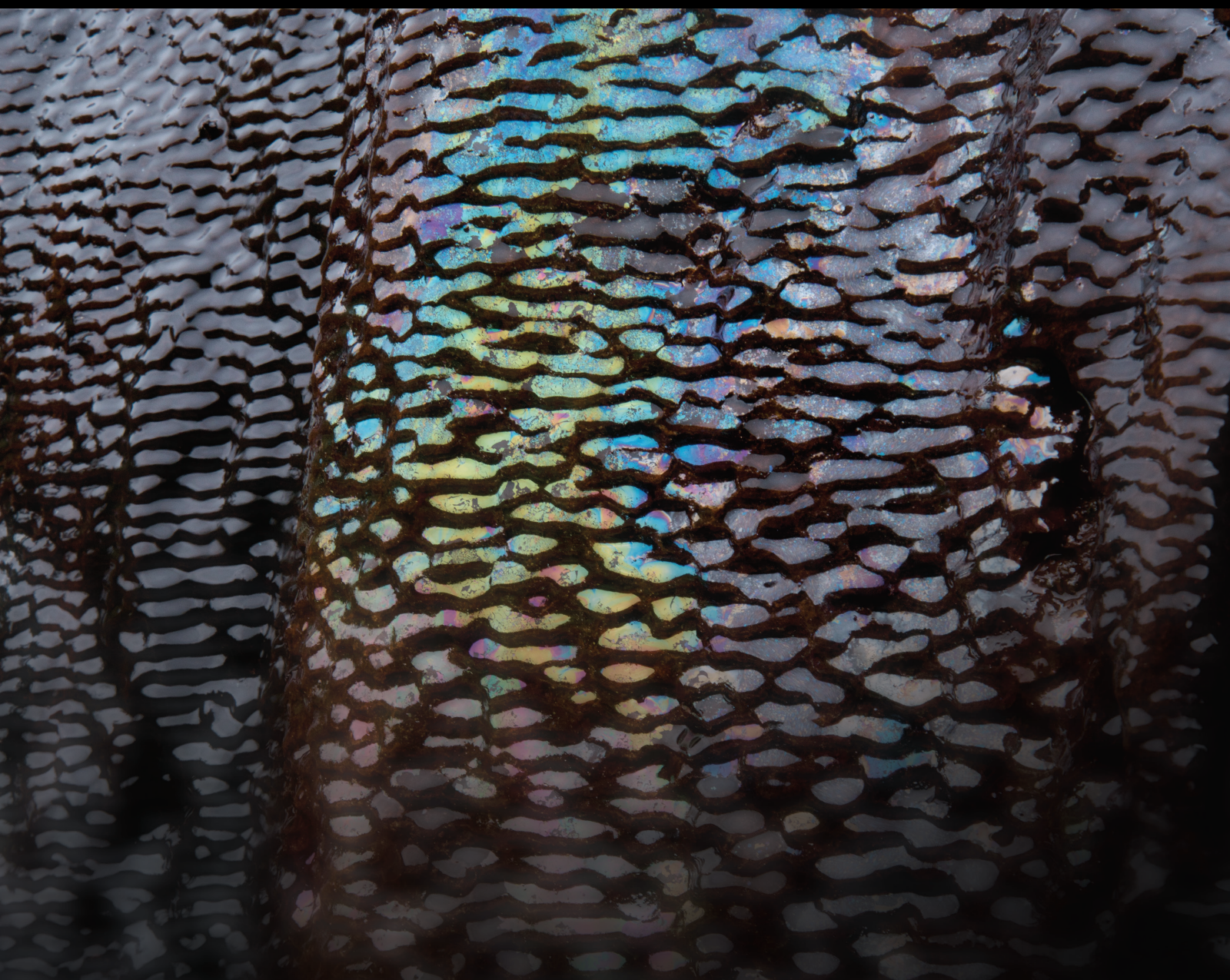


Advances in Freeze-Thaw Geomechanical Behavior of Rock Mass in Cold Regions

Lead Guest Editor: Yu Wang

Guest Editors: Zhengyang Song, Shibing Huang, and Hailiang Jia





Advances in Freeze-Thaw Geomechanical Behavior of Rock Mass in Cold Regions

**Advances in Freeze-Thaw
Geomechanical Behavior of Rock Mass
in Cold Regions**

Lead Guest Editor: Yu Wang

Guest Editors: Zhengyang Song, Shibing Huang,
and Hailiang Jia







Copyright © 2021 Hindawi Limited. All rights reserved.

This is a special issue published in "Geofluids." All articles are open access articles distributed under the Creative Commons Attribution License, which permits unrestricted use, distribution, and reproduction in any medium, provided the original work is properly cited.



























Chief Editor

































Umberta Tinivella, Italy

Associate Editors

Paolo Fulignati , Italy
Huazhou Li , Canada
Stefano Lo Russo , Italy
Julie K. Pearce , Australia

Academic Editors

Basim Abu-Jdayil , United Arab Emirates
Hasan Alsaedi , USA
Carmine Apollaro , Italy
Baojun Bai, USA
Marino Domenico Barberio , Italy
Andrea Brogi , Italy
Shengnan Nancy Chen , Canada
Tao Chen , Germany
Jianwei Cheng , China
Paola Cianfarra , Italy
Daniele Cinti , Italy
Timothy S. Collett , USA
Nicoló Colombani , Italy
Mercè Corbella , Spain
David Cruset, Spain
Jun Dong , China
Henrik Drake , Sweden
Farhad Ehya , Iran
Lionel Esteban , Australia
Zhiqiang Fan , China
Francesco Frondini, Italy
Ilaria Fuoco, Italy
Paola Gattinoni , Italy
Amin Gholami , Iran
Michela Giustiniani, Italy
Naser Golsanami, China
Fausto Grassa , Italy
Jianyong Han , China
Chris Harris , South Africa
Liang He , China
Sampath Hewage , Sri Lanka
Jian Hou, China
Guozhong Hu , China
Lanxiao Hu , China
Francesco Italiano , Italy
Azizollah Khormali , Iran
Hailing Kong, China

Karsten Kroeger, New Zealand
Cornelius Langenbruch, USA
Peter Leary , USA
Guangquan Li , China
Qingchao Li , China
Qibin Lin , China
Marcello Liotta , Italy
Shuyang Liu , China
Yong Liu, China
Yueliang Liu , China
Constantinos Loupasakis , Greece
Shouqing Lu, China
Tian-Shou Ma, China
Judit Mádl-Szonyi, Hungary
Paolo Madonia , Italy
Fabien Magri , Germany
Micòl Mastroicco , Italy
Agnes Mazot , New Zealand
Yuan Mei , Australia
Evgeniy M. Myshakin , USA
Muhammad Tayyab Naseer, Pakistan
Michele Paternoster , Italy
Mandadige S. A. Perera, Australia
Marco Petitta , Italy
Chao-Zhong Qin, China
Qingdong Qu, Australia
Reza Rezaee , Australia
Eliahu Rosenthal , Israel
Gernot Rother, USA
Edgar Santoyo , Mexico
Mohammad Sarmadivaleh, Australia
Venkatramanan Senapathi , India
Amin Shokrollahi, Australia
Rosa Sinisi , Italy
Zhao-Jie Song , China
Ondra Sracek , Czech Republic
Andri Stefansson , Iceland
Bailu Teng , China
Tivadar M. Tóth , Hungary
Orlando Vaselli , Italy
Benfeng Wang , China
Hetang Wang , China
Wensong Wang , China
Zhiyuan Wang , China
Ruud Weijermars , Saudi Arabia

Bisheng Wu , China
Da-yang Xuan , China
Yi Xue , China
HE YONGLIANG, China
Fan Yang , China
Zhenyuan Yin , China
Sohrab Zendeboudi, Canada
Zhixiong Zeng , Hong Kong
Yuanyuan Zha , China
Keni Zhang, China
Mingjie Zhang , China
Rongqing Zhang, China
Xianwei Zhang , China
Ye Zhang , USA
Zetian Zhang , China
Ling-Li Zhou , Ireland
Yingfang Zhou , United Kingdom
Daoyi Zhu , China
Quanle Zou, China
Martina Zucchi, Italy





Contents

Study on Stability of Tunnel Surrounding Rock and Precipitation Disaster Mitigation in Flowing Sand Body

Yongyi He , Bole Sun , and Mingnian Wang


Research Article (13 pages), Article ID 6043807, Volume 2021 (2021)

Effect of Temperature and Strain Rate on the Brittleness of China Sandstone

Xiuyuan Yang , Zhenlong Ge , Qiang Sun , and Weiqiang Zhang 

Research Article (10 pages), Article ID 6782146, Volume 2021 (2021)

The Responses of Injection Pressure and Fracture Width during Height Extension in Sand-Mud Interbed Reservoirs in the Dongsheng Gas Field

Di Wang , Haibo Wang, Fengxia Li, Fuhu Chen, and Xinchun Zhu

Research Article (13 pages), Article ID 2500912, Volume 2021 (2021)

Overlying Strata Movement and Abutment Pressure Evolution Process of Fully Mechanized Top Coal Caving Mining in Extra Thick Coal Seam

Yongqiang Zhao, Yingming Yang , Xiaobin Li , and Zhiqi Wang 


Research Article (11 pages), Article ID 7839888, Volume 2021 (2021)

Variations on Reservoir Parameters of Oil Shale Deposits under Periodic Freeze-Thaw Cycles: Laboratory Tests

Rui-heng Li, Zhong-guang Sun , Jiang-fu He , Zhi-wei Liao , Lei Li, and Fang Qian


Research Article (11 pages), Article ID 2269733, Volume 2021 (2021)

Particle Flow Analysis of Macroscopic and Mesoscopic Failure Process of Salt Rock under High Temperature and Triaxial Stress

Haoran Li, Ziheng Wang, Dekang Li , and Yajun Zhang



Research Article (15 pages), Article ID 8238002, Volume 2021 (2021)

Dynamic Mechanical Response and Dissipated Energy Analysis of Sandstone under Freeze-Thaw Cycles

Ke Man , Zongxu Liu, Zhifei Song , and Xiaoli Liu

Research Article (9 pages), Article ID 7724455, Volume 2021 (2021)

Hydrogeology Response to the Coordinated Mining of Coal and Uranium: A Transparent Physical Experiment

Tong Zhang , Xiang He, Kai Zhang, Xiaohan Wang, and Yang Liu 



Research Article (10 pages), Article ID 6236455, Volume 2021 (2021)

A Practical Design Method for Reducing Postconstruction Settlement of Highway Subgrade Induced by Soil Creep

Fei Zhou , Tangdai Xia , Bingqi Yu, Fan Xia, and Fan Yu

Research Article (10 pages), Article ID 4029439, Volume 2021 (2021)

Research on Deformation Mechanisms of a High Geostress Soft Rock Roadway and Double-Shell Grouting Technology

Fengnian Wang , Shizhuang Chen, Pan Gao, Zhibiao Guo, and Zhigang Tao 
Research Article (13 pages), Article ID 6215959, Volume 2021 (2021)


Study on Damage Constitutive Model of High-Concentration Cemented Backfill in Coal Mine

Baogui Yang and Haigang Yang 
Research Article (12 pages), Article ID 1866042, Volume 2021 (2021)


Investigation of Dynamic Mechanical Properties of Coal after Freeze-Thaw Cyclic Conditions

Shuang Gong , Wen Wang , Furui Xi , and Wenlong Shen 
Research Article (10 pages), Article ID 8602301, Volume 2021 (2021)

Freeze-Thaw Effects on Stability of Open Pit Slope in High-Altitude and Cold Regions

Yong Hong, Zhushan Shao , Guangbin Shi, Yong Dou, Weiqin Wang, and Wen Zhang
Research Article (10 pages), Article ID 8409621, Volume 2021 (2021)

Optical Fiber Frequency Shift Characterization of Overburden Deformation in Short-Distance Coal Seam Mining

Dingding Zhang , Qiang Chen, Zhengshuai Wang, Jianfeng Yang, and Jing Chai
Research Article (16 pages), Article ID 1751256, Volume 2021 (2021)

Migration of the Industrial Wastewater in Fractured Rock Masses Based on the Thermal-Hydraulic-Mechanical Coupled Model

Yanan Gao , Peng Guo, Zetian Zhang , Minghui Li , and Feng Gao
Research Article (13 pages), Article ID 5473719, Volume 2021 (2021)






Study on Air Void Characteristics and Hydraulic Characteristics of Porous Asphalt Concrete Based on Image Processing Technology

Zhanqi Wang , Jianguang Xie , Lei Gao , Yanping Liu , and Kuan Li 
Research Article (13 pages), Article ID 9432323, Volume 2021 (2021)



Application of 3D Printing Technology in the Mechanical Testing of Complex Structural Rock Masses

Yingjie Xia, Qingkun Meng, Chuanqing Zhang , Ning Liu, Zhenxing Zhao, Jun Chen, and Gao Yang
Review Article (23 pages), Article ID 7278131, Volume 2021 (2021)

Characteristics Evolution of Multiscale Structures in Deep Coal under Liquid Nitrogen Freeze-Thaw Cycles


Yingfeng Sun , Yixin Zhao , Yulin Li , Nima Noraei Danesh , and Zetian Zhang 
Research Article (9 pages), Article ID 8921533, Volume 2021 (2021)

Study on the Catastrophic Evolution of Tianshan Road Slope under the Freeze-Thaw Cycles

Luqi Wang , Yibing Zhang, Jian Guo, Qiang Ou, Songlin Liu, and Lin Wang 
Research Article (12 pages), Article ID 6128843, Volume 2021 (2021)



Contents

Degradation of Strength and Stiffness of Sandstones Caused by Wetting-Drying Cycles: The Role of Mineral Composition

Lu Chen , Yichao Rui , and Yihan Zhao




Research Article (8 pages), Article ID 3483506, Volume 2021 (2021)

Parametric Study of the Borehole Drilling in Jointed Rock Mass

Yanan Gao, Yudong Zhang, Zetian Zhang , Minghui Li , Yingfeng Sun, Donghao Lan, and Feng Gao

Research Article (14 pages), Article ID 8237199, Volume 2021 (2021)

Coupling Effect of Strain Rate and Freeze-Thaw Temperature on Dynamic Mechanical Properties and Fractal Characteristic of Saturated Yellow Sandstone

Peng Wu , Lianying Zhang , Xianbiao Mao, Yanlong Chen , Ming Li, Liang Chen, and Lan Wang



Research Article (14 pages), Article ID 7511467, Volume 2021 (2021)

Loading Behavior and Soil-Structure Interaction for a Floating Stone Column under Rigid Foundation: A DEM Study

Feng Liu , Panpan Guo , Haibo Hu , Chengwei Zhu , and Xiaonan Gong 

Research Article (13 pages), Article ID 9508367, Volume 2021 (2021)

A Simulation Study on the Swelling and Shrinking Behaviors of Nanosized Montmorillonite Based on Monte Carlo and Molecular Dynamics

Kaiwen Tong, Jianhua Guo, Shanxiong Chen, Fei Yu , Shichang Li, and Zhangjun Dai 





Research Article (13 pages), Article ID 1038205, Volume 2021 (2021)

Frost-Heaving Cracking Sensitivity of Single-Flaw Rock Mass Based on a Numerical Experimental Method

Tingting Wang , Chun'an Tang , Pingfeng Li , Shibin Tang , Minghao Liu , and Bingbing Zhang 



Research Article (13 pages), Article ID 3436119, Volume 2021 (2021)

Influence of Lightweight Foamed Concrete as Backfill Material on Stress and Deformation of Buttressed Earth-Retaining Wall

Youqiang Qiu , Yang Liu , Liujun Zhang , and Zhanqi Wang 



Research Article (14 pages), Article ID 7610933, Volume 2021 (2021)

Experimental Study of a New Concrete Admixture and Its Function in Filling and Reinforcing Granite Fissures

Songnan Ru, Zuozhou Li, Handong Liu, Huaichang Yu , Chunlei Wei, Guangzhu Hu, Fangfang Xue, Congxian Wang, and Jiali Wang 





Research Article (9 pages), Article ID 8587258, Volume 2021 (2021)

Stability Analysis and Protection Measures of Large Section Tunnel in Coal Rich Weak Rock Stratum

Guannan Zhou, Zijiang Zhao , Zhanping Song , and Hongjian Wang


Research Article (15 pages), Article ID 9394145, Volume 2021 (2021)

Undrained Cyclic Response and Resistance of Saturated Calcareous Sand considering Initial Static Shear Effect

Baojian Li , Panpan Guo , Gaoyun Zhou, Zhe Wang, Gang Lei , and Xiaonan Gong 

Research Article (12 pages), Article ID 4616747, Volume 2021 (2021)

Analysis of Mechanical Properties of Sandstone under Freeze-Thaw Cycles Based on Digital Image Correlation (DIC)

Daguo Quan, Shuailong Lian, Jing Bi , and Chaolin Wang

Research Article (12 pages), Article ID 7101873, Volume 2021 (2021)

Investigation into Macro- and Microcrack Propagation Mechanism of Red Sandstone under Different Confining Pressures Using 3D Numerical Simulation and CT Verification

Wen Zhang , Yan-yu Chen , Jin-ping Guo , Sai-sai Wu , and Cheng-yuan Yan 

Research Article (12 pages), Article ID 2871687, Volume 2021 (2021)

A Damage Constitutive Model for a Rock under Compression after Freeze-Thaw Cycles Based on the Micromechanics

Hongyan Liu , Xiaochen Zhang , and Xidong Yan 



Research Article (11 pages), Article ID 3177464, Volume 2021 (2021)

Numerical Simulation of the Effect of Stress on the Seepage of Fractured Rock Mass

Liang Shiwei , Wang Hongmei, Ge Di, and Zhao Cunqing

Research Article (20 pages), Article ID 4242337, Volume 2021 (2021)

Observed Performance and FEM-Based Parametric Analysis of a Top-Down Deep Excavation in Soil-Rock Composite Stratum

Gang Lei , Panpan Guo , Fucai Hua, Xiaonan Gong, and Lina Luo

Research Article (17 pages), Article ID 6964940, Volume 2021 (2021)

Research Article

Study on Stability of Tunnel Surrounding Rock and Precipitation Disaster Mitigation in Flowing Sand Body

Yongyi He ^{1,2}, Bole Sun ^{1,2} and Mingnian Wang¹

¹School of Civil Engineering, Southwest Jiaotong University, Chengdu 610065, China

²China Railway Third Bureau Group Co., Ltd., Taiyuan 030001, China

Correspondence should be addressed to Yongyi He; 340097@my.swjtu.edu.cn

Received 5 September 2021; Accepted 2 November 2021; Published 14 December 2021

Academic Editor: Yu Wang

Copyright © 2021 Yongyi He et al. This is an open access article distributed under the Creative Commons Attribution License, which permits unrestricted use, distribution, and reproduction in any medium, provided the original work is properly cited.

Flowing sand is a special surrounding rock encountered by tunnel construction. Due to the looseness and low viscosity of the flowing sand, after excavation, the sand body is easy to flow along the open surface. In addition, the water seepage also causes tunnel instability. Considering the characteristics of water seepage, how to improve the stability of flowing sand bodies and prevent the instability of surrounding rocks has become a difficult problem. In this paper, a parametric experiment on the surrounding rock taken from the project site was carried out, and then, a numerical simulation of the flowing sand body was conducted to study the precipitation construction method and stability of the flowing sand body. Other than that, the tunnel face vacuum dewatering, vertical vacuum dewatering at the top of the tunnel, and the vacuum dewatering technology of the gravity well in poor geological section were systematically analyzed in our research. A radial vacuum enclosed precipitation process for the face of the tunnel was proposed, which effectively solved the problem concerning continuous seepage of water in the front. Through numerical simulation and field experiments, the basis for determining the precipitation parameters of the tunnel face was obtained, while aiming at the top position of the tunnel, a vertical vacuum negative pressure precipitation method of intercepting the top seepage water and the water supply behind the top of the tunnel was proposed. For the bottom of the tunnel, setting gravity wells on the side walls for the purpose of preventing seepage at the bottom was put forward. The application of these methods in the project ensured the safety of construction and improved the construction schedule. After the completion of the dewatering construction, the method of inserting plywood into the small pipe was adopted to avoid the collapse of the dry sand. Then, to solve the problem of borehole collapse in flowing sand bodies, pipe feeding was introduced, thus further enhancing the precipitation effect. Furthermore, in view of the problem that the dewatering hole in the flowing sand body is easy to collapse, resulting in the failure of 60% of the dewatering hole and the sand body is extracted from the dewatering pipe, causing the risk of the cavity at the top of the tunnel, a method of pipe following is presented to avoid the damage of geotextile caused by directly inserting the dewatering pipe and further improve the dewatering effect. All the above processes together form an omnidirectional three-dimensional negative pressure precipitation method that considers the special sand body flow and water seepage of unfavorable geology and that has been proved to enhance the stability of surrounding rock in practice.

1. Introduction

With the development of society and economy, the tunnel construction process is gradually accelerating. Quicksand formation is a type of formation sometimes encountered in tunnel engineering. It is generally characterized by poor diagenesis, and its engineering properties are closer to compacted silt fine sand. During the construction of the tunnel,

the support is prone to crack in dry sand, and the sand will flow out from the cracks, resulting in a cavity at the top of the tunnel, thus further causing engineering accidents. When the water content is large, the mechanical properties of the quicksand layer deteriorate rapidly under the action of water. To be specific, the surrounding rock is deformed and collapsed, and the quicksand is severe, while the stability is extremely poor. In this condition, the construction is

extremely difficult, and the risk is extremely high [1–3]. Especially, when the water-rich quicksand stratum has worse stability, the safety of tunnel construction is threatened. Therefore, it is necessary to carry out precipitation construction in the stratum with rich water and quicksand.

Regarding the precipitation construction technology of water-rich quicksand formations, there are few domestic and foreign construction cases, and corresponding research materials are also scarce. However, some scholars have conducted some research, mainly focusing on the research of advanced grouting and reinforcement [4, 5], advanced precipitation, and excavation methods. Wu et al. conducted research on Xiamen Xiang'an Subsea Tunnel [6]. In order to ensure a smooth passage through the water-rich sand layer, underground diaphragm walls and drain relief wells were used on the surface to control groundwater, and advanced pregrouting was taken to consolidate sand in the tunnel, while as for the construction plan of layer combination, the CRD method of excavation is adopted. Wang et al. aimed to reduce the risk of water inrush and mud outburst in the Bieyancao tunnel on the Yiwu railway and adopted full-face curtain grouting to reinforce the surrounding rock [7]. Besides, radial reinforcement and grouting were implemented to reinforce the ground. After the construction, the full-face pregrouting reinforcement measures were applied to guarantee the construction safety [8]. Moreover, Deng introduced the differential equation of seepage movement in the phreatic aquifer, which laid the foundation for the theory of groundwater steady flow [9]. Beyond that, Deift et al. proposed the differential equation of unsteady flow motion in the phreatic aquifer [10], while Mroueh and Shahrouh [11] used the three-dimensional finite element method to study the influence of the ground loss caused by tunnel excavation on the existing foundation.

Analytical methods, finite difference methods, boundary element methods, and finite element methods are main precipitation calculation methods. In general, the finite element method not only maintains the advantages of the original variational method but also has the flexibility of the difference method, which makes up for the shortcomings of the classical variational method. Considering that, it is currently the most effective method for numerical calculations [12–15]. From the study on well-point precipitation in 1950, Gong et al. [16] put forward the viewpoint of precipitation “funnel.” Shang [17] observed the change of the vacuum degree in the soft foundation reinforcement project with the vacuum-heap loading method and then found that the vacuum degree decreased with the increase of depth. In addition, Huang [18] studied the stress state, constructed a mathematical model of foundation stability under vacuum conditions, and finally proposed the attenuation formula of vacuum degree under vacuuming, while Liang [19] researched the water-rich sections of Beijing subway tunnels and obtained the control methods of vertical jet grouting piles and horizontal jet grouting piles in the tunnel, which provided a safe construction environment for tunnel excavation. Besides, Wu et al. [20] analyzed and summarized the construction of tunnels in the water-rich sand layer in Hangzhou and concluded that the liquefac-

tion of the water-rich sandy silt layer was solved by the full-section pregrouting, combined with the auxiliary measures such as the advanced pipe shed and precipitation problems with piping. Through the application analysis and research on the construction method of the rich water section belonging to Shenzhen subway tunnel, it is concluded that the water-stop curtain, the dewatering well, the surface chemical grouting, the deep hole grouting in the cave, and the advanced small pipe grouting in the cave are the main factors [21]. Here, it should be noted that auxiliary construction methods can improve the stability of surrounding rock and ensure construction safety and quality. Li [22] obtained a small pipe dense grouting, advanced drainage in the tunnel, and enhanced initial support strength via the application research on the construction technology of Shenzhen cross-street tunnel through the water-rich sand layer to ensure the smooth passage of the tunnel. Furthermore, Peng et al. [23] analyzed the groundwater treatment in the water-rich sandy silt section of Hangzhou Jiefang Road tunnel and found that the light well point in the tunnel is an effective and economical way of precipitation. Apart from that, compared with grouting and blocking water, its cost is reduced to a great extent.

Scholars have gained rich results when concerning researching precipitation technology in the formation of water-rich quicksand. Studies have shown that water and temperature have a certain impact on the physical and mechanical properties of rocks [24–29]. In engineering excavation and construction, mining method and stratum buried depth also have an impact on rock mechanical properties. For example, in coal mining, mining rate and coal seam occurrence depth are important factors affecting the physical and mechanical properties and mechanical response of coal and rock [30, 31]. In addition, under complex geological environment, freezing thawing and cyclic loading have a significant impact on rock fracture [32, 33]. It can be seen that for the engineering of excavating rock and soil or underground resource reservoir, the stability and safety of surrounding rock are affected by a variety of environmental and complex human factors. Then, for tunnel engineering, complex conditions will cause instability risk of surrounding rock and then form hidden dangers of geological disasters. A water-rich sand stratum is a kind of extremely unstable geological area. When considering its stability and safe excavation, how to reduce precipitation and reduce disasters have a very important impact on the safe implementation of the project and the stable operation of the tunnel. However, there are few reports about the precipitation problem in the large-deformation section in water-rich and soft rock. Due to the special stratum status of the project, using traditional methods, the effect is not ideal, and the construction progress and construction quality are difficult to be effectively solved. Therefore, the vacuum negative pressure precipitation method is optimized and improved, followed by good results having been achieved. In this case, a certain coal-transport railway tunnel is taken as the engineering background to analyze and discuss the precipitation problem in the water-rich soft rock section with large deformation in this paper.

2. Sample Preparation and the Parameter Test Experiment

2.1. Sample Preparation. The sampling site is a special railway tunnel for coal transportation in southwestern China, which traverses the soft rock of the Tertiary fine sandstone formation and is featured with loose rock quality and extremely bad diagenesis. Besides, it belongs to the extremely soft rock with extremely poor stability and is easy to soften in contact with water. When the groundwater is developed or the water content is high, the surrounding rock softening is obvious. In addition, the sandstone is mostly silt-like, and water gushing occurs in the base, while the water is immersed into silt, and the arches and side walls collapse, and blocks are serious. In this case, sand samples were collected at different locations in this tunnel.

2.2. The Quicksand Parameter Test Experiment. During the tunnel construction process, the sand body is very easy to slide, which brings great risks to the construction. In order to better guide the construction, corresponding experiments on the physical and chemical properties of sand are conducted.

2.2.1. Density and Moisture Content Determination. During the construction process, due to the phenomenon of sand gushing and sand boiling in some areas, great risks appeared in the construction. Thus, in order to better guide the construction, tests were conducted on four different water gushing sections, mainly on the density and moisture content of quicksand, as shown in Figure 1.

The results are obtained through experiments, as shown in Table 1. Through the mastery of these data, theoretical data is provided for the optimization of the construction process, and at the same time, a basis is presented for the selection of construction methods.

2.2.2. Particle Size Analysis. The particle size of dry sand was tested, as shown in Table 2.

The composition of the sand particle size is not much different, and the particle size is relatively fine, with more than 90% less than 0.5 mm, which is a poor gradation. Besides, the cementation is not good and it is easy to collapse. At the same time, the tunnel is medium-coarse sand, but the mud content is small and about 5% on average. Moreover, the mud content of sand bodies in domestic and foreign tunnels was investigated, and most of them were around 20%, which is one of the reasons why the tunnel construction in this study is extremely difficult.

2.2.3. Surrounding Rock Reinforcement Measures. In order to study the stability of the dry sand tunnel, a compressibility experiment was carried out on the dry sand here to determine the corresponding reinforcement measures, so as to provide the necessary parameters for the effective maintenance design of the surrounding rock. Apart from that, the experimental results show that the dry sand possesses a higher compression rate, and the compression rate corresponds directly to the water content. Therefore, the sand can easily collapse without taking measures.



FIGURE 1: Test experiments on the physical properties of quicksand in the water gushing section of the tunnel.

2.3. Reinforcement Measures. In this study, due to the low mud content of the sand body in the project (as shown in Figure 2(a)), many problems occurred in the construction. Considering that, a series of measures have been taken in reinforcement, and curtain grouting has been adopted for the tunnel face. At the same time, horizontal jet grouting piles were used to reinforce the periphery of the tunnel face, and the side walls of the lower steps and the bottom of the pavement were excavated and supported with jet grouting piles to strengthen the side walls. At this time, the strength of the tunnel consolidation construction process has reached the highest level and cannot be further enhanced, but the effect is still not apparent. In this case, it can be seen that the pure reinforcement measures still have large defects for this project.

In order to improve the surrounding rock and increase the stability of the sand body, curtain grouting reinforcement, horizontal jet grouting pile reinforcement, and oblique jet grouting pile reinforcement are adopted. In the curtain grouting reinforcement, the grouting parameters are changed on site to adjust the setting time of the grout, but the final effect is still not ideal, as shown in Figure 2(b). After the overall grouting, it becomes ring-shaped, layered, and vein-shaped, and its self-stabilization ability is poor. Due to the high pressure of the surrounding rock water body, the place where the grouting is not tight will be the easiest point for water to flow out, which will eventually lead to instability of the tunnel face and affect the progress of the project. Besides, in the construction of horizontal jet grouting piles along the periphery, it is effective in some parts, but the whole is not very ideal. To be specific, insufficient occlusion is common, and it is difficult to operate at the angle of construction and to ensure the quality of jet grouting piles. Apart from that, the grouting consolidation strength itself is insufficient. Affected by water and sand inrush, the water pressure is large, which makes it easy to break through the water inrush at the poor local effect and then enlarges the overall effect of grouting, as shown in Figure 2(c). Furthermore, in the construction concerning of the side wall of the lower step, the bottom of the paving and the supporting construction with the inclined side wall jet grouting piles, the side wall jet grouting piles are well occluded, as displayed in Figure 2(d). However, the pile-forming distance in each cycle is limited,

TABLE 1: Test results of physical properties of quicksand.

Bulk density (kg/m^3)	Apparent density (kg/m^3)	Water content before precipitation (%)	Water content after precipitation (%)
1546.3	2565.5	19.2	6.4

TABLE 2: The composition of sand bodies with different particle sizes.

No.	D10 (mm)	D30 (mm)	D50 (mm)	D60 (mm)	Dav (mm)	Nonuniformity coefficient (C_u)	Curvature coefficient (C_c)
1#	0.095	0.15	0.19	0.22	0.241	2.32	1.08
2#	0.120	0.18	0.24	0.27	0.274	2.25	1.00
3#	0.086	0.14	0.22	0.27	0.263	3.14	0.84
4#	0.098	0.16	0.19	0.22	0.219	2.24	1.19

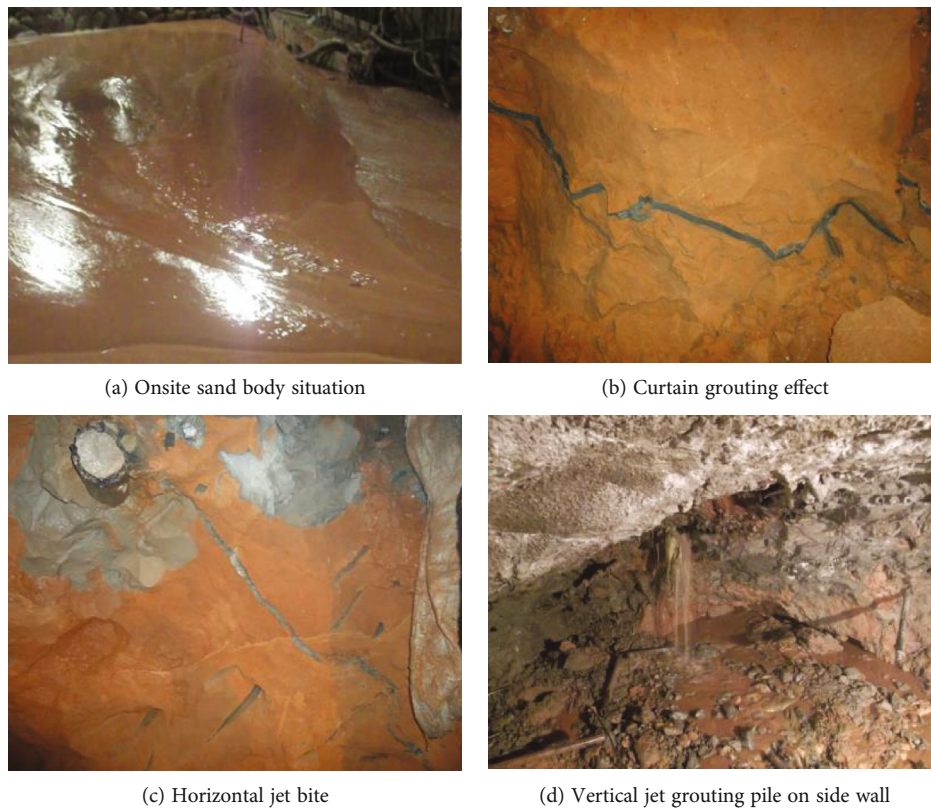


FIGURE 2: Construction effect of grouting reinforcement.

generally up to about 6 meters, and during the actual excavation process, only 2 to 3 meters can be dug, and then supplementary reinforcement construction of horizontal jet grouting piles is required.

3. Theoretical Analysis of Precipitation in Shifting Sand Formation

3.1. Precipitation Numerical Simulation Calculation. FLAC 3D numerical simulation software is commonly employed in the research of tunnels, mining, and rock and soil instability analysis [34–40]. For the water-rich sand layer encountered during the construction process, FLAC 3D finite difference software was used to analyze the sand layer

precipitation. Besides, a single downpipe is simulated to dewater the sand layer under negative pressure conditions (-0.05 MPa, -0.06 MPa, -0.07 MPa, and -0.08 MPa). Thus, the influence radius of different negative pressure drops can be obtained, which can provide a theoretical basis for the arrangement of dewatering holes in engineering construction, whereas the numerical simulation takes the water-rich sand layer as the research object simplifies the calculation model and assumes that the sand layer is uniformly distributed. The physical and mechanical parameters of the sand layer are shown in Table 3.

The size of the model is $5\text{ m} \times 2\text{ m} \times 5\text{ m}$, and the precipitation hole is set at a position of 2 m from the bottom. Other than that, the precipitation hole adopts a cylindrical grid,

TABLE 3: Physical and mechanical parameters of sand layer.

Permeability coefficient (cm/s)	Poisson's ratio	Void ratio	Cohesion (kPa)	Internal friction angle (°)	Modulus of elasticity (MPa)	Density (kg/m ³)
4.47×10^{-3}	0.20	0.42	3.0	25.0	20.5	1547

and its periphery is surrounded by a radial grid around the cylindrical body, while the remaining sand layers are all rectangular grids. The model is divided into 58149 nodes and 53440 units, and the geometric model is presented in Figure 3.

In the model, displacement boundary conditions are selected to define the model, when five surfaces, namely, the front, rear, left and right sides, and the bottom are subjected to displacement constraints. Besides, the upper surface is a free boundary, and the initial stress field is considered in accordance with the self-weight stress field. Furthermore, a water level is set on the upper boundary of the model, and the software automatically generates pore pressure based on the water level and the porosity of the soil. Apart from that, we set the leakage boundary condition on the outer boundary of the precipitation hole and add negative pressures of -0.05 MPa, -0.06 MPa, -0.07 MPa, and -0.08 MPa to the outer boundary of the precipitation hole and then calculate. After that, during the calculation process, we observe and record the distribution of sand pore pressure, as shown in Figure 4, while the influence radius of negative pressure precipitation is determined by the distribution of sand pore pressure, and the calculation results are seen in Table 4.

The negative pressure precipitation has a greater impact on the pore pressure of the upper part of the precipitation hole. Then, a closed elliptical isobaric area with upper and lower sides will be established near the precipitation hole. In this area, the precipitation hole has the greatest impact on the sand body. Leaving this area, the influence of negative pressure precipitation gradually decreases, while the isobar formed by precipitation basically coincides with the precipitation funnel curve. According to the calculation results, the influence radius of different negative pressure precipitations is obtained, as displayed in Table 4:

As the precipitation pressure continues to increase, the precipitation radius increases. In the actual construction process, the size of the precipitation pressure should be determined according to the onsite hydrogeological conditions. For precipitation in areas with poor stratum stability, the precipitation pressure should not be too high and should be determined in conjunction with onsite protective measures. From Figure 5, in the numerical model, the precipitation displacement is acquired.

During the precipitation process, the sand will flow with the extraction of water, resulting in an increase in the sand within the radius of the precipitation hole, while there will be sand erosion in a certain area above the precipitation hole. Besides, during the construction process, the support measures in this area should be strengthened. From Figures 5(b)–5(d), it can be seen that there is a triangular strain concentration area within 1 m of the influence radius

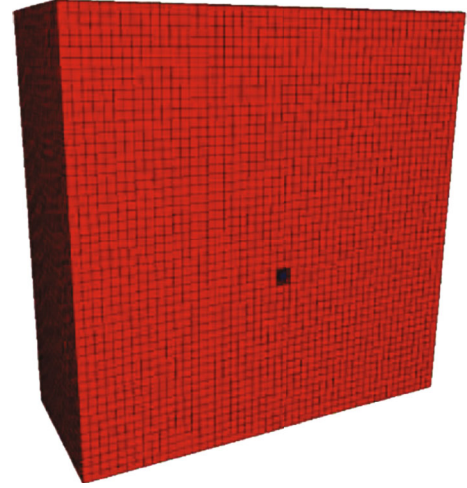


FIGURE 3: Numerical simulation geometric model.

just above the precipitation hole, and the sand in this area accepts the lost sand from above. Compared with other areas, the soil will deform to a great extent, and the density of sand particles will be relatively increased. Moreover, affected by the negative pressure of precipitation, the stress is relatively concentrated within the radius of precipitation, and the stress outside the radius of precipitation is basically and evenly distributed, as presented in Figure 5(c). Therefore, in the actual project, the support measures for the soil above the dewatering hole should be enhanced. In addition to that, monitoring equipment should be installed within 2 m above the dewatering hole to monitor the deformation of the soil in real time in order to respond to the danger in time.

3.2. Theoretical Calculation. The process of precipitation completion is also that of reducing the water content of the semicylinder to the water content of the sand body when it can be excavated. Therefore, the following formula can be derived:

$$Q_2 - Q_1 = \frac{1}{2} \pi r^2 (q_1 - q_2). \quad (1)$$

Among them, Q_1 represents the normal water inflow (m³) within the precipitation range of a single downpipe; Q_2 refers to the pumping capacity of a single downpipe (m³); and q_1 denotes the moisture content (%) of the quicksand without pumping water, while q_2 indicates the water content (%) after pumping. By further derivation, the

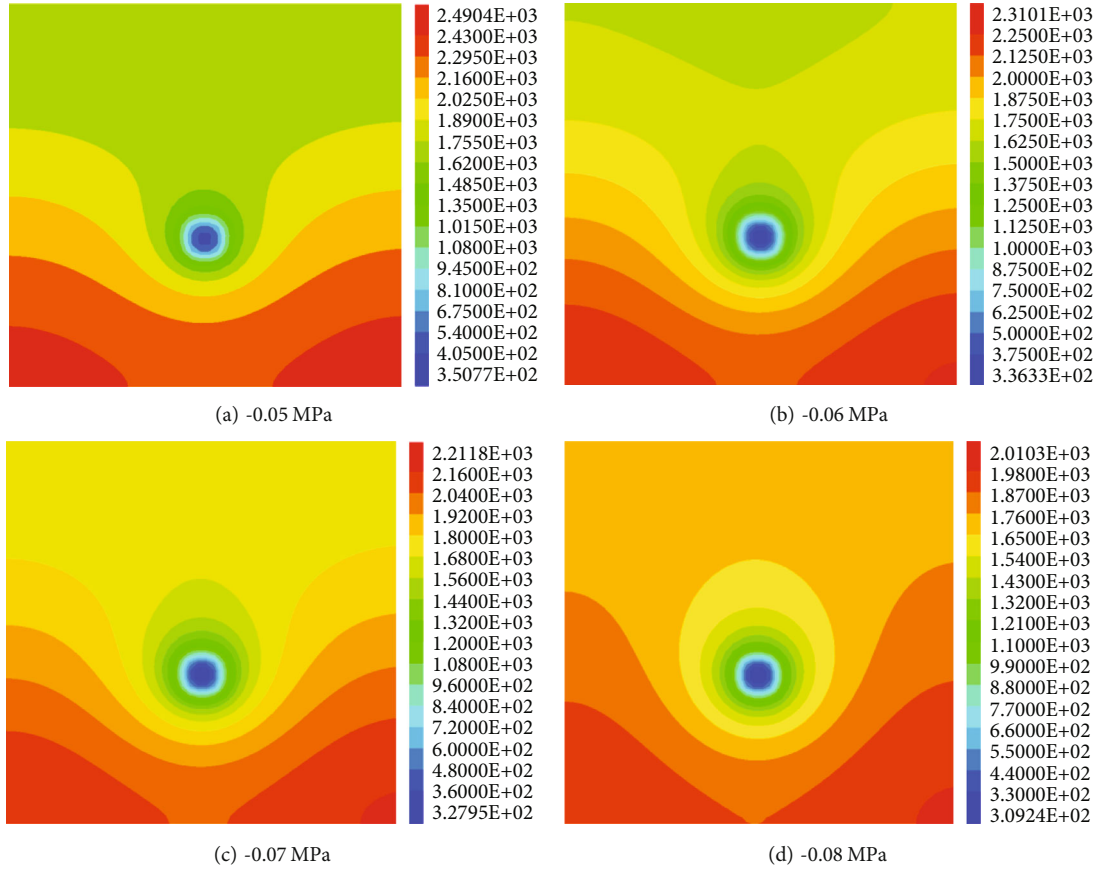


FIGURE 4: Different negative pressure precipitation pore pressure cloud map.

TABLE 4: Different negative pressure precipitation radius.

Negative pressure (MPa)	-0.05	-0.06	-0.07	-0.08
Precipitation radius (m)	0.83	1.04	1.15	1.28

calculation formula of the precipitation radius can be obtained:

$$r = \sqrt{\frac{2(Q_2 - Q_1)}{\pi(q_1 - q_2)}} \quad (2)$$

According to the measurement results of field practice, the difference between the absolute value Q_2 and Q_1 of the pumping water of a single downpipe is calculated, as shown in Table 5.

Through the monitoring data, the precipitation radius under different pressures of the specific water inflow is calculated here, and the calculation result of the formula is brought into it, as shown in Table 6.

By comparing the results obtained from the theoretical computer field measurement, it is shown that the precipitation radius calculated by the numerical simulation is very close to that calculated by the theoretical calculation, and there are only a few errors. Besides, the reasons for these errors are related to the simplification of the model. There-

fore, the calculation result can be used as a reference for the layout of downwater pipes in actual construction.

4. Onsite Vacuum Negative Pressure Precipitation Technology

Through the above experiments and theoretical analysis, the theoretical values of precipitation water pressure and precipitation radius are obtained and are applied in the field to formulate reasonable precipitation parameters. At the same time, during the application process, it was found that there was still water leakage at the top and bottom after the construction was completed, which brought certain difficulties to the construction. Therefore, the measures for omnidirectional precipitation of the tunnel face, the top of the tunnel and the bottom of the tunnel were optimized and designed.

4.1. Vacuum Negative Pressure Precipitation Technology for the Face. Vacuum negative pressure precipitation in the cave sucks the air in the well point pipe, horizontal pipe, and water storage tank through a vacuum pump to form a certain degree of vacuum (i.e., negative pressure). The groundwater outside the pipeline system is pressed into the well point pipe under the action of the pressure difference and then to the storage tank through the horizontal pipe. Besides, it is pumped away. As a result, the water level drops, the void ratio decreases, the soil is consolidated, and the operation reaches a dry and wet state. Furthermore, in order

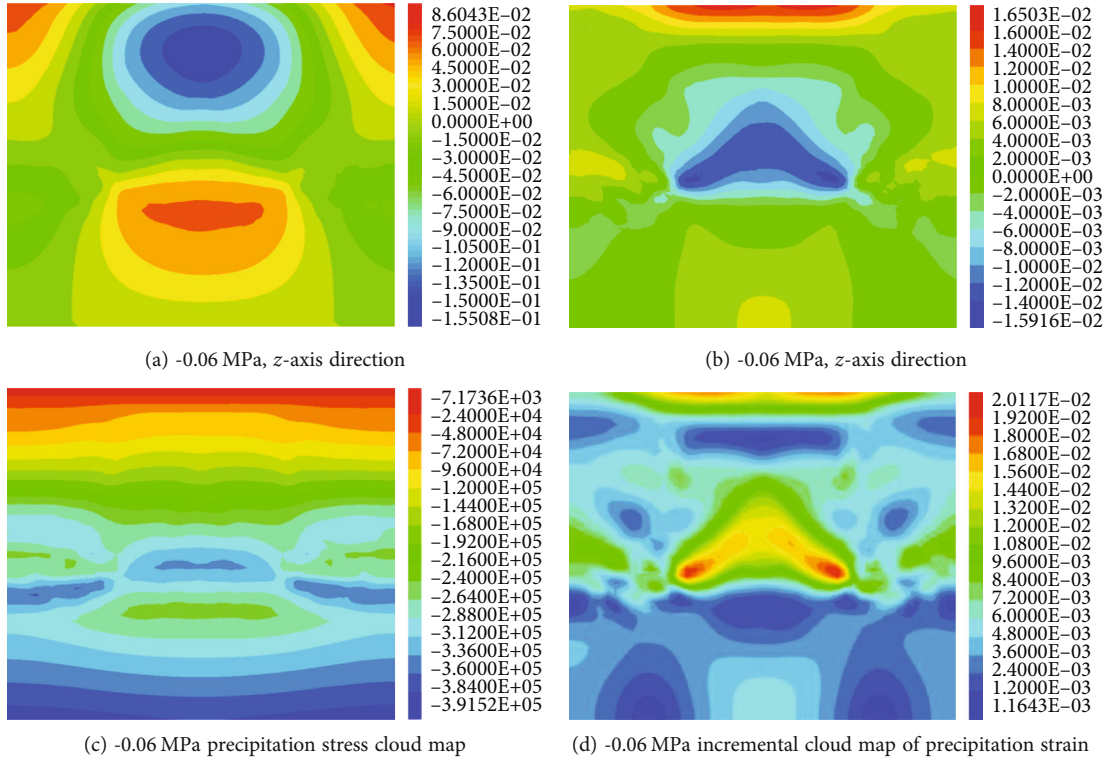


FIGURE 5: -0.06 MPa negative pressure precipitation soil stress and deformation cloud map.

TABLE 5: Absolute value table of different negative pressures and pumping.

Negative pressure (MPa)	-0.05	-0.06	-0.07	-0.08
Absolute pumping capacity (m ³)	0.256	0.464	0.766	1.149

TABLE 6: Table of negative pumping pressure and precipitation radius.

Negative pressure (MPa)	-0.05	-0.06	-0.07	-0.08
Precipitation radius (m)	0.8	1	1.1	1.25

to achieve a better effect of vacuum negative pressure precipitation in this section, the length of the precipitation pipe here is 9 m, and that of the precipitation pipe in the actual precipitation range is 7 m. The vacuum precipitation process of the entire tunnel face is displayed in Figure 6:

The precipitation pressure of this project is generally -0.06 MPa, while the precipitation radius is 1 m, and the mutual influence coefficient is 0.8, so that the most suitable distance between the precipitation pipes is 0.8 m at this time. Besides, the layout of the downpipe at the tunnel face is shown in Figure 7.

Each of the downfall pipes is 9 m, and they are formed by welding 1.5 m long steel pipes in sections. Besides, the pipe body is drilled with 8 mm holes with the 10 cm spacing in a plum blossom pattern. Apart from that, no precipitation drilling is provided for the pipe end of 2 m and the pipe head

of 0.5 m. After each section of the pipe is drilled, two layers of geotextile are used to wrap it, and a layer of the 100-mesh filter screen is wrapped around it. After winding, every 20 cm interval is used to tie tightly. Other than that, the 32 mm diameter precipitation steel pipe uses 25 steel pipes as the joints of each section and is welded and connected. Furthermore, each downfall pipe is equipped with a special structure pipe head of 10 cm, and the bottom end of the pipe head adopts a steel welded crosshead with a diameter of 8 mm and is sealed at the bottom. The schematic diagram of the downwater pipe layout is shown in Figure 8.

When the vacuum negative pressure was employed for precipitation at the beginning, PVC pipes were used. At the same time, after drilling the holes, we retreat the drill and directly stuff the processed and wrapped precipitation pipes into the holes. Besides, the filter screen layer wrapped around the downfall pipe has a large friction with the sand body, which can easily damage the filter screen layer. As a result, the extracted water contains a large amount of sediment, causing blockage of the pipe and even the upper sand body to empty with the precipitation, forming a cavity and resulting in a large area of landslides. When the PVC pipe is used for precipitation, the construction will have a great impact on the precipitation pipe, and it is very likely to cause damage to the precipitation pipe. Besides, during the construction, the rear water will continue to penetrate into the face of the tunnel, and it is difficult to guarantee the tunneling length. Clear water flows out after the pipe is down, as shown in Figure 9(a).

The process has been improved as follows. After the drilling is completed, do not retract the drill and insert the

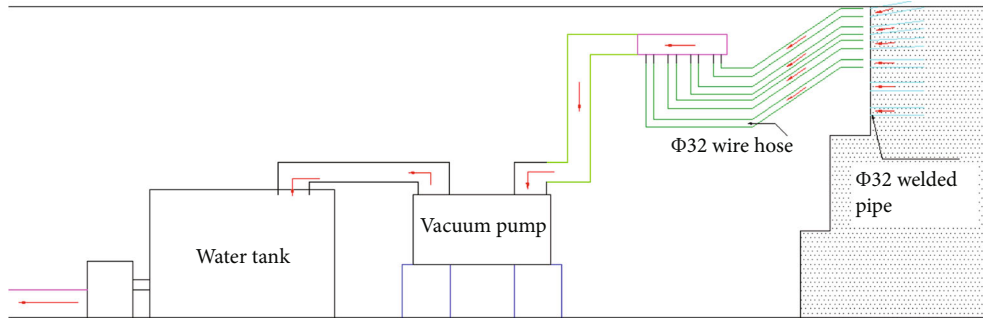
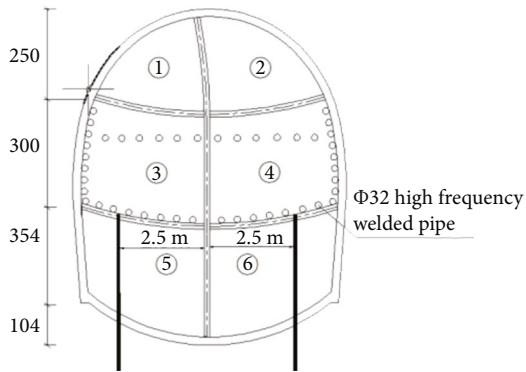


FIGURE 6: General layout of vacuum precipitation.



(a) Dewatering pipe layout



(b) On-site layout of downwater pipes

FIGURE 7: Layout of the downwater pipe.

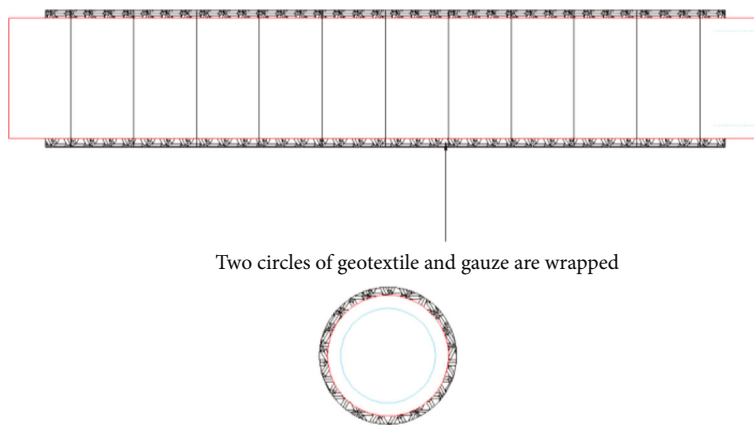


FIGURE 8: Structure diagram of downwater pipe.

wrapped downpipe through the middle of the hollow drill rod. Then, we slowly withdraw the pipe and leave the downpipe in the borehole to ensure the integrity of the downpipe

and improve the quality of the precipitation. Apart from that, we pull out the cork of the branch pipe section connected with the main pipe, connect the branch pipe with



(a) Clear water flows out after the tube is down



(b) Effect drawing after stepping method construction on steps

FIGURE 9: Effect picture after downpipe and after precipitation.

the well point pipe, tie it firmly with 10# lead wire, and wrap it tightly with a sealing tape. After that, we check the connection of each pipe. Furthermore, through the above operation process, the precipitation effect is obvious, the safety of the construction is ensured, the construction progress is accelerated, and the benefit is improved. As for the effect, it is given in Figure 9(b).

4.2. Vertical Vacuum Negative Pressure Dewatering Technology on Tunnel Top. In order to speed up the construction and precipitation progress, in addition to precipitation at the tunnel face, vertical precipitation at the top of the tunnel was also coordinated, as shown in Figure 10. Besides, the precipitation process is the same as that of the tunnel face. The length of the precipitation pipe is 9 m and the row spacing is 6 m, while the precipitation effect is obvious. Apart from that, the construction process is almost the same as the horizontal vacuum precipitation process, and only the differences are explained. Furthermore, we arrange the parameters as required for the precipitation section, use red paint positioning marks for the drilling points and spacing according to the design, and prepare in advance for the hole positions that affect the drilling.

By adopting vacuum negative pressure precipitation technology on the top of the tunnel, the emergence of water strands at the top of the tunnel is effectively avoided, thereby controlling the phenomenon of voiding at the top due to the flow of pressurized water along the gap and taking away the sand at the top. In addition to that, the rear water penetrates to the face of the tunnel, indirectly speeding up the precipitation progress and ensuring the safety of construction.

4.3. Vacuum Negative Pressure Dewatering Technology of the Gravity Dewatering Well in the Cave. Vacuum negative pressure precipitation ensures that there is no running water phenomenon in the upper and middle guide construction faces. In order to prevent water from gushing out during invert construction and avoid sand boiling, in this research, a dewatering technique for dewatering wells in the cave is proposed, when the diameter of the drilled hole is 290 mm, while XY-2B drilling rig is adopted, and the protective barrel should be 0.30 m above the ground next to the hole to prevent surface sewage from infiltrating into the well. Besides, the shaft wall pipes are all bridge steel pipes, and their diameter is 108 mm (outer diameter). Apart from that, the water



FIGURE 10: Vertical vacuum precipitation.



FIGURE 11: Gravity well dewatering and its effect.

filter pipe is wrapped with a layer of geotextile and a layer of 100 mesh nylon gauze. In addition, the diameter of the water filter pipe is the same as that of the well wall pipe, whereas the sedimentation tube exists at the bottom of the filter tube, when the diameter is the same as that of the filter tube; the length is 0.50 m, and the bottom of the sedimentation tube is sealed. Furthermore, the area that is 4.00 m below the bottom of the diving well is filled with gravel as a filter layer. In order to prevent the infiltration of ground sewage and ensure the effect, high-quality clay must be used to fill the ground surface and compacted above the surrounding filling surface of the gravel material.

After the completion of the well construction, the deep well pump should be run in time, while drainage pipes,



FIGURE 12: The implementation of advanced conduit and plywood installation.

cables, etc. should be laid, and the pumping and drainage system should be installed, followed by the pumping test being able to start. Besides, these devices shall be marked on site. Moreover, during well washing and dewatering operation, pipes shall be used to drain water into the sump, and the water shall be discharged into the preset drainage ditches outside the site through the drainage pipes preset outside the site that should be cleaned regularly to ensure the smooth flow of the drainage system. The effect is shown in Figure 11.

In the reinforcement measures, in order to control the sand boiling phenomenon, the oblique rotary jet grouting pile is adopted to form the partition wall. Since the sand layer is a whole, it cannot prevent water from penetrating from the bottom of the partition wall to the bottom plate. Therefore, through the gravity dewatering wells, it is possible to achieve no water gushing during the invert excavation of the tunnel in the water-rich quicksand formation and to ensure the dryness of the construction surface. In addition, this technology can well control the groundwater level line to be lower than the lowest point of invert construction and overcome the difficulty of invert construction in rich water and quicksand formations.

5. Tunnel Excavation Technology after Precipitation Is Completed

After the completion of the tunnel precipitation, the sand layer is almost dry. However, dry sand is a kind of soil with special properties, with different water content, and its mechanical indexes are quite different. Moreover, the mechanical behavior of the surrounding rock varies with the size of the tunnel span and section. Because of its small cohesive force, an empty surface is formed when the tunnel is excavated, and it is prone to collapse under the action of gravity due to the disturbance of the excavation. Moreover, its deformation is abrupt, discontinuous, and irreversible, and tunnel construction is very risky. Therefore, deformation control and collapse prevention must be put in the first place in tunnel construction in dry sand formations.

5.1. Tunnel Excavation Technology. The dry sand tunnel is excavated with the CD method or three-step arc reserved core soil, while both the upper part and the lower part are

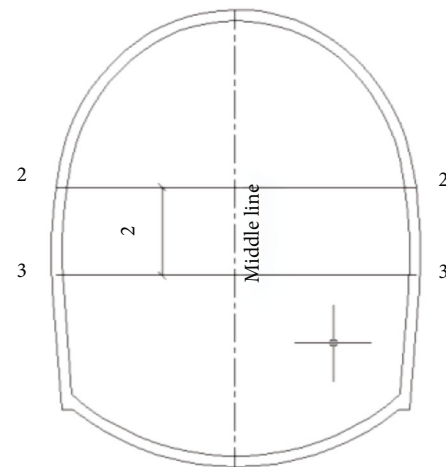


FIGURE 13: Layout of the measurement section.

excavated by pneumatic shovels and pneumatic picks. Besides, dump trucks tracklessly transport the ballast out. Since the tunnel in this study is a single-track tunnel with a small cross-section, the natural collapse angle of dry sand is generally 45° . Therefore, the three-step arc-shaped reserved core soil construction method is selected.

The advanced support will use advanced small conduits for prereinforcement, which will cause less disturbance to the surrounding rock during the excavation process. Due to the small particle size of dry sand, it must be encrypted when carrying out advanced support. Therefore, the reinforcement measures of the encrypted small conduits have been taken, as shown in Figure 12(a). Apart from that, the length of the leading small pipe is 3.0 m, the circumferential spacing is 0.15 cm, the excavation is carried out every 1.5 m, and the overlap length is 1.5 m. In construction, holes are arranged on the steel frame web at intervals along the 158° range of the vault to ensure that the extrapolation angle of the small catheter is $5^\circ \sim 10^\circ$. In addition, the first shotcrete is used to seal the face, and then, the small pipe is drilled and installed. Besides, the dry sand layer advanced small pipe construction technology mainly includes two processes of hole layout and drilling and pipe installation. Moreover, to guarantee that the dry sand does not collapse, a wooden

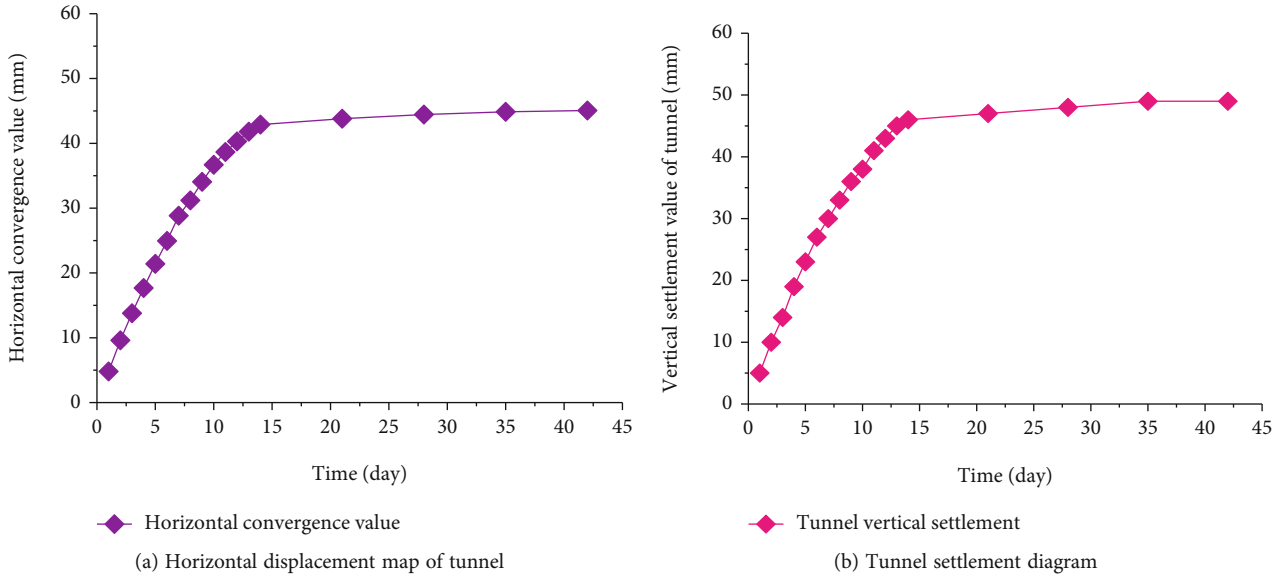


FIGURE 14: Displacement diagram around the tunnel.

insert plate is installed between the steel arch and the small pipe so as to prevent the dry sand from slipping. After drilling the bolt hole with the YT-28 air gun, the small pipe is driven in from the middle of the section steel frame, and the exposed end is supported on the steel frame behind the excavation surface, which forms a presupport system with the steel frame, whereas, after the construction of the small pipe is completed, the steel arch is erected on the face of the tunnel, and the flexible plywood of $250 \times 500 \times 5$ mm is made at the same time, as shown in Figure 12(b).

The installation of plywood has played a great role in preventing the collapse of dry sand, avoiding large-scale landslide accidents caused by the sliding of dry sand from the middle of the small pipe, ensuring the stability of the surrounding rock, and solving the collapse problem fundamentally.

The following points should be paid attention to when adopting this construction technology. During the excavation process, a special person is responsible for following up and commanding, and the operation must be carried out in strict accordance with the requirements. Besides, the upper guide is designed to change the original double-row small catheter into a single-row small catheter, with one in every 15 cm. After excavation, it must be closed and formed into a ring in time, and the lock-foot anchor pipe must be installed in time, while the temporary invert should be set reasonably, whereas, after overexcavation and small-area landslides are treated, it should be ensured that the backfilling behind the steel frame is compact, and grouting holes should be reserved for large landslides. In addition, the bottom of the invert tunnel is supported and sealed well in time. Apart from that, we follow up the invert in time as required to ensure that the step distance of the invert and the second liner is always kept within a safe step distance, and as close as possible to the tunnel face.

5.2. Analysis on Monitoring Measurement Data Results. One vault sinking point and two clearance horizontal conver-

gence measurement lines are arranged on each measurement section of the tunnel. Besides, measure until the lining structure is closed and the sinking basically stops. Furthermore, the measurement section layout is shown in Figure 13, while the convergence of the tunnel in the vertical and horizontal directions is displayed in Figure 14.

From the horizontal convergence data, it can be seen that the maximum displacement is 45.06 mm. Besides, the curve is smooth, and the data slightly fluctuates. Apart from that, it is judged that the surrounding rock is stable. Furthermore, the total displacement of the vault subsidence is 49 mm, and the temporal curve regression analysis shows that the data tends to be stable, and the surrounding rock is judged to be stable.

6. Conclusion

Aiming at the construction of quicksand tunnels, in this paper, laboratory parameter measurement experiments and numerical calculations are performed, when combined with field experiments, to study the precipitation technology, construction methods, and stability of quicksand surrounding rocks for tunnels in quicksand formations. The main conclusions are as follows:

- (1) For tunnel construction in the quicksand stratum, the disadvantages of reinforcement measures under such geology are analyzed, and a comprehensive three-dimensional negative pressure dewatering construction method is proposed. For the phenomenon of the sand influx on the tunnel face and sand boiling on the bottom, the tunnel face is put forward, whereas, for the water replenishment behind the top of the tunnel, a construction method of intercepting the water replenishment by the vertical vacuum dewatering on the top of the tunnel is introduced. Besides, for the phenomenon of sand boiling

on the bottom plate, a method of setting gravity dewatering wells on the side walls is presented to ensure the safety of construction and improve the construction progress, and it is obviously reflected in the construction progress. Furthermore, before this method is adopted, the excavation is 15 m in 8 months, and after this method is used, the average excavation is 25 m per month

- (2) Since the borehole in the quicksand formation is easy to collapse, the method of feeding the dewatering pipe from the drill pipe avoids the damage of the geotextile caused by the direct insertion of the dewatering pipe, enhances the precipitation effect, reduces the construction risk, and realizes the rapid construction
- (3) When the precipitation is completed, considering that the natural collapse angle of dry sand is generally 45°, it is more reasonable to use the three-step arc-shaped reserved core soil construction method. At the same time, the plywood is inserted into the back of the small duct during the construction, which eliminates the risk of the tunnel construction caused by the collapse of the dry sand radically and ensures the safety of the construction

Data Availability

The data used to support the findings of this study are available from the corresponding author upon request.

Conflicts of Interest

The authors declare that there are no conflicts of interest regarding the publication of this paper.

References

- [1] M. Q. Zhang, Z. J. He, G. Z. Xiao, and R. Chengmin, "Research on the tunnel engineering characteristics and construction technology of the tertiary water rich sand," *Journal of Railway Engineering Society*, vol. 2016, no. 9, pp. 76–81, 2016.
- [2] F. Cao, "Special research on water-stability characteristics of tertiary system sandstone in Lanzhou area during tunnel construction," *Journal of Railway Engineering Society*, vol. 12, no. 31, pp. 21–25, 2012.
- [3] B. G. Zhen, "Characteristics analysis of the tertiary sandstone in Lanzhou-Chongqing tunnel Taoshuping tunnel," *Railway Engineering*, vol. 5, pp. 55–57, 2013.
- [4] M. Eriksson, H. Stille, and J. Andersson, "Numerical calculations for prediction of grout spread with account for filtration and varying aperture," *Tunnelling and Underground Space Technology*, vol. 15, no. 4, pp. 353–364, 2000.
- [5] E. C. Almer, *Grouting for pile foundation improvement*, [Ph.D. Thesis], Delft University, Delft, Netherlands, 2001.
- [6] S. J. Wu, H. Q. Tang, W. X. Meng, X. L. He, and Y. G. Li, "Construction technology of Xiamen Xiang'an subsea tunnel crossing water-rich sand layer," *Chinese Journal of Rock Mechanics and Engineering*, vol. 26, no. 2, pp. 3386–3821, 2007.
- [7] S. G. Wang, M. Q. Zhang, H. J. Huang, W. Y. Chen, and H. L. Yin, "Construction technology of F1 high pressure and water-rich fault in Bieyancao tunnel on Yiwan railway," *Journal of Railway Engineering Society*, vol. 9, no. 120, pp. 66–70, 2008.
- [8] J. Hai, "Construction method of the rich water surrounding rock section of Xiangshan tunnel," *Shanxi Architecture*, vol. 35, no. 3, pp. 316–317, 2009.
- [9] X. F. Deng, *A study on rock deformation control of a tunnel underpassing flyover bridges in rich water and shifting sand strata*, Southwest Jiaotong University, Chengdu, 2009.
- [10] P. Deift, C. Tomei, and E. Trubowitz, "Inverse scattering and the Boussinesq equation," *Pure and Applied Mathematics*, vol. 35, no. 5, pp. 567–628, 1982.
- [11] H. Mroueh and I. Shahrour, "Three-dimensional finite element analysis of the interaction between tunneling and pile foundations," *International Journal for Numerical and Analytical Methods in Geomechanics*, vol. 26, no. 3, pp. 217–230, 2002.
- [12] G. L. Li and F. Wang, *Study on the main technical measures of the Tertiary argillaceous weakly cemented water-rich fine sandstone tunnel*, Journal of Chongqing Jiaotong University, 2015.
- [13] S. C. Li, G. R. Shi, and J. Wu, "The pre-reinforcement construction technology of Taoshuping tunnel with water-rich undiagenetic silt fine sand," *Modern Tunnel Technology*, vol. 48, no. 2, pp. 116–119, 2011.
- [14] F. Y. Yang, "Construction technology of water-rich tertiary silt sandstone section of Chengershan tunnel," *Tunnel Construction*, vol. 42, no. 8, pp. 65–66, 2013.
- [15] C. J. Xu, "The key construction technology of the H series siltstone section of Humaling tunnel," *National Defense Traffic Engineering and Technology*, vol. 6, pp. 55–58, 2011.
- [16] X. N. Gong, *Examples of Foundation Pit Engineering 5*, vol. 6, China Construction Industry Press, Beijing, 2014.
- [17] S. Z. Shang, "Hoegnotger static probe performance and application," *Water Transport Engineering*, vol. 1, pp. 53–56, 1996.
- [18] T. Huang, "Experimental study on the use of vacuum preloading method to deal with highway soft foundation slumping," *China Civil Engineering Journal*, vol. 6, no. 7, pp. 133–139, 2009.
- [19] Y. S. Liang, "Construction technology of rotary jet grouting pile in urban subway," *Tunnel Construction*, vol. 27, no. 3, pp. 84–87, 2007.
- [20] Q. L. Wu, Z. W. Liu, and W. Q. Zhang, "Super shallow buried short-distance double-hole tunnel construction in water-rich fine sandy soil layer," *Construction Technology*, vol. 33, no. 10, pp. 18–20, 2004.
- [21] F. Zhang, "Water-stop construction technology for surrounding rock of water-rich sand tunnel," *Journal of Shijiazhuang Railway Institute*, vol. 18, no. 1, pp. 99–102, 2005.
- [22] Y. C. Li, "Construction technology of large-span flat-top and shallow-buried tunnels in water-rich sand," *National Defense Traffic Engineering and Technology*, vol. 4, pp. 61–63, 2007.
- [23] Z. H. Peng, C. T. Yan, and Q. J. Meng, "Application of well point precipitation in tunnel construction in water-rich silt sand," *Western Exploration Engineering*, vol. 12, pp. 118–120, 2004.
- [24] G. Feng, X. C. Wang, Y. Kang, and Z. T. Zhang, "Effect of thermal cycling-dependent cracks on physical and mechanical properties of granite for enhanced geothermal system," *International Journal of Rock Mechanics and Mining Sciences*, vol. 134, article 104476, 2020.

- [25] G. Feng, X. C. Wang, M. Wang, and Y. Kang, "Experimental investigation of thermal cycling effect on fracture characteristics of granite in a geothermal-energy reservoir," *Engineering Fracture Mechanics*, vol. 235, article 107180, 2020.
- [26] A. Nakao, Y. Nara, and T. Kubo, "P-wave propagation in dry rocks under controlled temperature and humidity," *International Journal of Rock Mechanics and Mining Science*, vol. 86, pp. 157–165, 2016.
- [27] J. J. Hu, H. P. Xie, Q. Sun, C. B. Li, and G. K. Liu, "Changes in the thermodynamic properties of alkaline granite after cyclic quenching following high temperature action," *International Journal of Mining Science and Technology*, vol. 31, no. 5, pp. 843–852, 2021.
- [28] P. H. Jin, Y. Q. Hu, J. X. Shao, G. K. Zhao, X. Z. Zhu, and C. Li, "Influence of different thermal cycling treatments on the physical, mechanical and transport properties of granite," *Geothermics*, vol. 78, pp. 118–128, 2019.
- [29] T. Meng, R. C. Liu, X. X. Meng, D. H. Zhang, and Y. Q. Hu, "Evolution of the permeability and pore structure of transversely isotropic calcareous sediments subjected to triaxial pressure and high temperature," *Engineering Geology*, vol. 253, pp. 27–35, 2019.
- [30] M. Z. Gao, J. Xie, Y. Gao et al., "Mechanical behavior of coal under different mining rates: a case study from laboratory experiments to field testing," *International Journal of Mining Science and Technology*, vol. 31, no. 5, pp. 825–841, 2021.
- [31] M. Z. Gao, J. Xie, J. Guo, Y. Q. Lu, Z. Q. He, and C. Li, "Fractal evolution and connectivity characteristics of mining-induced crack networks in coal masses at different depths," *Geomechanics and Geophysics for Geo-Energy and Geo-Resources*, vol. 7, no. 1, p. 9, 2021.
- [32] Y. Wang, B. Zhang, B. Li, and C. H. Li, "A strain-based fatigue damage model for naturally fractured marble subjected to freeze-thaw and uniaxial cyclic loads," *International Journal of Damage Mechanics*, vol. 30, no. 10, pp. 1594–1616, 2021.
- [33] Y. Wang, Y. F. Yi, C. H. Li, and J. Q. Han, "Anisotropic fracture and energy characteristics of a Tibet marble exposed to multi-level constant-amplitude (MLCA) cyclic loads: a lab-scale testing," *Engineering Fracture Mechanics*, vol. 244, article 107550, 2021.
- [34] S. Chuang, C. Dongxu, W. Laigui, and W. Lin, "Quantitative evaluation of the constraint effect and stability of tunnel lining support," *Tunnelling and Underground Space Technology*, vol. 112, article 103920, 2021.
- [35] F. Yue, B. Liu, B. Zhu, X. L. Jiang, L. Chen, and K. Liao, "Shaking table test and numerical simulation on seismic performance of prefabricated corrugated steel utility tunnels on liquefiable ground," *Soil Dynamics and Earthquake Engineering*, vol. 141, article 106527, 2021.
- [36] D. W. H. Su, P. Zhang, H. Dougherty, M. van Dyke, and R. Kimutis, "Longwall mining, shale gas production, and underground miner safety and health," *International Journal of Mining Science and Technology*, vol. 31, no. 3, pp. 523–529, 2021.
- [37] S. Sinha and G. Walton, "Integration of three-dimensional continuum model and two-dimensional bonded block model for studying the damage process in a granite pillar at the Creighton mine, Sudbury, Canada," *Journal of Rock Mechanics and Geotechnical Engineering*, vol. 13, no. 2, pp. 275–288, 2021.
- [38] R. F. Wang, F. T. Zeng, and L. Li, "Stability analyses of side-exposed backfill considering mine depth and extraction of adjacent stope," *International Journal of Rock Mechanics and Mining Sciences*, vol. 142, article 104735, 2021.
- [39] C. B. Basnet and K. K. Panthi, "Evaluation on the minimum principal stress state and potential hydraulic jacking from the shotcrete-lined pressure tunnel: a case from Nepal," *Rock Mechanics and Rock Engineering*, vol. 52, no. 7, pp. 2377–2399, 2019.
- [40] N. A. Do and D. Dias, "A comparison of 2D and 3D numerical simulations of tunnelling in soft soils," *Environmental Earth Sciences*, vol. 76, no. 3, p. 102, 2017.

Research Article

Effect of Temperature and Strain Rate on the Brittleness of China Sandstone

Xiuyuan Yang ^{1,2,3} **Zhenlong Ge** ⁴ **Qiang Sun** ⁴ and **Weiqliang Zhang** ^{1,2}

¹Key Laboratory of Coalbed Methane Resources and Reservoir Formation Process of the Ministry of Education, China University of Mining and Technology, Xuzhou, Jiangsu Province 221116, China

²School of Resources and Geosciences, China University of Mining and Technology, Xuzhou, Jiangsu Province 221116, China

³Center for Hydrogeology and Environmental Geology, China Geological Survey, Baoding, Hebei Province 071051, China

⁴College of Geology and Environment, Xi'an University of Science and Technology, Xi'an, Shaanxi Province 710054, China

Correspondence should be addressed to Zhenlong Ge; gezhenlong04@cumt.edu.cn

Received 25 August 2021; Revised 28 October 2021; Accepted 11 November 2021; Published 7 December 2021

Academic Editor: Shi-bing Huang

Copyright © 2021 Xiuyuan Yang et al. This is an open access article distributed under the Creative Commons Attribution License, which permits unrestricted use, distribution, and reproduction in any medium, provided the original work is properly cited.

To quantitatively study the influence of temperature and strain rate on the brittleness of sandstone, the mechanical parameters of sandstone under different temperatures and strain rates are collected from the previous literature, and two empirical equations for calculating rock brittleness are used to quantitatively calculate and evaluate the brittleness of sandstone. The results show that both BI_1 and BI_2 can characterize the brittleness of sandstone, but the applicable conditions are different. The BI_1 method is more accurate in calculating the variation in the sandstone brittleness with a strain rate, while the BI_2 method is more accurate in calculating its variation with temperature. The brittleness of sandstone increases with the increase in the strain rate, especially when the strain rate exceeds 100 s^{-1} . Under low-temperature conditions, the strength and brittleness of rocks increase due to the strengthening of ice. Under the condition of high temperature, the thermal damage to sandstone is intensified after 400°C , and the quartz phase changes after 600°C , which leads to the increase in microcrack density and the decrease in brittleness of sandstone. The conditions of low temperature and high strain rate are beneficial to the enhancement of sandstone brittleness.

1. Introduction

Brittleness is a very important property of rock. It can be used as an index of safety risk in resource exploitation and engineering construction projects. For example, brittleness is an important property for shale gas compressibility measurement and evaluation and is a basic parameter for reservoir evaluation. Rock bursts are directly related to the brittle fracture of rock masses and the instability failure of surrounding rock structures [1]. Brittleness also is a key index of rock drillability, which plays an important role in improving tunneling speed and reducing tool wear [2]. Therefore, it is important to evaluate the brittleness of rock accurately in the process of resource development and engineering construction.

Definitions of brittleness vary across disciplines and fields, and at present, there is no unified definition. Nevertheless, many scholars have carried out in-depth research

on the brittleness of rock and established different evaluation indexes of brittleness [3, 4]. For example, Jarvie et al. [5] defined the percentage of brittle minerals in rocks as a BI. Altindag [6] defined the BI of rock as the ratio of compressive strength to tensile strength. There are many definitions of BI based on curve shapes [7–9] and energy relationships [10] in stress-strain curves. Hucka and Das [11] defined a BI as the ratio of elastic strain to total strain in a stress-strain curve. Tarasov and Potvin [12] defined a BI for rocks as the ratio of rupture energy to excess (released) energy.

Temperature is one of the important factors affecting rock mechanical properties. Geotechnical engineering and artificial freezing engineering in cold areas make the surrounding rock of the engineering structure be subject to periodic low-temperature effects or long-term low-temperature freezing, and its strength characteristics are very different from normal temperature conditions. Under high-temperature conditions, sandstone produces thermally

TABLE 1: Characteristics of the reviewed dynamic loading of sandstone.

Rock type	Ref.	Site	Main mineral	Number of samples	Sample size (mm)	Test equipment	Test process
Sandstone	Gong et al. [49]	Shandong, China	42% Qtz; 35% Pl; 9% Cal; 8% Zeo; 5% Kfs; 1% Op	22	$\Phi 50 \times 100$ mm	Conventional SHPB system	45 s^{-1} , 59 s^{-1} , 66 s^{-1} , 84 s^{-1} , 91 s^{-1} , 96 s^{-1} , 116 s^{-1} , 135 s^{-1}
Fine sandstone	Hou [50]	Shanxi, China	/	36	$\Phi 50 \times 25$ mm	$\Phi 74$ mm SHPB test device	10 s^{-1} , 25 s^{-1} , 95 s^{-1} , 100 s^{-1} ; 100°C , 200°C , 300°C , keep 20 min
Roof sandstone	Li [24]	Xuzhou, China	/	18	$\Phi 50 \times 25$ mm	$\Phi 50$ mm SHPB test device	25°C , 800°C , $5^\circ\text{C}/\text{min}$, keep 1 h; impact load of 0.30, 0.35, 0.40, 0.45, 0.50, and 0.55 MPa
Sandstone	Li et al. [25]	China	/	12	$\Phi 50 \times 25$ mm	$\Phi 50$ mm SHPB test device	18.6 s^{-1} , 24.3 s^{-1} , 46.3 s^{-1} , 132.7 s^{-1}
Medium-grained sandstone	Liu and Xu [51]	Qinling, China	52% Qtz; 27% Cal; 8% Pl; 6% Kfs; 3% Ill; 2% Chl; 1% Mot; 1% Dol	35	$\Phi 100 \times 50$ mm	$\Phi 100$ mm SHPB test device	25, 100, 200, 400, 600, 800, and 1000°C ; keep 2 h; impact velocity of 11.0–15.0 m/s
Sandstone	Liu et al. [52]	China	/	18	$\Phi 50 \times 50$ mm	$\Phi 50$ mm SHPB test device	82 s^{-1} , 92 s^{-1} , 106 s^{-1} , 118 s^{-1} , 156 s^{-1} , 164 s^{-1}
Sandstone	Lv et al. [53]	China	41% Qtz; 26% Cal; 17% Pl; 9% Kfs; 1% Talc; 2% Chl; 2% Ill; 1% Hem	12	$\Phi 97 \times 43$ mm	$\Phi 100$ mm SHPB test device	31.0 s^{-1} , 43.5 s^{-1} , 48.2 s^{-1} , 81.4 s^{-1}
Fine sandstone	Ma et al. [54]	Shanxi, China	/	20	$\Phi 50 \times 25$ mm	SHPB test device	25°C , 100°C , 200°C , 300°C
Sandstone	Mahanta et al. [55]	Rajasthan, India	80.2% Qtz; 7.3% Di; 6.8% Kln; 5.4% Cal; 0.4% Spl	/	$\Phi 50 \times 100$ mm	AG-X universal testing machine	25°C , 100°C , 200°C , 300°C , 500°C , 600°C , 800°C , 1000°C , $10^\circ\text{C}/\text{min}$, keep 3 h
Sandstone	Wang et al. [56]	Shaanxi, China	/	/	/	$\Phi 100$ mm SHPB test device	25°C , 100°C , 200°C , 400°C , 600°C , 700°C , 800°C , 900°C , $5^\circ\text{C}/\text{min}$, keep 3 h
Red sandstone	Wang et al. [57]	China	81% Qtz; 10% Pl; 3% Kfs; 3% Cal; Chl; Ill; Hem	6	$\Phi 96 \times 48$ mm	$\Phi 100$ mm SHPB test device	$1.5^\circ\text{C}/\text{min}$, 200°C , keep 4 h; $-2.25^\circ\text{C}/\text{min}$, water bath (20°C), keep 6 h; 0, 10, 20, 30, and 40 TS cycles
Siltstone	Yin et al. [58]	China	/	24	$\Phi 50 \times 30$ mm	$\Phi 50$ mm SHPB test device	25°C , 100°C , 200°C , 300°C , 400°C , $3.33^\circ\text{C}/\text{min}$, keep 2 h
Sandstone	Yin et al. [59]	China	/	25	$\Phi 50 \times 100$ mm	SHPB test device	25°C , 200°C , 400°C , 600°C , 800°C ; $3.33^\circ\text{C}/\text{min}$, keep 4 h
Sandstone	Zhu et al. [26]	China	/	15	$\Phi 50 \times 30$ mm	$\Phi 50$ mm SHPB test device	71.5 s^{-1} , 92.3 s^{-1} , 118.3 s^{-1} , 126.7 s^{-1}

Cal: calcite; Chl: chlorite; Di: dickite; Dol: dolomite; Hem: hematite; Ill: illite; Kfs: K-feldspar; Mot: montmorillonite; Op: opaque minerals; Pl: plagioclase; Qtz: quartz; Spl: spinel; Zeo: zeolite.

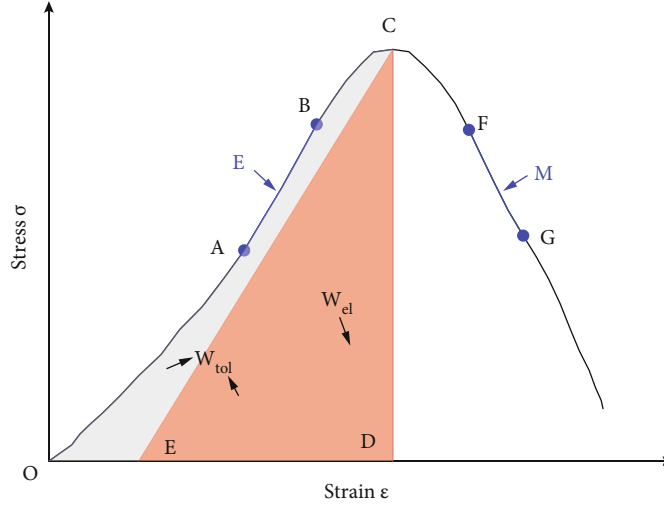


FIGURE 1: Stress-strain curve of brittle rock.

induced cracks, which affect its strength and integrity and brings great hidden dangers to engineering constructions. Therefore, it is necessary to understand the mechanical behavior of rock under different temperature conditions. On the other hand, underground engineering construction often involves ore and rock crushing, pile driving, explosives, and other engineering techniques, which are almost all related to fracturing and stress wave propagation in rocks under impact loads. This is related to the dynamic mechanical properties of rock.

At present, there has been much in-depth research on the influence of different temperatures and strain rates on the physical and mechanical properties of rocks. However, there are relatively few studies on the evaluation of rock brittleness under these two influencing factors. Based on this, this study selected sandstone as the research object and studied the effects of temperature and strain rate on the brittleness of sandstone.

2. Experimental Results of Previous Studies

In previous experiments, some researchers focused on the influences of tensile strength, mineral composition, and other factors on the brittleness of the specific rocks, while neglecting important common characteristics. In this paper, we summarized the effects of the strain rate and different treatment temperatures on the brittleness of sandstone based on the previous research results, as shown in Table 1. In these studies, sandstone is collected from different areas and processed into different sizes and then treated at different temperatures. With different loading rates, the impact load test or static compression test of sandstone treated at different temperatures was carried out with SHPB, and the stress-strain curves under different test conditions were obtained. In this paper, the brittleness of sandstone is quantitatively calculated according to these stress-strain curves, to explore the influence of temperature and strain rate on the brittleness of sandstone.

3. Methods of Calculating Rock Brittleness

After many years of theoretical exploration, researchers have put forward nearly 80 brittleness indexes (BI) of rock [13]. Because of differences in test conditions, some of these indexes can reflect differences in rock brittleness, while others need further experiments to verify their accuracy. In this study, based on stress-strain curves, two typical empirical formulas for evaluating rock BI are selected [14] (formulas (1) and (2)).

$$BI_1 = \frac{E}{M}, \quad (1)$$

where E is the prepeak elastic modulus and M is the postpeak elastic modulus.

$$BI_2 = \frac{W_{el}}{W_{tot}}, \quad (2)$$

where W_{el} is the elastic energy at failure and W_{tot} is the total energy at failure.

As shown in the stress-strain curve in Figure 1, BI_1 is approximately the ratio of the AB segment to the FG segment. BI_2 is equal to the ratio of the areas for CDE and OABCD in the stress-strain curve in Figure 1.

4. Analysis and Discussion

4.1. Influence of the Strain Rate. Figure 2 shows the relationship between the brittleness index and strain rate calculated by formulas (1) and (2). As shown in Figure 2(a), there is an overall increasing trend in BI_1 with an increasing strain rate. When the strain rate is lower than 100 s^{-1} , BI_1 slowly increases from 0.2 to about 0.7. When the strain rate is between 100 s^{-1} and 180 s^{-1} , BI_1 increases rapidly from 0.7 to about 2.5. As shown in Figure 2(b), BI_2 decreases with the increase in the strain rate. When the strain rate is lower

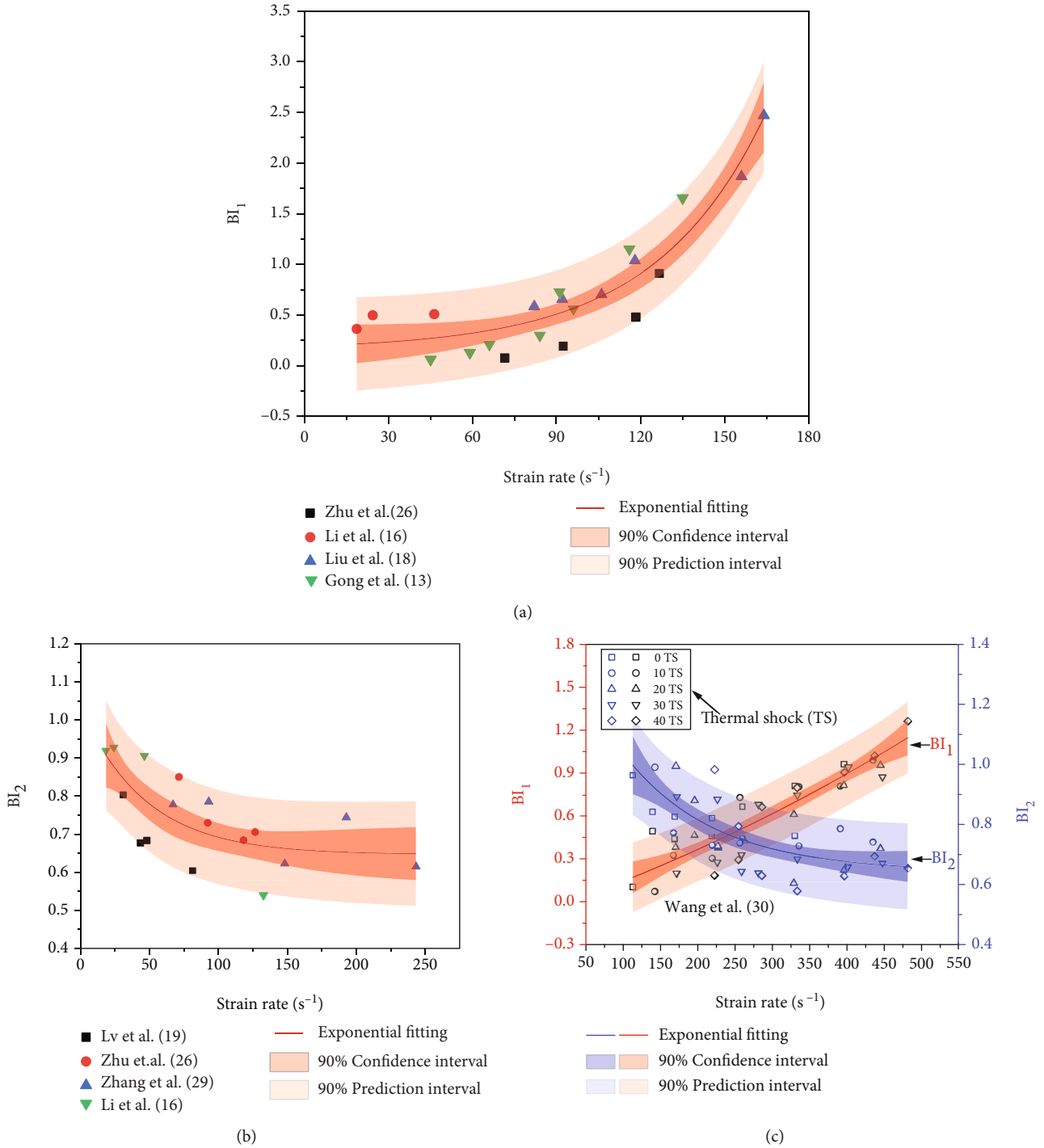


FIGURE 2: Changes in the BI of sandstone with strain rate. (a) BI₁ [25, 26, 51, 53]; (b) BI₂ [25, 26, 54, 60]; (c) BI₁ and BI₂ [58].

than 100 s⁻¹, BI₁ decreases rapidly from 0.9 to about 0.7. When the strain rate is between 100 s⁻¹ and 180 s⁻¹, the BI₁ decreases slowly from 0.7 to about 0.65. At a higher strain rate, with the increase in the strain rate, BI₁ increases slowly, while BI₂ decreases rapidly, as shown in Figure 2(c).

4.2. Influence of Temperature. To facilitate the comparison of the variation of the brittleness index with temperature, the data for the calculated brittleness indexes from different

literature are standardized as shown in equation (3). The BI₁^{*} and BI₂^{*} denote the standardized brittleness indexes calculated in equations (1) and (2), respectively. Figure 3 shows the variation in the BI^{*} of sandstone with treatment temperature. It can be seen that under low-temperature conditions, BI₁^{*} and BI₂^{*} both shows a downward trend with increasing temperature, as shown in Figures 3(a) and 3(c). Under high-temperature conditions, BI₁^{*} and BI₂^{*} can be divided into two stages as the temperature increases, but they show

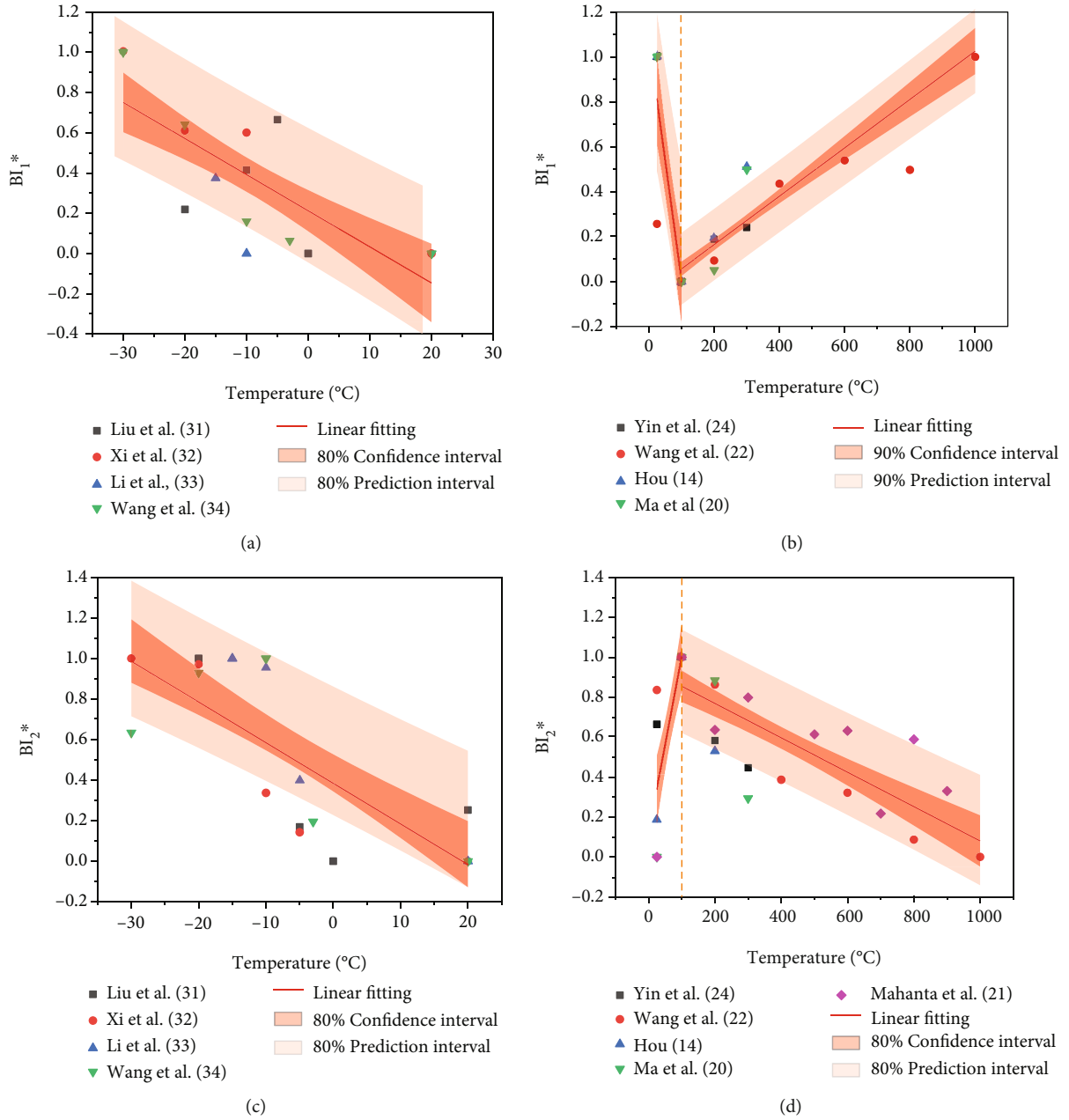


FIGURE 3: Changes in the BI^* of sandstone with temperature: (a, b) BI_1^* ; (c, d) BI_2^* . [38, 52, 55–57, 59, 61–63].

opposite trends. When the heating temperature is about 100°C, BI_1^* drops to the minimum and BI_2^* increases to the maximum, as shown in Figures 3(b) and 3(d).

$$BI^* = \frac{BI - BI_{\min}}{BI_{\max} - BI_{\min}}, \quad (3)$$

where BI^* represents the standardized brittleness index. BI represents the brittleness index at different temperatures, and BI_{\max} and BI_{\min} represent the maximum and minimum values of the brittleness index at different temperatures, respectively.

5. Discussion

Brittleness is a very important property of rocks (especially deep rocks). The brittleness of rock is affected by many factors such as mineral composition, Young's modulus, Poisson's ratio, compressive strength, and tensile strength [15–17]. In this paper, the effects of the strain rate and temperature on the brittleness of sandstone were studied and the mechanisms of influence were discussed.

The brittleness of rock is closely related to its failure stress. According to previous studies, the variation in failure stress with a strain rate of brittle materials is shown in Figure 4(a), which is roughly divided into three stages. Among them, point A is the end of stage I, and the

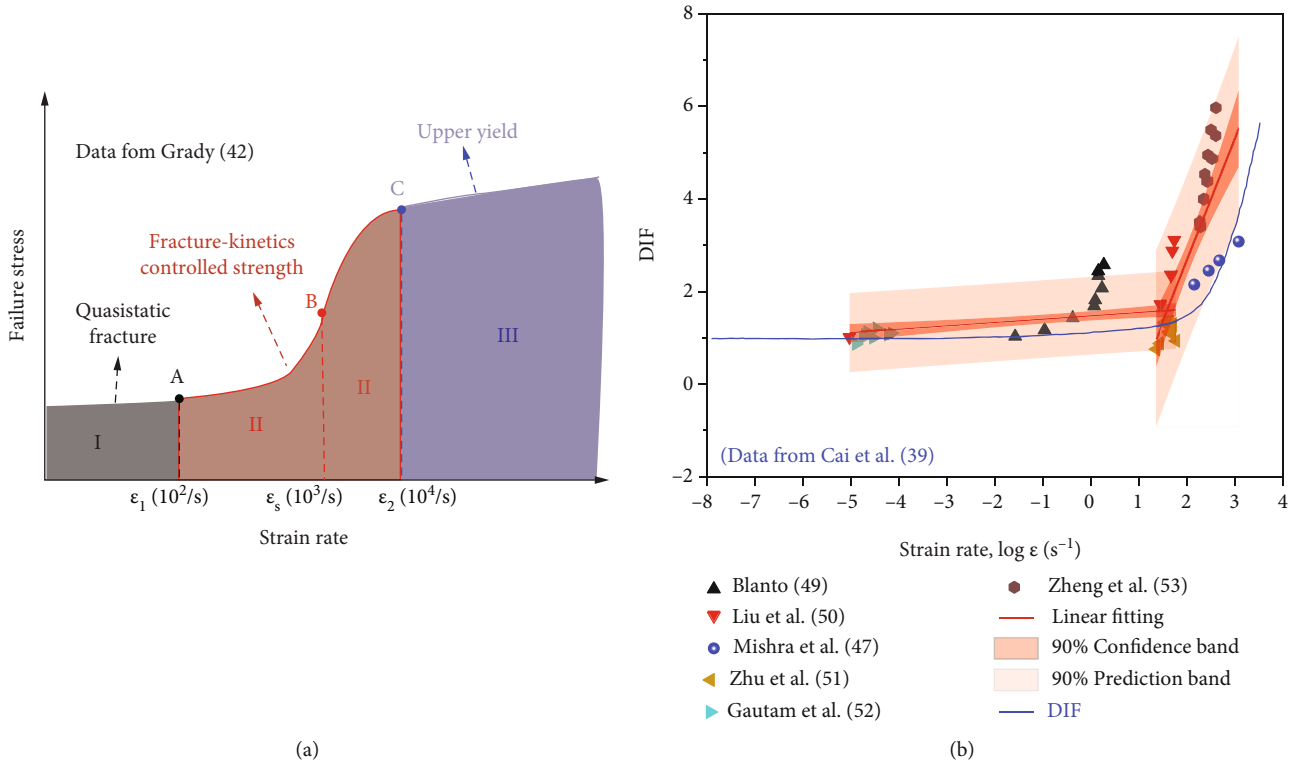


FIGURE 4: Variations in dynamic strength and dissipated energy with strain rate. (a) Failure stress with strain rate [22]. (b) DIF with strain rate [30, 64–68].

corresponding strain ϵ_1 is $10^2 s^{-1}$; point B is the inflection point of the stage II curve, and the corresponding strain ϵ_s is $10^3 s^{-1}$; and point C is the starting point of stage III, and the corresponding strain ϵ_2 is $10^4 s^{-1}$ [18]. In stage I, that is, in the area of low strain, a quasistatic fracture mainly occurs in rocks. The original pore closures and microcracks in sandstone are compressed and compacted with the increase in the strain rate, resulting in a slow increase in rock strength and brittleness [19]. This stage is mainly controlled by the thermoactivation mechanism [20, 21]. In stage II, with the continuous increase in the strain rate, the fracture damage controlled by dynamics in the sandstone gradually increases [22, 23], and the energy consumed gradually increases [24–26]. The energy required for crack generation is greater than the energy required for crack expansion [27]. In rock dynamics tests, due to the short duration of the impact loading action, the specimen does not have enough time for energy accumulation and can only be used for energy accumulation by increasing the strength of the rock [11, 28, 29]. The dynamic increase coefficient (DIF), which is the ratio of dynamic strength to static strength, is usually used to express the increase in rock strength [30], as shown in Figure 4(b). It can be seen that when $\log \epsilon$ is close to $2.0 s^{-1}$ ($\epsilon = 100 s^{-1}$), the DIF value increases significantly, which leads to a rapid increase in the brittleness of the rock. When the strain rate is close to $10^3 s^{-1}$ (point B), the failure stress growth rate reaches the maximum. In stage II, the macroviscosity mechanism is dominant [31], the inertia of the rock is gradually obvious, and the viscosity coefficient decreases

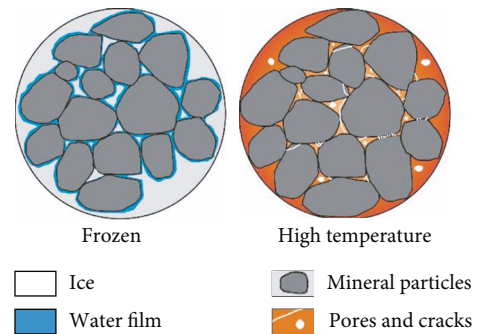


FIGURE 5: Schematic diagram of low-temperature freezing and high-temperature thermal damage to the rock.

with the increase in the strain rate. When the upper yield is reached in the shock compression process, that is, entering stage III, the rate of increase in rock strength with the increase in the strain rate slows down. With the continuous increase in the strain rate, the rock enters the high strain zone, and defects of different sizes begin to grow in the rock. The sandstone will produce permanent damage, and the rock will change from brittleness to ductility. The strain rates involved in this study includes stage I and a portion of stage II.

The temperature has a great influence on the physical and mechanical properties of sandstone [32]. Under low-temperature conditions, bulk water, capillary water, and adsorbed water in the rock gradually freeze into ice, and some of the unfrozen adsorbed water forms a water film (as shown in Figure 5) [33]. As the temperature continues to decrease,

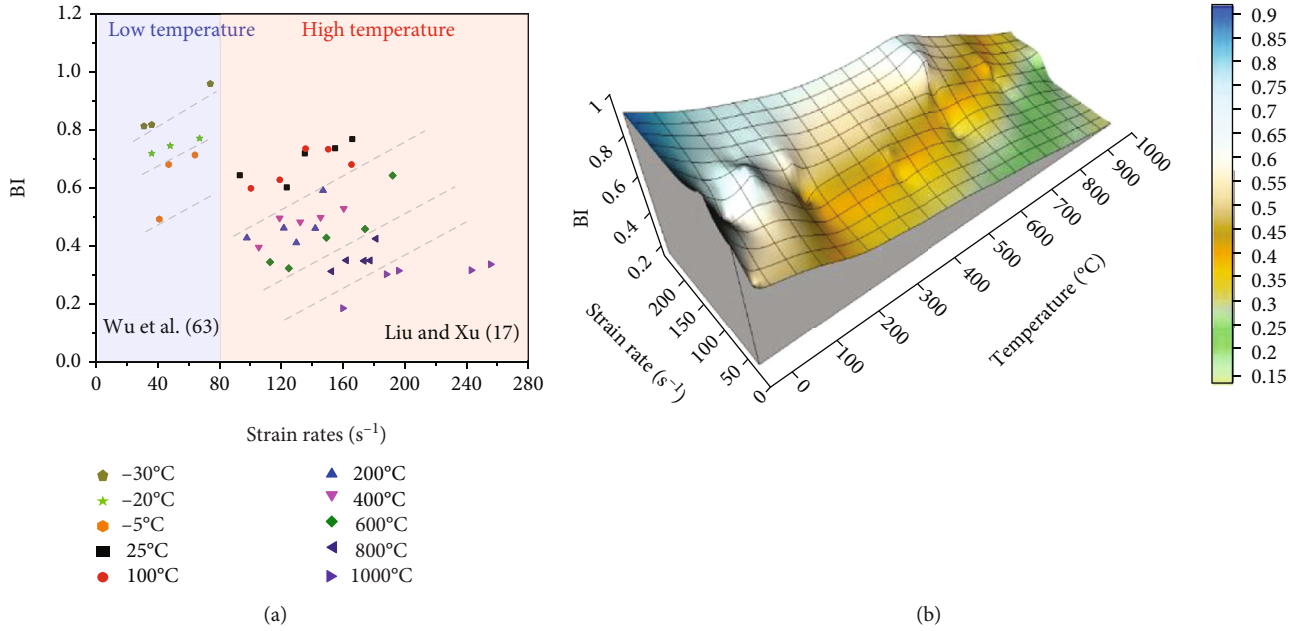


FIGURE 6: Relationship between BI and strain rate and temperature [51, 69]: (a) variation in BI with the strain rate at different heat treatment temperatures; (b) 3-D variations of BI with the strain rate and temperature.

the thickness of the unfrozen water film becomes progressively thinner [34]. Due to the supporting force of the ice, the connection force between the mineral particles becomes stronger, and the mineral skeleton becomes more stable, which strengthens the strength of the rock [35]. At the same time, due to the rapid expansion of ice in the formation process, it squeezes the surrounding minerals and produces microcracks, weakening the mechanical properties of the rock [36]. According to the study of Wang et al. [37], during the freezing process of rock, the strengthening effect inhibits the weakening effect, which leads to the continuous increase in the strength of the rock. Therefore, the brittleness of the rock gradually increases as the temperature decreases [38], as shown in the low-temperature area in Figure 6(a). Under high-temperature conditions, due to the different thermal expansion coefficients of mineral particles [39], nonuniform expansion occurs and thermally induced cracks occur. At the same time, the adsorbed water and crystal water in the sandstone overflowed, causing the pore structure of the sandstone to change [40]. As the temperature continues to rise, different degrees of defects and cracks occur after the rock cools [41, 42]; especially after 400°C, thermal cracks are gradually obvious, and the internal microcracks of the sandstone increase, the strength decreases, and the brittleness is weakened, as shown in the high-temperature area in Figure 6(a). Around 600°C, quartz begins to undergo a phase transformation from α -quartz to β -quartz [43, 44], and the internal and intergranular cracks between the mineral particles become increasingly serious [45–47]. Under high temperatures, these changes in the internal structure of sandstone lead to a gradual decrease in its strength, reduced brittleness, and enhanced plasticity [48].

In summary, temperature and strain rate have significant effects on the brittleness and plasticity of sandstone due to its water content, pore and crack distribution, mineral struc-

ture, and so on. Low temperature and high strain rate are conducive to the enhancement of sandstone brittleness, as shown in Figure 6(b). Both BI₁ and BI₂ can reflect the brittleness of sandstone but have different applicable conditions. Within the strain rate range of this study, as the strain increases, the internal pores and cracks of the sandstone decrease and the strength of the sandstone increases. For the calculation of BI₁, because the prepeak and postpeak elastic moduli are considered, the calculation result is more accurate. Under low-temperature conditions, the strength of sandstone increases, and the BI₁ and BI₂ changes show the same change trend. However, under high-temperature conditions, the plastic characteristics of sandstone are enhanced, which leads to the unreliable selection of the post-peak elastic modulus of some samples for BI₁, so the BI₂ value is more reliable. At around 100°C, BI₂ suddenly increases, which may be due to the high-water content of sandstone. The water evaporates during the heat treatment process, and the original pores and cracks of the sandstone are exposed. When subjected to a load, the strain rate increases, increasing brittleness.

6. Conclusions

In this paper, based on existing research data, the variation in the brittleness of sandstone with temperature and strain rate was studied and discussed from a microscopic point of view. At the same time, the variation in sandstone brittleness under the combined action of temperature and strain rate was analyzed. The main conclusions are as follows:

- (1) Temperature and strain rate are two important parameters that affect the brittleness of sandstone. Based on previous studies, two empirical formulas

for the quantitative calculation of sandstone brittleness are selected. Among them, the BI_1 method is more accurate in calculating the variation in the sandstone brittleness index with the strain rate, while the BI_2 method is more accurate in calculating its variation with temperature

- (2) Under dynamic load, with the increase in the strain rate, the failure stress and brittleness of sandstone are positively correlated. When the strain rate exceeds 100 s^{-1} , the failure stress of sandstone begins to increase significantly, resulting in a significant increase in the brittleness index
- (3) Under low-temperature conditions, the water inside the rock gradually freezes into ice. Due to the strengthening effect of ice, the strength and brittleness of the rock increase. Under the condition of high temperature, the thermal damage to sandstone is intensified after 400°C , and the quartz phase changes after 600°C , which leads to the increase in microcrack density and the decrease in brittleness in sandstone. The conditions of low temperature and high strain rate are beneficial to the enhancement of sandstone brittleness

Notations

BI:	Brittleness index
BI^* :	Standardized brittleness index
E :	Prepeak elastic modulus
M :	Postpeak elastic modulus
W_{el} :	Elastic energy and total energy at failure
W_{tot} :	Slab top surface temperature.

Data Availability

The data used to support the findings of this study are available from the corresponding author upon request.

Conflicts of Interest

The authors declare that they have no conflicts of interest.

Acknowledgments

This research was supported by the National Natural Science Foundation of China (Grant Nos. 41672279, 41807233, and 41972288) and the Natural Science Foundation of Jiangsu Province (Grant No. BK20180662).

References

- [1] J. L. Zhang and B. J. Fu, "Rockburst and its criteria and control," *Chinese Journal of Rock Mechanics and Engineering*, vol. 27, no. 10, pp. 2034–2042, 2008.
- [2] O. Yarali and S. Kahraman, "The drillability assessment of rocks using the different brittleness values," *Tunnelling and Underground Space Technology*, vol. 26, no. 2, pp. 406–414, 2011.
- [3] J. G. Ramsay, *Folding and Fracturing of Rocks*, McGraw Hill, New York, 1967.
- [4] L. Obert and W. I. Duvall, *Rock Mechanics and the Design of Structures in Rock*, John Wiley Sons, New York, 1967.
- [5] D. M. Jarvie, R. J. Hill, T. E. Ruble, and R. M. Pollastro, "Unconventional shale-gas systems: the Mississippian Barnett Shale of North-Central Texas as one model for thermogenic shale-gas assessment," *AAPG Bulletin*, vol. 91, no. 4, pp. 475–499, 2007.
- [6] R. Altindag, "Assessment of some brittleness indexes in rock-drilling efficiency," *Rock Mechanics and Rock Engineering*, vol. 43, no. 3, pp. 361–370, 2010.
- [7] A. W. Bishop, "Progressive failure-with special reference to the mechanism causing it," *Proceedings of the Geotechnical Conference on Shear Strength Properties of Natural Soils and Rocks, Oslo*, vol. 2, pp. 142–150, 1967.
- [8] V. Hajiabdolmajid, P. K. Kaiser, and C. D. Martin, "Modelling brittle failure of rock," *International Journal of Rock Mechanics and Mining Sciences*, vol. 39, no. 6, pp. 731–741, 2002.
- [9] T. Feng, X. B. Xie, W. X. Wang, and C. L. Pan, "Brittleness of rocks and brittleness indexes for describing rockburst proneness," *Mining and Metallurgical Engineering*, vol. 20, no. 4, pp. 18–19, 2000.
- [10] M. Aubertin, D. E. Gill, and R. Simon, "On the use of the brittleness index modified (BIM) to estimate the post-peak behavior of rocks," in *Proceedings of the 1st North American Rock Mechanics Symposium*, pp. 945–952, Austin, Texas, 1994.
- [11] V. Hucka and B. Das, "Brittleness determination of rocks by different methods," *International Journal of Rock Mechanics and Mining Sciences & Geomechanics Abstracts*, vol. 11, no. 10, pp. 389–392, 1974.
- [12] B. Tarasov and Y. Potvin, "Universal criteria for rock brittleness estimation under triaxial compression," *International Journal of Rock Mechanics and Mining Sciences*, vol. 59, pp. 57–69, 2013.
- [13] F. Meng, L. N. Y. Wong, and H. Zhou, "Rock brittleness indices and their applications to different fields of rock engineering: a review," *Journal of Rock Mechanics and Geotechnical Engineering*, vol. 13, no. 1, pp. 221–247, 2021.
- [14] D. Zhang, P. G. Ranjith, and M. A. S. Perera, "The brittleness indices used in rock mechanics and their application in shale hydraulic fracturing: a review," *Journal of Petroleum Science and Engineering*, vol. 143, pp. 158–170, 2016.
- [15] H. Horii and S. Nemat-nasser, "Brittle failure in compression: splitting, faulting and brittle-ductile transition," *Philosophical Transactions of The Royal Society A Mathematical Physical and Engineering Science*, vol. 319, no. 1549, pp. 337–374, 1986.
- [16] T. F. Wong and P. Baud, "The brittle-ductile transition in porous rock: a review," *Journal of Structural Geology*, vol. 44, pp. 25–53, 2012.
- [17] M. Duda and J. Renner, "The weakening effect of water on the brittle failure strength of sandstone," *Geophysical Journal International*, vol. 192, no. 3, pp. 1091–1108, 2013.
- [18] C. Z. Qi and Q. H. Qian, "Physical mechanism of dependence of material strength on strain rate for rock-like material," *Chinese Journal of Rock Mechanics and Engineering*, vol. 22, no. 2, pp. 177–181, 2003.
- [19] M. Cai, P. K. Kaiser, F. Suorineni, and K. Su, "A study on the dynamic behavior of the Meuse/Haute-Marne argillite," *Physics and Chemistry of the Earth*, vol. 32, no. 8–14, pp. 907–916, 2007.

- [20] A. Kumar, "The effect of stress rate and temperature on the strength of basalt and granite," *Geophysics*, vol. 33, no. 3, pp. 501–510, 1968.
- [21] P. Perzyna, "Constitutive modelling of dissipative solids for localization and fracture," in *Localization and Fracture Phenomena in Inelastic Solids*, pp. 99–241, Springer, Vienna, 1998.
- [22] D. E. Grady, "Shock-wave properties of brittle solids," *Office of Scientific and Technical Information Technical Reports*, vol. 370, no. 1, pp. 9–20, 1996.
- [23] M. E. Kipp, D. E. Grady, and E. P. Chen, "Strain-rate dependent fracture initiation," *International Journal of Fracture*, vol. 16, no. 5, pp. 471–478, 1980.
- [24] M. Li, *Research on Rupture Mechanism of Coal Measures Sandstone under High Temperature and Impact Load*, China University of Mining Technology, Xuzhou, China, 2014.
- [25] X. F. Li, H. B. Li, K. Liu, Q. B. Zhang, and L. Zou, "Dynamic properties and fracture characteristics of rocks subject to impact loading," *Chinese Journal of Rock Mechanics and Engineering*, vol. 36, no. 10, pp. 2393–2405, 2017.
- [26] J. J. Zhu, X. B. Li, F. Q. Guan, S. M. Wang, and W. He, "Study on dynamic characteristics and damage characteristics of sandstone under impact load," in *China Proceedings 6th High-level Forum on Highway science and technology innovation*, pp. 278–285, 2013.
- [27] D. R. Wang and S. S. Hu, "Influence of aggregate on the compression properties of concrete under impact," *Journal of Experimental Mechanics*, vol. 17, no. 1, pp. 23–27, 2002.
- [28] X. B. Li, T. S. Lok, and J. Zhao, "Dynamic characteristics of granite subjected to intermediate loading rate," *Rock Mechanics and Rock Engineering*, vol. 38, no. 1, pp. 21–39, 2005.
- [29] J. Z. Liu, J. Y. Xu, X. C. Lu, L. Zhang, and Z. D. Wang, "Experimental study on dynamic mechanical properties of amphibolites under impact compressive loading," *Chinese Journal of Rock Mechanics and Engineering*, vol. 28, no. 10, pp. 2113–2121, 2009.
- [30] S. Mishra, H. Meena, V. Parashar et al., "High strain rate response of rocks under dynamic loading using split Hopkinson pressure bar," *Geotechnical & Geological Engineering*, vol. 36, no. 1, pp. 531–549, 2018.
- [31] J. D. Campbell and W. G. Ferguson, "The temperature and strain-rate dependence of the shear strength of mild steel," *Philosophical Magazine*, vol. 21, no. 169, pp. 63–82, 1970.
- [32] Z. L. Ge, Q. Sun, L. Xue, and T. Yang, "The influence of microwave treatment on the mode I fracture toughness of granite," *Engineering Fracture Mechanics*, vol. 249, article 107768, 2021.
- [33] J. G. Dash, A. W. Rempel, and J. S. Wettlaufer, "The physics of premelted ice and its geophysical consequences," *Reviews of Modern Physics*, vol. 78, no. 3, pp. 695–741, 2006.
- [34] A. W. Rempel, "Formation of ice lenses and frost heave," *Journal of Geophysical Research: Earth Surface*, vol. 112, no. F2, 2007.
- [35] H. L. Jia, S. Ding, Y. Wang, F. Zi, Q. Sun, and G. S. Yang, "An NMR-based investigation of pore water freezing process in sandstone," *Cold Regions Science and Technology*, vol. 168, article 102893, 2019.
- [36] H. L. Jia, F. Zi, G. S. Yang et al., "Influence of pore water (ice) content on the strength and deformability of frozen argillaceous siltstone," *Rock Mechanics and Rock Engineering*, vol. 53, no. 2, pp. 967–974, 2020.
- [37] T. Wang, Q. Sun, H. L. Jia, J. X. Ren, and T. Luo, "Linking the mechanical properties of frozen sandstone to phase composition of pore water measured by LF-NMR at subzero temperatures," *Bulletin of Engineering Geology and the Environment*, vol. 80, no. 6, pp. 4501–4513, 2021.
- [38] J. M. Xi, G. S. Yang, L. Pang, X. T. Lv, and F. L. Liu, "Experimental study on basic mechanical behaviors of sandy mudstone under low freezing temperature," *Journal of China Coal Society*, vol. 39, no. 7, pp. 1262–1268, 2014.
- [39] Z. L. Ge and Q. Sun, "Acoustic emission characteristics of gabbro after microwave heating," *International Journal of Rock Mechanics and Mining Sciences*, vol. 138, article 104616, 2021.
- [40] Y. Nara, N. Hiroyoshi, T. Yoneda, and K. Kaneko, "Effects of relative humidity and temperature on subcritical crack growth in igneous rock," *International Journal of Rock Mechanics and Mining Sciences*, vol. 47, no. 4, pp. 640–646, 2010.
- [41] J. J. Hu, Q. Sun, and X. H. Pan, "Variation of mechanical properties of granite after high-temperature treatment," *Arabian Journal of Geosciences*, vol. 11, no. 2, pp. 1–8, 2018.
- [42] J. J. Hu, H. P. Xie, Q. Sun, C. B. Li, and G. K. Liu, "Changes in the thermodynamic properties of alkaline granite after cyclic quenching following high temperature action," *International Journal of Mining Science and Technology*, vol. 31, no. 5, pp. 843–852, 2021.
- [43] I. Ohno, "Temperature variation of elastic properties of α -quartz up to the α - β transition," *Journal of Physics of the Earth*, vol. 43, no. 2, pp. 157–169, 1995.
- [44] I. Ohno, K. Harada, and C. Yoshitomi, "Temperature variation of elastic constants of quartz across the α - β transition," *Physics and Chemistry of Minerals*, vol. 33, no. 1, pp. 1–9, 2006.
- [45] W. H. Somerton and G. D. Boozer, "Thermal characteristics of porous rocks at elevated temperatures," *Journal of Petroleum Technology*, vol. 12, no. 6, pp. 77–81, 1960.
- [46] H. C. Heard and L. Page, "Elastic moduli, thermal expansion, and inferred permeability of two granites to 350°C and 55 megapascals," *Journal of Geophysical Research*, vol. 87, no. B11, pp. 9340–9348, 1982.
- [47] H. F. Wang, B. P. Bonner, S. R. Carlson, B. J. Kowallis, and H. C. Heard, "Thermal stress cracking in granite," *Journal of Geophysical Research*, vol. 94, no. B2, pp. 1745–1758, 1989.
- [48] G. Wu, D. Y. Wang, and S. T. Zhai, "Acoustic emission characteristics of sandstone after high temperature under uniaxial compression," *Rock and Soil Mechanics*, vol. 33, no. 11, pp. 3237–3242, 2012.
- [49] F. Q. Gong, X. F. Si, X. B. Li, and S. Y. Wang, "Dynamic triaxial compression tests on sandstone at high strain rates and low confining pressures with split Hopkinson pressure bar," *International Journal of Rock Mechanics and Mining Sciences*, vol. 113, pp. 211–219, 2019.
- [50] Y. Hou, *Experimental Study on Mechanical Properties of Deep Fine Sandstone under Impact Load*, Henan University Technology, Henan, China, 2015.
- [51] S. Liu and J. Y. Xu, "Effect of strain rate on the dynamic compressive mechanical behaviors of rock material subjected to high temperatures," *Mechanics of Materials*, vol. 82, pp. 28–38, 2015.
- [52] Y. Liu, K. Pan, and X. G. Zhou, "Study on impact failure properties of post-peak cracked sandstone," *Journal of West Anhui University*, vol. 34, no. 2, pp. 123–127, 2018.

- [53] X. C. Lv, J. Y. Xu, H. H. Ge, D. H. Zhao, and E. L. Bai, "Effects of confining pressure on mechanical behaviors of sandstone under dynamic impact loads," *Chinese Journal of Rock Mechanics and Engineering*, vol. 29, no. 1, pp. 193–201, 2010.
- [54] D. F. Ma, Y. Hou, D. N. Chen, H. R. Wang, and G. Y. Wang, "Compression tests and failure characteristic research of fine sandstones under impact loading," *Acta Armamentarii*, vol. 37, no. 2, pp. 42–48, 2016.
- [55] B. Mahanta, P. G. Ranjith, V. Vishal, and T. N. Singh, "Temperature-induced deformational responses and microstructural alteration of sandstone," *Journal of Petroleum Science and Engineering*, vol. 192, article 107239, 2020.
- [56] P. Wang, J. X. Xu, S. Liu, and T. F. Chen, "Research on dynamic mechanical properties of sandstone at high temperature," *Acta Armamentarii*, vol. 32, no. 2, pp. 203–208, 2013.
- [57] P. Wang, J. Y. Xu, S. H. Liu, and H. Y. Wang, "Dynamic mechanical properties and deterioration of red-sandstone subjected to repeated thermal shocks," *Engineering Geology*, vol. 212, pp. 44–52, 2016.
- [58] T. B. Yin, X. B. Li, Z. L. Zhou, L. Hong, and Z. Y. Ye, "Study on mechanical properties of post-high-temperature sandstone," *Chinese Journal of Underground Space and Engineering*, vol. 12, no. 6, pp. 1060–1063, 2007.
- [59] T. B. Yin, X. B. Li, B. Wang, Z. Q. Ying, and J. F. Jin, "Mechanical properties of sandstones after high temperature under dynamic loading," *Chinese Journal of Geotechnical Engineering*, vol. 33, no. 5, pp. 777–784, 2011.
- [60] Y. Zhang, Q. W. Li, M. Li, and M. Cui, "Research into the dynamic mechanical characteristics of sandstone under different strain rate," *China Mining Magazine*, vol. 24, no. 2, pp. 162–166, 2015.
- [61] Q. S. Liu, G. M. Xu, Y. H. Hu, and X. Chang, "Study on basic mechanical behaviors of rocks at low temperatures," *Key Engineering Materials*, vol. 306–308, pp. 1479–1484, 2006.
- [62] C. Li, G. Y. Cao, Y. W. Wu, Y. S. Huang, and Z. M. Huang, "Experimental study on frozen uniaxial strength of Jurassic sandstone in western China," *Journal of Henan University of Urban Construction*, vol. 28, no. 2, pp. 39–44, 2019.
- [63] H. Y. Wang and Q. Zhang, "Mechanical behavior of frozen porous sandstone under uniaxial compression," *Geofluids*, vol. 2021, Article ID 1872065, 6 pages, 2021.
- [64] T. L. Blanton, "Effect of strain rates from 10^{-2} to 10 sec^{-1} in triaxial compression tests on three rocks," *International Journal of Rock Mechanics and Mining Sciences & Geomechanics Abstracts*, vol. 18, no. 1, pp. 47–62, 1981.
- [65] J. Z. Liu, J. Y. Xu, X. C. Lv, D. H. Zhao, and B. L. Leng, "Experimental study on dynamic mechanical properties of amphibolites, sericite-quartz schist and sandstone under impact loadings," *International Journal of Nonlinear Encees and Numerical Simulation*, vol. 13, no. 2, pp. 209–217, 2012.
- [66] J. J. Zhu, X. B. Li, F. Q. Gong, S. M. Wang, and W. He, "Experimental test and damage characteristics of sandstone under uniaxial impact compressive loads," *Journal of Central South University*, vol. 43, no. 7, pp. 2701–2707, 2012.
- [67] P. Gautam, A. K. Verma, M. K. Jha, K. Sarkar, T. N. Singh, and R. K. Bajpai, "Study of strain rate and thermal damage of Dholpur sandstone at elevated temperature," *Rock Mechanics and Rock Engineering*, vol. 49, no. 9, pp. 3805–3815, 2016.
- [68] G. H. Zheng, J. Y. Xu, P. Wang, S. Liu, and H. Y. Wang, "Research on strain rate effects of red-sandstone under water-rock coupling," *Chinese Journal of Underground Space and Engineering*, vol. 13, no. 1, pp. 79–85, 2017.
- [69] J. H. Wu, H. B. Wang, Q. Zong, and Y. Xu, "Experimental investigation of dynamic compression mechanical properties of frozen fine sandstone," *Advances in Civil Engineering*, vol. 2020, Article ID 8824914, 10 pages, 2020.

Research Article

The Responses of Injection Pressure and Fracture Width during Height Extension in Sand-Mud Interbed Reservoirs in the Dongsheng Gas Field

Di Wang^{1,2,3}, Haibo Wang^{1,2,3}, Fengxia Li^{1,2,3}, Fuhu Chen⁴ and Xinchun Zhu⁴

¹State Key Laboratory of Shale Oil and Gas Enrichment Mechanisms and Effective Development, Beijing 100083, China

²National Energy Shale Oil Research and Development Center, Beijing 100083, China

³SINOPEC Petroleum Exploration and Production Research Institute, Beijing 102206, China

⁴Petro-Engineering Research Institute of Sinopec North China Oil and Gas Branch, Zhengzhou 450006, China

Correspondence should be addressed to Di Wang; wangdi304@126.com

Received 9 September 2021; Accepted 12 October 2021; Published 28 November 2021

Academic Editor: Yu Wang

Copyright © 2021 Di Wang et al. This is an open access article distributed under the Creative Commons Attribution License, which permits unrestricted use, distribution, and reproduction in any medium, provided the original work is properly cited.

The Dongsheng gas field is characterized by low porosity and low permeability. Its principal producing reservoir is the H-1 zone, belonging to the Lower Shihezi Formation. Sand is the main lithology in the H-1 zone, while mud interlayers are also well developed in a vertical direction. As a result, the reservoir is a sand-mud interbed, which brings difficulty to fracture height extension. In order to understand the process of fracture height growth in a sand-mud interbed reservoir and obtain the responses of injection pressure and fracture width during a hydraulic fracturing, a hydromechanical-coupled model is established. Mud interlayers are fully considered and a cohesive zone model is adopted to deal with fracture propagation. Numerical results show that the fracture extends quickly to the sand-mud interface after initiation and breaks through rather than propagating along the interfaces. Pressure and width both increase continuously when fracture propagates in the mud interlayer. High-viscosity and high-injection rates are helpful for the fracture to break through the mud interlayer, especially at an early period. When the mud interlayers are asymmetric, pressure and width fluctuate several times once fracture propagates inside and breaks through the mud interlayer. Perforations close to the thinner mud interlayer can increase the fracture width and reduce fracturing risks.

1. Introduction

The Dongsheng gas field belongs to the Erdos basin, which locates in North China. The principal producing reservoir of the Dongsheng gas field is Lower Shihezi Formation, especially the H-1 zone. Without too many complex structures, the formation is flat overall and has a good continuity horizontally. The thickness of the H-1 zone ranges from 10 m to 50 m and there are multiple gas formations in the vertical direction.

The main sedimentary system of the H-1 zone includes the alluvial fan and braided stream. As a result, the lithology is very complicated, including pebbly sandstone, coarse sandstone, medium sandstone, fine sandstone, siltstone, and dark mud. Particularly, the coarse sandstone, medium sandstone, and fine sandstone are the main reservoirs.

Due to the influence of river channel migration and the variation of the flood scale, barely permeable and impermeable interlayers are well developed vertically in the H-1 zone [1]. The most common interlayers in the H-1 zone are mud and property interlayers [2], as shown in Figure 1. The lithologies of mud interlayers have the characteristic of high clay content, such as pure mudstone, silty mudstone, and argillaceous siltstone, while the lithologies of the property interlayer are primarily siltstone or argillaceous fine siltstone. Compared with the mud interlayer, the property interlayer has higher porosity and permeability but they are still below the lower limit of the effective reservoirs. In this paper, only mud interlayers are considered to investigate its influence on fracture height growth. The thickness of the mud interlayer varies widely from several centimeters to

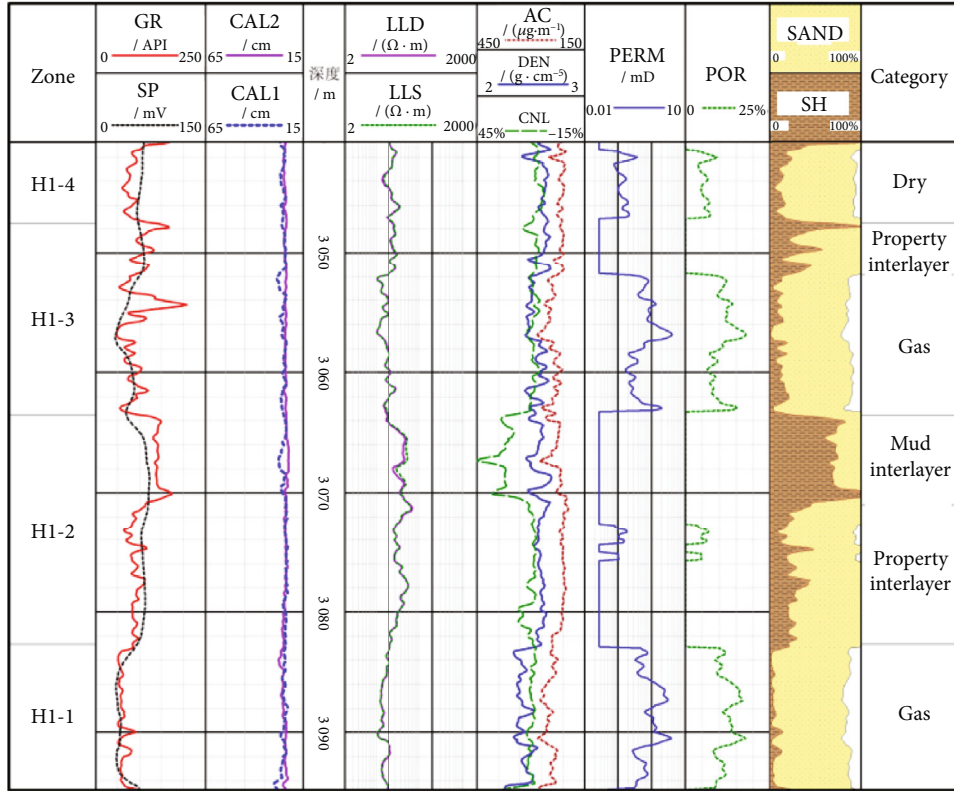


FIGURE 1: The characteristics of the H-1 zone in the Dongsheng gas field [3].

25 m. The thick mud interlayers can be treated as caps which can prevent fracture propagation.

The lithologies of gas reservoirs are also complex, including coarse sandstone, medium sandstone, and fine sandstone. The porosity ranges from 5.0% to 16.9% and the permeability is mainly in the range from 0.3 mD to 0.9 mD [4, 5]. Both porosity and permeability are very low, and hydraulic fracturing is the most effective way to develop the Dongsheng gas field. Therefore, it is especially important to understand fracture height growth and specify the responses of injection pressure and fracture width during fracture propagation. In this paper, a hydromechanical coupled numerical model about fracture height extension is established based on the reservoir characteristics in the Dongsheng gas field taking into account of mud interlayers and stress difference. The numerical results illustrate the process of fracture height growth and are instructive to the design of a hydraulic fracturing.

2. Model

Classic linear elastic fracture mechanics (LEFM) is a widely used method to evaluate fracture propagation. When the stress intensity factor (SIF) at fracture tip is larger than fracture toughness which is an inherent property of the solid material, fracture initiates and propagates [6, 7]. At the fracture tip, there is a stress singularity which is described by SIF in LEFM. But the SIF is usually difficult to obtain and this stress singularity bothers numerical simulations at times.

Instead of using the classic LEFM to deal with an elastic crack tip region where stress singularity exists, the cohesive zone model [8–11] assumes the existence of a fracture process zone (where the rock has yielded or experienced micro-cracking) in front of the material crack tip, which is governed by a traction-separation law. The stress singularity at the crack tip is avoided in cohesive zone models through this constitutive law. In this way, the cohesive zone model provides an alternative approach to explicitly simulate the fracture process near the tip and is often applied in modeling hydraulic fracturing.

2.1. Cohesive Zone Model. In this work, we use a hydromechanical model utilizing the finite element method with a special zero-thickness interface element based on the cohesive zone model which has shown its effectiveness in previous work [12–15].

Indeed, there are numerous kinds of T-S models [16, 17] and the classic bilinear traction-separation criteria [18–20] are used in this paper, as shown in Figure 2. These criteria evaluate the stress ratios between a given stress value and the peak nominal stress value in each of the three directions and is based on a quadratic combination of all three ratios [21], as shown in equation (1) as follows:

$$\left(\frac{\langle t_n \rangle}{t_n^0}\right)^2 + \left(\frac{t_{s1}}{t_{s1}^0}\right)^2 + \left(\frac{t_{s2}}{t_{s2}^0}\right)^2 = 1, \quad (1)$$

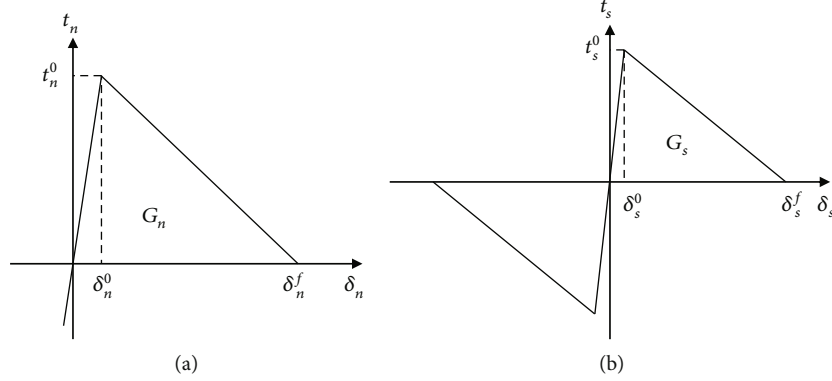


FIGURE 2: Bilinear traction-separation constitutive law for (a) tensile and (b) shear failure of the cohesive element.

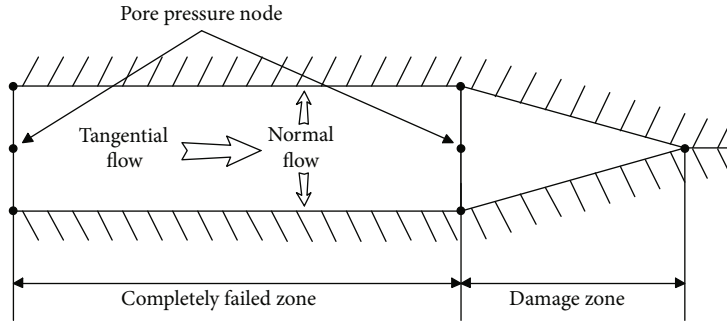


FIGURE 3: Sketch of fluid flow within cohesive elements.

where t_n , t_{s1} , t_{s2} are nominal stress, first direction shear stress, and second direction shear stress. t_n^0 , t_{s1}^0 , t_{s2}^0 represent the peak values of the nominal stress when the deformation is either purely normal to the interface or purely in the first or the second shear direction. $\langle \cdot \rangle$ is the Macaulay bracket with the usual interpretation $\langle t_n \rangle = t_n$ if $t_n \geq 0$ and $\langle t_n \rangle = 0$ if $t_n < 0$.

The fracture initiation and propagation are natural outcomes of a cohesive zone model. After cohesive element debonds, fluid flows in the hydromechanical interface and transmit pressure on the cohesive element, as shown in Figure 3.

2.2. Fluid Flow. We assume that the rock surrounding the hydraulic fractures is permeable. Leakoff and poroelastic effects are considered during fracture propagation. Therefore, the fluid flow can be divided into three processes: flow inside the fracture, leakage through fracture, and seepage in the matrix.

As to incompressible fluid, flow in the hydromechanical cohesive interface is derived from the fluid mass balance equation:

$$\frac{\partial w}{\partial t} + \nabla \cdot \mathbf{q} + q_L = Q(t)\delta(x, y), \quad (2)$$

where w is normal opening, which equals to the displacement jump in the normal direction of the interface, \mathbf{q} is

the longitudinal fluid flux, q_L is fluid leakoff, $Q(t)$ is the source term, and $\delta(x, y)$ is the Dirac delta function.

The lubrication equation for fluid flow between parallel plates is used to simulate flow in the fracture. It is given as follows:

$$\mathbf{q} = \mathbf{v}w = -\frac{w^3}{12\mu} \nabla p, \quad (3)$$

where \mathbf{v} is the average fluid velocity over the cross-section of the hydraulic fracture, μ is the viscosity of the Newtonian fluid, and p is fluid pressure inside the fracture.

Combining equations (2) and (3), we obtain the equation for fluid flow in a hydraulic fracture:

$$\frac{\partial w}{\partial t} - \nabla \cdot \left(\frac{w^3}{12\mu} \nabla p \right) + q_L = Q(t)\delta(x, y). \quad (4)$$

For the seepage in the matrix, according to the theory of poroelasticity, the continuity equation utilized in numerical formulation is as follows [22]:

$$\nabla \cdot \left(\frac{k}{\gamma_l} (\nabla p_0 - \mathbf{b}_l) \right) + \mathbf{m}^T \dot{\boldsymbol{\varepsilon}} = 0, \quad (5)$$

where k is matrix permeability coefficient, γ_l is specific weight of liquid, p_0 is the pore pressure, \mathbf{b}_l is the body force

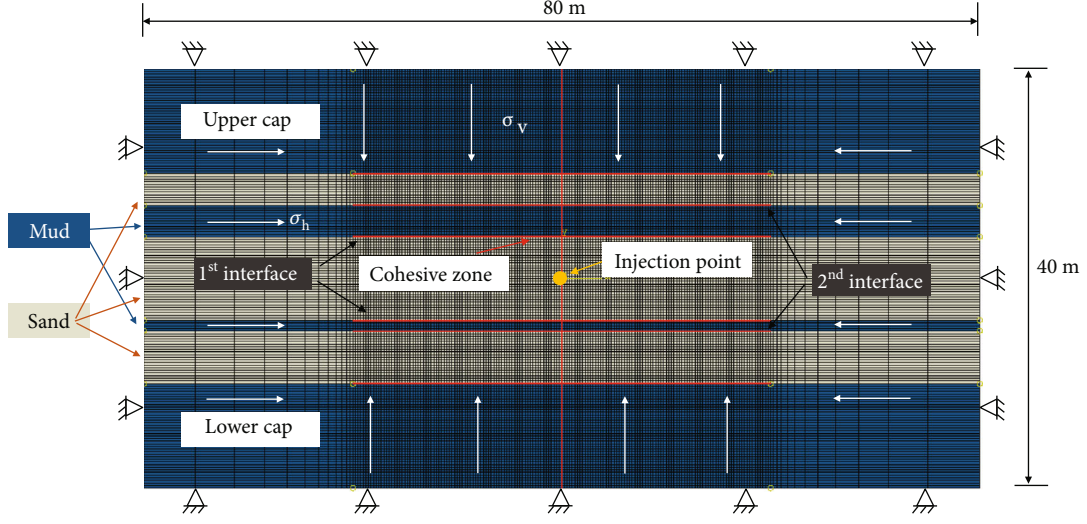


FIGURE 4: Sketch of the sand-mud interbed numerical model.

of the liquid phase, $\boldsymbol{\varepsilon}$ is the strain tensor, and $\mathbf{m} = [1, 1, 1, 0, 0, 0]$.

In addition, fluid leakage through the fracture wall can be expressed by the following:

$$q_L = C_L(p - p_0), \quad (6)$$

where C_L is leakoff coefficient.

2.3. Rock Deformation. The governing equations of rock deformation include the equilibrium equation, geometric equation, and constitutive equation [23, 24]. The equilibrium equation is written as follows:

$$\nabla \cdot \boldsymbol{\sigma} + \mathbf{b} = 0, \quad (7)$$

where $\boldsymbol{\sigma}$ is stress tensor and \mathbf{b} is body force vector of the rock.

According to Biot's theory, effective stress can be expressed as follows:

$$\boldsymbol{\sigma}' = \boldsymbol{\sigma} + \alpha p_0 \mathbf{I}, \quad (8)$$

where $\boldsymbol{\sigma}'$ is the effective stress tensor, α is the Biot coefficient, and \mathbf{I} is the Kronecker delta.

The geometric equation is written as follows:

$$\boldsymbol{\varepsilon} = \frac{1}{2} (\nabla \mathbf{u} + \nabla \mathbf{u}^T). \quad (9)$$

The constitutive relationship can be expressed as

$$\begin{aligned} \boldsymbol{\sigma} &= \lambda \varepsilon_{\text{vol}} \boldsymbol{\delta} + 2G \boldsymbol{\varepsilon} - C \zeta \boldsymbol{\delta}, \\ p &= C \varepsilon_{\text{vol}} - M \zeta, \end{aligned} \quad (10)$$

where λ and G are the Lamé parameters of the porous material, while C and M are additional elastic moduli required to describe a two-phase medium. ε_{vol} is the volumetric strain. ζ is a strain parameter describing the volumetric deformation

TABLE 1: Rock mechanical properties for simulation.

Property	Fine sand	Coarse sand	Mud cap/interlayer
Young's modulus (GPa)	35	59	20
Poisson's ratio	0.2	0.25	0.3
Tensile strength (MPa)	2.5	2.4	7.51
Cohesion (MPa)	36	6.4	13
Friction angle (°)	19	48	18

TABLE 2: Basic parameters for simulation.

Category	Sand	Mud cap/interlayer
Damage displacement (m)	10^{-4}	10^{-4}
Porosity (%)	10	1
Permeability (mD)	1	0.1
Leakoff coefficient (m/Pa·s)	10^{-13}	10^{-14}
Vertical stress (MPa)	75	75
Minimum horizontal stress (MPa)	60	64
Pore pressure (MPa)		30
Fluid viscosity (mPa·s)		2
Injection rate (m ² /s)		6×10^{-4}

of the fluid relative to that of the solid. $\boldsymbol{\delta}$ is the Kronecker function.

2.4. Model Construction. In this study, a sand-mud interbed model is established. In Figure 4, the whole model is 80 m × 40 m in size. The thicknesses of upper and lower caps are both 10 m. Between the upper and lower caps, there are two asymmetric mud interlayers as the thicknesses of the upper and lower interlayers are 3 m and 1 m, respectively. The first and second interfaces are defined according to the sequence when hydraulic fracture is encountered. Injection point is right at the center of the model. Cohesive zones are presented along the fracture height path and sand-mud

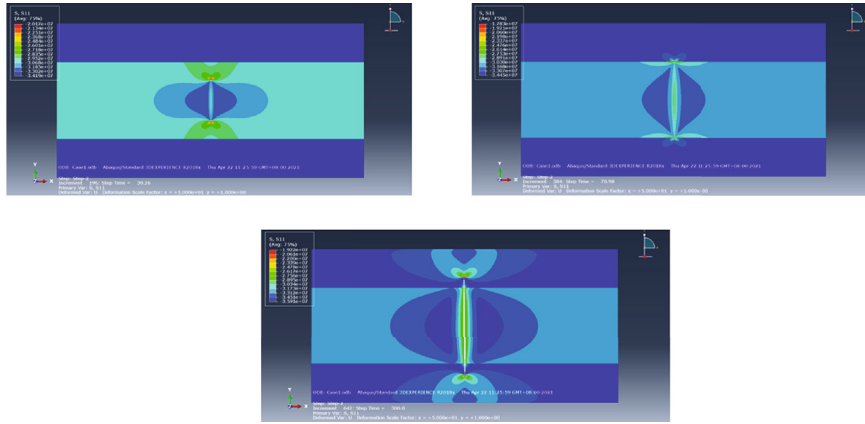


FIGURE 5: Height growth process in the reservoir without mud interlayers.

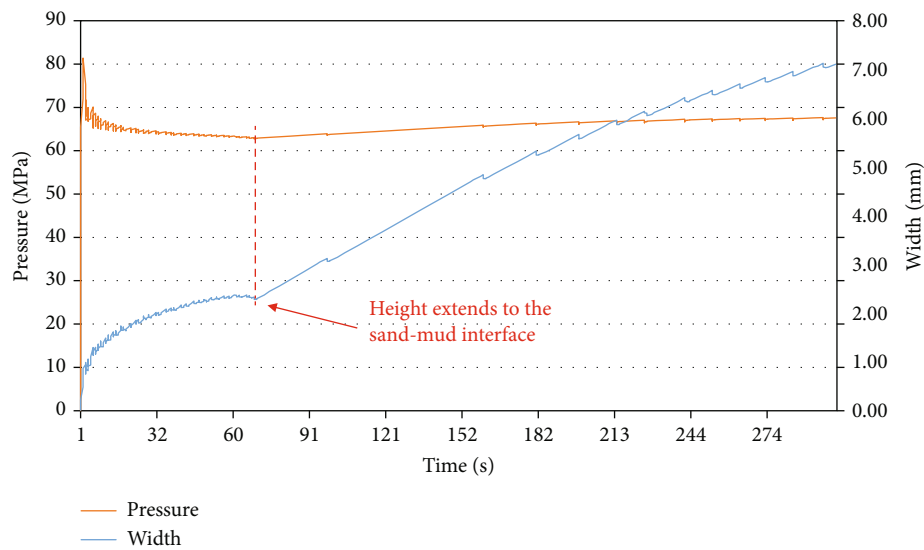
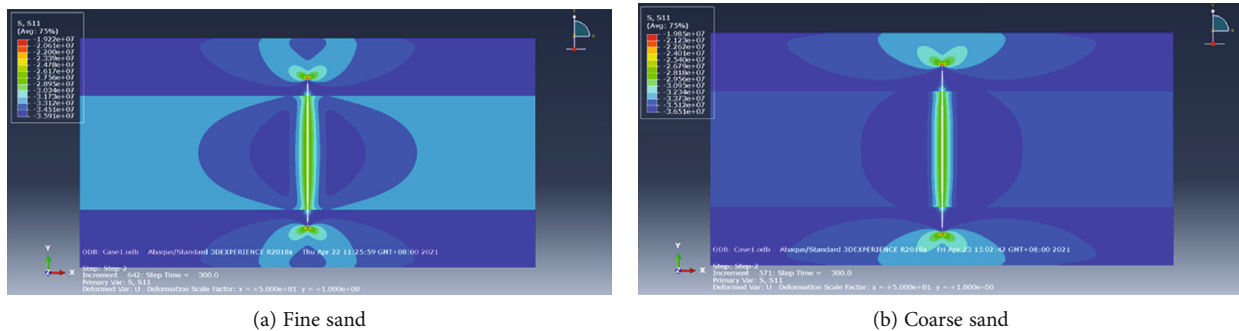


FIGURE 6: The responses of injection pressure and fracture width during height growth in the reservoir without mud interlayers.



(a) Fine sand

(b) Coarse sand

FIGURE 7: The influence of the rock property on height growth.

interfaces in order to investigate fracture height growth behavior at sand-mud interfaces.

Rock mechanical parameters adopted in numerical simulations are shown in Table 1, and they are all obtained from experimental measurements using downhole cores from the Dongsheng gas field. In order to investigate the influence of

rock mechanics on fracture height growth, both fine sand and coarse sand are tested.

Table 2 includes basic parameters except for rock mechanics. The reservoir parameters are all used according to the Dongsheng gas field so that the numerical models are consistent with the actual reservoir conditions as much as possible.

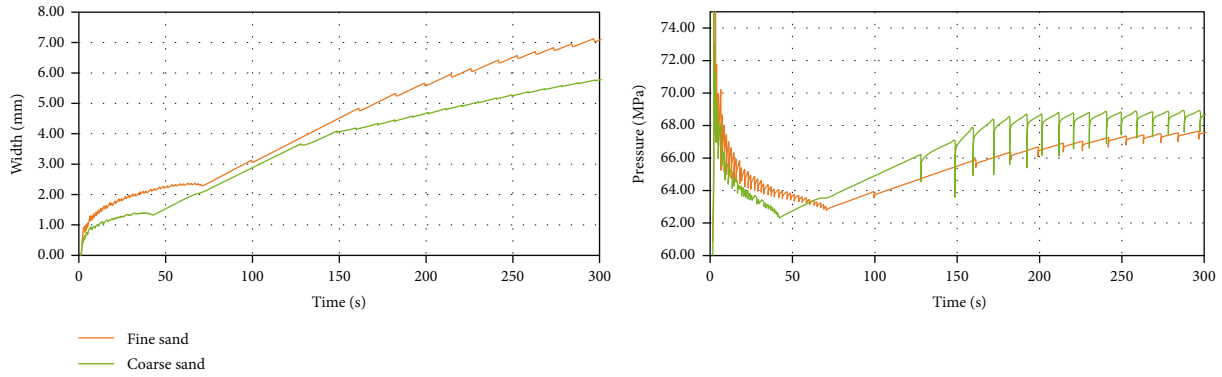


FIGURE 8: The influence of the rock property on injection pressure and fracture width.

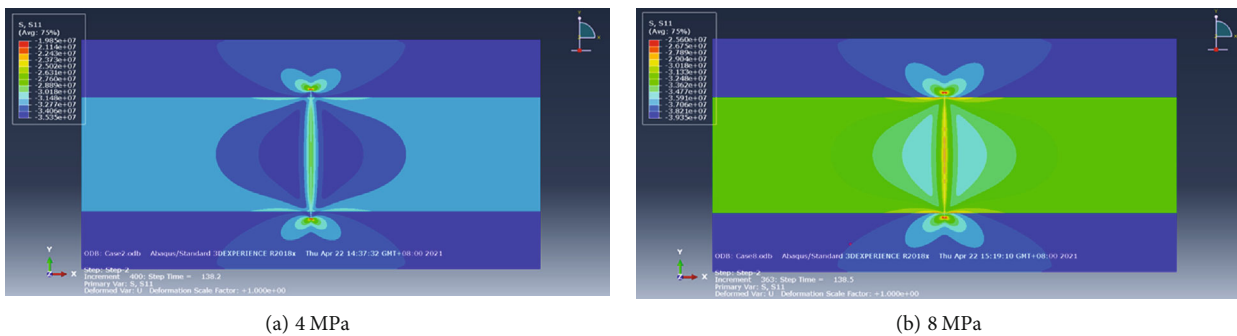


FIGURE 9: The influence of minimum horizontal stress difference on height growth.

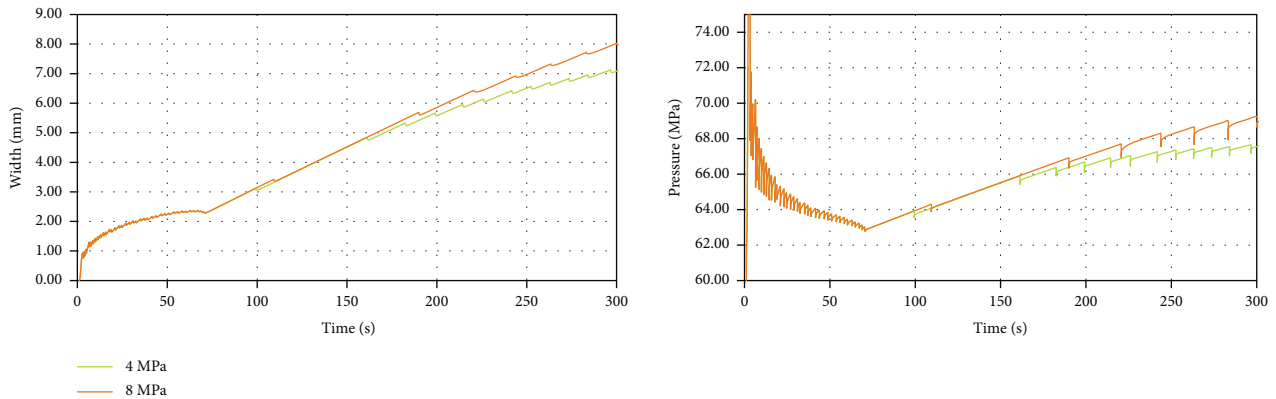


FIGURE 10: The influence of minimum horizontal stress difference on injection pressure and fracture width.

3. Results

In order to clearly illustrate about fracture height growth in sand, we first study the cases neglecting mud interlayers. Afterwards, we consider two symmetric mud interlayers whose thicknesses are both 3 m. In the end, two asymmetric mud interlayers as shown in Figure 4 are taken into account which is in accordance with the characteristics of the Dongsheng gas field.

3.1. Reservoirs without Mud Interlayers. Figure 5 shows fracture height extension in sand. At the sand-mud interface, the fracture passes through directly and extends to the cap. This

is because the reservoir shear strength is much larger than tensile strength and tensile failure dominates. Besides, when fluid wants to flow into the interface, it needs to overcome overburden stress or vertical stress, which is very difficult because the reservoir is deeper than 3000 m. But at the interface, it still can be observed that stress discontinuity exists.

Figure 6 clearly shows the fracture width and pressure responses during propagation. When fracture propagates in sand, pressure drops rapidly after initiation and keeps being smooth, while the width increases slowly. When the fracture reaches the interface and extends in the cap, propagation slows down. As a result, pressure increases and width

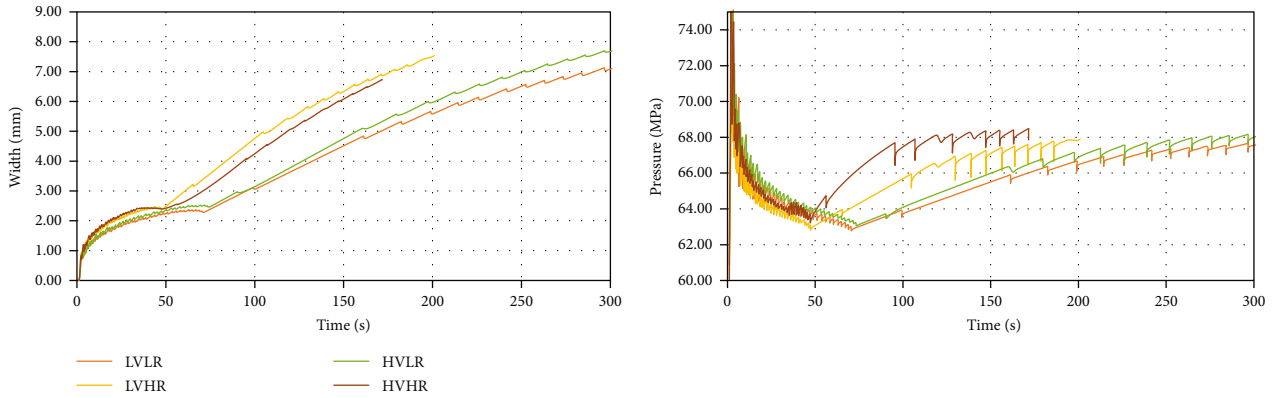


FIGURE 11: The influence of fluid viscosity and injection rates on injection pressure and fracture width.

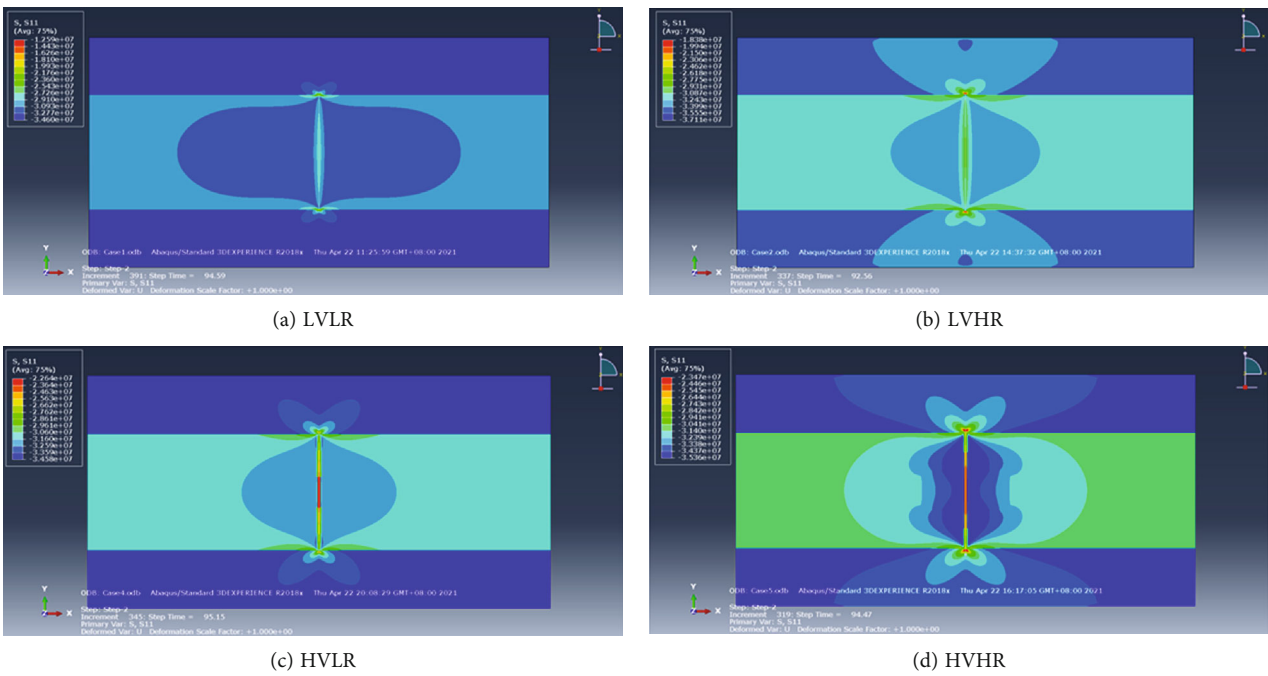


FIGURE 12: The influence of fluid viscosity and injection rates on height growth.

expands. In reality, when pressure is large enough, fracture will propagate horizontally in sand rather than keep the extension in the cap. The zigzags shown in Figure 6 are due to the mesh size used in the numerical model. With smaller meshes, the lines will be much more smooth but the calculation will be tremendous. Therefore, the element size along fracture is 0.25 m in this model and calculation accuracy is not affected.

3.1.1. The Effect of Sand Property. Figures 7 and 8 show that the fracture propagates in fine and coarse sands, respectively. With a lower tensile strength, the fracture propagates much easier in coarse sand. As a result, pressure is lower and width is smaller. However, when the fracture extends to the interface, pressure in coarse sand increases rapidly and surpasses that in fine sand. This is because the elastic modulus of coarse sand is lower. Under the same condition, fracture width is smaller and the friction along fracture is higher. If

the fracture continuously propagates in the cap, it requires higher pressure to overcome friction.

3.1.2. The Effect of Minimum Horizontal Stress Difference between Cap and Sand. Before the fracture reaches the interface, the responses of pressure and width are exactly the same. But after fracture extends into cap with higher stress, pressure increases higher and fracture opens wider, as shown in Figures 9 and 10.

3.1.3. The Effects of Fluid Viscosity and Injection Rate. We consider four cases to investigate the influence of fluid viscosity and injection rate on height growth, and they are the low viscosity and low injection rate (LVLR), low viscosity and high injection rate (LVHR), high viscosity and low injection rate (HVLR), and high viscosity and high injection rate (HVHR). Compared with viscosity, it seems that the injection rate has the most influence on fracture width.

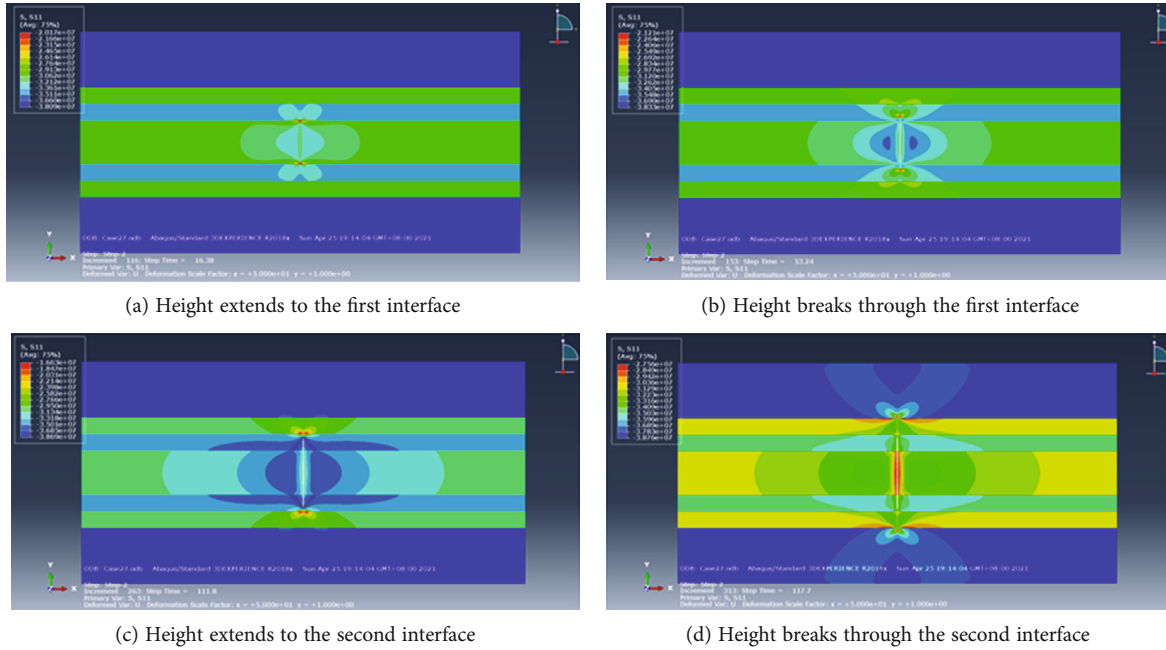


FIGURE 13: Height growth process in the reservoir with symmetric mud interlayers.

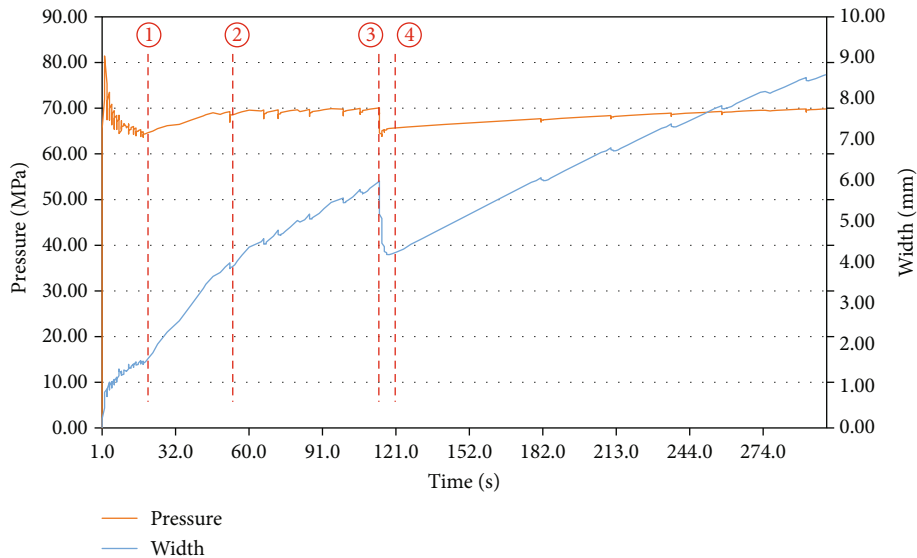


FIGURE 14: The responses of injection pressure and fracture width during height growth in the reservoir with symmetric mud interlayers.

Figure 11 clearly shows that with the high injection rate, fracture width is larger. At the same time, when the fracture extends to the interface, pressure increases rapidly. With higher viscosity, fluid friction along the fracture is higher, as shown in Figures 12(c) and 12(d).

3.2. Reservoirs within Symmetric Mud Interlayers. In this section, two symmetric mud interlayers are inserted in sand. Figure 13(a) shows that fracture extends to the first interface which is corresponding to ① in Figure 14 when fracture pressure and width are about to increase rapidly. The pressure keeps increasing until ② when the fracture tip extends into the mud interlayer. While the fracture propagates in

the mud interlayer, it seems that pressure no longer increases. Due to the high in situ stress of the mud interlayer, fracture propagation velocity slows down at the moment and friction along the fracture reduces. Therefore, pressure inside the fracture is much more uniform and pressure at the injection point tends to be similar to the pressure at the tip of fracture. As a result, fracture width keeps growing until ③, when the fracture breaks through the second interface and exits the mud interlayer. Afterwards, fracture extends to the interface of sand and cap. But it is a very short period from ③ to ④. This is because when the fracture propagates inside the mud, it requires a higher pressure. When the fracture leaves the mud and goes into the sand, the high

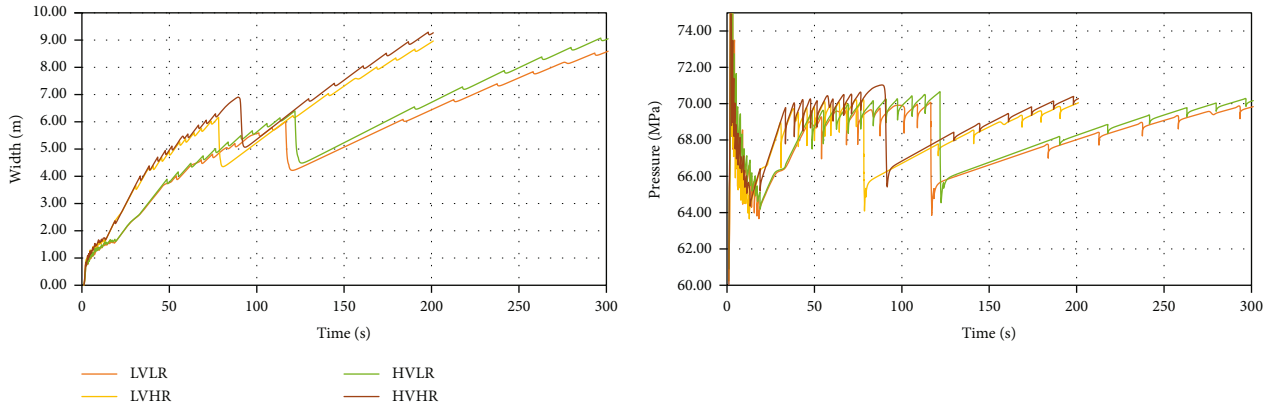


FIGURE 15: The influence of fluid viscosity and injection rates on injection pressure and fracture width.

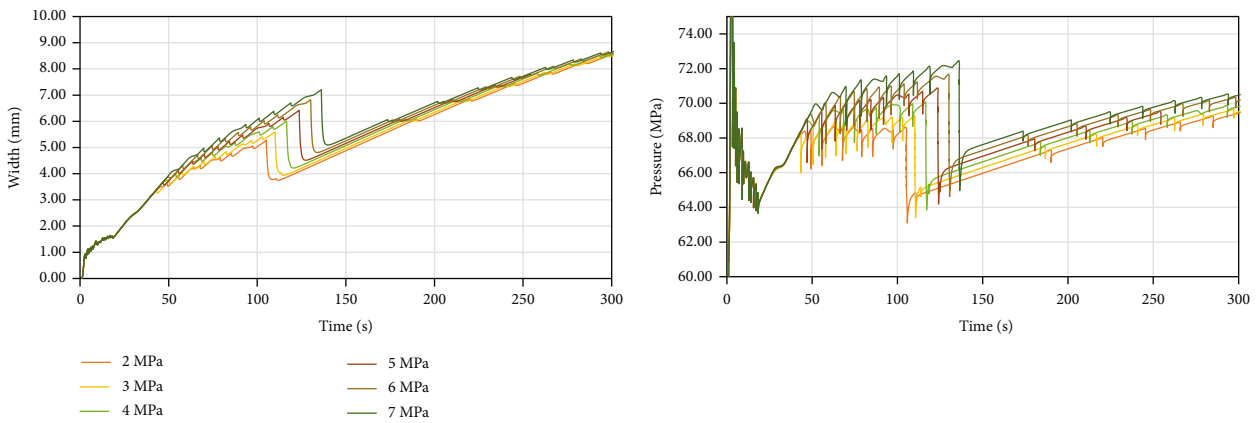


FIGURE 16: The influence of stress difference between the mud interlayer and sand on injection pressure and fracture width.

pressure will accelerate fracture growth. Therefore, the fracture reaches the sand and cap interface quickly as shown in Figure 13(c). In the end, the fracture extends inside the cap and the pressure increases integrally although the pressure at the injection point does not rise up obviously, which results in fracture width increasing continuously.

3.2.1. Effect of Fluid Viscosity and Injection Rate. When the mud interlayers are imbedded in sand, the treatment parameters affect height growth differently. With a high injection rate, the fracture propagates to the first interface and breaks through the mud interlayer quickly. As shown in Figure 15, it seems that under the low fluid viscosity condition, the pressure required to break through mud interlayer is a little bit smaller. This may be resulted from the lower friction when fluid viscosity is low. Under the high viscosity and high injection rate conditions, pressure inside the fracture is the highest. Therefore, when we hope that the fracture breaks through mud interlayers in sand, high viscosity and high injection rate are the best choices especially at the early period.

3.2.2. Effect of Stress Difference between Sand and Mud Interlayers. As shown in Figure 16, before the fracture reaches the first interface, the responses of pressure and

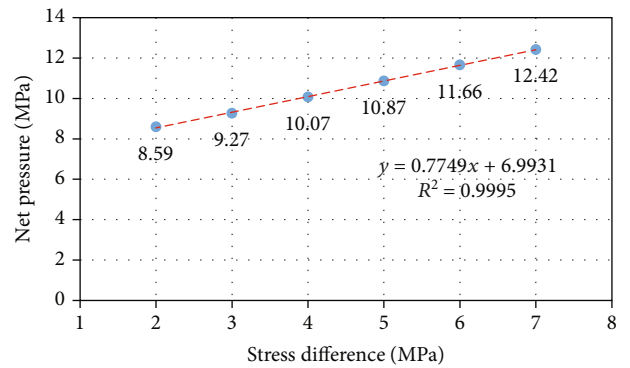


FIGURE 17: The relationship between required net pressure and stress difference.

width are exactly the same. But when the stress difference between sand and mud interlayers increases, the pressure required to break through the mud interlayer is higher and the fracture opens wider. Besides, it takes more time to break through the mud interlayers.

As shown in Figure 17, when the stress difference increases from 2 MPa to 7 MPa, the net pressure required to break through the mud interlayer rises up linearly from 8.59 MPa to 12.42 MPa. The increment of net pressure,

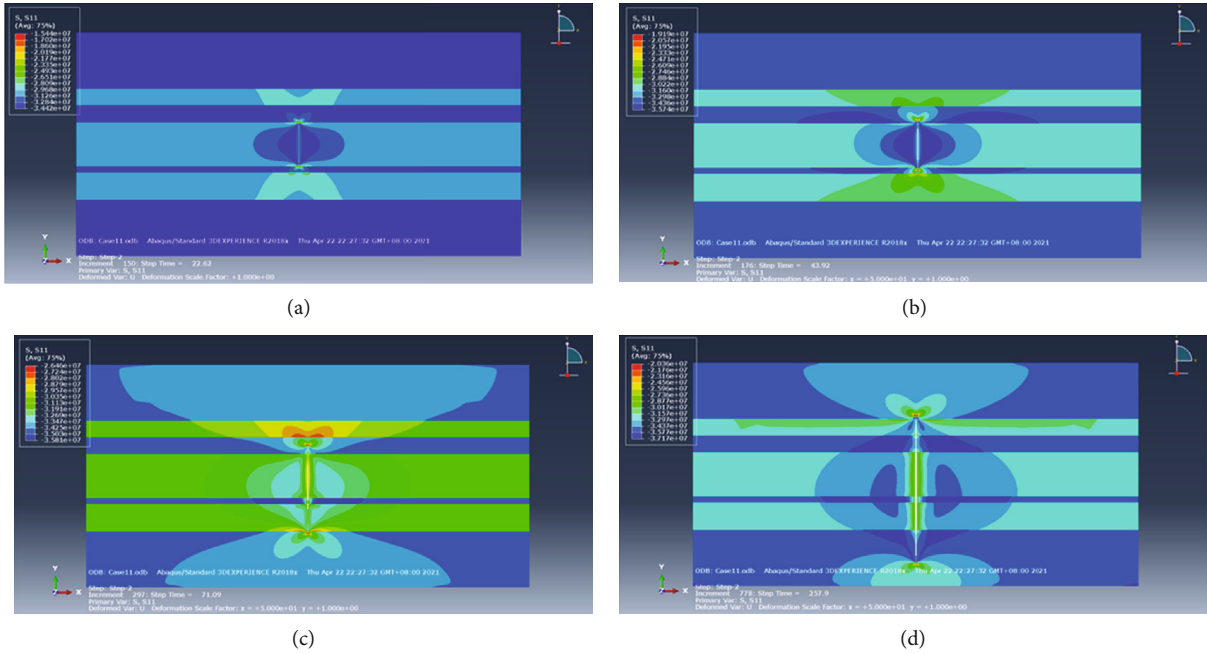


FIGURE 18: Height growth process in the reservoir with asymmetric mud interlayers: (a) height extends to the first interface, (b) height breaks through the first interface, (c) the lower branch breaks through the mud interlayer and extends to the lower cap, and (d) the upper branch extends to the upper cap.

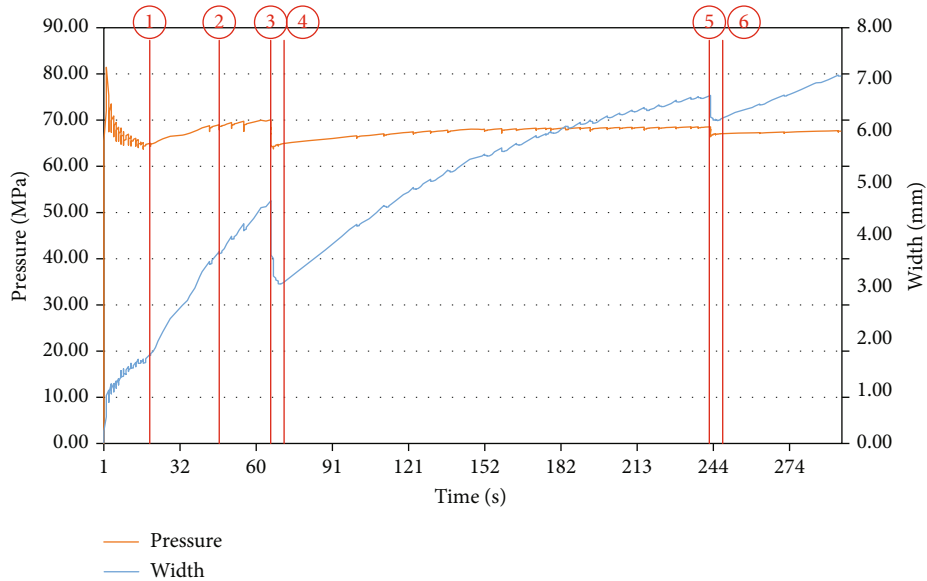


FIGURE 19: The responses of injection pressure and fracture width during height growth in the reservoir with asymmetric mud interlayers.

3.83 MPa, is smaller than the increment of stress difference, 5 MPa. This is because when the minimum horizontal stress is large, it becomes much more difficult for fracture to break through. Fracture propagation slows down and fluid friction along the fracture drops. As a result, pressure inside the fracture trends to be uniform and only a small increment of net pressure can keep the fracture propagating.

3.3. Reservoirs within Asymmetric Mud Interlayers. Asymmetric mud interlayers are more common in reality and are considered in this section. The numerical model is the

same as shown in Figure 4. The distances between the injection point to the upper and lower first interface are the same.

It can be observed that fracture extension becomes much more complex from that in Figure 18 and the process is divided into several stages, as shown in Figure 19. The upper and lower fracture branches reach ① and breaks through the first interface ② at the same time. But the stress distribution is no longer in symmetry from the reservoir top to bottom due to the influence of asymmetric mud interlayers. Afterwards, both upper and lower branches extend in the mud interlayer. But the lower branch quickly reaches the second

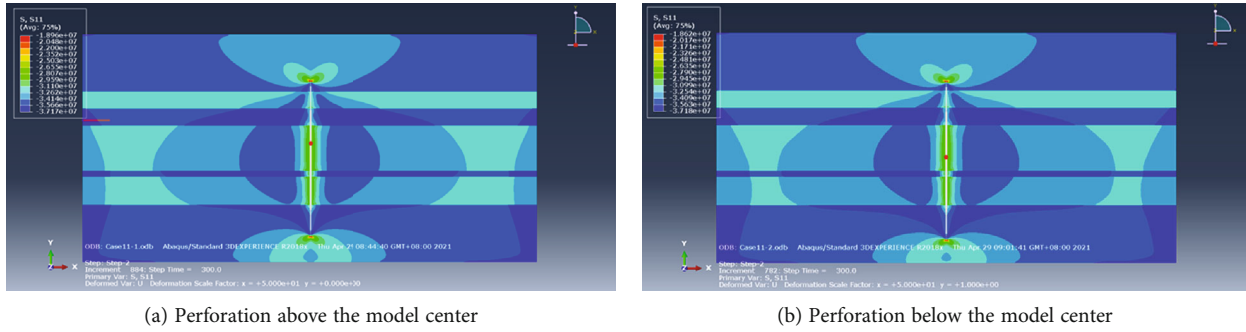


FIGURE 20: The influence of the perforation position on height growth.

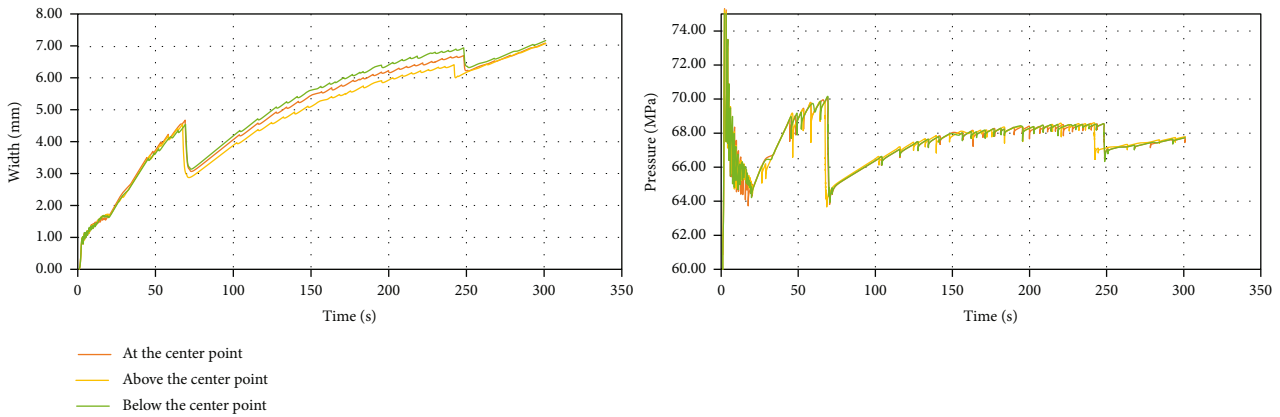


FIGURE 21: The influence of the perforation position on injection pressure and fracture width.

interface and the fracture width keeps growing ③. Right after the lower branch breaks through the lower thin mud interlayer, it goes quickly to the interface between sand and lower cap ④. Figure 18(c) shows at the moment when the lower branch reaches the cap interface, the upper branch is still inside the upper mud interlayer and does not break through. As both branches extend in mud, the pressure increases continuously. Finally, the upper branch breaks through the second interface and the width decreases immediately once more ⑤. As the number of mud asymmetric interlayers increases, the fluctuation of pressure and width will be more frequent. Every time the fracture breaks through the mud interlayer, it requires a higher pressure. Therefore, in reality, it may be difficult for the fracture to run through all interlayers. But at the early period, fluid with high viscosity and high rate is helpful for fracturing all sand reservoirs. Once the height extends into the multiple sand layers, it will become much easier for the fracture to propagate inside the sand.

In order to understand the influence of the perforation position on fracture height growth when the mud interlayers are asymmetric, two cases are studied. The distance between perforation to the center of the model in both Figures 20(a) and 20(b) is 1 m. In Figure 20(a), perforation is above the center of model. In Figure 20(b), perforation is below the center of the model. It can be observed that after both branches extend into the cap, these two cases have no difference from the perspective of stress field. But during the

propagation process, it can be observed in Figure 21 that when the perforation is below the center point, which means the position of perforation is close to the thinner mud interlayer, fracture width is much larger during fracture propagation. This is because the upper thick mud layer is difficult to break through and the fracture is asymmetric. That is to say, perforating close to the thinner mud layer can enlarge fracture width and make sand transport inside the fracture smoothly, which can reduce the risks of sand plugging.

4. Conclusions

This paper focuses on fracture height growth during hydraulic fracturing in the Dongsheng gas field. A hydromechanical sand-mud interbed model is established taking into full consideration reservoir characteristics. Besides, the parameters used in the simulations are from the experimental tests on downhole cores. Based on the numerical simulations, it can be concluded that fluid is difficult to flow inside the interfaces between sand and mud as it requires a much higher pressure to overcome overburden stress. As a result, the fracture extends vertically and breaks through mud interlayers without orientation. With a larger Young's modulus, fracture width in coarse sand is smaller than that in fine sand.

When there are mud interlayers within sand, the process of fracture height growth is complicated especially when the mud interlayers are asymmetric. Injection pressure and fracture width vibrate as fracture extends to and breaks through

the mud interface. As the minimum horizontal stress difference between the mud interlayer and the sand layer increases, the net pressure required to break through the mud interlayer increases linearly. What is more, when the mud interlayers are asymmetric, the fracture branch near the thinner mud interlayer breaks through the interlayer and reaches cap interface first. Afterwards, the other side branch propagates to the cap interface as the pressure inside the fracture increases. What needs to be stressed is that what we studied in this paper is a 2D height growth problem. In a hydraulic fracturing, when fracture height extends to the mud interlayers, it may propagate continuously in sand rather than break through the mud interlayer. This is because the stress of mud is larger than that of sand under normal circumstance. Fracture propagates much easier horizontally. If we want the fracture height to break through multiple mud interlayers, a high net pressure inside the fracture is required. Therefore, according to the simulation results in this paper, high viscosity fluid and high injection rate are beneficial to build a high net pressure inside the fracture, especially at the early period. In addition, when the mud interlayers are asymmetric, perforation close to the thinner mud interlayer can enlarge fracture width and make sand transport inside the fracture smoothly, which can reduce the risk of sand plug.

Data Availability

The data presented in this paper are available upon request from the corresponding author.

Conflicts of Interest

The authors declare no conflict of interest.

Acknowledgments

This work was financially supported by the Sinopec Science and Technology project (P20065).

References

- [1] Z. Lu, S. Ma, Y. He, and D. Niu, "Characteristics of sandy braided river intercalations in Ordos Basin: taking Sudong 27-36 tight well area for example," *Fault-Block Oil & Gas Field*, vol. 25, no. 6, pp. 704–708, 2018.
- [2] Z. Li, Y. Yang, J. Hou et al., "Reservoir architecture of turbidity channels in the 5th area of Bonan Oilfield," *Journal of China University of Petroleum (Edition of Natural Science)*, vol. 39, no. 5, pp. 36–42, 2015.
- [3] X. Xun, "Geological characteristics of Shihezi 1 member in Dongsheng gasfield and countermeasures against horizontal-well stimulation," *Natural Gas Technology and Economy*, vol. 13, no. 6, pp. 34–39, 2019.
- [4] X. Xun, "Reservoir characteristics and classification evaluation of Shihezi 1 member, Jin 58 wellblock, Dongsheng Gasfield," *Natural Gas Technology and Economy*, vol. 12, no. 5, pp. 9–11, 2018.
- [5] J. Cui, H. Li, J. Feng, C. N. Liu, and Y. J. Ju, "Barrier-beds and inter-beds characteristics and their effects on remaining oil distribution in braided river reservoirs," *Special Oil & Gas Reservoirs*, vol. 20, no. 4, pp. 26–30, 2013.
- [6] G. Irwin, "Relation of stresses near a crack to the crack extension force," in *9th Cong App Mech*, Brussels, 1957.
- [7] G. Irwin, "Analysis of stresses and strains near the end of a crack traversing a plate," *Journal of Applied Mechanics*, vol. 24, no. 3, pp. 361–364, 1957.
- [8] G. I. Barenblatt, "The mathematical theory of equilibrium cracks in brittle fracture," *Advances in Applied Mechanics*, vol. 7, pp. 55–129, 1962.
- [9] D. S. Dugdale, "Yielding of steel sheets containing slits," *Journal of the Mechanics and Physics of Solids*, vol. 8, no. 2, pp. 100–104, 1960.
- [10] A. Hillerborg, M. Modeer, and P. Petersson, "Analysis of crack formation and crack growth in concrete by means of fracture mechanics and finite elements," *Cement and Concrete Research*, vol. 6, no. 6, pp. 773–781, 1976.
- [11] M. Elices, G. Guinea, J. Gómez, and J. Planas, "The cohesive zone model: advantages, limitations and challenges," *Engineering Fracture Mechanics*, vol. 69, no. 2, pp. 137–163, 2002.
- [12] Y. Li, J. Deng, W. Liu, and Y. Feng, "Modeling hydraulic fracture propagation using cohesive zone model equipped with frictional contact capability," *Computers and Geotechnics*, vol. 91, pp. 58–70, 2017.
- [13] Y. Li, W. Liu, J. Deng, Y. Yang, and H. Zhu, "A 2D explicit numerical scheme-based pore pressure cohesive zone model for simulating hydraulic fracture propagation in naturally fractured formation," *Energy Science & Engineering*, vol. 7, no. 5, pp. 1527–1543, 2019.
- [14] Y. Li, J. Deng, W. Liu et al., "Numerical simulation of limited-entry multi-cluster fracturing in horizontal well," *Journal of Petroleum Science and Engineering*, vol. 152, pp. 443–455, 2017.
- [15] Q. Gao and A. Ghassemi, "Three dimensional finite element simulations of hydraulic fracture height growth in layered formations using a coupled hydro-mechanical model," *International Journal of Rock Mechanics and Mining Sciences*, vol. 125, article 104137, 2020.
- [16] K. Park, G. Paulino, and J. Roesler, "A unified potential-based cohesive model of mixed-mode fracture," *Journal of the Mechanics and Physics of Solids*, vol. 57, no. 6, pp. 891–908, 2009.
- [17] K. Volokh, "Comparison between cohesive zone models," *Communications in Numerical Methods in Engineering*, vol. 20, no. 11, pp. 845–856, 2004.
- [18] P. Camanho and C. Davila, *Mixed-Mode Decohesion Finite Elements for the Simulation of Delamination in Composite Materials*, NASA-Technical Paper, 2002.
- [19] A. Taleghani, M. Gonzaleiz, and A. Shojaei, "Overview of numerical models for interactions between hydraulic fractures and natural fractures: challenges and limitations," *Computers and Geotechnics*, vol. 71, pp. 361–368, 2016.
- [20] V. Tomar, J. Zhai, and M. Zhou, "Bounds for element size in a variable stiffness cohesive finite element model," *International Journal for Numerical Methods in Engineering*, vol. 61, no. 11, pp. 1894–1920, 2004.
- [21] D. Simulia, *Abaqus 6.13 User's Manual*, Dassault Systems, Providence, RI, 2013.
- [22] E. Detournay and H. Cheng, *Fundamentals of Poroelasticity Comprehensive Rock Engineering: Principles. Practice & Projects*, Pergamon Press, Oxford, 1993.

- [23] Y. Wang, Y. Yi, C. Li, and J. Q. Han, "Anisotropic fracture and energy characteristics of a Tibet marble exposed to multi-level constant-amplitude (MLCA) cyclic loads: a lab-scale testing," *Engineering Fracture Mechanics*, vol. 244, article 107550, 2021.
- [24] Y. Wang, B. Zhang, B. Li, and C. H. Li, "A strain-based fatigue damage model for naturally fractured marble subjected to freeze-thaw and uniaxial cyclic loads," *International Journal of Damage Mechanics*, vol. 30, no. 10, pp. 1594–1616, 2021.

Research Article

Overlying Strata Movement and Abutment Pressure Evolution Process of Fully Mechanized Top Coal Caving Mining in Extra Thick Coal Seam

Yongqiang Zhao,¹ Yingming Yang¹, Xiaobin Li², and Zhiqi Wang³

¹State Key Laboratory of Water Resource Protection and Utilization in Coal Mining, Beijing 102209, China

²School of Energy and Mining Engineering, China University of Mining and Technology (Beijing), Beijing 100083, China

³College of Energy and Mining Engineering, Shandong University of Science and Technology, Qingdao 266590, China

Correspondence should be addressed to Yingming Yang; yangym1988@163.com, Xiaobin Li; lxb162197@126.com, and Zhiqi Wang; 981477881@qq.com

Received 7 September 2021; Accepted 10 November 2021; Published 25 November 2021

Academic Editor: Zhengyang Song

Copyright © 2021 Yongqiang Zhao et al. This is an open access article distributed under the Creative Commons Attribution License, which permits unrestricted use, distribution, and reproduction in any medium, provided the original work is properly cited.

Taken overlying strata of fully mechanized top coal caving mining (FMTCCM) in 15 m extra thick coal seam as the research object, the comprehensive research methods such as field investigation, theoretical calculation, and numerical analysis are used to systematically analyze. During the mining of extra thick coal seam, the overlying strata form the structure of lower cantilever beam and upper hinged rock beam. The downward transmission caused by the interaction of this combined structure is the fundamental reason for the strong periodic ground pressure behavior of working face and roadway blow. The movement process of overlying strata movement is divided into four stages, and dynamic distribution characteristics of lateral abutment pressure in different stages are obtained. It is considered that the gob side roadway can be in a relatively stable overburden structure and stress environment during the stable stage of abutment pressure. The distribution range of the internal and external stress fields is determined, which provides a theoretical basis for the reasonable roadway layout. At last, the fracture position and abutment pressure evolution process of overlying strata along the goaf side of the extra thick coal seam are further verified by drilling stress measurement.

1. Introduction

China is rich in thick coal seam and extra thick coal seam, whose reserves and production account for about 45% of the total reserves. In recent years, extra thick and thick coal seams have become the main coal seam in China. During the mining of extra thick coal seam, the ground pressure behavior is severe and the peak value of abutment pressure is large. During the mining of the upper section working face, along the advancing direction of the vertical working face, the overlying strata will break, rotate, and sink successively after the first weighting, and the basic roof will be broken periodically to form a stable structure [1–3]. The distribution of lateral abutment pressure is directly related to the occurrence

state of the overlying basic roof rock and the macrostructure formed after fracture [4, 5].

At present, many studies have been carried on the overburden activity characteristics and abutment pressure evolution law. Zhu [6] put forward the point of view that the “triangle hanging plate” structure is formed in the end of working face and established a mechanical model of the stope roof structure. It is considered that the shape size and movement characteristics of the overlying hanging plate structure are closely related to the mine pressure behavior law of driving along the goaf. Song et al. [7, 8] developed a mechanical model of overlying strata of a roadway driving along the goaf, divided the lateral basic roof fracture position into the internal and external stress fields before and after,

and considered that digging roadway within the scope of the internal stress field can effectively avoid major accidents. On the contrary, when the roadway is excavated within the scope of the external stress field, the stability of roadway is poor and maintenance is difficult. Yu et al. [9] think that after the working face is mined, the rupture, rotation, and subsidence of the arc triangle block above the goaf force the lateral abutment pressure to transfer to the deep part of the solid coal, and a stress reduction area will be formed at the edge of the goaf. The serious stress disaster can be avoided by driving along the goaf in the lower stress area, and a large number of field tests have been conducted underground. Ma et al. [10] conducted field measurement and analysis on the ground pressure of some fully mechanized top coal caving faces and mining roadways and found that the mining and caving ratio of the working face have an effect on the distribution characteristics of lateral abutment pressure. Meanwhile, the peak point of lateral abutment pressure moves far away with the increase of caving ratio, which is favorable for driving roadway along the goaf with a narrow coal pillar. Wang et al. [11] obtained the dynamic evolution process of the lateral abutment pressure and microseismic activity through mine pressure observation and considered that the vertical stress trend of lateral coal seam in the goaf presented different stage characteristics. The stress and elastic-plastic evolution law of coal seam in each stage and interval were obtained through the measured data. Taking the 8.5 m mining height fully mechanized working face of Shangwan coal mine as the research background, Di et al. [12] adopted the methods of engineering analogy, theoretical calculation, and physics simulation to analyze the characteristics of overburden movement and abutment pressure. Based on the D-P criterion, Lode parameter correction statistical calculation formula was introduced to quantitatively analyze the size, location, and range of the abutment pressure peak point. Wang [13] established the strata movement model at the end of the goaf and studied the structural characteristics of the stable front end and the evolution law of lateral support pressure in the goaf. The results show that the fracture of the rock above the solid coal side in the goaf forms a triangular slip zone; with the instability of the fracture in the triangular sliding zone, the lateral support pressure of the solid coal decreases due to the transfer of some loads to the goaf. Based on the engineering and technical problems of the abnormal ground pressure of Datong mining area, Yu et al. [14] established the structural mechanical model of breaking “triangular plate” in the far-field key layer and clarified the relationship between the structural movement of the far-field “triangular plate” and the mine pressure behavior of the working face.

The above scientific research achievements have laid a foundation for exploring the temporal and spatial relationships between the overburden activity and abutment pressure in the goaf under the condition of an extra thick coal seam. However, because of the complexity and particularity of overburden structure and activity law in the goaf of a fully mechanized top coal caving face in the extra thick coal seam, it is necessary that the analysis model is established in order to explore the temporal and spatial evolu-

tion laws of lateral abutment pressure in different stages of the overburden activity. It can provide theoretical guidance for the excavation time and layout space of roadway along the goaf.

2. Engineering Background

The 8211 working face is located in the second panel of Madaotou coal mine, the north side is the undeveloped solid coal, the south side is the 8210 goaf which has been mined out, and the west side is the panel roadway. The relative position of the 8211 working face is shown in Figure 1. The fully mechanized caving mining method is adopted in the working face. The main mining coal seam is 3-5, the average dip angle is 2.5°, the average thickness of the coal seam is 15 m, the structure is complex, and the endogenous fractures are developed. There is a multilayer gangue intercalated between the coal seams, with the thickness of 0.7 m~3.6 m. The lithology is mainly mudstone, carbonaceous mudstone, and kaolinite mudstone.

The roof of the 8211 working face contains multilayer hard roof with large thickness, good integrity, high strength, and strong compactness. It is basically composed of gray medium coarse sandstone and coarse sandstone. The immediate roof is the interbedding of mudstone and sandstone, the immediate floor is carbonaceous mudstone, and the floor is gray white medium grained sandstone and fine sandstone. The main mineral composition is quartz, feldspar, and calcareous cementation (see Table 1 for the rock properties of 8211 working face).

3. Stability Evaluation of Surrounding Rock

Combined with the observation results of roof strata (Figure 2) and physical and mechanical tests of coal samples, the mechanical parameters and properties of the coal and rock are obtained [15]. The uniaxial compressive strength of coal is 11 MPa, the uniaxial tensile strength is 1.28 MPa, the elastic modulus is 6.16 MPa, and the internal friction angle is 15.3°. Coal seam has poor integrity, low strength, and easy breakage, which is not conducive to the roadway surrounding rock control. The uniaxial compressive strength of sandstone is 79.4 MPa, the uniaxial tensile strength is 5.83 MPa, the elastic modulus is 42.84 MPa, and the internal friction angle is 36.26°. Roof sandstone is relatively complete with hard and high strength, which has a huge impact on the working face and roadway below.

4. Overburden Structure Characteristics of FMTCCM in Extra Thick Coal Seam

4.1. Structural Form of Overburden. In the process of studying the strata control in mines, it is found that the mine pressure behavior law of stopes and roadways is closely related to the structural form and activity characteristics of overlying strata, especially the key strata that play a decisive role in controlling the strata behaviors of stopes and roadways. According to the “three zones” theory of overlying strata movement, the distribution and location

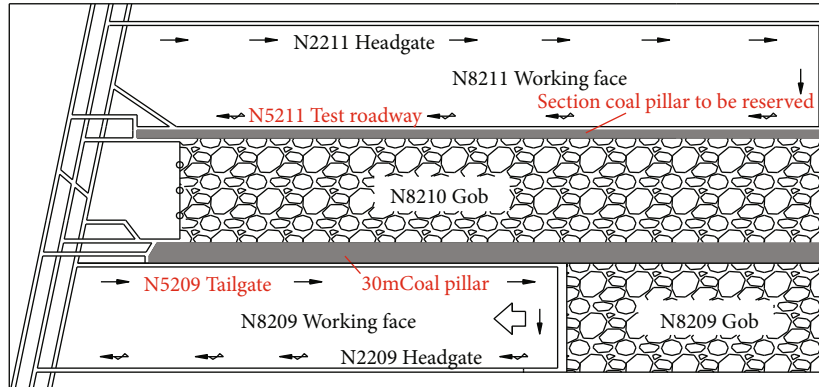


FIGURE 1: Relative position relationship of the 8211 working face.

TABLE 1: Lithology of the 8211 working face.

Lithology	Thickness (m)	Depth (m)	Lithology description
Aluminous mudstone and sandy mudstone interbedding	28.4	332.9	The upper part is purple patchy aluminum mudstone, and the lower part is yellow green sandy mudstone.
Medium coarse sandstone	9.2	342.1	It is grayish white coarse-grained massive structure, with gravel gradually increasing at the bottom.
Sandy mudstone and siltstone interbedding	39.4	381.5	It is mainly composed of light gray sandy mudstone and siltstone interbedded with thin layer of clay rock.
Medium coarse sandstone	13.5	395.0	Gray white coarse-grained massive structure intercalated with thin-layer siltstone.
Siltstone	3.2	398.2	The main mineral composition is quartz and calcareous cementation.
Carbonaceous mudstone	2.3	400.5	Black muddy structure, containing root plant fossils.
Coal seam	15.0	415.8	It is mainly black and semi dark coal with multilayer gangue and developed endogenous fractures.
Carbonaceous mudstone	5.3	421.1	Black muddy structure, containing root plant fossils.
Medium fine sandstone	14.5	435.6	Gray medium fine structure, containing a thin layer of silt and fine sandstone.

characteristics of bending subsidence zone, fracture zone, and caving zone of overlying strata are mainly affected by the mining height, and the relative position of key strata in “three zones” determines the structural form and movement form [16]. For the conventional working face with general mining height, during the mining process, with the increase of the hanging roof area, the roof gradually breaks. The adjacent broken rock blocks will be hinged and occluded with each other to form a relatively stable articulated structure under the action of horizontal thrust, as shown in Figure 3.

For the mining of the extra thick coal seam, the amount of coal mined out at one time is doubled, resulting in a large space increase in gob. Due to the large space size of the goaf, the broken rock above the coal body can not smoothly touch the gangue. Instead, the cantilever beam structure is located above the coal body. Stable hinged structures can be formed in the key strata of higher layers above the cantilever [17]. The structural form of the key strata is mainly determined by the mining height and the position of the key strata. The occurrence state of the key strata and the activity pattern have a direct impact on the mine pressure behavior of the stope and roadway. Therefore, it is the primary problem

to determine the structure of the upper key strata after the lower coal body is mined out.

According to the relevant calculation [18, 19], the structural form of the cantilever beam is formed in the lower key strata after the lower coal body is mined out. It can be seen that the overlying strata of FMTCCM in the extra thick coal seam has a structural form of low cantilever beam (LCB) and high hinged rock beam (HHRB). The structural model is shown in Figure 4.

4.2. Mechanical Analysis of Overburden Structure. With the continuous mining of coal, LCB gradually turns and deforms and forms a separation layer with the HHRB, which forces the HHRB structure to lose its support and slide. The unstable hinged rock beam structure acts on the LCB, causing the LCB breaking and further rotation deformation. The movement of the whole “cantilever beam + hinged rock beam” structure is the main factor causing the strong underground pressure behavior of the working face and roadway below. Therefore, it is necessary to carry out mechanical analysis of the whole overburden structure, so as to clarify the relationship between the key overburden structures.

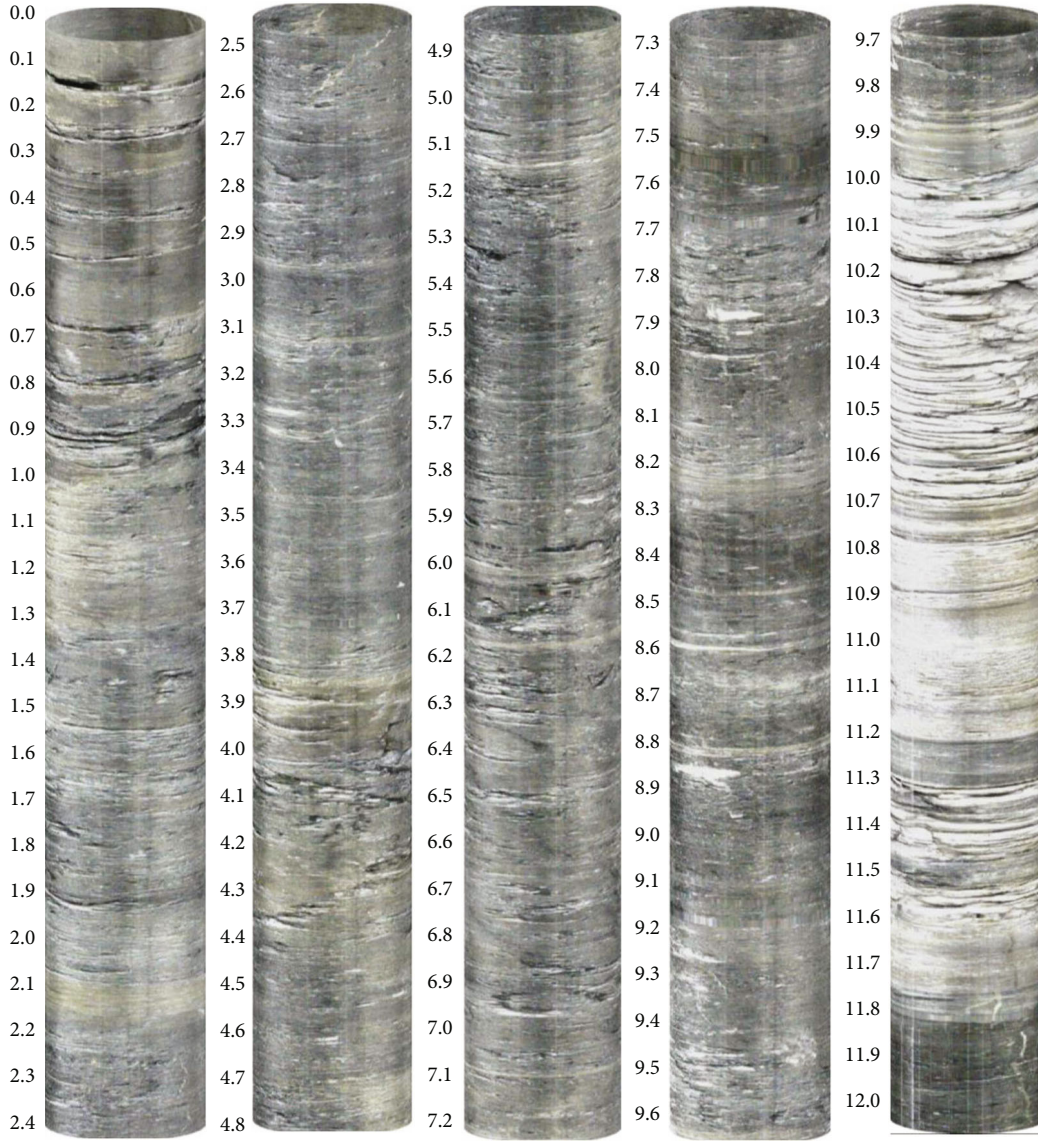


FIGURE 2: Observation results of roof strata structure.

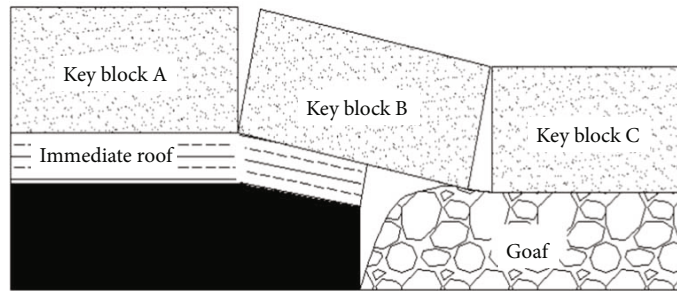
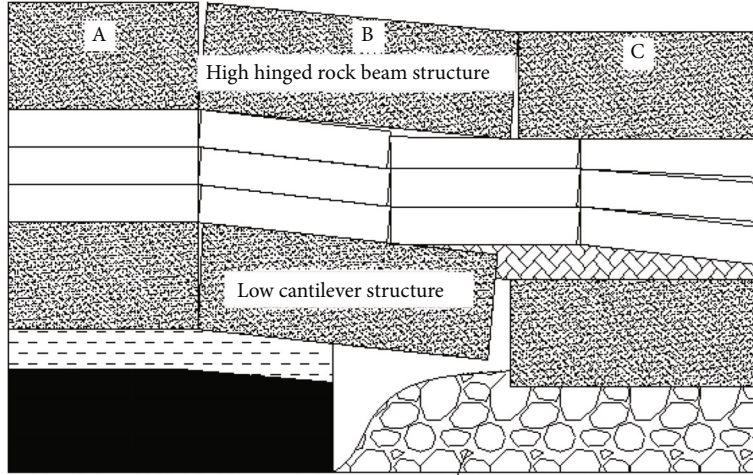


FIGURE 3: Structural characteristics of overburden for the conventional working face.

4.2.1. Mechanical Analysis of Hinged Rock Beam Structure. The mechanical model of hinged rock beam structure is established, and the force of each key block is analyzed. The bearing state of key block C is shown in Figure 5, where the adjacent key blocks are hinged to O_3 , the hori-

zontal thrust between them is T_{BC} and T_{CD} , the uniform load of overlying strata is q_4 , the supporting force of caving gangue on key block B is q_3 , the downward force of key block B on key block C is f_{BC} , and the weight of key block C is Q_C .



Goaf of 8210 fully mechanized caving face

FIGURE 4: Overburden structure characteristics.

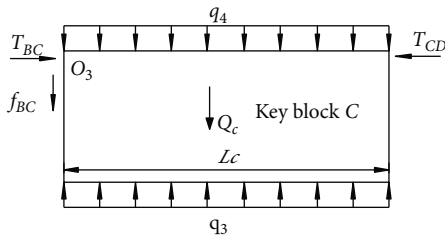


FIGURE 5: Mechanical analysis of key block C.

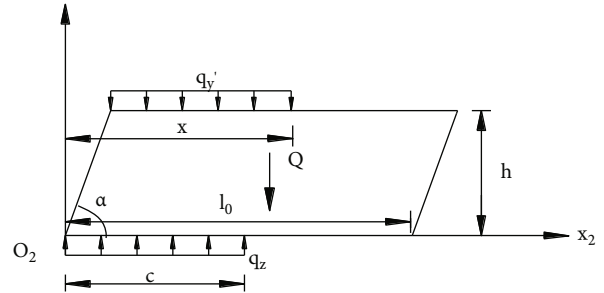


FIGURE 7: Force analysis of the cantilever beam structure.

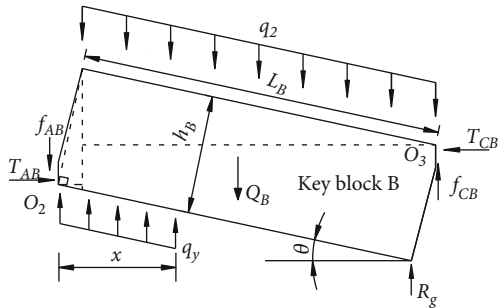


FIGURE 6: Mechanical analysis of key block B.

If $\sum x = 0$ and $\sum y = 0$ in the vertical and horizontal directions, then

$$T_{BC} = T_{CD}, \quad (1)$$

$$f_{BC} = q_4 L_C - q_3 L_C - Q_C. \quad (2)$$

T_{BC} can be obtained by the following formula [20, 21]:

$$T_{BC} = \frac{L_B(Q_B + q_2 L_B)}{2h_B - L_B \sin \theta}, \quad (3)$$

where the length and thickness of key block B are L_B and h_B , respectively, and the uniform loads imposed on blocks B

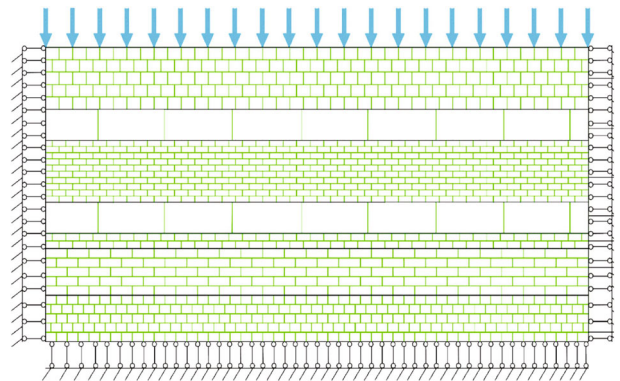


FIGURE 8: Numeric calculation model.

and C by the overlying weak rock layer are q_2 and q_4 , respectively, which can be obtained by controlling the unit weight of the weak rock layer by the key block. The weight of key block B is Q_B , the rotating angle of key block B is θ , and the breaking distances of key blocks B and C are L_B and L_C , respectively.

Key block B is hinged with key blocks A and C at points O_2 and O_3 , respectively. The bearing state of key block C is shown in Figure 6. Where the supporting force of weak rock stratum on key block B is q_y , the length of the supporting

force is x , and the supporting force of goaf gangue on key block is R_g . The vertical forces imposed by key blocks A and C on key block B are f_{AB} and f_{BC} , and the both are mutual forces. The horizontal forces imposed by key blocks A and C on key block B are T_{CB} and T_{AB} , respectively. Taking $\sum x = 0$, $\sum y = 0$, and calculate the moment for O_2 , $\sum M_{O_2} = 0$, then

$$q_y x^2 = \left[\begin{array}{c} q_2 \left(\frac{L_B}{2} \cos \theta + h_B \sin \theta \right) + Q_B \frac{(L_B \cos \theta + h_B \sin \theta)}{2} \\ -T_{CB}(h_B \cos \theta - L_B \sin \theta) - f_{CB}(L_B \cos \theta + h_B \sin \theta) \\ -R_g L_B \cos \theta \end{array} \right] \cos \theta. \quad (4)$$

4.2.2. Mechanical Analysis of Cantilever Beam Structure. The mechanical model of the cantilever beam structure is established, as shown in Figure 7. For the force analysis of

cantilever beam structure, $\sum M_{O_2} = 0$, which satisfies the following balance equation:

$$\frac{1}{2} Q(l_0 + h \cot \alpha) + q_y' [x^2 - (h \cot \alpha)^2] - q_z c^2 = 0, \quad (5)$$

where the sum of the gravity of the cantilever beam and the strata load controlled by cantilever beam is Q ; the thickness and fracture distance of the cantilever beam are h and l_0 , respectively; the dip angle of the fracture is α ; the load under the action of the hinged rock beam structure is q_y' ; and the force of the underlying coal and rock mass on the cantilever beam is q_z , and the distance from the fracture position of the cantilever beam to Q_2 is c .

Through simultaneous equations (3), (4), and (5), the following q_z is obtained.

$$q_z = \left(\frac{1}{c} \right)^2 \left\{ \left[\begin{array}{c} q_2 \left(\frac{L_B}{2} \cos \theta + h_B \sin \theta \right) + Q_B \frac{(L_B \cos \theta + h_B \sin \theta)}{2} \\ -\frac{L_B(Q_B + q_2 L_B)}{2h_B - L_B \sin \theta} (h_B \cos \theta - L_B \sin \theta) \\ -(q_3 L_C - q_4 L_C - Q_C)(L_B \cos \theta + h_B \sin \theta) \\ -R_g L_B \cos \theta \end{array} \right] \frac{\cos \theta}{x^2} [x^2 - (h \cot \alpha)^2] + \frac{1}{2} Q(l_0 + h \cot \alpha) \right\}. \quad (6)$$

From the above formula, it can be seen that the stress environment of the coal body near the goaf is closely related to the breaking position of the cantilever beam structure. The bearing capacity of the coal body near goaf is inversely proportional to the square of the breaking position c of the cantilever beam structure.

5. Movement Characteristics of Overlying Strata Structure

Considering the overlying strata in the goaf are mostly in discrete state, UDEC numerical simulation software is used to analyze the characteristics of overlying strata structure movement and its correlation with lateral abutment pressure distribution law of coal body [22, 23].

5.1. Establishment of Numerical Calculation Model. Combined with engineering conditions of the 8210 working face in Madaotou coal mine, the numerical model is established (Figure 8). The simulated working face length along the x -axis direction is 300 m. The deformation of the model is constrained by fixed boundary. The horizontal boundary of the model and the vertical direction of the bottom boundary are fixed. The equivalent uniform load of 8.5 MPa is applied at the upper boundary. The coal and rock mechanical parameters are shown in Table 2.

5.2. Overburden Movement along Goaf and Evolution of Lateral Abutment Pressure. During the mining of the upper working face, overlying rock structure undergoes the whole process of deformation, fracture, rotary subsidence, and stability. Combined with numerical analysis results and the internal and external stress field theory [24], the formation and development of lateral abutment pressure can be divided into four stages (Figure 9).

The first stage is before the change of support capacity of the coal wall. At this stage, the key strata in relatively stable state gradually transmit the pressure of overburden to the upper part of the coal seam, and the stress of the coal body has not reached its ultimate bearing strength. Therefore, the whole coal seam, including the side coal wall of the goaf, is in elastic deformation state. The process of abutment pressure is a monotone decline curve with the peak value at the edge of the coal wall, as shown in Figure 9(a).

The second stage is from the beginning of coal abutment pressure changed to the key strata broken. With the increasing of overburden activity, the lateral abutment pressure in a certain range increases to exceed the strength limit of the coal seam. With the destruction of the coal body, its bearing capacity begins to decrease. The process of abutment pressure on the coal seam will divide into the plastic zone and elastic zone. The pressure increases gradually in the plastic zone and decreases monotonically in the elastic zone. The

TABLE 2: Joint mechanical parameters of coal and rock.

Lithology	Normal stiffness (GPa)	Shear stiffness (GPa)	Shear modulus (GPa)	Bulk modulus (GPa)	Cohesion (MPa)	Internal friction angle (°)	Tensile strength (MPa)
Overlying strata 2	4.1	2.3	7.1	8.1	10.5	33.3	3.2
Medium coarse sandstone	5.2	2.9	10.2	15.3	26.5	35.4	5.8
Overlying strata 1	3.8	2.1	8.3	8.9	11.9	28.1	3.3
Medium coarse sandstone	5.2	2.9	10.2	15.3	26.5	35.4	5.8
Siltstone	4.8	2.6	9.8	12.1	15.5	33.2	4.3
Carbonaceous mudstone	2.6	1.4	2.8	3.6	10.8	28.1	3.8
Coal seam	2.2	1.2	1.7	2.2	5.9	15.3	1.3
Carbonaceous mudstone	3.6	1.7	2.8	3.6	10.8	28.1	3.8
Siltstone	5.6	2.8	8.2	10.3	7.2	34.8	3.7

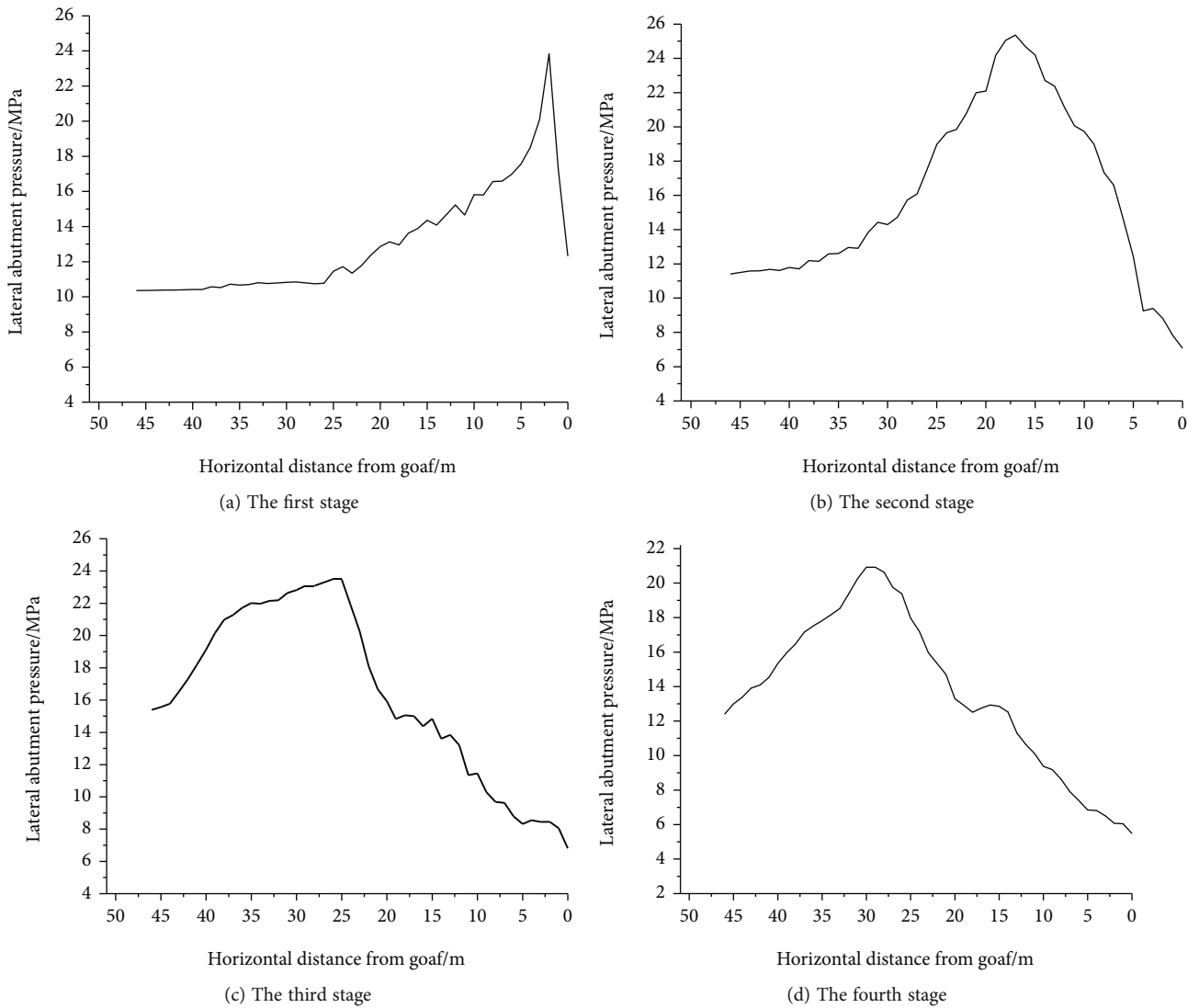


FIGURE 9: Structural characteristics of overburden movement and dynamic distribution curve of lateral abutment pressure in different stages.

peak position of the pressure is at the junction of the elastic-plastic zone, as shown in Figure 9(b).

The third stage is from the key strata broken to touch gangue. Before the key strata are broken, it is in a state of

tensile stress concentration near the broken line. When the tensile stress exceeds the tensile strength limit, the strata will break in front of the coal wall on the goaf side. The abutment pressure distribution is clearly divided by the broken line.

The two parts are the internal stress field controlled by the LCB and HHRB structure located within the broken line, and the external stress field that bears the additional stress of the upper rock layer beyond the broken line, as shown in Figure 9(c).

The fourth stage is from a low-level key stratum and high-level key stratum movement, touch- gangue to stability. At this stage, the overall failure height of overlying strata does not increase any more, the arch height of fracture arch reaches the maximum value, and the relative positions of the internal and external stress fields and stress peaks are basically stable. The lateral coal mass of the goaf is in a relatively stable overburden structure and stress environment, as shown in Figure 9(d).

The average thickness of the coal seam in Madaotou coal mine is 15 m, which belongs to the extra thick coal seam. The overlying strata will go through the movement process described in the above four stages. Because of the large thickness of the coal seam, the huge mining space will be formed, which leads to a violent and long lag period overlying rock activity. The peak value of abutment pressure formed is high, and the influence range is large. At the same time, it will take a long time for the overlying rock movement to reach a stable state. It can be seen that roadway driving along the goaf in the fourth stage, namely, the stable abutment pressure stage, can ensure that the gob side roadway is in a relatively stable overburden structure and stress environment.

6. Field Measurement

The lateral abutment pressure is monitored by installing a borehole stress meter on the coal pillar side. Firstly, it can reveal the dynamic evolution law of the coal pillar abutment pressure on the goaf side, which can reflect the movement state of the overlying strata in the goaf, and clarify the activity and stability stage of the overlying strata. Secondly, it can also judge the bearing capacity of different areas in the coal pillar according to the influence range and distribution state of the coal pillar bearing pressure on the goaf side [25].

The borehole stress gauge is installed at the coal pillar side of gob side roadway of the N8209 working face to monitor lateral abutment pressure, so as to verify the broken position of overburden rock and the evolution law of abutment pressure. The layout of monitoring station is shown in Figure 10.

As mentioned above, monitoring the abutment pressure in the coal pillar can reflect the strata movement state in the gob. According to Figure 11, when the working face is mined to about 30 m behind the station, the abutment pressure with a borehole depth of 13 m (17 m from the edge of the goaf) has dropped significantly and then slowly rises as the working face continues to advance. It is indicated that overlying strata is fractured near 17 m from the coal wall edge of the goaf, and the fractured rock masses squeeze the coal in the subsequent rotation process. The abutment pressure stress with a borehole depth of 8 m (22 m from the edge of the goaf) increased significantly and then gradually slowed down and stabilized with the distance of the working face,

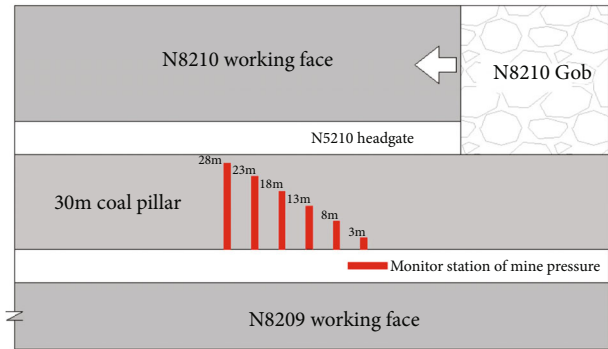


FIGURE 10: The layout of monitoring station.

indicating that the partial load was transferred to the front of fracture position after the rock block is fractured. Compared with a borehole depth of 28 m, the abutment pressure with a borehole depth of 3 m (27 m from the edge of the goaf) always maintains a higher stress level, and the coal body within this range still has a certain bearing capacity. However, in the mining process of the working face, it becomes a potential deformation and failure area due to strong mining, which is prone to plastic deformation and failure.

The abutment pressure with a borehole depth of 28 m (2 m from the edge of the goaf) decreased significantly at 30 m behind the working face. It shows that the coal bearing capacity at the location was reduced, and yield failure occurred, causing the stress to transfer to the depth of the coal pillar. The abutment pressure with borehole depths of 23 m and 18 m (7 m and 12 m from the goaf, respectively) have a small increase in front of the work face but little change. It indicates that the coal body is still elastic state and has a large bearing capacity within the range of 7 m~12 m from the goaf. From the above discussion, it can be concluded that field measurement results are consistent with theoretical analysis.

The stress distribution law of coal pillar drilling at different positions from the 8210 working face is shown in Figure 12.

- (1) With the advance of the working face, the abutment pressure of the coal pillar redistributes during the movement of the overlying strata. Before the overlying strata is broken, the stress curve of the coal pillar presents a “single hump” type, and the peak value of the overall stress is shifted to the side of the roadway along the goaf. After the overlying strata is broken, the stress curve of the coal pillar presents the “asymmetric saddle” type, and the stress value of the coal pillar side in the goaf is smaller than that of the coal pillar side along the roadway, which indicates that the mining roadway under the condition of 30 m protective coal pillar is always in a high stress environment during the movement of the overlying strata
- (2) The coal body within a certain range from the edge of the goaf wall is in a low stress state, and the coal body has a certain bearing capacity. If the mining

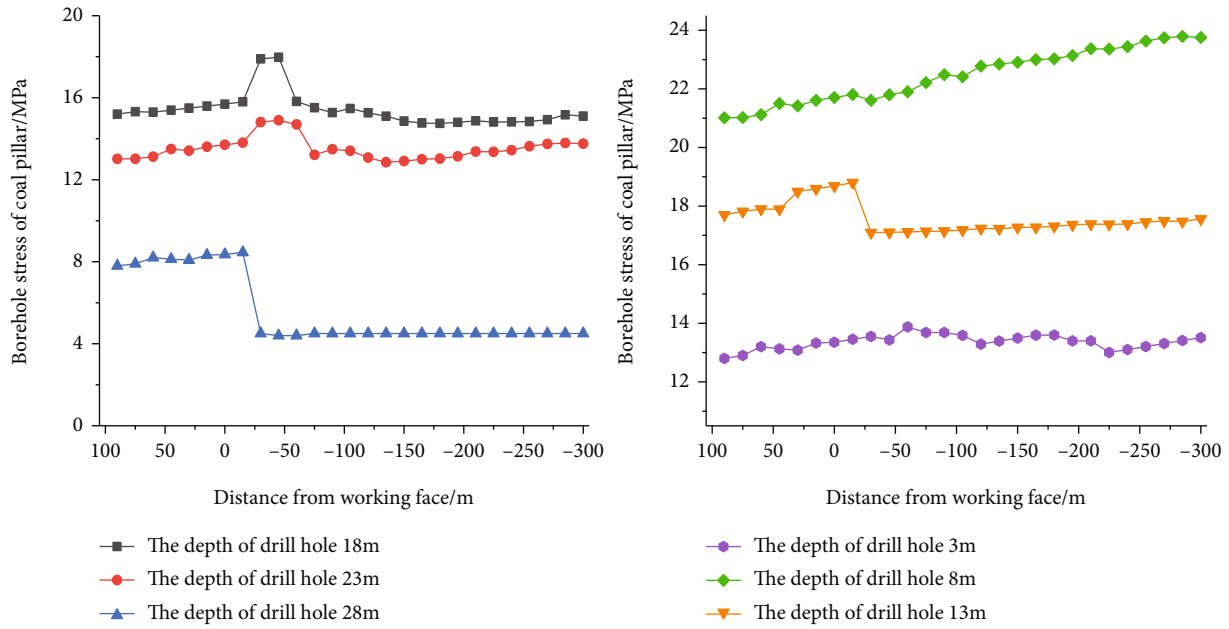


FIGURE 11: Relation between borehole stress of coal pillar and distance from working face.

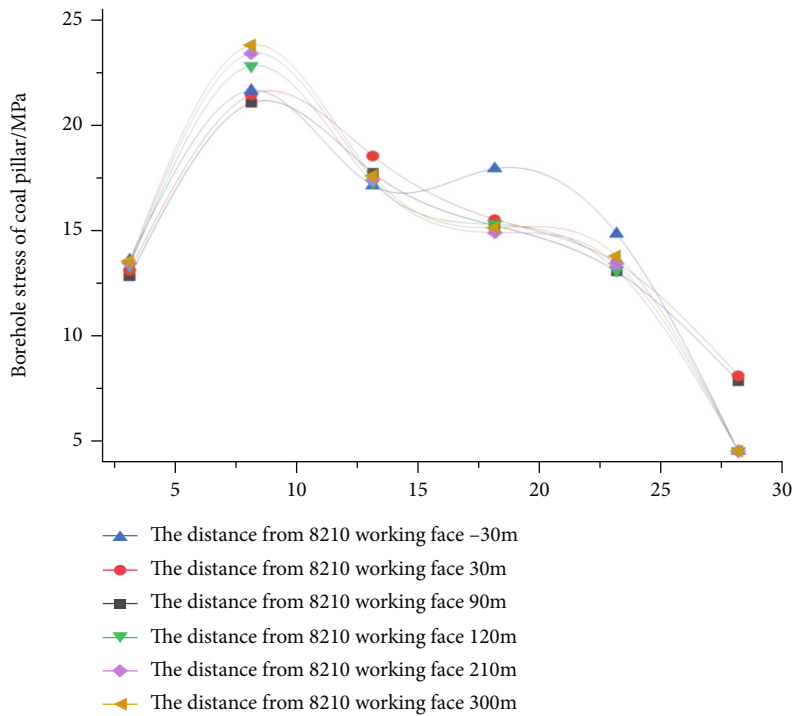


FIGURE 12: Dynamic evolution of bearing stress in the coal pillar.

roadway is arranged in this area, it is easier to maintain the roadway under the strong mining influence. Within the range of 300 m behind the working face, the abutment pressure of the coal pillar is always in the state of dynamic adjustment. Until the working face is pushed over 300 m, the abutment pressure in the coal pillar tends to be stable, and the activity of the overlying strata gradually is stopped

7. Conclusion

- (1) As the coal body is continuously mined, the unstable hinged rock beam structure acts on the low cantilever beam and causes the low cantilever beam to break and further turn to be deformed, which is the main factor causing the strong mine pressure behavior of the working face and roadway below

- (2) Four different movement stages of overlying rock structure along the goaf side of the extra thick coal seam are obtained and analyzed in detail. It is proposed that roadway driving along the goaf in stable abutment stress stage can avoid roadway in unstable overburden structure and stress environment
- (3) The fracture position and lateral abutment pressure evolution process of overlying strata on the gob side of the extra thick coal seam are confirmed by field measurement, which provides reference for the reasonable driving time and location of roadway

Data Availability

The data used to support the findings of this research are included within the paper.

Conflicts of Interest

The authors declare that there are no conflicts of interest.

Acknowledgments

This work was supported by The Program of State Key Laboratory of Water Resource Protection and Utilization in Coal Mining (SHGF-16-25). The authors gratefully acknowledge the financial support of the abovementioned agency.




References

- [1] H. Yavuz, "An estimation method for cover pressure re-establishment distance and pressure distribution in the goaf of longwall coal mines," *International Journal of Rock Mechanics and Mining Sciences*, vol. 41, no. 2, pp. 193–205, 2004.
- [2] H. Yan, F. L. He, T. Yang, L. Y. Li, S. B. Zhang, and J. X. Zhang, "The mechanism of bedding separation in roof strata overlying a roadway within a thick coal seam: a case study from the Pingshuo coalfield, China," *Engineering Failure Analysis*, vol. 62, pp. 75–92, 2016.
- [3] J. Wang, S. Yang, W. Wei, J. Zhang, and Z. Song, "Drawing mechanisms for top coal in longwall top coal caving (LTCC): a review of two decades of literature," *International Journal of Coal Science & Technology*, 2021.
- [4] Z. Song, T. Frühwirt, and H. Konietzky, "Fatigue characteristics of concrete subjected to indirect cyclic tensile loading: insights from deformation behavior, acoustic emissions and ultrasonic wave propagation," *Construction Building Material*, vol. 302, article 124386, 2021.
- [5] Z. Song, Y. Wang, H. Konietzky, and X. Cai, "Mechanical behavior of marble exposed to freeze-thaw-fatigue loading," *International Journal of Rock Mechanics and Mining Sciences*, vol. 138, article 104648, 2021.
- [6] D. R. Zhu, *Fracture Law of Basic Roof in Longwall Face and Its Application*, China University of mining and technology, Xuzhou, 1987.
- [7] Z. Q. Song and Z. D. Cui, "Study on green safe and efficient mining mode and engineering theoretical basis of filling without coal pillar research stone," *Journal of China Coal Society*, vol. 35, no. 5, pp. 705–708, 2010.
- [8] Z. Q. Song, Y. Y. Jiang, and J. K. Liu, "Theory and model of practical mine pressure control," *Coal Science and Technology*, vol. 2, no. 2, pp. 1–10, 2017.
- [9] Y. Yu, J. B. Bai, X. Y. Wang, and L. Y. Zhang, "Control of the surrounding rock of a goaf-side entry driving heading mining face," *Sustainability*, vol. 12, no. 7, 2020.
- [10] Q. H. Ma, Z. P. Guo, and K. G. Fan, "Characteristics of ground pressure behavior and feasibility of roadway driving along goaf in fully mechanized top coal caving face," *Mine Pressure and Roof Management*, vol. 1997, pp. 153–155, 1997.
- [11] S. W. Wang, D. B. Mao, and J. F. Pan, "Experimental study on lateral abutment pressure evolution and microseismic activity in goaf," *Journal of China Coal Society*, vol. 40, no. 12, pp. 2772–2779, 2015.
- [12] S. Di, J. R. Wang, and G. J. Song, "Theoretical study on roof movement and abutment pressure distribution characteristics of fully mechanized mining face with 8.5 m mining height," *Journal of China Coal Society*, vol. 42, no. 9, pp. 2254–2261, 2017.
- [13] Y. B. Wang, "End structure and lateral abutment pressure evolution mechanism of fully mechanized top coal caving face in extra thick coal seam," *Journal of China Coal Society*, vol. 42, pp. 30–35, 2017.
- [14] B. Yu, Z. Y. Zhang, T. J. Kuang, and J. R. Liu, "Stress changes and deformation monitoring of longwall coal pillars located in weak ground," *Rock Mechanics and Rock Engineering*, vol. 49, no. 8, pp. 3293–3305, 2016.
- [15] Z. Y. Song, H. Konietzky, and M. Herbst, "Bonded-particle model-based simulation of artificial rock subjected to cyclic loading," *Acta Geotechnica*, vol. 14, no. 4, pp. 955–971, 2019.
- [16] M. Shabanimashcool and C. C. Li, "Analytical approaches for studying the stability of laminated roof strata," *International Journal of Rock Mechanics and Mining Sciences*, vol. 79, pp. 99–108, 2015.
- [17] J. F. Ju, J. L. Xu, and Q. X. Wang, "Movement pattern of "cantilever beam" structure in key layer of large mining height stope and its influence on mine pressure," *Journal of China Coal Society*, vol. 36, no. 12, pp. 2115–2120, 2011.
- [18] J. F. Ju and J. L. Xu, "Surface stepped subsidence related to top-coal caving longwall mining of extremely thick coal seam under shallow cover," *International Journal of Rock Mechanics & Mining Sciences*, vol. 78, pp. 27–35, 2015.
- [19] S. H. Yan, X. W. Yin, and H. J. Xu, "Determination of short cantilever hinged rock beam structure and support working resistance in fully mechanized mining with large mining height," *Journal of China Coal Society*, vol. 36, no. 11, pp. 1816–1820, 2011.
- [20] L. L. Wang, C. W. Zang, and S. Liang, "Mechanical model of roadway roof and analysis of surrounding rock instability mechanism," *Coal Technology*, vol. 33, no. 12, pp. 47–49, 2014.
- [21] D. F. Yang, L. F. Zhang, and M. Chai, "Study on roof breaking law of fully mechanized top coal caving mining in extra thick coal seam based on fracture mechanics," *Geotechnical mechanics*, vol. 37, no. 7, pp. 2033–2039, 2016.
- [22] Y. Z. Feng, H. Lu, and B. Jiao, "Law of mine pressure behavior in 8 m high-cutting working face based on key strata theory," *Coal Engineering*, vol. 53, no. 3, pp. 1–5, 2021.
- [23] Z. Song, H. Konietzky, and X. Cai, "Modulus degradation of concrete exposed to compressive fatigue loading: insights from lab testing," *Structural Engineering and Mechanics*, vol. 78, pp. 281–296, 2021.

- [24] S. Y. Dong and W. Z. Li, "Influence analysis of principal stress deflection on fault stability based on theory of internal and external stress fields," *Safety in Coal Mines*, vol. 52, no. 1, pp. 213–219, 2021.
- [25] Y. T. Liu, J. D. Wang, and Z. G. Su, "Technology of delay in solving danger in small pillar roadway of kilometer gas mine," *Safety in Coal Mines*, vol. 52, no. 8, pp. 102–106, 2021.

Research Article

Variations on Reservoir Parameters of Oil Shale Deposits under Periodic Freeze-Thaw Cycles: Laboratory Tests

Rui-heng Li,¹ Zhong-guang Sun ^{1,2,3}, Jiang-fu He ¹, Zhi-wei Liao ¹, Lei Li,^{1,3} and Fang Qian⁴

¹Chongqing University, State Key Laboratory of Coal Mine Disaster Dynamics and Control, Chongqing 400030, China

²State Key Laboratory of Gas Disaster Detecting, Preventing and Emergency Controlling, Chongqing 400037, China

³China Coal Technology and Engineering Group Chongqing Research Institute, Chongqing 400039, China

⁴College of Construction Engineering, Jilin University, Changchun 130021, China

Correspondence should be addressed to Jiang-fu He; hejf2016@cqu.edu.cn

Received 1 August 2021; Accepted 30 October 2021; Published 16 November 2021

Academic Editor: Zhengyang Song

Copyright © 2021 Rui-heng Li et al. This is an open access article distributed under the Creative Commons Attribution License, which permits unrestricted use, distribution, and reproduction in any medium, provided the original work is properly cited.

As one of the most important unconventional hydrocarbon resources, the oil shale has been extracted with a frozen wall to successfully increase the shale oil production and reduce environmental pollution, which results from the harmful liquids in the in situ conversion processing of oil shale. Thereby, the strength and permeability of the frozen wall are extremely critical to reduce the harmful chemicals leaching into the groundwater. However, the permeability and strength of the frozen wall can be influenced by periodic freeze-thaw cycles. In order to investigate the damage and deterioration characteristics of oil shale samples after various periodic freeze-thaw cycles, the oil shale samples were periodically frozen and thawed as many as 48 times, after which the sample mass, stress-strain, freeze-thaw coefficient, uniaxial compressive strength, elastic modulus, and longitudinal wave velocity of the oil shale samples were separately measured. According to the measured results, the number of freeze-thaw cycles greatly influenced the physical and mechanical properties of oil shale samples. The uniaxial compressive strength and elastic modulus of the oil shale samples were changed with maximum variation rates of 64% and 65%, respectively. Meanwhile, the freeze-thaw coefficient of measured oil shale samples exponentially decreased with the increased number of freeze-thaw cycles, whereas the longitudinal wave velocity of tested samples ranged from 1602 m/s to 2464 m/s as a result of the new micropores inside the oil shale sample. Research results have enormous significance to the efficient and safe in situ exploitation of oil shale deposits.

1. Introduction

Oil shale is considered an important unconventional hydrocarbon resource, and its worldwide reservoir volume is huge. According to the latest report of the World Energy Council [1], the converted reserves of oil shale resources into shale oil reaches up to 4.8×10^{12} bbl throughout the world, which is 4 times as much as the world's oil resources. It can be confirmed that there are more than 300 shale deposits distributed in 40 countries, though the most abundant oil shale resources are located in the United States [2]. With the increasing price of the crude oil, the new energy resources, such as oil shale, have received further attention due to their

tremendous prospects for the production and utilization [3, 4]. Therefore, various production technologies of the shale oil have been proposed, such as true in situ (TIS) and modified in situ (MIS) for the conversion of oil shale [5]. In addition, the in situ conversion and restoration of shale oil are mainly accomplished by means of heat and chemistry activation, which intensively change the underground environment and reservoir property of the oil shale [6].

In shell's in situ retorting and conversion process, the kerogen of shale oil is thermally decomposed and converted into shale oil gas, which will be collected and separated above ground [7, 8]. However, the uncollected liquids in the spent shale or the vapour produced during in situ

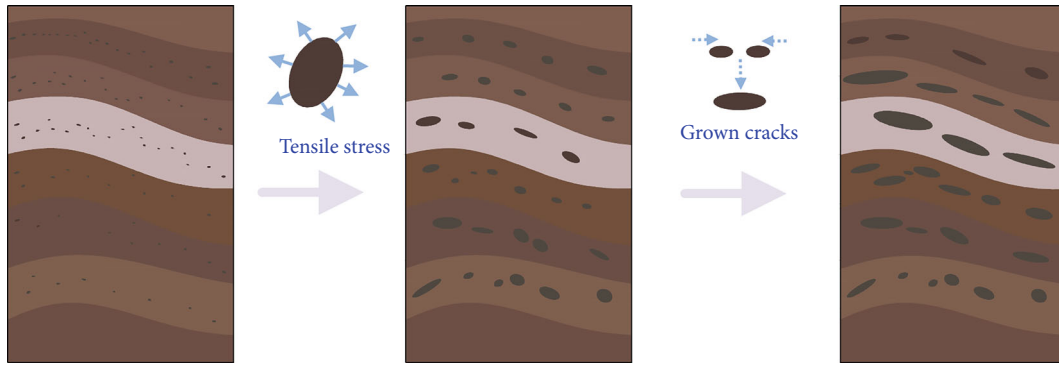


FIGURE 1: Schematic diagram of periodic freeze-thaw action process in oil shale samples.

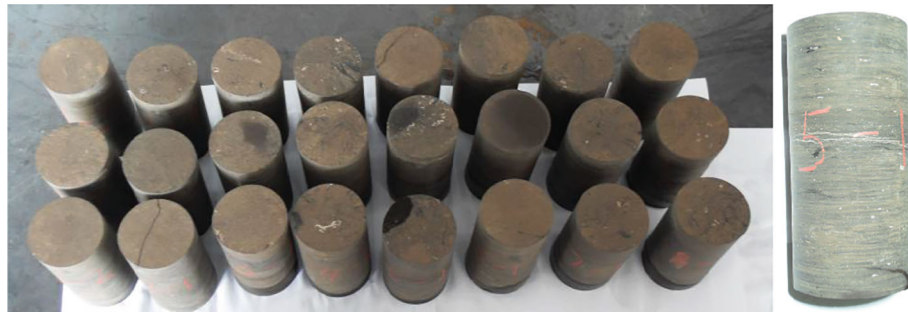


FIGURE 2: The tested oil shale samples with a diameter of 35 mm.

TABLE 1: Physical parameters of the tested oil shale samples.

Dry density ρ (g/cm ³)	Natural moisture content (%)	Porosity (%)
1.40	5.5490	1.7972

retorting may leach into groundwater; thereby, a frozen wall acts as an underground barrier around the oil shale site [9]. Besides, the freezing technology was applied to form a water-proof structure during the in situ production of underground energy [10]. In order to prevent groundwater from entering the oil shale site and prevent the harmful liquids produced by the in situ retorting from leaching out at the site, the frozen wall has been successfully utilized for the in situ conversion processing of oil shale [11, 12]. Initially, the targeted oil shale reservoir is enclosed with a cluster of freezing boreholes, which facilitates the rapid formation of underground frozen wall with expected coolant temperature of minus 42.8°C. Due to the permeability and strength of the frozen wall are determined by the physical and mechanical properties of oil shale deposits, the potential production capacity of shale oil may also be reduced when the conditions of the frozen wall, such as temperature, stress, and confining pressure, are changed. Once the strength and permeability of frozen wall have been weakened by freezing-thawing conditions, the underground water will be directly polluted, and the production efficiency will be subsequently reduced. In addition, the deformation and failure of frozen wall eventually leads to the potential pipe breakages, which dramatically increase the production cost of shale oil [13, 14]. Thereby, the influence of freeze-thaw condition

on the quality of frozen wall is extremely crucial for improving the exploitation of oil shale reservoir [15].

In previous studies, great advancements about the effects of periodic freeze-thaw conditions on variations of the mechanical and physical properties of other rocks have been made in recent years [16]. [17] from Spain conducted series of freeze-thaw experiments on various types of granites for 56 cycles with time intervals of 4 h, 8 h, and 12 h while the temperature was ranging from 12°C to 20°C. Subsequently, the ultrasonic wave velocity of granite samples was tested after every freeze-thaw cycle. The test results showed that the ultrasonic velocity of granite samples decreases with the lithology and freeze-thaw cycles, which result from the increased number of pores and microcracks caused by the freeze-thaw action. Yavuz [18] also found that the hardness, comprehensive strength, and P-wave velocity of andesite samples reduced after 10 freeze-thaw cycles and 50 thermal shock cycles, whereas the porosity and water absorption rate of the measured samples increased.

The rock mechanical properties under periodic freeze-thaw cycles were researched by Yang and Zhang, and the influence of freezing temperatures and freezing speed on the deterioration characteristics of rocks was obtained by using CT scanning equipment [19–21]. Besides, the temperature variation of frozen soil wall and the evolution characteristics of the specific heat capacity are analyzed by Yang et al. [22]. Wu Gang [23] separately tested the deterioration characteristics of saturated and dry rock samples with 60 freeze-thaw cycles, and the ultrasonic longitudinal wave and shear wave velocities were measured by the ultrasonic tester. Working with granite samples obtained from Jilin,



FIGURE 3: Experimental apparatus of TDS-300 periodic freeze-thaw cycles.

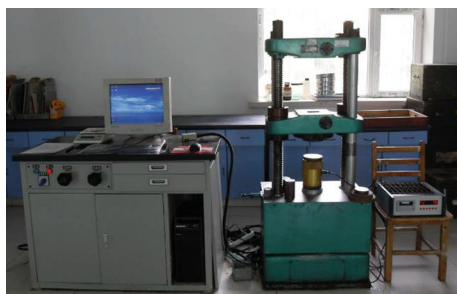


FIGURE 4: DNS100 microcomputer controlled electronic test machine.

China, Liu [24] conducted freeze-thaw experiments for 20 cycles under the condition of local minimum temperature. The test results showed that low-temperature freeze-thaw cycles have no obvious effect on the quality of granite, whereas these cycles have a great impact on the strength, stiffness, and Poisson's ratio of the tested samples. In addition, Bellanger [25] analyzed the calculation method of tunnel frost heaving force corresponding to the physical and mechanical properties of rock samples. Overall, several effective methods for controlling the freezing deterioration of soft rock have been proposed, including changing the physical and mechanical properties of the rock, extruding the pore water from the frozen area, and increasing the internal temperature of the tunnel [26].

In present studies, the influence of periodic freeze-thaw cycles on the deterioration characteristics of undermined oil shale is adequately analyzed according to the changes in physical and mechanical properties of rock samples. Studies on the physical and mechanical characteristics of oil shale samples will facilitate the development and utilization of oil shale resources. In addition, the oil shale samples recovered from Huadian Oil Field were utilized to measure the physical and mechanical properties of the tested samples. The freeze-thaw testing machine and mechanical testing machine were used to assess the damage and deterioration characteristics of oil shale samples under conditions of periodic freeze-thaw cycles, and the influence of periodic freeze-thaw cycle on the variation of mechanical and physical properties was investigated. The findings will contribute to the comprehensive study of oil shale samples, especially for the exploitation and production of oil shale deposits.

2. Mechanism of the Periodic Freeze-Thaw Cycle

Freeze-thaw cycles refer to the periodic freezing or thawing of rock and soil while the temperature falls below zero or rises above zero, which belongs to the physical and geological process phenomenon. Under minus temperature condition, water in the fractures of rock and soil will be frozen and expanded; thus, excessive pressure produced by ice particles will be accumulated inside the rock fracture. However, the frozen ice existed inside the fractures will be melted while the temperature rises, and the water droplets as well as moisture move along the pores or capillary pathway of the structure surface to the internal structure. Hence, the pressure on two walls of the rock fracture was dramatically decreased, and two walls between rock fractures push back to the center. Moisture in the structure surface and internal fractures will be alternately frozen and melted, which is known as periodic freeze-thaw cycle. As shown in Figure 1, during the process of periodic freeze-thaw cycle, fractures inside the rock will be expanded and grown in quantity; accordingly, the stones are separated by rock particles [27].

Freeze-thaw deterioration of rocks is an integrated process derived from the physical, chemical, and mechanical phenomena. It is a complicated process coupling with a multifield of temperature, water, and force, especially the energy transfer, phase change, and migration of water [28]. The essence of freeze-thaw damage and deterioration is that the compositions of rock, such as water, ice, and mineral, have different thermal physical properties [29]. Due to different crystalline orientations have different thermoelastic properties, as well as different shrink and expansion ratios of various mineral particles, shrinkages and expansions across the grain boundary are unbalanced, which applies a gravity force between mineral grains and micropore. The weakly cemented rock particles will be destroyed by such internal stress and cause partial damage and deterioration inside the rock matrix. While the temperature dropping to the freezing point, water transforms from liquid to solid, and this process will generate inflation tensile stress, which will lead to the damage of some weak rock particles. When the temperature rises, pore fissure water in the rock melts, freezing stress releases, moisture migrates, and fracture in local damage area interconnects, eventually aggravating this damage. With the increase of periodic freeze-thaw cycle, internal stress

TABLE 2: State of each group of samples.

Group	Group 1	Group 2	Group 3	Group 4	Group 5	Group 6	Group 7	Group 8
Hydrous conditions	Dry	Saturated	Saturated	Saturated	Saturated	Saturated	Saturated	Saturated
Cycle times	0	0	2 times	4 times	8 times	16 times	24 times	48 times



FIGURE 5: Samples in the periodic freeze-thaw experimental apparatus.

alternately acts on the skeleton of rock mass with the external temperature circulation, which causes irreversible deterioration inside the rock matrix.

According to Lemaitre's brittle damage model, the deterioration characteristic of oil shale sample can be specified by the uniaxial compression strain, as shown in formula (1):

$$D = \left(\frac{\varepsilon}{\varepsilon_r} \right)^k. \quad (1)$$

According to the relationship between stress and strain obtained from uniaxial compression, the stress can be expressed as

$$\sigma = E(1 - D)\varepsilon. \quad (2)$$

Thereby, the damage constitutive equation of oil shale samples can be presented as formula (3) after various freeze-thaw cycles:

$$\sigma = E(n) \left[1 - \left(\frac{\varepsilon}{\varepsilon_r} \right)^k \right] \varepsilon. \quad (3)$$

Besides,

$$E(n) = E_0[1 - D(n)]. \quad (4)$$

Eventually,

$$\sigma = E_0[1 - D(n)] \left[1 - \left(\frac{\varepsilon}{\varepsilon_r} \right)^k \right] \varepsilon, \quad (5)$$

where D denotes the damage degree of oil shale, n denotes the freeze-thaw cycles, E denotes the elasticity modulus of

raw oil shale, $E(n)$ denotes the elasticity modulus of frozen oil shale, ε denotes the initial strain of oil shale sample, and ε_r denotes the strain of frozen oil shale.

It can be indicated that the uniaxial compression strength of the oil shale sample is closely influenced by freeze-thaw cycles, which conversely changes the physical and mechanical properties of oil shale samples. Therefore, the variation of uniaxial compressive strength, mass, freeze-thaw coefficient, stress, and strain of tested oil shale samples will be discussed with various freeze-thaw cycles in the present research.

3. Tests on the Oil Shale Samples with Periodic Freeze-Thaw Cycle

3.1. Preparation of Tested Oil Shale Samples. The tested oil shale samples were recovered from Huadian Basin, Jilin Province, China. The dimension of all tested samples is $\varphi 50\text{mm} \times 100\text{mm}$, and the dry density of all samples is approximately 1.4g/m^3 . The reservoir depth of tested oil shale sample is 600 m, and the seam deposition age in Huadian belongs to the Tertiary period of the Cenozoic [30]. Besides, the tested samples were prepared by drilling and coring in oil shale mass with a water drilling method in the laboratory. According to the requirements for thin samples, the height-diameter ratio of prepared samples was 2:1, which accords with the requirement for improving measurement errors. In present experiments, a total of 24 pieces of oil shale samples with good integrity were tested, and the tested samples were as shown in Figure 2.

Meanwhile, other specified physical parameters of the tested oil shale samples are as shown in Table 1. The dry density was tested by dehydrating for 48 hours in a drying oven, whereas the natural moisture content and porosity were simultaneously measured with a QKY-11 gassy porosity detector manufactured by Nantong Experimental Apparatus Company. The porosity of oil shale samples can be calculated based on the solid volume and physical volume of the tested samples. The solid volume is derived from the balance pressure of a standard curve.

3.2. Experimental Apparatus. The test apparatus with a specified cryogenic bath is termed as TDS-300 freeze-thaw cycle test machine, which was manufactured by Suzhou Donghua Test Instrument Co., Ltd., as shown in Figure 3. The minimum working temperature of the test machine is -40°C , and the periodic freeze-thaw cycle of the oil shale samples can be conducted by freezing in the test machine and thawing in the water. Once the freezing temperature of the tested sample is confirmed, the periodic freeze-thaw cycles of oil shale samples will be automatically completed without extra

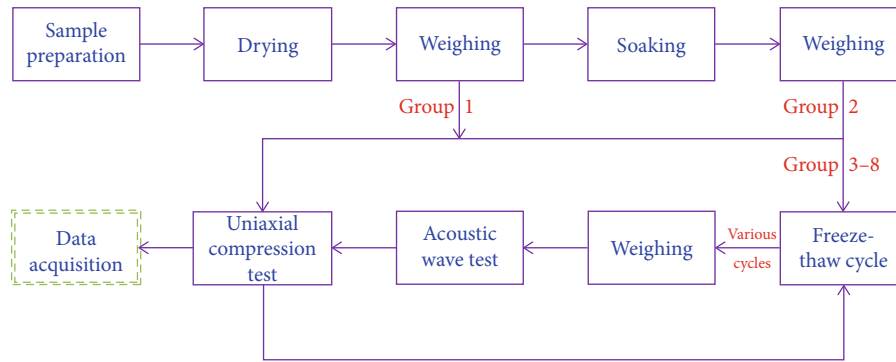


FIGURE 6: Flow diagram of the periodic freeze-thaw experiments.



FIGURE 7: Test on the mechanical properties of the measured oil shale samples.



FIGURE 8: Ultrasonic detection on oil shale samples after periodic freeze-thaw cycles.

operations. Overall, relevant requirements of the standard measurement of periodic freeze-thaw cycles are qualified.

The mechanical and physical properties of the oil shale samples were measured with a DNS100 microcomputer, controlled by electronic universal testing machine, as shown in Figure 4. The universal testing machines are mainly used for testing the tensile, compression, bending, shear, peel, tear, and other mechanical properties for all types of metallic, non-metallic, and composite materials. The maximum force, tensile strength, bending strength, compression strength, elastic modulus, breaking elongation, yield strength, and other parameters can be obtained. Meanwhile, the ZBL-U520 ultrasonic detector, electronic balance (tolerance of 0.0001 g) accuracy, vernier caliper, and drying oven have been utilized in all experiments.

3.3. *Experimental Methods and Proposals.* According to the operation specification of conventional rock experiments under conditions of periodic freeze-thaw cycles in water conservancy and hydroelectric engineering (SL264-2001), all periodic freeze-thaw experiments were conducted with -20°C freezing temperature and 20°C thawing temperature.

The experimental procedures were as follows: firstly, the oil shale samples were frozen for 4 hours in the test apparatus with a temperature of -20°C , then being thawed for 4 hours in the water at a temperature of 20°C , namely, each freeze-thaw time step was 8 hours. There were 8 groups of oil shale samples in all freeze-thaw experiments, and each group included 3 samples. Six groups of samples were processed under conditions of periodic freeze-thaw cycles with 2, 4, 8, 16, 24, and 48 hours, separately. Before the periodic freeze-thaw experiments, all the oil shale samples were placed in the oven (temperature at 105°C) for 48 hours, which is aimed at dehydrating all the samples to a constant weight (mass changes no greater than 0.1% in 24 hours). Then, the mass of each oil shale sample can be weighed and recorded. As shown in Table 2, totally, 2-8 groups of samples were continuously vacuumed for 4 hours until no air bubbles existed in the sample.

Subsequently, the oil shale sample was placed in distilled water for 48 hours until to be saturated; thus, the mass of each oil shale sample can also be weighed and recorded. The oil shale samples in group 1 and group 2 were prepared for the uniaxial compressive strength experiment, and the rest of the samples were placed in the freeze-thaw experimental apparatus for periodic freeze-thaw experiment, as

TABLE 3: Mass changes of oil shale samples before and after periodic freeze-thaw cycles.

Freeze-thaw cycle times (time)	Sample no.	Mass before freeze-thaw cycles (g)	Mass after freeze-thaw cycles (g)	Rate of mass change (%)	Average rate of mass change (%)
0	OS-2-1	139.5024	—	—	—
	OS-2-2	147.6156	—	—	—
	OS-2-3	138.8170	—	—	—
2	OS-3-1	138.2813	141.5362	2.35	2.22
	OS-3-2	134.1621	136.6143	1.83	
	OS-3-3	145.2909	148.9062	2.49	
4	OS-4-1	137.6229	141.5727	2.87	2.75
	OS-4-2	139.3990	143.5113	2.95	
	OS-4-3	145.2748	148.8195	2.44	
8	OS-5-1	138.0036	142.5931	3.33	3.20
	OS-5-2	146.2784	151.6432	3.67	
	OS-5-3	135.9549	139.5099	2.61	
16	OS-6-1	138.2125	143.9026	4.12	4.20
	OS-6-2	139.4651	145.5730	4.38	
	OS-6-3	142.9672	148.8533	4.12	
24	OS-7-1	134.2431	139.8679	4.19	4.26
	OS-7-2	147.3052	153.5951	4.27	
	OS-7-3	141.9107	148.0412	4.32	
48	OS-8-1	138.8485	141.8060	2.13	2.27
	OS-8-2	135.6381	139.3410	2.73	
	OS-8-3	140.9224	143.6704	1.95	

shown in Figure 5. After the designed freeze-thaw cycles were completed, the mass variation of tested oil shale samples will be weighted and recorded. The ultrasonic detection and uniaxial compression experiments were conducted once the weight of oil shale samples has been measured. Overall, the oil shale samples were continuously tested under conditions of periodic freeze-thaw cycles until all the experiments were entirely completed. The flow diagram of the periodic freeze-thaw experiments is shown in Figure 6.

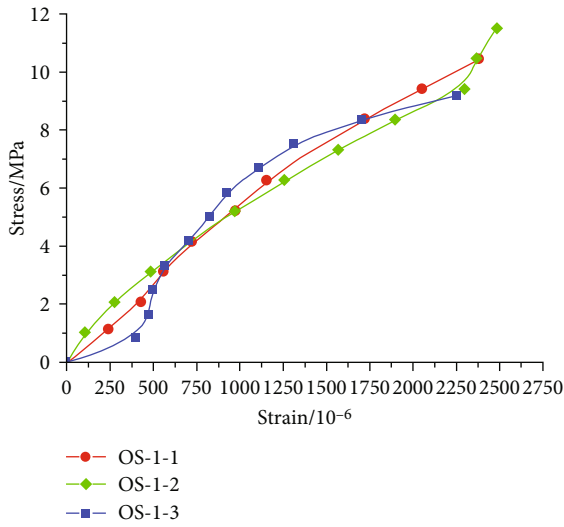
3.4. Uniaxial Compression Test on Oil Shale Samples after Periodic Freeze-Thaw Cycles. Once the oil shale samples were processed under conditions of periodic freeze-thaw cycles, the mechanical properties were measured with the uniaxial compression experiments in the rock mechanics laboratory (locates in the College of Construction Engineering, Jilin University). Under average ambient temperature conditions, the experiments were carried out using a DNS100 microcomputer-controlled electronic universal testing machine, and the strain and stress measurement were acquired with the electric resistance strain gauge. Meanwhile, the axial loading rate was controlled and assigned to 0.5 MPa/s in all experiments. The process used for testing the mechanical properties of the measured oil shale samples is shown in Figure 7.

3.5. Ultrasonic Detection on Oil Shale Samples after Periodic Freeze-Thaw Cycles. In order to investigate the influence of

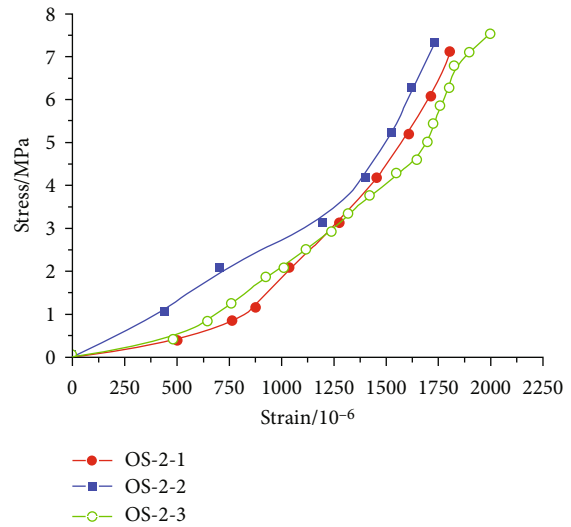
periodic freeze-thaw cycles on the deterioration characteristics of measured oil shale samples, the ultrasonic propagation velocity of measured sample has been obtained by ultrasonic detection on frozen-thawed samples, as shown in Figure 8. The ultrasonic propagation velocity is varying with various materials, which is highly related to the density of measured samples. While the fractures inside the oil shale samples are extended by internal stress derived from periodically freezing and thawing, the density of oil shale samples is changed. Besides, the nondestructive and ultrasonic longitudinal wave tests on oil shale samples have been completed after various freeze-thaw cycles, and the effect of periodic freeze-thaw cycles on longitudinal wave velocity of oil shale samples was subsequently analyzed and recorded.

4. Results and Discussions

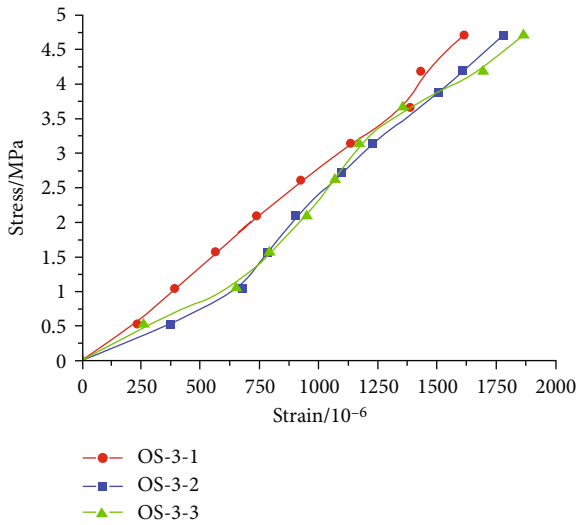
4.1. Influence of Periodic Freeze-Thaw Cycles on the Mass Changes of Oil Shale Sample. The mass variation of the measured samples before and after different periodic freeze-thaw cycles has been shown in Table 3. Test results have shown that the mass of each measured sample is increasing after periodic freeze-thaw cycles, and the sample in serial number of OS-6-2 has the maximum mass changes, which goes up to 4.38%. It can be implied that the internal micropore of measured sample is increasing, and the new micropore inside the oil shale appears due to the effect of frost heaving and melt shrinkage. Thereby, the water migrated into the internal



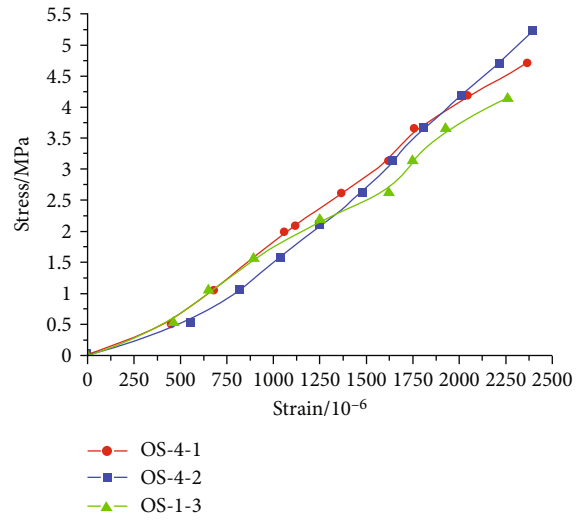
(a) Obtained stress-strain of dry rock sample



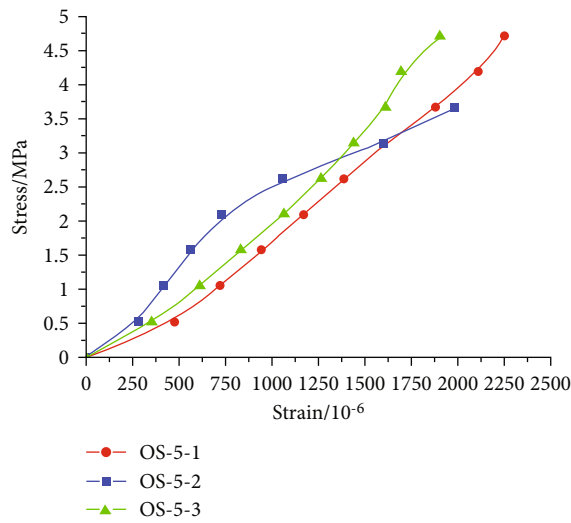
(b) Obtained stress-strain of saturated rock sample



(c) Stress-strain under 2 times of freeze-thaw cycle



(d) Stress-strain under 4 times of freeze-thaw cycle



(e) Stress-strain under 8 times of freeze-thaw cycle

FIGURE 9: Continued.

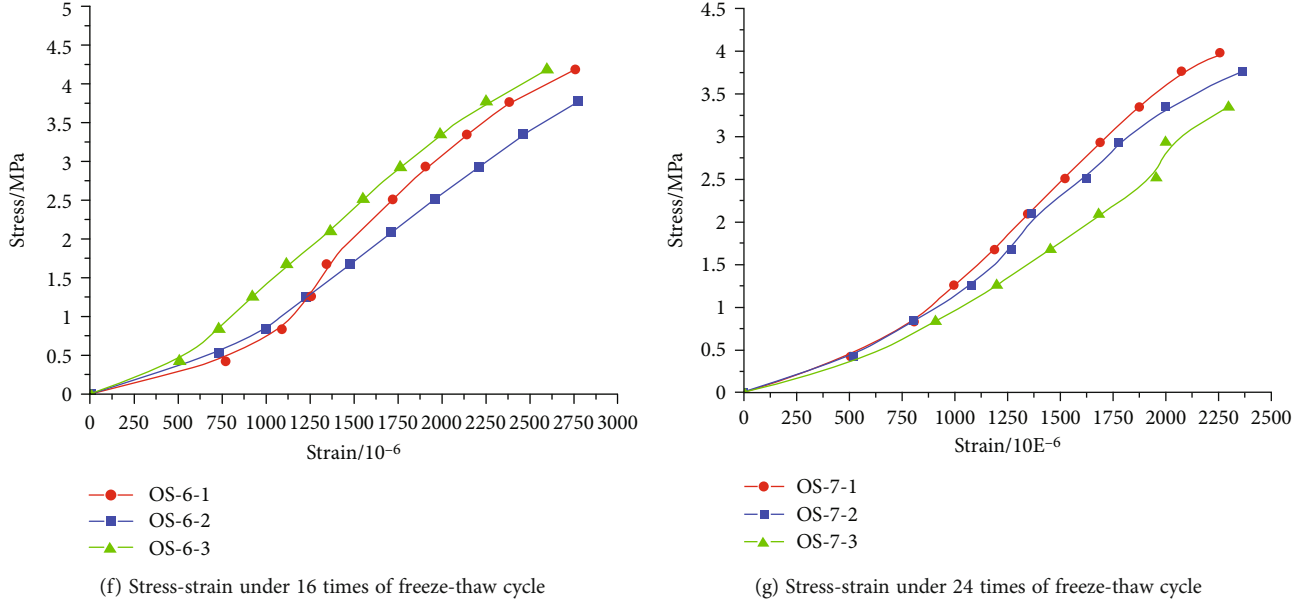


FIGURE 9: Variation of freeze-thaw cycles on the stress and strain of the measured oil shale samples.

TABLE 4: Relationship between the freeze-thaw coefficient and freeze-thaw cycles.

	Fresh and dry	Fresh and saturated	2 cycles	4 cycles	8 cycles	16 cycles	24 cycles
Freeze-thaw coefficient	—	1	0.64	0.64	0.60	0.55	0.50

TABLE 5: Relationship among uniaxial compressive strength, elastic modulus, and freeze-thaw cycles.

	Fresh and dry	Fresh and saturated	2 cycles	4 cycles	8 cycles	16 cycles	24 cycles
Average uniaxial compressive strength (MPa)	10.3941	7.3274	4.7087	4.6953	4.3599	4.0460	3.6972
Average elastic modulus (GPa)	4.3710	3.9822	2.6942	2.1367	2.0031	1.6045	1.4961

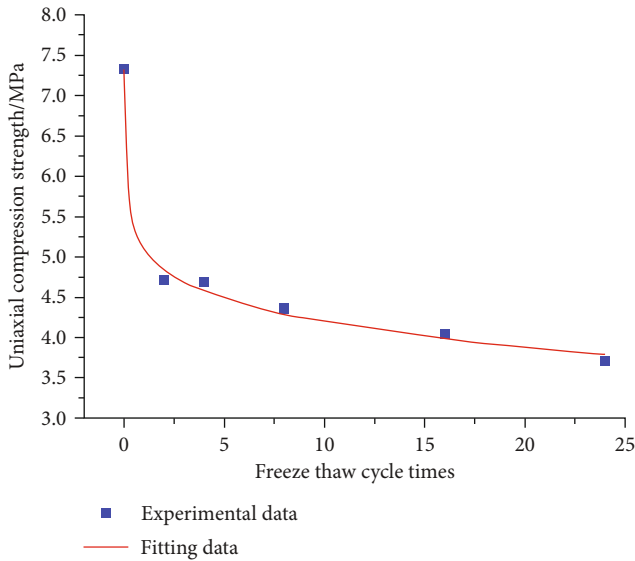


FIGURE 10: Variation of freeze-thaw cycles on the uniaxial compressive strength of oil shale samples.

rock fractures, which resulted in the mass increase of oil shale samples. In addition, the average mass change rate of each group of oil shale samples is increasing while the periodic freeze-thaw cycles are less than 24. However, the average mass change rate of measured samples will slightly decline with the increase of periodic freeze-thaw cycles while the freeze-thaw cycle is more than 24. It can be indicated that the expansion of micropore is hindered and the fractures inside the oil shale samples are squeezed; thus, it is difficult for moisture to come into the fractures inside the oil shale samples.

In essence, the volume of fissure water occupied in the rock matrix or the external water enters through the rock fractures will increase by approximately 9% after the ice is frozen. Besides, the ice exerts pressure on both sides of the cracks, leading to the increase of depth and width of cracks. While the ice is melting, generated water will flow into the new cracks. The water will be refrozen when the temperature drops, which enlarges the internal cracks inside the oil shale samples. Therefore, the periodic freeze-thaw cycle will weaken the oil shale samples until it is completely destroyed.

4.2. Influence of Periodic Freeze-Thaw Cycles on the Stress-Strain of Oil Shale Samples. As shown in Figure 9, the

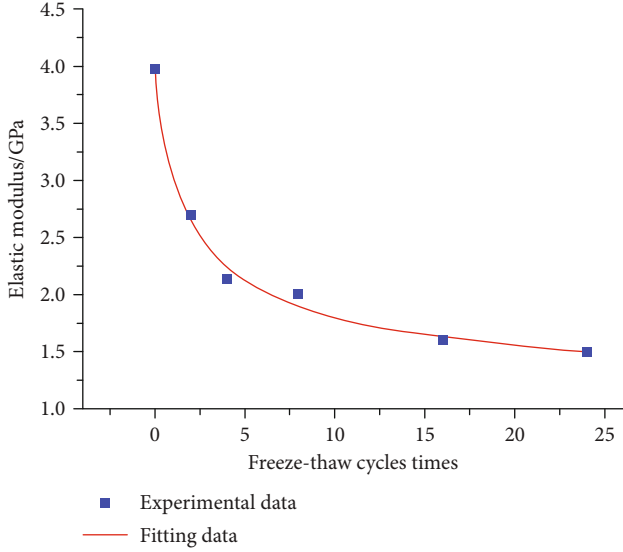


FIGURE 11: Elastic modulus of oil shale sample varies with the number of freeze-thaw cycles.

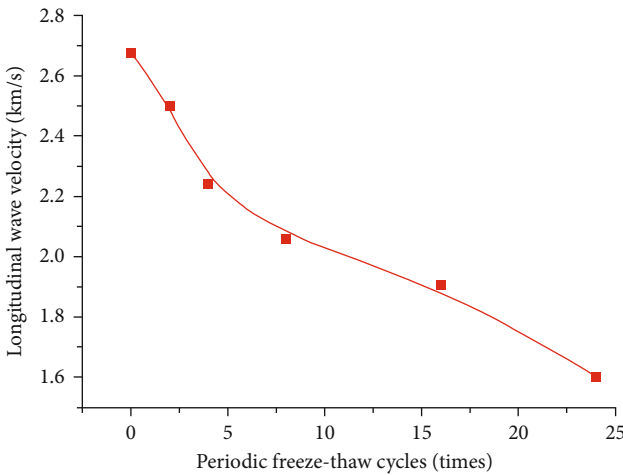


FIGURE 12: Longitudinal wave velocity of oil shale sample varies with periodic freeze-thaw cycles.

stress-strain curves of all the tested oil shale samples were obtained based on the test results of uniaxial compressive strength after various periodic freeze-thaw cycles. The stress and strain of the dry rock samples, saturated samples, and measured samples were obtained and checked. In addition, Young’s modulus of the oil samples was determined by the ratio of compression stress and longitudinal strain; hence, the compression stress and longitudinal strain of all samples should be precisely confirmed. Moreover, all tested results about periodic freeze-thaw experiments should be repeatedly measured for 3 times in order to reduce the measurement uncertainty.

It can be inferred that the damage and deterioration on the mechanical properties of the oil shale samples can be influenced by the periodic freeze-thaw cycles. Due to the hardness of the oil shale samples being low, excessive fractures are present inside the oil shale samples; thus, the

stress-strain variation on the oil samples is determined by the freeze-thaw cycles. When the number of freeze-thaw cycles is 48, the deterioration on the mechanical properties of the oil shale sample is the greatest. Although individual differences of the oil shale samples result in diverse effects on the stress-strain of tested samples, the deterioration of the oil shale samples can be illustrated by the obtained stress-strain.

Under the effect of periodic freeze-thaw cycles, there is an obvious drop in uniaxial compressive strength, and the downtrend is also obvious, especially in the initial cycles of the freeze-thaw process. Comparing the stress-strain changes of oil shale samples before and after the periodic freeze-thaw process, a similar variation tendency can be found throughout the periodic freeze-thaw process, which can be divided into three stages: the pressure stage, elastic deformation stage, and the crack extension stage.

4.3. *Influence of Freeze-Thaw Cycles on the Freeze-Thaw Coefficient of Oil Shale Samples.* The rock’s ability to resist freeze-thaw damage and deterioration can be expressed by the freeze-thaw coefficient. According to the specifications for rock tests in water conservancy and hydroelectric engineering (SL264-2001), the formula of the rock freeze-thawing coefficient is shown as follows:

$$K_f = \frac{\overline{R}_f}{\overline{R}_s}, \quad (6)$$

where K_f is the freeze-thaw coefficient, \overline{R}_f is the saturated uniaxial compressive strength after freeze-thaw test (MPa), and \overline{R}_s is the saturated uniaxial compressive strength before the periodic freeze-thaw tests (MPa). The freeze-thaw coefficients of the tested oil shale samples are shown in Table 4.

According to the measured results in Table 4, the freeze-thaw coefficient of oil shale samples significantly reduces with the increased number of freeze-thaw cycles. In the first 2 freeze-thaw cycles, the freeze-thaw coefficient of the tested samples rapidly decreases. Subsequently, the freeze-thaw coefficient of the samples continues to decrease. However, the decreasing rate of the freeze-thaw coefficient significantly reduces after the initial 2 freeze-thaw cycles. It can be inferred that the pore space inside the oil shale sample has been gradually reduced, and the sample will be compacted during the freeze-thaw process; thus, the freeze-thaw coefficient of oil shale samples decreases.

4.4. *Variation of the Uniaxial Compressive Strength and Elastic Modulus.* As shown in Table 5, the average uniaxial compressive strength and elastic modulus are reduced with the increased number of freeze-thaw cycles, and the maximum compressive strength and elastic modulus are obtained from the fresh and dry oil shale samples. Due to the pore matrix of oil shale samples is connected by rock particles, the fresh and dry oil shale samples have little moisture inside the pore volume, causing the compressive strength and elastic modulus of oil shale samples to be maximized, which reach up to 10.39 MPa and 4.37 GPa, respectively. Once the

TABLE 6: Relationship between longitudinal wave velocity and freeze-thaw cycles.

Freeze-thaw cycle	Dry	0 times	2 times	4 times	8 times	16 times	24 times
Average longitudinal wave velocity (km/s)	2.4644	2.6751	2.4.991	2.2418	2.0581	1.9055	1.6025

tested oil shale samples have been processed by several periodic freeze-thaw cycles, the compressive strength and elastic modulus of oil shale samples gradually decrease. It can be inferred that the water inside the pore volume is periodically frozen and melted; thereby, the connection between rock particles has been broken by the interaction force of rock particles, which results in the reduction of the average compressive strength and elastic modulus. The tested oil shale samples processed with 24 periodic freeze-thaw cycles exhibited the minimum compressive strength and elastic modulus among all the tested oil shale samples, which is simply 3.69 MPa and 1.49 GPa, respectively.

Meanwhile, the uniaxial compressive strength of the oil shale sample varied closely with the numbers of freeze-thaw cycles. As shown in Figure 10, the uniaxial compressive strength of oil shale is greatly influenced by the periodic freeze-thaw cycles. It can be implied that the uniaxial compressive strength of the oil shale sample exponentially decreased with the increased number of freeze-thaw cycles. In the first 2 freeze-thaw cycles, the uniaxial compressive strength dramatically decreased; then, the amplitude reduces, and eventually, the uniaxial compressive strength was only slightly decreasing with the remaining freeze-thaw cycles. After the oil shale samples have undergone 24 freeze-thaw cycles, the maximum variation rate of uniaxial compressive strength was reached up to 64%.

According to the experimental results, the relationship between the uniaxial compressive strength and the number of freeze-thaw cycles can be fitted

$$\sigma = -\frac{19.82058 + 27.14498}{(1 + nE0.15905/11.09104)}, \quad (7)$$

where σ is the uniaxial compressive strength (MPa), n is the number of freeze-thaw cycles, and the correlation coefficient is 0.98587.

Additionally, the elastic modulus of the tested oil shale sample was obtained under conditions of different freeze-thaw cycles. As shown in Figure 11, the elastic modulus of the oil shale sample exponentially decreased with the increasing of freeze-thaw cycles, and the maximum elastic modulus was approximately 4 GPa, whereas the minimum elastic modulus of tested oil shale sample is approximately 1.5 GPa. After processing the oil shale samples with 24 freeze-thaw cycles, the maximum variation rate of the elastic modulus reached up to 65%, which is greatly influenced and determined by the number of freeze-thaw cycles.

According to the obtained elastic modulus results, the relationship between the elastic modulus and freeze-thaw cycles can be fitted as

$$E = \frac{1.14961 + 2.83426}{(1 + n^{0.82524/1.99395})}, \quad (8)$$

where E is the elastic modulus (GPa), n is the number of freeze-thaw cycles, and the correlation coefficient is 0.98423.

4.5. Influence of Freeze-Thaw Cycles on Longitudinal Wave Velocity of Oil Shale Samples. According to the obtained wave velocity of tested oil shale sample, the longitudinal wave velocity of processed oil shale sample is shown in Figure 12. With the increase of periodic freeze-thaw cycles, the longitudinal wave velocity of oil shale sample dramatically decreases. The periodic freeze-thaw cycle has a significant influence on the longitudinal wave velocity of tested oil shale samples. As shown in Table 6, once the oil shale samples have been proceeded with 24 periodic freeze-thaw cycles, the minimum wave velocity of 1602 m/s can be accomplished.

Due to the performance of periodic freeze-thaw cycles on measured oil shale sample, the frozen ice particles inside the fractures will be melted while the temperature rises; otherwise, the water or moisture will be repeatedly frozen, which enlarges the fractures inside the oil shale samples. Thereby, the density of oil shale sample is decreasing due to the pore volume of the measured sample being increased. However, the wave velocity positively varies with the density of measured materials; thus, the longitudinal wave velocity reduces with the increase of periodic freeze-thaw cycles.

5. Conclusions

Under conditions of periodic freeze-thaw cycles, the physical and mechanical properties of oil shale samples were dramatically varied, and related conclusions and findings can be obtained:

- (1) Periodic freeze-thaw cycles greatly influence the physical and mechanical properties of oil shale samples. Once the oil shale samples were frozen and thawed for 24 cycles, the maximum compressive strength and elastic modulus were 10.39 MPa and 4.37 GPa, respectively, besides the maximum variation rates of uniaxial compressive strength and elastic modulus reaches up to 64% and 65%, respectively
- (2) The freeze-thaw coefficient of measured oil shale samples exponentially decreased with the increased number of freeze-thaw cycles, whereas the longitudinal wave velocity of tested samples ranged from 1602 m/s to 2464 m/s, as a result of the new micro-pores inside the oil shale sample

Data Availability

The data used to support the findings of this study are included within the article.

Conflicts of Interest

No conflict of interest exists in the submission of this manuscript.

Authors' Contributions

The manuscript is approved by all authors for publication.

Acknowledgments

This study was supported by the Fundamental Research Funds for the Central Universities (Project No. 2021CDJQY-028 and No.2019CDXYZH0019), the Natural Science Foundation of Chongqing Province, China (Grant No. cstc2019jcyj-msxmX0633), and the Special Project funded by Chongqing Postdoctoral Science Foundation (Project No. Xm2017068).

References

- [1] M. L. SJMK and H. M. Boak, "Panel discussion on the state of the U.S. and global oil shale development: introductory comments," in *32nd Oil Shale Symposium Golden*, p. 53, Curran Associates, Inc, Colorado, USA, 2012.
- [2] L. I. Shuyuan, X. Tang, H. Jilai, and Q. Jiashan, "Global oil shale development and utilization today-two oil shale symposiums held in 2012," *Sino-Globe Energy*, vol. 1, pp. 3–11, 2013.
- [3] C. H. A. I. N. SSL, *Case study of oil shale production*, Universiti Tunku Abdul Rahman, 2016.
- [4] X. Zhang, S. Zhang, Y. Luo, and D. Wu, "Experimental study and analysis on a fluidic hammer—an innovative rotary-percussion drilling tool," *Journal of Petroleum Science and Engineering*, vol. 173, pp. 362–370, 2019.
- [5] L. Jian and L. Weiguo, "Problems and environmental impacts induced by mining technology of shale oil and gas and coalbed methane," *Science Technology and Engineering*, vol. 17, no. 30, pp. 121–134, 2017.
- [6] Z. Chuanwen, M. Qingqiang, and T. Xuan, "Present situation and prospect of oil shale mining technology," *Mineral Exploration*, vol. 12, no. 8, pp. 1798–1805, 2021.
- [7] E. Elmer, *Method and apparatus for the destructive of kerogen in situ: US, 5058675*, U.S. Patent and Trademark Office, 1991.
- [8] S. L. Wellington, I. E. Berchenko, E. P. De Rouffignac et al., *In situ thermal processing of an oil shale formation to produce a condensate: US6, 923, 257.2005-8-2*, 2005.
- [9] J. M. D. R. Karanikas, *In-situ thermal processing of an oil shale formation while inhibiting coking*, 2005.
- [10] Z. Jinxun, Y. Qi, H. Yang, and S. Yongwei, "Temperature field expansion of basin-shaped freezing technology in sandy pebble stratum of Beijing," *Rock and Soil Mechanics*, vol. 41, no. 8, pp. 2796–2807, 2020.
- [11] M. Josh, L. Esteban, C. Delle Piane, J. Sarout, D. N. Dewhurst, and M. B. Clennell, "Laboratory characterisation of shale properties," *Journal of Petroleum Science and Engineering*, vol. 88–89, pp. 107–124, 2012.
- [12] S. Youhong, W. Guo, and S. Deng, "The status and development trend of in-situ conversion and drilling exploitation technology for oil shale," *Drilling Engineering*, vol. 48, no. 1, pp. 57–67, 2021.
- [13] U. Smolczyk, *Geotechnical Engineering Handbook, Volume 2: Procedures*, John Wiley & Sons, 2003.
- [14] Z. Bo, W. Yang, and B. Wang, "Plastic design theory of frozen wall thickness in an ultradeep soil layer considering large deformation characteristics," *Mathematical Problems in Engineering*, vol. 2018, Article ID 8513413, 2018.
- [15] Li, *Experimental Study on the Influence of Freezing Wall on Groundwater Temperature Field and Flow Field during Oil Shale In-Situ Mining*, Jilin University, 2020.
- [16] A. Momeni, Y. Abdilor, G. R. Khanlari, M. Heidari, and A. A. Sepahi, "The effect of freeze-thaw cycles on physical and mechanical properties of granitoid hard rocks," *Bulletin of Engineering Geology and the Environment*, vol. 75, no. 4, pp. 1649–1656, 2015.
- [17] L. M. Del Roa, F. Lopez, F. J. Esteban et al., "Ultrasonic study of alteration processes in granites caused by freezing and thawing," in *IEEE Ultrasonics Symposium, 2005*, pp. 415–418, Rotterdam, Netherlands, 2005.
- [18] H. Yavuz, "Effect of free e-thaw and thermal shock weathering on the physical and mechanical properties of an andesite stone," *Bulletin of Engineering Geology and the Environment*, vol. 70, no. 2, pp. 187–192, 2011.
- [19] Z. Q. P. Y. Yang Gengshe, "On the microdamage characteristics of rock under the frost and thaw conditions," *Journal of Xi'an University of Science and Technology*, vol. 139, 2003.
- [20] Z. Q. P. Y. Yang Gengshe, "CT scanning test of meso-damage propagation of rock under different freezing temperature," *Journal of Chang'an University (Natural Science Edition)*, vol. 24, no. 6, pp. 40–46, 2004.
- [21] Z. Q. R. J. Yang Gengshe, "Study on the effect of freezing rate on the damage CT values of Tongchuan sandstone," *Chinese journal of rock mechanics and engineering*, vol. 23, no. 24, pp. 4099–4104, 2004.
- [22] Y. Yang, D. Lei, H. Cai, S. Wang, and Y. Mu, "Analysis of moisture and temperature fields coupling process in freezing shaft," *Thermal Science*, vol. 23, no. 3 Part A, pp. 1329–1335, 2019.
- [23] H. G. Z. J. Wu Gang, "Experimental study on cycles of freeze-thaw of marble," *Chinese Journal of Rock Mechanics and Engineering*, vol. 25, pp. 2930–2938, 2006.
- [24] H. M. W. S. Liu Chengyu, "Experimental investigation on freeze-thawing damage characteristics of granite at low temperature," *Journal of Hunan University of Science & Technology: Natural Science Edition*, vol. 20, no. 1, pp. 37–40, 2005.
- [25] M. Bellanger, "HFR (1993) water behavior in limestone as a function of pores structure: application to frost resistance of some lorraine limestones," *Engineering Geology*, vol. 36, no. 1–2, pp. 99–108, 1993.
- [26] J. Haibin, *Theoretical Damage Models of Porous Rocks and Hard Jointed Rocks Subjected to Frost Action and Further Experimental Verifications*, China University of Geosciences, Wuhan, 2016.
- [27] J. Li, *Experiment study on deterioration mechanism of rock under the conditions of freezing-thawing cycles in cold regions based on NMR technology*, Central South University, 2012.
- [28] Q. W. X. P. Tong Cong, "Progress of theoretical research of rock damage," *Copper Engineering*, vol. 7, 2011.
- [29] L. Q. Xu Guangmiao, "Analysis of mechanism of rock failure due to freeze thaw cycling and mechanical testing study of frozen-thawed rocks," *Chinese Journal of Rock Mechanics and Engineering*, vol. 24, no. 17, pp. 3076–3082, 2005.
- [30] Q. Wang, *Experiment on thermal and electrical physical properties of oil shale in Jinlin Huadian area*, Jilin University, 2011.

Research Article

Particle Flow Analysis of Macroscopic and Mesoscopic Failure Process of Salt Rock under High Temperature and Triaxial Stress

Haoran Li,¹ Ziheng Wang,¹ Dekang Li^{1,2} and Yajun Zhang¹

¹Shijiazhuang Tiedao University, Shijiazhuang, Hebei, China

²Institute of Geophysics, China Earthquake Administration, Beijing, China

Correspondence should be addressed to Dekang Li; dekangli@163.com

Received 3 August 2021; Revised 2 October 2021; Accepted 15 October 2021; Published 15 November 2021

Academic Editor: Yu Wang

Copyright © 2021 Haoran Li et al. This is an open access article distributed under the Creative Commons Attribution License, which permits unrestricted use, distribution, and reproduction in any medium, provided the original work is properly cited.

In order to reveal the mechanism of thermal-induced deformation and fracture development of salt rock under high temperature, the particle flow program PFC^{2D} was used to study the triaxial compression failure process of salt rocks under different temperatures; at the same time, a combination model of Burge and Linearbond was proposed to simulate plastic deformation and heat conduction of salt rock. Finally, the simulation results were compared with the experimental results to verify the validity of the conclusion. The simulation results show that the elastic limit points of rock gradually descend, the dilatancy points rise gradually, and the plastic deformation characteristics of salt rock become more obvious with the increase of temperature. Due to the damage of the sample, the strong chains break and disappear, increasing the proportion of the weak chains, and the high temperature intensifies the rupture of the contact between the particles in the salt rock. As the temperature increases from 50°C to 120°C, the strong chains in the rock sample decrease significantly, and the damage gradually increases; when the temperature is 150°C, the contact force decreases sharply, and the damage of salt rock is significant. According to the particle displacement cloud diagrams, it is found that the expansion direction from the middle part of the rock sample to the left and right ends is 12.08°, 9.55°, 8.2°, 6.33°, and 0°, respectively. The displacement directions of the rock sample show obvious radial expansion tendency, and the higher the temperature, the more obvious the “drum-shaped” failure phenomenon in the middle of the rock sample. During the heating process, the thermal cracks are mainly tensile cracks, and transverse cracks are gradually formed in the middle of the model. The cementation failure points at the top and bottom of the model expand in an oblique direction and form oblique cracks of about 45°. From the three different mathematical models of macroscopic and mesoscopic views, it is concluded that the effect of temperatures on salt rock is more significant after 90°C. This research is important for exploring the macroscopic and microscopic mechanics evolution of salt rock and provides a reference for determining the long-term mechanical strength of salt rock.

1. Introduction

Salt rock can create an ideal environment for the storage of underground oil and gas energy, and salt cavern energy storage is generally built in the salt rock ore layer with a depth of 1500 m [1]. However, with the rapid development of shallow favourable deposits, the development of salt cavern underground energy storage is expanded from shallow (buried depth < 1500 m) to deep (buried depth 1500-2500 m) and ultradeep (buried depth > 2500 m), during which the construction and operation of underground storage also face more complex geological conditions, such as high in situ stress and

high ground temperature. Therefore, it is very important to study the physical and mechanical properties of salt rock in a high-temperature environment to ensure the safe operation of storage.

Many scholars have done a lot of experimental research on the mechanical properties of salt rock under the influence of temperature. Gao et al. [2] carried out triaxial compression tests of salt rock under the temperature of 25°C, 50°C, and 100°C to study the variation of macroscopic mechanical parameters of rock mass with temperature from a macro perspective, and they found that the peak stress and elastic modulus of salt rock decreased with the increase of temperature.

Wu et al. [3] monitored the acoustic emission activities of salt rock in the process of thermal loading and explored the acoustic emission characteristics of rock at different stress stages under high temperatures. Kang et al. [4] designed the damage self-recovery test of salt rock and analyzed the damage and healing mechanism of salt rock from the perspective of crystal by using SEM technology. Under different temperatures and osmotic pressures, Yang et al. [5] carried out triaxial creep tests on calcium mirabilite salt rock and analyzed the influence of temperature on the creep process of calcium mirabilite. Because of the restriction of the test conditions, the temperature in the triaxial test of salt rock was not high (below 100°C), and the results had limitations.

In addition, the laboratory tests always try to explain the temperature effect from the macroscopic perspective, which cannot reflect the mesoscopic development of salt rock in the thermodynamic coupling process; the DEM makes up this defect and is widely used in the geotechnical engineering field. Shen et al. [6] used PFC^{2D} to simulate the dynamic failure process of shale rock under uniaxial compression and explored the evolution characteristics of microcracks in brittle shale failure under different stresses. Jiang et al. [7] used the discrete element method (DEM) to carry out triaxial simulation tests on structural sand and compared the results of numerical simulation and laboratory tests. Li et al. [8] applied the 3D-GBM model to PFC^{3D} to explore the micro-mechanical properties of salt rock practical scale and verified the effectiveness of this method. Based on the DEM, Li et al. [9, 10] adopted the thermal-mechanical creep constitutive model to explore the micromechanism of the influence of temperature on the creep behaviour of salt rock. Xu [11] and Liang et al. [12] used PFC^{2D} to establish the thermal-mechanical model and explored the fracture mechanism of granite under high temperature from a mesoscopic perspective. However, although the particle discrete element method has been widely used to analyze the damage evolution of rock mass, the research on the failure law of rock under a high-temperature environment is limited.

Given the complexity of rock and earth mass mesostructure and the limitation of the research, there is no accepted mechanical theory formed to characterize the relationship between macro- and mesoevolution of rock mass. Based on the particle flow simulation technology, this paper makes up for the inadequacy of indoor high-temperature rock mechanics tests, analyzes the triaxial compression failure process of salt rock under 20°C, 50°C, 90°C, 120°C, and 150°C, and systematically studies the correlation characteristics of salt rock from mesoscopic change to macroscopic response, revealing the macro-mesoevolution mechanism of salt rock damage under high-temperature environment.

2. Constitutive Contact Model and Thermal Module Implementation

2.1. Selection of Constitutive Model

- (1) Burger model: Burger's model is an elastoviscous rheological model, which consists of the Maxwell body in series with the Kelvin body (Figure 1(a)).

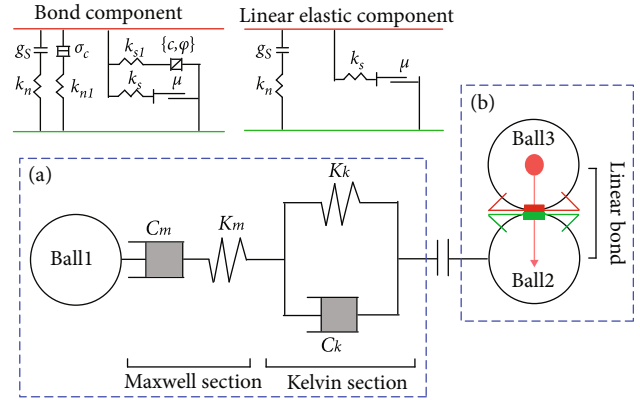


FIGURE 1: A combinatorial constitutive contact model of Burger and Linearbond.

The main contact parameters are the stiffness (K_m , K_n) of the elastic element and the bond coefficient (C_m , C_k) of the viscous element. The stiffness of the elastic element is the stiffness of contact between particles. The bond coefficient of the viscous element is the contact damping of the particles, which is related to the deformation strength. This model can well reflect the viscoplastic deformation characteristics of salt rock; however, during heating and loading, the internal thermal damage of the salt rock cannot be reflected by Burger's model, and the built-in program of the model does not have related functions, such as crack control network, force chain, and energy

- (2) Linearbond model: the Linearbond model consists of a bond component and a linear elastic component (Figure 1(b)), which establishes an elastic contact and can better simulate the linear elastic stage of salt rock. In addition, stiffness ratio (k_n/k_s), bond strength (c), and effective modulus (E^*) are the main contact parameters in the Linearbond model. The stiffness ratio is the ratio of normal stiffness to tangential stiffness (related to particle deformation). Bond strength is the contact bond strength of the particles. Effective modulus is the elastic modulus assigned to a single particle at the microscopic scale. After the contact bond is broken, the model allows the contacts between particles to produce cementation failure points, which can simulate the microcrack propagation during loading to better reflect the degradation of mechanical properties of rock and thermal expansion effects
- (3) Combination constitutive model: during the triaxial compression test, the salt rock exhibits strong viscoplastic deformation characteristics, and microcracks grow significantly. In addition, the high temperature increases the ductility of the rock mass, and the thermal response of the internal cementation is strong. When the temperature reaches a certain value, the salt rock may enter a creep stage. Therefore, to better simulate the mesoscopic failure process of salt rock

under high-temperature triaxial stress, the combination constitutive contact model of Burger and Linearbond was adopted, as shown in Figure 1. The constitutive models, burger and linear bond, and their parameters are quoted from the built-in database of PFC^{2D} of Itasca commercial [13, 14]

2.2. Heat Transfer Mechanism of the Model. To study the displacement and stress changes of rock particles under the action of thermal effect, the model needs to have the ability of heat storage and heat conduction. In the particle flow program, the heat conduction between particles is realized by the heat source through the heat pipe and finally forms the network heat transfer channel. The heat pipe represents the heat transfer process, which is related to predetermined thermal parameters of the model. Thermal parameters include thermal expansion coefficient (α), thermal resistance (η), thermal conductivity (k^*), and specific heat capacity (C_v). These parameters work together to generate heat conduction between particles. These parameters are determined following Section 3.4 of this paper. The thermal effect of particles produces the following effects: thermal strain causes particle expansion, which leads to the change of contact force; at the same time, the heat transferred through the contact between particles causes the expansion of the bond; their combined effect causes rock sample deformation. In addition, when heat is transferred to the inside of the model, the force and range of contact between particles will increase, and the parallel bond between particles will be broken, or particles will be moved, resulting in partial failure of the heat pipes between particles. The number of effective heat pipes decreases, and the overall heat conduction ability of the model decreases. The above process is consistent with the actual situation [15], so the PFC^{2D} model can better simulate the heat conduction process of rock.

2.3. Thermal Strain Constitutive Model. In the PFC^{2D}, the heat source completes heat conduction through the heat pipe and finally forms a network heat transfer channel. We assume that the effect of strain on temperature can be ignored, and the continuity equation of heat conduction involving thermal-mechanical coupled quasistatic mechanics is shown in

$$-\frac{\partial q_i}{\partial x_i} + q_v = \rho C_v \frac{\partial T}{\partial t}, \quad (1)$$

where q_i is the heat flow vector, q_v is the volumetric heat source intensity or energy density, ρ is the density, C_v is the specific heat capacity, and T is the temperature.

In the PFC^{2D}, the thermal strain is obtained by calculating the expansion of the adhesion between particles, and the thermal strain of the particles under the action of temperature is calculated by

$$\Delta R = \alpha R \Delta T, \quad (2)$$

where ΔT is the temperature increment, α is the linear expansion coefficient of the particle, and ΔR is the change in radius under temperature.

3. Numerical Modeling and Parameter Calibration

3.1. The Establishment of the Geometric Model. Referring to the high-temperature triaxial compression test in the salt rock chamber [16], numerical simulation was carried out to perform comparative analysis and verify the conclusion drawn in numerical simulation. The two-dimensional plane stress model was established, and the size of the model is $\Phi 100 \text{ mm} \times 200 \text{ mm}$, which is consistent with the laboratory test. In the model, the particle size range is $0.7 \text{ mm} \sim 1.05 \text{ mm}$, obeying uniform probability distribution. The reasonable ratio of the sample size to the average grain diameter is greater than $30 \sim 40$ [17]. The combination constitutive model is adopted to simulate the contacts between particles; the contacts between the wall and the particle adopt Linear's model, forming a total of 17,993 contacts. The density of the rock sample is 2300 kg/m^3 , and the porosity is 0.03. The salt rock model is shown in Figure 2.

3.2. Test Scheme of Numerical Simulation. The first step is to calibrate the parameters of the constitutive contact model based on the laboratory test results. The test temperature was set to 20°C (indoor temperature), and the axial loading speed was set to 0.05 m/s . In the quasistatic simulation, a higher local damping coefficient is usually used to remove the kinetic energy in the system effectively, making the quasistatic deformation occur at a much higher rate than the actual situation [18, 19]. Triaxial compression tests with confining pressures of 10 MPa, 20 MPa, and 30 MPa were, respectively, simulated to obtain the stress-strain curves; data processing was studied by trial and error method and comparison method. Then, the results were compared with laboratory test results to confirm the reasonable parameters of the numerical simulation constitutive contact model.

The second step is to determine the thermal model parameters and the new contact parameters. The triaxial compression tests were carried out at environment temperatures of 50°C , 90°C , 120°C , and 150°C while setting the triaxial confining pressure as 10 MPa and the axial loading speed as 0.05 m/s . Through parameter optimization, the stress-strain curves of salt rock were obtained. By comparing to laboratory test results, the reasonability of numerical simulation thermal model parameters was verified, and new contact parameters were determined.

The third step is to conduct the triaxial high-temperature numerical simulation test of salt rock. According to the parameters determined above, the triaxial confining pressure was set to be 10 MPa, and the axial loading speed was set to be 0.05 m/s . The stress-strain curves of salt rock under the environment temperatures of 20°C , 50°C , 90°C , 120°C , and 150°C were to obtain to further explore the damage evolution mechanism and macroscopic and mesoscopic characteristics of salt rock model at high temperatures.

3.3. Determination of Constitutive Contact Model Parameters. Since the cross-sectional area of the salt rock changes greatly after compression, the assumption of small strain is no longer applicable. Therefore, based on the results of the laboratory test [16], the area correction method [20] was used to process

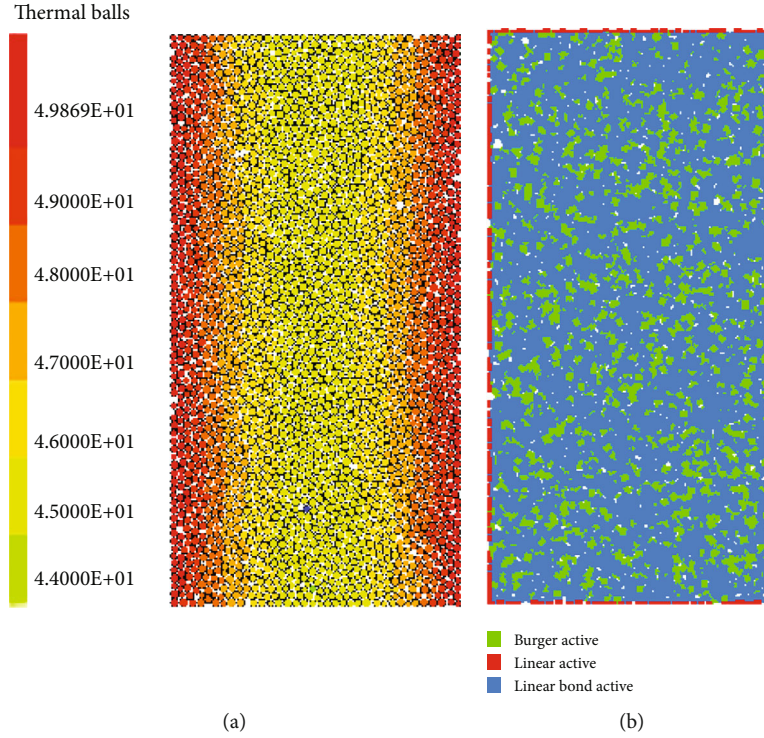


FIGURE 2: Numerical model of the salt rock: (a) particle model of heat transfer; (b) different contact models between particles.

the stress-strain data (Figure 3). The principle of the area correction method is as follows.

As the deformation changes the cross-sectional area of the rock sample, the corresponding pressure can be corrected by engineering strain; the specific expression is as follows.

$$\sigma_{\text{luc}} = \frac{F_1}{A'}, \quad A' = \frac{A_0}{1 - \varepsilon_t}, \quad (3)$$

where σ_{luc} is linear corrected axial pressure, A_0 is the cross-sectional area of the unpressurized sample, F_1 is the axial force, and ε_t is the engineering strain value.

In addition, according to the current research results [21–25], a set of constitutive model mesoparameters (Table 1) are determined by comparing the revised laboratory test results of salt rock so that the basic macroscopic parameters and stress-strain curves from the triaxial numerical simulation at room temperature are in good agreement with the laboratory test results (Figure 3). Comparison of stress-strain curves between laboratory test and numerical simulation shows that the correlation coefficients between the test curves and numerical curves are 0.9652, 0.9402, and 0.9601, respectively. The selected mesoparameters can reasonably reflect the macromechanical properties of the laboratory triaxial tests.

3.4. Determination of Thermal Model Parameters and New Contact Parameters. The heat conduction of the salt rock model was simulated by using the heat module of PFC^{2D}, in which the upper and lower boundary of the salt rock model was set to be adiabatic, so the heat was transmitted

from the lateral boundary of the model. With the reference data [9, 26, 27] and optimized parameters, a set of mesoscopic parameters of the thermal model were determined (Table 2). Specific heat capacity, C_v (J/kg°C), indicates the amount of heat required to raise the temperature of 1 kg of material by 1°C. The microscopic properties could be the same as the macroscopic specific heat capacity of the material. The thermal coefficient of expansion, α (1/°C), is the relative change in length of a unit length object when its temperature increases by 1°C. This microscopic property can be set by the macroscopic thermal coefficient of expansion α of the material. Upper and lower boundary thermal resistance, η (°C/W·m), is the ratio of the temperature difference between the two ends of the object and the power of the heat source when heat is transmitted through the object. The value of η can be calculated by traversing the thermal network of a given granular material. Macroscopic thermal conductivity, k^* (W/m°C), refers to the heat transfer per unit time through per unit horizontal cross-sectional area when the temperature gradient is 1°C/m vertically downward.

In addition, as the temperature rose, the cohesion between the particles was weakened, the particles moved, and the cementation points were destroyed, resulting in the contact of the particles, the local organization, and even the overall structure greatly changed. Therefore, it is necessary to update the contact parameters of the model after the rock temperature rising to better simulate the loading process of salt rock after heating up. The contact model parameters at 20°C were used as the reference parameters, and the new contact parameters were determined through

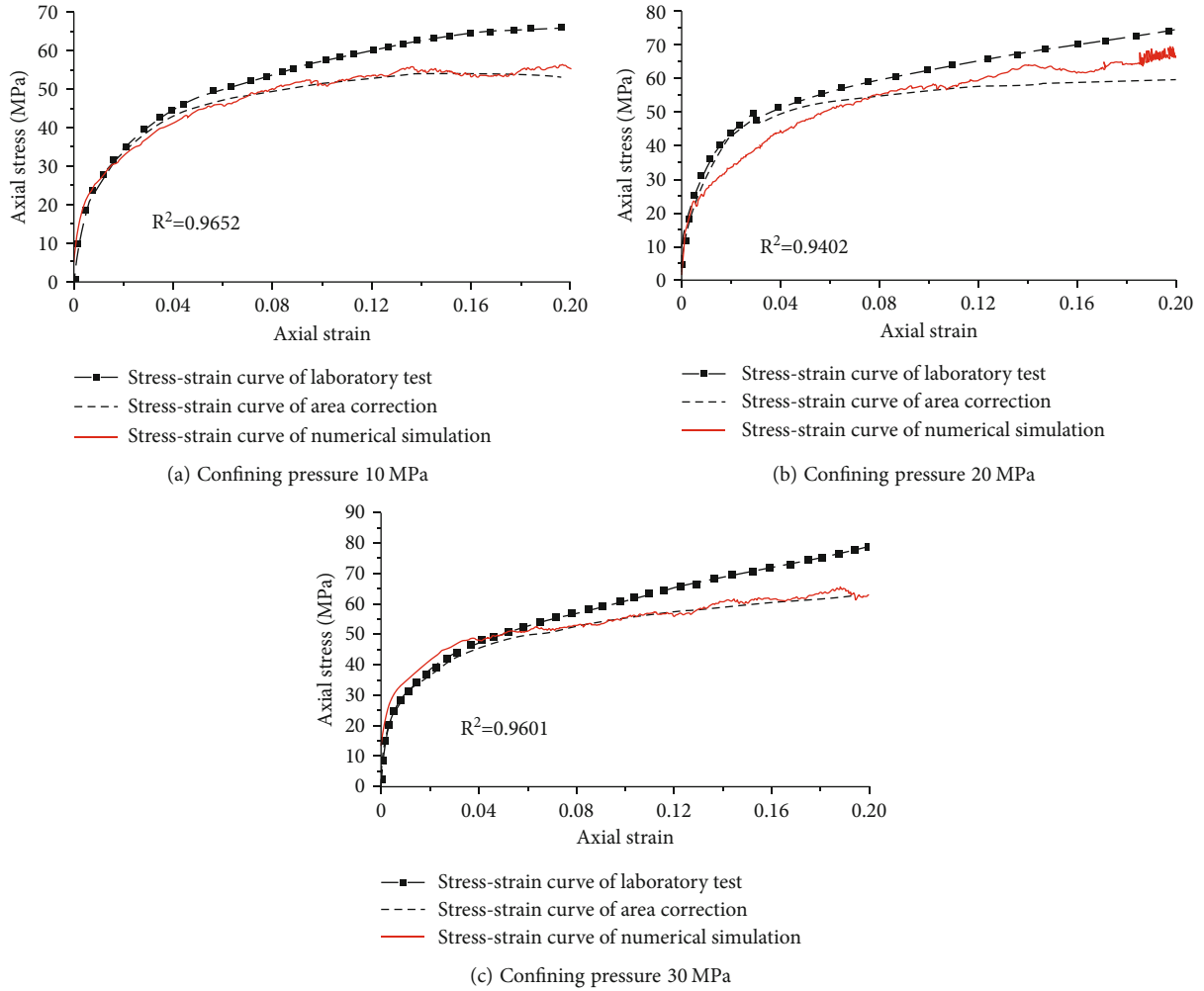


FIGURE 3: Stress-strain curves of different confining pressures at 20°C: (a) confining pressure 10 MPa; (b) confining pressure 20 MPa; (c) confining pressure 30 MPa.

TABLE 1: Microstructure parameters of PFC^{2D} constitutive contact model.

Contact model	Mesosopic parameter	Numerical value
Linear	Density (kg/m ³)	2300
	Linear contact modulus (Pa)	3 × 10 ⁹
	Stiffness ratio k_n/k_s	1.0
	Coefficient of intergranular friction (μ)	0.6
Parallel bond	Bond contact modulus (Pa)	3 × 10 ⁹
	Normal bond strength (Pa)	2.6 × 10 ⁸
	Shear bond strength (Pa)	2.0 × 10 ⁸
Burger's	Kelvin elastic coefficient (Pa)	1 × 10 ⁹
	Kelvin viscosity coefficient (Pa·s)	1 × 10 ⁵
	Maxwell elastic coefficient (Pa)	5 × 10 ¹¹
	Maxwell viscosity coefficient (Pa·s)	1 × 10 ⁷
	Friction coefficient (μ)	0.6

TABLE 2: Microstructure parameters of PFC^{2D} thermal model.

Model parameter	Units	Numerical value
Coefficient of thermal conductivity (k^*)	W/(m°C)	2.5
Specific heat capacity (C_v)	J/kg°C	1015
Thermal coefficient of expansion (α)	1/°C	2.8×10^{-6}
Upper and lower boundary thermal resistance (η)	°C/W · m	1×10^{300}

TABLE 3: New contact parameters of rock sample model at high temperature.

Model parameter	Numerical value					
	Temperature (°C)	20	50	90	120	150
Kelvin elastic coefficient (Pa)		1×10^9	5×10^8	2.5×10^8	2.2×10^8	2.0×10^8
Maxwell elastic coefficient (Pa)		5×10^{11}	4×10^{11}	3.0×10^{11}	2.5×10^{11}	1.5×10^{11}
Maxwell viscosity coefficient (Pa·s)		1×10^7	0.8×10^7	0.6×10^7	0.4×10^7	0.2×10^7
Normal bond strength (Pa)		2.6×10^8	2.4×10^8	2.2×10^8	2.0×10^8	1.8×10^8
Shear bond strength (Pa)		2.0×10^8	1.8×10^8	1.7×10^8	1.54×10^8	1.4×10^8

parameter optimization (Table 3). Under temperatures of 50°C, 90°C, 120°C, and 150°C, the simulation results of salt rock experiments with confining pressure of 10 MPa were obtained (Figure 4). The stress-strain characteristics of the laboratory test and numerical simulation test show good agreement, which verifies the rationality of the selection of thermal parameters and new contact parameters.

4. Analysis of Numerical Calculation Results

4.1. Characteristic Analysis of Salt Rock Strain Curves. In this section, triaxial compression simulations were carried out on salt rock under a different confining pressure of 10 MPa and 20°C, 50°C, 90°C, 120°C, and 150°C, respectively. The transverse strain, stress-strain curves, and volume strain curves of the samples were monitored and recorded, as shown in Figures 5–7.

Generally, the deformation process of rock can be divided into a linear elastic stage, a nonlinear elastic stage, a plastic stage, and a failure stage. As shown in Figure 5, the turning point from the nonlinear elastic stage to the plastic stage is defined as the elastic limit point, and it can be seen that the elastic limit points (a–e) of the rock gradually descended with the increase of temperature. The result shows that with the increase of temperature, the plastic deformation of salt rock becomes more obvious, and the stress-strain curves of salt rock tend to be flatter. Figure 6 shows that with the temperature increase from 20°C, 50°C, 90°C, 120°C, to 150°C, respectively, the dilatancy points (a–e) of salt rock continuously increase at 20°C, 50°C, 90°C, 120°C, and 150°C. The result shows that with the increase of temperature, the internal particles of the rock sample expand, which causes the volume to increase and the same sample becomes loose. Therefore, the volume strain values of the sample reaching the expansion points increase during axial loading.

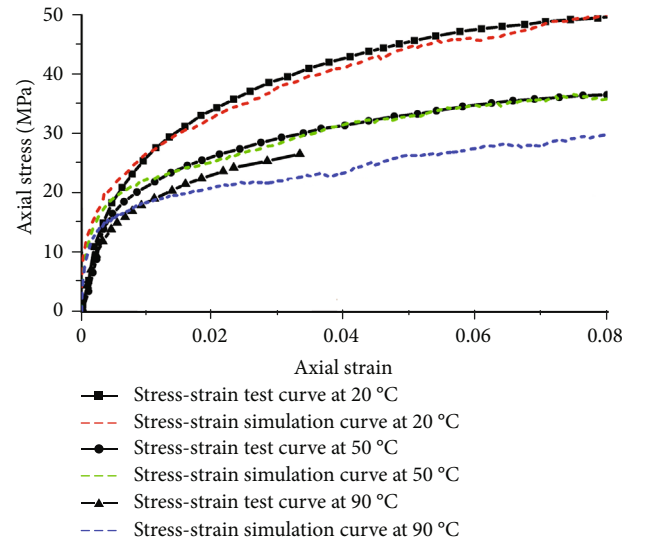


FIGURE 4: Stress-strain curves of different temperatures under the confining pressure of 10 MPa.

Figure 7 shows the transverse strain of salt rock after heating, and it can be seen that with the increase of termination temperature, the transverse strain was 0.0147, 0.0170, 0.018, and 0.0182, respectively, and the corresponding increments were 0.0023, 0.001, and 0.0002; this can be explained as that the temperature causes the increase of thermal motion of particles. However, when the particles collided with the wall, particles moved in reverse, resulting in the decrease of the increments of transverse strain.

4.2. Evolution of Force Chain Network in Rock Mass during Loading. The force chain network represents the distribution of the interparticle contact force in the soil framework

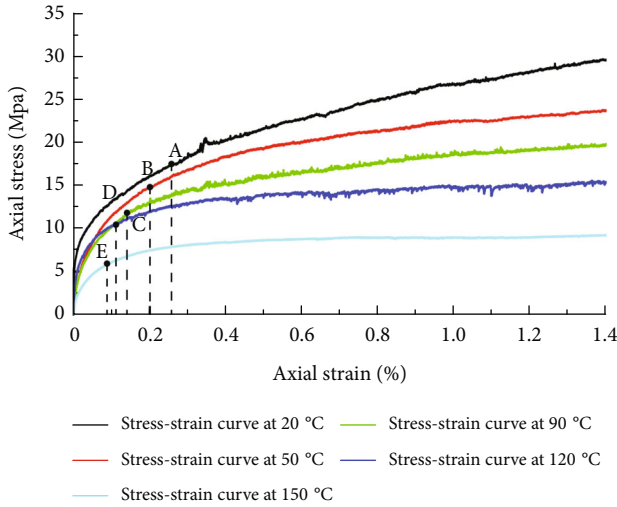


FIGURE 5: Stress-strain simulation curves of salt rock samples at different temperatures.

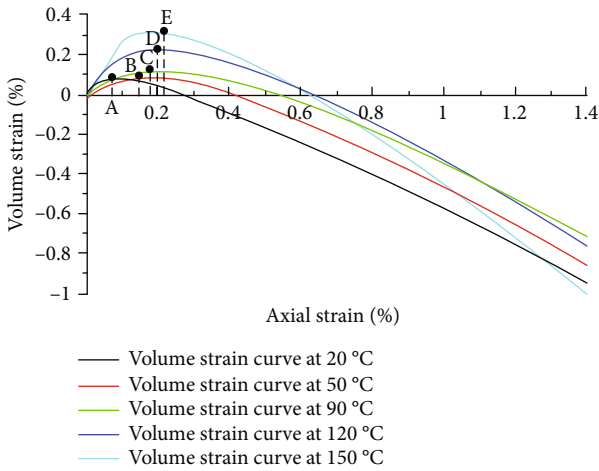


FIGURE 6: Volume strain simulation curves of salt rock samples at different temperatures.

system, which can reflect the sensitivity of the particle system to the force. Figure 8 shows the variation of the force chain network of the sample at different temperatures under the axial strain of 0.15. The contact force in the force chain was generalized to visually reflect the variation of the internal stress field of the sample at different temperatures.

- (1) It can be seen from Figures 8(a)–8(e) that the contact force inside the salt rock gradually decreased, and the strong chains broke and disappeared with the damage of the samples; at the same time, as the temperature increased, the proportion of weak chains increased under the same strain of 0.15, showing that the high temperature intensifies the rupture of contact between particles in the salt rock
- (2) The maximum contact force changed from 0.787 MPa to 0.649 MPa as the temperature changed from 20°C to 50°C. When the temperature changed from 120°C to 150°C, the maximum contact force varied from

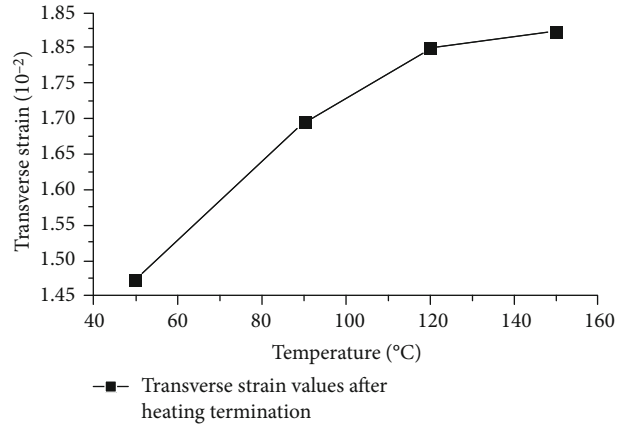


FIGURE 7: Transverse strain values of salt rock model after heating termination.

0.6 MPa to 0.417 MPa. For the temperature of 50°C, 90°C, and 120°C, the contact force slightly changed from 0.649 MPa, 0.62 MPa, to 0.6 MPa. However, Figures 8(b)–8(d) show that the force chains inside the rock sample significantly became disperse from 50°C to 120°C, indicating that the damage began to intensify gradually. The contact force decreased sharply at 150°C, indicating that the salt rock was damaged significantly

4.3. Evolution Law of Cloud Image of Displacement Field inside the Model. Figure 9 shows the change of displacement field in the sample under the temperature of 20°C, 50°C, 90°C, 120°C, and 150°C, respectively, and the axial strain was 0.15.

- (1) By analyzing the displacement direction of particles, it can be known that the displacement direction of the particles in the middle of the sample showed an obvious radial expansion trend at different temperatures, and the salt rock model appeared a “drum shape” destruction phenomenon
- (2) The arrows in Figures 9(a)–9(e) indicate the outward expansion direction of the central particles. It can be seen that the expansion direction from the middle of the sample to the left and right ends was 12.08°, 9.55°, 8.2°, 6.3°, and 0°, respectively, with the increase of temperature, which gradually changed from incline to horizontal. Therefore, during the loading, the phenomenon of “drum shape” in the middle of the rock sample became more obvious with the increase of temperature

4.4. Expansion Analysis of Mesofailure of Rock Mass during Heating. This section studies the initiation and evolution of thermal cracks in the salt rock during the heating process when the confining pressure of the test is 10 MPa, the initial temperature of the test is 20°C, and the heating termination temperatures are 50°C, 90°C, 120°C, 130°C, and 150°C, respectively. Figure 10 shows the distribution and extension of thermal cracks inside rock samples when the temperature

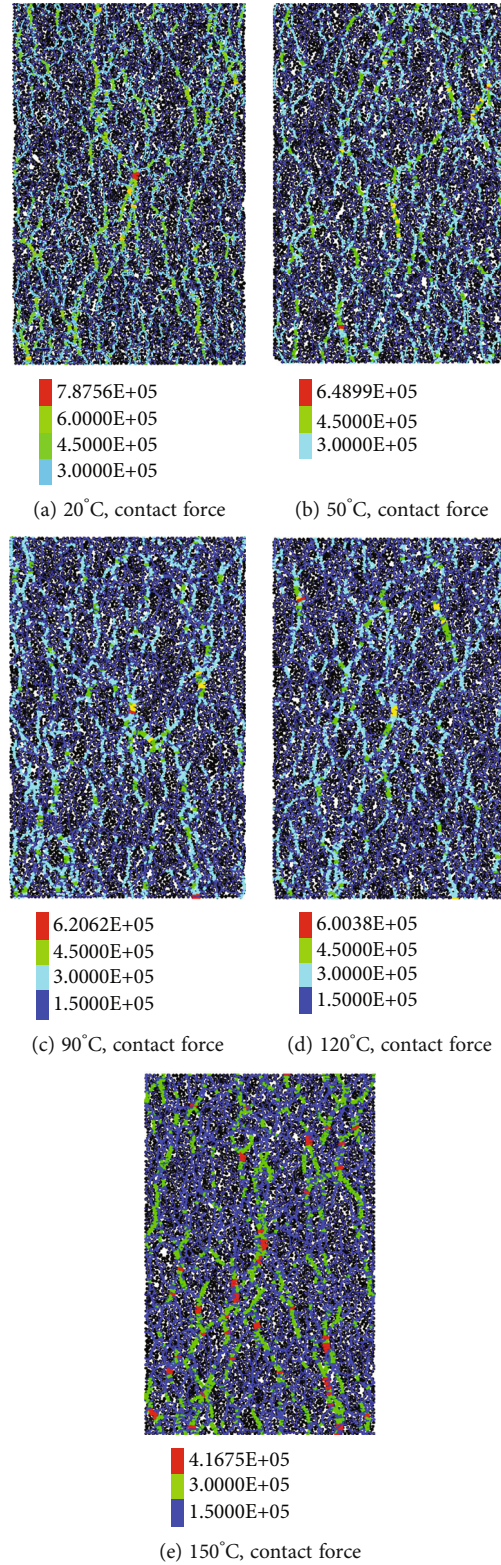


FIGURE 8: The force chain network evolution diagram of salt rock samples at different temperatures.

changed from 20°C to 50°C. A certain bonding distance is set between particles. The bonding force will be generated between particles due to the bonding action, which is called

the state of cementation when the distance between two particles is smaller than this distance. Cementation failure occurred under the action of thermal stress and thermal

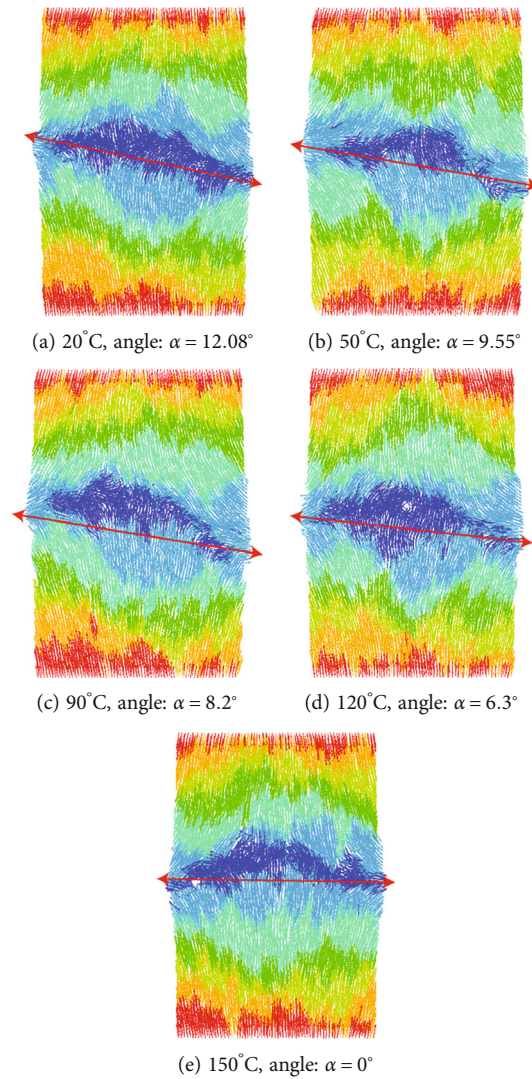


FIGURE 9: Displacement field nephograms of sample model at different temperatures.

strain. The failure criterion is as follows: the failure occurs between particles, generating cementation failure point, when the tensile stress, compressive stress, or shear stress generated between particles is greater than the cementation strength between particles.

- (1) It can be seen from Figures 10(a)–10(e) that there was a temperature gradient between the boundary and the internal particles of rock mass, and the cementation failure occurred first at the edge of the sample under the combined effect of thermal stress and thermal strain. As the heat was transferred to the interior of the model, the number of cementation failures increased, and the cementation failure points near the edge of the sample gradually connected. After reaching the termination temperature, the cementation failure points became stable
- (2) In the middle of the model, the cementation failure points expanded along the transverse direction. At

the top and bottom of the model, the cementation failure points expanded obliquely, and the direction was about 45° from the horizontal direction

- (3) Figure 11 shows the curve of the number of cementation failures under different temperatures. Figure 11 (a-b1-c1-d1) is the segment point of the cementation failure curve at 50°C, and Figure 11 (a-b2-c2-d2) is the segment point of the cementation failure curve at 90°C, 120°C, 130°C, and 150°C. It can be seen that at the initial stage of temperature rising (a-b1 and a-b2), the number of internal cementation failures in the salt rock increased linearly. With the transmission of heat (b1-c1 and b2-c2), the internal temperature gradient of rock mass became smaller, and the number of cementation failures grew smoothly. However, with the increase of temperature, the thermal motion of the particles increased, the cohesion decreases, and the

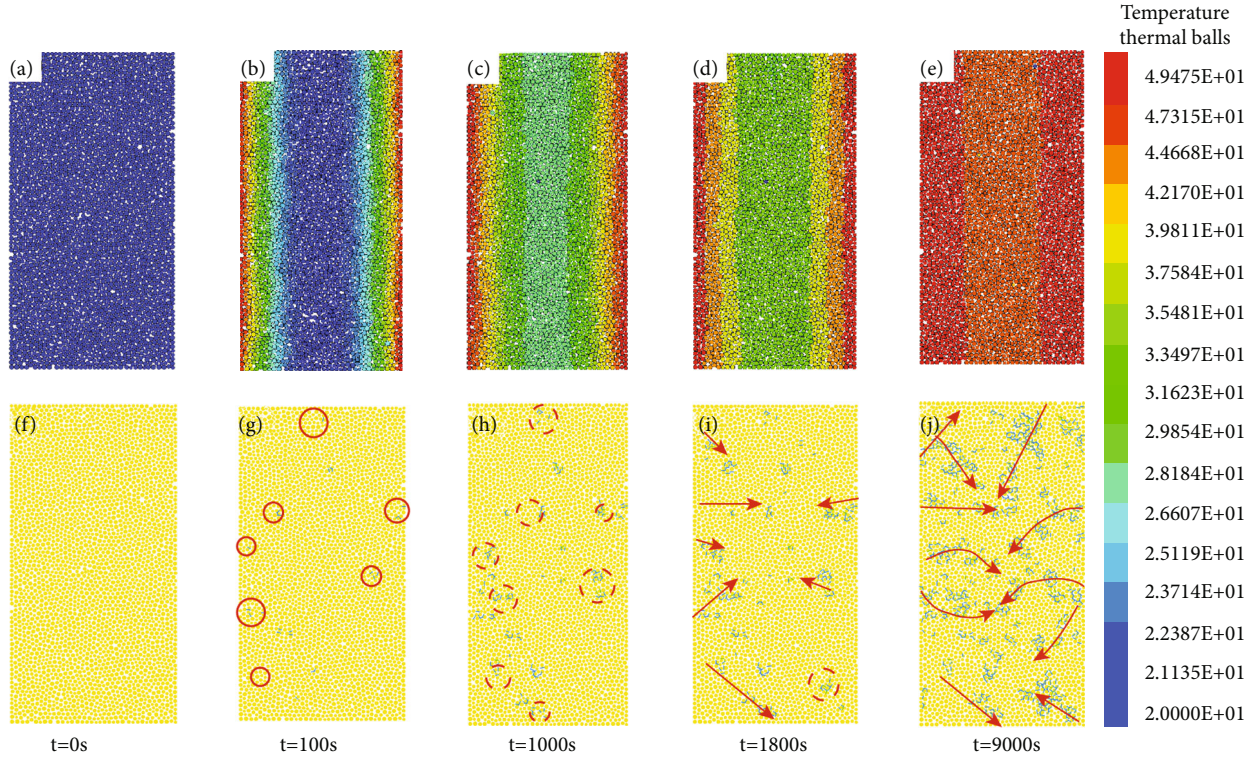


FIGURE 10: Distribution and propagation of cementation failure points in the salt rock model at 50°C (blue is the tensile failure points, green is the shear failure points, and red arrow represents the microcrack propagation direction).

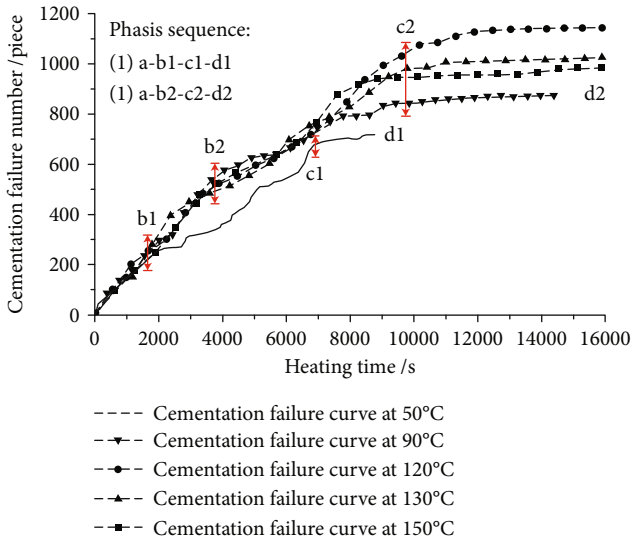


FIGURE 11: Cementation failure curves of sample model at different temperatures during temperature rising.

cementation failure points continued to increase at a slower rate. After the termination of heat transfer (c1-d1 and c2-d2), the cementation failure of rock mass no longer increased

- (4) According to the statistics of rock cementation failure points during the whole process of heating (Table 4), it was found that the number of cementation failure

points gradually increased with the termination temperature. However, when the temperature exceeded 120°C, the number of cementation failure points decreased, which may be because the significant enhancement of thermal movement and diffusion of particles in this temperature range move particles no longer a single movement, but a granular organizational movement. At the same time, the wall became more sensitive to the movement of particles, and the confining pressure of the wall also largely prevented contact fractures caused by particle dislocations

5. Quantitative Analysis of Thermal Damage of Salt Rock

5.1. Damage Analysis Based on the Elastic Modulus. In this section, the damage value is defined by the change of elastic modulus of the sample before and after heating [28], and the damage variable $D(T)$ is calculated as follows.

$$D(T) = 1 - \frac{E_T}{E_0}, \quad (4)$$

where E_T is elastic modulus at temperature T (MPa) and E_0 is elastic modulus at 20°C (MPa).

By analyzing the stress-strain curves at 20°C, 50°C, 90°C, 120°C, and 150°C, the corresponding elastic modulus of salt rock was calculated to be 4.989 GPa, 4.56 GPa, 3.72 GPa, 2.33 GPa, and 1.089 GPa, respectively. $D(T)$ at different temperatures were 0, 0.0860, 0.2543, 0.533, and 0.7817, respectively,

TABLE 4: Cementation failure number of sample model at different temperatures.

Serial number	Initial temperature (°C)	Termination temperature (°C)	Cementation failure numbers (piece)
1#	20	50	720
2#	20	90	874
3#	20	120	1148
4#	20	130	1041
5#	20	150	998

and the change curves of damage variables and elastic modulus with temperature are drawn in Figure 12.

It can be seen that the elastic modulus gradually decreased with increasing temperature, while the damage variables gradually increased, showing a negative correlation of them. Before reaching 90°C, the damage variables increased slowly from 0 to 0.2543 by 0.2543, and after 90°C, it increased by 0.5274. Between 90°C and 120°C, the damage variables changed from 0.2543 to 0.5330 by 0.2787. From 120°C to 150°C, they changed from 0.533 to 0.7817 by 0.2487. In conclusion, the damage of the salt rock model was relatively gentle before 90°C, while the influence of temperature on the salt rock was more significant after 90°C, but the higher the temperature did not cause more damage.

5.2. Damage Analysis Based on Cementation Accumulation Numbers. The particles are connected by the Linearpbond model and the Burger model. When the contact force is greater than the bonding strength, the contact bond will be broken and produce cementation failure points; then, the cementation failure points extend and penetrate each other to form microcracks, finally leading to the damage and deterioration of the salt rock model.

In addition, the rock damage index is usually defined by the development of microcracks as the basic variable. However, in the actual test, the number of cracks is not easy to obtain [29]. Therefore, many scholars define the damage variables as the ratio of cumulative acoustic emission ringing numbers to the cumulative ringing numbers under peak stress [30, 31]; the cementation failure numbers can represent cumulative acoustic emission ringing numbers in numerical simulation of particle flow [32, 33]. Therefore, with the particle flow discrete element method, the rock damage index was calculated as follows to quantitatively analyze the damage degree of salt rock at different temperatures.

$$D(T) = \frac{N(T)}{N_{0(T)}}, \quad (5)$$

where $N(T)$ is the cumulative cementation failure number at temperature T and $N_{0(T)}$ is the cementation failure number corresponding to peak stress at temperature T .

Generally, the point where the axial strain of salt rock is 0.1 is defined as the peak stress point. It can be seen from Figure 13 that at different temperatures, the variation trend

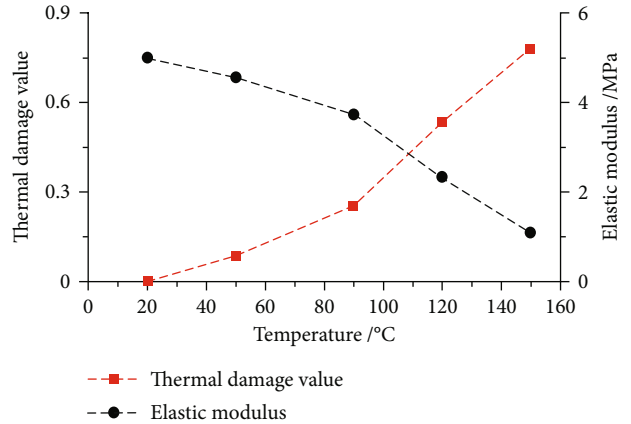


FIGURE 12: Damage variable curves of salt rock at different temperatures.

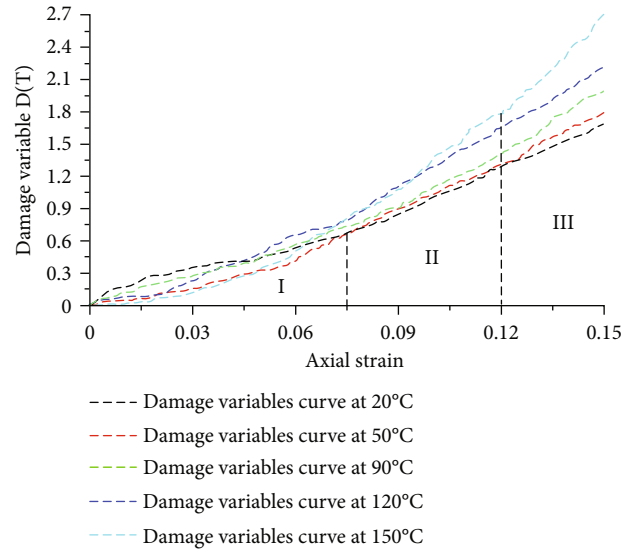


FIGURE 13: Variation curves of damage variables with axial strain at different temperatures.

of the salt rock damage variable $D(T)$ with the axial strain was basically the same, which can be divided into three stages. In stage I, the curve showed a slow-growth trend. In stage II, the slopes of all curves began to increase, and the damage started to be gradually intensified when the axial strain reached 0.075. In stage III, the damage variable sharply increased, and the higher the temperature, the more obvious the increment.

In the early stage of loading ($\varepsilon = 0 \sim 0.075$), the damage variable of salt rock did not change obviously at different temperatures. At the end of loading ($\varepsilon = 0.075 \sim 0.15$), the temperature showed a great influence on the damage of salt rock. In order to visually show the influence of temperature on the internal damage of salt rock, at different temperatures, the damage variables of salt rock when the axial strain was 0.09, 0.12, and 0.15 were obtained, as shown in Table 5.

TABLE 5: Damage variables of salt rock at different temperatures.

Temperature (°C)	Strain ($\epsilon = 0.09$)	Strain ($\epsilon = 0.12$)	Strain ($\epsilon = 0.15$)
20	0.7243	1.2949	1.6872
50	0.9192	1.3113	1.7962
90	0.9203	1.4162	1.9930
120	1.10	1.6432	2.2162
150	1.0645	1.7871	2.7097

It is found that from 20°C to 50°C, the damage increments under different strains were 0.1949, 0.0164, and 0.109, respectively. From 50°C to 90°C, the damage increments were 0.0011, 0.1049, and 0.1968, respectively. From 90°C to 120°C, the damage increments were 0.1797, 0.227, and 0.229, respectively. From 120°C to 150°C, the damage increments were -0.0355, 0.1439, and 0.4935, respectively. In conclusion, under different strains, the damage increments increase significantly with the temperatures after 90°C.

5.3. Damage Analysis Based on Crack Density Parameters. In the particle flow program, the rock model was established based on the assumptions of nonintersecting cracks, uniform crack distribution, and simple crack shape, which is the hypothetical model without cracks interaction (NIA). Based on NIA, Budiansky and O'Connell deduced the calculation model of rock elastic modulus and crack density parameters [34, 35], as follows.

$$\rho = \frac{45(2 - \nu_0)}{16(1 - \nu_0^2)(10 - 3\nu_0)} \left(\frac{E_0}{E} - 1 \right), \quad (6)$$

where E_0 is the elastic modulus of undamaged rock (MPa), ν_0 is Poisson's ratio of undamaged rock, E is the elastic modulus of damaged rock (MPa), and ρ is the crack density parameters.

Referring to the elastic modulus and Poisson's ratio of undamaged salt rock at room temperature, this paper explored the damage degree of salt rock at 20°C, 50°C, 90°C, 120°C, and 150°C. The elastic modulus and Poisson's ratio of undamaged salt rock are 7.157 MPa and 0.187, respectively [16]. Formula (3) is used to calculate the crack density of salt rock at different temperatures (see Table 6) and draw the curve of crack density with temperature, as shown in Figure 14.

When there is no thermal damage, the crack density parameter of rock is set to 0. It can be seen from Figure 14 that the crack density parameters increased slowly from 0.2433 to 0.5172, totally by 0.2739 before 90°C. From 90°C to 120°C, the value changed from 0.5172 to 1.1597 by 0.6425. From 120°C to 150°C, it changed from 1.1597 to 3.1192 by 1.9595. It can be seen that the number of cracks in the unit volume sharply increased after 90°C, and the temperature had a significant impact on the damage of salt rock at 150°C.

TABLE 6: Crack density parameters of salt rock at different temperatures.

Temperature (°C)	Elastic modulus (MPa)	Crack density parameters
20	4.989	0.2433
50	4.56	0.3188
90	3.72	0.5172
120	2.33	1.1597
150	1.089	3.1192

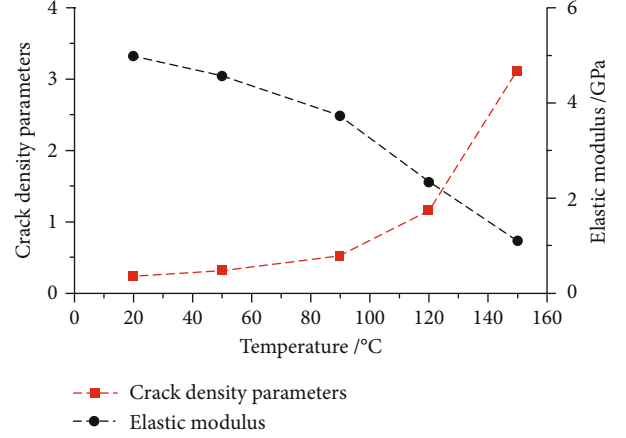


FIGURE 14: Crack density parameter curve of salt rock at different temperatures.

5.4. Comparative Analysis of Calculation Models. The elastic modulus, cumulative cementation numbers, and derived crack density parameters are closely related to the damage deterioration of rock mechanical properties.

- (1) The elastic modulus and crack density showed a consistent variation with temperature, indicating that the temperature has a significant effect on the damage of salt rock after 90°C
- (2) According to the calculation of cementation accumulation numbers, it was found that the damage of salt rock gradually increased after the axial strain reaching 0.075. Under different strains, the increments were 0.196, 0.1213, and 0.3018 from 20°C to 90°C, while the increments were 0.1442, 0.3079, and 0.7225, respectively, from 90°C to 150°C. After 90°C, the damage variables increased significantly with the change of temperatures; with the increase of loading, the damage variables increased significantly at 150°C. In addition, the crack density parameter also represents the damage of salt rock from the perspective of microcracks. The crack density parameter increased by 0.2739 from 20°C to 90°C, while it increased by 2.602 from 90°C to 150°C. After 90°C, the number of cracks per unit volume increased sharply. It can be seen from Figure 13 that the temperature has a significant effect on the

damage of salt rock at 150°C. The damage analysis of microcracks in salt rock from two different calculation models reflects the damage of salt rock under the action of temperature

- (3) Model ①: the calculation model is established from the perspective of macroscopic elastic modulus. Model ②: the calculation model is established from the perspective of mesoscopic cementation failure points. Model ③: the microcrack density parameter is established by using the macroscopic modulus, and the microphysical quantity characterizing the material is connected with the macroscopic modulus. From three different mathematical models, it is concluded that the temperature has a significant effect on the damage of salt rock after 90°C

6. Discussions

The physical and mechanical properties of the salt rock are affected by temperature, and the mechanism is complicated. On the one hand, the temperature is related to the thermal motion of the crystal particles. The higher the temperature, the weaker the binding force between particles, resulting in the enhanced plasticity of the rock and the decreased strength. The cohesion between rock particles is composed of true cohesion and apparent cohesion; true cohesion represents the bonding strength between particles, while apparent cohesion represents the frictional occlusal effect between particles [36]. In the low-temperature environment, the occlusal effect plays a dominant role, so the particle displacement is small, the elastic tensile deformation between the particles is not obvious, and the bonding strength is not weakened. In the high temperature, the friction and occlusion strength between particles are basically destroyed, and true cohesion plays a major role. With the increase of temperature, the bonding strength between particles is gradually destroyed, and the plastic deformation characteristics of rock become obvious. On the other hand, salt rock has damage repair function, including damage microcrack healing based on diffusion, microcrack filling based on NaCl crystal recrystallization, and the healing and bonding of NaCl crystal particles in the fracture zone [4]. The energy recovery, healing speed, and crystallization development of salt rock are closely related to the ambient temperature. The simultaneous occurrence of damage and repair of salt rock is also the reason for the complexity of the research topic. Through numerical simulation, it is found that there exists a postpeak hardening stage during triaxial compression of salt rock at high temperatures; the higher the ambient temperature, the more obvious this stage is. Due to the restriction of test instruments and high-temperature conditions, the curves of this stage generally cannot be obtained in laboratory rock mechanics tests. In this stage, the salt rock still has a higher load-bearing capacity, the stress increment is small, and the strain keeps increasing. In addition, it is found in the numerical simulation that the number of cementation failures in the salt rock model decreases when the temperature exceeds 120°C. Meanwhile, the damaged salt rock has short-term self-healing characteristics under temperature conditions in

laboratory tests. To sum up, the formation mechanism and physical significance of the above problems need to be further studied.

7. Conclusions

In this paper, through particle flow simulation analysis technology, the triaxial compression failure process and strength characteristics of salt rock under a high-temperature environment were systematically studied, and the following conclusions can be drawn.

- (1) With the increase of temperature, the elastic limit points (a–e) of rock gradually decrease, which indicates that the plastic deformation characteristics of salt rock become more obvious. In addition, as the termination temperature gradually increases, the transverse strain values are 0.0147, 0.0170, 0.018, and 0.0182, respectively, and the increments of transverse strain are 0.0023, 0.001, and 0.0002, which maybe because of the decrease of the increment of transverse strain caused by the limitation of the wall and confining pressure.
- (2) With the increase of temperature, the strong chains break and disappear, and the proportion of weak chains increase, which shows that the high temperature intensifies the rupture of contact between particles in the salt rock. The strength chains inside the rock sample decrease significantly from 50°C to 120°C, indicating that the damage begins to intensify gradually. The contact force decreases sharply at 150°C, indicating that the salt rock is damaged significantly at a temperature of 150°C during the loading process
- (3) By analyzing the displacement direction of particles in the cloud map of the displacement field, it can be known that the displacement direction of the particles in the middle of the sample shows an obvious radial expansion trend at different temperatures, and the salt rock model shows a “drum shape” destruction phenomenon. With the increase of temperature, the expansion direction from the middle of the sample to the left and right ends is 12.08°, 9.55°, 8.2°, 6.33°, and 0°, respectively, and the phenomenon of “drum shape” in the middle of rock sample becomes more obvious
- (4) During the heating process, the salt rock model is mainly controlled by tensile stress, so the thermal cracks in the sample are mainly tensile cracks. In the middle of the sample model, the microcracks roughly expand along the transverse direction. At the top and bottom of the model, the microcracks expand diagonally, and the direction of expansion is about 45° in the horizontal direction. In addition, the number of microcracks in the salt rock decreases when the temperature exceeds 120°C, which is different from the general rock, indicating that the damage self-healing phenomenon seems to occur in this temperature range

- (5) The damage variables of salt rock are analyzed from the macro and micro perspectives; it is concluded that the damage of salt rock is more significant after 90°C. In addition, it is found that the damage of salt rock is significantly aggravated at 150°C in the mathematical model of cumulative cementation numbers and crack density parameter, which is also consistent with the evolution law of the force chain network in salt rock

Data Availability

All data are available on request.

Conflicts of Interest

The authors declare no conflict of interests related to this article.

Acknowledgments

This research is supported by the Natural Science Foundation of Hebei Province of China (No. D2021210006), the Hebei Province Key Research and Development Program of China (No. 21374101D), and the Program for the Top Young Talents of Hebei Province Education Department (No. BJ2019011). The authors are thankful for all of the support for this basic research.

References

- [1] J. W. Chen, *Study on Temperature Effect and Meso-Mechanism of Salt Rock*, Graduate University of Chinese Academy of Sciences (Institute of Rock and Soil Mechanics), 2008.
- [2] X. P. Gao, C. H. Yang, W. Wu, and J. Liu, "Experimental study on influence of temperature effect on mechanical properties of salt rock," *Rock and Soil Mechanics*, vol. 37, no. 11, pp. 84–87, 2005.
- [3] G. Wu, S. T. Zhai, H. Sun, and Y. Zhang, "Experimental study on acoustic emission characteristics of salt rock at high temperature," *Chinese Journal of Rock Mechanics and Engineering*, vol. 33, no. 6, pp. 1203–1211, 2014.
- [4] Y. F. Kang, J. Chen, D. Y. Jiang et al., "Damage self-recovery characteristics of salt rock brine after immersion under different temperature conditions," *Rock and Soil Mechanics*, vol. 40, no. 2, pp. 601–609, 2019.
- [5] Y. L. Yang, W. G. Liang, X. Q. Yang, M. T. Cao, J. Li, and N. Xiao, "Study on temperature effect of creep under multi-field coupling action of glauberite salt rock," *Journal of China Coal Society*, vol. 45, no. 3, pp. 1070–1080, 2020.
- [6] H. M. Shen, Q. Li, X. Y. Li, and J. L. Ma, "Laboratory experiment and numerical simulation study on brittle failure characteristics of Longmaxi Formation shale under different stress conditions in southern Sichuan," *Rock and Soil Mechanics*, vol. 39, no. S2, pp. 254–262, 2018.
- [7] M. J. Jiang, A. N. Shi, J. Liu, and F. G. Zhang, "Three-dimensional discrete element analysis of mechanical properties of structured sand," *Chinese Journal of Geotechnical Engineering*, vol. 41, no. S2, pp. 1–4, 2019.
- [8] H. Li, H. L. Ma, X. L. Shi, J. Zhou, H. N. Zhang, and J. J. K. Daemen, "A 3D grain-based model for simulating the micromechanical behavior of salt rock," *Rock Mechanics and Rock Engineering*, vol. 53, no. 6, pp. 2819–2837, 2020.
- [9] W. J. Li, Y. H. Han, T. Wang, and J. W. Ma, "DEM micromechanical modeling and laboratory experiment on creep behavior of salt rock," *Journal of Natural Gas Science and Engineering*, vol. 46, no. 2, pp. 38–46, 2017.
- [10] W. J. Li, C. Zhu, C. H. Yang, K. Duan, and W. R. Hu, "Experimental and DEM investigations of temperature effect on pure and interbedded rock salt," *Journal of Natural Gas Science & Engineering*, vol. 56, no. 1, pp. 29–41, 2018.
- [11] Z. Y. Xu, *Study on Micro-Anisotropic Brittle Fracture Mechanism of Hard Rock under Thermal-Mechanical Coupling*, Chengdu University of Technology, Sichuan, 2014.
- [12] Y. K. Liang, Z. C. Feng, J. Bai, X. C. Li, and C. Wang, "Particle flow analysis of granite thermal fracture characteristics under thermodynamic coupling," *Water Resources and Power*, vol. 38, no. 1, pp. 127–130+193, 2020.
- [13] Itasca Consulting Group Inc, *PFC2D (Version 5.0) Users Manual*, Itasca Consulting Group Inc., USA, 2019.
- [14] H. Lin, W. H. Kang, J. Oh, I. Canbulat, and B. Hebblewhite, "Numerical simulation on borehole breakout and borehole size effect using discrete element method," *International Journal of Mining Science and Technology*, vol. 30, no. 5, pp. 623–633, 2020.
- [15] J. Kang, *Research and Application of Rock Thermal Fracture*, Dalian University of Technology Press, Dalian, 2008.
- [16] Z. Li, *Experimental Study on Mechanical Properties of Salt Rock under the Coupling of Stress and Temperature*, Chongqing University, Sichuan, 2012.
- [17] R. P. Jensen, P. J. Bosscher, M. E. Plesha, and T. B. Edil, "DEM simulation of granular media—structure interface: effects of surface roughness and particle shape," *International Journal for Numerical & Analytical Methods in Geomechanics*, vol. 23, no. 6, pp. 531–547, 1999.
- [18] X. B. Ding, L. Y. Zhang, H. H. Zhu, and Q. Zhang, "Effect of model scale and particle size distribution on PFC3D simulation results," *Rock Mechanics and Rock Engineering*, vol. 47, no. 6, pp. 2139–2156, 2014.
- [19] X. Cai, Z. Zhou, and X. Du, "Water-induced variations in dynamic behavior and failure characteristics of sandstone subjected to simulated geo-stress," *International Journal of Rock Mechanics and Mining Sciences*, vol. 130, article 104339, 2020.
- [20] G. Wang, L. Z. Xie, Z. M. Hou, J. F. Liu, and W. Xing, "Comparative study on rock salt triaxial compression test methods and data processing methods," *Rock and Soil Mechanics*, vol. 35, no. 2, pp. 429–434+458, 2014.
- [21] C. Shi, Q. Zhang, and S. N. Wang, *Numerical Simulation Technology and Application of Particle Flow*, China Construction Industry Press, Beijing, 2018.
- [22] S. Li, Y. Liu, and K. J. Wu, "Study on discrete element numerical simulation and meso deformation mechanism of sand direct shear test," *Journal of Yangtze River Scientific Research Institute*, vol. 34, no. 4, pp. 104–110+116, 2017.
- [23] C. Shi and W. Y. Xu, *Numerical Simulation Technique and Practice of Particle Flow*, China Construction Industry Press, Beijing, 2015.
- [24] B. K. Mishra and S. P. Mehrotra, "Modelling of particle stratification in jigs by the discrete element method," *Minerals Engineering*, vol. 11, no. 6, pp. 511–522, 1998.
- [25] X. Cai, Z. Zhou, H. Zang, and Z. Song, "Water saturation effects on dynamic behavior and microstructure damage of

- sandstone: phenomena and mechanisms,” *Engineering Geology*, vol. 276, article 105760, 2020.
- [26] C. Ma, Y. H. Tan, E. B. Li, and M. Yang, “Study on thermal conductivity of salt rock in the range of $-20^{\circ}\text{C} \sim 50^{\circ}\text{C}$,” *Journal of Rock Mechanics and Engineering*, vol. 31, no. S2, pp. 3725–3730, 2012.
- [27] X. Cai, Z. Zhou, L. Tan, H. Zang, and Z. Song, “Fracture behavior and damage mechanisms of sandstone subjected to wetting-drying cycles,” *Engineering Fracture Mechanics*, vol. 234, article 107109, 2020.
- [28] Z. W. Lou, *Damage Mechanics Foundation*, Xi’an Jiaotong University Press, Xi’an, 1991.
- [29] H. Y. Liu and G. W. Wang, “CHEN Fugang Research progress of rock damage theory characterized by damage variables,” *Blasting*, vol. 29, no. 1, pp. 9–12, 2004.
- [30] Z. W. Zhou, J. F. Liu, H. Zou, Y. Zhuo, and M. D. XuYang, “Acoustic emission characteristics and damage evolution of salt rock under uniaxial compression,” *Journal of Yangtze River Scientific Research Institute*, vol. 33, no. 5, pp. 63–68+75, 2016.
- [31] G. Xiang, J. F. Liu, T. Y. Li, M. D. XuYang, C. F. Deng, and C. Wu, “Research on fractal and damage characteristics of salt rock deformation and failure process based on acoustic emission,” *Rock and Soil Mechanics*, vol. 39, no. 8, pp. 2905–2912, 2018.
- [32] X. Cai, Z. Zhou, L. Tan, H. Zang, and Z. Song, “Water saturation effects on thermal infrared radiation features of rock materials during deformation and fracturing,” *Rock Mechanics and Rock Engineering*, vol. 53, no. 11, pp. 4839–4856, 2020.
- [33] L. Zhang and Y. Liu, “Damage evolution and acoustic emission characteristics analysis of coal rock based on particle discrete element model,” *Safety in Coal Mine*, vol. 48, no. 11, pp. 213–216, 2017.
- [34] M. D. Yao, *Experimental Study on Mechanical Properties and Crack Growth of Thermal Damaged Rock*, Wuhan University, Wuhan, 2017.
- [35] F. F. Meng, H. Pu, T. Sasaoka et al., “Time effect and prediction of broken rock bulking coefficient on the base of particle discrete element method,” *International Journal of Mining Science and Technology*, vol. 31, no. 4, pp. 643–651, 2021.
- [36] Z. J. Lu, H. M. Zhang, J. H. Chen, and M. Feng, “Shear strength and swelling pressure of unsaturated soil,” *Chinese Journal of Geotechnical Engineering*, vol. 14, no. 3, pp. 1–8, 1992.

Research Article

Dynamic Mechanical Response and Dissipated Energy Analysis of Sandstone under Freeze-Thaw Cycles

Ke Man ¹, Zongxu Liu,¹ Zhifei Song ¹ and Xiaoli Liu²

¹School of Civil Engineering, North China University of Technology, Beijing 100144, China

²State Key Laboratory of Hydro Science and Hydraulic Engineering, Tsinghua University, Beijing 100084, China

Correspondence should be addressed to Zhifei Song; song59672@163.com

Received 24 August 2021; Accepted 22 October 2021; Published 10 November 2021

Academic Editor: Yu Wang

Copyright © 2021 Ke Man et al. This is an open access article distributed under the Creative Commons Attribution License, which permits unrestricted use, distribution, and reproduction in any medium, provided the original work is properly cited.

Based on the sandstone from the slope of Baorixile open-pit mining area in Hulunbuir City, Inner Mongolia, the dynamic uniaxial compression test of sandstone with different freeze-thaw cycles has been carried out by Split Hopkinson Pressure Bar test (SHPB). The test results show that the crushing degree of sandstone becomes serious with the freeze-thaw cycle times and strain rate increases. The dynamic compressive strength increases with the raise of strain rate under the same freeze-thaw cycles, while it reduces with the increases of freeze-thaw cycles at the same strain rate. It is found that the 10 freeze-thaw cycles are an obvious inflection point. When it is less than 10 cycles, the dynamic compressive strength of sandstone specimens decreases rapidly, it is more than 10 cycles, and the strength decreases gradually. This is due to that the evolution progress of pores in sandstone is more uniform after a certain number of freeze-thaw cycles. Meantime, the effect of freezing and thawing is mostly restrained by the pore evolution. On the other hand, the dissipated energy required for sandstone failure grows up with the increase of the number of freeze-thaw cycles. It shows that more energy is needed for the engender of pores and fractures in sandstone caused by freeze-thaw cycle. This led to the deterioration of sandstone structural stability and the decrease of dynamic mechanical properties.

1. Introduction

More than 70% of the land area of China is perennially frozen and seasonally frozen. Among them, some areas in the northeast and high-altitude areas in the west are permafrost regions, while north and south China are seasonal permafrost regions [1]. These frozen regions are rich in mineral resources, and the rock mass will inevitably receive dynamic loads such as impact of drilling and blasting in the process of mineral mining. In addition, the effect of temperature change on rock freezing and thawing mechanics cannot be ignored [2]. Therefore, the study of mechanical properties and failure law of rock under the combined action of freeze-thaw and dynamic load is of great significance to rock mass engineering in frozen regions.

At present, the mechanical properties of rock under conventional freeze-thaw cycles have been deeply studied by many scholars [3–18]. Zhou et.al [19–21] used the NMR system to study the pore structure change and damage mecha-

nism of granite under freeze-thaw cycle. Amitrano et.al [22] tested the failure characteristics of rock under the action of freeze-thaw cycle by acoustic emission test and found that a large number of internal cracks occurred with the progress of freeze-thaw cycle. Wu et.al [23] studied the longitudinal wave velocity, mass, and volume of marble after freeze-thaw cycle and summed up the physical and mechanical properties of marble after freeze-thaw cycle. Yang et.al [24] used uniaxial and triaxial compression tests of sandstone and coal under different temperatures and confining pressures to study the strength properties of rocks under freeze-thaw cycles. Nicholson et.al [25] carried out freeze-thaw cycle tests on fractured rocks to study the effect of primary fractures on the degree of freeze-thaw damage. Huseyin et.al [26] tested the compressive strength and other parameters of andesite after freeze-thaw cycle and obtained the deterioration law of andesite. Jihwan Park et.al [27] used CT scanning and SEM techniques to analyze the microstructure changes of rocks under freeze-thaw cycles. Bellanger



FIGURE 1: Sandstone samples under impact loading test.

TABLE 1: The basic mechanical parameters of the tested sandstone.

Uniaxial compressive strength/MPa	Longitudinal strain/ 10^{-2}	Tensile strength/MPa	Transverse strain/ 10^{-2}	Elastic modulus/GPa	Poisson's ratio
28.05	0.84	3.91	0.09	3.82	0.14

et.al [28] studied the saturated water content, porosity, and permeability of limestone in northeastern France and obtained the relationship between them.

Moreover, the internal damage and fracture process of rock under dynamic load will be accompanied by the transformation and dissipation of energy. Energy dissipation is the most important factor in rock failure; so, many scholars have made an indepth study on the mechanism of rock energy dissipation [29–32]. For instance, Xie et.al [33, 34] found that the internal damage and fracture of rock are caused by external energy, and the rock damage equation based on energy dissipation can better describe the damage process of rock. Gong et.al [35, 36] carried out static uniaxial compression test and Brazilian splitting test of red sandstone and found the law of linear energy storage and energy consumption in compression tension failure of rock.

However, the current research on the dynamic mechanical properties of rock under freeze-thaw is relatively few. In this paper, the dynamic uniaxial compression tests of sandstone under different freeze-thaw cycles are studied in detail, and its failure mechanism is analyzed from the point of view of energy.

2. Samples and Test Methods

2.1. Sample Making. The test samples are taken from sandstone with good particle uniformity and structural integrity in Baorixile open-pit mining area in Hulunbuir City, Inner Mongolia. According to the *Standard of Experimental method for Engineering Rock Mass* [37], the sandstone sample is polished into a disc sample with a height of 25 mm and a diameter of 50 mm, as shown in Figure 1, and the basic mechanical parameters of the tested sandstone are shown in Table 1.

2.2. Test Equipment. TDS-300 freeze-thaw cycle test machine is used in the freeze-thaw cycle test, as shown in Figure 2. The temperature can be controlled by the device is -40°C – 90°C , and the temperature fluctuation is $\pm 0.05^{\circ}\text{C}$.

The impact load test of sandstone using the Split Hopkinson Pressure Bar test device (SHPB) is shown in



FIGURE 2: TDS-300 freeze-thaw cycle testing machine.

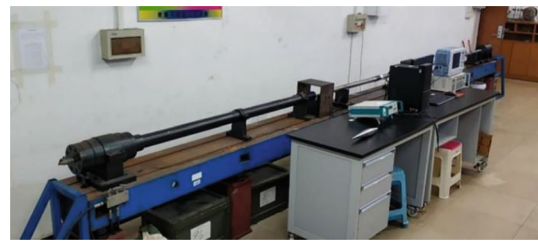


FIGURE 3: Split Hopkinson Pressure Bar test device (SHPB).

Figure 3. The device can be used to test the impact dynamic characteristics of rock, concrete, and other materials. It is mainly composed of transmitting cavity, incident rod, transmission rod, and data acquisition and processing system. The rod is made of chromium alloy steel. The diameter of the incident rod and the transmission rod is 50 mm, and the lengths are 2 m and 1.5 m.

TABLE 2: Bullet velocity and strain rate under different pressure.

Grouping and numbering of samples	Air pressure (MPa)	Bullet velocity (m/s)	Average speed (m/s)	Strain rate (s^{-1})	Average strain rate (s^{-1})
Y0-1	0.5	11.25	11.03	54.8	53.15
Y1-1		10.41		50.2	
Y5-1		11.09		53.8	
Y10-1		11.16		51.7	
Y15-1		11.27		53.2	
Y20-1		11.02		55.2	
Y0-2	0.6	12.82	13.09	75.3	75.07
Y1-2		12.98		70.5	
Y5-2		13.32		73.8	
Y10-2		12.93		77.8	
Y15-2		13.29		77.7	
Y20-2		13.19		75.3	
Y0-3	0.7	14.41	14.92	98.9	99.07
Y1-3		15.12		102.6	
Y5-3		14.77		96.7	
Y10-3		15.09		96.1	
Y15-3		14.84		98.3	
Y20-3		15.28		101.8	

TABLE 3: Dynamic uniaxial compression mechanical parameters of sandstone under different freeze-thaw cycles.

Grouping and numbering of samples	Strain rate (s^{-1})	Compression strength (MPa)	Axial strain (10^{-2})
Y0-1	54.8	155.54	0.73
Y0-2	75.3	179.11	0.97
Y0-3	98.9	221.03	1.18
Y1-1	50.2	140.28	0.87
Y1-2	70.5	167.99	1.04
Y1-3	102.6	200.36	1.27
Y5-1	53.8	130.46	0.98
Y5-2	73.8	157.33	1.16
Y5-3	96.7	185.65	1.36
Y10-1	51.7	121.75	1.09
Y10-2	77.8	148.94	1.28
Y10-3	96.1	176.21	1.44
Y15-1	53.2	112.23	1.16
Y15-2	77.7	140.07	1.33
Y15-3	98.3	166.83	1.52
Y20-1	55.2	105.28	1.21
Y20-2	75.3	135.68	1.39
Y20-3	101.8	158.76	1.59

2.3. *Test Scheme and Process.* First of all, the sandstone samples were saturated with water, and after the samples were completely saturated, the freeze-thaw cycle test was carried out, and the single freeze-thaw cycle was set to 12 h. The samples were frozen at -20°C for 6 h and thawed at 20°C for 6 h. The experiment was divided into 6 groups according to differ-

ent freeze-thaw cycles, and the freeze-thaw times were 0, 1, 5, 10, 15, and 20 times. After different freeze-thaw cycles, the Split Hopkinson Pressure Bar device was used to carry out impact loading tests on the samples with different impact pressures of 0.5 MPa, 0.6 MPa, and 0.7 MPa, and the dynamic characteristics of sandstone samples were tested.

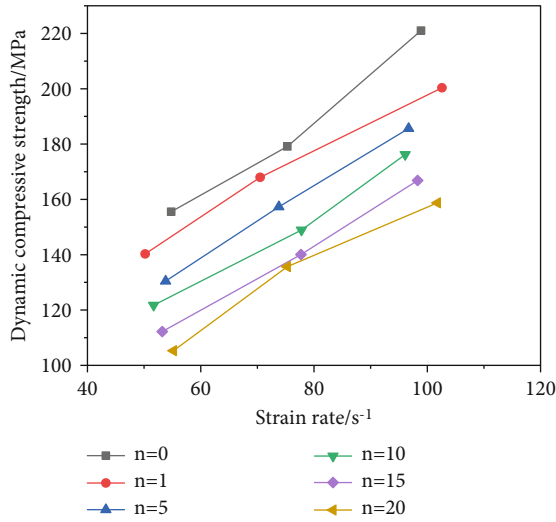


FIGURE 4: Dynamic compressive strength of sandstone under different strain rates.

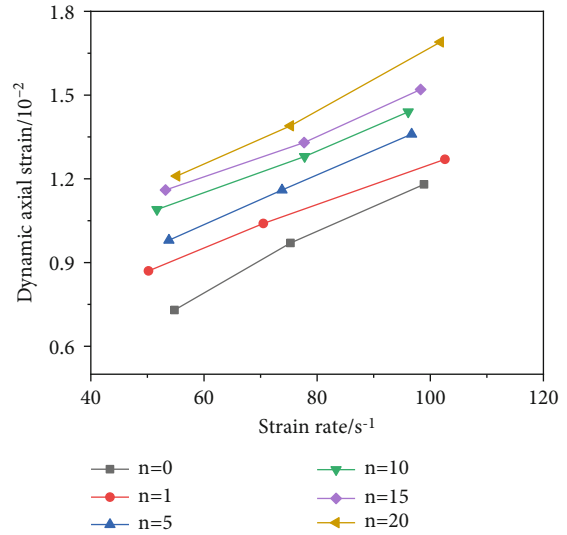


FIGURE 6: Dynamic axial strain of sandstone under different strain rates.

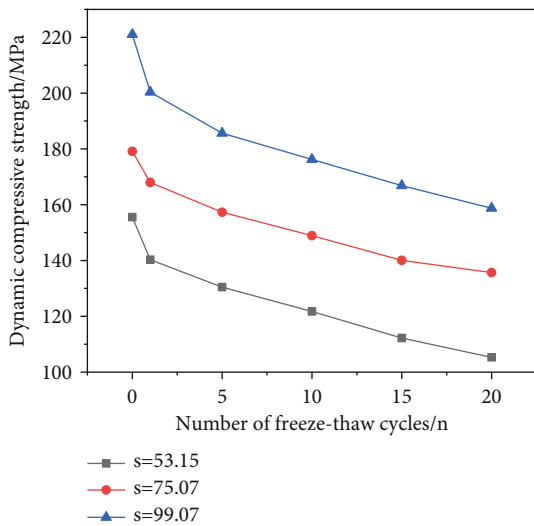


FIGURE 5: Dynamic compressive strength of sandstone under different freeze-thaw cycles.

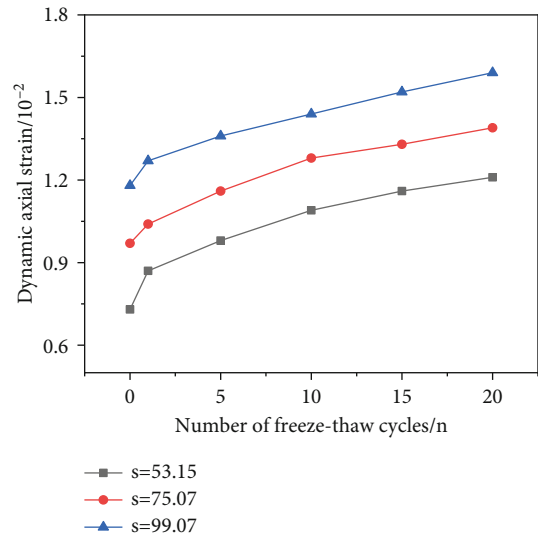


FIGURE 7: Dynamic axial strain of sandstone under different freeze-thaw cycles.

3. Test Results

The bullet velocity and strain rate of uniaxial compression test under different impact pressure are shown in Table 2, and the peak dynamic compressive strength and peak strain of sandstone under different freeze-thaw cycles and strain rates are shown in Table 3.

3.1. Dynamic Uniaxial Compression Strength Analysis. The influence of strain rate and freeze-thaw cycles on dynamic compressive strength is as follows. Figure 4 shows the dynamic compression strength curve of sandstone under different strain rates, and n is the number of freeze-thaw cycles. Figure 5 is the dynamic compression strength curve of sandstone under different freeze-thaw cycles, and s is the strain rate.

As shown in Figure 4, the dynamic compressive strength of sandstone rises with the increase of strain rate. This is due to that under the impact load of high strain rate, the sandstone with the same number of freeze-thaw cycles needs more stress, which leads to the failure of sandstone samples. The compressive strength declines with the increase of freeze-thaw cycles. It is clear that both strain rate and freeze-thaw affect the dynamic compressive strength of sandstone, but the effect of freeze-thaw is higher than that of strain rate.

As illustrated in Figure 5, the dynamic compressive strength of sandstone declines with the increase of freeze-thaw cycles. The reason is that repeated freeze-thaw cycles lead to repeated expansion and contraction of pores in sandstone, resulting in pores gradually developing into cracks and seriously destroying the internal structure of sandstone;

TABLE 4: Energy statistical table.

Sample number	Strain rate/s ⁻¹	W_I/J	W_R/J	W_T/J	W_S/J
Y0-1	54.8	126.38	39.10	36.78	50.5
Y0-2	75.3	179.07	61.01	59.92	58.14
Y0-3	98.9	230.24	86.51	54.51	89.22
Y1-1	50.2	127.30	37.92	36.02	53.36
Y1-2	70.5	178.84	58.64	47.34	72.86
Y1-3	102.6	233.03	88.62	44.36	100.05
Y5-1	53.8	126.84	38.86	34.17	53.81
Y5-2	73.8	180.14	58.62	45.68	75.84
Y5-3	96.7	230.17	80.27	32.80	117.1
Y10-1	51.7	127.99	37.44	31.41	59.14
Y10-2	77.8	180.37	62.14	35.76	82.47
Y10-3	96.1	232.27	85.79	31.87	114.61
Y15-1	53.2	126.95	38.69	28.01	60.25
Y15-2	77.7	180.28	60.25	32.40	87.63
Y15-3	98.3	230.81	81.22	30.12	119.47
Y20-1	55.2	126.33	37.53	28.12	60.68
Y20-2	75.3	179.72	59.42	31.84	88.46
Y20-3	101.8	231.45	83.18	28.86	119.41

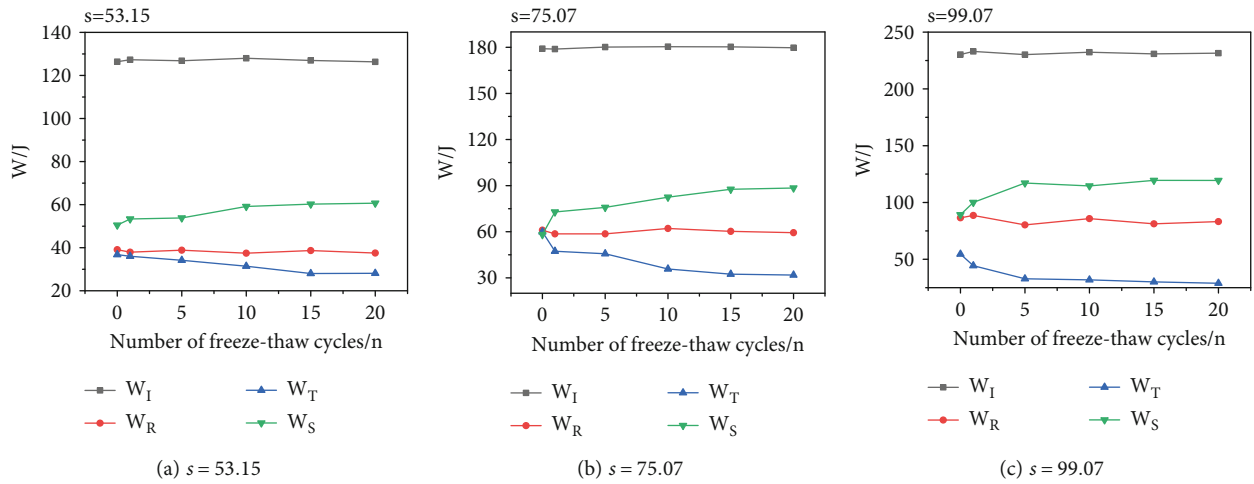


FIGURE 8: Four kinds of energy change curves under different strain rates and freeze-thaw cycles.

so, freeze-thaw cycles will significantly reduce the mechanical properties of sandstone.

3.2. *Variation Law of Dynamic Axial Strain.* The effect of strain rate and freeze-thaw cycle on strain: Figure 6 shows the dynamic axial strain curve of sandstone under different strain rates. Figure 7 shows the dynamic axial strain curve of sandstone under different freeze-thaw cycles.

As it can be seen from Figure 6: the dynamic axial strain of sandstone growth with the increase of strain rate, the reason is that the higher stress is needed to destroy the sandstone sample at high strain rate; so, the axial strain increases.

In Figure 7, the axial strain of sandstone ascends with the increase of freeze-thaw cycles. This is due to those different times of freeze-thaw cycles will destroy the internal structure of sandstone and make the internal pores growth into through fissures, resulting in the axial strain of sandstone samples will rise with the increase of the number of freeze-thaw cycles.

4. Discussion

4.1. *Energy Dissipation Law.* In the impact load test of sandstone, the destruction process of sandstone must be accompanied by the absorption and dissipation of energy. Energy

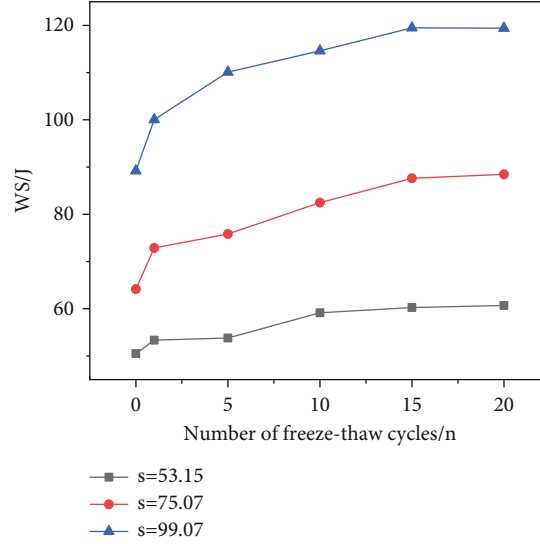


FIGURE 9: The variation curve of dissipative energy with the number of freeze-thaw cycles under different strain rates.

absorption in sandstone depends on factors such as pore space. The development and expansion of pores and fractures within the sandstone require the absorption of energy [21]. The dissipated energy required for sandstone failure can be calculated by incident energy, reflection energy, and transmission energy. The formula is as follows:

$$W_I = E_o C_o A_o \int_0^t \varepsilon_I^2(t) dt, \quad (1)$$

$$W_R = E_o C_o A_o \int_0^t \varepsilon_R^2(t) dt, \quad (2)$$

$$W_T = E_o C_o A_o \int_0^t \varepsilon_T^2(t) dt. \quad (3)$$

In the formula, W_I is the incident energy, W_R is the reflected energy, W_T is the transmission energy, E_o is the elastic modulus of rod, C_o is the longitudinal wave velocity of the rod, A_o is the cross-sectional area of the rod, $\varepsilon_I(t)$ is the incident stress wave strain signal, $\varepsilon_R(t)$ is the reflected stress wave strain signal, and $\varepsilon_T(t)$ is the transmitted stress wave strain signal.

The dissipated energy in the failure process of sandstone specimen is expressed by W_S , and the formula is

$$W_S = W_I - W_R - W_T. \quad (4)$$

Table 4 shows the energy statistics of dynamic uniaxial compression test of sandstone under different freeze-thaw cycles.

Figure 8 shows the variation curve of four kinds of energy with the number of freeze-thaw cycles when the average strain rates are 53.15, 75.07, and 99.07. It can be seen from Figure 8 that the incident energy and transmission energy remain stable under different freeze-thaw cycles.

However, the incident energy and transmission energy grow up with the increase of strain rate, and the higher the strain rate, the greater their growth. It shows that the incident energy and reflection energy are not sensitive to the number of freeze-thaw cycles. The transmission energy reduces with the increase of freeze-thaw cycles and increases at first and then declines with the increase of strain rate. The dissipated energy ascends with the increase of the number of freeze-thaw cycles, and the higher the strain rate, the greater the increase of dissipative energy.

4.2. Failure Mechanism of Sandstone Sample. The strain rate effect of dynamic compressive strength of sandstone is analyzed from the point of view of energy. The interior of the sandstone sample is full of natural pores and fissures, and the failure process of sandstone is also the process of the development and expansion of pores and fissures. The crack rises with the increase of strain rate and so does the energy require [38]. Because the time of impact load is very short, the sample can only increase the stress to balance the external energy; so, the dynamic compressive strength of sandstone samples ascends with the increase of strain rate.

Figure 9 shows the curve of dissipated energy varying with the number of freeze-thaw cycles at different strain rates. It can be seen that the dissipated energy of sandstone sample rises obviously with the increase of the number of freeze-thaw cycles, and the growth rate of dissipative energy gains in with the increase of strain rate. It shows that the failure of sandstone under the combined action of freeze-thaw cycle and high strain rate impact load will absorb more energy and illustration of the development of pores and cracks in sandstone needs higher energy. Therefore, with the increase of strain rate and the number of freeze-thaw cycles, the failure degree of sandstone specimens becomes larger and larger, as shown in Figure 10.

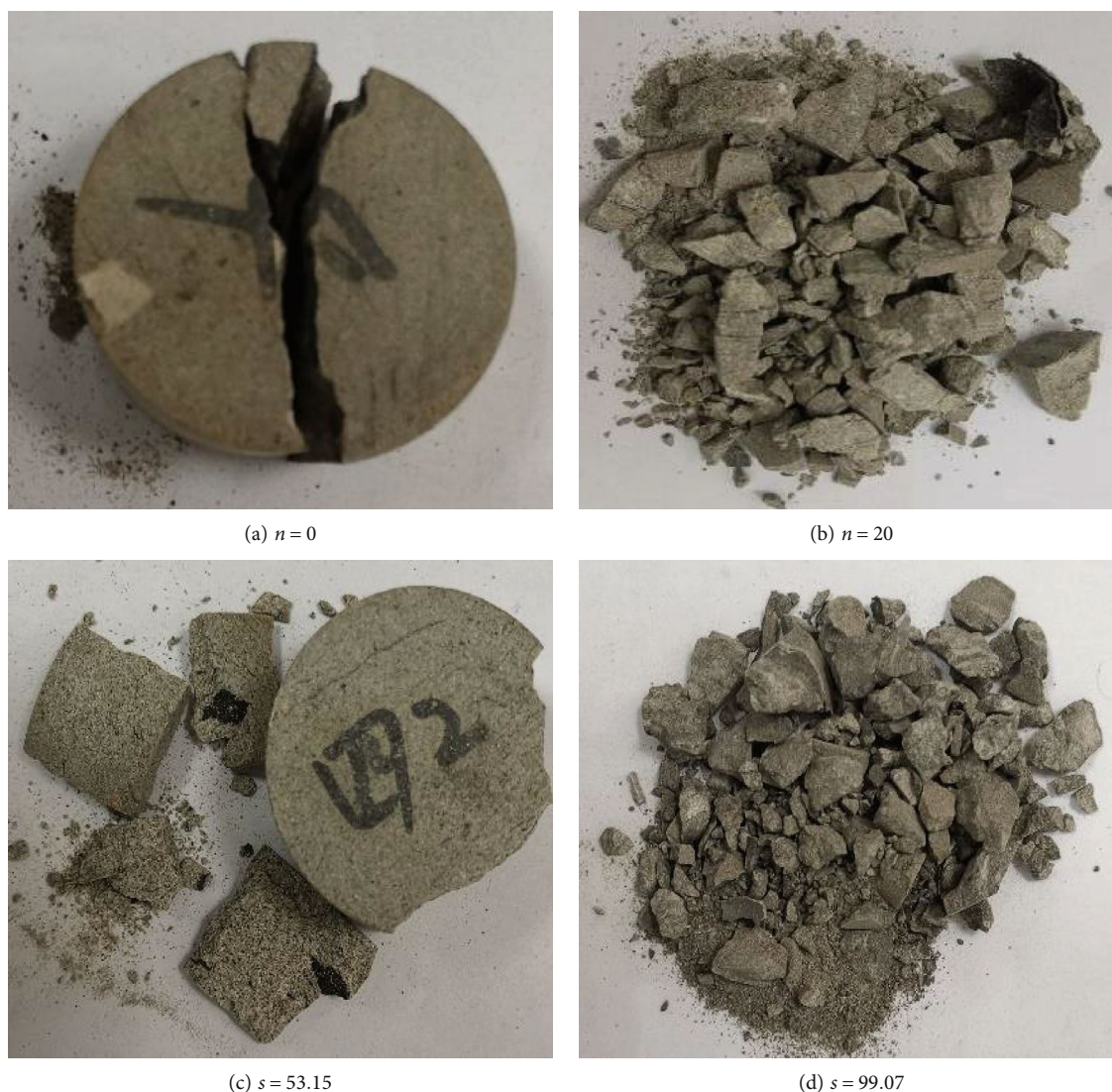


FIGURE 10: Failure morphology of sandstone specimens under different freeze-thaw cycles and strain rates.

5. Conclusions

- (1) The dynamic mechanical properties of sandstone are significantly affected by freeze-thaw cycles and strain rate. With the increase of freeze-thaw cycles, the strength of sandstone decreases and the strain increases and the strength and strain of sandstone growth with the increase of strain rate
- (2) When the number of cycles is less than 10, the dynamic compressive strength of sandstone decreases rapidly, and the image is obviously concave. When the number of cycles is more than 10 times, the strength decreases gradually, and the image shows a convex shape. 10 freeze-thaw cycles are an obvious inflection point. The reason is that after a certain number of freeze-thaw cycles, the internal pores of sandstone develop more evenly, which suppresses the effect of freeze-thaw on sandstone and slows the decrease of strength

- (3) With the increase of the number of freeze-thaw cycles, the dissipative energy is required for sandstone failure growth. The reason is that the freeze-thaw cycle makes the sandstone loose, and the development of cracks aggravates. When the sandstone is destroyed by external forces, it is easy to produce more cracks, resulting in a greater degree of failure of the samples, showing a powder clastic shape

Data Availability

The data that support the findings of this study are available from the corresponding author, upon reasonable request.

Conflicts of Interest

The authors declare no conflict of interest.

Acknowledgments

Thank you for the review experts for their comments on this article. At the same time, thanks for all those who are helpful to this experiment. This work was supported by the National Natural Science Foundation of China [Grant Nos. 51522903, 51774184], Excellent Project Fund in North China University of Technology [Grant No. 216051360020XN199/006], and Scientific Research Fund in North China University of Technology [Grant No. 110051360002].

References

- [1] Y. Yang, "Experimental study on dynamic mechanical properties of rock under low temperature," *China University of mining and Technology (Beijing)*, 2016.
- [2] G. M. Xu and Q. S. Liu, "Analysis of freeze-thaw failure mechanism of rock and experimental study of freeze-thaw mechanics," *Acta rock mechanics and engineering*, vol. 24, no. 17, pp. 3076–3082, 2005.
- [3] J. R. Ma and G. S. Yang, "Preliminary study on water thermal mechanical coupling of freeze-thaw damage of soft rock," *Journal of rock mechanics and engineering*, vol. 25, no. z1, pp. 4373–4377, 2004.
- [4] D. M. Lang and T. C. Li, "Energy evolution and damage ontology of rocks under freeze-thaw cycles," *Mining Research and Development*, vol. 40, no. 4, pp. 74–78, 2020.
- [5] N. Liu, *Mechanical Experiment and Hydro Thermal Coupling Analysis of Rock Freezing and Thawing*, Xi'an University of science and technology, 2010.
- [6] G. Q. Chen, Y. Wan, X. Sun, and G. Z. Zhang, "Research on the effect of temperature range on the creep behaviour of sandstone subjected to freeze-thaw cycles and its fractional order damage model," *Chinese Journal of Rock Mechanics and Engineering*, pp. 1–14, 2021.
- [7] Y. Wang, B. Zhang, B. Li, and C. H. Li, "A strain-based fatigue damage model for naturally fractured marble subjected to freeze-thaw and uniaxial cyclic loads," *International Journal of Damage Mechanics*, vol. 30, no. 10, pp. 1594–1616.
- [8] L. Zhang, "On mechanical properties and failure characteristics of surrounding rock of tunnel with weak interlayer under freeze-thaw cycles," *Hydrogeology & Engineering Geology*, pp. 1–7, 2021.
- [9] Y. Wang, Y. F. Yi, C. H. Li, and J. Q. Han, "Anisotropic fracture and energy characteristics of a Tibet marble exposed to multi-level constant-amplitude (MLCA) cyclic loads: a lab-scale testing," *Engineering Fracture Mechanics*, vol. 244, p. 107550, 2021.
- [10] J. Zhang, R. Xu, Y. Liu, H. Zhang, X. Tan, and M. Chen, "Experimental study on mechanical properties of grouted fractured rock under the action of freeze-thaw cycles," *Journal of Experimental Mechanics*, vol. 36, no. 3, pp. 378–388, 2021.
- [11] S. A. Ghoreishi-Madiseh, F. Hassani, A. Mohammadian, and F. Abbasy, "Numerical modeling of thawing in frozen rocks of underground mines caused by backfilling," *International Journal of Rock Mechanics & Mining Sciences*, vol. 48, no. 7, pp. 1068–1076, 2011.
- [12] S. Chang, J. Y. Xu, and G. H. Zheng, "Study on strain rate characteristics of frozen-thawed bedding sandstone under impact load," *Chinese Journal of Underground Space and Engineering*, vol. 17, no. 1, pp. 53–61, 2021.
- [13] H. Liao, Y. Chen, S. Li, Y. Yin, C. Peng, and Z. Li, "Mechanical properties of sandstone under freeze-thaw cycling and chemical corrosion," *Journal of Disaster Prevention and Mitigation Engineering*, vol. 40, no. 6, pp. 1009–1017, 2020.
- [14] L. N. Wang, X. M. Yi, J. Han, and J. Z. Wang, "Strength degradation and forecast model of siltstone under combined effect of chemical solutions and freeze-thaw cycles," *Journal of Central South University (Science and Technology)*, vol. 51, no. 8, pp. 2361–2372, 2020.
- [15] J. J. Zhao, M. L. Xie, J. L. Yu, and W. H. Zhao, "Experimental study on mechanical properties and damage evolution of fractured rock under freeze-thawing action," *Journal of Engineering Geology*, vol. 27, no. 6, pp. 1199–1207, 2019.
- [16] Y. Hou, X. Zhang, P. Li, P. Ding, S. Cao, and D. Han, "Mechanical properties and non-destructive testing of cemented mass of unclassified tailings under freeze-thaw cycles," *Chinese Journal of Engineering*, vol. 41, no. 11, p. 1443, 2019.
- [17] H. M. Zhang, X. Z. Meng, C. Peng et al., "Rock damage constitutive model based on residual intensity characteristics under freeze-thaw and load," *Journal of China Coal Society*, vol. 44, no. 11, pp. 3404–3411, 2019.
- [18] X. Zhang and C. A. Yanyan, "Meso-damage and mechanical properties degradation of sandstone under combined effect of water chemical corrosion and freeze-thaw cycles," *Rock and Soil Mechanics*, vol. 40, no. 2, pp. 455–464, 2019.
- [19] K. Zhou, J. Li, Y. Xu, Y. Zhang, P. Yang, and L. Chen, "Experimental study on nuclear magnetic resonance characteristics of rocks under freeze-thaw cycles," *Journal of rock mechanics and engineering*, vol. 31, no. 4, pp. 731–737, 2012.
- [20] Y. J. Xu, K. P. Zhou, and J. L. Li, "Z Y M. nuclear magnetic resonance detection of freeze-thaw rock and analysis of freeze-thaw damage mechanism," *Geotechnical mechanics*, vol. 33, no. 10, pp. 3001–3006, 2012.
- [21] B. Ke, K. Zhou, H. Deng, and F. Bin, "NMR pore structure and dynamic characteristics of sandstone caused by ambient freeze-thaw action," *Shock and Vibration*, vol. 2017, 10 pages, 2017.
- [22] D. Amitrano, S. Gruber, and L. Girard, "Evidence of frost-cracking inferred from acoustic emissions in a high-alpine rock-wall," *Earth and Planetary Science Letters*, vol. 341–344, pp. 86–93, 2012.
- [23] G. Wu, G. L. He, L. Zhang, and Y. P. Qiu, "Experimental study on cyclic freeze-thaw of marble," *Journal of rock mechanics and engineering*, vol. S1, pp. 2930–2938, 2006.
- [24] G. Yang, J. Xi, X. Shao, H. Li, and L. Cheng, "Experimental study on rock strength characteristics under freezing conditions," *Journal of Xi'an University of science and technology*, vol. 30, no. 1, pp. 14–18, 2010.
- [25] D. T. Nicholson and F. H. Nicholson, "Physical deterioration of sedimentary rocks subjected to experimental freeze-thaw weathering," *Earth Surface Processes and Landforms*, vol. 25, no. 12, pp. 1295–1307, 2000.
- [26] Y. Huseyin, "Effect of freeze-thaw and thermal shock weathering on the physical and mechanical properties of an andesite stone," *Bulletin of Engineering Geology and the Environment*, vol. 70, no. 2, pp. 187–192, 2011.
- [27] J. Park, C. U. Hyun, and H. D. Park, "Changes in microstructure and physical properties of rocks caused by artificial freeze-thaw action," *Bulletin of Engineering Geology and the Environment*, vol. 74, no. 2, pp. 555–565, 2015.
- [28] M. Bellanger, F. Homand, and J. M. Remy, "Water behaviour in limestones as a function of pores structure: application to

- frost resistance of some Lorraine limestones,” *Engineering Geology*, vol. 36, no. 1-2, pp. 99–108, 1993.
- [29] Y. Bernabé and A. Revil, “Pore-scale heterogeneity, energy dissipation and the transport properties of rocks,” *Geophysical Research Letters*, vol. 22, no. 12, pp. 1529–1532, 1995.
- [30] V. Sujatha and J. M. C. Kishen, “Energy release rate due to friction at bimaterial interface in dams,” *Journal of Engineering Mechanics*, vol. 129, no. 7, pp. 793–800, 2003.
- [31] Y. Ju, H. J. Wang, Y. M. Yang, Q. A. Hu, and R. D. Peng, “Numerical simulation of mechanisms of deformation, failure and energy dissipation in porous rock media subjected to wave stresses,” *SCIENCE CHINA Technological Sciences*, vol. 53, no. 4, pp. 1098–1113, 2010.
- [32] R. Peng, Y. Ju, J. G. Wang, H. Xie, F. Gao, and L. Mao, “Energy dissipation and release during coal failure under conventional triaxial compression,” *Rock Mechanics and Rock Engineering*, vol. 48, no. 2, pp. 509–526, 2015.
- [33] H. Xie, L. Li, R. Peng, and Y. Ju, “Energy analysis and criteria for structural failure of rocks,” *Journal of Rock Mechanics and Geotechnical Engineering*, vol. 1, no. 1, pp. 11–20, 2009.
- [34] H. Xie, L. Li, Y. Ju, R. Peng, and Y. Yang, “Energy analysis for damage and catastrophic failure of rocks,” *Science China Technological Sciences*, vol. 54, no. 1, pp. 199–209, 2011.
- [35] F. Q. Gong, J. Y. Yan, and X. B. Li, “A new criterion of rock burst proneness based on the linear energy storage law and the residual elastic energy index,” *Chinese Journal of Rock Mechanics and Engineering*, vol. 37, no. 9, pp. 1993–2014, 2018.
- [36] F. Q. Gong, S. Luo, X. B. Li, and J. Y. Yan, “Linear energy storage and dissipation rule of red sandstone materials during the tensile failure process,” *Chinese Journal of Rock Mechanics and Engineering*, vol. 37, no. 2, pp. 352–363, 2018.
- [37] *Standard of Experimental method for Engineering Rock Mass* GB/T 50266-1999.
- [38] J. Liu, J. Xu, X. Lu, L. Zhang, and Z. Wang, “Experimental study on dynamic mechanical properties of Amphibolite’s under impact compressive loading,” *Chinese Journal of Rock Mechanics and Engineering*, vol. 28, no. 10, pp. 2113–2121, 2009.

Research Article

Hydrogeology Response to the Coordinated Mining of Coal and Uranium: A Transparent Physical Experiment

Tong Zhang ^{1,2,3,4}, Xiang He,^{2,3} Kai Zhang,¹ Xiaohan Wang,^{2,3} and Yang Liu ^{2,3}

¹State Key Laboratory of Water Resource Protection and Utilization in Coal Mining, Beijing 100000, China

²State Key Laboratory of Mining Response and Disaster Prevention and Control in Deep Coal Mines, Anhui University of Science and Technology, Huainan, Anhui 232001, China

³School of Mining and Safety Engineering, Anhui University of Science & Technology, Anhui 232001, China

⁴Beijing Key Laboratory for Precise Mining of Intergrown Energy and Resources, University of Mining and Technology (Beijing), Beijing 100083, China

Correspondence should be addressed to Tong Zhang; 1099731996@qq.com

Received 3 July 2021; Accepted 28 September 2021; Published 8 November 2021

Academic Editor: Hailiang Jia

Copyright © 2021 Tong Zhang et al. This is an open access article distributed under the Creative Commons Attribution License, which permits unrestricted use, distribution, and reproduction in any medium, provided the original work is properly cited.

The migration of fracture and leaching solute caused by mining activity is critical to the hydrogeology. To characterize liquid and solid migration in a mining area of intergrown resources, the coordinated mining of coal and uranium was considered, and a physical experiment based on transparent soil was conducted. A well experimental performance of transparent soil composed of paraffin oil, n-tridecane, and silica gel and the leaching solution comprised of saturated oil red O dye was observed for hydrogeology characterization. An “arch-shaped” fracture zone with a maximum height of 90 m above the mined goaf and a “horizontal-shaped” fracture zone with a fractured depth of 9.97–16.09 m in the uranium-bearing layer were observed. The vertical leachate infiltration of 4.83 m was observed in the scenario of uranium mining prior to coal, which is smaller than those in the scenarios of comining of coal and uranium (10.26 m) and coal mining prior to uranium (16.09 m). A slight strata movement below the uranium was observed, and the leaching solution infiltration in the coal mining area was not observed in a short period in the scenario of uranium mining prior to coal; both of those was presented in the scenarios of comining of coal and uranium and coal mining prior to uranium.

1. Introduction

The natural resource mining of coal, oil, uranium, etc. concerns a series of safety and environmental problems. Visualizing the strata movement, failure mechanism, and seepage distribution attracts numerous attention, and many achievements have been obtained [1–5]. To investigate the mechanism and characteristics of the geotechnical problems, transparent soil, including a refractive index-matched skeleton and a saturating fluid, has been accepted in the field of physical modeling [6, 7]. The internal deformation and flow path in the case of multiscale geotechnical experiments can be appropriately described in a continuous and nonintrusive manner [8–10]. Further, the time-dependent spatial behaviors and seepage features inside the transparent soil can be appropriately measured using optical technologies and

image processing techniques, including particle image velocimetry (PIV) and digital image correlation (DIC) [11–13].

The soil skeleton materials and their corresponding fluids, including amorphous silica powder, silica gel, hydrogels, and fused quartz, have been extensively developed to mimic different natural soils [14]. Xu [15] developed the transparent soil, comprising silica gel powder, mineral oil, and n-tridecane, to study the deformation damage mechanism and fracture evolution of the surrounding rock. Ahmed and Iskander [16] evaluated the tunnel construction stability based on the prepared transparent soil and mineral oil solution. Wei et al. [17] introduced transparent cemented soil as a surrogate for the physical modeling of geotechnical problems. Zhang [18] developed a transparent rock similar material, which was applied in the stress and deformation experiments of the tunnel. Ye [19] conducted a 3D crack

growth test using similar materials containing transparent brittle rock, which were similar to the epoxy resin, curing agent, and rosin materials via the high- and low-temperature treatment processes. Fu et al. [20] studied the fracture process based on a new material having a three-dimensional internal fracture surface, which contained a C-type epoxy resin, curing agent, and thin mica sheet. Li et al. [21] developed a type of transparent rock, which was a similar test material and contained a mixed solution of silicon powder and mineral oil (liquid paraffin and n-tridecane).

The intergrown resource mining concerns the stress-fracture-seepage-solute transportation coupling process, which is directly related to groundwater and mining safety. The transparent soil and developed coordinated mining equipment were employed to investigate the development of the mining-induced fracture and leaching solution in this study. Taking coordinated mining of coal and uranium as an example, a physical experiment was conducted in different mining scenarios, and the migration and distribution of the fracture zone and leaching solute were analyzed.

2. Hydrogeology

The intergrown resource deposit of coal and uranium is located in Yijinhuoqi in the northeast of the Ordos Basin. In the coal mine with a production capacity of 26 million t/a and a mining area of 399.94 km², the mining coal seam 3-1 is buried at a depth of 600 m with an average thickness of 3.36 m. The sandstone-type uranium is grown in the Jurassic and located in the east wing of the coal mine with an area of 4.17 km². The thickness of the uranium varies from 1.10 m to 7.90 m, and the average thickness of the uranium is 3.44 m. Additionally, the uranium is located above the 3-1 coal seam at a distance of 90–150 m, and the uranium-bearing stratum is a direct aquifer of the 3-1 coal seam. The occurrence of coal and uranium is shown in Figure 1, and the specific hydrogeology is shown in Figure 2.

3. Mathematical Model of the Physical Experiment

To characterize the hydrogeology of the intergrown resource, a mathematical model as a function of a hydromechanical coupling equation, elasticity equilibrium equation, and effective stress equation is employed as

$$\begin{cases} K_x \frac{\partial^2 p}{\partial x^2} + K_y \frac{\partial^2 p}{\partial y^2} + K_z \frac{\partial^2 p}{\partial z^2} = S \frac{\partial p}{\partial t} + \frac{\partial e}{\partial t} + W, \\ \sigma_{ij,i} + X_j = \rho \frac{\partial^2 u_i}{\partial t^2}, \\ \sigma_{ij} = \bar{\sigma}_{ij} + \alpha \delta p, \end{cases} \quad (1)$$

where K_x , K_y , and K_z are the permeability coefficients in the Cartesian system, and $K_x = K_y = K_z = K$ is assumed; P is the hydraulic pressure; S is the water storage coefficient; W is the source-sink term; e is the volume strain; σ_{ij} is the total

stress tensor; $\bar{\sigma}_{ij}$ is the effective stress tensor; X_j is the volume force; ρ is the density; α is Biot's effective stress coefficient; and δ is the Kronecker symbol.

Combining the elasticity balance equation, geometric equation, and physical equation, the stress and strain components are eliminated, and the displacement equation is obtained by

$$\begin{cases} G \nabla^2 u + (\lambda + G) \frac{\partial e}{\partial x} + X = \rho \frac{\partial^2 u}{\partial t^2}, \\ G \nabla^2 v + (\lambda + G) \frac{\partial e}{\partial y} + Y = \rho \frac{\partial^2 v}{\partial t^2}, \\ G \nabla^2 w + (\lambda + G) \frac{\partial e}{\partial z} + Z = \rho \frac{\partial^2 w}{\partial t^2}, \end{cases} \quad (2)$$

where $\nabla^2 = (\partial^2/\partial x^2) + (\partial^2/\partial y^2) + (\partial^2/\partial z^2)$ is the Laplace operator notation; $G = E/2(1 + \mu)$ is the shearing modulus of elasticity; $\lambda = \mu E/(1 + \mu)(1 - 2\mu)$ is Lamé's constant; $e = (\partial u/\partial x) + (\partial v/\partial y) + (\partial w/\partial z)$ is the volumetric strain; and X, Y, Z are the volume force in the Cartesian coordinate system.

The coefficients in the prototype characterized by (') and physical model represented by (') are suitable in the given mathematical model: $C_G = G'/G''$, $C_E = E'/E''$, $C_l = x'/x''$, $C_\lambda = \lambda'/\lambda''$, $C_e = e'/e''$, $C_u = u'/u''$, $C_\gamma = X'/X''$, $C_\rho = \rho'/\rho''$, $C_t = t'/t''$, $K' = C_K K''$, $S' = C_S S''$, $Q' = C_Q Q''$, $y' = C_\gamma y''$, $z' = C_z z''$, $\partial e'/\partial x' = (1/C_l)(\partial e''/\partial x'')$, $\nabla^2 u' = (C_u/C_l^2)\nabla^2 u''$, and $\partial^2 u'/\partial t'^2 = (C_u/C_t^2)(\partial^2 u''/\partial t''^2)$, where C_i is the similarity coefficient. Based on a similar principle [22], the following expressions are given:

$$C_G \frac{C_u}{C_l^2} = C_\lambda \frac{C_e}{C_l} = C_G \frac{C_e}{C_l} = C_\gamma = C_\rho \frac{C_u}{C_t^2}, \quad (3)$$

$$C_K \frac{C_p}{C_l^2} = C_S \frac{C_p}{C_t} = \frac{C_e}{C_t} = C_w. \quad (4)$$

- (1) Geometric similarity: $C_u = C_e C_l$ and $C_e = 1$ were assumed and $C_u = C_l$ was obtained
- (2) Stress similarity: combining $C_G C_e = C_\gamma C_l$, $C_e = 1$, and the similarity principle and the homogeneous principle of dimension, the $C_G = C_\lambda = C_E = C_p = C_\gamma C_l$ was obtained
- (3) Time similarity: integrating $C_\gamma = C_\rho C_g$, $C_u = C_e C_l$, $C_g = 1$, and $C_e = 1$ into $C_\gamma = C_\rho (C_u/C_t^2)$, then $C_t = \sqrt{C_l}$ was obtained
- (4) Loading similarity: integrating $K_x = K_y = K_z = K$ into equation (1), then $C_e = 1$, $C_p = C_\lambda C_l$, and $C_t = \sqrt{C_l}$ were obtained
- (5) Source and sink term similarity: $C_w = 1/\sqrt{C_l}$

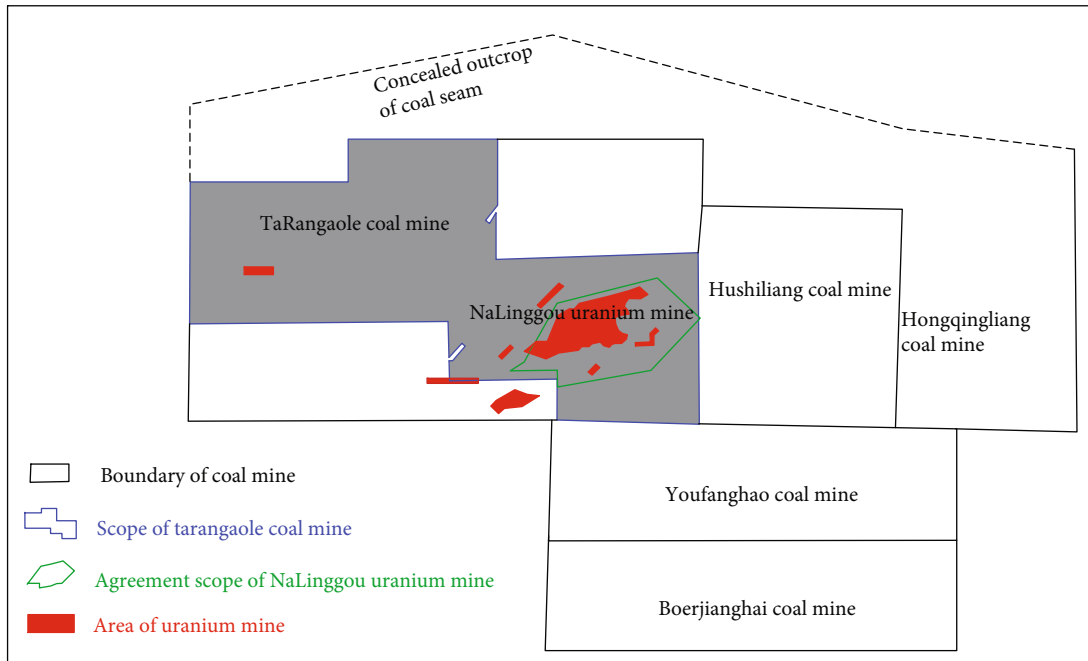


FIGURE 1: The spatial distribution of coal and uranium in the Ordos Basin.

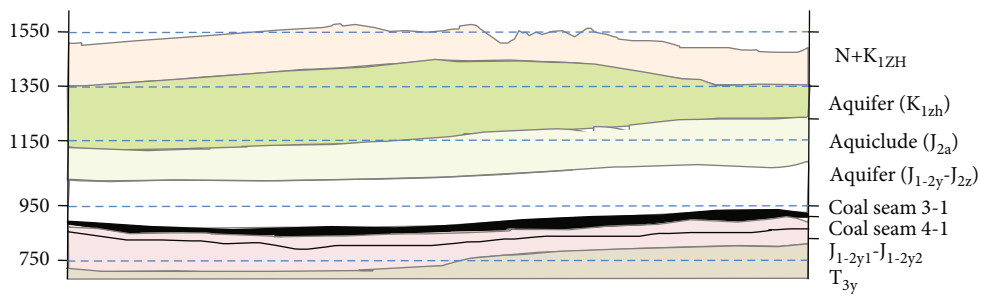


FIGURE 2: Hydrogeology condition of the coal and uranium reservoir.

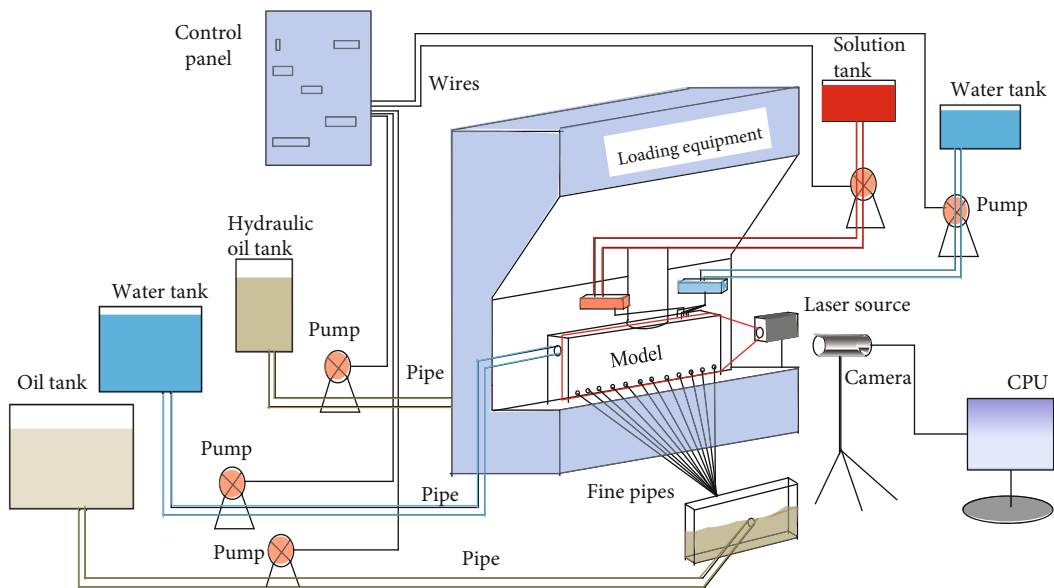


FIGURE 3: Schematic diagram of coordinated mining equipment.

TABLE 1: Key technical parameters of the equipment.

Category	Power	Stress/pressure	Measuring range	Accuracy	Flow rate	Operating system
Loading pump	5.5 kW	10 t	400 mm	0.1 mm	—	PLC
Fluid pump	1 kW	0-10 MPa	—	0.01 mL	0-1.2 L/minute	PLC



FIGURE 4: Preparation of the leaching solution.

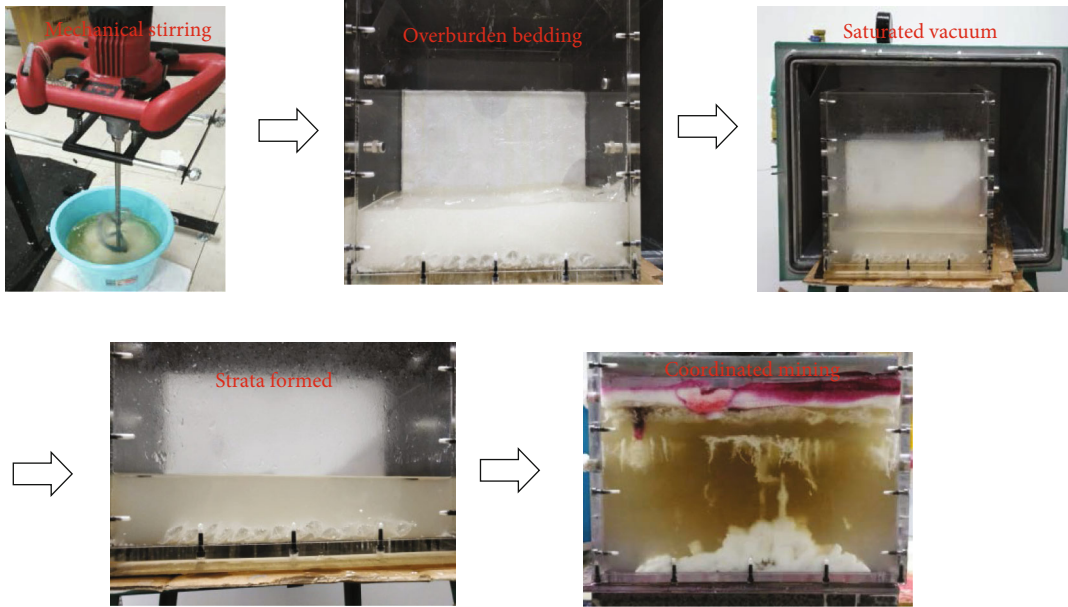


FIGURE 5: Preparation process of the transparent strata.

(6) Water storage coefficient similarity: $C_S = 1/C_\gamma \sqrt{C_l}$

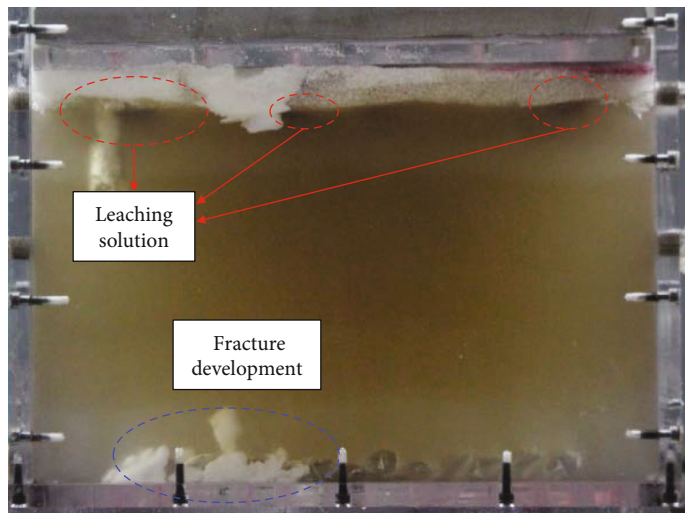
(7) Permeability similarity: $C_K = \sqrt{C_l}/C_\gamma$

4. Physical Experiment

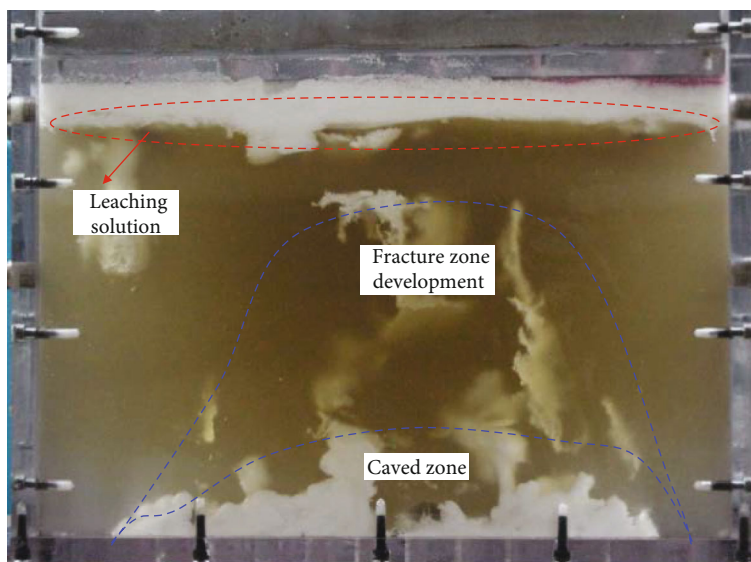
4.1. Experiment Setup. The geological and hydrology properties were characterized by the transparent soil and leaching solution. The behaviors of fracture development and fluid migration were studied in different mining scenarios. A “seven-point” pattern technology was adopted for the in situ leaching of uranium. The space of pumping wells is set to 30 m, the pumping volume is set to 8 m³/h, and the coal mining speed is assumed as 16 m/d.

The experiment equipment is composed of the control, loading, and monitoring systems, and a good performance function for the in situ leaching of uranium and coal mining was developed, as shown in Figure 3. In detail, the underground mining of coal and in situ leaching of uranium were performed by hydraulic pumping. The seepage migration, fracture movement, and strata displacement were captured by the monitoring system. And the specific technical parameters are shown in Table 1.

The physical model includes transparent acrylic glass and is sealed by bolts and colloids, and the dimension is 40 cm × 20 cm × 40 cm (length × width × height). The transparent soil is prepared by aggregate particles and saturated liquid. The aggregate particle was made by the mixture of 200–300- and 20–40-mesh silica gel powder, and the

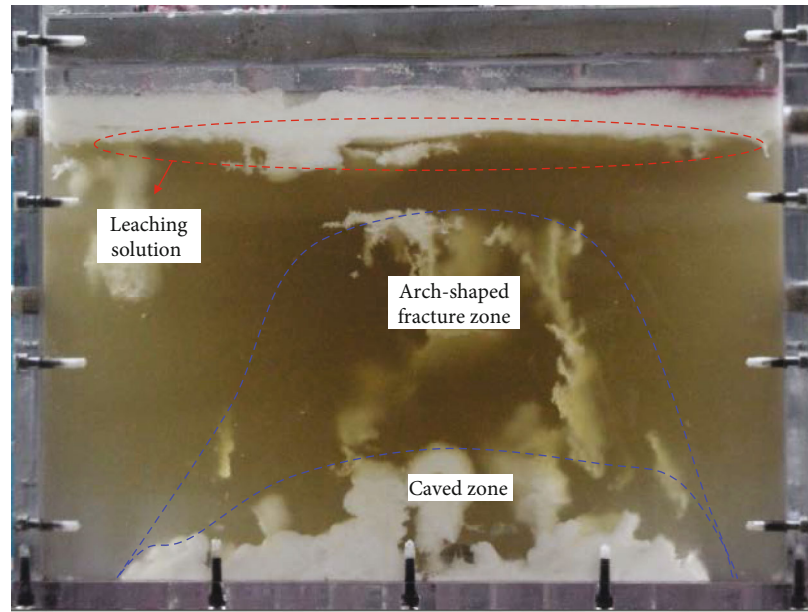


(a) 48 m

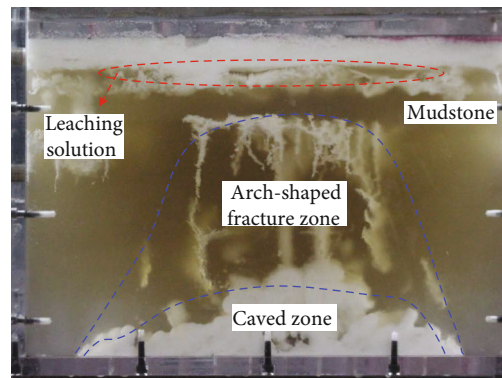


(b) 112 m

FIGURE 6: Continued.



(c) 132 m



(d) 150 m

FIGURE 6: Development of fracture field and migration of leaching solution.

saturated liquid was made by the mixture of paraffin oil and n-tridecane.

4.2. Experimental Procedure. The sandy mudstone layer, conglomerate aquifer, and coarse-grained sandstone layer were characterized by transparent soil. The coal seam was described by an oil bag located in the bottom of the physical model. The sandy mudstone layer was characterized by a mixture of 200–300-mesh silica gel powder and mineral oil. The conglomerate aquifer and coarse-grained sandstone were characterized by a mixture of 200–300- and 20–40-mesh silica and mineral oil, respectively. The preparation procedure is shown in Figure 4, and the specific experiment steps are shown:

- (1) The saturated liquid was obtained by the mixture of paraffin oil and n-tridecane at a mass ratio of 0.85 : 1. Subsequently, the silica gel powder and saturated liquid were mixed in a mass ratio of 1 : 0.65, and the mixture was stirred using the stirrer for 1 h
- (2) The mixture was poured into the transparent abrasive tool to be vacuumized and saturated for 12 h until the bubbles of the material completely disappeared. Subsequently, the mixture was consolidated with respect to a certain amount of mechanical stress for 7 days until the transparent material of the sandy mudstone, conglomerate aquifer, and coarse-grained rock approached the physical strength. Further, the transparent rock layer presented appropriate transparency with a refractive index of 1.42
- (3) The saturated oil red O dye and saturated liquid were mixed and retained for 24 h. Then, the solution tracer was obtained as the in situ leaching solution of uranium, as shown in Figure 5
- (4) For uranium mining prior to coal, in situ leaching was conducted with the prepared solution tracer using a pumping system. For the scenario of the coming of uranium and coal, the coal seam was mined at a rate of 16 m/d through the pumping fluid

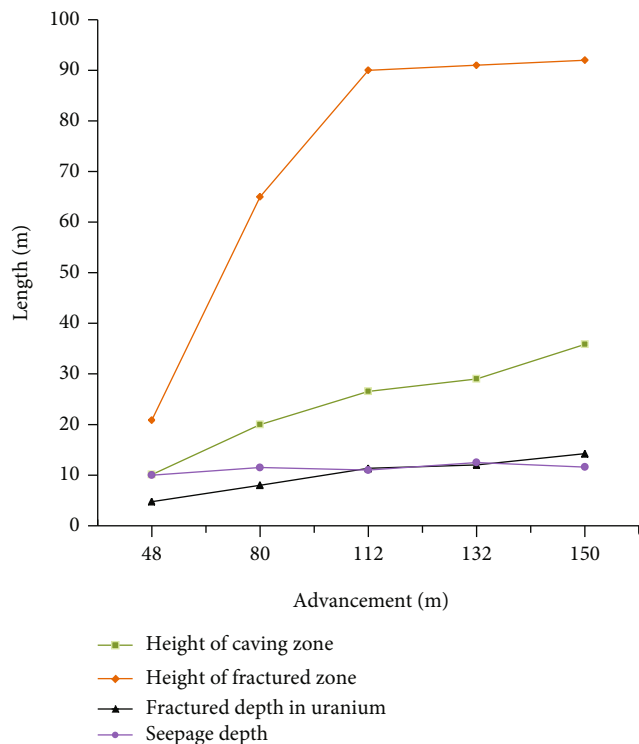


FIGURE 7: Correlation between the coal mining and development of the fracture and seepage zone.

from the oil bag, and the in situ leaching was conducted with the solution tracer using a pumping system. For the scenario of coal mining prior to uranium, the coal seam was initially mined, and the stability of the mining-induced fractured zone was obtained; then, the in situ leaching was performed using the solution tracer

5. Results and Analyses

5.1. Hydrogeology Response to the Comining of Coal and Uranium. During the coordinated mining of coal and uranium, the fracture growth and the solution diffusion were investigated. The specific characteristics of multifield coupling are shown in Figures 6 and 7.

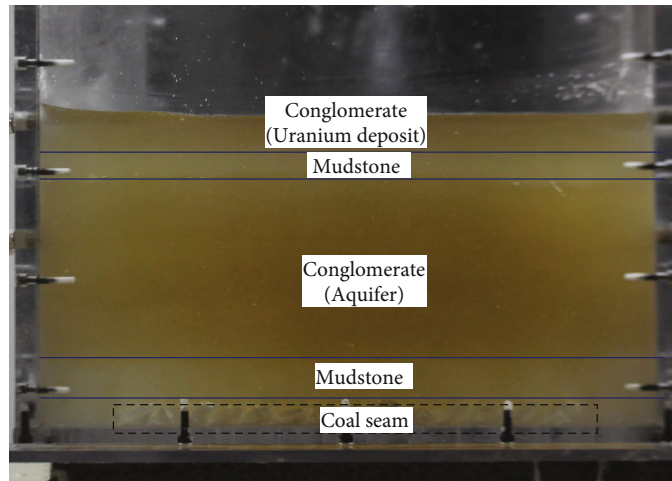
In Figure 6, a “cone-shaped” leaching solution diffusion area around the injection well was observed, as the in situ leaching of uranium at a constant speed of 0.14 m/s. The leaching solution diffused and was transported from the injection well to the pumping well under the effect of the negative pressure. With the advancement of coal mining, the fracture zone and caving zone could be observed in the sandy mudstone above the coal seam. In addition, a “horizontal-shaped” fracture zone was observed in the uranium-bearing layer due to the hydraulic and mechanical fracturing effect. In Figure 7, an increasing trend in the height of the fractured zone and the caving zone and fractured depth was presented, and seepage depth varied around 11 m, as the process of the in situ leaching of uranium. As the coal mining advanced to 48 m, the height of the caving

zone approached to 10 m, the height of the fractured zone had grown into 21 m, and the fractured depth evolved into 4.77 m. Meanwhile, the uranium was normally mined, and a 10 m vertical infiltration of leaching solution along the horizontal direction was observed. As the coal mining advanced to 112 m, the height of the caving zone is 26.6 m and the maximum height of the fractured zone is 90 m above the coal goaf. Further, a plastic zone with a length of 20 m was formed in front of the mining face, as shown in Figure 6(b), and a balanced horizontal flow state was obtained with a seepage depth of 11 m and a fracture depth of 11.35 m. As the mining advanced to 150 m, the maximum height of 90 m was maintained with respect to the fractured zone; in contrast, the height of the caving zone is 35.8 m. In addition, a fracture depth of 14.2 m and a seepage depth of 11.6 m are obtained. Further, the stability of the horizontal flow was maintained with respect to the in situ leaching, and the increase in vertical infiltration of the leaching solution was presented. Figure 6(d) shows that the morphology of the fractured zone is characterized by an “arched-shape” structure and the maximum height of the fractured zone is 90 m, as the mining advanced to 150 m. The decrease in fracture zone height from the middle to the end of the stope was presented. No obvious vertical infiltration was observed, as the in situ leaching was performed.

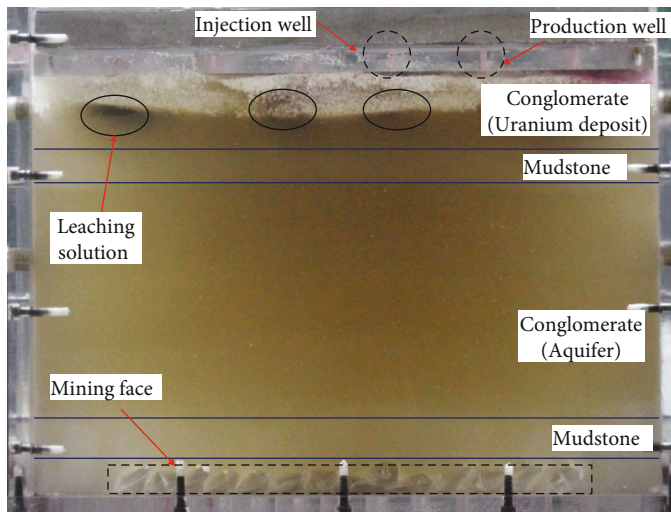
The vertical infiltration of the solution was not obvious in the scenario of the comining of coal and uranium; however, the horizontal and dynamic movements of the solution were observed between the injection well and the pumping well. A fracture zone characterized by the existence of an “arched-shape” structure was observed in the stope, and the stability was maintained for a long time. The maximum height is 90 m, which is 20 times the coal seam thickness. The “arched-shape” boundary of the fracture zone is observed under the no-key-layer condition in the overlying strata, and the coal mining was protected under the “arched-shape” structure.

5.2. Comparison of the Different Mining Scenarios of Coal and Uranium. The diffusion of the leaching solution, the development of a mining-induced fracture zone, and the influence of convection and dispersion of the underground fluid on the diffusion of the leaching solution are presented in Figures 8 and 9.

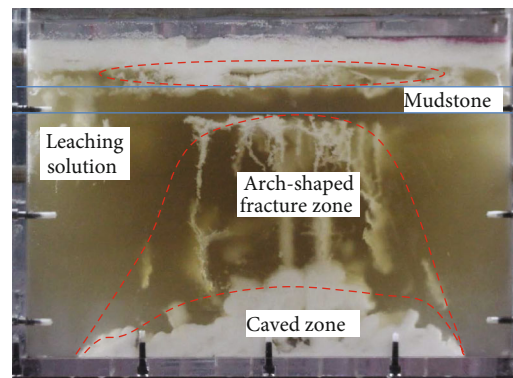
Figure 8(b) presents that the horizontal movement dominated the distribution of the leaching solution and that vertical infiltrate cannot be formed in the scenario of uranium mining prior to coal. This illustrates that the pressure difference between the coal seam and uranium-bearing strata plays an important role in the distribution of the leaching solution. For the comining of coal and uranium, the fracture zone, characterized by an “arched-shape” morphology, was generated with the advance of coal mining, as shown in Figure 8(c). Further, the stability of the uranium deposit was observed based on the protective effect of the undisturbed layer located below the uranium deposit. The maximum penetration depth of the solution was limited, and the vertical penetration behavior of the solution was not observed in a short period. The accelerated infiltration of



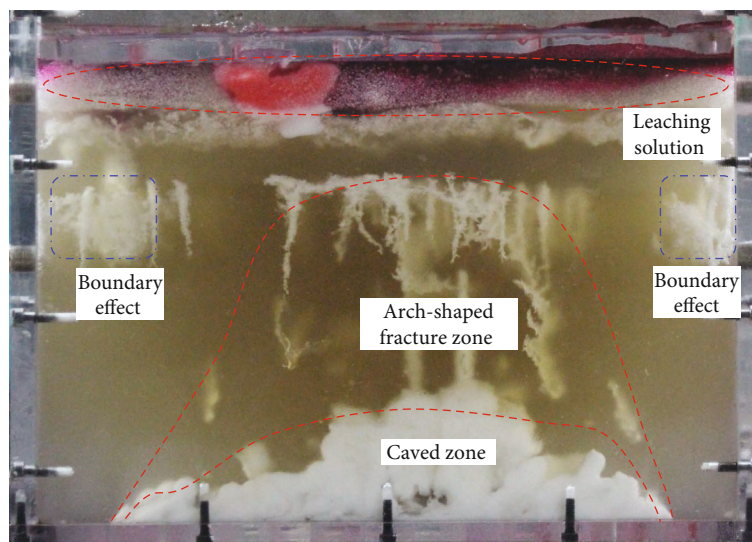
(a) Hydrogeology of the coal and uranium



(b) In situ leaching of uranium



(c) Coming of coal and uranium



(d) Coordinated mining of coal prior to uranium

FIGURE 8: Development of the fracture and migration of leaching solution in different mining scenarios.

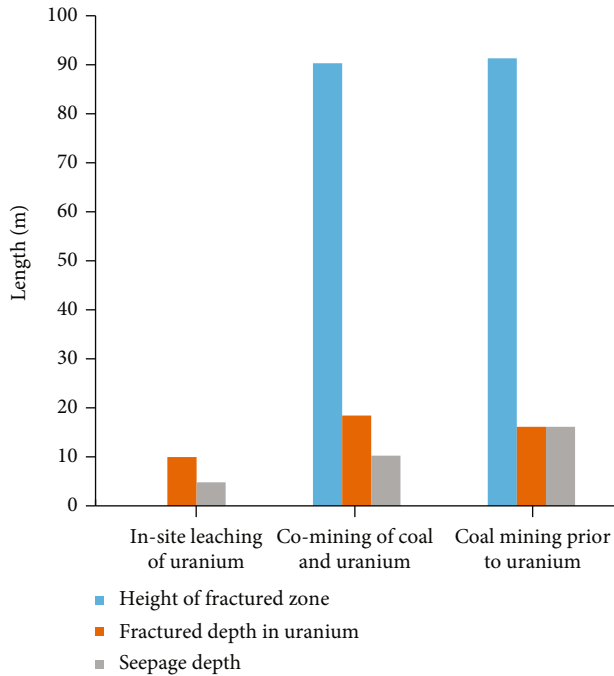


FIGURE 9: Comparison in the development of fracture and seepage for coordinated mining of coal and uranium.

the solution influenced by the convection effect would be presented in the goaf, as the solution approached the fracture zone in a long period.

Figure 9 shows that a stable 90 m height of the fractured zone was presented in the coming of coal and uranium and coal mining prior to uranium. The fracture depth in the uranium layer in the coming of coal and uranium was larger than that of coal mining prior to uranium and uranium mining prior to coal. However, the seepage depth of the leaching solution in coordinated mining of coal prior to uranium was higher than that in the coming of coal and uranium and uranium mining prior to coal. The maximum fractured depth in the uranium layer was observed in the coming of coal and uranium, because the physical influence and hydraulic fracturing effect caused by coal mining dynamically changed the hydrogeology. Considering the time-dependent effect, the maximum seepage depth was observed in coal mining prior to uranium. The vertical infiltration of the leaching solution was limited to 10–12 m because of the presence of an undisturbed layer during uranium mining in the uranium prior to coal.

6. Discussion

The geotechnical mechanics and permeability of the transparent soil composed of the different skeletons and saturating fluids were studied [7, 14]. And the displacement in embankment road, tunneling, and slope slipping were investigated using the transparent soil [1–5, 23]. However, the development of the mining-induced fracture and leaching solute was rarely characterized by the transparent soil. In this study, the hydrogeology of intergrown resources was described by transparent soil, which comprises paraffin oil,

n-tridecane, and silica gel in different mass ratios. The coordinated mining of coal and uranium in different scenarios was performed. The hydrogeology response characterization with respect to the mining can be given as follows:

- (1) Considering a matching refractive index, the sandy mudstone was characterized by the mixture of 200–300-mesh silica gel powder and mineral oil; the conglomerate aquifer and coarse-grained sandstone were represented by 200–300- and 20–40-mesh silica gel powder and mineral oil
- (2) The mining-induced fracture zone was well characterized by the “white zone” caused by air, and the leaching solution was characterized by the saturated red O dye
- (3) The “arch-shaped” fractured zone exhibits a maximum height of 90 m, and the “horizontal-shaped” fractured zone exhibits a maximum height of 14.24 m in the uranium-bearing layer. The leaching solution seepage depth of 12 m was determined by the distribution of the saturated red O dye
- (4) The difference in the scope of the fractured zone and seepage area was characterized by the white zone and red zones

7. Conclusions

Based on the physical experiment through transparent soil, the diffusion and migration of the in situ leaching solution and the development of mining-induced fracture zones were observed in different mining scenarios of coal and uranium, and the main conclusions are given:

- (1) The hydrogeology was appropriately characterized by a mixture of silica gel powder and mineral oil. The sandy mudstone was characterized by a mixture of 200–300-mesh silica gel powder particles with low permeability. The conglomerate aquifer was characterized by 20–40-mesh silica gel powder. And the mud pebble was characterized by a mixture of 200–300- and 20–40-mesh silica gel powder
- (2) With the oil separation and air diffusion along the fracture net, a white zone covering the mining-induced fracture zone was observed; the migration of the leaching solution was characterized by the saturated oil red O dye. A fracture zone characterized by an “arch-shape” morphology was observed with a maximum height of 90 m above the mined goaf, and the mining face was protected by the “arch-shape” structure. “Horizontal-shaped” fracture zones with depths of 9.97, 18.4, and 16.09 m were observed in the uranium-bearing layer for the scenario of uranium prior to coal, coming of coal and uranium, and coal mining prior to uranium, respectively
- (3) A smaller leaching solution vertical infiltration of 4.83 m was observed, compared with those of

10.26 m in the coming of coal and uranium and 16.09 m in coal mining prior to uranium. The layer below uranium was stable, and the leaching solution infiltration in the coal mining area was not observed in a short time for coordinated mining in different scenarios

Data Availability

The data used to support the findings of this study are included within the article.

Conflicts of Interest

The authors declared that they have no conflicts of interest to this work.

Acknowledgments

This study was supported by the Open Fund of State Key Laboratory of Water Resource Protection and Utilization in Coal Mining (Grant No. GJNY-18-73.7), National Youth Science Foundation (No. 51904011), Anhui Provincial Natural Science Foundation (No. 1908085QE183), Anhui University Scientific Research Foundation (No. QN2018108), and Institute of Energy, Hefei Comprehensive National Science Center (Grant No. 21KZS216).

References

- [1] E. D. Guzman and M. Alfaro, "Modelling a highway embankment on peat foundations using transparent soil," *Procedia Engineering*, vol. 143, pp. 363–370, 2016.
- [2] E. M. B. De Guzman and M. C. Alfaro, "Laboratory-scale model studies on corduroy-reinforced road embankments on peat foundations using transparent soil," *Transportation Geotechnics*, vol. 16, pp. 1–10, 2018.
- [3] W. Zhang, H. Zhong, Y. Xiang, D. Wu, Z. Zeng, and Y. Zhang, "Visualization and digitization of model tunnel deformation via transparent soil testing technique," *Underground Space*, 2020.
- [4] Y. Xiang, H. Liu, W. Zhang, J. Chu, D. Zhou, and Y. Xiao, "Application of transparent soil model test and DEM simulation in study of tunnel failure mechanism," *Tunnelling And Underground Space Technology*, vol. 74, pp. 178–184, 2018.
- [5] F. M. Ezzein and R. J. Bathurst, "A new approach to evaluate soil-geosynthetic interaction using a novel pullout test apparatus and transparent granular soil," *Geotextiles and Geomembranes*, vol. 42, no. 3, pp. 246–255, 2014.
- [6] M. G. Iskander, J. Liu, and S. Sadek, "Transparent amorphous silica to model clay," *Journal of Geotechnical and Geoenvironmental Engineering*, vol. 128, no. 3, pp. 262–273, 2002.
- [7] J. Liu, M. G. Iskander, and S. Sadek, "Consolidation and permeability of transparent amorphous silica," *Geotechnical Testing Journal*, vol. 26, no. 4, pp. 11056–11401, 2003.
- [8] B. Yuan, M. Sun, L. Xiong, Q. Luo, S. P. Pradhan, and H. Li, "Investigation of 3D deformation of transparent soil around a laterally loaded pile based on a hydraulic gradient model test," *Journal of Building Engineering*, vol. 28, p. 101024, 2020.
- [9] M. G. Iskander, S. Sadek, and J. Liu, "Optical measurement of deformation using transparent silica gel to model sand," *International Journal of Physical Modelling in Geotechnics*, vol. 2, no. 4, pp. 13–26, 2002.
- [10] I. L. Guzman, M. Iskander, and S. Bless, "Observations of projectile penetration into a transparent soil," *Mechanics Research Communications*, vol. 70, pp. 4–11, 2015.
- [11] S. Sadek, M. G. Iskander, and J. Liu, "Accuracy of digital image correlation for measuring deformations in transparent media," *Journal of Computing in Civil Engineering*, vol. 17, no. 2, pp. 88–96, 2003.
- [12] M. Iskander, S. Sadek, and J. Liu, "Soil structure interaction in transparent synthetic soils using digital image correlation," *proc*, vol. 03-2360, pp. 1–23, 2003.
- [13] S. Kashuk, S. R. Mercurio, and M. Iskander, "Visualization of dyed NAPL concentration in transparent porous media using color space components," *Journal of Contaminant Hydrology*, vol. 162-163, pp. 1–16, 2014.
- [14] G. Q. Kong, L. D. Zhou, and Z. T. Wang, "Shear modulus and damping ratios of transparent soil manufactured by fused quartz," *Materials Letters*, vol. 182, pp. 257–259, 2016.
- [15] G. Xu, *Research on the mechanism and evolution law of rock deformation and cracking around deep tunnels*, China Univ. Min. Tech, 2011.
- [16] M. Ahmed and M. Iskander, "Evaluation of tunnel face stability by transparent soil models," *Tunnelling & Underground Space Technology Incorporating Trenchless Technology Research*, vol. 27, no. 1, pp. 101–110, 2012.
- [17] L. Wei, Q. Xu, S. Wang, C. Wang, and J. Chen, "Development of transparent cemented soil for geotechnical laboratory modelling," *Engineering Geology*, vol. 262, p. 105354, 2019.
- [18] J. Zhang, *Study on the development of transparent similar materials for rock mass and its experimental applications*, J. China University Min. Techn, 2014.
- [19] W. Ye, *Experiment study of internal 3d crack propagation in brittle and transparent rock-like material*, Chongqing University, 2016.
- [20] J. Fu, W. Zhu, and X. Luo, "Study on failure process of fractured rock by using a new material containing three-dimensional internal fracture surfaces," *Zhongnan Daxue Xuebao (Ziran Kexue Ban)/Journal of Central South University (Science and Technology)*, vol. 45, no. 9, pp. 3257–3263, 2014.
- [21] L. I. Yuanhai, Z. Lin, and X. Qin, *Study of development of transparent rock mass for physical similarity experiment and its mechanical properties*, Journal of China University of Mining & Technology, 2015.
- [22] Y. Q. Hu, Y. S. Zhao, and D. Yang, "Simulation theory and method of 3D solid-liquid coupling," Journal of Liaoning Technical University, 2007.
- [23] J. Sun and J. Liu, "Visualization of tunnelling-induced ground movement in transparent sand," *Tunnelling and Underground Space Technology*, vol. 40, pp. 236–240, 2014.

Research Article

A Practical Design Method for Reducing Postconstruction Settlement of Highway Subgrade Induced by Soil Creep

Fei Zhou ¹, Tangdai Xia ¹, Bingqi Yu,¹ Fan Xia,¹ and Fan Yu²

¹Research Center of Coastal and Urban Geotechnical Engineering, Zhejiang University, Hangzhou 310058, China

²Zhejiang Provincial Institute of Communications Planning, Design & Research, Zhejiang, Hangzhou 310006, China

Correspondence should be addressed to Tangdai Xia; xtd@zju.edu.cn

Received 10 September 2021; Accepted 15 October 2021; Published 5 November 2021

Academic Editor: Yu Wang

Copyright © 2021 Fei Zhou et al. This is an open access article distributed under the Creative Commons Attribution License, which permits unrestricted use, distribution, and reproduction in any medium, provided the original work is properly cited.

The postconstruction settlement of the bridge approach is usually uneven, which could create a bump in the roadway. Indeed, this is a typical situation at the end of the bridge approach and requires a solution. One of the main causes of postconstruction settlement is the creep of soil. This paper is aimed at generalizing a new design method for controlling highway postconstruction settlement by replacing subgrade with expanded polystyrene (EPS). In the new method, the creep coefficient can be calculated based on the Yin-Graham EVP model. Thus, the relationship between the overloading ratio (OLR) and overconsolidation ratio (OCR) is obtained. The new method involves five steps: (a) determine the creep coefficient based on the relationship between the creep coefficient and over consolidation ratio, (b) divide the ground into a suitable number of sublayers, (c) select groups of different overloading ratios and then calculate the average values of the additional stress and overconsolidation ratio for each sublayer under different OLRs, (d) calculate the postconstruction settlement under different OLRs, and (e) determine the replacement capacity for different sections. This method can be used for quantitative design according to different requirements of postconstruction settlement of foundation. Taking Huzhou Avenue as an example, the case study illustrates the calculation process of the new method in detail.

1. Introduction

The bridge approaches provide a smooth transition of cars from roadway pavements to bridge structures. However, the postconstruction settlement of bridge approaches is usually uneven, which could create a bump in the roadway. Indeed, this is a typical situation at the bridge approach and requires a solution.

The bump at bridge-head is a complicated technical problem. The creep of soil is one of the main causes of postconstruction settlement. The soil exhibits creep properties. Compared with primary consolidation settlement, creep settlement is small but significant, especially for soft clay. In the past several decades, extensive studies have been conducted on the creep of soft clay. Ladd et al. [1] first proposed the

question of whether creep settlement occurs in the process of primary consolidation settlement. And there are two different views on whether the creep occurs during primary consolidation. They summed them up as Hypothesis A and Hypothesis B. Hypothesis A holds that creep occurs only in the secondary consolidation stage, and no creep occurs in the primary consolidation stage. Mesri et al. [2–4], Wang et al. [3], and Mesri and Vardhanabhuti [4] support Hypothesis A. However, Hypothesis B believes that the soil creep is caused by its own viscosity and occurs from the beginning of the primary consolidation process. It is supported by Bjerrum [5], Stolle et al. [6], Nash and Ryde [7], Yin et al. [8], Suklje [9], Bouchard et al. [10], Berre and Iversen [11], Leoni et al. [12], Karim et al. [13], and Nash and Brown [14]. As is known, with the effective stress changes, the creep always

exists actually, which means that Hypothesis B is reasonable. Based on Hypothesis B and the equivalent time concept, Yin and Graham [15–18] proposed a 1D elastic viscoplastic (EVP) model for creep behavior, which can be used to calculate the creep settlement. According to the EVP model, the creep coefficient is closely related to the over consolidation ratio (OCR).

Some compression tests [19–21] have shown that the creep coefficient decreases with the increase of OCR. Therefore, the use of a preload larger than the final construction load is an effective method to reduce postconstruction settlement [22–26]. However, in the actual project, for some sections, the preloading period is insufficient so that it is difficult to achieve the original effect within the time limit of the project. The method of replacing part of subgrade with lightweight materials to reduce the permanent load of subgrade can solve the problem [27, 28]. Expanded polystyrene (EPS) is one of the high-quality lightweight materials [29]. EPS has the characteristics of ultralightweight, compressibility resistance, self-reliance, water resistance, flame retardant, and so on. The density of the EPS material is generally $0.2 \sim 0.3 \text{ kN/m}^3$, which is equivalent to $1/100 \sim 1/60$ of the soil density. EPS has high compressive strength and varies with density, so it can be used as an embankment filling material in the elastic range of $80 \sim 140 \text{ kN/m}^2$. EPS is a synthetic resin foam containing independent bubbles that do not absorb water. The physical properties and mechanical indexes of the EPS material change little in the aging process, excellent aging resistance, and its aging life is more than 60 years.

It is important to determine the appropriate thickness of EPS to control the postconstruction settlement but there are only few studies in this area. Chen et al. [30] suggest that consolidation, compression, and other parameters can be calculated according to the monitoring data, and the calculation program of foundation settlement reflecting the process of overloading-unloading and reloading should be compiled. Then, the relationship between different capacities of lightweight material and postconstruction settlement is obtained. Thus, the thickness of the lightweight material can be determined according to the allowable postconstruction settlement. Many factors are considered in this method, but it is difficult to be generalized and applied in engineering due to its complex calculation. Jiang et al. [31] come up with a formula to calculate the thickness. However, this formula also relies on monitoring data and the postconstruction settlement is only estimated according to the measured data. Therefore, this formula may not be used in the stage of design.

This paper is aimed at proposing a new practical design method for controlling highway postconstruction settlement by replacing subgrade with EPS. First, the functional relationship between the creep coefficient and overconsolidation ratio is established by fitting the one-dimensional compression test data. Second, the relationship between the overloading ratio (OLR) and overconsolidation ratio (OCR) is deduced. Then, groups of different OLR are selected and the postconstruction settlement under different OLRs is calculated. This method can be used for quantitative design according to different requirements of postconstruction settlement of foundation. And it can make the OLR greater than 1.3 without the limitation of foundation stability.

2. Creep Coefficient of Overconsolidated Soil

Buisman proposed the concept of secondary consolidation coefficient (C_α). As is shown in Figure 1, it is believed that the $e - \lg t$ curve is close to a straight line after primary consolidation. The slope of the straight line part i is defined as secondary consolidation coefficient C_α .

$$C_\alpha = \frac{e_0 - e_1}{\lg t_1 - \lg t_0}, \quad (1)$$

where t_0 is the time at the end of primary consolidation and t_1 is any time after the end of primary consolidation.

However, Equation (1) is not applicable to the overconsolidated soil because overconsolidated soil has finished primary consolidation before test. In 1964, Crawford [32] conducted normally consolidated soil compressive rheological tests and plotted $e - \lg p$ curves of different consolidation times. In 1967, Bjerrum made a creep diagram. As is shown in Figure 2, he divided the displacements which he observed in the actual engineering into “instant compression” and “delayed compression” and proposed that the delayed compression can be described with parallel lines in $e - \lg \sigma$ space.

Based on Bjerrum’s creep diagram, Yin-Graham proposed the 1-D EVP model, and the total strains can be written as follows:

$$\varepsilon_z = \varepsilon_{z_0} + \frac{\lambda}{V} \ln \left(\frac{\sigma'_z}{\sigma'_{z_0}} \right) + \frac{\psi}{V} \ln \left(\frac{t_e + t_0}{t_0} \right), \quad (2)$$

where ε_{z_0} is a reference strain and ε_z is the total strain. σ'_{z_0} is a reference stress that corresponds, respectively, to the strain at the beginning of loading. For normally consolidated soil, σ'_{z_0} corresponds to strain ε_{z_0} . V is the specific volume of the soil ($1 + e$), that is, the volume occupied by unit volume of solids. So $\lambda = C_c/2.303$ and $\psi = C_{ae}/2.303$, where C_c and C_{ae} are the compression index and creep coefficient under logarithmic coordinates. Here, we call C_{ae} “creep coefficient” instead of the “secondary consolidation coefficient”, because Equation (2) considers creep occurs during and after “primary consolidation.” And t_0 is a parameter that can be measured by one-dimensional compression test, which is usually taken as unit time or the boundary point between the primary consolidation and secondary consolidation [33]. t_e is called the equivalent time as defined by Yin and Graham.

According to Equation (2), the void ratio e , the effective stress σ , and the equivalent t_e have a unique relationship.

$$e = e_0 - C_c \lg \left(\frac{\sigma'_z}{\sigma'_{z_0}} \right) - C_{ae} \lg \left(\frac{t_e + t_0}{t_0} \right). \quad (3)$$

As is shown in Figure 3, no matter if it is normal consolidation soil or overconsolidated soil, the zero point of time is taken as the loading start time of its corresponding normal

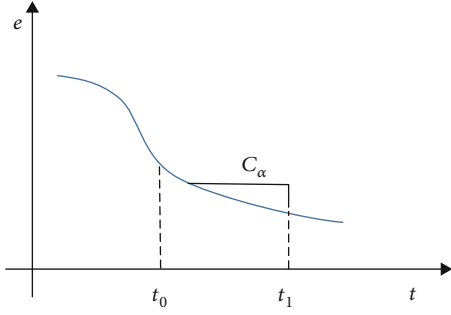


FIGURE 1: Primary consolidation and secondary consolidation of normally consolidated soil.

consolidation condition. For example, point 2 in Figure 3 is under overconsolidation condition, and its corresponding normal consolidation condition is point 5 on the normal consolidation line. The time corresponding to point 5 is the beginning time. And t_e is the equivalent time that is from point 5 to point 2. Such a time coordinate system combines normal consolidation and overconsolidation into a unified time coordinate system, so it is called an absolute time coordinate system. Now, t_e can be found from

$$C_{\alpha e0} \lg \left(\frac{t_e + t_o}{t_o} \right) = (C_c - C_e) \lg \left(\frac{\sigma'_z}{\sigma'_{z0}} \right), \quad (4)$$

where $C_{\alpha e0}$ is the normal consolidation soil creep coefficient and C_e is the expansion coefficient. From which

$$t_e = t_o \left(\frac{\sigma'_z}{\sigma'_{z0}} \right)^{(C_c - C_e)/C_{\alpha e0}} - t_o. \quad (5)$$

Let

$$\text{OCR} = \frac{\sigma'_z}{\sigma'_{z0}}, \quad \delta = \frac{C_c - C_e}{C_{\alpha e0}}. \quad (6)$$

t_e can be expressed as follows:

$$t_e = t_o (\text{OCR})^\delta - t_o. \quad (7)$$

According to Equation (7), t_e is a parameter related to OCR, and it can reflect the stress history and the state of soil. For overconsolidated soil, the creep coefficient of overconsolidated soils can be expressed as

$$\begin{aligned} C_{\alpha e} &= \frac{e_1 - e_2}{\lg \left(\frac{(t_{e2} + t_o)/(t_{e1} + t_o)}{e_1 - e_2} \right)} \\ &= \frac{e_1 - e_2}{\lg \left(\frac{(t_{e1} + \Delta t + t_o)/(t_{e1} + t_o)}{e_1 - e_2} \right)} \\ &= \frac{e_1 - e_2}{\lg \left(1 + (\Delta t / (t_{e1} + t_o)) \right)}, \end{aligned} \quad (8)$$

where t_{e1} and t_{e2} are the equivalent time; e_1 and e_2 are the

void ratios at equivalent time t_{e1} and t_{e2} , respectively; and Δt is the current load duration from t_{e1} to t_{e2} .

According to Equations (7) and (8), the creep coefficient is not a constant. It can be expressed as a function with overconsolidation ratio.

$$C_{\alpha e} = f(\text{OCR}). \quad (9)$$

3. The Relationship between Overconsolidation Ratio (OCR) and Overloading Ratio (OLR)

The maximum value of load in the past, namely, the preload, divided by the present value of load, is defined as the overload ratio (OLR). Overload ratio (OLR) was proposed to reflect overload state, which can be expressed as follows:

$$\text{OLR} = \frac{p_o}{p_f}, \quad (10)$$

where p_o is the preload, that is, the load under the condition of overload preloading. p_f is the present value of load, that is, the final construction load on the ground surface.

The maximum value of effective stress in the past, namely, the preconsolidation pressure, divided by the present value of effective value of effective stress, is defined as the overconsolidation ratio (OCR).

$$\text{OCR} = \frac{\sigma_c}{\sigma_o}, \quad (11)$$

where σ_o is the present effective stress and σ_c is the preconsolidation pressure.

When the load on the ground surface changes, the stress state of each point in the soil stratum will change, and OCR will also change. For example, as is shown in Figure 4, point A is under normal consolidation condition before loading. That is, σ_o is equal to $\gamma_i z$.

In soil mechanics, when load p_o is applied to the ground surface, the vertical additional stress σ_m is equal to αp_o . Here, α is the additional stress coefficient which can be calculated based on the depth of soil and the load distribution type. It is convenient that we can look up the additional stress coefficient table to determine its value. And when final load p_f is applied to the ground surface, the vertical additional stress σ_f is equal to αp_f . So, the OCR of point A can be expressed as follows:

$$\text{OCR} = \frac{\sigma_o + \sigma_m}{\sigma_o + \sigma_f} = \frac{\gamma_i z + \alpha p_o}{\gamma_i z + \alpha p_f}. \quad (12)$$

As is shown in Figure 4,

$$H = h + \Delta h + h_s, \quad (13)$$

$$p_f = \gamma h + \gamma_E \Delta h + \gamma_s h_s, \quad (14)$$

$$p_o = \gamma H = \gamma(h + \Delta h + h_s), \quad (15)$$

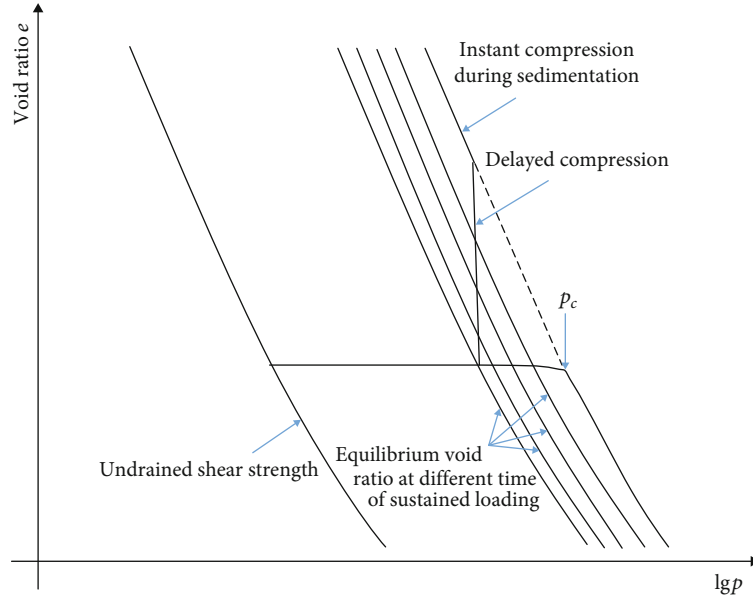
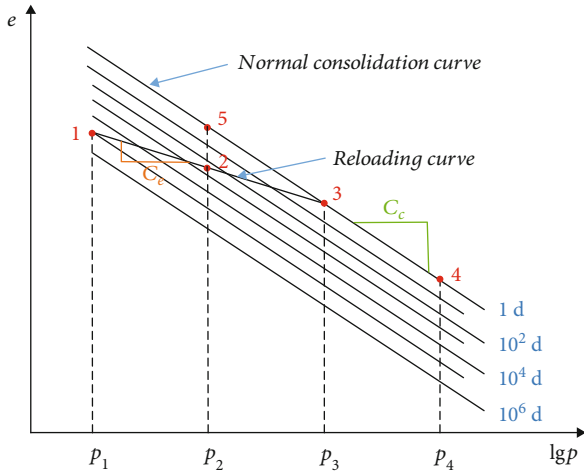


FIGURE 2: Bjerrum's creep diagram.

FIGURE 3: Equitime $e - \lg p$ curves.

where γ , γ_E , γ_i , and γ_s indicate the unit weight of filling soil, EPS, soft soil, and pavement, respectively; h , Δh , and h_s indicate the thickness of soft soil, EPS, and pavement, respectively; and H is the designed height of embankment fill.

Let us establish the relationship between the OCR and OLR. Based on Equations (10) and (11),

$$\begin{aligned} \text{OCR} &= \frac{\gamma_i z + \alpha \gamma (h + \Delta h + h_s)}{\gamma_i z + \alpha (\gamma h + \gamma_E \Delta h + \gamma_s h_s)} \\ &= \frac{\gamma_i z + \alpha \gamma h + \alpha (\gamma_E + (\gamma - \gamma_E)) \Delta h + \alpha (\gamma_s + (\gamma - \gamma_s)) h_s}{\gamma_i z + \alpha (\gamma h + \gamma_E \Delta h + \gamma_s h_s)} \\ &= 1 + \frac{(\gamma - \gamma_E) \Delta h + (\gamma - \gamma_s) h_s}{\gamma h + \gamma_E \Delta h + \gamma_s h_s + (\gamma_i z / \alpha)}, \end{aligned} \quad (16)$$

$$\begin{aligned} \text{OLR} &= \frac{\gamma (h + \Delta h + h_s)}{\gamma h + \gamma_E \Delta h + \gamma_s h_s} \\ &= \frac{\gamma h + (\gamma_E + (\gamma - \gamma_E)) \Delta h + (\gamma_s + (\gamma - \gamma_s)) h_s}{\gamma h + \gamma_E \Delta h + \gamma_s h_s} \\ &= 1 + \frac{(\gamma - \gamma_E) \Delta h + (\gamma - \gamma_s) h_s}{\gamma h + \gamma_E \Delta h + \gamma_s h_s}. \end{aligned} \quad (17)$$

According to Equations (14) and (15).

$$\frac{1}{\text{OCR} - 1} - \frac{1}{\text{OLR} - 1} = \frac{\gamma_i z}{\alpha (\gamma - \gamma_E) \Delta h + (\gamma - \gamma_s) h_s}. \quad (18)$$

Let

$$\beta(z) = \frac{\gamma_i z}{\alpha (\gamma - \gamma_E) \Delta h + (\gamma - \gamma_s) h_s}. \quad (19)$$

Thus, OCR, OLR, and z have a relationship:

$$\text{OCR} = 1 + \frac{1}{(1/(\text{OLR} - 1)) + \beta(z)}. \quad (20)$$

4. The New Method for Controlling Postconstruction Settlement

4.1. Procedures of Applying the Practical Design Method. The new method for controlling postconstruction settlement involves the following 5 steps:

- (a) Determine the creep coefficient. Based on the Yin-Graham EVP model, the functional relationship between the creep coefficient and overconsolidation ratio is established by fitting the one-dimensional compression test data

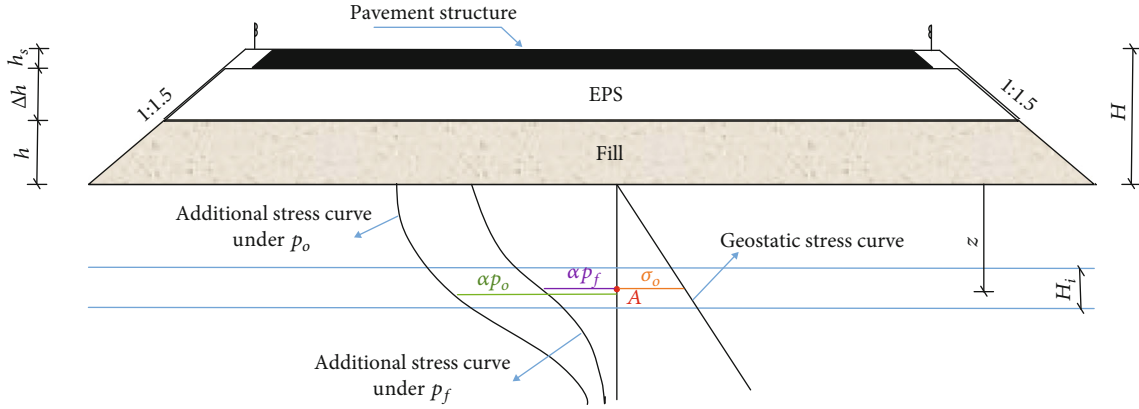


FIGURE 4: Cross-section of EPS filling.

- (b) Divided the ground into a suitable number of sublayers. Each sublayer within a same soil layer should not be overly thick. The thickness of each sublayer should be controlled within 2 m-4 m. For each sublayer, it is assumed that pressure is uniformly distributed
- (c) Select groups of different OLRs and calculate the average values of the additional stress and OCR for each sublayer under different OLRs. The OLR usually ranges from 1.1 to 1.6 in actual projects. Based on Equation (19), the additional stress and OCR at the center point of each sublayer are calculated and the values are taken as the average additional stress and OCR for each sublayer
- (d) Calculate the postconstruction settlement under different OLRs. Based on the functional relationship between C_{ae} and OCR, the creep coefficient of each layer is determined according to the average overconsolidation ratio for each sublayer. According to Equation (20), the settlement of each sublayer was calculated and the total postconstruction settlement of ground can be calculated as follows:

$$s = \sum_{i=1}^n \frac{H_i}{1 + e_{oi}} C_{aei} \lg \left(\frac{t_1 + \Delta t}{t_1} \right), \quad (21)$$

where s is the total postconstruction settlement of ground, H_i is the thickness of each sublayer, C_{aei} is the creep coefficient of each sublayer, t_1 is the preloading period, and Δt is the service period which is usually taken as 15 years

- (e) Correct the settlement value with the safety factor μ and determine the overload ratio and the replacement capacity under the requirements of postconstruction settlement

4.2. Advantages of the New Method. On the one hand, the subgrade soils become overconsolidated soil after replacement with EPS, so the creep coefficient is greatly reduced. As a lightweight material, EPS itself has the characteristics

of ultralightweight, compressibility resistance, self-reliance, water resistance, flame retardant, and so on. Therefore, this method can better control the postconstruction settlement.

On the other hand, this method can be used for the quantitative design according to different requirements of postconstruction settlement of foundation. In the process of the engineering design, the calculation of postconstruction settlement is often calculated by empirical formula or correction coefficient. This is often unable to meet the strict requirements of some engineering. Using the creep coefficient, this method can realize the quantitative calculation of postconstruction settlement.

Besides, this method can make the overloading ratio greater than 1.3 without the limitation of foundation stability. It is necessary to control the overloading ratio to ensure the stability of the foundation when using the overload preloading method for ground treatment. Thus, when the overloading is relatively small, a longer preloading time is needed to ensure the effect of controlling the postconstruction settlement, which would prolong the construction period. This method can make the overloading ratio greater than 1.3, which is like a strategy using space to exchange for time.

5. Case Study

5.1. Project Background. The considered Huzhou Avenue is constructed on soft clay on the Huzhou plain, southeast of the city of Huzhou in China. As is shown in Figure 5, the bridge approach is about 140 m long, which is divided into 5 transition sections (S1 to S5) and 1 general section (GS). The soft clay beneath it is about 13 m deep. In order to provide a smooth transition of vehicles from highway pavements to bridge structures, the design scheme is different for each section. Cement-soil mixed piles are used in S1 and S2. EPS lightweight materials are used in S3, S4, and S5. The plastic drainage plate is used in all sections.

The soft clay has high water content, a high void ratio, high compressibility, low strength, and low permeability. The soil profile is depicted in Figure 6, obtained from geological survey. The soil consists of 2 layers: (a) hard crust and (b) soft clay.

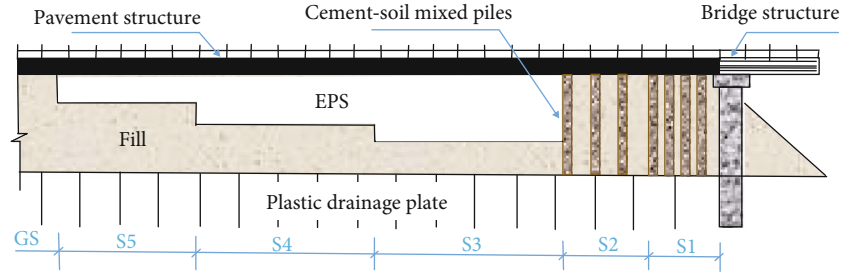


FIGURE 5: Profile of bridge approach.

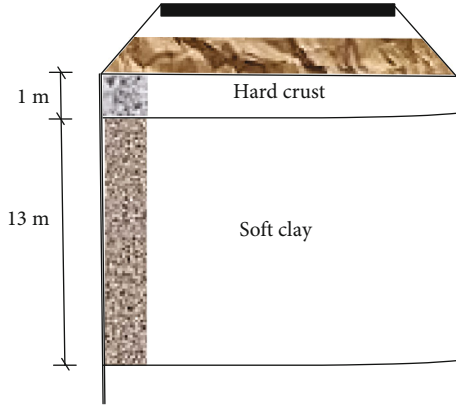


FIGURE 6: Profile of soil.

5.2. One-Dimensional Compression Test

5.2.1. Test Apparatus. As is shown in Figure 7, the sixteen automatic pneumatic consolidation apparatus is adopted to carry out one-dimensional compression test. The ring knife is 2 cm high, and the base area is 45.6 cm². Compared with traditional apparatus, the system has the advantage of automatic data acquisition during the test and overcomes the disadvantages of traditional manual recording. In order to ensure the reliability of the test results, the apparatus was proofread before the test.

5.2.2. Test Scheme and Description. In order to determine the stress history of the ground soils, the preconsolidation pressure should be first determined. Casagrande proposed an empirical graphical method using the $e - \lg p$ curve to obtain the maximum effective stress that had acted on the clay in the past. It is known through tests that the soft clay belongs to normally consolidated soil. The sample soils are taken from a depth of 5 m, and the preconsolidation pressure is about 110 kPa. In order to ensure that the maximum load is greater than the preconsolidation pressure, it is set as 150 kPa. The test loading path is divided into overloading, unloading, and reloading in order to simulate the actual construction condition. The soft clay is overconsolidated after reloading. For excluding the influence of the loading ratio factor, the loading ratio of each group is set as 1. Since the overconsolidation ratio is small and the creep coefficient changes greatly, the overconsolidation ratios are set as 1.1, 1.2, 1.4, and 1.8. It takes a long time for the creep coefficient

to stabilize, so the duration of the last stage test should be at least 7 d. The specific scheme for one-dimensional compression tests is shown in Table 1.

5.2.3. Test Results. Figure 8 shows the $s - \lg t$ curve of sample 1. Since the sample soil belongs to normally consolidated soil, it is obvious that the boundary between the primary and secondary consolidations is at about $t_0 = 100$ min. According to Equation (1),

$$C_{\alpha} = \frac{e_0 - e_1}{\lg t_1 - \lg t_0} = \frac{1.469 - 1.437}{\lg 1440 - \lg 100} = 0.0271. \quad (22)$$

Figure 9 shows the $e - \lg t$ curve of soil sample 2, sample 3, sample 4, and sample 5 under the last stage load. From Figure 9, we can learn that the lines of all samples are smooth after 100 min, so t_0 is 100 min. And the duration should be reduced by 100 minutes, so $\Delta t = 7d - 100 \text{ min} = 9980 \text{ min}$. Since each stage of load, except the last stage, lasts for 1 day, the equivalent time should be taken as 1 day. According to Equation (8), the creep coefficient can be calculated.

Taking sample 2 as an example, $t_e = 1d = 1440 \text{ min}$, $t_0 = 100 \text{ min}$, $\Delta t = 9980 \text{ min}$, $e_1 = 1.245$, and $e_2 = 1.228$. So, when OCR is 1.1, the creep coefficient.

$$\begin{aligned} C_{ae} &= \frac{e_1 - e_2}{\lg \left(1 + \frac{\Delta t}{(t_{e1} + t_0)} \right)} \\ &= \frac{1.245 - 1.228}{\lg \left(1 + \frac{9980}{(1440 + 100)} \right)} \\ &\approx 0.0197. \end{aligned} \quad (23)$$

The creep coefficients under each overconsolidation ratio are calculated as shown in Table 2.

The relationship between the creep coefficient and OCR is depicted in Figure 10.

It is found that the relationship between the creep coefficient and overconsolidation ratio can be fitted by an exponential function as follows, and the correlation coefficient R^2 is 0.991.

$$C_{ae} = -0.0031 + 0.2446e^{-2.1184\text{OCR}}. \quad (24)$$

5.3. Calculate the Postconstruction Settlement. As is shown in Figure 11, to facilitate the analysis, it is assumed that p_o is divided into 2 stages that are abruptly applied on the ground

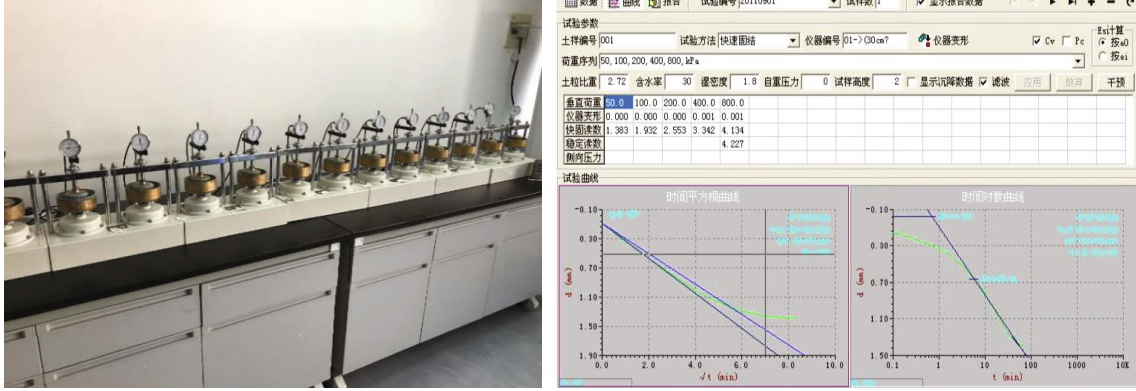


FIGURE 7: Automatic consolidation apparatus.

TABLE 1: Scheme for one-dimensional compression tests.

Sample	OCR	Load path and duration
1	1.0	37.5 kPa (1 d) → 75 kPa (1 d) → 150 kPa (7 d)
2	1.1	37.5 kPa (1 d) → 75 kPa (1 d) → 150 kPa (1 d) → 60.6 kPa (1 d) → 90.9 kPa (1 d) → 136.4 kPa (7 d)
3	1.2	37.5 kPa (1 d) → 75 kPa (1 d) → 150 kPa (1 d) → 55.5 kPa (1 d) → 83.33 kPa (1 d) → 125 kPa (7 d)
4	1.4	37.5 kPa (1 d) → 75 kPa (1 d) → 150 kPa (1 d) → 47.5 kPa (1 d) → 71.3 kPa (1 d) → 107 kPa (7 d)
5	1.8	37.5 kPa (1 d) → 75 kPa (1 d) → 150 kPa (1 d) → 37.0 kPa (1 d) → 55.5 kPa (1 d) → 83.3 kPa (7 d)

Note: the arrow direction in the loading path represents the next level stress. The number before the brackets is the value of the load, and the number in the brackets is the duration of the load. For example, 37.5 kPa (1 d) represents that the load is 37.5 kPa (duration is 1 day).

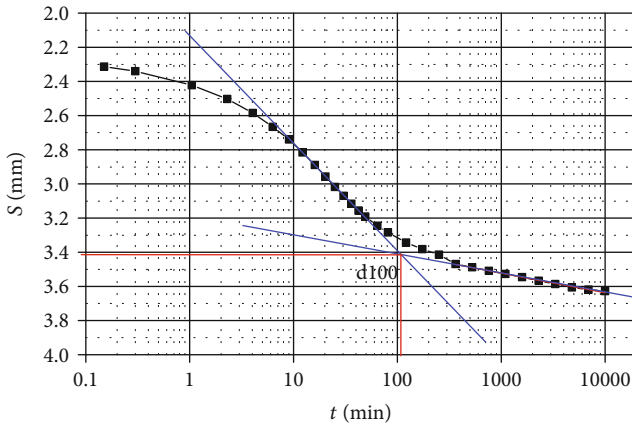


FIGURE 8: $s - \lg t$ curve.

surface. When the final stage is applied up to t_2 , the additional surcharge is replaced with lightweight EPS, and the preload is reduced from p_o to p_m . And then, the pavement is laid and the load is up to p_f .

As is shown in Figure 6, the thickness of hard crust is approximate 1 m. Due to its low compressibility, the post-construction settlement of this layer is negligible. The designed height of embankment fill H is 4.4 m. The unit weight of filling soil γ is taken as 20 kN/m³. According to Equation (13),

$$p_o = \gamma H = 20 \times 4.4 = 88 \text{ kPa.} \quad (25)$$

The designed thickness of pavement structure layer h_s is 0.9 m. And its unit weight γ_s is taken as 23 kN/m³. When the thickness of EPS Δh is taken as 0.5 m, according to Equations (13) and (15), the final load p_f and OLR are calculated below.

$$\begin{aligned} p_f &= \gamma h + \gamma_E \Delta h + \gamma_s h_s \\ &= 20 \times 3 + 0.2 \times 0.5 + 23 \times 0.9 \\ &= 80.47 \text{ kPa,} \end{aligned} \quad (26)$$

$$\text{OLR} = \frac{p_o}{p_f} = \frac{88}{80.47} = 1.093. \quad (27)$$

For the first soil layer, the depth of the middle point $z = 1$ m. Having looking up the additional stress coefficient table, we obtain $\alpha = 1.0$. According to Equations (18), (19), and (21),

$$\begin{aligned} \beta(z) &= \frac{\gamma_i z}{\alpha(\gamma - \gamma_E)\Delta h + (\gamma - \gamma_s)h_s} \\ &= \frac{16 \times 1}{1 \times (20 - 0.3) \times 0.5 + (20 - 23) \times 0.9} \\ &= 1.838, \end{aligned} \quad (28)$$

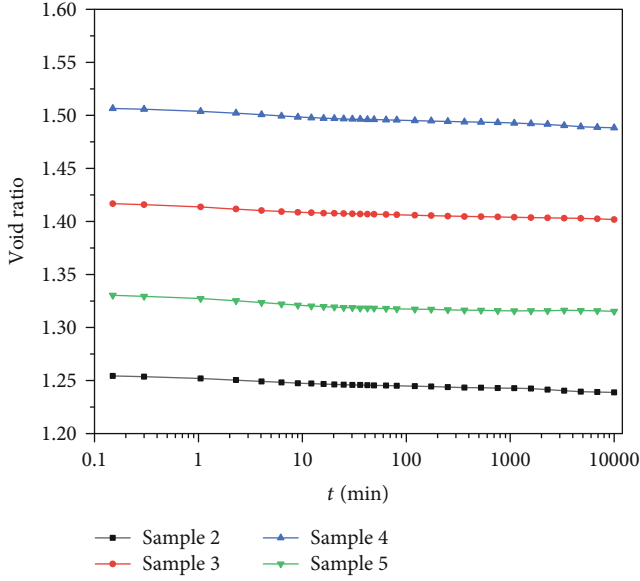
FIGURE 9: $e - \lg t$ curve of overconsolidated soil.

TABLE 2: Creep coefficient under different OCRs.

OCR	C_{ae}
1.0	0.0271
1.1	0.0197
1.2	0.0156
1.4	0.0107
1.8	0.0019

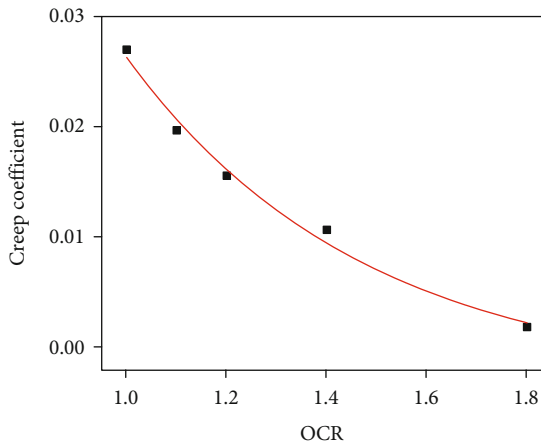


FIGURE 10: The relationship between the creep coefficient and OCR.

$$\begin{aligned}
 \text{OCR} &= 1 + \frac{1}{(1/(\text{OLR} - 1)) + \beta(z)} \\
 &= 1 + \frac{1}{(1/(1.093 - 1)) + 1.838} \\
 &= 1.077,
 \end{aligned} \tag{29}$$

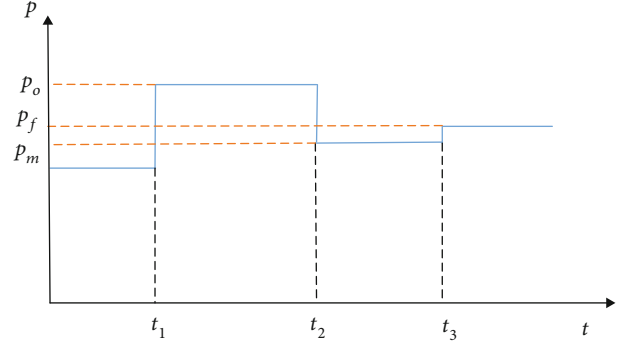


FIGURE 11: Schematic diagram of load-time.

$$C_{ae} = -0.0031 + 0.2446e^{-2.1184\text{OCR}} = 0.0227. \tag{30}$$

In this project, the timing of replacement is the timing of unloading. As the timing of unloading is mainly determined based on the degree of primary consolidation, the timing of replacement could be determined with traditional method. The preloading period lasts 1 year, so $t_1 = 1$ year. The postconstruction settlement at the end of the service period can be calculated according to Equation (19).

$$\begin{aligned}
 s_1 &= \frac{H_1}{1 + e_o} C_{ae} \lg \left(\frac{t_1 + \Delta t}{t_1} \right) \\
 &= \frac{2}{1 + 1.574} \times 0.0227 \lg \left(\frac{1 + 15}{1} \right) \\
 &= 0.021\text{m}.
 \end{aligned} \tag{31}$$

The postconstruction settlement of other soil layers is calculated in turn, and the calculation results are shown in Table 3.

Actually, the degree of consolidation cannot reach 100%, so the calculated postconstruction settlement should be corrected. The correction factor μ can be evaluated according to the degree of consolidation. The correction factor μ is an empirical coefficient. Here, according to existing engineering experience, as is shown in Table 4, we suggest the value of the correction factor should be determined based on the degree of consolidation after preloading. In this project, the degree of consolidation after preloading is about 80%, so the correction coefficient is 1.3.

According to the above calculation process, the postconstruction settlement under different OLRs is calculated as Table 5.

The allowable postconstruction settlement of the general section is 30 cm, which is the requirement in the specification. The longitudinal grade allowable value is 4‰. As is shown in Figure 5, the distance between the general section and Section 3 is 65 m. If the OLR of Section 3 is set as 1.09, the longitudinal grade is $(300 - 141.7)/65000 = 2.4‰ < 4‰$.

As is shown in Figure 12, the settlement curve of the cross-section is distributed in parabolic shape roughly. However, the calculated overloading ratio above is that of the

TABLE 3: Settlement calculation results.

i	H_i	α	β	OCR	C_{ae}	s
1	2(1.0)	1	4.900	1.062	0.0227	0.021
2	3(4.5)	1	7.351	1.054	0.0231	0.032
3	2(7.0)	0.95	18.054	1.034	0.0242	0.023
4	2(9.0)	0.93	23.712	1.028	0.0245	0.023
5	2(11.0)	0.89	30.284	1.024	0.0248	0.023
6	2(13.0)	0.86	37.038	1.020	0.0251	0.023
Sum						0.145

Note: the number in parenthesis is the depth of the middle of each layer.

TABLE 4: Correction factor.

The degree of consolidation	μ
>95%	1.1
85% ~ 95%	1.2
75% ~ 85%	1.3
<75%	1.4

$$[s] = \mu \times s = 1.3 \times 145 = 188.5 \text{ mm.}$$

TABLE 5: Postconstruction settlement under different OLRs.

Δh	OLR	s (mm)	$[s]$ (mm)
0.5	1.09	145	188.5
1.0	1.25	126	163.8
1.5	1.45	109	141.7

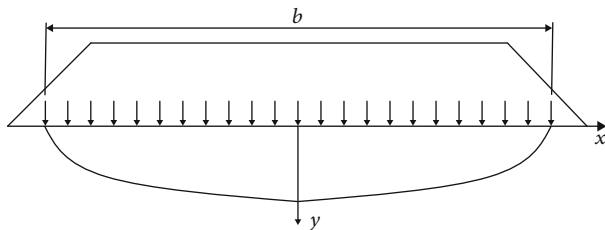


FIGURE 12: Settlement curve of cross-section of embankment.

midpoint of each section. So, the cross-section can be optimized to get more economical. The specific optimization content will be introduced in another article.

6. Conclusions

Based on practical engineering, a new design method for controlling postconstruction settlement is proposed in this paper. Main conclusions are drawn as follows:

- Based on the 1D EVP model and the concept of equivalent time, the functional relationship between the creep coefficient and overconsolidation ratio can be established by fitting one-dimensional compression test data. It is found that the creep coefficient

decreases with the overconsolidation ratio increasing

- The relationship between the overloading ratio and overconsolidation ratio is deduced. In practical engineering, the overconsolidation ratio can be changed by adjusting the overloading ratio, and then, the creep coefficient can be changed to control the post-construction settlement
- The new method can be used for the quantitative design according to different requirements of postconstruction settlement of foundation. The case study shows that the method is operable in engineering

Data Availability

The data used to support the findings of this study are available from the corresponding author upon request.

Conflicts of Interest

The authors declare that there are no conflicts of interest regarding the publication of this paper.

References

- C. C. Ladd, R. Foott, K. Ishihara, F. Schlosser, and H. G. Poulos, "Stress–deformation and strength characteristics," in *State of the Art Report, 9th International Conference on Soil Mechanics and Foundation Engineering*, 1977.
- G. Mesri, "Effects of friction and thickness on long-term consolidation behavior of Osaka Bay Clays¹," *Soils and Foundations*, vol. 49, no. 5, pp. 823–824, 2009.
- Y. Wang, Y. F. Yi, C. H. Li, and J. Q. Han, "Anisotropic fracture and energy characteristics of a Tibet marble exposed to multi-level constant-amplitude (MLCA) cyclic loads: a lab-scale testing," *Engineering Fracture Mechanics*, vol. 244, p. 107550, 2021.
- G. Mesri and B. Vardhanabhuti, "Closure to "secondary compression" by G. Mesri and B. Vardhanabhuti," *Journal of Geotechnical and Geoenvironmental Engineering*, vol. 132, no. 6, pp. 817–818, 2006.
- L. Bjerrum, "Engineering geology of Norwegian normally-consolidated marine clays as related to settlements of buildings," *Géotechnique*, vol. 17, no. 2, pp. 83–118, 1967.
- D. Stolle, P. A. Vermeer, and P. G. Bonnier, "A consolidation model for a creeping clay," *Canadian Geotechnical Journal*, vol. 36, no. 4, pp. 754–759, 1999.
- D. Nash and S. J. Ryde, "Modelling consolidation accelerated by vertical drains in soils subject to creep," *Géotechnique*, vol. 51, no. 3, pp. 257–273, 2001.
- J.-H. Yin, J.-G. Zhu, and J. Graham, "A new elastic viscoplastic model for time-dependent behaviour of normally and over-consolidated clays: theory and verification," *Canadian Geotechnical Journal*, vol. 39, no. 1, pp. 157–173, 2002.
- L. Suklje, "On some controversial effects of the viscous structural resistance of soil," *Acta Geotechnica*, vol. 84, pp. 1–25, 1982.
- R. Bouchard, F. Tavenas, M. Kabbaj, and S. Leroueil, "Stress–strain–strain rate relation for the compressibility of sensitive natural clays," *Géotechnique*, vol. 35, no. 2, pp. 159–180, 1985.

- [11] T. Berre and K. Iversen, "Oedometer test with different specimen heights on a clay exhibiting large secondary compression," *Géotechnique*, vol. 22, no. 1, pp. 53–70, 1972.
- [12] M. Leoni, M. Karstunen, and P. A. Vermeer, "Anisotropic creep model for soft soils," *Géotechnique*, vol. 58, no. 3, pp. 215–226, 2008.
- [13] M. R. Karim, C. T. Gnanendran, S.-C. R. Lo, and J. Mak, "Predicting the long-term performance of a wide embankment on soft soil using an elastic viscoplastic model," *Canadian Geotechnical Journal*, vol. 47, no. 2, pp. 244–257, 2010.
- [14] D. Nash and M. Brown, "Influence of destructuration of soft clay on time-dependent settlements: comparison of some elastic viscoplastic models," *International Journal of Geomechanics*, vol. 15, no. 5, 2015.
- [15] J. H. Yin and J. Graham, "Viscous-elastic-plastic modelling of one-dimensional time-dependent behaviour of clays," *Canadian Geotechnical Journal*, vol. 26, no. 2, pp. 199–209, 1989.
- [16] Y. Wang, B. Zhang, B. Li, and C. H. Li, "A strain-based fatigue damage model for naturally fractured marble subjected to freeze-thaw and uniaxial cyclic loads," *International journal of damage mechanics*, vol. 6, 2021.
- [17] J. H. Yin and J. Graham, "Equivalent times and one-dimensional elastic viscoplastic modelling of time-dependent stress-strain behaviour of clays," *Canadian Geotechnical Journal*, vol. 31, no. 1, pp. 42–52, 1994.
- [18] J. H. Yin, "Non-linear creep of soils in oedometer tests," *Géotechnique*, vol. 49, no. 5, pp. 699–707, 1999.
- [19] W.-Q. Feng and J.-H. Yin, "A new simplified hypothesis b method for calculating consolidation settlements of double soil layers exhibiting creep," *International Journal for Numerical and Analytical Methods in Geomechanics*, vol. 41, no. 6, pp. 899–917, 2017.
- [20] Y. Wang, C. H. Li, and J. Q. Han, "On the effect of stress amplitude on fracture and energy evolution of pre-flawed granite under uniaxial increasing-amplitude fatigue loads," *Engineering Fracture Mechanics*, vol. 240, p. 107366, 2020.
- [21] Y.-Y. Hu, W.-H. Zhou, and Y.-Q. Cai, "Large-strain elastic viscoplastic consolidation analysis of very soft clay layers with vertical drains under preloading," *Canadian Geotechnical Journal*, vol. 51, no. 2, pp. 144–157, 2014.
- [22] S. J. Johnson, "Precompression for improving foundation soil," *Soil Mechanics and Foundation Division Journal*, vol. 96, no. 1, 1970.
- [23] Y. Wang, W. K. Feng, H. J. Wang, C. H. Li, and Z. Q. Hou, "Rock bridge fracturing characteristics in granite induced by freeze-thaw and uniaxial deformation revealed by AE monitoring and post-test CT scanning," *Cold Regions Science and Technology*, vol. 177, p. 103115, 2020.
- [24] A. C. Stamatopoulos and P. C. Kotzais, "Settlement-time predictions in preloading," *Journal of Geotechnical Engineering*, vol. 109, no. 6, pp. 807–820, 1983.
- [25] Y. Y. Hu, "Particular behaviors of quasi-plastic viscous elastic model under consolidation," *International Journal of Geomechanics*, vol. 16, no. 4, pp. 04016003–04016018, 2016.
- [26] G. W. Li, T. Yang, and Z. Z. Yin, "Study of mechanism about surcharge preloading method on the soft ground of highways," *Chinese Journal of Geotechnical Engineering*, vol. 28, no. 7, pp. 896–901, 2006.
- [27] S. Saride, A. J. Puppala, R. Williammee, and S. K. Sirigiripet, "Use of lightweight ECS as a fill material to control approach embankment settlements," *Journal of Materials in Civil Engineering*, vol. 22, no. 6, pp. 607–617, 2010.
- [28] S. V. Deijk, "A review of the Netherlands approach to the use of foam concrete in Holland and at canary wharf," *Concrete*, vol. 25, no. 5, pp. 49–54, 1991.
- [29] D. J. Thompsett, A. Walker, R. J. Radley, and B. M. Grieveson, "Design and construction of expanded polystyrene embankments: practical design methods as used in the United Kingdom," *Construction and Building Materials*, vol. 9, no. 6, pp. 403–411, 1995.
- [30] Y. H. Chen, C. G. Shi, D. H. Cao, H. J. Ying, and X. Q. Wang, "Control of post-construction settlement by replacing subgrade with foamed cement banking," *Chinese Journal of Geotechnical Engineering*, vol. 33, no. 12, pp. 1854–1862, 2011.
- [31] Q. Z. Jiang, Z. P. Chen, J. B. Wang, and J. F. Liu, "the method of determining the thickness of foamed cement banking," *Highway*, vol. 4, pp. 84–88, 2019.
- [32] C. B. Crawford, "Interpretation of the consolidation test," *Soil Mechanics and Foundation Division Journal*, vol. 90, no. 5, pp. 87–102, 1964.
- [33] Z. Y. Liu and Z. L. Zheng, "Estimation of reference time in EVP model," *Chinese Journal of Underground Space and Engineering*, vol. S1, no. 14, pp. 134–139, 2018.

Research Article

Research on Deformation Mechanisms of a High Geostress Soft Rock Roadway and Double-Shell Grouting Technology

Fengnian Wang ^{1,2}, Shizhuang Chen,³ Pan Gao,^{1,2} Zhibiao Guo,^{1,2} and Zhigang Tao ^{1,2}

¹State Key Laboratory for Geomechanics and Deep Underground Engineering, China University of Mining and Technology (Beijing), Beijing 100083, China

²School of Mechanics and Civil Engineering, China University of Mining and Technology (Beijing), Beijing 100083, China

³Research Institute of Geotechnical Engineering, Hohai University, Nanjing 210098, China

Correspondence should be addressed to Zhigang Tao; taozhigang@263.net

Received 3 September 2021; Revised 29 September 2021; Accepted 6 October 2021; Published 31 October 2021

Academic Editor: Yu Wang

Copyright © 2021 Fengnian Wang et al. This is an open access article distributed under the Creative Commons Attribution License, which permits unrestricted use, distribution, and reproduction in any medium, provided the original work is properly cited.

In this study, the deformation characteristics and mechanical properties of coal and rock mass in the S2N5 working face of the Xiaokang coal mine are analyzed to address the problem of large deformation of soft rocks with high in situ stress surrounding roadways. Through a newly developed grouting pipe, a double-shell grouting technology, consisting of low-pressure grouting and high-pressure split grouting, is proposed for the Xiaokang coal mine. In addition, the effect of grouting is evaluated by borehole peeping and deformation monitoring. The results show that the double-shell grouting technology can effectively improve the overall mechanical properties of the surrounding coal and rock mass, preventing the large deformation and failure of the roadway. This technology can be useful when analyzing and preventing large deformation of soft rock roadways.

1. Introduction

Controlling the soft rock strata surrounding roadways is important when conducting mining activities [1, 2]. To control the large deformation of soft rock roadways, it has become necessary to support them with bolt/cable + steel mesh + shotcrete technology [3, 4]. However, bolts and anchor cables could not play a full role because of insufficient anchoring force in soft rock, and grouting reinforcement is an effective method to control the deformation of roadway surrounding rock [5, 6]. Grouting reinforcement technology is an indispensable part of the support design for tunnels with high ground stress and complex geological conditions [7]. Grouting reinforcement technology can effectively improve the mechanical properties and integrity of broken surrounding rock. At the same time, grouting reinforcement can prevent the surrounding rock from becoming unstable and also prevent its damage and failure during mining [8]. There have been many studies on the

mechanism and control of large deformation of roadways in soft rock with high in situ stress.

Li et al. analyzed the failure mechanism of a large span intersection through numerical simulation and proposed a double-bolt control technology to effectively control the deformation of the surrounding rock in roadways [9]. Li et al. proposed a coupling support technology consisting of a high-toughness sealing layer + hollow grouting cables + full-length anchoring bolts in deep boreholes to effectively control the large deformation of roadways [10]. Fangtian et al. implemented a whole section anchor-grouting reinforcement technology in a coal mine based on a double-shell anchor-grouting reinforcement mechanism to control the deformation of the rock surrounding a roadway [11]. Wang et al. put forward the concept of “high strength, integrity, and decompression” based on the large deformation mechanism of soft rock surrounding a roadway and developed a confined concrete (CC) support system, which was verified by field tests [12]. Chen et al. proposed a whole

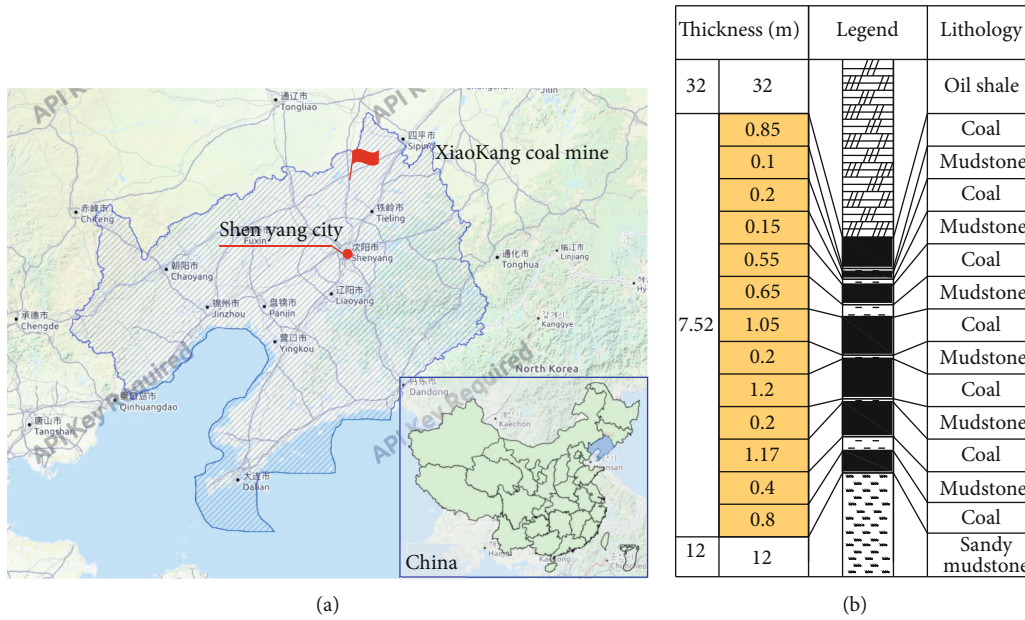


FIGURE 1: General situation of the Xiaokang coal mine. (a) Geographical location of the Xiaokang coal mine. (b) Coal seam of S2N5.

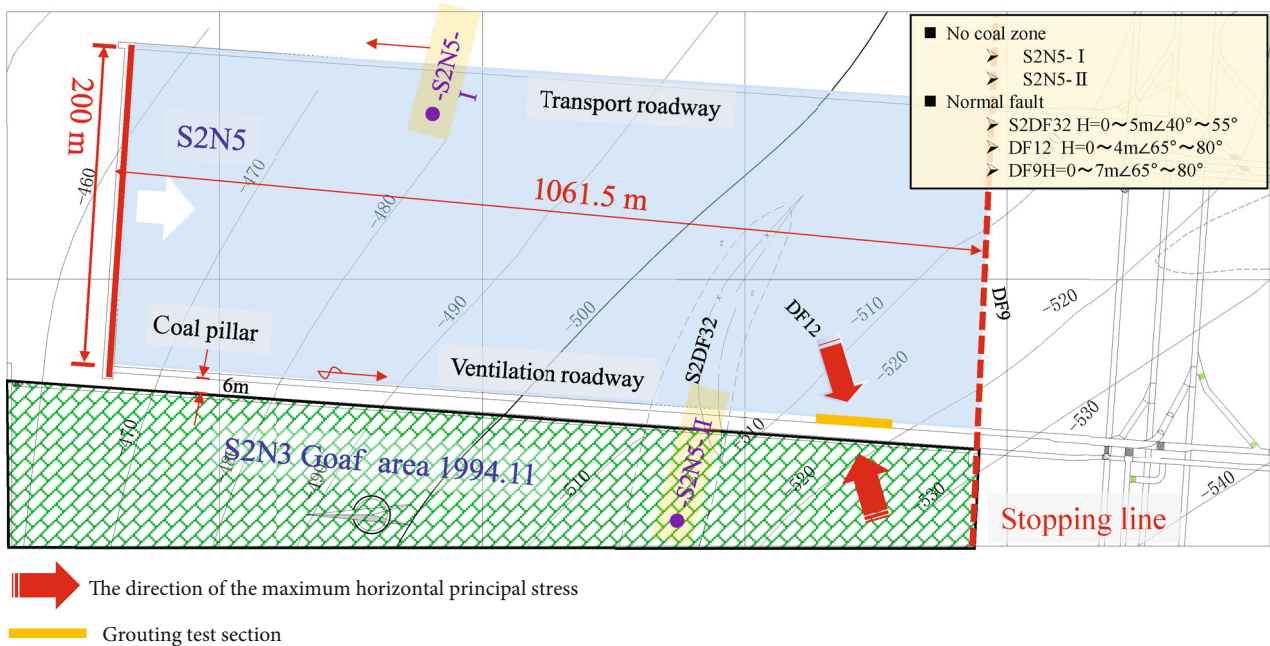


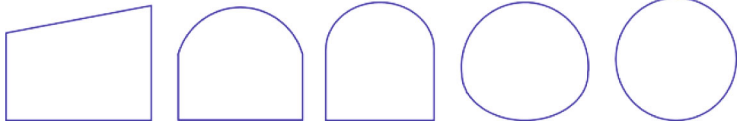


FIGURE 2: Basic situation of the S2N5 working face.

section double arch synergy reinforcement technology of “sprayed concrete + grouting + anchor bolt + anchor cable” to control the deformation of inclined shaft in soft surrounding rock [13]. Zhang et al. proposed a grouting material with low cost and high density for the reinforcement of large-scale floor cracks; the optimal proportion of constituents for the new grouting material (including 1% foaming agent) was 40% of cement, 30% of clay, and 30% of fly ash [14]. Yang et al. put forward a new grouting method based on the CFD-DEM coupling principle; one typical subgrade section in the Shanghai–Nanjing intercity railway was used

to simulate the grouting process and the diffusion mechanism of the slurry at the microlevel [15].

This study mainly analyzes the mechanism of large deformation occurring in roadways surrounded by soft rock with high geostress and the reinforcement of soft broken coal rock mass using inorganic grouting material. Modified coal and rock mass can be effectively reinforced in a roadway surrounded by rock using double-shell grouting technology (low-pressure grouting in shallow surrounding rock and high-pressure split grouting technology in deep surrounding rock) to enhance the strength and the deformation resistance

TABLE 1: Development of the support system in the Xiaokang coal mine.

Supporting design	Parameters				
Section	 Trapezoid → Three-center arch → Semicircle arch → Horseshoe arch → Circular				
Steel arch	 25U-shape steel arch → 29U-shape steel arch → 36U-shape steel arch				
Bolts and anchor cables	 Screw steel bolt → Equal-strength rebar bolt → Anchor cable (17.8 mm → 21.8 mm → 21.6 mm)				

of the surrounding rock under mining activity. The field application of double-shell grouting technology is achieved using a newly developed grouting conduit and good results are obtained.

2. Field Overview

2.1. Engineering Background. The Xiaokang coal mine is located in Kangping County, Shenyang City, Liaoning Province, China, as shown in Figure 1(a). It is 40 km away from Shenyang City. The mine area is 28.99 m², and the output is 270 Wt/a. There are no hydrological characteristics of large rivers in the mine area. The structure of the Xiaokang coal mine is influenced by the second subsidence zone of the Neocathaysian system and the Yinshan zonal structural zone of the Tianshan Mountains, where tension-torsion normal faults are well-developed. The sliding structure of the mine has multilevel sliding surfaces and small faults in the oil shale on the roof of the coal seam. In addition, the widespread development of gravity sliding structures in the Xiaokang coal mine has destroyed the integrity of the coal roof and increased the mine pressure.

The maximum buried depth of the coal seam in the S2N5 working face is 585 m, and the coal seam inclination is generally 3°~6°. The length of the mining area is 1061.5 m, and the width is 200 m as shown in Figure 2. The average thickness of the coal seam is about 7.52 m as shown in Figure 1(b). The adjacent working face S2N3 was mined in 1994 with a small pillar 6 m away from the S2N5 area as shown in Figure 2. Affected by the S2DF32H fault, the roadway deformation in the working face is obvious and the stability of the roadway is difficult to control. Therefore, near the DF12 fault, grouting reinforcement is proposed to control the deformation of S2N5's ventilation roadway.

2.2. Original Support Design of the S2N5 Tunnel. The problem of implementing an adequate support system has been restricting the development of the Xiaokang coal mine [16]. A series of reforms have been carried out on the selection of an appropriate roadway support section, the supporting material of the arch frame, and the anchor cable as shown in Table 1.

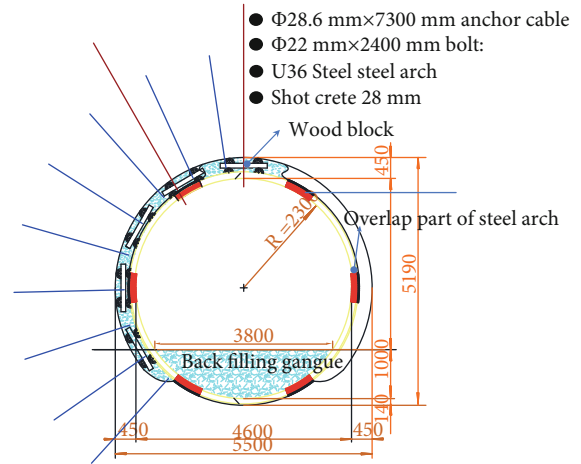


FIGURE 3: Support design of the ventilation roadway of S2N5.

It can be seen from Table 1 that the supporting methods selected for the Xiaokang coal mine have become increasingly more complex and that the support strength has gotten increasingly higher. At present, the roadway in the Xiaokang coal mine has adopted a compound lining structure. The initial support consists of bolts (2.4 m) and anchor cables (7.3 m). The row spacing between bolts is 800 mm × 600 mm and anchor cables is 1600 mm × 1200 mm. The diameter of mining roadway in the S2N5 working face is 4.6 m. Comprehensive mechanized caving mining technology is adopted with a mining height of 3.8 m, and the height of caving mining is 3.72 m. The secondary lining is composed of steel arch (U36) and shotcrete (28 mm) as shown in Figure 3. However, the mining roadway, which has had a long service period and a complex engineering-geological environment, still needs to be improved to achieve normal production of the mine.

3. Failure Characteristics and Mechanism of the Surrounding Rock

3.1. Failure Characteristics of the Surrounding Rock. Observations of the deformation of the rock surrounding the roadway at the S2N5 working face show that the influence range

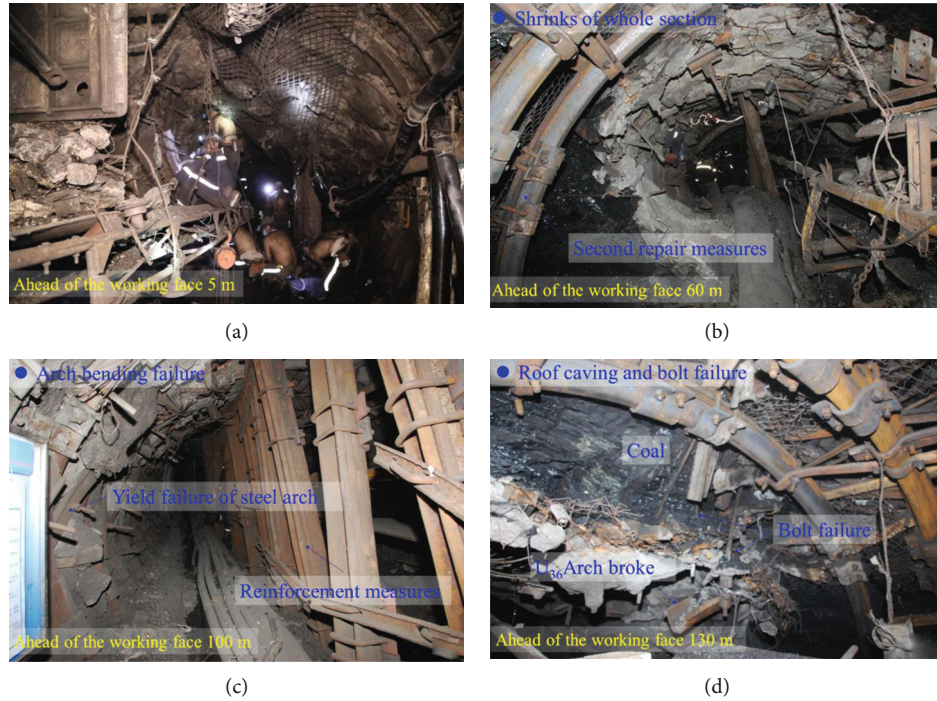


FIGURE 4: Failure phenomenon of the S2N5 working face.

of the advance working face is up to 200 m. The zoning statistics of the influence area of the working face are as follows.

- (1) Abutment pressure affects damage zone I (0-20 m). The roadway is seriously affected by the mining pressure of the working face. Under mining pressure, the roadway section shrinks overall, and the bottom heave phenomenon is particularly obvious. The arch frame of the roadway needed to be dismantled and repaired twice to achieve normal production as shown in Figure 4(a)
- (2) Abutment pressure affects damage zone II (20-75 m). The roadway shows the rheological properties of soft rock, and the support structure shrinks overall. The plastic zone is far beyond the control depth of the support structure as shown in Figure 4(b).
- (3) Abutment pressure affects damage zone III (75-120 m). The pressure around the roadway causes the support structure to shrink overall under pressure. Because the support structure does not have certain pressure relief characteristics, the U36 arch frame presents different shapes of yielding states, such as folding, bending, and falling off
- (4) Abutment pressure affects the IV area (120-200 m). As the strength of surrounding rock is not coupled with the strength of support body, the failure of roadway starts from a certain point, which is mainly manifested in the form of falling blocks of shotcrete, bending deformation of the steel arch, and the failure of the anchors in the shallow surrounding rock

3.2. Failure Mechanism of the Surrounding Rock in S2N5

3.2.1. Low Strength of the Surrounding Rock. The roof of the roadway in the S2N5 working face is mainly composed of coal and shale, and the floor is composed of sandy mudstone. In the laboratory, the strengths of the roof, floor, and coal were tested using the rock strength test system shown in Figure 5. The strength parameters are shown in Table 2. The strengths of the coal, shale, and sandy mudstone are 14.20 MPa, 19.70 MPa, and 17.71 MPa, respectively. The surrounding rock belongs to the typical three-soft coal seam, which has low compressive strength, poor stability, and poor load-bearing capacity [17–20]. In the process of coal mining, areas of stress expansion and collapse of the surrounding rock easily occur due to the concentrated stress in the surrounding rock. The low strength of the rock mass surrounding the roadway is the main cause of the large deformation of the roadway.

3.2.2. Clay Minerals and Microstructure. The rock mineral content and the clay mineral relative content were tested using an X-ray diffractometer, and the results are shown in Tables 3 and 4:

It can be seen from Table 3 that the clay content of the bottom sandy mudstone is 45.7%, and the illite-smectite layer-mixed clay mineral is the main component with a content of 58%, followed by kaolinite (19%) and illite (15%). The shale clay composition of the roof is 39.5%, and the main constituents of the clay are the illite-smectite layer-mixed content (58%) followed by kaolinite (30%) and illite (12%). Both the imonite mixed layer and the kaolinite show strong hydrophilicity and easily soften and disintegrate in contact with water. After the excavation of the working face,

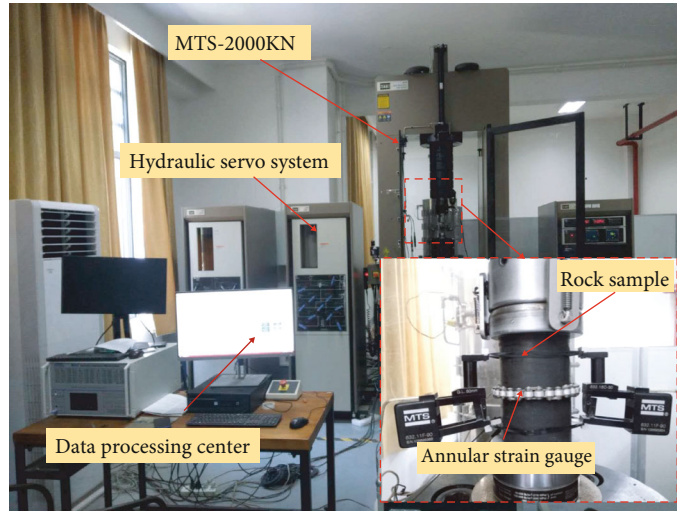


FIGURE 5: Rock strength testing system.

TABLE 2: Physical and mechanical parameters of the surrounding rock.

No.	Lithology	Tensile strength (MPa)	Friction angle (°)	Poisson's ratio	Cohesion (MPa)	Compressive strength (MPa)	Elastic modulus (GPa)
1	Coal	0.64	47.20	0.11	2.35	14.20	5.8×10^3
2	Shale	0.79	33.60	0.12	4.28	19.70	6.3×10^3
3	Mudstone	1.32	47.70	0.18	1.52	17.71	8.8×10^3

TABLE 3: Mineral content of the surrounding rock.

Lithology	Mineral content (%)								
	Quartz	Feldspar	Anorthose	Calcite	Dolomite	Siderite	Pyrite	Kaolinite	Clay mineral
Mudstone	47.5	1.8	5.0	/	/	/	/	/	45.7
Shale	29.3	0.8	2.6	12.1	/	14.7	1.0	/	39.5

TABLE 4: Clay mineral relative content of the surrounding rock.

Lithology	Clay mineral relative content (%)						Mixed layer than (%)	
	S	I/S	It	Kao	C	C/S	I/S	C/S
Mudstone	/	58	15	19	8	/	40	/
Shale	/	58	12	30	/	/	50	/

S: smectite; I/S: illite-smectite layer-mixed; It: illite; K: kaolinite; C: chlorite; C/S: chlorite -smectite layer-mixed.

the surrounding rock encounters water and wind, causing significant expansion in the soft rock, which leads to the destruction of the soft rock. This is another cause of the floor heave and roof failure.

SEM (scanning electron microscopy) shows that the shale surface is smoother after magnification of 36 times perpendicular to the bedding direction. After magnification by 27740 times, it is found that the shale surface has curved flaky illite and imonite mixed layer, clay minerals, fine clastic particles, and microholes as shown in Figure 6(a). The paral-

lel bedding direction shows the directional distribution of thin-bedded illite and imonite mixed layers, and there are some biofossil fragments and micropores in the shale, which is also one of the reasons for the high oil content of the shale, as shown in Figure 6(b). Extremely well-developed horizontal and vertical cracks penetrate the coal body as shown in Figure 6(c), which is the main reason for the low strength of the coal body. The mudstone has a thin layer with a flocculent structure, as shown in Figure 6(d). Due to its high clay content, the structure of mudstone is relatively loose.

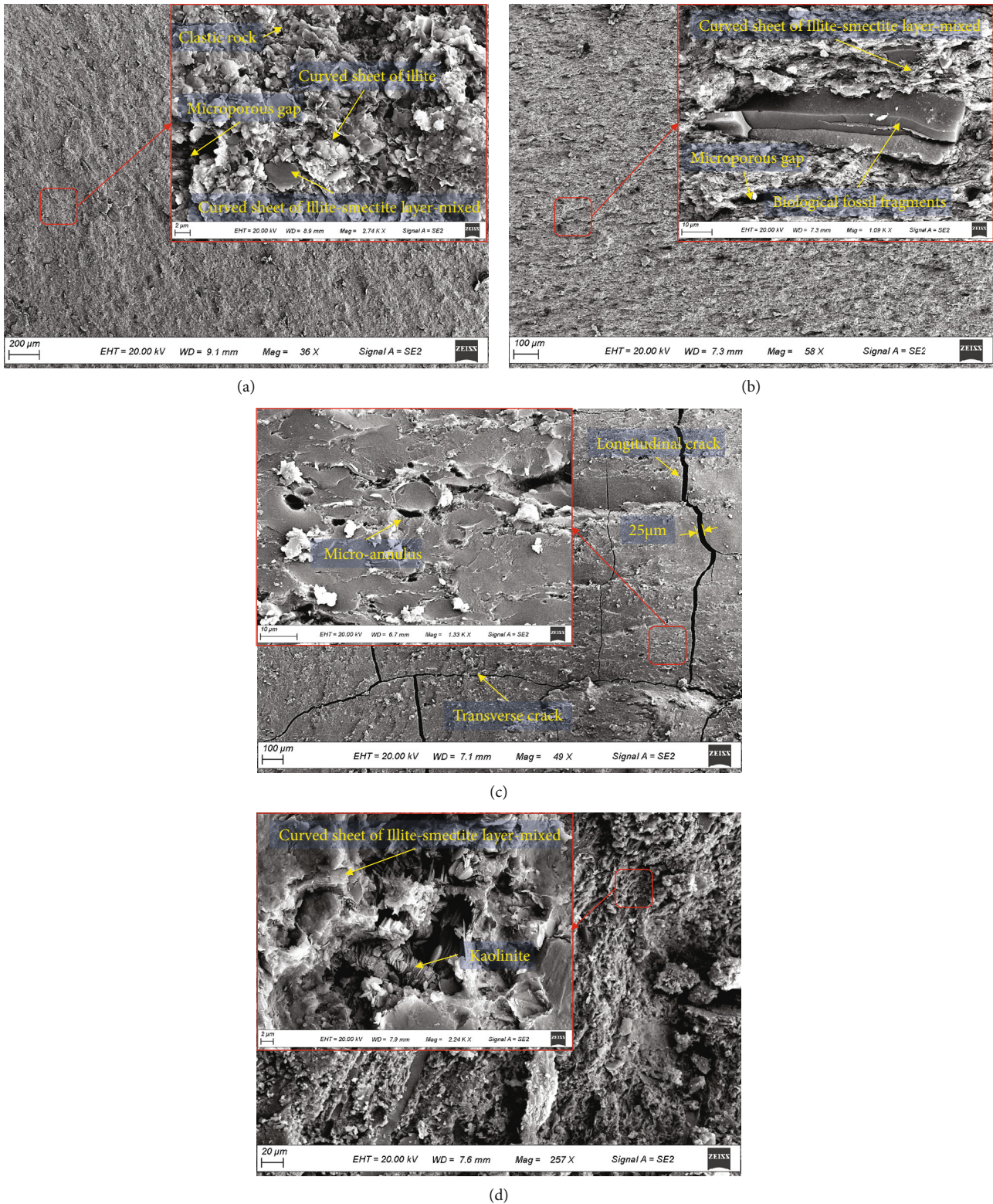


FIGURE 6: SEM of surrounding rock. (a, b) SEM of mudstone. (c, d) SEM of shale.

3.2.3. *Measurement of the Geostress.* We conducted on-site measurements of the geostress on the working face. The results show that the S2 mining area is dominated by horizontal tectonic stress, with a maximum value of 22.76 MPa, which is 1.22 times the self-weight stress. The

direction of the maximum horizontal principal stress is east-west (EW). The angle between the direction of the roadway and the maximum stress is greater than 70°, which is also one of the reasons for the large deformation of the roadway.

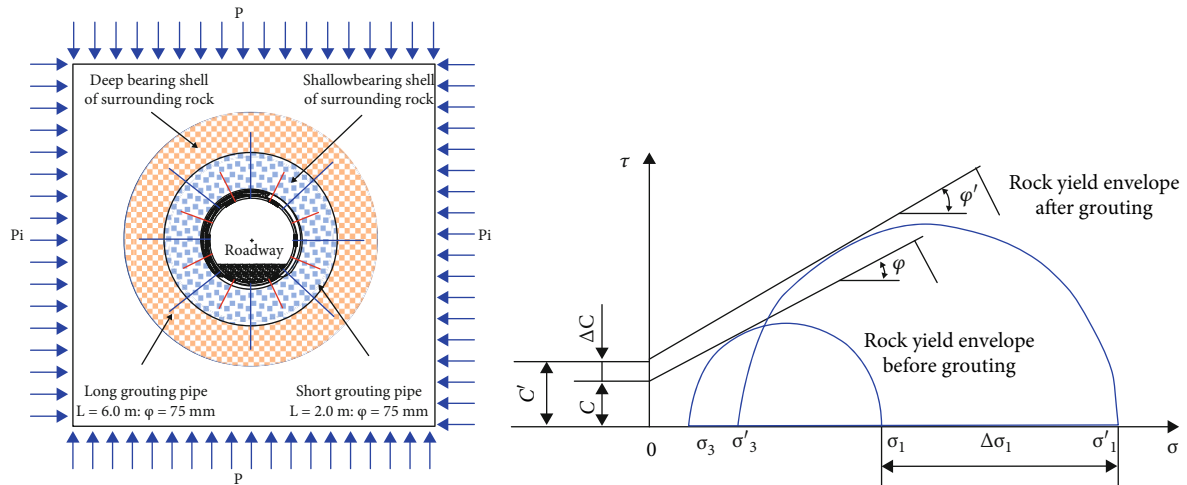


FIGURE 7: Double-shell grouting reinforcement mechanism.

TABLE 5: Physical and mechanical properties of grouting materials.

1	Initial grouting time		2018.6.20	Water: solid		0.52 : 1		
Cement (92%)		Cement and admixtures						
2	P.O 52.5	Water reducing agent	Bentonite	Accelerator	Expansive agent	Other		
		2.0	0.4	0.2	5.0	0.4		
Physical and mechanical properties of grouting materials								
3	Liquid viscosity	Liquid time	Softening plasticity time	Hardening plastic time	Final setting time	Inflation rate	Bulk density	Compressive strength
	/s			/min		%	g/cm ³	MPa
	37.26	40	20	20	70	0.43	1.75	>30

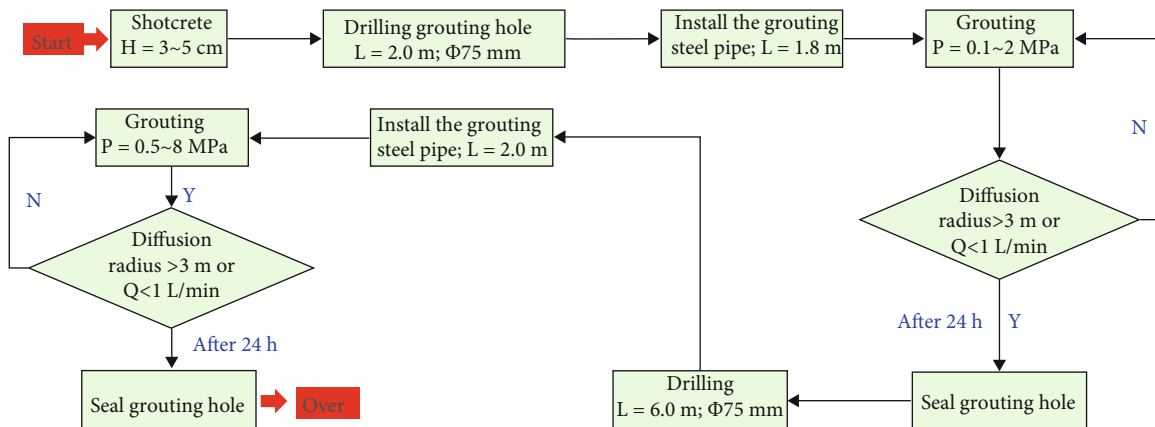


FIGURE 8: Grouting process and control standards.

The analysis above shows that the strength values of the surrounding rock are all lower than 20 MPa, which shows that it is a typical soft rock. Although the maximum horizontal principal stress is only 12.05 MPa, the strength-to-stress ratio is about 3, and the coal and rock mass are in a state of high in situ stress. However, due to the high content

of clay in the roof and bottom and the developmental cracks, which become the main channels to conduct water under certain conditions, the strength of the surrounding rock is greatly reduced after encountering water. In addition, in the original support plan, although the anchor cable of φ28.6 was used, the initial pretightening force was only

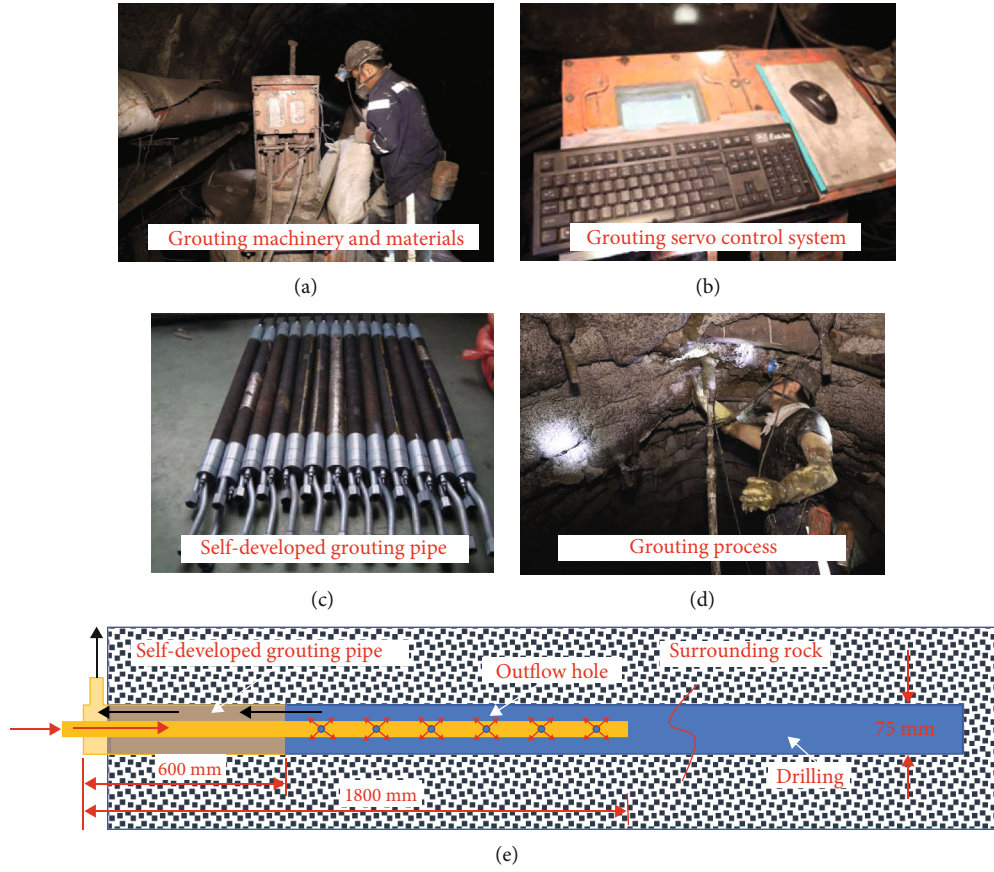


FIGURE 9: On-site grouting process and a newly developed grouting pipe installation method.

175 kN. The tension test of the anchor cable shows that the pretightening force is only 150 kN, but the anchoring force can reach 380 kN after field testing. This shows that the anchor cable with the low pretension cannot mobilize the stress of the deep surrounding rock. The short anchor bolt and the long anchor cable with low pretension cannot form a stress overlap, and their stress-bearing arch strengths are low and not enough to resist the strong mining activity. The U36 circular arch is used as the last line of defense against the deformation of the soft rock roadway. Its rigidity is high, but it cannot be adapted to the rheological characteristics of the soft rock. The rheological properties of the bottom argillaceous siltstone after encountering water and the nonuniformly distributed load under the deviator stress caused by roof engineering leading to obvious asymmetric deformation, finally causing the metal shed to be destroyed first from the bottom heave and then successively form severe shrinkage and deformation, resulting in complete instability.

4. Double-Shell Grouting Technology

Grouting and reinforcement of broken coal and rock mass can improve the mechanical properties of the weak structural surface and increase the cohesive force and internal friction angle of the broken coal and rock mass [21]. The cementation effect of the grouting material can increase the internal relative displacement resistance between the discon-

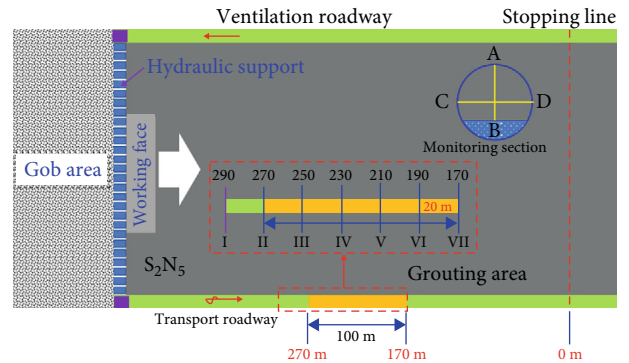


FIGURE 10: Overview of the testing site.

tinuous blocks of broken coal and rock mass, thereby improving the overall stability and integrity of the surrounding rock [22]. In addition, grouting materials can penetrate the fissures of the surrounding rock to form a skeleton bearing structure, improve the residual strength of the crushed surrounding rock, and give full play to the self-stability of the coal and rock mass [23].

According to the engineering geological conditions of Xiaokang Coal Mine, the concept of double-shell grouting is proposed, namely, shallow low-pressure grouting and deep high-pressure split grouting, as shown in Figure 7(a).

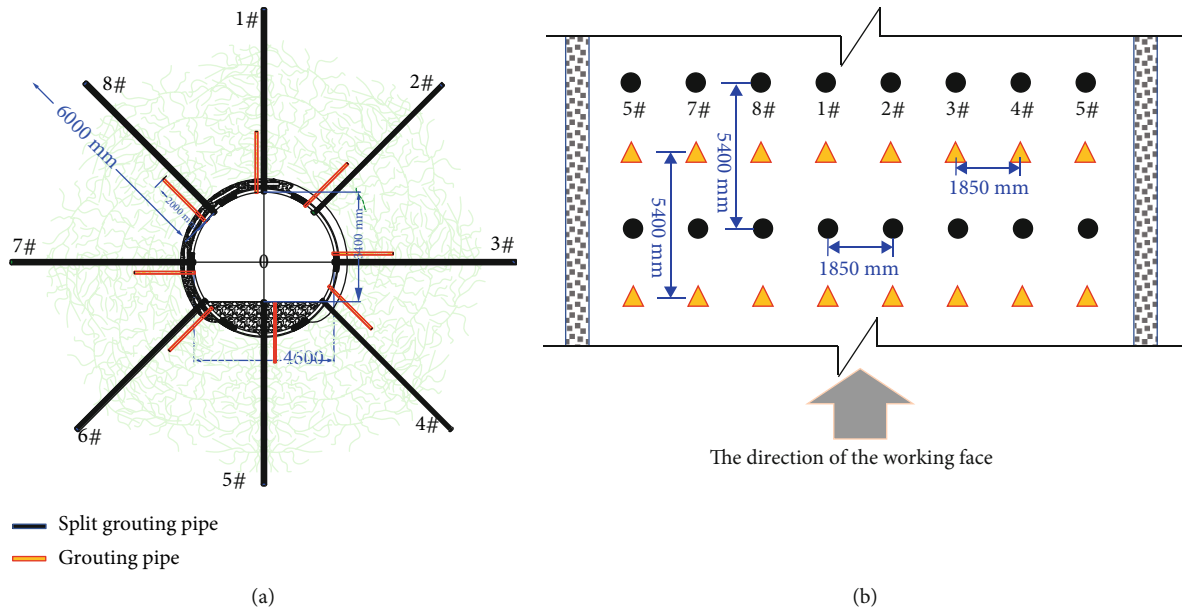


FIGURE 11: Support design of grouting reinforcement.

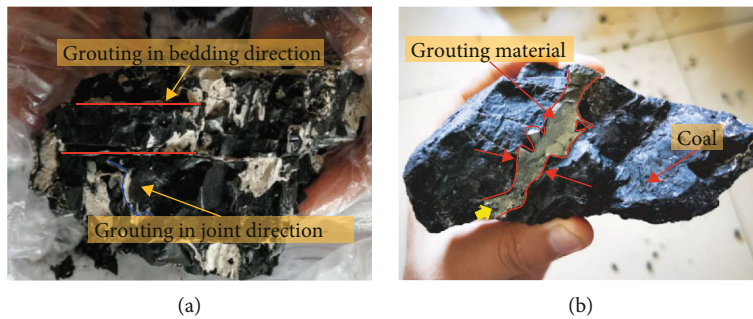


FIGURE 12: Sample of the grouting block. (a) Sample of the shallow coal. (b) Sample of the deep coal.

In addition, considering that the length of the initial supporting anchor cable is 7.3 m, it is hoped that the internal grouting can be carried out on the surrounding rock within its range without damaging the anchor section of the anchor cable. The grouting is carried out as follows:

- (1) A large amount of grouting material is poured into the coal body so that a harder thin plate is formed in the shallow coal body to resist the deformation of the surrounding rock. At the same time, it also provides an isolation layer for the high-pressure fracturing grouting
- (2) Compared with the shallow surrounding rock, the deep surrounding rock has fewer fissure channels. High-pressure fracturing grouting technology can inject the grouting material into the surrounding rock along its structural plane to improve the cohesion (c) and friction angle (φ) of the coal mass as shown in Figure 7(b). At the same time, a fissure framework is formed inside the coal body to further enhance the coal body's ability to resist deformation

Grouting technology is widely used in surrounding rock reinforcement [24]. Cement materials have the characteristics of low cost and good performance and are commonly used to manage soft rock roadways in coal mines [25]. In the Xiaokang coal mine, the deformation of the soft rock roadway before mining was about 300 mm, which was able to stay steady. In addition, a large number of cracks were detected in the surrounding rock by borehole visitation. Therefore, P.O52.5 concrete was chosen as the grouting material. In order to fill the cracks in the coal and rock mass, an expansion agent which accounts for about 0.4% of the total composition is specially added. The volume expansion rate of the grouting material is about 0.43%, the final setting time is 70 minutes, and the final strength is not less than 30 MPa. The mechanical properties of the grouting materials are shown in Table 5.

4.1. Low-Pressure Grouting Technology. To prevent the grouting material from leaking, the surrounding rock was sprayed with 3 ~ 5 cm of thick concrete. Then, holes with a diameter of 75 mm and a depth of 2.0 m and 8.0 m were

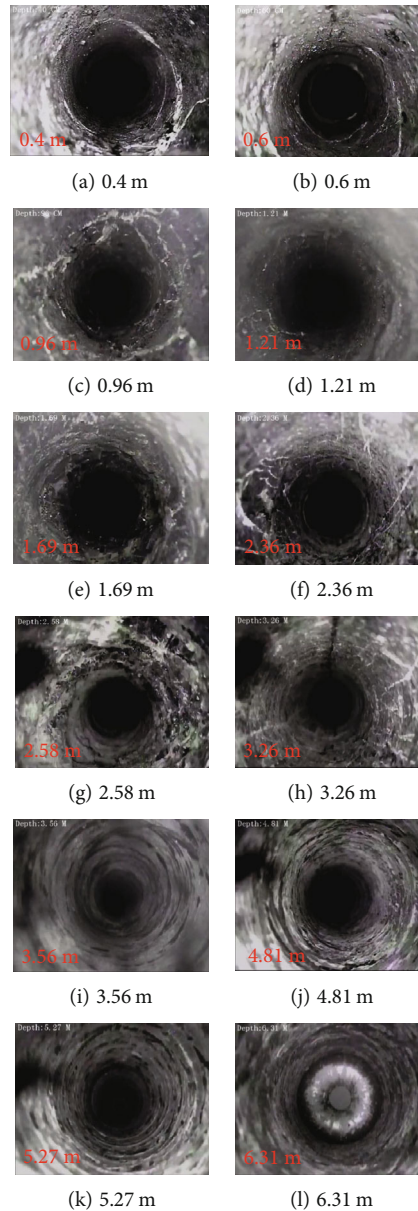


FIGURE 13: Results of the borehole observations.

drilled in the shallow and deep surrounding rock. The detailed grouting process is shown in Figure 8. The on-site grouting process is shown in Figures 9(a), 9(b), and 9(d). A newly developed grouting pipe with a length of 1.8 m and an outer diameter of 75 mm as shown in Figure 9(c) was installed as shown in Figure 9(e).

4.2. High-Pressure Split Grouting Technology. Split grouting technology uses high-pressure grouting pumps to split the surrounding rock along the bedding or weak surfaces. By injecting thick slurry into the fissures, the surrounding rock is compacted and the strength of the surrounding rock is increased. The grouting flow rate should be kept at 20L/min as much as possible. If the flow rate is too small, it will cause the slurry to condense in the equipment and pipelines, and the flow rate will be prone to slurry leakage.

Since the grout enters the initial setting state in about 40 minutes, the grouting time of each barrel of grout should not exceed 40 minutes. The detailed grouting process is shown in Figure 8.

5. Field Test and Evaluation of the Controlling Effect

5.1. Selection of the Testing Site. The grouting test was carried out on 100 m (270 m~170 m) of the S2N5 transport roadway. Monitoring points were created at 20 m intervals and numbered II-VII in sequence. I monitoring point was used for data analysis and comparison as shown in Figure 10. In the grouting test section, the deformation of the roadway between the roof and floor (AB) and that of the two sides of the roadway were measured (CD).

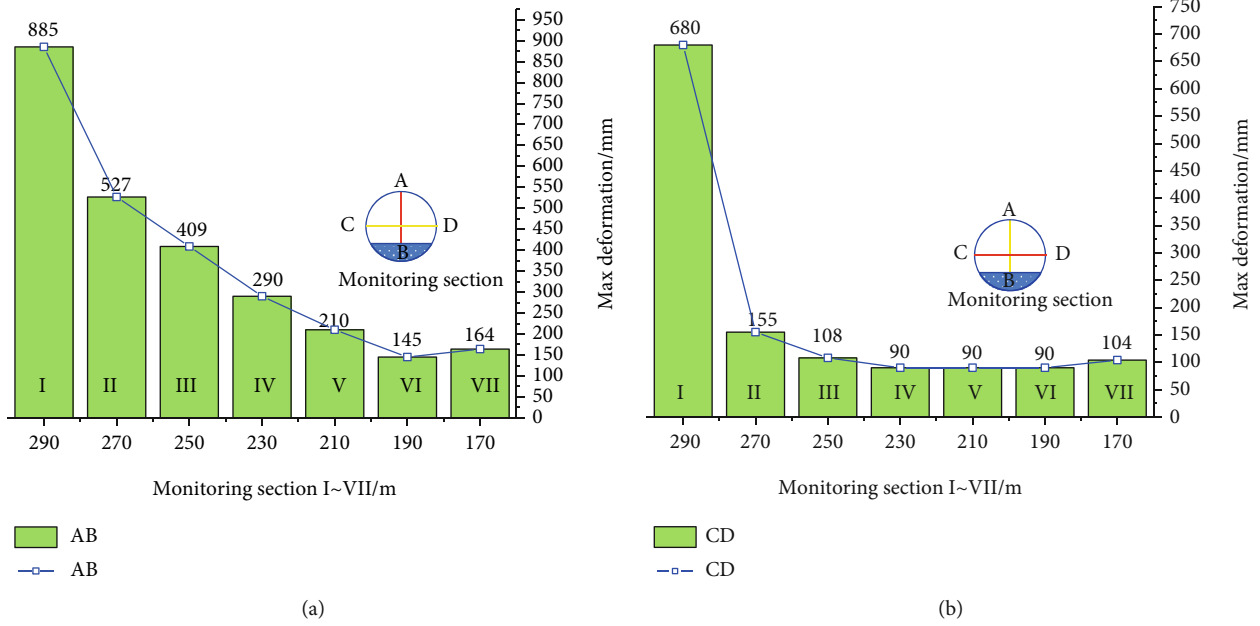


FIGURE 14: Statistics of the maximum deformation of the test section. (a) Displacement between the roof and floor. (b) Displacement of the two sides of the roadway.

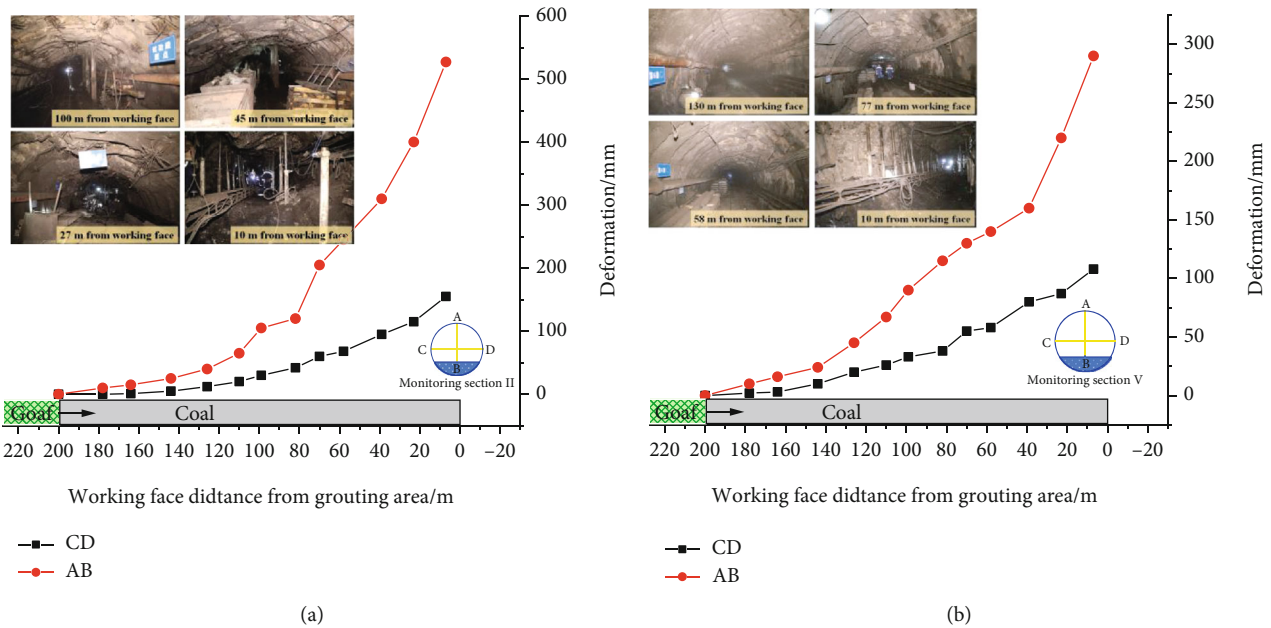


FIGURE 15: Statistics of the maximum deformation of the test section. (a) Displacement between the roof and floor. (b) Displacement of the two sides of the roadway.

5.2. *Grouting Reinforcement Support Design.* Considering the original roadway support form in the Xiaokang coal mine, a double-shell grouting reinforcement scheme is proposed as shown in Figure 11(a). The alternate arrangement of the shallow and deep drilling holes is shown in Figure 11(b).

5.3. *Evaluation of Grouting*

5.3.1. *Grouting Block Analysis.* To evaluate the effect of grouting, rock samples were evaluated. The shallow coal seam was

relatively broken, and the grouting material could penetrate the bedding and joints of the coal under the action of lower pressure as shown in Figure 12(a). The grouting material had a high bonding force to the fracture surface, which improved the deformation rigidity of the fractured coal and rock mass structure so that the integrity of the coal mass was improved. The deep coal seam was relatively complete, and the grouting material could expand the microcracks in the coal under the action of high-pressure splitting. Through the

squeezing action, the c and φ of the coal body were enhanced as shown in Figure 12(b).

5.3.2. Borehole Observations. An electronic borehole observation instrument, which is an effective method for grouting evaluation, was used to observe the grouting borehole [26–29]. Observations showed that the shallow surrounding rock fissures were relatively developed and that the grouting material could fully fill the coal seam fissures to improve the integrity of the coal seam as shown in Figures 13(a)–13(e). Although there were fewer fissures in the deep surrounding rock, the internal structural surface of the coal seam was still filled under the action of the high-pressure fracturing grouting as shown in Figures 13(f)–13(l).

5.3.3. Deformation Curve of the Surrounding Rock. The statistics of the maximum deformation of the surrounding rock in the grouting test area are shown in Figure 14, and the maximum displacement between the roof and floor is shown in Figure 14(a). After grouting, the displacement between the roof and floor decreased from a maximum of 885 mm to 145 mm, which is a decrease of 83.5%. The deformation of the two sides of the roadway decreased from a maximum of 680 mm to 90 mm, which is a decrease of 86.8%, as shown in Figure 14(b). Sections II and V were selected for detailed analysis, as shown in Figures 15(a) and 15(b). The results show that the deformation of the mining roadway is obviously reduced and normal production can be maintained after grouting. The influence of the advanced abutment pressure was reduced to about 150 m. The roadway deformation was still dominated by roof subsidence, but the deformation was significantly reduced.

6. Conclusion

- (1) The S2N5 working face is a typical three-soft coal seam, which shows obvious rheological characteristics under the action of high geostress. The original support structure could not control the deformation of the surrounding rock, resulting in the failure of supporting structures
- (2) The pretension of the bolts and anchor cables was too low to consolidate the broken surrounding rock and form a stress-bearing structure. The superposition of the advanced abutment pressure and the geostress is the dynamic source of the large deformation in the S2N5 working face
- (3) Grouting reinforcement can effectively improve the value of cohesion (c), friction angle (φ), and strength of the broken surrounding rock (σ_1 and σ_3). The surrounding rock bonded by grouting materials and bolts and anchor cables forms a stress-bearing structure that prevents large deformation from occurring in the roadway
- (4) Double-shell grouting technology can effectively improve the overall mechanical properties of the surrounding coal and rock mass and prevent the large deformation and failure of the roadway using a newly developed grouting pipe made in this study

Data Availability

All the data, models, or codes that support the findings of this study are available from the corresponding author upon reasonable request.

Conflicts of Interest

The authors declare that they have no conflicts of interest.

Acknowledgments

The authors gratefully acknowledge the funding provided by the National Natural Science Foundation of China (41941018).

References

- [1] M. C. He, H. P. Xie, S. P. Peng, and Y. D. Jiang, "Study on rock mechanics in deep mining engineering," *Chinese Journal of Rock Mechanics and Engineering*, vol. 24, no. 16, pp. 2803–2813, 2005.
- [2] M. C. He, Q. Wang, and Q. Y. Wu, "Innovation and future of mining rock mechanics," *Journal of Rock Mechanics and Geotechnical Engineering*, vol. 13, no. 1, pp. 1–21, 2021.
- [3] S. Xie, E. Li, S. Li, J. Wang, C. He, and Y. Yang, "Surrounding rock control mechanism of deep coal roadways and its application," *International Journal of Mining Science and Technology*, vol. 25, no. 3, pp. 429–434, 2015.
- [4] Q. Wang, M. C. He, S. C. Li et al., "Comparative study of model tests on automatically formed roadway and gob-side entry driving in deep coal mines," *International Journal of Mining Science and Technology*, vol. 31, no. 4, pp. 591–601, 2021.
- [5] H. P. Kang and Z. Q. Feng, "Status and development tendency of roadway grouting reinforcement technology in coal mine," *Coal Mining Technology*, vol. 18, no. 3, pp. 1–7, 2013.
- [6] F. N. Wang, Z. B. Guo, X. B. Qiao et al., "Large deformation mechanism of thin-layered carbonaceous slate and energy coupling support technology of NPR anchor cable in Minxian Tunnel: A case study," *Tunnelling and Underground Space Technology*, vol. 117, p. 104151, 2021.
- [7] N. Yang, W. T. Li, C. Xuan, and Y. H. Zhang, "Solid support system construction technology of U- type concrete filled steel tube arch of soft rock roadway in kilometer deep mine," *Journal of China Coal Society*, vol. 47, no. 12, pp. 82–86, 2016.
- [8] Z. F. Zhang, H. P. Kang, Z. Y. Jiang et al., "Study and application of high-pressure splitting grouting modification technology in coalmine with depth more than 1000 m," *Journal of China Coal Society*, vol. 45, no. 3, pp. 972–981, 2020.
- [9] G. Li, M. He, G. Zhang, and Z. Tao, "Deformation mechanism and excavation process of large span intersection within deep soft rock roadway," *Mining Science and Technology (China)*, vol. 20, no. 1, pp. 28–34, 2010.
- [10] G. C. Li, Z. H. Jiang, C. X. Lv, C. Huang, G. Chen, and M. Li, "Instability mechanism and control technology of soft rock roadway affected by mining and high confined water," *International Journal of Mining Science and Technology*, vol. 25, no. 4, pp. 573–580, 2015.
- [11] W. Fangtian, Z. Cun, W. Shuaifeng, Z. Xiaogang, and G. Shenghua, "Whole section anchor-grouting reinforcement technology and its application in underground roadways with

- loose and fractured surrounding rock,” *Tunnelling and Underground Space Technology*, vol. 51, pp. 133–143, 2016.
- [12] Q. Wang, R. Pan, B. Jiang et al., “Study on failure mechanism of roadway with soft rock in deep coal mine and confined concrete support system,” *Engineering Failure Analysis*, vol. 81, pp. 155–177, 2017.
- [13] S. Chen, A. Wu, Y. Wang, X. Chen, R. Yan, and H. Ma, “Study on repair control technology of soft surrounding rock roadway and its application,” *Engineering Failure Analysis*, vol. 92, pp. 443–455, 2018.
- [14] W. Zhang, X. Zhu, S. Xu, Z. Wang, and W. Li, “Experimental study on properties of a new type of grouting material for the reinforcement of fractured seam floor,” *Journal of Materials Research and Technology*, vol. 8, no. 6, pp. 5271–5282, 2019.
- [15] C. Yang, J. Guo, J. Lian, and Z. Wang, “Study on microscopic roadbed grouting mechanism based on CFD-DEM coupling algorithm,” *Mathematical Problems in Engineering*, vol. 2020, 9 pages, 2020.
- [16] Z. C. Wang, J. Tang, W. Li, X. G. Zhu, and D. S. Zhao, “Combined support technology of bolting net and U section steel support in soft rock roadway,” *Safety of Coal Mine*, vol. 45, no. 12, pp. 156–159, 2014.
- [17] J. Shen and Y. Zhang, “Theory and application of gob-side entry retaining in thick three-soft coal seam,” *Geofluids*, vol. 2021, Article ID 6157174, 16 pages, 2021.
- [18] C. Zhu, K. Zhang, H. Cai et al., “Combined application of optical fibers and CRLD bolts to monitor deformation of a pit-in-pit foundation,” *Advances in Civil Engineering*, vol. 2019, Article ID 2572034, 16 pages, 2019.
- [19] T. Zhigang, Z. Chun, W. Yong, W. Jiamin, H. Manchao, and Z. Bo, “Research on stability of an open-pit mine dump with fiber optic monitoring,” *Geofluids*, vol. 2018, Article ID 9631706, 20 pages, 2018.
- [20] D. D. Zhang, C. Y. Ma, Y. Y. Duan, W. G. Du, J. X. Liu, and J. Chai, “Wavelength characteristic analysis of a FBG array embedded in quaternary unconsolidated strata during a deep borehole installation,” *Journal of Sensors*, vol. 2021, Article ID 1207374, 13 pages, 2021.
- [21] C. J. Deng, F. N. Dang, X. Z. Chen, Z. Miao, and L. L. Chen, “Experimental study on grouting effect and mechanical properties of the rockfill materials grouted with SCM,” *Advances in Civil Engineering*, vol. 2020, Article ID 8834686, 9 pages, 2020.
- [22] J. Wu, B. Chen, S. Chai, and W. Kong, “Experimental study on compression characteristics of gangue grouting filling materials,” *Geotechnical and Geological Engineering*, vol. 38, no. 5, pp. 4557–4565, 2020.
- [23] X. Wang, Q. Qin, and Z. Xiong, “Comprehensive evaluation for grouting effect of fractured surrounding rock in deep roadway,” *Chinese Journal of Underground Space and Engineering*, vol. 15, no. 2, p. 576, 2019.
- [24] H. Wu, D. Ma, A. J. S. Spearing, and G. Y. Zhao, “Fracture phenomena and mechanisms of brittle rock with different numbers of openings under uniaxial loading,” *Geomechanics and Engineering*, vol. 25, no. 6, pp. 481–493, 2021.
- [25] Y. Wang, B. Zhang, B. Li, and C. H. Li, “A strain-based fatigue damage model for naturally fractured marble subjected to freeze-thaw and uniaxial cyclic loads,” *International Journal of Damage Mechanics*, vol. 30, no. 9, pp. 1305–1323, 2021.
- [26] Q. Wang, Z. Jiang, B. Jiang, H. Gao, Y. Huang, and P. Zhang, “Research on an automatic roadway formation method in deep mining areas by roof cutting with high-strength bolt-grouting,” *International Journal of Rock Mechanics and Mining Sciences*, vol. 128, p. 104264, 2020.
- [27] X. S. Li, K. Peng, J. Peng, and H. Xu, “Effect of cyclic wetting-drying treatment on strength and failure behavior of two quartz-rich sandstones under direct shear,” *Rock Mechanics and Rock Engineering*, pp. 1–8, 2021.
- [28] F. N. Wang, S. S. Yin, A. P. Guo et al., “Frame structure and engineering applications of the multisource system cloud service platform of monitoring of the soft rock tunnel,” *Geofluids*, vol. 2021, Article ID 6672732, 15 pages, 2021.
- [29] F. Wu, H. Zhang, Q. L. Zou, C. B. Li, J. Chen, and R. B. Gao, “Viscoelastic-plastic damage creep model for salt rock based on fractional derivative theory,” *Mechanics of Materials*, vol. 150, p. 103600, 2020.

Research Article

Study on Damage Constitutive Model of High-Concentration Cemented Backfill in Coal Mine

Baogui Yang and Haigang Yang 

School of Energy and Mining Engineering, China University of Mining and Technology (Beijing), Beijing 100083, China

Correspondence should be addressed to Haigang Yang; haigangy@163.com

Received 30 August 2021; Revised 13 October 2021; Accepted 16 October 2021; Published 29 October 2021

Academic Editor: Yu Wang

Copyright © 2021 Baogui Yang and Haigang Yang. This is an open access article distributed under the Creative Commons Attribution License, which permits unrestricted use, distribution, and reproduction in any medium, provided the original work is properly cited.

In order to construct the damage constitutive model (DCM) of high-concentration cemented backfill (HCCB) in coal mine, the generalized Hoek-Brown strength criterion was used as the failure criterion. For the difference of theoretical derivation of constitutive relation, a new DCM based on residual strength was proposed. Combined with the conventional triaxial compression test, the correctness and rationality of the DCM were verified. The damage evolution characteristics of HCCB were analyzed, and the physical meaning of model parameters was clarified. The results show that (a) the theoretical curves of stress-strain relation are in good agreement with its experimental curves, which means DCM can simulate the deformation and failure process of HCCB. (b) The damage evolution curve of HCCB is S-shaped. To some extent, the confining pressure can inhibit the development of damage. (c) The parameter F_0 reflects the position of the peak point of the DCM, and parameter n is the slope of the straight line segment in the postpeak strain softening stage, which are, respectively, used to characterize the strength level and brittleness of HCCB. The establishment of DCM of HCCB is helpful to reveal its deformation and failure mechanism and provides theoretical basis for its strength design.

1. Introduction

While coal mining has made great contribution to national economy, it has also brought serious environmental problems. Backfilling mining is one of the effective ways to solve the above problems. With the increasing popularity of environmental protection concept, backfilling mining will be applied more widely. High-concentration cemented backfill (HCCB) in coal mine is a goaf backfilling material composed of coal gangue, fly ash, cement, admixture, and water in a certain proportion. It has good flow characteristics before coagulating and high strength after coagulating. HCCB is mainly used to support the overlying strata in the coal mine goaf to effectively control the surface settlement and reduce all kinds of mining damage [1]. Constitutive relation is one of the key and hot issues in the study of mechanical properties of rock and other materials. The damage constitutive model (DCM) is established by combining the damage mechanics and statistical analysis theory, a stress-strain ($\sigma_1 - \varepsilon_1$) relation which can characterize the deformation and failure pro-

cess of rock and other materials, used to analyze and solve the deformation and failure problems of materials [2–5]. The damage constitutive relation of HCCB is directly related to its stability in goaf and control effect of coal mine surface collapse.

At present, the research on damage constitutive relation is mainly focused on rock materials and has achieved fruitful research results. The reasonable measurement of rock microelements strength is one of the key problems in the establishment of DCM. Many experts and scholars regard the strength failure criterion as the random distribution variable of rock microelement strength. According to the randomness of the distribution of defects in rock materials, the damage in rock deformation and failure process was studied based on the maximum strain criterion and a DCM with simple form and parameter easy to obtain was established [6–9]. Using the Mohr-Coulomb (M-C) criterion as the expression method of microelement strength and assuming the microelement strength follows Weibull random distribution, a three-dimensional damage statistical

constitutive model was established to reflect the postpeak softening characteristics of rock [10–14]. Based on the theory of probability statistics and continuous damage mechanics, the Drucker-Prager (D-P) criterion was introduced as the failure criterion of rock microelements, and the damage evolution equation of rock was deduced strictly, which greatly improved the degree of agreement between the theoretical curve of $\sigma_1 - \varepsilon_1$ relation and the test data [15–19]. Yan et al. [20], Pan et al. [21], and Zhang et al. [22] used the triple shear energy yield criterion, the unified strength criterion, and the double shear unified strength criterion to characterize the rock microelement strength, respectively, and constructed the DCM based on the above strength criterion. The failure criteria of rock materials involved in the above study include maximum strain criterion, M-C criterion, D-P criterion, triple shear energy yield criterion, unified strength criterion, and double shear unified strength criterion, among which M-C criterion and D-P criterion are in the majority.

As an artificial composite material, HCCB has a short diagenetic time and a large number of soft structural planes such as pores and cracks. The deformation and failure process after loading shows obvious nonlinear characteristics. The generalized Hoek-Brown strength criterion can reflect the nonlinear failure characteristics of rock mass better by comprehensively considering a variety of influencing factors, while D-P criterion is relatively conservative, and M-C criterion is more suitable to represent the linear relation [23–27]. Therefore, the generalized Hoek-Brown strength criterion was selected as the failure criterion of HCCB. In view of the difference of the theoretical derivation of constitutive relation, the theoretical derivation model was modified and a new DCM was proposed. The correctness and rationality of the model were verified by conventional triaxial compression tests. The damage evolution characteristics of HCCB were analyzed. The related studies are helpful to reveal the deformation and failure mechanism of HCCB under triaxial compression and provide a theoretical basis for its strength design.

2. Test Equipment, Materials, and Results

2.1. Test Equipment. The conventional triaxial compression test was carried out on the RTR-2000 triaxial dynamic test system for high-pressure rock (see Figure 1). The system is mainly used for testing physical and mechanical parameters in normal- and high-temperature and high-pressure environment. The system is equipped with a high stiffness loading frame, the load stiffness is up to 10 mN/mm, the maximum axial pressure is 2000 kN, the maximum confining pressure is 140 MPa, the maximum pore pressure is 140 MPa, and the maximum temperature is 200°C. Samples of different sizes can be tested according to the requirements of users. The sample is a cylinder with a diameter of 25~100 mm and a height of 50~200 mm. The change of test conditions and data acquisition can be completely controlled by a computer. The operator can control the operation of the test by means of load, displacement, strain, and stress.



FIGURE 1: Test system.

Axial displacement control was adopted in the test. The axial loading rate was strictly in accordance with standard for test method of concrete physical and mechanical properties (GB/T50081-2019) [28]. During the test, the specimen was first installed in the pressure chamber. Specimens with insufficient end flatness should be polished in advance. Secondly, the specimen was preloaded to make the pressure head contact with the specimen. Then, the confining pressure was applied to the predetermined value according to the hydrostatic pressure condition. The loading rate of confining pressure was 0.25 MPa/min, and the predetermined values were 0 MPa, 1 MPa, 2 MPa, and 3 MPa, respectively. After the confining pressure loading, the specimen was under hydrostatic pressure. Finally, the load was applied along the axis at a constant displacement rate until the specimen was in the residual strength stage. In order to reduce the adverse effects of specimen discreteness on the test and ensure the success of the test, three groups of tests were carried out under each confining pressure, and one group of tests was selected for analysis.

2.2. Test Materials. The coal gangue used in the test was taken from Xinyang Coal Mine in Xiaoyi City, the fly ash was selected from the coal-fired power plant around Xinyang Mine, the cement was commercially available ordinary Portland cement, the admixture was cellulose hydroxypropyl methyl ether, and the preparation water was laboratory tap water. Combined with the practice of backfilling mining in Xinyang Coal Mine, the mass fractions of coal gangue, fly ash, cement, cellulose hydroxypropyl methyl ether, and water were set as 49.94%, 18%, 12%, 0.06%, and 20%, respectively. The weighed raw materials were mixed in turn to prepare the backfilling slurry with mass concentration of 80%. The specimens ($\phi 50 \times 100$ mm) were poured in time and maintained to the prescribed age (28 days). All specimens used the same batch of raw materials. Slurry preparation strictly referred to standard for test method of performance of ordinary fresh concrete (GB/T50080-2016) [29]. The pouring and maintaining of specimens strictly referred to standard for test method of concrete physical and mechanical properties (GB/T50081-2019) [28]. The specimens after maintaining are shown in Figure 2.

2.3. Test Results. The $\sigma_1 - \varepsilon_1$ curves of HCCB are similar under different confining pressures. Taking the specimen with confining pressure of 2 MPa as an example, the deformation and failure process of HCCB is analyzed. Similar to the deformation and failure process of materials such as



FIGURE 2: Specimens.

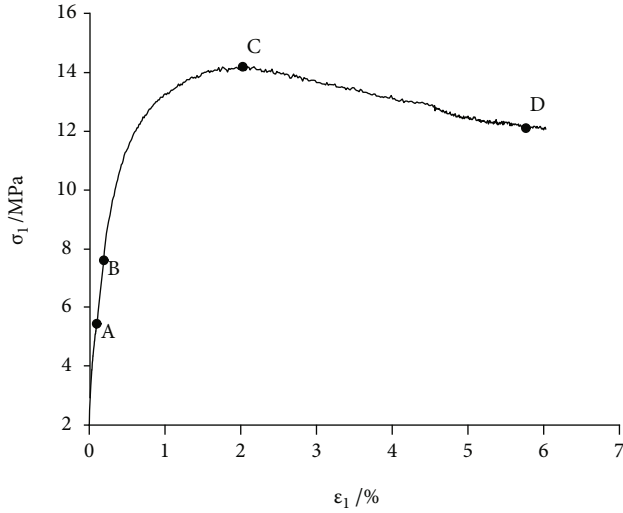


FIGURE 3: Curve of $\sigma_1 - \varepsilon_1$.

rocks, the $\sigma_1 - \varepsilon_1$ curve of the specimens can be divided into five stages, as shown in Figure 3.

- (1) Initial compaction stage (before point A): at the initial stage of compression, the original defects inside the HCCB are pressed and closed. The curve of $\sigma_1 - \varepsilon_1$ is approximately linear. The reason why there is no typical concave section is that the HCCB is so soft that most of the original defects have been compressed in the process of confining pressure loading. The deformation at this stage is close to elastic deformation and can be mainly restored after unloading
- (2) Elastic deformation stage (AB section): the HCCB bears the load stably. The curve $\sigma_1 - \varepsilon_1$ is close to a straight line. This stage is dominated by elastic deformation which can be recovered, but also contains a small amount of plastic deformation which cannot be recovered
- (3) Yield deformation stage (BC section): when the external load reaches the yield stress of the HCCB, new cracks initiate, expand, and gradually connect. The curve of $\sigma_1 - \varepsilon_1$ is convex, whose slope of tangent decreases until it drops to 0. With the increase of axial strain, the unrecoverable plastic deformation increases gradually

- (4) Strain softening stage (CD section): when the peak strength is reached, the HCCB is damaged and then enters the strain softening stage. The slope of the tangent of the $\sigma_1 - \varepsilon_1$ curve changes from zero to negative. The bearing capacity is gradually decreasing. The plastic deformation increases significantly. The specimens show obvious dilatancy characteristics
- (5) Residual strength stage (after point D): with the increase of axial strain, the axial stress does not change. The curve of $\sigma_1 - \varepsilon_1$ is a horizontal line. Although HCCB in this stage has been completely destroyed, it still maintains a certain bearing capacity

3. Establishment of DCM

According to the general pattern of damage mechanics, in order to obtain the DCM of materials, the damage variables are defined in a certain way and damage evolution equation is derived accordingly. Then, the damage evolution equation is substituted into the constitutive relation to obtain the DCM.

3.1. *Damage Evolution Equation.* Assuming that the number of damaged microelements of the HCCB under a certain level of load is N_d , the damage variable D is defined as the ratio of the number of damaged microelements N_d to the number of total microelements N [2, 15]; then,

$$D = \frac{N_d}{N}. \quad (1)$$

When the stress level S reaches the strength F of the microelement, the microelement is destroyed. Assuming that F obeys a certain probability distribution, the number of microelements that fail in any stress level interval $[S, S + dS]$ is as follows:

$$dN_d = Np(S)dS, \quad (2)$$

where p is the density function of the probability distribution satisfied by F . For F , the commonly used distribution types include Weibull distribution and normal distribution.

When the stress level reaches a certain S , the number of damaged microelements is as follows:

$$N_d = \int_0^S Np(x)dx = NP(S), \quad (3)$$

where P is the distribution function of the probability distribution satisfied by F .

It can be obtained from Equations (1) and (3) that

$$D = P(S). \quad (4)$$

Equation (4) is the deduced damage evolution equation. For any probability distribution, the value of the distribution function changes from 0 to 1 as S increases, which is consistent with the change law of D .

A microelement is taken from any section of the specimen of HCCB, and it is assumed that (1) the microelement conforms to the generalized Hoek theorem, (2) the yield of microelements follows Hoek-Brown criterion, and (3) microelement strength strictly follows Weibull random distribution [8]. Then, the probability density function of the microelement strength is as follows:

$$p(F) = \frac{n}{F_0} \left(\frac{F}{F_0}\right)^{n-1} \exp \left[-\left(\frac{F}{F_0}\right)^n \right], \quad (5)$$

where F_0 and n are the Weibull distribution parameters.

The distribution function of the microelement strength is as follows:

$$P(F) = 1 - \exp \left[-\left(\frac{F}{F_0}\right)^n \right]. \quad (6)$$

It can be obtained from Equations (4) and (6) that

$$D = 1 - \exp \left[-\left(\frac{S}{F_0}\right)^n \right]. \quad (7)$$

According to the assumption of point (2) satisfied by the microelement, S can be determined by the Hoek-Brown criterion. The expression of the generalized Hoek-Brown strength criterion [24] is as follows

$$\sigma_{1c} = \sigma_{3c} + \sigma_c \left(m \frac{\sigma_{3c}}{\sigma_c} + s \right)^\alpha, \quad (8)$$

where σ_{1c} is the maximum principal stress under rock failure, MPa; σ_{3c} is the minimum principal stress under rock failure, MPa; σ_c is the uniaxial compressive strength of rock, MPa; M is the material parameter, which can be obtained according to the rock mass classification index GSI; S and α are constants related to material characteristics. For materials with good quality, $\alpha = 0.5$.

The generalized Hoek-Brown strength criterion expressed by the effective stress invariants [24] is as follows:

$$\begin{cases} S = f(\sigma^*) = m\sigma_c \frac{I_1^*}{3} + 4J_2^* \cos^2 \theta_\sigma + m\sigma_c \sqrt{J_2^*} \left(\cos \theta_\sigma + \frac{\sin \theta_\sigma}{\sqrt{3}} \right) = s\sigma_c^2, \\ I_1^* = \sigma_1^* + \sigma_2^* + \sigma_3^*, \\ J_2^* = \frac{(\sigma_1^* - \sigma_2^*)^2 + (\sigma_2^* - \sigma_3^*)^2 + (\sigma_1^* - \sigma_3^*)^2}{6}, \end{cases} \quad (9)$$

where $f(\sigma^*)$ is the strength of microelement, MPa; I_1^* is the first invariant of effective stress, MPa; J_2^* is the second invariant of effective stress deviator, MPa; θ_σ is Lord's angle. For conventional triaxial compression test, $\theta_\sigma = 30^\circ$; σ_i^* is the effective stress in the direction i , $i = 1, 2, 3$ MPa.

According to the generalized Hoek law and the concept of effective stress, the corresponding effective stress can be obtained as follows:

$$\begin{cases} \sigma_1^* = \frac{\sigma_1 E \varepsilon_1}{\sigma_1 - \mu(\sigma_2 + \sigma_3)}, \\ \sigma_2^* = \frac{\sigma_2 E \varepsilon_1}{\sigma_1 - \mu(\sigma_2 + \sigma_3)}, \\ \sigma_3^* = \frac{\sigma_3 E \varepsilon_1}{\sigma_1 - \mu(\sigma_2 + \sigma_3)}, \end{cases} \quad (10)$$

where σ_i is the nominal stress in the direction i , MPa; E is the elastic modulus, GPa; ε_1 is the axial strain, %; μ is Poisson's ratio.

Substituting Equation (10) into Equation (9), the following can be obtained.

$$\begin{cases} I_1^* = \frac{E \varepsilon_1 (\sigma_1 + \sigma_2 + \sigma_3)}{\sigma_1 - \mu(\sigma_2 + \sigma_3)}, \\ J_2^* = \frac{E^2 \varepsilon_1^2 (\sigma_1^2 + \sigma_2^2 + \sigma_3^2)}{3[\sigma_1 - \mu(\sigma_2 + \sigma_3)]^2} - \frac{(\sigma_1 \sigma_2 + \sigma_2 \sigma_3 + \sigma_1 \sigma_3)}{3[\sigma_1 - \mu(\sigma_2 + \sigma_3)]^2}, \\ S = \frac{m\sigma_c E \varepsilon_1 \sigma_1}{\sigma_1 - \mu(\sigma_2 + \sigma_3)} + \frac{E^2 \varepsilon_1^2 (\sigma_1 - \sigma_3)^2}{[\sigma_1 - \mu(\sigma_2 + \sigma_3)]^2}. \end{cases} \quad (11)$$

3.2. Damage Constitutive Relation. Lemaitre [30] established the strain equivalence hypothesis. The damage model established is as follows:

$$\sigma_i^* = \frac{\sigma_i}{1 - D}. \quad (12)$$

According to Hoek's law, the principal strain can be as follows:

$$\varepsilon_i = \frac{1}{E} [(1 + \mu)\sigma_i^* - \mu(\sigma_1^* + \sigma_2^* + \sigma_3^*)]. \quad (13)$$

It can be obtained from Equations (12) and (13) that

$$\sigma_1 = E \varepsilon_i (1 - D) + \mu(\sigma_2 + \sigma_3). \quad (14)$$

According to Equation (14), when the HCCB is completely damaged, that is, $D = 1$, $\sigma_1 = \mu(\sigma_2 + \sigma_3)$. Then, the residual strength of HCCB is $\mu(\sigma_2 + \sigma_3)$. However, the actual residual strength of HCCB is σ_r . There is an absolute difference in value between them. In order to eliminate this difference, make the established constitutive model more in line with the reality and better characterize the $\sigma_1 - \varepsilon_1$ relation of HCCB. Equation (14) is modified based on the σ_r of HCCB. A new constitutive model of HCCB is proposed, that is,

$$\sigma_1 = E \varepsilon_i (1 - D) + \mu(\sigma_2 + \sigma_3) + \sigma_m D, \quad (15)$$

where σ_m is the difference between σ_r and $\mu(\sigma_2 + \sigma_3)$, that is, $\sigma_m = \sigma_r - \mu(\sigma_2 + \sigma_3)$.

In the conventional triaxial compression test, $\sigma_2 = \sigma_3$, the DCM of HCCB can be expressed as follows:

$$\sigma_1 = E\varepsilon_1(1 - D) + (\sigma_r - 2\mu\sigma_3)D + 2\mu\sigma_3. \quad (16)$$

It can be seen from Equations (16) and (7) that the determination of distribution parameters F_0 and n is one of the key issues in the establishment of DCM. The unknown parameters of the model can be determined according to the extreme value characteristics of the $\sigma_1 - \varepsilon_1$ curve. The specific determination process is as follows.

Assuming that the stress and strain at the peak point corresponding to $\sigma_1 - \varepsilon_1$ curve under different confining pressures are σ_{1c} and ε_{1c} , respectively, then,

$$\left. \frac{\partial \sigma_1}{\partial \varepsilon_1} \right|_{\sigma_1 = \sigma_{1c}, \varepsilon_1 = \varepsilon_{1c}} = 0. \quad (17)$$

The derivative of Equation (16) can be obtained.

$$\frac{\partial \sigma_1}{\partial \varepsilon_1} = E(1 - D) + (\sigma_r - 2\mu\sigma_3 - E\varepsilon_1) \frac{\partial D}{\partial \varepsilon_1}. \quad (18)$$

According to Equations (17) and (18), the following can be obtained.

$$\left. \frac{\partial D}{\partial \varepsilon_1} \right|_{\sigma_1 = \sigma_{1c}, \varepsilon_1 = \varepsilon_{1c}} = \frac{E(D_{1c} - 1)}{\sigma_r - 2\mu\sigma_3 - E\varepsilon_{1c}}, \quad (19)$$

where D_{1c} is D when $\sigma_1 = \sigma_{1c}$ and $\varepsilon_1 = \varepsilon_{1c}$, and it can be determined from Equation (16), that is,

$$D_{1c} = \frac{\sigma_{1c} - 2\mu\sigma_3 - E\varepsilon_{1c}}{\sigma_r - 2\mu\sigma_3 - E\varepsilon_{1c}}. \quad (20)$$

Partial differentiation of Equation (7) can be obtained.

$$\frac{\partial D}{\partial \varepsilon_1} = \exp \left[-\left(\frac{S}{F_0} \right)^n \right] \left[n \left(\frac{S}{F_0} \right)^{n-1} \right] \frac{1}{F_0} \frac{\partial S}{\partial \varepsilon_1}. \quad (21)$$

Partial differentiation of Equation (11) can be obtained.

$$\begin{aligned} \frac{\partial S}{\partial \varepsilon_1} &= \frac{m\sigma_c\sigma_1 E}{\sigma_1 - 2\mu\sigma_3} + \frac{2E^2\varepsilon_1(\sigma_1 - \sigma_3)^2}{(\sigma_1 - 2\mu\sigma_3)^2} \\ &= \frac{m\sigma_c\sigma_1 E(\sigma_1 - 2\mu\sigma_3) + 2E^2\varepsilon_1(\sigma_1 - \sigma_3)^2}{(\sigma_1 - 2\mu\sigma_3)^2}. \end{aligned} \quad (22)$$

The transformation of Equation (7) can be obtained.

$$\exp \left[-\left(\frac{S}{F_0} \right)^n \right] = 1 - D. \quad (23)$$

It can also be expressed as follows:

$$\left(\frac{S}{F_0} \right)^{n-1} = -\frac{F_0}{S} \ln(1 - D). \quad (24)$$

By substituting Equations (22)–(24) into Equation (21) and then substituting Equation (21) into Equation (19), it can be obtained that

$$n = \frac{S_{1c}}{(\sigma_r - 2\mu\sigma_3 - E\varepsilon_{1c}) \ln(1 - D_{1c})} \cdot \frac{(\sigma_{1c} - 2\mu\sigma_3)^2}{m\sigma_c\sigma_{1c}(\sigma_{1c} - 2\mu\sigma_3) + 2E\varepsilon_{1c}(\sigma_{1c} - \sigma_3)^2}, \quad (25)$$

where S_{1c} is S when $\sigma_1 = \sigma_{1c}$ and $\varepsilon_1 = \varepsilon_{1c}$, and it can be determined from Equation (11), that is,

$$S_{1c} = \frac{m\sigma_c E\varepsilon_{1c}\sigma_{1c}(\sigma_{1c} - 2\mu\sigma_3)}{(\sigma_{1c} - 2\mu\sigma_3)^2} + \frac{E^2\varepsilon_{1c}^2(\sigma_{1c} - \sigma_3)^2}{(\sigma_{1c} - 2\mu\sigma_3)^2}. \quad (26)$$

By substituting $D = D_{1c}$ and $S = S_{1c}$ into Equation (23), it can be obtained that

$$F_0 = \frac{S_{1c}}{[-\ln(1 - D_{1c})]^{1/n}}. \quad (27)$$

4. Model Verification

According to conventional triaxial compression test with $\sigma_3 = 0$ MPa, the uniaxial compressive strength of HCCB was 8.5 MPa, that is, $\sigma_c = 8.5$ MPa. The material parameter m of the generalized Hoek-Brown strength criterion was fitted by the least square method and $m = 5.58$. Combined with conventional triaxial compression test results, DCM parameters under different confining pressures were obtained, as shown in Table 1.

In order to verify the correctness and rationality of the established DCM, the obtained model parameters were replaced into the DCM to draw the theoretical curve of $\sigma_1 - \varepsilon_1$ relation. The theoretical curves were compared with the test curves under different confining pressures, as shown in Figure 4.

As can be seen from Figure 4, under low confining pressure, the postpeak curve of $\sigma_1 - \varepsilon_1$ relation has an obvious strain softening stage. The postpeak axial stress decreases significantly with the increase of axial strain, as shown in Figures 4(a)–4(c). When the confining pressure reaches a certain value, the postpeak curve of $\sigma_1 - \varepsilon_1$ relation no longer has obvious strain softening stage. After the specimen reaches the peak strength, with the increase of axial strain, the axial stress decreases but not significantly, as shown in Figure 4(d). In Figure 4(d), the peak strength is 16.6 MPa and the residual strength is 16.3 MPa, which are very similar, but the postpeak strain softening stage still exists. For the $\sigma_1 - \varepsilon_1$ relation whose postpeak curve has obvious strain softening stage, its theoretical curve agrees well with the experimental curve, especially in the prepeak stage and the residual strength stage. In the strain softening stage, the theoretical curve and the test curve are in relatively low agreement, showing a certain difference. However, in Figures 4(a)–4(c), the maximum difference between theoretical and experimental values in the strain softening stage is

TABLE 1: Parameters of DCM.

Specimens number	σ_3 (MPa)	E (GPa)	μ	σ_{1c} (MPa)	ε_{1c} (%)	σ_r (MPa)	S_{1c} (MPa)	D_{1c}	F_0	n
SJ-0	0	2.595	0.135	8.5	0.5270	1.8	836.10	0.44	1173.92	1.64
SJ-1	1	3.540	0.149	12.0	0.7320	7.9	1831.17	0.77	1046.47	0.72
SJ-2	2	1.932	0.132	14.3	1.9950	12.0	3082.34	0.91	354.61	0.42
SJ-3	3	1.102	0.110	16.7	3.9976	16.3	3593.18	0.99	13.85	0.26

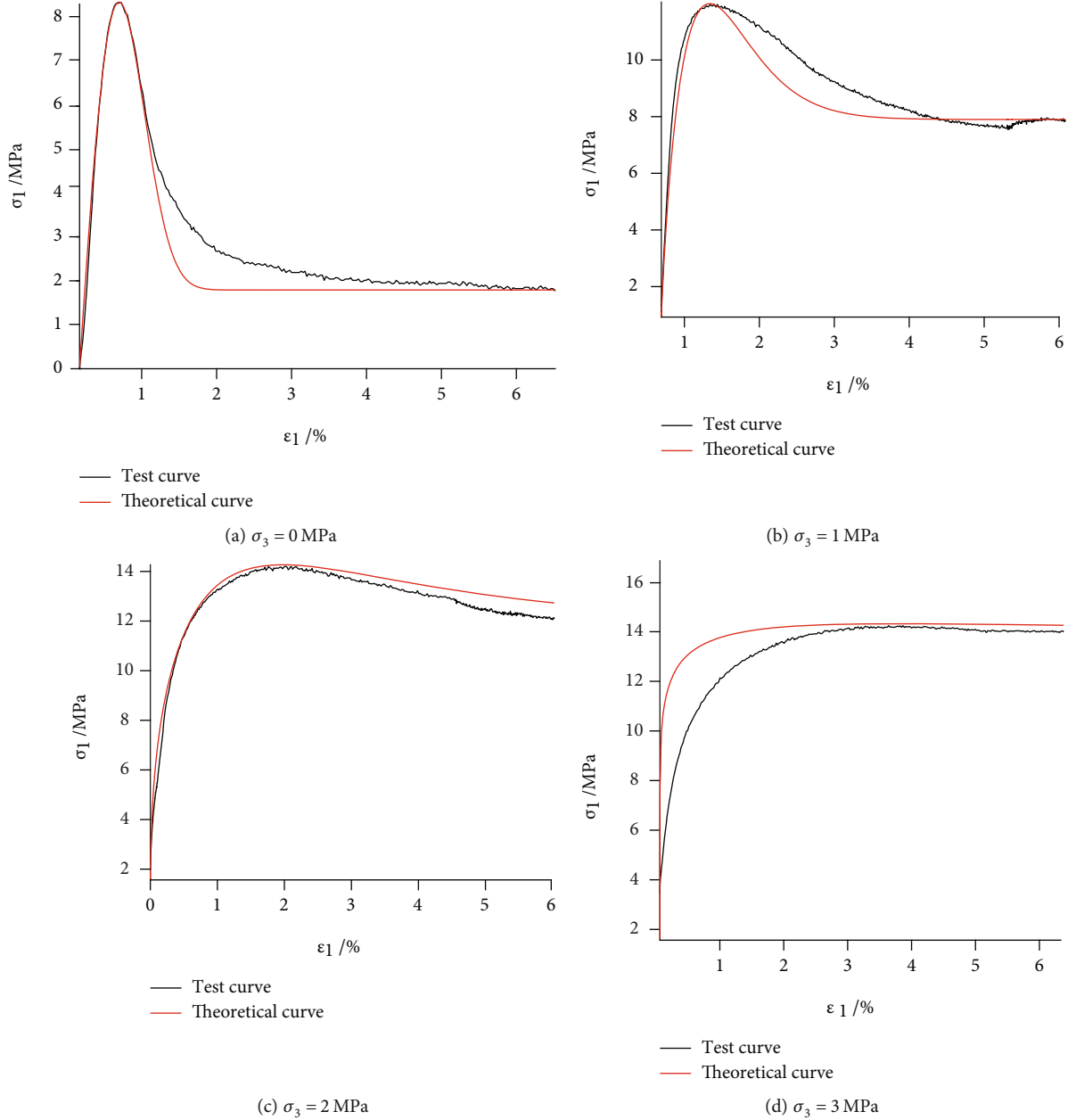


FIGURE 4: Damage constitutive models.

1.35 MPa. Compared to local differences of tens of megapascals in the rocks, the degree of match has been greatly improved. For the $\sigma_1 - \varepsilon_1$ relation whose postpeak curve has no obvious strain softening stage, there is a great difference between the theoretical curve and the experimental curve, especially in the prepeak stage. The maximum differ-

ence between theoretical value and experimental value is 7 MPa. From the initial compaction to the peak strength, the difference gradually decreases between them. In the post-peak stage, the theoretical curve can simulate the experimental curve well. In view of the relatively large difference between the theoretical value and the experimental value in

the prepeak stage, it is considered that the damage constitutive equation established can only characterize the $\sigma_1 - \varepsilon_1$ relation whose postpeak curve has no obvious strain softening stage to a certain extent. When a DCM with a higher degree of consistency is needed, its damage constitutive relation can be reconstructed.

When the confining pressure is 0 MPa, the postpeak axial stress decreases rapidly with the increase of axial strain. The absolute value of the slope of the straight segment of the postpeak curve is large. The difference between peak strength and residual strength is large. HCCB shows obvious brittleness. With the increase of confining pressure, the axial stress after the peak decreases slowly with the increase of axial strain. The absolute value of the slope of the straight section of the postpeak curve is small. The difference between the peak strength and the residual strength is reduced. The brittleness of the HCCB weakens, showing a certain plasticity. When the confining pressure is 3 MPa, the HCCB shows the lowest brittleness. The DCM can reflect the trend of brittleness decreasing and plasticity increasing.

5. Analysis of Damage Evolution Characteristics and Parameter Effect

5.1. Damage Evolution Characteristics. The theoretical curves of $\sigma_1 - \varepsilon_1$ relation are in good agreement with the experimental curves, which indicates that the established DCM is correct and the damage evolution equations are reasonable. Based on damage evolution equations, the damage evolution characteristics in the process of deformation and failure of HCCB will be discussed. The evolution equation of damage variable is shown in Equation (28).

$$\begin{cases} D = 1 - \exp \left[- \left(\frac{S}{F_0} \right)^n \right], \\ S = \frac{m\sigma_c E \varepsilon_1 \sigma_1 (\sigma_1 - 2\mu\sigma_3) + E^2 \varepsilon_1^2 (\sigma_1 - \sigma_3)^2}{(\sigma_1 - 2\mu\sigma_3)^2}. \end{cases} \quad (28)$$

According to Equation (28), combined with the parameters of DCM, damage evolution curves of HCCB under different confining pressures can be drawn, as shown in Figure 5.

Most of the damage evolution curves of rock materials show S-shaped [2, 24]. The damage evolution curves increase monotonically under different confining pressures. With the increase of axial strain, the damage variable increases from 0 and gradually approaches 1, completing the continuous accumulation of damage until it reaches saturation. The whole damage evolution process can be divided into no damage stage, damage beginning stage, damage accelerating stage, damage slowing stage, and damage stabilizing stage. The corresponding deformation and failure stages are initial compaction and elastic deformation stage, yield deformation stage, early strain softening stage, late strain softening stage, and residual strength stage. As can be seen from Figure 5, the damage evolution curves of

HCCB are half S-shaped and are the upper part of S. The damage evolution curves mainly include the damage slowing stage and damage stabilizing stage. The reasons are as follows: due to the confining pressure, the starting point of the damage evolution curve and the stress-strain curve is not the origin, resulting in no damage stage, damage beginning stage, and damage accelerating stage that are not shown in Figure 5. The dashed line in Figure 5 is the dividing line between the damage slowing stage and the damage stabilizing stage. Among them, the damage stabilizing stage corresponds to the residual strength stage of HCCB, and the damage slowing stage almost corresponds to all deformation and failure stages except the residual strength stage. The reason for the above differences is that the strength of cemented matrix forming HCCB is low. The cemented matrix is rapidly damaged from the beginning of axial loading. In the damage slowing stage, the damage of HCCB increases rapidly at first and then slowly. The increase rate gradually slows down. In the early part of this stage, most of the damage of the HCCB is completed within a small axial strain range. In the later part of this stage, the damage increment is limited, but this part lasts for a long time, which is several times of the early part. In the damage stabilizing stage, the damage of HCCB does not increase any more. D is always 1, which means that the HCCB has been completely damaged.

Figure 5 shows that the damage slowing stage of HCCB will last for a long time no matter under low or high confining pressure. The axial strain of HCCB is maintained at a high value when it is completely damaged. When $D = 1$, the HCCB is completely damaged. The axial strain under complete damage is defined as ε_r . The curve of ε_r changing with σ_3 is shown in Figure 6.

It can be seen from Figure 6 that ε_r increases with the increase of σ_3 . There is a roughly linear relation between them; that is, the greater the confining pressure is, the greater the axial strain is when the HCCB is completely damaged. The main reason is that confining pressure can inhibit the development of damage to some extent. With the increase of confining pressure, when HCCB achieves the same damage amount, the axial deformation required is larger.

5.2. Parametric Effect. Most of the parameters in the DCM have clear physical meanings. For example, E is the elastic modulus, reflecting the elastic level of the material. At the same time, there are also some parameters whose physical meanings are unclear, such as Weibull distribution parameters F_0 and n . The following is to determine the physical significance of F_0 and n by analyzing their influence on DCM. Weibull distribution parameters F_0 and n are the common reflection of material characteristics and confining pressure of HCCB. Under the same confining pressure, F_0 and n are bound to be different for HCCB with different proportions. Similarly, for HCCB with the same proportion, F_0 and n are different under different confining pressures and show certain regularity. It can be seen from Table 1 that with the increase of confining pressure of HCCB, both F_0 and n of the DCM decrease.

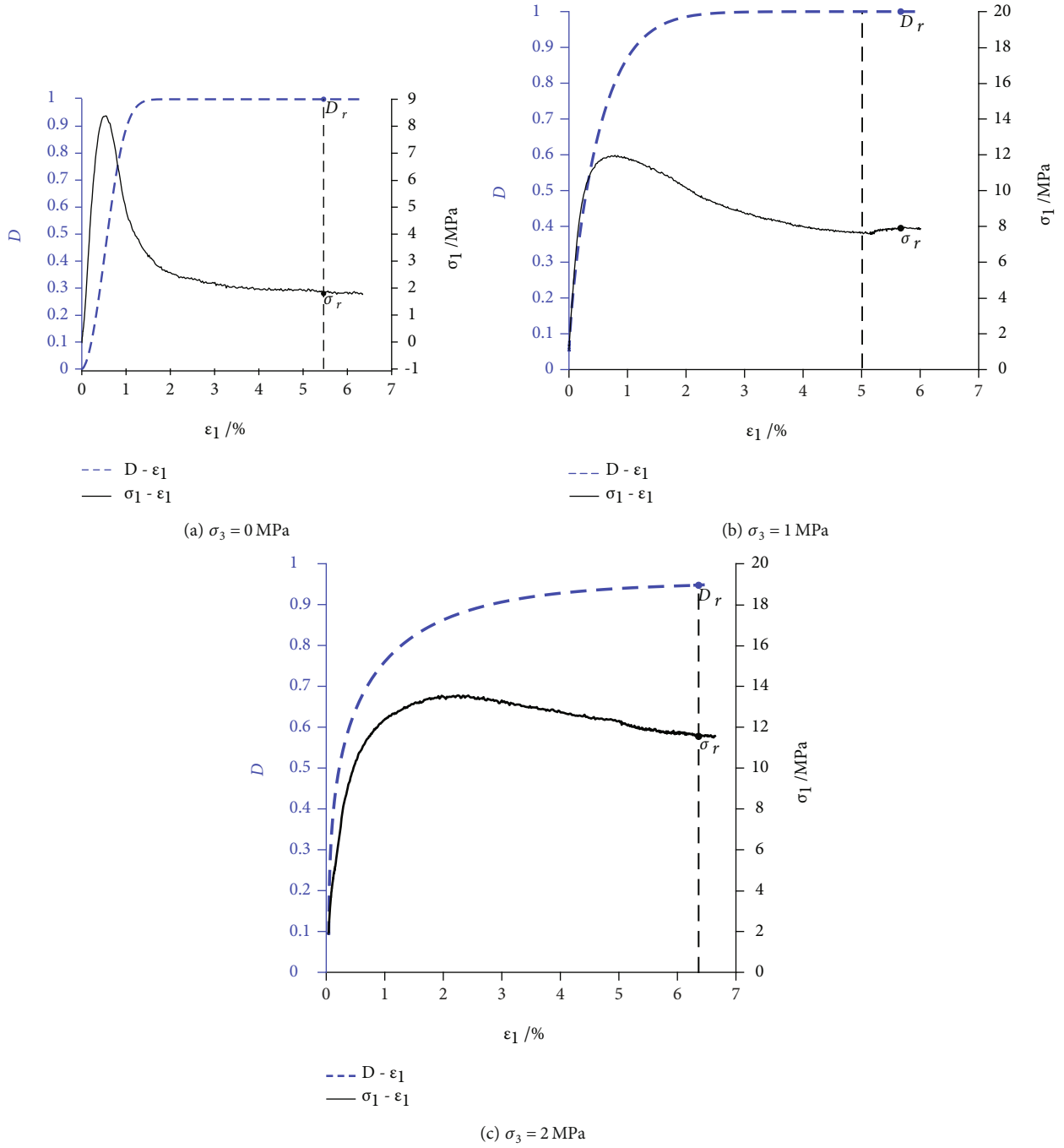


FIGURE 5: Continued.

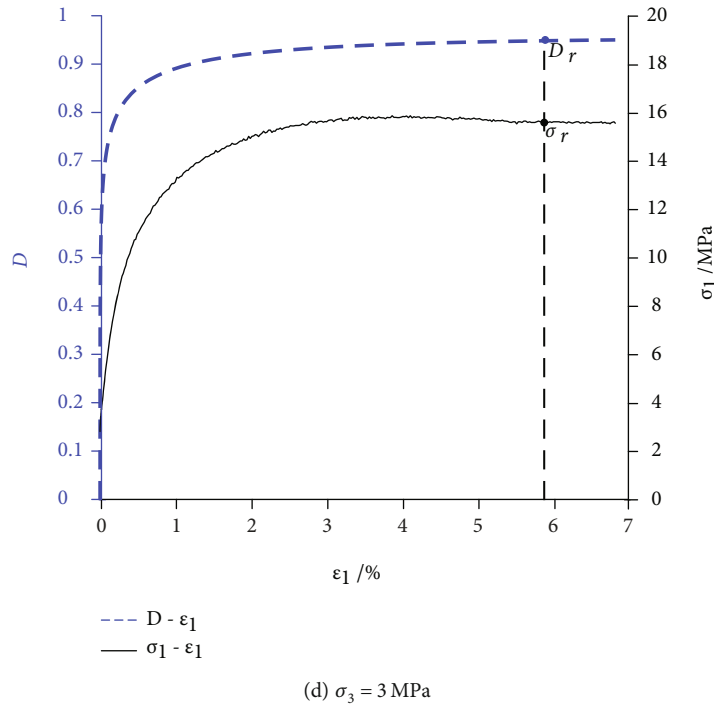


FIGURE 5: Damage evolution curves.

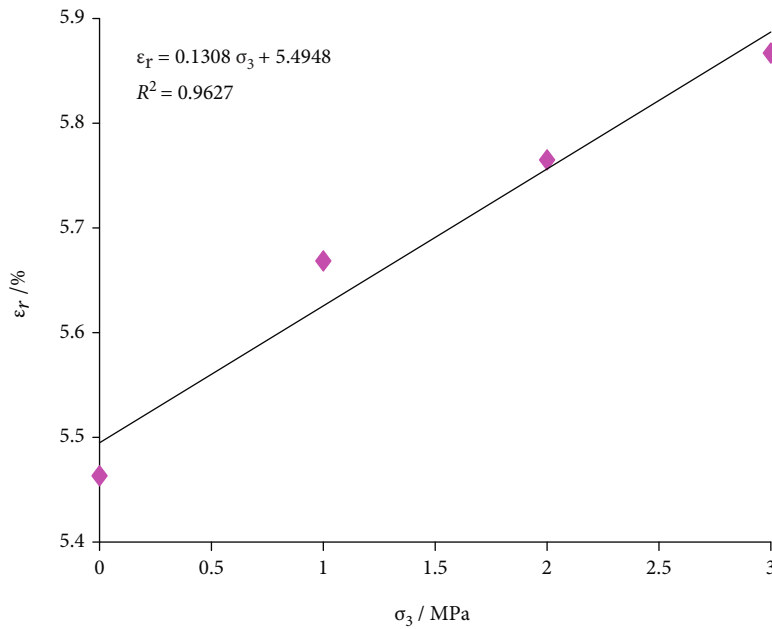
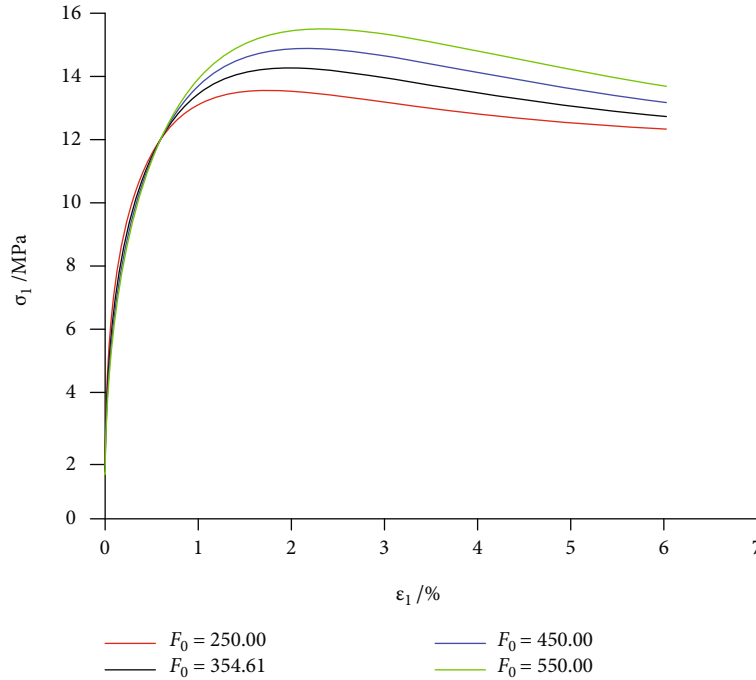
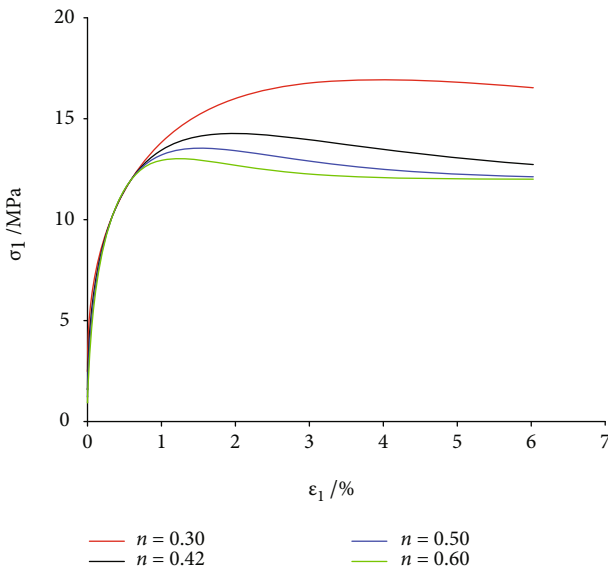


FIGURE 6: Change curve between ϵ_r and σ_3 .

5.2.1. *Effect of F_0 on DCM.* Based on the specimen with confining pressure of 2 MPa, other parameters remain unchanged and only parameter F_0 is changed. When F_0 varies approximately in amplitude of 100, the DCM was obtained under different values of F_0 , as shown in Figure 7.

Figure 7 shows that the linear elastic deformation stage of the DCM is almost not affected by F_0 . The linear elastic deformation stages under different F_0 are approximately

coincident. With the increase of F_0 , the peak strength, peak strain, and residual strength of the DCM all increase. The peak point of the DCM moves outward and is further and further away from the origin in the horizontal and vertical directions. But the shape of the DCM basically remains unchanged. The postpeak strain softening stages under different F_0 are approximately parallel. F_0 has no significant effect on the slope of straight line segment in strain softening

FIGURE 7: Effect of F_0 .FIGURE 8: Effect of n .

stage. Therefore, F_0 reflects the location of the peak point of the DCM, which can be regarded as a physical quantity representing the strength level of HCCB.

5.2.2. Effect of n on DCM. Based on the specimen with confining pressure of 2 MPa, other parameters remain unchanged and only parameter n is changed. When n varies approximately in amplitude of 0.10, the DCM was obtained under different values of n , as shown in Figure 8.

Figure 8 shows that the linear elastic deformation stage of the DCM is almost not affected by n . The linear elastic

deformation stages under different n are approximately coincident. With the increase of n , the peak strength, peak strain, and residual strength of the DCM all decrease. The peak point of the DCM moves inward and is closer to the origin in the horizontal and vertical directions. On the other hand, the shape of DCM changes obviously. n changes the softening and steepening degree of the straight line segment in the strain softening stage. As n increases, the line segment becomes steeper and the brittleness of HCCB increases. Therefore, n reflects the slope of the straight section in the strain softening stage, which can be regarded as a physical quantity representing the brittleness degree of HCCB.

6. Conclusions

The following conclusions can be drawn from this study:

- For the $\sigma_1 - \varepsilon_1$ relation whose postpeak curve has obvious strain softening stage, the theoretical curve agrees well with the experimental curve. The DCM can characterize the deformation and failure process of HCCB. For the $\sigma_1 - \varepsilon_1$ relation whose postpeak curve has no obvious strain softening stage, the damage constitutive relation with higher degree of coincidence can be established according to the demand
- The damage evolution curve of HCCB is S-shaped. The damage evolution process only shows damage slowing stage and damage stabilizing stage because of the confining pressure. When the HCCB is completely damaged, the axial strain remains high. Confining pressure can inhibit the development of damage to some extent

- (c) The linear elastic deformation stage of the DCM is almost not affected by the distribution parameters F_0 and n . F_0 reflects the position of the peak point of DCM and n reflects the slope of the straight line segment in the strain softening stage, respectively, used to characterize the strength level and brittleness degree of HCCB

Data Availability

The data used to support the findings of this study are available from the corresponding author and first author upon request.

Conflicts of Interest

The authors declare that they have no conflicts of interest.

Acknowledgments

This study was supported by the National Key Research and Development Plan (Grant No. 2017YFC0603002).





References

- [1] B. G. Yang, *Mining Technology of High Concentration Cemented Filling in Coal Mine*, China Coal Industry Press, Beijing, 2015.
- [2] D. Q. Liu, Z. Wang, and X. Y. Zhang, "Characteristics of strain softening of rocks and its damage constitutive model," *Rock and Soil Mechanics*, vol. 38, no. 10, pp. 2901–2908, 2017.
- [3] Y. Wang, Y. F. Yi, C. H. Li, and J. Q. Han, "Anisotropic fracture and energy characteristics of a Tibet marble exposed to multi-level constant-amplitude (MLCA) cyclic loads: a lab-scale testing," *Engineering Fracture Mechanics*, vol. 244, p. 107550, 2021.
- [4] X. B. Yang, Y. P. Qin, and F. Ye, "Damage constitutive relation of sandstone considering residual stress," *Journal of China Coal Society*, vol. 40, no. 12, pp. 2807–2811, 2015.
- [5] Y. Wang, B. Zhang, B. Li, and C. H. Li, "A strain-based fatigue damage model for naturally fractured marble subjected to freeze-thaw and uniaxial cyclic loads," *International Journal of Damage Mechanics*, vol. 30, no. 10, pp. 1594–1616, 2021.
- [6] X. Q. Yuan, H. Y. Liu, and J. P. Liu, "3-D constitutive model for rock masses with non-persistent joints based on compound damage," *Chinese Journal of Geotechnical Engineering*, vol. 38, no. 1, pp. 91–99, 2016.
- [7] D. KRAJCINOVIC and M. A. G. SILVA, "Statistical aspects of the continuous damage theory," *International Journal of Solids and Structures*, vol. 18, no. 7, pp. 551–562, 1982.
- [8] J. B. Wang, Z. P. Song, B. Y. Zhao, X. R. Liu, J. Liu, and J. X. Lai, "A study on the mechanical behavior and statistical damage constitutive model of sandstone," *Arabian Journal for Science and Engineering*, vol. 43, no. 10, pp. 5179–5192, 2018.
- [9] G. Li and C. A. Tang, "A statistical meso-damage mechanical method for modeling trans-scale progressive failure process of rock," *International Journal of Rock Mechanics and Mining Sciences*, vol. 74, pp. 133–150, 2015.
- [10] L. L. Li, M. L. Xiao, L. Zhuo, Q. Yuan, and J. D. He, "Compound constitutive model considering damage evolution of non-persistent fractured rock mass," *Journal of Harbin Institute of Technology*, vol. 49, no. 6, pp. 96–101, 2017.
- [11] S. Chen, C. S. Qiao, Q. Ye, and B. Deng, "Composite damage constitutive model of rock mass with intermittent joints based on Mohr-Coulomb criterion," *Rock and Soil Mechanics*, vol. 39, no. 10, pp. 3612–3622, 2018.
- [12] W. B. Liu, S. G. Zhang, and B. Y. Sun, "Energy evolution of rock under different stress paths and establishment of a statistical damage model," *KSCSE Journal of Civil Engineering*, vol. 23, no. 10, pp. 4274–4287, 2019.
- [13] S. W. Zhou, C. C. Xia, H. B. Zhao, S. H. Mei, and Y. Zhou, "Statistical damage constitutive model for rocks subjected to cyclic stress and cyclic temperature," *Acta Geophysica*, vol. 65, no. 5, pp. 893–906, 2017.
- [14] T. C. Li, L. X. Lyu, S. L. Zhang, and J. C. Sun, "Development and application of a statistical constitutive model of damaged rock affected by the load-bearing capacity of damaged elements," *Journal of Zhejiang University Science A*, vol. 16, no. 8, pp. 644–655, 2015.
- [15] X. D. Zhang, J. Q. Cai, N. N. Tang, Q. W. Li, and C. Sun, "Experimental study on mechanical properties of deep sandstone and its constitutive model," *Journal of China Coal Society*, vol. 44, no. 7, pp. 2087–2093, 2019.
- [16] T. B. Li, M. B. Gao, G. Q. Chen et al., "A thermal-mechanical-damage constitutive model for hard brittle rocks and its preliminary application," *Chinese Journal of Geotechnical Engineering*, vol. 39, no. 8, pp. 1477–1484, 2017.
- [17] J. Deng and D. S. Gu, "On a statistical damage constitutive model for rock materials," *Computers & Geosciences*, vol. 37, no. 2, pp. 122–128, 2011.
- [18] C. Gao, L. Z. Xie, H. P. Xie et al., "Coupling between the statistical damage model and permeability variation in reservoir sandstone: theoretical analysis and verification," *Journal of Natural Gas Science and Engineering*, vol. 37, pp. 375–385, 2017.
- [19] M. B. Gao, T. B. Li, T. Wei, L. B. Meng, and M. Zhang, "A statistical constitutive model considering deterioration for brittle rocks under a coupled thermal-mechanical condition," *Geofluids*, vol. 2018, 10 pages, 2018.
- [20] J. B. Yan, Z. X. Zou, F. Wang, Q. Zhang, and T. Luo, "Statistical damage constitutive model of strain softening rock based on triple shear energy yield criterion," *Safety and Environmental Engineering*, vol. 27, no. 6, 2020.
- [21] J. L. Pan, Q. F. Guo, L. M. Tian, X. Wu, and M. Wang, "Study on rock statistical damage softening constitutive model and its parameters based on the unified strength theory," *Mining Research & Development*, vol. 39, no. 8, pp. 38–42, 2019.
- [22] Y. Zhang, L. D. Yang, and L. X. Xiong, "Study on the statistical model of rock damage based on twin shear unified failure criterion," *Journal of Hebei University of Engineering (Natural Science Edition)*, vol. 3, 2008.
- [23] Y. D. Zhang, H. Q. Xie, H. Z. Liu, M. L. Xiao, L. Zhuo, and J. D. He, "Compound damage constitutive model and evolution characteristics of intermittent joint rock mass under high stress conditions based on Hoek-Brown criterion," *Water Resources and Power*, vol. 39, no. 2, pp. 109–113, 2021.
- [24] R. L. Cao, S. H. He, J. Wei, and F. Wang, "Study of modified statistical damage softening constitutive model for rock considering residual strength," *Rock and Soil Mechanics*, vol. 34, no. 6, 2013.

- [25] M. Ismael and H. Konietzky, "Constitutive model for inherent anisotropic rocks: ubiquitous joint model based on the Hoek-Brown failure criterion," *Computers and Geotechnics*, vol. 105, pp. 99–109, 2019.
- [26] X. L. Xu, F. Gao, and Z. Z. Zhang, "Thermo-mechanical coupling damage constitutive model of rock based on the Hoek-Brown strength criterion," *International Journal of Damage Mechanics*, vol. 27, no. 8, pp. 1213–1230, 2017.
- [27] S. Q. Yang, B. Hu, and P. Xu, "Study on the damage-softening constitutive model of rock and experimental verification," *Acta Mechanica Sinica*, vol. 35, no. 4, pp. 786–798, 2019.
- [28] Standardization Administration of the People's Republic of China, *Standard for Test Method of Concrete Physical and Mechanical Properties: GB/T50081-2019*, China Building Industry Press, Beijing, 2019.
- [29] Standardization Administration of the People's Republic of China, *Standard for Test Method of Performance on Ordinary Fresh Concrete: GB/T50080-2016*, China Building Industry Press, Beijing, 2016.
- [30] J. Lemaitre, "A continuous damage mechanics model for ductile fracture," *Journal of Engineering Materials & Technology*, vol. 107, no. 1, pp. 83–89, 1985.

Research Article

Investigation of Dynamic Mechanical Properties of Coal after Freeze-Thaw Cyclic Conditions

Shuang Gong ^{1,2,3}, Wen Wang ^{1,3}, Furui Xi ^{4,5} and Wenlong Shen ^{1,3}

¹School of Energy Science and Engineering, Henan Polytechnic University, Jiaozuo 454000, China

²Henan Key Laboratory for Green and Efficient Mining & Comprehensive Utilization of Mineral Resources, Jiaozuo 454000, China

³Collaborative Innovation Center of Coal Work Safety, Henan Province, Jiaozuo 454000, China

⁴China Institute of Geo-Environment Monitoring, Beijing 100081, China

⁵Key Laboratory of Mine Ecological Effects and Systematic Restoration, Ministry of Nature Resource, Beijing 100081, China

Correspondence should be addressed to Wen Wang; wwang306@foxmail.com and Furui Xi; xifurui@mail.cgs.gov.cn

Received 9 September 2021; Accepted 7 October 2021; Published 28 October 2021

Academic Editor: Yu Wang

Copyright © 2021 Shuang Gong et al. This is an open access article distributed under the Creative Commons Attribution License, which permits unrestricted use, distribution, and reproduction in any medium, provided the original work is properly cited.

Due to the extensive excavation of the mine pit, a special frozen rock slope is formed, which transforms the permafrost (coal rock) of certain thickness in the frozen state to the melting state. To evaluate the dynamic mechanical properties and deformation characteristics of coal under cyclic freeze-thaw conditions, freeze-thaw experiments with different cycle times were conducted. And the mechanical properties of coal under quasistatic and dynamic conditions were investigated by using GCTS multifunctional rock mechanic experimental apparatus and SHPB dynamic loading apparatus, respectively. The results show that with the increase of freeze-thawing times, mass of both water-saturated and dried coal samples gradually decreased, the postpeak becomes gentler, and the specimens show ductile damage characteristics. The damage of the coal samples changed more after 30 freeze-thaw cycles, when deterioration of the coal samples was highest. The elastic modulus of the coal sample after freeze-thawing decreases continuously with the increase of the number of freeze-thaw cycles, and its trend decreases approximately linearly. Dynamic compressive strength of the coal samples decreases after freeze-thaw cycles, and this trend is consistent with the quasistatic loading conditions.

1. Introduction

With the decreasing amount of coal resources in China and the increasing energy demand year by year, several cities with depleted coal resources have emerged in the Middle East [1–3]. Coal resource development has been gradually extended to the northwest planning area, where several large open-pit coal mines are located in the high-altitude perennial permafrost zone. Due to the extensive excavation of the mine pit, a special frozen rock slope is formed, which transforms the permafrost (coal rock) of certain thickness in the frozen state to the melting state. With the change of temperature and the two-state cycle of freezing and melting, the nature of coal rock medium is also changing, thus, mak-

ing the frozen rock slope of open pit mine in high altitude permafrost area a special slope. The special characteristics of high-altitude areas are mainly manifested in two aspects: climatic conditions and stratigraphic conditions [4–6]. Wang et al. [7] investigate the fatigue mechanical characteristics of marble having different interbed orientation subjected to multilevel constant-amplitude (MLCA) cyclic loads. The experimental results reveal that the deformation, strength, lifetime, damping characteristics, and energy release and dissipation are all impacted by the interbed structure. The rock structural deterioration and damage accumulation were investigated as well as the stimulated natural fracture pattern. Results show the frost heaving force acted on natural fracture results in the rock volumetric

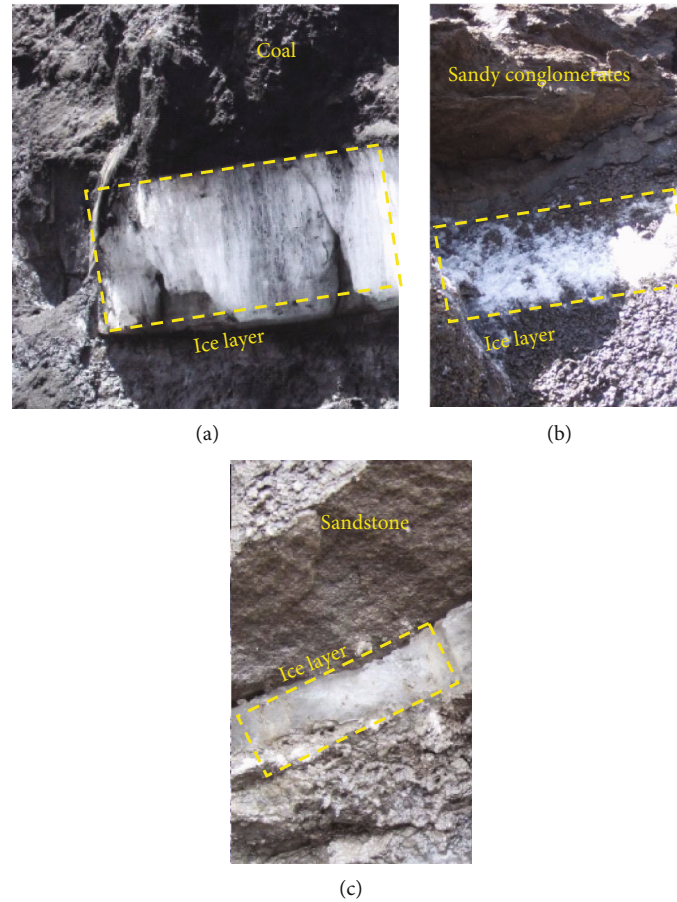


FIGURE 1: Picture of ice layer in coal and rock mass of open pit slope.

changes [8]. A typical open pit mine in Qinghai Province is taken as the study site, and the ice layer in its coal rock mass is shown in Figure 1.

The altitude of this area is above 4000 m. Spatially, it belongs to the high-altitude cold area of Qinghai-Tibet Plateau, and the surface water system is more developed. The annual and monthly temperature changes in the area are shown in Figure 2, from which it can be seen that the coal-field area has a large temperature difference and has the distinctive characteristics of an alpine area. In the high-altitude zone, due to the peculiarities of the natural environment, as shown in Figure 2, the slope is in the alternating state of above-zero and below-zero temperature for many years and months, and the surface water-saturated rock and structural surface of the slope are in the cyclic and repeated freezing and melting state. Due to the direct influence of atmospheric environment, the rock properties of frozen rock slopes of open pit mines in high altitude areas undergo unstable changes related to temperature and moisture, which is the essential difference between these slopes and those of conventional open pit mines.

The analysis of the evolution law of slope stability based on the changes of ambient temperature and moisture can more accurately describe the safety status and change trend of the slopes of open pit coal mines in high altitude areas. Appropriate safety protection can be carried out accordingly

to improve the safety of mining operations. There is a freezing period of more than half a year, the temperature starts to rise gradually in April, and the stratum starts to melt gradually. The high-temperature period is basically from June to September, during which the ground surface is in a state of ablation, and the strata gradually freeze from October. In addition, during most months, there is often a cycle of above- and below-zero temperatures within a day. The surface will undergo a phase cycle of melting and freezing. In the actual production process of open pit coal mine, there are external forces such as blasting, earthquake, excavation, and mechanical vibration. The slope structure of coal rock mass is disturbed by different degrees of dynamic loads, and there is a safety risk of instability [9–11]. The dynamic loading mode of coal rock under freeze-thaw damage conditions is a common phenomenon in current engineering practice. Therefore, the study of rock mechanical properties of freeze-thaw damaged rocks under dynamic loading form has important guiding significance and practical engineering application value, which can provide a reliable theoretical basis for the construction design and scheme optimization of related projects.

Many scholars have made a series of achievements in the research of rock freezing and thawing and introduced a series of modern means. Yang et al. [12] proposed the development direction of rock mass freeze-thaw multiscale

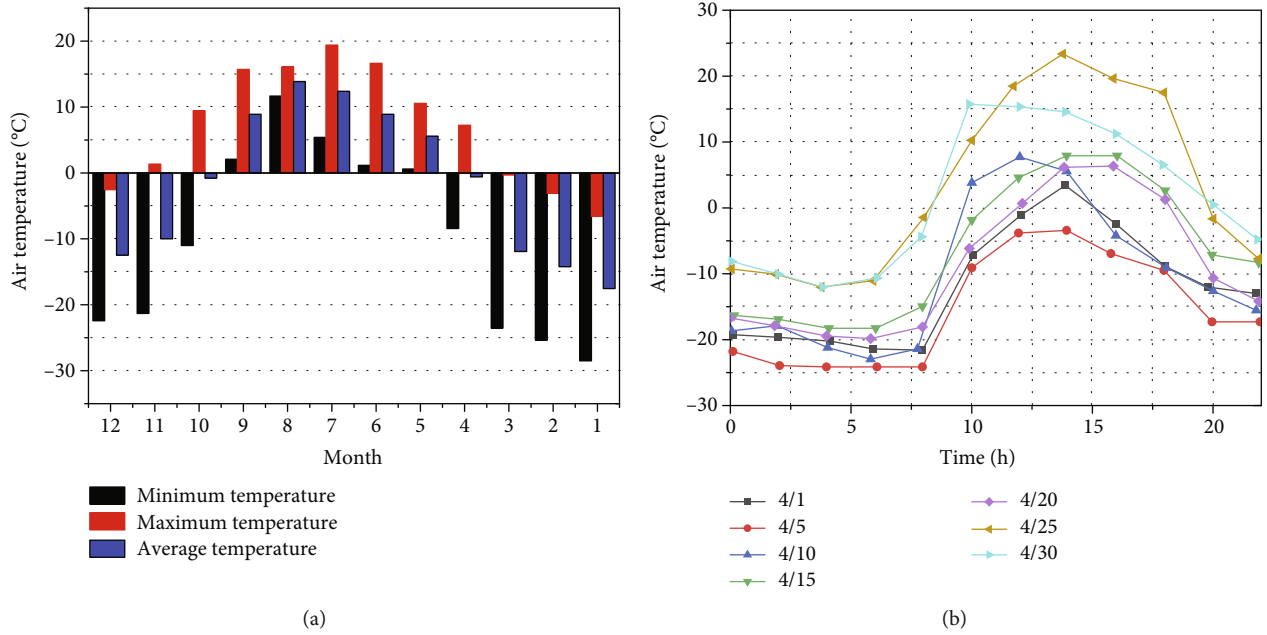


FIGURE 2: Variation law of annual and daily temperature in coalfield area where open-pit coal mine is located. (a) Variation law of temperature over the years. (b) Variation law of calendar day temperature.

damage identification and evaluation mechanism and preliminarily discussed the microfine macrocross-scale cognitive idea of rock mass damage induced by freeze-thaw. Xu et al. [13] established a theoretical model of rock freeze-thaw deterioration of sandstone samples selected from the slope of open-pit mine. Wen et al. [14] preliminarily discussed the engineering application of freezing and thawing rock test results. İsmailİnce [15] analyzed the microscopic images of frozen and thawed rocks. Fener [16] analyzed the porosity characteristic of rock and studied the polarizing microscope image. Khanlari and Abdilor and Park et al. [17, 18] analyzed the rock freeze-thaw damage qualitatively and quantitatively from the microscopic point of view by means of electron microscope scanning and CT scanning. Therefore, scholars generally pay attention to the laboratory tests of mechanical properties and freezing and thawing mechanism of freeze-thaw rocks.

The dynamic and static combined loading characteristics of frozen and thawed rock have developed rapidly in recent years. However, the research in this field is still in the development stage, and there is some relevant literature for reference. Wang et al. [19, 20] used the automatic freezing and thawing cycle system to freeze and thaw the red sandstone sample, and the visible cracks were generated after the rock freezing and thawing. Dynamic mechanical properties of rock sample before and after freezing and thawing were studied by using a one-dimensional SHPB device with a diameter of 100 mm, and the changes of the physical, static, and dynamic mechanical properties of the rock sample were analyzed. Zhou et al. [21] studied the changes of saturated porosity of rocks with different freeze-thaw cycles and made a subtle study by NMR technology. Wen et al. [22] conducted multiple freezing and thawing of granite porphyry samples, used one-dimensional SHPB experimental device

for impact loading, and analyzed the dynamic strength of rock samples with different freezing and thawing times under the same strain rate in combination with numerical simulation software.

At present, the design and protection theories of frozen rock slopes of open pit coal mines in high altitude areas are based on the theories of conventional open pit slopes. The research on the evolution of slope stability under the influence of multiple factors is carried out in a targeted manner, especially the mechanical characteristics of coal rock under the disturbance of external dynamic load after freeze-thaw cycles. The conclusion can complement the theory of stability of frozen rock slopes in open pit mines and provide theoretical basis for sound slope design and safety protection in special areas. Therefore, it is of great theoretical significance to study the mechanical properties and deformation characteristics of coal rock masses in open pit coal mines in cold regions under the combined effects of freeze-thaw cycles and dynamic load disturbances to ensure the safe mining of open pit coal mines.

2. Test Preparation

2.1. Sample Preparation. The coal samples were taken from Muli mine field, an open pit mine in the cold area of Northwest China. Muli mining area is located in northwest China, with mountains and valleys. Table 1 shows the industrial analysis parameters of coal samples. Calorific value of the coal sample is 6850 cal/g, the moisture content is 2.065%, the air-dry ash is 15.9, the dry basis ash is 6.083, and the vitrinite reflectance is 3.16. Table 2 shows the chemical composition. Nitrogen value is 0.795%, the carbon is 78.032%, the hydrogen is 2.851%, the oxygen is 1.169%, the sulphur is 0.43%, and the other elements are 16.723. The coal

TABLE 1: Industrial analysis parameters of coal samples.

Calorific value (cal/g)	Moisture (%)	Air dry ash	Dry basis ash	Vitrinite reflectance
6850	2.065	15.9	6.083	3.16

TABLE 2: Chemical composition of coal sample.

Nitrogen (%)	Carbon (%)	Hydrogen (%)	Oxygen (%)	Sulphur (%)	Other elements (%)
0.795	78.032	2.851	1.169	0.43	16.723

specimen is processed into a cylinder. Accuracy of specimen meets the requirements of the rock dynamic properties test procedure (T/CSRME001-2019). Ensure that the error of flatness of both ends of the specimen is not more than 0.05 mm. Loading displacement was set to 0.02 mm/s for the quasistatic condition, and the impact air pressure was set to 0.4 MPa for the dynamic impact test. Four freeze-thaw cycles (0, 10, 20, and 30) were set, and three coal rock specimens were set for each condition. The selected specimens were numbered.

The selected and numbered specimens were put into the water-saturated dish, and distilled water was injected into the water-saturated dish to submerge the specimens. The water-filled dish is continuously pumped with 0.1 MPa pressure for 4 h until no bubble overflows on the surface of the specimen and then soaked for more than 24 h to obtain the water-saturated specimen. The saturated specimen is put into the automatic low temperature freeze-thaw test chamber (temperature accuracy: $\pm 0.5^\circ\text{C}$; temperature range: $50^\circ\text{C} \sim -40^\circ\text{C}$) for freeze-thaw cycle test. Considering the historical minimum temperature of the sampling site and referring to the relevant specifications, the temperature was set to $-20^\circ\text{C} \sim 20^\circ\text{C}$. Each freeze-thaw cycle lasted 720 min, as shown in Figure 3.

2.2. Experimental System. The specimens that reached the freeze-thaw limited number of times were subjected to quasistatic and dynamic uniaxial compression tests, and the instruments used were the GCTS rock mechanics loading device and the $\Phi 50$ mm SHPB system, respectively, as shown in Figure 4.

3. Results and Discussion

3.1. Mechanical Properties of Coal after Freeze-Thaw Cycle. No macroscopic cracks were observed in the coal samples throughout the freeze-thawing process, and all of the coal samples showed surface particle exfoliation. The drying and water-saturated masses of the coal samples at different freeze-thaw times (0, 10, 20, and 30) are shown in Figure 5. With the increase of freeze-thawing times, the mass of both water-saturated and dried coal samples gradually decreased, and the decreasing trend was basically consistent. However, there is a slight difference in the degree of change

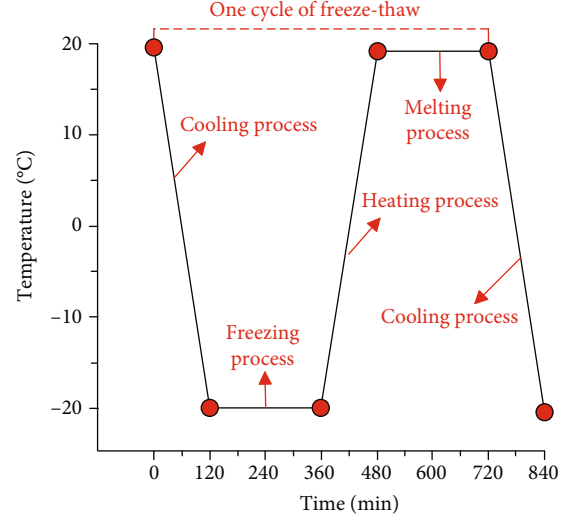


FIGURE 3: Temperature-time curve of freeze-thaw cycle.

between the two, which is due to the change in the degree of open fracture penetration caused by the formation and change of internal debris in the rock after different freeze-thawing times. Compared with the nonfreeze-thawed rock samples, the quality of the water-saturated rock samples decreased by 8.33% after 10 freeze-thaw cycles, 18.33% after 20 freeze-thaw cycles, and 33.33% after 30 freeze-thaw cycles. After each freeze-thaw cycle, the mass of rock samples decreased significantly, and the surface layer further spalling occurred significantly.

Typical stress-strain curves for coal samples subjected to 0, 10, 20, and 30 freeze-thaw cycles are shown in Figure 6. The peak strength of unfrozen-thawed specimens is the largest. With the increase of the number of freeze-thawing, the postpeak becomes gentler and specimens show ductile damage characteristics. The stress-strain curves before and after freeze-thawing can be divided into four stages, i.e., compression-density stage, elastic stage, crack development stage, and damage stage. With the increase of the number of freeze-thawing, compressive phase was significantly extended. In particular, the compressive stage of freeze-thawed samples with 20 times of freeze-thawing increased significantly compared with those without freeze-thawing. This indicates that the first 20 freeze-thaw cycles led to the significant development of microfractures inside the specimens.

The longitudinal wave velocity of rock is affected by various factors such as mineral composition, cement and condition, and porosity and structural form. The wave velocities of saturated rock samples and dried rock samples all decrease gradually with the increase of freeze-thawing times, mainly because the pores in the rock samples keep increasing with the increase of freeze-thawing times. The denseness of the rock sample decreases, and the voids are filled with water or air, which leads to the decrease of the longitudinal wave velocity after freeze-thawing because the velocity of longitudinal waves in water or air is much smaller than the propagation velocity in rock. Since the open pores of the rock sample are filled with water after the sample is full of



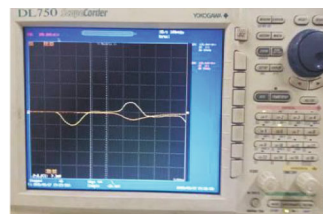
(a)



(b)



(c)



(d)

FIGURE 4: Continued.

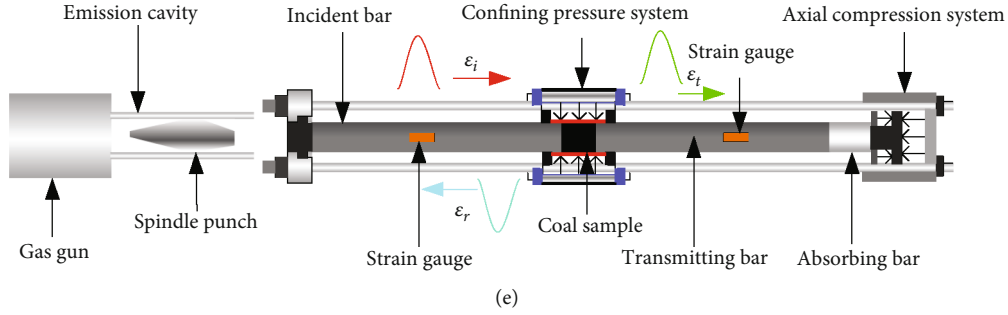


FIGURE 4: Rock mechanics loading device with different strain rate. (a) GCTS loading device. (b) Hopkinson bar dynamic loading device. (c) Spindle punch. (d) Sine wave waveform recording instrument. (e) Hopkinson bar.

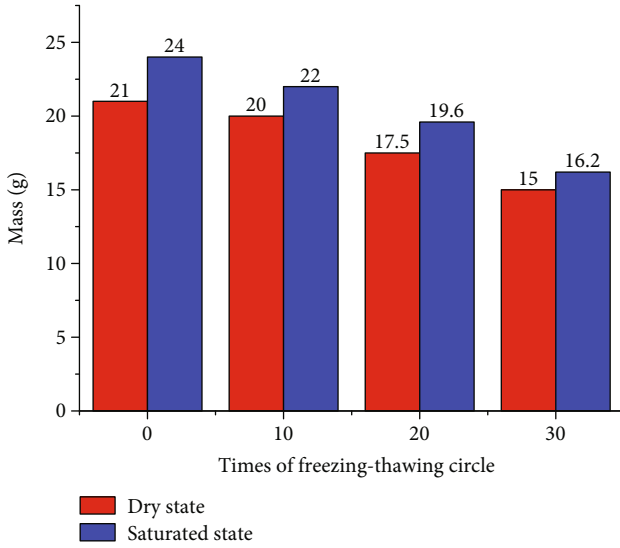


FIGURE 5: Histogram of the average mass of coal samples versus the number of freeze-thaws.

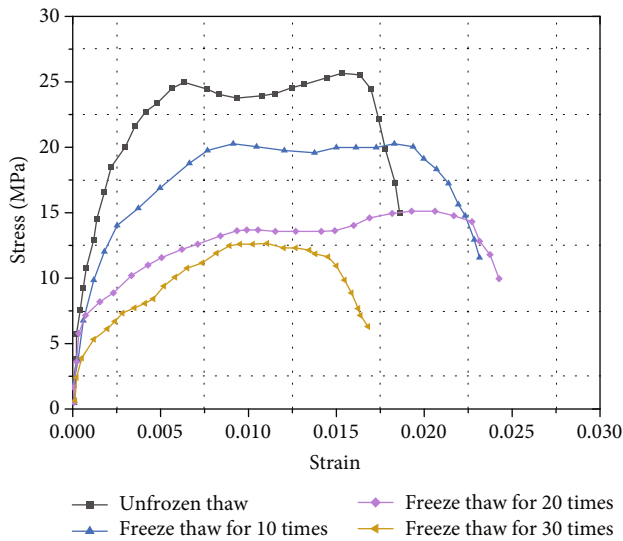


FIGURE 6: Average stress-strain curve of coal samples.

water, the wave speed of the water-saturated rock sample is slightly larger than that of the dry rock sample. Figure 7 shows the histogram of the average wave velocity of coal samples versus the number of freeze-thaws. It can be found that the wave velocities of saturated coal samples after freeze-thaw cycles are all lower than those in the dry state. The wave velocity of saturated coal samples decreased by 10.03% after 10 freeze-thaw cycles, 12.16% after 20 cycles, and 33.46% after 30 freeze-thaw cycles.

In general, the damage of the material can indirectly reflect the internal crack expansion characteristics. To further evaluate the damage to coal samples by freeze-thaw cycles, damage factor D was defined based on the variation of the wave velocity test values of the P -wave as follows:

$$D = 1 - \left(\frac{V_{PF}}{V_p} \right)^2, \quad (1)$$

where V_p is the wave velocity value before the freeze-thaw cycle of the coal sample, and V_{PF} is the wave velocity value after the freeze-thaw cycle.

Soviet scholar L.M. Kachanov first proposed the concept of damage. Solid materials in an unsuitable environment or mechanical action (such as temperature, external loading, and corrosion), the internal microscopic cracks, microscopic hole generation, convergence, and expansion will cause local deterioration of the material, known as the material damage. The damage of the material will cause the material strength, stiffness, and toughness decline and shorten the service life. In order to give a proper description of the material micro-structure change phenomenon, it is necessary to introduce the damage variable as an internal variable of the intrinsic structure relationship. Because the change of material structure is generally said to be irreversible, according to the thermodynamic point of view, the entropy of the material increases during the damage process, i.e., the damage occurs cumulatively, so the damage variable is not only an invisible internal variable but also an increasing quantity. Figure 8 shows the relationship between damage factors and freeze-thaw times of coal samples. As shown in Figure 8, the average values of damage factors for coal samples after 0, 10, 20, and 30 freeze-thaw cycles were 0, 0.21, 0.24, and 0.54, respectively. The damage of the coal samples changed more after 30 freeze-thaw cycles, when the deterioration of coal

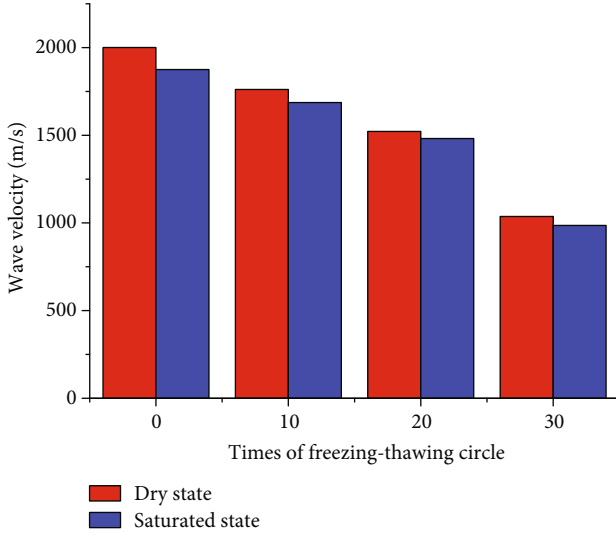


FIGURE 7: Histogram of the average wave velocity of coal samples versus the number of freeze-thaws.

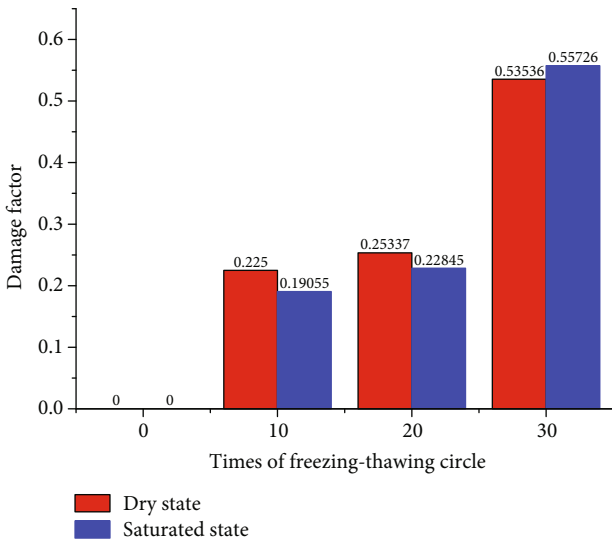


FIGURE 8: Relationship between damage factors and freeze-thaw times of coal samples.

samples was highest. Table 3 shows the change of porosity of coal samples tested by the NMR method, and it can be seen that the characteristics of the change of deterioration degree of coal samples reflected from the porosity are basically consistent with the damage factor.

3.2. Mechanical Properties of Coal after Freeze-Thaw Cycle under Dynamic Loading. In civil engineering construction, mining development, road construction, and other production fields, dynamic load is a factor that cannot be ignored. The physical and mechanical properties of slope rocks exposed to the air for a long time are changed after freeze-thaw damage. Due to the possible stress effect of the rock itself, it is also subjected to the impact of earthquake, blasting, landslide, etc. In-depth understanding of the impact

TABLE 3: Porosity of coal samples before and after freezing and thawing.

Group	Cycle freeze-thaw times	Porosity before freezing and thawing (%)	Porosity after freezing and thawing (%)
Group 1	0	3.97	3.97
Group 2	10	4.23	6.39
Group 3	20	4.15	10.85
Group 4	30	4.35	12.93

loads on freeze-thaw damaged rocks during the construction can avoid unnecessary losses. In order to ensure the safe production of open pit mines in cold regions, the study of their dynamical properties after freeze-thawing is particularly crucial.

Table 4 shows the mechanical parameters of coal samples after cyclic freezing and thawing. As shown in Figure 9, the elastic modulus of the coal sample after freeze-thawing decreases continuously with the increase of the number of freeze-thaw cycles, and its trend decreases approximately linearly. Moreover, the overall dispersion of the modulus of elasticity of the coal samples increases when the number of freeze-thaw cycles is 30. The elastic modulus of coal samples varied from 1.2 to 4.5 GPa within 30 freeze-thaw cycles. When the number of freeze-thaw cycles is lower than 20, the Poisson’s ratio of coal samples decreases continuously with the increasing number of cycles. However, when the number of cycles continued to increase to 30, the Poisson’s ratio increased to some extent. When the number of freeze-thaw cycles reached 20, the Poisson’s ratio of coal samples was the smallest. Figure 10 shows the relationship between dynamic compressive strength and freeze-thaw cycle times of coal samples after freeze-thaw. Dynamic compressive strength of the coal samples decreases after freeze-thaw cycles, and this trend is consistent with the quasistatic loading conditions.

The fitted functions between the mechanical parameters (modulus of elasticity, Poisson’s ratio, and dynamic compressive strength) of the coal samples after freeze-thaw cycles and the number of cycles are as follows:

$$E = 4.369 \times 0.978^N, \quad R^2 = 0.83, \quad (2)$$

$$\nu = 0.397 - 0.011N + 6.667N^2 + 7.222, \quad R^2 = 0.85, \quad (3)$$

$$\sigma_{ct} = 61.162 \times 0.951^N, \quad R^2 = 0.95. \quad (4)$$

Rocks are aggregates of mineral particles cemented together with various complex forms of cracks, holes, and other defects inside. During the freeze-thaw cycle, more holes and small cracks expand under the action of water-ice phase change. At the same time, the mineral particles are deformed by the temperature stress, and the different

TABLE 4: Mechanical parameters of coal samples after cyclic freezing and thawing.

Cycle freeze-thaw times	Sample	Diameter (mm)	Height (mm)	Dynamic UCS (MPa)	Elastic modulus (GPa)	Poisson's ratio
0	F1	49.6	99.87	57.35	4.45	0.42
	F2	49.7	101.10	64.50	4.28	0.40
	F3	49.6	99.78	57.53	4.38	0.37
	F4	49.8	99.45	40.42	3.54	0.32
10	F5	49.5	99.86	41.56	3.56	0.29
	F6	49.7	100.35	38.56	3.38	0.28
	F7	49.6	99.87	27.65	2.91	0.25
20	F8	49.8	98.78	24.68	2.85	0.27
	F9	49.6	98.69	18.65	2.70	0.24
	F10	49.6	99.53	8.56	1.32	0.28
30	F11	49.8	101.20	7.69	2.56	0.32
	F12	49.7	100.52	12.89	2.84	0.33

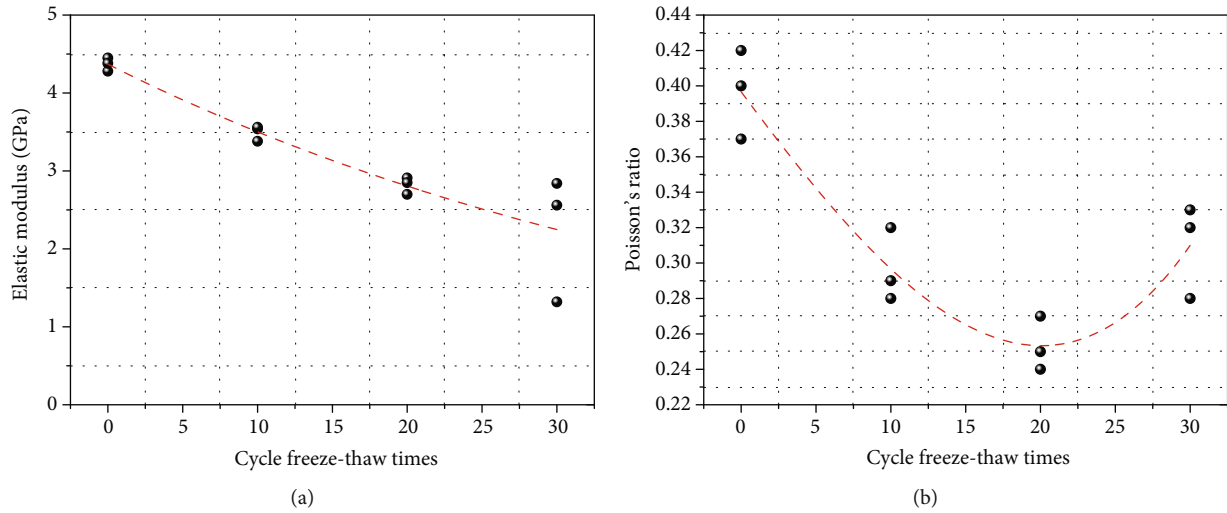


FIGURE 9: Relationship between deformation parameters and freeze-thaw cycles of coal samples. (a) Dynamic uniaxial compressive strength. (b) Poisson's ratio.

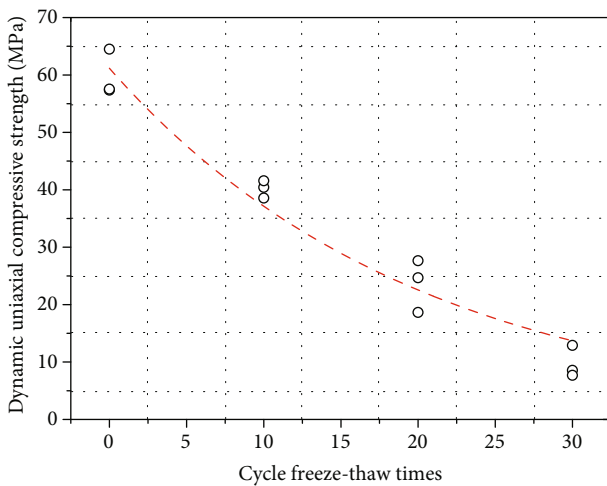


FIGURE 10: Relationship between dynamic UCS and freeze-thaw cycle times of coal samples after freeze-thaw.

expansion coefficients lead to the uncoordinated deformation of different mineral particles. This leads to the expansion and accumulation of primary cracks, the initial state of the interparticle interface is destroyed, and even particle freeze-thaw damage. As a result, more debris is formed around the mineral particle interface, resulting in the loss of macroscopic freeze-thaw integrity of the rock, which is an important reason for freeze-thaw damage to occur in coal with low water content. The degree of crack extension and connectivity varies at different freeze-thaw stages. This leads to different degrees of degradation of physical and mechanical properties of coal samples after freeze-thaw cycles. The coal sample is saturated with water, and the microscopic observation of crumb-like material is more abundant. During the freeze-thaw process, the temperature stress is concentrated inside the rock, and the freeze-thaw cycle causes greater structural damage to the coal samples. This causes greater damage and destruction of coal samples, and therefore, this type of coal rock has poor freeze-thaw resistance.

4. Conclusions

- (a) With the increase of freeze-thawing times, the mass of both water-saturated and dried coal samples gradually decreased, and the decreasing trend was basically consistent. However, there is a slight difference in the degree of change between the two, which is due to the change in the degree of open fracture penetration caused by the formation and change of internal debris in the rock after different freeze-thawing times. Compared with the nonfreeze-thawed rock samples, the quality of the water-saturated rock samples decreased by 8.33% after 10 freeze-thaw cycles, 18.33% after 20 freeze-thaw cycles, and 33.33% after 30 freeze-thaw cycles
- (b) The peak strength of the unfrozen-thawed specimens is the largest. With the increase of the number of freeze-thawing, the postpeak becomes gentler, and the specimens show ductile damage characteristics. The stress-strain curves of the specimens before and after freeze-thawing can be divided into four stages, i.e., compression-density stage, elastic stage, crack development stage, and damage stage. In particular, the compressive stage of freeze-thawed samples with 20 times of freeze-thawing increased significantly compared with those without freeze-thawing. This indicates that the first 20 freeze-thaw cycles led to the significant development of microfractures inside the specimens
- (c) The wave velocities of saturated coal samples after freeze-thaw cycles are all lower than those in the dry state. The wave velocity of saturated coal samples decreased by 10.03% after 10 freeze-thaw cycles, 12.16% after 20 cycles, and 33.46% after 30 freeze-thaw cycles. The damage of the coal samples changed more after 30 freeze-thaw cycles, when the deterioration of the coal samples was the highest
- (d) The elastic modulus of the coal sample after freeze-thawing decreases continuously with the increase of the number of freeze-thaw cycles, and its trend decreases approximately linearly. Moreover, the overall dispersion of the modulus of elasticity of the coal samples increases when the number of freeze-thaw cycles is 30. The dynamic compressive strength of the coal samples decreases after freeze-thaw cycles, and this trend is consistent with the quasistatic loading conditions

Data Availability

Some or all data, models, or code that support the findings of this study are available from the corresponding author upon reasonable request.

Conflicts of Interest

The authors declare that they have no conflicts of interest.

Acknowledgments

This work was financially supported by the Fundamental Research Funds for the Universities of Henan Province (Grant no. NSFRF200332), Key Research and Development and Promotion of Special (Science and Technology) Project of Henan Province (nos. 212102310379 and 202102310542), National Natural Science Foundation of China (nos. 41907402 and 51604093), the research fund of Henan Key Laboratory for Green and Efficient Mining & Comprehensive Utilization of Mineral Resources (Henan Polytechnic University) (no. KCF201804), the Key Scientific Research Project Fund of Colleges and Universities in Henan Province (no. 21A610005 and no. 20B440001), and the Doctoral Foundation of Henan Polytechnic University (no. B2019-22). All support is greatly appreciated.

References

- [1] H. Xie, Y. Ju, M. Gao et al., "Theories and technologies for in-situ fluidized mining of deep underground coal resources," *Journal of China Coal Society*, vol. 43, no. 5, pp. 1210–1219, 2018.
- [2] W. Shen, G. Shi, Y. Wang, J. Bai, R. Zhang, and X. Wang, "Tomography of the dynamic stress coefficient for stress wave prediction in sedimentary rock layer under the mining additional stress," *International Journal of Mining Science and Technology*, vol. 31, no. 4, pp. 653–663, 2021.
- [3] S. Gong, L. Zhou, Z. Wang, and W. Wang, "Effect of bedding structure on the energy dissipation characteristics of dynamic tensile fracture for water-saturated coal," *Geofluids*, vol. 2021, Article ID 5592672, 10 pages, 2021.
- [4] N. Kivekäs, J. Sun, M. Zhan et al., "Long term particle size distribution measurements at Mount Waliguan, a high-altitude site in inland China," *Atmospheric Chemistry and Physics*, vol. 9, no. 15, pp. 5461–5474, 2009.
- [5] S. Gong, "Investigation of tensile and fracture mechanical properties of bituminous coal at different strain rates," *Journal of Materials Research and Technology*, vol. 15, pp. 834–845, 2021.
- [6] Y. L. Duan, G. Bellis, L. Li et al., "Potential vectors of bluetongue virus in high altitude areas of Yunnan Province, China," *Parasites & Vectors*, vol. 12, no. 1, pp. 1–11, 2019.
- [7] Y. Wang, Y. F. Yi, C. H. Li, and J. Q. Han, "Anisotropic fracture and energy characteristics of a Tibet marble exposed to multi-level constant-amplitude (MLCA) cyclic loads: a lab-scale testing," *Engineering Fracture Mechanics*, vol. 244, p. 107550, 2021.
- [8] Y. Wang, B. Zhang, B. Li, and C. H. Li, "A strain-based fatigue damage model for naturally fractured marble subjected to freeze-thaw and uniaxial cyclic loads," *International Journal of Damage Mechanics*, vol. 10567895211021629, p. 105678952110216, 2021.
- [9] G. Liu, D. Song, Z. Chen, and J. W. Yang, "Dynamic response characteristics and failure mechanism of coal slopes with weak intercalated layers under blasting loads," *Advances in Civil Engineering*, vol. 2020, 18 pages, 2020.
- [10] Z. Li, S. Yu, W. Zhu et al., "Dynamic loading induced by the instability of voussoir beam structure during mining below the slope," *International Journal of Rock Mechanics and Mining Sciences*, vol. 132, p. 104343, 2020.

- [11] D. Deb, K. N. R. Kaushik, B. H. Choi, C. H. Ryu, Y. B. Jung, and C. Sunwoo, "Stability assessment of a pit slope under blast loading: a case study of Pasir coal mine," *Geotechnical and Geological Engineering*, vol. 29, no. 4, pp. 419–429, 2011.
- [12] G. Yang, Y. Shen, H. Jia, R. Wei, H. Zhang, and H. Liu, "Research progress and tendency in characteristics of multi-scale damage mechanics of rock under freezing-thawing," *Chinese Journal of Rock Mechanics and Engineering*, vol. 37, no. 3, pp. 545–563, 2017.
- [13] S. Xu, N. Li, X. Wang et al., "Damage test and degradation model of saturated sandstone due to cyclic freezing and thawing of rock slopes of open-pit coal mine," *Chinese Journal of Rock Mechanics and Engineering*, vol. 35, no. 12, pp. 2561–2571, 2016.
- [14] L. Wen, X. Li, H. Tang, and L. Weng, "Study of physico-mechanical characteristics of rock under different frozen-thawed circle temperature range and its engineering application," *Engineering Mechanics*, vol. 34, no. 5, pp. 247–256, 2017.
- [15] İ. İnce and M. Fener, "A prediction model for uniaxial compressive strength of deteriorated pyroclastic rocks due to freeze-thaw cycle," *Journal of African Earth Sciences*, vol. 120, pp. 134–140, 2016.
- [16] M. Fener and İ. İnce, "Effects of the freeze-thaw (F-T) cycle on the andesitic rocks (Sille- Konya/Turkey) used in construction building," *Journal of African Earth Sciences*, vol. 109, pp. 96–106, 2015.
- [17] G. Khanlari and Y. Abdilor, "Influence of wet–dry, freeze–thaw, and heat–cool cycles on the physical and mechanical properties of Upper Red sandstones in Central Iran," *Bulletin of Engineering Geology and the Environment*, vol. 74, no. 4, pp. 1287–1300, 2015.
- [18] J. Park, C. U. Hyun, and H. D. Park, "Changes in microstructure and physical properties of rocks caused by artificial freeze–thaw action," *Bulletin of Engineering Geology and the Environment*, vol. 74, no. 2, pp. 555–565, 2015.
- [19] P. Wang, J. Xu, S. Liu, H. Wang, and S. Liu, "Static and dynamic mechanical properties of sedimentary rock after freeze-thaw or thermal shock weathering," *Engineering Geology*, vol. 210, pp. 148–157, 2016.
- [20] P. Wang, J. Xu, S. Liu, S. Liu, and H. Wang, "A prediction model for the dynamic mechanical degradation of sedimentary rock after a long-term freeze-thaw weathering: considering the strain-rate effect," *Cold Regions Science and Technology*, vol. 131, pp. 16–23, 2016.
- [21] K. P. Zhou, B. Li, J. L. Li, H. W. Deng, and F. Bin, "Microscopic damage and dynamic mechanical properties of rock under freeze-thaw environment," *Transactions of Nonferrous Metals Society of China*, vol. 25, no. 4, pp. 1254–1261, 2015.
- [22] L. Wen, X. Li, Y. Yin, and L. Gao, "Study of physico-mechanical properties of granite porphyry and limestone in slopes of open-pit metal mine under freezing-thawing cycles and their application," *Journal of Glaciology and Geocryology*, vol. 36, no. 3, pp. 632–639, 2014.

Research Article

Freeze-Thaw Effects on Stability of Open Pit Slope in High-Altitude and Cold Regions

Yong Hong,¹ Zhushan Shao ,¹ Guangbin Shi,¹ Yong Dou,² Weiqin Wang,¹ and Wen Zhang¹

¹*Xi'an University of Architecture and Technology, Xi'an, Shaanxi 710055, China*

²*China Coal Xi'an Design Engineering Co., Ltd., Xi'an, Shaanxi 710055, China*

Correspondence should be addressed to Zhushan Shao; shaozhushan@xauat.edu.cn

Received 23 August 2021; Revised 28 September 2021; Accepted 4 October 2021; Published 27 October 2021

Academic Editor: Yu Wang

Copyright © 2021 Yong Hong et al. This is an open access article distributed under the Creative Commons Attribution License, which permits unrestricted use, distribution, and reproduction in any medium, provided the original work is properly cited.

The cycle of the freeze-thaw action must be taken into account in the stability analysis of an open pit slope in the high-altitude and cold regions, because the natural process of freeze-thaw poses a significant effect on mechanical properties of the rock mass. To achieve this purpose, a linear relationship between the geological strength index (GSI) and the Tianshan slope rock mass rating (TSMR) system is established considering the effect of the freeze-thaw action by introducing a freeze-thaw correction coefficient δ . The GSI value is modified for rock mass in high-altitude and cold regions. The improved Hoek-Brown criterion considers the influences of the freeze-thaw action and steep and gentle slopes. The research outcome is applied in the No. 4 minefield open pit coal mine in the Muli mining area. Numerical calculations are performed by inputting rock mass mechanical parameters obtained in traditional and modified criteria, to discuss the influences of the freeze-thaw action on the stabilities of both the present mining slope and the final slope at the end of the designed mining. The results show that the safety factors of the original slope are 2.33 and 1.67, respectively, while after the modification, they are 2.14 and 1.61, respectively. In terms of the No. 4 minefield open pit coal mine, the slope stability meets the design requirement, although taking the freeze-thaw cycle into account.

1. Introduction

Slope stability analysis has always been one of the basic problems in the field of geotechnical engineering. At present, some fruitful results have been achieved in the analysis of slope stability under normal temperature [1]. However, the research of rock slope stability under freeze-thaw cycles in cold regions is still in its infancy [2]. The freeze-thaw cycle normally causes the deterioration of mechanical properties of the rock mass [3–5], thus leading to slope instability. It is an urgent task to study the influence of the freeze-thaw action on rock slope stability.

Reasonable determination of rock mass mechanical parameters is the basis of slope stability analysis and slope treatment, and it is also one of the difficulties in rock mechanics research and development [6]. At present, many methods have been widely used to determine rock mechan-

ical parameters [7–17]. Practice has proven that when rock mechanical parameters are modified and converted into rock mass mechanical parameters, the results could better meet the engineering needs [17]. Such modification is based on laboratory rock experiments and tests and by taking a comprehensive list of factors into account such as the types and characteristics of rock structural planes, stress state, rock disturbance, size effect, and groundwater. The Hoek-Brown criterion as a typical example has attracted wide attention from both academia and engineering geological fields, and it has been widely applied as well. Currently, it has become one of the most recommended methods by the International Society for Rock Mechanics and Rock Engineering (ISRM) [17–21].

The Hoek-Brown criterion could reflect the intrinsic and nonlinear failure characteristics of the rock and rock mass as well as the influence that the structural plane and stress state



FIGURE 1: Location of the area under study.

exert on rock mass strength. It could also be used to explain the influence of the low stress zone, tension stress zone, and minimum principal stress on rock mass strength. In addition to the above, it can be extended to the description of the fractured rock mass and anisotropic rock mass. The latest edition is the generalized Hoek-Brown strength criterion [18, 21], which was proposed in 2002. In its expression, the disturbance factor D which considers the effect of stress relaxation and near blast damage is introduced, and a parameter selection method based on the geological strength index (GSI) is proposed. The Hoek-Brown strength criterion is empirical. Determining the two parameters is crucially significant for selecting rock mass strength parameters. Hence, many scholars have carried out in-depth analysis and research on the values of D and GSI [22, 23].

The freeze-thaw action causes damage to rocks and thus is not conducive to the stability of the rock slope. Under the action of freeze-thaw cycles, the rock mass undergoes freeze-thaw damage and its strength decreases. Especially for the fractured rock mass containing water, water-ice phase transformation occurs at low temperature. As the ice body grows and volume expands, tensile stress occurs around the pore and at the tip of the fracture, which causes rock mass frost heave and cracking. Recurrent freeze-thaw weakens the integrity and strength index of the rock mass. When the Hoek-Brown criterion is used to determine rock mass parameters, the effect of freeze-thaw cycles on GSI must be considered. At present, the experimental method is a major one applied to study the physical and mechanical properties of rock mass in cold regions. According to this method, the effects of freeze-thaw cycles on the physical and mechanical parameters of the rock mass under different conditions have been discussed. However, the problem remains unsolved regarding how to determine the mechanical parameters of the rock mass based on the experimental results.

This paper establishes the relationship between GSI and TSMR and presents an improved Hoek-Brown criterion. The proposed theoretical analysis is applied in an engineering case, well demonstrating the influence of freeze-thaw cycles on the slope stability. The outcome of this research is useful for the slope design of similar projects.

TABLE 1: Rock strength parameters after freeze-thaw tests.

Number of freeze-thaw cycles	Average saturated compressive strength (MPa)		
	Coarse sandstone	Fine sandstone	Muddy siltstone
0	104.1	114.8	89.6
30	90.1	98.8	73.1
60	83.9	86.7	58.7
90	74.2	79.6	50.1
120	64.4	72.3	42.3

TABLE 2: Freeze-thaw coefficients of rock samples.

Number of freeze-thaw cycles	Average saturated compressive strength (MPa)		
	Coarse sandstone	Fine sandstone	Muddy siltstone
0	1	1	1
30	0.87	0.95	0.82
60	0.81	0.76	0.66
90	0.71	0.69	0.56
120	0.62	0.63	0.47

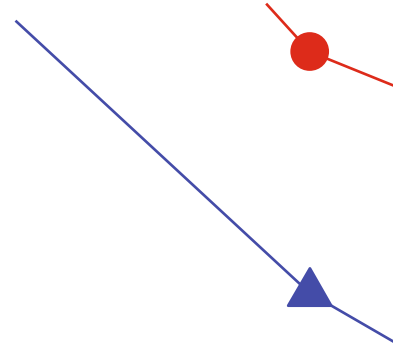


FIGURE 2: Relationship between freeze-thaw coefficients and freeze-thaw cycle times.

2. Quality Evaluation of Rock Mass Slope in Cold Regions

The No. 4 Minefield open pit coal mine is located in the Juhugeng Coal Mine Area in the Northeast of Qinghai Province. It is part of the Qinghai-Tibet Plateau. Its approximate location is shown in Figure 1. The highest altitude in the area is 4083.20 m, and the lowest altitude is 3814.30 m. The lowest temperature is mainly in January to February and the lowest recorded temperature is -36°C , whereas the highest temperature is in July to August with the highest recorded temperature of 19.8°C . The annual average temperature is -4°C and the annual average ground temperature is -1.0°C to -3.5°C . Surface water freezes from October and thaws until April next year; as a result, it is below 0°C for nearly six months every year. The maximum seasonal freezing depth of the Muli mining area is about 8.25 m. Because the

TABLE 3: Corresponding relationship between rock uniaxial compressive strength, rock hardness, and rock freeze-thaw correction coefficients.

Rock uniaxial compressive strength	$R_c > 60$ MPa	$30 \text{ MPa} < R_c \leq 60 \text{ MPa}$	$15 \text{ MPa} < R_c \leq 30 \text{ MPa}$	$5 \text{ MPa} < R_c \leq 15 \text{ MPa}$	$R_c \leq 5 \text{ MPa}$
Rock types	Hard rock	Relatively hard rock	Relatively soft rock	Soft rock	Special soft rock
Freeze-thaw correction coefficients (δ)	≥ 0.9	0.7-0.9	0.5-0.7	0.2-0.5	≤ 0.2

TABLE 4: Freeze-thaw correction coefficients of rock mass in Muli mining area.

Lithology	Freeze-thaw correction coefficient
Coarse sandstone	0.9
Fine sandstone	0.85
Muddy siltstone	0.7

coal mine is located in the permafrost area of the Qinghai-Tibet Plateau, the influence of freeze-thaw action on open pit slope stability must be considered.

2.1. Freeze-Thaw Coefficient. At present, the relevant regulations and standards about freeze-thaw tests in China are as follows: *Rock Test Rules for Water Conservancy and Hydropower Engineering* (SL264-2001), *Rock Test Rules for Highway Engineering* (JTGE41-2005), and *Engineering Rock Test Method Standard* (GBT 50266-2013). However, these codes and standards do not provide fully unified standards for the operation and requirements of freeze-thaw experiments, and due to lack of consistent understanding of freeze-thaw experiments at the international level, even the ISRM recommended standards for rock experiments are no exception.

According to the geological investigation report and the temperature variation pattern in the Muli mining area, the freeze-thaw cycling experiments were carried out with coarse sandstone, fine sandstone, and muddy siltstone as representative rock samples. The samples were set to freeze at -25°C for 8 hours in a cryogenic refrigerator before being taken out. Lukewarm water would then be injected into the test box and the water temperature was kept at 25°C for 8 hours for sample thawing. The rock uniaxial compressive strength was measured after the freeze-thaw cycle times were set at 0, 30, 60, 90, and 120. The experimental results are as shown in Table 1 [24, 25].

The definition of the rock freeze-thaw coefficient is consistent in the preceding specification standards. In this paper, the definition of the freeze-thaw coefficient is quoted from the *Engineering Rock Mass Test Method Standard* (GBT 50266-2013):

$$K_{fm} = \frac{\bar{R}_{fm}}{\bar{R}_w}, \quad (1)$$

where K_{fm} is the freeze-thaw coefficient of rock samples, \bar{R}_{fm} is the average rock saturated uniaxial compressive strength after freeze-thaw cycles, and \bar{R}_w is the average rock

saturated uniaxial compressive strength before freeze-thaw cycle tests. The freeze-thaw coefficient of rock samples can be obtained as shown in Table 2.

Table 2 shows that as the number of freeze-thaw cycle times increases; the freeze-thaw coefficients of the three kinds of rock samples gradually decreased to quite a different extent, which can also be seen from Figure 2. As a matter of fact, the freeze-thaw coefficients reflect the sensitivity of different rocks to freeze-thaw action. Specifically, the coefficient reduction of muddy siltstone is the largest, followed by coarse sandstone and fine sandstone. Since the influence of freeze-thaw action on rock mass quality is not limited to a single factor, it is necessary to modify the whole evaluation system before the introduction of the freeze-thaw coefficient. Therefore, the correction coefficient δ of rock freeze-thaw action is introduced to evaluate the influence of freeze-thaw action on rock mass quality. The quantification of the correction coefficients is mainly based on some existing rock freeze-thaw coefficient data. In addition, the hardness of rock mass, in combination with experience and field investigation, should also be considered.

The relationship between rock hardness, uniaxial compressive strength, and freeze-thaw correction coefficient is shown in Table 3. Combined with joint fissure investigation and uniaxial compression, the results suggest that coarse sandstone is hard rock and fine sandstone and muddy siltstone are relatively hard rock. The freeze-thaw correction coefficients are shown in Table 4.

2.2. Quality Classification of Slope Rock Mass. So far, many empirical rock mass quality classification systems have been put forward around the world. Some of them are directly or indirectly used in slope rock mass such as Q, RMR, MRMR, SMR, M-RMR, SRMR, and CSMR [26]. At present, there are still no relevant standard operational procedures and evaluation systems for slope engineering rock mass in open pit mines with high-altitude and cold conditions. The CSMR evaluation system introduces a height correction coefficient and structural plane correction coefficient, which are suitable for high slopes where hydropower projects are constructed. On this basis, Zhang et al. [27] introduced the freeze-thaw coefficient and established the rock mass quality evaluation system TSMR, which is suitable for highway slope engineering in a cold and high-altitude environment. Luo et al. [28], based on the TSMR evaluation system, analyzed the slope stability in the Mengku Iron Mine. No.4 minfield open pit mine in the Muli mining area which is located in high-altitude and cold areas, which meets the application conditions of the TSMR evaluation system. Hence, TSMR

TABLE 5: Adjustment values of occurrence on discontinuous planes in Muli mining area.

Condition	Very favorable	Favorable	Ordinary	Unfavorable	Very unfavorable	
Plane failure	$ \alpha_j - \alpha_s $	$>30^\circ$	$30^\circ-20^\circ$	$20^\circ-10^\circ$	$10^\circ-5^\circ$	$<5^\circ$
	$ \alpha_j - \alpha_s - 180^\circ $					
	F_1	0.15	0.4	0.70	0.85	1.00
Plane failure	$ \beta_j $	$<20^\circ$	$20^\circ-30^\circ$	$30^\circ-35^\circ$	$35^\circ-45^\circ$	$>45^\circ$
	F_2	0.15	0.4	0.70	0.85	1.00
Plane failure	$\beta_j - \beta_s$	$>10^\circ$	$10^\circ-0^\circ$	0°	$0^\circ-10^\circ$	$<-10^\circ$
	F_3	0	6	10	25	30

Note: α_j : discontinuous plane inclination; α_s : slope inclination; β_j : discontinuous plane angle; β_s : slope angle.

TABLE 6: TSMR values of slope rock mass in Muli mining area.

Lithology	TSMR values
Coarse sandstone	56
Fine sandstone	58
Muddy siltstone	50

TABLE 7: GSI values of slope rock mass in Muli mining area.

Lithology	GSI
Coarse sandstone	51
Fine sandstone	53
Muddy siltstone	45

is used herein to evaluate the rock mass quality in the No. 4 minefield open pit mine. The TSMR expression is as follows:

$$\text{TSMR} = \delta\xi\text{RMR} - \lambda(F_1F_2F_3) + F_4, \quad (2)$$

where δ and ξ are the freeze-thaw correction coefficient and slope height correction coefficient, respectively; $\xi = 0.57 + 0.43(H_r/H)$, where $H_r = 80$ m and H is the slope height; λ is the structural plane condition coefficient, and a geological report shows that there are faults in the mining area and $\lambda = 1$; F_1 refers to the adjustment value of the dip direction between discontinuity and the slope surface; F_2 is the adjustment value of the dip angle of discontinuities; and F_3 is the adjustment value of the dip angle between discontinuity and the slope surface. The values of F_1 , F_2 , and F_3 are shown in Table 5. $F_4 = 10$ which is the adjustment factor of slope excavation and can be obtained through engineering practice experience and pre-splitting blasting. Based on Equation (2) and the correction of slope parameters, the TSMR calculation results of the slope rock mass are shown in Table 6.

3. Rock Mass Quality Parameters of Open Pit Slope

Since Hoek-Brown failure criterion was put forward in 1980 by E. Hoek and E. T. Brown, it has been widely applied in

the field of rock mass engineering, and a series of practical engineering problems have been solved. At the same time, it has also attracted more scholars to conduct theoretical discussion. The latest version is expressed as follows [20]:

$$\sigma_1 = \sigma_3 + \sigma_c \left(m_b \frac{\sigma_3}{\sigma_c} + s \right)^a, \quad (3)$$

$$m_b = m_i \exp \left(\frac{\text{GSI} - 100}{28 - 14D} \right), \quad (4)$$

$$s = \exp \left(\frac{\text{GSI} - 100}{9 - 3D} \right), \quad (5)$$

$$a = \frac{1}{2} + \frac{1}{6} \left(e^{-\text{GSI}/15} - e^{-20/3} \right), \quad (6)$$

where σ_1 and σ_3 are the major and minor principal stresses, respectively; σ_c is the uniaxial compressive strength of the intact rock; m_b , s , and a are the empirical parameters reflecting rock mass characteristics; the value of m_i is 13, 15, and 5 for coarse sandstone, fine sandstone, and muddy siltstone, respectively; D is the disturbance factor, which is related to the rock mass excavation mode and disturbance degree. The research object herein is located in a large open pit coal mine and is excavated by blasting, so $D = 1$; GSI is the geological strength index for short. With regard to the determination of the GSI value, Hoek, Kaiser, and Brown established the relationship between the GSI and RMR values, namely,

$$\text{GSI} = \text{RMR}_{76}, \text{RMR}_{76} > 18, \quad (7)$$

$$\text{GSI} = \text{RMR}_{89} - 5, \text{RMR}_{89} > 23, \quad (8)$$

where RMR_{76} and RMR_{89} are rock mass classification systems established by Bieniawski in 1976 and 1989, respectively. Based on the RMR system, TSMR is a rock mass quality evaluation method that takes into account the freeze-thaw behavior, rock mass structure, and slope height. Therefore, for rock mass slope engineering in cold and high-altitude regions, the GSI value can be expressed as follows:

$$\text{GSI} = \text{TSMR}_{76}, \text{TSMR}_{76} > 18, \quad (9)$$

TABLE 8: Strength parameters of rock mass on No. 4 minefield slope under freeze-thaw environment.

Lithology	Internal friction angle φ ($^\circ$)		Cohesion c (MPa)		Poisson ratio	Deformation modulus E (GPa)	Unit weight (kN/m ³)
	Improved Hoek-Brown criterion	RocLab	Improved Hoek-Brown criterion	RocLab			
Coarse sandstone	44.5	37.8	0.412	0.669	0.17	5.25	26.89
Fine sandstone	49.9	42.1	0.259	0.436	0.20	4.89	26.39
Muddy siltstone	36.9	22.8	0.249	0.270	0.19	2.66	26.59

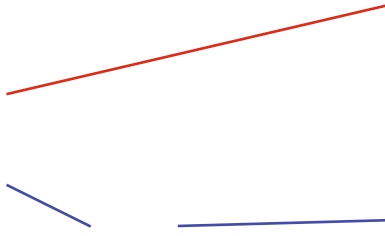


FIGURE 3: Comparison of rock mass internal friction angle and cohesion obtained by two methods.

$$\text{GSI} = \text{TSMR}_{89} - 5, \text{TSMR}_{89} > 23. \quad (10)$$

The GSI values of different lithologies in the No. 4 minefield open pit coal mine of the Muli mining area can be obtained from the above equation. The results are tabulated in Table 7.

In addition, in 2002, Hoek also gave the estimation equation of the deformation modulus of rock mass.

$$E = \left(1 - \frac{D}{2}\right) \sqrt{\frac{\sigma_c}{100}} 10^{(\text{GSI}-10)/40} (\sigma_{ci} < 100 \text{ MPa}), \quad (11)$$

$$E = \left(1 - \frac{D}{2}\right) 10^{(\text{GSI}-10)/40} (\sigma_{ci} > 100 \text{ MPa}). \quad (12)$$

In the stability analysis of rock slope engineering, the limit equilibrium method and many kinds of numerical software are based on the Mohr-Coulomb failure criterion. On the basis of the strength parameters of the Hoek-Brown criterion, E. Hoek proposed the following expressions for calculating the internal friction angle and cohesion of the Mohr-Coulomb criterion:

$$c = \frac{\sigma_c [(1+2a)s + (1-a)m_b \sigma_{3n}] (s + m_b \sigma_{3n})^{a-1}}{(1+a)(2+a) \sqrt{1 + 6am_b (s + m_b \sigma_{3n})^{a-1} / [(1+a)(2+a)]}}, \quad (13)$$

$$\varphi = \sin^{-1} \left[\frac{6am_b (s + m_b \sigma_{3n})^{a-1}}{2(1+a)(2+a)6am_b (s + m_b \sigma_{3n})^{a-1}} \right], \quad (14)$$

where $\sigma_{3n} = \sigma_{3 \max} / \sigma_c$, and the relationship between $\sigma_{3 \max}$, the upper limit of the confining stress, and σ_{cm} , the rock mass strength, is as follows:

$$\frac{\sigma_{3 \max}}{\sigma_{cm}} = k \left(\frac{\sigma_{cm}}{\gamma H} \right)^m, \quad (15)$$

where k and m are empirical parameters, γ is the unit weight of rock mass, and H is the engineering burial depth. The compressive strength of the rock mass can be determined as

$$\sigma_{cm} = \sigma_c \frac{[m_b + 4s - a(m_b - 8s)](m_b/4 + s)^{a-1}}{2(1+a)(2+a)}. \quad (16)$$

In slope engineering, Li et al. [29] have corrected the values of k and m in Equation (15) based on the limit analysis method. The modified k and m are 0.2 and -1.07 for the steep slope and 0.41 and -1.23 for the gentle slope.

According to the above expressions, the rock mass mechanical parameters of the No. 4 minefield open pit coal mine in the Muli mining area are determined as shown in Table 8. At the same time, the calculated results herein are compared with those obtained by generalized the Hoek-Brown criterion, and the latter are calculated using RocLab software. Figure 3 shows that the internal friction angle of the rock mass calculated in this paper is larger than that calculated by the generalized Hoek-Brown criterion. The reason is that under the influence of the freeze-thaw action, rock mass damage occurs inducing new cracks. As a consequence, the joint surface of rock mass becomes rougher, and the internal friction angle of the rock mass becomes larger. The case is especially true for muddy siltstone. Because of freeze-thaw susceptibility, the numerical results obtained through the two methods are quite different. As can be seen from Figure 3, as a result of the freeze-thaw action, the overall strength of rock mass decreases, and the calculated cohesion values are smaller than that calculated by the generalized Hoek-Brown criterion.

4. Engineering Application

4.1. Engineering Survey. The lithology of the strata in the No. 4 minefield open pit coal mine is mainly fine sandstone, coarse sandstone, and muddy siltstone. The present situation of open pit mining is shown in Figure 4. The minimum mining elevation is +4000 m and the maximum mining depth is 135 m. The stability analysis herein is made according to the geological environment conditions, the present production situation of open pit mine, and the structural

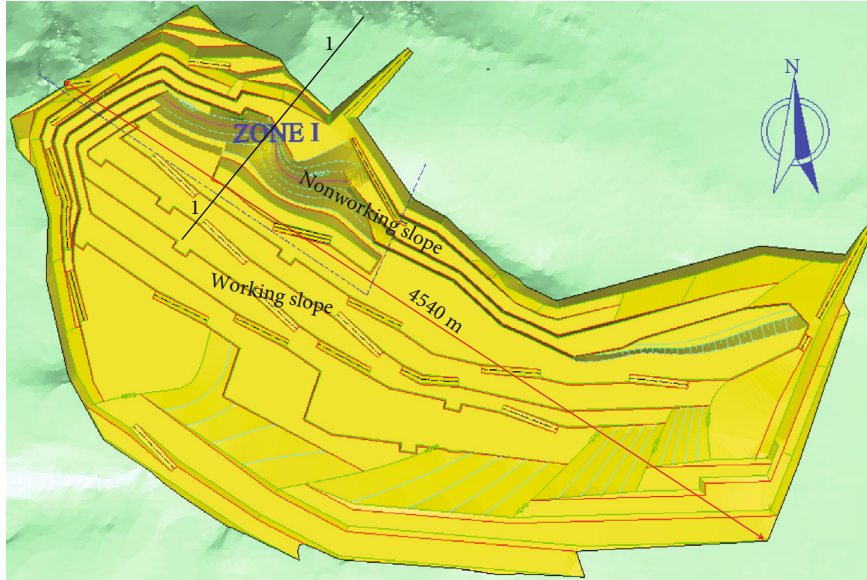


FIGURE 4: Present situation of open pit mine.

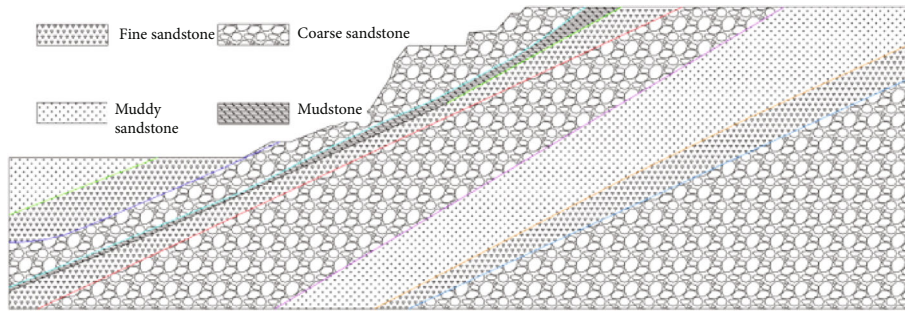


FIGURE 5: Profile of nonworking slope under the present open pit mining situation.

TABLE 9: Strength parameters of mudstone rock mass on No. 4 minefield slope.

Lithology	Deformation modulus E (GPa)	Internal friction angle φ ($^{\circ}$)	Cohesion c (MPa)	Poisson ratio	Unit weight (kN/m ³)
Mudstone	2.78	21.4	0.220	0.25	23.42

characteristics of the slope rock mass. More specifically, the working slope is a mining face with a small slope angle of about 12 degrees and good stability, so it is not considered. Likewise, the end slope is clamped and its stability is good, so it is not considered either. However, the nonworking slope has a larger slope angle and higher slope height in comparison with the working slope and the end slope. On top of this, a complete working platform has not yet been formed in Zone I, and the north slope suffered from landslides, hence resulting in its poor stability. Therefore, the present slope stability analysis is conducted at the 1-1 typical section of Zone I, which is located on the north side of the nonworking slope. Such stability analysis is also conducted for the final slope angle designed for the end of mining.

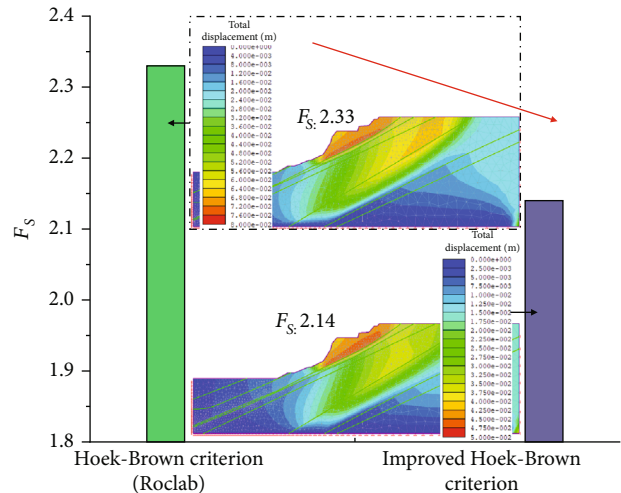


FIGURE 6: Slope safety factor and total displacement of the present nonworking slope in open pit mining (by RocLab and improved Hoek-Brown criterion).

4.2. Stability Analysis of Present Slope. According to the geological profile and rock mass structure characteristics, the typical section of the nonworking slope at Zone I is shown

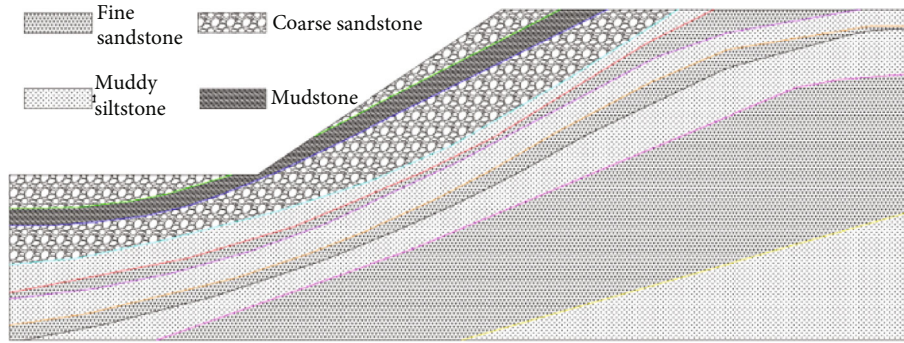


FIGURE 7: Profile of nonworking slope at the end of designed mining.

in Figure 5. The model contains a group of weak planes with mudstone as lithology, and its strength parameter is shown in Table 9. The height of the model slope is 94 m. With the influence of the boundary area of the model on the calculation results considered, the distance from the bottom to the left boundary is 145 m, the top to the right boundary is 240 m, and the total height of the model is 188 m [30]. Phase 2 (Ver.8.014) software is used to establish a model and analyze the slope stability. After meshing, there are 5830 units and 3042 nodes. The slope surface is a free boundary, with the bottom boundary of the model fixed, and the left and right end boundaries constrained horizontally. The rock mass parameters calculated by the two methods in Table 8 are entered into the model for analysis and calculation, and the slope safety factor is calculated by the strength reduction method. The slope safety factors are 2.33 and 2.14, respectively, based on the rock mass parameters obtained by using RocLab software and the improved Hoek-Brown criterion. The reason for the difference is that the rock mass strength is reduced by freeze-thaw action, which is consistent with the previous analysis. On the whole, no matter which method is used to calculate the rock mass parameters, the safety factor of the present slope is highly larger than specification requirements. This is because the present slope angle is small, about 28 degrees; therefore, the safety factor is large and the stability of the slope is good. The overall displacement and meshing of the slope calculated by the two methods are shown in Figure 6. It shows that the maximum displacements are 8 cm and 5 cm, respectively, both occurring on steep slopes and weak layers. The analysis shows that although freeze-thaw cycling reduces the strength of rock mass, the slope angle of the nonworking side is relatively gentle, so the safety factor of the slope is large and the stability of the slope is good.

4.3. The Final Slope Stability Analysis of Open Pit Mine. The final slope angle of the open pit mine is a significant technical parameter, which directly affects the safety and economic benefits of the mine [30–38]. In the design process of the No.4 minefield open pit mine, a technical study is carried out to the final slope angle. In the study of slope engineering stability, when mining to the designed mining depth (slope height of 160 m), the final slope angle is recommended to be 34 degrees. The current working conditions are the same

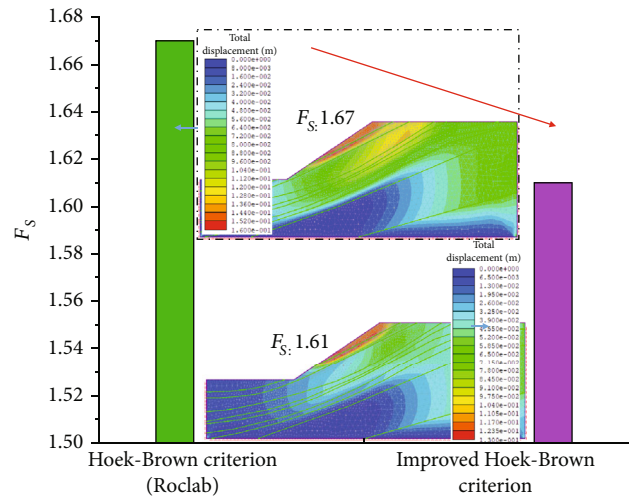


FIGURE 8: Slope safety factor and total displacement of nonworking slope at the end of designed mining (by RocLab and improved Hoek-Brown criterion).

as in the research report. A typical section of the northern slope (Zone I) is selected as the study section (Figure 7). Finite element model is established. The model parameters are the same as that of the present slope as mentioned earlier. The calculation results are shown in Figure 8. The slope safety factors are 1.67 and 1.61, respectively, based on the rock mass parameters obtained by using RocLab software and the improved Hoek-Brown criterion. The maximum displacement is 16 cm and 13 cm, respectively. The analysis indicates that the safety factor of the slope calculated by the improved Hoek-Brown criterion decreased. The reasons and rules are also due to the freeze-thaw action, which reduces the strength of the rock mass. The seasonal freezing depth of the Muli mining area is about 8.25 m. Considering the influence of moisture migration and blasting vibration, the slope is stable when the final slope angle is 34 degrees, and the slope angle design is relatively reasonable.

4.4. Discussion. Figure 9 presents the calculation process of modified rock mass parameters. The freeze-thaw correction coefficient is introduced to obtain the modified rock mass TSMR values. The linear relationship between TSMR and GSI is established to further achieve the values of other

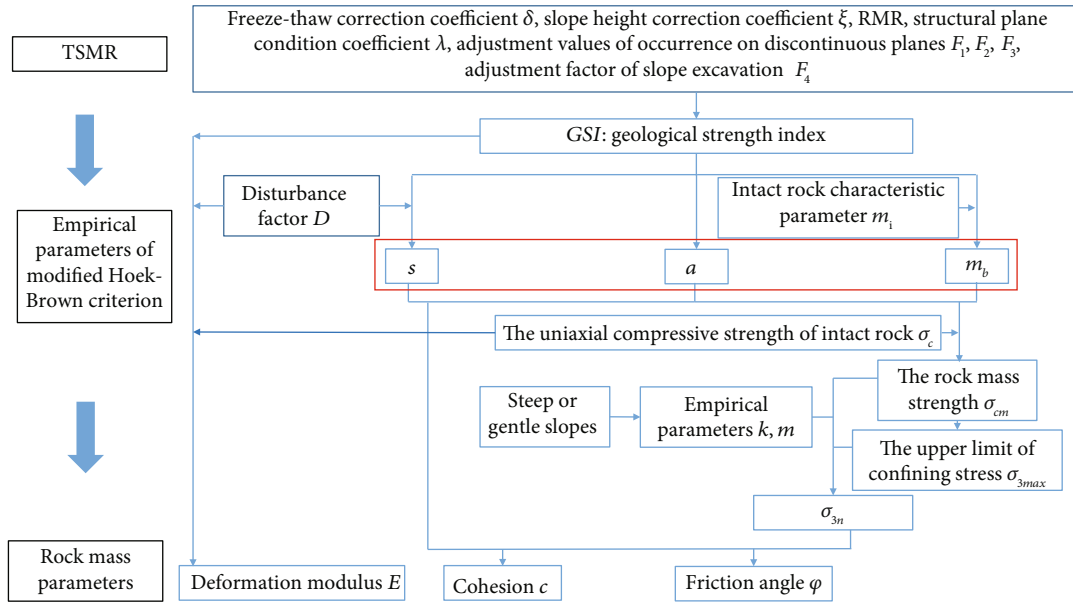


FIGURE 9: Calculation process of rock mass parameters.

parameters in the Hoek-Brown criterion. In addition, the values of empirical parameters k and m are corrected for the steep slope and the gentle slope. Then, equivalent conversion of the Hoek-Brown criterion to Mohr-Coulomb criterion is performed. Finally, the values of the rock mass parameters in the numerical calculation are obtained. All the parameters of the Hoek-Brown criterion are corrected throughout the calculation process, because the freeze-thaw correction coefficient is introduced at the beginning. The modified rock mass parameters can better describe the mechanical properties of slopes in high-altitude and cold regions. Absolutely, the correction of the empirical parameters k and m has more conformity with the actual slope engineering of the open pit mine.

As shown in Figures 6 and 8, it can be seen that after considering freeze-thaw action, the slope safety factor decreases by 8.15% and 3.59%, respectively. The decreased slope safety factor may affect the magnitude of slope inclination in slope design. Generally, the slope inclination is designed as large as possible for the economic benefit, when considering the specification requirements and safety premise. The reduction of slope inclination caused by the decreases of the slope safety factor can also affect the mine production. In addition, it can be seen from Figure 2 that the rock freeze-thaw coefficient decreases as the number of freeze-thaw cycles increases, which generally shows that the freeze-thaw coefficient is reduced with the decrease of the rock strength. It can be seen from Figure 3 that when the freeze-thaw action is considered, the internal friction angle of the rock increases, while the cohesion decreases. Comprehensive analysis shows that under the effect of freeze-thaw of rock, the water-ice phase change causes the initial fractures of rock. The initiated cracks then expand until new fractures are formed. The forming of the new cracks may increase the roughness of rock joints which increase the internal friction angle and

decreases the cohesion. However, the overall integrity is of the rock destroyed by the forming of the new fractures, thus reducing its mechanical properties. Since the freeze-thaw actions have significant effects on the slope stability, the freeze-thaw effects should be involved in the design process of the slope as well as production despite the effects of slope height, slope inclination, and slope rock parameters on slope stability.

5. Conclusions

According to the characteristics of freeze-thaw effects on rock mass in high-altitude and cold regions, mechanical parameters of rock mass are calculated and determined based on the improved Hoek-Brown criterion. The No. 4 minefield open pit coal mine in the Muli mining area is taken as an engineering case, and the differences between the traditional method and the modified method in calculating slope stability are compared and analyzed. The main conclusions are drawn as below:

- (1) The experimental results show that the strength parameters of rock mass decrease under the situation of freeze-thaw cycles, after 120 freeze-thaw cycles, leading to the freeze-thaw coefficients of coarse sandstone, fine sandstone, and muddy siltstone decreasing to 0.62, 0.63, and 0.47, respectively
- (2) The Hoek-Brown criterion is modified based on the linear relationship between TSMR and GSI in the Hoek-Brown criterion and by considering whether the slope is steep or gentle. According to the correlation between the Hoek-Brown criterion and the Mohr-Coulomb criterion, mechanical parameters of the slope rock mass are determined in open pit mines in the case of freeze-thaw cycles. Based on

improved calculation results, the internal friction angle of the rock mass is increases by 17.7%, 18.5%, and 61.8%, and the cohesion is decreased by 38.4%, 40.6%, and 7.8%, respectively

- (3) The slope stability in the open pit mine slope is calculated considering the effects of freeze-thaw. The calculated results show that in terms of the current slope, the safety factor of its nonworking slope is 2.14, and the maximum displacement occurred at the steep slope and weak surface with the values of 5 cm. At the end of mining, the slope safety factor is 1.61, and the maximum displacement is 13 cm. These decrease the slope safety factor by 8.15% and 3.59%. The improved calculation method of rock mass parameters can quantitatively reflect the influence law of freeze-thaw on rock mass strength. Compared with the traditional method, the calculated safety factor of the slope is more consistent with the reality of the open pit slope in high-altitude and cold regions. The improved calculation method provides theoretical guidance for the design and evaluation of an open pit slope

Data Availability

The data used to support the findings of this study are available from the corresponding author upon request.

Conflicts of Interest

The authors declare that they have no conflicts of interest.

Acknowledgments

The authors would like to thank the financial support provided by the National Natural Science Foundation of China (Grant no. 11872287, 51904220), Natural Science Foundation of Shaanxi Provincial Department of Education (Grant no. 21JK0719), and Science and Technology Foundation of Xi'an University of Architecture and Technology (Grant no. ZR19063).

References

- [1] Y. Hong, Z. S. Shao, G. B. Shi, and J. Liu, "Stability and countermeasures for a deposit slope with artificial scarp: numerical analysis and field monitoring," *Advances in Civil Engineering*, vol. 2020, Article ID 8822080, 13 pages, 2020.
- [2] Q. S. Liu, S. B. Huang, Y. S. Kang, and X. Z. Cui, "Advance and review on freezing-thawing damage of fractured rock," *Chinese Journal of Rock Mechanics and Engineering*, vol. 34, no. 3, pp. 452–471, 2015.
- [3] S. B. Huang, Y. Z. Liu, Y. L. Guo, Z. Zhang, and Y. Cai, "Strength and failure characteristics of rock-like material containing single crack under freeze-thaw and uniaxial compression," *Cold Regions Science and Technology*, vol. 162, pp. 1–10, 2019.
- [4] Y. Wang, Y. F. Yi, C. H. Li, and J. Q. Han, "Anisotropic fracture and energy characteristics of a Tibet marble exposed to multi-level constant-amplitude (MLCA) cyclic loads: a lab-scale testing," *Engineering Fracture Mechanics*, vol. 244, article 107550, 2021.
- [5] Y. Wang, B. Zhang, B. Li, and C. H. Li, "A strain-based fatigue damage model for naturally fractured marble subjected to freeze-thaw and uniaxial cyclic loads," *International Journal of Damage Mechanics*, vol. 30, article 105678952110216, 2021.
- [6] K. Wu, Z. Shao, S. Qin, N. Zhao, and Z. Chu, "An improved non-linear creep model for rock applied to tunnel displacement prediction," *International Journal of Applied Mechanics*, vol. 13, article 2150094, 2021.
- [7] M. G. Culshaw and R. Ulusay, "The ISRM suggested methods for rock characterization, testing and monitoring: 2007–2014," *Bulletin of Engineering Geology and the Environment*, vol. 74, no. 4, pp. 1499–1500, 2015.
- [8] H. Zheng, X. T. Feng, Z. Y. Chen, J. A. Hudson, and Y. Wang, "ISRM suggested method for reporting rock laboratory test data in electronic format," *Rock Mechanics and Rock Engineering*, vol. 47, no. 1, pp. 221–254, 2014.
- [9] D. Mas Ivars, M. E. Pierce, C. Darcel et al., "The synthetic rock mass approach for jointed rock mass modelling," *International Journal of Rock Mechanics & Mining Sciences*, vol. 48, no. 2, pp. 219–244, 2011.
- [10] K. Wu, Z. Shao, M. Sharifzadeh, Z. Chu, and S. Qin, "Analytical approach to estimating the influence of shotcrete hardening property on tunnel response," *Journal of Engineering Mechanics*, vol. 148, pp. 1–10, 2022.
- [11] Z. T. Bieniawski, "Engineering classification of jointed rock masses," *Civil Engineer in South Africa*, vol. 15, no. 12, pp. 335–343, 1973.
- [12] E. Hoek, P. K. Kaiser, and W. F. Bawden, *Support of Underground Excavations in Hard Rock*, A A Balkema Publishers, Rotterdam, Netherlands, 1st edition, 2000.
- [13] N. Barton, "Some new Q-value correlations to assist in site characterisation and tunnel design," *International Journal of Rock Mechanics and Mining Sciences*, vol. 39, no. 2, pp. 185–216, 2002.
- [14] E. Hoek and E. T. Brown, "Practical estimates of rock mass strength," *International Journal of Rock Mechanics and Mining Sciences*, vol. 34, no. 8, pp. 1165–1186, 1997.
- [15] E. Hoek and M. S. Diederichs, "Empirical estimation of rock mass modulus," *International Journal of Rock Mechanics & Mining Sciences*, vol. 43, no. 2, pp. 203–215, 2006.
- [16] I. Yilmaz and A. G. Yuksek, "An example of artificial neural network (ANN) application for indirect estimation of rock parameters," *Rock Mechanics and Rock Engineering*, vol. 41, no. 5, pp. 781–795, 2008.
- [17] K. Wu, Z. Shao, M. Sharifzadeh, S. Hong, and S. Qin, "Analytical computation of support characteristic curve for circumferential yielding lining in tunnel design," *Journal of Rock Mechanics and Geotechnical Engineering*, vol. 14, pp. 1–9, 2022.
- [18] E. Hoek and E. T. Brown, "Empirical strength criterion for rock masses," *Journal of Geotechnical Engineering Division*, vol. 106, no. 9, pp. 1013–1035, 1980.
- [19] E. Hoek, D. Wood, and S. Shah, "A modified Hoek–Brown failure criterion for jointed rock masses," in *Rock Characterization: ISRM Symposium, Chester, UK, September 1992*, Thomas Telford Publishing, 1992.
- [20] E. Hoek, C. Carranza-Torres, and B. Corkum, "Hoek-Brown failure criterion-2002 edition," *Proceedings of NARMS-Tac*, vol. 1, no. 1, pp. 267–273, 2002.

- [21] E. Eberhardt, "The Hoek-Brown failure criterion," *Rock Mechanics & Rock Engineering*, vol. 45, no. 6, pp. 981–988, 2012.
- [22] H. Sonmez and R. Ulusay, "Modifications to the geological strength index (GSI) and their applicability to stability of slopes," *International Journal of Rock Mechanics and Mining Sciences*, vol. 36, no. 6, pp. 743–760, 1999.
- [23] W. K. Feng, S. Dong, Q. Wang, X. Yi, Z. Liu, and H. Bai, "Improving the Hoek-Brown criterion based on the disturbance factor and geological strength index quantification," *International Journal of Rock Mechanics and Mining Sciences*, vol. 108, pp. 96–104, 2018.
- [24] S. H. Xu, N. Li, X. D. Wang et al., "Damage test and degradation model of saturated sandstone freezing and thawing of rock slopes of open-pit coal mine," *Chinese Journal of Rock Mechanics and Engineering*, vol. 35, no. 12, pp. 2561–2571, 2016.
- [25] B. Y. Deng, *Research of stability for the Muli slope of open-pit coal mine on freezing-thawing cycle*, Xi'an University of Technology, Xi'an, China, 2015.
- [26] L. Pantelidis, "Rock slope stability assessment through rock mass classification systems," *International Journal of Rock Mechanics & Mining Sciences*, vol. 46, no. 2, pp. 315–325, 2009.
- [27] Y. C. Zhang, R. Q. Huang, L. D. Zhao, R. H. Fu, and X. J. Pei, "Study of Tianshan slope rock mass rating (TSMR) system," *Chinese Journal of Rock Mechanics and Engineering*, vol. 29, no. 3, pp. 617–623, 2010.
- [28] X. D. Luo, N. Jiang, X. Y. Fan, N. Mei, and H. Luo, "Effects of freeze-thaw on the determination and application of parameters of slope rock mass in cold regions," *Cold Regions Science and Technology*, vol. 110, pp. 32–37, 2015.
- [29] A. J. Li, R. S. Merifield, and A. V. Lyamin, "Stability charts for rock slopes based on the Hoek-Brown failure criterion," *International Journal of Rock Mechanics & Mining Sciences*, vol. 45, no. 5, pp. 689–700, 2008.
- [30] Y. R. Zheng and S. Y. Zhao, "Application of strength reduction FEM in soil and rock slope," *Chinese Journal of Rock Mechanics and Engineering*, vol. 23, no. 19, pp. 3381–3388, 2004.
- [31] M. Cai, P. K. Kaiser, H. Uno, Y. Tasaka, and M. Minami, "Estimation of rock mass deformation modulus and strength of jointed hard rock masses using the GSI system," *International Journal of Rock Mechanics & Mining Sciences*, vol. 41, no. 1, pp. 3–19, 2004.
- [32] H. Saroglou and G. Tsiambaos, "A modified Hoek-Brown failure criterion for anisotropic intact rock," *International Journal of Rock Mechanics and Mining Sciences*, vol. 45, no. 2, pp. 223–234, 2008.
- [33] K. Wu, Z. Shao, and S. Qin, "An analytical design method for ductile support structures in squeezing tunnels," *Archives of Civil and Mechanical Engineering*, vol. 20, no. 3, p. 91, 2020.
- [34] R. Bertuzzi, K. Douglas, and G. Mostyn, "Improving the GSI Hoek-Brown criterion relationships," *International Journal of Rock Mechanics and Mining Sciences*, vol. 89, pp. 185–199, 2016.
- [35] S. H. Xu, N. Li, G. G. Xu et al., "Thermal transfer and heat balance of saturated rock under freezing-thawing environment," *Chinese Journal of Rock Mechanics and Engineering*, vol. 35, no. 11, pp. 2225–2236, 2016.
- [36] K. Wu, Z. Shao, S. Qin, W. Wei, and Z. Chu, "A critical review on the performance of yielding supports in squeezing tunnels," *Tunnelling and Underground Space Technology*, vol. 115, article 103815, 2021.
- [37] K. Wu, Z. Shao, S. Qin, N. Zhao, and H. Hu, "Analytical-based assessment of effect of highly deformable elements on tunnel lining within viscoelastic rocks," *International Journal of Applied Mechanics*, vol. 12, no. 3, article 2050030, 2020.
- [38] N. Zhao, Z. Shao, K. Wu, Z. Chu, and S. Qin, "Time-dependent solutions for lined circular tunnels considering rockbolts reinforcement and face advancement effects," *International Journal of Geomechanics*, vol. 21, no. 10, article 04021179, 2021.

Research Article

Optical Fiber Frequency Shift Characterization of Overburden Deformation in Short-Distance Coal Seam Mining

Dingding Zhang ^{1,2}, Qiang Chen,³ Zhengshuai Wang,⁴ Jianfeng Yang,^{1,2} and Jing Chai^{1,2}

¹School of Energy Engineering, Xi'an University of Science and Technology, Xi'an 710054, China

²Key Laboratory of Western Mine Exploitation and Hazard Prevention, Xi'an 710054, China

³Jining No. 3 Coal Mine, Yanzhou Coal Mining Co., Ltd., Jining 272000, China

⁴China Coal Technology Engineering Group Chongqing Research Institute Co., Ltd., Chongqing 400037, China

Correspondence should be addressed to Dingding Zhang; zhangdd@xust.edu.cn

Received 9 September 2021; Accepted 6 October 2021; Published 19 October 2021

Academic Editor: Yu Wang

Copyright © 2021 Dingding Zhang et al. This is an open access article distributed under the Creative Commons Attribution License, which permits unrestricted use, distribution, and reproduction in any medium, provided the original work is properly cited.

Overburden deformation is an important concern for the safe and green mining of coal resources. Similarity simulation testing is the main approach used to study the deformation characteristics of the overburden in coal mining. In the application of Brillouin optical time-domain analysis (BOTDA) in similarity simulation tests, the capability of distributed optical fiber sensing (DOFS) to detect the characteristics of the overburden deformation and the evolution is a key factor affecting the testing accuracy. In this study, the relationships between DOFS and overburden deformation and the face impact pressure under geological conditions in short-distance coal seam mining were explored. The results show that DOFS can be used to monitor the strain conditions of the overburden during the entire mining process and can provide the peak positions of the advance support pressure on the face. A DOFS characterization model for investigating the spatial and temporal evolutions of overburden deformation was established. A new method of characterizing the face impact pressure based on the fiber frequency shift variation was developed. The method was demonstrated to be effective through comparison of monitored results of impact pressure counts detected using pressure sensors. The characteristics of the face impact pressure in short-distance coal seam mining were obtained. The results of this study provide valuable guidance for the development of similarity simulation testing and intelligent mining engineering techniques.

1. Introduction

The mining of coal resources can destroy the overburden rock layers, resulting in soil and water losses at the ground surface, damage to the regional ecological balance, and many other serious environmental problems [1–3]. Current mining techniques have evolved from shallow, single coal seam to multi-layer mining. The overlying rocks are affected by repeated mining disturbances [4]. The overburden migration characteristics caused by the mining are fundamentally important to the development of mining techniques, and they are of great significance to the prevention and control of mining-related geological disasters such as rock burst, coal (rock) body pro-

trusion, roadway deformation, and water inrush from the roof and floor [5–7]. However, the on-site in situ research has been limited by high costs, great technical difficulties, and restricted monitoring equipment [8, 9]. Therefore, similarity simulation testing is the main approach used to investigate the characteristics of the overburden deformation, fracturing, and roof impact pressure [10, 11]. At present, close-range photography, total station instruments, and dial indicators are usually used to obtain displacement measurements in similarity simulation tests, while strain gauges and pressure sensors are widely used for stress and strain monitoring. Due to the low test accuracy and disadvantages of scattered measurements only at selected locations, these

testing methods are difficult to use for the continuous measurement of the entire field in real time [12, 13].

Optical fiber monitoring techniques have many advantages such as high precision, corrosion resistance, and electromagnetic interference resistance. They are widely used in monitoring the quality of structures in the electric power, mining, and construction industries [14, 15]. Among them, Brillouin optical time-domain analysis (BOTDA) is outstanding due to its high precision, distributed measurements, and the measurements of the absolute temperature and strain [16–18]. Horiguchi et al. [19] first proposed the distributed optical fiber sensor monitoring technique based on stimulated Brillouin scattering in 1989. Bao et al. [20] proposed Brillouin optical time-domain analysis with differential pulse-width pairs (DPP-BOTDA) based on a difference method in order to further improve the spatial resolution of optical fiber monitoring. Kishida et al. [21] proposed pulse-prepump Brillouin optical time-domain analysis (PPP-BOTDA) to obtain high spatial resolution and high-precision strain measurements via optical fiber sensing. Song et al. [22] proposed a new monitoring technique for distributed optical fiber sensing to achieve a centimeter-level spatial resolution.

BOTDA can be used for internal strain monitoring of rock strata, and it is an important monitoring method for detecting rock deformation [23, 24]. Moffat et al. [25] used a distributed optical fiber sensing monitoring system based on BOTDA to detect the displacement of the tunnel roof and the tunnel's two sides in order to evaluate rock deformation due to mining activities. Buchoud et al. [26] used artificial collapse pits to simulate surface collapse pits and to carry out surface subsidence displacement monitoring based on distributed optical fiber sensing (DOFS) and achieved submillimeter-level vertical surface displacement measurements. Zhang et al. [27] used inclined drilling to implant distributed sensing optical cables in the sampling field of their similarity simulation test in order to accomplish strain field monitoring of overburden deformation during mining. Chai et al. [28] applied the distributed strain fiber technique to a three-dimensional physical similarity simulation test to conduct quantitative characterization of the internal deformation and failure of mining-induced overburden.

In this study, a distributed optical fiber sensing technique (BOTDA) was applied in a physical similarity simulation test. Distributed optical fiber sensors were used to test the internal strain of the overburden under repeated mining conditions and to explore the relationships between the overburden failure, face impact pressure, and optical fiber monitoring results. The results of this study provide a useful basis for the application of distributed optical fiber sensing in similarity simulation testing in mining engineering.

2. Similarity Simulation Test Based on Distributed Optical Fiber Sensing Monitoring

2.1. Principle of PPP-BOTDA. The propagation of light in an optical fiber produces three scattering signals: Rayleigh scat-

tering, Raman scattering, and Brillouin scattering. Brillouin scattered light is caused by nonlinear interactions between incident light and phonons that are thermally excited within the light propagation medium. This scattered light shifts in frequency by a Brillouin shift and propagates in the opposite direction relative to the incident light [29]. Figure 1 shows the monitoring principle of BOTDA.

Compared to BOTDA, PPP-BOTDA (i.e., pulse-prepump-Brillouin optical time domain analyzer) [26], higher spatial resolution can be obtained. This is done by loading an appropriate pulse-prepumped light to preexcite phonons before introducing the pulsed light (pumped light.) The PPP-BOTDA has a smaller half-value full width and higher frequency resolution of the Brillouin gain spectrum, achieving a spatial resolution of 10 mm and 0.0025% strain test accuracy.

It has been found that there is a relationship between Brillouin frequency shift (BFS) ν_B and temperature T or strain ε ; the relationship can be expressed as follows [30]:

$$\nu_{B2} = \nu_{B1} + C_T(T - T_0) + C_\varepsilon\Delta\varepsilon, \quad (1)$$

where ν_{B2} is Brillouin scattered frequency shift with strain at a certain temperature T , ν_{B1} is Brillouin scattered frequency shift without strain at temperature T_0 , C_T is the sensitivity coefficient of the fiber to temperature, C_ε is the sensitivity coefficient of the fiber to strain, and T_0 is the initial temperature. The C_{VT} is 1.07 MHz/°C, and the $C_{V\varepsilon}$ is 0.0497 MHz/ $\mu\varepsilon$.

It is worth noting that the temperature-induced Brillouin frequency shift is much smaller than that caused by strain (0.002%/°C). Therefore, when measuring the Brillouin frequency shift caused by strain, if the temperature changes within 5°C, the temperature can be ignored.

2.2. Similarity Simulation Test Design. Research on the movement of the overlying strata in mining engineering has been a black box problem. Similarity material simulation tests provide an effective solution for studying overburden deformation and rock structure evolution during coal mining [31]. The similarity model was constructed using a 3000 × 200 × 2000 mm (length × width × height) plane stress model frame and based on the geological conditions of the Ningtiaota coal mine. The similarity model contained two coal seams that could be excavated. The thickness of the upper coal seam 1⁻² was 1.95 m, and the thickness of its overburden was 123.05 m. The thickness of the lower coal seam 2⁻² was 4.65 m, and the thickness of its overburden was 158.35 m. The inclination angle of the coal seam ranged from 1°47' to 0°13'. The distance between the two coal seams was 33.35 m, i.e., short-distance coal seams. The similarity materials were composed of quartz sand, gypsum, and mica powder. These materials were mixed with ratios based on calculation results and the similarity theory [31] (Table 1). The geometric similarity ratio, bulk density similarity ratio, and stress similarity ratio were 1:150, 1:1.56, and 1:234, respectively.

The coal seam was excavated from the left side of the model to the rear side. One 30 cm wide boundary coal pillar

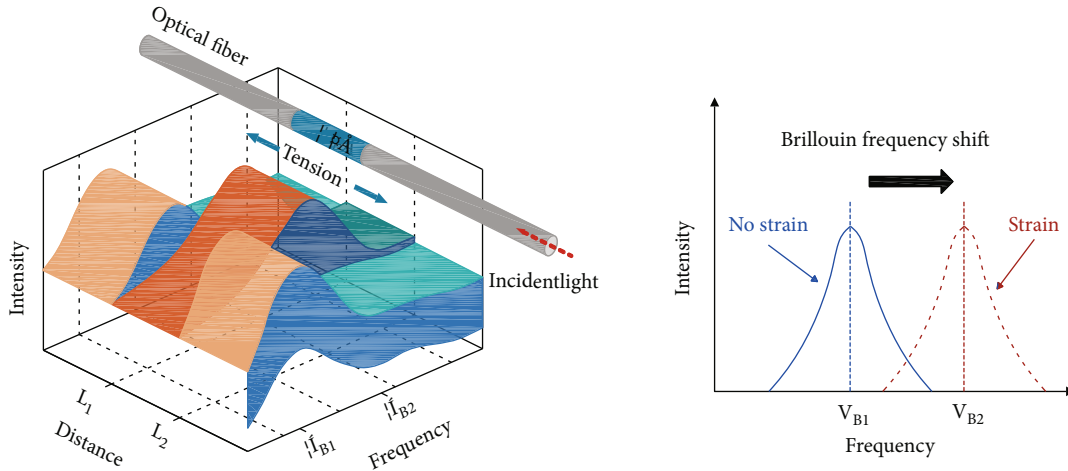


FIGURE 1: Monitoring principle of BOTDA.

TABLE 1: Material ratios used in the similarity material model.

Lithology of simulated stratum	Stratum thickness (m)	Simulated thickness (cm)	Accumulated height (cm)	Material ratio	Dosage of analogous materials (kg)		
					Sand	Gypsum	Mica powder
Loess	42.00	28.0	117.1	1019	238.25	2.38	21.44
Sandy mudstone	14.76	9.8	89.1	919	82.89	0.92	8.29
Siltstone	21.55	14.4	79.3	837	119.53	4.48	10.46
Medium-grained sandstone	28.75	19.2	64.9	837	159.47	5.98	13.95
Siltstone	6.70	4.5	45.8	937	37.63	1.25	2.93
Medium-grained sandstone	9.96	6.6	41.3	828	55.24	1.38	5.52
1 ⁻² coal seam	1.89	1.3	34.7		5.13	0.19	1.28
Fine-grained sandstone	9.4	6.3	33.4	937	52.34	1.89	4.42
Siltstone	3.80	2.5	27.1	828	21.08	0.53	2.11
Fine-grained sandstone	5.90	3.9	24.6	837	32.73	1.23	2.86
Siltstone	1.00	0.7	20.7	937	5.62	0.19	0.44
Fine-grained sandstone	12.16	8.7	20.0	828	73.14	1.8	7.18
2 ⁻² coal seam	4.60	3.1	11.2		12.48	0.47	3.12
Siltstone	3.54	2.4	8.2	937	19.88	0.66	1.55
Fine-grained sandstone	8.70	5.8	5.8	837	48.26	1.81	4.22

was left on each side of the model to eliminate the influence of the boundary effect on the similarity simulation test. In each coal seam, the excavation step was 3 cm, the number of excavations was 77, and the excavation length was 240 cm. Coal seam 1⁻² was excavated first in the similarity simulation test. After the excavation, the model was allowed to settle for two weeks. After the overburden of the goaf behind the face was compacted, coal seam 2⁻² was excavated.

2.3. *Monitoring System Layout.* The similarity simulation test monitoring system included a NX-6055 Brillouin scattering optical time-domain analyzer, distributed optical fiber sensors, CL-YB-114 pressure sensors, and a micrometer. The distributed optical fiber sensors (DOFSs) were common single-mode fibers with a diameter of 2 mm. The distributed

optical fiber sensor layout is shown in Figure 2. Four vertically distributed optical fiber sensors (V1, V2, V3, and V4) were embedded in the similarity model to monitor the deformation characteristics of the overlying rocks. The spacing between the vertically distributed optical fiber sensors was 60 cm, and that between the horizontally distributed sensors was 39 cm. Each fiber sensor was connected in series with another fiber sensor and then connected with an NBX-6055 optical stress analyzer.

3. Analysis of Monitoring Results

Figure 3 shows the strain monitoring results of DOFS V1-V4 for the working-face mining of coal seam 1⁻². Figure 4 shows the strain monitoring results of the DOFS for the working-

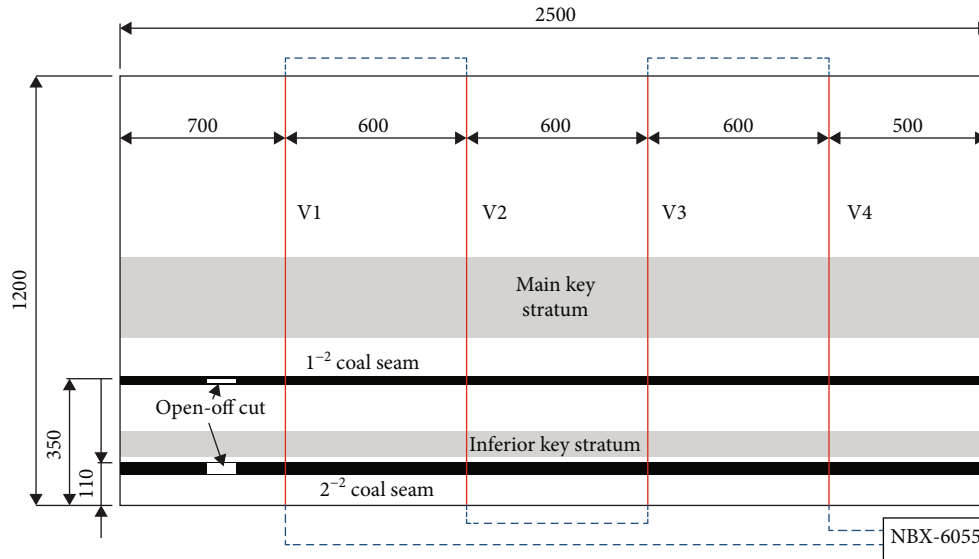


FIGURE 2: Layout of the distributed optical fiber sensors.

face mining of 2^{-2} coal seam. The vertical axis in Figures 3 and 4 represents the similarity model height, and the horizontal axis shows the strain monitoring value provided by the optical fiber. When the strain value is positive, the optical fiber is stretched. When the strain value is negative, the optical fiber is compressed.

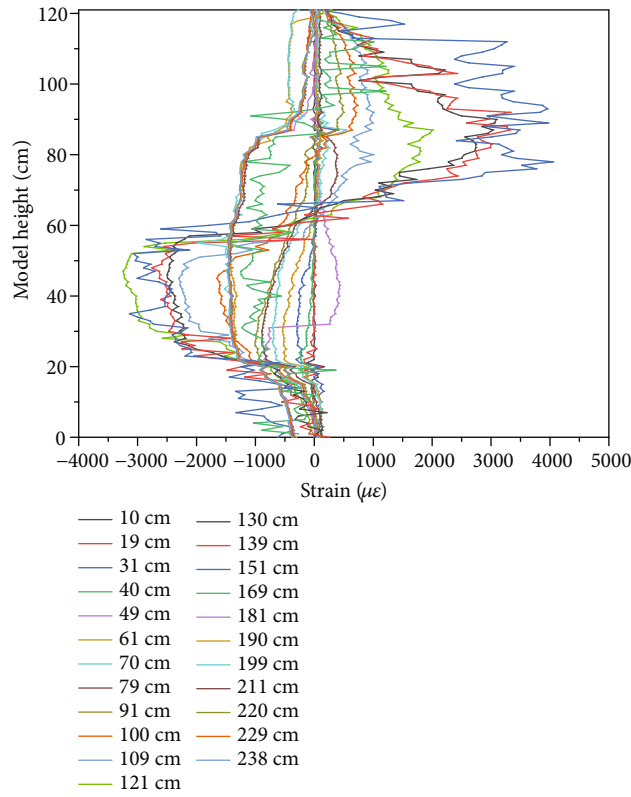
When the optical fiber was far away from the face, the overlying rock containing the optical fiber was under the stress conditions of the original rock, and the strain value provided by the optical fiber was not affected by the mining. As the face was excavated, the strains of DOFSs V1-V4 were successively affected by the excavation. When the face was close to the rock in which the optical fiber was placed, the optical fiber reported negative growth with a small amplitude, and the strain peak occurred in the rock near the top of the coal seam. As the distance between the face and the optical fiber decreased, the strain peak value initially increased and then decreased. When the face reached and passed through the rock in which the optical fiber was placed, the strain peak value changed from negative to positive with a continuous increase. The strain peak value in the overburden also increased gradually and occurred in the middle and upper parts of the overburden. As the face moved far away from the optical fiber, the strain peak value decreased and then became stable. During the excavation of coal seams 1^{-2} and 2^{-2} , the strain monitoring curves of optical fibers V1-V4 exhibited clear trends in both their numerical values and structural forms as the face was excavated. Therefore, optical fiber strain monitoring can be used to invert the overburden failure characteristics during the mining process.

4. Analysis of Temporal and Spatial Distribution Characteristics of Overburden Strain

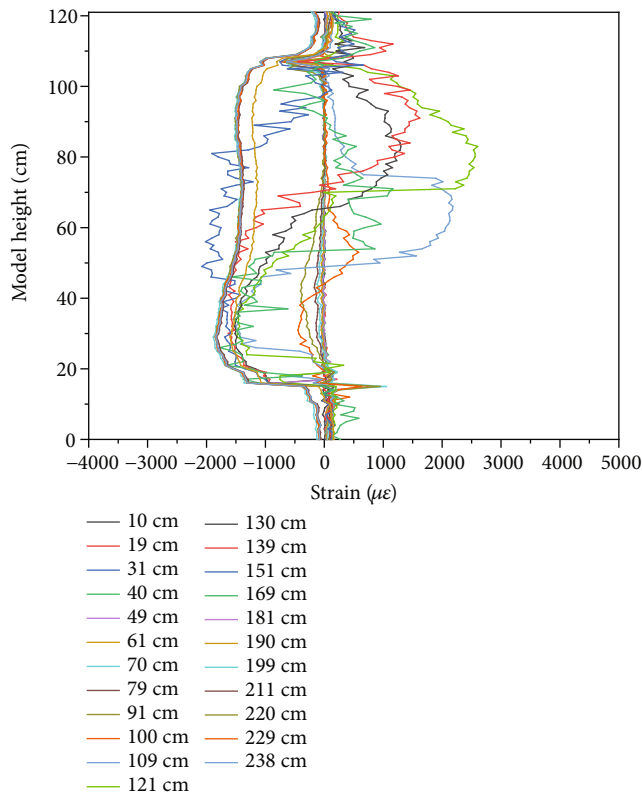
4.1. Analysis of Temporal and Spatial Evolutions of Overburden Strain. Figure 5 shows the strain distribution of optical fiber V3 during the mining of the face of coal seam

1^{-2} , with the vertical axis representing the similarity model height and the horizontal axis representing the distance between the face and V3. When the distance was negative, the face was close to the optical fiber. When the distance was positive, the face was far away from the optical fiber. The compression and tension regions are separated by the $0 \mu\epsilon$ curves. During the construction of the similarity model, a certain amount of prestress was applied to the distributed optical fiber sensors to make the distributed optical fiber sensors more sensitive to the changes in the overburden pressure during mining of the face. Therefore, before the face was mined, the lower part of the model in the height range of 0-53 cm was under slight compression, while the upper part of the model in the height range of 53-120 cm was under slight tension. As the face approached optical fiber V3, the compressive strain range of V3 increased due to the influence of the advanced support pressure. When the face was advanced to the position of V3, the compressive stress affected an expanded height range of 0-79 cm in the similarity model. The compressive strain provided by the optical fiber sensor near the face was the greatest, reaching $-452.29 \mu\epsilon$. After the face passed V3, tensile strain appeared in the overlying strata. As the face was excavated, the range of the tensile strain expanded, and the peak strain position moved upward. When the face had advanced to 42 cm past optical fiber V3, the peak tensile strain reached the maximum value of $7627.85 \mu\epsilon$, occurring in the overlying rock at a height of 51.0 cm above the face of coal seam 1^{-2} . As the face progressed farther away from V3, the fiber strain gradually changed from tensile to compressive, indicating that the overburden in the goaf was gradually compacted.

Figure 6 shows the strain distribution of V3 during the mining of coal seam 2^{-2} . After the face was excavated during the mining of coal seam 1^{-2} , the overburden gradually recovered to the stress level of the original rock. The bottom part of the similarity model (height range of 0-24 cm) was affected by the impact pressure. As the face approached

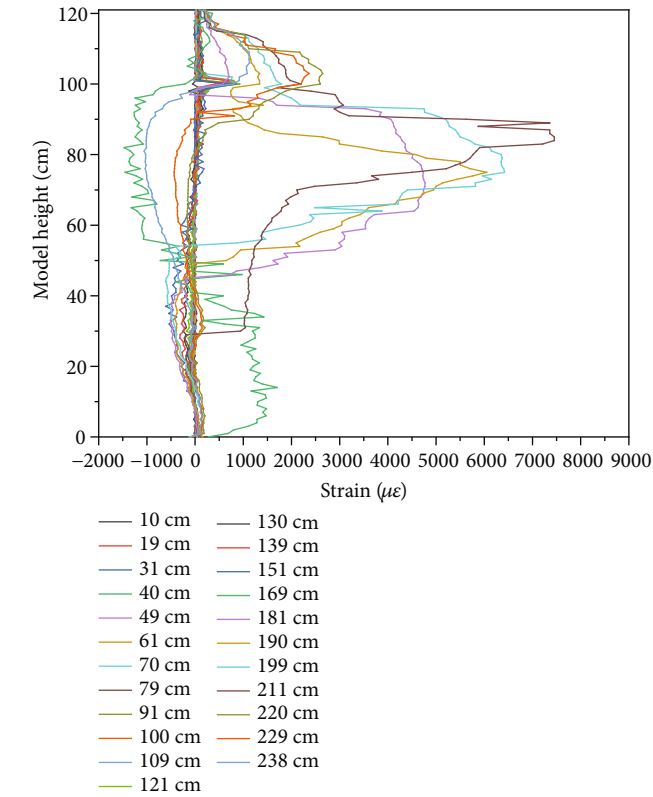


(a) DOFS V1

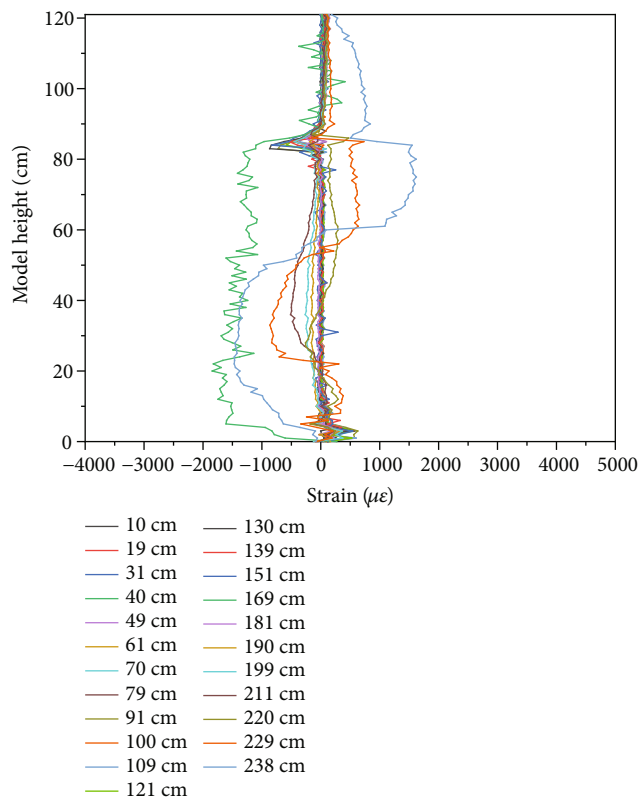


(b) DOFS V2

FIGURE 3: Continued.

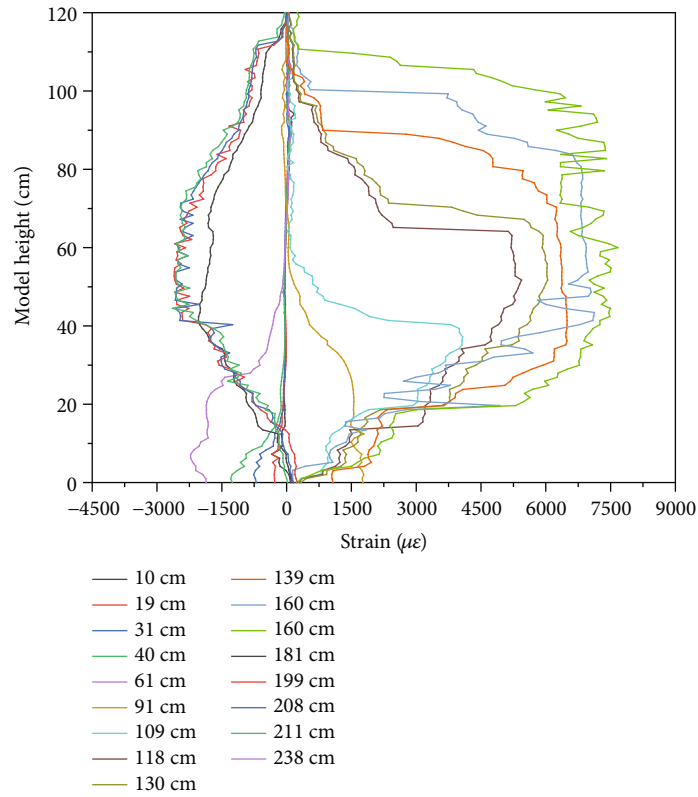


(c) DOFS V3

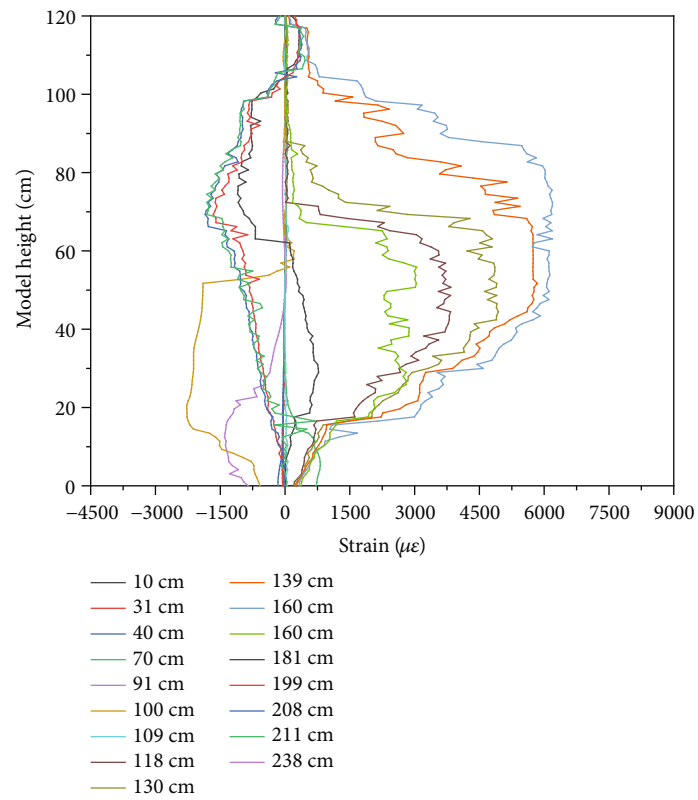


(d) DOFS V4

FIGURE 3: Strain monitoring results of DOFS V1-V4 in the mining of coal seam 1⁻².

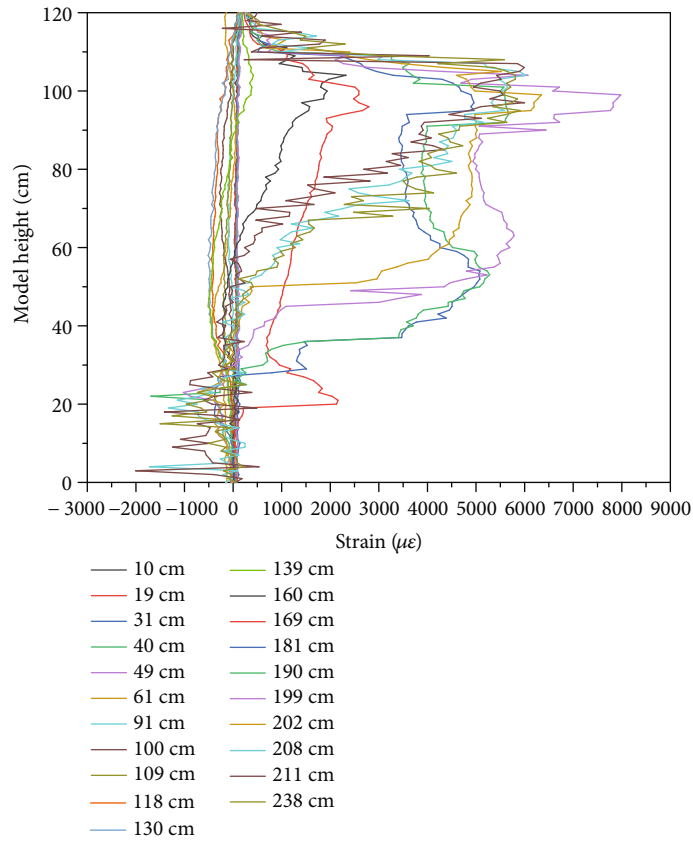


(a) DOFS V1

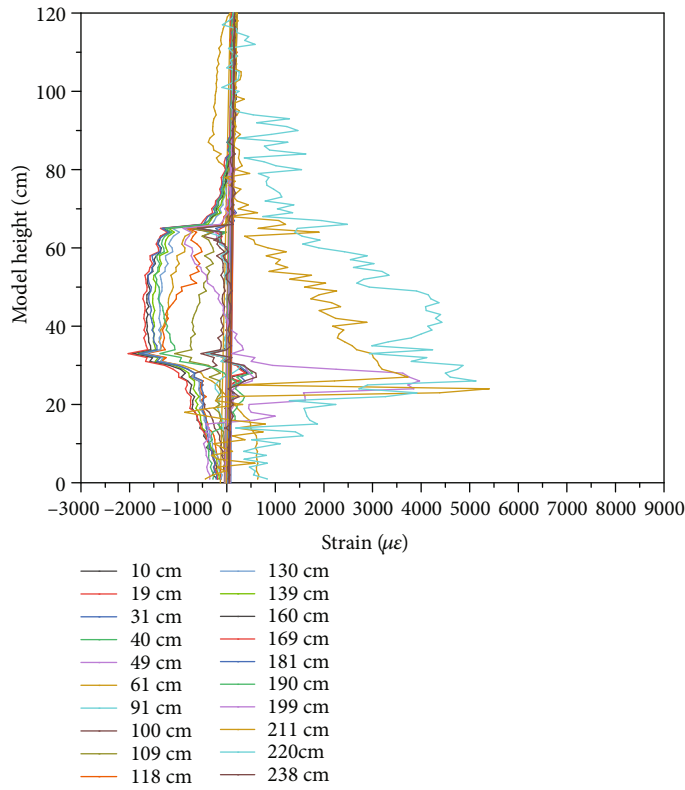


(b) DOFS V2

FIGURE 4: Continued.



(c) DOFS V3



(d) DOFS V4

FIGURE 4: Strain monitoring results of DOFSs V1-V4 in the mining of coal seam 2².

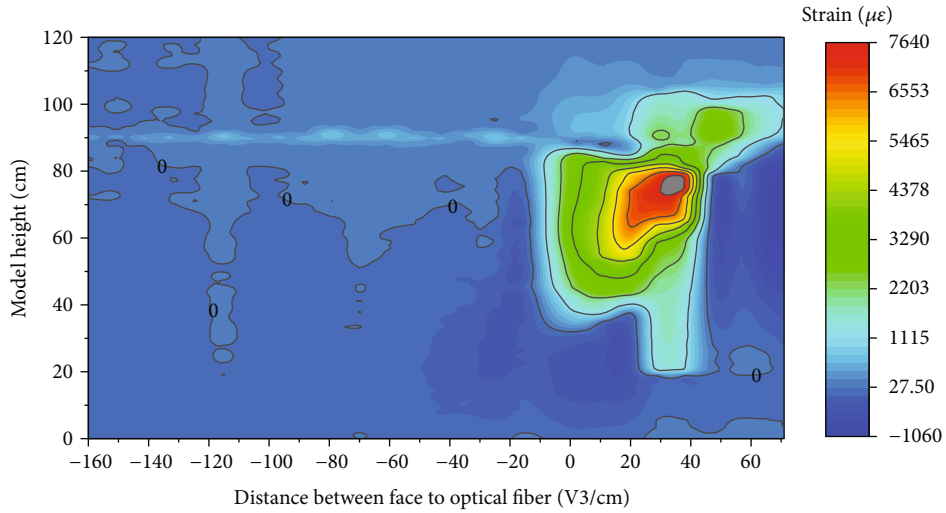


FIGURE 5: Strain distribution of fiber V3 during the mining of coal seam 1⁻² (the abscissa is the model height, and the ordinate is the distance between the face and the optical fiber).

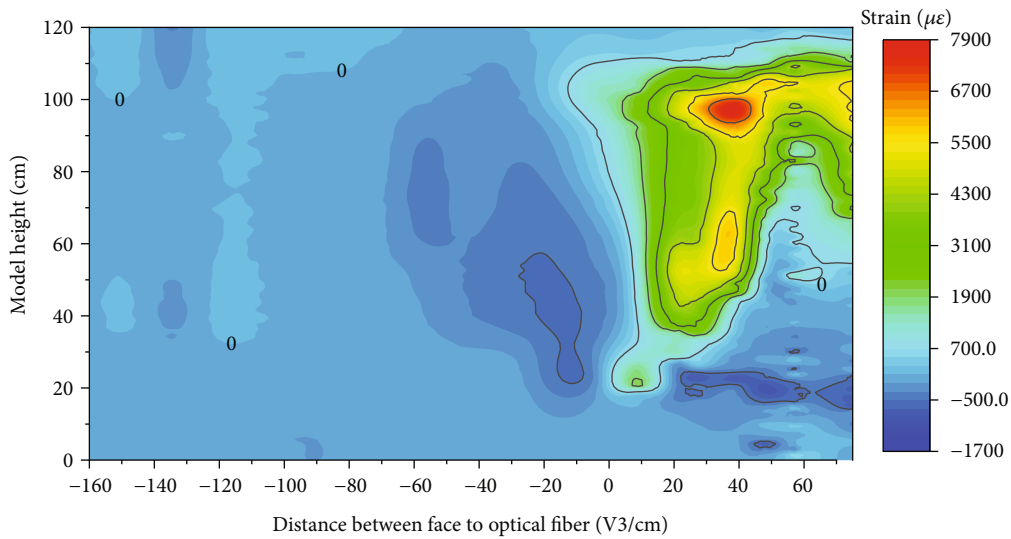


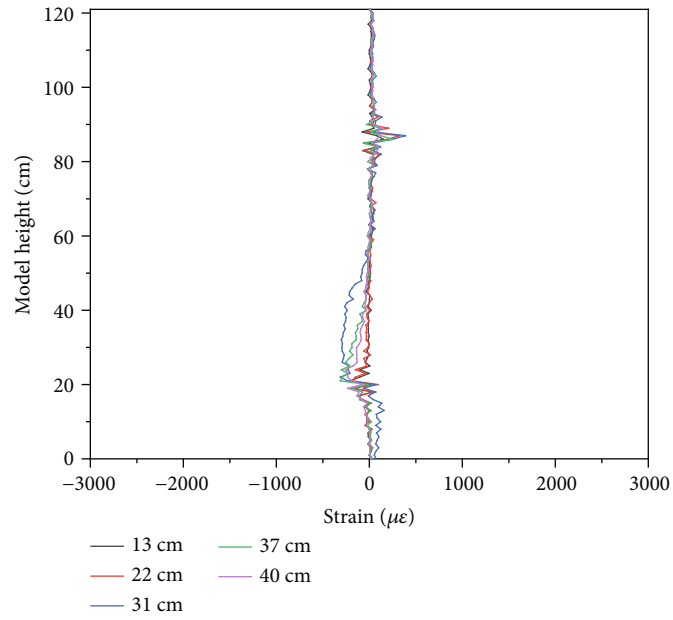
FIGURE 6: Strain distribution of fiber V3 during the mining of coal seam 2⁻² (the abscissa is the model height, and the ordinate is the distance between the face and the optical fiber).

V3, the broken overburden rocks in the goaf of coal seam 1⁻² did not have any capacity to sustain loads. Therefore, the rocks all caved downward into the goaf of coal seam 2⁻² under the influence of the secondary mining, resulting in the compression range of the optical fiber gradually increasing. When the face was 21-58 cm away from V3, the compressive strain range of the overburden was the greatest, and the entire height range of 0-114 cm in the similarity model was under compressive strain. When the face passed through and progressed farther away from the position of V3, the deformation characteristics were similar to the deformation characteristics of the overlying strata during the excavation of coal seam 1⁻². When the face was 39 cm away from V3, both the range and peak value of the tensile strain reached their maxima, with a maximum tensile strain

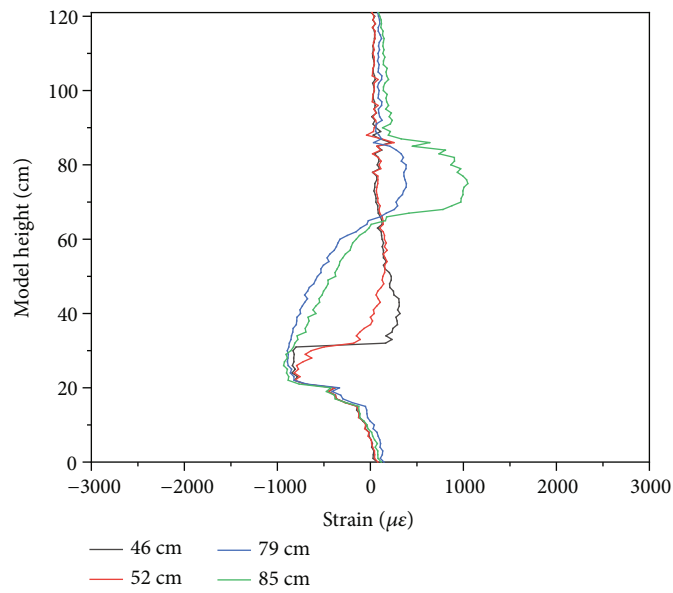
of 7867.18 $\mu\epsilon$ and the position of the maximum tensile strain located at a height of 88 cm above the face of coal seam 2⁻².

4.2. *Optical Fiber Monitoring Analysis of Overburden Damage.* Figure 7 shows the fiber strain curves as the face successively approached, passed through, and progressed farther away from the fiber sensor. A direct relationship between the fiber strain curves and the overburden deformation characteristics was established under these different excavation conditions.

The strain monitoring curve for the case of the face approaching V1 is shown in Figure 7(a). When the face was excavated from 0 to 40 cm, it became gradually closer to the optical fiber. The optical fiber was in a coal wall support area of the face. Under the influence of the advance

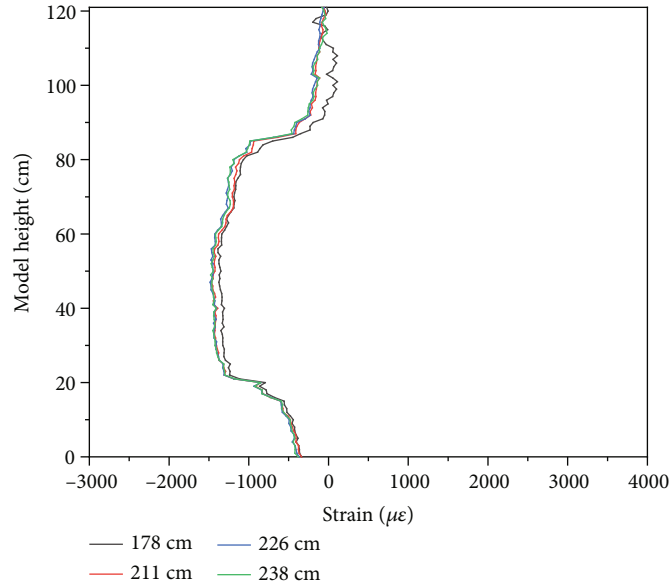


(a) Stage 1: the face is close to the optical fiber



(b) Stage 2: the face passes the optical fiber

FIGURE 7: Continued.



(c) Stage 3: the face is far away from the optical fiber

FIGURE 7: Strains of vertical fiber V1 at different positions relative to the face.

support pressure, compressive strain occurred in the lower part of the optical monitoring fiber. As the face advanced toward the optical fiber, the compressive strain initially increased and then decreased. The maximum compressive strain was $-295.52 \mu\epsilon$, and it occurred when the excavation advanced to 31 cm from V1. The variation trends of the optical fiber's compressive strain in front of the face verify the distribution characteristics of the advance support pressure in front of the face [5]. The position of the peak compressive strain was the same as the position of the maximum advanced support pressure in front of the face.

The strain monitoring curve for the case of the face passing through V1 is shown in Figure 7(b). When the face was excavated from 43 to 85 cm, the face passed through the optical fiber. When the face passed through the optical fiber by 0-12 cm, the optical fiber sustained tensile strain. As the face was excavated further, the fiber's strain curve exhibited a three-step distribution. The optical fiber's strain was negative in the height range of 0-31 cm above the face, corresponding to heights of 35-66 cm in the similarity model, and the compressive strain gradually increased. The fiber's strain was positive in the height range of approximately 31-52 cm above the face, corresponding to heights of 66-87 cm in the similarity model. According to the three-zone theory of the overburden [32], the step in the negative strain curve corresponded to the overburden fracture zone, where the fractured rocks were gradually compacted, causing a gradually increase in the compressive strain. The step in the positive strain curve corresponded to the overburden crack zone, where the optical fiber was strained. A bending subsidence zone was located above the crack zone. The fiber's strain decreased in the bending subsidence zone.

The strain monitoring results for the case of the face being far away from V1 are shown in Figure 7(c). When the face was excavated from 88 to 240 cm, the face was far

away from the optical fiber. In this stage, because the face had been fully excavated, the overburden rocks collapsed in a large area and gradually and firmly pressed on the lower caving zone, eliminating the cracks in the middle crack zone and causing a negative strain in the optical fiber due to the overall compression effect. The upper part of the similarity model was a bending subsidence zone, in which the fiber's strain varied very little.

As the face progressed farther away from V1, the impact of the mining on optical fiber's signal became weak, while optical fibers V2, V3, and V4 were gradually influenced by the mining to a greater extent, and their strains' variation trends were similar to that of V1. These analysis results show that the peak position of the advanced support pressure on the face and the heights of the caving zone and fracture zone in the overburden goaf can be estimated based on the relative positions of the optical fiber and the face and on the optical fiber monitoring characteristic curves under different overburden deformation conditions.

5. Optical Fiber Monitoring Analysis of the Face Impact Pressure

5.1. Relationship between Face Impact Pressure and Optical Fiber Frequency Shift. When the coal seam was not excavated, the overlying rocks were not disturbed by mining, and the fiber's Brillouin frequency shift in the similarity model did not change. When the face was excavated, the large-scale collapse of the overlying strata caused the impact pressures to act on the face. The face impact pressure is of great importance to the safety of the face. The overburden collapse in a large area caused drastic variations in the fiber's Brillouin frequency shift in the similarity model. Therefore, the variation of the fiber frequency shift can be used to characterize the occurrence of the face impact pressure.

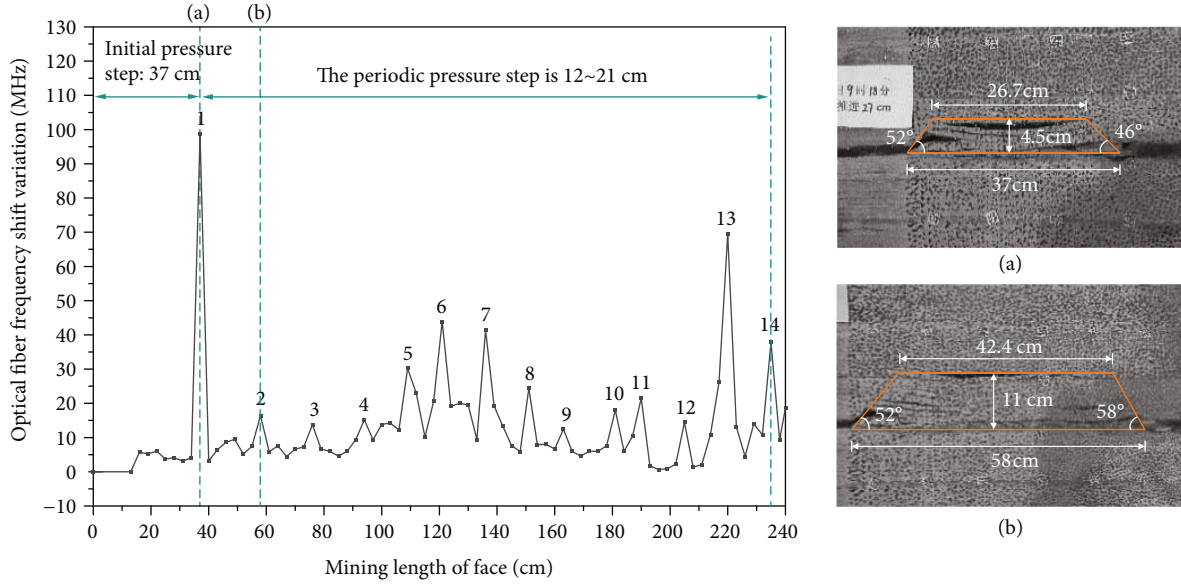


FIGURE 8: Impact pressure identification curves during the mining of coal seam 1⁻² (the abscissa is the face excavation distance, and the ordinate is the variation degree of the optical fiber frequency shift). (a) Face excavation distance of 37 cm. (b) Face excavation distance of 58 cm.

The concept of the variation degree of the optical fiber frequency shift can be explained as follows. There are j collected samples of the frequency shift in the optical fiber monitoring database, and there are n sampling points for each data sample. The difference in the frequency shifts of two collected samples in a given space is normalized to characterize the deformation degree of the rock structure and to reflect the intensity of the rock movement. The variation degree is expressed as follows:

$$D_x = \frac{1}{n} \left(\sum_{j=1}^n |\text{BFS}_j| - \sum_{j=1}^n |\text{BFS}_{j-1}| \right), \quad (2)$$

where D_x is the variation degree of the optical fiber frequency shift in the testing when the face is excavated for a distance x , and n is the number of sampling points for the optical fiber. When the overburden strata experience small deformations, the frequency shift variation of the monitoring fiber is small. When the overburden strata experience a large separation or are even broken and fall, the frequency shift variation is large.

5.2. Characterization of Face Impact Pressure Based on Optical Fiber Frequency Shift Variation. During the face mining, the strata containing fibers V1-V4 were affected by the mining disturbances. Therefore, the variation degree of the optical fiber frequency shift throughout the entire process of mining the face was the sum of the variation degree of each optical fiber (V1, V2, V3, and V4) (Figures 8 and 9). The horizontal axis in the figures represents the mining distance of the face, and the vertical axis represents the variation degree of the optical fiber frequency shift.

Figure 8 shows that there were a total of 14 spikes in the optical fiber frequency shift curve during the mining of the

face of coal seam 1⁻², indicating that there were 14 episodes in which the impact pressures acted on the face, corresponding to excavation distances of 37, 58, 76, 91, 109, 124, 136, 151, 163, 178, 190, 205, 220, and 235 cm. The first peak corresponded to the appearance of the first impact pressure when the face was excavated to 37 cm, with a frequency shift of 98.69 MHz, and the first impact pressure acted on the face. It occurred when the basic overburden roof overhang reached the span limit, shear fractures formed along the coal wall of the face under the effects of the rock weight and the pressure caused by the upper overburden rocks. The step distance, the mining length of the working face from the time of impact pressure to the time of last pressure, of the initial impact pressure was 37 cm. The height of the fracture zone was 4.5 cm. The overburden caving angle was 52° on the side farther away from the face. The overburden caving angle was 46° on the side closer to the face. Rock separation occurred above the basic overburden roof, and the maximum height of the stratum gap was 1 cm. The stratum gap gradually closed as the excavation continued. The overlying rocks located in the goaf were entered the pressure relief zone. The second peak in Figure 8 occurred when the face was excavated to 58 cm, with a frequency shift variation degree of 16.41 MHz, and the first periodic impact pressure occurred on the face. The broken rocks rotated unstably toward the goaf. The step distance of the first periodic impact pressure was 21 cm. After the second peak, multiple periodic impact pressures acted on the face. It can be observed that the step distances of the periodic impact pressures were 12-21 cm, with an average of 15.5 cm. The variation degrees of the optical fiber frequency shift were 12.44-98.69 MHz.

Figure 9 shows that there were 16 peaks in the variation degree curve of the optical fiber frequency shift for the face of coal seam 2⁻² during the mining process, indicating that

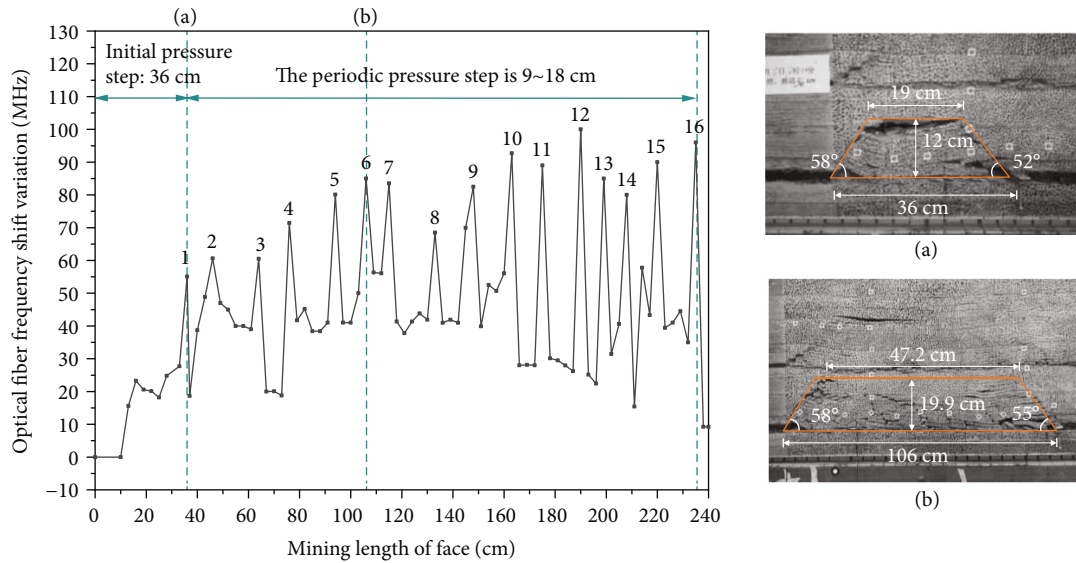


FIGURE 9: Impact pressure identification curve during the mining of the face of coal seam 2⁻² (the abscissa is the face excavation distance, and the ordinate is the variation degree of the optical fiber frequency shift). (a) Face excavation distance of 36 cm. (b) Face excavation distance of 106 cm.

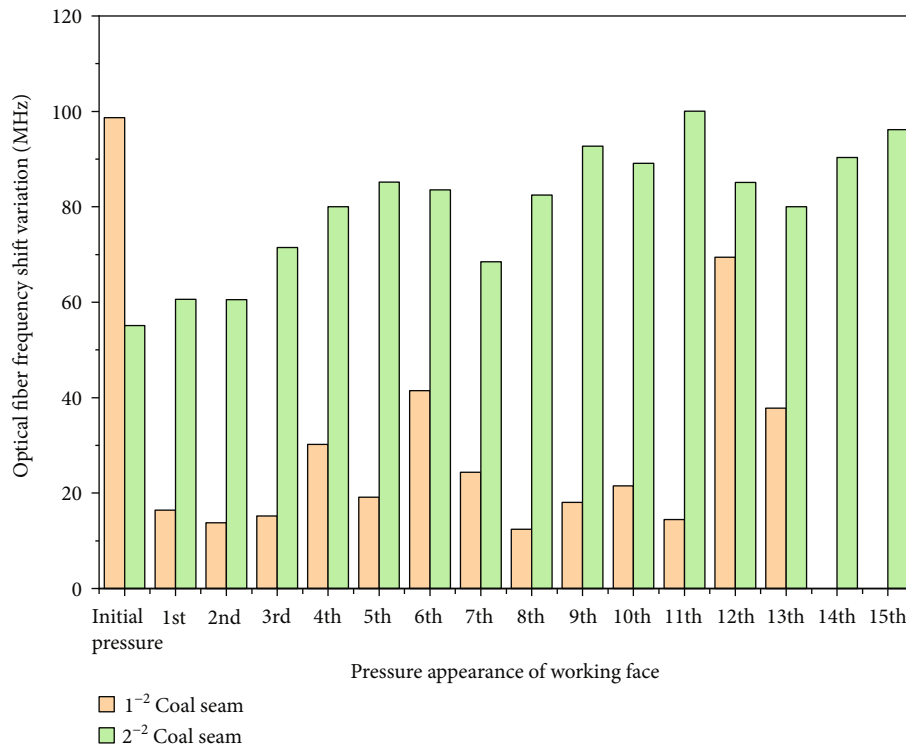


FIGURE 10: Comparison of the variation degree of the optical fiber frequency shift with the impact pressure (the ordinate is peak values in the mining of coal seams 1⁻² and 2⁻²).

the impact pressures acted on the face 16 times, including one initial impact pressure and 15 periodic pressures. The step distance of the initial impact pressure was 36 cm, while the step distances of the periodic pressures were 9-18 cm, with an average of 13.27 cm. The variation degrees of the frequency shift were 60.52-103.45 MHz. It can be seen that the step distances of the impact pressures in the mining of the

lower coal seam were less than those in the mining of the upper coal seam in the short-distance coal mining.

5.3. Comparison of the Face Impact Pressure in Short-Distance Coal Seam Mining. The mining of lower coal seam 2⁻² caused repeated disturbances to the stress of the overlying strata, resulting in the intensity of the impact pressures

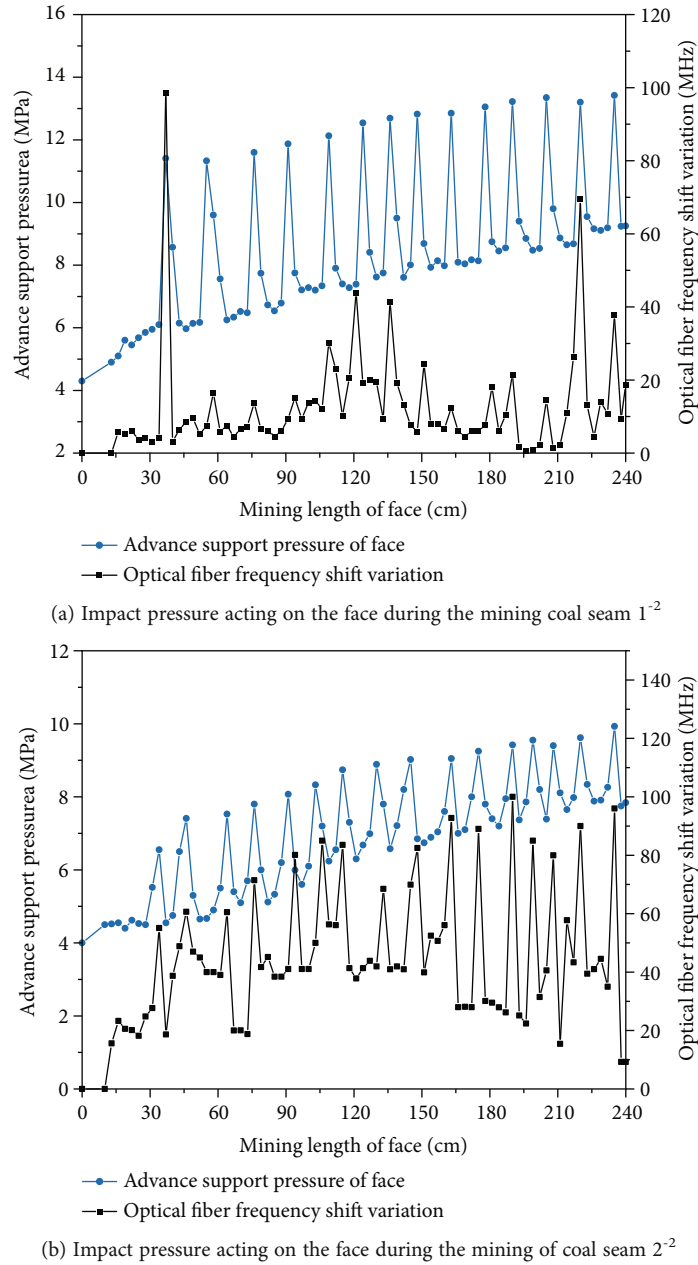


FIGURE 11: Comparison of the impact pressures monitored by the optical fiber sensors and the pressure sensors.

acting on the face in the lower coal mining differing from that in the upper coal mining. Figure 10 shows the comparison of the variation degree of the optical fiber frequency shift in the impact pressure events on the face during the mining of coal seams 1⁻² and 2⁻².

Figure 10 shows that the average variation degrees of the mining of coal seams 1⁻² and 2⁻² were 30.92 and 80.06 MHz, respectively, with a ratio of 1:2.64. This indicates that the average intensity of the impact pressures in the mining of coal seam 2⁻² was 2.64 times that in the mining of coal seam 1⁻², reflecting the more violent mining environment of coal seam 2⁻². The reason for this phenomenon was that after the upper coal mining was completed, the overburden chan-

ged from intact rocks to broken rocks, and the caved rocks fell into the goaf. The load-sustaining capacity of the caved rocks was greatly reduced, causing its load to directly act on the coal seam floor in the goaf. When a single key layer in lower coal seam 2⁻² overburden was broken during face mining, the caving of the overburden in the original goaf was affected by the secondary mining, causing overall clipped collapse and step subsidence of the overburden. This is the reason why the intensity of the impact pressures in this type of mining is greater than that in single-coal-seam mining. Moreover, the mining height of the lower coal seam was 2.38 times that of the upper coal seam. The higher mining height caused greater vertical deformation of the overburden. When the

coal seam spacing was smaller, it was easier for the cracks in the overburden of the lower coal seam to penetrate into the goaf of the upper coal seam. Therefore, the impact pressures during the short-distance mining of the lower coal seam mining were more violent than those in single-coal-seam mining.

5.4. Comparative Analysis of Pressure Sensor Measurement Results. The pressure of the overlying strata during the coal mining process was measured using CL-YB-114 pressure sensors installed at the bottom of the similarity model. The coal seam excavation caused the advanced support pressure of the overburden, which was sustained by the coal wall in front of the face. When the impact pressure occurred, the peak value of the advanced support pressure increased rapidly. Therefore, the peak value of the monitored curve of the advanced support pressure can be used to judge whether an impact pressure event occurred.

For the mining of the faces of coal seams 1⁻² and 2⁻², the comparisons of the variation degrees of the optical fiber frequency shifts and the peak values of the advanced support pressures provided by the pressure sensors are shown in Figure 11. The initial pressure of the overburden was measured by the pressure sensors before the face was excavated. The initial support pressure measured in coal seam mining 1⁻² was 4.30 MPa, while that in coal seam 2⁻² was 4.00 MPa. This is because the overburden pressure was reduced by the mining of coal seam 1⁻². The overburden pressure sustained by the coal wall increased gradually during the excavation of the face, and the peak values of the advanced support pressures also increased gradually. The curve of the pressure sensors exhibits continuous convex peaks. When the peaks occurred, the initial impact pressure or periodic pressures occurred on the face. During the mining of coal seams 1⁻² and 2⁻², the pressure sensors detected 14 and 16 impact pressure events, respectively. Moreover, the step distances of the impact pressures detected by the pressure sensors were consistent with the signals reflected by the variation degree of the optical fiber frequency shift. Therefore, the frequency shift variation can be used to characterize the impact pressure acting on the face.

6. Conclusions

In this study, critical issues in applying distributed optical fiber sensing to monitoring overburden deformation using similarity simulation tests were investigated. The relationships between the optical fiber monitoring, overburden deformation, and face impact pressure were explored. The following conclusions were drawn.

- (1) Overburden strain monitoring during the entire mining process was achieved at different relative positions between the distributed optical fiber sensors and the face. The peak positions of the advanced support pressures acting on the face were obtained. The three-step characteristics of the Brillouin frequency shift curve of the vertically distributed fiber sensors reflect the dynamic variation of the overburden movement in the goaf. They can quantitatively

describe the height evolution characteristics of the overburden fracturing zone and the crack zone in the similarity model

- (2) A new method was proposed for characterizing the impact pressure acting on the face based on the variation degree of the optical fiber frequency shift. The number of impact pressure events detected by the optical fiber frequency shift variation was basically consistent with the pressure sensor monitoring results, thus validating the proposed method
- (3) The variation characteristics of the impact pressures acting on the face during short-distance coal mining were revealed by analyzing the characteristics of the optical fiber frequency shift variation curves. The step distances of the impact pressures during the mining of the lower coal seam were less than those during the mining of the upper coal seam, but the intensity of the impact pressures was greater than that during the mining of the upper coal seam

Data Availability

All the data, models, or codes that support the findings of this study are available from the corresponding author upon reasonable request.

Conflicts of Interest

The authors declare that they have no conflicts of interest.

Acknowledgments

We are grateful for financial support by the Key Program of the National Natural Science Foundation of China (Nos. 51804244, 41027002, and 52004203) and Scientific Research Project of Shaanxi Provincial Department of Education (16JK1488). Many thanks go to Professor J. Chai for the guidance in this paper. We would also like to thank Dr. Wang and Dr. Du for their valuable comments and suggestions for improving the manuscript.

References

- [1] J. C. Wang, "Sustainable coal mining based on mining ground control," *J. Min. Strat. Control Eng.*, vol. 1, pp. 1–8, 2019.
- [2] Q. Wang, M. He, S. Li et al., "Comparative study of model tests on automatically formed roadway and gob-side entry driving in deep coal mines," *International Journal of Mining Science and Technology*, vol. 31, no. 4, pp. 591–601, 2021.
- [3] C. Zhu, K. Zhang, H. Cai et al., "Combined application of optical fibers and CRLD bolts to monitor deformation of a pit-in-pit foundation," *Advances in Civil Engineering*, vol. 2019, Article ID 2572034, 16 pages, 2019.
- [4] W. Du, J. Chai, D. Zhang, and W. Lei, "The study of water-resistant key strata stability detected by optic fiber sensing in shallow-buried coal seam," *International Journal of Rock Mechanics and Mining Sciences*, vol. 141, p. 104604, 2021.

- [5] P. S. Zhang and B. Sun, "Distribution characteristics of the advance abutment pressure in a deep stope," *Journal of Geophysics and Engineering*, 2020.
- [6] T. Zhigang, Z. Chun, W. Yong, W. Jiamin, H. Manchao, and Z. Bo, "Research on stability of an open-pit mine dump with fiber optic monitoring," *Geofluids*, vol. 2018, Article ID 9631706, 20 pages, 2018.
- [7] F. N. Wang, Z. B. Guo, X. B. Qiao et al., "Large deformation mechanism of thin-layered carbonaceous slate and energy coupling support technology of NPR anchor cable in Minxian Tunnel: a case study," *Tunnelling and Underground Space Technology*, vol. 117, p. 104151, 2021.
- [8] X. Li, K. Peng, J. Peng, and H. Xu, "Effect of cyclic wetting-drying treatment on strength and failure behavior of two quartz-rich sandstones under direct shear," *Rock Mechanics and Rock Engineering*, 2021.
- [9] F. Wu, H. Zhang, Q. Zou, C. Li, J. Chen, and R. Gao, "Visco-elastic-plastic damage creep model for salt rock based on fractional derivative theory," *Mechanics of Materials*, vol. 150, p. 103600, 2020.
- [10] C. O. Aksoy, H. Kose, T. Onargan, Y. Koca, and K. Heasley, "Estimation of limit angle using laminated displacement discontinuity analysis in the Soma coal field, Western Turkey," *International Journal of Rock Mechanics and Mining Sciences*, vol. 41, no. 4, pp. 547–556, 2004.
- [11] Q. Ye, G. Wang, Z. Jia, C. Zheng, and W. Wang, "Similarity simulation of mining-crack-evolution characteristics of overburden strata in deep coal mining with large dip," *Journal of Petroleum Science and Engineering*, vol. 165, pp. 477–487, 2018.
- [12] J. Li, F. Li, M. Hu, X. Zhou, and Y. Huo, "Dynamic monitoring of the mining-induced fractured zone in overburden strata, based on geo-electrical characteristics," *Arabian Journal of Geosciences*, vol. 12, pp. 1–12, 2019.
- [13] W. Zhou, P. Zhang, R. Wu, and X. Hu, "Dynamic monitoring the deformation and failure of extra-thick coal seam floor in deep mining," *Journal of Applied Geophysics*, vol. 163, pp. 132–138, 2019.
- [14] D. D. Zhang, C. Ma, Y. Duan, W. du, J. Liu, and J. Chai, "Wavelength characteristic analysis of a FBG array embedded in quaternary unconsolidated strata during a deep borehole installation," *Journal of Sensors*, vol. 2021, Article ID 1207374, 13 pages, 2021.
- [15] F. N. Wang, S. Yin, A. Guo et al., "Frame structure and engineering applications of the multisource system cloud service platform of monitoring of the soft rock tunnel," *Geofluids*, vol. 2021, Article ID 6672732, 15 pages, 2021.
- [16] L. J. Butler, N. Gibbons, P. He, C. Middleton, and M. Z. E. B. Elshafie, "Evaluating the early-age behaviour of full-scale prestressed concrete beams using distributed and discrete fibre optic sensors," *Construction and Building Materials*, vol. 126, pp. 894–912, 2016.
- [17] C. Pandian, M. Kasinathan, S. Sosamma et al., "Single-fiber grid for improved spatial resolution in distributed fiber optic sensor," *Optics Letters*, vol. 35, no. 10, pp. 1677–1679, 2010.
- [18] W. Zou, Z. He, and K. Hotate, "Single-end-access correlation-domain distributed fiber-optic sensor based on stimulated Brillouin scattering," *Optics Index*, vol. 28, no. 18, pp. 2736–2742, 2010.
- [19] T. Horiguchi, T. Kurashima, and M. Tateda, "Tensile strain dependence of Brillouin frequency shift in silica optical fibers," *IEEE Photonics Technology Letters*, vol. 1, no. 5, pp. 107–108, 1989.
- [20] Y. Li, X. Y. Bao, Y. Dong, and L. Chen, "A novel distributed Brillouin sensor based on optical differential parametric amplification," *Journal of Lightwave Technology*, vol. 28, no. 18, pp. 2621–2626, 2010.
- [21] K. Kishida, C. H. Li, and K. Nishiguchi, "Pulse pre-pump method for cm-order spatial resolution of BOTDA," in *17th International Conference on Optical Fibre Sensors*, pp. 559–562, Bruges, Belgium, May 2005.
- [22] Kwang Yong Song, Sanghoon Chin, N. Primerov, and L. Thevenaz, "Time-domain distributed fiber sensor with 1 cm spatial resolution based on Brillouin dynamic grating," *Journal of Lightwave Technology*, vol. 28, no. 14, pp. 2062–2067, 2010.
- [23] W. Du, J. Chai, D. Zhang, and W. Lei, "Application of optical fiber sensing technology in similar model test of shallow-buried and thick coal seam mining," *Measurement*, vol. 181, p. 109559, 2021.
- [24] A. Klar and R. Linker, "Feasibility study of automated detection of tunnel excavation by Brillouin optical time domain reflectometry," *Tunnelling and Underground Space Technology*, vol. 25, no. 5, pp. 575–586, 2010.
- [25] R. A. Moffat, J. F. Beltran, and R. Herrera, "Applications of BOTDR fiber optics to the monitoring of underground structures," *Geo-mechanics and Engineering*, vol. 9, no. 3, pp. 397–414, 2015.
- [26] E. Buchoud, V. Vrabie, J. I. Mars et al., "Quantification of sub-millimeter displacements by distributed optical fiber sensors," *IEEE Transactions on Instrumentation and Measurement*, vol. 65, no. 2, pp. 413–422, 2016.
- [27] D. Zhang, J. Wang, P. Zhang, and B. Shi, "Internal strain monitoring for coal mining similarity model based on distributed fiber optical sensing," *Measurement*, vol. 97, pp. 234–241, 2017.
- [28] J. Chai, W. du, Q. Yuan, and D. Zhang, "Analysis of test method for physical model test of mining based on optical fiber sensing technology detection," *Optical Fiber Technology*, vol. 48, pp. 84–94, 2019.
- [29] D. D. Zhang, Y. Duan, W. du, and J. Chai, "Experimental study on physical similar model of fault activation law based on distributed optical fiber monitoring," *Shock and Vibration*, vol. 2021, Article ID 4846977, 11 pages, 2021.
- [30] D. D. Zhang, W. du, J. Chai, and W. Lei, "Strain test performance of Brillouin optical time domain analysis and fiber Bragg grating based on calibration test," *Sensors and Materials*, vol. 33, no. 4, pp. 1387–1404, 2021.
- [31] Q. Yuan, J. Chai, Y. Ren, and Y. Liu, "The characterization pattern of overburden deformation with distributed optical fiber sensing: an analogue model test and extensional analysis," *Sensors*, vol. 20, no. 24, p. 7215, 2020.
- [32] M. G. Qian and J. Xu, "Behaviors of strata movement in coal mining," *Journal of China Coal Society*, vol. 44, pp. 973–984, 2019.

Research Article

Migration of the Industrial Wastewater in Fractured Rock Masses Based on the Thermal-Hydraulic-Mechanical Coupled Model

Yanan Gao ^{1,2,3,4}, Peng Guo,^{1,2} Zetian Zhang ³, Minghui Li ⁴ and Feng Gao^{1,2}

¹State Key Laboratory for Geomechanics and Underground Engineering, China University of Mining and Technology, Xuzhou, Jiangsu 221116, China

²School of Mechanics and Civil Engineering, China University of Mining and Technology, Xuzhou, Jiangsu 221116, China

³Key Laboratory of Deep Earth Science and Engineering, Sichuan University, Chengdu, Sichuan 610025, China

⁴Guangdong Provincial Key Laboratory of Deep Earth Sciences and Geothermal Energy Exploitation and Utilization, Shenzhen University, Shenzhen 518060, China

Correspondence should be addressed to Zetian Zhang; zhangzetian@scu.edu.cn

Received 8 September 2021; Accepted 1 October 2021; Published 16 October 2021

Academic Editor: Yu Wang

Copyright © 2021 Yanan Gao et al. This is an open access article distributed under the Creative Commons Attribution License, which permits unrestricted use, distribution, and reproduction in any medium, provided the original work is properly cited.

Industrial wastewater may have a long-time effect on the environment and human life as it goes underground and causes serious pollution continuously. To have a well understanding of the migration of such wastewater is a basic task for industrial wastewater treatment as well as industrial design. To study the migration mechanism of industrial wastewater in rock formations, the governing equations such as mechanics, seepage, heat, and mass transfer are reviewed, referenced, and proposed. The thermal (T)-hydraulic (H)-mechanical (M) coupled model of the multimedia of matrix-fault and matrix-fracture-fault is established. The influence of the fault and the fractures on the pressure distribution and contaminant migration is analyzed. The influence of fault length, width, dip angle, permeability, and temperature of wastewater on contaminant migration is parametrically studied. The following results can be obtained. (1) The fracture quantitatively affects the concentration distribution, while the fault dominates the concentration distribution and contaminant migration. (2) The migration of the contaminants can be geometrically divided into 3 zones along the direction of the fault: the saturation zone, the rapid diffusion zone, and the concentration decrease zone. (3) There is a peak of the concentration along the bottom of the model. The position of the peak is the projection of the endpoint of the fault. (4) The fault length has the most significant effect on contaminant accumulation. The temperature of the wastewater has the minimum effect on the contaminant accumulation. (5) The accumulation of concentrations can be divided into 2 stages, the slow growth stage (before 20 years) and the rapid growth stage (after 20 years). The main channel of contaminant migration in the slow growth stage is a fault. During the rapid growth stage, the contaminants penetrate through the rock matrix as well as the fault.

1. Introduction

The great development of the society and economy of China leads the rapid growth in the industry. However, the development of the industry inevitably results in environmental problems as the wastewater discharge cannot be avoided. The wastewater that contains the contaminants will cause long-time pollution and risks for the social life and ecology because it migrates continuously in the underground, such as soil and rock. Such polluted soil or rock thus becomes poi-

sonous and harmful and has adverse effects on the environment and human life [1–3]. Therefore, the study of the transport process of contaminants in industrial wastewater in rock formations has been a hot topic for scholars in the last decades.

The simultaneous existence of different scales of physical structures in rock formations, such as matrix, fracture networks, and faults, leads to strongly nonhomogeneous behaviors [4–7]. The contaminants in the migration process thus penetrate from even microscale to macroscale. The flow

status also changes from linear Darcy seepage in the rock and natural microfracture network to the complicated non-linearity in faults. Meanwhile, the transport of contaminants in industrial wastewater in rock formation is the result of a combination of multiple physical fields, including thermal field, hydraulic field, and stress field. The fluid pressure changes in the hydraulic field due to the fluid flow behavior and affects the stress distribution in the rock formation, i.e., it influences the stress field. Also, the thermal characteristics are influenced by the change of velocity of the flow. The change of porosity and permeability of the rock formation due to the change of the stress field also affects the hydraulic field. The change of temperature in the thermal field influences the hydrodynamic viscosity coefficient and the fluid density, which affects the hydraulic field. Thermal stress has a consequent effect on the stress distribution of the stress field.

As mentioned above, the process of the migration of the industrial wastewater is a complex multiphysics coupled problem, such as thermal-hydraulic (TH), thermal-chemical (TC), thermal-mechanical (TM), and THM coupling [8–14]. Based on the energy conservation model, pore fluid mass conservation equation, and the elastic-plastic constitutive model, a more comprehensive multicomponent THM coupling model for unsaturated porous media was established by Seetharam et al. [15, 16]. However, the contribution of the rock formation with strong inhomogeneity to the fluid motion was not considered. et al. established a THMC coupling model for clay barriers in high radioactive waste storage [17]. However, the pore fluid flow and solute diffusion characteristics driven by the combined temperature gradient and concentration gradient were not included. For the study of the mathematical model of fluid seepage, many studies have been carried out. Three typical basic models of rock seepage are proposed, i.e., the equivalent continuous medium seepage model, the fracture network discontinuous medium seepage model, and the dual medium seepage model [18–20]. Rossen pointed out that the pore-fissure and interfracture seepage problems can be solved by the way of Darcy's law and an anisotropic permeability tensor and proposed a method to characterize the anisotropic seepage in fractured rock masses using continuous medium theory [21]. Such equivalence model is not applicable when the fractured rock mass cannot be treated as a continuous medium, and the discontinuous medium method should be employed [22]. Hsieh et al. introduced hydrodynamics into fracture-pore media by using the N-S equation and the continuity equation as governing equations and provided a new approach to solve this difficult problem [23].

Most of the current studies do not simultaneously consider the inhomogeneity of rock mass and the coupling effect of multiphysics during the migration of the contaminants. Therefore, the THM coupling model with the consideration of the multimedia, i.e., matrix-fracture-fault, is proposed. The influence of the fault and natural fractures on the pressure distribution and contaminant concentration during migration is firstly analyzed. Secondly, the influence of fault length, width, dip angle, permeability, and inflow temperature of wastewater on contaminant migration is studied.

The contaminants in industrial wastewater of this paper are not specified as this is a theoretical and parametric study. The contaminant can be referred to as the common heavy metal ion such as Pb (plumbum) or Hg (mercury).

2. The Coupled THM Model

The seepage of contaminants in rock formations is the result of a combination of physical, chemical, biological, and other factors. Therefore, the study of contaminant migration in rock formations requires the establishment of governing equations under the coupling of multifield such as the chemical field, thermal field, stress field, and hydraulic field. Meanwhile, the migration of contaminants involves convection, adsorption, desorption, hydrodynamic dispersion, chemical action, and microbial decomposition, which cause great difficulties for the research.

In this paper, the study focuses on the seepage mechanism of contaminants in rock formations under the coupled THM effect. The flow of industrial wastewater is considered to be unidirectional, and the effects of adsorption, desorption, chemical interaction, and microbial decomposition during the migration of contaminants are not considered.

In addition, to carry out the numerical modeling, the following simplifications and assumptions of the extremely complex process of THM coupling still required are put forward to establish the theoretical model. (1) The rock is a saturated, isotropic, homogeneous, and small deformation porous elastic medium. (2) The phase change is not considered, i.e., the transformation between gas and liquid phases due to temperature is not considered. (3) Only the heat conduction mode is considered in the rock mass, and thermal radiation is not considered. (4) The thermal strain in the rock mass due to temperature is isotropic.

2.1. Equivalent Continuous Medium Model Theory

2.1.1. Hydraulic Field. The density of wastewater is defined as a function of temperature and pressure [24] and can be expressed as

$$\rho = \rho_0 [1 + \eta_w (p - p_0) - \beta_w (T - T_0)] = \rho_0 (1 + \eta_w \Delta p - \beta_w \Delta T), \quad (1)$$

where η_w is the compression coefficient of the fluid, β_w is the thermal expansion coefficient of the fluid, ρ_0 is the fluid reference density, p and p_0 are the pore water pressure and initial pore water pressure, respectively, and T and T_0 are the fluid temperature and initial temperature, respectively.

The average value of the general ground temperature gradient is 3°C/100 m; thus, the temperature of the flow of wastewater in the rock formation is below 40°C.

The hydrodynamic viscosity decreases with increasing temperature, and the relationship between the hydrodynamic viscosity and the temperature conforms to the power function. The expression of the dynamic viscosity of

wastewater with temperature is as follows [25, 26]:

$$\mu = 1.787 \times 10^{-3} e^{[-0.333 + 1.962 \times 10^{-4} \times T] \times T}. \quad (2)$$

The flow of industrial wastewater in a rock formation can be assumed as the flow of a fluid in a porous medium. According to the law of conservation of mass and Darcy's law, the hydraulic field equation can be expressed as

$$\phi \rho c_p \frac{\partial p}{\partial t} + \nabla \cdot \left(-\rho \frac{k}{\mu} (\nabla p + \rho g \nabla H) \right) = Q_m - \phi \rho c_T \frac{\partial T}{\partial t} - \rho \frac{\partial \phi}{\partial t}, \quad (3)$$

where $c_p = 1/\rho \partial \rho / \partial p$, $c_T = 1/\rho \partial \rho / \partial T$, ϕ is the porosity, ρ is the density of wastewater, k is the permeability of the matrix, g is the acceleration of gravity, $\nabla H = (0, 0, 1)^T$, H represents the hydraulic head, and Q_m is the source term.

2.1.2. Thermal Field. The fluid flow in the rock mass is assumed in thermal equilibrium. Without the consideration of the heat exchange between the rock mass and the wastewater, the thermal field equation of the fluid flow process in saturated porous media can be obtained as [27]

$$(\rho C)_{\text{eff}} \frac{\partial T}{\partial t} + (1 - \phi) T K \alpha_T \frac{\partial \varepsilon_v}{\partial t} = \lambda_{\text{eff}} \nabla^2 T + \rho c_w \frac{k}{\mu} \nabla p \nabla T, \quad (4)$$

where $(\rho C)_{\text{eff}} = \phi \rho c_w + (1 - \phi) \rho_s c_s$ is the effective heat capacity, $\lambda_{\text{eff}} = \phi \lambda_w + (1 - \phi) \lambda_s$ is the effective thermal conductivity, α_T is the coefficient of thermal expansion of the rock matrix, ε_v is the volume strain of the rock matrix, c_w is the specific heat capacity of wastewater, λ_w is the thermal conductivity of wastewater, ρ_s is the density of the rock mass, c_s is the specific heat capacity of the rock matrix, and λ_s is the thermal conductivity of the rock matrix.

2.1.3. Stress Field. The constitutive relationship of the rock mass is idealized as isotropic, homogeneous, and linear medium with small deformation. The deformation of the rock mass will be caused by 3 factors: the stress of the rock mass, the pressure of fluid flow in the rock mass, and the temperature change of the rock mass. Therefore, the stress-strain relationship for the rock mass with consideration of pore pressure and temperature is obtained based on the linear principle:

$$\sigma_{ij} = \sigma'_{ij} + \alpha p \delta_{ij} = 2G \varepsilon_{ij} + \lambda \delta_{ij} \varepsilon_v - K \alpha_T \delta_{ij} (T - T_0) + \alpha p \delta_{ij}, \quad (5)$$

where σ_{ij} is the stress tensor, σ'_{ij} is the effective stress tensor, G is the shear modulus, $G = E/2(1 + \nu)$, ε_{ij} is the strain tensor, λ is the Lamé constant, $\lambda = 2G\nu/(1 - 2\nu)$, and α is the

Biot coefficient:

$$\alpha = 1 - \frac{K}{K_s}, \quad (6)$$

where K is the bulk deformation modulus of the rock matrix, $K = E/3(1 - 2\nu)$, and K_s is the bulk deformation modulus of the rock grains.

Based on the Cauchy strain theory and the static equilibrium, the geometry relationship and the equilibrium equation can be obtained:

$$\varepsilon_{ij} = \frac{1}{2} (u_{i,j} + u_{j,i}), \quad (7)$$

$$\varepsilon_v = \varepsilon_{kk} = \varepsilon_{11} + \varepsilon_{22} + \varepsilon_{33}, \quad (8)$$

$$\sigma_{ij,j} + f_i = 0. \quad (9)$$

Combined with Equation (5), we can get the equation of the stress field of rock mass under stress, pore pressure, and temperature:

$$G(u_{i,ij} + u_{j,ji}) + \lambda u_{j,ji} - \alpha_T T_{,i} + \alpha p_{,i} + F_i = 0, \quad (10)$$

where F_i is the volume force of the rock mass and u_i is the displacement component of the rock mass.

2.1.4. Porosity Model. Porosity is the key factor of pore pressure; thus, it is necessary to choose a porosity model of the rock mass. According to the derivation of the definition of porosity, the dynamic porosity equation of the rock mass is defined as follows [28]:

$$\phi = \alpha - (\alpha - \phi_0) \exp \left(-\frac{1}{K_s} (p - p_0) + \alpha_T (T - T_0) - (\varepsilon_v - \varepsilon_{v0}) \right). \quad (11)$$

2.1.5. Permeability Model. The Kozeny-Carman (KC) equation [29] is a semiempirical formulation widely used in the study of permeability evolution of the porous media. Based on the porosity model, the permeability model can be expressed as

$$k = k_0 \left\{ \left(\frac{1}{\phi_0} - \left(\frac{1}{\phi_0} - 1 \right) \left[1 - \frac{1}{K_s} (p - p_0) + \alpha_T (T - T_0) - (\varepsilon_v - \varepsilon_{v0}) \right] \right) \right\}^3. \quad (12)$$

2.2. THM Coupling Relationship. The coupled THM model defined based on the field equations provided above is illustrated in Figure 1. (1) The hydraulic field affects the mechanical field by changing the fluid pressure. (2) The mechanical field affects the porosity and permeability through the change of volume strain and thus affects the hydraulic field. (3) The hydraulic field affects the thermal convection term in the thermal field through the change of fluid velocity vector. (4) The thermal field affects the fluid density by changing the temperature and then affects the hydraulic field. (5) The mechanical field changes the thermal deformation

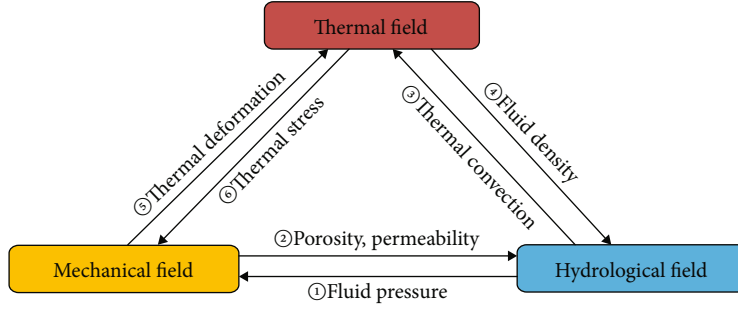


FIGURE 1: THM coupling diagram.

energy to affect the thermal field. (6) The change of temperature in the thermal field produces thermal stress and then affects the mechanical field.

2.3. Matrix-Fracture-Fault (MFF) Multimedia Model. The matrix-fracture-fault (MFF) multimedia model is different from the equivalent continuous medium model. It considers the porous medium separately from the fractured medium with discretization of the fractured medium and the influence of each fracture on the hydraulic and thermal fields. With the continuous improvement of the fracture network, the MFF multimedia model is trending toward perfection in terms of modeling [30].

2.3.1. Hydraulic Field. The equation controlling the seepage in the fracture can be expressed as follows [28]:

$$d_f S_f \frac{\partial p}{\partial t} + \nabla_T \cdot \left(-d_f \frac{k_f}{\mu} \nabla_T p \right) = -d_f \frac{\partial \varepsilon_v}{\partial t} + Q_f, \quad (13)$$

where d_f is the fracture width, S_f is the water storage coefficient of the fissure, ∇_T is the tangential gradient operator along the fissure boundary direction, which is the tangential differentiation on the boundary as a function of the x -direction and y -direction, and k_f is the fissure permeability.

2.3.2. Thermal Field. In contrast to the equivalent continuous medium case, when discrete fractures are present in the model, the discrete fractures become the main flow channels for the fluid in the matrix. Therefore, the effect of convective action in the matrix on the thermal field of the model can be neglected. The heat conduction effect is considered to be present in the matrix only, and therefore, the governing equation for the thermal field in the fracture can be expressed as follows:

$$d_f (\rho C)_{\text{eff}} \frac{\partial T}{\partial t} = \nabla_T \cdot (d_f \lambda_{\text{eff}} \nabla_T T) + d_f \rho c_w \frac{k}{\mu} \nabla p \nabla_T T + Q_w. \quad (14)$$

2.3.3. Stress Field. Same as the stress governing equation for the equivalent continuous medium, the stress field governing equation for the fracture part can be expressed as

$$G(u_{i,ij} + u_{j,ij}) + \lambda u_{j,ji} - \alpha_T T_{,i} + \alpha p_{,i} + F_i = 0. \quad (15)$$

Since the study in this paper is a 2-dimensional diffusion model, the discrete fractures are treated as a geometry model of line. Therefore, the deformation of the fractures is neglected. The relationship between permeability and stress of the fractures can be established based on the borehole test of water pressure measurement [31]:

$$k_f = k_{f0} \exp(-\alpha_f \sigma_n), \quad (16)$$

where k_{f0} is the permeability of the fracture when $\sigma_n = 0$, σ_n is the normal corresponding force of the fracture surface, α_f is the influence coefficient, and it determines the fracture state.

2.4. Contaminant Migration Model. The migration mechanism of contaminants in porous media consists of 3 parts: convection, i.e., the contaminant is driven by the water flow to migrate downstream; diffusion, where the contaminant diffuses from high concentration area to low concentration area under the effect of a concentration gradient; and dispersion, which is caused by the presence of a porous media, and the porous media cause the migration velocity of contaminants to be different in magnitude and direction from the average flow rate. Although the mechanisms of diffusion and mechanical dispersion are different, they are still difficult to distinguish. And they are generally named as hydrodynamic dispersion. The mechanism of contaminant migration in porous media can be expressed as follows:

$$\frac{\partial c}{\partial t} = \nabla \cdot (D \nabla c) - \nabla \cdot (uc) + I, \quad (17)$$

where c is the solute concentration, D is the hydrodynamic dispersion coefficient, and u is the convection velocity.

3. Migration in the Multimedia under the Coupled THM Effects

To investigate the migration of the contaminants under the coupled THM effects as well as the influence of the fault and fractures, 2 models are employed, i.e.,

- (1) matrix-fault (MF) model
- (2) MFF model

TABLE 1: The parameters and values.

Parameters	Value
Young's modulus of the rock matrix, E (Pa)	2×10^{10}
Young's modulus of the rock grains, E_s (Pa)	5×10^{10}
Poisson's ratio, ν	0.3
Coefficient of thermal expansion of rock matrix, α_T (1/K)	1.2×10^{-5}
Density of the rock grains, ρ_s (kg/m^3)	2652
Specific heat capacity of the rock matrix, c_s ($\text{J}/(\text{kg}\cdot^\circ\text{C})$)	2190
Thermal conductivity of the rock matrix, λ_s ($\text{W}/(\text{m}\cdot^\circ\text{C})$)	0.56
Density of the wastewater, ρ_0 (kg/m^3)	1100
Specific heat capacity of the wastewater, c_w ($\text{J}/(\text{kg}\cdot^\circ\text{C})$)	4210
Thermal conductivity of the wastewater, λ_w ($\text{W}/(\text{m}\cdot^\circ\text{C})$)	0.65
Initial porosity, ϕ_0	0.001
Initial permeability of the matrix, k_0 (m^2)	2.5×10^{-15}
Initial permeability of the fault, k_1 (m^2)	1×10^{-13}
Initial permeability of the fractures, k_2 (m^2)	2.5×10^{-14}
Width of the fault, d_1 (m)	0.002
Aperture of the fracture, d_2 (m)	0.0005

The MF model considers the rock matrix and the fault, and the MFF model considers the rock matrix, the fault, and the fractures.

The upper boundary of the model is the inflow boundary of the wastewater. The initial temperature of the rock formation is 318 K. The temperature of the inflowing contaminant at the upper boundary is 293 K. The concentration of contaminants is $1 \text{ mol}/\text{m}^3$. The head pressure of the upper boundary is 9000 Pa. The parameter used in the numerical study is listed in Table 1.

To study the concentration distribution of the contaminant around the fault and the accumulation of the concentration, 2 monitoring lines (AB and CD) are selected. The line of AB is along the direction of the fault. The line of CD is along the bottom of the geometry models. The coordinates of endpoints $A, B, C,$ and D are (23.66 m, 30 m), (6.34 m, 0 m), (0 m, 0 m), and (30 m, 0 m).

3.1. MF Model. As shown in Figure 2, a geometric model with the size $30 \text{ m} \times 30 \text{ m}$ is established. The incline angle of the fault is 60° , the width of the fault is 0.002 m, and the coordinate of the midpoint of the fault is (15 m, 15 m).

As shown in Figure 3, the pressure around the fault varies obviously as the contour lines concentrate. The pressure distribution in the model behaves nonhomogeneously due to the fault. The difference in permeability of the fault and the rock matrix may be the reason for this phenomenon as it may cause the nonhomogeneity in the seepage field.

Figure 4 is the distribution of the contaminant concentration after 20 years. The contaminants are mainly concentrated in the upper half of the model and along the fault. It may imply that the contaminants migrate very slowly, and the diffusion is more significant in the fault than in the matrix.

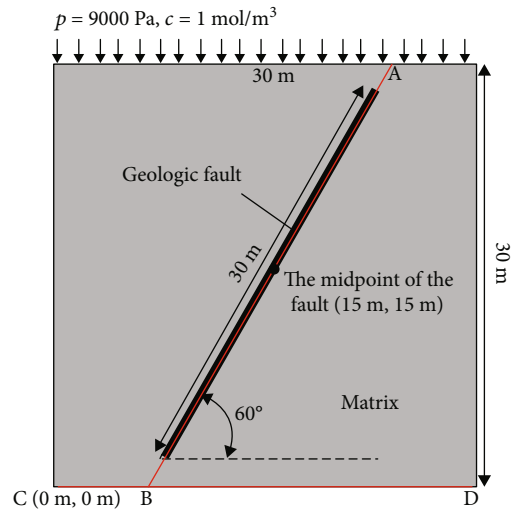


FIGURE 2: Geometry of the MF model.

As mentioned above, the fault may influence the flow of the wastewater and the migration of the contaminants greatly. The flow vector is employed to illustrate. As shown in Figure 5, both the direction and density of the vectors change obviously around the fault; thus, it can be another aspect to reflect the role of the fault for the distribution of the nonhomogeneity.

Although the fault has a dramatic effect on the flow field, the concentration of the contaminants is monitored along the fault direction, i.e., the line of AB . It is important to note that the length of AB in this paper is calculated based on the start point of A . As shown in Figure 6, the contaminants reach saturation as the concentration is close to $1 \text{ mol}/\text{m}^3$ within the length of 3 m toward the fault direction. And

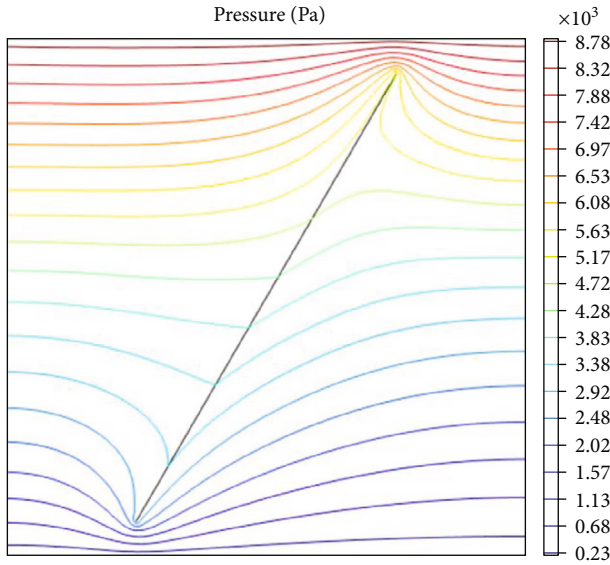


FIGURE 3: The pressure distribution contour of the MF model.

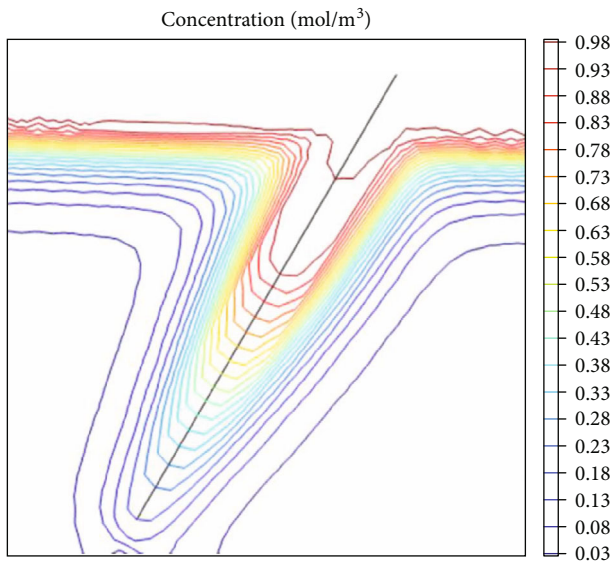


FIGURE 4: The concentration distribution contour of the MF model.

the diffusion of the contaminants becomes remarkable from about 3 m to 15 m along the fault. Thus, a rapid diffusion zone can be found. From 15 m to the bottom of the model (point B), the concentration decreases rapidly. Therefore, the migration of the contaminants can be divided into 3 zones along the direction of the fault, i.e., the saturation zone, the rapid diffusion zone, and the concentration decrease zone.

It can be also observed that the concentration increases with time. The concentration of the point of B reaches $0.23 \times 10^{-3} \text{ mol/m}^3$, $1.31 \times 10^{-3} \text{ mol/m}^3$, $1.3 \times 10^{-3} \text{ mol/m}^3$, 0.012 mol/m^3 , 0.074 mol/m^3 , and 0.138 mol/m^3 at the time of 5 years, 10 years, 15 years, 20 years, 25 years, and 30 years, respectively.

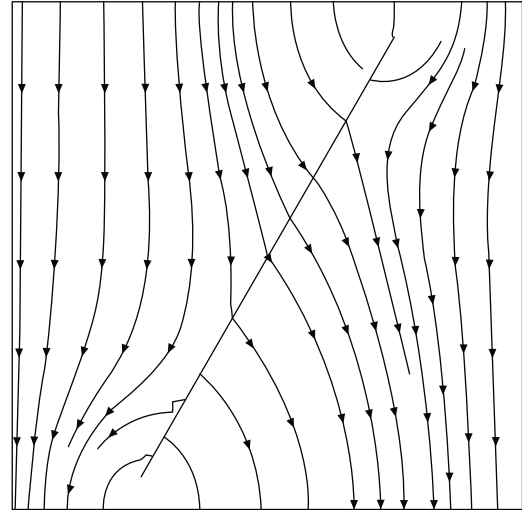


FIGURE 5: The flow vector of the wastewater of the MF model.

Figure 7 is the plot of the concentration along the line of CD, i.e., the bottom of the model. Similarly, the concentration increases with time, and it becomes the maximum after 30 years. Meanwhile, it can be found that this is a peak in each line of the plot. And the peak occurs at the point of the projection of the endpoint of the fault. The reason may be as follows. The fault has a significant effect on the migration of the contaminants as its permeability is much higher than that of the rock matrix. The projection of the endpoint of the fault is the point which is the nearest to the fault; therefore, the peak value of the concentration occurs around such a point.

3.2. MFF Model. In this section, the MFF model (Figure 8) with the consideration of the rock matrix, the fault, and the fractures is employed to study the effect of the fractures. 50 fractures are generated randomly by using MATLAB coding [32]. The length of the fractures varies from 0.8 m to 4 m. The direction of the fractures varies from 0° to 360° . The aperture of each fracture is 0.0005 m.

Compared with Figure 3, there are more drastic pressure changes in the model (Figure 9). The nonhomogeneity of the pressure distribution of the MFF model is more obvious than that of the MF model. The pressure contours change around the natural fractures. However, the main pattern of the pressure distribution of the MFF model is similar to that of the MF model. It can be also found that the distribution of the concentration of the MFF model (Figure 10) is similar to that of the MF model. The phenomena mentioned above may indicate that the fault has a dominant role in the concentration distribution and contaminant migration.

Based on Figure 11, it can be found that there are also 3 typical zones of the contaminant concentration, the saturation zone, the rapid diffusion zone, and the concentration decrease zone. And the geometry scale of the 3 zones is also similar to that of the MF model. The concentration of the point B reaches $1.15 \times 10^{-3} \text{ mol/m}^3$, $1.47 \times 10^{-3} \text{ mol/m}^3$, $1.79 \times 10^{-3} \text{ mol/m}^3$, 0.016 mol/m^3 , 0.086 mol/m^3 , and

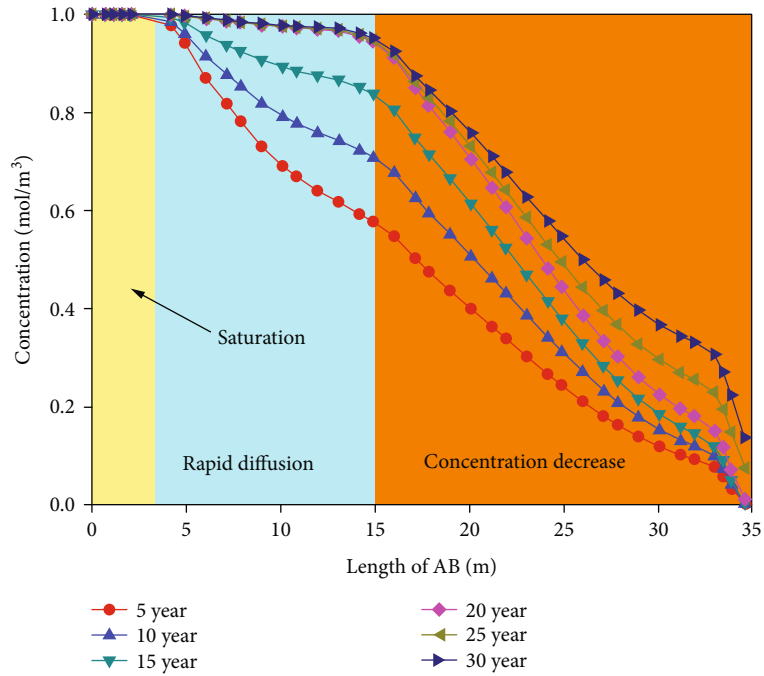


FIGURE 6: The contaminant concentration along the line of AB in the MF model.

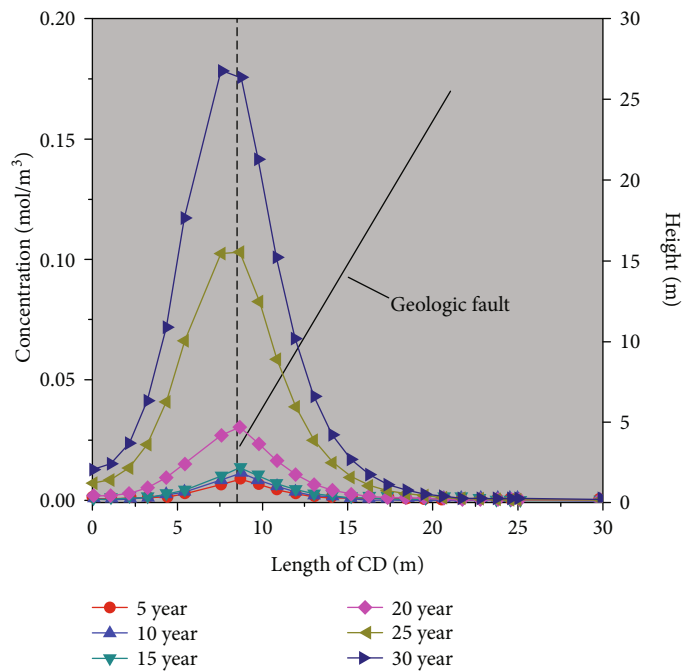


FIGURE 7: The contaminant concentration along the line of CD in the MF model.

0.157 mol/m³ at the time of 5 years, 10 years, 15 years, 20 years, 25 years, and 30 years, respectively.

Figure 12 is the plot of the concentration distribution along the bottom of the MFF model (the line of CD); there is also a peak for each line of the plot. Each peak value of MFF is higher than the corresponding one of the MF model. And the position where the peak occurs is almost the same as that of the MFF model. Therefore, the concentration dis-

tribution of the 2 models is similar, and the magnitude of the MFF model is higher than that of the MF model.

4. Effect of the Fault Parameters on Contaminant Migration

As discussed in Section 3, the fault has a dominant role in contaminant migration. The parametric study of the fault

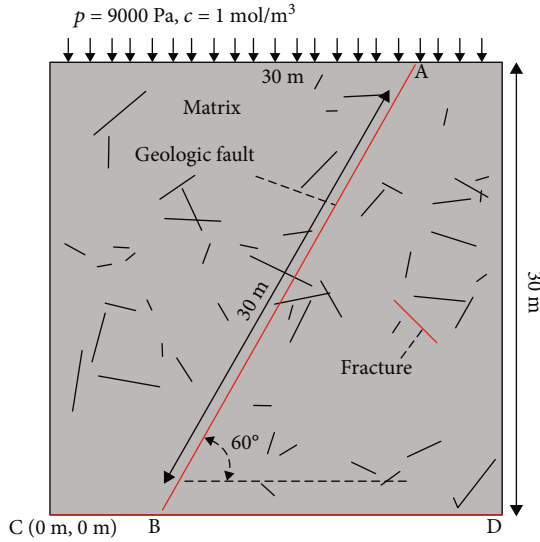


FIGURE 8: Geometry of the MFF model.

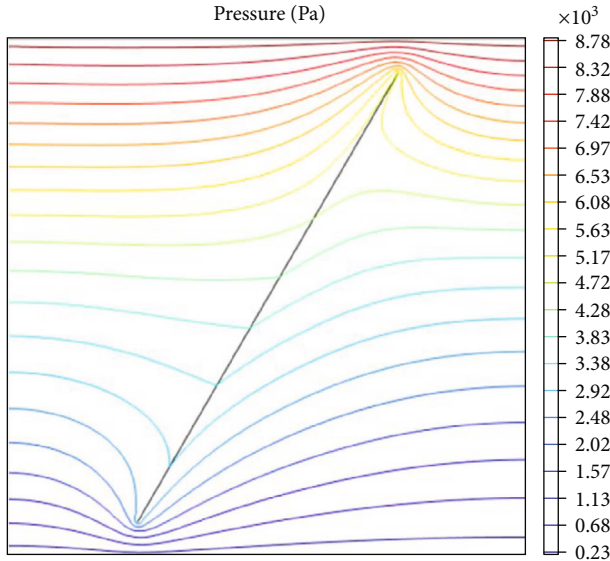


FIGURE 9: The pressure distribution contour of the MFF model.

is carried out in this section. The length, width, dip, permeability, and width of the fault are selected as the parameters. In addition, the effect of the initial temperature of industrial wastewater is also studied.

4.1. Length of the Fault. Based on the results of Section 3.1, the length of the fault may dominate the distribution of contaminants; it is thus a crucial factor affecting the migration of contaminants. In this section, 3 models with different fault lengths (Table 2) are employed to explore the effect of fault length on the migration of contaminants.

Figure 13 shows the accumulation of contaminants along the line of CD under the different fault lengths. The accumulation of contaminants at the line of CD increases gradually with time. After 30 years, the accumulation of contaminants at the CD reaches 3.68×10^{-4} mol (Model L1),

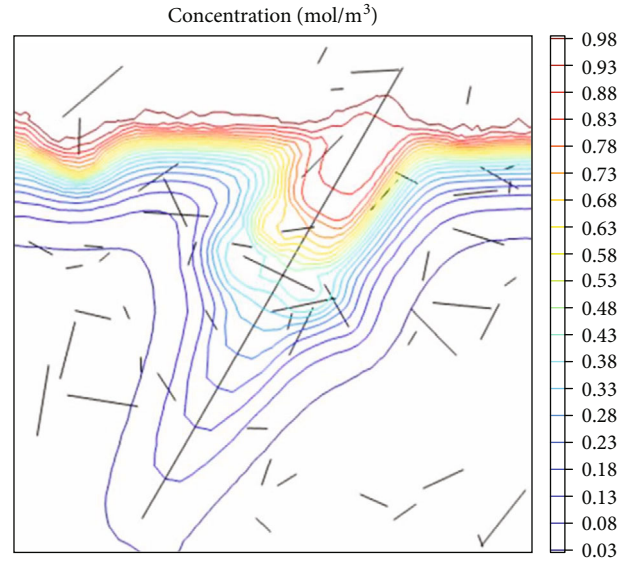


FIGURE 10: The concentration distribution contour of the MFF model.

0.064 mol (Model L2), and 1.58 mol (Model L3), respectively. The length of the fault has an obvious effect on the accumulation of contaminants. A longer fault will result in more accumulation of contaminants.

4.2. Width of the Fault. The width of a fault may not have a remarkable effect on the migration pattern of the contaminants while it is associated with permeability. It may also have an important effect on contaminant accumulation. In this section, 3 models with the different fault widths (Table 3) are established to study the influence of fault width on contaminant accumulation.

The accumulation of the contaminants along the line of CD under the different fault widths is plotted in Figure 14. After 30 years, the accumulation of contaminants at the line of CD reaches 0.69 mol (Model W1), 1.58 mol (Model W2), and 1.83 mol (Model W3), respectively. A larger fault width may lead to a larger accumulation. This indicates that the width of the fault can increase the local permeability of the model and enhance the diffusion of contaminants.

4.3. Fault Dip Angle. In the process of contaminant migration, the dip angle of the fault may determine the length of the fault; therefore, the migration distance of the contaminants as well as the distribution of the contaminants could be affected by such dip angle. Three models (Table 4) with different dip angles of the fault are considered for the accumulation of contaminants.

Figure 15 is the plot of the accumulation of contaminants along the line of CD under the different fault dip angles. After 30 years, the accumulation of contaminants along the line of CD reaches 0.67 mol (Model D1), 1.25 mol (Model D2), and 1.58 mol (Model D3), respectively. The 60° of dip angle of the fault may induce the maximum accumulation of contaminants.

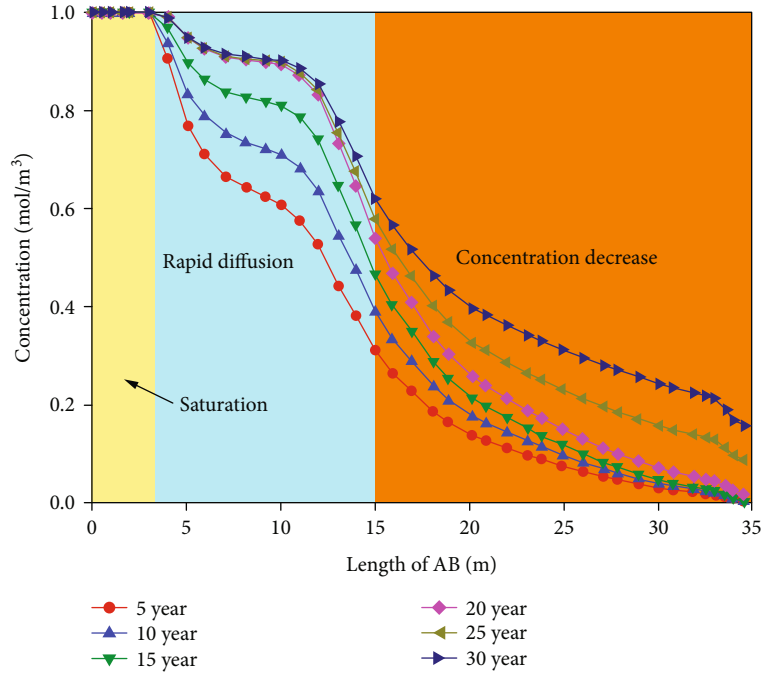


FIGURE 11: The contaminant concentration along the line of AB in the MFF model.

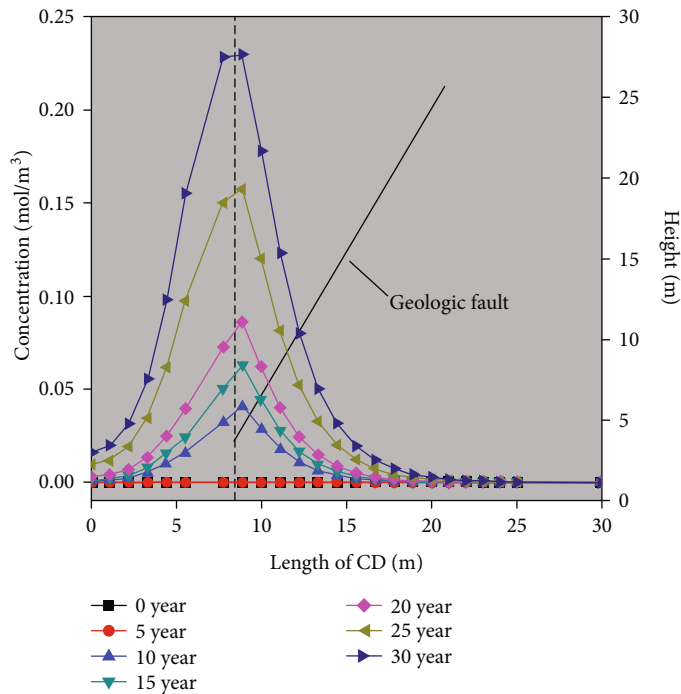


FIGURE 12: The contaminant concentration along the line of CD in the MFF model.

TABLE 2: The fault length in the different models.

Model no.	Model L1	Model L2	Model L3
Fault length (m)	10	20	30

4.4. *Fault Permeability.* The permeability coefficient is an index of the permeability of rock formations and has a critical influence on the migration of contaminants. In this sec-

tion, the initial permeability k of the fault is set as $1 \times 10^{-13} \text{ m}^2$. Three models (Table 5) with different permeability of the fault are employed to investigate the influence of fault permeability on the accumulation of contaminants.

Figure 16 shows the accumulation of contaminants along the line of CD with time under the different permeability. After 30 years, the accumulation of contaminants at

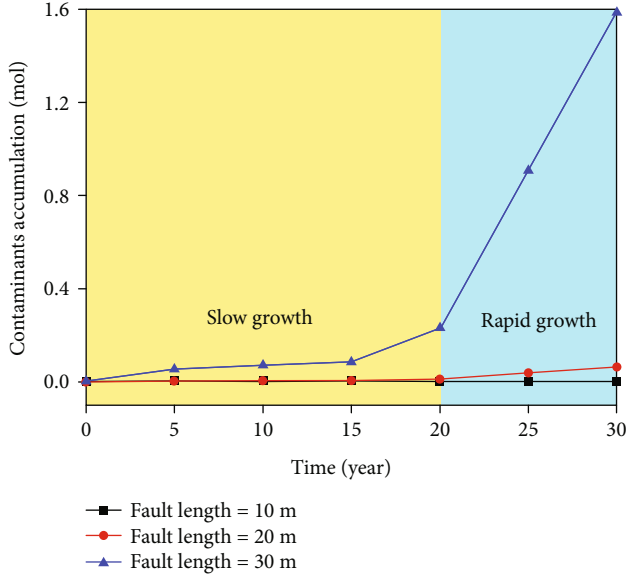


FIGURE 13: The contaminant accumulation along the line of CD under different fault lengths.

TABLE 3: The fault width in the different models.

Model no.	Model W1	Model W2	Model W3
Fault width (m)	0.001	0.002	0.003

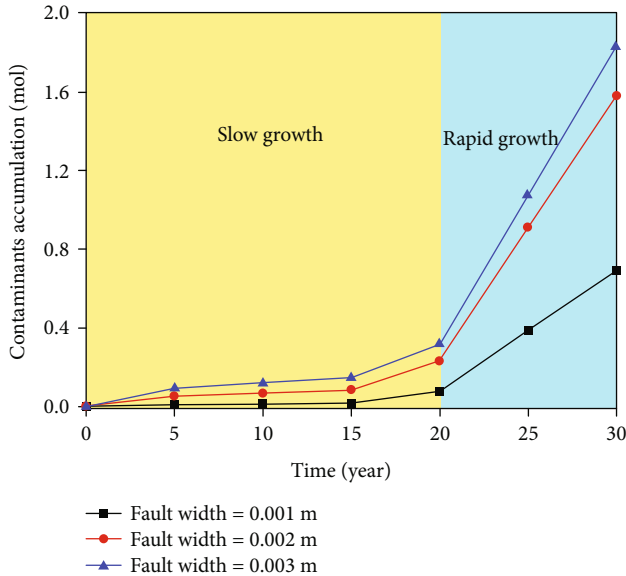


FIGURE 14: The contaminant accumulation along the line of CD under the different fault widths.

TABLE 4: The fault dip angle in different models.

Model no.	Model D1	Model D2	Model D3
Fault dip angle ($^{\circ}$)	30	45	60

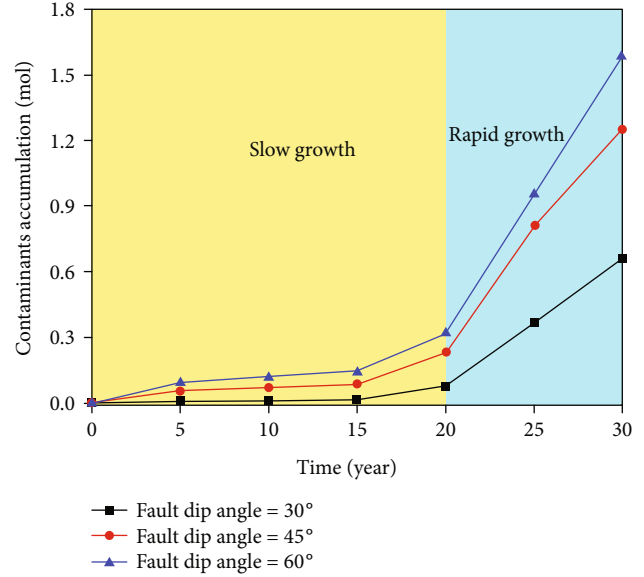


FIGURE 15: The contaminant accumulation along the line of CD under different fault dip angles.

CD reaches 0.67 mol (Model P1), 1.58 mol (Model P2), and 1.84 mol (Model P3), respectively. A larger permeability results in a larger accumulation of contaminants.

4.5. Inflow Temperature of Industrial Wastewater. When wastewater flows into a rock formation, the inflow temperature will impact the thermal field of the rock formation, and the intereffect of the THM coupling will thus influence the migration of the wastewater. In this section, the inflow temperature of wastewater (Table 6) is selected as a parameter to study the contaminant accumulation.

The accumulation of contaminants along the line of CD under different inflow temperatures is plotted in Figure 17. The accumulation of contaminants at the CD increases gradually with time. After 30 years, the accumulation of contaminants along the line of CD reaches 1.58 mol (Model T1), 1.69 mol (Model T2), and 1.76 mol (Model T3), respectively. The temperature of the inflow water has a positive relationship with contaminant accumulation, while it does not affect as much as the fault parameters.

4.6. Discussion. From Figures 13–17, it can be inferred that the fault length has the most remarkable effect on the contaminant accumulation, while the temperature of the wastewater has the minimum effect on the contaminant accumulation.

Meanwhile, the accumulation of contaminants is divided into 2 stages, slow growth stage and rapid growth stage. And for all the models, the slow growth stage is before 20 years, and the rapid growth stage begins after 20 years. The reason for the 2 stages may be that the main channel of contaminant migration in the slow growth stage is the fault; thus, the concentration accumulation increases slowly. During the rapid growth stage, the long-time scale seepage results in the entire penetration of the contaminants through the

TABLE 5: Permeability in different models.

Model no.	Model P1	Model P2	Model P3
Fault permeability (m^2)	$0.5 k$	$1.0 k$	$1.5 k$

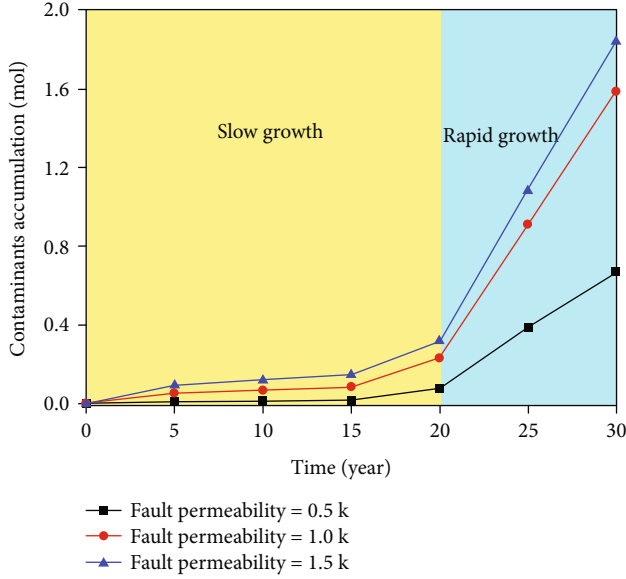


FIGURE 16: The contaminant accumulation along the line of CD under different permeability.

TABLE 6: The temperature of the inflow wastewater.

Model no.	Model T1	Model T2	Model T3
Inflow temperature ($^{\circ}C$)	20	30	40

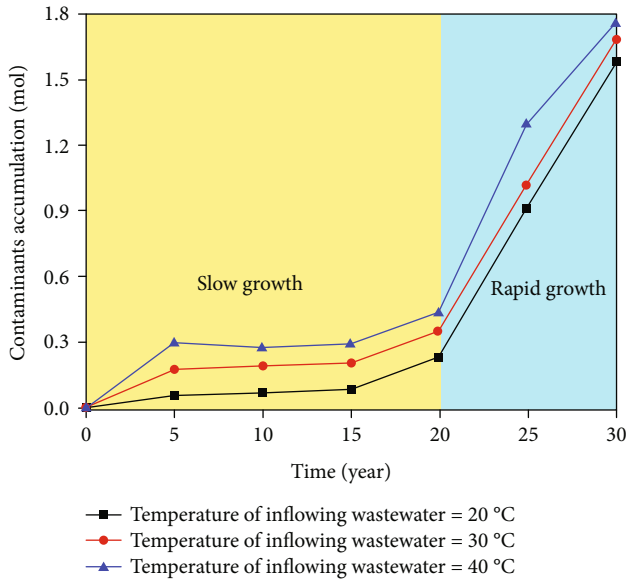


FIGURE 17: The contaminant accumulation along the line of CD under different inflow temperatures.

rock matrix as well as the fault; therefore, the concentration accumulation increases rapidly.

5. Conclusions

Based on the governing equations of the THM coupled theory, multimedia of MF and MFF is presented. The migration of the contaminants is analyzed. The parametric study of the fault geometry and the temperature of the wastewater is carried out. The conclusion can be summarized as follows:

- (1) The pressure distribution is strongly nonhomogeneous around the fault. The fracture quantitatively affects the concentration distribution, while the fault dominates the concentration distribution and contaminant migration
- (2) The migration of the contaminants can be geometrically divided into 3 zones along the direction of the fault, the saturation zone, the rapid diffusion zone, and the concentration decrease zone
- (3) There is a peak of the concentration along the bottom of the model. Such peak occurs at the point of the projection of the endpoint of the fault because this position is the nearest to the fault
- (4) The accumulation of contaminants is positively correlated with the fault length, width, dip angle, permeability, and temperature of wastewater. The fault length has the most significant effect on contaminant accumulation. The temperature of the wastewater has the minimum effect on the contaminant accumulation
- (5) The accumulation of concentrations can be divided into 2 stages, the slow growth stage (before 20 years) and the rapid growth stage (after 20 years). The main channel of contaminant migration in the slow growth stage is a fault. During the rapid growth stage, the contaminants penetrate through the rock matrix as well as the fault

Symbols

- η_w : The fluid compression coefficient
- β_w : The thermal expansion coefficient of the fluid
- ρ : The fluid reference density (kg/m^3)
- ρ_0 : The density of wastewater (kg/m^3)
- ρ_s : The density of the rock mass (kg/m^3)
- p : The pore pressure (MPa)
- p_0 : The initial pore pressure (MPa)
- T : The fluid temperature ($^{\circ}C$)
- T_0 : The initial temperature ($^{\circ}C$)
- φ : The porosity
- φ_0 : The initial porosity
- k : The permeability of the matrix (m^2)
- k_0 : The initial permeability of matrix (m^2)
- k_1 : The initial permeability of fault (m^2)
- k_2 : The initial permeability of fracture (m^2)

g : The acceleration of gravity (m/s^2)
 Q_m : The source term
 α_T : The coefficient of thermal expansion of the rock matrix
 λ_s : The thermal conductivity of the rock matrix ($\text{W}/(\text{m}\cdot^\circ\text{C})$)
 λ_w : The thermal conductivity of wastewater ($\text{W}/(\text{m}\cdot^\circ\text{C})$)
 c_w : The specific heat capacity of wastewater ($\text{J}/(\text{kg}\cdot^\circ\text{C})$)
 c_s : The specific heat capacity of the rock matrix ($\text{J}/(\text{kg}\cdot^\circ\text{C})$)
 K : The bulk deformation modulus of the rock matrix (Pa)
 K_s : The bulk deformation modulus of the rock grains (Pa)
 E : Young's modulus of the rock matrix (Pa)
 E_s : Young's modulus of the rock grains (Pa)
 ν : Poisson's ratio of the rock matrix
 ε_v : The volume strain of the rock matrix
 d_1 : The width of fault (m)
 d_2 : The aperture of fracture (m).

Data Availability

The data used to support the findings of this study are available from the first author upon request.

Conflicts of Interest

The authors declare that they have no conflicts of interest.

Acknowledgments

This project is supported by the National Natural Science Foundation of China (Nos. 52078477 and 51827901), Key Laboratory of Deep Earth Science and Engineering (Sichuan University), Ministry of Education (DESE202106 and DESE202004), and Guangdong Provincial Key Laboratory of Deep Earth Sciences and Geothermal Energy Exploitation and Utilization (Shenzhen University) (2020-3). The authors acknowledge the supports of the abovementioned funding agencies.

References

- [1] M. Chen and H. Q. Chen, "Spatiotemporal coupling measurement of industrial wastewater discharge and industrial economy in China," *Environmental science and pollution research international*, 2021.
- [2] I. Mantis, D. Voutsas, and C. Samara, "Assessment of the environmental hazard from municipal and industrial wastewater treatment sludge by employing chemical and biological methods," *Ecotoxicology and Environmental Safety*, vol. 62, no. 3, pp. 397–407, 2005.
- [3] L. Chen, H. Zheng, and H. Yang, "Rule design and status quo evaluation on cross-industrial wastewater emissions trading in China's typical industrial sectors," *Environmental Sciences Europe*, vol. 32, no. 3, pp. 7077–7084, 2020.
- [4] B. Liang, H. J. Jiang, J. J. Li, and C. Gong, "A systematic study of fracture parameters effect on fracture network permeability based on discrete-fracture model employing finite element analyses," *Journal of Natural Gas Science and Engineering*, vol. 28, pp. 711–722, 2016.
- [5] Y. Wang, Y. F. Yi, C. H. Li, and J. Q. Han, "Anisotropic fracture and energy characteristics of a Tibet marble exposed to multi-level constant-amplitude (MLCA) cyclic loads: a lab-scale testing," *Engineering Fracture Mechanics*, vol. 244, p. 107550, 2021.
- [6] Y. Wang, B. Zhang, B. Li, and C. H. Li, "A strain-based fatigue damage model for naturally fractured marble subjected to freeze-thaw and uniaxial cyclic loads," *International Journal of Damage Mechanics*, vol. 30, p. 105678952110216, 2021.
- [7] H. G. Zhu, H. P. Xie, C. Yi et al., "Analysis of properties of fluid flow in rock fractures," *Chinese Journal of Rock Mechanics Engineering*, vol. 32, no. 4, pp. 657–663, 2013.
- [8] Y. Zhou, R. K. N. D. Rajapakse, and J. Graham, "A coupled thermoporoelastic model with thermo-osmosis and thermal-filtration," *International Journal of Solids and Structures*, vol. 35, no. 34-35, pp. 4659–4683, 1998.
- [9] J. M. Soler, "The effect of coupled transport phenomena in the Opalinus clay and implications for radionuclide transport," *Journal of Contaminant Hydrology*, vol. 53, no. 1-2, pp. 63–84, 2001.
- [10] X. H. Chen, W. Pao, and X. K. Li, "Coupled thermo-hydro-mechanical model with consideration of thermal-osmosis based on modified mixture theory," *International Journal of Engineering Science*, vol. 64, pp. 1–13, 2013.
- [11] G. Q. Cai, C. G. Zhao, and H. Tian, "Numerical simulation of coupled thermo-hydro-mechanical behavior for engineered barriers in high-level radioactive waste disposal," *Chinese Journal of Geotechnical Engineering*, vol. 35, no. 1, pp. 1–8, 2013.
- [12] W. Z. Chen, Z. Gong, H. D. Yu, M. Yong-shang, and T. Hong-ming, "Review of thermo-hydro-mechanical coupled tests and constitutive models of clays," *Rock and Soil Mechanics*, vol. 36, no. 5, pp. 1217–1238, 2015.
- [13] G. Q. Cai, G. Yan-xin, L. Jian, Z. Xue-dong, and Z. Cheng-gang, "Elastoplastic modeling of volume change behaviour of unsaturated soils under thermo-hydro-mechanical coupling conditions," *Rock and Soil Mechanics*, vol. 38, no. 4, pp. 1060–1068, 2017.
- [14] Z. H. Zhang, Y. M. Shi, and M. Zhu, "Coupled hydro-mechanical-chemical model for clay liner," *Chinese Journal of Geotechnical Engineering*, vol. 38, no. 7, pp. 1283–1290, 2016.
- [15] S. C. Seetharam, H. R. Thomas, and P. J. Cleall, "Coupled thermo/hydro/chemical/mechanical model for unsaturated soils: numerical algorithm," *International Journal for Numerical Methods in Engineering*, vol. 70, no. 12, pp. 1480–1511, 2007.
- [16] P. J. Cleall, S. C. Seetharam, and H. R. Thomas, "Inclusion of some aspects of chemical behavior of unsaturated soil in thermo/hydro/chemical/mechanical models," *Journal of Engineering Mechanics*, vol. 133, no. 3, pp. 337–347, 2007.
- [17] A. Gens, L. D. N. Guimarães, S. Olivella, and M. Sánchez, "Modelling thermo-hydro-mechano-chemical interactions for nuclear waste disposal," *Journal of Rock Mechanics and Geotechnical Engineering*, vol. 2, no. 2, pp. 97–102, 2010.
- [18] M. Presho, S. Wo, and V. Ginting, "Calibrated dual porosity, dual permeability modeling of fractured reservoirs," *Journal of Petroleum Science and Engineering*, vol. 77, no. 3-4, pp. 326–337, 2011.
- [19] M. M. Lu, K. H. Xie, and S. Y. Wang, "Consolidation of vertical drain with depth-varying stress induced by multi-stage loading," *Computers and Geotechnics*, vol. 38, no. 8, pp. 1096–1101, 2011.
- [20] R. J. Rossen, "Simulation of naturally fractured reservoirs with semi-implicit source terms," *Society of Petroleum Engineers Journal*, vol. 17, no. 3, pp. 201–210, 1977.

- [21] D. T. Snow, "Rock fracture spacings, openings, and porosities," *ASCE Soil Mechanics and Foundation Division Journal*, vol. 94, no. 1, pp. 73–91, 1968.
- [22] P. Hsieh, S. P. Neuman, E. S. Simpson, and G. Stiles, "Field determination of the three-dimensional hydraulic conductivity tensor of anisotropic media: 1. Theory," *Water Resources Research*, vol. 21, no. 11, pp. 1655–1665, 1985.
- [23] F. Kuwahara, U. Takahiro, and A. Nakayama, "A macroscopic momentum equation for flows in porous media of dual structure," *Proceeding of Japan Chemical Society*, vol. 26, no. 6, pp. 837–841, 2000.
- [24] X. L. Huan, G. Xu, Y. Zhang, F. Sun, and S. Xue, "Study on thermo-hydro-mechanical coupling and the stability of a geothermal wellbore structure," *Energies*, vol. 14, no. 3, pp. 649–649, 2021.
- [25] B. P. Shi, Y. C. Wang, B. D. Lu, and X. X. Zhao, "Study on new relationship between viscosity of liquid and temperature," *Journal of Taiyuan University of Science and Technology*, vol. 28, no. 6, pp. 500–503, 2007.
- [26] B. G. Chen, *Study on Numerical Methods for Coupled Fluid Flow and Heat Transfer in Fractured Rocks of Doublet System*, Tsinghua University, 2014.
- [27] X. Y. Zhuang, R. Huang, C. Liang, and T. Rabczuk, "A coupled thermo-hydro-mechanical model of jointed hard rock for compressed air energy storage," *Mathematical Problems in Engineering*, vol. 2014, Article ID 179169, 11 pages, 2014.
- [28] K. Gao, *THM Coupling Model of Fractured Reservoir in Hot Dry Rock Mining and Its Application*, China University of Mining and Technology, 2020.
- [29] P. Xu and B. M. Yu, "Developing a new form of permeability and Kozeny-Carman constant for homogeneous porous media by means of fractal geometry," *Advances in Water Resources*, vol. 31, no. 1, pp. 74–81, 2008.
- [30] Y. D. Shou and X. P. Zhou, "A coupled hydro-mechanical non-ordinary state-based peridynamics for the fissured porous rocks," *Engineering Analysis with Boundary Elements*, vol. 123, pp. 133–146, 2021.
- [31] C. Louis, *Rock Hydraulics in Rock Mechanics*, Springer Verlag, New York, 1974.
- [32] J. Wu, *Hydraulic Characteristics of Fracture with Fractal Surface*, Dalian University of Technology, 2010.

Research Article

Study on Air Void Characteristics and Hydraulic Characteristics of Porous Asphalt Concrete Based on Image Processing Technology

Zhanqi Wang ¹, Jianguang Xie ¹, Lei Gao ¹, Yanping Liu ¹, and Kuan Li ^{1,2}

¹Department of Civil and Airport Engineering, Nanjing University of Aeronautics and Astronautics, Nanjing 211106, China

²Jiangsu Sinoroad Engineering Technology Research Institute Co. Ltd., Nanjing 211806, China

Correspondence should be addressed to Jianguang Xie; xiejg@nuaa.edu.cn and Lei Gao; glzjy@nuaa.edu.cn

Received 24 August 2021; Accepted 14 September 2021; Published 14 October 2021

Academic Editor: Yu Wang

Copyright © 2021 Zhanqi Wang et al. This is an open access article distributed under the Creative Commons Attribution License, which permits unrestricted use, distribution, and reproduction in any medium, provided the original work is properly cited.

The appearance of porous asphalt (PA) pavement is to solve the problem of road ponding in rainy days. The internal air voids in PA pavement are the main functional structure that determines its drainage performance. It is of great practical significance to find out the relationship between void drainage capacity and air voids. This paper is aimed at researching the relationship between three-dimensional (3D) pore structures and drainage performance of PA concrete. Four samples were formed and scanned by CT equipment to obtain the internal cross-sectional CT images. Image dodging algorithm and OTSU method were conducted to deal with these CT images for segmenting them into three subimages (void image, asphalt mortar image, and aggregate image) according to the three components of PA concrete. The voids on void images were identified and classified into three groups according to the three kind of pores (interconnected pore, semi-interconnected pore, and closed pore) and reshaped them into 3D pore structures according to the overlapping principle. Then, the volume and size distribution of the pores was analyzed. Besides, this research mainly focused on the influence of several parameters obtained from interconnected pores on the drainage performance of PA concrete at last. The permeability coefficient of PA concrete samples was tested, and equations between permeability coefficient and void content were fitted linearly. The distribution of hydraulic radius and cross-sectional area ratio was calculated and researched by statistical methods. A new parameter, perimeter variation coefficient, is proposed to study the influence of boundary wall roughness on the drainage performance. At last, equivalent drainage channel was drawn to reflect the drainage capacity of PA concrete.

1. Introduction

In the engineering field, water stability and drainage problems have always been perplexing engineers and scholars [1–4]. Porous asphalt (PA) pavement is known as a kind of environmental friendly pavement due to its drainage, noise reduction, and antiskid properties [5–7]. PA pavement was originally designed for rapidly draining the rainwater to improve driving safety on rainy days. The drainage performance is closely linked with its interconnected pore structures [8, 9]. However, pore structures usually exist in PA concrete in extremely complex geometry, which poses a great challenge to study the relationship between drainage performance and characteristic parameters of pore structures.

Void parameters (such as void content and size) are commonly used indicators instead of characteristic parameters of pore structures for researching its influence on drainage performance or other properties by most researchers [10–14]. Void parameters are usually obtained from two-dimensional cross-sectional images by using computed tomography (CT) technology combined with image processing technology. Although it is relatively easy to obtain void parameters, more efforts are needed to develop and propose pore characteristic parameters of pore structures, so as to study its influence on drainage performance more accurately. Three-dimensional (3D) reconstruction of pore structures is an important step to research its influence on drainage performance or other properties. Due to the

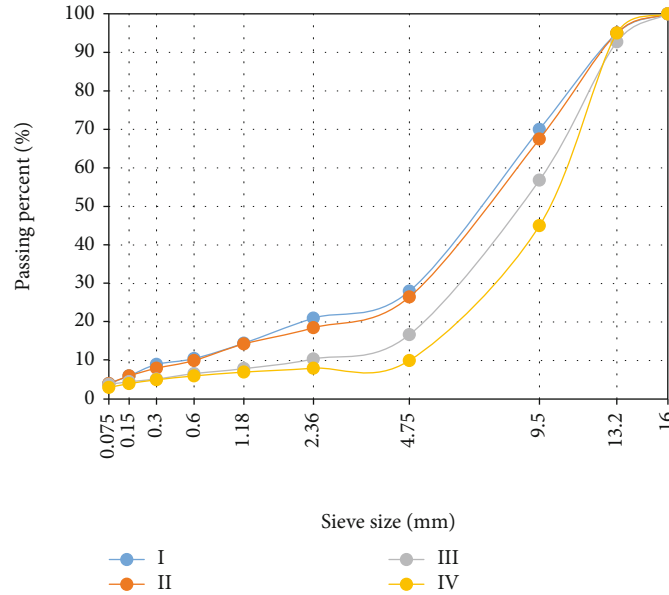


FIGURE 1: Aggregate gradation.

complexity of pore geometry, there is still a lack of effective methods to reconstruct the 3D geometry and obtain characteristic parameters of pore structures at present, and only a few researchers have done some work in this field [15–17]. Gruber et al. [15] reconstructed the 3D model of pores and simulated the fluid flow in PA concrete sample by Avizo and ANSYS 12.0. Zhao et al. [16] proposed a method to separate the valid and invalid interconnected pores in PA concrete. Besides, in terms of drainage performance, most researches generally regarded PA concrete as permeable medium to study its macro drainage performance, but not to study the impact of its structure properties on drainage performance from the micro structure perspective [18–20]. Garcia et al. [18] analyzed the permeability reduction in drainage asphalt mixtures through a self-developed device and using the coefficient of permeability as the indicator to reflect the drainage performance of drainage asphalt mixtures. Aboufoul et al. [19] investigated the effects of air void topology on hydraulic conductivity in asphalt mixtures by using 3D printing technology, and permeability coefficient was also used for predicting the hydraulic conductivity.

In this paper, the authors tried to find the key parameters affecting hydraulic characteristics based on image processing technology, which paves the way for further revealing the drainage characteristics of PA concrete. First, 3D pore structures were successfully reconstructed by overlapping principle. Second, the volume and size distribution of pores was analyzed. Third, the permeability coefficient of PA concrete samples was tested and equations between permeability coefficient and void content were fitted linearly. At last, several key hydraulic parameters affecting hydraulic characteristics were studied.

2. Materials and Mix Design

Four PA concrete (PAC-13) specimens were taken as the research object in this paper whose target void content was

set to be 16%, 18%, 20%, and 22%, respectively. Due to mold size, the specimens were formed with the same size of 300 mm × 300 mm × 40 mm, in which the coarse aggregate was basalt, the fine aggregate was basalt machine-made sand, and appropriate amount of limestone powder was used as mineral powder filler. In addition, SBS-modified asphalt mixed high-viscosity additives (HVA) were used as binder to increase the adhesion between asphalt mortar and aggregates. The aggregate gradation is shown in Figure 1.

3. CT Image Processing

CT scanning technology was used to scan the specimens to observe the internal structure, mainly observing the pore structures in PA concrete. Due to the allowed sample size of CT equipment, the four specimens were, respectively, cut into nine pieces with the same size of 100 mm × 100 mm × 40 mm, and the central piece was taken as target sample I~IV to be scanned. Besides, the samples were scanned along the thickness direction with an interval of 0.14 mm. In the process, 275, 272, 270, and 273 CT images were generated from the sample I~IV, respectively.

Image processing is an important step to obtain and evaluate the characteristic of pore structures. A reliable image segmentation algorithm is indispensable and essential to segment these CT images. Image processing generally involves four steps: image graying (RGB to gray), median filtering, contrast enhancement, and image segmentation [6, 16]. Image segmentation is the most important step in the whole process; the segmentation algorithm directly determines the accuracy of subimages after segmentation. As we know, the OTSU algorithm [21] is a commonly used method to segment gray images due to its advantages such as simplicity, efficiency, and accuracy. The OTSU algorithm describes a method to separate target object and background in a digital image by finding out the key thresholds for

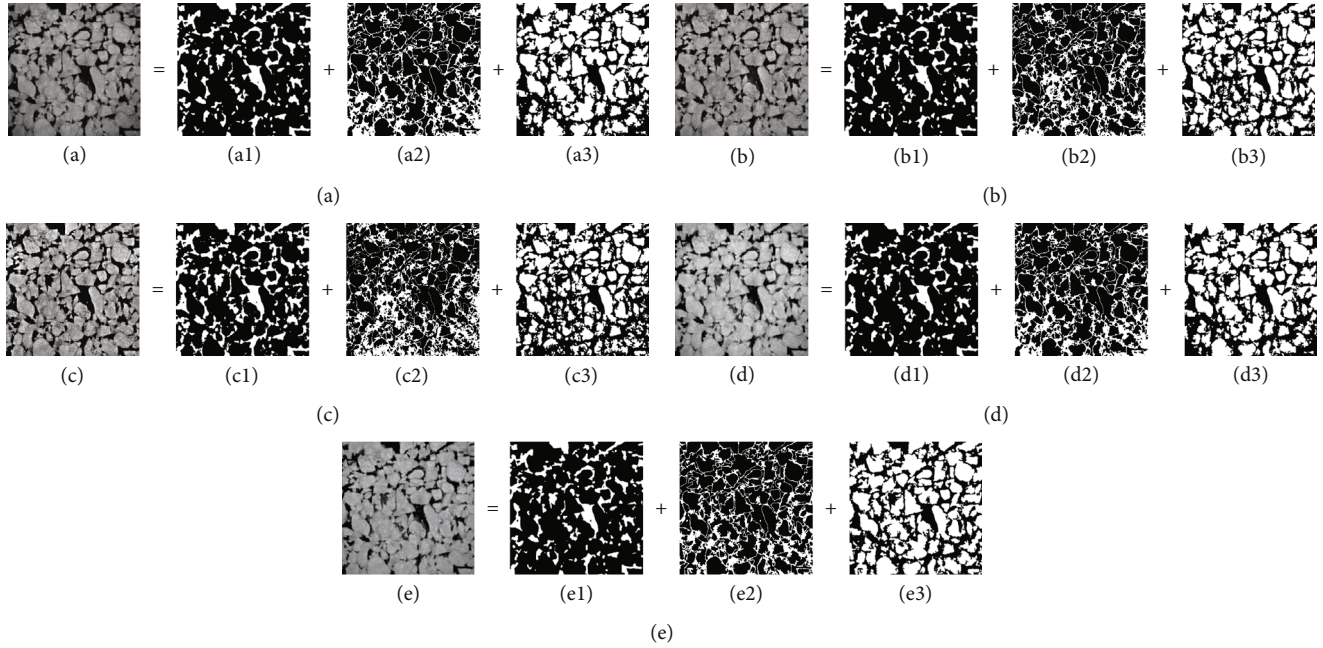


FIGURE 2: CT image segmentation: (a) without dodging; (b) MASK dodging; (c) Retinex dodging; (d) homomorphic filter dodging; (e) 2D gamma dodging; (*1) void; (*2) asphalt mortar; (*3) aggregate. The range of “*” is (a)–(e).

classifying all the pixels into different groups. In this paper, the OTSU algorithm was also used in image segmentation. All the CT images were separated into three subimages by the OTSU algorithm according to the three components (void, asphalt mortar, and aggregate) of PA concrete, as shown in Figure 2. However, the quality of subimages was always disappointing while CT images without further improved process. For example, Figures 2(a1), 2(a2), and 2(a3) are subimages of CT image Figure 2(a), whose white areas stand for void, asphalt mortar, and aggregate, respectively. It is obvious in the figures that a part of aggregate was missing and wrongly classified as asphalt mortar or void. In most cases, CT images need to be preprocessed by specific methods before segmentation to eliminate some specific defects that affect the accuracy of segmentation. In this research, a universal phenomenon was found in most CT images that the aggregate in the center shows brighter (with larger intensity) while the aggregate at four corners shows darker (with smaller intensity), as shown in Figure 2(a). So it can be inferred that the uneven illumination may be the main defect that affects the accuracy of segmentation which needs to be preprocessed. Subsequently, a series of image dodging algorithms were conducted to unify the illuminance component of CT images before segmentation.

To meet different image processing demands in different fields, a variety of image dodging algorithms have been developed by researchers, such as MASK dodging [22], homomorphic filter dodging [23], Retinex dodging [24], and 2D gamma dodging [25]. In this paper, they were all conducted on the CT images to unify the illuminance component and then separated into three subimages, respectively, as shown in Figure 2. It is easy to find that CT image preprocessed by 2D gamma dodging shows the best segmentation effect: less aggregate missing and asphalt mortar and

TABLE 1: Proportion of pore structures that connected with the outside space (%).

Sample		I	II	III	IV
Without dodging	V_c	13.10	14.88	21.67	25.12
	E	34.89	7.15	7.30	3.26
2D gamma	V_c	12.93	14.42	21.03	24.47
	E	33.18	3.85	4.12	5.77
MASK	V_c	13.05	15.11	22.27	25.89
	E	34.44	8.80	10.23	0.27
Retinex	V_c	18.25	21.53	29.13	30.21
	E	87.99	55.04	44.21	16.33
Homomorphic	V_c	13.28	15.08	21.91	25.35
	E	36.82	8.60	8.47	2.37
V_p		9.71	13.89	20.20	25.97

void being closest to actual situation. It should be noted, however, that this research mainly focused on the pore structures in PA concrete. A novel method to identify and reconstruct pore structures was introduced in Section 4, and the proportion of pore structures that connected with the outside space was calculated by MATLAB. The results are shown in Table 1.

Furthermore, the four samples were placed into a measuring cup with proper amount of distilled water to measure the proportion of pore structures that connected with the outside space according to Equation (1). The measuring cup is shown in Figure 3, and measuring results are listed in Table 1. In addition, the errors between measured values

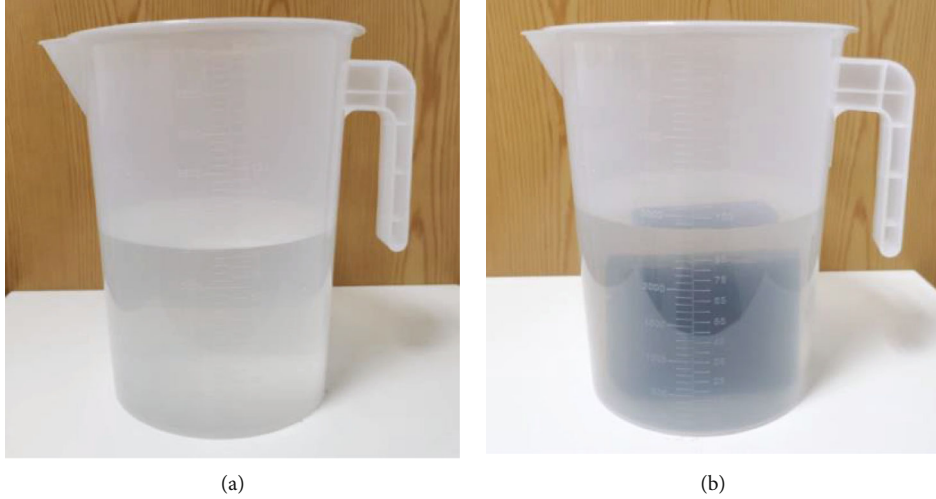


FIGURE 3: Measuring device.

and calculated values were obtained by Equation (2) and also listed in Table 1.

$$V_p = \frac{(V_a - V_w)}{V_s}, \quad (1)$$

$$E = \frac{|(V_p - V_c)|}{V_p}, \quad (2)$$

where V_p is the measured proportion of pore structures that connected with the outside space, V_a is the volume of distilled water, V_w is the volume of distilled water with sample, V_s is the volume of sample, V_c is the calculated proportion of pore structures that connected with the outside space, and E is the error between V_p and V_c .

From Table 1, it can be concluded that image dodging could improve the visual and sensory effects, but limited help for image segmentation. Compared with the measured values and errors, values calculated from the CT images that are preprocessed by 2D gamma image dodging are more accurate and reliable than the others. Values calculated from images preprocessed by Retinex image dodging show the maximum error. Considering the image segmentation effect and calculation accuracy, 2D gamma dodging algorithm was chosen to unify illumination of CT images for further research, eventually.

4. Identification and Reconstruction of Pore Structures

4.1. Identification of Pore Structures. As mentioned above, a series of CT images was obtained and separated into three subimages, including void image, asphalt mortar image, and aggregate image. Pore structures in PA concrete could be reconstructed through an appropriate algorithm by using air voids in void images. Actually, such an algorithm is available: overlapping principle. It is easy to imagine that air

voids in two adjacent void images that share a common overlapping area, from the top view, must belong to the same pore structure if the interval of the two void images is close enough along the thickness direction. According to the overlapping principle, all the air voids in different CT images can be identified and classified into independent groups that belong to different pore structures. Thus, all the air void groups can be reshaped into pore structures by MATLAB, respectively.

4.2. Reconstruction of Pore Structures. Pore structures in PA concrete mainly can be classified into three types: interconnected pore (IP), semi-interconnected pore (SP), and closed pore (CP). Interconnected pore refers to the pore with two open ends that connected with the outside space at the top and bottom of samples. Semi-interconnected pore refers to the pore with an open end and a dead end. Closed pore refers to the pore with two dead ends that isolated from the outside space. According to the overlapping principle, a MATLAB program was properly edited and executed to reconstruct all the pore structures. Figure 4 shows all the interconnected pore structures in the four samples. It can be seen that samples I~IV contain 3, 3, 1, and 1 interconnected pore, respectively. Pore structures in image (a)~(c) were reconstructed from sample I, images (d)~(f) were reconstructed from sample II, images (g) and (h) were reconstructed from samples III and IV, respectively. However, it is discouraged that all the pores have a complex and disorderly structure which turned out to be a challenge for further research. Besides, the samples also contain thousands of closed pores and dozens of semi-interconnected pores, which are not listed in Figure 4 due to the space limitation of the paper. In addition, it also can be inferred that the sample formed by the aggregate gradation with smaller target void content is more likely to form multiple independent interconnected pores, while the sample formed by the aggregate gradation with larger target void content is more likely to form single overall interconnected pore.

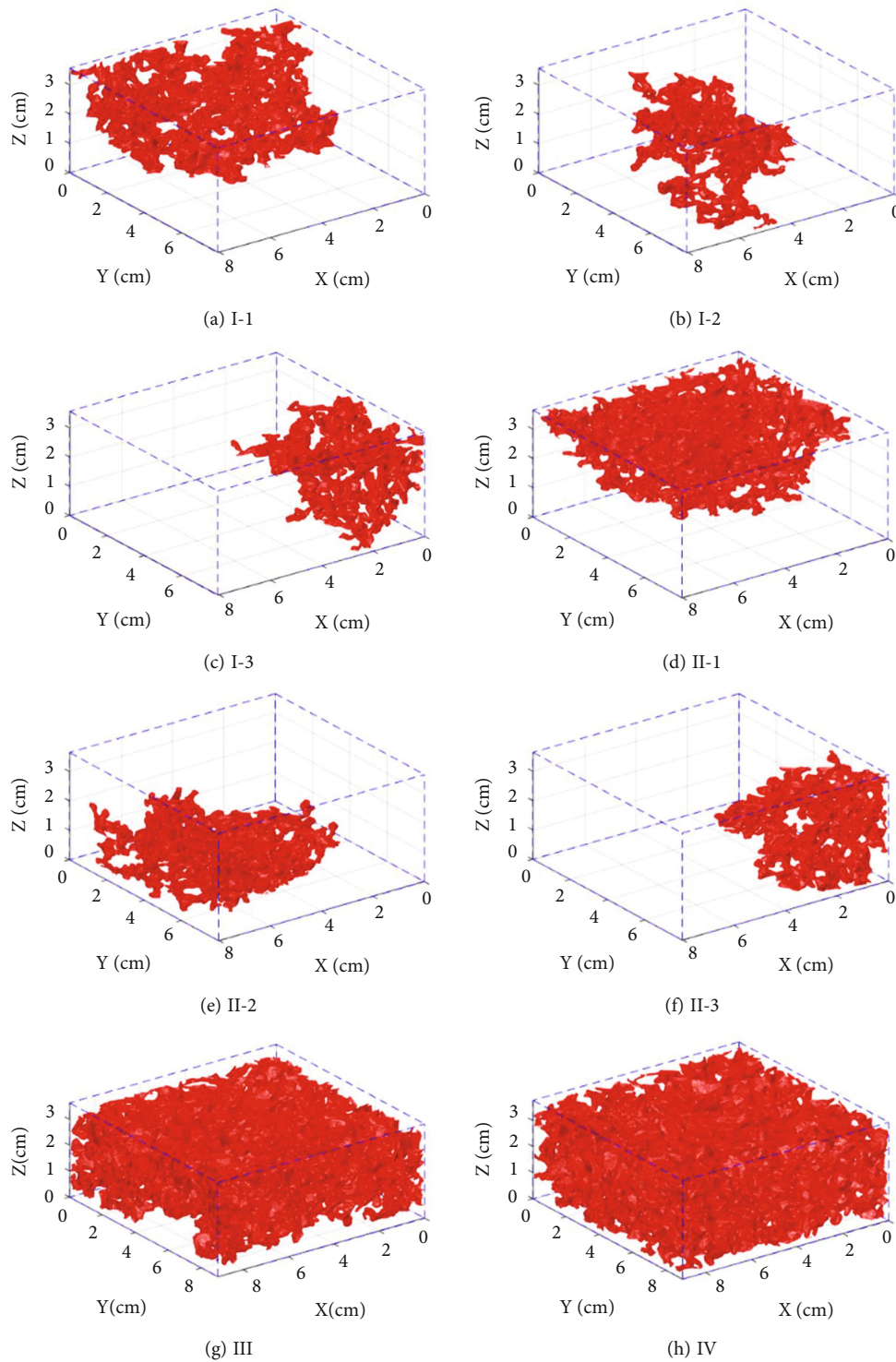


FIGURE 4: Interconnected pore structures.

5. Distribution of Pore Structures

5.1. Volume Distribution. There are generally thousands of pore structures in PA concrete, most of which are micro closed pores. The number and volume of pore structures in the four samples were calculated and listed in Table 2 after 3D reconstruction process. It can be seen that the number

of closed pores with volume less than 1 mm^3 accounts for more than 70% of the total number; however, their cumulative volume accounts for a very small proportion of the total volume of all the pores in the samples, which is less than 0.5%. In specimens I-V, the cumulative volume of all closed pores accounts for 8.53%, 7.62%, 1.97%, and 0.28% of the total pore volume, respectively. And the cumulative volume

TABLE 2: Number and volume distribution of pore structures.

Volume range (mm ³)		I		II		III		IV	
		Num.	Vol.	Num.	Vol.	Num.	Vol.	Num.	Vol.
0~1	IP	0	0.00	0	0.00	0	0.00	0	0.00
	SP	31	9.94	29	9.51	38	7.96	38	8.56
	CP	945	158.94	1101	193.64	1378	120.29	378	38.53
1~10	IP	0	0.00	0	0.00	0	0.00	0	0.00
	SP	19	76.93	21	64.22	5	19.03	6	11.13
	CP	212	675.86	263	838.51	111	358.68	42	136.78
10~100	IP	0	0.00	0	0.00	0	0.00	0	0.00
	SP	6	179.23	8	377.49	3	70.19	2	21.75
	CP	68	2060.12	68	2182.76	28	574.10	5	69.49
100~500	IP	0	0.00	0	0.00	0	0.00	0	0.00
	SP	5	927.52	2	374.09	0	0.00	0	0.00
	CP	7	1141.29	5	782.71	3	401.34	0	0.00
>500	IP	1	41566.90	1	47654.50	1	72185.50	1	87136.70
	SP	1	530.80	0	0.00	0	0.00	0	0.00
	CP	0	0.00	0	0.00	0	0.00	0	0.00
Total		1295	47327.53	1498	52477.43	1567	73737.09	472	87422.94

of all semi-interconnected pores accounts for 3.64%, 1.57%, 0.13%, and 0.05% of the total pore volume, respectively. The volume of interconnected pore is the absolutely dominant part of the total pore volume in samples I~IV, accounting for 87.83%, 90.81%, 97.90%, and 99.67%, respectively. It should be noted that each sample contains only one interconnected pore in the table. Actually, PA concrete with lower void content may contain several independent interconnected pores. It was found that the surface texture of samples has an important influence on 3D reconstruction process. The surface texture is an open boundary with a certain depth. All the independent interconnected pores will intersect with the surface texture at the top or bottom to form a whole. Therefore, the CT image within the texture depth must be deducted in the 3D reconstruction process to achieve the purpose of separating independent interconnected pores. For instance, three independent interconnected pores are separated from samples I and II when deducting CT images covering the texture depth in the 3D reconstruction process.

5.2. Size Distribution. As we know, the size of pore structures is definitely a significant factor that directly determines the drainage performance of PA concrete. However, due to the complex geometry of pore structures, it is difficult to find a reasonable parameter to characterize its size. In this research, equivalent diameter of voids on each CT images was calculated to reflect the size of pore structures from the perspective of statistics, as shown in Figure 5. Equivalent diameter refers to the diameter of a circle whose area equal to the void. It can be seen that the void size is mainly distributed below 2.61 mm, most of which belongs to interconnected pores. The size of voids belonging to closed pores and semi-interconnected pores is mainly distributed below 5.21 mm. In terms of interconnected pores, void size is

mainly below 5.21, but the distribution range is relatively wide, and the maximum value is greater than 20.86 mm. With the increase of void content, the proportion of void with large size gradually increases.

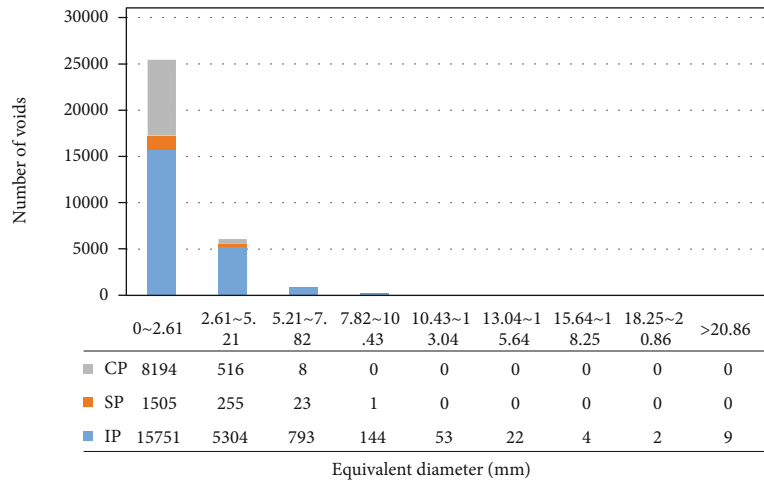
6. Hydraulic Characteristics

PA pavement is aimed at quickly removing the rain water, increasing the skid resistance of pavement to improve the driving safety when it was born in the world. Pore structures act as a drainage pipe to drain rain water from pavement surface. The drainage performance of PA pavement depends on the size and geometry of pores. Due to the complex geometry of pores, it is hard to find a representative parameter to evaluate its drainage performance. Some researchers [18, 19] considered PA concrete sample as a whole to test its permeability coefficient for evaluating its drainage performance according to Darcy's law [26] (Equation (3)) which was first proposed and used to test the permeability of soils. Although permeability coefficient may be a good choice for evaluating drainage performance in a sense, it is still a challenge to reveal the internal relationship between drainage performance and geometry of pores.

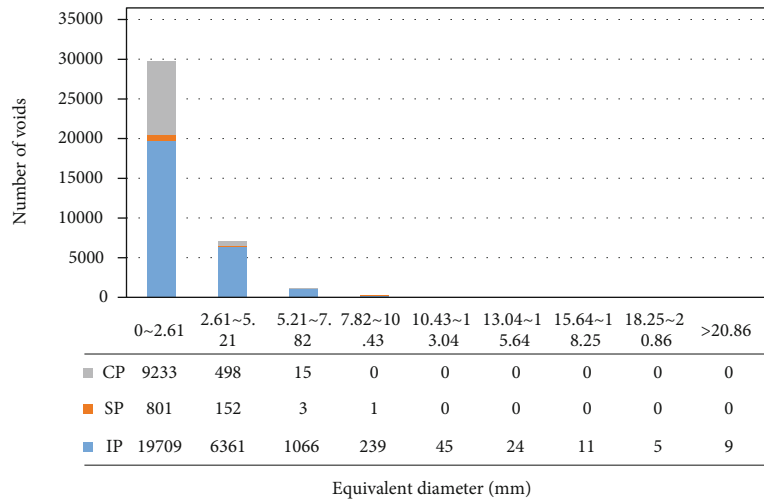
$$Q = kA \frac{\Delta H}{L}, \quad (3)$$

where Q is the seepage water volume per unit time, cm³/s; k is the permeability coefficient, cm/s; A is the top surface area of sample to be tested, cm²; ΔH is the water head difference between top and bottom of sample to be tested, cm; and L is the thickness of sample to be tested, cm.

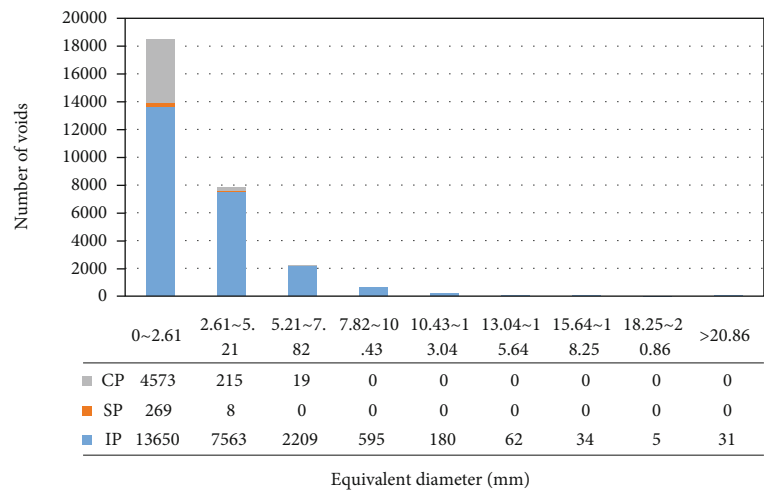
6.1. Permeability Coefficient. According to Darcy's law, permeability coefficient of samples I-IV was tested by constant



(a) I



(b) II



(c) III

FIGURE 5: Continued.

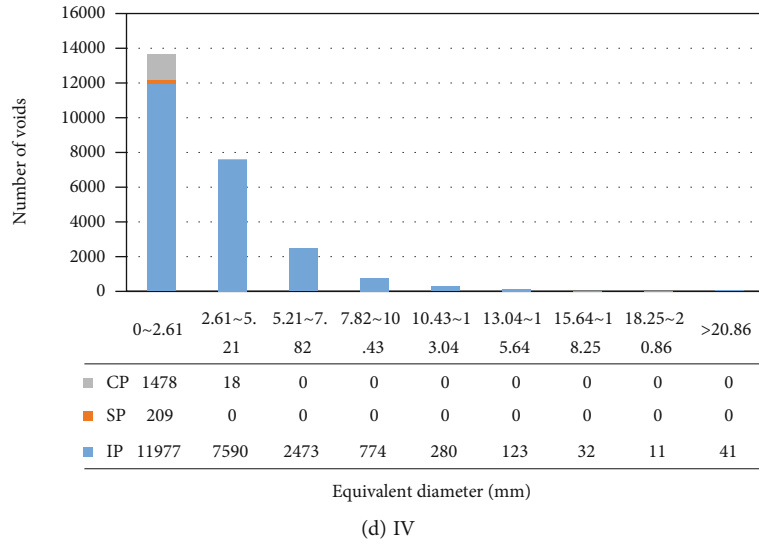


FIGURE 5: Size distribution of voids.

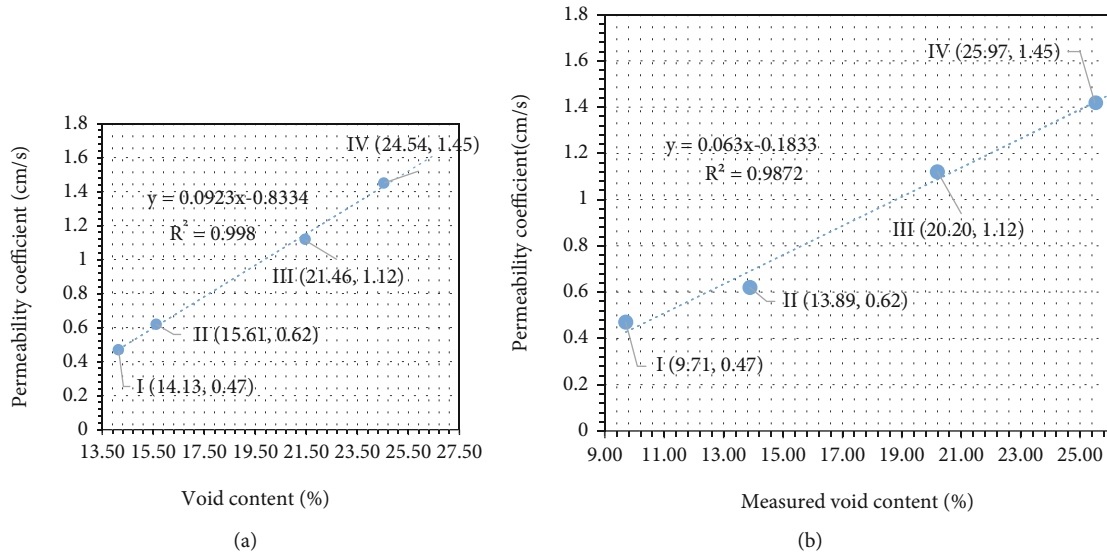


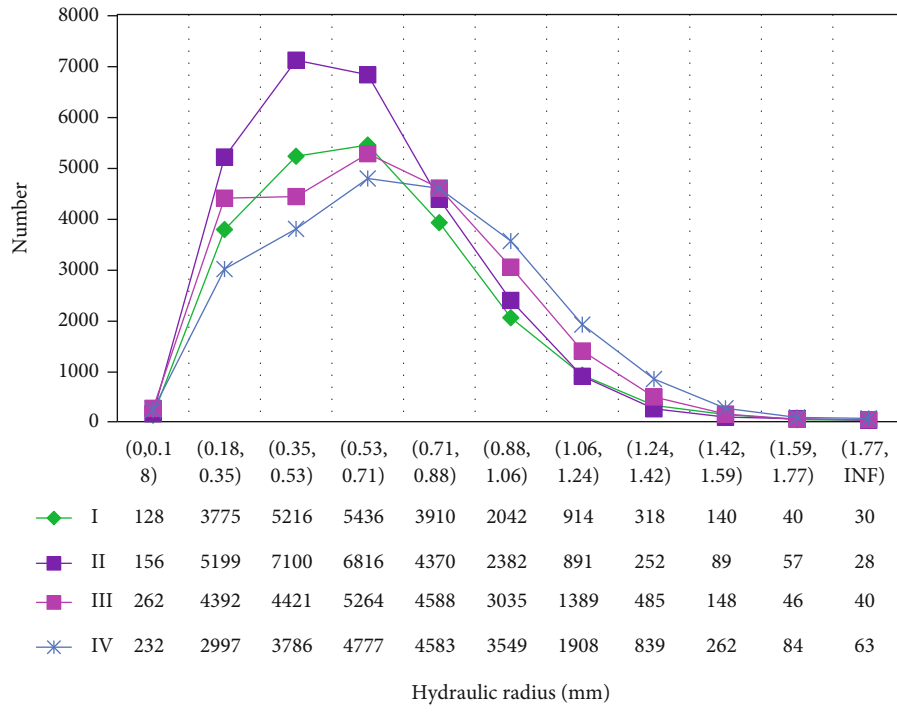
FIGURE 6: Relationship between permeability coefficient and void content.

water head method [26] in this research and the results are shown in Figure 6. Figure 6(a) shows the relationship between permeability coefficient and void content which was calculated from CT images. It can be seen that there is a highly linear positive correlation between permeability coefficient and void content. The correlation coefficient reaches 0.998. Figure 6(b) shows the relationship between permeability coefficient and measured void content V_p . It should be noticed that measured void content only involves the proportion of pore structures that connected with the outside space. Likewise, it can be found that the permeability coefficient also shows a high linear correlation with the measured void content, and the correlation coefficient reaches 0.987.

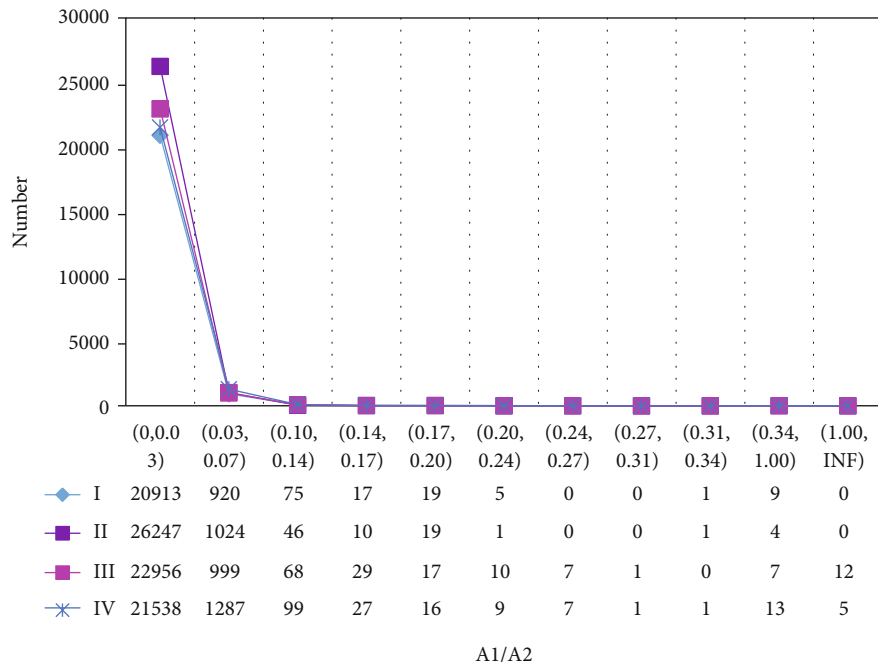
6.2. Hydraulic Parameters. In Equation (3), ΔH refers to the mean value of water head loss, and L refers to the sample thickness rather than the seepage path. Actually, the flow pat-

tern of water in the pore structures is extremely complex; due to the complex geometry of pores, it is hard to find an effective method for revealing the relationship between water head loss and flow pattern of water. This research mainly focused on some key parameters and analyzed their variation law, which lays a foundation for further study of hydraulic characteristics.

As a kind of Newtonian fluid, flow resistance will be produced in the process of water flow due to its viscosity. To overcome the resistance, a part of mechanical energy will be consumed, resulting in head loss. There are two main reasons for the water head loss. One is the influence of viscosity. The interaction between water and solid wall boundary causes uneven velocity distribution on the cross section, which leads to friction resistance in the water flow. The liquid needs to consume a part of energy to overcome the friction resistance. The other is the influence of solid wall boundary. The sharp change of boundary shape will change



(a)



(b)

FIGURE 7: Distribution of hydraulic radius and A_1/A_2 .

the internal structure of water flow and produce vortex flow. The particles in the flow will collide with each other to convert kinetic energy and potential energy. In this process, a part of mechanical energy is converted into heat energy, resulting in energy loss. Besides, the head loss is also related to the microscopic motion of the liquid. Due to the microscopic motion, flow patterns of water can be divided into

two types: laminar flow and turbulent flow. Osborne Reynolds [27, 28] has revealed the different nature of the two flow patterns through experiments in the 1880s and studied the relationship between head loss and pipe diameter, wall roughness, and velocity. According to the different reasons causing the water head loss, it can be generally divided into two parts, namely, the water head loss along

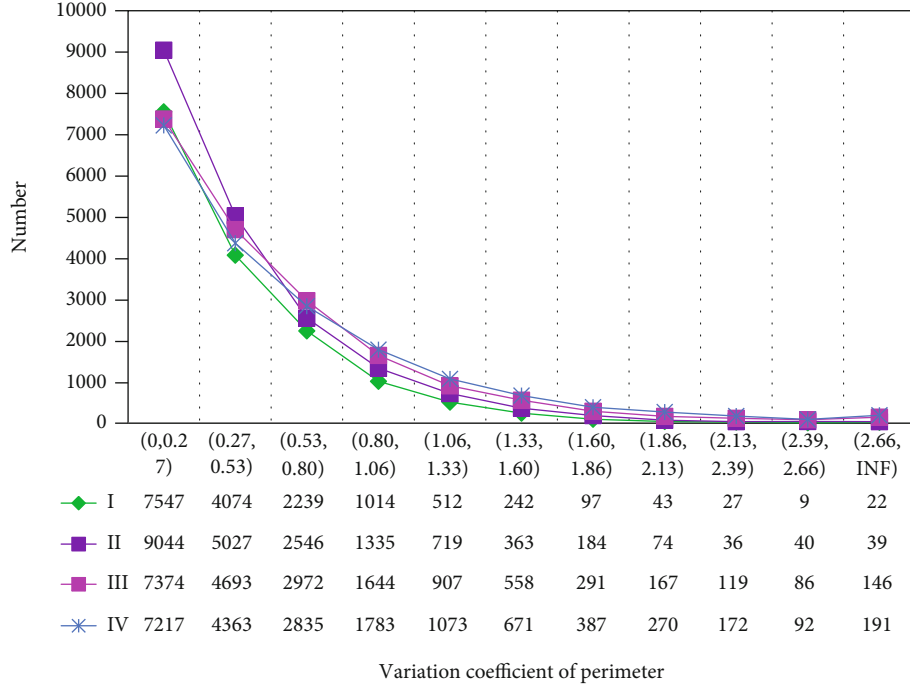


FIGURE 8: Distribution of perimeter variation coefficient.

flow path and the local water head loss. The general calculation equations are as follows [27]:

$$h_f = \lambda \frac{l}{4R} \frac{v^2}{2g}, \quad (4)$$

$$\lambda = f\left(R_e, \frac{\Delta}{R}\right), \quad (5)$$

$$h_j = \zeta \frac{v^2}{2g}, \quad (6)$$

$$\zeta = f\left(\frac{A_1}{A_2}\right), \quad (7)$$

where h_f is the water head loss along flow path, λ is the resistance coefficient along flow path, l is the flow path, R is the hydraulic radius, Δ is the boundary wall roughness, R_e is the Reynolds number, v is the flow velocity, g is the acceleration of gravity, h_j is the local water head loss, ζ is the local resistance coefficient, and A_1/A_2 is the cross-sectional area ratio at cross section change.

In Equations (4)–(7), there are many unknown parameters that need to be determined. Only R and A_1/A_2 can be directly calculated from the CT images while the others are hard to obtain. Figure 7 shows the distribution of R and A_1/A_2 of interconnected pores in samples I~IV. Hydraulic radius is an important parameter that can comprehensively reflect the influence of cross-sectional shape and size on average velocity. A_1/A_2 can reflect the size change on each cross section of pores. It can be concluded from Figure 7(a) that hydraulic radius is mainly distributed in

the range of [0.18, 0.88) mm, accounting for 83.54%, 85.90%, 77.54%, and 69.94% of the total number, respectively, in samples I~V, and the curves gradually flatten with the increase of specimen number, indicating that with the increase of void content, the number of larger voids increases gradually, and the drainage capacity increases in a sense. Besides, it can be seen from Figure 7(b) that the area ratio of adjacent cross sections of interconnected pores is mainly below 0.1, accounting for 99.43%, 99.71%, 99.38%, and 99.24% of the total number, respectively, in samples I~IV, indicating that the geometry of pore structures in PA concrete is extremely complex, which poses a very difficult challenge to the study of its drainage performance or other performances. Meanwhile, it can be found that almost all the values of A_1/A_2 are less than 1, indicating that the size of voids near the top is larger than that near the bottom.

In Equation (5), λ is the function of R_e , R , and Δ , called boundary wall roughness, refers to the average value of bulge height of boundary wall, which is an important factor that cannot be ignored. For pipe with regular shape, the roughness can be easily obtained, but for the pore structure in porous asphalt concrete, it is almost impossible to define and obtain the boundary wall roughness due to its complex shape. In this research, another similar parameter, called perimeter variation coefficient, was defined to reflect the boundary wall roughness. The perimeter variation coefficient is defined as follows:

$$C_R = \frac{P_o - P_c}{P_c}, \quad (8)$$

where C_R is the perimeter variation coefficient, P_o is the

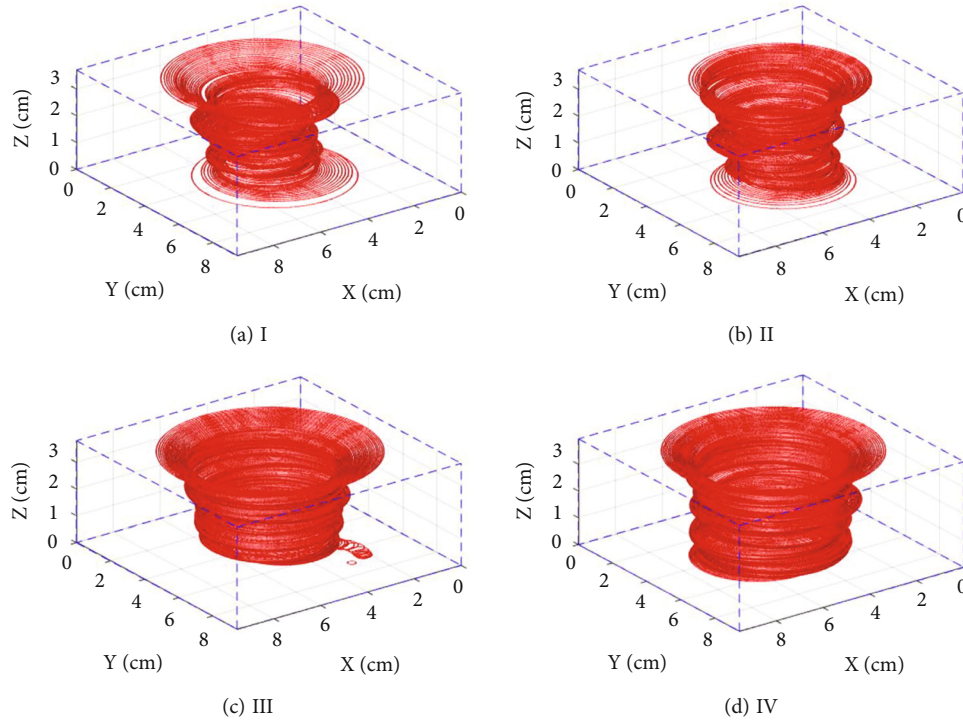


FIGURE 9: Equivalent drainage channel.

perimeter of void, and P_c is the perimeter of a circle equal to the area of the void.

Figure 8 shows the distribution of perimeter variation coefficient in samples I~IV.

It can be seen that the values less than 1.06 account for 93.98%, 92.5%, 88.00%, and 85.01%, respectively, in samples I~V; likewise, the values larger than 1.06 account for 6.07%, 7.50%, 12.00%, and 14.99%, respectively. It can be concluded that the perimeter variation coefficient of samples with more void content is generally larger than that with less void content. The larger perimeter variation coefficient means that the perimeter contacting with the water flow becomes larger, which produces greater resistance to the water flow and is not conducive to the pavement drainage.

It is easy to imagine that larger area for water passing on a cross section will show greater drainage capacity. Considering the interconnected pores as a whole pipe with only one water passing channel, take the centroid of all the voids on each CT images as the center of the pipe, and take the accumulated area value of each void on an image as the area of the channel; then, draw a circle on each cross section, respectively, as shown in Figure 9. It can be seen that the size of the channel near the top is larger than that near the middle and lower part. The size of channels with larger sample number is generally larger than that with smaller sample number, indicating that sample with larger void content tends to show better drainage performance.

7. Further Research

Although the 3D geometry of pore structures in PA concrete has been successfully reconstructed, it still remains a chal-

lenge to propose several key parameters for describing the geometry characteristics. Besides, there is no doubt that the drainage performance of pavement is related to the shape, size, roughness, and other related parameters of interconnected pores, but there is still a lack of effective way to obtain these parameters to evaluate its drainage performance, which needs further research.

8. Conclusions

This paper is aimed at researching the relationship between 3D pore structures and drainage performance of PA concrete. Four samples were formed and scanned by CT equipment to obtain the internal cross-sectional CT images. Image processing technology and OTSU method were conducted to deal with these CT images for segmenting them into three sub-images (void image, asphalt mortar image, and aggregate image) according to the three components of PA concrete. The voids on void images were identified and classified into three groups according to the three kind of pores (interconnected pore, semi-interconnected pore, and closed pore) and reshaped them into 3D pore structures. Then, the volume and size distribution of the pores was analyzed. Besides, this research mainly focused on the influence of several parameters obtained from interconnected pores on the drainage performance of PA concrete at last. The conclusions are as follows:

- (1) Image dodging plays an important role in CT image segmentation process. 2D gamma dodging shows an excellent performance in unifying the illumination component of CT images to improve the image segmentation effect

- (2) Pore structures in PA concrete can be classified into three types according to the interconnectivity, including interconnected pore, semi-interconnected pore, and closed pore. Pore structures in the PA concrete can be reconstructed according to the overlapping principle
- (3) PA concrete generally contains a lot of pores, most of which are closed pores, but their cumulative volume only accounts for about 0.5% of the total pore volume. The other small parts are semi-interconnected pores and interconnected pores; however, their cumulative volume accounts for more than 99% of the total pore volume
- (4) The void size is mainly distributed below 2.61 mm, most of which belongs to interconnected pores. The size of voids belonging to closed pores and semi-interconnected pores is mainly distributed below 5.21 mm. With the increase of void content, the proportion of void with large size gradually increases
- (5) There is a highly linear positive correlation between permeability coefficient and void content. The correlation coefficient reaches 0.998. The permeability coefficient also shows a high linear correlation with the measured void content, and the correlation coefficient reaches 0.987
- (6) Hydraulic radius is mainly distributed below 0.88 mm. With the increase of void content, the number of larger voids increases gradually, indicating that the drainage capacity increases in a sense. The geometry of pore structures in PA concrete is extremely complex. Meanwhile, almost all the values of A_1/A_2 are less than 1, indicating that the size of voids near the top is larger than that near the bottom
- (7) The perimeter variation coefficient of samples with more void content is generally larger than that with less void content. The larger perimeter variation coefficient means that the perimeter contacting with the water flow becomes larger, which produces greater resistance to the water flow and is not conducive to the pavement drainage. PA concrete with larger void content is more likely containing larger water passing channel, which tends to show a better drainage performance

Data Availability

Some or all data that support the findings of this study are available from the corresponding author (xiejj@nuaa.edu.cn) and first author (wangzq911201@nuaa.edu.cn) upon reasonable request.

Conflicts of Interest

The authors declare that they have no known competing financial interests or personal relationships that could have appeared to influence the work reported in this paper.

Acknowledgments

This study was supported by the National Key R&D Program of China (2018YFB1600101), National Natural Science Foundation of China (51908286), and Natural Science Foundation of Jiangsu Province (BK20191278). Also, all the authors of the following references are much appreciated.

References

- [1] P. P. Guo, F. F. Liu, G. Lei et al., "Predicting response of constructed tunnel to adjacent excavation with dewatering," *Geofluids*, vol. 2021, Article ID 5548817, 17 pages, 2021.
- [2] Y. Wang, W. K. Feng, H. J. Wang, C. H. Li, and Z. Q. Hou, "Rock bridge fracturing characteristics in granite induced by freeze-thaw and uniaxial deformation revealed by AE monitoring and post-test CT scanning," *Cold Regions Science and Technology*, vol. 177, article 103115, 2020.
- [3] H. N. Wu, P. Li, T. F. Nian, G. H. Zhang, T. He, and X. Y. Wei, "Evaluation of asphalt and asphalt mixtures' water stability method under multiple freeze-thaw cycles," *Construction and Building Materials*, vol. 228, article 117089, 2019.
- [4] J. G. Xie, C. H. Wu, H. Li, and G. T. Chen, "Study on storm-water management of grassed swales and permeable pavement based on SWMM," *Water*, vol. 9, no. 11, p. 840, 2017.
- [5] Y. Wang, Y. F. Yi, C. H. Li, and J. Q. Han, "Anisotropic fracture and energy characteristics of a Tibet marble exposed to multi-level constant-amplitude (MLCA) cyclic loads: a lab-scale testing," *Engineering Fracture Mechanics*, vol. 244, article 107550, 2021.
- [6] M. Z. H. Mahmud, N. A. Hassan, M. R. Hainin et al., "Characterisation of microstructural and sound absorption properties of porous asphalt subjected to progressive clogging," *Construction and Building Materials*, vol. 283, article 122654, 2021.
- [7] P. Rungruangvirojn and K. Kanitpong, "Measurement of visibility loss due to splash and spray: porous, SMA and conventional asphalt pavements," *International Journal of Pavement Engineering*, vol. 11, no. 6, pp. 499–510, 2010.
- [8] X. Ma, J. W. Jiang, Y. J. Zhao, and H. Wang, "Characterization of the interconnected pore and its relationship to the directional permeability of porous asphalt mixture," *Construction Building Materials*, vol. 258, article 121233, 2020.
- [9] M. Z. H. Mahmud, N. A. Hassan, M. R. Hainin, and C. R. Ismail, "Microstructural investigation on air void properties of porous asphalt using virtual cut section," *Construction and Building Materials*, vol. 155, pp. 485–494, 2017.
- [10] W. L. Wu, D. Y. Wang, X. N. Zhang, and Z. Li, "Air voids distribution of asphalt mixtures based on industrial computerized tomography," *Journal of Central South University*, vol. 43, no. 6, pp. 2343–2348, 2012.
- [11] F. Zhang, R. S. Chen, and F. J. Ni, "Techniques of permeability testing for porous asphalt pavement mixture," *Journal of Southeast University*, vol. 40, no. 6, pp. 1288–1292, 2010.
- [12] W. Jiang, A. Sha, and J. Xiao, "Experimental study on relationships among composition, microscopic void features, and performance of porous asphalt concrete," *Journal of Materials in Civil Engineering*, vol. 27, no. 11, article 04015028, 2015.
- [13] N. A. Hassan, M. Z. H. Mahmud, K. A. Ahmad, M. R. Hainin, R. P. Jaya, and N. Mashros, "Air voids characterisation and permeability of porous asphalt gradations used in different

- countries,” *Journal of Engineering and Applied Science*, vol. 11, pp. 14043–14047, 2016.
- [14] A. Garcia, M. Aboufoul, F. Asamoah, and D. Jing, “Study the influence of the air void topology on porous asphalt clogging,” *Construction and Building Materials*, vol. 227, article 116791, 2019.
- [15] I. Gruber, I. Zinovik, L. Holzer, A. Flisch, and L. D. Poulikakos, “A computational study of the effect of structural anisotropy of porous asphalt on hydraulic conductivity,” *Construction and Building Materials*, vol. 36, pp. 66–77, 2012.
- [16] Y. J. Zhao, X. W. Wang, J. W. Jiang, and L. Zhou, “Characterization of interconnectivity, size distribution and uniformity of air voids in porous asphalt concrete using X-ray CT scanning images,” *Construction and Building Materials*, vol. 213, pp. 182–193, 2019.
- [17] Y. Wang, C. H. Li, and J. Q. Han, “On the effect of stress amplitude on fracture and energy evolution of pre-flawed granite under uniaxial increasing-amplitude fatigue loads,” *Engineering Fracture Mechanics*, vol. 240, article 107366, 2020.
- [18] E. S. H. Garcia, L. P. Thives, E. Ghisi, and L. N. Antunes, “Analysis of permeability reduction in drainage asphalt mixtures due to decrease in void volume,” *Journal of Cleaner Production*, vol. 248, article 119292, 2020.
- [19] M. Aboufoul, A. Chiarelli, I. Triguero, and A. Garcia, “Virtual porous materials to predict the air void topology and hydraulic conductivity of asphalt roads,” *Powder Technology*, vol. 352, pp. 294–304, 2019.
- [20] T. F. Fwa, E. Lim, and K. H. Tan, “Comparison of permeability and clogging characteristics of porous asphalt and pervious concrete pavement materials,” *Transportation Research Record Journal of the Transportation Research Board*, vol. 2511, no. 1, pp. 72–80, 2015.
- [21] Z. Q. Wang, J. G. Xie, L. Gao, Y. P. Liu, and L. Tang, “Three-dimensional characterization of air voids in porous asphalt concrete,” *Construction and Building Materials*, vol. 272, article 121633, 2021.
- [22] S. Li, H. Wang, L. Y. Wang, X. Z. Yu, and L. Yang, “Adaptive dodging method based on variational mask for remote sensing images,” *Journal of Remote Sensing*, vol. 22, no. 3, pp. 450–457, 2018.
- [23] R. Pullagura, U. S. Valasani, and P. P. Kesari, “Hybrid wavelet-based aerial image enhancement using georectification and homomorphic filtering,” *Arabian Journal of Geosciences*, vol. 14, no. 13, p. 1235, 2021.
- [24] W. D. Liu, J. Y. Li, W. B. Zhang, and L. Li, “Underwater image enhancement method with non-uniform illumination based on Retinex and ADMM,” *Journal of Northwestern Polytechnical University*, vol. 39, no. 4, pp. 824–830, 2021.
- [25] C. Wang, X. J. Xue, H. Li, G. Y. Zhang, H. R. Wang, and L. Zhao, “Underwater image enhancement based on color correction and improved 2D gamma function,” *Journal of Electronic Measurement and Instrumentation*, vol. 35, no. 2, pp. 171–178, 2021.
- [26] G. X. Li, B. Y. Zhang, and Y. Z. Yu, *Soil Mechanics*, Tsinghua University Press, 2nd edition, 2013.
- [27] Y. L. Wang, *Hydromechanics*, China Communications Press Co. Ltd., 2nd edition, 2015.
- [28] P. P. Guo, X. N. Gong, Y. X. Wang, H. Lin, and Y. Zhao, “Minimum cover depth estimation for underwater shield tunnels,” *Tunnelling and Underground Space Technology*, vol. 115, article 104027, 2021.

Review Article

Application of 3D Printing Technology in the Mechanical Testing of Complex Structural Rock Masses

Yingjie Xia,^{1,2} Qingkun Meng,¹ Chuanqing Zhang^{1b},² Ning Liu,³ Zhenxing Zhao,⁴ Jun Chen,³ and Gao Yang²

¹State Key Laboratory of Coastal and Offshore Engineering, Dalian University of Technology, Dalian 116024, China

²State Key Laboratory of Geomechanics and Geotechnical Engineering, Institute of Rock and Soil Mechanics, Chinese Academy of Sciences, Wuhan, Hubei 430071, China

³Power China Huadong Engineering Corporation, Hangzhou, Zhejiang 310014, China

⁴China Railway Construction Bridge Engineering Bureau Group 3rd Engineering Co., Shenyang, Liaoning 110043, China

Correspondence should be addressed to Chuanqing Zhang; cqzhang@whrsm.ac.cn

Received 28 August 2021; Accepted 17 September 2021; Published 13 October 2021

Academic Editor: Yu Wang

Copyright © 2021 Yingjie Xia et al. This is an open access article distributed under the Creative Commons Attribution License, which permits unrestricted use, distribution, and reproduction in any medium, provided the original work is properly cited.

In the engineering of underground construction, the discontinuous structures in rock mass have important influences on the mechanical behaviors of the subsurface of rock mass. The acquisition of mechanical parameters is the basis of rock mass engineering design, construction, safety, and stability evaluation. However, the mechanical parameters and failure characteristics of the same rock mass under different mechanical conditions cannot be obtained due to the limitations of specimen preparation techniques. In recent years, with the continuous development of 3D printing (3DP) technology, it has been successfully applied to the repetitive preparation of rock mass samples. The combinations of 3DP and other techniques, such as 3D scanning and CT scanning, provided a new approach to study the mechanical behavior of complex structural rock masses. In this study, through a comprehensive review of the technical progress, equipment situation, application fields, and challenges of the use of 3DP technology, the following conclusions were obtained: (1) 3DP technology has advantages over traditional rock mass specimen preparation techniques, and the verification of test results using 3D printed samples shows that the 3DP has broad application prospects in geotechnical engineering. (2) The combination of 3DP and other advanced techniques can be used to achieve the accurate reconstruction of complex structural rock masses and to obtain the mechanical and failure characteristics of the same rock mass structure under different mechanical boundary conditions. (3) The development of 3DP materials with high strength, high brittleness, and low ductility has become the major bottleneck in the application of 3DP in geotechnical engineering. (4) 3D printers need to meet the high precision and large size requirements while also having high strength and long-term printing ability. The development of 3D printers that can print different types of materials is also an important aspect of the application of 3DP in geotechnical engineering.

1. Introduction

Rock mass is characterized by discontinuity, inhomogeneity, and anisotropy. It is composed of various weak structural joints within certain engineering scales [1–4]. The internal structures of rock mass are generally complex and contain defects such as pores, joints, and fissures that directly affect the strength, deformation, and seepage characteristics of the rock mass, which are closely related to the stability of rock engineering [5–8]. Therefore, the mechanical behavior

and failure characteristics of complex structural rock masses have become the key factors of rock mass engineering design, construction, safety, and stability evaluation [9–11].

Currently, the acquisition of mechanical parameters of rock mass is carried out using three main methods: in situ field tests [12–14], laboratory tests [15, 16], and numerical simulation [17, 18]. Specifically, in situ testing is the most effective method of obtaining the mechanical parameters of rock mass on an engineering scale. However, the large size of rock mass specimens used in in situ testing causes many

problems, such as a long test period, high costs, and influences on construction, leading to less data being obtained through in situ testing. Laboratory tests have been the most important means of obtaining the mechanical parameters of rocks because they can visualize the mechanical characteristics, such as the strength, deformation, and failure characteristics, of rock mass specimens under different mechanical boundary conditions. However, due to the limitations of the testing equipment in terms of the size of rock samples and the difficulty in preparing samples of complex structures, it is hard to obtain the mechanical parameters via laboratory tests. Moreover, since the experimental testing of rocks is generally destructive, it is impossible to accurately obtain the change rule of mechanical properties of the same rock mass. Numerical simulation has the advantages of low cost and repeatability, so it has become an effective supplement to in situ tests and laboratory tests on rock masses. However, the complex structures of rock mass are often simplified in the simulation process due to the limitations of calculation conditions, making the numerical model differ from the real structures of rock mass. In addition, the selection of material parameters and determination of constitutive relation in the simulation process would affect the calculation results [19–21].

As was discussed above, when laboratory tests are used to study the mechanical and failure properties of rock mass, the specimens need to be representative of their structural characteristics. Due to the complexity of natural rock mass structures, it is difficult to obtain rock mass specimens with identical structures and properties. So, it is impossible to obtain the mechanical properties of the same rock mass structure under different mechanical boundary conditions. Such problems can be solved by using similar material model tests. However, it is difficult to make specimens with natural joint surfaces, special internal structures, and chamber excavation models, although these structural characteristics have important influences on the strength, deformation, and failure characteristics of rock masses [22–25]. Therefore, the repetitive preparation of complex structural specimens is the key to carrying out laboratory tests.

As an additive manufacturing technology, the 3DP differs from traditional manufacturing techniques such as cutting and grinding because it uses a layer-by-layer accumulation method to achieve the precise reconfiguration of complex structures. In recent years, the 3DP has been widely used in many fields such as biomedicine, aerospace, automobile manufacturing, and electronic components [26–29]. With the development of 3DP technology, some studies have begun to explore the applications of 3DP in the field of rock mechanics. For example, the combination of technologies of 3DP, stress freezing technique, CT scanning, and X-ray scanning has enabled the quantitative characterization and visualization of complex structures inside deep rock masses [30–34]. Based on this technology, transparent natural sand conglomerate specimens have been produced to investigate the effects of complex structures on the stress field and plastic zone [35, 36]. Furthermore, some materials such as polylactic acid (PLA), gypsum, and photosensitive resin have also been used in the preparation of rock-like specimens.

The feasibility of 3DP in rock mechanics tests was initially verified by comparing the mechanical and failure properties of rock specimens [37, 38]. After that, several regular rock masses were assessed using 3DP, and the influences of the structural characteristics on the overall mechanical properties were studied [39–41]. Recently, the 3DP technique has been applied to the structural reconstruction of irregular columnar jointed rock masses, and the feasibility and superiority of this method in the reconstruction of complex structural rock masses have been demonstrated by comparing the results of mechanical and laboratory tests [42–44].

Thus, it is clear that the 3DP has advantages over other techniques used in rock mechanics testing, such as the accurate and rapid specimen preparation of complex structural rock masses [45]. However, compared with the mechanical and failure characteristics of high strength and high brittleness in rock mechanics tests, the specimens prepared using 3DP usually have low strength and high plasticity, which limit the applications of 3DP in rock engineering. Therefore, on the basis of 3DP technology in complex structural rock mass reconstruction and mechanical testing, the applications and progress of the use of 3DP technology in the rock mass are reviewed from the aspects of materials, equipment, and test methods. In addition, the deficiencies of current 3DP technology in rock mass engineering are discussed to provide guidance for its engineering application.

2. The Technologies, Materials, and Equipment of 3DP

2.1. The Technologies of 3DP. The difference between 3DP technologies and traditional methods lies in the printing materials and accumulation methods. Table 1 describes the common 3DP technologies and their corresponding materials, which are mainly divided into three categories: (1) Extrusion 3DP technology includes fused deposition manufacturing (FDM), fused filament fabrication (FFF), directed ink writing (DIW), and continuous fibre fabrication (CFF) [46–49]. The principle of this method is that the material is melted at a high temperature and ejected from the nozzle; then, the material solidifies quickly after being ejected. (2) 3DP using photography includes stereolithography (SLA), digital light processing (DLP), and continuous liquid interface production (CLIP) [50, 51]. The principle of this method is that the liquid photosensitive resin is sprayed from the nozzle, and the liquid in the target area is irradiated with ultraviolet light, so that the liquid can be rapidly solidified. (3) The 3DP via layer powder bonding includes powder-based 3DP, electron beam melting (EBM), selective laser melting (SLM), selective heat sintering (SHS), selective laser sintering (SLS), and direct metal laser sintering (DMLS) [52–57]. The principle of SLS consists in spreading the first layer of powder, and then, the infrared laser is used to sinter the powder into the desired solid object. The powder bed is preheated a few degrees below the melting temperature of the polymer, and the laser locally provides only the thermal energy necessary to melt the polymer. In addition, the commonly used 3DP techniques also include laminated object manufacturing (LOM) [58],

TABLE 1: Classifications of 3DP technology [43].

Technical types	Technical names	Materials	Printer manufacturer	Sources
Melt extrusion	Fused deposition manufacturing (FDM)	Thermoplast, eutectic alloy, rubber		[46]
	Fused filament fabrication (FFF)	Thermoplast, eutectic alloy, rubber, etc.	Stratasys	[47]
	Directed ink writing (DIW)	Ceramics, alloy, metal ceramic, etc.	3D Systems	[48]
	Continuous fibre fabrication (CFF)	Nylon, straps, glassfibre, etc.		[49]
Photopolymerization	Stereolithography (SLA)	Photosensitive resin		
	Digital light processing (DLP)	Photosensitive resin	3D Systems	[51]
	Continuous liquid interface production (CLIP)	Photosensitive resin		
Layer powder bonding	Powder-based 3DP	Almost any alloy, powdered polymer, gypsum		[52]
	Electron beam melting (EBM)	Almost any alloy (including titanium alloys)		[53]
	Selective laser melting (SLM)	Titanium alloy, cobalt chromium alloy, stainless steel, aluminum	Z Corporation	[54]
	Selective heat sintering (SHS)	Thermoplastic powder	3D Systems	[55]
	Selective laser sintering (SLS)	Hot plastic, metal powder, ceramic powder	Stratasys	[56]
	Direct metal laser sintering (DMLS)	Almost any alloy		[57]
Lamination	Laminated object manufacturing (LOM)	Paper, sheet metal, plastic film	Helisys	[58]
Powder feeding	Directed energy deposition (DED)	Almost any alloy	Fraunhofer	[59]
Metal wire	Electron beam freeform fabrication (EBF ³)	Almost any alloy	LARC	[58]

directed energy deposition (DED) [58, 59], and electron beam freeform fabrication (EBF³) [58].

The general processes of 3DP technologies are mostly similar and can be divided into four steps: (1) 3DP model building, which usually uses computer-aided design (CAD) software to build a 3D solid model. In this process, the solid 3D model can be built independently or can be acquired using other means such as CT scanning. (2) Model format conversion and slicing. In this process, it is necessary to convert the established 3D model into a format that can be recognized by the 3D printer. Then, the model is sliced according to the accuracy of the 3D printer. (3) The 3DP path and parameter setting to printing. (4) Postprocessing of printed models. For some 3D printed models, redundant materials (such as the supporting materials) may need to be removed after printing.

2.2. The Materials of 3DP. Different 3DP techniques require different materials (Wang and Qi [54]). Table 2 describes the 3DP materials used in different 3DP techniques. Currently, the 3DP materials such as polylactic acid (PLA), gypsum-like materials, photosensitive resins, and acrylonitrile butadiene styrene (ABS) have been used in the production of rock mass specimens [60–64]. The failure of rock materials generally shows high strength and high brittleness. However, from the test data of these materials, the specimens made from these materials exhibit low strength and high ductility which are different from the mechanical and failure characteristics of real rocks. To address this issue, Fereshtenejad and Song [65] investigated the material properties of powder

layer printing technique and found that by using appropriate posttreatment techniques and changing printing parameters, the strength of 3DP specimens could be improved. However, the test results still differed from the mechanical and failure properties of natural rocks. Perras and Vogler [66] made specimens with two different particle sizes using the powder layer and inkjet head technology to carry out Brazilian splitting tests. Through comparative testing of three types of natural sandstone specimens, it was found that the specimens made using 3DP were close to the sandstone specimens with the weakest roughness, tensile strength, and fracture processes. Zhou and Zhu [67] compared specimens made of five 3DP materials and conducted mechanical analyses, which found that the photosensitive resin is the most ideal material for building hard and brittle rocks. According to the test results shown in Figure 1, the photosensitive resin specimens printed using stereolithography (SLA) have better strength, but their brittleness characteristics are still less than those of natural rocks. Therefore, the brittleness of the specimens should be improved by freezing at low temperatures and adding internal macro- or microcracks.

2.3. 3D Printers. In addition to the printing materials, the printing equipment is another factor limiting the applications of 3DP in the related fields. In 1986, the first 3DP device (SLA-250) was produced by 3D Systems Corporation. Since then, the 3DP technology has developed rapidly in industrial applications, and the corresponding 3D printers have been developed on the basis of different printing technologies. In 1989, Deckard invented selective laser sintering

TABLE 2: 3D printed rock specimens.

Materials	Specimen	Description of mechanical properties	Failure properties of specimen	Sources
Sand-based materials		Unconfined compressive strength (UCS) at about 20 MPa		[35] [36] [71]
		Young's modulus at about 1.8 GPa		[72]
Resin		Unconfined compressive strength (UCS) at about 80 MPa		[30, 31]
		Young's modulus at about 1.5 GPa		[67]
Gypsum powder		Unconfined compressive strength (UCS) at about 55 MPa		[73–76]
		Young's modulus at about 7 GPa		
Ceramics power		Unconfined compressive strength (UCS) at about 3 MPa		[67]
		Young's modulus at about 0.15 GPa		[77]
Mixed materials		Unconfined compressive strength (UCS) at about 55 MPa		[78] [79] [80]
		Young's modulus at about 5 GPa		[81]
Polylactic acid (PLA)		Young's modulus at about 1.391 GPa		[37]
Acrylonitrile butadiene styrene (ABS)		$K_{IC} \approx 0.789 \pm 0.131 \text{ MPa}\cdot\text{m}^{1/2}$		[64]
		$J_{IC} \approx 256 \pm 84 \text{ J/m}^2$		

(SLS), which enabled the application of laser sintering technology in the field of 3DP [68]. In 1995, Z Corporation obtained a license from MIT and produced this type of 3DP device. In 2005, the company also invented the first high-precision colour 3D printer. Subsequently, several printers have been developed and widely used. In 2009,

Organovo, USA, used 3DP to manufacture artificial blood vessels. In 2011, Southampton University, UK, printed the first unmanned aircraft using 3DP. In 2011, Kor Ecological Company launched the first car whose surface and parts were manufactured using 3DP. In 2013, British researchers printed embryonic stem cells and similar biological tissues

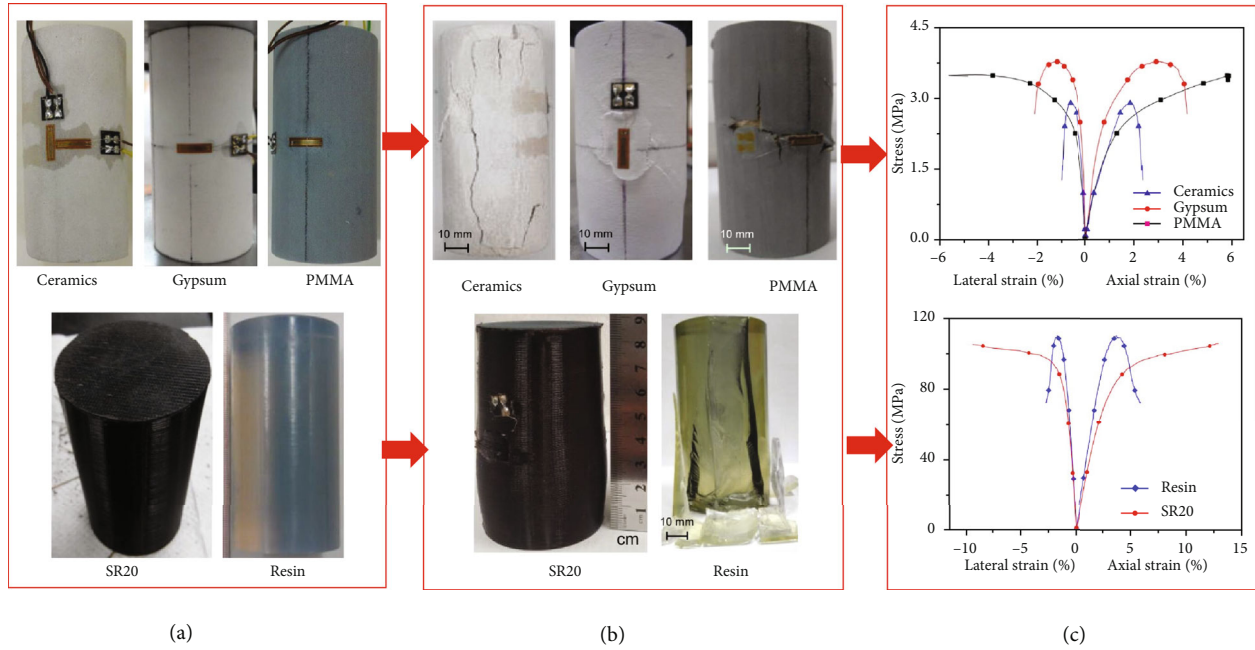


FIGURE 1: Standard specimens prepared using different 3DP materials and their failure modes: (a) standard specimens, (b) failure modes, and (c) stress-strain curves related to the specimens [67].

for the first time with a 3D printer. Since 2014, the 3DP applications in shipbuilding, aerospace science and technology, medicine, construction, automobiles, and other fields have appeared [69, 70].

The current 3D printer manufacturers are mainly located in the United States, Israel, Germany, Japan, Sweden, and other countries. Among them, 3D Systems and Stratasys account for almost 90% of the production of 3D printers. In 2011, 3D Systems acquired Z Corporation, and in 2012, Stratasys acquired Israel’s Objet Company and completed resource integration. The current equipment manufacturers corresponding to different 3DP technologies are also listed in Table 1. From Table 1, it can be seen that for 3DP technologies such as FEM, FFF, DIW, and CFF, the related manufacturers of 3D printers are mainly Stratasys and 3D Systems. For 3DP technologies such as SLA, DLP, and CLIP, the main equipment manufacturer is 3D Systems. For 3DP technologies such as powder-based 3DP, EBm, SLM, SHS, SLS, and DMLS, the manufacturers mainly include Z Corporation, 3D Systems, and Stratasys. For LOM, DED, and EBF³ technologies, the major equipment manufacturers are Helisys, Fraunhofer, and LARC, respectively.

Although there are many kinds of 3DP techniques and printers, the applications of 3DP technology and its materials in rock mass engineering reconstruction are limited because of the following requirements. (1) The natural rocks are generally characterized by high strength; the applications of 3DP in rock mass engineering should meet the high strength conditions. (2) The failure of rock materials is generally brittle. When the rock structure is reconstructed via 3DP, the reconstructed specimens should meet the characteristic of high brittleness. (3) The structure of rock contains joints and cracks, so the corresponding 3DP materials and printers need to meet the characteristics of high precision.

(4) It is necessary to obtain the mechanical parameters of rock mass on the engineering scale. Therefore, in order to reconstruct the large size of rock mass specimens, the 3D printer that meets the requirement of printing large-size rock mass is also needed.

3. Applications of 3DP in Rock Mass Experimental Tests

With the development of 3DP technology, it has been preliminarily applied in the field of rock mass engineering. In this section, the use of 3DP in rock mass experimental tests was summarized.

3.1. Preparation of Specimens in Laboratory Tests

3.1.1. Experimental Tests on 3D Printed Specimens. The mechanical and failure properties of 3D printed specimens are the basis for the applications of 3DP technology in rock mass experimental tests. In the process of making rock specimens, some materials are selected to reconstruct the 3DP rock mass. Table 2 describes the 3DP materials used for reconstructing rock specimens and the mechanical and failure properties (such as UCS and Young’s modulus) of corresponding materials. As is shown in Table 2, the sandstone-based materials were used to prepare standard size specimens using 3DP [66, 71, 72]. It was found that the uniaxial compressive strength of the specimens was about 20 MPa, and Young’s modulus reached about 1.8 GPa. The failure mode exhibits brittle failure characteristics, which is consistent with natural sandstone specimens.

Zhou and Zhu [67] reported that the resin is the most ideal material for simulating rock materials based on the comparison of mechanical and failure properties of five

standard 3DP materials. Therefore, the resin has been used in several studies due to its mechanical and failure characteristics [30–32]. However, the ductility of resin is large, exhibiting plastic characteristics under uniaxial compression, which is different from the brittle failure of rocks. To solve this problem, the brittle failure can be increased by freezing it at low temperatures and adding macro- or microcracks within the specimen [67]. In addition to the sandstone-based materials and photosensitive resin, gypsum has been used in several studies to reconstruct rock specimens using 3DP [73–76]. The 3D printed specimens reconstructed by gypsum generally have low strength, which is suitable for simulating soft rock structures. Wu et al. [73] used glue immersion with evacuation to enhance the rock specimens and achieved better results. The failure characteristics of 3D printed gypsum specimens under uniaxial compression are also presented in Table 2. As can be seen from Table 2, the 3D printed gypsum specimens exhibit brittle failure, which is consistent with the failure of natural rocks. However, the specimens prepared from gypsum have anisotropic characteristics [73]. In addition, since the gypsum specimens need to be soaked with glue to improve their strength, the glue cannot penetrate into the interior of specimens uniformly, leading to the uneven strength of specimens.

Several studies have mixed the cement with printing materials when preparing the 3D printed specimens. For example, as is shown in Table 2, Feng et al. [78] printed the specimens using 525R ordinary Portland cement and obtained the mechanical and failure characteristics of the specimens under uniaxial compression. The uniaxial compressive strength of specimens reached 60 MPa, and the elastic moduli reached about 5 GPa. For the failure characteristics of 3D printed specimens prepared from this material, the brittle failure was predominant. Like the 3D printed specimens prepared using gypsum, the specimens are anisotropic which can be used to simulate the mechanical and failure characteristics of shale.

3.1.2. Repetitive Preparation of Rock Mass with Complex Structures. Since the 3DP has the characteristics of high precision and repeatability, it has been used in the preparation of specimens containing different structures. The mechanical and failure characteristics of the same structural specimens under different mechanical conditions were tested on this basis. Compared with the traditional laboratory specimens containing joints and fissures, the 3DP method allows for the repetitive preparation of rock specimens with the same structures. For example, several studies have used 3DP methods to prepare specimens with single and multiple fractures and studied the mechanical and failure properties of rock specimens under different loading conditions (Table 3) [82–85].

The reconstruction of rock masses requires higher precision because of the influence of mechanics and structure on the failure process. Compared with traditional rock mass reconstruction methods, the 3DP has the advantages of higher precision and efficiency. Therefore, the repeatability of 3D printed specimens is better than that of specimens prepared by traditional methods, which makes it easier to

analyze the effects of different external factors (e.g., rock structure, surrounding pressure state, and loading conditions) on the failure characteristics. For example, the mechanical properties of structural planes in rock masses are related to geological disasters such as landslides and rock bursts, which play an important role in the safety and stability control of rock mass engineering. Therefore, the determination of the mechanical properties of rock mass structural planes is the basis of rock mass engineering design, construction, and stability evaluation. The repetitive preparation of identical specimens containing structural planes is the factor for studying the mechanical and failure characteristics of rock masses [88]. Compared with the regularity of joints and fissures prepared in the laboratory, the natural joint planes have irregular characteristics, so it is difficult to prepare the representative specimens in experiments. Moreover, it is hard to obtain the failure and mechanical characteristics of the same structural planes under different mechanical conditions.

Due to the advantages of 3DP technology, such as the high precision and reproducibility, several studies have attempted to use 3DP to prepare identical rock mass specimens containing structural surfaces. Table 4 presents the typical cases of rocks containing structural planes produced by 3DP technology. Ban et al. [89] printed the scanned data of structural planes using 3DP and then achieved the repetitive production of natural structural planes. The advantage of this method is that they used 3DP as the bridge of obtaining structural plane information and repetition reconstruction. However, the mechanical similarity between natural rocks and casting materials should be considered. Ishibashi et al. [90] used acrylic resin to produce the 3D printed shear specimens with specific roughness coefficients. The tests results showed that the 3DP is an effective method for producing structural planes with specific roughness coefficients. Specifically, it allows for the repeated tests on the shear seepage characteristics of identical rock mass specimens.

The main advantage of 3DP is the precise reconstruction of complex structures. Taking advantage of this, several studies have used 3DP to reconstruct the rock masses with complex structures. Suzuki et al. [92, 93] produced the rock mass specimen containing complex fracture networks using 3DP (Figure 2). The analysis of CT scanning results revealed that the rock mass specimens reconstructed using 3DP reduced the uncertainty of laboratory tests and numerical calculations, which are important for the acquisition of mechanical and failure characteristics of complex fractured rock masses.

In rock mass engineering, understanding the mechanical and failure characteristics of complex structural rock masses is the basis of engineering safety design, analysis, and stability evaluation. The structure of rock mass is the controlling factor that determines the mechanical and failure characteristics. However, it was difficult to reconstruct structural rock masses for either experimental testing or numerical calculations. Xia et al. [43, 44] used 3DP to reconstruct the columnar jointed rock mass at Baihetan hydropower station (Figure 3). By comparing the mechanical properties, failure characteristics, and acoustic emission characteristics of the

TABLE 3: 3DP fractured rock specimens.





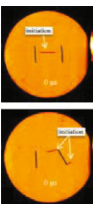
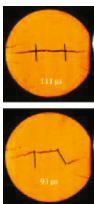
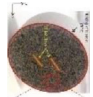
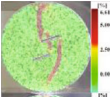

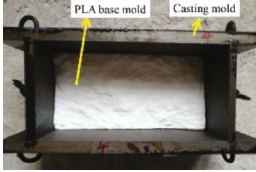
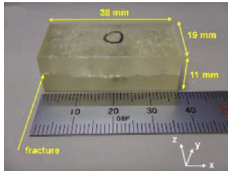
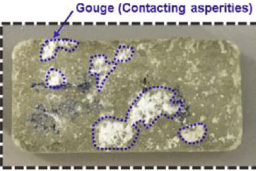


No.	Specimen	Specimen materials and test conditions	Test results	Relevant mechanical parameters	Comments	Sources
1		Photosensitive resin Dynamic loading		Dynamic compressive stress and strain, longitudinal wave velocity, elastic modulus, etc.	Symmetrical wing cracks initiated The specimen cannot completely reflect the mechanical behavior of brittle rocks	[86]
2		Photosensitive resin Static uniaxial compression		Compressive strength and axial strain at the peak stress influenced by the flaw number and angles.	Wing and antiwing cracks wrapped around the flaw edge The maximum crack propagation velocity in single flawed specimens is higher than that in double flawed specimens	[87]
3		Gypsum-like material Dynamic loading		Dynamic compressive stress and strain, longitudinal wave velocity, elastic modulus, etc.	The 3DP technique could prepare specimens with preset cracks The failure patterns of gypsum-like specimens are close to the rock mechanical tests	[40]
4		Gypsum-like material Brazilian tests		Young's modulus, Poisson's ratio, uniaxial compressive strength, tensile strength.	3D printed rock-like Brazilian discs with preexisting flaws were investigated The 3DP technology combined with DIC method shows the superiority in the laboratory test	[82-84]

TABLE 4: 3D printed natural structural planes.

No.	Specimen	Specimen material and target test	Test type	Specimen preparation	Sources
1		Polyactic acid Shear tests		Scanning of natural rock mass structural plane using 3D scanning technology The information on the structural plane of the natural rock mass was printed and used as a mold, and the repetitive pouring of the structural plane was achieved on this basis	[89]
2		Acrylic resin Shear tests		Acrylic resin was used to prepare the structural plane, and shear tests were carried out	[90]
3		Polyactic acid Shear test		3DP method was used to make the shear sample mold, and then, the sample was poured	[91]

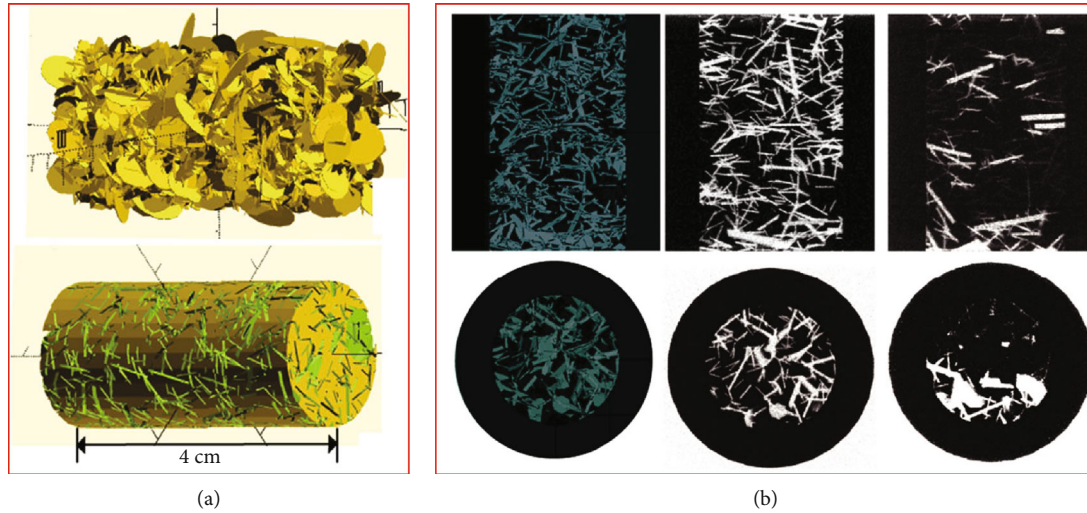


FIGURE 2: Precise reconstruction of complex rock mass structures using 3DP [92, 93]: (a) 3DP preparation of complex rock mass structures; (b) CT scanning results of the 3D printed rock specimens.

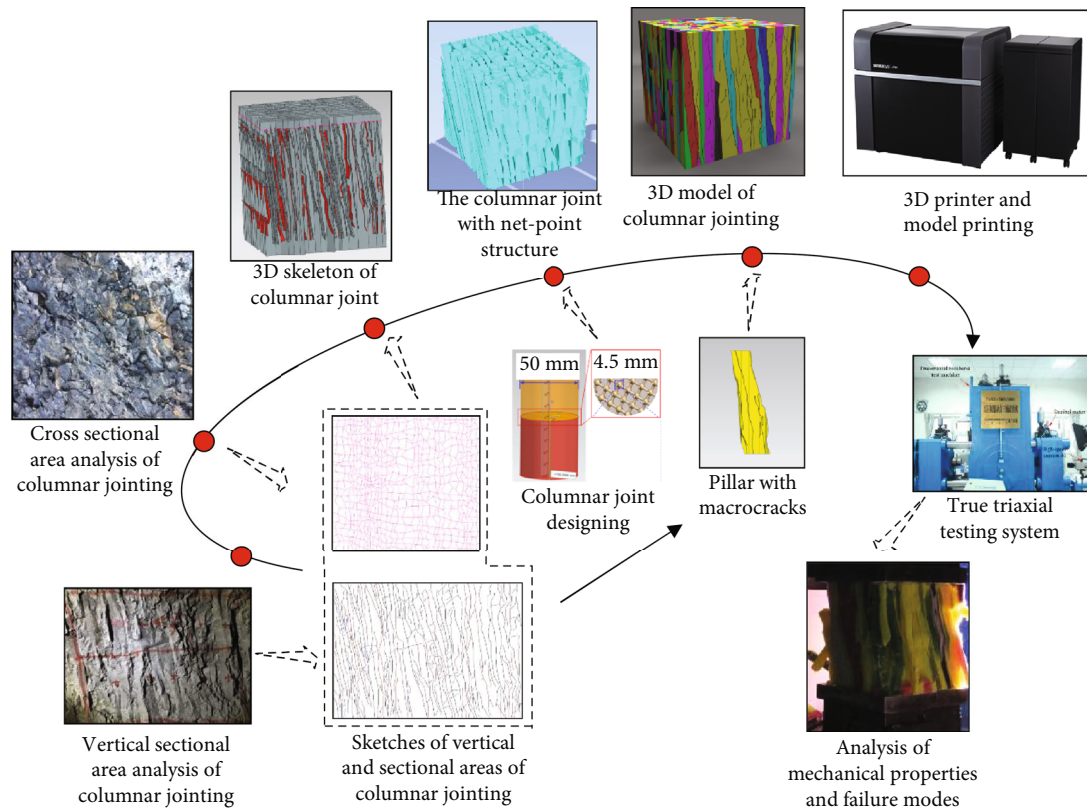
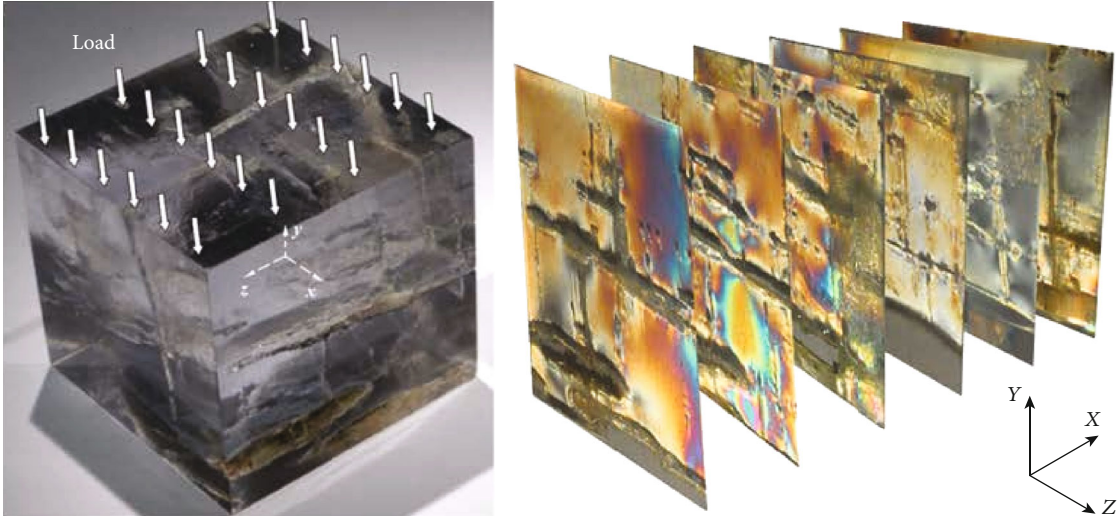


FIGURE 3: Accurate reconstruction of columnar jointed rock mass using 3DP [44].

3DP reconstructed columnar jointed rock mass with the results of in situ and laboratory tests, the mechanical properties of the 3DP reconstructed columnar jointed rock mass were verified, which demonstrates the effectiveness of 3DP in the structural reconstruction of complex rock masses.

The accurate description and visualization of complex internal structures and stress distribution of rock mass are important for solving the various underground engineering

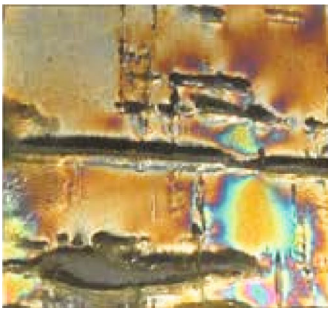
problems [30]. By comparing stress and failure characteristics of the 3DP reconstructed model with natural coal specimens, the discontinuity and stress freezing technique can be intuitively quantified by the combined application of 3DP and CT scanning (Figure 4). The method of combining 3DP with the stress freezing technique is a promising method for quantifying and visualizing the complex fracture structures of underground rock masses and their influences



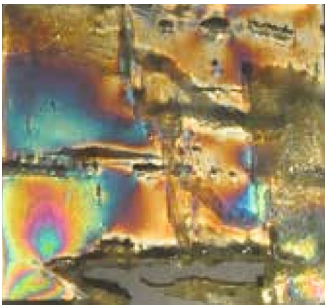
(a)



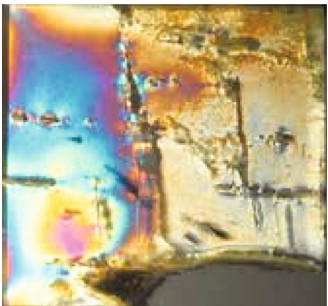
(b)



(c)



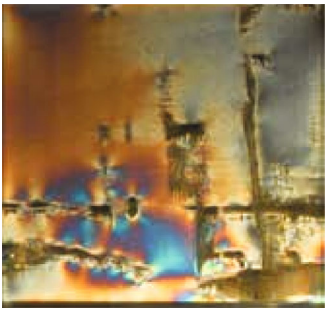
(d)



(e)



(f)



(g)

FIGURE 4: Accurate reconstruction of fractured rock mass using 3DP [30].

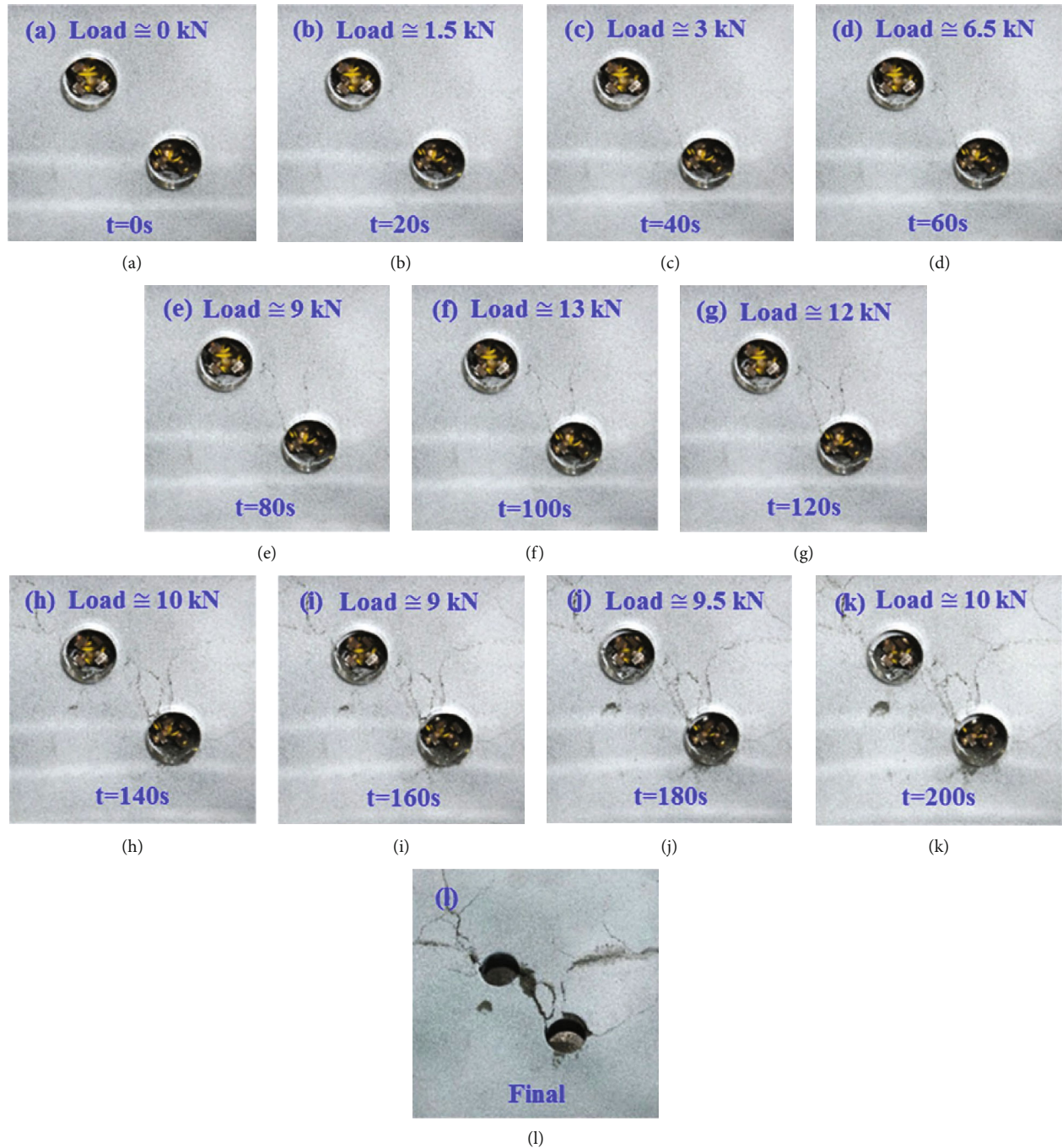


FIGURE 5: Failure processes of the 3D printed twin-hole tunnel [105].

on the 3D stress distribution. In addition, this method can also be used to verify the numerical simulation results.

3.2. Tunnel Failure Simulation. Geomechanical model tests can accurately reflect the spatial relationship between engineering geology and the structure of rock mass. The test results can provide an intuitive interpretation of mechanical properties, deformation trends, and stability characteristics of rock masses. Therefore, the experimental tests have become an important method for studying the stability of rock structures and verifying numerical simulations [74,

94–96]. In deep underground projects, there are widely adjacent tunnels and caverns, such as the twin railroad tunnels for urban and mountain highways [97–100], large caverns in hydroelectric power plants [101, 102], and the deep mine tunnels [103, 104]. The quantitative stability evaluation of multitunnel structures is an important issue related to the safety evaluation and stable construction of underground tunnels. Jiang et al. [105] simulated the overall failure process of the twin-tunnel structure based on a 3D printed sandstone reconstruction model (Figure 5). In addition, they proposed the safety factor method for evaluating the overall

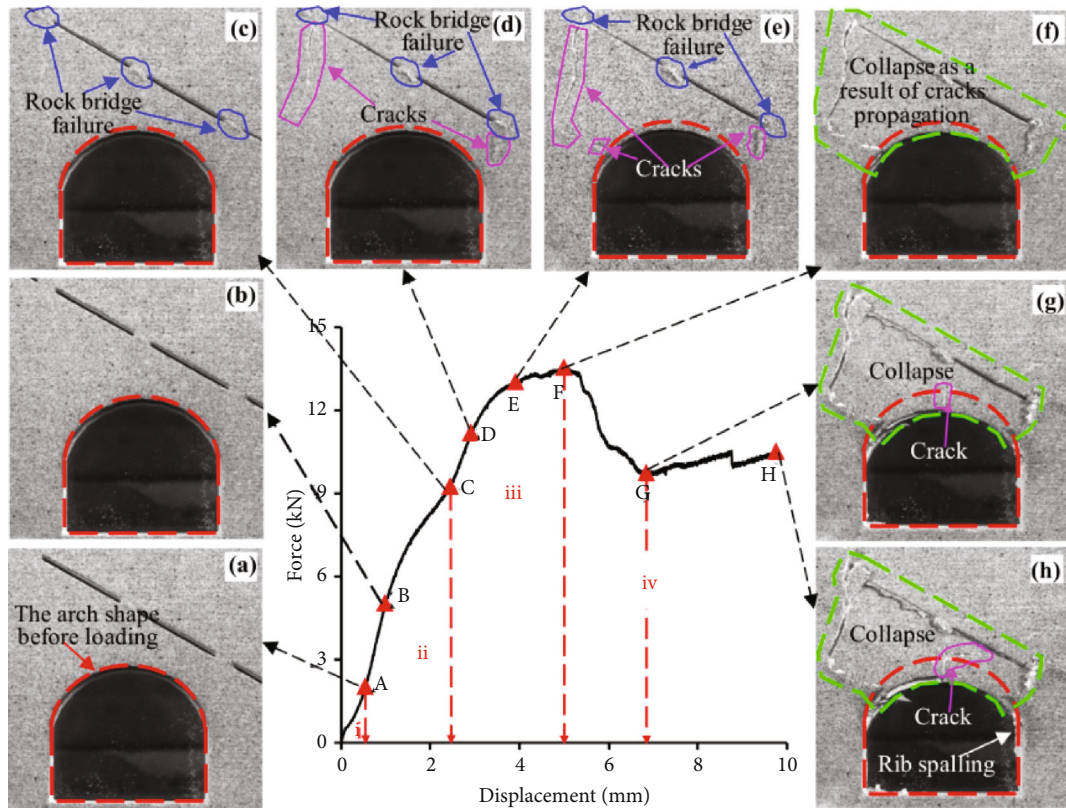


FIGURE 6: Failure processes of the 3D printed tunnel model [74].

safety of multitunnel structures. The experimental results and corresponding numerical analysis showed that the reconstruction of the twin-tunnel structure using 3DP is an effective method for studying tunnel failure and stability analysis. It was determined that for the double tunnel structures, the plastic strain connectivity between tunnels can be used as a conservative instability criterion, and the tunnel displacement inflection point can be used as the overall instability criterion, respectively.

The repetitive preparation of tunnel models and mechanical testing are some of the most commonly used research methods for studying tunnel stability [106–108]. However, the preparation of rock specimens using traditional methods has disadvantages, including time-consuming and unavoidable human errors [30]. The reconstruction method of 3DP may overcome the disadvantages of traditional geotechnical modelling methods. Song et al. [74] prepared four tunnel models via 3DP with gypsum powder and PLA (polylactic acid) materials. The uniaxial compression test results showed that the failure characteristics of the conventional tunnel and single fault tunnel models are similar to the failure process of the 3D printed model (Figure 6). The results of the experimental tests are in general agreement with the artificial model tests, tunnel engineering examples, and numerical simulations, indicating that the 3DP technology can be applied to the experimental study of tunnels.

3.3. Integration of the 3DP with Other Techniques. As the new technique, the 3DP can be combined with other advanced techniques in the failure analysis of rock masses,

thus making up for the disadvantages of traditional testing methods. This section focuses on the applications of 3DP in the combination with other related techniques.

3.3.1. Integration of 3DP with 3D Scanning and CT Scanning.

The mechanical properties of structural planes are the important factors affecting the stability of rock mass. Therefore, the typical strength of structural planes has been concerned in the field of rock mechanics [109–113]. However, the structural planes of the natural rock masses are complex, and the morphology is characterized by anisotropy and size effects. So, it is difficult to accurately evaluate the shear strength of natural structural planes.

In the traditional experimental tests, since it is difficult to make irregular rock mass structures in the preparation processes, the specimen needs to be simplified. The influences of irregular rock mass structures on the mechanical and failure characteristics are ignored, which makes the mechanical characteristics of rock mass differ from the test results. With the development of measurement technology, several studies have applied digital photogrammetry methods to rock mass structure measurements [115–119]. In particular, 3D laser scanners can achieve real replication and are now gradually being used in the field of engineering measurements and detection. The 3D laser scanner can obtain 3D information for complex, irregular, and nonstandard objects. So, it has become an important method for obtaining information on the irregular structures of rock masses [114]. As is shown in Figure 7 [114], the surface information for irregular rock structures was acquired via

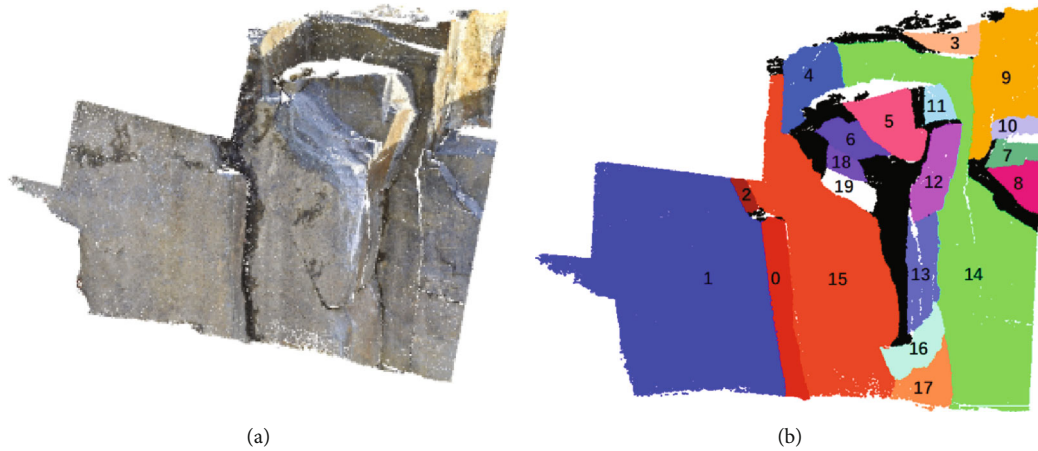


FIGURE 7: Acquisition of 3D scanning data for rock masses [114]: (a) photographs of natural rock mass structures and (b) the 3D information of rock masses regenerated by postprocessing point cloud data.

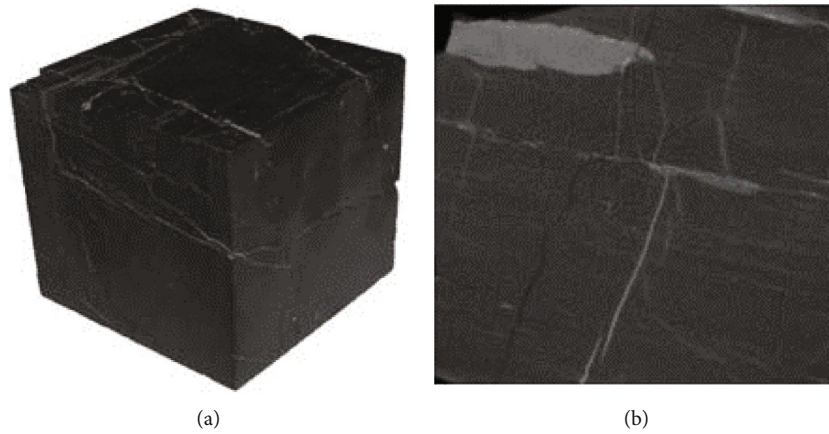


FIGURE 8: Acquisition of CT scanning data for rock masses [30].

3D scanning, and the 3D data for rock masses was regenerated by postprocessing point cloud data. Then, the data can be output by the 3DP printer, which solved the problem of an irregular rock mass structure that cannot be reproduced by general methods of laboratory tests.

In addition to the surface irregularities, defects such as joints and fissures also exist within rock masses [120–122]. Nondestructive CT identification can be used to obtain images of internal structures of rock mass under different environments without disturbance. The CT images are expressed as the colour of CT number, which finally reflects the distribution of each medium inside rocks. The CT technique can be used to obtain the information of joints and fissures inside rock masses (Figure 8) [30]. Therefore, through the combination of CT scanning and 3DP, the irregular joints and fissures can be replicated, and the mechanical properties of the same rock masses under different stress conditions can be obtained.

3.3.2. Integration of 3DP and Numerical Simulations. The 3DP can transform digital models of rock masses into experimental models, thus providing the possibility of repeated failure tests on the complex structure of rock mass. Similarly,

the 3D digital models can also be imported into the numerical software for numerical calculations, such as the finite element [123–125] and discrete element [126] analysis. Therefore, the 3DP is compatible with the laboratory tests and numerical simulations and can be regarded as a virtual bridge connecting laboratory tests and numerical simulations. For example, the 3DP was used to verify the reliability of numerical methods [76]. In addition, the 3DP in combination with numerical simulation has focused on the verification of mechanical and failure modes of rock mass specimens (Figure 9) [85].

By comparing the results of uniaxial compression and Brazilian splitting tests of 3D printed specimens with numerical results, it was concluded that the failure mode of specimens produced using 3DP is consistent with the classical numerical simulations. Furthermore, several studies have used a combination of 3DP and numerical simulation to verify the results of laboratory tests, thus demonstrating the effectiveness of 3DP in studying failure modes of rock masses [76, 85].

Since the 3DP can transform digital models of rock masses into laboratory specimens, its main advantage lies in the accurate reconstruction of complex rock mass

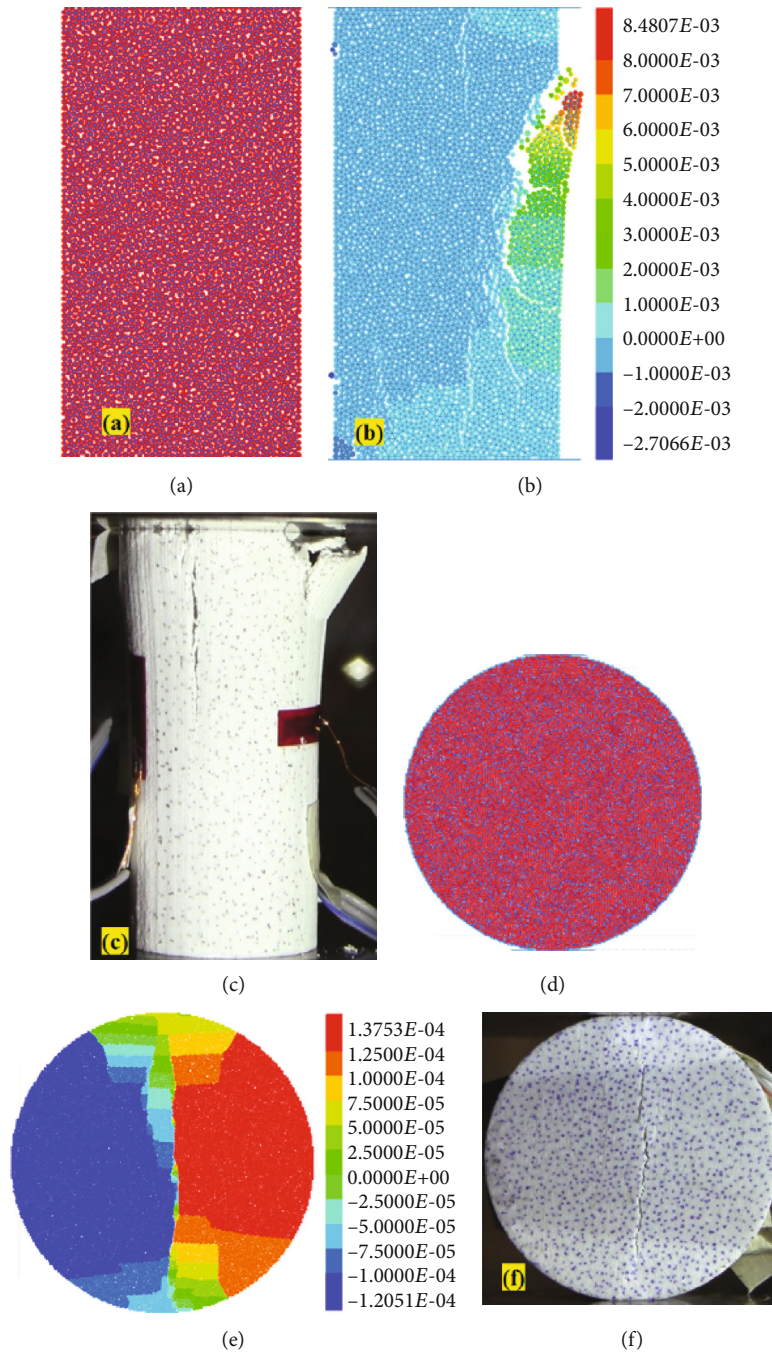
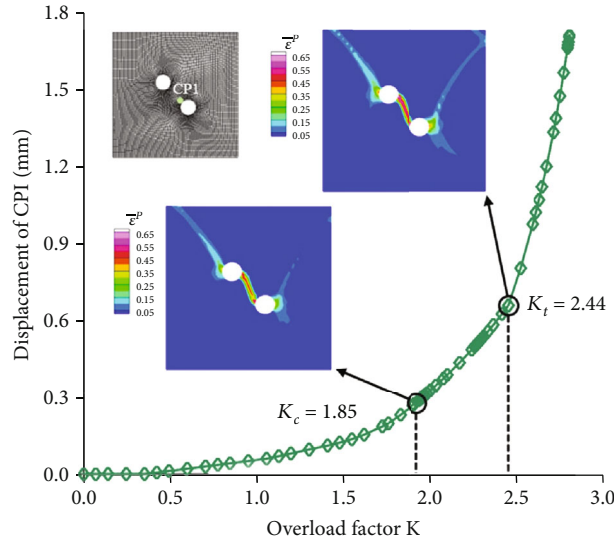


FIGURE 9: Mutual verification of test results for 3D printed specimen and numerical test [85].

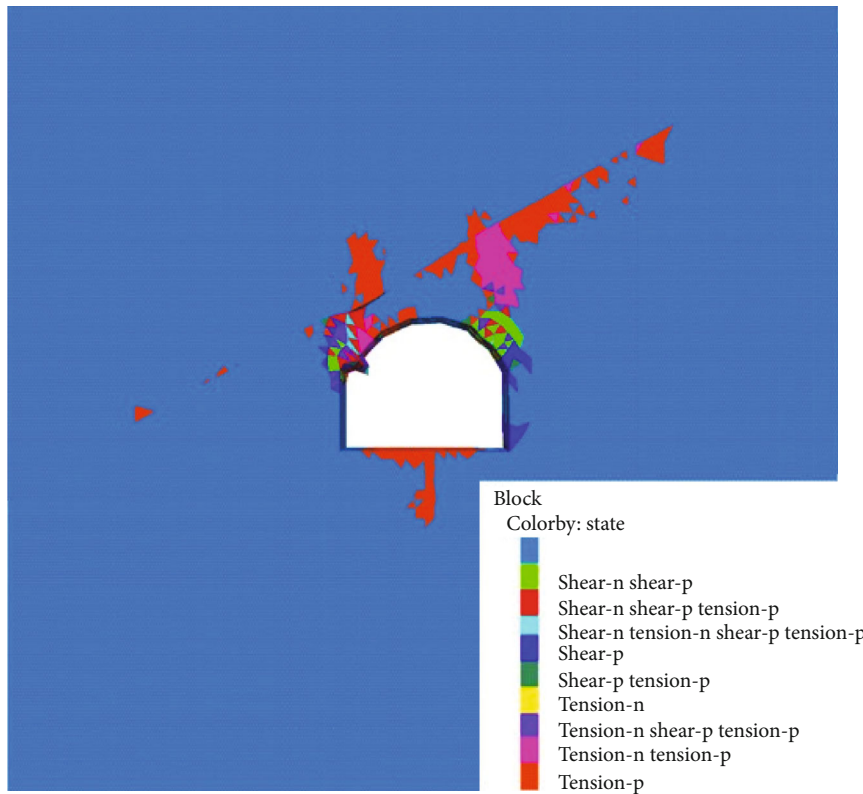
structures. Based on this, Song et al. [74] and Jiang et al. [105] produced tunnel models using 3DP and carried out numerical simulations for comparison. The numerical results are shown in Figure 10. As can be seen in this figure, the combination of 3DP and numerical analysis enabled the thorough analysis of strength, deformation, and failure mode of the rock mass' structure.

3.3.3. Integration of 3DP and the Stress Freezing Technique. The stress freezing technique is an effective method for quantitatively analyzing the three-dimensional stress field

within a complex solid structure. The property of isotropic stress or isotropic stripes caused by external loads in a warmed environment can be “frozen” and recorded when the specimen returns to room temperature [30, 126–128]. With the development of optical mechanics experimental technologies, the solid 3D stress freezing method has been used to make progress in the photoelastic material properties, model preparation, 3D optical measurement theory, fringe picking and resolution analysis, and free-surface stress measurements [129–133]. It is a convenient, economical, and effective way to intuitively and quantitatively analyze



(a)



(b)

FIGURE 10: Mutual verification of test results for 3DP rock tunnel model and numerical test: (a) verification of double-hole tunnel and numerical results [105] and (b) verification of numerical results of the tunnel model with a structural plane [74].

the complex stress field in the solid structure. However, the traditional method of model preparation in 3D photoelastic analysis is mainly making the mold and then casting and molding. This method not only requires the solving of casting process challenges but also leads to high costs and long preparation cycles. For the complex solid structures, when using traditional methods to make 3D photoelastic models, the complex local features have to be omitted. In particular,

the complex structures within a solid are difficult to set up using conventional methods. For example, it is difficult to prepare photoelastic models of subsurface rock mass media with internal pores or fractures. Therefore, it prevents the 3D stress freezing method from being used to visually display the internal stress field of complex solid structures.

The 3DP technology has enabled the rapid production of complex 3D solid models. Based on the digital model of files,

the 3DP technology uses powdery (or liquid) photosensitive resin, ceramic, or metal materials to build a 3D solid via rapid laser curing and layer-by-layer spraying [134–138]. Compared with the traditional photoelastic material of epoxy resin, the photosensitive resin has similar composition, photoelasticity, and stress freezing characteristics, which ensures the feasibility of making photoelastic models of complex structures with 3DP technology. Therefore, the applications of 3DP and 3D stress freezing methods provide a promising path for realizing the quantitative characterization and visualization of complex analyses. The typical test results obtained using 3DP and stress freezing technique are shown in Figure 11 [31].

3.3.4. Integration of 3DP and Other Electronic Technologies. The numerical and laboratory tests have been used to investigate the factors influencing the mechanical properties of anchored rock joints [139, 140]. Feng et al. [29] used 3DP rock bolts and anchoring glue to reinforce the specimens with joints. The surface morphology of the 3DP rock bolt is consistent with the actual rock bolt with better strength. In addition, the digital image correlation (DIC) method was used to capture the changes of strain/displacement fields of the specimen, and the effects of joint planes and joint angles on the crack process, DIC variation pattern, and stress-strain evolution were discussed in conjunction with the test results.

The scanning electron microscope (SEM) is a high-resolution electrooptical instrument used for observing the microscopic fields of objects [141–143]. The micromorphology of the sample surface can be observed, and this method has been used in the experimental fields because of its high scanning resolution [144–148]. By combining the technologies of 3DP and SEM, the mesostructural features of the 3DP reconstructed rock mass specimens can be obtained. Then, the mesostructural features of the 3DP reconstructed rock mass specimens can be compared with those of natural rock mass structures. It ensures the consistency between the macrostructural features and natural rock mass structures and also describes the structural features of 3D printed specimens on the mesoscale, thus measuring the structural features of rock mass from macroscale to microscale.

4. Discussions

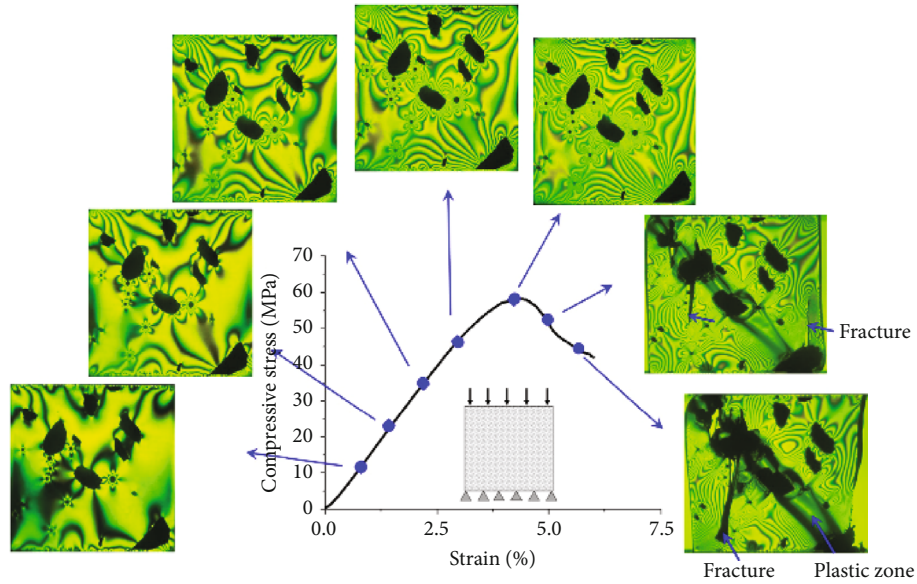
4.1. Improvement of Rock Mass Experimental Methods Using 3DP. As was previously mentioned, the main methods of testing the mechanical properties of jointed rock masses are in situ testing, laboratory tests, and numerical simulations. There are mutual influences and verifications among the three methods [149–153]. In situ testing is the most effective method of obtaining the mechanical parameters of rock masses in engineering. But it takes a long time and is expensive. In addition, in situ testing is mainly used for verification, while laboratory tests are used to obtain the mechanical characteristics of rock masses. Moreover, there are problems such as size effects and anisotropy between in situ and laboratory tests. Due to the limitations of experimental testing equipment such as the size of the rock speci-

men and the difficult preparation of complex rock mass structures, it is impossible to accurately obtain the change rule of the mechanical properties of the same rock masses under different mechanical conditions. Thus, the reconstruction of complex rock masses has become the bottleneck of obtaining the mechanical parameters of complex rocks. Numerical simulation analysis has the advantages of low cost and repeatability, which are generally used to supplement the in situ and laboratory tests. However, the numerical processes are always limited by the computational model, selection of material parameters, constitutive relationship, etc.

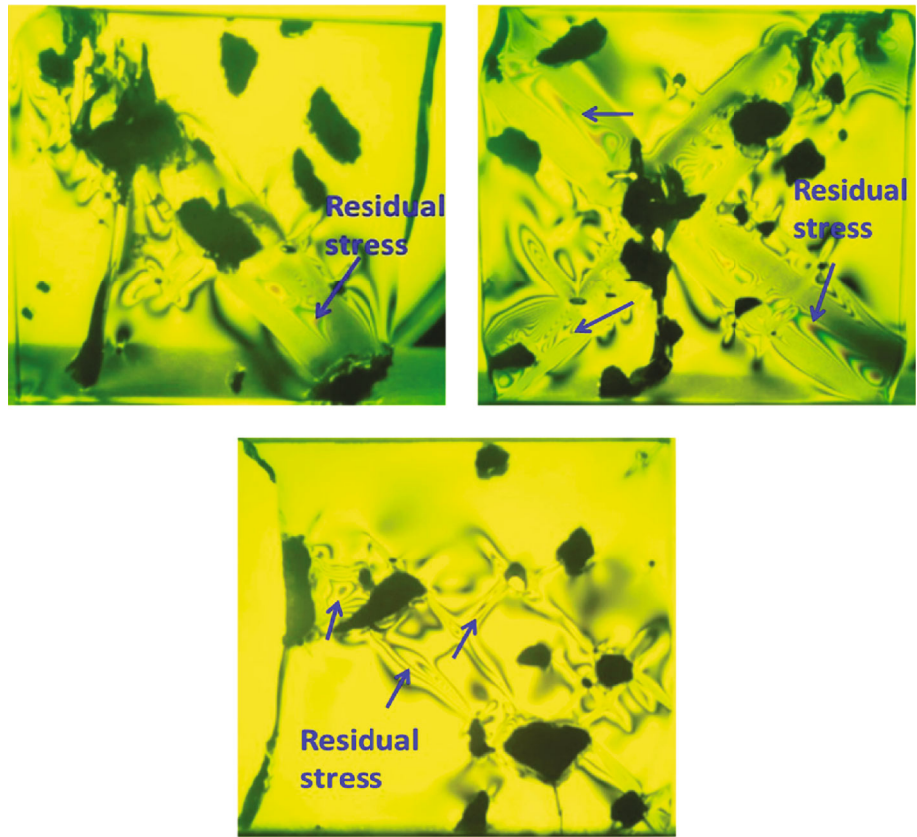
Based on the discussions above, it is clear that the in situ testing, laboratory tests, and numerical simulations mutually validate and support each other. However, due to the limitations of laboratory tests and numerical simulations, there are problems of producing physical and numerical models, which make the obtained physical and numerical model structures differ from the actual rock masses. With the development of 3DP, the methods of obtaining physical and numerical models have been changed (Figure 12). As can be seen from Figure 12, due to the emergence of the 3DP and other techniques, a bridge has been created between in situ tests, laboratory tests, and numerical simulation. Based on the geological surveys and in situ testing of rock masses, the information on the surface and internal structures can be obtained via 3D scanning and CT scanning. Through the digital reconstruction of model structure, the 3DP can be used to output the reconstructed digital model. Thus, a physical model of rock mass with completely consistent structures can be made. Based on this, the mechanical and failure tests can be conducted on identical specimens. Similarly, the reconstructed digital model of rock mass can be imported into the numerical software for calculations. Thus, more accurate mechanical parameters for the engineering design can be obtained by comparing the results of in situ tests, laboratory tests, and numerical simulations. After the comparison, the obtained mechanical parameters can be corrected through the feedback analysis of designing and construction.

4.2. Problems and Challenges regarding the 3DP Technology. Although the 3DP technology has obvious advantages in the reconstruction of rock mass structures, there are still several challenges in the applications of engineering. In this section, we describe the problems that need to be solved.

4.2.1. The 3DP Materials. Rock mass failure has the typical characteristics of high strength, high brittleness, and low ductility. But there is no 3DP material that can satisfy all of these characteristics. Currently, the materials that can be used for 3DP of rock mass structures mainly include photosensitive resin, gypsum, and sandstone-based self-made materials [43, 44]. The rock specimens prepared from these materials often possess one or two of the mechanical and failure characteristics of the real rocks. For example, photosensitive resin is a liquid material before printing. The rock specimens prepared from these materials can meet the characteristics of high strength and precision. However, the



(a)



(b)

FIGURE 11: Applications of 3D printed structures combined with stress freezing technique: (a) monochromatic illumination of the isochromatic fringe pattern of M-III at different loading stages and (b) illustration of the residual stress distribution of the specimens after the removal of the compressive stress [31].

problems of ductility and low brittleness lead to the need for additional treatment [67]. For example, the 3D printed specimen made of gypsum has high brittleness during the failure process, but the strength does not meet the requirements of general rocks [73]. The sandstone-based material specimen

is brittle, but the strength differs from those of natural rocks [35].

In terms of the limitations of 3DP materials regarding the mechanical and failure characteristics of rocks, the solution is to modify one material that meets the requirements of

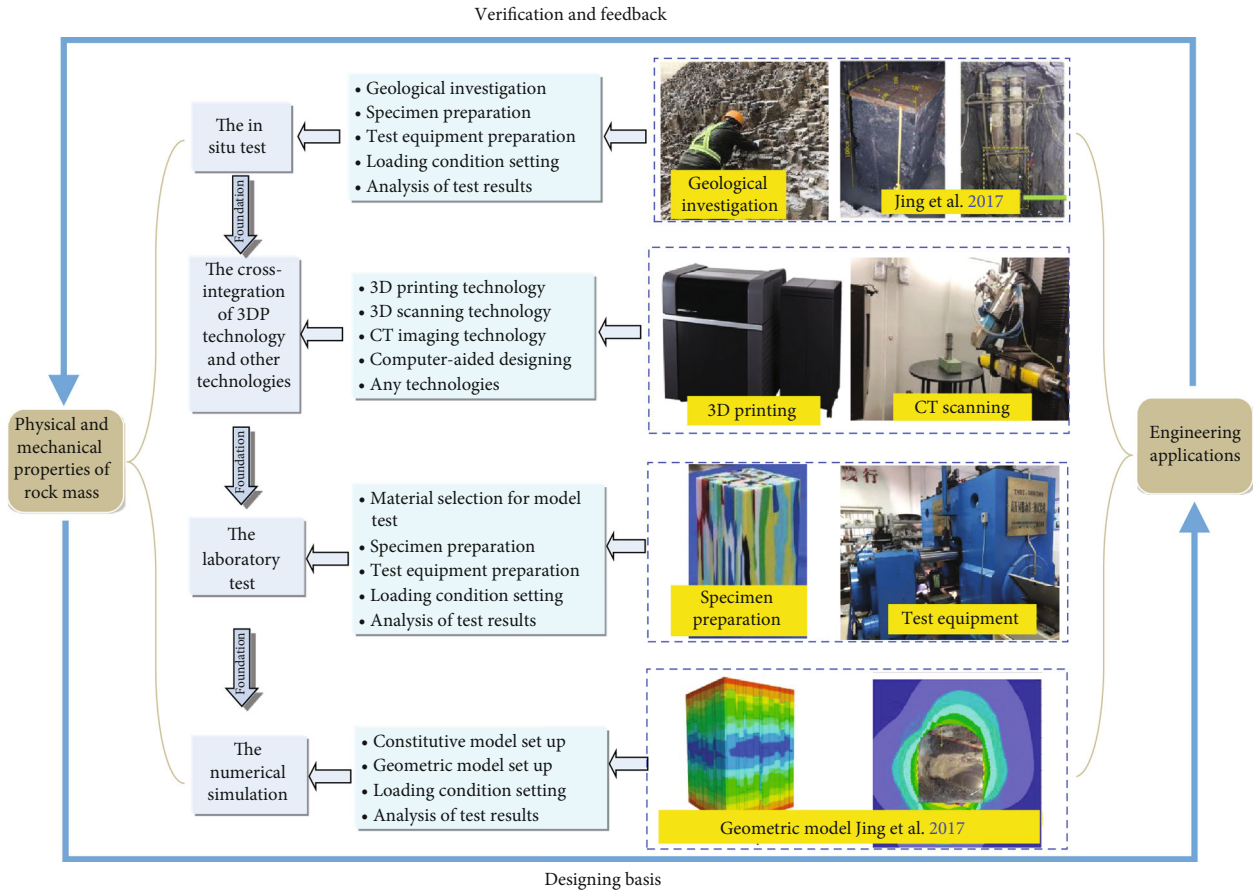


FIGURE 12: Method changes of obtaining mechanical properties of rock mass by 3DP.

the natural rock masses. For example, photosensitive resin can be modified by adding materials with high brittleness characteristics in order to obtain the characteristics of high brittleness, low ductility, and high strength. But it requires the intersection of geotechnical engineering, chemical engineering, and other related subjects.

4.2.2. *The 3D Printers.* The 3D printers and printing materials are closely related. Due to the different 3DP processes, most 3D printers can print using one or two types of materials. Therefore, it is necessary to develop 3D printers that can utilize a wide range of 3DP materials. In addition, the 3D printers are relatively expensive, and most researchers cannot afford them, which is one of the main factors that limit the application of 3DP to the accurate reconstruction of rock mass structures.

Since the material of 3DP is accumulated layer by layer in an incremental manner, the preparation of complex structures can be achieved. Thus, making the reconstructed structure anisotropic is one main characteristic but unavoidable. In addition, the defects such as joints and fissures in the rock mass are generally small in size. In order to achieve the accurate reconstruction of these structures, the 3D printers need to have high precision. Therefore, in the aspects of reducing anisotropy of 3D printed specimens and meeting the requirements of preparing small joints and fissures, the 3D printers need to have the property of high precision.

The size effect is a basic feature for the jointed rock masses. To obtain more accurate mechanical parameters of jointed rock masses and to meet the relevant requirements for engineering design, it is necessary to reconstruct the 3D printed models to be a large size in the model tests. This imposes the requirements on the printing size and capability of the 3D printers. First, since the 3D printed specimens need to meet the requirements of large size, it needs to have the capability of printing large specimens. Second, due to the contradiction between the overall size of the modelled rock mass structure and its small structures such as joints and fissures, the 3D printer also needs to be able to produce large specimens containing small structures. Third, due to the large size and high precision requirements of the 3DP, it requires the 3D printer to have long-term printing capability. Overall, these are the main bottlenecks that limit the applications of 3DP technology in rock engineering. With the development of the 3DP technology, those problems can be solved, and the 3DP technology will be widely used in rock mass engineering.

5. Conclusions

In this paper, the technical development, equipment situation, application fields, and challenges involved in using 3DP technology in rock mass mechanics were

comprehensively reviewed, and the following conclusions were obtained.

- (1) As an emerging technology, the 3DP has obvious advantages in terms of the production of experimental rock models compared to previous sample preparation techniques. This technology has been used in the precise reconstruction of rock mass structures. The results of the 3D printed specimens used in uniaxial compression show that the 3DP has broad application prospects in the geotechnical engineering
- (2) The 3DP technology has been successfully applied in the specimen preparation for laboratory tests and repetitive preparation of natural rock masses containing structural planes. By combining the technology of 3DP with 3D scanning, CT scanning, numerical calculations, stress freezing technique, and other advanced techniques, the complex structural rock masses can be accurately reconstructed. Based on this, the mechanical and failure characteristics of the identical rock masses under different mechanical boundary conditions can be obtained
- (3) The mechanics and failure modes of the general rock specimens have the characteristics of high strength, high brittleness, and low ductility. However, the 3DP materials containing all of those above characteristics have not yet been developed, which has become the main constraint in the use of 3DP in the geotechnical engineering
- (4) Due to the size effect of rock masses and anisotropic characteristics of the 3D printed specimens, it is necessary for the 3D printers to have high precision, be able to print large specimens, be suitable for long-term printing, and have the capability to print using different types of materials

Data Availability

All data, models, and code generated or used during the study appear in the submitted article.

Conflicts of Interest

The authors declared that they have no conflicts of interest in this work. We declare that we do not have any commercial or associative interest that represents a conflict of interest in connection with the work submitted.

Acknowledgments

The study was funded by the National Natural Science Foundation of China (Grant Nos. 42077251, 41807269, and U1865203). The work presented in this paper was also supported by the Open Research Fund of State Key Laboratory of Geomechanics and Geotechnical Engineering, Institute of Rock and Soil Mechanics, Chinese Academy of Sciences (Grant No. Z020011), and Fundamental Research Funds for the Central Universities (Grant No. DUT20RC(3)011).

References

- [1] Y. H. Hatzor, X. T. Feng, S. J. Li, G. Yagoda-Biran, Q. Jiang, and L. X. Hu, "Tunnel reinforcement in columnar jointed basalts: the role of rock mass anisotropy," *Tunnelling and Underground Space Technology*, vol. 46, no. 1, pp. 1–11, 2015.
- [2] H. L. Tu, C. S. Qiao, and Z. M. Han, "Elastic-brittle-plastic analysis of the radial subgrade modulus for a circular cavity based on the generalized nonlinear unified strength criterion," *Tunnelling and Underground Space Technology*, vol. 71, pp. 623–636, 2018.
- [3] X. Wang, W. Yuan, Y. Yan, and X. Zhang, "Scale effect of mechanical properties of jointed rock mass: a numerical study based on particle flow code," *Geomechanics and Engineering*, vol. 21, no. 3, pp. 259–268, 2020.
- [4] Y. Zheng, C. X. Chen, T. T. Liu, and Z. H. Ren, "A new method of assessing the stability of anti-dip bedding rock slopes subjected to earthquake," *Bulletin of Engineering Geology and the Environment*, vol. 80, no. 5, pp. 3693–3710, 2021.
- [5] W. Q. Mu, L. C. Li, T. H. Yang, G. Yu, and Y. Han, "Numerical investigation on a grouting mechanism with slurry-rock coupling and shear displacement in a single rough fracture," *Bulletin of Engineering Geology and the Environment*, vol. 78, no. 8, pp. 6159–6177, 2019.
- [6] W. Q. Mu, L. C. Li, T. H. Yang, L. J. Yao, and S. X. Wang, "Numerical calculation and multi-factor analysis of slurry diffusion in an inclined geological fracture," *Hydrogeology Journal*, vol. 28, no. 3, pp. 1107–1124, 2020.
- [7] T. Xu, T. F. Fu, M. J. Heap, P. G. Meredith, T. M. Mitchell, and P. Baud, "Mesoscopic damage and fracturing of heterogeneous brittle rocks based on three-dimensional polycrystalline discrete element method," *Rock Mechanics and Rock Engineering*, vol. 53, no. 12, pp. 5389–5409, 2020.
- [8] Y. J. Yu, W. C. Zhu, L. C. Li, C. H. Wei, B. X. Yan, and S. Li, "Multi-fracture interactions during two-phase flow of oil and water in deformable tight sandstone oil reservoirs," *Journal of Rock Mechanics and Geotechnical Engineering*, vol. 12, no. 4, pp. 821–849, 2020.
- [9] W. J. Darlington, P. G. Ranjith, and S. K. Choi, "The effect of specimen size on strength and other properties in laboratory testing of rock and rock-like cementitious brittle materials," *Rock Mechanics and Rock Engineering*, vol. 44, no. 5, pp. 513–529, 2011.
- [10] Y. X. Xiao, X. T. Feng, B. R. Chen, G. L. Feng, Z. B. Yao, and L. X. Hu, "Excavation-induced microseismicity in the columnar jointed basalt of an underground hydropower station," *International Journal of Rock Mechanics and Mining sciences*, vol. 97, no. 9, pp. 99–109, 2017.
- [11] Y. J. Xia, L. C. Li, C. A. Tang, X. Y. Li, S. Ma, and M. Li, "A new method to evaluate rock mass brittleness based on stress-strain curves of class I," *Rock Mechanics and Rock Engineering*, vol. 50, no. 5, pp. 1123–1139, 2017.
- [12] G. Herget and K. Unrug, "In situ rock strength from triaxial testing," *International Journal of Rock Mechanics and Mining sciences and Geomechanics Abstracts*, vol. 13, no. 11, pp. 299–302, 1976.
- [13] Q. Jiang, X. T. Feng, J. Chen, K. Huang, and Y. L. Jiang, "Estimating in-situ rock stress from spalling veins: a case study," *Engineering Geology*, vol. 152, no. 1, pp. 38–47, 2013.
- [14] F. K. Nizamtdinov, A. A. Nagibin, V. V. Levashov, R. F. Nizamtdinov, N. F. Nizamtdinov, and A. E. Kasymzhanova, "Methods of in situ strength testing of rocks and

- joints,” *Journal of Mining Science*, vol. 52, no. 2, pp. 226–232, 2016.
- [15] K. Kovari, A. Tisa, and H. H. Einstein, “Suggested methods for determining the strength of rock materials in triaxial compression: revised version,” *International Journal of Rock Mechanics and Mining Sciences and Geomechanics Abstracts*, vol. 20, no. 6, pp. 285–290, 1983.
- [16] J. Yu, W. Yao, K. Duan, X. Y. Liu, and Y. L. Zhu, “Experimental study and discrete element method modeling of compression and permeability behaviors of weakly anisotropic sandstones,” *International Journal of Rock Mechanics and Mining sciences*, vol. 134, no. 10, article 104437, 2020.
- [17] R. E. Goodman, R. L. Taylor, and T. L. Brekke, “A model for the mechanics of jointed rock,” *Journal of Soil Mechanics and Foundations Division*, vol. 94, no. 3, pp. 637–659, 1968.
- [18] J. Yu, G. Y. Liu, Y. Y. Cai, J. F. Zhou, S. Y. Liu, and B. X. Tu, “Time-dependent deformation mechanism for swelling soft-rock tunnels in coal mines and its mathematical deduction,” *International Journal of Geomechanics*, vol. 20, no. 3, article 04019186, 2020.
- [19] E. J. Garboczi, G. S. Cheok, and W. C. Stone, “Using LADAR to characterize the 3-D shape of aggregates: preliminary results,” *Cement and Concrete Research*, vol. 36, no. 6, pp. 1072–1075, 2006.
- [20] S. Häfner, S. Eckardt, T. Luther, and C. Konke, “Mesoscale modeling of concrete: geometry and numerics,” *Computers and Structures*, vol. 84, no. 7, pp. 450–461, 2006.
- [21] Z. M. Wang, A. K. H. Kwan, and H. C. Chan, “Mesoscopic study of concrete I: generation of random aggregate structure and finite element mesh,” *Computers and Structures*, vol. 70, no. 5, pp. 533–544, 1999.
- [22] H. Z. Cui, T. Y. Lo, S. A. Memon, and W. T. Xu, “Effect of lightweight aggregates on the mechanical properties and brittleness of lightweight aggregate concrete,” *Construction and Building Materials*, vol. 35, no. 10, pp. 149–158, 2012.
- [23] H. Kim and W. G. Buttler, “Discrete fracture modeling of asphalt concrete,” *International Journal of Solids and Structures*, vol. 46, no. 13, pp. 2593–2604, 2009.
- [24] K. R. Wu, B. Chen, W. Yao, and D. Zhang, “Effect of coarse aggregate type on mechanical properties of high-performance concrete,” *Cement and Concrete Research*, vol. 31, no. 10, pp. 1421–1425, 2001.
- [25] L. P. Li, J. Hu, S. C. Li et al., “Development of a novel triaxial rock testing method based on biaxial test apparatus and its application,” *Rock Mechanics and Rock Engineering*, vol. 54, no. 3, pp. 1597–1607, 2021.
- [26] M. Bourke, H. Viles, J. Nicoli, P. Lyew-Ayee, R. Ghent, and J. Holmlund, “Innovative applications of laser scanning and rapid prototype printing to rock breakdown experiments,” *Earth Surface Processes and Landforms*, vol. 33, no. 10, pp. 1614–1621, 2008.
- [27] W. Otten, R. Pajor, S. Schmidt, P. C. Baveye, R. Hague, and R. E. Falconer, “Combining X-ray CT and 3D printing technology to produce microcosms with replicable, complex pore geometries,” *Soil Biology and Biochemistry*, vol. 51, pp. 53–55, 2012.
- [28] D. P. Germann, W. Schatz, and P. Eggenberger Hotz, “Artificially evolved functional shell morphology of burrowing bivalves,” *Palaeontologia Electronica*, vol. 17, no. 1, pp. 1–25, 2014.
- [29] X. W. Feng, F. Xue, T. Z. Wang, L. X. Wang, T. Y. Zhao, and X. X. Liu, “Reinforcing effects of 3D printed bolts on joint-separated standard soft rock specimens,” *Composites Part B: Engineering*, vol. 193, article 108024, 2020.
- [30] Y. Ju, H. P. Xie, Z. M. Zheng et al., “Visualization of the complex structure and stress field inside rock by means of 3D printing technology,” *Science Bulletin*, vol. 59, no. 36, pp. 5354–5365, 2014.
- [31] Y. Ju, L. Wang, H. P. Xie, G. W. Ma, Z. M. Zheng, and L. T. Mao, “Visualization and transparentization of the structure and stress field of aggregated geomaterials through 3D printing and photoelastic techniques,” *Rock Mechanics and Rock Engineering*, vol. 50, no. 6, pp. 1383–1407, 2017.
- [32] Y. Ju, L. Wang, H. Xie et al., “Visualization of the three-dimensional structure and stress field of aggregated concrete materials through 3D printing and frozen-stress techniques,” *Construction and Building Materials*, vol. 143, no. 7, pp. 121–137, 2017.
- [33] P. Liu, Y. Ju, P. G. Ranjith, Z. M. Zheng, L. Wang, and A. Wanniarachchi, “Visual representation and characterization of three-dimensional hydrofracturing cracks within heterogeneous rock through 3D printing and transparent models,” *International Journal of Coal Science and Technology*, vol. 3, no. 3, pp. 284–294, 2016.
- [34] J. Jaber, M. Conin, O. Deck, M. Moumni, O. Godard, and S. Kenzari, “Investigation of the mechanical behavior of 3D printed polyamide-12 joints for reduced scale models of rock mass,” *Rock Mechanics and Rock Engineering*, vol. 53, no. 6, pp. 2687–2705, 2020.
- [35] B. Primkulov, J. Chalaturnyk, R. Chalaturnyk, and G. Zambrano Narvaez, “3D printed sandstone strength: curing of furfuryl alcohol resin-based sandstones,” *3D Printing and Additive Manufacturing*, vol. 4, no. 3, pp. 149–156, 2017.
- [36] J. S. Gomez, R. J. Chalaturnyk, and G. Zambrano-Narvaez, “Experimental investigation of the mechanical behavior and permeability of 3D printed sandstone analogues under triaxial conditions,” *Transport in Porous Media*, vol. 129, no. 2, pp. 541–557, 2019.
- [37] C. Jiang and G. F. Zhao, “A preliminary study of 3D printing on rock mechanics,” *Rock Mechanics and Rock Engineering*, vol. 48, no. 3, pp. 1041–1050, 2015.
- [38] C. Jiang, G. F. Zhao, J. B. Zhu, Y. X. Zhao, and L. M. Shen, “Investigation of dynamic crack coalescence using a gypsum-like 3D printing material,” *Rock Mechanics and Rock Engineering*, vol. 49, no. 10, pp. 3983–3998, 2016.
- [39] Q. Jiang, X. T. Feng, Y. H. Gong, L. B. Song, S. G. Ran, and J. Cui, “Reverse modelling of natural rock joints using 3D scanning and 3D printing,” *Computers and Geotechnics*, vol. 73, no. 3, pp. 210–220, 2016.
- [40] Q. Jiang, X. T. Feng, L. B. Song, Y. H. Gong, H. Zheng, and J. Cui, “Modeling rock specimens through 3D printing: tentative experiments and prospects,” *Acta Mechanica Sinica*, vol. 32, no. 1, pp. 101–111, 2016.
- [41] D. Head and T. Vanorio, “Effects of changes in rock microstructures on permeability: 3-D printing investigation,” *Geophysical Research Letters*, vol. 43, no. 14, pp. 7494–7502, 2016.
- [42] Y. J. Xia, C. Q. Zhang, H. Zhou et al., “Structural characteristics of columnar jointed basalt in drainage tunnel of Baihetan hydropower station and its influence on the behavior of P-wave anisotropy,” *Engineering Geology*, vol. 264, article 105304, 2020.

- [43] Y. J. Xia, C. Q. Zhang, H. Zhou et al., "Mechanical behavior of structurally reconstructed irregular columnar jointed rock mass using 3D printing," *Engineering Geology*, vol. 268, article 105509, 17 pages, 2020.
- [44] Y. J. Xia, C. Q. Zhang, H. Zhou et al., "Study on model structure and mechanical anisotropy of columnar jointed rock mass based on three-dimensional printing method," *International Journal of Geomechanics*, vol. 20, no. 11, article 04020208, 2020.
- [45] E. M. Gell, S. M. Walley, and C. H. Braithwaite, "Review of the validity of the use of artificial specimens for characterizing the mechanical properties of rocks," *Rock Mechanics and Rock Engineering*, vol. 52, no. 9, pp. 2949–2961, 2019.
- [46] D. Espalin, D. W. Muse, E. Macdonald, and R. B. Wicker, "3D printing multifunctionality: structures with electronics," *International Journal of Advanced Manufacturing Technology*, vol. 72, no. 5-8, pp. 963–978, 2014.
- [47] S. R. Rajpurohit and H. K. Dave, "Flexural strength of fused filament fabricated (FFF) PLA parts on an open-source 3D printer," *Advances in Manufacturing*, vol. 6, no. 4, pp. 430–441, 2018.
- [48] V. C. F. Li, C. K. Dunn, Z. Zhang, Y. L. Deng, and H. J. Qi, "Direct ink write (DIW) 3D printed cellulose nanocrystal aerogel structures," *Scientific Reports*, vol. 7, no. 1, pp. 1–8, 2017.
- [49] M. Spoerk, C. Savandaiah, F. Arbeiter et al., "Anisotropic properties of oriented short carbon fibre filled polypropylene parts fabricated by extrusion-based additive manufacturing," *Composites Part A: Applied Science and Manufacturing*, vol. 113, no. 1, pp. 95–104, 2018.
- [50] X. Feng, F. Xue, T. Wang, L. Wang, T. Zhao, and X. Liu, "3D printing a mechanically-tunable acrylate resin on a commercial DLP-SLA printer," *Additive Manufacturing*, vol. 1, no. 23, pp. 374–380, 2018.
- [51] C. J. Bloomquist, M. B. Mecham, M. D. Paradzinsky et al., "Controlling release from 3D printed medical devices using CLIP and drug-loaded liquid resins," *Journal of Controlled Release*, vol. 278, no. 28, pp. 9–23, 2018.
- [52] H. S. Shang and Y. P. Song, "Triaxial compressive strength of air-entrained concrete after freeze-thaw cycles," *Cold Regions Science and Technology*, vol. 90-91, no. 91, pp. 33–37, 2013.
- [53] A. T. Sidambe, I. Todd, and P. V. Hatton, "Effects of build orientation induced surface modifications on their vitrobiocompatibility of electron beam melted Ti6Al4V," *Powder Metallurgy*, vol. 59, no. 1, pp. 57–65, 2016.
- [54] C. L. Wang and S. W. Qi, "Application and prospect of 3D printing for rock mechanics," *Progress in Geophysics*, vol. 33, no. 2, pp. 842–849, 2018, (in Chinese).
- [55] Q. B. Nguyen, D. N. Luu, S. M. L. Nai, Z. Zhu, Z. Chen, and J. Wei, "The role of powder layer thickness on the quality of SLM printed parts," *Archives of Civil and Mechanical Engineering*, vol. 18, no. 3, pp. 948–955, 2018.
- [56] F. Fina, A. Goyanes, C. M. Madla et al., "3D printing of drug-loaded gyroid lattices using selective laser sintering," *International Journal of Pharmaceutics*, vol. 547, no. 1-2, pp. 44–52, 2018.
- [57] M. A. al-Tarifi and D. S. Filipovic, "On the design and fabrication of W-band stabilised-pattern dual-polarised horn antennas with DMLS and CNC," *IET Microwaves, Antennas & Propagation*, vol. 11, no. 14, pp. 1930–1935, 2017.
- [58] W. Gao, Y. B. Zhang, D. Ramanujan et al., "The status, challenges, and future of additive manufacturing in engineering," *Computer-Aided Design*, vol. 69, pp. 65–89, 2015.
- [59] H. Jee and M. Kim, "Spherically curved layer (SCL) model for metal 3-D printing of overhangs," *Journal of Mechanical Science and Technology*, vol. 31, no. 12, pp. 5729–5735, 2017.
- [60] Y. Ju, Z. Y. Ren, X. L. Li, Y. T. Wang, L. T. Mao, and F. P. Chiang, "Quantification of hidden whole-field stress inside porous geomaterials via three-dimensional printing and photoelastic testing methods," *Journal of Geophysical Research Solid Earth*, vol. 124, no. 6, pp. 5408–5426, 2019.
- [61] Y. Ju, Z. Zheng, H. Xie, J. Lu, L. Wang, and K. He, "Experimental visualisation methods for three-dimensional stress fields of porous solids," *Experimental Techniques*, vol. 41, no. 4, pp. 331–344, 2017.
- [62] Y. Ju, C. B. Wan, Z. Y. Ren, L. T. Mao, G. Fu, and F. P. Chiang, "Quantification of continuous evolution of full-field stress associated with shear deformation of faults using three-dimensional printing and phase-shifting methods," *International Journal of Rock Mechanics and Mining Sciences*, vol. 126, article 104187, 2020.
- [63] Y. Ju, Z. Y. Ren, J. T. Zheng et al., "Quantitative visualization methods for continuous evolution of three-dimensional discontinuous structures and stress field in subsurface rock mass induced by excavation and construction - an overview," *Engineering Geology*, vol. 265, article 105443, 2020.
- [64] K. R. Hart and E. D. Wetzel, "Fracture behavior of additively manufactured acrylonitrile butadiene styrene (ABS) materials," *Engineering Fracture Mechanics*, vol. 177, pp. 1–13, 2017.
- [65] S. Fereshtenejad and J. J. Song, "Fundamental study on applicability of powder-based 3D printer for physical modeling in rock mechanics," *Rock Mechanics and Rock Engineering*, vol. 49, no. 6, pp. 2065–2074, 2016.
- [66] M. A. Perras and D. Vogler, "Compressive and tensile behavior of 3D-printed and natural sandstones," *Transport in Porous Media*, vol. 129, no. 2, pp. 559–581, 2019.
- [67] T. Zhou and J. B. Zhu, "Identification of a suitable 3D printing material for mimicking brittle and hard rocks and its brittleness enhancements," *Rock Mechanics and Rock Engineering*, vol. 51, no. 3, pp. 765–777, 2018.
- [68] C. R. Deckard, *Method and apparatus for producing parts by selective sintering*, no. article 5017753, 1989DC: US Patent Office, 1989.
- [69] X. L. Li, J. X. Ma, P. Li, Q. Chen, and W. M. Zhou, "3D printing technology and its application trend," *Process Automation Instrumentation*, vol. 35, no. 1, pp. 1–5, 2014.
- [70] Z. L. Li, L. Li, C. Wang, and G. Liu, "The 3D printing technology and the application research in petrochemical industry," *Guangdong Chemical Industry*, vol. 41, no. 23, pp. 100–101, 2014.
- [71] K. J. Hodder and J. A. Nychka, "Silane treatment of 3D-printed sandstone models for improved spontaneous imbibition of water," *Transport in Porous Media*, vol. 129, no. 2, pp. 583–598, 2019.
- [72] K. Barbosa, R. Chalaturnyk, B. Bonfils, J. Esterle, and Z. W. Chen, "Testing impact load cell calculations of material fracture toughness and strength using 3D-printed sandstone," *Geotechnical and Geological Engineering*, vol. 38, no. 2, pp. 1065–1096, 2020.




- [73] Z. J. Wu, B. Zhang, L. Weng, Q. S. Liu, and L. N. Y. Wong, "A new way to replicate the highly stressed soft rock: 3D printing exploration," *Rock Mechanics and Rock Engineering*, vol. 53, no. 1, pp. 467–476, 2020.
- [74] L. B. Song, Q. Jiang, Y. E. Shi et al., "Feasibility investigation of 3D printing technology for geotechnical physical models: study of tunnels," *Rock Mechanics and Rock Engineering*, vol. 51, no. 8, pp. 2617–2637, 2018.
- [75] L. Y. Kong, M. Ostadhassan, B. Liu, C. X. Li, and K. Q. Liu, "Multifractal characteristics of MIP-based pore size distribution of 3D-printed powder-based rocks: a study of post-processing effect," *Transport in Porous Media*, vol. 129, no. 2, pp. 599–618, 2019.
- [76] L. Y. Kong, M. Ostadhassan, S. Zamiran, B. Liu, C. X. Li, and G. G. Marino, "Geomechanical upscaling methods: comparison and verification via 3D printing," *Energies*, vol. 12, no. 3, article 382, 2019.
- [77] M. H. Shen, W. Qin, B. H. Xing et al., "Mechanical properties of 3D printed ceramic cellular materials with triply periodic minimal surface architectures," *Journal of the European Ceramic Society*, vol. 41, no. 2, pp. 1481–1489, 2021.
- [78] X. T. Feng, Y. H. Gong, Y. Y. Zhou, Z. W. Li, and X. F. Liu, "The 3D-printing technology of geological models using rock-like materials," *Rock Mechanics and Rock Engineering*, vol. 52, no. 7, pp. 2261–2277, 2019.
- [79] G. W. Ma, Z. J. Li, L. Wang, F. Wang, and J. Sanjayan, "Mechanical anisotropy of aligned fiber reinforced composite for extrusion-based 3D printing," *Construction and Building Materials*, vol. 202, pp. 770–783, 2019.
- [80] R. Song, Y. Wang, S. Shutov et al., "A comprehensive experimental study on mechanical behavior, microstructure and transport properties of 3D-printed rock analogs," *Rock Mechanics and Rock Engineering*, vol. 53, no. 12, pp. 5745–5765, 2020.
- [81] K. J. Hodder, J. A. Nychka, and R. J. Chalaturnyk, "Process limitations of 3D printing model rock," *Progress in Additive Manufacturing*, vol. 3, no. 3, pp. 173–182, 2018.
- [82] M. Sharafisafa, L. M. Shen, Y. G. Zheng, and J. Z. Xiao, "The effect of flaw filling material on the compressive behaviour of 3D printed rock-like discs," *International Journal of Rock Mechanics and Mining Sciences*, vol. 117, pp. 105–117, 2019.
- [83] M. Sharafisafa and L. M. Shen, "Experimental investigation of dynamic fracture patterns of 3D printed rock-like material under impact with digital image correlation," *Rock Mechanics and Rock Engineering*, vol. 53, no. 8, pp. 3589–3607, 2020.
- [84] M. Sharafisafa, Z. Aliabadian, F. Tahmasebinia, and L. M. Shen, "A comparative study on the crack development in rock-like specimens containing unfilled and filled flaws," *Engineering Fracture Mechanics*, vol. 241, article 107405, 2021.
- [85] Z. Aliabadian, M. Sharafisafa, F. Tahmasebinia, and L. M. Shen, "Experimental and numerical investigations on crack development in 3D printed rock-like specimens with pre-existing flaws," *Engineering Fracture Mechanics*, vol. 241, article 107396, 2020.
- [86] T. Zhou, J. B. Zhu, and H. P. Xie, "Mechanical and volumetric fracturing behaviour of three-dimensional printing rock-like samples under dynamic loading," *Rock Mechanics and Rock Engineering*, vol. 53, no. 6, pp. 2855–2864, 2020.
- [87] T. Zhou, J. B. Zhu, Y. Ju, and H. P. Xie, "Volumetric fracturing behavior of 3D printed artificial rocks containing single and double 3D internal flaws under static uniaxial compression," *Engineering Fracture Mechanics*, vol. 205, pp. 190–204, 2019.
- [88] L. F. Zhang, F. J. Zhou, J. Y. Mou et al., "Large-scale true triaxial fracturing experimental investigation on diversion behavior of fiber using 3D printing model of rock formation," *Journal of Petroleum Science and Engineering*, vol. 181, article 106171, 2019.
- [89] L. R. Ban, C. Z. Qi, H. X. Chen, F. Y. Yan, and C. M. Ji, "A new criterion for peak shear strength of rock joints with a 3D roughness parameter," *Rock Mechanics and Rock Engineering*, vol. 53, no. 4, pp. 1755–1775, 2020.
- [90] T. Ishibashi, Y. Fang, D. Elsworth, N. Watanabe, and H. Asanuma, "Hydromechanical properties of 3D printed fractures with controlled surface roughness: insights into shear-permeability coupling processes," *International Journal of Rock Mechanics and Mining Sciences*, vol. 128, article 104271, 2020.
- [91] Q. Jiang, L. B. Song, F. Yan, C. Liu, B. Yang, and J. Xiong, "Experimental investigation of anisotropic wear damage for natural joints under direct shearing test," *International Journal of Geomechanics*, vol. 20, no. 4, article 04020015, 2020.
- [92] A. Suzuki, N. Watanabe, K. W. Li, and R. N. Horne, "Fracture network created by 3-D printer and its validation using CT images," *Water Resources Research*, vol. 53, no. 7, pp. 6330–6339, 2017.
- [93] A. Suzuki, J. M. Minto, N. Watanabe, K. Li, and R. N. Horne, "Contributions of 3D printed fracture networks to development of flow and transport models," *Transport in Porous Media*, vol. 129, no. 2, pp. 485–500, 2019.
- [94] D. Bachmann, S. Bouissou, and A. Chemenda, "Influence of weathering and pre-existing large scale fractures on gravitational slope failure: insights from 3-D physical modelling," *Natural hazards and earth system sciences*, vol. 4, no. 5/6, pp. 711–717, 2004.
- [95] M. C. He, W. L. Gong, H. M. Zhai, and H. P. Zhang, "Physical modeling of deep ground excavation in geologically horizontal strata based on infrared thermography," *Tunnelling and Underground Space Technology*, vol. 25, no. 4, pp. 366–376, 2010.
- [96] Q. Y. Zhang, K. Duan, Y. Y. Jiao, and W. Xiang, "Physical model test and numerical simulation for the stability analysis of deep gas storage cavern group located in bedded rock salt formation," *International Journal of Rock Mechanics and Mining Sciences*, vol. 94, pp. 43–54, 2017.
- [97] S. Suwansawat and H. H. Einstein, "Describing settlement troughs over twin tunnels using a superposition technique," *Journal of Geotechnical and Geoenvironmental Engineering*, vol. 133, no. 4, pp. 445–468, 2007.
- [98] D. Merlini, D. Stocker, M. Falanesca, and R. Schuerch, "The Ceneri Base Tunnel: construction experience with the southern portion of the flat railway line crossing the Swiss Alps," *Engineering*, vol. 4, no. 2, pp. 235–248, 2018.
- [99] M. Afifipour, M. Sharifzadeh, K. Shahriar, and H. Jamshidi, "Interaction of twin tunnels and shallow foundation at Zand underpass, Shiraz metro, Iran," *Tunnelling and Underground Space Technology*, vol. 26, no. 2, pp. 356–363, 2011.
- [100] M. Sharifzadeh, A. Tarifard, and M. A. Moridi, "Time-dependent behavior of tunnel lining in weak rock mass based on displacement back analysis method," *Tunnelling and Underground Space Technology*, vol. 38, pp. 348–356, 2013.

- [101] M. Tezuka and T. Seoka, "Latest technology of underground rock cavern excavation in Japan," *Tunnelling and Underground Space Technology*, vol. 18, no. 2-3, pp. 127-144, 2003.
- [102] N. Plasencia, J. M. Carvalho, and T. Cavaco, "Groundwater monitoring impacts of deep excavations: hydrogeology in the Venda Nova repowering schemes (NW Portugal)," *Environmental Earth Sciences*, vol. 73, no. 6, pp. 2981-2995, 2015.
- [103] M. R. Islam and R. Shinjo, "Mining-induced fault reactivation associated with the main conveyor belt roadway and safety of the Barapukuria Coal Mine in Bangladesh: constraints from BEM simulations," *International Journal of Coal Geology*, vol. 79, no. 4, pp. 115-130, 2009.
- [104] X. Huang, Q. Liu, K. Shi, Y. C. Pan, and J. P. Liu, "Application and prospect of hard rock TBM for deep roadway construction in coal mines," *Tunnelling and Underground Space Technology*, vol. 73, pp. 105-126, 2018.
- [105] Q. Jiang, X. P. Liu, F. Yan, Y. Yang, D. P. Xu, and G. L. Feng, "Failure performance of 3DP physical twin-tunnel model and corresponding safety factor evaluation," *Rock Mechanics and Rock Engineering*, vol. 54, no. 1, pp. 109-128, 2021.
- [106] S. Jeon, J. Kim, Y. Seo, and C. Hong, "Effect of a fault and weak plane on the stability of a tunnel in rock—a scaled model test and numerical analysis," *International Journal of Rock Mechanics and Mining Sciences*, vol. 41, no. 3, pp. 486-486, 2004.
- [107] D. Sterpi and A. Cividini, "A physical and numerical investigation on the stability of shallow tunnels in strain softening media," *Rock Mechanics and Rock Engineering*, vol. 37, no. 4, pp. 277-298, 2004.
- [108] S. Seki, S. Kaise, Y. Morisaki, S. Azetaka, and Y. J. Jiang, "Model experiments for examining heaving phenomenon in tunnels," *Tunnelling and Underground Space Technology*, vol. 23, no. 2, pp. 128-138, 2008.
- [109] J. C. Jaeger, "Friction of rocks and stability of rock slopes," *Géotechnique*, vol. 21, no. 2, pp. 97-134, 1971.
- [110] P. H. S. W. Kulatilake, G. Shou, T. H. Huang, and R. M. Morgan, "New peak shear strength criteria for anisotropic rock joints," *International Journal of Rock Mechanics and Mining Sciences and Geomechanics Abstracts*, vol. 32, no. 7, pp. 673-697, 1995.
- [111] F. Homand, T. Belem, and M. Souley, "Friction and degradation of rock joint surfaces under shear loads," *International Journal for Numerical and Analytical Methods in Geomechanics*, vol. 25, no. 10, pp. 973-999, 2001.
- [112] G. C. Zhang, M. Karakus, H. M. Tang, Y. F. Ge, and L. Zhang, "A new method estimating the 2D joint roughness coefficient for discontinuity surfaces in rock masses," *International Journal of Rock Mechanics and Mining Sciences*, vol. 72, pp. 191-198, 2014.
- [113] C. Q. Zhang, G. J. Cui, X. R. Chen, H. Zhou, and L. Deng, "Effects of bolt profile and grout mixture on shearing behaviors of bolt-grout interface," *Journal of Rock Mechanics and Geotechnical Engineering*, vol. 12, no. 2, pp. 242-255, 2020.
- [114] L. P. Liu, J. Xiao, and Y. Wang, "Major orientation estimation-based rock surface extraction for 3D rock-mass point clouds," *Remote Sensing*, vol. 11, no. 6, article 635, 2019.
- [115] A. J. Riquelme, A. Abellán, R. Tomás, and M. Jaboyedoff, "A new approach for semi-automatic rock mass joints recognition from 3D point clouds," *Computers and Geosciences*, vol. 68, pp. 38-52, 2014.
- [116] A. J. Riquelme, A. Abellán, and R. Tomás, "Discontinuity spacing analysis in rock masses using 3D point clouds," *Engineering Geology*, vol. 195, pp. 185-195, 2015.
- [117] P. T. Wang, T. H. Yang, Q. L. Yu, H. L. Liu, and P. H. Zhang, "Characterization on jointed rock masses based on PFC2D," *Frontiers of Structural and Civil Engineering*, vol. 7, no. 1, pp. 32-38, 2013.
- [118] J. Q. Chen, H. H. Zhu, and X. J. Li, "Automatic extraction of discontinuity orientation from rock mass surface 3D point cloud," *Computers and Geosciences*, vol. 95, pp. 18-31, 2016.
- [119] Y. F. Ge, Z. G. Xie, H. M. Tang, H. Z. Chen, Z. S. Lin, and B. du, "Determination of shear failure regions of rock joints based on point clouds and image segmentation," *Engineering Geology*, vol. 260, article 105250, 2019.
- [120] B. C. Yang, L. Xue, and K. Zhang, "X-ray micro-computed tomography study of the propagation of cracks in shale during uniaxial compression," *Environmental Earth Sciences*, vol. 77, no. 18, article 652, 2018.
- [121] S. Q. Yang, P. F. Yin, and Y. H. Huang, "Experiment and discrete element modelling on strength, deformation and failure behaviour of shale under Brazilian compression," *Rock Mechanics and Rock Engineering*, vol. 52, no. 11, pp. 4339-4359, 2019.
- [122] Y. T. Duan, X. Li, B. Zheng, J. M. He, and J. Hao, "Cracking evolution and failure characteristics of Longmaxi shale under uniaxial compression using real-time computed tomography scanning," *Rock Mechanics and Rock Engineering*, vol. 52, no. 9, pp. 3003-3015, 2019.
- [123] G. W. Ma, Q. Q. Dong, L. F. Fan, and J. W. Gao, "An investigation of non-straight fissures cracking under uniaxial compression," *Engineering Fracture Mechanics*, vol. 191, pp. 300-310, 2018.
- [124] G. W. Ma, Q. Q. Dong, and L. Wang, "Experimental investigation on the cracking behavior of 3D printed kinked fissure," *Science China Earth Sciences*, vol. 61, no. 12, pp. 1872-1881, 2018.
- [125] W. Yang, D. Zhang, and G. Lei, "Experimental study on multiphase flow in fracture-vug medium using 3D printing technology and visualization techniques," *Journal of Petroleum Science and Engineering*, vol. 193, article 107394, 2020.
- [126] C. Jiang and G. F. Zhao, "Implementation of a coupled plastic damage distinct lattice spring model for dynamic crack propagation in geomaterials," *International Journal for Numerical and Analytical Methods in Geomechanics*, vol. 42, no. 4, pp. 674-693, 2017.
- [127] M. A. Schroedl, J. J. McGowan, and C. W. Smith, "An assessment of factors influencing data obtained by the photoelastic stress freezing technique for stress fields near crack tips," *Engineering Fracture Mechanics*, vol. 4, no. 4, pp. 801-809, 1972.
- [128] J. S. Epstein, D. Post, and C. W. Smith, "Three-dimensional photoelastic measurements with very thin slices," *Experimental Techniques*, vol. 8, no. 12, pp. 34-37, 1984.
- [129] C. Pappalettre and U. Galietti, "Polycarbonate for frozen stress photoelasticity," *Strain*, vol. 31, no. 2, pp. 69-74, 1995.
- [130] T. H. Hyde and N. A. Warrior, "An improved method for the determination of photoelastic stress intensity factors using the westergaard stress function," *International Journal of Mechanical Sciences*, vol. 32, no. 3, pp. 265-273, 1990.

- [131] C. Buckberry and D. Towers, "New approaches to the full-field analysis of photoelastic stress patterns," *Optics and Lasers in Engineering*, vol. 24, no. 5-6, pp. 415-428, 1996.
- [132] A. Baldi, F. Bertolino, and F. Ginesu, "A temporal phase unwrapping algorithm for photoelastic stress analysis," *Optics and Lasers in Engineering*, vol. 45, no. 5, pp. 612-617, 2007.
- [133] P. Pinit and E. Umezaki, "Digitally whole-field analysis of isoclinic parameter in photoelasticity by four-step color phase-shifting technique," *Optics and Lasers in Engineering*, vol. 45, no. 7, pp. 795-807, 2007.
- [134] J. P. Kruth, M. C. Leu, and T. Nakagawa, "Progress in additive manufacturing and rapid prototyping," *CIRP Annals*, vol. 47, no. 2, pp. 525-540, 1998.
- [135] H. J. Jee and E. Sachs, "A visual simulation technique for 3D printing," *Advances in Engineering Software*, vol. 31, no. 2, pp. 97-106, 2000.
- [136] B. W. Miller, J. W. Moore, H. H. Barrett et al., "3D printing in X-ray and gamma-ray imaging: a novel method for fabricating high-density imaging apertures," *Nuclear Instruments and Methods in Physics Research Section A: Accelerators, Spectrometers, Detectors and Associated Equipment*, vol. 659, no. 1, pp. 262-268, 2011.
- [137] T. A. Campbell and O. S. Ivanova, "3D printing of multifunctional nanocomposites," *Nano Today*, vol. 8, no. 2, pp. 119-120, 2013.
- [138] V. Kostakis and M. Papachristou, "Commons-based peer production and digital fabrication: the case of a RepRap-based, Lego-built 3D printing-milling machine," *Telematics and Informatics*, vol. 31, no. 3, pp. 434-443, 2014.
- [139] M. Salcher and R. Bertuzzi, "Results of pull tests of rock bolts and cable bolts in Sydney sandstone and shale," *Tunnelling and Underground Space Technology*, vol. 74, pp. 60-70, 2018.
- [140] A. H. Hoiem, B. Nilsen, and R. Olsson, "Main aspects of deformation and rock support in Norwegian road tunnels," *Tunnelling and Underground Space Technology*, vol. 86, pp. 262-278, 2019.
- [141] G. Desbois, J. Urai, and P. Kukla, "Morphology of the pore space in claystones - evidence from BIB/FIB ion beam sectioning and cryo-SEM observations," *eEarth Discuss*, vol. 4, no. 1, pp. 1-19, 2009.
- [142] S. Hemes, G. Desbois, J. L. Urai, M. De Craen, and M. Honty, "Variations in the morphology of porosity in the Boom Clay Formation: insights from 2D high resolution BIB-SEM imaging and mercury injection porosimetry," *Netherlands Journal of Geosciences*, vol. 92, no. 4, pp. 275-300, 2013.
- [143] R. Yang, S. He, J. Z. Yi, and Q. H. Hu, "Nano-scale pore structure and fractal dimension of organic-rich Wufeng- Longmaxi shale from Jiaoshiba area, Sichuan Basin: investigations using FE- SEM, gas adsorption and helium pycnometry," *Marine and Petroleum Geology*, vol. 70, pp. 27-45, 2016.
- [144] M. E. Houben, G. Desbois, and J. L. Urai, "A comparative study of representative 2D microstructures in shaly and sandy facies of opalinus clay (Mont Terri, Switzerland) inferred from BIB-SEM and MIP methods," *Marine and Petroleum Geology*, vol. 49, pp. 143-161, 2014.
- [145] M. E. Houben, G. Desbois, and J. L. Urai, "Pore morphology and distribution in the Shaly facies of Opalinus Clay (Mont Terri, Switzerland): insights from representative 2D BIB-SEM investigations on mm to nm scale," *Applied Clay Science*, vol. 71, pp. 82-97, 2013.
- [146] K. Jiao, S. P. Yao, C. Liu et al., "The characterization and quantitative analysis of nanopores in unconventional gas reservoirs utilizing FESEM-FIB and image processing: an example from the lower Silurian Longmaxi Shale, upper Yangtze region, China," *International Journal of Coal Geology*, vol. 128-129, pp. 1-11, 2014.
- [147] J. Klaver, G. Desbois, R. Littke, and J. L. Urai, "BIB-SEM characterization of pore space morphology and distribution in postmature to overmature samples from the Haynesville and Bossier Shales," *Marine and Petroleum Geology*, vol. 59, pp. 451-466, 2015.
- [148] J. Klaver, G. Desbois, J. L. Urai, and R. Littke, "BIB-SEM study of the pore space morphology in early mature Posidonia Shale from the Hils area, Germany," *International Journal of Coal Geology*, vol. 103, no. 1, pp. 12-25, 2012.
- [149] Y. Wang, Y. F. Yi, C. H. Li, and J. Q. Han, "Anisotropic fracture and energy characteristics of a Tibet marble exposed to multi-level constant-amplitude (MLCA) cyclic loads: a lab-scale testing," *Engineering Fracture Mechanics*, vol. 244, article 107550, 2021.
- [150] Y. Wang, B. Zhang, B. Li, and C. H. Li, "A strain-based fatigue damage model for naturally fractured marble subjected to freeze-thaw and uniaxial cyclic loads," *International Journal of Damage Mechanics*, 2021.
- [151] Y. Wang, C. H. Li, and J. Q. Han, "On the effect of stress amplitude on fracture and energy evolution of pre-flawed granite under uniaxial increasing-amplitude fatigue loads," *Engineering Fracture Mechanics*, vol. 240, article 107366, 17 pages, 2020.
- [152] Y. Wang, W. K. Feng, H. J. Wang, C. H. Li, and Z. Q. Hou, "Rock bridge fracturing characteristics in granite induced by freeze-thaw and uniaxial deformation revealed by AE monitoring and post-test CT scanning," *1036 Cold Regions Science and Technology*, vol. 177, article 103115, 2020.
- [153] Y. Wang, C. H. Li, J. Hao, and R. Q. Zhou, "X-ray microtomography for investigation of meso-structural changes and crack evolution in Longmaxi formation shale during compressive deformation," *Journal of Petroleum Science and Engineering*, vol. 164, pp. 278-288, 2018.

Research Article

Characteristics Evolution of Multiscale Structures in Deep Coal under Liquid Nitrogen Freeze-Thaw Cycles

Yingfeng Sun ^{1,2}, Yixin Zhao ^{3,4}, Yulin Li ⁴, Nima Noraei Danesh ⁴
and Zetian Zhang ²

¹School of Civil and Resource Engineering, University of Science and Technology Beijing, Beijing 100083, China

²Key Laboratory of Deep Earth Science and Engineering (Sichuan University), Ministry of Education, Chengdu 610065, China

³Beijing Key Laboratory for Precise Mining of Intergrown Energy and Resources, China University of Mining and Technology (Beijing), Beijing 100083, China

⁴School of Energy and Mining Engineering, China University of Mining and Technology (Beijing), Beijing 100083, China

Correspondence should be addressed to Zetian Zhang; zhangzetian@scu.edu.cn

Received 17 August 2021; Accepted 22 September 2021; Published 13 October 2021

Academic Editor: Yong liu

Copyright © 2021 Yingfeng Sun et al. This is an open access article distributed under the Creative Commons Attribution License, which permits unrestricted use, distribution, and reproduction in any medium, provided the original work is properly cited.

Liquid nitrogen freeze-thaw fracturing has attracted more and more attention in improving the coal reservoir permeability. In order to reveal the impact of liquid nitrogen freeze-thaw on the multiscale structure of deep coal, the multiscale structure evolution law of deep and shallow coal samples from the same seam in the Qinshui coalfield during the liquid nitrogen freeze-thaw cycling was investigated using NMR T_2 spectrum, NMRI, and SEM. The connectivity between mesopores and macropores in deep and shallow coal is improved after liquid nitrogen freeze-thaw cycles. The influence of liquid nitrogen freeze-thaw cycles on the structure evolution of deep and shallow coal is the formation and expansion of microscopic fractures. The initial NMR porosity of deep coal is lower than that of shallow coal from the same coalfield and coal seam. The NMR porosity of both the deep and shallow coal samples increases with the increase of the number of freeze-thaw cycles, and the NMR porosity growth rate of the deep sample is lower than that of the shallow sample.

1. Introduction

Global reserves of deep coalbed methane (CBM) are approximately $47.6 \times 10^{12} \text{ m}^3$ [1], and the development of deep CBM in the United States started early and has been gradually commercialized [2–7]. Although China developed deep CBM production relatively late, it has achieved success in deep CBM development in recent years in the Cainan area of Junggar Basin [8–10], Yanchuannan on the eastern edge of the Ordos Basin, Linfen block, and Zhengzhuang and Shizhuang block of Qinshui Basin [11], indicating great potential for the development of deep CBM production.

The multiscale structure of coal is not only the main flow channel of CBM but also the main factor influencing its development. Qin et al. investigated the pore-fracture characteristics of deep coal with a depth of more than 1000 m in the Daning-Jixian area using nuclear magnetic resonance

(NMR) and found that the development of macropores and fractures is superior to that of micropores [12]. Gao studied the influence of temperature and stress on the characteristics evolution of pore-fracture structures in deep coal reservoirs in the Linxing block by NMR and found that the deformation of fractures and mesopores is more significant than that of micropores under the same stress and the negative effect of temperature on fractures and mesopores is greater than that of micropores [13]. Xu et al. analyzed the pore structure of medium-high rank coal samples from depths of 100–1800 m in Yichuan of Shaanxi Province and Shizhuang of Shanxi Province by mercury intrusion, low-temperature liquid nitrogen adsorption, and NMR. Their results show an increase in micropores and a decrease in mesopores and macropores with depth [14]. Lu et al. analyzed the pore-fracture structure of coal samples from different depths of 14 coal mines in the south of Qinshui Basin and found that

fracture density is not affected by depth and is distributed between 7 and 15 fractures/5 cm. Compared with shallow coal samples, the average diameter of the pore-throat in deep coal decreases, the volume of micropores increases slightly, and the volume of mesopores and macropores decreases slightly; when the depth exceeds 1000 m, the porosity is generally less than 6% [15, 16]. Zheng et al. studied the variation in porosity with depth in Qinshui Basin and found that the porosity of coal in the depth greater than 800 m is generally less than 6.5% [17]. Liang et al. studied the pore structure characteristics of samples at different depths in the Huainan coalfield and found that porosity decreased with depth, and the ratio of the macropore specific pore volume to the total specific pore volume is decreasing, while that of micropores is increasing [18]. Zhang found there is a binomial relationship between porosity and effective stress in deep coal reservoirs in the Yushe-Wuxiang block and Shizhuang south block [19].

Due to the low permeability of CBM reservoirs, hydraulic fracturing has become a common method to improve coal seam permeability. However, the solid particles in the fracturing fluid may block the flow channel, and the adsorption of the fracturing fluid on the coal surface and the water-swelling minerals in the coal seam leads to expansion of the coal matrix during the fracturing, thus reducing the permeability of the seam [20]. In addition, hydraulic fracturing consumes large amounts of water, pollutes groundwater, and induces earthquakes [21]. In view of these factors, exploration of new coal seam fracturing technology is urgent. Liquid nitrogen fracturing has attracted increasing attention in recent years [22, 23]. The vaporization and expansion of liquid nitrogen injected into the coal seam, the solidification and expansion of water in the coal seam caused by low temperature, and the thermal stress caused by low temperature will damage and destroy the coal body, and then, the permeability of the coal seam is improved [24]. Qin systematically studied the effect of liquid nitrogen freeze-thaw on the coal pore-fracture structure. He suggested that more freeze-thaw cycles are better than a longer freezing time in improving coal seam permeability [24], and it is the difference in the initial porosity that causes the different increments of permeability under liquid nitrogen freeze-thaw conditions [25]. Sun et al. found that the impact of freeze-thaw on rocks pores and fractures is sandstone > limestone > granite, which is also related to their initial porosities [26]. Using nitrogen adsorption and mercury injection, Qin et al. found that the cumulative seepage pore volume and total pore volume have an exponential relationship with freezing time, and cumulative pore volume has a quadratic relationship with freeze-thaw cycles [27]. Using NMR and SEM, Qin et al. observed that when the freezing time increased from 1 minute to 1 hour, the maximum fracture width increases from 5.56 μm to 100 μm [28]. Yan analyzed the pore structure of coal samples with different water content before and after liquid nitrogen freeze-thaw cycling using nitrogen adsorption and found that the variation in pore structure increases with increasing water content [29]. Sun et al. found that the pores and fractures become more developed when the freezing temperature decreases under

freeze-thaw conditions [30]. Zhai et al. found that freeze-thaw cycles increase the proportion of mesopores and macropores and reduce the proportion of micropores [31].

Liquid nitrogen freeze-thaw cycling, a nonwater fracturing technology, has many advantages over hydraulic fracturing. In recent years, scholars have conducted a lot of researches on the effect of liquid nitrogen freeze-thaw cycles on the multiscale coal structure, mainly focusing on the effects of the liquid nitrogen freeze-thaw cycle on shallow coal. In view of this, using the NMR T_2 spectrum, NMRI, and SEM, this paper compares the evolution of multiscale structures in deep and shallow coal after different numbers of liquid nitrogen freeze-thaw cycles to reveal the multiscale structure evolution law of deep and shallow coal in liquid nitrogen freeze-thaw cycling.

2. Laboratory Experiments: Methodology and Procedures

2.1. Samples. The two samples used in the experiments were collected from Qinshui coalfield. The HL sample was collected from coal seam no. 15 in the Hengling block, and the SJZ sample was collected from coal seam no. 15 in the Sijiazhuang coal mine, with sampling depths of 1436 and 420 meters, respectively. The sample was prepared by wire-electrode cutting, as shown in Figure 1. The sample used in the liquid nitrogen freeze-thaw experiment is cylindrical, with a diameter of 25 mm and a length of 50 mm.

2.2. Multiscale Structure Evolution Experiment of Deep Coal under Liquid Nitrogen Freeze-Thaw Cycles

2.2.1. Principles of NMR. This paper mainly uses nuclear magnetic resonance imaging (NMRI) and NMR relaxation spectrum. The basic principle of NMRI is to apply the radio frequency pulse, layer selection gradient field, phase encoding gradient field, and frequency encoding gradient field to the test sample; then, the signal source in three dimensions is located through slice selection, phase encoding, and frequency encoding. The signal is then collected and decoded (Fourier transform). Finally, NMRI is achieved according to the relationship between the signal intensity and image gray value (pixels with larger signals are more bright, while those with smaller signals are less bright) [32, 33]. The NMRI flowchart is shown in Figure 2 [34].

The quantitative relationship between transverse relaxation time T_2 and pore radius r is mainly used to analyze the multiscale structure of coal in the NMR relaxation spectrum analysis [35, 36],

$$r = \rho F_s T_2, \quad (1)$$

where r is the pore radius, ρ is the surface transverse relaxation rate (m/s), and F_s is the shape factor; $F_s = 1, 2, 3$ for the pore shape of the slit, columnar, and spherical, respectively [37].

As shown in Equation (1), the larger the multiscale structure is, the longer the corresponding transverse relaxation time T_2 is.

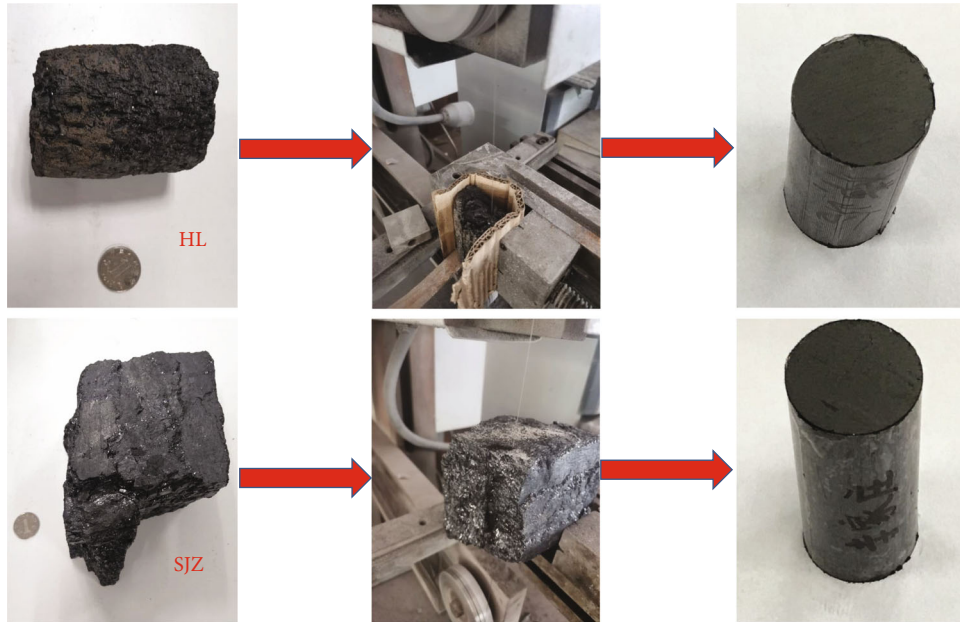


FIGURE 1: Coal sample wire-electrode cutting.

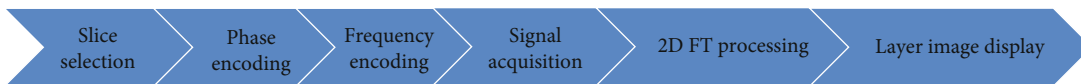


FIGURE 2: Flowchart of nuclear magnetic resonance imaging.



FIGURE 3: Drying oven for coal samples.

2.2.2. *Experimental Procedures.* The coal samples were dried at 60°C for 24 hours before liquid nitrogen freeze-thaw cycling. The drying oven is shown in Figure 3. The T_2 spectrum of the dried samples was used as the base signal. The SEM, porosity, and permeability tests were carried out before the freeze-thaw cycling. Then, vacuum-water saturation treatment was performed (12 hours). The vacuum-water saturation device is shown in Figure 4. The T_2 spectrum and NMRI tests were conducted under water satura-

tion, and then, the sample was dried (60°C for 24 hours). Next, the liquid nitrogen freeze-thaw cycles and related tests were carried out, using liquid nitrogen to freeze the sample for 1 hour. Figure 5 shows the liquid nitrogen freeze-thaw device and frozen samples. Then, the samples were melted at room temperature for 1 hour, and vacuum-water saturation treatment was carried out (12 hours) after every two liquid nitrogen freeze-thaw cycles. The T_2 spectrum test was performed under water saturation, and then, the samples



FIGURE 4: Vacuum-water saturation device.



FIGURE 5: Liquid nitrogen freeze-thaw device and frozen samples.

were dried at 60°C for 24 hours and the porosity and permeability tests were conducted. Finally, after 10 liquid nitrogen freeze-thaw cycles, NMRI and SEM imaging of the samples were implemented.

3. Results and Discussion

3.1. SEM Comparison before and after Freeze-Thaw Cycles. The deep and shallow coal samples were imaged before and after the freeze-thaw cycles using an EVO scanning electron microscope customized from Zeiss, to investigate the effect of freeze-thaw cycles on coal microstructure, as shown in Figure 6.

As can be seen in Figure 6, the expansion of fractures can be observed in the deep coal sample (HL), and the formation of new fractures can be observed in the shallow sample (SJZ), after the liquid nitrogen freeze-thaw cycles. Therefore, the influence of the freeze-thaw cycles on the microstructure evolution of deep and shallow coal mainly manifests the formation of new fractures and the expansion of original fractures, which verifies the improved connectivity between mesopores and macropores and the fracture (macropores in NMR tests) development found in subsequent NMR tests after the liquid nitrogen freeze-thaw cycles. Zhai et al. observed the formation of new fractures in coal by SEM after

freeze-thaw cycles [31]. Qin et al. also observed the expansion of fractures in coal by SEM after freeze-thaw cycles [28].

3.2. NMRI Comparison before and after Liquid Nitrogen Freeze-Thaw Cycles. In order to visually display the microstructure evolution of the deep and shallow coal before and after the freeze-thaw cycle, NMRI was carried out on the HL (deep) and SJZ (shallow) samples before and after 10 liquid nitrogen freeze-thaw cycles. The MesoMR23-60H medium-size NMRI analyzer developed by the Suzhou Niumag Analysis Instrument Corporation was used in this paper, as shown in Figure 7. In NMRI, the center frequency is 21.240 MHz, the echo time is 5.885 ms, the repetition time is 500 ms, the slice thickness is 25 mm, the stacking times is 16, the frequency code is 256, and the phase code is 192.

The NMRI results are shown in Figure 8. The bright spots represent the development of the pore structure in the NMRI images. The brighter and larger spots reflect the more developed pore structure [38]. Comparing the NMRI images of deep and shallow samples before and after the freeze-thaw cycle, it can be found that the pore structure of the shallow sample before cycling is better developed than that of the deep samples, and the variation in pore structure of the shallow sample is also more significant than that of the deep coal after liquid nitrogen freeze-thaw cycles, which

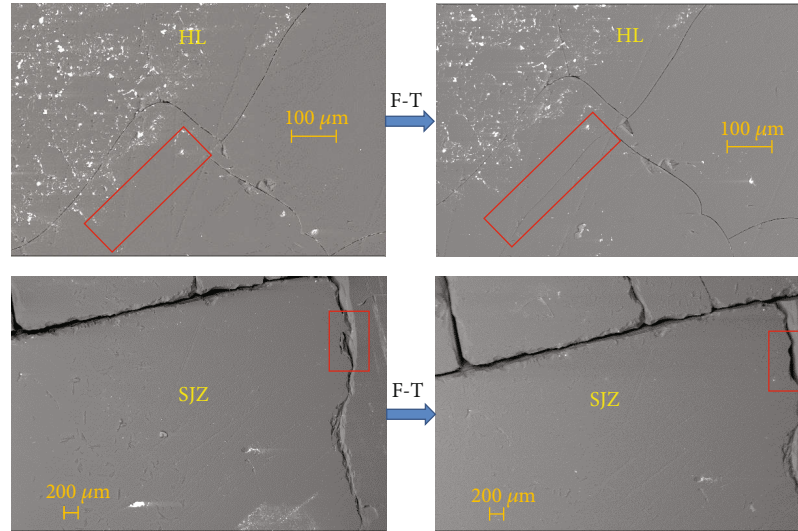


FIGURE 6: SEM images before and after freeze-thaw cycle.

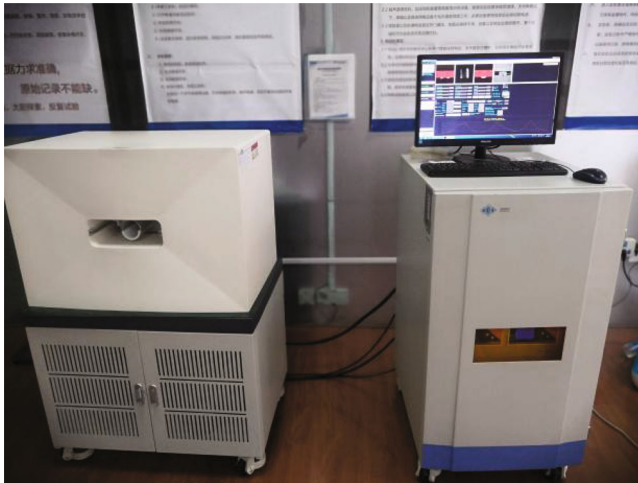


FIGURE 7: MesoMR23-60H medium-size NMRI analyzer.

can be seen from the initial porosity of the deep and shallow samples before the freeze-thaw cycle and the variation patterns of porosity during the freeze-thaw cycles (Figure 9).

3.3. Evolution Law of Multiscale Coal Structure during Liquid Nitrogen Freeze-Thaw Cycles. Considering that the NMR T_2 spectrum comprehensively can reflect the multiscale micropore, mesopore, and macropore structure characteristics, the NNM T_2 spectra of the deep (HL) and shallow (SJZ) samples were tested before freeze-thaw and after the 2nd, 4th, 6th, 8th, and 10th cycles. The MesoMR23-60H medium-size NMRI analyzer developed by Suzhou Niumag Analysis Instrument Corporation was also used in the NMR T_2 spectrum test. In the test, the main value of the RF signal frequency was 23 MHz, the RF signal frequency offset was 401587.9 Hz, the RF 90° pulse width was $10.00 \mu\text{s}$, and the RF 180° pulse width was $19.52 \mu\text{s}$; the signal frequency range and the sampling frequency received by the receiver during sampling were 250 kHz, the sampling repeat

interval was 3000 ms, the RF delay was 0.08 ms, the analog gain was 20, the digital gain was 3, the count of cumulative samples was 16, the preamplifier gain was 0, the number of echoes was 10000, and the echo time was 0.20 ms.

Figure 10 shows three peaks in the T_2 spectrum during liquid nitrogen freeze-thaw cycles for the HL and SJZ samples. Based on the relationship between pore size and relaxation time (Equation (1)), with the increase of relaxation time, the three peaks in the T_2 spectrum represent micropores, mesopores, and macropores, from left to right, respectively. From the evolution law of the T_2 spectrum in the process of liquid nitrogen freeze-thaw cycles, it can be found that with the increase of the number of freeze-thaw cycles, the peak areas corresponding to micropores, mesopores, and macropores increase. Namely, with the increase of the number of liquid nitrogen freeze-thaw cycles, the volumes of micropores, mesopores, and macropores increase, which can be verified by Figure 9 (variation law of porosity over freeze-thaw cycles). Also, the valleys between the peaks corresponding to mesopores and macropores gradually become less visible with more freeze-thaw cycles, which indicates that the connectivity between mesopores and macropores is gradually enhanced [38].

In order to investigate the individual evolution of micropores, mesopores, and macropores, the proportion of the peak areas corresponding to micropores, mesopores, and macropores in the total area of the three peaks after different cycle numbers is calculated over the process of liquid nitrogen freeze-thaw cycles, as shown in Figure 11.

It can be observed from Figure 11 that the proportion of micropores in the total pore volume decreases with the increase of freeze-thaw cycles, and the proportion of mesopores and macropores in the total pore volume increases. Compared to macropores, mesopores increase more obviously. Zhai et al. investigated the coal pore structure evolution under freeze-thaw cycles by NMR; they also observed that the proportion of micropores decreased and the proportion of mesopores and macropores increased [31].

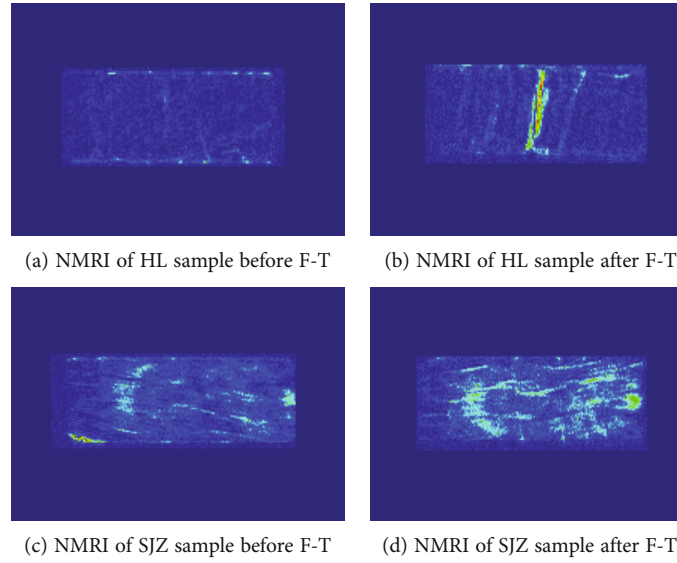


FIGURE 8: Comparison of NMRI before and after freeze-thaw cycle.

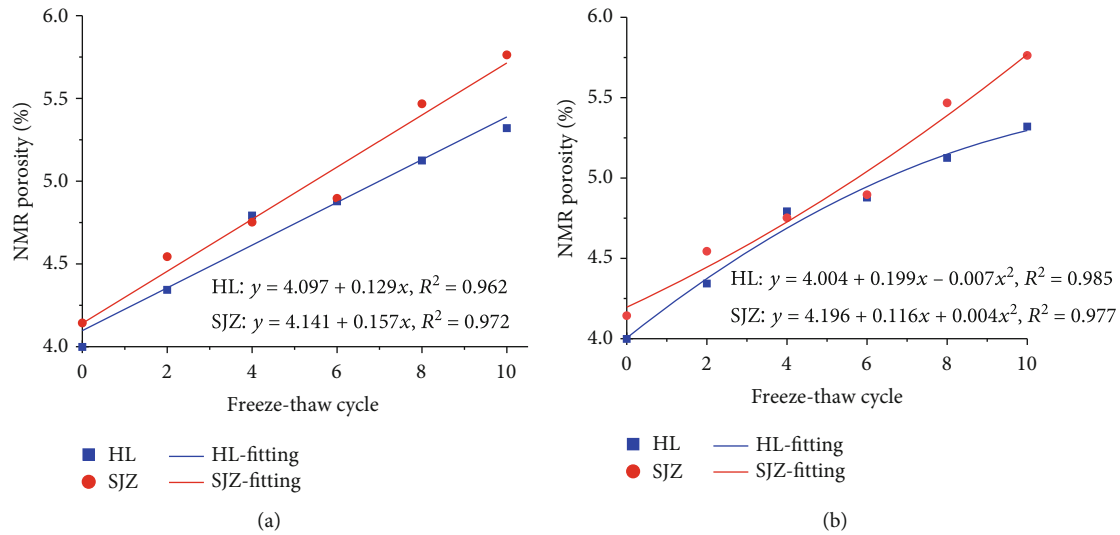


FIGURE 9: Evolution of the porosity measured by NMR during liquid nitrogen freeze-thaw cycle.

There is a linear relationship between NMR signal intensity and water mass in pore structure [39]. In view of this, this paper investigates the linear relationship between NMR signal intensity and water mass in the pore structure of the coal sample, as shown in Figure 12.

After obtaining the relationship between NMR signal intensity and water mass, the mass of water in the coal sample pore structure can be obtained by NMR signal intensity, from which the volume of the pore structure in the sample can be further obtained. Finally, the evolution law of NMR porosity with the number of freeze-thaw cycles was obtained, as shown in Figure 9.

Figure 9 indicates that the porosity of the deep (4.00%) sample before liquid nitrogen freeze-thaw cycling is less than that of the shallow (4.14%) sample. A linear positive correla-

tion exists between the porosity of both samples and the number of freeze-thaw cycles, and the growth rate of the deep coal sample is less than that of the shallow coal sample (Figure 9(a)). Qin et al. found that the coal with larger initial porosity has a larger porosity growth rate during freeze-thaw cycling [34]. In this study, the initial porosity in shallow coal is larger than that in deep coal, which can explain the growth rate of shallow coal being larger than that of deep coal. Sun et al. and Qin et al. found that there is a quadratic function relation between the porosity and the number of freeze-thaw cycles in shallow coal and shallow rock, respectively [25, 26]. Therefore, in this study, the relationship between the porosity and the number of freeze-thaw cycles was also fitted by the quadratic function (Figure 9(b)). It can be found that the quadratic function is better than the linear function

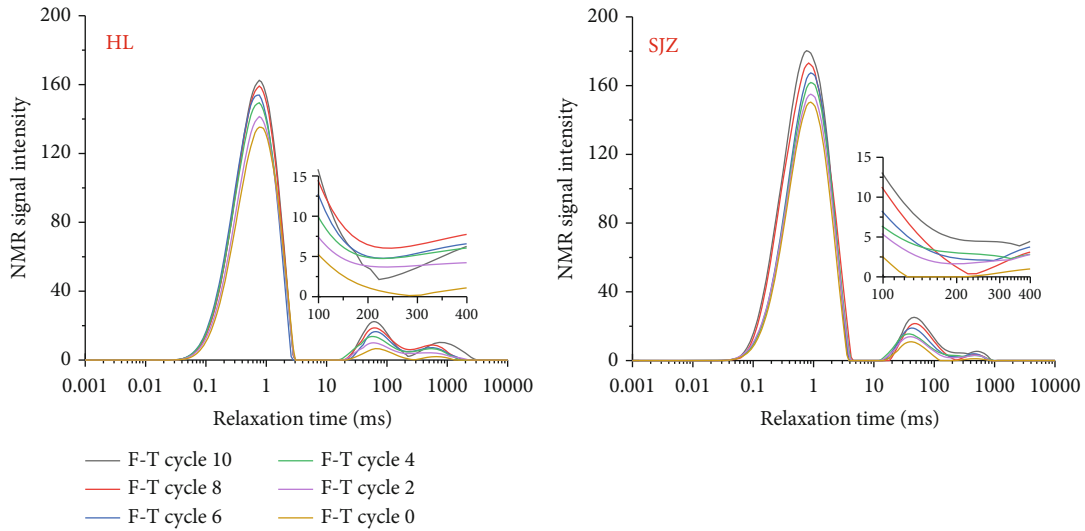


FIGURE 10: Evolution of NMR T_2 spectrum during liquid nitrogen freeze-thaw cycle.

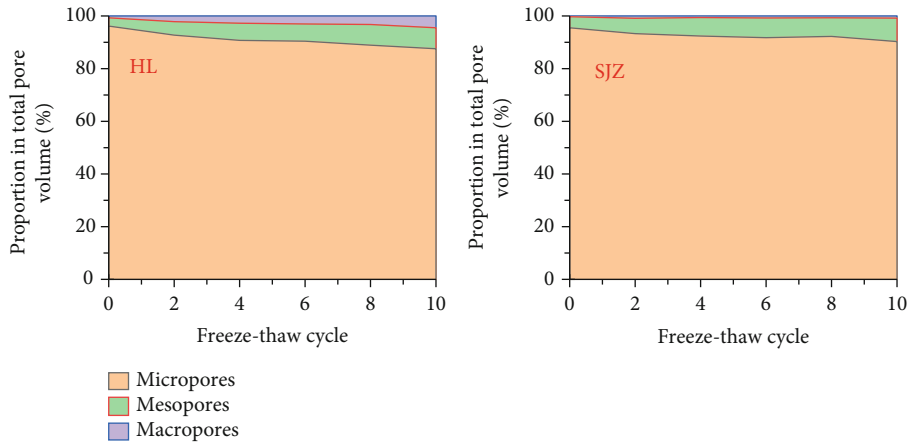


FIGURE 11: Evolution of pore structure at different scales during liquid nitrogen freeze-thaw cycles.

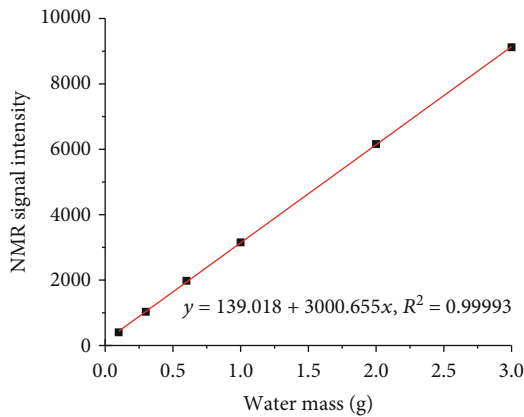


FIGURE 12: Relationship between NMR signal intensity and water mass.

in fitting the relation between the porosity and the number of freeze-thaw cycles in both deep and shallow coals. The coefficient of the quadratic term is positive in shallow coal,

while the coefficient of quadratic term is negative in deep coal, which indicates that the effect of increasing the freeze-thaw number on improving the structure is more significant in shallow coal than in deep coal. The difference between deep and shallow coals in response to freeze-thaw cycles may be also caused by the difference of rock mechanical properties. Li and Li found that the compressive strength, shear strength, and cohesion of rock increase with the increase of depth [40].

4. Conclusions

The multiscale structure evolution law of deep and shallow coal samples from the same seam in the Qinshui coalfield during the liquid nitrogen freeze-thaw cycles was investigated using the NMR T_2 spectrum, NMRI, and SEM. The following conclusions can be drawn:

- (1) The initial NMR porosity of deep coal is lower than that of shallow coal from the same coalfield and coal seam

- (2) The connectivity between mesopores and macropores in deep and shallow coal is both improved after liquid nitrogen freeze-thaw cycles, and the connectivity is gradually enhanced over freeze-thaw cycles
- (3) The influence of the liquid nitrogen freeze-thaw cycle on the structure evolution of deep and shallow coal is mainly the formation and expansion of microscopic fractures
- (4) During the liquid nitrogen freeze-thaw cycles, the volumes of micropores, mesopores, and macropores in deep and shallow coal increase. The proportion of micropores in the total pore structure volume decreases, and the proportion of mesopores and macropores in the total pore structure volume increases. Compared to macropores, the increase of the proportion of the mesopore volume in the total pore volume is more significant
- (5) The NMR porosity of both deep and shallow coal samples increases with the number of freeze-thaw cycles, and the NMR porosity growth rate of the deep sample is lower than that of the shallow sample

Data Availability

The experimental data used to support the findings of this study are included within the article.

Conflicts of Interest

The authors declare that they have no conflicts of interest.

Acknowledgments

The research is financially sponsored by the National Natural Science Foundation of China (Grant Nos. 52004293, U1910206, 51861145403, and 51874312); the Open Project Program of Key Laboratory of Deep Earth Science and Engineering (Sichuan University), Ministry of Education (No. DESE 202004); the Fundamental Research Funds for the Central Universities (No. FRF-TP-20-034A1); the China Postdoctoral Science Foundation (No. 2018M641526); and the Yue Qi Distinguished Scholar Project of the China University of Mining & Technology (Beijing).

References

- [1] S. Li, D. Z. Tang, H. Xu, and S. Tao, "Progress in geological researches on the deep coalbed methane reservoirs," *Earth Science Frontiers*, vol. 23, no. 3, pp. 10–16, 2016.
- [2] L. J. Zhao and Y. Qin, "Current status on deep coalbed methane in China," *China Coalbed Methane*, vol. 7, no. 2, pp. 38–40, 2010.
- [3] R. R. Tonnsen and J. L. Miskimins, "Simulation of deep coalbed methane permeability and production assuming variable pore volume compressibility," *Proceedings of Canadian Unconventional Resources and International Petroleum Conference*, Society of Petroleum Engineers, Calgary, Alberta, Canada, 2010.
- [4] D. D. Rice, "Composition and origins of coalbed gas," *AAPG Studies in Geology*, vol. 38, pp. 159–184, 1993.
- [5] R. C. Johnson and R. M. Flores, "Developmental geology of coalbed methane from shallow to deep in Rocky Mountain basins and in Cook Inlet-Matanuska basin, Alaska, U.S.A. and Canada," *International Journal of Coal Geology*, vol. 35, no. 1–4, pp. 241–282, 1998.
- [6] R. R. Tonnsen and J. L. Miskimin, "A conventional look at an unconventional reservoir: coalbed methane production potential in deep environments," in *Proceedings of AAPG Annual Convention and Exhibition*, New Orleans, Louisiana, 2010.
- [7] C. R. Nelson, "Deep coalbed gas plays in the U.S. rocky mountain region," in *Proceedings of AAPG Annual Meeting*, Salt Lake City, Utah, 2003.
- [8] C. B. Che, *Report on the New Round of National Oil and Gas Resource and Coalbed Methane Resource Evaluation Results*, Beijing, 2006.
- [9] C. H. Liu, J. Zhu, C. B. Che, H. L. Yang, and M. Z. Fan, "Methodologies and results of the latest assessment of coalbed methane resources in China," *Natural Gas Industry*, vol. 29, no. 11, pp. 130–132, 2009.
- [10] Y. T. Wang and W. F. Lan, "Origin of hydrocarbons and its exploration in Cainan oilfield," *Xinjiang Petroleum Geology*, vol. 15, no. 1, pp. 30–36, 1994.
- [11] S. H. Cui, H. L. Liu, B. Wang, N. Ning, and S. X. Sang, "Trapping characteristics of coalbed methane in low-rank coal of Zhungaer basin," *Geoscience*, vol. 21, no. 4, pp. 719–724, 2007.
- [12] H. L. Qin, H. F. Yao, X. B. Jia, P. F. Li, and Y. J. Meng, "Pore and fissure characteristics of deep coal reservoir based on NMR," *Coal Technology*, vol. 38, no. 8, pp. 55–89, 2019.
- [13] X. D. Gao, *Study on porosity and permeability evolution mechanism and fracturing reconstruction feasibility of deep coal reservoirs in Linxing area*, China university of Mining and Technology-Beijing, 2019.
- [14] Q. L. Xu, W. H. Huang, S. H. Tang et al., "Pore structure and adsorption of deep medium-high rank coal reservoirs," *Geoscience*, vol. 30, no. 2, pp. 413–419, 2016.
- [15] X. X. Lu, *The reservoir characteristics of deep coal seam in Southern Qinshui basin*, China university of Geosciences-Beijing, 2013.
- [16] X. X. L. W. H. Huang, Y. P. Chen, S. R. Zhang, J. Wu, and Y. Y. Xu, "Pore structure of deep coal seam in southern Qinshui basin," *Journal of Northeast Petroleum University*, vol. 39, no. 3, pp. 41–49, 2015.
- [17] G. Q. Zheng, D. F. Yang, and X. L. Zhou, "Comparative study on reservoir properties of deep and shallow coal seams in Qinshui basin," *Coal Technology*, vol. 37, no. 3, pp. 108–110, 2018.
- [18] H. X. Liang, P. Chen, L. H. Tong, and C. H. Lu, "Pore characteristics of deep part coal and significance in Huainan coalfield," *Coal Geology of China*, vol. 22, no. 6, pp. 5–8, 2010.
- [19] M. Zhang, *The variation law of deep coal measure gas reservoirs physical properties with the increase of temperature and pressure*, China university of Mining and Technology, 2019.
- [20] X. Y. Wen, X. Y. Yi, Y. Lu, B. S. Guan, L. Liang, and P. Liu, "Evaluation and primary exploration of damage experiment of coal rock permeability caused by different fracture fluid," *Petrochemical Industry Application*, vol. 30, no. 3, pp. 12–15, 2011.

- [21] K. Zhu, "Impact of shale gas hydraulic fracturing development on environment," *China Petroleum and Chemical Standard and Quality*, vol. 36, no. 22, pp. 57–78, 2016.
- [22] C. Z. Cai, F. Gao, G. S. Li, Z. W. Huang, and P. Hou, "Evaluation of coal damage and cracking characteristics due to liquid nitrogen cooling on the basis of the energy evolution laws," *Journal of Natural Gas Science and Engineering*, vol. 29, pp. 30–36, 2016.
- [23] C. Zhai, L. Qin, S. M. Liu, J. Z. Xu, Z. Q. Tang, and S. L. Wu, "Pore structure in coal: pore evolution after cryogenic freezing with cyclic liquid nitrogen injection and its implication on coalbed methane extraction," *Energy & Fuels*, vol. 30, no. 7, pp. 6009–6020, 2016.
- [24] L. Qin, *Pore evolution after fracturing with cyclic liquid nitrogen and the mechanism of permeability enhancing*, China university of Mining and Technology, 2018.
- [25] L. Qin, C. Zhai, S. M. Liu, J. Z. Xu, G. Q. Yu, and Y. Sun, "Changes in the petrophysical properties of coal subjected to liquid nitrogen freeze-thaw - a nuclear magnetic resonance investigation," *Fuel*, vol. 194, pp. 102–114, 2017.
- [26] Y. Sun, C. Zhai, J. Z. Xu, Y. Z. Cong, L. Qin, and C. Zhao, "Characterisation and evolution of the full size range of pores and fractures in rocks under freeze-thaw conditions using nuclear magnetic resonance and three-dimensional X-ray microscopy," *Engineering Geology*, vol. 271, 2020.
- [27] L. Qin, S. G. Li, Z. Cheng et al., "Changes in the pore structure of lignite after repeated cycles of liquid nitrogen freezing as determined by nitrogen adsorption and mercury intrusion," *Fuel*, vol. 267, pp. 117214–117214, 2020.
- [28] L. Qin, C. Zhai, J. Z. Xu, S. M. Liu, C. Zhong, and G. Q. Yu, "Evolution of the pore structure in coal subjected to freeze-thaw using liquid nitrogen to enhance coalbed methane extraction," *Journal of Petroleum Science and Engineering*, vol. 175, pp. 129–139, 2019.
- [29] D. C. Yan, *Experimental study on the effects of liquid nitrogen freezing and thawing damage in coal with different water content*, China university of Mining and Technology, 2019.
- [30] Y. Sun, C. Zhai, L. Qin, J. Z. Xu, and G. Q. Yu, "Coal pore characteristics at different freezing temperatures under conditions of freezing-thawing cycles," *Environmental Earth Sciences*, vol. 77, p. 525, 2018.
- [31] C. Zhai, S. L. Wu, S. M. Liu, L. Qin, and J. Z. Xu, "Experimental study on coal pore structure deterioration under freeze-thaw cycles," *Environmental Earth Sciences*, vol. 76, no. 15, p. 507, 2017.
- [32] P. C. Lauterbur, "Image formation by induced local interactions: examples employing nuclear magnetic resonance," *Nature*, vol. 242, no. 5394, pp. 190–191, 1973.
- [33] M. R. Mitchell, R. W. Tarr, T. E. Conturo, C. L. Partain, and A. E. James, "Spin echo technique selection: basic principles for choosing MRI pulse sequence timing intervals," *Radio-graphics*, vol. 6, no. 2, pp. 245–260, 1986.
- [34] Suzhou Niumag Analytical Instrument Corporation, "Nuclear magnetic resonance imaging MRI-introduction to the principle of nuclear magnetic resonance imaging," <https://www.niumag.com/he-ci-gong-zhen-cheng-xiang-mri-he-ci-gong-zhen-cheng-xiang.html>, 2016.
- [35] W. Kenyon, "Nuclear magnetic resonance as a petrophysical measurement," *Nuclear Geophysics*, vol. 6, no. 2, pp. 153–171, 1992.
- [36] S. Li, D. Tang, Z. Pan, H. Xu, and W. Huang, "Characterization of the stress sensitivity of pores for different rank coals by nuclear magnetic resonance," *Fuel*, vol. 111, pp. 746–754, 2013.
- [37] W. Looyestijin and J. Hofman, "Wettability-index determination by nuclear magnetic resonance," *SPE Reservoir Evaluation and Engineering*, vol. 9, no. 2, pp. 146–153, 2006.
- [38] S. Li, M. K. Luo, C. J. Fan, H. J. Bi, and Y. P. Ren, "Quantitative characterization of the effect of acidification in coals by NMR and low-temperature nitrogen adsorption," *Journal of China Coal Society*, vol. 42, no. 7, pp. 1748–1756, 2017.
- [39] Y. X. Zhao, Y. F. Sun, S. M. Liu, K. Wang, and Y. D. Jiang, "Pore structure characterization of coal by NMR cryoporometry," *Fuel*, vol. 190, pp. 359–369, 2017.
- [40] J. R. Li and H. B. Li, "Experimental study on mechanical properties of rocks with different depths," *Chinese Journal of Rock Mechanics and Engineering*, vol. 21, no. S1, pp. 948–951, 2001.

Research Article

Study on the Catastrophic Evolution of Tianshan Road Slope under the Freeze-Thaw Cycles

Luqi Wang , Yibing Zhang, Jian Guo, Qiang Ou, Songlin Liu, and Lin Wang 

School of Civil Engineering, Chongqing University, Chongqing 400045, China

Correspondence should be addressed to Lin Wang; sdxywanglin@cqu.edu.cn

Received 24 August 2021; Accepted 7 September 2021; Published 4 October 2021

Academic Editor: Yu Wang

Copyright © 2021 Luqi Wang et al. This is an open access article distributed under the Creative Commons Attribution License, which permits unrestricted use, distribution, and reproduction in any medium, provided the original work is properly cited.

The maximum temperature difference of Tianshan Road can reach 77.4°C in a year. Under such complex mechanical environment, the mechanical properties of rock mass and structural planes will change significantly as the increase of freeze-thaw cycles (FTC). Consequently, the FTC has become a key factor in the instability and failure of rocky slopes along the Tianshan Road. In this paper, the progressive deformation of rocky slopes and sudden failure process after critical instability were studied through the FTC tests of rock mass and structural planes, discrete element method, and theoretical analysis. The results show that the structural planes and internal microcracks of the rock mass expand under the action of the FTC, causing a gradual decrease in the stability of the slope. The dynamic collapse of the rocky slope has a certain degree of randomness caused by the spatial distribution of structural planes and the interaction between the rock fragments. Due to the limitation of the slipping space and the tilt angle of the trailing edge of the slope, long-distance migration did not occur, and the in situ accumulation of the slope was obvious after failure. The analysis method in this paper can provide an important reference for guiding the catastrophe mechanism analysis and protection of engineering slopes in cold regions.

1. Introduction

The Tianshan Mountains are composed of more than 20 parallel high-steep mountains [1]. As a result, many high-altitude areas do not melt all year round [2]. The Tianshan Road is a major traffic artery that traverses the northern, central, and southern parts of the Tianshan Mountains and connects southern Xinjiang with northern Xinjiang. Therefore, its geographic location is very important ([3]; Figure 1).

The Tianshan Road has a total length of 537 km, most of which is through the alpine mountains above 2000 m, and the geological conditions of the entire line are extremely complicated. It starts at Dushanzi and ends at Kuche; the eastern part is connected to the Bayinbulak grassland, and the western part is connected to the Tangbula grassland. Specifically, it passed through Bingdaban at an altitude of more than 4000 m three times. The Tianshan Road has almost all the geological disasters that can occur on the world's highways, such as collapses, landslides, mudslides, frozen soil, and avalanches.

The study area can be characteristic of complex lithological changes, high-steep slopes, intense unloading, and multiple cracks. Furthermore, the mechanical characteristics of rocky slope change significantly as the increase of the freeze-thaw cycles (FTC), which has become the dominant factor of rocky slope failure [4]. Once the deformation and instability of road slope occur, the operation of highway engineering will be seriously affected. As for these mechanical environments, indoor rock mechanics tests [5, 6], similar model tests [7], numerical simulations [8, 9], in situ monitoring [10, 11], and failure mechanisms [12–14] are used to study the evolution trend of rock mass. However, there are still significant gaps between the existing research methods and the research motivation to effectively reveal the catastrophic evolution of rocky slopes under the FTC, especially in the changing mechanical state and the collapse process after the critical state.

A typical rocky slope along the Tianshan Road was taken as a research object in this paper. Its progressive deformation and sudden failure process were studied through the

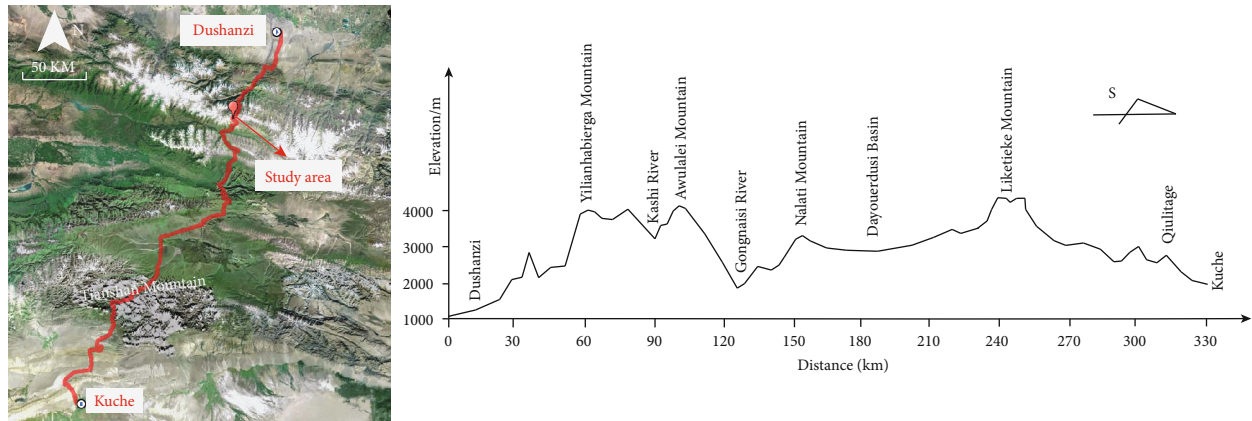


FIGURE 1: General situation of the Tianshan Road.

FTC test results of rock mass and structural planes, discrete element methods (DEM), and theoretical analysis. These analysis methods can provide important references for guiding the evolution trend and protection of engineering slopes in cold regions.

2. Study Area

Through the comparative analysis of the high- and low-temperature climate along the Tianshan Road, it can be found that the maximum temperature difference between day and night can reach about 45°C . And the maximum temperature difference in different seasons of the year can reach 77.4°C , of which the extreme maximum temperature is 41.8°C in the Wusu section in the northern part of the study area, and the extreme minimum temperature is -48.1°C in the Bayinbulak area. Due to intense ultraviolet radiation, the surface temperature of the rocky slope is about 12°C higher than the expected temperature. Under this extreme climate, the rocky slopes are affected by the high temperature stress, ice cleavage force, and frost heave and thawing shrinkage [15].

In the study area, the terrain is higher in the west and lower in the east, and the altitude is between 2000 m and 5000 m. Caused by the subduction and compression of the Indian plate to the Eurasian plate, the topography of the mountain crisscross basin is formed. Meanwhile, many glaciers are developed in high-altitude areas along the Tianshan Road. And due to the deep cutting of the valleys, the terrain is undulating, and the natural conditions are harsh.

3. Engineering Geologic Conditions

3.1. Topography. The study area is the alpine valley of the North Tianshan Mountains, specifically on the southern slope of Hashelekandaban. The slope height is about 25~30 m, and the average slope is about 75° . This section is convex and developed in the conglomerate. The leading edge of the slope is the Kuitun River that is about 10~15 m wide and about 80 m away from the road.

3.2. Formation Lithology and Geological Structures. The stratigraphy of the study area is relatively simple, mainly

outcropping the Quaternary and the Middle Carboniferous strata. Among them, the Quaternary deposits are distributed above the Kuitun River. It is a mainly fragmented conglomerate with a particle size of 5~15 cm. The Carboniferous Middle System belongs to the Bayingou Formation in the Yilianhaergabishan district, and the lithology is sandstone. A small fault, about 1 km south of the study area, is derived from a regional structure.

3.3. Earthquake and Neotectonic Movement. The study area is located near the North Tianshan seismic belt, which spreads in the east-west direction, starting from the east of Barkol and extending westward to the piedmont of the North Tianshan Mountains. The thrust-wrinkle active zone in this area is related to earthquakes. And the earthquake occurrence scope is distributed in an elliptical shape, with features of low occurrence frequency, high intensity, and concentrated time distribution.

3.4. Hydrogeological Conditions. The formation, occurrence, and migration of groundwater are dominated by climatic conditions, topography, stratum lithology, and geological structure. Rainfall and glacier snowmelt are the main supplies of groundwater. Groundwater discharges to rivers through runoff from structure zones or fracture zones. The annual rainfall in the area ranges from 250 mm to 500 mm. Except for a small amount of evaporation, the rest rainfall is supplied to groundwater and rivers. Fracture water of detrital rocks is the main type of groundwater. Meanwhile, the tuffaceous sandstone is the main aquifer.

3.5. Climate. Through analysis of weather station data in the study area, the extreme cold weather in winter occurs in January, with an average temperature of -9.0°C . The maximum thickness of snow can reach 60~150 cm, and the maximum melting thickness of seasonally frozen soil is 80 cm. The study area suffers the most severe snow damage in winter along the Tianshan Road. Meanwhile, the extreme high-temperature weather of summer occurs in July, with an average temperature of 22.0°C . The annual precipitation ranges from 250 mm to 500 mm. The spring and summer are the seasons with heavy rains, accounting for 65 to 80% of the annual precipitation.

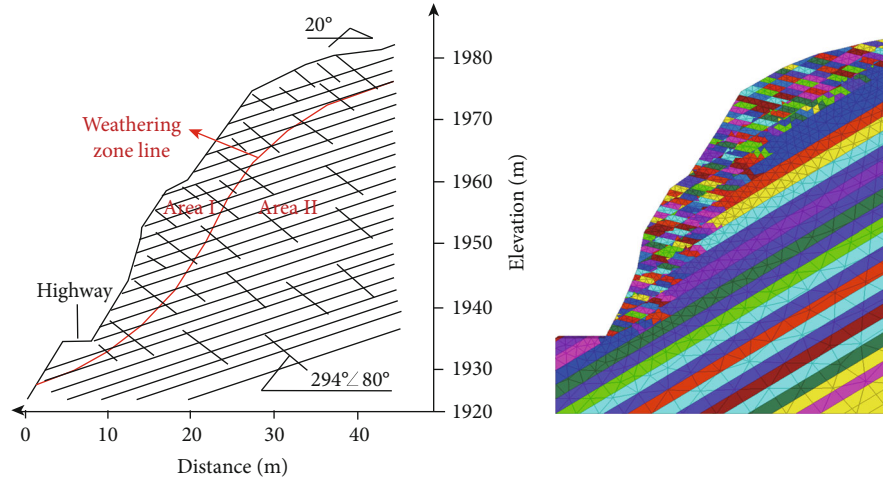


FIGURE 2: The typical section applied in numerical calculations.

TABLE 1: Parameters of materials in freeze-thaw area (area I).

Material	Parameters	Time of the freeze-thaw cycles			
		0	15	30	50
Rock mass	Density (kg/m^3)	2600	2626	2678	2704
	Volume modulus (GPa)	5.9	3.1	2.8	2.6
	Shear modulus (GPa)	5.1	2.9	2.6	2.4
	Cohesion (MPa)	6.2	5.3	4.7	4.2
	Internal friction angle ($^\circ$)	48	41	36	32
	Tensile strength (MPa)	3.2	2.7	2.4	2.2
Layer	Normal stiffness (GPa)	13.2	12.6	12.2	11.9
	Shear stiffness (GPa)	11.6	11.0	10.6	10.3
	Cohesion (kPa)	86	56	50	43
	Internal friction angle ($^\circ$)	42	38	35	34
Structural planes	Normal stiffness (GPa)	11.3	10.7	10.3	10.0
	Shear stiffness (GPa)	0.94	0.88	0.84	0.81
	Cohesion (kPa)	82	53	47	41
	Internal friction angle ($^\circ$)	40	36	33	31

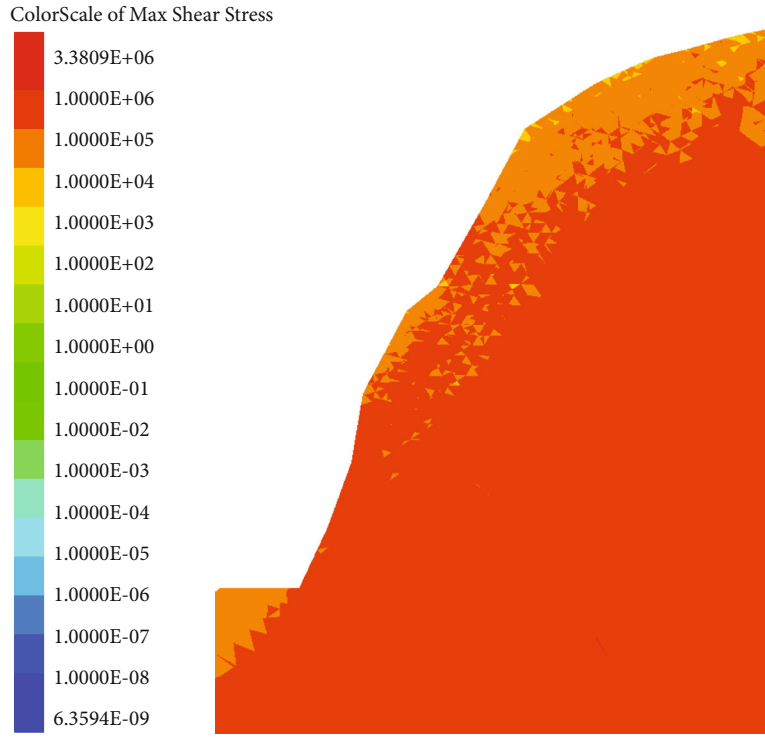
TABLE 2: Parameters of materials in nonfreeze-thaw area (area II).

Parameters	Density (kg/m^3)	Volume modulus (GPa)	Shear modulus (GPa)	Cohesion (kPa)	Internal friction angle ($^\circ$)	Tensile strength (MPa)
Rock mass	2750	6.2	5.4	7.6	52	3.9
Parameters	Normal stiffness (GPa)	Shear stiffness (GPa)	Cohesion (kPa)	Internal friction angle ($^\circ$)	Tensile strength (MPa)	/
Layer	18.2	13.6	180	45	1.2	/
Structural planes	16.4	11.3	160	42	0.8	/

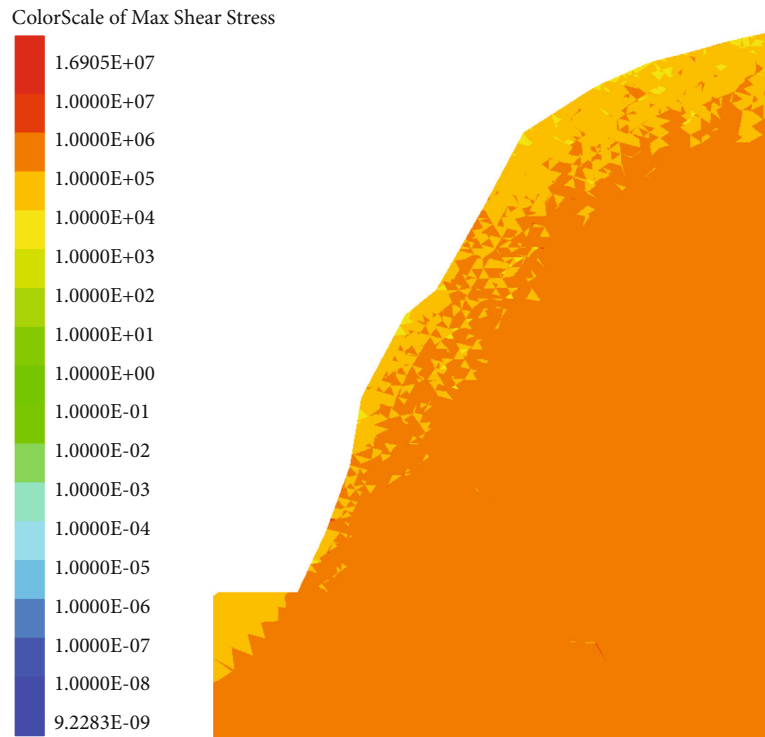
4. Structure and Stability Factors of the Typical Slope

The rock stratum ($180^\circ \angle 35^\circ$) of the typical slope is the medium-thick layered sandstone. The primary structural planes ($294^\circ \angle 80^\circ$) have a spacing of about 1 m, an opening

of 5 mm, straight and smooth, no fillings, and an extension length over 10 m. The rock mass is divided into approximately $1 \text{ m} \times 1 \text{ m} \times 0.5 \text{ m}$, and the linear fissure rate is 55.1%. The shape of the slope is convex, without the influence of groundwater. Due to the excavation and blasting caused the unloading and rebound of the rock mass, this

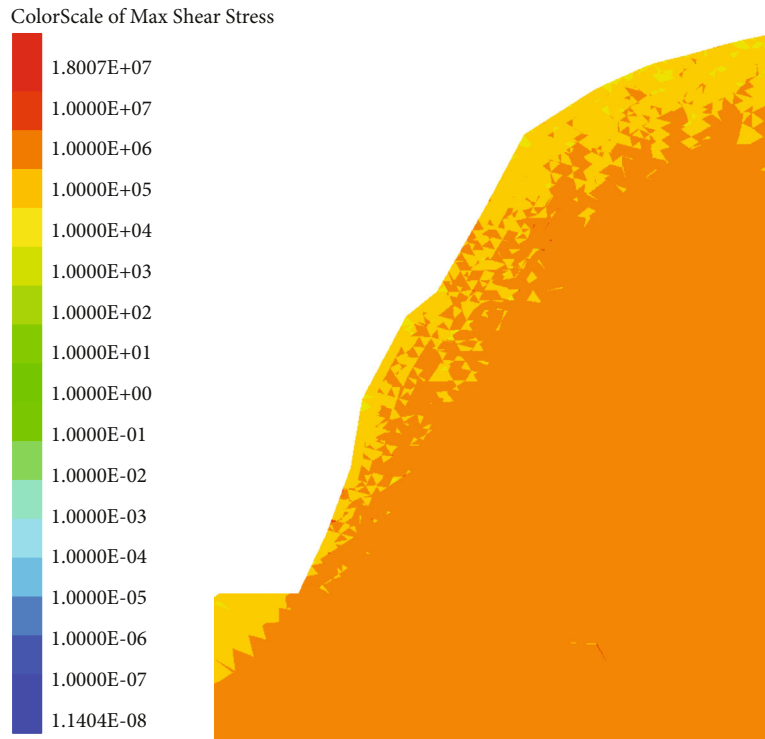


(a) 0 times

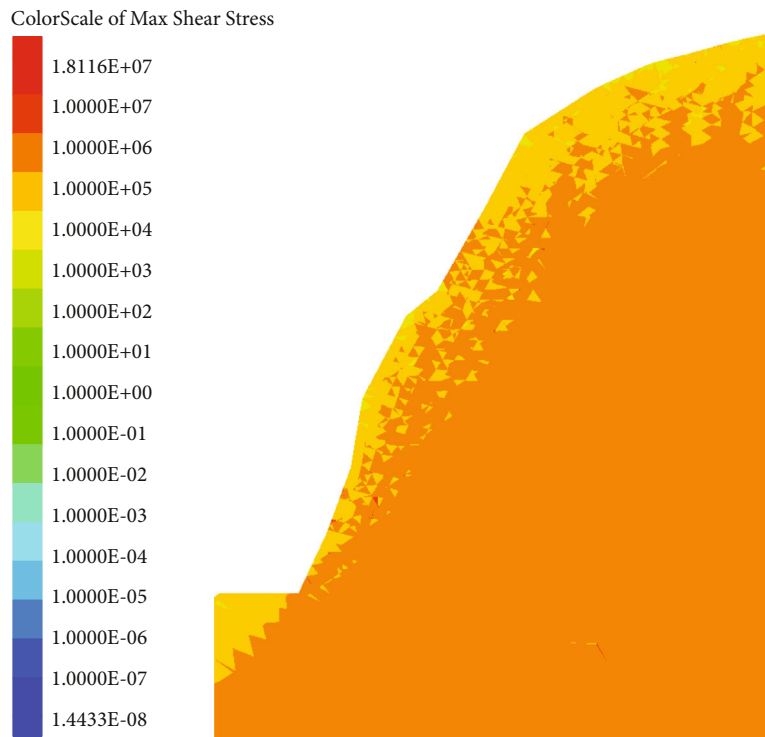


(b) 15 times

FIGURE 3: Continued.



(c) 30 times



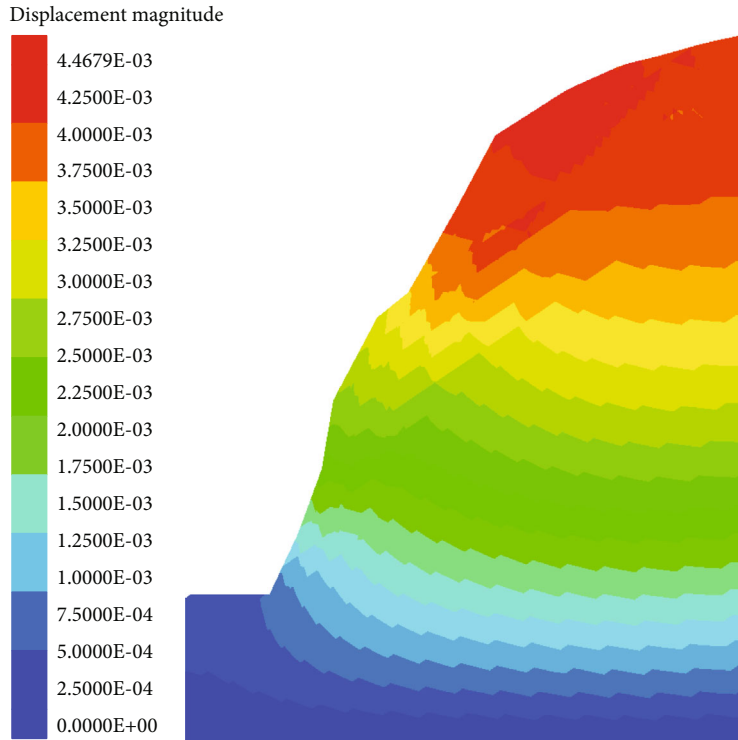
(d) 50 times

FIGURE 3: Max-shear stress distribution of the typical rocky slope.

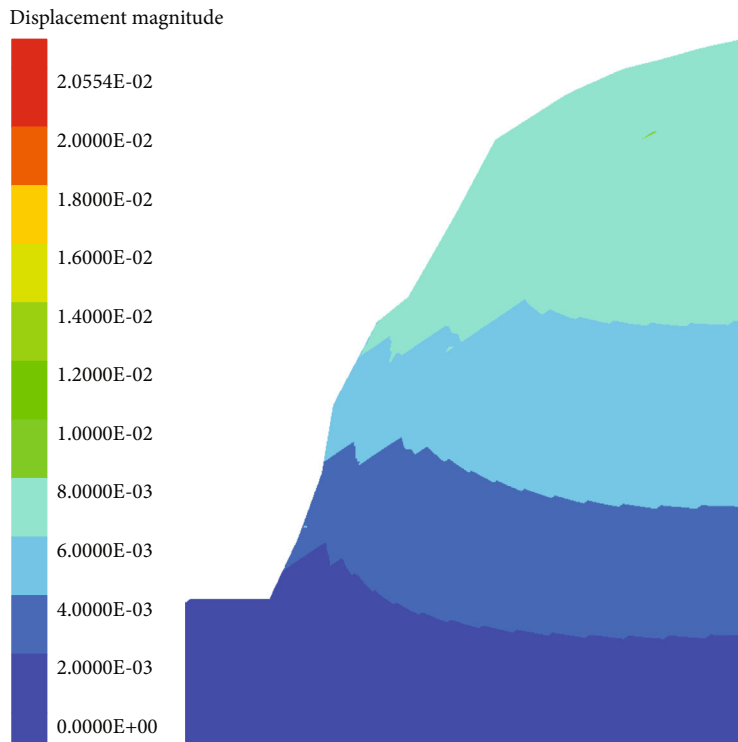
section of the Tianshan Road has fallen blocks year-round. The weathering thickness of the slope is about 10 m. The dominant structural planes make the rock mass more fragmented with a block-to-fragmental structure. With the combination of discontinuities and the free face, it is prone to

slide along the structural planes under the self-weight and external dynamics.

The freezing conditions are the main external forces for the slope failure. The study area is in snowy weather from January to March. In this case, the rainfall and glacier snow



(a) 0 times



(b) 15 times

FIGURE 4: Continued.

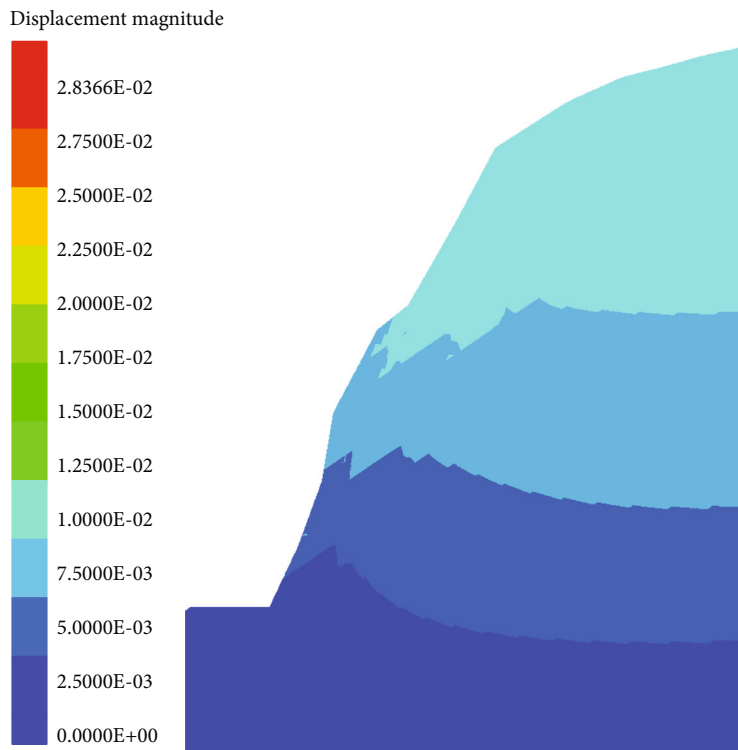
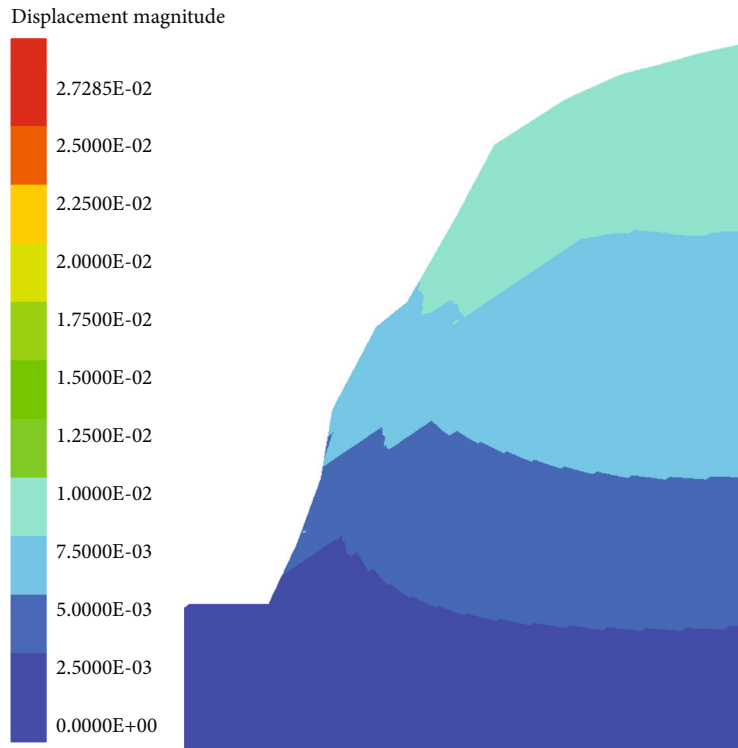


FIGURE 4: Displacement distribution of the typical rocky slope.

melting make water enter the joints network of the rocky slope, which freeze into ice in winter, expand the volume, generate ice splitting force, and push the rock mass. Meanwhile, the rock mass is subjected to the FTC of seasonal

reciprocation and the temperature difference between day and night, causing the cracks to expand and the mechanical properties of the rock mass to reduce. Taking one year as a period, the deformation of the rock mass gradually increases.

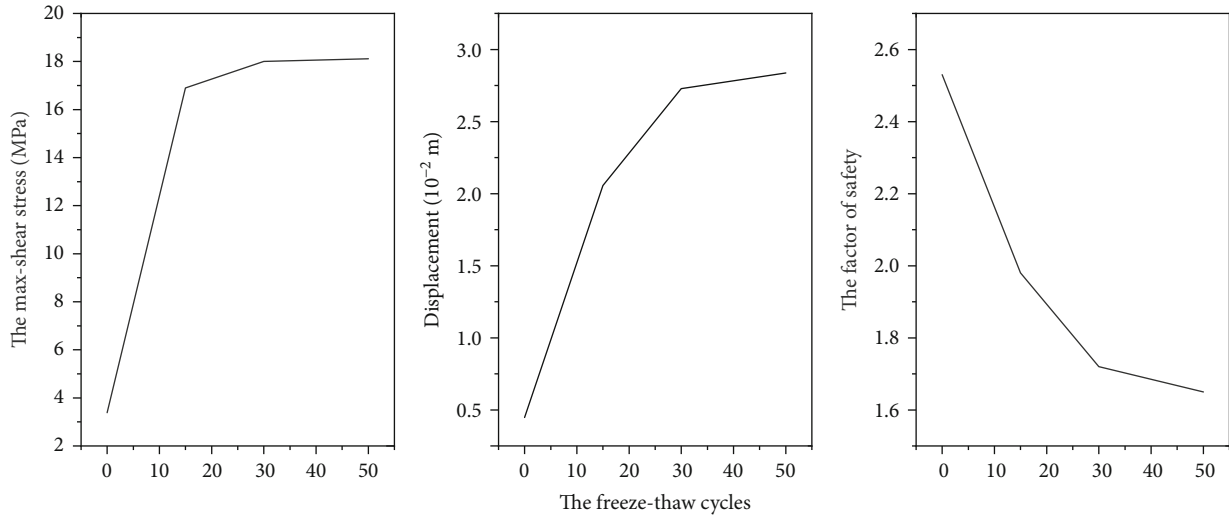


FIGURE 5: The mechanic features of the typical rocky slope under different FTC.

In summary, the failure mechanism of the rocky slope can be determined to the excavation of highway makes the leading-edge to form the slipping space, and the layer of the down-dip slope is cut by the antidip structural planes to form dangerous rock mass. Then, under the action of the internal and external forces, the sliding-cracking deformation is generated. After instability, it slips to the free face, causing a typical sliding-type collapse.

5. Methods

Based on the field investigation, 3DEC is used to simulate the large deformations of block systems [16, 17]. The typical section was divided into two areas ([3, 18]; Figure 2). The mechanical parameters of rock mass and structural planes in area I are changing with the FTC. And area II is defined as the nonfreeze-thaw-affected zone. In 3DEC, the blocks and the structural planes are set to the Mohr-Coulomb model. The mechanical parameters of the rocks and structural planes in each area are comprehensively selected through field survey and indoor test results ([19]; Tables 1 and 2).

After the parameters assignments of all the blocks and structural planes, the fixed velocity boundary conditions and load conditions are applied to the numerical model. The left, right, and bottom boundaries of the model are fixed, and the upper part of the model has a free boundary. The times of FTC are taken as the driven parameter, and the self-weight is considered in the load process. When the maximum unbalanced force of the node approaches zero or is relatively small compared with the total force initially applied, the model is taken as a state of equilibrium.

6. Results

The analysis of 0 times, 15 times, 30 times, and 50 times of FTC is simulated for the typical rocky slope. And the distri-

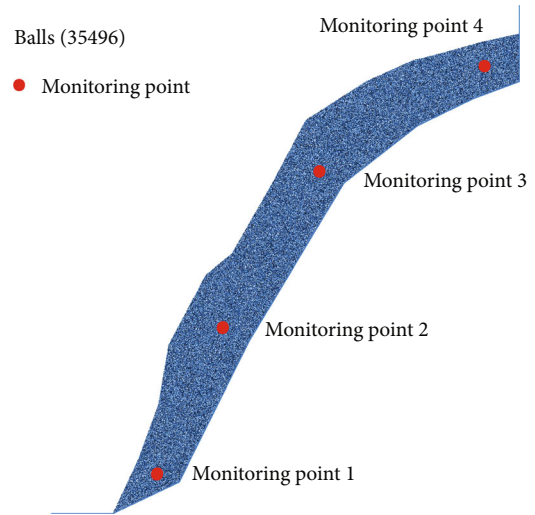


FIGURE 6: A dynamic simulation model of the typical rocky slope.

bution of max-shear stress (Figure 3) and displacement (Figure 4) is obtained.

After 15 times of the FTC, a stress concentration zone appeared along the structural planes in the freeze-thaw affected area. With the increase of FTC, the concentration distribution of the max-shear stress in the freeze-thaw affected area gradually expands. After 50 times of the FTC, a slipping zone is formed and basically penetrated.

Under the action of the FTC, the maximum displacement of the slope has increased from 4.468 mm to 20.554 mm after 15 times of the FTC. After the 50 times of the FTC, the maximum displacement increased to 28.366 mm, and the factor of safety was reduced from 2.56 to 1.64, which shows that the deformation of the slope will increase and the stability of the slope will decrease.

From the perspective of stability trend (Figure 5), the factor of safety decreases sharply under 0~15 times of the

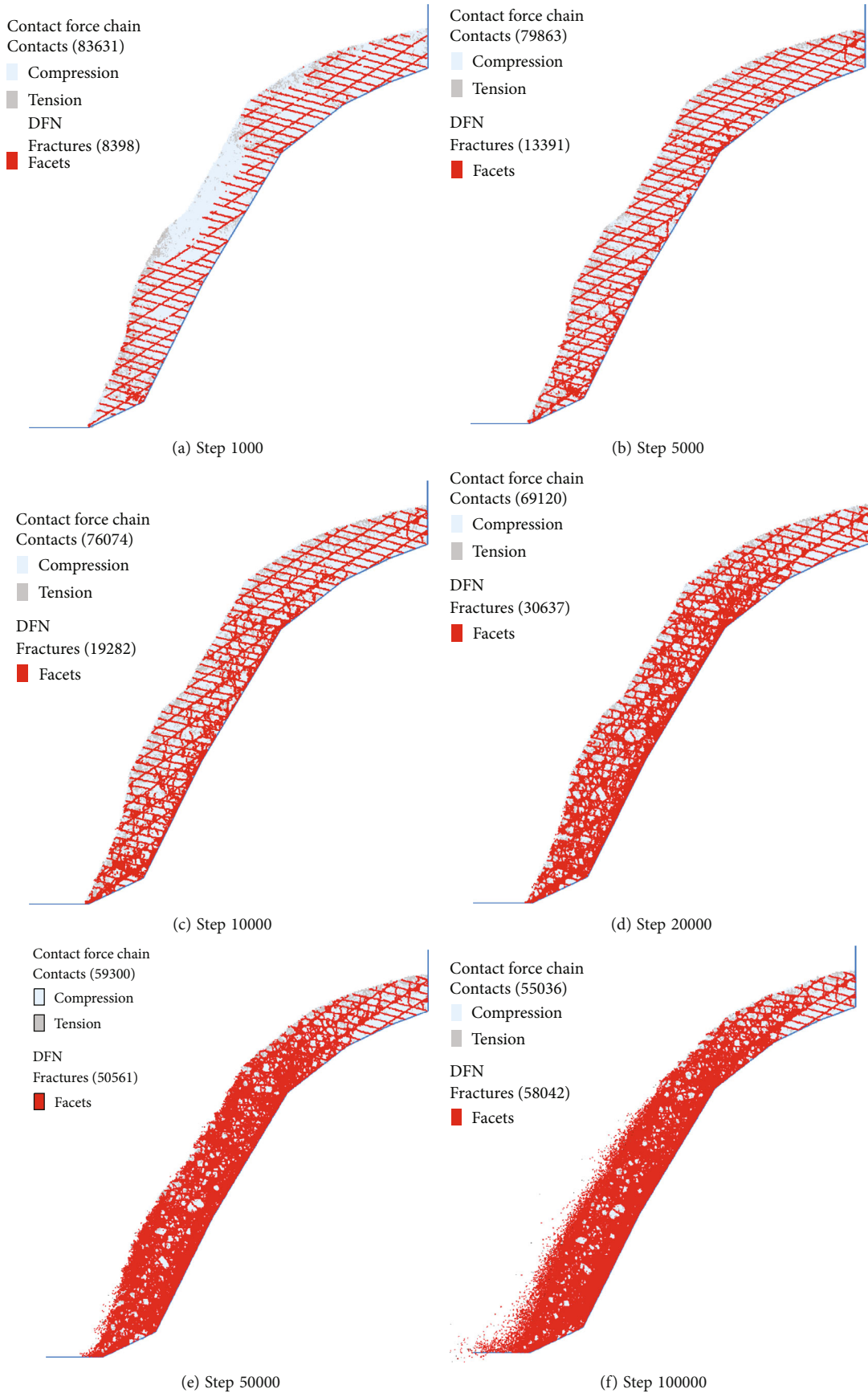


FIGURE 7: Continued.

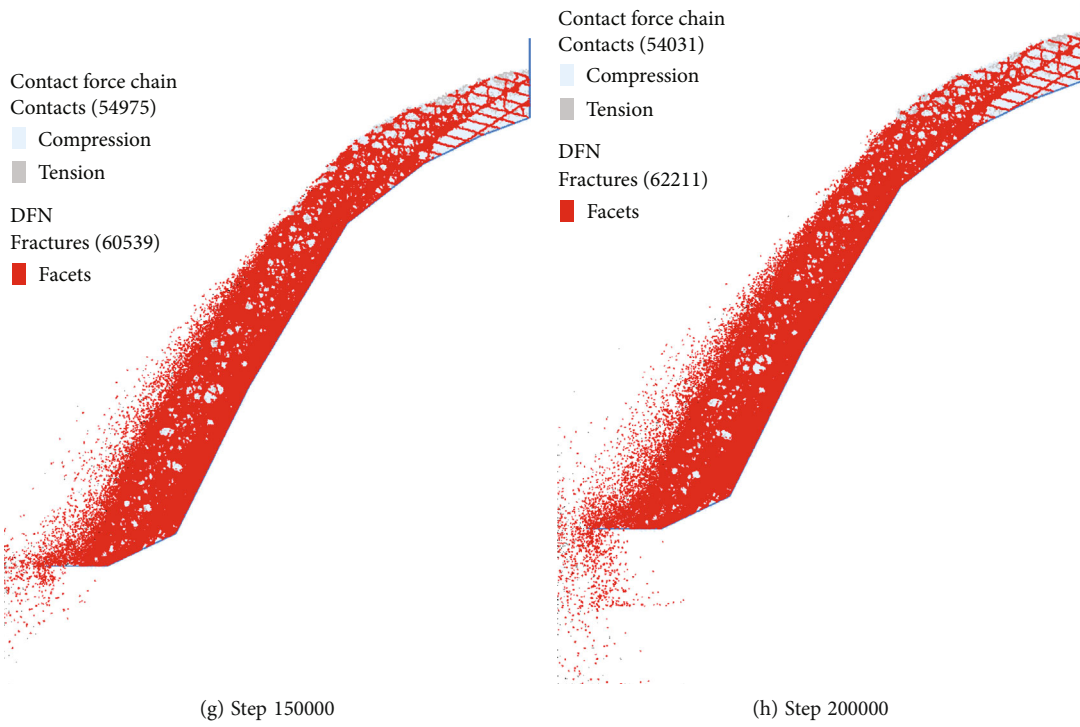


FIGURE 7: The dynamic collapse process of the typical section.

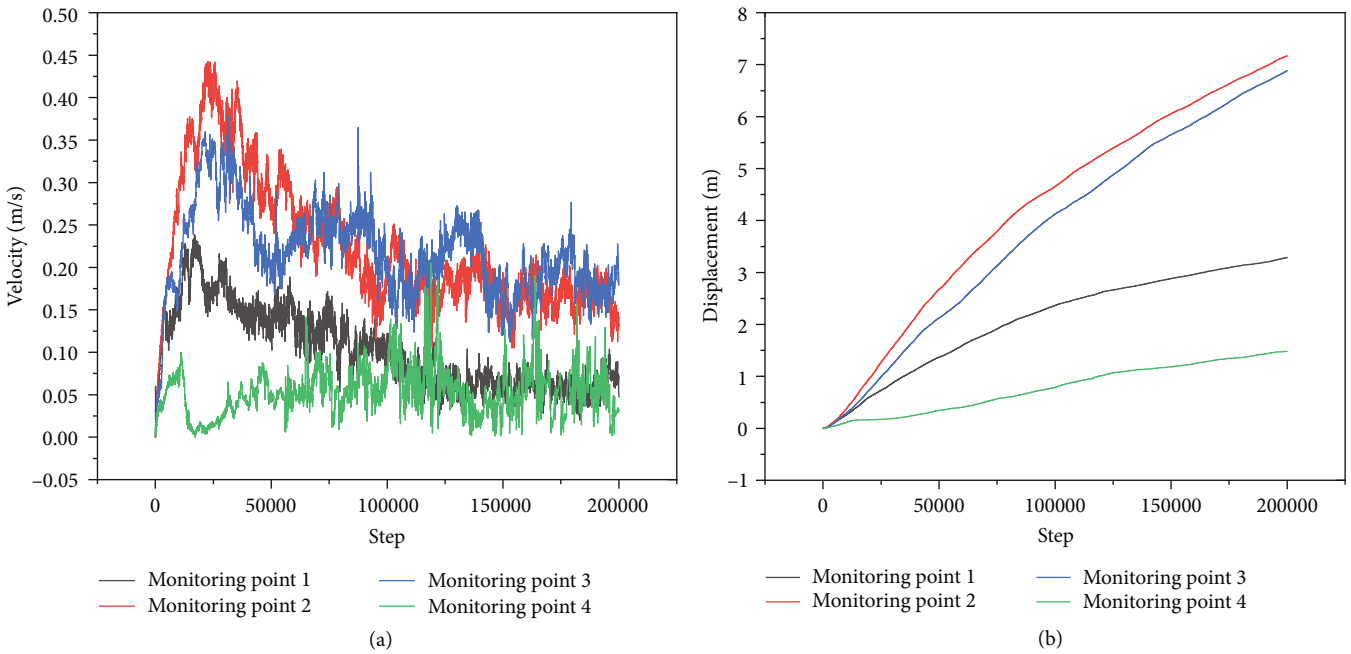


FIGURE 8: The dynamic characteristics of monitoring points during the collapse process.

FTC, and then the decreasing tendency tends to be gentle after 30 times of the FTC. It can be inferred that the sliding collapse may undergo local instability under the action of the FTC with intense weathering or unloading. Affected by external factors such as heavy rainfall or earthquakes, the slope may be a failure.

7. Discussions

According to the previous theoretical analysis, the critical state was predicted by the evolution trend [20]. The related mechanical parameters of the rock mass and discontinuities were determined by the existing test data [21]. Furthermore,

the microscopic parameters were calibrated according to the macroscopic parameters in the critical state, and the related methods will not be described in detail [22, 23].

A numerical model was established based on the typical section involving 35496 particles (Figure 6). The bedrock without weathering at the trailing edge was simplified as a wall to reduce the amount of calculation. Notably, this simplification of trailing edge may affect the simulation results of the slip rate of the rocky slope, but it can still effectively reveal the whole collapse process. Four monitoring points were placed on the typical section.

The dynamic collapse process of the typical section (Figure 7) led to several conclusions. As the concentration of shear stress in rocky slope, dense cracks expand from the toe to the middle part along the structural planes. The cracks increase and gradually penetrate, forming a gradual cumulative failure, which leads to further collapse of the slope under the action of gravity.

According to the dynamic characteristics of monitoring points (Figure 8), the displacement continues to increase, and the velocity begins to fall after reaching the peak values. Specifically, the peak values of slip velocity and the final slip distance of monitoring point 2 in the leading edge are the largest, while the related values of monitoring point 4 are the smallest. This phenomenon shows that due to the spatial distribution of multiple structural planes and the interaction between the rock fragments, the movement characteristics of the particles have a certain randomness during the failure process. Moreover, the sliding space at the leading edge is limited, and the sliding inclination angle of the trailing edge is small. As a result, there is no long-distance migration, and the in situ accumulation phenomenon of the slope is obvious after slope failure. Even so, the sliding failure of the rocky slope would still cause great damage to Tianshan Road.

The dynamic characteristics of monitoring points are consistent with the data monitored by the Zhenziyan collapse [24], which shows that the numerical simulations are effective.

8. Conclusions

Driven by the times of FTC, the mechanical parameters of the rock mass and structural planes were reduced. And the numerical calculations of DEM were used to reveal the disaster-causing effect of the freezing and weathering environment in the alpine area.

Specifically, as the increase of FTC, the structural planes and internal microcracks of the rock mass would expand under the action of frost heave force. Moreover, the physical and mechanical properties of the rock mass on the surface are further deteriorated, leading to a gradual decrease in slope stability.

The dynamic collapse results show that the cracks gradually extend from the toe to the middle part of the rocky slope along the structural planes. The cracks continue to increase and gradually penetrate, forming a progressive failure, which causes further collapse of the slope under the action of gravity. Due to the spatial distribution of multiple structural planes and the interaction between rock frag-

ments, the movement characteristics of rock masses have a certain degree of randomness in the collapse process. And the sliding failure of the rocky slope will cause great damage to Tianshan Road. Therefore, it is necessary to strengthen the monitoring of the rocky slope of Tianshan Road. In this case, the real-time deformation and mechanical state can be obtained, and the threat of landslide can be prevented.

Data Availability

The data used to support the findings of this study are available from the corresponding author upon request.

Conflicts of Interest

The authors declare that they have no conflicts of interest.

Acknowledgments

This study was supported by the National Natural Science Foundation of China (52008058 and 52108299).

References

- [1] J. Charvet, L. S. Shu, S. Laurent-Charvet et al., "Palaeozoic tectonic evolution of the Tianshan belt, NW China," *Science China-Earth Sciences*, vol. 54, no. 2, pp. 166–184, 2011.
- [2] F. H. Chen, J. Jia, J. H. Chen et al., "A persistent Holocene wetting trend in arid central Asia, with wettest conditions in the late Holocene, revealed by multi-proxy analyses of loess-paleosol sequences in Xinjiang, China," *Quaternary Science Reviews*, vol. 146, pp. 134–146, 2016.
- [3] J. Q. Mu, *The Rock Degradation Damage Characteristics and the Disaster-Causing Effects under the Cyclic Freeze-Thaw Action*, Chengdu University of Technology, 2013, (in Chinese).
- [4] Y. Wang, B. Zhang, B. Li, and C. H. Li, "A strain-based fatigue damage model for naturally fractured marble subjected to freeze-thaw and uniaxial cyclic loads," *International Journal of Damage Mechanics*, 2021.
- [5] İ. İnce and M. Fener, "A prediction model for uniaxial compressive strength of deteriorated pyroclastic rocks due to freeze-thaw cycle," *Journal of African Earth Sciences*, vol. 120, pp. 134–140, 2016.
- [6] D. M. Gu, H. L. Liu, X. C. Gao, D. Huang, and W. G. Zhang, "Influence of Cyclic Wetting–Drying on the Shear Strength of Limestone with a Soft Interlayer," *Rock Mechanics and Rock Engineering*, vol. 54, no. 8, pp. 4369–4378, 2021.
- [7] S. B. Huang, Q. S. Liu, A. P. Cheng, and Y. Z. Liu, "A statistical damage constitutive model under freeze-thaw and loading for rock and its engineering application," *Cold Regions Science and Technology*, vol. 145, pp. 142–150, 2018.
- [8] M. Li, Y. Song, and F. Chen, "Analysis on stability of slope in a typical cold region based on thermo-mechanical coupling," *Bulgarian Chemical Communications*, vol. 48, pp. 96–103, 2016.
- [9] J. W. Zhou, P. Cui, and M. H. Hao, "Comprehensive analyses of the initiation and entrainment processes of the 2000 Yigong catastrophic landslide in Tibet, China," *Landslides*, vol. 13, no. 1, pp. 39–54, 2016.

- [10] X. D. Luo, N. Jiang, X. Y. Fan, N. F. Mei, and H. Luo, "Effects of freeze-thaw on the determination and application of parameters of slope rock mass in cold regions," *Cold Regions Science and Technology*, vol. 110, pp. 32–37, 2015.
- [11] L. Q. Wang, Y. P. Yin, B. L. Huang, Z. H. Zhang, P. Zhao, and Y. J. Wei, "A study of the treatment of a dangerous thick submerged rock mass in the three gorges reservoir area," *Bulletin of Engineering Geology and the Environment*, vol. 79, no. 5, pp. 2579–2590, 2020.
- [12] P. P. Guo, X. N. Gong, and Y. X. Wang, "Displacement and force analyses of braced structure of deep excavation considering unsymmetrical surcharge effect," *Computers and Geotechnics*, vol. 113, p. 103102, 2019.
- [13] P. P. Guo, X. N. Gong, Y. X. Wang, H. Lin, and Y. L. Zhao, "Minimum cover depth estimation for underwater shield tunnels," *Tunnelling and Underground Space Technology*, vol. 115, p. 104027, 2021.
- [14] Y. Wang, Y. F. Yi, C. H. Li, and J. Q. Han, "Anisotropic fracture and energy characteristics of a Tibet marble exposed to multi-level constant-amplitude (MLCA) cyclic loads: a lab-scale testing," *Engineering Fracture Mechanics*, vol. 244, p. 107550, 2021.
- [15] M. Xu, S. C. Kang, H. Wu, and X. Yuan, "Detection of spatio-temporal variability of air temperature and precipitation based on long-term meteorological station observations over Tianshan Mountains, Central Asia," *Atmospheric Research*, vol. 203, pp. 141–163, 2018.
- [16] L. Q. Wang, Y. P. Yin, C. Y. Zhou, B. L. Huang, and W. P. Wang, "Damage evolution of hydraulically coupled Jianchuan dong dangerous rock mass," *Landslides*, vol. 17, no. 5, pp. 1083–1090, 2020.
- [17] L. Q. Wang, B. L. Huang, Z. H. Zhang, Z. W. Dai, P. Zhao, and M. J. Hu, "The analysis of slippage failure of the HuangNanBei slope under dry-wet cycles in the three gorges reservoir region, China," *Geomatics, Natural Hazards and Risk*, vol. 11, no. 1, pp. 1233–1249, 2020.
- [18] Y. Wang, W. K. Feng, H. J. Wang, C. H. Li, and Z. Q. Hou, "Rock bridge fracturing characteristics in granite induced by freeze-thaw and uniaxial deformation revealed by AE monitoring and post-test CT scanning," *Cold Regions Science and Technology*, vol. 177, p. 103115, 2020.
- [19] J. Q. Mu, X. J. Pei, Y. Huang, and W. K. Min, "Experimental research on mechanical characteristics of rock with cycles of freezing-thawing action," *Journal of Engineering Geology*, vol. 21, no. 1, pp. 103–108, 2013.
- [20] J. J. Zhao, X. Wan, Y. B. Shi, J. B. Wei, and M. L. Lee, "Deformation behavior of mining beneath flat and sloping terrains in mountainous areas," *Geofluids*, vol. 2021, 16 pages, 2021.
- [21] P. A. Cundall, *A Computer Model for Simulating Progressive Large Scale Movements in Blocky Rock Systems*, Proceedings of the symposium of the International Society for Rock Mechanics, Society for Rock Mechanics (ISRM), France, 1971.
- [22] D. O. Potyondy, "The bonded-particle model as a tool for rock mechanics research and application: current trends and future directions," *Geosystem Engineering*, vol. 18, no. 1, pp. 1–28, 2015.
- [23] L. Q. Wang, Y. P. Yin, B. L. Huang, and Z. W. Dai, "Damage evolution and stability analysis of the Jianchuan dong dangerous rock mass in the three gorges reservoir area," *Engineering Geology*, vol. 265, p. 105439, 2019.
- [24] K. He, C. L. Chen, and B. Li, "Case study of a rockfall in Chongqing, China: movement characteristics of the initial failure process of a tower-shaped rock mass," *Bulletin of Engineering Geology and the Environment*, vol. 78, no. 5, pp. 3295–3303, 2019.

Research Article

Degradation of Strength and Stiffness of Sandstones Caused by Wetting-Drying Cycles: The Role of Mineral Composition

Lu Chen ^{1,2} Yichao Rui ³ and Yihan Zhao ⁴

¹School of Civil Engineering, Changsha University of Science and Technology, Changsha, China 410114

²Engineering Research Center of Catastrophic Prophylaxis and Treatment of Road and Traffic Safety of Ministry of Education, Changsha University of Science & Technology, Changsha 410114, China

³School of Resources and Safety Engineering, Central South University, Changsha, China 410010

⁴PowerChina Zhongnan Engineering Corporation Limited, Changsha, China 410010

Correspondence should be addressed to Yichao Rui; ruiyichao@csu.edu.cn

Received 26 July 2021; Accepted 31 August 2021; Published 1 October 2021

Academic Editor: Yu Wang

Copyright © 2021 Lu Chen et al. This is an open access article distributed under the Creative Commons Attribution License, which permits unrestricted use, distribution, and reproduction in any medium, provided the original work is properly cited.

Rock mechanical parameters are of great importance for the construction and design of rock engineering. Rocks are usually subjected to the deteriorating effect of cyclic wetting-drying because of the change in moisture content. The main objective of this study is to reveal the degradation effects of wetting-drying cycles on strength and modulus on varying rocks. Three kinds of sandstones with different mineral constituents are selected for testing. Artificial treatments of cyclic wetting-drying are conducted on respective specimens of the three sandstones (0, 10, 20, 30, and 40 cycles) to simulate the damage of rocks exposed to natural weathering. Uniaxial compressive tests are carried out on sandstone specimens to obtain their strength and modulus. Test results show that, for the tested sandstones, both of the uniaxial compressive strength (UCS) and modulus are reduced as the cyclic number rises. In the first ten cycles, the losses of UCS and modulus are very significant. Subsequently the changes of UCS and modulus become much more placid against cyclic number. When the cyclic number is the same, the loss percentages of rock mechanical properties of the three sandstones are very different which mainly depends on the contents of expandable and soluble minerals.

1. Introduction

In the pluvial region, rock masses are commonly exposed to cyclic wetting-drying (WD) interactions in many rock engineering applications, such as slope, mining, tunnelling, and underground storage [1–3]. The periodic cyclic WD can deteriorate the mechanical characteristics of rocks, which would cause some engineering geological hazards, e.g., ground subsidence, landslide, and mine collapse [4–7]. Thus, on account of the stability and safety of rock engineering, a deep understanding the deformation and mechanical behavior of rocks exposed to WD cycles is of great significance.

So far, the impact of WD weathering on rock mechanical properties has been widely explored. For instance, Hale and Shakoor [8] performed uniaxial compressive tests on six kinds of sandstones after 50 WD cycles. They reported that no remarkable correlation between uniaxial compressive

strength (UCS) and WD cycles can be found. Similar tests have been widely carried out under quasistatic and dynamic conditions. More researchers however hold the opinion that as the number of WD cycles increases, the UCS of rocks is decreased [9–20]. Except for uniaxial compressive tests, many other types of experimental tests were also performed on rock specimens exposed to cyclic WD treatments, such as triaxial compressive test [13, 21, 22], Brazilian disc test [17, 23, 24], bending test [25–27], and shear test [28, 29]. For example, Zhang et al. [29] found that under the same vertical stress, the shear strength of siltstone declines after cyclic WD treatments. Hua et al. [26, 27] measured mode I and mode II fracture toughness of a Chongqing sandstone of sandstone and found that the two modes of fracture toughness are decreased by 52.4% and 56.2% when the sandstone specimen is endured seven WD cycles. Zhou et al. [24] first investigated the dynamic tensile properties of sandstone

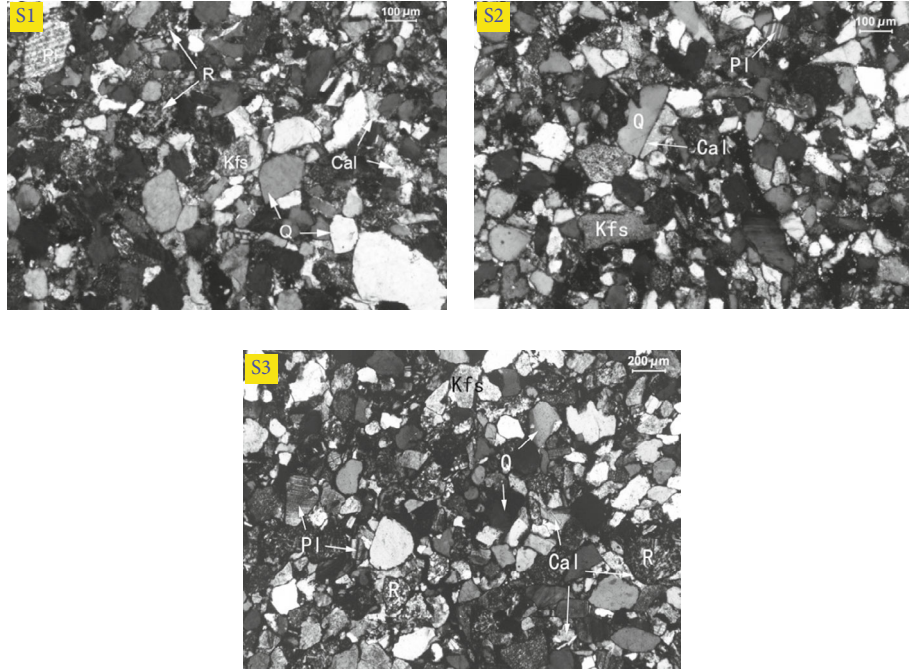


FIGURE 1: Optical microscope images of the three tested sandstones.

subjected to cyclic WD treatments by means of a split Hopkinson pressure bar. They discovered that as the WD cycles rises, the dynamic tensile strength of sandstone declines significantly at given loading rates. Also, they established a strength prediction model considering rate effect and WD deterioration. Overall, the strength, stiffness, and fracture toughness of different rocks experience varying deterioration levels after cyclic WD. However, the underlying mechanism is not understood. Technically speaking, the test data in different publications are not comparable due to the differences in lab weathering methods and testing conditions, such as wetting or drying method, testing machine, and loading speed.

This research is aimed at understanding the deterioration of mechanical behavior of rock caused by cyclic WD; a series of uniaxial compressive tests are conducted on three kinds of sandstone specimens. The strength and elastic modulus of sandstone specimens after different WD cycles are obtained. The sensitivity of mechanical behavior for the three sandstones to cyclic WD deterioration is revealed. The weakening mechanisms induced by cyclic WD are elucidated.

2. Experimental Method

2.1. Testing Materials and Specimen Preparation. Three kinds of sandstones with different engineering properties are selected for test materials, which are labelled as S1, S2, and S3, respectively. The optical image of thin sections for the three sandstones is shown in Figure 1. Their mineralogical constituents are measured via X-ray diffraction (XRD) technique, as listed in Table 1. As seen in Table 1, mineral contents of the three sandstones are very different. S1 holds abundant content of clay minerals (about 13.77%), while S3 has few clay minerals (less than 1%). S2 has a moderate clay content of 2.03%.

TABLE 1: Mineral constituents of the three sandstones.

Mineral	Mass percentage (%)		
	S1	S2	S3
Quartz	57.20	44.94	63.39
Feldspar	13.48	28.71	29.09
Calcite	5.26	17.36	1.79
Hematite	6.45	5.35	1.07
Mica	3.84	1.61	2.21
Clay	Smectite	9.72	0
	Chlorite	4.05	2.03
	Clinochlore	0	0
			<1

50 mm rock cores are first drilled from one single slate without visible discontinuities. Then, the cores are sliced into cylindrical specimens with the length slightly greater than 100 mm. Subsequently, all ends of each specimen are polished by a grinding machine to the top and bottom surfaces planar to each other and perpendicular to the long axis of this specimen. After specimen manufacturing, the internal moisture of all specimens is removed via the oven-dried method under a constant temperature of 50°C for more than 48 hours. These specimens are considered the specimens free from cyclic WD treatments for comparison.

The whole artificial WD treatment includes a free-soaking period and oven-drying period, as depicted in Figure 2. In the former period, the specimens are submerged a tank full of distilled water at 25°C for 48 hours to get a nominal complete water-saturated state. In the later period, the water-saturated specimens are put into the oven at 50°C for 48 hours for drying. Then, the specimens are cooled in the oven at 25°C for 2

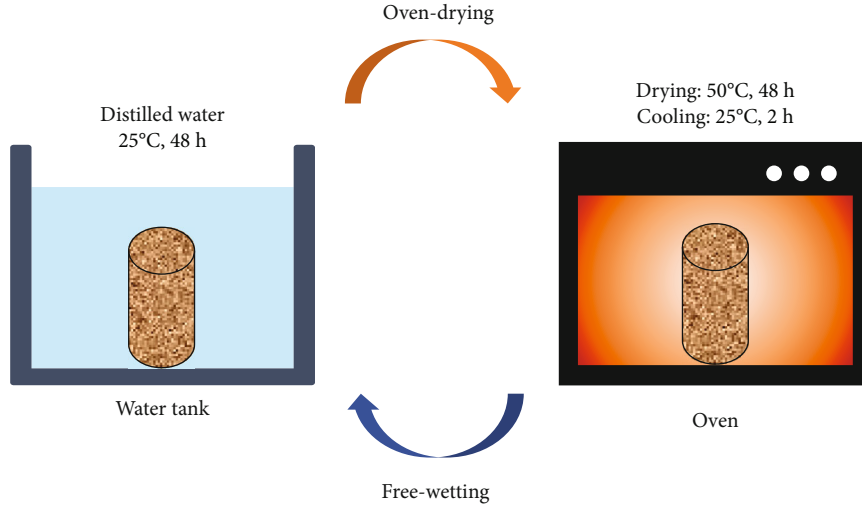


FIGURE 2: Schematic of a whole wetting-drying treatment process.

hours. For each type of rock, we design five groups of specimens experiencing 0, 10, 20, 30, and 40 WD cycles for testing. Each group prepares five specimens.

2.2. Experimental Setup. A servocontrolled material testing system (MTS 332) is used to perform all uniaxial compressive tests are performed on a servocontrolled material testing system (MTS 332), as seen in Figure 3. The MTS 332 has a global stiffness of 1370 kN/mm and a loading capacity of 500 kN. The displacement-control loading approach is adopted. During tests, the displacement speed is maintained at 0.24 mm/min until specimen failure, i.e., the axial deformation rate of the specimen is nearly $4 \times 10^{-5} \text{ s}^{-1}$. The applied axial load is recorded by a load cell in the machine. The axial deformation of the specimen is determined by a linear variable differential transformer attached besides the specimen.

3. Test Results and Discussion

3.1. Effect of WD Cycles on Rock Strength. Figure 4 shows the uniaxial compressive strength (UCS) of the tested sandstones after cyclic WD treatments. We can observe that, for the original specimen, the rank of UCS is $S3 > S2 > S1$. With the increasing number of WD cycles (n), the UCS of each sandstone decreases with different declining rates. For S1 and S2, their UCS experiences relatively remarkable changes with the increasing cyclic number. However, the UCS of S1 has very slight reduction induced by cyclic WD.

Figure 5 further presents the normalized UCS of the tested sandstones. It is found that the UCS of the three tested sandstones drops dramatically in the first ten WD cycles and then stabilizes. This phenomenon agrees with test data in many prior studies [10–12, 14, 20]. After 40 WD cycles, the percentage of UCS reduction for S1, S2, and S3 is 29.99%, 17.78%, and 7.15%, respectively.

As reported by Zhou et al. [20], the relationships between rock properties and the number of WD cycles (n) can be characterized by the exponential form:



FIGURE 3: Photographic view of the loading apparatus.

$$\sigma_c(n) = a + be^{-cn}, \tag{1}$$

where σ_c is UCS and a , b , and c are fitting constants. Specifically, the term of b is a dimensionless constant, which represents the strength reduction rate as the increase of n . The higher value of b means the stronger sensitivity of UCS to WD cycles.

To compare the UCS sensitivity of the tested sandstones to WD cycles, we fit the test data according to Equation (1) as shown in Figure 4. The specific relation expressions are

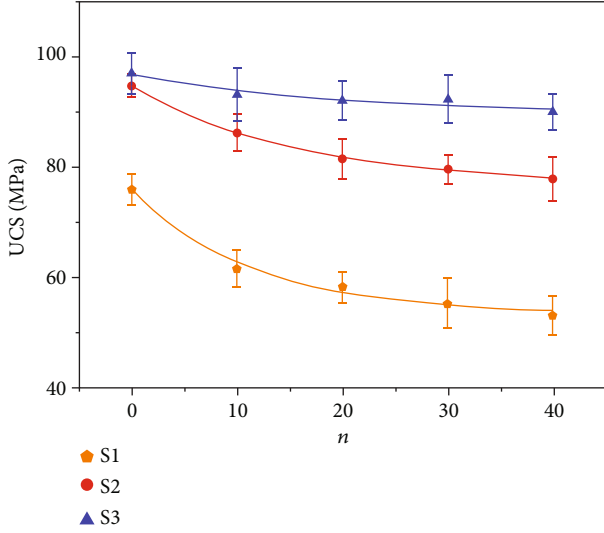


FIGURE 4: Variation in the UCS of tested sandstones versus the number of WD cycles.

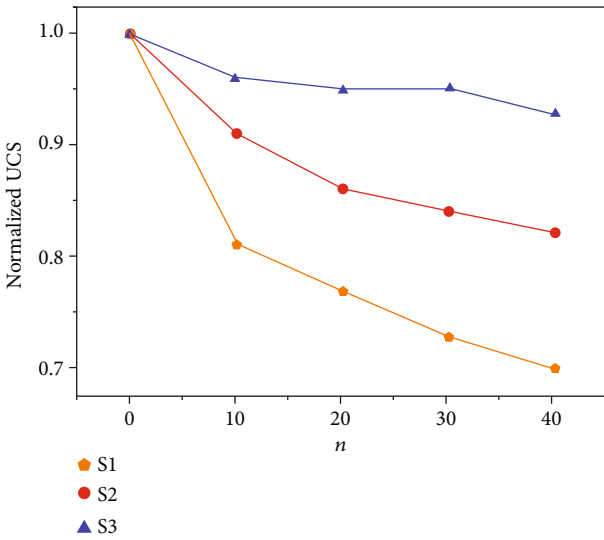


FIGURE 5: Normalized UCS of tested sandstones versus the number of WD cycles.

$$\begin{cases} \sigma_{c1}(n) = 53.49 + 22.41e^{-0.087n} \quad (R^2 = 0.978), \\ \sigma_{c2}(n) = 76.84 + 17.92e^{-0.064n} \quad (R^2 = 0.999), \\ \sigma_{c3}(n) = 89.73 + 7.18e^{-0.053n} \quad (R^2 = 0.885), \end{cases} \quad (2)$$

where σ_{c1} , σ_{c2} , and σ_{c3} are the UCS of S1, S2, and S3, respectively; R^2 is the coefficient of determination. From Equation (2), we can see that S1 has the largest UCS sensitivity to WD cycles, followed by S2 and S3.

3.2. Effect of WD Cycles on Rock Modulus. Initial modulus and Young's modulus are compared in the section. They are measured from the stress-strain curve. The former is

calculated according to the secant modulus at the strain of 0.2%, and the latter is the gradient of the linear portion.

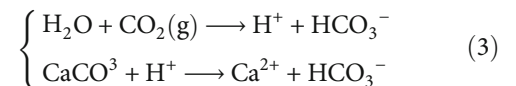
Figure 6 shows the changes in initial modulus and Young's modulus of the tested three sandstones versus the number of WD cycles. From Figure 6(a), for all tested sandstones, the average values of initial modulus decrease as the cyclic number increases. Initially, the average initial modulus of S1, S2, and S3 are 3.59 GPa, 4.28 GPa, and 2.88 GPa, respectively. After 10 cyclic WD treatments, they are decreased to 2.44 GPa, 3.46 GPa, and 2.63 GPa. Thereafter, the initial modulus declines more slowly and tends to become stable as cyclic number rises. It also can be seen from Figure 6(b) that, when a rock specimen is experienced a given number of WD cycle, its Young's modulus is greater than initial modulus. Also, Young's modulus follows a similar decreasing pattern as the initial modulus.

Figure 7 further displays the modulus reduction of sandstones after 40 WD cycles. We can observe that when the tested three sandstones are subjected to 40 WD cycles, the initial modulus of S1, S2, and S3 is reduced by 49.03%, 33.88%, and 16.32%, respectively. The loss percentage of Young's modulus is 38.38%, 18.14%, and 4.16% for S1, S2, and S3, which is much lower than that of initial modulus.

4. Discussion

4.1. Weakening Mechanism for Strength Reduction Induced by WD Cycles. It is extensively shared that the presence of water plays a dominant weakening role on rock strength and stiffness due to physical-chemical-mechanical water-rock interactions [19, 30–34]. Some water-weakening effects will be vanished when the rock is dried again, but some are not and lead to irreversible damage of rock structure [35]. Cyclic WD treatments further aggregate the cumulative damage. The underlying mechanisms for the rock damage induced by WD cycles are as follows [25]:

- (1) Mechanical cracking induced by expandable minerals: when the rock is immersed in water, some expandable minerals, e.g., smectite, will absorb water molecules and dilate. The swelling pressure on the pore wall will promote the creation and propagation of intergranular cracks [36]. Also, in the oven-drying period, the swelling pressure will decrease as the free water evaporates. During cyclic WD treatments, the pores containing expandable minerals are actually subjected to repeated tensile loads. This fatigue loading further damages the rock structure [25]
- (2) Mineral dissolution: mineral grains are commonly insoluble in distilled water. However, under atmospheric condition, the calcite will react with distilled water due to the presence of gaseous carbon dioxide as follows [37]:



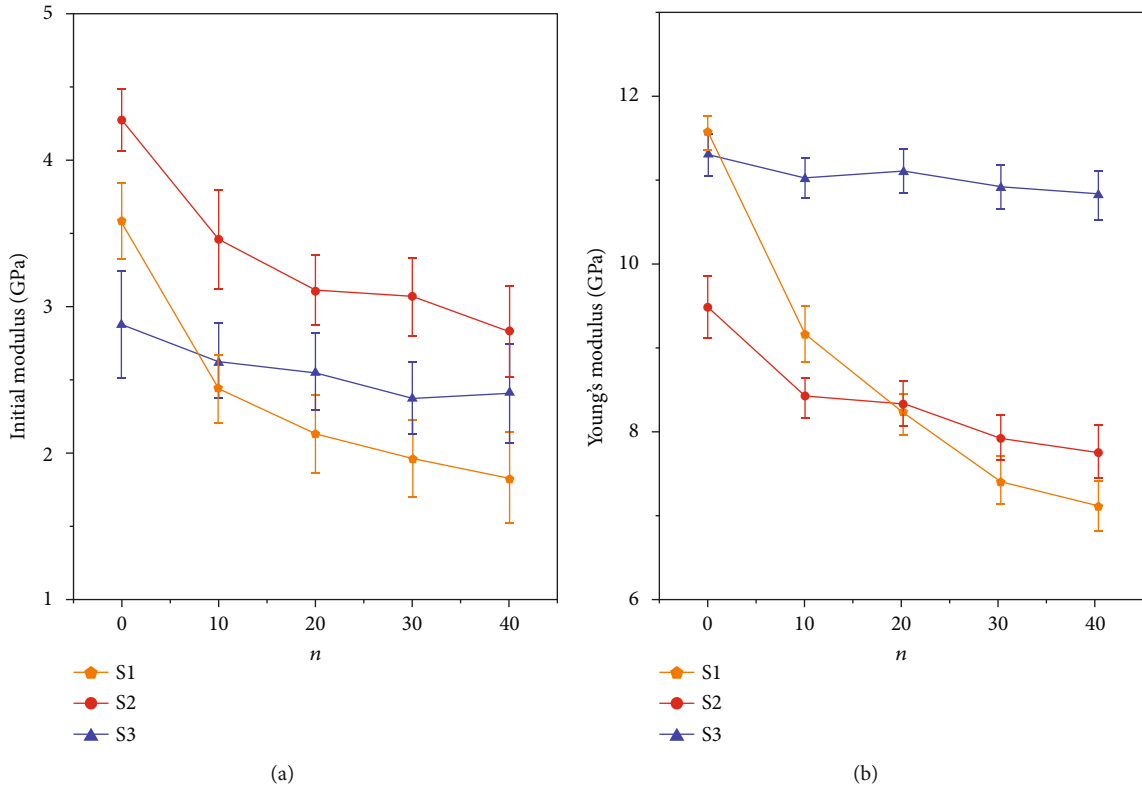


FIGURE 6: Variation in (a) initial modulus and (b) Young's modulus of tested sandstones versus the number of WD cycles.

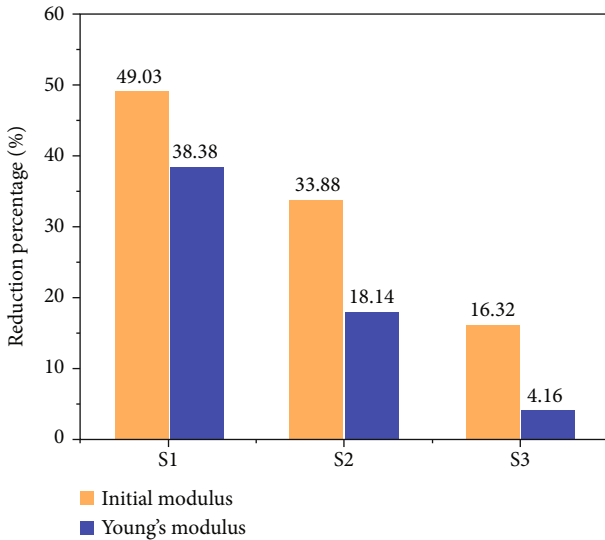


FIGURE 7: Reduction percentage of initial modulus and Young's modulus after 40 WD cycles.

The abovementioned two reactions can increase the crack density in rock, which is verified from scanning electron microscope [13, 25] and computerized tomography [17]. This will further decrease the rock strength. Hence, we can deduce that the strength reduction induced by cyclic WD is highly controlled by the content of expansible min-

erals (smectite) and soluble minerals (calcite). It can be seen from Figure 8 that the percentage of UCS loss after 40 cycles rises as the percentage of clay mineral increases. However, there is no clear correlation between the UCS loss and calcite content. Thus, we can infer that the smectite swelling plays a more important role in rock deterioration than calcite dissolution. Among the tested three sandstones, S1 has the most content of smectite (9.72%) and a moderate content of calcite (5.26%); thus, it experiences the greatest UCS loss caused by cyclic WD and is most sensitive to cyclic WD. Though there is no smectite in S2, it has a considerable content of calcite, such that the UCS reduction of S2 is the second largest after S1. In S3, no expandable minerals and a little content of calcite exist. These results in the UCS of S3 are not sensitive to WD cycles.

4.2. Weakening Mechanisms for Modulus Reduction Induced by WD Cycles. As known, the initial modulus is an indicator of the volume of microdefects within the rock specimen. The lower initial modulus means the greater volume of initial defects. As discussed in Section 4.1, after cyclic WD treatments, the crack density in rock specimen will increase primarily due to mechanical cracking and mineral dissolution. The decrease of initial modulus verifies our hypothesis to some extent. The loss percentage of modulus is related to the increment of defect volume caused by WD cycles. Similar with UCS, the different sensitivities of modulus to cyclic WD depend on the content of smectite and calcite.

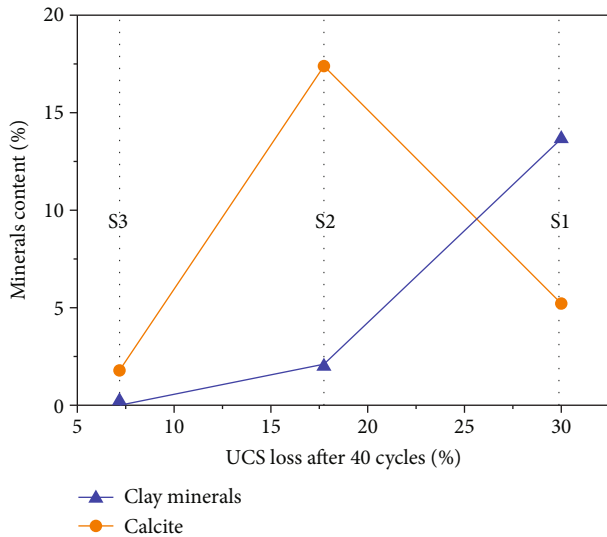


FIGURE 8: Relationship between UCS loss percentage and mineral content.

4.3. Engineering Significance. Rock strength and modulus are very crucial parameters for rock engineering design and construction [38]. In practice, rock structures are commonly exposed to water erosion and cyclic wetting-drying degradation. Our test results reveal that rock strength and modulus will be decreased after cyclic WD treatments. The declining extent is mainly controlled by the contents of expandable and soluble minerals. Thus, it should be noted that the weakening effects of WD on rock strength and modulus should be considered. Before rock engineering design, the rainy period or the variation of water table should be surveyed; the engineering indicators of rock are predicted according to the water cyclic period and the service life of project. Moreover, some potential protection methods can be adopted to alleviate water-weakening effects [25]:

- (1) Rocks containing high contents of expandable (e.g., smectite) and soluble (e.g., calcite) minerals cannot be used for critical structures, such as the key pillar in underground cavern
- (2) Waterproof measures must be applied in critical rock structures
- (3) To clog the channels of water seepage, specific binders can be used on rock structures to repair the visible fractures and cracks

5. Conclusions

In the present study, we aim to understand the effects of wetting-drying cycles on the strength and modulus of different rocks; uniaxial compressive tests were carried out on three kinds of sandstone specimens suffering different numbers of artificial cyclic wetting-drying treatments (up to 40 cycles). The following specific conclusions can be made:

- (1) For the tested sandstones, when they suffer wetting-drying cycles, their uniaxial compressive strength and modulus are decreased in different contents
- (2) The losses of strength and modulus are commonly remarkable in the first ten cycles, and then, the declining rate is much gentler
- (3) The sensitivity of rock strength and modulus to wetting-drying cycles is controlled by the mineral composition of rock. The clay swelling and calcite dissolution are probably the dominating mechanisms for the degradation of rock properties after wetting-drying cycles

Data Availability

Data can be available from the corresponding author by request.

Conflicts of Interest

The authors declare that there is no conflict of interest regarding the publication of this paper.

Acknowledgments

This work was supported by the National Natural Science Foundation for Young Scientists of China (52004036), the Research Foundation of Education Bureau of Hunan Province (20B040), and the Open Fund of Engineering Research Center of Catastrophic Prophylaxis and Treatment of Road & Traffic Safety of Ministry of Education (Changsha University of Science & Technology), China (kfj190402).

References

- [1] C. Gökçeoglu, R. Ulusay, and H. Sönmez, "Factors affecting the durability of selected weak and clay-bearing rocks from Turkey, with particular emphasis on the influence of the number of drying and wetting cycles," *Engineering Geology*, vol. 57, pp. 215–237, 2000.
- [2] G. Pardini, G. V. Guidi, R. Pini, D. Regüés, and F. Gallart, "Structure and porosity of smectitic mudrocks as affected by experimental wetting-drying cycles and freezing-thawing cycles," *Catena*, vol. 27, no. 3-4, pp. 149–165, 1996.
- [3] L. Zeng, J. Liu, Q. F. Gao, and H. Bian, "Evolution characteristics of the cracks in the completely disintegrated carbonaceous mudstone subjected to cyclic wetting and drying," *Advances in Civil Engineering*, vol. 2019, Article ID 1279695, 10 pages, 2019.
- [4] K. Liao, Y. Wu, F. Miao, L. Li, and Y. Xue, "Time-varying reliability analysis of Majiagou landslide based on weakening of hydro-fluctuation belt under wetting-drying cycles," *Landslides*, vol. 18, no. 1, pp. 267–280, 2021.
- [5] P. D. Loubser and M. Sumner, "Experimental sandstone weathering using different wetting and drying moisture amplitudes," *Earth Surf Process Landforms*, vol. 33, pp. 985–990, 2008.
- [6] A. Momeni, S. S. Hashemi, G. R. Khanlari, and M. Heidari, "The effect of weathering on durability and deformability

- properties of granitoid rocks,” *Bulletin of Engineering Geology and the Environment*, vol. 76, pp. 1037–1049, 2017.
- [7] L. Wang, Y. Yin, B. Huang, and Z. Dai, “Damage evolution and stability analysis of the Jianchuandong Dangerous Rock Mass in the Three Gorges Reservoir Area,” *Engineering Geology*, vol. 265, article 105439, 2020.
- [8] P. A. Hale and A. Shakoor, “A laboratory investigation of the effects of cyclic heating and cooling, wetting and drying, and freezing and thawing on the compressive strength of selected sandstones,” *Environmental and Engineering Geoscience*, vol. 9, pp. 117–130, 2003.
- [9] B. Du, H. Bai, M. Zhai, and S. He, “Experimental study on dynamic compression characteristics of red sandstone under wetting-drying cycles,” *Advances in Civil Engineering*, vol. 2020, Article ID 6688202, 10 pages, 2020.
- [10] S. Huang, J. Wang, Z. Qiu, and K. Kang, “Effects of cyclic wetting-drying conditions on elastic modulus and compressive strength of sandstone and mudstone,” *Processes*, vol. 6, no. 12, p. 234, 2018.
- [11] G. Khanlari and Y. Abdilor, “Influence of wet-dry, freeze-thaw, and heat-cool cycles on the physical and mechanical properties of Upper Red sandstones in central Iran,” *Bulletin of Engineering Geology and the Environment*, vol. 74, pp. 1287–1300, 2015.
- [12] M. L. Lin, F. S. Jeng, L. S. Tsai, and T. H. Huang, “Wetting weakening of tertiary sandstones - microscopic mechanism,” *Environmental Geology*, vol. 48, pp. 265–275, 2005.
- [13] X. Liu, M. Jin, D. Li, and L. Zhang, “Strength deterioration of a Shaly sandstone under dry-wet cycles: a case study from the Three Gorges Reservoir in China,” *Bulletin of Engineering Geology and the Environment*, vol. 77, no. 4, pp. 1607–1621, 2017.
- [14] A. Özbek, “Investigation of the effects of wetting-drying and freezing-thawing cycles on some physical and mechanical properties of selected ignimbrites,” *Bulletin of Engineering Geology and the Environment*, vol. 73, pp. 595–609, 2014.
- [15] C. Wang, W. Pei, M. Zhang, Y. Lai, and J. Dai, “Multi-scale experimental investigations on the deterioration mechanism of sandstone under wetting-drying cycles,” *Rock Mechanics and Rock Engineering*, vol. 54, no. 1, pp. 429–441, 2021.
- [16] X. Yang, J. Wang, C. Zhu, M. He, and Y. Gao, “Effect of wetting and drying cycles on microstructure of rock based on SEM,” *Environment and Earth Science*, vol. 78, no. 6, 2019.
- [17] W. Yao, C. Li, H. Zhan et al., “Multiscale study of physical and mechanical properties of sandstone in Three Gorges Reservoir region subjected to cyclic wetting-drying of Yangtze River water,” *Rock Mechanics and Rock Engineering*, vol. 53, no. 5, pp. 2215–2231, 2020.
- [18] P. Yuan, N. N. Wei, Q. Y. Ma, and J. C. Chang, “Coupled effect of water temperature and cyclic wetting and drying on dynamic mechanical characteristics of sandstone,” *Advances in Civil Engineering*, vol. 2019, Article ID 8167651, 15 pages, 2019.
- [19] Z. Zhang, Y. Niu, X. Shang, P. Ye, R. Zhou, and F. Gao, “Deterioration of physical and mechanical properties of rocks by cyclic drying and wetting,” *Geofluids*, vol. 2021, 15 pages, 2021.
- [20] Z. Zhou, X. Cai, L. Chen, W. Cao, Y. Zhao, and C. Xiong, “Influence of cyclic wetting and drying on physical and dynamic compressive properties of sandstone,” *Engineering Geology*, vol. 220, pp. 1–12, 2017.
- [21] M. C. Torres-Suarez, A. Alarcon-Guzman, and R. Berdugo-De Moya, “Effects of loading-unloading and wetting-drying cycles on geomechanical behaviors of mudrocks in the Colombian Andes,” *Journal of Rock Mechanics and Geotechnical Engineering*, vol. 6, pp. 257–268, 2014.
- [22] Z. Zhang, Q. Jiang, C. Zhou, and X. Liu, “Strength and failure characteristics of Jurassic Red-Bed sandstone under cyclic wetting-drying conditions,” *Geophysical Journal International*, vol. 198, pp. 1034–1044, 2014.
- [23] Z. Zhao, J. Yang, D. Zhang, and H. Peng, “Effects of wetting and cyclic wetting-drying on tensile strength of sandstone with a low clay mineral content,” *Rock Mechanics and Rock Engineering*, vol. 50, pp. 485–491, 2017.
- [24] Z. Zhou, X. Cai, D. Ma, L. Chen, S. Wang, and L. Tan, “Dynamic tensile properties of sandstone subjected to wetting and drying cycles,” *Construction and Building Materials*, vol. 182, pp. 215–232, 2018.
- [25] X. Cai, Z. Zhou, L. Tan, H. Zang, and Z. Song, “Fracture behavior and damage mechanisms of sandstone subjected to wetting-drying cycles,” *Engineering Fracture Mechanics*, vol. 234, p. 107109, 2020.
- [26] W. Hua, S. Dong, Y. Li, J. Xu, and Q. Wang, “The influence of cyclic wetting and drying on the fracture toughness of sandstone,” *International Journal of Rock Mechanics and Mining Sciences*, vol. 78, pp. 331–335, 2015.
- [27] W. Hua, S. Dong, Y. Li, and Q. Wang, “Effect of cyclic wetting and drying on the pure mode II fracture toughness of sandstone,” *Engineering Fracture Mechanics*, vol. 153, pp. 143–150, 2016.
- [28] Z. C. Tang, Q. Z. Zhang, and Y. Zhang, “Cyclic drying-wetting effect on shear behaviors of red sandstone fracture,” *Rock Mechanics and Rock Engineering*, vol. 54, no. 5, pp. 2595–2613, 2021.
- [29] B. Y. Zhang, J. H. Zhang, and G. L. Sun, “Deformation and shear strength of rockfill materials composed of soft siltstones subjected to stress, cyclical drying/wetting and temperature variations,” *Engineering Geology*, vol. 190, pp. 87–97, 2015.
- [30] X. Cai, Z. Zhou, L. Tan, H. Zang, and Z. Song, “Water saturation effects on thermal infrared radiation features of rock materials during deformation and fracturing,” *Rock Mechanics and Rock Engineering*, vol. 53, no. 11, pp. 4839–4856, 2020.
- [31] X. Cai, Z. Zhou, H. Zang, and Z. Song, “Water saturation effects on dynamic behavior and microstructure damage of sandstone: phenomena and mechanisms,” *Engineering Geology*, vol. 276, p. 105760, 2020.
- [32] C. Li, N. Liu, and W. Liu, “Experimental investigation of mechanical behavior of sandstone with different moisture contents using the acoustic emission technique,” *Advances in Civil Engineering*, vol. 2020, Article ID 8877921, 10 pages, 2020.
- [33] Z. Zhou, X. Cai, D. Ma et al., “Water saturation effects on dynamic fracture behavior of sandstone,” *International Journal of Rock Mechanics and Mining Sciences*, vol. 114, pp. 46–61, 2019.
- [34] Z. Zhou, X. Cai, D. Ma, W. Cao, L. Chen, and J. Zhou, “Effects of water content on fracture and mechanical behavior of sandstone with a low clay mineral content,” *Engineering Fracture Mechanics*, vol. 193, pp. 47–65, 2018.
- [35] Z. Zhou, X. Cai, W. Cao, X. Li, and C. Xiong, “Influence of water content on mechanical properties of rock in both saturation and drying processes,” *Rock Mechanics and Rock Engineering*, vol. 49, no. 8, pp. 3009–3025, 2016.

- [36] D. A. Laird, "Influence of layer charge on swelling of smectites," *Applied Clay Science*, vol. 34, no. 1–4, pp. 74–87, 2006.
- [37] M. Violay, S. Nielsen, E. Spagnuolo, D. Cinti, G. di Toro, and G. di Stefano, "Pore fluid in experimental calcite-bearing faults: abrupt weakening and geochemical signature of coseismic processes," *Earth and Planetary Science Letters*, vol. 361, pp. 74–84, 2013.
- [38] L. Tan, T. Ren, L. Dou, X. Yang, M. Qiao, and H. Peng, "Analytical stress solution and mechanical properties for rock mass containing a hole with complex shape," *Theoretical and Applied Fracture Mechanics*, vol. 114, p. 103002, 2021.

Research Article

Parametric Study of the Borehole Drilling in Jointed Rock Mass

**Yanan Gao,^{1,2,3,4} Yudong Zhang,^{1,2} Zetian Zhang^{1,2,3},, Minghui Li^{1,2,4},, Yingfeng Sun,^{3,5}
Donghao Lan,^{1,2} and Feng Gao^{1,2}**

¹State Key Laboratory for Geomechanics and Underground Engineering, China University of Mining and Technology, Xuzhou, Jiangsu 221116, China

²School of Mechanics and Civil Engineering, China University of Mining and Technology, Xuzhou, Jiangsu 221116, China

³Key Laboratory of Deep Earth Science and Engineering, Sichuan University, Chengdu, Sichuan 610025, China

⁴Guangdong Provincial Key Laboratory of Deep Earth Sciences and Geothermal Energy Exploitation and Utilization, Shenzhen University, Shenzhen 518060, China

⁵School of Civil and Resource Engineering, University of Science and Technology Beijing, Beijing 100083, China

Correspondence should be addressed to Zetian Zhang; zhangzetian@scu.edu.cn

Received 21 August 2021; Accepted 17 September 2021; Published 30 September 2021

Academic Editor: Bailu Teng

Copyright © 2021 Yanan Gao et al. This is an open access article distributed under the Creative Commons Attribution License, which permits unrestricted use, distribution, and reproduction in any medium, provided the original work is properly cited.

Gas is associated with coal mining; it commonly exists in the coal seam. It is one of the major dangers during the production because its reaction between the coal masses may induce the gas-coal outburst as well as it being an expositive matter. The gas accident has caused a huge amount of property damage and casualties. Therefore, the primary precaution for coal mining is gas control. At present, drilling and extraction are the main approaches for gas accident prevention. After drilling, the ground pressure will be released; the gas which is in a free state or absorbed in the coal seam will be easy to extract as the migration channel is enhanced. Hence, one of the most concerned problems is the stress redistribution of the coal and rock mass around the borehole. In practical engineering, there are many joints distributed in the coal and rock strata, so it is necessary to investigate the effect of the drilling in the jointed coal and rock mass. In this paper, the boundary element model of the borehole in the jointed coal and rock mass is established to study the influence of joints on the stress and displacement field. The following results can be obtained. The number of joints has a significant effect on the maximum displacement of the coal and rock mass. The maximum displacement increases with the number of the joint. The position of the maximum displacement shifts from the boundary of the borehole to the far field. Meanwhile, it can be found that the displacement may reach a peak value when the joint angle is 30° and if the joint number is less than 4, and the maximum displacement may occur under the joint angle of 45° and if the joints number continuous increases. The von Mises stress has a trend of increasing with the number of joints when the joint angle is less than 30° , while it has a decreasing trend when the joint angle is larger than 30° . The max stress may occur at the joint angle of 15° . The maximum shear stress occurs mostly in the No. 4 joint and the No.7 joint. When the joint angle is 30° , the maximum shear stress occurs in the No. 3 joint and the No. 4 joint. The overlap of the position of the maximum von Mises stress or the maximum displacement with different joint angles or different numbers of joint leads to a reexploration of such positions. The position of the maximum von Mises stress and the maximum displacement σ is relatively steady, which locates symmetrically around the borehole. The line between the points that behaves as the maximum von stress is approximately perpendicular to the joint direction.

1. Introduction

Gas is associated with coal mining; it commonly exists in the coal seam. It is one of the major dangers during the production, because its reaction between the coal masses may induce dynamic disasters such as gas-coal outburst, as well

as it being an expositive matter. The gas accident has caused a huge amount of property damage and casualties [1–5].

Therefore, the primary precaution for coal mining is gas control. At present, mining of the protective layer and drilling-extraction are the main approaches for gas accident prevention. However, a suitable protective layer cannot be

always found, especially in the deep underground. Thus, drilling-extraction may be the preferred method for the regional gas control under this circumstance [6–10]. After the drilling, the ground pressure will be released, the gas which is in a free state or absorbed in the coal seam will be easy to extract as the migration channel is enhanced. Hence, one of the most concerned problems is the stress redistribution of the coal and rock mass around the borehole.

At present, many studies have been carried out to investigate the process, effect, and the mechanism of pressure relief by drilling. Wang optimized the surface drilling position and drainage pressure of Yuwu coal mine. The results show that the position in horizontal of surface drilling should arrange inside of “O” ring, and in vertical, it should be arranged between the collapse zone to the middle part of the fracture zone [11]. Tong et al. studied the behavior of gas extraction from the protected layer by surface drilling. It is found that, after the protected layer working face was advanced through the surface drilling, the gas extracted by surface drilling behaves as 3 periods, i.e., the rising period, stable period, and decay period [12]. Lian studied the key factors of well completion such as well layout, well structure, drilling technology, and drilling management and provided reference for the application of gas extraction in surface wells [13]. Liu et al. proposed an efficient strategy to minimize air leakage for underground gas extraction based on the controlling of the fracture permeability of the coal rock mass. A good strategy to minimize air leakage for underground gas extraction is to seal the developed fractures around the borehole [14]. Based on the results of the drainage from pressure release area, Wu indicated that the coalbed methane drainage from coal seams with low permeability in the release area of pressure is not only advantageous to the coal mine safety production but also can enhance recovery ratio of the coalbed methane enormously and enhances the economic efficiency of the coalbed methane development [15]. Chen et al. carried out a hydraulic flushing technology with cross-seam boreholes to solve this problem. Furthermore, the optimal spacing of hydraulic flushing boreholes (HFB) is determined to provide the basis for field testing [16]. Hu et al. conducted an experimental study on the permeability enhancement of boreholes by using liquid CO_2 phase-transition blasting (LCPTB). The results indicated a significant increase in the permeability of the coal seam, and the efficiency of gas drainage can be obtained by using LCPTB. The amount of gas extracted from the LCPTB-enhanced holes was 1.8–8 times greater than that extracted from common borehole [17]. Gao et al. studied the effect of the borehole and the borehole-slotting on the pressure relieve. The parametric study of the geometry of the slotting, and the in situ stress is carried out [18]. Wei et al. optimized the process parameters of gas extraction and carried out the application study in the field. The results show that the reduction of gas pressure around the borehole group is larger than that from a single borehole. The borehole spacing is suggested to be 2 times of or over the effective drainage radius [19]. Zhao et al. studied the influence of coal gas seepage law between boreholes for gas extraction and proposed the law of gas pressure distributions, gas seepage

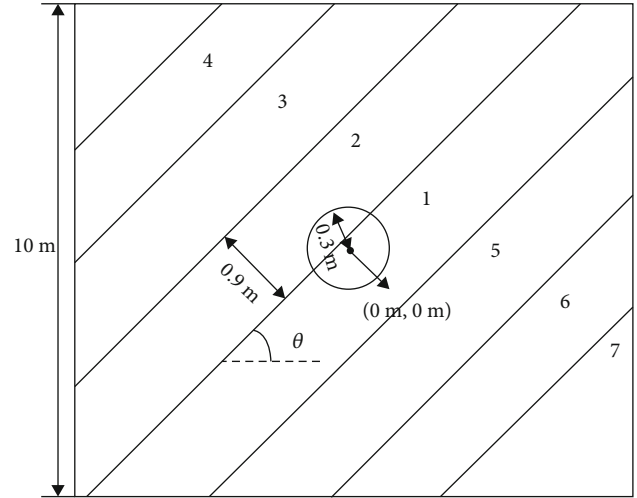


FIGURE 1: Geometry model.

TABLE 1: The mechanical parameters of the coal rock mass.

Parameter	Poisson's ratio	Frictional angle	Cohesion	Elasticity modulus	Tensile strength
Value	0.25	50°	2 MPa	10 GPa	0.3 MPa

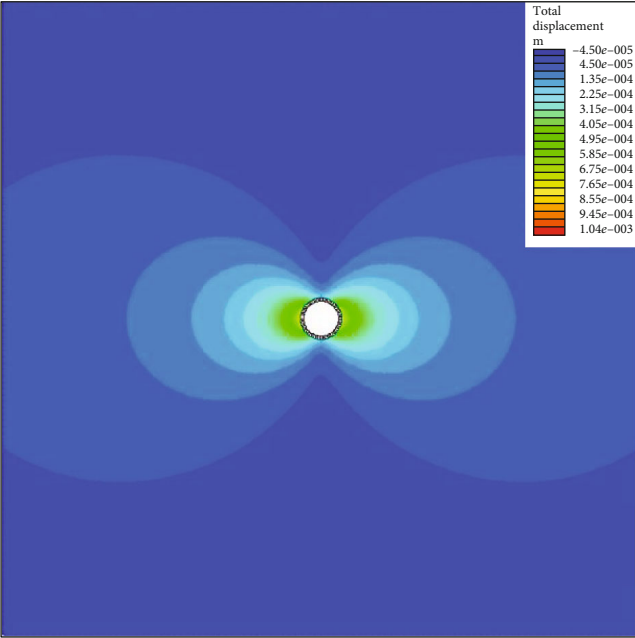
velocity distributions, and permeability change in the coal rock mass between two drilled boreholes and around the two boreholes [20].

As we know, the underlying mechanism of drilling-extraction is pressure relief. When a borehole is drilled in the coal rock mass, the stress will be released and the permeability of the coal mass is also changed as the deformation. Therefore, the stress and displacement may be the important indexes for describing the drilling effect. Meanwhile, there are many joints in the coal rock mass which may also impact the drilling effect. In this paper, a boundary element model of a borehole in jointed coal rock mass is established and simulated. The stress and displacement of the coal rock mass around the borehole is analyzed. The influence of the angles and number of joints on the stress and displacement field is discussed. The results can be a reference for borehole drilling evaluation of coal bed methane gas engineering.

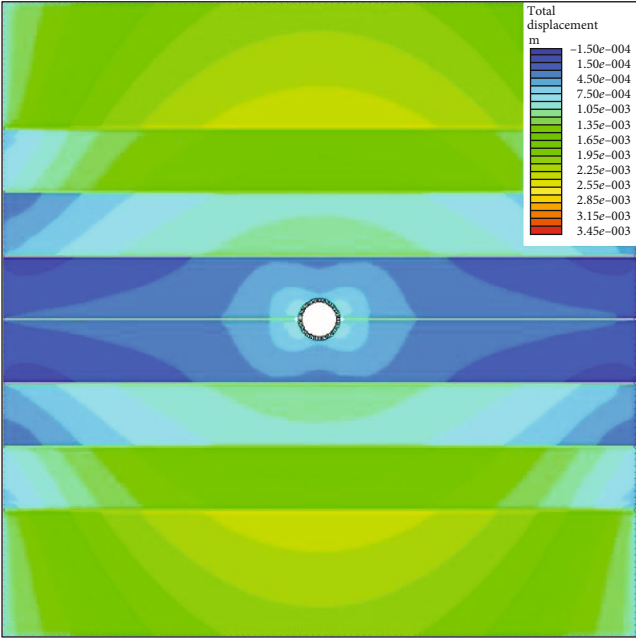
2. Model Establishment

The analysis domain is a $10\text{ m} \times 10\text{ m}$ square. The borehole is a circle with a radius of 0.3 m, and the center of the borehole is located at the point of (0, 0). The in situ stress in the horizontal direction is 10 MPa, and the in situ stress in the vertical direction is 17 MPa. As shown in Figure 1, there are 7 paralleled joints in a group. And the joint direction θ varies from 0° to 75° with the interval of 15° . The spacing of the joints in each group is about 0.9 m.

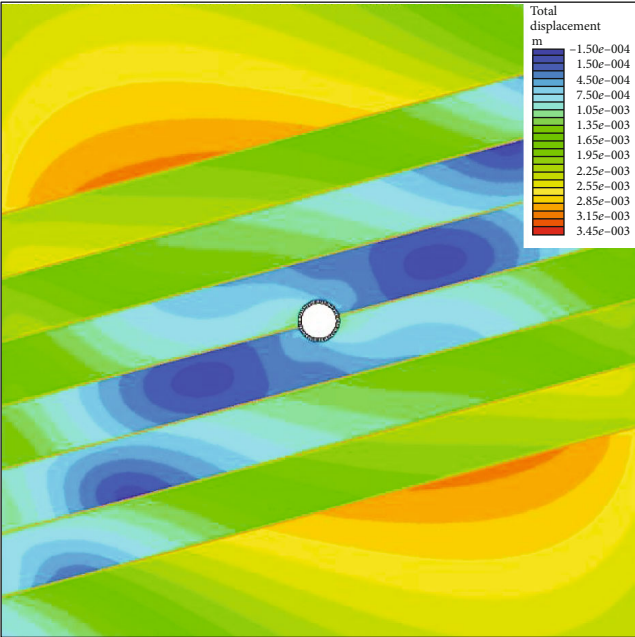
The mechanical parameters of the coal rock mass are listed in Table 1. The normal stiffness and the shear stiffness of the joint are assumed as 10000 MPa/m and 1000 MPa/m,



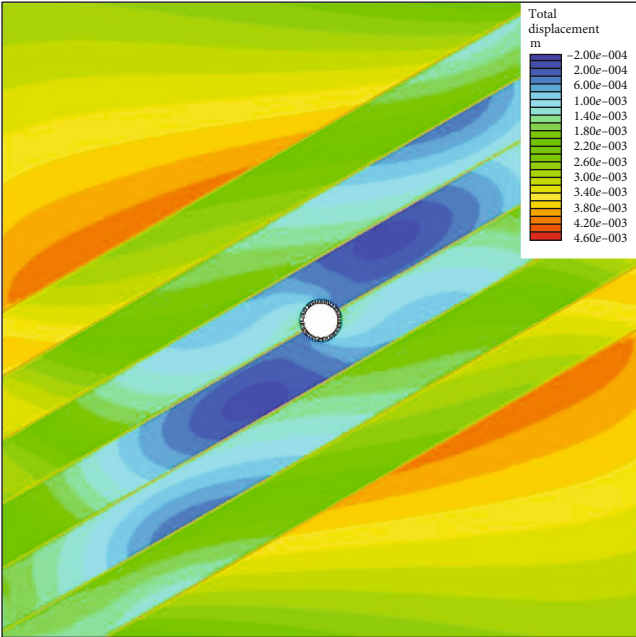
(a) Without joint



(b) Joint angle: 0°



(c) Joint angle: 15°



(d) Joint angle: 30°

FIGURE 2: Continued.

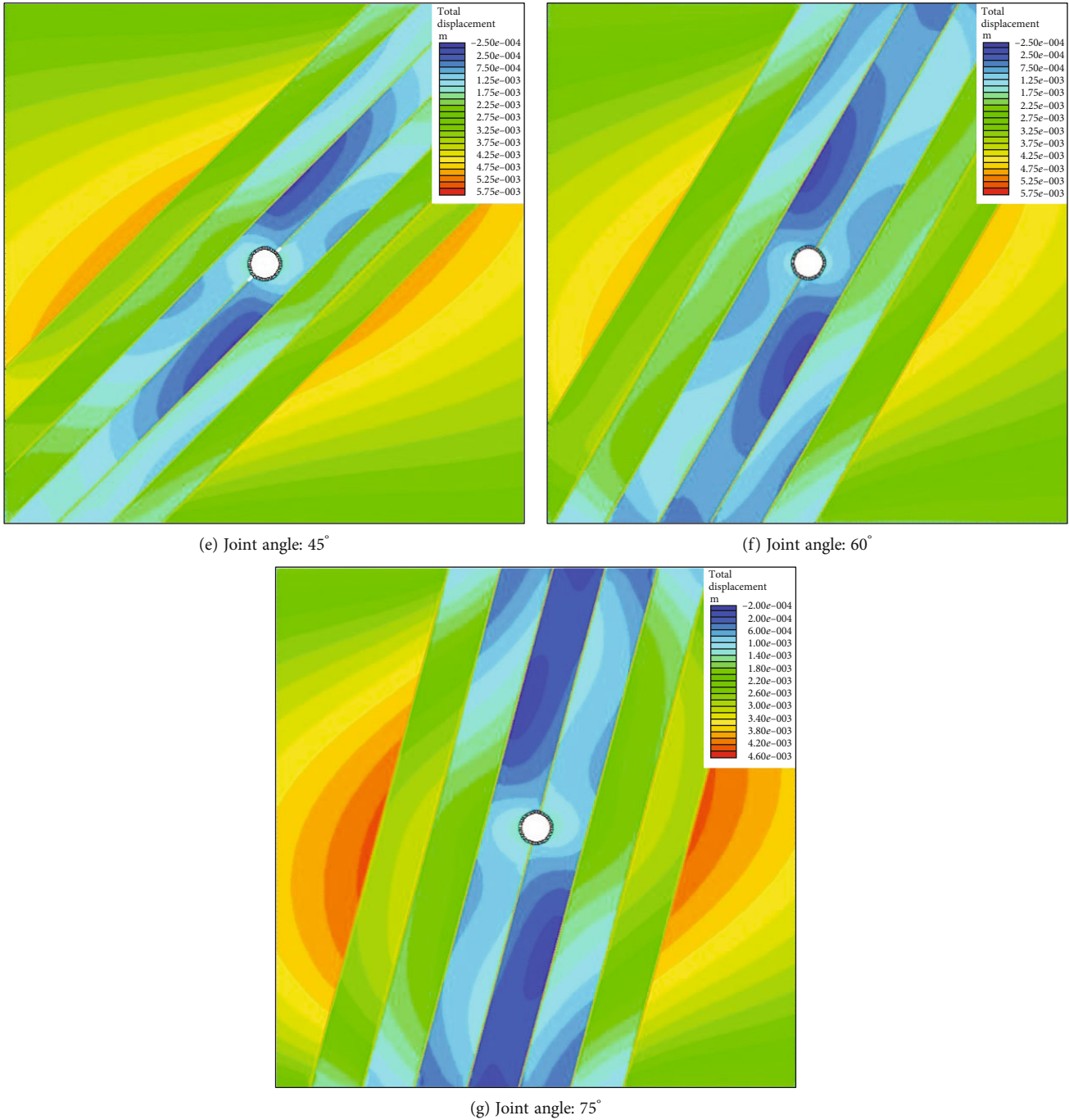


FIGURE 2: Displacement nephogram.

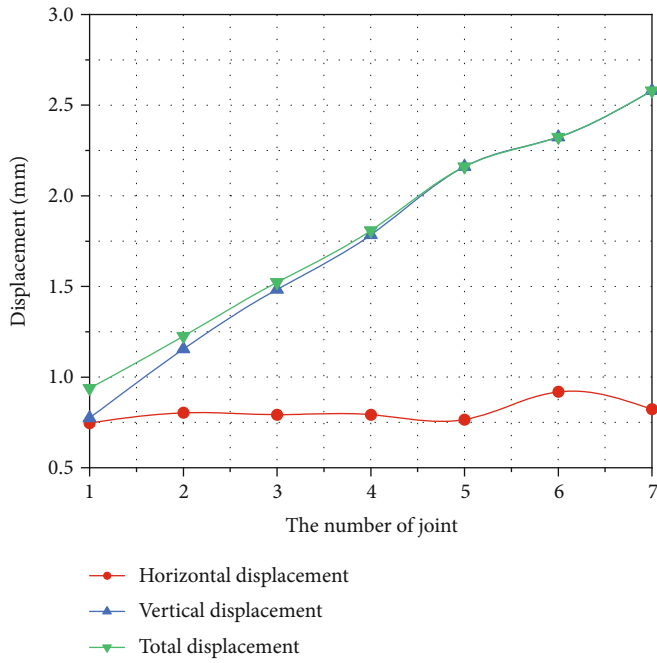
respectively. In this paper, the maximum stress and the maximum displacement are most concerned as such physical values may result in key issues that represent the drilling effect in practical engineering.

3. Analysis of the Numerical Results

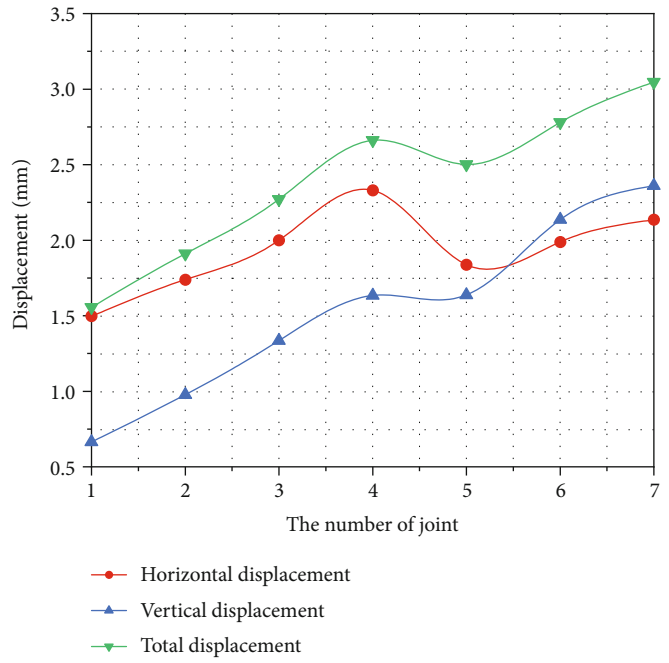
3.1. Displacement Field. As shown in Figure 2(a), the total displacement of the model is symmetric in vertical and horizontal directions as there is no joint distributed in the model. The maximum displacement occurs at the boundary

of the borehole. As shown in Figures 2(b)–2(g), compared with the model of Figure 2(a), the displacement field changes greatly under the effect of the joints. The position of the maximum displacement shifts from boundary of the borehole to the far field. The maximum displacement of the coal rock mass can be found around the No. 4 joint and No. 7 joint (Figure 1).

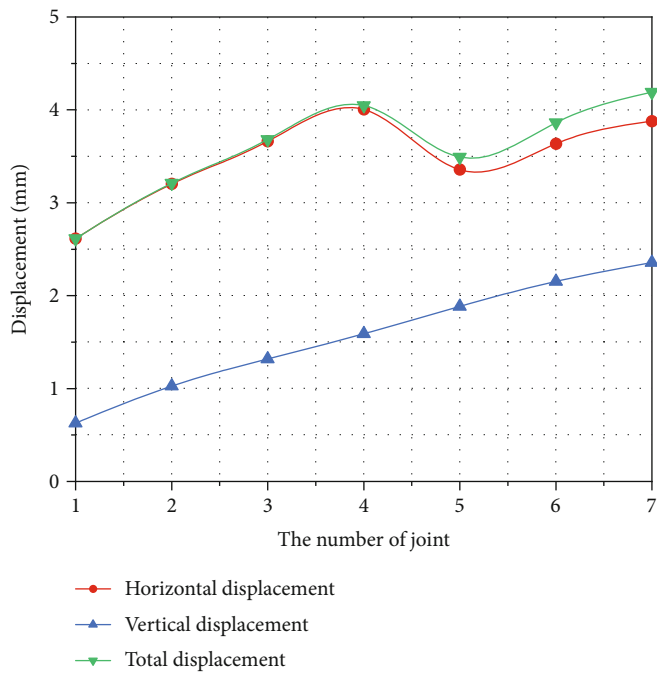
The max displacement is the maximum total displacement of the model under different conditions, including the horizontal displacement and the vertical displacement. The total displacement is the vector sum of the vertical



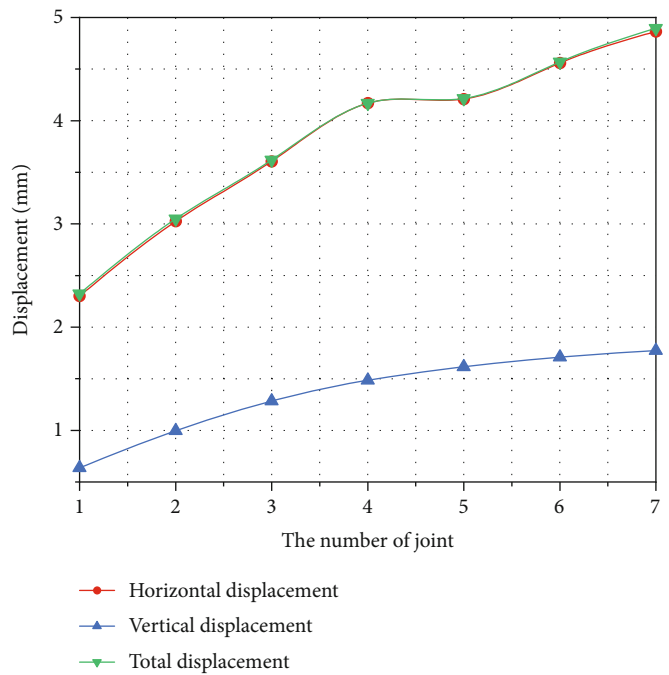
(a) Joint angle: 0°



(b) Joint angle: 15°



(c) Joint angle: 30°



(d) Joint angle: 45°

FIGURE 3: Continued.

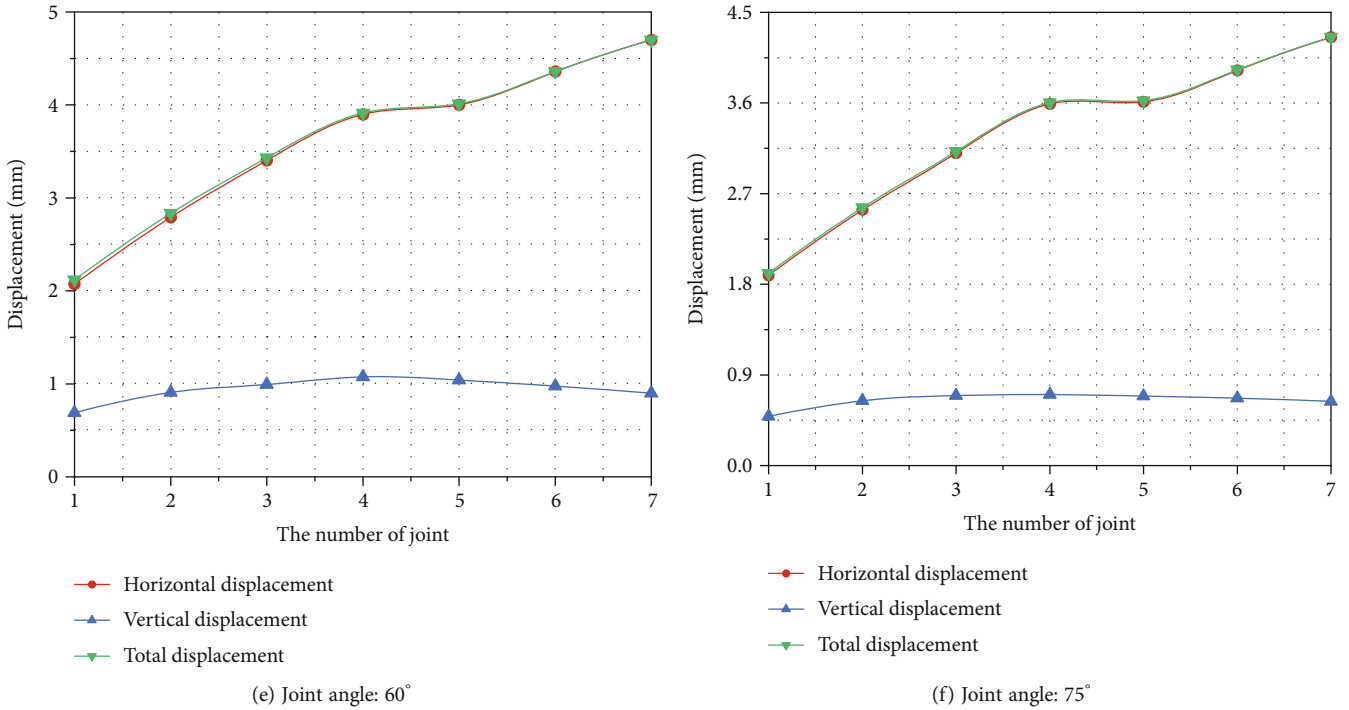


FIGURE 3: Variation of the displacement.

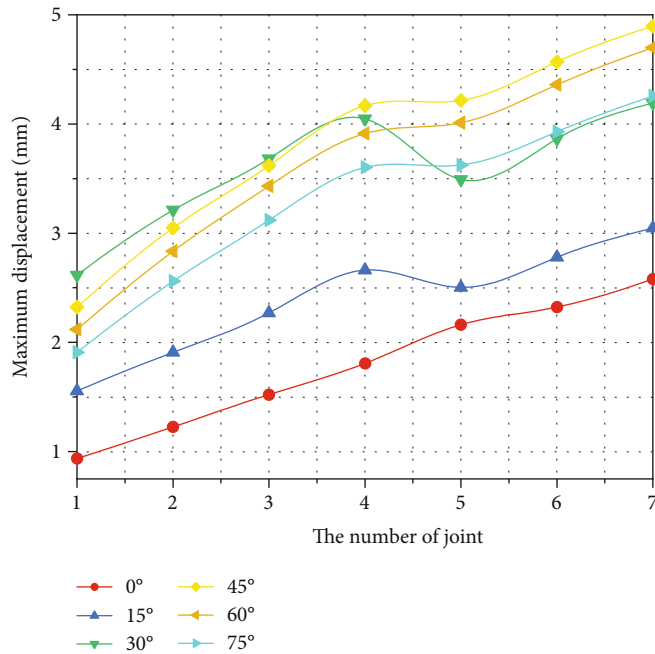
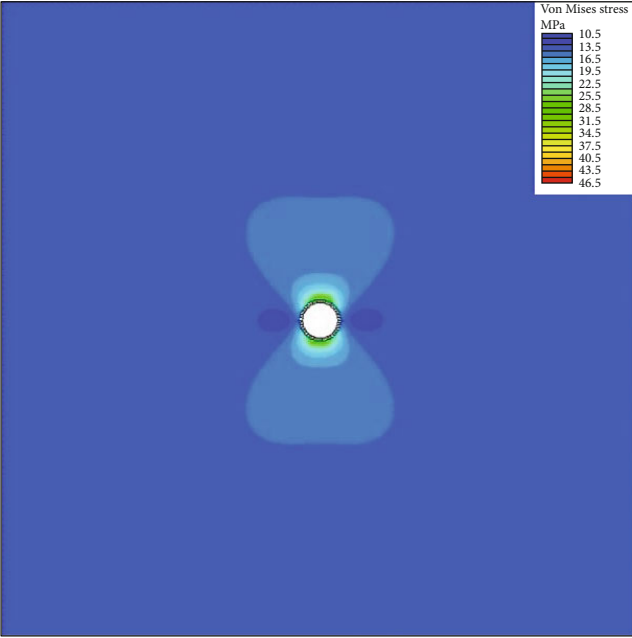


FIGURE 4: Maximum displacement with the number of joints.

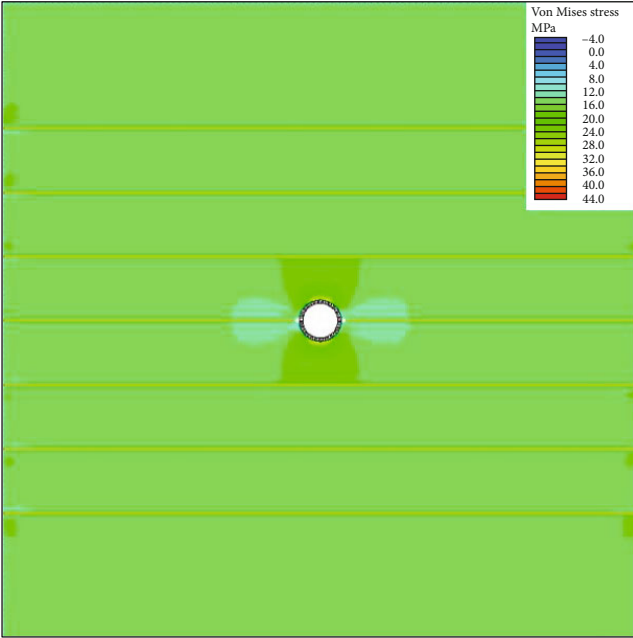
displacement and the horizontal displacement. As shown in Figure 3, the maximum displacement of the coal rock mass is impacted significantly by the number of joints as it has an entire trend of rapid increase rapidly with the number of joints. Meanwhile, it can be seen that there is a slight drop of the displacement when the joints distributed at 15° (Figure 3(b)) or 30° (Figure 3(c)). And the drop occurs when

the joint number rises by 4 to 5. It also can be found that the domination component of the maximum displacement gradually transits from vertical displacement to horizontal displacement as the joint angle varies from 0° to 75°.

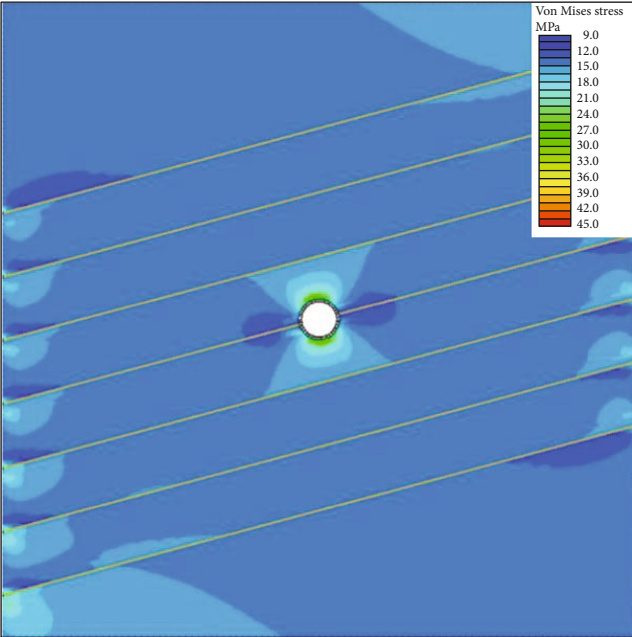
As shown in Figure 4, if the joint number is less than 4, the maximum displacement increases with the angle of the joint ($0^\circ \leq \text{joint angle} \leq 30^\circ$). However, the maximum



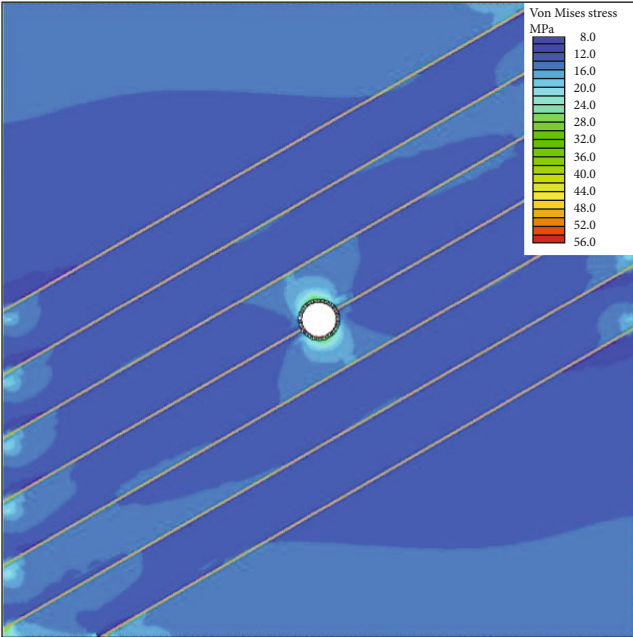
(a) Without joint



(b) Joint angle: 0°



(c) Joint angle: 15°



(d) Joint angle: 30°

FIGURE 5: Continued.

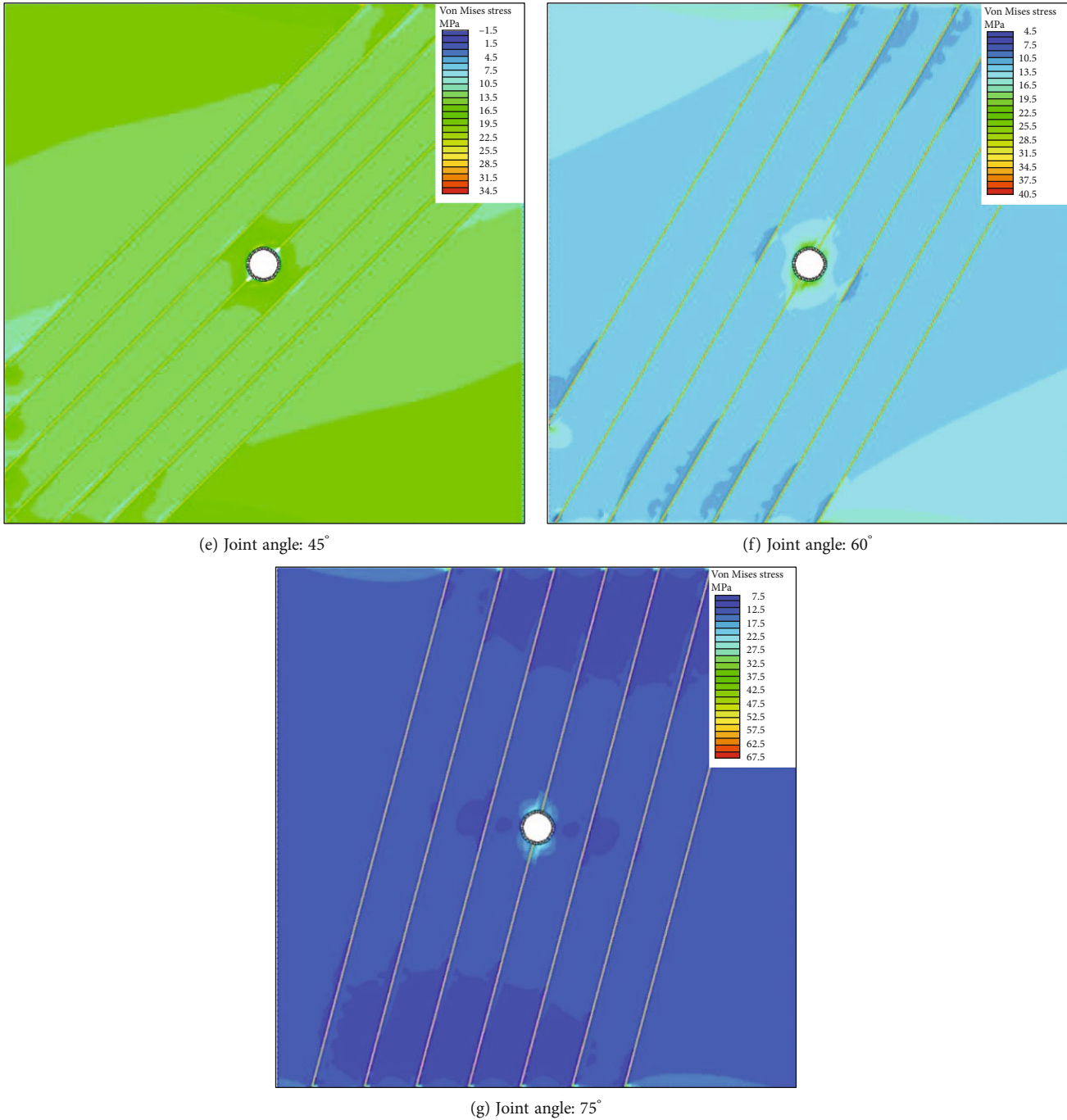


FIGURE 5: Von Mises stress nephogram.

displacement behaves in an opposite trend when the joint angle is larger than 30° , i.e., $30^\circ \leq \text{joint angle} \leq 75^\circ$. And it can be concluded that the displacement may reach a peak value when the joint angle is 30° if the joint number is less than 4.

3.2. Stress Field. As shown in Figure 5, the maximum von Mises stress is around the boundary of the borehole with any joint angle. It means that the joints have little effect on the position of the maximum von Mises.

As shown in Figure 6, the von Mises stress has a trend of increase with the number of joints when the joint angle is less than 30° , while it has a decreasing trend when the joint angle is larger than 30° . It also can be found that the stress generally decreases with the incline joints (joint angle $> 0^\circ$). In addition, the max stress may occur at the joint angle of 15° .

For each joint angle, the maximum shear stress of the joints is summarized in Table 2. The value in the table is calculated with the distribution of 7 joints for each joint angle. It can be seen that the maximum shear stress occurs mostly

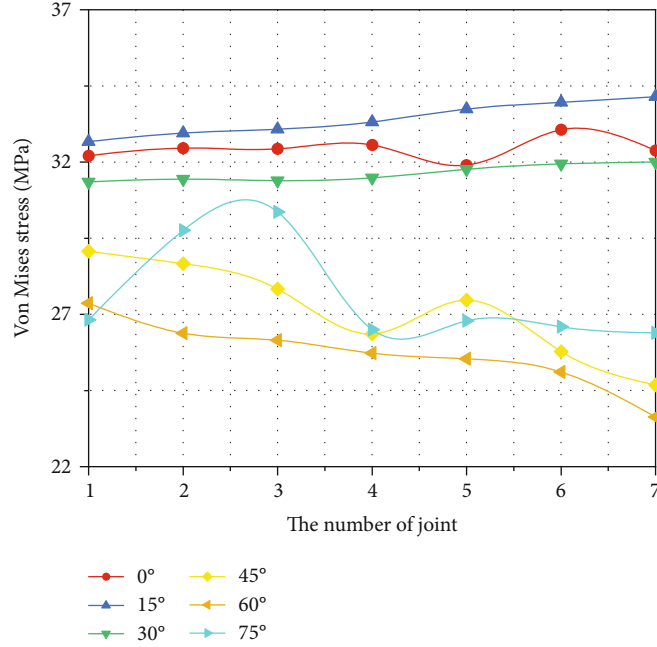


FIGURE 6: Maximum von Mises stress with the number of joints.

TABLE 2: Summary of the maximum shear stress of the joints (MPa).

Joint number	Joint angle					
	0°	15°	30°	45°	60°	75°
1						
2						
3			1.67			
4	0.32	1.22		1.61	1.50	1.01
5						
6			1.67			
7	0.32	1.22		1.61	1.50	1.01

in the No. 4 joint and the No.7 joint. When the joint angle is 30°, the maximum shear stress occurs in the No. 3 joint and the No. 4 joint. And it should be noted that the relationship between the shear stress and shear displacement is a linear relationship with one parameter, i.e., the shear stress divided by the shear stiffness is the shear displacement. Thus, the shear displacement is not listed in this paper. And it can be concluded that the maximum shear displacement occurs in the same position of the maximum shear stress. This indicates that the farther the joint is from the borehole, the joint behaves the greater the shear displacement.

3.3. Discussion. In Sections 3.1 and 3.2, the displacement field and the stress field are analyzed in the view of the joint angle and the number of the joints, while to get a well understanding of the evolution of such physical fields should be not only focused on the quantity that was affected by the joints but also focused on the position evolution.

Figure 7 is the plot of the occurrence of the maximum von Mises stress. As described in Section 3.2, the maximum von Mises in each distribution model of the joints may occur around the borehole. A, B, C, D, E, F, and G are denoted as the position that the maximum stress occurs. Besides, the relevant data is summarized in Table 3. It should be pointed that each model has a characteristic of symmetry, and the position may be not unique. Here, only one position for each model is listed.

It is obvious that all the position of the maximum von Mises stress occurs in the same position which is close to the borehole boundary. It means that such position does not change with the number of joints or the joint angle. This finding is not very reasonable as the joint angle varies. However, it can be found that the similarity in position or the same positions may be due to the computation element/unit size after a double check of the results obtained by software. Therefore, further exploration of the results is needed. And the refined results of the position are then obtained. The positions of the maximum von Mises stress and the displacement for each joint angle are plotted in Figure 8. A1 and A2 are the position that the maximum von Mises stress behaves. Similarly, B1 and B2 are the position that the maximum stress behaves.

Based on Figure 8, the symmetry of A1 and A2 (B1 and B2) can be observed. And in accordance with the current results, those positions are located around the borehole. In addition, it can be inferred from Figure 8 that the line between A1 and A2 is approximately perpendicular to the joint direction. The reexplored values of the maximum von Mises stress and the maximum displacement are listed in Tables 4 and 5. The trend of the stress and the displacement generally agrees with the results of Section 3.1 and Section 3.2 in terms of the joint angle and joint number.

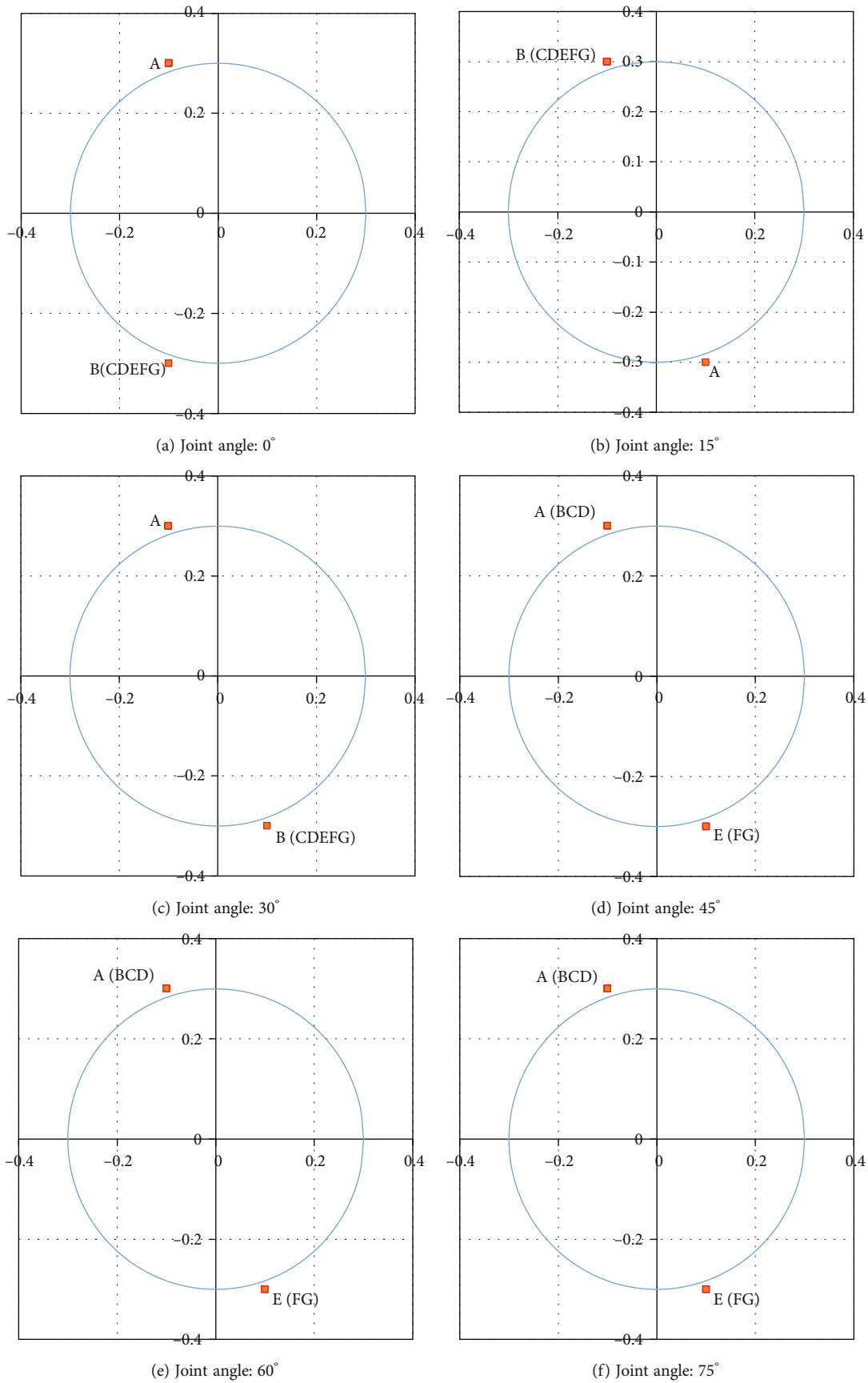


FIGURE 7: The position of the maximum von Mises stress.

TABLE 3: Summary of the maximum von Mises stress and the coordinates.

Joint angle	Parameter	A	B	C	D	E	F	G
0°	Stress (MPa)	32.2	32.5	32.40	32.6	31.9	33.1	32.4
	x, y (m)	-0.1, 0.3	-0.1, 0.3	-0.1, 0.3	-0.1, 0.3	-0.1, 0.3	-0.1, 0.3	-0.1, 0.3
15°	Stress (MPa)	32.7	33.0	33.1	33.3	33.7	34.0	34.1
	x, y (m)	0.1, -0.3	-0.1, 0.3	-0.1, 0.3	-0.1, 0.3	-0.1, 0.3	-0.1, 0.3	-0.1, 0.3
30°	Stress (MPa)	31.4	31.4	31.4	31.5	31.8	31.9	32.0
	x, y (m)	0.1, -0.3	-0.1, 0.3	-0.1, 0.3	-0.1, 0.3	-0.1, 0.3	-0.1, 0.3	-0.1, 0.3
45°	Stress (MPa)	29.1	28.7	27.8	26.4	27.5	25.8	24.7
	x, y (m)	-0.1, 0.3	-0.1, 0.3	-0.1, 0.3	-0.1, 0.3	0.1, -0.3	0.1, -0.3	0.1, -0.3
60°	Stress (MPa)	27.4	26.4	26.1	25.7	25.5	25.1	23.6
	x, y (m)	-0.1, 0.3	-0.1, 0.3	0.1, 0.3	0.1, 0.3	0.1, 0.3	0.1, 0.3	-0.1, 0.3
75°	Stress (MPa)	26.8	29.8	30.4	26.5	26.8	26.6	26.4
	x, y (m)	0.1, -0.3	-0.1, -0.3	-0.1, -0.3	-0.1, 0.3	0.1, -0.3	-0.1, 0.3	0.1, -0.3

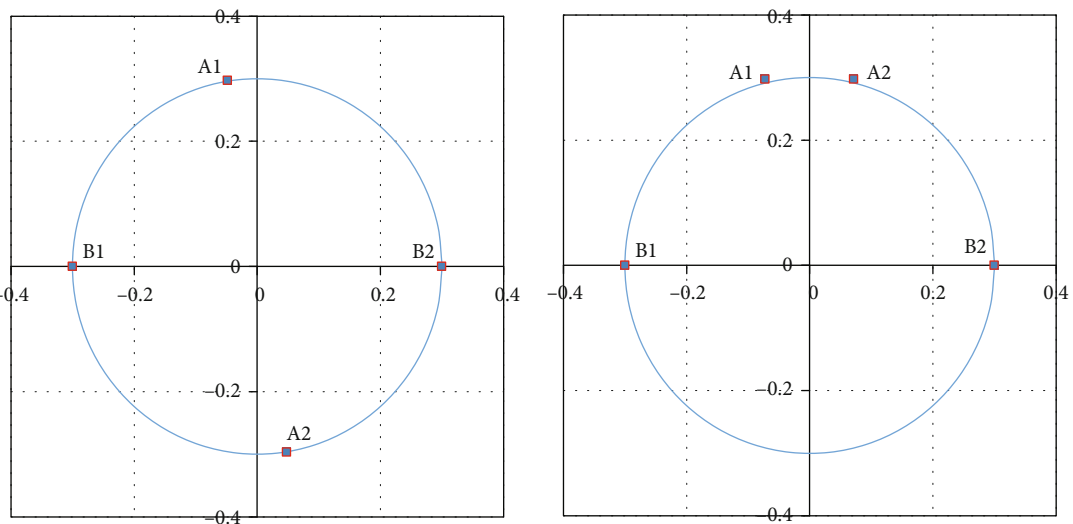
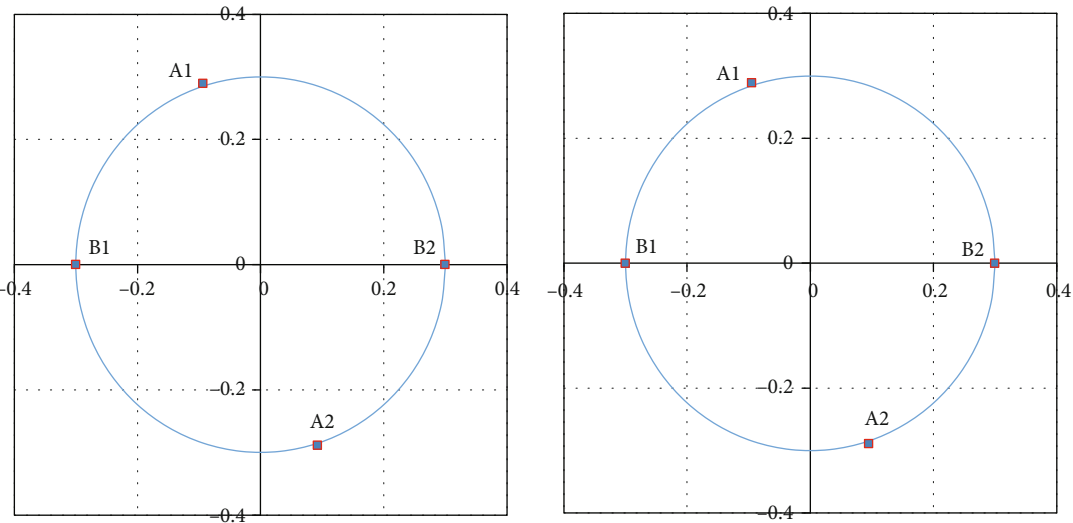
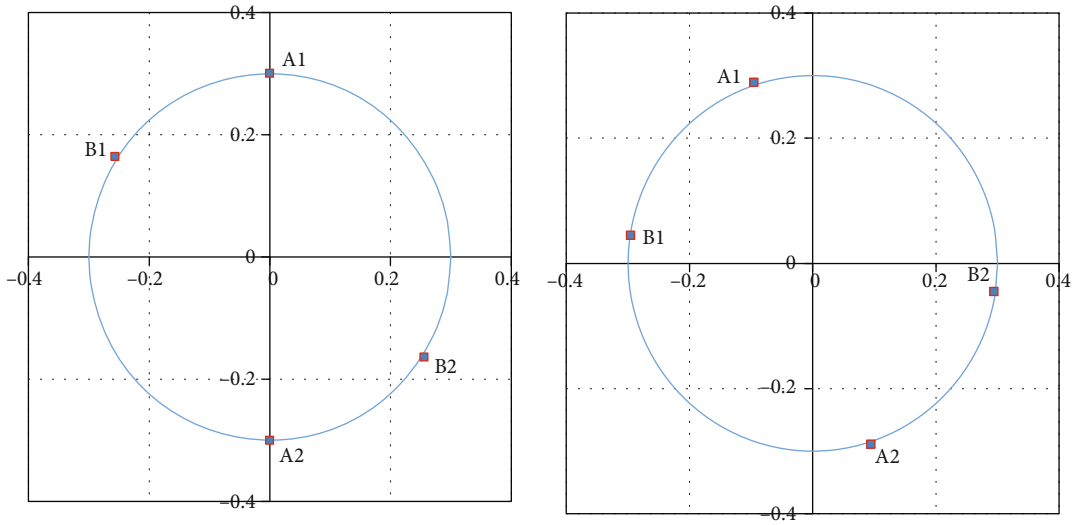


FIGURE 8: The reexplored position of the maximum von Mises stress and the maximum displacement.

TABLE 4: The maximum shear stress around the borehole (MPa).

Number of joints	Joint angle					
	0°	15°	30°	45°	60°	75°
1	33.6	33.0	31.6	29.3	27.5	27.0
2	33.6	33.0	31.4	28.3	26.4	28.6
3	33.2	33.1	32.0	27.8	25.8	27.1
4	33.3	33.0	31.8	26.5	25.3	26.6
5	32.7	33.9	32.2	27.7	24.8	27.0
6	32.8	34.2	32.1	26.0	24.0	26.8
7	32.5	34.6	32.4	24.9	23.8	26.5

TABLE 5: The maximum displacement around the borehole (mm).

Number of joints	Joint angle					
	0°	15°	30°	45°	60°	75°
1	0.95	1.5	2.4	2.4	2	1.9
2	1.1	1.9	3	3	2.8	2.7
3	1.5	2.6	3.8	3	3.4	3
4	1.8	2.6	3.8	3.8	3.8	3.4
5	1.9	1.9	1.9	2.9	2.8	2.6
6	1.4	1.7	2.4	2.8	2	1.8
7	1.2	1.2	1.8	1.5	1.3	1.4

4. Conclusions

Based on the boundary element, the numerical model of the coal rock mass with the distribution of the joints is established to study the influence of borehole drilling on the stress and displacement field. The parametric study is carried out in terms of the joint angle and the number of joints. The following conclusions can be obtained.

- (1) The maximum displacement increases with the number of joints. The position of the maximum displacement shifts from the boundary of the borehole to the far field. The maximum displacement of coal rock mass can be found around the No. 4 joint and No. 7 joint. There is a slight drop of the displacement when the joints are distributed at 15° or 30°. The displacement may reach a peak value when the joint angle is 30° and if the joint number is less than 4. The drop occurs when the joint number rises by 4 to 5. The domination component of the maximum displacement gradually transits from vertical displacement to horizontal displacement as the joint angle varies from 0° to 75°
- (2) The von Mises stress has a trend of increase with the number of joints when the joint angle is less than 30°. It has a decreasing trend when the joint angle is larger than 30°. Such stress generally decreases with the incline joints (joint angle > 0°). The maximum von Mises stress may occur at the joint angle of 15°. The maximum shear stress occurs mostly in

the No. 4 joint and the No.7 joint. When the joint angle is 30°, the maximum shear stress occurs in the No. 3 joint and the No. 4 joint

- (3) The overlap of the position of the maximum von Mises stress or the maximum displacement with different joint angles or different numbers of joints leads to a reexploration of such positions. The position of the maximum von Mises stress and the maximum displacement is relatively steady, which locates symmetrically around the borehole. The line between the points that behaves as the maximum von stress is approximately perpendicular to the joint direction

Data Availability

The data used to support the findings of this study are available from the first author upon request.

Conflicts of Interest

The authors declare that they have no conflicts of interest.

Acknowledgments

This project is supported by the National Natural Science Foundation of China (Nos. 52078477 and 51827901), Key Laboratory of Deep Earth Science and Engineering (Sichuan University), Ministry of Education (DESE202106 and DESE202004), and Guangdong Provincial Key Laboratory of Deep Earth Sciences and Geothermal Energy Exploitation and Utilization (2020-3).

References

- [1] Q. Wang and X. Jin, "Key technologies of directional drilling construction for gas extraction and pressure relief in protective layer mining," *Coal Engineering*, vol. 53, no. 5, pp. 63–67, 2021.
- [2] Q. J. Liu, "Exploring green governance gas model with "using to promote pumping "," *Coal Technology*, vol. 37, no. 12, pp. 169–171, 2018.
- [3] H. J. Duan and S. J. Hao, "Application of gas drainage technology for high-position borehole with large diameter in extremely thick coal seam mining area," *Exploration Engineering (Rock & Soil Drilling and Tunneling)*, vol. 40, no. 12, pp. 40–42, 2013.
- [4] M. Gao, J. Xie, Y. Gao et al., "Mechanical behavior of coal under different mining rates: a case study from laboratory experiments to field testing," *International Journal of Mining Science and Technology*, vol. 31, 2021.
- [5] J. W. Yan, X. B. Zhang, and Z. M. Zhang, "Research on geological control mechanism of coal-gas outburst," *Journal of China Coal Society*, vol. 38, no. 7, pp. 1174–1178, 2013.
- [6] Y. He and Y. F. Xu, "Investigation and analysis of drainage effect of large diameter pressure relief borehole through layer," *Scientific and Technological Innovation*, vol. 18, pp. 156–158, 2021.
- [7] Z. K. Yang, Z. H. Cheng, and Y. Q. Liu, "Influence of multiple mining of outburst coal seam group on gas extraction of cross-

- layer borehole,” *China Safety Science Journal*, vol. 30, no. 5, pp. 66–73, 2020.
- [8] G. Q. Ma, R. Z. Cheng, and G. Cui, “Gas comprehensive control technology of upper protective seam in contiguous outburst seams,” *Coal Science and Technology*, vol. 43, no. 3, pp. 52–55, 2015.
- [9] C. H. Ji, “Application and practice of coal-gas co-extraction technology by floor drainage roadway in single low-permeability outburst seam,” *Mining Safety & Environmental Protection*, vol. 42, no. 3, pp. 86–98, 2015.
- [10] N. Zhao, G. L. Dai, and R. Zhang, “Practice on gas control technology of floor drainage gateway with two uses,” *Coal Science and Technology*, vol. 42, no. 2, pp. 44–46, 2014.
- [11] X. Z. Tong, H. Wen, X. J. Cheng et al., “Characteristics of pressure relief gas extraction in the protected layer by surface drilling in Huainan,” *Advances in Civil Engineering*, vol. 2021, 11 pages, 2021.
- [12] Z. J. Wang, “Optimum surface drilling gas drainage technique based on “O” ring theory,” *Coal Mining Technology*, vol. 22, no. 5, pp. 96–101, 2017.
- [13] F. X. Lian, “Completion technology of surface gas extraction wells,” *Coal Geology & Exploration*, vol. 40, no. 6, pp. 29–38, 2012.
- [14] P. Liu, J. Y. Fan, D. Y. Jiang, and J. Li, “Evaluation of underground coal gas drainage performance: mine site measurements and parametric sensitivity analysis,” *Process Safety and Environmental Protection*, vol. 148, pp. 711–723, 2021.
- [15] J. G. Wu, “Integrated technology of coalbed methane drainage with ground well in Luling coal mine,” *Coal Geology & Exploration*, vol. 1, pp. 27–29+33, 2008.
- [16] D. D. Chen, W. R. He, S. R. Xie, F. He, Q. Zhang, and B. Qin, “Increased permeability and coal and gas outburst prevention using hydraulic flushing technology with cross-seam borehole,” *Journal of Natural Gas Science and Engineering*, vol. 73, article 103067, 2019.
- [17] G. Z. Hu, W. R. He, and M. Sun, “Enhancing coal seam gas using liquid CO₂ phase-transition blasting with cross-measure borehole,” *Journal of Natural Gas Science and Engineering*, vol. 60, pp. 164–173, 2018.
- [18] Y. Gao, G. Dong, H. Wang, and X. Chang, “Slotting effect on pressure relief during gas drainage of low permeability coal,” *Thermal Science*, vol. 23, no. 3 Part A, pp. 1547–1553, 2019.
- [19] P. Wei, S. W. Huang, X. Li, S. Peng, and Y. Lu, “Numerical simulation of boreholes for gas extraction and effective range of gas extraction in soft coal seams,” *Energy Science & Engineering*, vol. 7, no. 5, pp. 1632–1648, 2019.
- [20] D. Zhao, J. Liu, and J. T. Pan, “Study on gas seepage from coal seams in the distance between boreholes for gas extraction,” *Journal of Loss Prevention in the Process Industries*, vol. 54, pp. 266–272, 2018.

Research Article

Coupling Effect of Strain Rate and Freeze-Thaw Temperature on Dynamic Mechanical Properties and Fractal Characteristic of Saturated Yellow Sandstone

Peng Wu ^{1,2}, Lianying Zhang ¹, Xianbiao Mao², Yanlong Chen ², Ming Li², Liang Chen,³ and Lan Wang⁴

¹Civil Engineering Department, Xuzhou Institute of Technology, Xuzhou, China 221000

²State Key Laboratory for Geomechanics and Deep Underground Engineering, China University of Mining & Technology, Xuzhou, China 221116

³State Key Laboratory of Coal Resources and Safe Mining, China University of Mining and Technology, Xuzhou 221116, China

⁴School of Mechanics and Civil Engineering, China University of Mining and Technology, Xuzhou 221116, China

Correspondence should be addressed to Lianying Zhang; zhanglianying@126.com and Yanlong Chen; chenyanlong@cumt.edu.cn

Received 22 June 2021; Accepted 31 August 2021; Published 26 September 2021

Academic Editor: Yu Wang

Copyright © 2021 Peng Wu et al. This is an open access article distributed under the Creative Commons Attribution License, which permits unrestricted use, distribution, and reproduction in any medium, provided the original work is properly cited.

Strain rate is not only an important influence factor for deformation property but also an important parameter for analyzing the dynamic mechanical behavior of rock material. In this study, the dynamic compressive mechanical properties of saturated yellow sandstone at four strain rates and six freeze-thaw temperatures are investigated by using the SHPB test system. The coupling effect of strain rate and freeze-thaw temperatures on the mechanical parameters of rock material are discussed in detail, and the relationship formula of peak strain and dissipated energy with strain rate and freeze-thaw temperature are also established. Finally, the fractal dimension characteristic of fracture specimens with the strain rate and temperature are analyzed by using the fractal dimension method. The research results indicate that (1) with the increase of strain rate, the increase speed of peak strain, peak strength, and dissipated energy at medium strain rate level was obviously higher than that at high strain rate level, indicating that the strain rate effect weakened at high strain rate. (2) Freeze-thaw temperature can improve the brittleness-ductile transformation rate of saturated specimens. (3) According to the strain rate sensitivity coefficient, at room temperature, the strain rate effects on peak strain and peak strength are weakest, while at $-20^{\circ}\text{C} \sim -30^{\circ}\text{C}$, they are most significant. In addition, the strain rate effect on dissipated energy is significant at room temperature, while weakest at -30°C . (4) The fractal dimension gradually increases with strain rate increasing or freeze-thaw temperature decreasing, indicating that the freeze-thaw environment has a positive function for increasing the damage and fracture degree of specimens for saturated specimen. Our research results can provide an extremely important theoretical basis for the dynamic disaster prevention and structural design of rock engineering in cold regions.

1. Introduction

The dynamic mechanical properties of rock material are an extremely important evaluation index for rock structural engineering stability, such as tunnel excavation, blasting engineering, mining excavation, and oil drilling engineering. Therefore, the structural design and stability assessment of underground engineering need to take the dynamic mechanical properties of rock material into account for preventing

the impact of earthquake and impact load on the structure strength [1, 2]. Strain rate is an extremely effective parameter which can reflect the deformation and dynamic mechanical behaviors of rock materials. Meanwhile, the mechanical properties of rock material are closely related to the strain rate [3–5]. According to the amplitude, it can be divided into the low strain rate (10^{-5} – 10^{-2} s^{-1}), medium strain rate (10^{-2} – 10^2 s^{-1}), high strain rate (10^2 – 10^4 s^{-1}), and ultrahigh strain rate (more than 10^4 s^{-1}) [2, 6–8]. In the lower strain rate range, the material strength

parameter gradually increases with the increase of strain rate, while rapidly increases under the medium strain rate condition. At the high or ultrahigh strain rate level, the strain rate effect of the material strength parameter becomes weak again [9]. The split Hopkinson pressure bar (SHPB) system, as the most commonly used and stable dynamic test device, has been widely used to obtain the dynamic mechanical properties of rock or rock-like materials at the high strain rate. In fact, the strain rate effect of various rock-like materials, e.g., concrete, earth-rock aggregate, and rock, have been investigated and achieved fruitful research results by experimental and numerical simulation methods [10–17]. However, the dynamic mechanical properties of rock materials are not only related to the strain rate but also closely related to the freeze-thaw (F-T) effect. The coupling influence of temperature and impact loading was ignored in the above investigation.

In fact, many rock engineering techniques in cold regions, such as highway construction, open-pit slope stability, and roadway and tunnel excavation, are concerned with the freeze-thaw problem of rock materials. Hence, the design of these engineering must fully take the impact of freeze-thaw effect on rock mechanical properties into account. At present, a lot of studies have been carried out on the freeze-thaw effect of rock materials under static or dynamic loading conditions [18–25]. However, the above works were mainly limited to static or dynamic mechanical investigation by considering the effect of freeze-thaw cycle times at different strain rates or freeze-thaw temperatures at low or medium strain rate. This does not reveal the influence of freeze-thaw temperature on the dynamic impact mechanical properties of rock materials subjected to the high strain rate loading condition.

In addition, the fragmentation distribution characteristic of specimens after impact loading are also an extremely important index for evaluating the damage degree of rock materials by statistical or fractal methods. A large number of investigations related to the failure characteristics of rock materials have been carried out at different strain rates, stress state, high temperatures, or freeze-thaw effect [9, 26–28]. However, few reports about the coupling effect of the medium-high strain rate and freeze-thaw temperature on dynamic fracture characteristics have been published in literature. In this paper, we mainly focus on the following two issues for detailed discussion:

- (1) How does the strain rate affect the dynamic mechanical properties of rock materials subjected to different freeze-thaw temperatures and whether the strain rate hardening effect still exists?
- (2) How do the strain rate and freeze-thaw temperature affect the fracture degree of specimens?

Based on the above proposed problems, the dynamic compressive test of saturated yellow sandstone is carried out under different strain rates and temperatures. Then, the coupling effect of strain rate and freeze-thaw temperatures on the dynamic mechanical behaviour of rocks are analyzed in detail and the expression formula of dynamic

mechanical parameters related to temperature and strain rate are also deduced in Section 3. Finally, after the impact test, we collected the fragments of saturated yellow sandstone and analyzed its fractal characteristic by using the fractal dimension calculation method. Our research results can provide an extremely important theoretical basis for the dynamic disaster prevention and structural design of rock engineering in cold regions.

2. Experimental

2.1. Material Preparation. In this study, the test rock material was yellow sandstone, gathered from the Haerwusu open-pit coal mine (Figure 1) located in Inner Mongolia Autonomous Region, China. The main mineral contents were 54% albite, 19.9% quartz, 17.4% anorthoclase, 5.8% laumontite, and 2.9% santafite. The sandstone specimens were taken from the same block and cut into cylinders 50 mm in diameter and 25 mm in height with errors less than 0.05 mm in height and 0.02 mm in diameter [9]. Then, the nondestructive ultrasonic P-wave velocity tests carried out in specimen indicated that the yellow sandstone materials exhibit an obvious isotropic behavior. Its P-wave and density were, respectively, 1.58 km/s and 2287 kg/m³ with the average uniaxial compressive strength of 50.89 MPa, elastic modulus 5.67 GPa, and Poisson's ratio 0.22.

2.2. Testing Equipment. The main testing equipment included the freeze-thaw testing system, SHPB testing system, and particle size screening device for separating fragment. Firstly, the JC-ZDR-5 freeze-thaw testing machine was used to treat the saturated yellow sandstone materials with eight freeze-thaw cycles under normal temperature (25°C) and low temperatures (-5°C, -10°C, -15°C, -20°C, and -30°C). Then, an impact loading test was carried out on a 50 mm diameter SHPB test system, which consists of the loading drive system, pressure bar system, energy absorption system, and signal acquisition system, as shown in Figure 2. During the impact test, the striker bar could obtain different impact speeds by adjusting the air pressure produced by high-pressure nitrogen tank, and then, the striker bar collided with the incident bar with the occurrence of incident plus or stress plus in the incident bar which would be transmitted to the free end of the rock specimen. Some incident pulses were returned to the incident bar as reflected pulse, while others were transmitted to the transmission bar as a transmitted pulse. All of the stress plus information in the two bars would be recorded into a signal acquisition system by the strain gauge on the elastic compression bar. In this study, the elastic modulus and wave velocity of incident bar and transmission bar are, respectively, 210 GPa and 5450 m/s with the length 25 mm and diameter 50 mm of incident bar. After the impact test, the particle size screening device was used to research the fractal characteristic of the fragment by using the fractal dimension method.

2.3. Testing Procedure. In this study, the specific test procedures (Figure 2) were as follows:

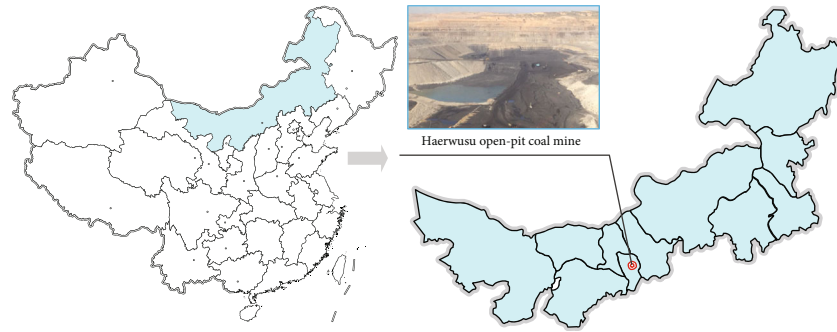


FIGURE 1: Sampling location.

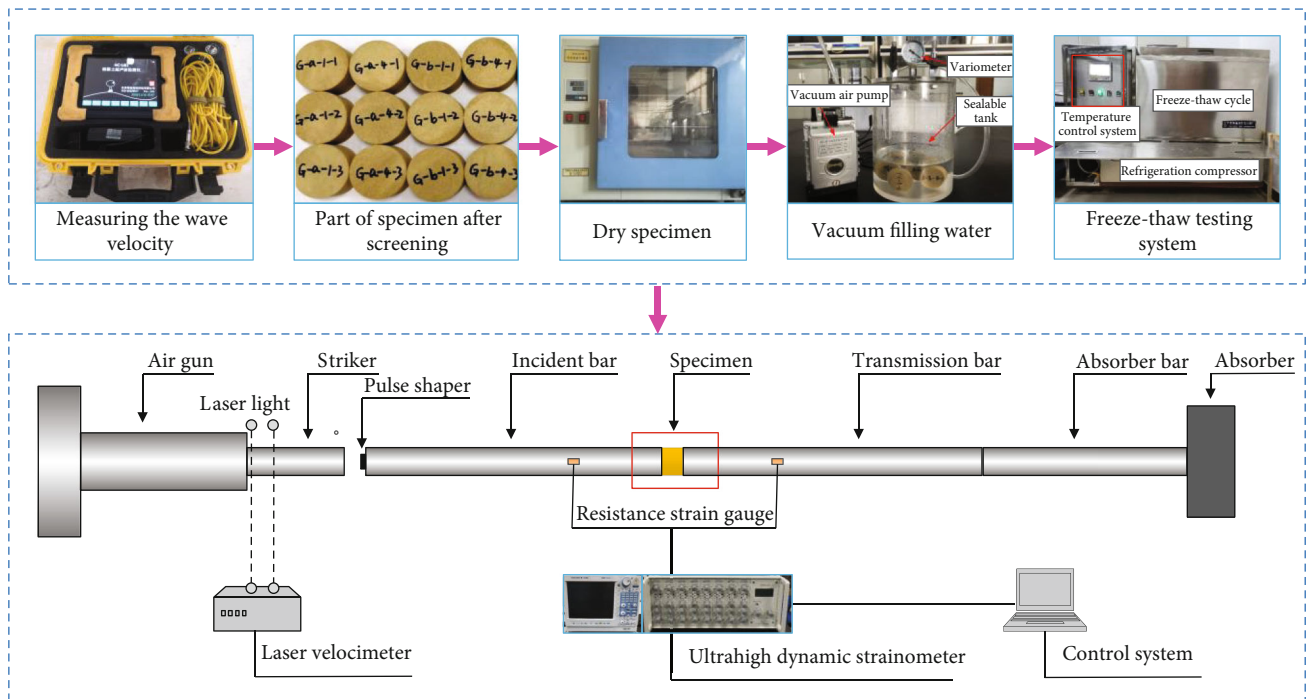


FIGURE 2: Structure characteristic of the SHPB and testing procedure.

- (1) The saturated experimental procedures: the P-wave velocity of nature specimen was firstly monitored. The specimens with the same P-wave velocity (approximately 1580 m/s) were selected to be dried in an incubator for 24 hours at 105°C. Next, the selected specimens were placed in the vacuum pumping saturation system (VPSS) to extract gas with water injection for 12 hours until the bubble-free overflow from the surface of the specimen. Then, the air pressure was adjusted in the sealed tank to the atmospheric pressure and kept for 12 hours. When the quality change of the specimen was less than 0.01 g per hour, it can be considered that it has reached the water saturation state
- (2) The freeze-thaw cycle test procedures: firstly, the saturated yellow sandstone specimens were taken out from the sealed tank. In order to eliminate the effect of moisture content, the saturated yellow sandstone

specimens with the same moisture content were selected as the test specimens and divided into 24 groups with five specimens of each group. The average saturated moisture content was about 5.71%. Then, the saturated specimens were placed in the freeze-thaw cycle tank and frozen to different temperatures (25°C, -5°C, -10°C, -15°C, -20°C, and -30°C) with eight freeze-thaw cycles. In addition, the temperature-fall stage, freezing stage, temperature-rise stage, and thawing stage lasted for 2 h, 6 h, 1 h, and 6 h, respectively; the total time of one freeze-thaw cycle is 15h. The temperature history curve of the freeze-thaw experiments is displayed in Figure 3

- (3) The impact load test procedures: the specimen was placed between the incident bar and transmission bar; the two ends of which were coated with the vaseline to reduce the friction effect at the specimen-

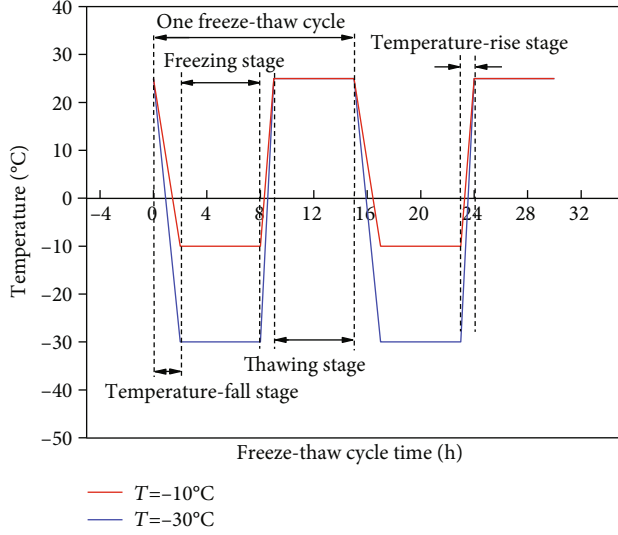


FIGURE 3: Temperature profile of the yellow sandstone specimens undergoing the F-T cycle.

incident bar or specimen-transmission bar interface. Then, an impact gas pressure (0.2~0.35 MPa) were, respectively, applied to the saturated specimens at the same temperatures to produce different strain rates. The average strain rate ranges of saturated yellow sandstone in this study were from 74.22 s^{-1} to 169.41 s^{-1} . In this experiment, there were 6 groups of temperature and 4 groups of strain rate. A total of 24 groups of experiments were combined in pairs, and each experiment was repeated 5 times

- (4) After the impact test, the fragments of specimens were collected and divided into different particle size ranges by using a classifying screen. Then, the fragment mass in different particle size ranges was measured, and the fractal characteristics were analyzed to reflect the coupling effect of freeze-thaw temperature and strain rate on the damage degree of saturated yellow sandstone

2.4. Data Processing

2.4.1. Dissipated Energy Calculation Process. Based on the one-dimensional stress wave theory and the uniform stress assumption, the stress $\sigma(t)$, strain $\varepsilon(t)$, and strain rate $\dot{\varepsilon}(t)$ of each specimen can be calculated by using three-wave analysis methods [2, 24].

$$\begin{cases} \dot{\varepsilon} = \frac{C_s}{l_s} [\varepsilon_i(t) - \varepsilon_r(t) - \varepsilon_t(t)], \\ \varepsilon = \frac{C_s}{l_s} \int_0^t [\varepsilon_i(t) - \varepsilon_r(t) - \varepsilon_t(t)] dt, \\ \sigma = \frac{A_0 E_0}{2A_s} [\varepsilon_i(t) + \varepsilon_r(t) + \varepsilon_t(t)], \end{cases} \quad (1)$$

where $\varepsilon_i(t)$, $\varepsilon_r(t)$, and $\varepsilon_t(t)$, respectively, represent the

strain signals of the incident wave, the reflected wave, and the transmitted wave; E_0 , A_0 , and C_s are, respectively, Young's modulus, the cross-sectional area, and the elastic wave speed of the bar; l_s and A_s are the height and the cross-sectional area of the specimen, respectively; and t is the duration time of elastic wave.

Then, the incident energy W_i , reflected energy W_r , and transmitted energy W_t can be calculated by

$$W_j = \frac{A_0 C_s}{E_0} \int_0^t \sigma_j^2 dt \quad j = i, r, t, \quad (2)$$

where $\sigma_i(t)$, $\sigma_r(t)$, and $\sigma_t(t)$, respectively, represent the stress of incident wave, reflected wave, and transmitted wave.

In the SHPB test, the incident energy (W_i) caused by the impact between the striker bar and incident bar can be treated as the total energy input to the system, which mainly includes four parts [24]. The energy reflected to the incident bar (reflected energy, W_r), the energy transferred to the transmitted bar (transmitted energy, W_t), the energy absorbed by the specimens (dissipated energy (DE), W_s), and the energy lost at the specimen-incident and specimen-transmitted bar interfaces due to the friction effect, which accounted for a very small proportion, can be ignored. Hence, the energy dissipation W_s can be expressed as

$$W_s = W_i - W_r - W_t. \quad (3)$$

2.4.2. Definition of Strain Rate Sensitivity Coefficient. In order to more clearly and effectively describe the strain rate effect of dynamic compression mechanical properties of saturated yellow sandstone under different low temperatures, the strain rate sensitivity coefficient of peak strength, peak strain, elastic modulus, and energy dissipation were defined as follows [2]:

$$\begin{cases} \gamma_\sigma = \frac{\sigma_2 - \sigma_1}{\dot{\varepsilon}_2 - \dot{\varepsilon}_1}, \\ \gamma_\varepsilon = \frac{\varepsilon_2 - \varepsilon_1}{\dot{\varepsilon}_2 - \dot{\varepsilon}_1}, \\ \gamma_E = \frac{E_2 - E_1}{\dot{\varepsilon}_2 - \dot{\varepsilon}_1}, \\ \gamma_W = \frac{W_{s2} - W_{s1}}{\dot{\varepsilon}_2 - \dot{\varepsilon}_1}, \end{cases} \quad (4)$$

where γ_σ , γ_ε , γ_E , and γ_W are the strain rate sensitivity coefficient of peak strength, peak strain, elastic modulus, and energy dissipation, respectively. $\dot{\varepsilon}_2$ and $\dot{\varepsilon}_1$ represent the maximum and minimum value of strain rates at each low temperature. σ , ε , E , and W_s are the corresponding peak stress, peak strain, elastic modulus, and dissipated energy of specimens, respectively. The larger the strain rate sensitivity coefficient is, the more significant the strain rate effect is.

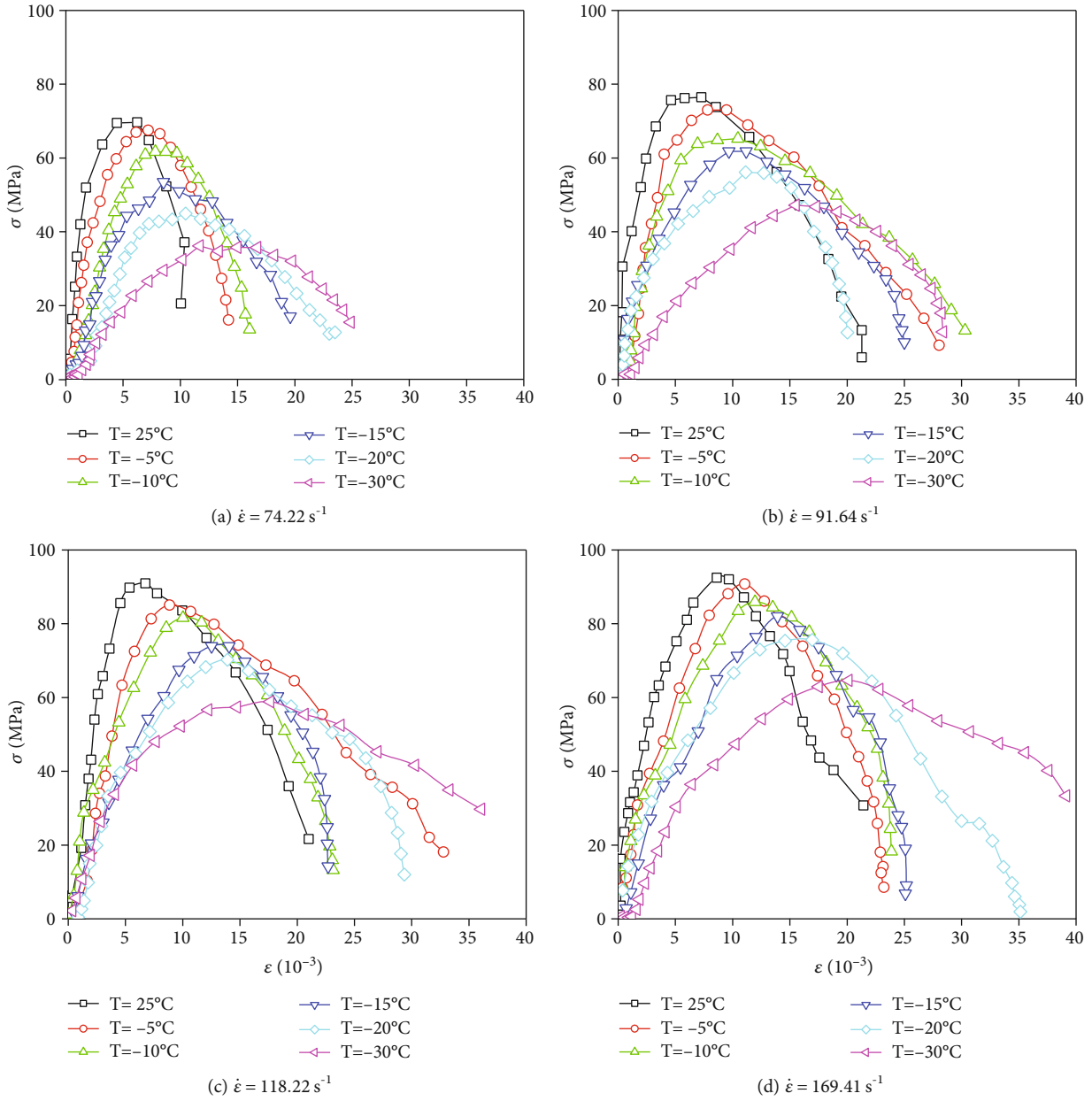


FIGURE 4: The dynamic compression stress-strain curve of saturated yellow sandstone under different temperatures and strain rates.

3. Experimental Result Analysis

The dynamic peak stress, dynamic peak strain, dynamic elastic modulus, and brittle/ductile behaviour of specimens under the coupling effect of freeze-thaw temperatures and strain rates could be inferred from the stress-strain curve. Figure 4 presented the typical dynamic compressive stress-strain curves obtained from the SHPB test at four loading levels and six freeze-thaw temperature levels. It can be seen clearly that the strain rates and freeze-thaw temperatures have an extremely important influence on the dynamic compression behavior of rock specimens [29]. The stress-strain curve can be roughly divided into four stages as a whole: nonlinear compression deformation stage with the initial crack closure, elastic deformation stage, crack unsteady

propagation stage, and postpeak plastic deformation stage. Although under different strain rates and temperatures, the shape feature of the stress-strain curve is basically similar with their process of nonlinear compression deformation stage relatively short. When the temperature is less than -20°C , the slope of the post-peak stress-strain curve decreases significantly. It means that the brittleness of the yellow sandstone specimens weakens whereas their plastic or ductile enhances. In addition, the strength parameters, such as peak stress, peak strain, dynamic elastic modulus, and dissipated energy, of specimens varied as the temperature and strain rates changed. The experimental results of dynamic compressive mechanical behavior for yellow sandstone under different temperatures and strain rates are shown in Table 1. It should be noted that the experiment

TABLE 1: Experimental result of dynamic compressive mechanical behavior for yellow sandstone under different temperatures and strain rates.

Number	Temperature T (°C)	Strain rate $\dot{\epsilon}$ (s^{-1})	Average value $\dot{\epsilon}$ (s^{-1})	Dynamic compressive strength (MPa)	Peak strain (10^{-3})	Elastic modulus (GPa)	DE (J)
1	25	72.51	74.22	70.41	5.02	34.42	30.13
2	-5	74.57		67.16	6.70	23.48	27.81
3	-10	76.00		61.83	7.84	13.46	24.77
4	-15	73.87		53.55	8.55	9.13	23.52
5	-20	75.02		44.97	10.40	7.97	24.20
6	-30	73.95		36.39	11.72	3.68	20.19
1	25	92.35	91.64	76.49	6.61	35.36	48.64
2	-5	91.58		73.68	8.16	17.46	43.55
3	-10	91.10		66.20	9.14	11.91	38.93
4	-15	92.47		62.92	10.36	5.69	34.00
5	-20	91.93		56.84	11.91	4.83	34.45
6	-30	90.41		47.49	15.50	3.08	30.69
1	25	116.94	118.22	90.94	6.61	23.92	72.22
2	-5	118.27		85.67	8.70	21.56	61.74
3	-10	119.33		82.46	10.26	17.71	54.54
4	-15	118.93		74.85	12.44	9.45	49.74
5	-20	117.86		70.76	13.57	7.63	46.08
6	-30	117.99		60.23	17.30	6.42	44.74
1	25	168.43	169.41	92.42	8.61	23.46	85.47
2	-5	169.35		90.38	11.04	12.48	82.66
3	-10	170.39		86.30	12.09	10.33	78.87
4	-15	169.47		82.22	14.00	8.82	66.74
5	-20	168.98		76.09	15.57	8.53	63.41
6	-30	169.84		65.02	19.57	7.70	54.23

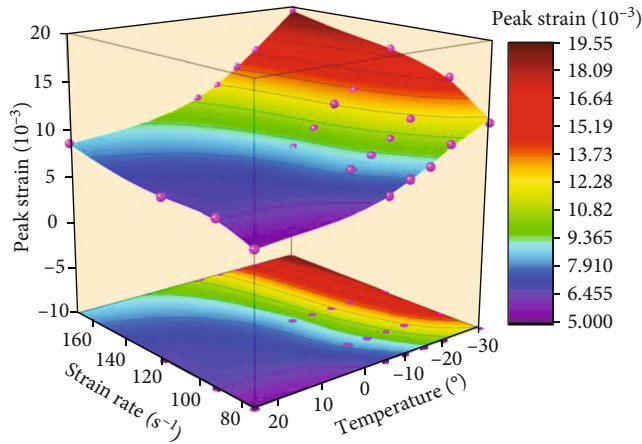


FIGURE 5: Dynamic peak strain under different temperatures and strain rates.

results are the average value of three specimens after removing two groups' data with larger error.

3.1. Coupling Effect of Strain Rate and Low Temperatures on Dynamic Peak Strain. Figure 5 shows dynamic peak strain under different temperatures and strain rates. It can be seen

clearly that the two variables exist good regularity and the uniform fitting equation of these curves can be expressed as

$$\epsilon_c = [d_1(T)\dot{\epsilon} + d_2(T)] \times 10^{-3}, \quad (5)$$

where $d_1(T)$ and $d_2(T)$ are, respectively, the fitting

TABLE 2: Fitting coefficient values in Equation (5).

	25°C	-5°C	-10°C	-15°C	-20°C	-30°C
d_1	0.033	0.042	0.042	0.055	0.052	0.074
d_2	2.888	3.788	4.972	5.088	6.894	7.592
R^2	0.906	0.969	0.976	0.922	0.968	0.867

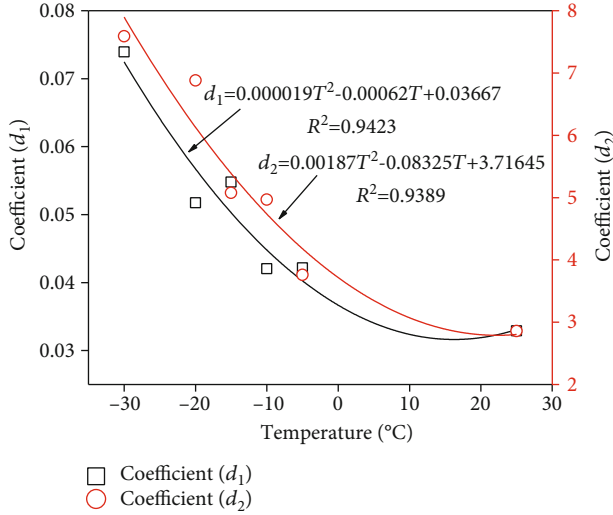


FIGURE 6: Variation of fitting coefficients with the temperature.

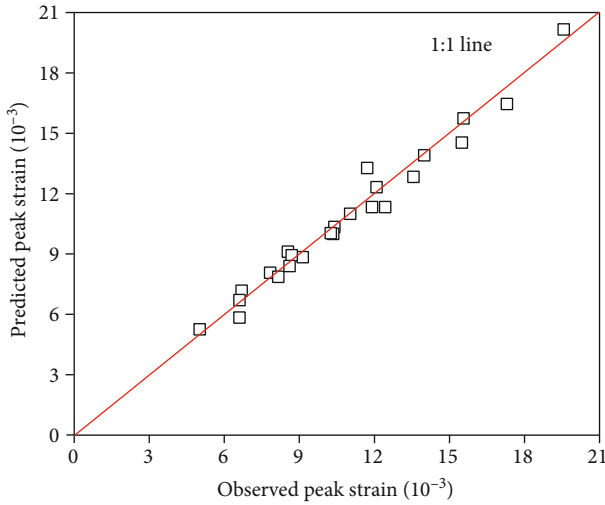


FIGURE 7: Plots of predicted peak strain against observed peak strain.

coefficients related to temperature, of which the value and correlation coefficient are shown in Table 2.

In order to obtain the specific expression of peak strain under coupling effect of the strain rate and temperature, it is needed to analyze the relationship between the fitting coefficients and temperatures. As shown in Figure 6, the variation of fitting coefficients with the temperature also exists good regularity. The fitting equation is shown in

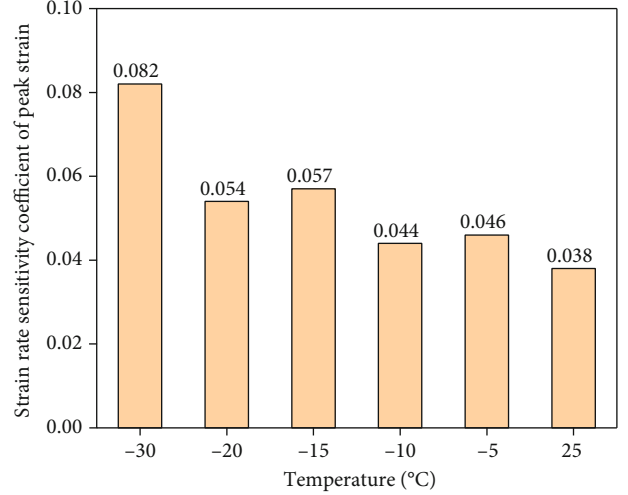


FIGURE 8: Strain rate sensitivity coefficient of peak strain variation with temperature.

$$\begin{cases} d_1 = 0.000019T^2 - 0.00062T + 0.03667, & R^2 = 0.9423, \\ d_2 = 0.00187T^2 - 0.08325T + 3.71645, & R^2 = 0.9389. \end{cases} \quad (6)$$

Substituting Equation (6) into Equation (5), the relationship formula of peak strain with strain rate and temperature can be deduced as follows:

$$\epsilon_c = [(0.000019T^2 - 0.00062T + 0.03667)\dot{\epsilon} + 0.00187T^2 - 0.08325T + 3.71645] \times 10^{-3}. \quad (7)$$

The dynamic peak strain of rock is predicted by Equation (7) and compared with the laboratory observation; as shown in Figure 7, the 1 : 1 inclined line is given in the figure. The distance between the predicted value and the 1 : 1 inclined line represents the error between the predicted value and the observation value [30]. It can be seen from the figure that the predicted value is basically distributed near the 1 : 1 inclined line; Equation (7) can be used to predict dynamic peak strain at any temperature and impact rate.

Figure 8 shows the strain rate sensitivity coefficient of peak strain variation with temperature. Figure 9 shows the increased ratio of peak strain compared to room temperature under different temperatures and strain rates. It can be seen from Figures 8 and 9 that the enhanced effect of strain rate always exists under low temperature. However, according to the strain rate level [7, 8], the increase speed of peak strain at medium strain rate level (74.22 s^{-1} and 91.64 s^{-1}) is obviously higher than that at high strain rate level (118.22 s^{-1} and 169.41 s^{-1}) with strain rate increasing. At room temperature, the strain rate sensitivity coefficient of peak strain is 0.038. With temperature decreasing, the value changes in volatility. From -5°C to -25°C , the strain rate sensitivity coefficient increased by 21.05%, 15.79%, 50.00%, and 42.11% compared to room temperature,

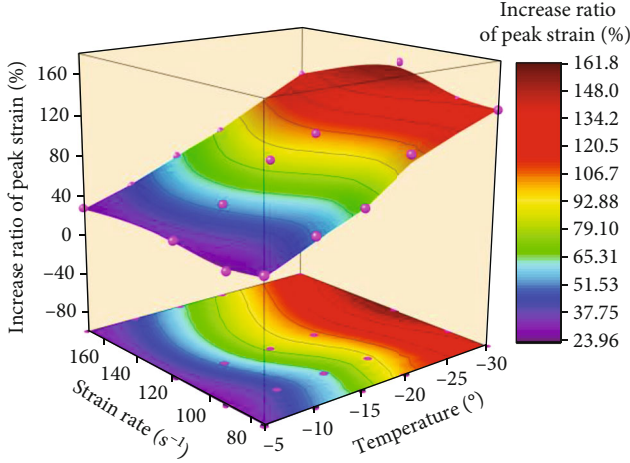


FIGURE 9: Increase ratio of peak strain under different temperatures and strain rates.

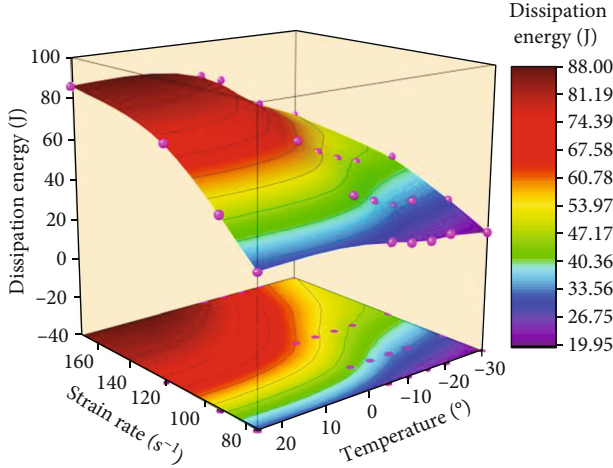


FIGURE 10: Dissipated energy under different temperatures and strain rates.

TABLE 3: Fitting coefficient values in Equation (8).

	25°C	-5°C	-10°C	-15°C	-20°C	-30°C
d_1	67.73	66.41	65.22	53.04	47.34	41.73
d_2	258.00	257	256.10	204.80	179.60	157.90
R^2	0.956	0.996	0.999	0.997	0.999	0.972

respectively. When the temperature reach -30°C , the strain rate sensitivity coefficient reaches the maximum value of 0.082 increased by 115.79%, indicating that the strain rate effect has a most important influence at this temperature.

In addition, it can be seen from Figure 9 that the increase ratio of peak strain compared to room temperature shows the scattered distribution with the increase of strain rate, indicating that the influence of strain rate on the increase ratio of peak strain is not regular. However, the increase ratio of peak strain gradually increases with decreasing of

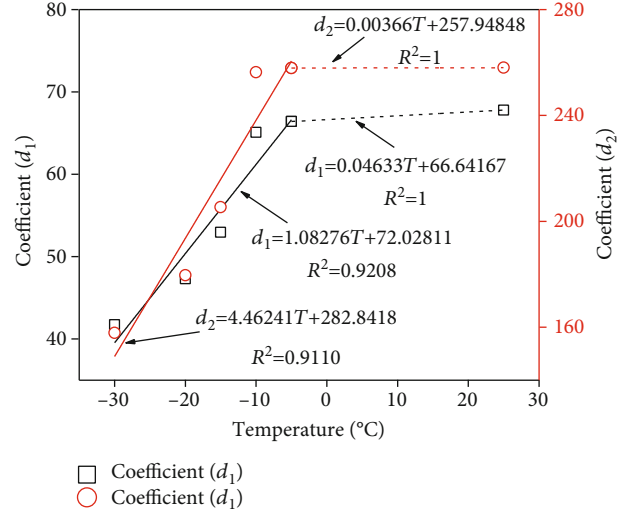


FIGURE 11: Variation of fitting coefficients with the temperature.

temperature and reaches the maximum value when the temperature reaches -30°C . It means that the freeze-thaw temperature has a certain enhancement effect on the plastic behavior of yellow sandstone. The lower the freeze-thaw temperature is, the greater the ductility of saturated yellow sandstone is.

3.2. Coupling Effect of Strain Rate and Low Temperatures on Dissipated Energy. Figure 10 shows dissipated energy under different temperatures and strain rates. As can be seen clearly from Figure 10 that the dissipated energy presents obvious strain rate and temperature effects and the uniform fitting equation of these curves is as follows:

$$W_L = d_1(T) \ln(\dot{\epsilon}) - d_2(T). \quad (8)$$

The fitting coefficients $d_1(T)$ and $d_2(T)$ as well as the correlation coefficient of fitting curves are shown in Table 3.

For obtaining the certain equation of dissipated energy under coupling influence of strain rate and temperature, the relationship between fitting coefficients and temperature should be firstly determined.

Figure 11 shows the fitting curve of the above variables, indicating a good regularity. The fitting equation can be written as shown in Equation (9).

$$d_1 = \begin{cases} 1.08276T + 72.02811, & -30 \leq T \leq -5, \quad R^2 = 0.9208, \\ 0.04633T + 66.64167, & -5 < T \leq 25, \quad R^2 = 1, \end{cases}$$

$$d_2 = \begin{cases} 4.46241T + 282.8418, & -30 \leq T \leq -5, \quad R^2 = 0.9110, \\ 0.00366T + 257.9485, & -5 < T \leq 25, \quad R^2 = 1. \end{cases} \quad (9)$$

Substituting Equation (9) into Equation (8), the certain expression of dissipated energy under the coupling effect of

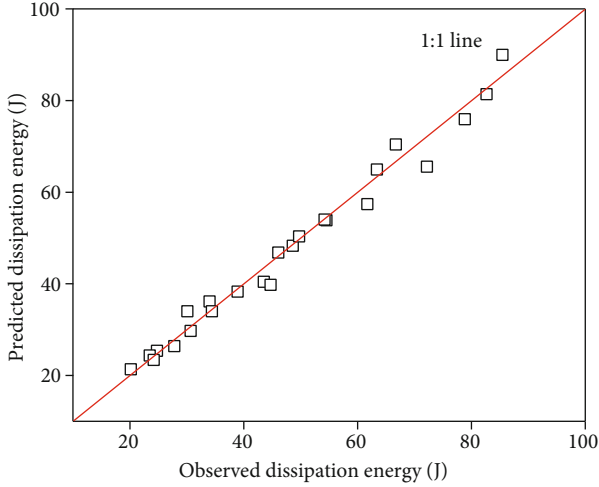


FIGURE 12: Plots of predicted dissipation energy against observed dissipation energy.

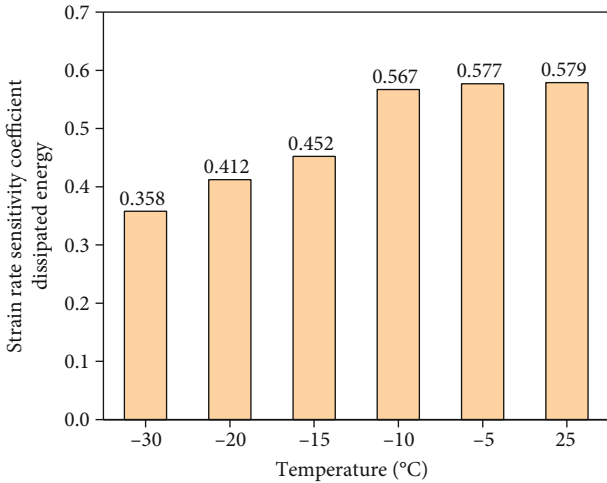


FIGURE 13: Strain rate sensitivity coefficient of dissipated energy variation with temperature.

strain rate and temperature can be obtained as follows:

$$W_L = \begin{cases} (1.08276T + 72.02811) * \ln(\dot{\epsilon}) - 4.46241T - 282.8418, & -30 \leq T \leq -5, \\ (0.04633T + 66.64167) * \ln(\dot{\epsilon}) - 0.00366T - 257.9485, & -5 < T \leq 25. \end{cases} \quad (10)$$

Equation (10) is used to predict the dissipated energy of rock and compare it with the laboratory observation value. As shown in Figure 12, the 1:1 inclined line is given in the figure. The distance between the predicted value and the 1:1 inclined line represents the error between the predicted value and the observation value. It can be seen from the figure that the predicted value is basically distributed near the 1:1 inclined line; Equation (11) can be used to predict the dissipated energy at any temperature and impact rate.

Figure 13 shows the strain rate sensitivity coefficient of dissipated energy variation with temperature. As can be seen

from Figure 13 that the enhancement effect of strain rate on dissipated energy under different temperatures also exists and the increase speed under different temperatures also have an obvious strain rate effect. The increased ratio of dissipated energy at high strain rate level (118.22 s^{-1} and 169.41 s^{-1}) is lower than that at medium strain rate level (74.22 s^{-1} and 91.64 s^{-1}), indicating that the strain rate effect gradually weakens with strain rate increasing. At room temperature, the strain rate sensitivity coefficient of dissipated energy is 0.579. As the temperature goes down, the value gradually nonlinearly decreases until it reaches minimum value (0.358) at -30°C , showing that the strain rate effect on dissipated energy gradually weakens with the decrease of freeze-thaw temperature.

Figure 14 shows the increase ratio of dissipated energy compared to room temperature under different temperatures and strain rates. It can be seen from Figure 14 that the increased ratio of dissipated energy under different freeze-thaw temperatures shows a change characteristic of decreasing first in the range of $74.22 \text{ s}^{-1} \sim 118.22 \text{ s}^{-1}$ and then increasing in the range of $118.22 \text{ s}^{-1} \sim 169.41 \text{ s}^{-1}$, indicating that the influence of strain rate on the increase ratio of dissipated energy has an obvious interval effect. On the whole, with the increase of freeze-thaw temperature, regardless of individual discrete points, the increase ratio of dissipated energy gradually increases, of which the values are substantially negative. From -30°C to -5°C , the increase ratio changes from -36.9% to -10.47% at strain rate 91.64 s^{-1} or from -36.55% to -3.29% at strain rate 118.22 s^{-1} . At -30°C , the increase ratio of dissipated energy reaches minimum value, indicating that the energy absorption capacity of rock material has reached weakest.

This maybe mainly because that the freeze-thaw temperature has significantly resulted in the serious inner damage degree of rock material by the frost heaving effect. As a result, the energy absorbed by specimens will be greatly reduced in the process of impact test.

3.3. Coupling Effect of Strain Rate and Low Temperatures on Elastic modulus. The dynamic elastic modulus is an extremely important mechanics index for evaluating the impact deformation resistance of rock materials. In general, there are many various methods to determine elastic modulus, which mainly include secant modulus, tangent modulus, and average modulus. In this paper, we take the slope of approximate straight line at the elastic stage of the stress-strain curve as the elastic modulus of rock material. The methods have already been used in other papers [9].

Figure 15 shows the elastic modulus evolution law under different temperatures and strain rates. Figure 16 shows the strain rate sensitivity coefficient of elastic modulus under different temperatures. As can be seen from Figures 15 and 16, the elastic modulus fluctuates with the strain rate increasing. It means that there is no obvious strain rate effect on the elastic modulus under different temperatures. The experimental phenomenon has already been verified in some experiments [2]. In addition, with the freeze-thaw temperature increasing, the elastic modulus gradually increases, indicating that the lower the freeze-thaw temperature is, the

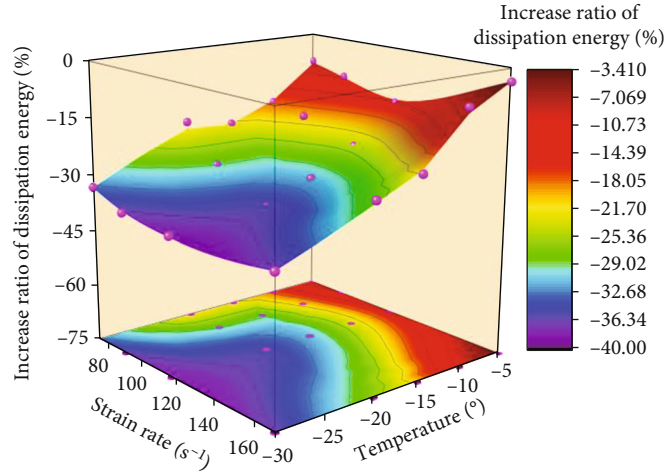


FIGURE 14: Increase ratio of dissipated energy under different temperatures and strain rates.

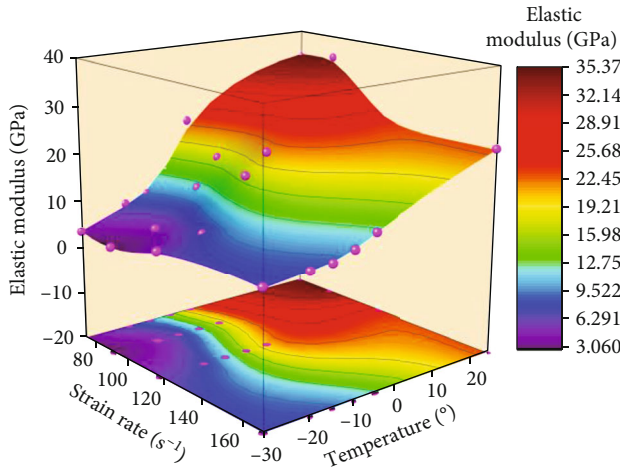


FIGURE 15: Elastic modulus under different temperatures and strain rates.

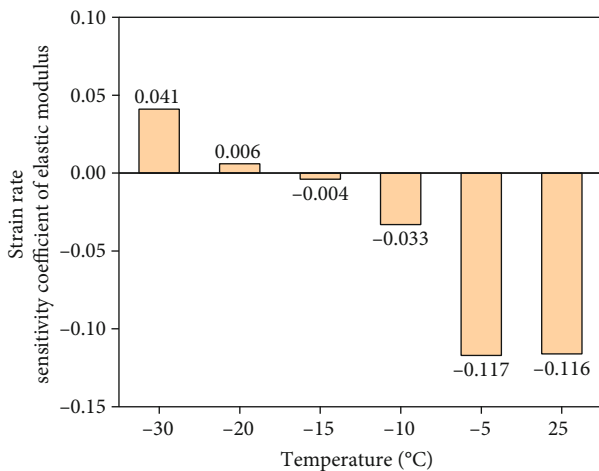


FIGURE 16: Strain rate sensitivity coefficient of elastic modulus variation with temperature.

weaker the deformation resistance of yellow sandstone will be.

Figure 17 shows the increase ratio of elastic modulus compared to room temperature. As can be seen from Figure 17, the increased ratio of the elastic modulus presents obvious fluctuation characteristic with strain rate increasing. In addition, the increased ratio of the elastic modulus gradually decreases with the temperature decreasing. From -5°C to -30°C , the increase ratio changes from -31.77% to -89.3% at strain rate 74.22 s^{-1} or from -9.8% to -73.14% at strain rate 118.22 s^{-1} . At -30°C , the increase ratio of elastic modulus compared to room temperature reaches minimum value, indicating that the ability to resist deformation of rocks has reached weakest under this temperature.

3.4. Coupling Effect of Strain Rates and Low Temperatures on Dynamic Peak Strength. Figure 18 shows dynamic peak stress under different temperatures and strain rates. Figure 19 indicates the strain rate sensitivity coefficient of peak stress variation with temperature. As can be seen from Figures 18 and 19, the enhanced effect of strain rate on peak strength of yellow sandstone under different temperatures also always exists. It has an obvious regularity with temperature and strain rate. On the whole, the increase speed of peak stress at high strain rate level (118.22 s^{-1} and 169.41 s^{-1}) is lower than that at medium strain rate level (74.22 s^{-1} and 91.62 s^{-1}), showing that, at the same temperature, the strain rate effect gradually weakens with the increase of strain rate. In addition, the strain rate sensitivity coefficient of peak stress is always positive and dramatically increases with the temperature decreasing from 25°C to -20°C , indicating that the strain rate effect on peak strength gradually strengthened with the decrease of freeze-thaw temperature. Otherwise, the strain rate sensitivity coefficient of 0.30 at -30°C is slightly lower than that of 0.33 at -20°C , but higher than that under other temperatures. It may be because that, at -30°C , the surface of specimens appeared an obvious particle spalling phenomenon, which increased the frost heave damage degree and destroyed the integrity of rock material

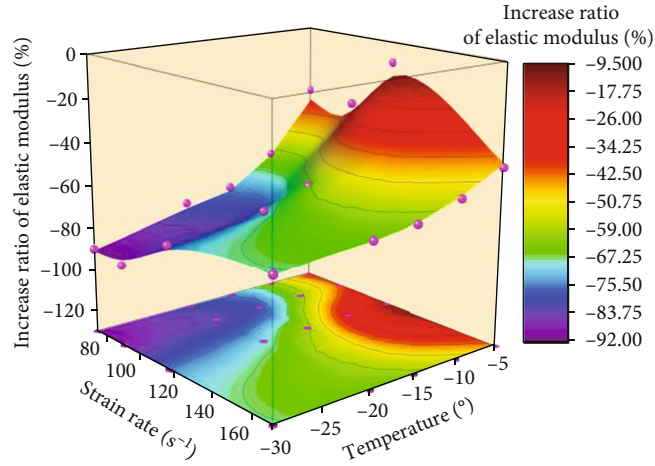


FIGURE 17: Increased ratio of the elastic modulus under different temperatures and strain rates.

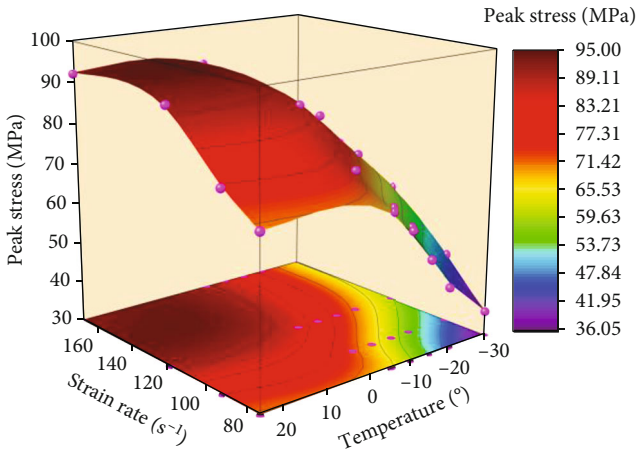


FIGURE 18: Dynamic peak stress under different temperatures and strain rates.

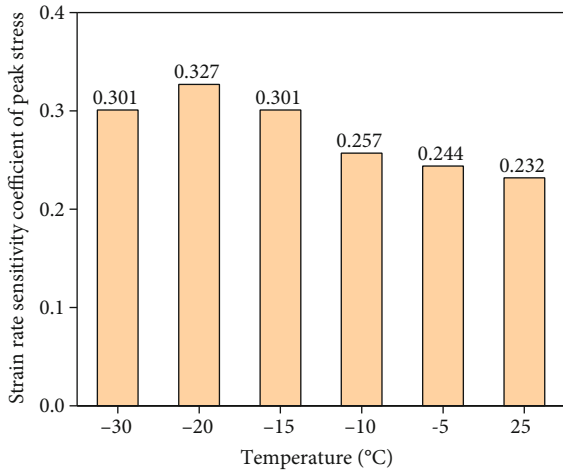


FIGURE 19: Strain rate sensitivity coefficient of peak stress variation with temperature.

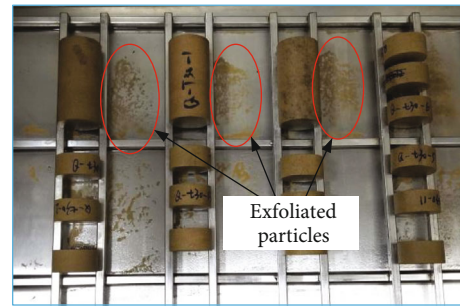


FIGURE 20: Particle spalling phenomenon at -30°C under different size specimens.

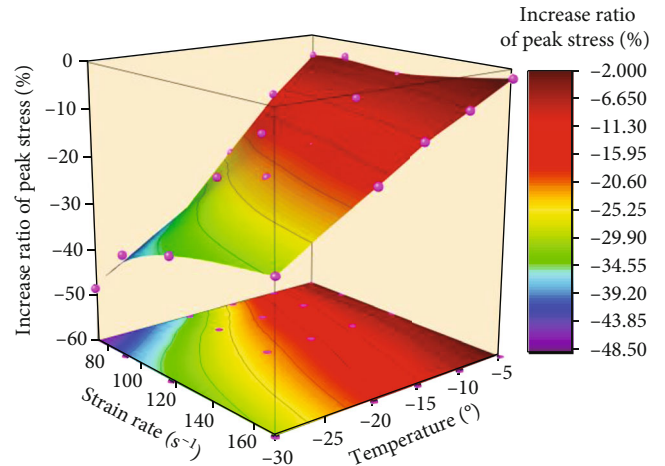


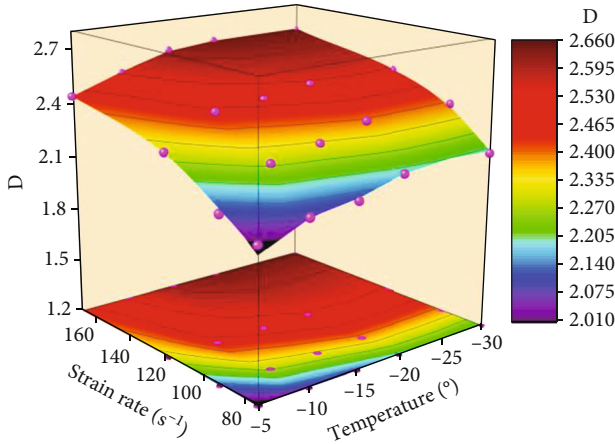
FIGURE 21: Increased ratio of peak stress compared to the room temperature under different temperatures and strain rates.

so that caused errors in the test results. The particle spalling phenomenon is shown in Figure 20.

Figure 21 shows the increase ratio of peak stress compared to the room temperature under different temperatures and strain rates. It can be seen from Figure 21 that, on the whole, the increase ratio of peak stress has an obvious

TABLE 4: Fractal characteristic parameters of fractured sandstone.

T (°C)	$\dot{\epsilon}$ (s ⁻¹)	M_R/M								d	D
		$R=1$	$R=2.5$	$R=4$	$R=6$	$R=8.5$	$R=11$	$R=13$	$R=15$		
-5	74.22	0.13	0.11	0.09	0.06	0.04	0.03	0.02	0.02	0.99	2.01
	91.64	0.37	0.37	0.29	0.21	0.11	0.08	0.06	0.04	0.91	2.09
	118.22	0.60	0.54	0.48	0.38	0.30	0.24	0.19	0.13	0.58	2.29
	169.41	0.74	0.65	0.59	0.48	0.37	0.30	0.25	0.16	0.56	2.44
-10	74.22	0.16	0.15	0.13	0.09	0.06	0.04	0.03	0.02	0.92	2.08
	91.64	0.46	0.41	0.33	0.27	0.18	0.13	0.10	0.07	0.72	2.28
	118.22	0.61	0.60	0.54	0.48	0.38	0.28	0.23	0.15	0.54	2.46
	169.41	0.89	0.84	0.82	0.71	0.60	0.48	0.39	0.26	0.47	2.53
-15	74.22	0.24	0.23	0.16	0.11	0.06	0.05	0.04	0.02	0.90	2.10
	91.64	0.54	0.53	0.48	0.37	0.26	0.19	0.15	0.10	0.67	2.33
	118.22	0.69	0.64	0.55	0.45	0.36	0.29	0.25	0.17	0.52	2.48
	169.41	0.92	0.92	0.90	0.85	0.69	0.56	0.51	0.34	0.38	2.62
-20	74.22	0.35	0.30	0.28	0.16	0.10	0.08	0.06	0.04	0.82	2.18
	91.64	0.61	0.54	0.52	0.42	0.34	0.27	0.22	0.14	0.60	2.40
	118.22	0.68	0.68	0.67	0.58	0.47	0.38	0.32	0.21	0.48	2.52
	169.41	0.96	0.96	0.93	0.89	0.77	0.64	0.55	0.37	0.36	2.64
-30	74.22	0.44	0.44	0.35	0.29	0.21	0.16	0.13	0.08	0.65	2.35
	91.64	0.71	0.65	0.59	0.47	0.37	0.29	0.25	0.16	0.57	2.43
	118.22	0.72	0.70	0.68	0.57	0.45	0.36	0.30	0.21	0.45	2.55
	169.41	0.97	0.97	0.96	0.91	0.83	0.71	0.61	0.44	0.30	2.70

FIGURE 22: Variation of fractal dimension, D , with strain rate and freeze-thaw temperature.

correlation with the temperature and strain rate. As the strain rate increases, the increase ratio gradually nonlinear increases and the phenomenon is more significant with the temperature decreasing. When the temperature reaches -30°C , the phenomenon is most pronounced. In addition, the increase ratio of peak stress gradually decreases with decreasing of temperature and reaches the minimum value of -48.32% for 74.22 s^{-1} , 37.92% for 91.64 s^{-1} , 33.76% for 118.22 s^{-1} and 29.65% for 169.41 s^{-1} when the temperature reaches -30°C , indicating that the freeze-thaw temperature

has a serious weakening effect on rock strength, which can reduce the bearing capacity of rocks.

4. Coupling Effect of Strain Rate and Low Temperature on Fractal Characteristics

4.1. Fractal Dimension Calculation Methods. In order to quantitatively study the effect of strain rate on the fracture degree of specimens at different freeze-thaw temperatures, the mass-equivalent dimension method as an effective fractal dimension calculation method is used to explore the fractal characteristics of the fracture specimens after impact test in this literature. The specific calculation formula is as follows [27]:

$$D = 3 - d, \quad (11)$$

$$d = \frac{\lg(M_R/M)}{\lg R}, \quad (12)$$

where D is the fractal dimension of fracture specimens. The larger parameter D is, the higher the fracture degree of specimen is. d is the slope of the fitting line in the logarithmic coordinates ($\lg(M_R/M) - \lg R$). M_R is the cumulative mass of fragments smaller than particle size R for each specimen. M is the total mass of fragment.

After the impact test, the fragment of specimen firstly be collected, and then, a classifying screen with eight layers is used to divide the particle size range of fragments into 50-

15 mm, 15-13 mm, 13-11 mm, 11-8.5 mm, 8.5-6 mm, 6-4 mm, 4-2.5 mm, 2.5-1 mm, and 1-0 mm. The maximum particle size is 50 mm. The fragment mass in different ranges of particle size will be measured by electronic scales and the parameters M , M_R , and M_R/M will also be calculated. Next, parameter d can be obtained by taking the slope of fitting line in the logarithmic coordinates ($\lg(M_R/M) - \lg R$). Finally, substituting parameter d into Equation (11), the fractal dimension of fragments (D) can be easily calculated at different temperatures and strain rates. The fractal characteristic parameters of fractured sandstone are shown in Table 4.

4.2. Variation of Fractal Dimension under Strain Rate and Freeze-Thaw Temperature. Figure 22 shows the variation of fractal dimension with strain rate and freeze-thaw temperature.

It can be seen from Figure 22 that the strain rate effect on the fractal dimension under different freeze-thaw temperatures always exists. The fractal dimension presents a positive correlation with strain rate. When the strain rate increases from 74.22 s^{-1} to 169.41 s^{-1} , the fractal dimension of fragments increases from 2.01 to 2.44, up 21.39% for -5°C ; from 2.08 to 2.53, up 21.63% for -10°C ; from 2.10 to 2.62, up 24.76% for -15°C ; from 2.18 to 2.64, up 21.10% for -20°C ; and from 2.38 to 2.70, up 14.89% for -30°C . In addition, on the whole, the increased speed of fractal dimension gradually decreases with strain rate increasing, showing that high strain rate is more likely to increase the fracture degree of rock material, but the strain rate effect weakened at high strain rate. In addition, the fractal dimension also gradually increases with freeze-thaw temperature decreasing, indicating that the low freeze-thaw temperature environment has a positive function for increasing the damage and fracture degree of specimens for the saturated specimen. When the temperature reaches -30°C and the strain rate reaches 169.41 s^{-1} , the fractal dimension reaches the maximum value, indicating that the fracture degree of specimens at this state is the most serious.

5. Conclusion

In this paper, the coupling effect of strain rate and freeze-thaw temperature on dynamic compressive mechanical and fracture behavior of saturated yellow sandstone are studied by SHPB test. Moreover, the relationship formula of the peak strain and dissipated energy with the strain rate and freeze-thaw temperature is also established. Finally, the fractal dimension method is introduced to analyze the fractal characteristics of fractured specimens subjected to different strain rates and temperatures after impact test. The main conclusions summed up are as follows:

- (1) The enhanced effects of strain rates on the peak strain, peak strength, and dissipated energy of saturated yellow sandstone under different freeze-thaw temperatures still exist. With the increase of strain rate, the increase speed of above parameters at medium strain rate level (74.22 s^{-1} and 91.64 s^{-1})

was obviously higher than that at high strain rate level (118.22 s^{-1} and 169.41 s^{-1}), indicating that the strain rate effect gradually weakens at high strain. The elastic modulus change has nothing to do with the strain rate

- (2) At the same strain rate, the parameters of peak strength, elastic modulus, and dissipated energy gradually decrease with the decrease of freeze-thaw temperature whereas peak strain opposite
- (3) At room temperature, the strain rate effect on peak strain and peak strength is weakest, while at $-20^\circ\text{C} \sim -30^\circ\text{C}$, it is most significant. When the temperature is higher than -10°C , the increased speed of strain rate sensitivity coefficient has no obvious change, while the increase rapidly with temperature decreasing when it is below -10°C . In addition, the strain rate effect on dissipated energy is significant at room temperature, while weakest at -30°C
- (4) The strain rate and freeze-thaw temperature have a significantly important effect on the fractal dimension of fractured specimens. With the strain rate increasing, the fractal dimension gradually increases. However, the increased speed gradually decreases, showing that high strain rate is more likely to increase the fracture degree of rock material, but the strain rate effect weakened at high strain rate. In addition, the fractal dimension also gradually increases with freeze-thaw temperature decreasing, indicating that the freeze-thaw temperature environment with low temperature has a positive function for increasing the damage and fracture degree of specimens for saturated specimen

Data Availability

Most of the data generated or analyzed during this study are included in this manuscript, and all of the data are available from the corresponding author on reasonable request.

Conflicts of Interest

The authors declare that they have no conflicts of interest.

Acknowledgments

This work was financially supported by the National Natural Science Foundation of China (52074240, 51974295) and the Research Project of "333 Project" in Jiangsu Province of China (BRA2019236).

References

- [1] D. Asprone, E. Cadoni, F. Iucolano, and A. Prota, "Analysis of the strain-rate behavior of a basalt fiber reinforced natural hydraulic mortar," *Cement & Concrete Composites*, vol. 53, pp. 52–58, 2014.
- [2] S. Liu and J. Xu, "Effect of strain rate on the dynamic compressive mechanical behaviors of rock material subjected to high

- temperatures,” *Mechanics of Materials*, vol. 82, pp. 28–38, 2015.
- [3] M. Li, X. Mao, L. Cao, H. Pu, R. Mao, and A. Lu, “Effects of thermal treatment on the dynamic mechanical properties of coal measures sandstone,” *Rock Mechanics and Rock Engineering*, vol. 49, no. 9, pp. 3525–3539, 2016.
- [4] Y. Chen, G. Lin, R. Mao, M. Li, X. Mao, and K. Zhang, “Strain rate effect on the mechanical properties and fracture surface roughness of sandstone subjected to dynamic direct tension,” *IEEE Access*, vol. 8, pp. 107977–107992, 2020.
- [5] M. Li, L. Gang, and X. Mao, “Dynamic fracture and energy consumption characteristics of coal-series sandstone after heat treatment,” *Thermal Science*, vol. 23, Suppl. 3, pp. 967–974, 2019.
- [6] S. J. Green, J. D. Leasia, R. D. Perkins, and A. H. Jones, “Triaxial stress behavior of Solenhofen limestone and westerly granite at high strain rates,” *Journal of Geophysical Research*, vol. 77, no. 20, pp. 3711–3724, 1972.
- [7] T. L. Blanton, “Effect of strain rates from 10^{-2} to 10 sec^{-1} in triaxial compression tests on three rocks,” *International Journal of Rock Mechanics & Mining Sciences & Geomechanics Abstracts*, vol. 18, no. 1, pp. 47–62, 1981.
- [8] Q. B. Zhang and J. Zhao, “A review of dynamic experimental techniques and mechanical behaviour of rock materials,” *Rock Mechanics and Rock Engineering*, vol. 47, no. 4, pp. 1411–1478, 2014.
- [9] M. Li, X. Mao, L. Cao, H. Pu, and A. Lu, “Influence of heating rate on the dynamic mechanical performance of coal measure rocks,” *International Journal of Geomechanics*, vol. 17, no. 8, article 04017020, 2017.
- [10] U. S. Lindholm and L. M. Yeakley, “High strain-rate testing: tension and compression,” *Experimental Mechanics*, vol. 8, no. 1, pp. 1–9, 1968.
- [11] W. F. Brace and A. H. Jones, “Comparison of uniaxial deformation in shock and static loading of three rocks,” *Journal of Geophysical Research*, vol. 76, no. 20, pp. 4913–4921, 1971.
- [12] J. R. Klepaczko, “Behavior of rock-like materials at high strain rates in compression,” *International Journal of Plasticity*, vol. 6, no. 4, pp. 415–432, 1990.
- [13] Q. M. Li and H. Meng, “About the dynamic strength enhancement of concrete-like materials in a split Hopkinson pressure bar test,” *International Journal of Solids and Structures*, vol. 40, no. 2, pp. 343–360, 2003.
- [14] S. G. Grantham, C. R. Siviour, W. G. Proud, and J. E. Field, “High-strain rate Brazilian testing of an explosive simulant using speckle metrology,” *Measurement Science & Technology*, vol. 15, no. 9, pp. 1867–1870, 2004.
- [15] X. Liu, R. Zhang, and J. Liu, “Dynamic test study of coal rock under different strain rates,” *Journal of China Coal Society*, vol. 37, no. 9, pp. 1528–1534, 2012.
- [16] Y. Li, D. Huang, and X. Li, “Strain rate dependency of coarse crystal marble under uniaxial compression: strength, deformation and strain energy,” *Rock Mechanics and Rock Engineering*, vol. 47, no. 4, pp. 1153–1164, 2014.
- [17] T. Saksala, “On the strain rate sensitivity of coarse-grained rock: a mesoscopic numerical study,” *Rock Mechanics and Rock Engineering*, vol. 52, no. 9, pp. 3229–3240, 2019.
- [18] R. Altindag, I. S. Alyildiz, and T. Onargan, “Mechanical property degradation of ignimbrite subjected to recurrent freeze-thaw cycles,” *International Journal of Rock Mechanics and Mining Sciences*, vol. 41, no. 6, pp. 1023–1028, 2004.
- [19] H. Yavuz, “Effect of freeze-thaw and thermal shock weathering on the physical and mechanical properties of an andesite stone,” *Bulletin of Engineering Geology and the Environment*, vol. 70, no. 2, pp. 187–192, 2011.
- [20] X. Tan, W. Chen, J. Yang, and J. Cao, “Laboratory investigations on the mechanical properties degradation of granite under freeze-thaw cycles,” *Cold Regions Science and Technology*, vol. 68, no. 3, pp. 130–138, 2011.
- [21] G. Charrier, K. Charra-Vaskou, J. Kasuga, H. Cochard, S. Mayr, and T. Ameglio, “Freeze-thaw stress: effects of temperature on hydraulic conductivity and ultrasonic activity in ten woody angiosperms,” *Plant Physiology*, vol. 164, no. 2, pp. 992–998, 2014.
- [22] L. Wen, L. I. Xibing, W. U. Qiuhong, L. Weng, and S. U. Wei, “Dynamic strength of granite porphyry under freezing-thawing cycles,” *Chinese Journal of Rock Mechanics and Engineering*, vol. 34, no. 7, pp. 1297–1306, 2015.
- [23] J. Eslami, C. Walbert, A. Beaucour, A. Bourges, and A. Noumowe, “Influence of physical and mechanical properties on the durability of limestone subjected to freeze-thaw cycles,” *Construction and Building Materials*, vol. 162, pp. 420–429, 2018.
- [24] Q. Ma, D. Ma, and Z. Yao, “Influence of freeze-thaw cycles on dynamic compressive strength and energy distribution of soft rock specimen,” *Cold Regions Science and Technology*, vol. 153, pp. 10–17, 2018.
- [25] G. H. Zheng, J. Y. Xu, P. Wang, X. Y. Fang, and M. Wen, “Physical characteristics and degradation model of stratified sandstone under freeze-thaw cycling,” *Yantu Lixue/Rock and Soil Mechanics*, vol. 40, no. 2, pp. 632–641, 2019.
- [26] M. Grenon, J. Hadjigeorgiou, and Q. Liu, “Quantifying in-situ rock block size and resulting fragment size distributions due to blasting,” *Fragblast*, vol. 2, no. 2, pp. 205–218, 1998.
- [27] D. J. Li, X. N. Jia, J. L. Miao, M. C. He, and D. D. Li, “Analysis of fractal characteristics of fragments from rock burst test of granite,” *Chinese Journal of Rock Mechanics and Engineering*, vol. 29, no. 1, pp. 3280–3289, 2010.
- [28] A. H. Bakhshandeh and H. R. Malekinezhad, *An Empirical Model to Predict Particle Size Reduction Caused by Blasting in the Conglomerate Rock-Mass at Gotvand Olya Dam*, Energy Engineering and Management, 2012.
- [29] L. Chen, X. Mao, S. Yang, C. An, and P. Wu, “Experimental investigation on dynamic fracture mechanism and energy evolution of saturated yellow sandstone under different freeze-thaw temperatures,” *Advances in Civil Engineering*, vol. 2019, Article ID 2375276, 16 pages, 2019.
- [30] L. Chen, P. Wu, Y. Chen, and W. Zhang, “Experimental study on physical-mechanical properties and fracture behaviors of saturated yellow sandstone considering coupling effect of freeze-thaw and specimen inclination,” *Sustainability*, vol. 12, no. 3, article 1029, 2020.

Research Article

Loading Behavior and Soil-Structure Interaction for a Floating Stone Column under Rigid Foundation: A DEM Study

Feng Liu ¹, Panpan Guo ¹, Haibo Hu ¹, Chengwei Zhu ^{1,2} and Xiaonan Gong ¹

¹Research Center of Coastal and Urban Geotechnical Engineering, Zhejiang University, Hangzhou 310058, China

²Institute of Geotechnical Engineering, University of Natural Resources and Life Sciences Vienna, Vienna 1180, Austria

Correspondence should be addressed to Panpan Guo; pp_guo@zju.edu.cn and Chengwei Zhu; zhuchengwei@zju.edu.cn

Received 12 August 2021; Accepted 30 August 2021; Published 21 September 2021

Academic Editor: Yu Wang

Copyright © 2021 Feng Liu et al. This is an open access article distributed under the Creative Commons Attribution License, which permits unrestricted use, distribution, and reproduction in any medium, provided the original work is properly cited.

This paper investigates the loading behavior and soil-structure interaction associated with a floating stone column under rigid foundation by using the discrete element method (DEM). The aggregates and soft soil are simulated by particles with different sizes. The rigid foundation is simulated by two loading plates at the same position with the same velocity. The stress distributions and microscopic interaction between the column and soft soil are investigated. The vertical stress of the column increases with settlement and decreases with the depth. The position of the column with large radial stress also has large deformation, which decreases from top to bottom. The vertical and radial stresses of the soft soil increase with settlement, and the radial stress shows high value in the upper part of soft soil. The stress concentration ratio is obtained by two loading plates, which decreases from 2.5 to 1.55 during loading. The interaction between column and soft soil shows that the column does not penetrate into the underlying stratum but drags the surrounding soil down.

1. Introduction

Stone columns have been proved to be effective, economical, and environment friendly to improve the soft soils [1, 2]. They can increase bearing capacity, reduce final and differential settlement, accelerate soil consolidation, improve slope stability, and decrease liquefaction potential [3–5]. Since this technique was first recorded in 1839 in Bayonne (France), it has been widely used around the world [6–8]. Numerous studies have been done to reveal the engineering characteristics of stone column-improved soft soils, especially in recent decades.

Based on one-dimensional (1D) consolidation theory by Terzaghi and ideal drain well solution by Barron, many analytical, semianalytical solutions of soft clay with stone column have been obtained. Most of them considered pore water pressure and time factor, derived consolidation equations under various geological states and boundary conditions. The average degree of consolidation can be well predicted by using the solutions [9–15].

Field monitoring can get the settlement and deformation of structure; the data can be used to reliably analyze settlement and bearing capacity of stone columns in soft clay. In situ monitoring generally lasts for several years, even more than ten years, which is time-consuming and uneconomical [1, 2]. Laboratory tests can overcome those disadvantages, which simulate field structure in small scale. Experimental study on behavior of stone column can be carried out by various parameters like shear strength of soft clay, loading conditions, and diameter and spacing of stone columns [16–21]. Obvious bulging deformation can be observed when only pile is loaded; the maximum bulging location is 0.5 times the column diameter from the top [20]. No significant bulging is seen when the load is applied to the entire model tank area [20, 21].

The finite element method (FEM) is widely used to analyze the behavior of stone columns. It is assumed that stone column is isotropic and continuous, and part of the model is usually taken as research object due to the axial symmetry [22–30]. Some studies convert individual stone columns to

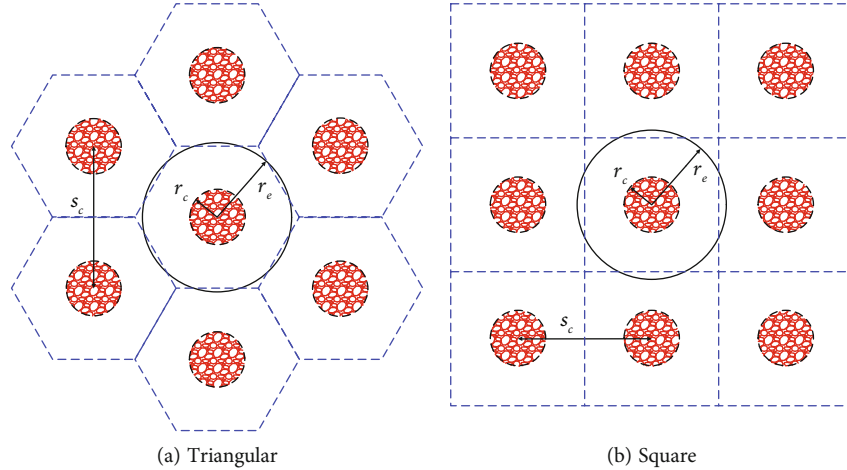


FIGURE 1: Layout of stone columns.

column walls using plane strain analysis. The results coincide with equivalent area method in long-term conditions [26]. The computational efficiency of FEM is relatively high, but its results mainly focus on the macroscopic level of model.

DEM-FDM is a coupled numerical modeling scheme. Isolated stone column can be simulated by DEM, and surrounding soil is simulated by FDM with Mohr-Coulomb yield criterion. Many studies using this method have been done to understand the behavior of stone columns and surrounding soils [31–35]. It is found that the failure mode of isolated stone column in soft clay is related to soil elastic modulus and soil cohesion [31]. The force and displacement between stone column and soil are transferred by a series of walls, which cannot be captured directly.

The DEM is widely used in geotechnical engineering, such as slopes, embankments, roads, and rocks [36–46]. In geotechnical engineering, DEM can simulate the discontinuity of soil and rock and reveal the microscopic failure mechanism. Wang et al. [40] have used DEM to study the effects of confining pressure and load path on deformation and strength of cohesive granular materials. Yu et al. [42] have investigated the failure mechanism of sandstones under different bedding angles and osmotic pressures by DEM. DEM is an effective simulation method because of the granularity of stone column aggregate; it can simulate microscopic response of granular materials. Gu et al. built a 3D DEM model for an end-bearing stone column in soft clay, and the stone column and surrounding soil were simulated by DEM. They analyzed the stress and deformation of an isolated stone column under load [47]. However, in practice, stone columns do not always penetrate the soft soil layer and sit on a hard bearing layer [19, 21]. Stone columns are ordinary installed under rigid foundation or uniform distributed load [22]. Until now, according to the author’s knowledge, there is no DEM research on the stress and deformation of floating stone column under rigid foundation.

In this study, a 3D model for floating stone column in soft clay is built, and the model is loaded uniformly on the

TABLE 1: Microscopic properties of aggregate.

Parameter	Value
Particle density (g/cm^3)	2.65
Coefficient of particle friction	0.8
Particle normal stiffness (N/m)	6.0×10^7
Particle shear stiffness (N/m)	1.0×10^7
Contact bond normal strength (N)	130
Contact bond shear strength (N)	130

TABLE 2: Microscopic properties of soil particles in the top layer.

Parameter	Value
Particle density (g/cm^3)	2.65
Coefficient of particle friction	0.25
Particle normal stiffness (N/m)	4.0×10^4
Particle shear stiffness (N/m)	4.0×10^4
Contact bond normal strength (N)	3.2
Contact bond shear strength (N)	3.2

top. The vertical and radial stress of the column and the soft soil, the porosity, coordination number and deformation of the column, the stress concentration ratio, and the column-soil interaction are analyzed.

2. Numerical Simulation

2.1. Unit Cell. Stone columns are usually arrayed in triangular or square as depicted in Figure 1. Thus, the part of column and surrounding soil is a hexagon (Figure 1(a)) or square (Figure 1(b)). Due to axial symmetry conditions, the hexagon or square can be transformed into a circle (cylinder) with the same area. The diameter of unit cell is $2r_e = 1.05 - 1.13s_c$ for triangular and square form, respectively, where s_c is the distance from center to center between

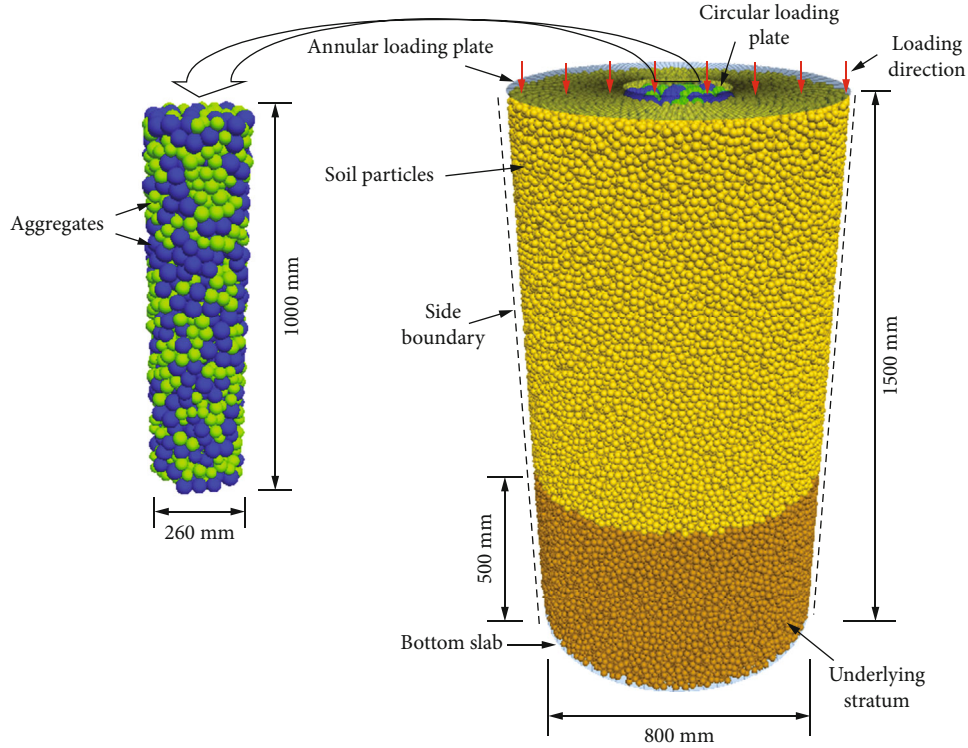


FIGURE 2: 3D model for unit cell of a floating stone column in soft clay.

columns, r_c is the radius of the column, and r_e is the replacement radius of the column.

2.2. *Parameter Selection.* The DEM software, three-dimensional particle flow code (PFC3D, version 5.0), is applied in this study. PFC is a mature business software of Itasca company. The displacements and contact forces of each particle are calculated by Newton's second law.

The linear contact bond model is used in this study to simulate the aggregate and the soft clay. The parameters of aggregates and soil particles are shown in Tables 1 and 2, which have been validated by Gu. In the Gibson soil model, the undrained shear strength of soft clay increases with depth. According to Han's suggestion, the undrained shear strength of soft clay can be calculated [48]:

$$\tau_u = c + 0.25\gamma'z, \quad (1)$$

where c is the cohesion of soft clay and γ' is the effective specific weight of soft clay. The contact-bond strength of the lower six layers was 3.40 N, 3.65 N, 3.95 N, 4.20 N, 4.55 N, and 4.90 N, respectively.

2.3. *DEM Model of a Floating Stone Column under Rigid Foundation.* A 3D DEM model is built to simulate a floating stone column under rigid foundation. Figure 2 shows the unit cell for a floating stone column in soft clay. In order to effectively simulate stone column-soil interaction and improve the calculation efficiency, the diameter and height of the model are set as 800 mm and 1500 mm, respectively.

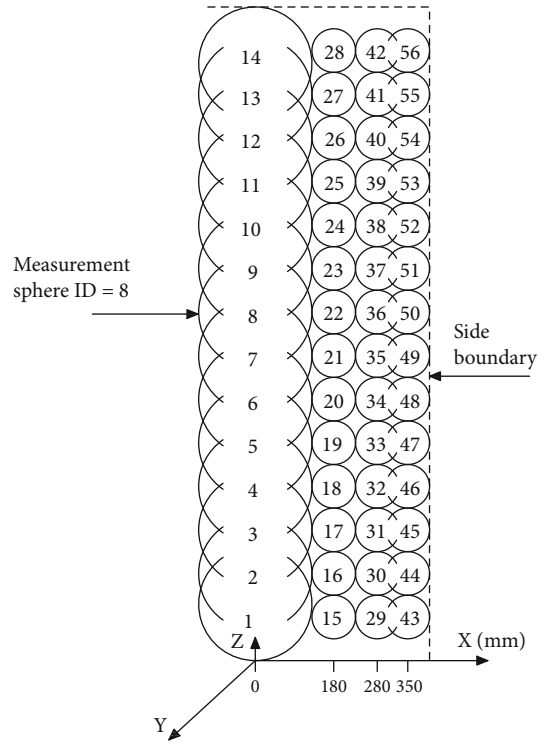


FIGURE 3: Position of measurement spheres within the model.

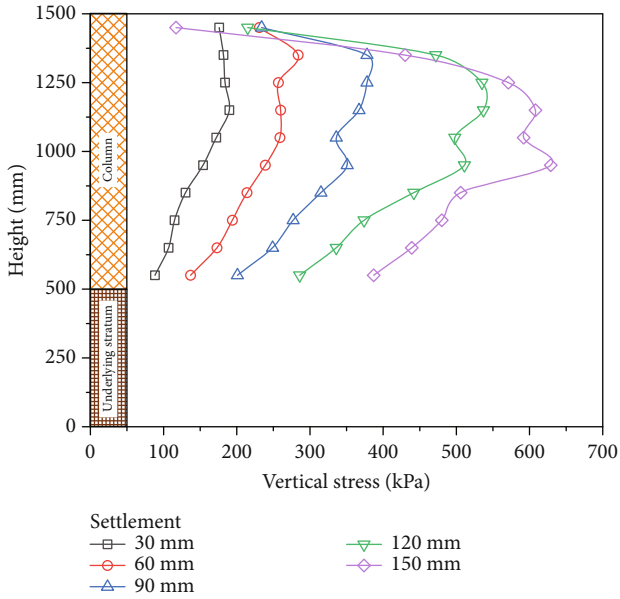


FIGURE 4: Vertical stresses of stone column under different settlements.

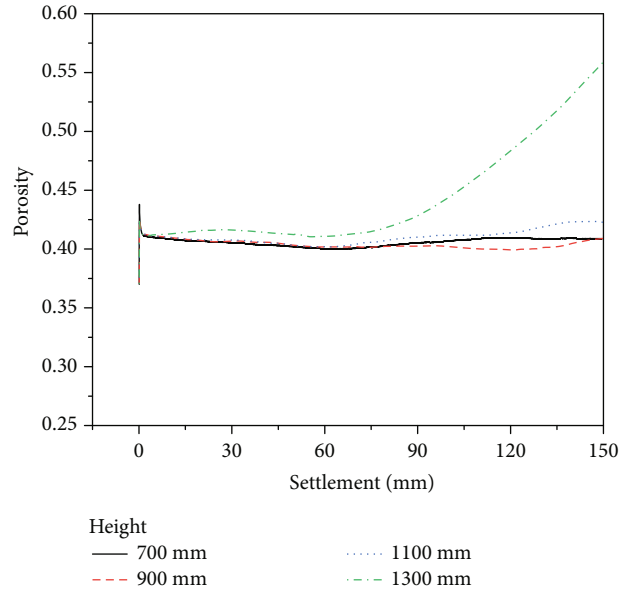


FIGURE 6: Porosity changes of the column during loading.

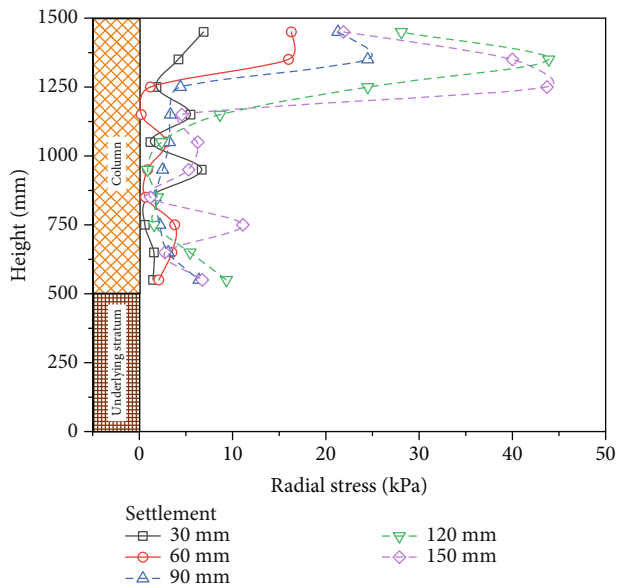


FIGURE 5: Radial stresses of stone column under different settlements.

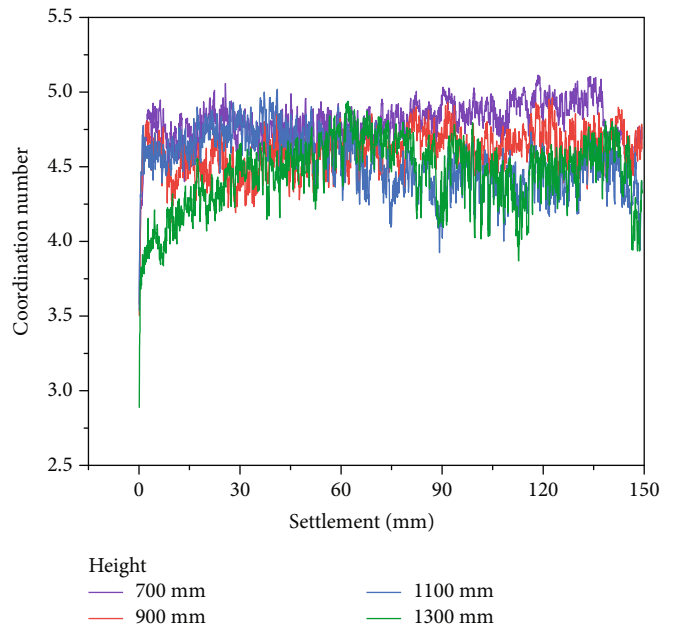


FIGURE 7: Coordination number in the column during loading.

The bottom slab of the model is fixed. The friction coefficient of side boundary is set as 0 to reduce the influence of the boundary on the model. The diameter of stone column is 260 mm, and the length is 1000 mm. The diameter of aggregates ranges from 30 to 50. Aggregates with a diameter of 30 to 40 mm make up 40% of the stone column, and aggregates with a diameter of 40-50 mm make up 60%. The porosity of stone column is 0.37. The area replacement ratio is 10.56%, between 10 and 35% [7].

Due to the irregular shape of soil particles and the influence of mineral component, the microscopic interaction of soil particles is very complex [49, 50]. DEM is difficult to simulate clayey soil accurately. This study makes some simplifications, ignores some properties, and focuses on the cohesive features of soft clay. The soft clay is simulated by linear contact bond model. The diameter of soil particles ranges from 18 to 20 mm. A total of 117930 particles are generated to simulate soft clay around and beneath the stone column. For clear display, the soil particles are divided into two groups, the soil around stone column and the

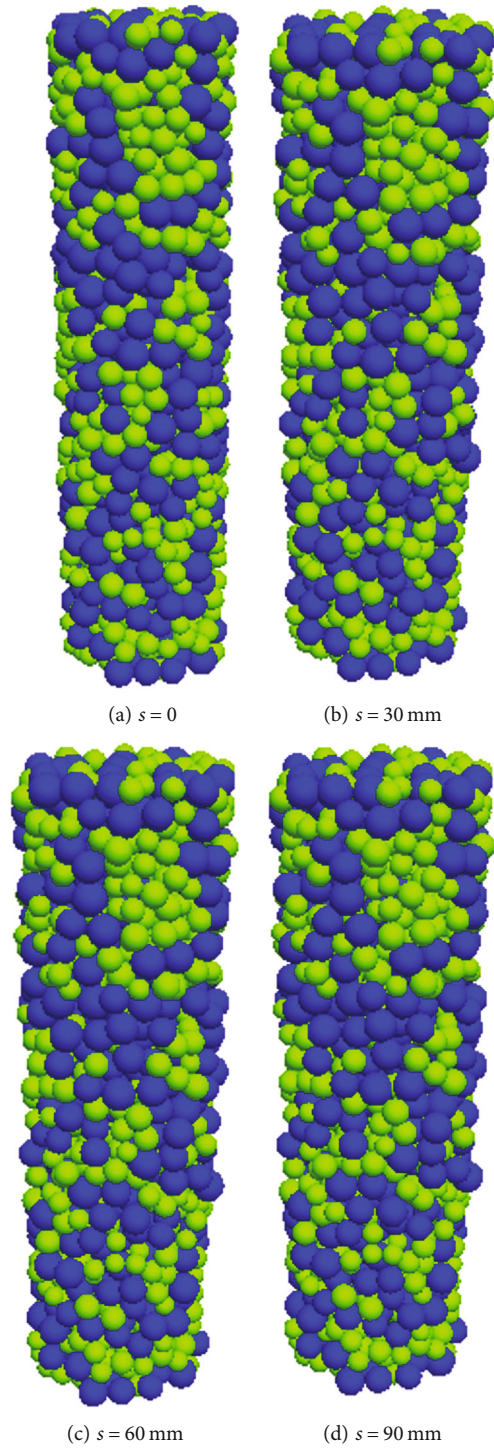


FIGURE 8: Continued.

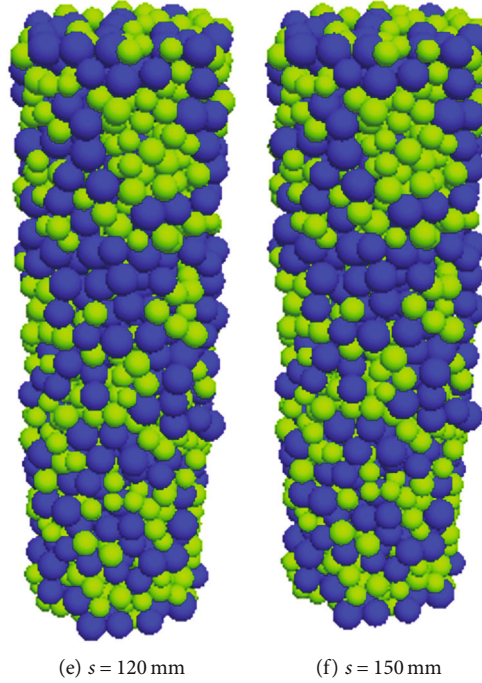


FIGURE 8: Deformation of the column during loading.

underlying stratum, which are shown in different colors. The initial porosity of soft clay is 0.4.

A circular plate and an annular plate are generated as loading plates. The two loading plates are rigid and will not be deformed during the loading process. The diameter of the circular plate is 260 mm. The inner diameter of the annular is 260 mm and the outer diameter is 800 mm. The two loading plates move down simultaneously to obtain an initial pressure of 5.0 kPa. Under the initial pressure, the particles of stone column and soil reach a certain compaction state. The displacement control method is used in the loading process. During the loading process, the two loading plates simultaneously move downward at a uniform speed of 0.008 m/s. This speed is small enough to ensure that the model remains quasistatic during loading. The ratio of the maximum unbalanced force to the maximum contact force is less than 0.003.

The parameter variation of aggregates and soft clay during loading can be monitored by measurement spheres. Figure 3 shows the location of measurement spheres within the model. There are fourteen measurement spheres of 260 mm diameter along the stone column to the bottom slab. These measurement spheres (ID from 1 to 14) overlapped each other, allowing for more intensive monitoring of data. Forty-two measurement spheres (ID from 15 to 56) are generated to monitor the surrounding soft soil at different position. The diameter of these measurement spheres is 100 mm.

3. Results

3.1. Stresses and Deformation of the Stone Column. The measurement sphere provided by PFC3D 5.0 can effectively obtain the stress and deformation changes of the column

and soil clay during loading. Because the medium is discrete, stress cannot be obtained directly. The average stress in a measurement sphere can be computed:

$$\bar{\sigma} = -\frac{1}{V} \sum_{N_c} F^{(c)} \otimes L^{(c)}, \quad (2)$$

where $\bar{\sigma}$ is the average stress in the measurement sphere, V is the volume of the measurement sphere, N_c is the number of contacts in the measurement sphere or on the boundary, $F^{(c)}$ is the contact force vector, $L^{(c)}$ is the branch vector joining the centroids of the two particles in contact, and \otimes denotes outer product.

3.1.1. Vertical and Radial Stresses. Figure 4 shows the distribution of vertical stress along the stone column under different settlements. On the whole, the vertical stress increases with the increase of settlement. When the settlement is more than 1000 mm, the stress on the top of stone column decreases significantly. This is because the horizontal constraint of the aggregates on the top of column is small, and the effective volume of the measurement sphere (ID = 14) is decreasing due to the increase of settlement. The vertical stress firstly increases and then decreases along the stone column, which means that the vertical load is transferred from the column to the surrounding soil. At the beginning, the maximum stress is about at the 200 mm below the column top; with the increase of settlement, it gradually moves down to 500 mm. The vertical load on the column is transferred downward, but not to the bottom of the column.

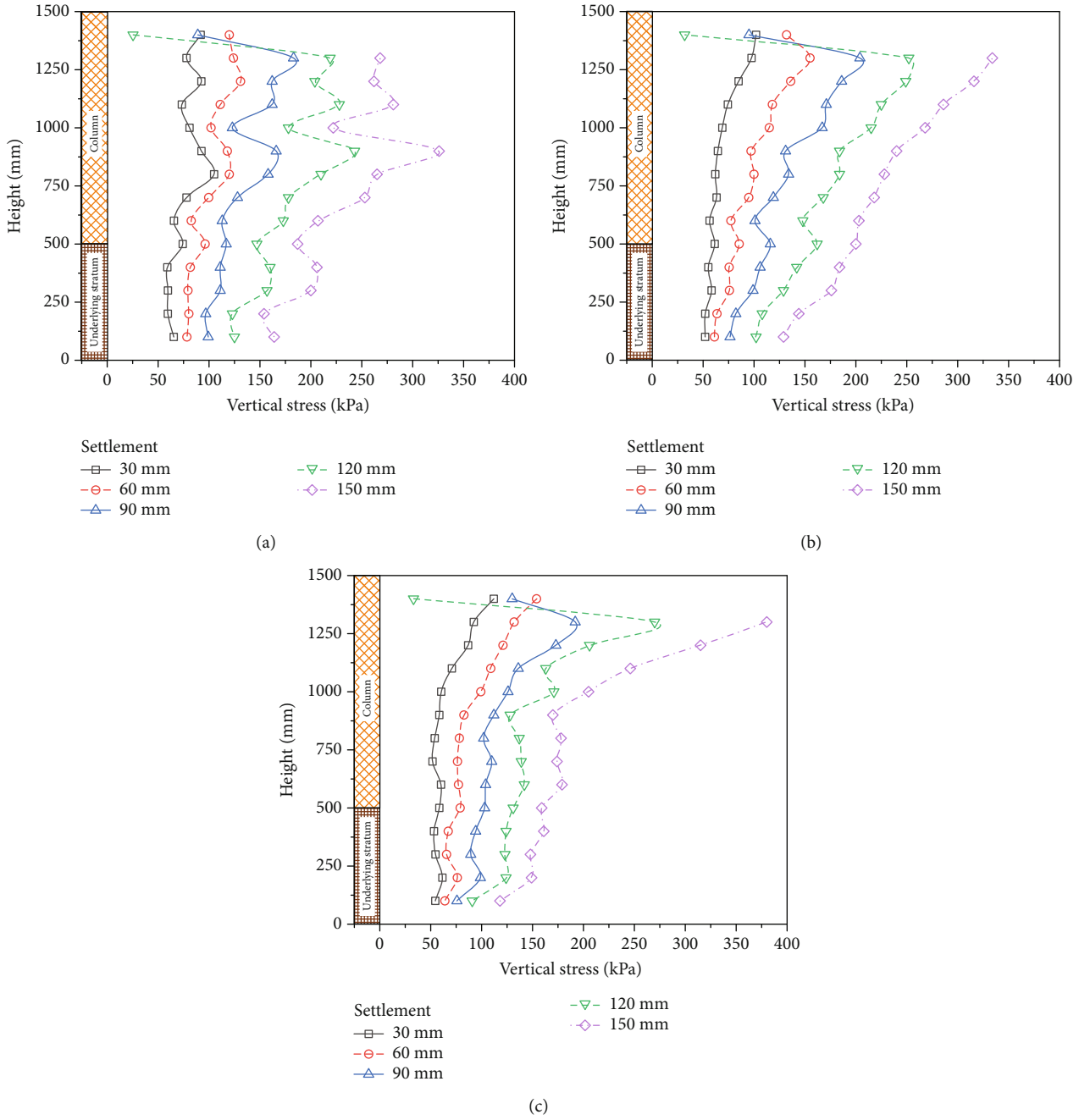


FIGURE 9: Vertical stresses of the soft soil: (a) 180 mm, (b) 280 mm, and (c) 350 mm away from the center of the column.

Figure 5 shows the distribution of radial stresses along the stone column under different settlements. As shown in the figure, the maximum radial stress occurs within the range of 400 mm below the column top. With the increase of settlement, the radial stress also increases, but the affected area does not increase.

3.1.2. Porosity Change. The change of porosity is an important index of stone column. It can reflect the change of relative density of the column during loading. However, the exact variation of porosity is difficult to obtain in laboratory

and field tests. The measurement sphere in PFC can easily measure the change of porosity with time. Porosity is the ratio of the volume of the void in the measurement sphere to the volume of the whole measurement sphere. Four measurement spheres are selected at the model heights of 700 mm, 900 mm, 1100 mm, and 1300 mm. The four positions correspond to 200 mm, 400 mm, 600 mm, and 800 mm in the column, respectively.

Figure 6 shows the porosity changes of the column during loading. The initial porosity of stone column is 0.37, which increases to 0.425 immediately after the initial

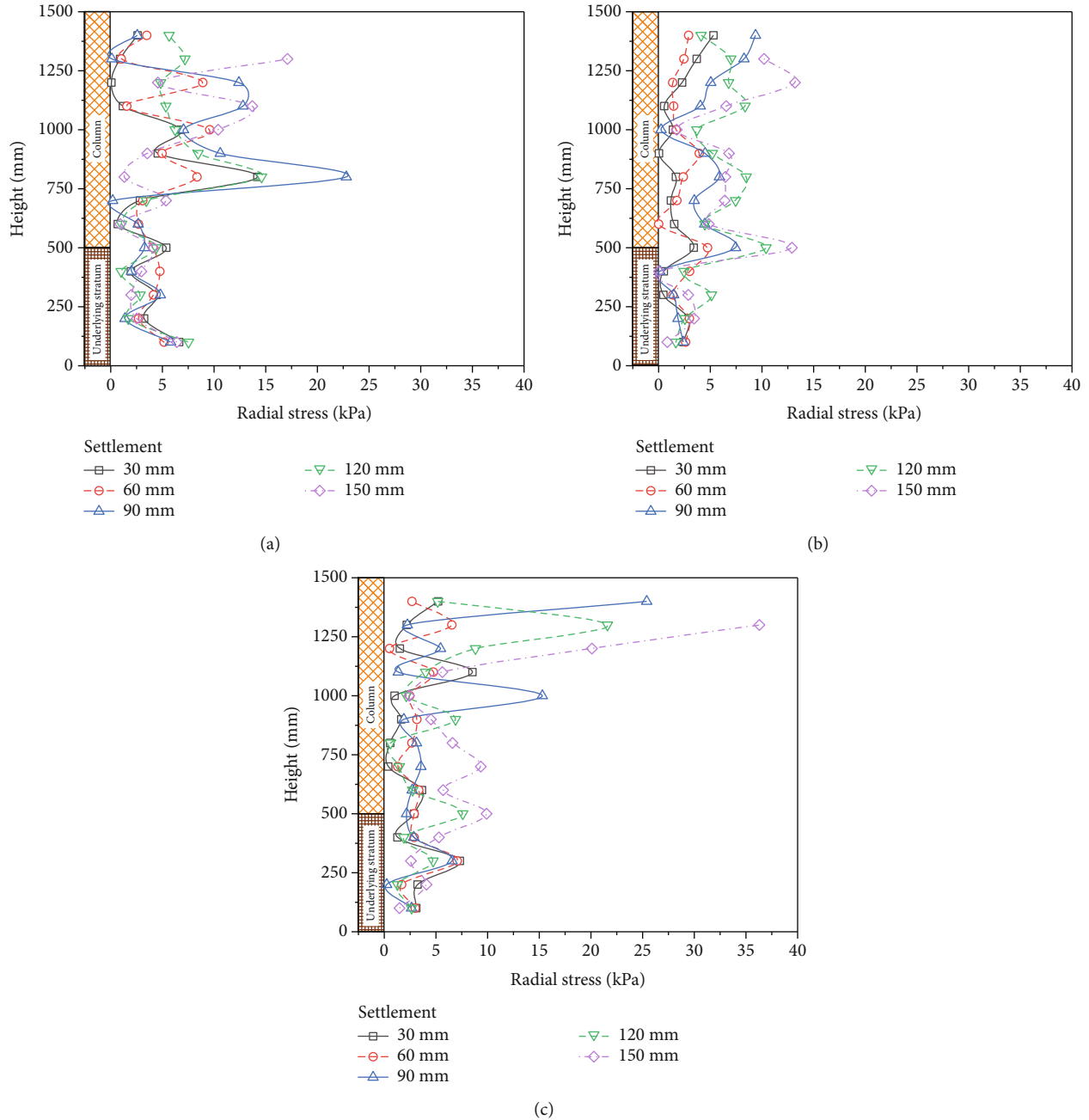


FIGURE 10: Radial stresses of the soft soil: (a) 180 mm, (b) 280 mm, and (c) 350 mm away from the center of the column.

pressure is applied. As the load continues to increase, the porosity of the three lower positions changes little and is basically stable between 0.41 and 0.42. The porosity of the upper position is stable at about 0.42, when settlement is less than 750 mm. When the settlement is greater than 700, the porosity increases with the increase of settlement. This indicates that when the settlement is less than 750 mm, the aggregates of the column are relatively dense. As the load continues to increase, the lower part of the column remains stable, and the upper part shows sign of failure.

3.1.3. Coordination Number. The coordination number is the average number of active contacts for each particle in a measurement sphere and is computed as

$$C_n = \frac{\sum_{N_b} n_c^{(b)}}{N_b}, \quad (3)$$

where C_n is coordination number, N_b is the number of particles with centroids in the measurement sphere, and $n_c^{(b)}$ is the number of active contacts of particle b .

The coordination number can be used to estimate the particle movement of the column. Four measurement spheres at the model heights of 700 mm, 900 mm, 1100 mm, and 1300 mm are selected. The four positions correspond to 200 mm, 400 mm, 600 mm, and 800 mm in the column, respectively. Figure 7 shows the coordination number in the column during loading. After the initial pressure was applied, the coordination number at the heights of 700 mm, 900 mm, 1100 mm, and 1300 mm was 4.9, 4.7, 4.5, and 4.0. As the load gradually increases, the coordination number of the four positions has some fluctuations, but the coordination number increases in general, which means that the aggregates became denser. At the end of loading, the coordination number at the height of 700 mm, 900 mm, 1100 mm, and 1300 mm was 4.7, 4.6, 4.3, and 3.8. The aggregates at the upper part of the column have a small coordination number, which also means that the aggregates are relatively loose. This is consistent with the result of porosity.

3.1.4. Deformation. The deformation of the column can reflect the failure mode intuitively. However, it is difficult to monitor the deformation process of stone column under load in laboratory test and in situ engineering practice. Numerical simulation can overcome this disadvantage and conveniently obtain the deformation of column under various loads. PFC 3D obtained the deformation of the column during loading, as shown in Figure 8. Under the action of load, the column is constantly compressed and expanded. Expansion becomes smaller from top to bottom. The deformation of the upper part of the column is large, and the radial stress is also large, which shows a certain positive correlation. When the settlement reaches 1500 mm, the shape of the column is close to the frustum of a cone. The results of the PFC numerical simulation are similar to those of the experiments [20, 21]. Wang et al. [20] and Guo et al. [21] conducted the model test of stone column under uniform load on the entire top of model. The deformation of stone column under rigid foundation is different from that under load only on the column top. When the load only applies on the column top, obvious expansion deformation will occur below the column top [29, 33]. This difference is related to the confined strength of the soil. When the load is applied to both column and soil, the soil can provide greater confined strength than when the load is applied only to the column.

3.2. Vertical and Radial Stresses of the Soft Soil. The vertical and radial stresses of the soft soil during loading are obtained using measurement spheres at different positions. Figure 9 shows the vertical stresses of the soft soil 180 mm, 280 mm, and 350 mm away from the center of the column. Figure 9(a) shows that the vertical stress fluctuates along the depth direction. This is because the soil in this area is close to the column and is greatly affected by the deformation of the column. The vertical stress distributions of the soft soil are relatively regular in Figures 9(b) and 9(c). The vertical stresses in Figure 9 all increase with the increase of load. At the same position away from the center of the column, the vertical stress decreases with the increase of

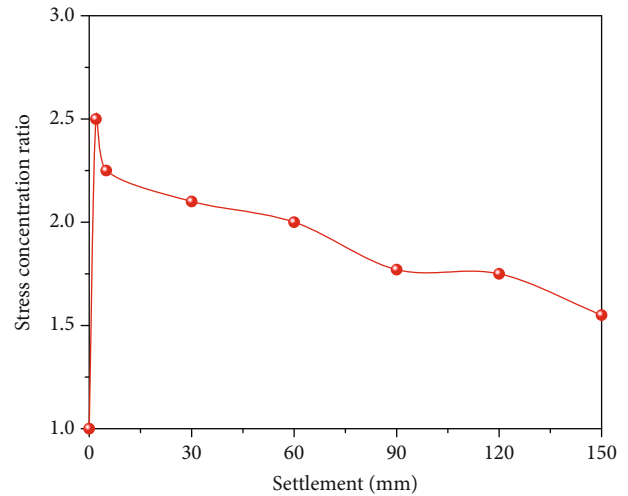


FIGURE 11: Stress concentration ratio with settlement.

the depth. As the loading plate gradually moves down, the volume of the measurement sphere at the top gradually decreases, so the stress measured by the measurement sphere at the top also decreases.

Figure 10 shows the radial stresses of the soft soil 180 mm, 280 mm, and 350 mm away from the center of the column. Figures 10(a) and 10(c) show that the radial stress of the upper part of the soil is relatively large. Figure 10(b) shows that the radial stress fluctuation of the soil in the middle is large, but the value of radial stress is small. At the height of 500 mm, that is, the position of column foot, the radial stress increases significantly.

The distribution of vertical and radial stress of the soft soil under rigid foundation is different from that load only on the column top. When load is only on the column top, the vertical stress increases along the depth, and the radial stress in the upper soil near the side boundary is large [47].

3.3. Column-Soil Interaction

3.3.1. Stress Concentration Ratio. The stress concentration ratio is an important parameter in geotechnical engineering, which reflects the load sharing between column and soil. In this study, a circular loading plate and an annular loading plate are generated to record the load on the column and soil, respectively. The stress concentration ratio can be obtained by calculating the recorded load. Figure 11 shows that the stress concentration ratio decreases with the increase of settlement. After the initial pressure applied, the stress concentration ratio reaches the maximum of 2.5. This is because the column had higher stiffness than the surrounding soil and carried more load. With the gradual increase of load, the settlement becomes larger, and the stress is transferred from the column to soil. When settlement reached 150 mm, the stress concentration ratio is 1.55. The results in this study are in the range of 2 to 4, which is consistent with other's literature [10, 26]. In Zhang et al.'s article, the typical stress concentration ratio of a stone column-improved ground under rigid foundation is 2 to 4

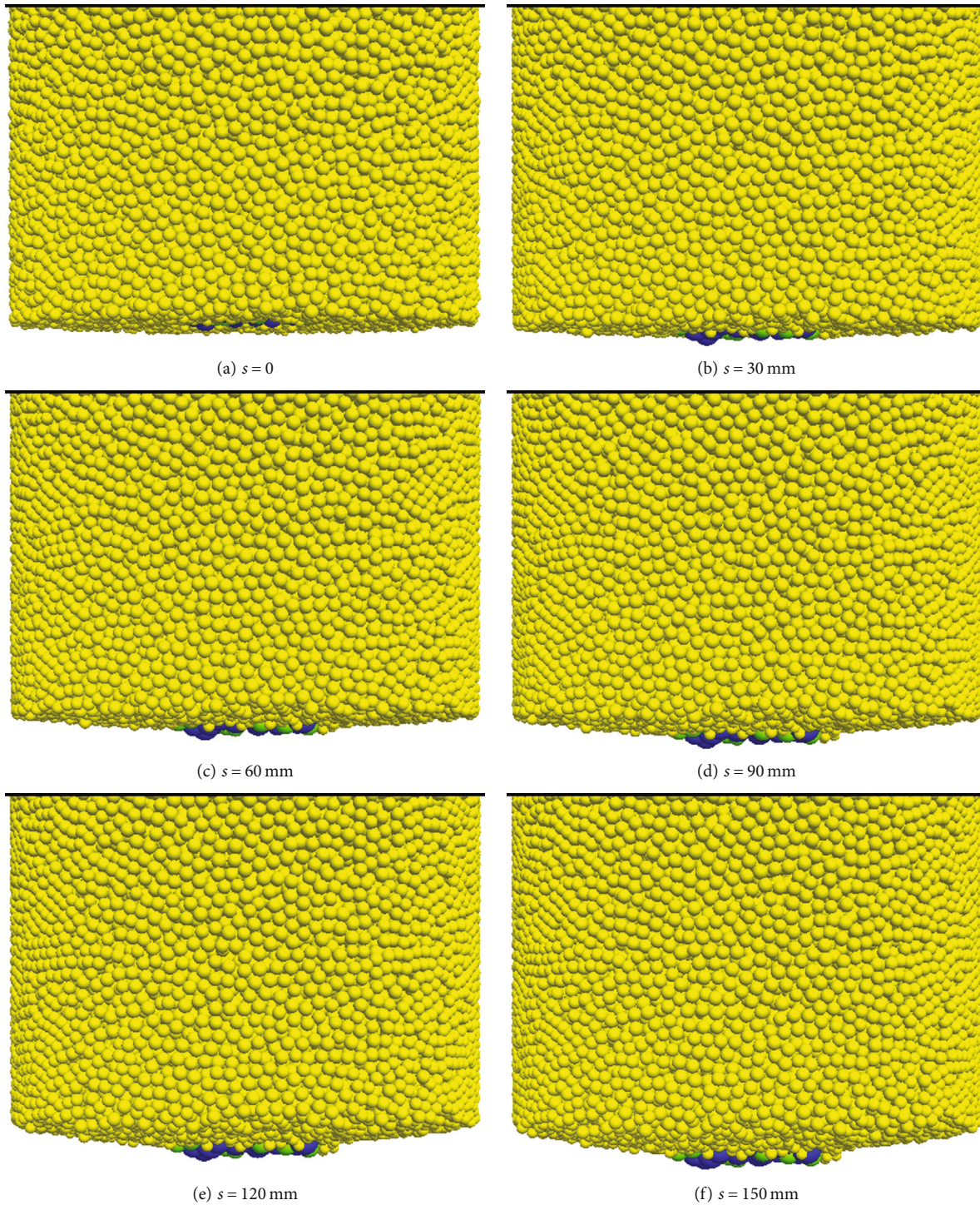


FIGURE 12: Deformation of column and soil at the bottom of column during loading.

[26]. When the settlement is greater than 90 mm, the stress concentration ratio is less than 2. This is due to the expansion of the column top; the circular loading plate cannot record accurately. The stress concentration ratio at the later stage of loading is an approximate value.

3.3.2. Deformation of Column and Soil at the Bottom of Column. PFC has the advantage to monitor the movement

of particles under load. Each particle can be divided into different groups before loading. Therefore, the trajectory of particles can be clearly seen during loading. In this study, as shown in Figure 2 the particles of soft clay are divided into two groups with different colors. The soil with yellow is the same height as the column. Figure 12 shows the deformation of column and soil at the bottom of column under different settlements. With the increase of load, the deformation of

column and soil becomes larger, and the protrusion is more obvious. When the settlement reaches 150 mm, the protrusion is close to cone. The column does not penetrate into the underlying stratum, and the column has a drag effect on the surrounding soil. In other words, the column and surrounding soil deform cooperatively, showing certain integrity. This is related to the large coefficient of friction between column and soil. The stress is transmitted from inside to outside through the column to the surrounding soil, thus making the protrusion to cone shape.

4. Discussion

Although the proposed DEM model can analyze the behavior of a floating stone column under rigid foundation, it still needs to be improved in the following aspects: (1) the linear contact model was used to simulate the soil particle for simplicity; the use of PFC to simulate soft soil requires further study; (2) the displacement-control method was adopted in the model, and the load-control method could be developed in further study; and (3) when the column top expanded during loading, the loading plate on the column did not expand simultaneously.

5. Conclusions

In this present work, a 3D DEM model of a floating stone column under rigid foundation is established. The aggregates of stone column and soft clay are simulated with particles, using the linear contact model. Two loading plates at the same position with the same velocity are used to simulate the rigid foundation. The stress and deformation of column and soft clay are investigated in this study. The interaction between column and soil is also analyzed. Based on the numerical simulation results, the following conclusions have been obtained:

- (i) The vertical stress of the column increases with the increase of settlement and decreases with the depth of the column. The radial stress of the column also increases with the settlement, but the affected area is concentrated in the shallow section
- (ii) With the settlement increasing, the porosity of the shallow section of the column increases and the coordination number is relatively small. This means that the aggregates in the upper part of the column become loose as settlement increases. The porosity and coordination number of the lower section of the column remain relatively stable with the increase of settlement. Therefore, the aggregates in the lower part remain relatively dense
- (iii) Under rigid foundation, the surrounding soil can provide great lateral strength. The expansion deformation of the column decreases gradually from top to bottom
- (iv) The vertical stress of the soft clay increases with the increase of settlement. The radial stress of the upper

part of soft clay is large, and at the position of column foot, the radial stress increases significantly

- (v) The stress concentration ratio decreases from 2.5 to 1.55 during loading. The column does not penetrate into the underlying stratum, and the column drags the surrounding soil down

Data Availability

The data used to support the findings of this study are available from the corresponding author upon request.

Conflicts of Interest

The authors declare that they have no known competing financial interests or personal relationships that could have appeared to influence the work reported in this paper.

Acknowledgments

This research was financially supported by the National Natural Science Foundation of China (grant numbers 51778575 and 52078457).

References

- [1] B. A. McCabe, G. J. Nimmons, and D. Egan, "A review of field performance of stone columns in soft soils," *Geotechnical Engineering*, vol. 162, no. 6, pp. 323–334, 2009.
- [2] O. Sadaoui and R. Bahar, "Field measurements and back calculations of settlements of structures founded on improved soft soils by stone columns," *European Journal of Environmental and Civil Engineering*, vol. 23, no. 1, pp. 85–111, 2019.
- [3] S. Pal and K. Deb, "Effect of stiffness of stone column on drainage capacity during soil liquefaction," *International Journal of Geomechanics*, vol. 18, no. 3, article 04018003, 2018.
- [4] A. W. Stuedlein and R. D. Holtz, "Bearing capacity of spread footings on aggregate pier reinforced clay," *Journal of Geotechnical and Geoenvironmental Engineering*, vol. 139, no. 1, pp. 49–58, 2013.
- [5] A. W. Stuedlein and R. D. Holtz, "Displacement of spread footings on aggregate pier reinforced clay," *Journal of Geotechnical and Geoenvironmental Engineering*, vol. 140, no. 1, pp. 36–45, 2014.
- [6] Y. Wang, Y. F. Yi, C. H. Li, and J. Q. Han, "Anisotropic fracture and energy characteristics of a Tibet marble exposed to multi-level constant-amplitude (MLCA) cyclic loads: a lab-scale testing," *Engineering Fracture Mechanics*, vol. 244, article 107550, 2021.
- [7] A. M. Hanna, M. Etehad, and T. Ayadat, "Mode of failure of a group of stone columns in soft soil," *International Journal of Geomechanics*, vol. 13, no. 1, pp. 87–96, 2013.
- [8] J. M. O. Hughes, N. J. Withers, and D. A. Greenwood, "A field trial of the reinforcing effect of a stone column in soil," *Geotechnique*, vol. 25, no. 1, pp. 31–44, 1975.
- [9] R. A. Barron, "Consolidation of fine-grained soils by drain wells by drain wells," *Transactions of the American Society of Civil Engineers*, vol. 113, no. 1, pp. 718–742, 1948.
- [10] J. Han and S. L. Ye, "Simplified method for consolidation rate of stone column reinforced foundations," *Journal of*

- Geotechnical and Geoenvironmental Engineering*, vol. 127, no. 7, pp. 597–603, 2001.
- [11] L. Wang, A. Zhou, Y. F. Xu, and X. H. Xia, “Consolidation of unsaturated composite ground reinforced by permeable columns,” *Computers and Geotechnics*, vol. 125, article 103706, p. 14, 2020.
- [12] H. B. Poorooshab and G. G. Meyerhof, “Analysis of behavior of stone columns and lime columns,” *Computers and Geotechnics*, vol. 20, no. 1, pp. 47–70, 1997.
- [13] J. Han, S. Oztoprak, R. L. Parsons, and J. Huang, “Numerical analysis of foundation columns to support widening of embankments,” *Computers and Geotechnics*, vol. 34, no. 6, pp. 435–448, 2007.
- [14] Y. Wang, B. Zhang, B. Li, and C. H. Li, “A strain-based fatigue damage model for naturally fractured marble subjected to freeze-thaw and uniaxial cyclic loads,” *International Journal of Damage Mechanics*, no. article 105678952110216, 2021.
- [15] K. H. Xie, M. M. Lu, and G. B. Liu, “Equal strain consolidation for stone columns reinforced foundation,” *International Journal for Numerical and Analytical Methods in Geomechanics*, vol. 33, no. 15, pp. 1721–1735, 2009.
- [16] R. Moradi, A. Marto, A. S. A. Rashid, M. M. Moradi, A. A. Ganiyu, and S. Horpibulsuk, “Bearing capacity of soft soil model treated with end-bearing bottom ash columns,” *Environmental Earth Sciences*, vol. 77, no. 3, p. 100, 2018.
- [17] D. Muir Wood, W. Hu, and D. F. T. Nash, “Group effects in stone column foundations: model tests,” *Geotechnique*, vol. 50, no. 6, pp. 689–698, 2000.
- [18] A. Cimentada, A. da Costa, J. Cañizal, and C. Sagaseta, “Laboratory study on radial consolidation and deformation in clay reinforced with stone columns,” *Canadian Geotechnical Journal*, vol. 48, no. 1, pp. 36–52, 2011.
- [19] J. Black, V. Sivakumar, and J. D. McKinley, “Performance of clay samples reinforced with vertical granular columns,” *Canadian Geotechnical Journal*, vol. 44, no. 1, pp. 89–95, 2007.
- [20] Y. Wang, C. H. Li, and J. Q. Han, “On the effect of stress amplitude on fracture and energy evolution of pre-flawed granite under uniaxial increasing-amplitude fatigue loads,” *Engineering Fracture Mechanics*, vol. 240, article 107366, 2020.
- [21] P. Guo, F. Liu, G. Lei et al., “Predicting response of constructed tunnel to adjacent excavation with dewatering,” *Geofluids*, vol. 2021, Article ID 5548817, 2021.
- [22] J. Castro, “An analytical solution for the settlement of stone columns beneath rigid footings,” *Acta Geotechnica*, vol. 11, no. 2, pp. 309–324, 2016.
- [23] A. K. Das and K. Deb, “Experimental and 3D numerical study on time-dependent behavior of stone column-supported embankments,” *International Journal of Geomechanics*, vol. 18, no. 4, article 04018011, p. 16, 2018.
- [24] A. Thakur, S. Rawat, and A. K. Gupta, “Experimental and numerical investigation of load carrying capacity of vertically and horizontally reinforced floating stone column group,” *Geotechnical and Geological Engineering*, vol. 39, no. 4, pp. 3003–3018, 2021.
- [25] P. Guo, X. Gong, and Y. Wang, “Displacement and force analyses of braced structure of deep excavation considering unsymmetrical surcharge effect,” *Computers and Geotechnics*, vol. 113, article 103102, 2019.
- [26] Z. Zhang, J. Han, and G. B. Ye, “Numerical investigation on factors for deep-seated slope stability of stone column-supported embankments over soft clay,” *Engineering Geology*, vol. 168, pp. 104–113, 2014.
- [27] B. Indraratna, S. Basack, and C. Rujikiatkamjorn, “Numerical solution of stone column–improved soft soil considering arching, clogging, and smear effects,” *Journal of Geotechnical and Geoenvironmental Engineering*, vol. 139, no. 3, pp. 377–394, 2013.
- [28] J. Castro and M. Karstunen, “Numerical simulations of stone column installation,” *Canadian Geotechnical Journal*, vol. 47, no. 10, pp. 1127–1138, 2010.
- [29] X. Tan, L. J. Feng, Z. B. Hu, and M. H. Zhao, “Failure modes and ultimate bearing capacity of the isolated stone column in soft soil,” *Bulletin of Engineering Geology and the Environment*, vol. 80, no. 3, pp. 2629–2642, 2021.
- [30] P. Guo, X. Gong, Y. Wang, H. Lin, and Y. Zhao, “Minimum cover depth estimation for underwater shield tunnels,” *Tunnelling and Underground Space Technology*, vol. 115, article 104027, 2021.
- [31] X. Tan, L. J. Feng, Z. B. Hu, and M. H. Zhao, “A DEM-FDM coupled numerical study on the deformation and failure process of the isolated stone column in soft soil,” *Bulletin of Engineering Geology and the Environment*, vol. 79, no. 4, pp. 1693–1705, 2020.
- [32] B. Indraratna, N. T. Ngo, C. Rujikiatkamjorn, and S. W. Sloan, “Coupled discrete element-finite difference method for analysing the load–deformation behaviour of a single stone column in soft soil,” *Computers and Geotechnics*, vol. 63, pp. 267–278, 2015.
- [33] X. Tan, M. H. Zhao, Z. B. Hu, and L. J. Feng, “Failure process of a single stone column in soft soil beneath rigid loading: numerical study,” *International Journal of Geomechanics*, vol. 20, no. 8, article 04020130, p. 13, 2020.
- [34] X. Tan, L. J. Feng, Z. B. Hu, and S. M. Abbas, “The equivalent shear strength properties of the composite soil reinforced by stone columns: an FDM-DEM-coupled numerical evaluation,” *Environmental Earth Sciences*, vol. 80, no. 4, article 125, p. 12, 2021.
- [35] A. Gholaminejad, A. Mahboubi, and A. Noorzad, “Hybrid continuous-discrete modeling of an ordinary stone column and micromechanical investigations,” *Geotechnical and Geological Engineering*, vol. 39, no. 4, pp. 3249–3264, 2021.
- [36] J. Cheng, H. Zhang, and Z. Wan, “Numerical simulation of shear behavior and permeability evolution of rock joints with variable roughness and infilling thickness,” *Geofluids*, vol. 2018, Article ID 1869458, 11 pages, 2018.
- [37] Z. Chen, X. Li, L. Weng, S. Wang, and L. Dong, “Influence of flaw inclination angle on unloading responses of brittle rock in deep underground,” *Geofluids*, vol. 2019, Article ID 4657645, 16 pages, 2019.
- [38] Y. Wu, Q. Liu, A. H. C. Chan, and H. Liu, “Implementation of a time-domain random-walk method into a discrete element method to simulate nuclide transport in fractured rock masses,” *Geofluids*, vol. 2017, Article ID 5940380, 13 pages, 2017.
- [39] X. Q. Gu, M. S. Huang, and J. G. Qian, “Discrete element modeling of shear band in granular materials,” *Theoretical and Applied Fracture Mechanics*, vol. 72, pp. 37–49, 2014.
- [40] Y. Wang, W. K. Feng, H. J. Wang, C. H. Li, and Z. Q. Hou, “Rock bridge fracturing characteristics in granite induced by freeze-thaw and uniaxial deformation revealed by AE monitoring and post-test CT scanning,” *Cold Regions Science and Technology*, vol. 177, article 103115, 2020.

- [41] Z. Li, Y. H. Wang, C. H. Ma, and C. M. B. Mok, "Experimental characterization and 3D DEM simulation of bond breakages in artificially cemented sands with different bond strengths when subjected to triaxial shearing," *Acta Geotechnica*, vol. 12, no. 5, pp. 987–1002, 2017.
- [42] J. Yu, W. Yao, K. Duan, X. Y. Liu, and Y. L. Zhu, "Experimental study and discrete element method modeling of compression and permeability behaviors of weakly anisotropic sandstones," *International Journal of Rock Mechanics and Mining Sciences*, vol. 134, article 104437, 2020.
- [43] J. M. Li, Y. L. Huang, H. Pu et al., "Influence of block shape on macroscopic deformation response and meso-fabric evolution of crushed gangue under the triaxial compression," *Powder Technology*, vol. 384, pp. 112–124, 2021.
- [44] K. C. S. S. R. J. Pillai, and H. Mudavath, "Influence of erodible layer on granular column collapse using discrete element analysis," *Geomechanics and Geoengineering*, pp. 1–13, 2021.
- [45] X. Q. Gu, Z. P. You, J. G. Qian, and W. Y. Li, "The deformation of granular materials under repeated traffic load by discrete element modelling," *European Journal of Environmental and Civil Engineering*, vol. 24, no. 8, pp. 1135–1160, 2020.
- [46] R. X. Zhang, D. Su, G. P. Lei, and X. S. Chen, "Three-dimensional granular column collapse: impact of column thickness," *Powder Technology*, vol. 389, pp. 328–338, 2021.
- [47] M. X. Gu, J. Cui, J. Yuan, Y. Wu, Y. D. Li, and H. Z. Mo, "The stress and deformation of stone column-improved soft clay by discrete element modelling," *European Journal of Environmental and Civil Engineering*, pp. 1–17, 2020.
- [48] J. Han, *Principles and Practice of Ground Improvement*, John Wiley & Sons, Hoboken, NJ, 2015.
- [49] A. A.-C. Guéry, F. Cormery, J. F. Shao, and D. Kondo, "A micromechanical model of elastoplastic and damage behavior of a cohesive geomaterial," *International Journal of Solids and Structures*, vol. 45, no. 5, pp. 1406–1429, 2008.
- [50] Z. Y. Yin, "Micromechanics based analytical model for soils: review and development," *Chinese Journal of Geotechnical Engineering*, vol. 35, pp. 993–1009, 2013.

Research Article

A Simulation Study on the Swelling and Shrinking Behaviors of Nanosized Montmorillonite Based on Monte Carlo and Molecular Dynamics

Kaiwen Tong,^{1,2} Jianhua Guo,^{1,2} Shanxiong Chen,¹ Fei Yu ,¹ Shichang Li,^{1,2} and Zhangjun Dai ¹

¹State Key Laboratory of Geomechanics and Geotechnical Engineering, Institute of Rock and Soil Mechanics, Chinese Academy of Sciences, Wuhan 430071, China

²University of Chinese Academy of Sciences, Beijing 100049, China

Correspondence should be addressed to Zhangjun Dai; zjdai@whrsm.ac.cn

Received 12 July 2021; Accepted 20 August 2021; Published 15 September 2021

Academic Editor: Yu Wang

Copyright © 2021 Kaiwen Tong et al. This is an open access article distributed under the Creative Commons Attribution License, which permits unrestricted use, distribution, and reproduction in any medium, provided the original work is properly cited.

Montmorillonite is the main mineral source for the swelling and shrinking of expansive soils. The macroscopic phenomena of soil are affected by the action of deep-level nanosized minerals. In order to illustrate the nanoscale mechanism from the molecular level, a combination of Monte Carlo and molecular dynamics was used to explore the swelling and shrinking characteristics of montmorillonite. The results showed that the basal spacing, free swelling ratio, and void ratio were positively correlated with water content but were inversely proportional to the change of CEC. The hysteresis phenomena of swelling and shrinking were the most significant at a water content of 40%. Compared with the expansive soil, the nanoscale shrinkage curve of montmorillonite also included three stages of normal shrinkage, residual shrinkage, and no shrinkage. The relative concentration of water molecules conveyed information such as the thickness and position of the hydration film and explained the difference in swelling and shrinking caused by the above variables. The changes in the number and length of hydrogen bonds revealed the order of formation and the process of destruction of hydrogen bonds during the reaction. The similarity of the trends between the basal spacing, binding energy, and the number of hydrogen bonds indicated that the swelling and shrinking of the crystal layer are a reflection of the molecular interaction, and the hydrogen bonding is particularly critical.

1. Introduction

Expansive soil is widely distributed worldwide and generally exists on the surface of the earth. It is mainly composed of clay minerals such as montmorillonite, illite, and kaolinite [1]. Due to its engineering characteristics of swelling and shrinking, it often causes damage to roadbeds, slopes, and buildings, bringing huge losses to the economic security of countries around the world [2, 3].

Both natural and remodeled expansive soils have extremely complex mineral compositions and random structures. The research scale ranges from nanosized minerals to macroscale clays, and there are complex interactions between particles, as well as between particles and electrolyte solution [4–7]. So far, the explanation of the swelling and shrinking mechanism

of expansive soil has not been unified. Most of them are based on the macrolevel, ignoring the coupling process of physics, mechanics, and chemistry on the microscale [8–10]. Studies have shown that montmorillonite plays an important role in the swelling and shrinking of expansive soil. Starting with nano-level minerals is a prerequisite to fully understand and clarify its deformation and destruction [11]. However, it is highly difficult to test the interaction between the solid and liquid molecules of crystal layer by experimental methods, which hinders the further development of clay mineralogy to a certain extent.

With the improvement of molecular simulation technology, many scholars have achieved remarkable results in the behaviors of montmorillonite and the influencing factors of swelling. Boek et al. [12] first used the Monte Carlo method to simulate the hydrated phenomena of Na-montmorillonite

and found the basic spacing increased with the rise of water content. Marry et al. [13] obtained its structure and kinetic features to calculate the diffusion coefficient of water molecules and interlayer cations. In order to determine the key factors affecting the swelling properties, Chang et al. [14] investigated the hydrated behaviors under the action of different cations such as Li^+ , Na^+ , and K^+ by molecular simulation. Furthermore, Wang and Zeng [15] regarded the water content and the types of interlayer cations as variables, sorting the ability of Li^+ , Na^+ , and K^+ to organize oxygen atoms through the radial distribution function. Katti et al. [16] relied on Fourier transform infrared and molecular dynamics to study the swelling behaviors of Na-montmorillonite in various organic fluids. Abduljawad et al. [17] considered the influence of dry density on swell potential and pressure of Na-montmorillonite from the perspective of cohesive energy density (CED). In addition to its own conditions, Li [18] reported the changes in the interlayer structure of Na-montmorillonite and Cs-montmorillonite in the range of 300 K–600 K. But up to date, there are few evaluations on the influence of cation exchange capacity (CEC), and most of the above researches are obviously insufficient in system and depth. Recently, studies involving the shrinking of montmorillonite after losing water have rarely been mentioned. In addition, the range of water content that the existing literature focused on is too narrow (0–30%). It cannot reflect the characteristics of montmorillonite in the entire stage of swelling and shrinking and lacking a connection with macroscopic experimental phenomena [19–21].

In this paper, based on the molecular dynamics, the influence of water content, types of interlayer cations, and cation exchange capacity on the swelling and shrinking behaviors of montmorillonite under normal temperature and pressure was explored. The simulation results of the nanoscale were utilized to figure out the microscopic mechanism and preliminarily explained the macroscopic experimental phenomena.

2. Methodology

2.1. Swelling Behaviors of Montmorillonite

2.1.1. Model Construction. The Wyoming montmorillonite (Mnt) selected in this article has been widely studied by scholars [22, 23]. The unit cell belongs to the monoclinic system, space group C2/m with $\alpha = \gamma = 90^\circ$, $\beta = 99^\circ$, $a \approx 5.23 \text{ \AA}$, and $b \approx 9.06 \text{ \AA}$. When montmorillonite is in a completely dry state, $c \approx 9.60 \text{ \AA}$. While adsorbing one, two, three, and four layers of water molecules, the c values are 12.5 \AA , 15.5 \AA , 18.5 \AA , and 21.5 \AA , respectively [21]. To keep the number of particles in the system constant and eliminate the boundary effect of the model, referring to the experience of Skipper [24], the simulation cell consisted of 8 unit cells ($4 \times 2 \times 1$ array of clay unit cell) using periodic boundary conditions and the space group in the simulated environment is P1. Considering the complicated forms and time-consuming calculation in the MCY and TIP4P, the SPC/E model was selected to better reflect the properties of water and describe the interaction between water and clay [23, 25]. By adjusting the bond

angle H-O-H and bond length H-O to 109.47° and 1 \AA , respectively, the dipole moment of the water molecule will be close to the real value [21]. The nanoscale Mnt and the macroscopic samples were bridged through water content, fully reflecting the whole stage of swelling and further establishing the connection between two scales. The initial water content (the percentage of the mass of water molecules to the mass of clay, namely, $m_{\text{H}_2\text{O}}/m_{\text{clay}} \times 100\%$), c value, and number of hydrated layers under different numbers of water molecules are listed in Table 1.

According to Lowenstein's nonadjacent principle [26] followed by multiple isomorphous replacement of montmorillonite, Si^{4+} in tetrahedral sheet and Al^{3+} in octahedral sheet will be replaced by Al^{3+} and Mg^{2+} , respectively. Take Na-Mnt or Ca-Mnt with a layer charge of 0.75 (0.38 per half unit cell) as an example; there are six Na^+ or three Ca^{2+} between the layers, and the molecular formula is $\text{Na}_{0.75}\{\text{Si}_{7.75}\text{Al}_{0.25}\}[\text{Al}_{3.5}\text{Mg}_{0.5}]\text{O}_{20}(\text{OH})_4 \cdot n\text{H}_2\text{O}$ or $\text{Ca}_{0.375}\{\text{Si}_{7.75}\text{Al}_{0.25}\}[\text{Al}_{3.5}\text{Mg}_{0.5}]\text{O}_{20}(\text{OH})_4 \cdot n\text{H}_2\text{O}$. The supercell configuration of Na-Mnt with 0–4 hydrated layers is depicted in Figure 1.

2.1.2. Simulation Design. Layer charge density and cation exchange capacity (CEC) are important criteria for the classification of clay minerals. In soil science, CEC means the milligram equivalent of cation exchange per 100 g of soil, namely, the molar charge per unit mass of soil. Layer charge and CEC can be transformed into each other, but a previous work has rarely linked the two indicators. To this end, this paper constructed three types of Mnt models according to the standard "geological exploration instruction of bentonite deposit" GB 12518-1990, including low-level charge type (0.20–0.35 per half unit cell), transition type (0.35–0.45 per half unit cell), and high-level charge type (0.45–0.60 per half unit cell). The transition from layer charge to CEC (eq/g) is realized by formula (1), so as to be related to the CEC detected by macroscopic experimental methods.

$$\text{CEC (eq/g)} = 1000 \times \frac{2\sigma/e'}{\text{FW}/100}, \quad (1)$$

where σ is the layer charges, e' is the charge of an electron, FW (g) represents the mass of the model. Equation (1) presents that the CEC of the mineral is affected by the volume, natural density, and layer charge of the model, and the CEC of Mnt is various under different water contents [27]. Tables 2 and 3 list the variable gradients of water content and layer charge density. The water content range of 16–232 water molecules corresponds to water content in the range of 5%–70%, covering all states of the soil when it expands and shrinks [28]. In view of the fact that the interlayer cations of Mnt are mostly Na^+ and Ca^{2+} under actual conditions and the layer charge density generally varies from 0.20 to 0.60 per half unit cell, so the total number of groups simulated is 66, corresponding to 66 CEC values. The CEC of Mnt is not greatly affected by the types of cations (Tables 2 and 3). According to the changes of CEC, it can be roughly divided

TABLE 1: The parameters of Mnt with different numbers of water molecules between layers.

Parameters	The number of water molecules										
	16	32	64	96	128	149	166	183	199	216	232
The number of hydrated layers	1	1	1	2	3	3	3	3	3	4	4
Initial c value (\AA)	12.5	12.5	12.5	15.5	18.5	18.5	18.5	18.5	18.5	21.5	21.5
Initial water content (%)	5	10	20	30	40	45	50	55	60	65	70

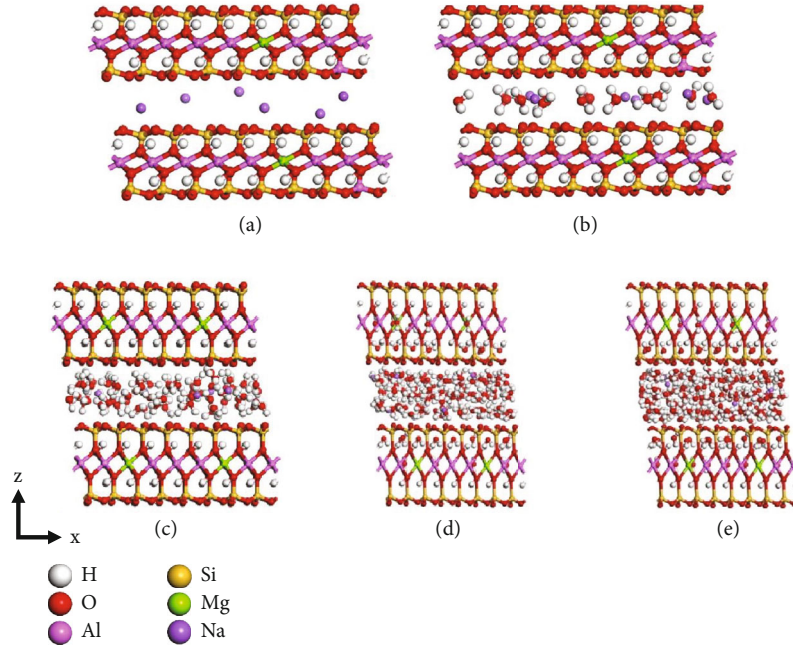


FIGURE 1: Na-Mnt in different hydrated layers: (a) dry state, (b) 1-layer hydrated, (c) 2-layer hydrated, (d) 3-layer hydrated, and (e) 4-layer hydrated.

TABLE 2: CEC of Na-Mnt.

Layer charge density (per half unit cell)	Type of layer charge	Number of Na^+	Water content (%)										
			5	10	20	30	40	45	50	55	60	65	70
0.20	Low-level	3	49	47	43	40	37	35	34	33	32	31	30
0.38	Transition	6	97	93	85	79	73	70	68	65	63	61	60
0.60	High-level	10	160	153	140	130	121	119	112	108	105	101	99

TABLE 3: CEC of Ca-Mnt.

Layer charge density (per half unit cell)	Type of layer charge	Number of Ca^{2+}	Water content (%)										
			5	10	20	30	40	45	50	55	60	65	70
0.25	Low-level	2	65	62	57	53	49	49	45	44	42	41	40
0.38	Transition	3	97	93	85	79	73	70	68	65	63	61	60
0.60	High-level	5	160	153	141	130	121	116	112	108	103	102	99

into three levels, namely, LCEC (30~60 eq/g), MCEC (60~100 eq/g), and HCEC (100~160 eq/g).

2.1.3. Computational Parameters and Procedure. The simulation was performed by Materials studio software package on the system containing Mnt, water, and ions. The force field, CLAYFF, proposed by Cygan et al. [29] was applied

to describe the process of molecular dynamics. With reference to the parameters of previous experience [15, 21], the long-range Coulomb electrostatic force was processed by the Ewald summation method with an accuracy of 10^{-4} kcal/mol. The van der Waals force of the short-range interaction was acquired by the atom-based method, and the cut-off distance, spline width, and buffer distance were set to

12 Å, 0.5 Å, and 0.5 Å, respectively. The basic steps included the adsorption of water molecules and interlayer cations, geometric optimization, structural relaxation, and the kinetic simulation of swelling. The specific details are as follows:

- (1) The adsorption of water molecules and interlayer cations: in accordance with the gradients of the layer charge, the isomorphous replacement was accomplished first, and then, the initial model was constructed. The corrected water molecules and Na or Ca were given the corresponding charges through CLAYFF force field, and specific parameters are listed in Table 4 [30]. Sorption of water molecules and interlayer cation (Na^+ or Ca^{2+}) was carried out using the Metropolis Monte Carlo method in the Sorption module of the software. Specifically, the parameters selected for ratios of “exchange,” “conformer,” “rotate,” “translate,” and “regrow” are 0.39, 0.2, 0.2, 0.2, and 0.2, respectively [9]. In this way, initial crystal structures after adsorption were built.
- (2) Geometric optimization: to gain the conformation with the lowest potential energy, the energy of adsorbed Mnt was minimized by the Smart algorithm. The convergence tolerance and displacement were controlled to $1.0e-4$ kcal/mol and $5.0e-5$ Å, respectively, and the maximum number of iteration steps was 5000. When the energy of the system dropped to a stable level and reached the convergence criterion, the optimized configuration was chosen to lay the foundation for the next step.
- (3) Structural relaxation: the model was further optimized globally to prevent the energy of the system from falling into the local optimum in the NVT ensemble, and a more stable configuration can be generated. In this section, the kinetic simulation of Na-Mnt and Ca-Mnt was carried out at 25°C (298 K). The temperature was controlled by the more efficient Velocity Scale method with an allowable error of 5.0 K. Considering that most models have reached equilibrium at the 50th ps, the total simulation time and time step were, respectively, 200 ps and 0.5 fs to improve accuracy [30].
- (4) The kinetic simulation of swelling: when simulating the swelling of Mnt in the NPT ensemble, all the atomic degrees of freedom need to be released to apply a fixed temperature (298.15 K) and pressure (1 atm). Since Mnt is an inorganic crystal and its structure and shape are known, the pressure can be fixed by the Berendsen method. To save simulation time and increase accuracy, this research integrated previous experience and set the total simulation time to 200 ps [30, 31]. The time step was conducted for 0.1 fs.

Using the method of Chang et al. [14] for reference, the new basic spacing of hydrated clay minerals after swelling

was taken as the initial basal spacing for the following simulation. The trajectory of the balanced model will be extracted and processed by Perl script.

2.2. Shrinking Characteristics of Montmorillonite. When the mineral undergoes swelling reaction, the water molecules in the pores of the soil will evaporate with the influence of temperature, leading to water content of soil decreasing and further shrinking under external force. If the water content is less than a certain critical value, the volume of the soil will no longer change. This study concentrated on the shrinking process of Mnt with atmospheric pressure after evaporation. For the Monte Carlo method, firstly, it can provide more detailed information without providing experimental data and calculate a reliable and balanced system by determining the energy, pressure, and temperature of the configuration. Secondly, this method can more realistically describe the water absorption and desorption of water molecules randomly distributed among the layers of clay particles to simulate the process of shrinking. Finally, the algorithm is less restricted by geometric conditions such as the size, number of atoms, and orientation of the system, which is convenient for obtaining more realistic and accurate simulated results [23, 32].

The fundamental difference between the swelling and shrinking of Mnt lies in the adsorption and desorption of water molecules. The current work was combined with the research of Zheng et al. [23] and desorbed a fixed amount of interlayer water molecules in the expanded model by Monte Carlo. During the shrinking period, the water content of the entire system changes from 70% to 0%. It means that when the process of swelling is completed at a higher water content (such as 70%), Monte Carlo will be used on this basis to make the system reach a lower water content (such as 65%) as a model premise of simulating shrinking by deleting a specific number of water molecules.

The parameters are the same as those in Section 2.1. Geometry optimization, structural relaxation, and simulation of shrinking (NPT ensemble) were executed in sequence, and finally the trajectory data after equilibrium was sorted.

2.3. Data Analyses. Before the discussion and analysis of the results, it is necessary to figure out the way and physical meaning of certain nanolevel parameters. For instance, the basal spacing, free swelling ratio, and void ratio can display the phenomena of swelling and shrinking from different aspects, as well as the relative concentration, binding energy, number, and length of hydrogen bonds reflecting its reaction mechanism. The ergodic hypothesis points out that even if the system is in an equilibrium state, its configuration will dynamically change with time and the system will experience all possible microscopic states at this time. Therefore, it is statistically significant to extract the data of the stable configuration to calculate the following indicators.

2.3.1. Basal Spacing (d_{001} -value). The change of the basal spacing represents the ability of swelling and shrinking of Mnt, including the thickness of solid minerals and interlayer spacing. The formula is defined as [21]

TABLE 4: Force field and charges of montmorillonite and water.

Type	Atom	Symbol	q (e)	σ_{ij} (Å)	ϵ_{ij} (kcal/mol·Å)
Montmorillonite	O (bridging oxygen)	ob	-1.050	3.5532	0.1554
	O (hydroxyl oxygen)	oh	-0.950	3.5532	0.1554
	Na (interlayer cation)	Na	1.0	2.6378	0.1301
	Ca (interlayer cation)	Ca	2.0	3.2237	0.1000
	H (hydroxyl hydrogen)	ho	0.425	—	—
	Mg (octahedral magnesium)	mgo	1.360	5.9090	9.0298×10^{-7}
	Al (tetrahedral aluminum)	at	1.5750	3.7064	1.8405×10^{-6}
	Al (octahedral aluminum)	ao	1.575	4.7943	1.3298×10^{-6}
	Si (tetrahedral silicon)	st	2.100	3.7064	1.8405×10^{-6}
Water	O (H ₂ O)	o*	-0.820	3.5532	0.1554
	H (H ₂ O)	h*	0.410	0.0000	0.0000

$$d_{001}\text{-value} (\text{Å}) = \frac{V}{a \times b \times \sin \alpha}, \quad (2)$$

where V (cm³) is the statistical average volume in the system and a (Å), b (Å), and $\sin \alpha$ are the average unit cell parameters.

2.3.2. Free Swelling Ratio (FS). Compared with the basal spacing, the free swelling rate is a professional measure of three-dimensional swelling. The larger the free swelling ratio, the stronger the swelling abilities of the soil. It is defined macroscopically as the ratio of the difference between the volume of loose dried soil particles when freely accumulated in the air and water to the volume when freely accumulated in the air; thus, Ahmed and Abduljawwad [9] gave a way to describe the free swelling ratio (FS) of expansive clays on a microscale and the specific form is expressed as

$$\text{FS} (\%) = \frac{\text{IDD} - \text{FDD}}{\text{FDD}} \times 100\%, \quad (3)$$

where IDD (g/cm³) is the initial dry density and FDD (g/cm³) is the final dry density.

2.3.3. Void Ratio (e). The shrinking of soil is mostly characterized by the shrinkage curve (the relationship curve between void ratio and water content) [28]. According to the Connolly algorithm, the porosity of the clay matrix can be calculated by the hard-sphere test-particle insertion (TPI) method. The Connolly radius was 1.0 Å. The van der Waals scale factor and grid interval were 1.0 and 0.25 Å. Hereby, the free volume (FV) and occupied volume (OV) can be solved, and the void ratio is given as

$$e = \frac{\text{OV}}{\text{FV}}, \quad (4)$$

where OV (Å³) and FV (Å³), respectively, are the free volume (including the volume of water molecules) and the solid phase volume of clay after swelling.

2.3.4. Relative Concentration. Relative concentration refers to the ratio of the number of atoms or molecules on a certain plane of the model to the number of atoms or molecules in the entire system, quantitatively depicting the position and distribution of atoms or molecules. With this parameter, the process of swelling and shrinking of Na-Mnt and Ca-Mnt under different CEC can be further explored.

2.3.5. Binding Energy (E_{bind}). Whitley and Smith [33] discovered that the main thermodynamic factor affecting the swelling of Mnt is the energy term in the free energy of swelling. To distinguish differences between the swelling and shrinking with different water content, types of cations, and CEC from the perspective of thermodynamics, the binding energy was introduced as [34]

$$E_{\text{bind}} (\text{kcal/mol}) = -E_{\text{inter}} = (E_{\text{solid}} + E_{\text{H}_2\text{O}}) - E_{\text{total}}. \quad (5)$$

The binding energy E_{bind} (kcal/mol) in (5) is the negative value of the interaction energy E_{inter} (kcal/mol), which is used to measure the interaction energy between the solid and liquid phase and quantitatively characterize the interaction force between molecules. The more positive the binding energy, the stronger the attraction between the solid and liquid molecules. The greater the absolute value of the negative binding energy, the more significant the attraction between water molecules and the clay wafer. E_{solid} (kcal/mol), $E_{\text{H}_2\text{O}}$ (kcal/mol), and E_{Total} (kcal/mol) are the energy of the solid phase, liquid phase, and the total energy of the system, respectively.

2.3.6. The Number and Length of Hydrogen Bonds. Hydrogen bonding is a special nonbonding interaction. For the force field, CLAYFF, it is reflected in the interaction between static electricity and van der Waals. It can be divided into intermolecular hydrogen bonds and intramolecular hydrogen bonds according to their types [35]. Relevant studies have shown [21] that intermolecular hydrogen bonds in Mnt are mainly formed between water molecules and bridging oxygen atoms on the surface of the wafer. On the one hand, the intermolecular hydrogen bonds are generated between the hydroxyl hydrogen

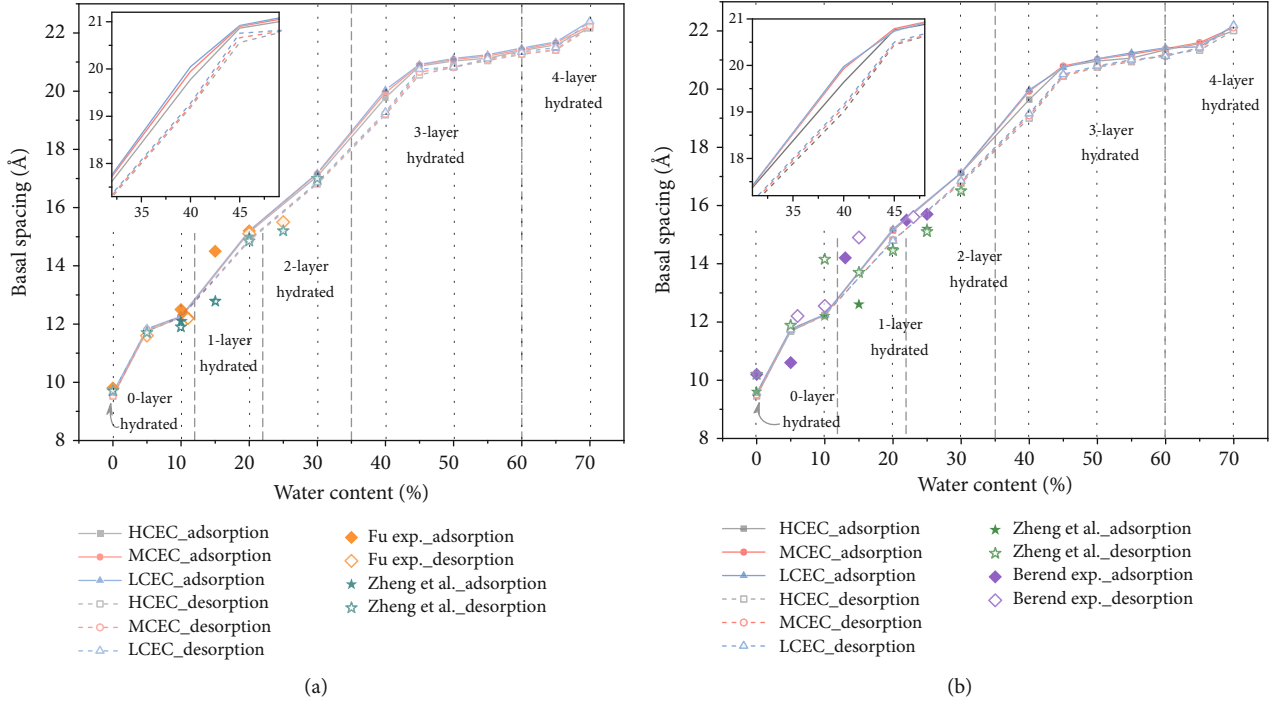


FIGURE 2: Hysteresis curve of Mnt during swelling and shrinking: (a) Na-Mnt and (b) Ca-Mnt.

in the structure and the common oxygen atoms of silicon-oxygen tetrahedron and aluminum-oxygen octahedron and between a few bridging oxygen atoms. When water molecules are adsorbed into the crystal layer or desorbed from the interlayer, the hydrogen bonds will vary accordingly. Thus, the changes of hydrogen bonds in the system may be related to the swelling and shrinking behaviors of Mnt.

In view of this, we determined the order of formation during swelling, the process of destruction during shrinking, and the distribution of water molecules between layers by the number of hydrogen bonds (N_{HB}), the number of hydrogen bonds per water molecule ($N_{HB,p}$), and the length of hydrogen bonds (L_{HB}). Using Perl script to define the bonding rule of hydrogen bonds is that the distance between the largest donor and acceptor was 2.5 \AA , and the smallest angle between the donor, hydrogen atom, and acceptor was 90° [21].

3. Results and Discussion

3.1. Hysteresis Curve of Swelling and Shrinking. Referring to (2), the relationships between d_{001} -value and water content of Na-Mnt and Ca-Mnt under different CEC are shown in Figures 2(a) and 2(b). d_{001} -value has slightly decreased with the increase of CEC (Figure 2), which is consistent with the test results of Ahmed and Abduljauwad [9]. In the process of Mnt from swelling to shrinking, d_{001} -value has undergone four hydrated states. Generally, it first grew with the rise of water content and then declined with the decrease of water content. The swelling and shrinking had evident hysteresis effects. Tang [28] also found the irreversibility of the swell-shrinking deformation of the sample in the macroscopic test. The experimental results of Fu [19] and Berend [20] using X-ray diffraction (the range of water content is 0%~30%),

and the simulation results of Zheng et al. [23] are in good agreement with the hysteresis curve in Figure 2, which largely confirms the accuracy of the simulation results in this work. Comparing the changes of d_{001} -value between Na-Mnt and Ca-Mnt, the interlayer cations had an effect on the swelling and shrinking of Mnt. However, Na-Mnt only had a smaller swelling advantage than Ca-Mnt, which may be related to the hydrated capacity of cations [21].

As shown in Figures 2(a) and 2(b), similar to the hysteresis behaviors of hydrated Mnt under the influence of temperature [36], the swell-shrinking phenomenon was the most significant when the water content varied from 30% to 50%. The difference in d_{001} -value between absorption and desorption of Mnt was the largest when the water content was around 40% (the partial enlarged view on the upper left side of Figure 2). By linking the macroscopic results, the corresponding critical water content is also about 40% when desiccation cracks are beginning to appear [27, 37]. The discovery suggested that the volumetric shrinkage of Mnt may create spatial conditions for the formation of cracks on expansive soils.

3.2. Swelling Properties of Montmorillonite. Figures 3(a) and 3(b) are the swelling curves of Na-Mnt and Ca-Mnt, where the dry state is considered the reference point for calculating FS. The changes of FS with water content under different CEC displayed that, similar to d_{001} -value, FS of Mnt presented an upward trend with the increase of water content as a whole. CEC had a negative correlation with FS, and the swelling performance of Na-Mnt was slightly better than that of Ca-Mnt.

Na-Mnt and Ca-Mnt with a water content of 0% to 70% have expanded by about 150% (Figure 3). From a completely

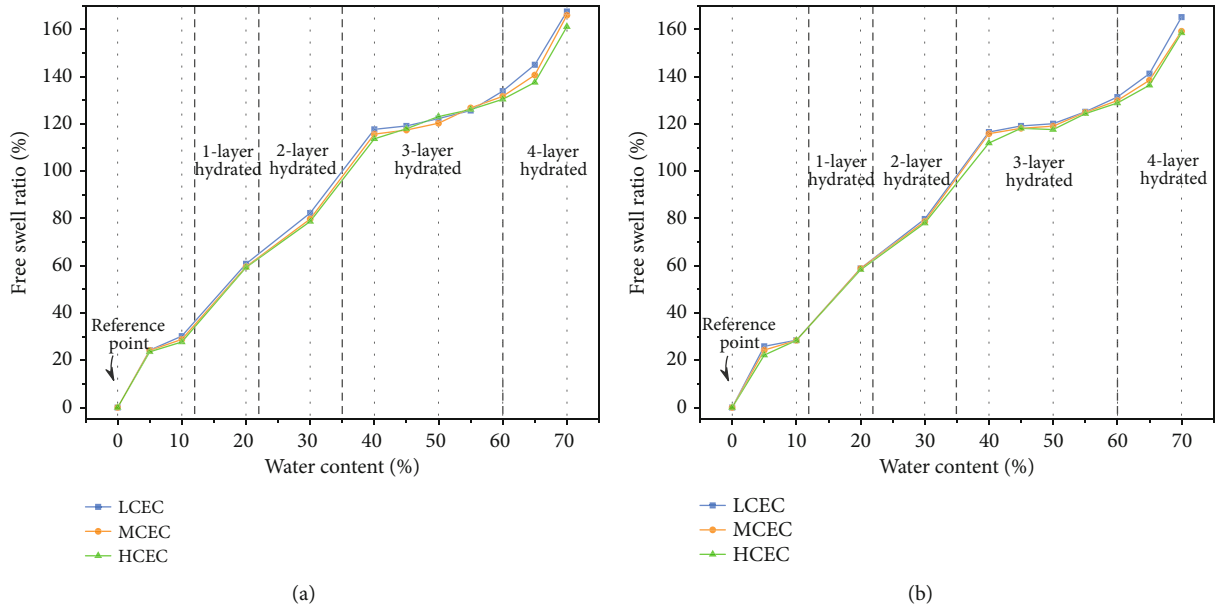


FIGURE 3: The relationship between free swelling ratio and water content: (a) Na-Mnt and (b) Ca-Mnt.

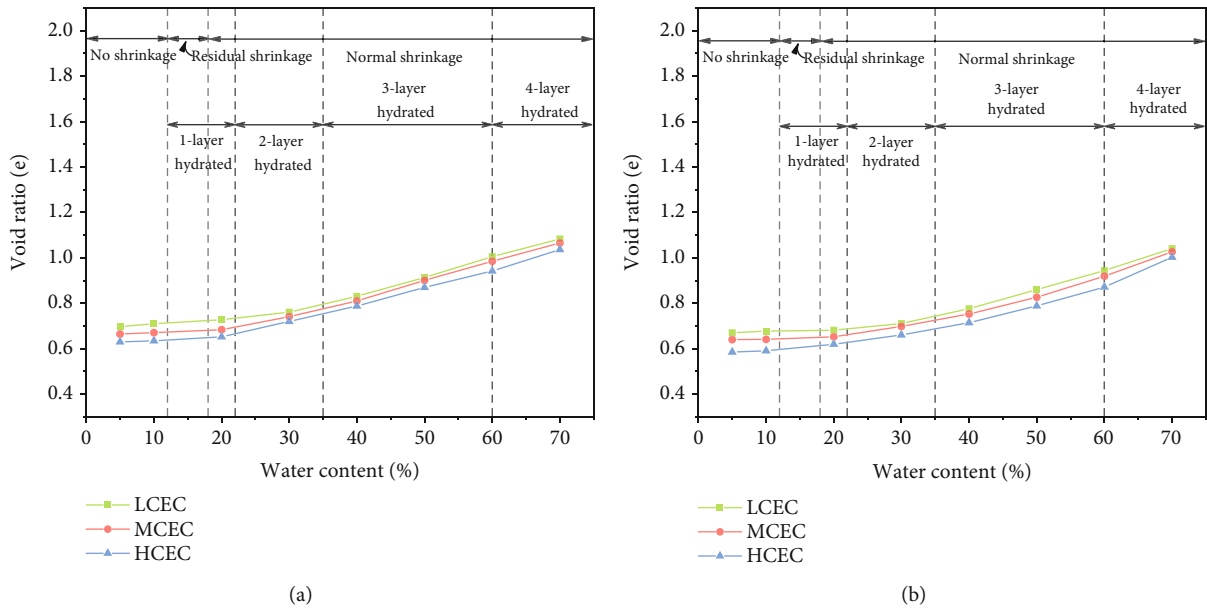


FIGURE 4: Nanoscale shrinkage curve of Mnt: (a) Na-Mnt and (b) Ca-Mnt.

dry state to adsorb 16 to 32 water molecules (a water content of 5% to 10%), the first layer of hydration was about to fill up. After entering the first hydrated state, FS of Mnt climbed rapidly, but the increasing trend slowed down when the second hydrated layer was formed. This may be closely connected with the aggregation of water molecules and the generation of hydrated layer. When the adsorption of the third hydrated layer was completed, FS at a water content of 40% reached 120%, while the FS of the expansive soil measured by Yu et al. [38] on the macroscale is about 100%. The difference between them may be due to the scale effect of the soil, but it largely indicated that Mnt is the main

source of clay minerals for swelling of expansive soil. FS at the water content of 40% to 60% increased mildly, suggesting that the three-layer water molecules gradually transitioned to the four-layer, and a small swelling occurred when the four-layer hydration was established.

3.3. Shrinkage Curve of Montmorillonite. Figure 4 presents the shrinkage curve (the relationship between void ratio and water content) of nanoscale Na-Mnt and Ca-Mnt. As shown in Figures 4(a) and 4(b), with the desorption of water molecules, the crystal layer gradually shrunk in volume under external pressure, resulting in a continuous drop in

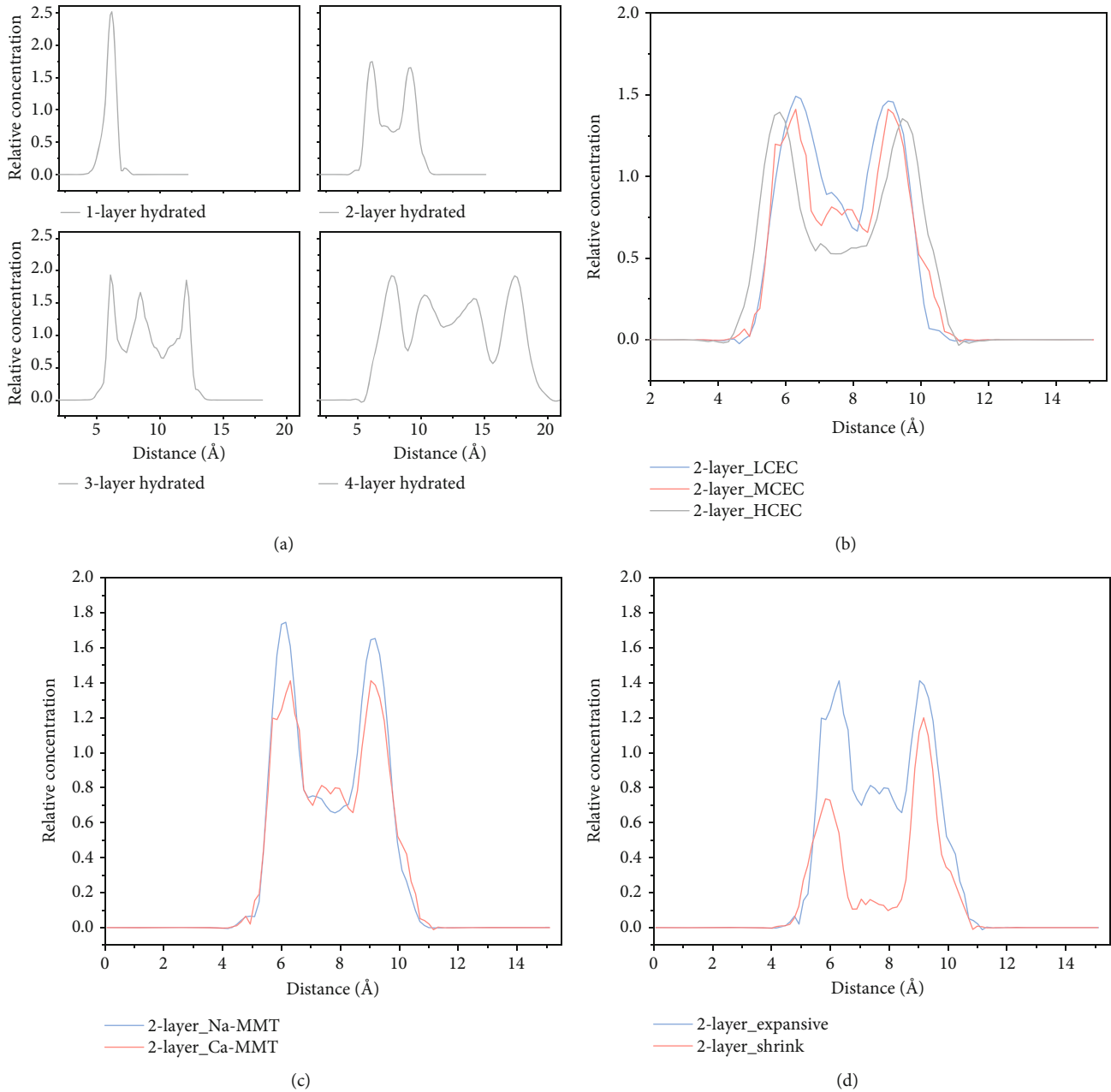


FIGURE 5: Distribution of water molecules along the z -axis: (a) different hydrated layers of Na-Mnt, (b) different CEC, (c) different types of interlayer cations, and (d) swelling and shrinking.

the void ratio of Mnt, and finally tended to stabilize. Compared with the expansive soil, the entire curve also roughly went through three stages [28]. The first was the linear development stage (water content $\geq 30\%$). Water molecules began to desorb from 70% of the water content, and the reduced volume of the system was equal to the dehydrated volume. After the fourth hydration film disappeared, the volume was compressed under external pressure until the third hydration film was removed. The second was residual deformation (from 10% to 30%). The dry density of Mnt gradually went up as the water content went down, and the void ratio decreased at a slower rate. When the water content dropped to less than 10%, in other words, when

the system was in the stage of no shrinkage, the molecules of the first hydrated layer were closely combined with the interlayer cations. At this moment, the dry density of the mineral has reached 2.1g/cm^3 . The void ratio stayed constant at about 0.65 and no longer deformed. The main reason for the distinction between the shrinkage curves of expansive soil and nanosized Mnt should be attributed to the multiscale effect of the soil and the difference in mineral composition and structure.

The effects of types of interlayer cation and CEC on the shrinking behaviors of Mnt revealed that influenced by the swelling states, the void ratio of Na-Mnt was slightly larger than that of Ca-Mnt under the same water content. The

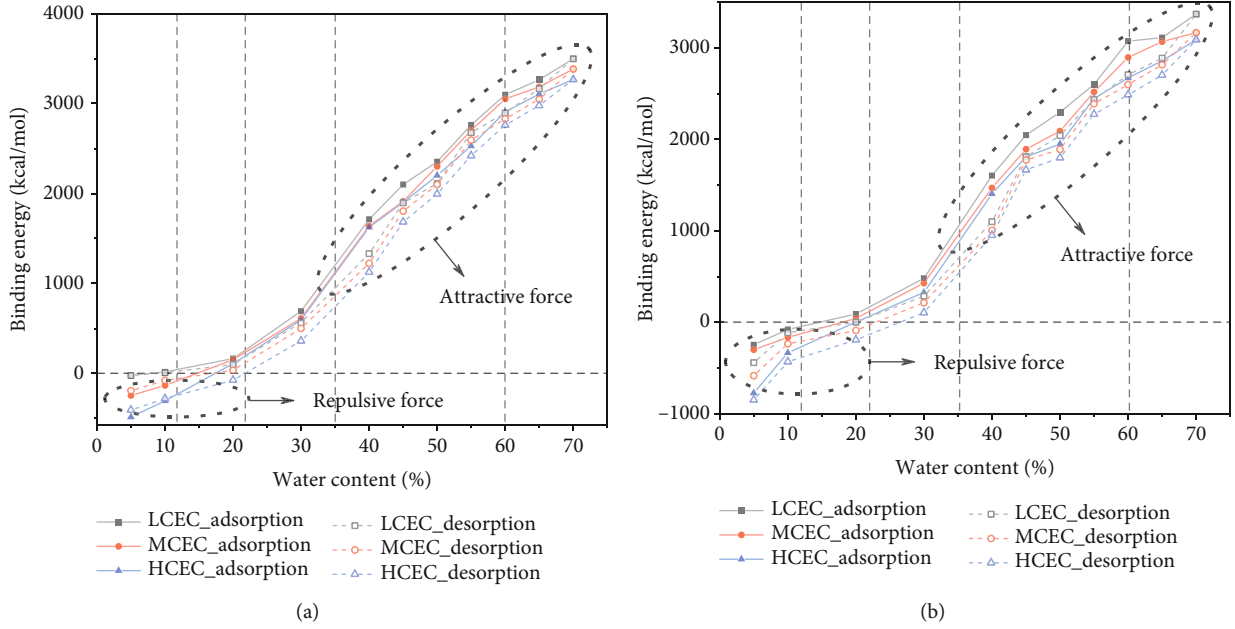


FIGURE 6: Changes in binding energy between solid and liquid molecules: (a) Na-Mnt and (b) Ca-Mnt.

higher the CEC, the smaller the void ratio, which is basically the same as the results of d_{001} -value in Figure 2.

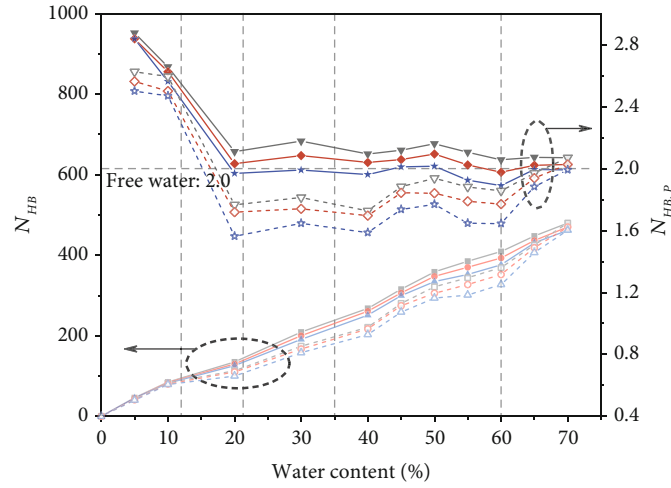
3.4. Swelling and Shrinking Mechanism. In order to explain the above-mentioned microscopic phenomena in depth, we will discuss the relative concentration of water molecules, the binding energy of solid-liquid molecules, and the number and length of hydrogen bonds.

3.4.1. Distribution of Water Molecules. The relative distribution of water molecules along the z -axis in the Na-Mnt model is presented in Figure 2(a). When Mnt adsorbed 32 water molecules, it appeared a peak along the z -axis, forming the first hydrated layer and concentrated in the center of the crystal layer. When water molecules were successively adsorbed and developed into a second hydrated layer, the main peak split into two symmetrical secondary peaks, and the peak value was reduced. Similarly, the third and fourth hydrated layers corresponded to 3 and 4 peaks, respectively. After the water molecules were arranged in layers, they became more dispersed. Fei [21] also obtained the related results. Figure 2(b) exhibits the distribution of water molecules between two layers of hydrated Ca-Mnt (with a water content of 20%) under different CEC. The higher the CEC, the narrower the peak width, leading to the thinner the thickness of the hydration film and the worse the final swelling performance. It also explained the influence of CEC on d_{001} -value and FS. The swelling effects of Na-Mnt and Ca-Mnt also depended on the thickness of the hydration film in the process of absorbing water molecules. In Figure 5(c), the hydration film of Na-Mnt was slightly thicker than Ca-Mnt, so the swelling properties of the former had advantages over the latter. It is given that the ionic radius of Na is smaller than that of Ca and the hydrated ability of ions is inversely proportional to the ionic radius, which ensures the correctness of the simulation results. The water film between the layers of 2-layer hydrated Ca-Mnt became thinner in the

shrinking state (Figure 5(d)). In comparison with the distribution of water molecules after swelling, the distance from the solid phase of the mineral was enlarged, promoting a certain agglomeration of water molecules. Hence, the interaction between the liquid and solid phases was weakened, and the crystal layer will shrink due to external pressure, generating hysteresis effects of swelling and shrinking.

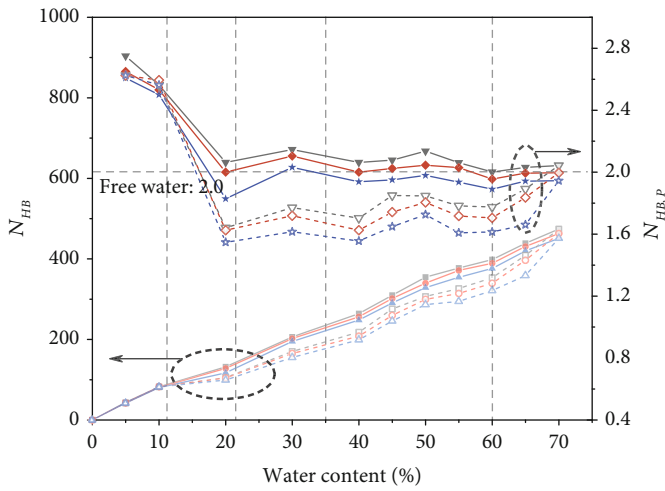
3.4.2. Solid-Liquid Interaction. The force field, CLAYFF, only relies on the interaction of Coulomb electrostatic force and van der Waals force. The total potential energy of each component in (5) is mainly derived from the Coulomb electrostatic potential, van der Waals nonbonding potential energy, bond stretching, and angle bending of water molecule and hydroxyl bond [21].

Figures 6(a) and 6(b) demonstrate that the binding energy (E_{bind}) between the solid phase of clay and the liquid phase of water molecules varied from -850 to 35000 kcal/mol in the range of 5% to 70% water content. When the water content of Mnt was nearly 20%, there is no interaction between the solid and liquid phases. Based on Figures 5(b) and 5(c), the distance between the two layers of water molecules and the solid surface was about 10^{-10} Å, which is in the same order of magnitude as the equilibrium value in the change of molecular force with molecular distance [39]. As the water content increased, the distance between the outermost water molecules and the surface of the solid phase expanded (Figure 5(a)), causing a descent in the attractive and repulsive forces of solid-liquid molecules. However, the attractive force declined faster than the repulsive force, so the molecular force between the two phases in this stage appeared as attraction. Conversely, the reduction of water content made the distance between the solid-liquid molecules smaller, and the repulsive force will dominate. Combining the previous statement that the swelling of Mnt is controlled by the balance between the repulsive force caused by the 2:1 layer interaction and the attractive force



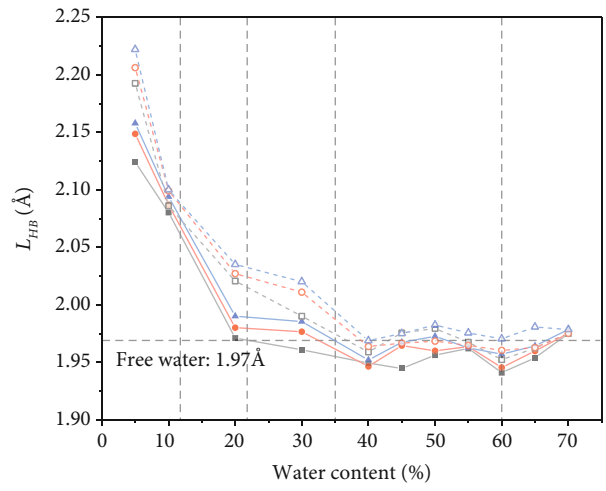
- ▼— LCEC_adsorption
- MCEC_adsorption
- ★— HCEC_adsorption
- -▼- - LCEC_desorption
- -●- - MCEC_desorption
- -★- - HCEC_desorption
- LCEC_adsorption
- MCEC_adsorption
- ▲— HCEC_adsorption
- -■- - LCEC_desorption
- -○- - MCEC_desorption
- -▲- - HCEC_desorption

(a)



- ▼— LCEC_adsorption
- MCEC_adsorption
- ★— HCEC_adsorption
- -▼- - LCEC_desorption
- -●- - MCEC_desorption
- -★- - HCEC_desorption
- LCEC_adsorption
- MCEC_adsorption
- ▲— HCEC_adsorption
- -■- - LCEC_desorption
- -○- - MCEC_desorption
- -▲- - HCEC_desorption

(b)



- LCEC_adsorption
- MCEC_adsorption
- ▲— HCEC_adsorption
- -■- - LCEC_desorption
- -●- - MCEC_desorption
- -▲- - HCEC_desorption

(c)

FIGURE 7: Continued.

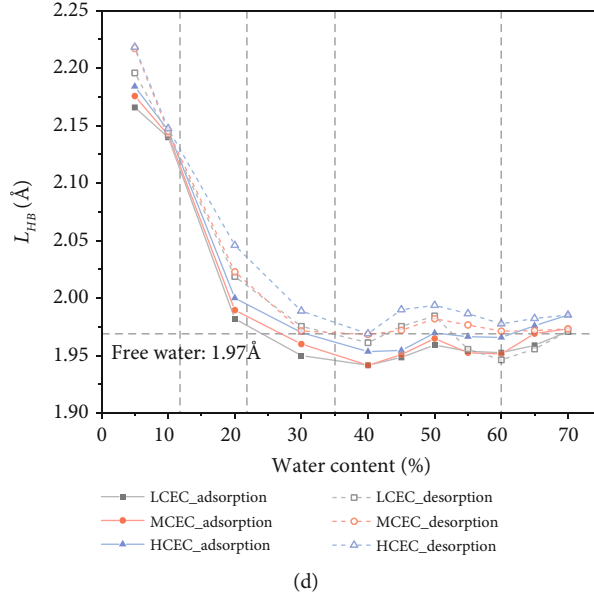


FIGURE 7: Changes in the number and length of hydrogen bonds: (a) Na-Mnt, (b) Ca-Mnt, (c) Na-Mnt, and (d) Ca-Mnt.

between the cations of the hydrated layer and the negatively charged surface of the siloxane layer [40], the above findings have revealed that solid-liquid interaction in the process of swelling and shrinking is mainly manifested by attraction and repulsive force.

The binding energy between the solid and liquid phases was positively correlated with the water content, implying that the filling of water molecules induced the interaction of the two phases more intense. The desorption of water molecules resulted in the disappearance of the hydration film and the agglomeration of water molecules, and the interaction between the two phases also weakened. As presented in Figure 6, the changes in E_{bind} are roughly similar to the trend in Figure 2. It can be inferred that the differences caused by factors such as water content, CEC, and types of cations could be mainly a reflection of the interaction between the two phases.

3.4.3. The Role of Hydrogen Bonds. As shown in Figures 7(a) and 7(b), the higher the water content of the mineral, the greater the number of hydrogen bonds in the system. The water content became lower, and the number of hydrogen bonds decreased. When the water content was within 20%, $N_{HB,p}$ and L_{HB} dropped the fastest. When the water content exceeded 20%, influenced by the hydrated state of Mnt, the fluctuation of $N_{HB,p}$ and L_{HB} gradually reduced, which is slightly larger than the average $N_{HB,p}$ and L_{HB} in free water. It can be speculated that in the process of swelling, in addition to hydrogen bonds between water molecules, bridging oxygen atoms on the surface of the wafer could be also generated until the occupancy of bridging oxygen atoms is completely utilized in the range of water content from 0% to 20%. After the water molecules reached a certain number (water content > 20%), the newly inhaled water molecules expanded the interlayer spacing and formed hydrogen bonds with the bridging oxygen atoms on the surface, but the over-

all increase in hydrogen bonds mainly came from the hydrogen bonds between water molecules. With the continuous adsorption of water molecules, the average $N_{HB,p}$ and L_{HB} between the layers were close to the stable value of free water (2.0 and 1.97 Å) [41].

For the shrinking of Mnt, the successive desorption of water molecules induced the rupture of the hydrogen bonds between the outermost hydration film and the bridging oxygen atoms of the wafer, as well as between the water molecules. Then, the distance between the new outermost water molecules and the surface of the crystal layer enlarged to weaken the interaction, so the volume shrunk because of external pressure and promoted new hydrogen bonds with the bridging oxygen atoms. As the water molecules further desorbed, the hydrogen bonds in the system continued to break. Until it is in the 1-layer hydrated state (the water content was less than 20%), the hydrogen bonds between the water molecules and between the water molecules and the bridging oxygen atoms were gradually and completely destroyed.

The dissimilarity in the number of hydrogen bonds between water molecules in this paper and free water may stem from the hydration of interlayer cations, which locally destroyed the tetrahedral coordination structure of water molecules. The hydrogen bonds formed between water molecules, and bridging oxygen caused the average $N_{HB,p}$ and L_{HB} to be different from free water during swelling and shrinking of Mnt. Equivalently, the distinction in the properties of hydrogen bonds with different CEC, state of swelling and shrinking, and types of cations can also be attributed to the above reasons. Since the longer the hydrogen bond, the weaker the hydrogen bond [42], namely, the smaller the interaction between molecules. Thus Figures 7(c) and 7(d) illustrate the disparity in the swelling and shrinking of different CEC and interlayer cations from another view. Judging from Figures 2 and 6, the changes in N_{HB} , d_{001} -value, and E_{bind} with water

content are almost similar, implying that the swelling and shrinking effects of Mnt may be mainly due to the results of molecular interaction, and this interaction is closely related to hydrogen bonding.

4. Conclusions

In the present study, the Monte Carlo and molecular dynamics methods were used to carry out a series of studies on the influence of CEC, water content, and types of interlayer cation. The phenomena of nanosized Mnt were discussed through the changes of basal spacing, free swelling ratio, and void ratio. Compared with previous simulation results and experimental data, the reaction mechanism was explained in terms of the relative distribution of water molecules, solid-liquid interaction, and hydrogen bonds. The key findings can be summarized as follows:

- (1) Water content, types of interlayer cations, and CEC have a certain influence on the basal spacing of Mnt. The higher the water content, the larger the basal spacing. As the CEC decreased, the basal spacing increased. Furthermore, Na-Mnt has a weak swelling advantage over Ca-Mnt. When the water content was in the range of 30%~50%, the swelling and shrinking of Mnt had apparent hysteresis phenomena
- (2) Affected by the hydrated state of Mnt, the changes of the free swelling ratio were basically consistent with the basal spacing in the swelling stage. When the water content was 70%, the free swelling ratio reached nearly 150%. By comparison with the expansive soil, the nanoscale shrinkage curves of Na-Mnt and Ca-Mnt also experienced three stages of linear normal shrinkage, residual shrinkage, and no shrinkage
- (3) The differences between the swelling and shrinking phenomena of Mnt with different water content, interlayer cation, and CEC were closely related to the distribution of water molecules. If the water content goes up, the number of hydrated layers will go down. With the rise of CEC, the thickness of the hydration film declined. The thickness of the hydration film in the shrinking state became thinner than that in the swelling state, and the agglomeration between water molecules was enhanced. The binding energy of the solid and liquid phases was directly proportional to the water content. The water content around 20% was the critical point of the attractive and repulsive forces in the intermolecular forces. The difference in swelling and shrinking caused by various factors could be mainly due to the molecular interaction between the two phases
- (4) The number of hydrogen bonds was roughly similar to the changes in binding energy and basal spacing. The distinction between the swelling and shrinking of Mt lies in the adsorption and desorption of water

molecules, and it is essentially reflected in the formation and breaking of hydrogen bonds. The hydration of interlayer cations and the hydrogen bonds between water molecules and bridging oxygen atoms on the surface of the wafer may make the number and length of hydrogen bonds slightly different from those of free water, which explains the influences of above variables

Data Availability

The data used to support the findings of this study are available from the corresponding author upon request.

Conflicts of Interest

The authors declare that they have no known competing financial interests or personal relationships that could have appeared to influence the work reported in this paper.

Acknowledgments

This research was financially supported by the National Natural Science Foundation of China (Grant Nos. 42172308 and 42077270).

References

- [1] S. X. Chen, *Study on Engineering Behaviors of Expansive Soils and Its Treatment Measures*, Huazhong University of Science and Technology, 2006.
- [2] D. E. Jones and W. G. Holtz, "Expansive soils-the hidden disaster," *Civil Engineering*, vol. 43, no. 8, pp. 49–51, 1973.
- [3] K. V. Ramana, "Expansive soils: problems and practice in foundation and pavement engineering," *Engineering Geology*, vol. 35, no. 1-2, pp. 136–138, 1993.
- [4] Y. Z. Wang, *Theoretical and Experimental Study on Scale Effects of Soil*, South China University of Technology, 2014.
- [5] D. L. Feng, Y. G. Fang, and M. X. Hou, "Theoretical and experimental studies of particle size effect of mechanical properties of soil," *Rock and Soil Mechanics*, vol. 36, no. 6, pp. 209–214, 2015.
- [6] Y. Wang, H. Meng, and D. Long, "Experimental investigation of fatigue crack propagation in interbedded marble under multilevel cyclic uniaxial compressive loads," *Fatigue & Fracture of Engineering Materials & Structures*, vol. 44, no. 4, pp. 933–951, 2021.
- [7] Y. Wang, Y. F. Yi, C. H. Li, and J. Q. Han, "Anisotropic fracture and energy characteristics of a Tibet marble exposed to multi-level constant-amplitude (MLCA) cyclic loads: a lab-scale testing," *Engineering Fracture Mechanics*, vol. 244, article 107550, 2021.
- [8] W. Sun and D. Sun, "Coupled modelling of hydro-mechanical behaviour of unsaturated compacted expansive soils," *International Journal for Numerical and Analytical Methods in Geomechanics*, vol. 36, no. 8, pp. 1002–1022, 2012.
- [9] H. R. Ahmed and S. N. Abduljawad, "Nano-level constitutive model for expansive clays," *Géotechnique*, vol. 67, no. 3, pp. 187–207, 2017.
- [10] Y. Wang, B. Zhang, B. Li, and C. H. Li, "A strain-based fatigue damage model for naturally fractured marble subjected to

- freeze-thaw and uniaxial cyclic loads,” *International Journal of Damage Mechanics*, 2021.
- [11] M. Eghbalian, M. Pouragha, and R. Wan, “Micromechanical approach to swelling behavior of capillary-porous media with coupled physics,” *International Journal for Numerical & Analytical Methods in Geomechanics*, vol. 43, no. 1, pp. 353–380, 2019.
- [12] E. S. Boek, P. V. Coveney, and N. T. Skipper, “Monte Carlo molecular modeling studies of hydrated Li-, Na-, and K-smectites: understanding the role of potassium as a clay swelling inhibitor,” *Journal of the American Chemical Society*, vol. 117, no. 50, pp. 12608–12617, 1995.
- [13] V. Marry, P. Turq, T. Cartailleur, and D. Levesque, “Microscopic simulation of structure and dynamics of water and counterions in a monohydrated montmorillonite,” *The Journal of Chemical Physics*, vol. 117, no. 7, pp. 3454–3463, 2002.
- [14] F.-R. C. Chang, N. T. Skipper, and G. Sposito, “Computer simulation of interlayer molecular structure in sodium montmorillonite hydrates,” *Langmuir*, vol. 11, no. 7, pp. 2734–2741, 1995.
- [15] J. Wang and F. Zeng, “Molecular dynamics simulations for hydration swelling and interlayer structure of Na-montmorillonite,” *Journal of The Chinese Ceramic Society*, vol. 33, no. 8, pp. 996–1001, 2005.
- [16] D. R. Katti, K. B. Thapa, and K. S. Katti, “The role of fluid polarity in the swelling of sodium-montmorillonite clay: a molecular dynamics and Fourier transform infrared spectroscopy study,” *Journal of Rock Mechanics and Geotechnical Engineering*, vol. 10, no. 6, pp. 1133–1144, 2018.
- [17] S. N. Abduljawad and H. U. R. Ahmed, “Use of nano-level constitutive model to predict the volume change behavior of the treated expansive clays,” in *IFCEE 2018*, pp. 143–153, Orlando, FL, 2018.
- [18] B. Li, *The Effect of Temperature on the Interlayerstructure of Na-, Cs-Montmorillonite Using Molecular Simulation*, Taiyuan University of Technology, 2013.
- [19] M. H. Fu, “Changes in the properties of a montmorillonite-water system during the adsorption and desorption of water: hysteresis1,” *Clays & Clay Minerals*, vol. 38, no. 5, pp. 485–492, 1990.
- [20] I. Berend, *Les Mécanismes d’Hydratation de Montmorillonites Homoioniques pour des Pressions Relatives Inferieures à 0.95*, Vandoeuvre-les-Nancy, INPL, 1991.
- [21] K. L. Fei, *Multi-Scale Study on the Basic Mechanisms of High Stress Mechanical Properties for Saturated Montmorillonite*, China University of Mining and technology, Xuzhou, 2013.
- [22] M. Chavez-Paez, K. V. Workum, and L. D. Pablo, “Monte Carlo simulations of Wyoming sodium montmorillonite hydrates,” *Journal of Chemical Physics*, vol. 114, no. 3, pp. 1405–1413, 2001.
- [23] Y. Zheng, A. Zaoui, and I. Shahrour, “A theoretical study of swelling and shrinking of hydrated Wyoming montmorillonite,” *Applied Clay Science*, vol. 51, no. 1-2, pp. 177–181, 2011.
- [24] N. T. Skipper, “Monte Carlo simulation of interlayer molecular structure in swelling clay minerals. 1. Methodology,” *Clays & Clay Minerals*, vol. 43, no. 3, pp. 285–293, 1995.
- [25] T. R. Underwood and I. C. Bourg, “Large-scale molecular dynamics simulation of the dehydration of a suspension of smectite clay nanoparticles,” *The Journal of Physical Chemistry C*, vol. 124, no. 6, pp. 3702–3714, 2020.
- [26] W. Loewenstein, “The distribution of aluminum in the tetrahedra of silicates and aluminates,” *American Mineralogist*, vol. 39, no. 1, pp. 92–97, 1954.
- [27] V. Romanov and E. M. Myshakin, “Experimental studies: clay swelling,” in *Greenhouse Gases and Clay Minerals. Green Energy and Technology*, V. Romanov, Ed., Springer, Cham, 2018.
- [28] C. S. Tang, “Study on desiccation cracking behaviour of expansive soil,” *Journal of Engineering Geology*, vol. 20, no. 5, pp. 663–673, 2012.
- [29] R. T. Cygan, J. J. Liang, and A. G. Kalinichev, “Molecular models of hydroxide, oxyhydroxide, and clay phases and the development of a general force field,” *The Journal of Physical Chemistry B*, vol. 108, no. 4, pp. 1255–1266, 2004.
- [30] W. N. Zhang, H. X. Hu, and X. C. Li, “Changes in micromechanical properties of Na-montmorillonite caused by CO₂/H₂O sorption,” *Computational Materials Science*, vol. 129, pp. 178–183, 2017.
- [31] R. Martos-Villa, S. Guggenheim, and M. P. Mata, “Interaction of methane hydrate complexes with smectites: experimental results compared to molecular models,” *American Mineralogist*, vol. 99, pp. 401–414, 2014.
- [32] W. Dai, Z. H. Shui, C. H. Shen, and K. Li, “Monte Carlo simulation on adsorption characteristics of water in kaolin,” *Journal of the Chinese Ceramic Society*, vol. 40, no. 1, pp. 149–153, 2012.
- [33] H. D. Whitley and D. E. Smith, “Free energy, energy, and entropy of swelling in Cs-, Na-, and Sr-montmorillonite clays,” *Journal of Chemical Physics*, vol. 120, no. 11, pp. 5387–5395, 2004.
- [34] X. L. Fu, X. Z. Fan, and X. H. Ju, “Molecular dynamic simulations on the interaction between an HTPE polymer and energetic plasticizers in a solid propellant,” *RSC Advances*, vol. 5, 2015.
- [35] G. Gilli and P. Gilli, “Towards a unified hydrogen-bond theory,” *Journal of Molecular Structure*, vol. 552, no. 1-3, pp. 1–15, 2000.
- [36] Y. Zheng, A. Zaoui, and I. Shahrour, “Evolution of the interlayer space of hydrated montmorillonite as a function of temperature,” *American Mineralogist*, vol. 95, no. 10, pp. 1493–1499, 2010.
- [37] H. Peron, T. Hueckel, L. Laloui, and L. B. Hu, “Fundamentals of desiccation cracking of fine-grained soils: experimental characterisation and mechanisms identification,” *Canadian Geotechnical Journal*, vol. 46, no. 10, pp. 1177–1201, 2009.
- [38] S. Yu, S. X. Chen, and X. C. Xu, “Testing study on relative free swelling ratio for expansive soil,” *Chinese Journal of Rock Mechanics and Engineering*, vol. 25, pp. 3330–3335, 2006.
- [39] E. R. Lippincott and R. Schroeder, “General relation between potential energy and internuclear distance for diatomic and polyatomic molecules. I,” *The Journal of Chemical Physics*, vol. 23, no. 6, pp. 1131–1141, 1955.
- [40] E. Ferrage, B. Lanson, and B. A. Sakharov, “Investigation of smectite hydration properties by modeling experimental X-ray diffraction patterns: part I. montmorillonite hydration properties,” *American Mineralogist*, vol. 90, no. 8-9, pp. 1358–1374, 2005.
- [41] M. Hakala and S. Manninen, “Correlation of hydrogen bond lengths and angles in liquid water based on Compton scattering,” *The Journal of Chemical Physics*, vol. 125, no. 8, article 084504, 2006.
- [42] E. R. Johnson, S. Keinan, and P. Mori-Sanchez, “Revealing noncovalent interactions,” *Journal of the American Chemical Society*, vol. 132, no. 18, pp. 6498–6506, 2010.

Research Article

Frost-Heaving Cracking Sensitivity of Single-Flaw Rock Mass Based on a Numerical Experimental Method

Tingting Wang ^{1,2}, Chun'an Tang ^{1,2,3}, Pingfeng Li ⁴, Shibin Tang ³, Minghao Liu ², and Bingbing Zhang ⁴

¹School of Resources and Civil Engineering, Northeastern University, Shenyang 110819, China

²State Key Laboratory of Frozen Soil Engineering, Northwest Institute of Eco-Environment and Resources, Chinese Academy of Sciences, Lanzhou 730000, China

³State Key Laboratory of Coastal and Offshore Engineering, Dalian University of Technology, Dalian 116024, China

⁴Hongda Blasting Engineering Group Co., Ltd., Guangzhou 510623, China

Correspondence should be addressed to Pingfeng Li; hdbplpf@163.com

Received 20 July 2021; Accepted 23 August 2021; Published 14 September 2021

Academic Editor: Yu Wang

Copyright © 2021 Tingting Wang et al. This is an open access article distributed under the Creative Commons Attribution License, which permits unrestricted use, distribution, and reproduction in any medium, provided the original work is properly cited.

A novel numerical experimental method is developed herein to study frost-heaving cracking in fractured rock masses by reproducing the physical experimental frost-heaving process. The failure mode of a preexisting closed and water-saturated single-flaw in a rock mass during the frost-heaving process is affected by the inclination angle, flaw width, crack length, and cooling rate. Additionally, a regression model for predicting secondary crack formation and propagation is established by combining multiple stepwise regressions. Overall, the results indicate that preexisting flaw with various inclination angles, flaw lengths, and cooling rates mainly propagates along the flaw-coplanar direction. The secondary crack failure mode is most affected by the flaw width, and the length of the secondary crack increases with increasing inclination angle, flaw width, and flaw length, but decreases with increasing cooling rate. The contributions of the investigated factors to the secondary crack length follow the order: flaw width > inclination angle > cooling rate > flaw length. The results presented herein provide crucial theoretical guidance for engineering and construction projects in cold regions.

1. Introduction

Rocks are heterogeneous composite materials, which can develop defects, such as cracks, holes, joints, weak surfaces, and interlayers as a result of long-term geological tectonic activity. Infrastructure construction projects at high altitudes or in cold regions often face the problem of freezing damage to fractured rock mass, which is a critical engineering challenge that cannot be ignored. There are many factors affecting the engineering stability of rock masses in cold regions [1–3], including microcracks (microscopic defects) and joint surfaces (macroscopic defects) [4, 5]. Under high rainfall and subsurface flow conditions, water typically accumulates in fissures. During the cooling process, the freezing of water

induces a volume expansion of approximately 9% [6, 7]. When cracked ice is restricted by the surrounding rock medium, it generates volumetric dilatancy pressure, also known as, frost-heaving pressure. The frost-heaving pressure tends to concentrate the stress at the crack tip, which is enough to induce the formation of a secondary crack that grows and breaks through; this may cause damage or even the destruction of the rock mass, thus hindering the construction and implementation of rock mass engineering in cold regions [8].

Currently, the frost-heaving and freezing-thawing engineering disasters involving fractured rock masses in cold regions are mainly studied through theoretical calculations and experimental measurements of the frost-heaving

pressure, as well as through analysis of the mechanical properties of the rock material after freeze-thawing.

There are two research ideas that are typically applied in theoretical calculations of the frost-heaving pressure. One involves determining the frost-heaving pressure based on the circular tunnel model [9, 10]. For example, Lai et al. [11] proposed a viscoelastic analytical computation of tunnel frost-heaving pressure in cold regions by using a Laplace transform method. Gao et al. [12] derived the analytical elastic-plastic solution of the frost-heaving pressure of a tunnel in a cold region using a continuity equation, and they proposed a semianalytical method to calculate the stress in the plastic zone of the surrounding rock. Feng et al. [13] developed a theoretical model to obtain the elastic-plastic solutions from the stress and deformation analysis around the tunnel in cold regions where the entire surrounding rock comprised a nonfrozen elastic zone, a frozen elastic zone, a frozen plastic zone, and a support zone. Zhao et al. [14] established an elastic-plastic analytical determination of the frost-heaving pressure by considering the transversely isotropic frost heave of the surrounding rock. The results indicated that the transversely isotropic frost heave of the surrounding rock had a significant impact on the frost-heaving pressure.

The second approach to such theoretical calculations involves computing the frost-heaving pressure based on a single flaw [15–17]. For example, Kang et al. [18] proposed a theoretical method to predict crack propagation under freezing pressure and far-field stress, and the authors determined the direction and length of crack propagation based on Griffith's theory of brittle fracture mechanics. Considering the influence of thermal stress on flaw deformation, Huang et al. [19] derived a mathematical model for calculating the frost-heaving pressure of elliptical flaws in low-permeability rock. Tan et al. [20] expanded on previous research and evaluated the influence of external loading conditions and other parameters.

Aiming to empirically determine the frost-heaving pressure, Davidson and Nye [21] exploited the photoelastic effect to measure the stress generated in transparent materials following ice expansion, and they also discussed the influence of the frost-heaving pressure on the freezing process of real rock materials. Matsuoka and Murton [22] studied the effects of porosity and lithology on the frost-heaving deformation of saturated rock in open and closed systems and discussed the law of flaw propagation during the melting and freezing stages. A new experimental device was designed by Amanuma et al. [23] to simultaneously measure the frost-heaving pressure in the temperature gradient direction and perpendicular to the temperature gradient direction. Xia et al. [24] conducted transverse isotropic frost-heaving experiments involving saturated rock under unidirectional freezing conditions and deduced the formula for tunnel frost-heaving pressure. Based on experimental research investigating the frost-heaving pressure characteristics of fractured red sandstone, Shan et al. [25] analyzed the factors affecting the frost-heaving pressure and cracking mode and discussed the frost-heaving expansion mechanism of a single-flaw rock mass.

Several research groups have also studied the mechanical properties of rock materials after freezing-thawing [26, 27]. For example, Jia et al. [28] studied the changes in the compressive tensile strength of sandstone based on freezing-thawing tests, and they also monitored the strain changes of specimens during a single freeze-thaw cycle to evaluate the damage mechanism. Huang et al. [29] analyzed the strength and failure characteristics of rock materials containing single cracks under freeze-thaw and uniaxial compression conditions, and they concluded that the new frost-heaving crack grew from the crack tip along the coplanar direction because of the boundary effect; then, most of it expanded toward the short side of the specimen. Bai et al. [30] carried out experimental research regarding the strength, deformation, and crack evolution characteristics of red sandstone samples containing double flaws and subjected to triaxial compression conditions at various temperatures and confining pressures.

The mechanical behavior of brittle rock is affected by the initiation, propagation, and coalescence of preexisting rock flaws. The development cracking mode and microcrack location of a secondary crack of fractured rock mass caused by frost-heaving pressure has important guiding significance for construction projects in cold regions. Considering the heterogeneity of rock materials, this study establishes a thermo-mechanical model based on elastic mechanics, thermodynamics, and fracture mechanics and proposes a novel numerical experimental method for evaluating frost-heaving cracking via RFPA^{2D}-thermal analysis. The numerical experimental system reproduces the physical frost-heaving cracking process, and the feasibility of this approach is verified (Section 2). Additionally, the failure mode of the single preexisting water-saturated flaw in the rock mass during frost-heaving, and the effects of the inclination angle, flaw width, crack length, and cooling rate are discussed (Sections 3.1–3.4). Ultimately, a prediction regression model of the secondary crack is derived by combining multiple stepwise regressions (Section 4). Finally, the few limitations of this study are discussed, and several significant conclusions are drawn (Section 5).

2. Verifying the Feasibility of Numerical Simulations of Rock Mass Frost-Heaving Cracking

Based on the theory of elastic damage mechanics, RFPA^{2D} discretizes rock materials into several elements with distinct physical and mechanical properties, while ensuring that their material properties obey the Weibull distribution [31–33]. The RFPA^{2D}-thermal module was developed by Tang and coworkers, and several reports have been published on this topic [34, 35]. This module is mainly employed for the simultaneous analysis of the temperature and stress fields for a brittle material. First, the temperature field in the model is computed according to the temperature conditions. Second, the stress field is deduced according to the mechanical conditions. Then, the selected phase transition criterion is used to evaluate the basic elements, and

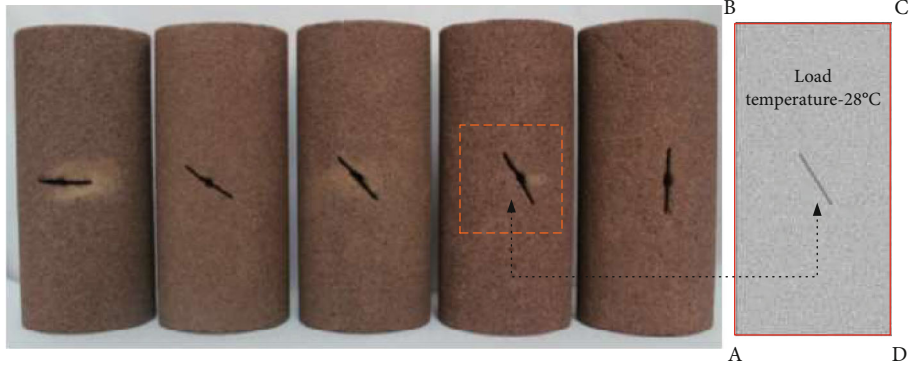


FIGURE 1: Comparisons of experimental specimens and the numerical simulation model.

TABLE 1: Mechanical parameters of rock and ice.

	Compressive strength	Compressive strength homogeneity	Poisson's ratio	Elasticity modulus	Elasticity modulus homogeneity	Internal friction angle
Unit	MPa	—	—	MPa	—	°
Rock	20	5	0.22	1840	5	26
Ice	50	100	0.35	700	100	30

TABLE 2: Thermal properties of rock and ice.

	Thermal conductivity	Thermal capacity	Thermal expansion coefficient
Unit	$W/(m \cdot ^\circ C)$	$J(m^3 \cdot ^\circ C) \times 10^6$	$1/^\circ C \times 10^{-5}$
Rock	2.2	2.3	0.2
Ice	2.1	1.9	-40

the corresponding damage treatment is carried out. The elements are treated as linearly elastic before and after phase transformation. RFPFA^{2D}-thermal can simulate the initiation and propagation of fractured rock mass cracking and reproduce the failure process. When analyzing the frost-heaving cracking of a fractured rock mass, the coupled temperature and stress effects are mainly considered, and the effect of the water-ice phase transition is generally ignored; rather, it is simplified as the damage to the surrounding rock medium induced by the expansion of cracked ice at low temperature.

2.1. Theoretical Model. The first set of heat conduction temperature boundary conditions is used for numerical simulations. The differential equation of heat conduction is described by

$$k_x \frac{\partial^2 T}{\partial x^2} + k_y \frac{\partial^2 T}{\partial y^2} = \rho c \frac{\partial T}{\partial t}, \quad (1)$$

where k_x and k_y represent the thermal conductivity of the elements in the X - and Y -directions, respectively; T is the temperature; ρ and c represent the density and specific heat of the material, respectively; t is the time.

For the frost-heaving analysis of a fractured rock mass, the stress-strain field equation is expressed as shown in

$$\sigma_{ij,j} + F_i = 0, \quad (2)$$

$$\varepsilon_{ij} = \frac{1}{2} (u_{i,j} + u_{j,i}), \quad (3)$$

$$\sigma_{ij} = \lambda \varepsilon_{kk} \delta_{ij} + 2G \varepsilon_{ij} - \beta \Delta T \delta_{ij}, \quad (4)$$

where σ_{ij} is the stress tensor; F_i is the body force; ε_{ij} and u_i represent the strain tensor and displacement vector, respectively; β , G , and λ are the thermal stress coefficient, shear modulus, and Lamé coefficient, respectively; δ_{ij} represents the Kronecker function ($i = j, \delta_{ij} = 1; i \neq j, \delta_{ij} = 0$).

In elastic mechanics, the elastic modulus of an element gradually decreases with damage aggravation, and the elastic modulus of a damaged material is defined by

$$E = (1 - D)E_0. \quad (5)$$

During frost-heaving, fractured rock cracking is mainly affected by tensile stress. When the tensile stress in an element reaches its uniaxial tensile strength σ_{t0} , the relationship in Equation (6) is satisfied.

$$\sigma_3 \leq -\sigma_{t0}. \quad (6)$$

In this case, tensile damage occurs in the element, the

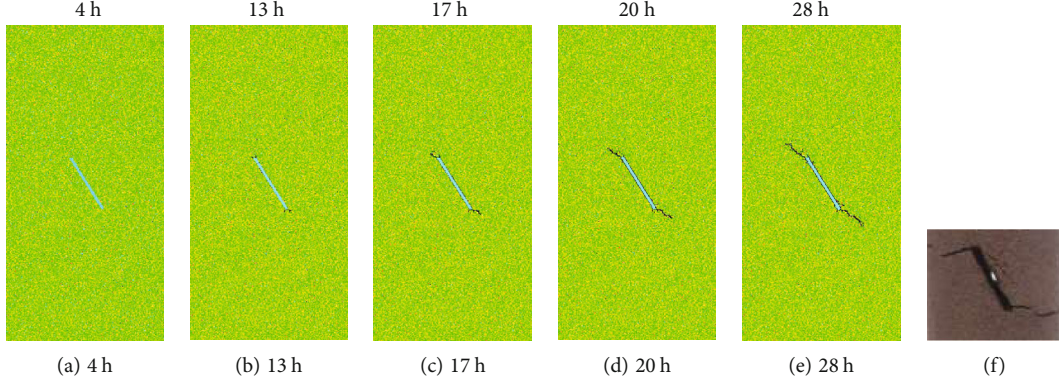


FIGURE 2: Simulated results (a–e) of the frost-heaving cracking mode compared with the experimental results (f).

damage variable D is defined by the conditions in

$$D = \begin{cases} 0, & \varepsilon \leq \varepsilon_{t0}, \\ 1 - \frac{\sigma_{tr}}{\varepsilon E_0}, & \varepsilon_{t0} < \varepsilon \leq \varepsilon_{tu}, \\ 1, & \varepsilon > \varepsilon_{tu}, \end{cases} \quad (7)$$

where E_0 represents the initial elasticity modulus; σ_{tr} is the residual strength of the tensile damage; ε_{t0} and ε_{tu} are the tensile strain at the elastic limit and the ultimate tensile strain of the element, respectively.

The tensile damage constitutive relationship for the frost-heaving cracking of a fractured rock mass can be expressed as shown in

$$\sigma_{ij} = \begin{cases} \lambda \varepsilon_{kk} \delta_{ij} + 2G\varepsilon_{ij} - \beta \Delta T \delta_{ij}, & \varepsilon \leq \varepsilon_{t0}, \\ \frac{\sigma_{tr}}{\varepsilon E_0} (\lambda \varepsilon_{kk} \delta_{ij} + 2G\varepsilon_{ij} - \beta \Delta T \delta_{ij}), & \varepsilon_{t0} < \varepsilon \leq \varepsilon_{tu}, \\ 0, & \varepsilon > \varepsilon_{tu}. \end{cases} \quad (8)$$

2.2. Numerical Simulations

2.2.1. Description of the Model. To verify the reliability of the rock frost-heaving analysis using the RFPA^{2D}-thermal module, the simulated results were compared with the experimental study regarding the frost-heaving pressure characteristics of fissured red sandstone conducted by Shan et al. [25]. The test specimen was a standard cylinder ($\phi = 50$ mm; $l = 100$ mm). The width and length of the flaw in the specimen were 1 mm and 20 mm, respectively (Figure 1). The frost-heaving analysis of the fractured rock was carried out by directly soaking the sample in water and cooling to -28°C over a total freezing time of 25 h. To maintain consistency with the test conditions, a numerical simulation model was established (Figure 1) based on a plane strain model. The temperature boundary conditions were applied to the boundary around the model, and the temperature drop was set to -28°C . The mechanical parameters and thermal properties of the model are summarized in Tables 1 and 2, respectively.

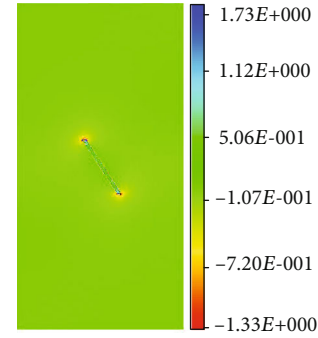


FIGURE 3: Cloud diagram showing the minimum principal stress before cracking.

2.2.2. Cracking Mode and Frost-Heaving Pressure Comparison. Figure 2 shows the cracking morphology of the fractured rock model as the temperature drops to -28°C . Initially, the preexisting closed and water-saturated single-flaw begins to expand and extrude into the surrounding media without causing any damage. As the frost-heaving pressure gradually increases, the extrusion effect of the surrounding medium becomes clearer. Under the applied crack tip stress concentration, microcracks appeared when the stress exceeded the tensile strength of the rock material. As the number of microcracks increases, individual microcracks gradually converge to form macrocracks.

The experimentally measured frost-heaving pressure was 0.23 MPa [25]. In the numerical simulation, the minimum principal stress at the center of the cracked ice was defined as the frost-heaving pressure, and the computed value was 0.45 MPa (Figure 3).

In Figures 2(e) and 2(f), the numerical results are similar to the experimental results. Although there are some differences in the cracking mode (i.e., inclination angle of the secondary crack), the numerical simulation results concerning the frost-heaving pressure closely reproduce the test results. The feasibility of the numerical experimental system is thus verified again.

2.2.3. Microcrack Analysis during the Frost-Heaving Process of a Fractured Rock. During the simulated frost-heaving process, the number of microcracks is relatively small at the

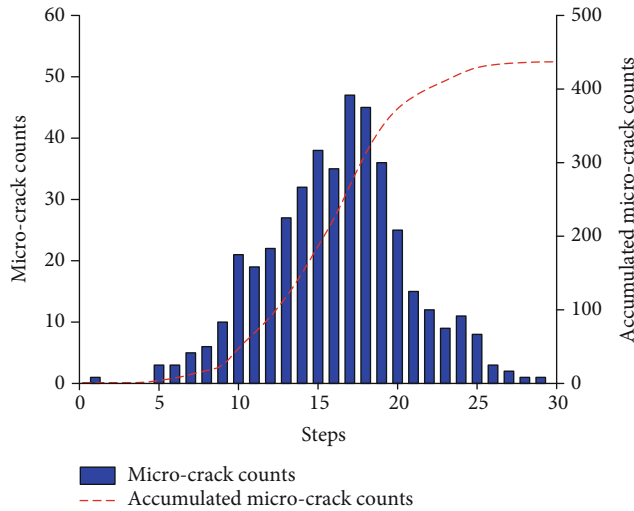


FIGURE 4: Statistical analysis of microcrack development during the frost-heaving of fractured rock.

early stages. The influence of the frost heave pressure on the surrounding medium is not clear at this time, before macrocracks have appeared. In the middle stages of frost-heaving, the number of microcracks increased rapidly, and macrocracks began to appear. Based on Figures 2(a)–2(f) and the quantitative microcrack analysis (Figure 4), the frost-heaving cracking process can be divided into a rupture incubation period (during which there were no obvious macrocracks and only a few damage units), a rupture growth period (during which macroscopic cracks appear and develop gradually), and a rupture steady period (wherein the macrocracks stop growing).

3. Sensitivity Analysis of a Preexisting Closed and Water-Saturated Single-Flaw during Frost-Heaving

The single flaw is the simplest and most important form of rock mass composition. The mechanical properties of a single-flaw rock mass also comprise the foundation for studying the mechanical properties of complex fractured rock masses. This section discusses and analyzes the effects of the flaw width, length, inclination angle, and cooling rate on the cracking mode. The feasibility of the numerical experimental system for frost-heaving analysis was verified in Section 2.2; to facilitate the computations, the model and material parameters in Tables 1 and 2 were used, and only the BC edge (Figure 1) was cooled to -28°C .

3.1. Influence of the Inclination Angle on the Frost-Heaving Cracking Process. Considering the inclination angles of 0° , 30° , 45° , 60° , and 90° and assuming a flaw length and width of 20 mm and 1 mm, respectively, the influence of the inclination angle on the frost-heaving cracking of a preexisting water-saturated single-flaw was analyzed.

From the real-time monitoring of the rock frost-heaving process at various inclination angles (Figure 5), it was concluded that the preexisting single-flaws with different incli-

nation angles mainly propagated along the flaw-coplanar direction.

With an inclination angle of 0° , the lengths of the left and right sides were approximately 3.475 mm. When the inclination angle was 30° , 45° , or 60° , the lengths of the left and right sides were about 6.243 mm, 7.218 mm, and 8.851 mm, respectively. When the inclination angle was 90° , the secondary crack was about 9.538 mm long; the secondary crack length increases with increasing inclination angle, mainly because the frost-heaving pressure reaches the strength limit of the rock medium sooner at a greater inclination angle. This causes tensile failure, and failure units gradually form a secondary crack. However, a secondary crack must appear at the tip of a preexisting flaw because of the stress concentrations, regardless of the inclination angle.

3.2. Influence of the Flaw Width on the Frost-Heaving Cracking Process. Setting the flaw length as 20 mm and the inclination angle at 60° , the width of the flaw was varied (i.e., 0.6, 1, 1.6, or 2 mm) to analyze the influence of the flaw width on the frost-heaving cracking of a preexisting closed and water-saturated single-flaw.

3.2.1. Cracking Mode Analysis. Figure 6 shows that the cracking modes of the secondary cracks produced by frost-heaving in a fractured rock mass with various flaw widths were quite diverse. When the flaw width was less than 1 mm, the initiation crack began from the tip and developed gradually along the direction of the flaw, thus forming a secondary crack. When the flaw width was greater than 1 mm, there were two stress concentration points at the end of the preexisting flaw, and secondary cracks developed from these two stress concentration points. It is clear that the flaw width affects the cracking mode of rock frost-heaving. As the flaw width increased, the larger frost-heaving pressure caused by the cooling effect causes a longer secondary crack to develop. When the flaw width was 0.6, 1, or 1.6 mm, the secondary crack length was about 3.855, 8.851, or 18.591 mm, respectively. When the flaw width was 2 mm, the secondary crack ran through the entire model, and the upper covering layer tends to lift; in this case, the secondary crack length is about 22 mm.

3.2.2. Multielement Stress Change Analysis. In Figure 6(a), path A–A' was taken as the research object to analyze the change in the minimum principal stress during the frost-heaving cracking process as a function of the flaw width. In the module, pressure is positive, and tension is negative. The plots in Figure 7 reveal that the minimum principal stress of the rock medium along path A–A' exhibits a concave trend in all simulated cases. The reason for this type of stress distribution is that the preexisting flaw was located in the middle of the whole model, and the rock medium above the flaw has the greatest influence on the frost-heaving pressure. When the flaw width was 0.6, 1, 1.6, or 2 mm, the minimum principal stress value along path A–A' reached -0.08 , -0.16 , -0.25 , and -0.5 MPa, respectively. The larger the flaw width, the greater the frost-heaving pressure. The stress curves fluctuate because the properties of the

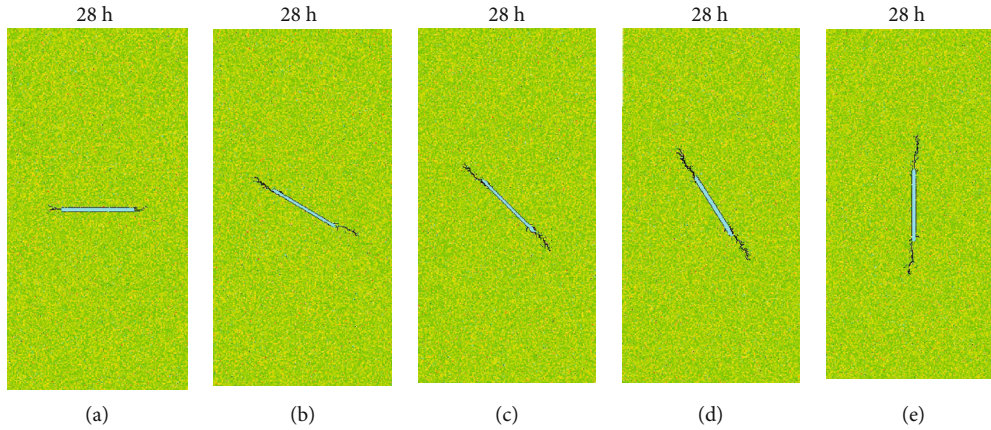


FIGURE 5: Frost-heaving cracking mode of fractured rocks containing different inclination angles: (a) 0°; (b) 30°; (c) 45°; (d) 60°; (e) 90°.

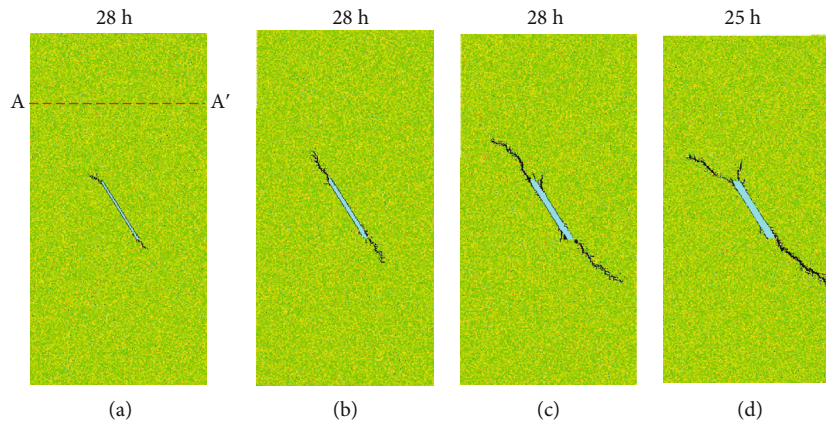


FIGURE 6: Frost-heaving cracking mode of fractured rocks containing various flaw widths: (a) 0.6 mm; (b) 1 mm; (c) 1.6 mm; (d) 2 mm.

rock materials are not uniform, and low strength elements are destroyed first. The stress acting on a given element disperses around it, thus causing the stress in adjacent elements to vary greatly.

3.3. Influence of the Flaw Length on the Frost-Heaving Cracking Process. Setting the inclination angle to 60° and the flaw width to 1 mm, the flaw length was varied (10, 15, 20, or 25 mm) to determine the influence of the flaw length on the frost-heaving cracking of preexisting closed and water-saturated single-flaws.

3.3.1. Cracking Mode Analysis. Figure 8 shows that as the flaw length increased, the secondary cracks gradually lengthen; however, the main trend of secondary crack development still followed the direction of the preexisting cracks. When the flaw length was 10, 15, 20, or 25 mm, the secondary crack length was about 5.6, 8.474, 8.851, or 11.97 mm, respectively.

3.3.2. Y-Direction Displacement Analysis. Figure 9 presents the Y-direction (vertical) displacement of preexisting flaws with various lengths along the B-B' path (Figure 8(a)). For example, when the flaw length was 10 mm, the vertical displacement of the upper part of the rock mass exhibited a convex trend (Figure 9(a)). The peak of this curve tends

toward the left side, mostly because the preexisting flaw's inclination angle was 60°, and the rock medium in the upper-left part of the specimens is more significantly affected by the frost-heaving pressure, so the peak value appears to be offset. A comparison of the plots in Figures 9(a)–9(d) indicates that as the length of the preexisting flaw increases, a frost-heaving pressure is generated, and the effect on the upper part of the specimen becomes more obvious. As a result, the deformation increases from 1.82×10^{-3} mm to 5.02×10^{-3} mm.

3.4. Influence of the Cooling Rate on the Rock Frost-Heaving Cracking Process. The frost-heaving cracking process for preexisting closed and water-saturated single-flaws was analyzed by setting an inclination angle of 45°, a flaw width of 1 mm, a flaw length of 20 mm, and modulating the cooling rate (−0.5, −1, −2, or −4°C/h).

3.4.1. Cracking Mode Analysis. Figure 10 shows that the secondary crack length gradually decreased with faster cooling rates, and the development direction still followed the direction of the flaw. This was because the faster the cooling rate, the more failure units generated around the tip of the preexisting flaw under the frost-heaving pressure, which consumes more energy, thus decreasing the length of the

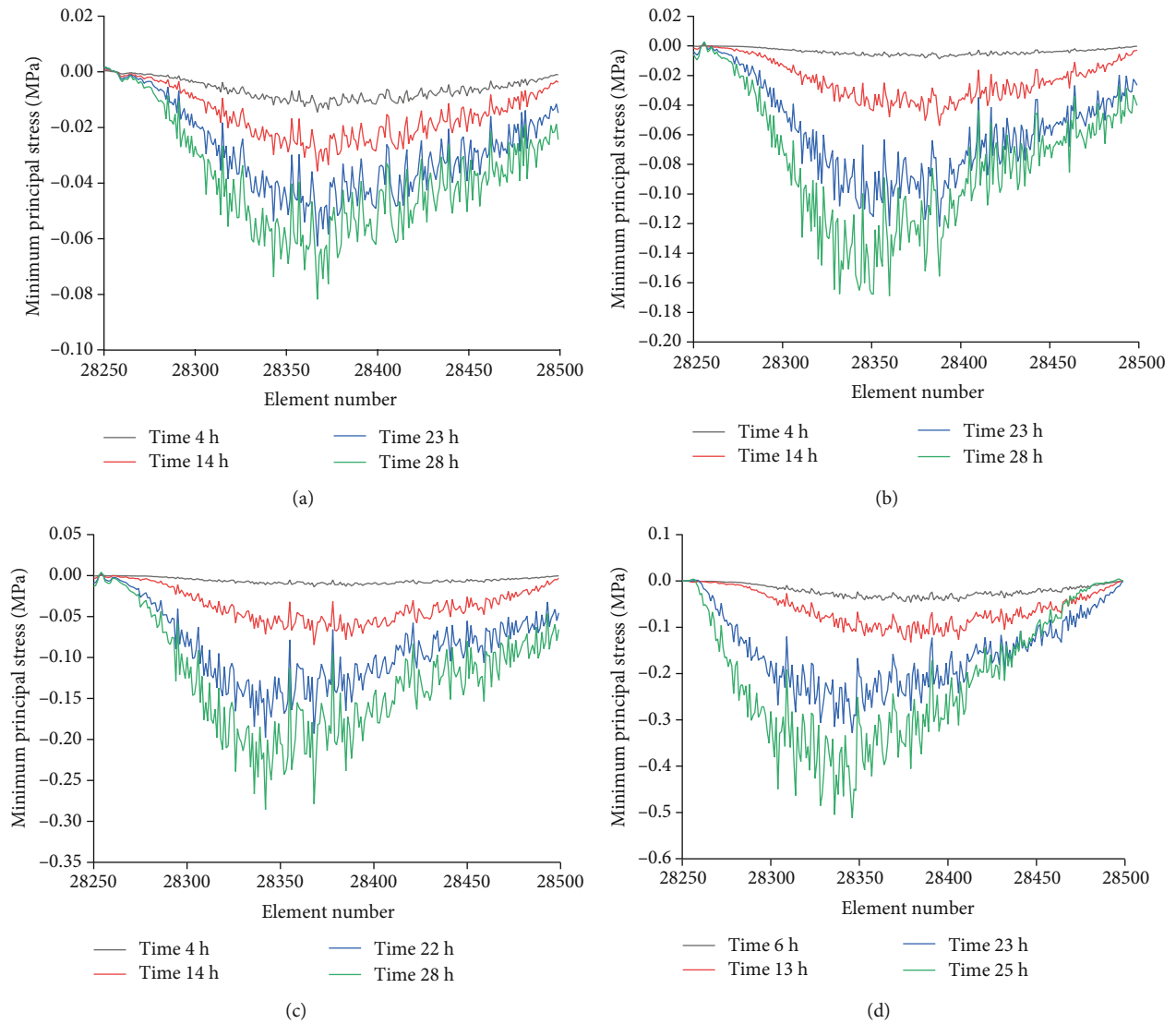


FIGURE 7: Variation in the multielement minimum principal stress along path A–A' over time for various flow widths: (a) 0.6 mm; (b) 1 mm; (c) 1.6 mm; (d) 2 mm.

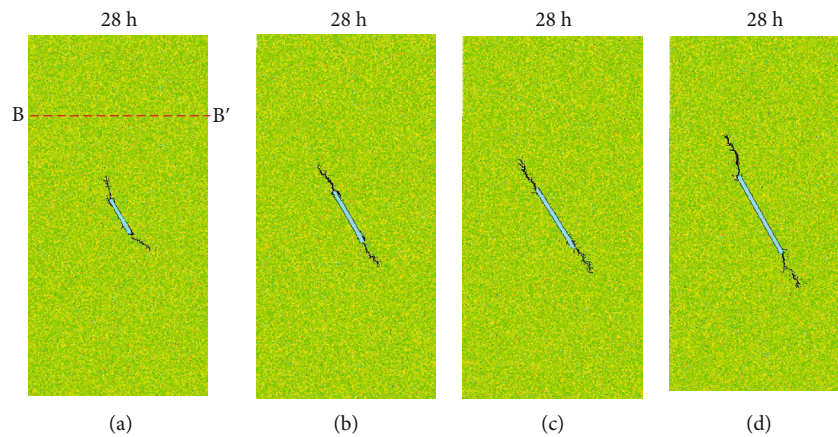


FIGURE 8: Frost-heaving cracking modes of fractured rocks with different flaw lengths: (a) 10 mm; (b) 15 mm; (c) 20 mm; (d) 25 mm.

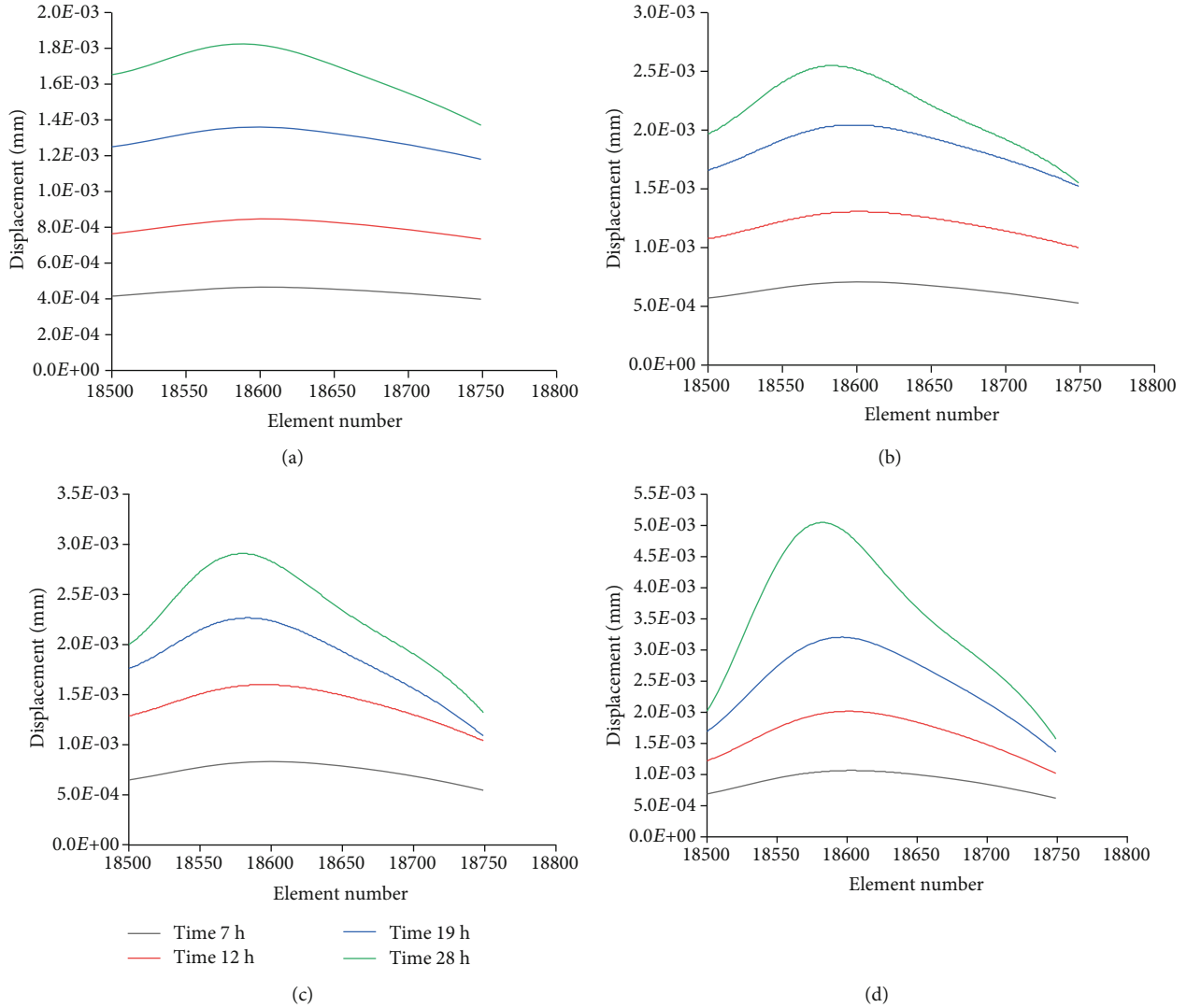


FIGURE 9: Variation in the multielement minimum principal stress along path B–B' over time for various flaw lengths: (a) 10 mm; (b) 15 mm; (c) 20 mm; (d) 25 mm.

secondary crack. When the cooling rate was -0.5 , -1 , -2 , or -4°C/h , the secondary crack length was about 9.758, 7.218, 4.903, or 3.583 mm, respectively.

3.4.2. Analysis of the Microcrack Initiation Process. The graphs in Figure 11 shows the microcrack changes under various cooling rates during the frost-heaving process. It is clear that as the cooling rate increases, the maximum number of accumulated microcracks gradually increases. When the cooling rate was -0.5 , -1 , -2 , or -4°C/h (each step took one hour), the number of microcracks reached about 20, 35, 80, or 130, respectively.

4. Multiple Stepwise Regression Analysis of the Secondary Crack Length Sensitivity

The variation in the secondary crack length as influenced by the inclination angle, flaw width, crack length, and cooling rate has been studied previously. Herein, a regression model

for predicting the secondary crack length has been established by applying a multiple stepwise regression method.

4.1. Multiple Stepwise Regression Analytical Model Setup. The main steps in the multiple stepwise regression analysis are describe here. First, independent variables are introduced, including the inclination angle, flaw width, flaw length, and cooling rate. The independent variable with the most significant effect on the secondary crack length y is introduced each time. Then, other variables are tested one by one to eliminate the variables associated with negligible changes.

The multiple stepwise regression equation is shown in

$$y = \beta_0 + \beta_1 x_1 + \beta_2 x_2 + \beta_3 x_3 + \beta_4 x_4 + \varepsilon, \quad (9)$$

where y is the secondary crack length; x_1, x_2, x_3, x_4 represent the independent variables affecting the secondary crack length (i.e., inclination angle, flaw width, crack length, and cooling rate, respectively); β_0 is a constant; $\beta_1, \beta_2, \beta_3, \beta_4$

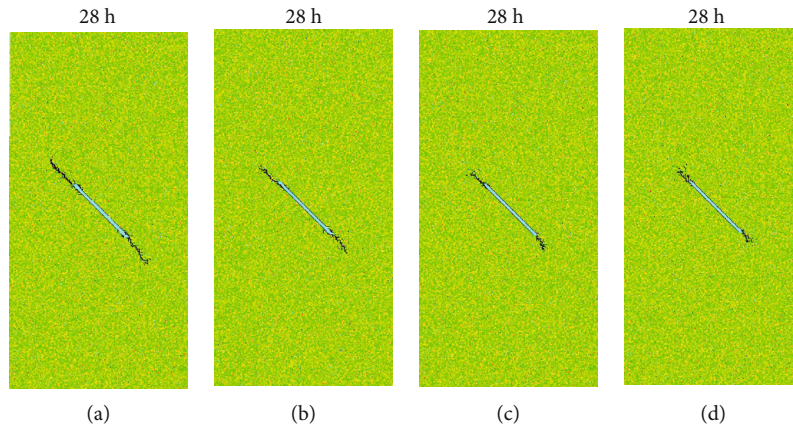


FIGURE 10: Frost-heaving cracking modes of fractured rock subjected to various cooling rates: (a) -0.5°C/h ; (b) -1°C/h ; (c) -2°C/h ; (d) -4°C/h .

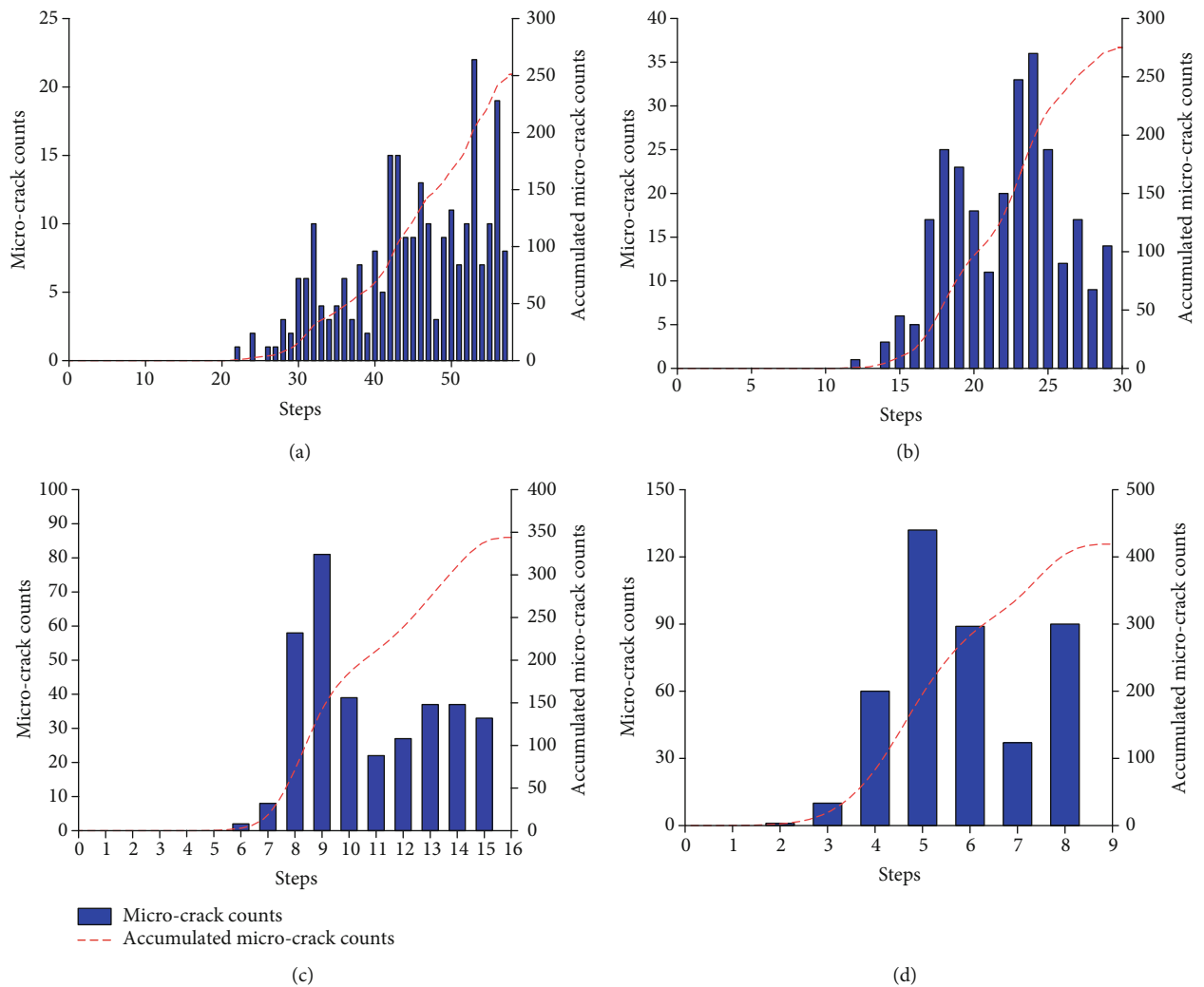


FIGURE 11: Statistical analysis of microcrack development during the frost-heaving of fractured rock masses: (a) -0.5°C/h ; (b) -1°C/h ; (c) -2°C/h ; (d) -4°C/h .

TABLE 3: Secondary crack length and related parameters.

No.	Secondary crack length y (mm)	Inclination angle x_1 ($^\circ$)	Flaw width x_2 (mm)	Flaw length x_3 (mm)	Cooling rate x_4 (mm)
1	5.6	60	1	10	1
2	8.474	60	1	15	1
3	8.851	60	1	20	1
4	11.97	60	1	25	1
5	3.855	60	0.6	20	1
6	18.591	60	1.6	20	1
7	22	60	2	20	1
8	9.758	45	1	20	0.5
9	4.903	45	1	20	2
10	3.583	45	1	20	4
11	6.243	30	1	20	1
12	7.218	45	1	20	1
13	3.475	0	1	20	1
14	9.538	90	1	20	1
15	10.308	60	1	20	0.5
16	6.965	60	1	20	2
17	7.786	30	1	20	0.5

TABLE 4: Model summary.

Model	R	R^2	Adjusted R^2	Standard error of estimate	Durbin-Watson (DW)
1	0.983	0.966	0.951	1.2158	2.003

TABLE 5: Analysis of variance.

Model	Sum of squares	df	Mean square	F	Sig.
Regression	382.860	4	95.715	64.748	0.000
1 Residual	13.304	9	1.478		
Total	396.164	13			

are the regression coefficients (indicating the degree of influence of the inclination angle, flaw width, crack length, and cooling rate, respectively, on the secondary crack length); ϵ is the random error.

In Table 3, entry nos. 1–14 show the numerical simulation results discussed above, and entry nos. 15–17 present the numerical simulation results regarding secondary cracks formed under conditions other than those used for the model test.

4.2. Analysis of Computed Results. The regression differentiation was carried out through the program, and the results are presented in Tables 4–6.

4.2.1. R Test. Both R and R^2 are very close to 1, thus proving (i) that the selected variables have a strong correlation with the length of the secondary cracks and (ii) that the degree of fitting is sufficient. Additionally, the DW value is close

to 2, there is no autocorrelation, and the model design meets the necessary requirements.

4.2.2. F Test. Considering the F distribution critical value table [36], $F_{0.05}(4, 9) = 3.633$. Since $F = 64.748 > 3.633$, the F test indicates that the regression equation is significant at $\alpha = 0.05$.

4.2.3. T Test. Considering the T distribution critical value table [36], $T_{0.05}(12) = 2.179$, and $t_0 = -5.966$, $t_1 = 13.213$, $t_2 = 4.728$, $t_3 = -4.042$, $t_4 = 3.362$. Comparative analysis confirms that each factor is significant at $\alpha = 0.05$.

The described analytical tests indicate that the regression equation of this model is suitable for use in predictions. In the established model, the flaw width is positively correlated with secondary crack length, with a correlation coefficient of 0.817. There is also a positive correlation between the inclination angle and the secondary crack length (correlation coefficient = 0.294). The cooling rate is negatively correlated with the length of the secondary crack, with a correlation coefficient of 0.249. Finally, the flaw length is positively correlated with the secondary crack length, and the correlation coefficient is 0.207. The relative contributions to the secondary crack length follow the order flaw width > inclination angle > cooling rate > flaw length.

The regression prediction equation for the secondary crack length is shown in

$$y = -14.751 + 13.668x_1 + 0.08x_2 + 1.621x_3 + 0.345x_4. \quad (10)$$

4.3. Inspection and Application. Equation (10) can be used to predict the length of the secondary cracks in entries 15–17 in Table 3, and the results are compared with the measured values in Table 7 as programs 1–3, respectively. The obtained relative error is within the allowable range, so the established regression prediction equation demonstrates suitable applicability.

5. Discussion and Conclusions

The simulations presented herein investigated the effects of the inclination angle, flaw width, flaw length, and cooling rate on crack propagation. The regression equation for predicting the secondary crack length was established via multiple stepwise regression analysis. The results confirmed that the frost-heaving pressure in a flaw was enough to drive crack initiation and propagation along the coplanar direction of a preexisting crack under unconfined conditions. Therefore, the frost-heaving process may easily destroy the unconfined rock mass near the surface when crack water is available. Based on the results of this study, the following conclusions can be drawn:

- (1) During the freeze-heaving process, preexisting closed and water-saturated single-flaws with various inclination angles, flaw widths, flaw lengths, and cooling rates mainly propagate along the flaw-coplanar direction. However, the secondary crack

TABLE 6: Coefficients for regression analysis.

Model		Unstandardized coefficients		Standardized coefficients	<i>t</i>	Sig.	Collinear statistics	
		<i>B</i>	Std. error				Tolerance	VIF
1	Constant	-14.751	2.472		-5.966	0.000		
	Flaw width	13.668	1.034	0.817	13.213	0.000	0.975	1.026
	Inclination angle	0.080	0.017	0.294	4.728	0.001	0.967	1.034
	Cooling rate	-1.621	0.401	-0.249	-4.042	0.003	0.981	1.020
	Flaw width	0.345	0.103	0.207	3.362	0.008	0.981	1.019

TABLE 7: Comparison between real and predicted values.

Program	Secondary crack length (mm)		Relative error (%)
	Real value	Predicted value	
1	10.308	9.8065	4.9%
2	6.965	7.375	5.9%
3	7.786	7.4065	4.9%

must appear at the tip of the preexisting flaw because of the stress concentration

- (2) The cracking mode of a rock mass is influenced by the flaw width of a preexisting single flaw. As the flaw width increases, the secondary crack changes from one main crack to two main cracks, and the minimum principal stress value along the path A–A' changes more dramatically. As the flaw width increases from 0.6 to 2 mm, the maximum minimum principal stress increases from 0.08 to 0.5 MPa
- (3) The secondary crack length increases with increasing inclination angle, flaw width, or flaw length, and decreases with increasing cooling rates. The entire process of secondary crack formation can be divided into a rupture incubation period, a rupture growth period, and a rupture steady period
- (4) The influencing factors of flaw width, inclination angle, cooling rate, and flaw length correspond to 0.817, 0.294, 0.249, and 0.207, respectively, leading to an order of contribution to the secondary crack length where flaw width > inclination angle > cooling rate > flaw length. The model for predicting the secondary crack length is thus established as follows: $y = -14.751 + 13.668x_1 + 0.08x_2 - 1.621x_3 + 0.345x_4$

Herein, simulations of the frost-heaving cracking of fractured rock masses are simplified to a model probing the coupled temperature and stress fields. The described work considered the cracking of the surrounding rock medium caused by the expansion of cracked ice under an ambient temperature of 0°C. This study also focused on elucidating the relationship between secondary crack formation and propagation and the preexisting cracked ice; however, it ignored the effect of the water-ice phase transition. Therefore, ongoing studies in our laboratory are aimed at further enriching the established theoretical model and redeveloping

the RFP software to incorporate the water-ice phase transition process.

Data Availability

The data used to support the findings of this study are available from the corresponding author upon request.

Conflicts of Interest

We declare that we have no financial and personal relationships with other people or organizations that can inappropriately influence our work; there is no professional or other personal interest of any nature or kind in any product, service and or company that could be construed as influencing the position presented in, or the review of, the manuscript entitled.

Acknowledgments

This project was supported by the National Key R&D Program of China (Grant no. 2018YFC1505001), the Open Fund of State Key Laboratory of Frozen Soil Engineering (Grant no. SKLFSE202013), and the National Natural Science Foundation of China (No. 51874065).

Supplementary Materials

Highlights. (*Supplementary Materials*)

References

- [1] N. Matsuoka, "Mechanisms of rock breakdown by frost action: an experimental approach," *Cold Regions Science and Technology*, vol. 17, no. 3, pp. 253–270, 1990.
- [2] Y. Wang, Y. F. Yi, C. H. Li, and J. Q. Han, "Anisotropic fracture and energy characteristics of a Tibet marble exposed to multi-level constant-amplitude (MLCA) cyclic loads: a lab-scale testing," *Engineering Fracture Mechanics*, vol. 244, article 107550, 2021.
- [3] D. D. Ma, H. Xiang, Q. Ma et al., "Dynamic damage constitutive model of frozen silty soil with prefabricated crack under uniaxial load," *Journal of Engineering Mechanics*, vol. 147, no. 6, article 04021033, 2021.
- [4] H. Y. Liu, X. C. Zhang, and X. Yan, "A damage constitutive model for a rock under compression after freeze-thaw cycles based on the micromechanics," *Geofluids*, vol. 2021, Article ID 3177464, 11 pages, 2021.

- [5] N. Fan, J. R. Wang, C. B. Deng, Y. P. Fan, T. T. Wang, and X. Y. Guo, "Quantitative characterization of coal microstructure and visualization seepage of macropores using CT-based 3D reconstruction," *Journal of Natural Gas Science and Engineering*, vol. 81, article 103384, 2020.
- [6] A. Prick, "Dilatometrical behaviour of porous calcareous rock samples subjected to freeze-thaw cycles," *Catena*, vol. 25, no. 1-4, pp. 7-20, 1995.
- [7] N. F. Liu, N. Li, C. B. Xu, G. F. Li, Z. P. Song, and M. Yang, "Mechanism of secondary lining cracking and its simulation for the Dugongling tunnel," *Rock Mechanics and Rock Engineering*, vol. 53, no. 10, pp. 4539-4558, 2020.
- [8] Y. Wang, B. Zhang, B. Li, and C. H. Li, "A strain-based fatigue damage model for naturally fractured marble subjected to freeze-thaw and uniaxial cyclic loads," *International Journal of Damage Mechanics*, vol. 6, 2021.
- [9] Y. M. Lai, Z. W. Wu, Y. L. Zhu, and L. Zhu, "Elastic viscoplastic analysis for earthquake response of tunnels in cold regions," *Cold Regions Science and Technology*, vol. 31, no. 3, pp. 175-188, 2000.
- [10] W. W. Liu, Q. Feng, S. G. Fu, and C. X. Wang, "Elasto-plastic solution for cold-regional tunnels considering the compound effect of non-uniform frost heave, supporting strength and supporting time," *Tunnelling and Underground Space Technology*, vol. 82, pp. 293-302, 2018.
- [11] Y. M. Lai, S. Zhang, and W. Yu, "A new structure to control frost boiling and frost heave of embankments in cold regions," *Cold Regions Science and Technology*, vol. 79-80, pp. 53-66, 2012.
- [12] G. Y. Gao, Q. S. Chen, Q. S. Zhang, and G. Q. Chen, "Analytical elasto-plastic solution for stress and plastic zone of surrounding rock in cold region tunnels," *Cold Regions Science and Technology*, vol. 72, pp. 50-57, 2012.
- [13] Q. Feng, S. G. Fu, C. X. Wang, W. W. Liu, Y. Wang, and W. G. Qiao, "Analytical elasto-plastic solution for frost force of cold-region tunnels considering anisotropic frost heave in the surrounding rock," *KSCSE Journal of Civil Engineering*, vol. 23, no. 9, pp. 3831-3842, 2019.
- [14] X. Zhao, X. Yang, H. Zhang, H. Lai, and X. Wang, "An analytical solution for frost heave force by the multifactor of coupled heat and moisture transfer in cold-region tunnels," *Cold Regions Science and Technology*, vol. 175, pp. 103077-103168, 2020.
- [15] J. Walder and B. Hallet, "A theoretical model of the fracture of rock during freezing," *Geological Society of America Bulletin*, vol. 96, no. 3, pp. 336-346, 1985.
- [16] B. Hallet, J. S. Walder, and C. W. Stubbs, "Weathering by segregation ice growth in microcracks at sustained subzero temperatures: verification from an experimental study using acoustic emissions," *Permafrost and Periglacial Process*, vol. 2, no. 4, pp. 283-300, 1991.
- [17] Y. Wang, C. H. Li, and J. Q. Han, "On the effect of stress amplitude on fracture and energy evolution of pre-flawed granite under uniaxial increasing-amplitude fatigue loads," *Engineering Fracture Mechanics*, vol. 240, article 107366, 2020.
- [18] Y. S. Kang, Q. S. Liu, X. Y. Liu, and S. B. Huang, "Theoretical and numerical studies of crack initiation and propagation in rock masses under freezing pressure and far-field stress," *Journal of Rock Mechanics and Geotechnical Engineering*, vol. 6, no. 5, pp. 466-476, 2014.
- [19] S. B. Huang, Q. S. Liu, Y. Z. Liu, Y. S. Kang, A. P. Cheng, and Z. Y. Ye, "Frost heaving and frost cracking of elliptical cavities (fractures) in low-permeability rock," *Engineering Geology*, vol. 234, pp. 1-10, 2018.
- [20] X. J. Tan, W. Z. Chen, H. Y. Liu, L. Y. Wang, W. Ma, and A. H. C. Chan, "A unified model for frost heave pressure in the rock with a penny-shaped fracture during freezing," *Cold Regions Science and Technology*, vol. 153, pp. 1-9, 2018.
- [21] G. P. Davidson and J. F. Nye, "A photoelastic study of ice pressure in rock cracks," *Cold Regions Science and Technology*, vol. 11, no. 2, pp. 141-153, 1985.
- [22] N. Matsuoka and J. Murton, "Frost weathering: recent advances and future directions," *Permafrost and Periglacial Processes*, vol. 19, no. 2, pp. 195-210, 2008.
- [23] C. Amanuma, T. Kanauchi, S. Akagawa, Z. Hao, and S. Kanie, "Evaluation of frost heave pressure characteristics in transverse direction to heat flow," *Procedia Engineering*, vol. 171, pp. 461-468, 2017.
- [24] C. C. Xia, Z. T. Lv, Q. Li, J. H. Huang, and X. Y. Bai, "Transversely isotropic frost heave of saturated rock under unidirectional freezing condition and induced frost heaving force in cold region tunnels," *Cold Regions Science and Technology*, vol. 152, pp. 48-58, 2018.
- [25] R. L. Shan, Y. Bai, P. F. Sun, Y. X. Wu, S. M. Sui, and H. H. Yuan, "Experimental study on frost heaving pressure properties in fractured red sandstone," *Journal of China Coal Society*, vol. 44, no. 6, pp. 1742-1752, 2019, (in Chinese).
- [26] A. Al-Omari, K. Beck, X. Brunetaud, Á. Török, and M. Al-Mukhtar, "Critical degree of saturation: a control factor of freeze-thaw damage of porous limestones at Castle of Chambord, France," *Engineering Geology*, vol. 185, pp. 71-80, 2015.
- [27] H. M. Zhang, X. Z. Meng, and G. S. Yang, "A study on mechanical properties and damage model of rock subjected to freeze-thaw cycles and confining pressure," *Cold Regions Science and Technology*, vol. 174, article 103056, 2020.
- [28] H. L. Jia, K. Leith, and M. Krautblatter, "Path-dependent frost-wedging experiments in fractured, low-permeability granite," *Permafrost and Periglacial Process*, vol. 28, no. 4, pp. 698-709, 2017.
- [29] S. B. Huang, Y. Z. Liu, Y. L. Guo, Z. L. Zhang, and Y. T. Cai, "Strength and failure characteristics of rock-like material containing single crack under freeze-thaw and uniaxial compression," *Cold Regions Science and Technology*, vol. 162, pp. 1-10, 2019.
- [30] Y. Bai, R. L. Shan, Y. Ju, Y. X. Wu, P. F. Sun, and Z. E. Wang, "Study on the mechanical properties and damage constitutive model of frozen weakly cemented red sandstone," *Cold Regions Science and Technology*, vol. 171, article 102980, 2020.
- [31] C. A. Tang, H. Liu, P. K. K. Lee, Y. Tsui, and L. G. Tham, "Numerical studies of the influence of microstructure on rock failure in uniaxial compression - part I: effect of heterogeneity," *International Journal of Rock Mechanics and Mining Sciences*, vol. 37, no. 4, pp. 555-569, 2000.
- [32] W. C. Zhu and C. A. Tang, "Micromechanical model for simulating the fracture process of rock," *Rock Mechanics & Rock Engineering*, vol. 37, no. 1, pp. 25-56, 2004.
- [33] W. C. Zhu and C. A. Tang, "Numerical simulation of Brazilian disk rock failure under static and dynamic loading," *International Journal of Rock Mechanics and Mining Sciences*, vol. 43, no. 2, pp. 236-252, 2006.
- [34] S. B. Tang, C. A. Tang, Z. Z. Liang, Y. Zhang, and L. C. Li, "Numerical study of the influence of material structure on

effective thermal conductivity of concrete,” *Heat Transfer Engineering*, vol. 33, no. 8, pp. 732–747, 2012.

- [35] S. B. Tang and C. A. Tang, “Crack propagation and coalescence in quasi-brittle materials at high temperatures,” *Engineering Fracture Mechanics*, vol. 134, pp. 404–432, 2015.
- [36] F. David, P. Robert, and P. Roger, *Statistics*, W. W. Norton & Company, Inc., New York, 4th Ed. edition, 2007.

Research Article

Influence of Lightweight Foamed Concrete as Backfill Material on Stress and Deformation of Buttressed Earth-Retaining Wall

Youqiang Qiu ^{1,2}, Yang Liu ¹, Liujun Zhang ², and Zhanqi Wang ³

¹School of Civil and Resource Engineering, University of Science and Technology Beijing, Beijing 100083, China

²CCCC First Highway Consultants Co., Ltd., Xi'an 710075, China

³Department of Civil and Airport Engineering, Nanjing University of Aeronautics and Astronautics, Nanjing 210016, China

Correspondence should be addressed to Yang Liu; yangliu@ustb.edu.cn and Liujun Zhang; zhanglj@ccroad.com.cn

Received 25 June 2021; Accepted 17 August 2021; Published 8 September 2021

Academic Editor: Afshin Davarpanah

Copyright © 2021 Youqiang Qiu et al. This is an open access article distributed under the Creative Commons Attribution License, which permits unrestricted use, distribution, and reproduction in any medium, provided the original work is properly cited.

Controlling settlement and earth pressure behind retaining wall in soft soil area are ongoing practical problems for the construction and operation of highway, which are mainly caused by the poor nature of soft soil. To reduce the pushing force on retaining wall and subgrade settlement, the authors propose the use of lightweight foamed concrete as subgrade filler behind the buttressed earth-retaining wall. However, the mechanical properties and deformation behavior of the buttressed earth-retaining wall remain unknown when lightweight foamed concrete is used as a backfill behind the wall. To solve this problem, a scale model of the subgrade filled with lightweight foamed concrete behind the buttressed earth-retaining wall is established to determine its stress and deformation characteristics under different factors. Lateral earth pressures and wall displacements at different elevations of the retaining wall model were monitored during the tests. Then, a series of orthogonal experiments are conducted to analyse and compare the effects of overload, density, and replacement thickness of lightweight foamed concrete on the earth pressure and displacement of this retaining wall. The results show that the size of earth pressures at the same position of retaining wall is affected by overload, density, and replacement thickness of lightweight foamed concrete, but its change of distribution form is only related to the replacement thickness of this backfill. Additionally, the primary-secondary relations of different factors' influence extent on the forces and deformation of the buttressed earth-retaining wall filled with lightweight foamed concrete as backfill are obtained by using range analysis method.

1. Introduction

With the new construction concept of “green, environmental protection and energy saving” actively advocated both at home and abroad in recent years, a large number of new materials and innovative technologies for infrastructure construction have been developed and applied in the practical engineering [1–3]. As a new type of lightweight material, lightweight foamed concrete has been widely valued and studied by many scholars and experts at home and abroad due to its advantages such as light weight, uprightness, high fluidity, good durability, convenient construction, and thermal insulation [4–9]. Besides, it has been gradually applied in various fields of civil engineering and achieved good engineering results, which has been vigorously promoted by the

industry and widely recognized by the society [10–14]. Thus, the authors propose the use of lightweight foamed concrete as a filler behind the buttressed earth-retaining wall in Guangzhou-Foshan-Jiangmen Freeway of Guangdong province in China, which provides a new method to control subgrade settlement and reduce the pushing force on retaining wall (as shown in Figure 1).

Regarding the research on replacement technology of cast in situ lightweight foamed concrete, its constitution, physical properties, and engineering applications have been studied by Valore [15, 16], Rudnai [17], Taylor [18], and Short and Kinniburgh [19]. As foam concrete developed further, a series of experimental studies on modification of lightweight foamed concrete were carried out by adding different admixtures. For example, Jones and McCarthy



FIGURE 1: Use of lightweight foamed concrete as a filler behind buttressed earth-retaining wall.

[20] and Kearsley and Wainwright [21] suggested that using unprocessed, run-of-station, low-lime fly ash can significantly improve the performance of foamed lightweight concrete. Chandni and Anand [22] studied the effect of superplasticizer inclusion and the corresponding change in the water to solid ratio on compressive strength of foam concrete, and incorporation of PCE-based superplasticizer was observed to be effective in enhancing the strength of foam concrete. Wang et al. [23] found that the small amount (3 wt%) of crumb rubber can improve the waterproof performance of foamed concrete. Besides, as for the research on durability and microscopic properties of lightweight foamed concrete, Chung et al. [24] investigated the characteristics and properties of lightweight aggregate concrete and foamed concrete with the same density levels by using image analysis method; Kashani et al. [25] revealed the effect of recycled glass fines on mechanical and durability properties of concrete foam in comparison with traditional cementitious fines; Su et al. [26] analyzed the mechanical behavior of foamed concrete by a series of uniaxial and triaxial experiments; results indicated that foamed concrete demonstrates brittle failure under a uniaxial tension and small compression deformation for uniaxial loading. According to the above references, although a large number of experimental studies on lightweight foamed concrete have been carried out at home and abroad, it is mainly limited to experimental research on its physical and mechanical properties. There are few researches on the use of lightweight foamed concrete as a backfill behind the buttressed earth-retaining wall, and its force and deformation characteristics are still unclear, which need to be further studied.

On the other hand, relevant researches [27–29] show that factors affecting earth pressures and wall displacements of the retaining wall are as follows: overload, shape of retaining wall, the nature of the filled soil, and filled soil height. Taking into account the limitations of laboratory test conditions, three main influencing factors are considered in this paper, including overload, density of lightweight foamed concrete, and replacement depth of lightweight foamed concrete.

The overall objective of this study is to determine and compare the stress and deformation characteristics of buttressed earth-retaining wall backfilled with lightweight foamed concrete under different factors through the indoor

model test. In addition, results of the model test can determine the primary and secondary relations of three factors' influence extent on the forces and deformation of this retaining wall through the range analysis, and the most suitable replacement thickness of lightweight foamed concrete behind buttressed earth-retaining wall can be also obtained by regression analysis, which can provide a reference in the practical engineering.

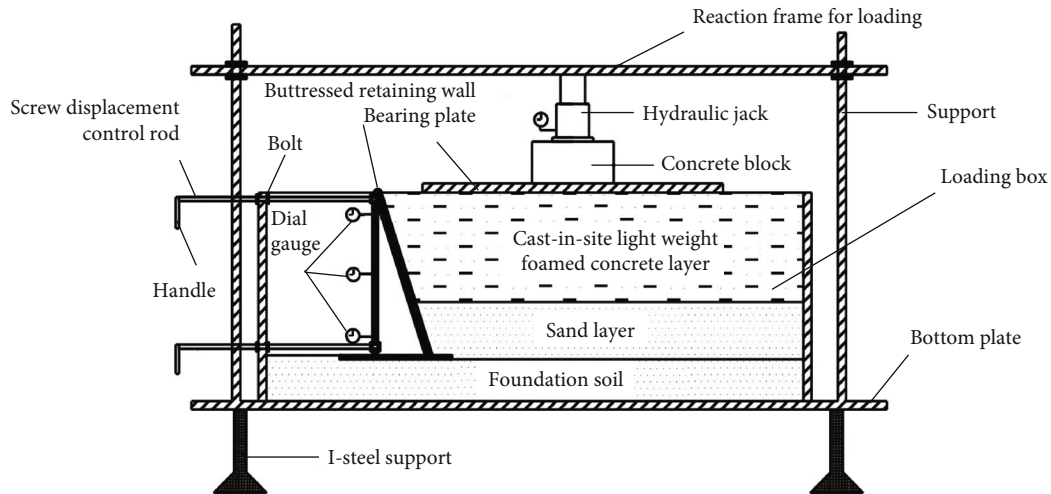
2. Experimental Procedure

2.1. Experimental Model Setup. In this paper, referring to the field structure size of Guangzhou-Foshan-Jiangmen Freeway of Guangdong province in China, a self-developed model box is used to carry out the model experiment with the reduced-scale of 25:1 (actual size: model size). The model box is mainly composed of the following parts: a loading box (backfill layer), a retaining wall, displacement control system of retaining wall, upper loading system, and measurement system (as shown in Figure 2).

2.1.1. Buttressed Earth-Retaining Wall and Backfill Layer. Taking the size of the on-site buttressed earth-retaining wall structure as a reference prototype, the size of buttressed earth-retaining wall in model is designed with reduced-scale of 25:1 (actual size: model size) (as shown in Figure 3). Besides, the design sizes of the model box and the loading box are 150 cm × 50 cm × 40 cm (length × width × height) and 100 cm × 50 cm × 40 cm (length × width × height), respectively. In the loading box, the cast in situ lightweight foamed concrete layer and sand layer are presented as packing layers from top to bottom. The thicknesses of two packing layers behind the retaining wall can be adjusted according to the test requirements.

2.1.2. Sensors Distribution. In order to reveal the stress and deformation characteristics of buttressed earth-retaining wall backfilled with lightweight foamed concrete under different conditions, 17 earth pressure cells and 3 dial indicators were buried at different elevations of the retaining wall model to, respectively, monitor the lateral earth pressures and wall displacements during the tests.

LY-350 series strain type miniature earth pressure sensors were selected to measure lateral earth pressures of this retaining wall in the tests. Among them, 3 earth pressure cells were arranged at the bottom plate, numbered 1 through 3, and the distances from the edge of the wall toe plate are 4, 13, and 22 cm in order; 4 earth pressure cells were buried on the inside of vertical wall, numbered 4 through 7, and distances from the top of the wall are 5, 14, 23, and 32 cm in order; 5 earth pressure cells were arranged on the left side of the soil facing surface of buttress; its stress surface is vertical to the horizontal surface, numbered 8 through 12, and distances from the top of the wall are 6, 13, 20, 27, and 34 cm in order; 5 earth pressure cells were buried on the right side of the buttress sidewall, numbered 13 through 17, and distances from the top of the wall are 6, 13, 20, 27, and 34 cm, respectively. The detailed buried positions of the earth pressure cells are shown in Figure 4.



(a) Schematic diagram of the model box



(b) Real image of the model box

FIGURE 2: The test model box.

In addition, 3 dial indicators were selected to measure displacements of the retaining wall in model tests, which were, respectively, arranged at the positions of 2, 16, and 32 cm from the top of the wall (as shown in Figure 5).

2.1.3. Loading System and Data Acquisition System. The upper loading system in the model is mainly composed of reaction beam, a hydraulic jack, concrete block, steel load bearing plate, and support rod. In the tests, the hydraulic jack with precision pressure gauge was selected, which can directly apply the required load and make up pressure at any time. Furthermore, the load exerted by the jack can be evenly transmitted to packing layers because of the load bearing plate with sufficient rigidity. The experimental model is loaded by using the stage loading method, which is divided into three stages. The deformation of the retaining wall can be considered to be stable when the loading interval time of each stage is 1 h, and the readings of dial indicators and earth pressure cells corresponding to the level of load shall be recorded.

Based on the above loading system and sensor distribution, the dynamic data are gathered by a dynamic acquisition system during the loading process. The CM-1A-20 digital static strain gauge produced by Qinhuangdao Xinheng Electronic Technology Co., Ltd. was used as the collection device in the test. The connection of the earth pressure cells adopts the full bridge mode, and the measurement data collection is controlled by the computer (as shown in Figure 6).

2.2. Model Test Scheme. According to the above experimental model, limited by laboratory test conditions, the effects of three factors, including surface load, density of lightweight foamed concrete, and replacement thickness of lightweight foamed concrete, on the stress and deformation of butressed earth-retaining wall backfilled with lightweight foamed concrete are considered in this paper.

With the support of Guangzhou-Foshan-Jiangmen Freeway, under vehicle loads, the uniform load at the top surface of lightweight foamed concrete subgrade is about 60.8 kPa according to local traffic volume and numerical calculations.

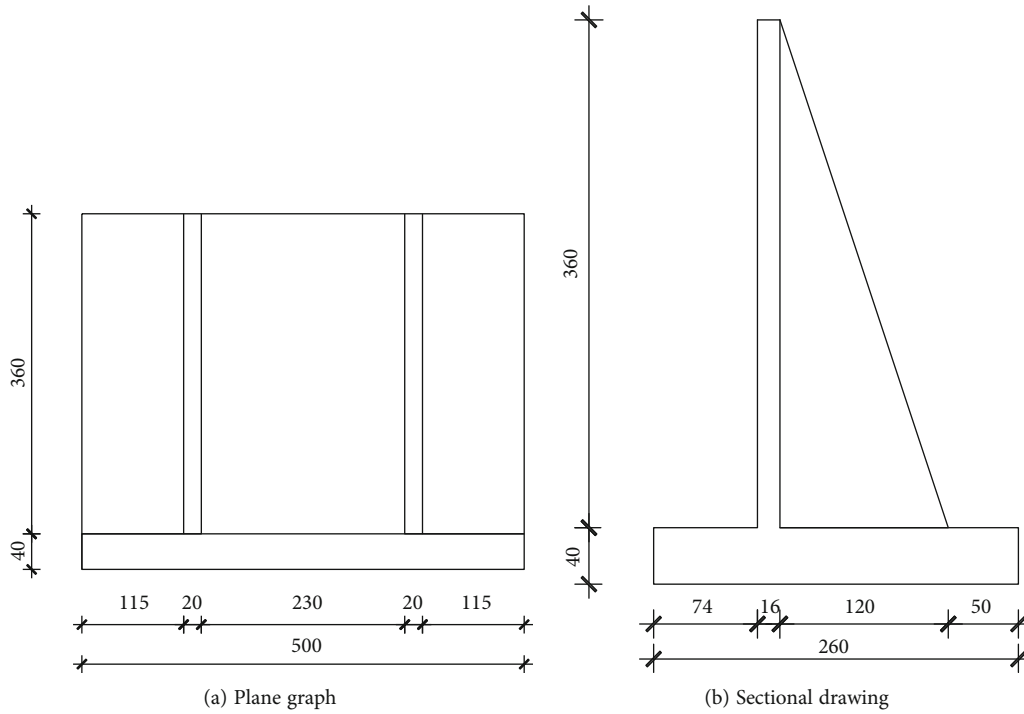


FIGURE 3: Size of buttressed earth-retaining wall (unit: mm).

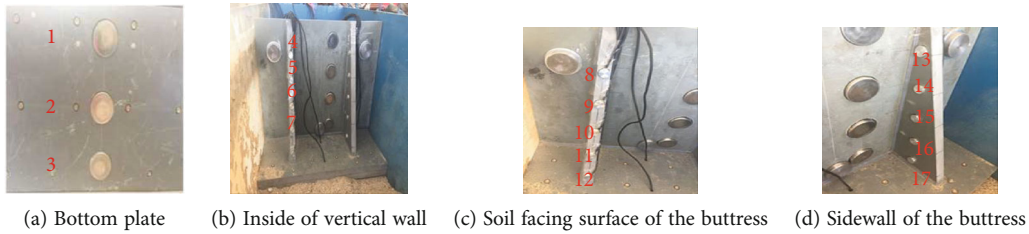


FIGURE 4: The distribution of earth pressure cells.



FIGURE 5: The distribution of dial indicators.

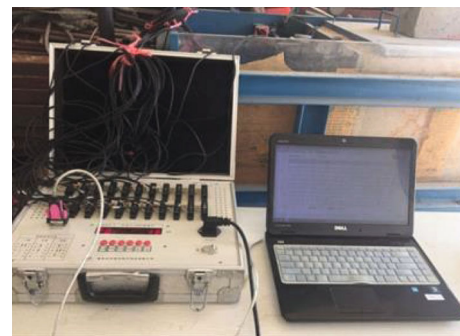


FIGURE 6: Data acquisition system.

In consideration of the three-stage loading method used in the model test, the overloads (concentrated load) of 14, 16, and 18 MPa at the top surface of lightweight foamed concrete layer behind the retaining wall are applied by controlling the loading system for interval 1 h, respectively. In fact, these overloads can be converted to the uniform loads of 61, 69.484 and 77.969 kPa by numerical calculations, which are consistent with the actual engineering.

TABLE 1: The single-factor orthogonal test scheme.

Test number	Overload (MPa)	Density of lightweight foamed concrete (kg/m ³)	Replacement thickness of lightweight foamed concrete (m)	Single factor
1-1	14	700	0.28	Overload
1-2	16	700	0.28	
1-3	18	700	0.28	
1-4	14	600	0.28	Density of lightweight foamed concrete
1-5	14	700	0.28	
1-6	14	800	0.28	
1-7	14	700	0.22	Replacement thickness of lightweight foamed concrete
1-8	14	700	0.28	
1-9	14	700	0.40	

TABLE 2: The multiple-factor orthogonal test scheme.

Test number	Overload (MPa)	Density of lightweight foamed concrete (kg/m ³)	Replacement thickness of lightweight foamed concrete (m)
2-1	14	600	0.22
2-2	14	700	0.28
2-3	14	800	0.40
2-4	16	600	0.28
2-5	16	700	0.40
2-6	16	800	0.22
2-7	18	600	0.40
2-8	18	700	0.22
2-9	18	800	0.28

As for the selection of density of lightweight foamed concrete in tests, the foamed lightweight concrete paste with density of 600, 700, and 800 kg/m³ are used to cast the lightweight foamed concrete layer referring to the cast-in-place lightweight foamed concrete density of 700 kg/m³ in actual engineering. In addition, according to the height of the buttressed retaining wall model, the replacement thicknesses of lightweight foamed concrete layer of 0.22, 0.28, and 0.40 m are selected to carry out the tests, and the corresponding thicknesses of the sand layer are 0.18, 0.12, and 0 m.

In order to more accurately reveal the force and deformation characteristics of the buttressed earth-retaining wall backfilled with lightweight foamed concrete, the influence laws of the changing single factor on the resultant earth pressure and the point of resultant force of retaining wall were studied first by means of single-factor orthogonal test. And then, using range analysis method, the primary and secondary relations of the influence extent of each factor on the forces and deformation of this retaining wall were analyzed by the multiple-factor orthogonal test.

The single-factor orthogonal test scheme is shown in Table 1, and the multiple-factor orthogonal test scheme is shown in Table 2.

2.3. *Materials, Mixture Proportion, and Properties.* As a new type of artificial lightweight cement material, lightweight

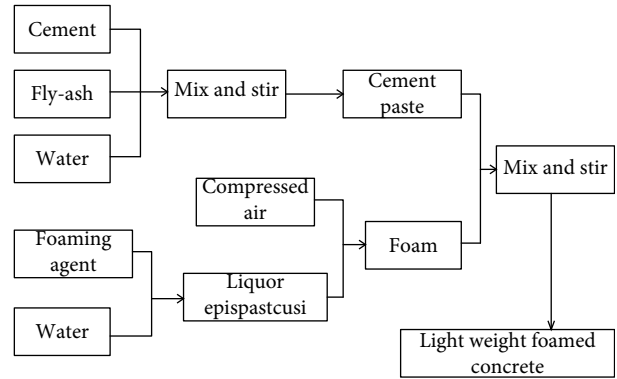


FIGURE 7: Preparation process of lightweight foamed concrete.

foamed concrete is firstly prepared by the physical method from the foaming agent into the foam, then the foam is mixed into the cement slurry which has been stirred evenly in a certain proportion, and finally, hardened by physical and mechanical effects. The preparation process of lightweight foamed concrete is shown in Figure 7.

In this paper, lightweight foamed concrete is produced under a controlled percentage of OPC (42.5), water, and foaming agent without adding aggregate or modifiers. On the basis of the Chinese *Technical Specification for Design and Construction of Cast-In-Situ Lightweight Foamed Concrete Subgrade (TJG F10 01-2011)* [30] and results of previous tests [31, 32], the most suitable water/solid ratio of lightweight foamed concrete under this condition is 1:2.0 by comparison of performances; the mix proportions of lightweight foamed concrete with target densities of 600, 700, and 800 kg/m³ are shown in Table 3. According to the Chinese *Technical Specification for Design and Construction of Cast-In-Situ Lightweight Foamed Concrete Subgrade (TJG F10 01-2011)* [30] and the Chinese *Test Methods of Soils for Highway Engineering (JTG E40-2020)* [33], the main performance indexes of lightweight foamed concrete and sand are measured in Tables 4 and 5, respectively.

As can be seen from the results in Table 4, with the increase of the target density of lightweight foamed concrete, the moist unit weight, compressive strength, flexural strength, and CBR of lightweight foamed concrete increase gradually, but its flow value and water absorption rate

TABLE 3: The mix proportions of lightweight foamed concrete.

Water/solid ratio	Density of lightweight foamed concrete (kg/m ³)	Density of cement (kg/m ³)	Density of foam (kg/m ³)	Cement (kg/m ³)	Water (kg/m ³)	Foam (kg/m ³)
1 : 2.0	600	3069	40.27	381.6	190.8	27.6
1 : 2.0	700	3069	40.27	449.8	224.9	25.3
1 : 2.0	800	3069	40.27	518.0	259.0	23.0

TABLE 4: The performance indexes of lightweight foamed concrete.

Density of lightweight foamed concrete (kg/m ³)	Flow value (mm)	Moist unit weight (kN/m ³)	Compressive strength (28 days) (MPa)	Flexural strength (28 days) (MPa)	Water absorption (%)	CBR (%)
600	186	5.08	0.99	0.34	23.5	12.5
700	178	5.74	1.45	0.47	21.7	15.6
800	170	6.48	1.86	0.63	20.1	18.9

TABLE 5: The performance indexes of sand.

Density (kg/m ³)	Moisture content (%)	Nonuniform coefficient	Curvature coefficient	Elasticity modulus (MPa)	Poisson ratio	Cohesion (kPa)	Internal friction angle (°)
1613	1.12	5.33	1.28	15.0	0.35	0	35.8

decrease gradually. According to the *Technical Specification for Design and Construction of Cast-In-Place Lightweight Foamed Concrete Subgrade (TJG F10 01-2011)* [30], the main performance indexes of lightweight foamed concrete in Table 4 meet the relevant requirements, which indicates that lightweight foamed concrete can be used as filler for the model.

In addition, results in Table 5 reveal that the nonuniform coefficient of sand is greater than 5 and that its curvature coefficient is between 1 and 3. This indicates that sand is well graded and can therefore be used as filler for the model.

3. Results and Discussion

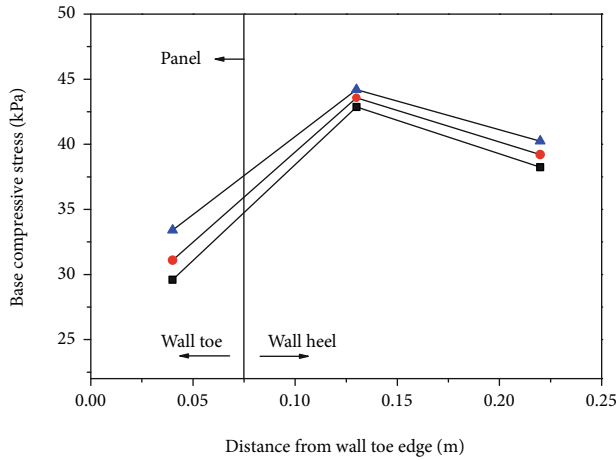
3.1. Results of the Single-Factor Orthogonal Test. Firstly, based on the single-factor orthogonal test scheme in Table 1, the effects of overload, density of lightweight foamed concrete, and replacement thicknesses of lightweight foamed concrete on the stress and deformation characteristics of buttressed earth-retaining wall backfilled with lightweight foamed concrete are analyzed and discussed, respectively, in this section of the paper.

3.1.1. Effects of Overload. According to the orthogonal test scheme in Table 1, the overloads of 14, 16, and 18 MPa were applied to the surface of backfill in order by using a jack on the premise of keeping the density and the replacement depth of lightweight foamed concrete unchanged.

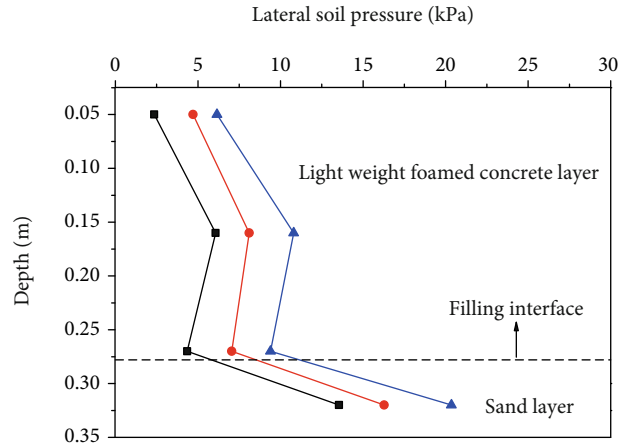
The effects of different overload on the lateral earth pressures and wall displacements at different elevations of the retaining wall model filled with lightweight foamed concrete are presented in Figure 8, which shows that the overload has

a great influence on the earth pressure of retaining wall filled with lightweight foamed concrete; the earth pressure at the same position increases with the increase of the overload, but it does not change the distribution laws of earth pressure at the same position of retaining wall. This effect is due to the larger of overload on the surface of the lightweight foamed concrete, the greater of compression force between the backfill and the retaining wall, which is reflected in the greater earth pressure of the retaining wall.

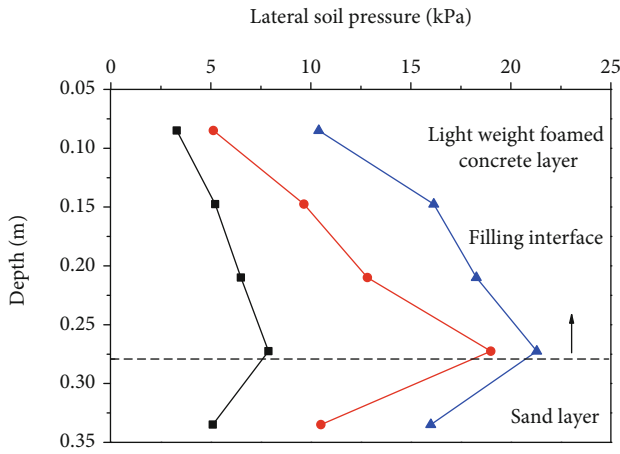
Compared with the size and distribution shape of earth pressure at different positions of the retaining wall in Figure 8, it can be seen that under the same overload, the size and distribution shape of earth pressure vary with the different positions of the retaining wall. As for the distribution shape of earth pressure under the same overload, the base compressive stress is not distributed in the triangle or trapezoid, but in a convex shape of "large in the middle and small on both sides", which indicates that there is a peak point of base compressive stress in the middle of the bottom plate. However, the earth pressure presents an "R" distribution shape along the height of the wall both on the inside of vertical wall and sidewall of the buttress. That is, the earth pressure increases first and then decreases along the lightweight foamed concrete layer depth, but the earth pressure suddenly increases along sand layer depth, showing a linear growth, which may be caused by the too large difference between the gravity of two filling layers. In the calculation of earth pressure, the gravity of filler is an important factor affecting the size of earth pressure, and the earth pressure increases with the increase of the gravity of fill. The density of sand is about 2.5 times as severe as that of lightweight foamed concrete, so the earth pressure in this two filling



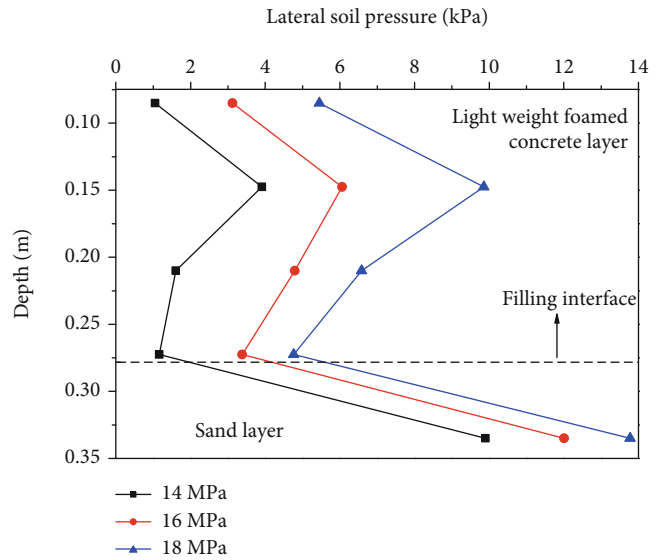
(a) Earth pressure distribution at the bottom plate



(b) Earth pressure distribution on the inside of vertical wall



(c) Earth pressure distribution on the soil facing surface of the buttress



(d) Earth pressure distribution on sidewall of the buttress

FIGURE 8: Earth pressure distributions of retaining wall under different overloads.

layers presents an “R” distribution as a whole. Furthermore, the earth pressure on the soil facing surface of the buttress presents a “D” distribution shape along the height of the wall, that is, the earth pressure increases gradually with the increase of wall depth and reaches the maximum value at the junction of two filling layers, but the earth pressure in sand layer decreases rapidly, which may be due to the tensile stress at the root of buttress.

On the other hand, the magnitudes of lateral earth pressures vary with positions of retaining wall under the same overload. Taking the overload of 14 MPa as an example, it can be seen from Figure 8 that the maximum earth pressure on the inside of vertical wall and the soil facing surface of the buttress are 6.10 and 7.88 kPa, respectively, while the earth pressures on sidewall of the buttress are obviously smaller, with the maximum value of 3.95 kPa. The reason is that the sidewall of the buttress is not smooth, which leads to the soil arch effect between two buttresses in the horizontal direction. Due to the existence of these soil arches, most of

the lateral earth pressures behind the wall are transmitted to the buttresses, which causes the earth pressure on the buttresses greater than that on sidewall of the buttress, reducing the lateral pressure on the retaining wall panels.

Figure 9 shows the displacement changes of retaining wall backfilled with lightweight foamed concrete along the height of the wall under different overload, “-” in Figure 9 indicates that the retaining wall moves away from the filling direction, and “-” in the following text is the same meaning, so it is not described in the following text.

As seen from Figure 9, the wall displacements at the same depth increases gradually in the process of continuous loading, and the increase of the displacement at the top of the wall is larger than that at the bottom of the wall, which shows that the overload has a greater impact on the displacement at the top of the wall. From the results shown in Figure 9, the displacement change laws of the retaining wall are basically similar under different overload conditions, that is, the horizontal displacement of the retaining wall

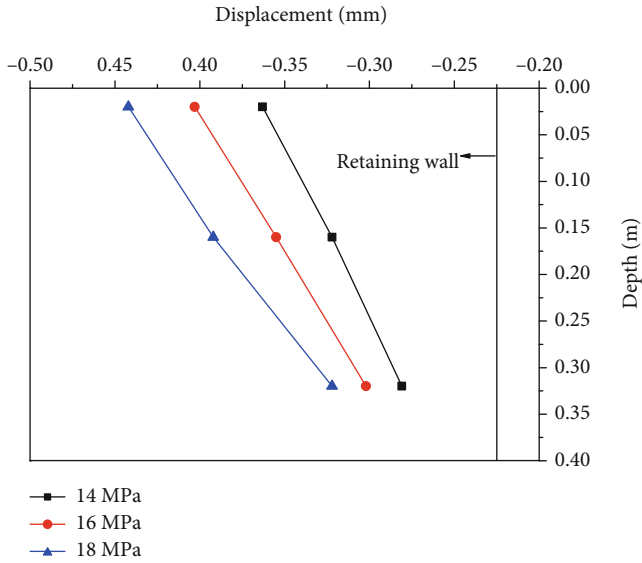


FIGURE 9: Displacement changes of retaining wall under different overloads.

decreases linearly with the increase of the retaining wall depth. The horizontal displacement at the top of the wall is larger than that at the bottom, which illustrates that the retaining wall not only rotates around the bottom of the wall but also moves away from the soil behind the wall. Therefore, it indicates that the displacement mode of the retaining wall backfilled with lightweight foamed concrete is an “RBT” mode in the actual project.

3.1.2. Effects of the Density of Lightweight Foamed Concrete.

In this study, lightweight foamed concrete with the target density of 600, 700, and 800 kg/m³ is used as the backfill behind the buttressed earth-retaining wall. Under the condition of overload and lightweight foamed concrete replacement thickness unchanged, the test results for earth pressure distribution law of retaining wall under different densities of lightweight foamed concrete are shown in Figure 10.

Compared with the test results in Figures 8 and 10, it can be seen that there are no significant differences in the distribution shapes of earth pressure at different positions of the retaining wall under the effect of overload or the density of lightweight foamed concrete. In other words, similar to the distribution shapes of earth pressure in Figure 8, Figure 10 shows that the base compressive stress is still distributed in a convex shape of “large in the middle and small on both sides”, and the earth pressure on the soil facing surface of the buttress still presents a “D” shape distribution along the height of the wall, and the earth pressure still presents an “R” distribution along the height of the wall both on the inside of vertical wall and sidewall of the buttress.

However, by contrasting the maximum values of lateral earth pressure at each location of retaining wall in Figures 8 and 10, it can be found that two factors have different effects on the magnitude of lateral earth pressure of retaining wall backfilled with lightweight foamed concrete.

Obviously, the magnitudes of lateral earth pressure at the same location under the effect of overload are greater than that under the effect of lightweight foamed concrete density. Therefore, it can be concluded that overload has a greater effect on the force performance of the retaining wall back-filled with lightweight foamed concrete, compared to the effect of density of lightweight foamed concrete.

Furthermore, the results in Figure 10 show that the earth pressure at the same position increases with the increase of the density of lightweight foamed concrete, but it does not change the distribution laws of earth pressure at the same position of retaining wall, which is similar to the effects of overload. Therefore, it can be concluded that both of two factors can only change the magnitude of the earth pressure of this retaining wall, but cannot change its distribution shapes.

The displacement changes of retaining wall backfilled with lightweight foamed concrete along the height of the wall under different densities of lightweight foamed concrete are shown in Figure 11.

As shown in Figures 9 and 11, the displacement of this retaining wall is less affected by the density of the lightweight foamed concrete compared to the effect of overload, but the horizontal displacement change laws of the retaining wall caused by these two factors are similar. Under the condition that the density of lightweight foamed concrete remains the same, the displacement of the retaining wall decreases linearly with the increase of the filling depth. However, as the density of lightweight foamed concrete increases, the displacement of wall at the same depth would increase slightly. According to the test results in Figures 9 and 11, it is worth noting that the displacement of the retaining wall is small when lightweight foamed concrete is used to as the backfill behind the retaining wall, which is far less than the displacement required to active earth pressure under normal filling (0.004H, H is the height of retaining wall). The reason is that the lightweight foamed concrete has good self-standing after curing, and it has almost no pushing force on the retaining wall after curing. Therefore, using lightweight foamed concrete as the backfill behind the retaining wall can significantly reduce the deformation of the retaining wall in the actual engineering.

3.1.3. Effects of the Replacement Thickness of Lightweight Foamed Concrete.

Based on the height of the buttressed earth-retaining wall model, lightweight foamed concrete with the target replacement thickness of 0.22, 0.28, and 0.40 m is used to cast the lightweight foam concrete layer behind the retaining wall, while the corresponding thicknesses of the sand layer are 0.18, 0.12, and 0 m, respectively. Under the premise of keeping overload and the density of lightweight foamed concrete unchanged, the effects of the replacement thickness of lightweight foamed concrete on the earth pressure at different positions of retaining wall are presented in Figure 12.

Different from the effects of overload and density of lightweight foamed concrete, it can be clearly seen from Figure 12, both the sizes of the earth pressure of the retaining wall and its distribution laws have changed significantly,

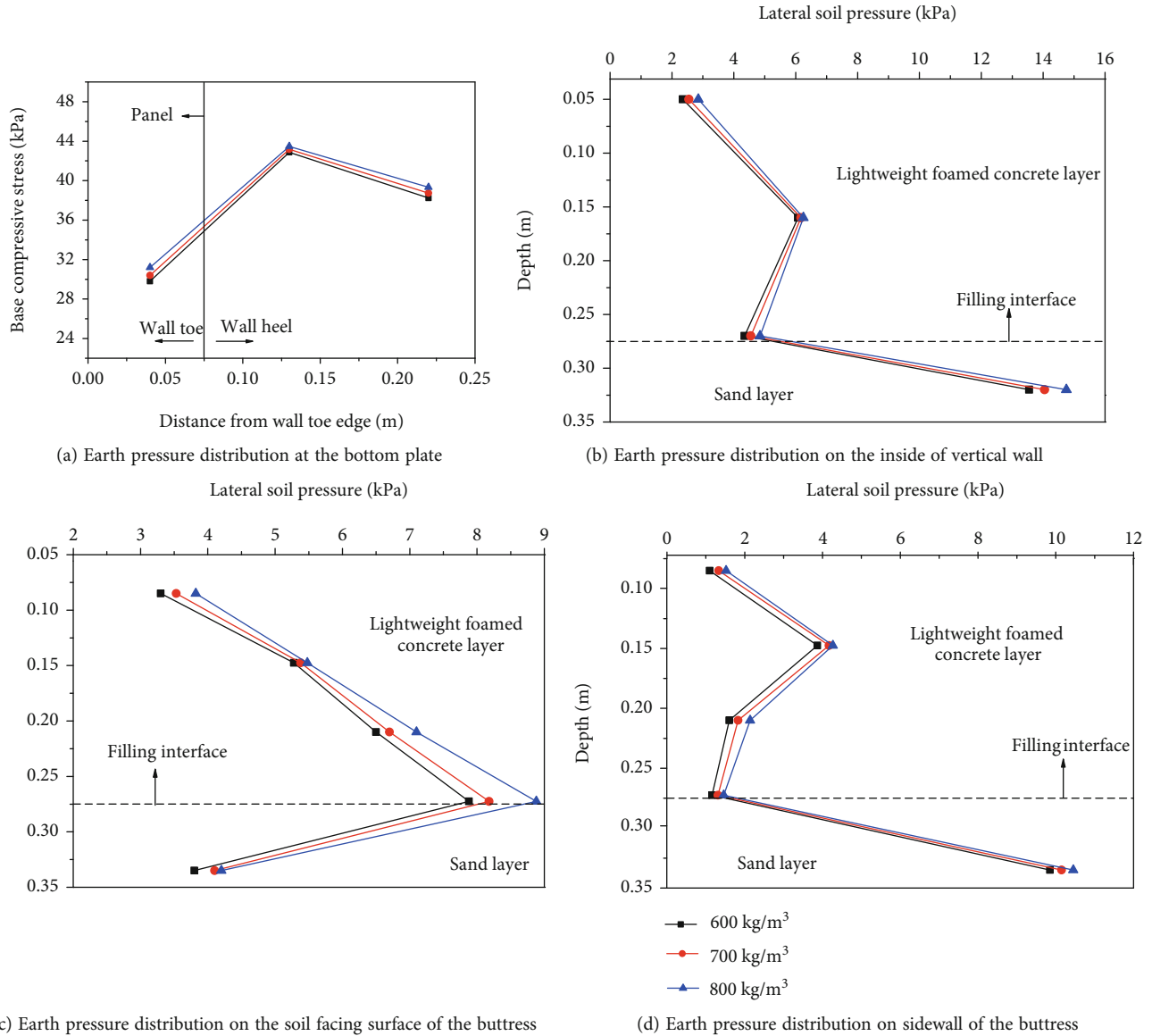


FIGURE 10: Earth pressure distributions of retaining wall under different densities of lightweight foamed concrete.

when using different replacement thicknesses of lightweight foamed concrete as the backfill in the model tests. The base compressive stress is still distributed in a convex shape of “large in the middle and small on both sides”, and it gradually decreases with the increase of the replacement depth of lightweight foamed concrete since the density of lightweight foamed concrete is about 1/3 of the general filling.

As for earth pressure distributions on the inside of vertical wall or on the sidewall of the buttress, three different replacement thicknesses of lightweight foamed concrete correspond to three different earth pressure distribution characteristics of retaining wall. When the replacement thickness is 0.28 m (the part backfill behind the wall is lightweight foamed concrete), the earth pressure still presents an “R” distribution shape, which is consistent with the previous distribution rule under the same conditions. When the thick-

ness of replacement is 0.22 m, the earth pressures presents firstly increases and then decreases, but this does not represent the distribution rule of earth pressure in this case, since only two earth pressure sensors are buried in the lightweight foamed concrete layer with target thickness of 0.22 m in model, and the distribution law of earth pressure was determined by at least three sensors. However, with the increase of thickness, when the replacement thickness of lightweight foamed concrete is 0.40 m (the filling soil behind the wall is all lightweight foamed concrete), the earth pressure presents a “D” distribution shape, the lateral earth pressure near the bottom of the retaining wall decreases gradually, and the back bending appeared, which may be caused by the restraint of the bottom plate of the retaining wall.

Furthermore, as for the earth pressure distribution on the soil facing surface of the buttress, the lateral earth

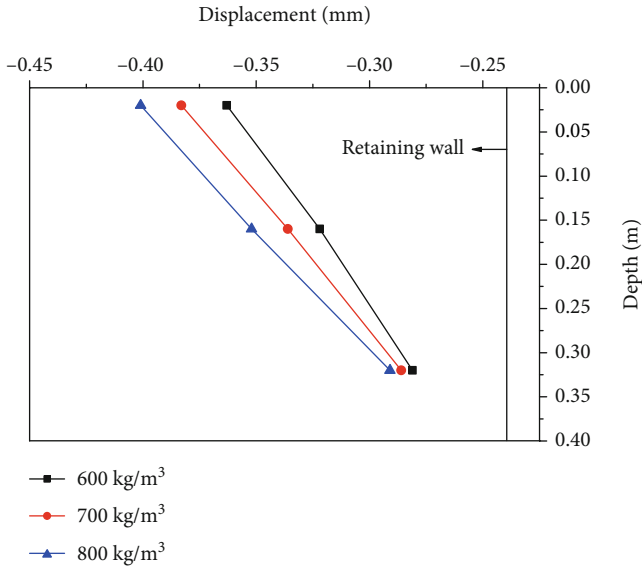


FIGURE 11: Displacement changes of retaining wall under different densities of lightweight foamed concrete.

pressure of the retaining wall is distributed as a “D” distribution shape along the depth of the wall when partially filled with foamed light soil, which is consistent with the previous distribution rule under the same conditions. However, the earth pressure distribution increased approximately linearly when all filled with lightweight foamed concrete, which means that the backfill is all filled with lightweight foamed concrete layer, and there is no difference in density between fillers.

To sum up, it can be concluded that the replacement thickness of lightweight foamed concrete has a great impact on the stress characteristics of this retaining walls. Therefore, it is very important to choose the suitable replacement thickness of lightweight foamed concrete as backfill in the actual engineering.

Figure 13 shows the effects of the replacement thickness of lightweight foamed concrete on the displacement of retaining wall. It can be seen from Figure 13 that the displacement of the retaining wall decreases approximately linearly as the depth of the retaining wall increases, which indicates that the displacement at the top of the retaining wall is the largest and the displacement at the bottom of the retaining wall is the smallest. Besides, with the increase of the replacement thickness of lightweight foamed concrete, the displacement of retaining wall at the same point decreases gradually, which indicates that increasing the replacement thickness of lightweight foamed concrete within a certain range is conducive to improving the stability of retaining wall.

3.1.4. Establishment of Regression Equations. In order to further reveal the relationships between the size of the resultant earth pressure, the point of resultant force of retaining wall, and above three factors, taking the earth pressure on the inside of vertical wall as an example, the resultant earth pressure and the point of resultant force of retaining wall are,

respectively, fitted with different influencing factors based on the above test results. The corresponding fitting equations are established in Table 6, which provide references in the practical engineering.

According to the results in Table 6, it is very convenient to obtain the resultant earth pressure and the points of resultant force of this retaining wall model through the above fitting equations, and corresponding indexes in practical engineering can be converted by the scale of 25:1 (actual size: model size).

On the other hand, through the above fitting equations in Table 6 and the scale of 25:1 (actual size: model size), we can deduce the appropriate construction parameters or design parameters of the foamed lightweight earth as the backfill behind the retaining wall in actual engineering, which has a significant guiding value for the construction and design of similar projects.

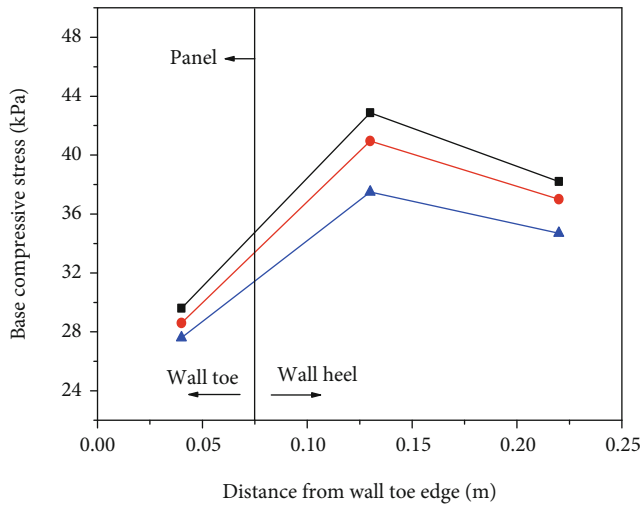
For example, as the conclusion mentioned previously, the replacement thickness of lightweight foamed concrete has great effects on the stress and deformation characteristics of retaining wall, which illustrates that choosing the suitable replacement thickness of lightweight foamed concrete as backfill is the key in the actual engineering. The suitable replacement thickness of lightweight foamed concrete layer behind the wall can be determined by the fitting equation in Table 6. According to the earth pressure theory of retaining wall, the smaller the earth pressure value is, the better the stability of retaining wall is. Therefore, combined with the fitting equation (No. 5) in Table 6, taking the size of the resultant earth pressure of the retaining wall as the control standard, when the replacement thickness of the lightweight foamed concrete in the model test is 0.346 m, the size of the resultant earth pressure of the retaining wall is the smallest. Then, through the scale ratio of 25:1 (actual size: model size), it can be calculated that the suitable replacement thickness of lightweight foamed concrete behind the buttressed earth-retaining wall in the supporting project is about 8.7 m.

3.2. Results of the Multiple-Factor Orthogonal Test. Through the analysis of the above single-factor test results, the lateral earth pressure distribution and deformation characteristics of the buttressed earth-retaining wall backfilled with lightweight foamed concrete under single factor are obtained. In order to further study the comprehensive influence of multiple factors on the stress and deformation characteristics of this retaining wall, taking the earth pressure on the inside of vertical wall as an example, the primary and secondary relations of three factors' influence extent on the forces and deformation of the retaining wall backfilled with lightweight foamed concrete are analyzed by using range analysis method.

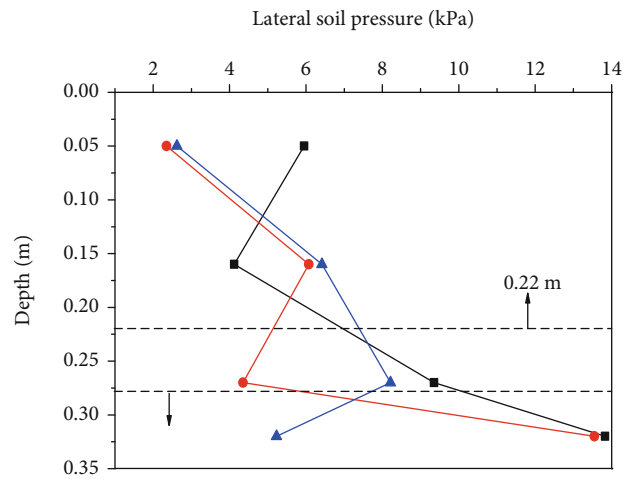
The range of each factor is calculated by Equation (1):

$$R = \max \{K_{ij}\} - \min \{K_{ij}\}. \quad (1)$$

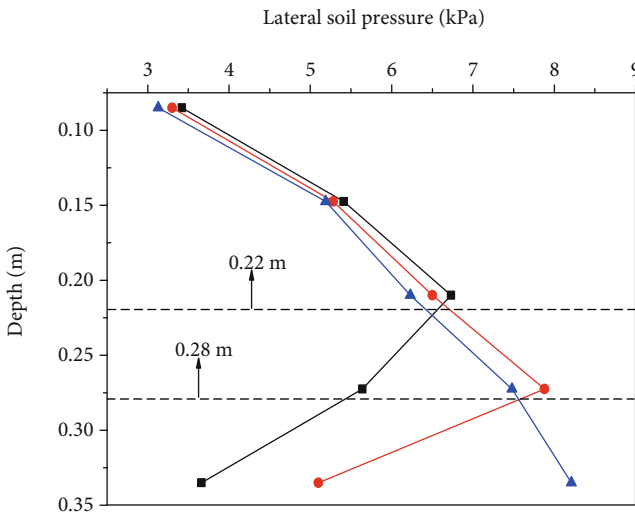
According to multiple-factor orthogonal test scheme in Table 2, the corresponding resultant earth pressure and the points of resultant force of retaining wall were calculated



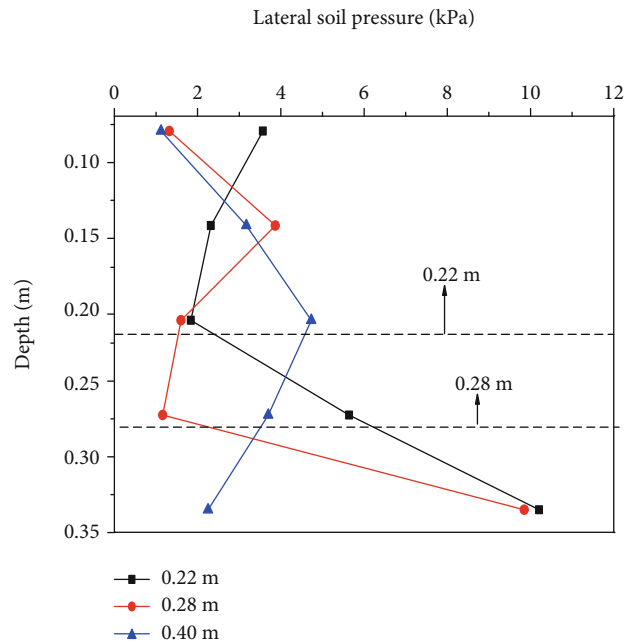
(a) Earth pressure distribution at the bottom plate



(b) Earth pressure distribution on the inside of vertical wall



(c) Earth pressure distribution on the soil facing surface of the buttress



(d) Earth pressure distribution on sidewall of the buttress

FIGURE 12: Earth pressure distributions of retaining wall under different replacement thicknesses of lightweight foamed concrete.

by the model tests, and the range analysis method was used to analyze the test results under multiple factors (as shown in Tables 7 and 8).

As can be seen from Tables 7 and 8, the resultant earth pressure and the point of resultant force would change when the level of any influencing factor changes, and the degree of change varies significantly with different influencing factors. In addition, three influencing factors, including overload, density of lightweight foamed concrete, and replacement thickness of lightweight foamed concrete, maintain a mutually independent and mutually restrictive relationship in the process of affecting the stress and deformation characteristics of retaining wall backfilled with lightweight foamed concrete.

According to the results in Table 7, the sequence of three factors' range for resultant earth pressure of the retaining wall is as follows: $R_1 = 1.071566666 > R_3 = 0.478883333 > R_2 = 0.2799$. In other words, it can be concluded that the primary and secondary relation of three factors' influence extent on the mechanical characteristics of the retaining wall filled with lightweight foamed concrete is as follows: overload > density of lightweight foamed concrete > replacement thickness of lightweight foamed concrete.

On the other hand, it can be seen from the results in Table 8 that the sequence of three factors' range for point of resultant force is as follows: $R_3 = 0.04031722 > R_2 = 0.022143565 > R_1 = 0.018589099$. Therefore, the primary and secondary relation of three factors' influence

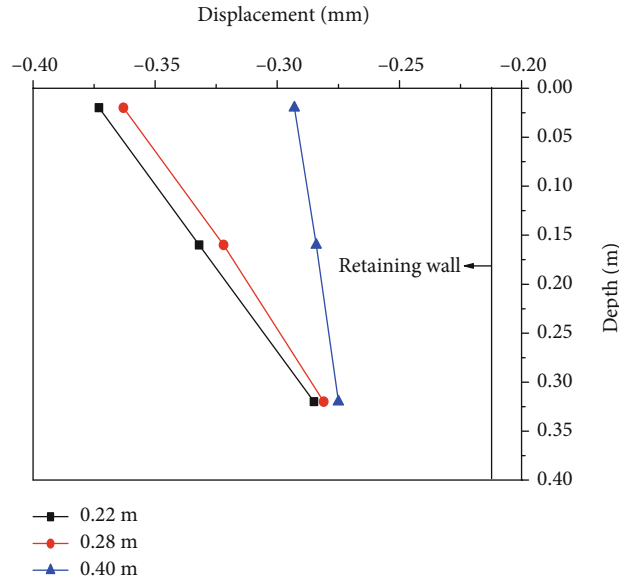


FIGURE 13: Displacement changes of retaining wall under different replacement thicknesses of lightweight foamed concrete.

TABLE 6: Regression equations with different factors.

Number	Dependent variable	Independent variable	Fixed parameter	Regression equation
1	y_1	x_1	$x_2 = 700, x_3 = 0.28$	$y_1 = 0.00507x_1^2 - 0.59728x_1 + 19.38062$
2	y_2			$y_2 = 0.0059x_1^2 - 0.034x_1 + 0.2361$
3	y_1	x_2	$x_1 = 14, x_3 = 0.28$	$y_1 = 0.00074x_2 + 1.37618$
4	y_2			$y_2 = -0.0005x_2^2 + 0.002x_2 + 0.1924$
5	y_1	x_3	$x_1 = 14, x_2 = 700$	$y_1 = 35.33565x_3^2 - 24.43032x_3 + 5.89528$
6	y_2			$y_2 = 0.0147x_3^2 - 0.0549x_3 + 0.1706$

TABLE 7: Results of resultant earth pressure by multiple-factor orthogonal tests.

Test number	Overload (MPa)	Density of lightweight foamed concrete (kg/m ³)	Replacement thickness of lightweight foamed concrete (m)	Resultant earth pressure (kPa)
2-1	14	600	0.22	2.23085
2-2	14	700	0.28	1.8886
2-3	14	800	0.40	1.8707
2-4	16	600	0.28	2.574295
2-5	16	700	0.40	2.31385
2-6	16	800	0.22	2.84595
2-7	18	600	0.40	2.59685
2-8	18	700	0.22	3.14125
2-9	18	800	0.28	3.46675
η_{j1}	1.996716667	2.467331667	2.73935	—
η_{j2}	2.578031667	2.4479	2.643215	—
η_{j3}	3.068283333	2.7278	2.260466667	—
R_j	1.071566666	0.2799	0.478883333	—

TABLE 8: Results of the point of resultant force by multiple-factor orthogonal tests.

Test number	Overload (MPa)	Density of lightweight foamed concrete (kg/m ³)	Replacement thickness of lightweight foamed concrete (m)	Point of resultant force (m)
2-1	14	600	0.22	0.130380918
2-2	14	700	0.28	0.193842579
2-3	14	800	0.40	0.141944335
2-4	16	600	0.28	0.191728314
2-5	16	700	0.40	0.141691374
2-6	16	800	0.22	0.13069862
2-7	18	600	0.40	0.144787266
2-8	18	700	0.22	0.134576483
2-9	18	800	0.28	0.131036786
α_{j1}	0.155389277	0.155632166	0.13188534	—
α_{j2}	0.154706103	0.156703479	0.17220256	—
α_{j3}	0.136800178	0.134559914	0.142807658	—
R_j	0.018589099	0.022143565	0.04031722	—

extent on the point of resultant force of the retaining wall filled with lightweight foamed concrete is as follows: replacement thickness of lightweight foamed concrete > density of lightweight foamed concrete > overload.

4. Conclusion

In this paper, a scale experimental model in which the backfill behind the buttressed earth-retaining wall is filled with lightweight foamed concrete is established to study its force and deformation characteristics under different factors. Based on the experimental results and numerical calculation study of this investigation, the following findings can be drawn:

- (i) The size and distribution characteristics of earth pressure vary with the different positions of the retaining wall backfilled with lightweight foamed concrete under different factors
- (ii) There are similarities and differences in the mechanical characteristics of the buttressed earth-retaining wall backfilled with lightweight foamed concrete under different influence factors by model tests: both of two factors (overload and density of lightweight foamed concrete) can only change the size of earth pressure of this retaining wall and cannot change its distribution laws; but both the size and the distribution form of earth pressure of this retaining wall have changed under the influence of different replacement thicknesses of lightweight foamed concrete
- (iii) There are good linear relationships between the displacement of the retaining wall filled with lightweight foamed concrete and each factor: the horizontal displacement of the retaining wall increases with the increase of overload or the density of the lightweight foamed concrete, while it decreases with the increase of the replacement thickness of lightweight foamed concrete
- (iv) Through regression analysis, the regression equations of the resultant earth pressure and the point of resultant force of this retaining wall under each single factor are obtained, which determined that the suitable replacement thickness of lightweight foamed concrete behind the buttressed earth-retaining wall in the supporting project is about 8.7 m
- (v) Through the range analysis method, it is concluded that the primary-secondary relation of three factors' influence extent on the resultant earth pressure of the retaining wall backfilled with lightweight foamed concrete is as follows: overload > density of lightweight foamed concrete > replacement thickness of lightweight foamed concrete, while the primary-secondary relation of three factors' influence extent on the point of resultant force of this retaining wall is as follows: replacement thickness

of lightweight foamed concrete > density of lightweight foamed concrete > overload

Abbreviations

- i : Orthogonal test level
 j : Number of orthogonal test factors
 K_{ij} : Sum of factor j test results at level i
 x_1 : Overload
 x_2 : Density of lightweight foamed concrete
 x_3 : Replacement thickness of lightweight foamed concrete
 y_1 : Resultant earth pressure
 y_2 : Point of resultant force
 η_{jk} : Average value of final resultant earth pressure when the index of the column j is at the level k ($k = 1, 2, 3$)
 R_j : Range of the index of the column j , defined as $R_j = \max \{\eta_{jk}\} - \min \{\eta_{jk}\}$, ($k = 1, 2, 3$)
 α_{jk} : Average value of final point of resultant force when the index of the column j is at the level k ($k = 1, 2, 3$)
 R_j : Range of the index of the column j , defined as $R_j = \max \{\alpha_{jk}\} - \min \{\alpha_{jk}\}$, ($k = 1, 2, 3$).

Data Availability

The data used to support the findings of this study are available from the corresponding author upon request.

Conflicts of Interest

The authors declare that there are no conflicts of interest regarding the publication of this paper.

Acknowledgments

This paper gets its funding from project (2016YFC0802203 and 2017YFC0805300) supported by National Key R&D Program of China.

References

- [1] R. Belakroum, A. Gherfi, M. Kadja et al., "Design and properties of a new sustainable construction material based on date palm fibers and lime," *Construction and Building Materials*, vol. 184, pp. 330–343, 2018.
- [2] Y.-l. Huang and A. Zhou, "Study on mechanical properties of PET fiber-reinforced coal gangue fine aggregate concrete," *Geofluids*, vol. 2021, Article ID 6627447, 13 pages, 2021.
- [3] M. Yang, Z. He, X. Chen, M. Li, and Z. Peng, "Comparative study on the macroscopic and microscopic properties of UHPC mixed with limestone powder and slag powder," *Geofluids*, vol. 2021, Article ID 5510490, 11 pages, 2021.
- [4] M. Kozłowski and M. Kadela, "Mechanical characterization of lightweight foamed concrete," *Advances in Materials Science and Engineering*, vol. 2018, Article ID 6801258, 8 pages, 2018.
- [5] M. R. Jones and A. McCarthy, "Preliminary views on the potential of foamed concrete as a structural material," *Magazine of Concrete Research*, vol. 57, no. 1, pp. 21–31, 2005.
- [6] D. Falliano, L. Restuccia, G. A. Ferro, and E. Gugliandolo, "Strategies to increase the compressive strength of ultra-

- lightweight foamed concrete,” *Procedia Structural Integrity*, vol. 28, pp. 1673–1678, 2020.
- [7] S. Feng, Y. Zhou, Y. Wang, and M.-d. Lei, “Experimental research on the dynamic mechanical properties and damage characteristics of lightweight foamed concrete under impact loading,” *International Journal of Impact Engineering*, vol. 140, p. 103558, 2020.
- [8] R. J. Sldozian, A. G. Tkachev, I. V. Burakova, and Z. A. Mikhaileva, “Improve the mechanical properties of lightweight foamed concrete by using nanomodified sand,” *Journal of Building Engineering*, vol. 34, p. 101923, 2021.
- [9] Z.-m. Huang, T.-s. Zhang, and Z.-y. Wen, “Proportioning and characterization of Portland cement-based ultra-lightweight foam concretes,” *Construction and Building Materials*, vol. 79, pp. 390–396, 2015.
- [10] J.-j. Huang, Q. Su, W.-h. Zhao, T. Li, and X.-x. Zhang, “Experimental study on use of lightweight foam concrete as subgrade bed filler of ballastless track,” *Construction and Building Materials*, vol. 149, pp. 911–920, 2017.
- [11] S. N. Shah, K. H. Mo, S. P. Yap, J. Yang, and T.-c. Ling, “Lightweight foamed concrete as a promising avenue for incorporating waste materials: a review,” *Resources, Conservation and Recycling*, vol. 164, p. 105103, 2021.
- [12] X.-n. Shi, J.-j. Huang, and Q. Su, “Experimental and numerical analyses of lightweight foamed concrete as filler for widening embankment,” *Construction and Building Materials*, vol. 250, p. 118897, 2020.
- [13] S. K. Lim, C. S. Tan, T.-c. Ling, M. U. Hossain, and C. S. Poon, “Utilizing high volumes quarry wastes in the production of lightweight foamed concrete,” *Construction and Building Materials*, vol. 151, pp. 441–448, 2017.
- [14] W. She, Y. Du, G.-t. Zhao, P. Feng, Y.-s. Zhang, and X.-Y. Cai, “Influence of coarse fly ash on the performance of foam concrete and its application in high-speed railway roadbeds,” *Construction and Building Materials*, vol. 170, pp. 153–166, 2018.
- [15] R. C. Valore, “Cellular concrete part 1 composition and methods of production,” *ACI Journal Proceedings*, vol. 50, no. 5, pp. 773–796, 1954.
- [16] R. C. Valore, “Cellular concrete part 2 physical properties,” *ACI Journal Proceedings*, vol. 50, no. 6, pp. 817–836, 1954.
- [17] G. Rudnai, *Lightweight Concretes*, Akademiado, Budapest, Hungary, 1963.
- [18] W. H. Taylor, *Concrete Technology and Practice*, Angus and Robertson, London, Britain, 1969.
- [19] A. Short and W. Kinniburgh, *Lightweight Concretes*, Applied Sciences Publishers, London, Britain, 1978.
- [20] M. R. Jones and A. McCarthy, “Utilising unprocessed low-lime coal fly ash in foamed concrete,” *Fuel*, vol. 84, no. 11, pp. 1398–1409, 2005.
- [21] E. P. Kearsley and P. J. Wainwright, “The effect of high fly ash content on the compressive strength of foam concrete,” *Cement and Concrete Research*, vol. 31, no. 1, pp. 106–112, 2001.
- [22] T. J. Chandni and K. B. Anand, “Utilization of recycled waste as filler in foam concrete,” *Journal of Building Engineering*, vol. 19, pp. 154–160, 2018.
- [23] R. Wang, P.-w. Gao, M.-h. Tian, and Y.-c. Dai, “Experimental study on mechanical and waterproof performance of lightweight foamed concrete mixed with crumb rubber,” *Construction and Building Materials*, vol. 209, pp. 655–664, 2019.
- [24] S. Y. Chung, M. A. Elrahman, J. S. Kim, T. S. Han, D. Stephan, and P. Sikora, “Comparison of lightweight aggregate and foamed concrete with the same density level using image-based characterizations,” *Construction and Building Materials*, vol. 211, pp. 988–999, 2019.
- [25] A. Kashani, T. D. Ngo, and A. Hajimohammadi, “Effect of recycled glass fines on mechanical and durability properties of concrete foam in comparison with traditional cementitious fines,” *Cement and Concrete Composites*, vol. 99, pp. 120–129, 2019.
- [26] B.-y. Su, Z.-w. Zhou, Z.-q. Li, Z.-h. Wang, and X.-f. Shu, “Experimental investigation on the mechanical behavior of foamed concrete under uniaxial and triaxial loading,” *Construction and Building Materials*, vol. 209, pp. 41–51, 2019.
- [27] O. L. Ertugrul and A. C. Trandafir, “Lateral earth pressures on flexible cantilever retaining walls with deformable geofoam inclusions,” *Engineering Geology*, vol. 158, pp. 23–33, 2013.
- [28] F. Molina-Moreno, T. García-Segura, J. V. Martí, and V. Yepes, “Optimization of buttressed earth-retaining walls using hybrid harmony search algorithms,” *Engineering Structures*, vol. 134, pp. 205–216, 2017.
- [29] Y.-l. Liu and S. K. Vanapalli, “Prediction of lateral swelling pressure behind retaining structure with expansive soil as backfill,” *Soils and Foundations*, vol. 59, no. 1, pp. 176–195, 2019.
- [30] TJG F10 01-2011, *Technical Specification for Design and Construction of Cast-In-Situ Lightweight Foamed Concrete Subgrade (in Chinese)*, Tianjin Municipal Road Administration, Tianjin, China, 2011.
- [31] Z.-p. Chen, *The New Technology of Bubble Mixed Light Soil about Filling (in Chinese)*, China Communications Press, Beijing, China, 2004.
- [32] Y.-q. Qiu, *Study on Engineering Properties of Lightweight Foamed Concrete Subgrade in the Soft Soil Foundation (in Chinese)*, Master Thesis of Chang’an University, 2018.
- [33] JTG E40-2020, *Test Methods of Soils for Highway Engineering (in Chinese)*, Ministry of Transport of the People’s Republic of China, Beijing, China, 2020.

Research Article

Experimental Study of a New Concrete Admixture and Its Function in Filling and Reinforcing Granite Fissures

Songnan Ru,¹ Zuozhou Li,² Handong Liu,³ Huaichang Yu ,³ Chunlei Wei,¹ Guangzhu Hu,² Fangfang Xue,² Congxian Wang,¹ and Jialiang Wang ³

¹State Grid Xin Yuan Company Limited, Beijing 100761, China

²Shaanxi Zhenan Pumped Storage Company Limited, Xi'an 710061, China

³North China University of Water Resources and Electric Power, Zhengzhou 450011, China

Correspondence should be addressed to Huaichang Yu; yuhuaichanghb@126.com

Received 17 June 2021; Accepted 21 August 2021; Published 6 September 2021

Academic Editor: Yu Wang

Copyright © 2021 Songnan Ru et al. This is an open access article distributed under the Creative Commons Attribution License, which permits unrestricted use, distribution, and reproduction in any medium, provided the original work is properly cited.

A concrete admixture with water retention and superhydrophobic properties was developed according to the high tensile strength, fissure resistance, and antiseepage requirements of concrete linings. Capillary water absorption, early-age anticracking, cube compressive strength, and splitting tensile tests were employed to study the effects of the new concrete admixture on the basic performance of concrete. On this basis, a triaxial compression test was conducted on granite fissures filled with concrete containing the admixture; the stress-strain and failure characteristics under different admixture dosages, confining pressures, and fracture widths were analyzed, and the reinforcement effect of the concrete with the admixture on the fractured rock mass was studied. The results show that the admixture can effectively improve the ability of concrete to resist water and fissures, and the concrete with the admixture significantly reinforced the fractured rock mass. Therefore, it can be widely applied in filling and reinforcing fractured rock masses.

1. Introduction

With the increase in the scale and complexity of underground engineering, the performance requirements of concrete lining structures for underground tunnels and caverns are increasingly stringent. Modern tunnel theory focuses on the mechanical evolution of surrounding rock-lining systems [1, 2], and many scholars have studied the mechanical properties of concrete linings. Ding et al. [3] studied the influence of lining deterioration on the seismic vulnerability of tunnels through model tests and pointed out that the impact produced by lining deterioration increased over time. Considering the time and spatial effects of sprayed concrete, Xu et al. [4] studied the stress characteristics of shotcrete layers with different rock mass qualities and the response of the surrounding rock and proposed an applicable evaluation method for concrete shotcrete layers. Oreste [5] studied the mechanical properties of sprayed concrete linings and provided a method for calculating the lin-

ing safety factor. Gschwandtner and Galler [6] studied the application of the convergence confinement method in concrete linings, considering the time effect. Lu et al. [7] studied the performance of cement grouting in filling rocks. However, damage and failure of concrete linings in engineering projects are still common. For example, the Shiziya Tunnel, which was completed and began use in 2003, experienced a serious collapse of its lining supports and water leakage in 2004 [8]. The lining structures of the Sanchaling Tunnel [9], the Jinjiguan Tunnel [10], and the Liupanshan Tunnel [11] were damaged to varying degrees after these tunnels entered operation, which has had a substantial impact on both engineering safety and social and economic development.

Lining cracking is a common issue for underground caverns. Upon investigation of the tunnels in the Wenchuan earthquake area, Ji et al. [12] found that most of the earthquake damage to the surrounding rock caverns was caused by lining fissures. Many factors are likely to cause lining

fissures in the surrounding rocks of engineering projects, including improper surveys and designs and unsatisfactory construction and maintenance. In particular, the use of unqualified lining materials is a major factor that causes lining fissures. Therefore, the application of new high-performance materials to solve the problem of lining cracking is worthy of further study. High-performance concrete materials have been studied, but there are still a limited number of studies on the use of these materials in the lining supports of the surrounding rocks in underground engineering projects. Through laboratory model tests, Cui et al. [13] found that after becoming deformed, the initial support of steel-fiber concrete may intersect with the characteristic curve of the surrounding rock, thereby enabling the surrounding rock structure to remain stable. Guo [14] studied the concrete used for grouting reinforcement, compared the setting times of phosphoric acid-water glass and cement-water glass with different mix ratios, and proposed relevant design parameters. Li et al. [15] studied the influences of the concrete grain size and nanosilica content on the grouting reinforcement effect in rock fissures. Cui [16] studied the possibility of using geopolymers, which are a type of cementitious material, to treat fissures in tunnel linings. It is generally believed that the addition of fly ash can significantly improve the impermeability of concrete. Naik et al. [17] conducted experiments to study the influence of a large amount of fly ash on the impermeability of concrete. Their results show that as long as the amount of fly ash being substituted for cement does not exceed 50%, the addition of fly ash will reduce the chloride ion permeability of concrete. Yu and Wang [18] developed a concrete admixture that successfully promotes the hydration degree of cement to significantly improve the crack resistance and tensile properties of concrete.

A limited number of high-performance materials have been developed for use in surrounding rock-lining supports in underground engineering projects, so the research and development of new concrete materials with superior anti-seepage, fissure resistance, and tensile resistance properties are important for the stabilization of the surrounding rocks in underground engineering projects. In this study, a new concrete admixture for use in the linings of surrounding rocks was developed. Through capillary water absorption, early-age anticracking, cube compressive strength, and splitting tensile tests, the performance of the admixture when added to concrete was investigated in this study. In addition, triaxial compression tests were conducted after filling granite fissures with concrete containing the admixture, and the working performance of this amended concrete in the linings of surrounding rocks was analyzed to determine the reinforcement effect that the concrete with the admixture had on fractured rock masses.

2. Materials and Methods

2.1. Materials. The high-strength (HS) admixture, which has a particle size of $100\ \mu\text{m}$, is a superhydrophobic powder containing both inorganic and organic materials. It has a floor structure, a flat structure, a spherical structure, and a smooth

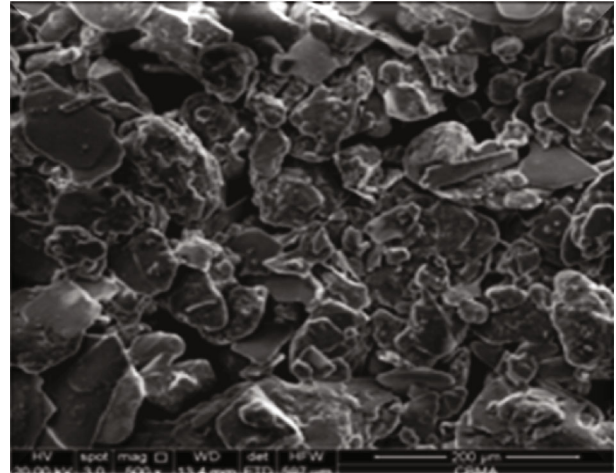


FIGURE 1: Microstructure of the HS admixture.

sphere structure (see Figure 1). The thin sheet inorganic substrate has the properties of heat resistance, corrosion resistance, and high strength. The sheet structure, which has a high diameter to thickness ratio, can hinder the penetration of water and other corrosive substances in concrete linings. The chemical bonding between the surfaces of organic compounds and inorganic powders under alkaline conditions gives concrete materials hydrophobic properties.

Adding the HS admixture to concrete materials can improve the separation and seepage of the concrete mixture, strengthen the connection between concrete aggregates, and promote a sufficient reaction between cementitious grouting materials and hydration products to generate a high-strength and highly stable gel, with the HS admixture as the crystal nucleus. Then, many hydrophobic membranes are generated in the capillary channels, and bubbles and thin films with thicknesses of approximately 20 nanometers are introduced to form an impermeable “isolation zone” for permeable materials, which improves the waterproof performance of concrete linings.

To verify its performance, the HS admixture was added to concrete, and capillary water absorption, early-age anticracking, cube compressive strength, splitting tensile, and triaxial compression tests were performed. The materials used in the sample concrete mixtures are as follows: tested Portland cement with a grade of 42.5, in compliance with Chinese national standard GB175-2007 (equivalent to Eurocode CEM I 42.5, ENV197-1: 2000); natural river sand with a fineness of 2.8 as fine aggregate; limestone with a diameter of 5-20 mm as coarse aggregate; water reducing agent; and the HS admixture. Table 1 shows the mix ratio of the concrete used in each test.

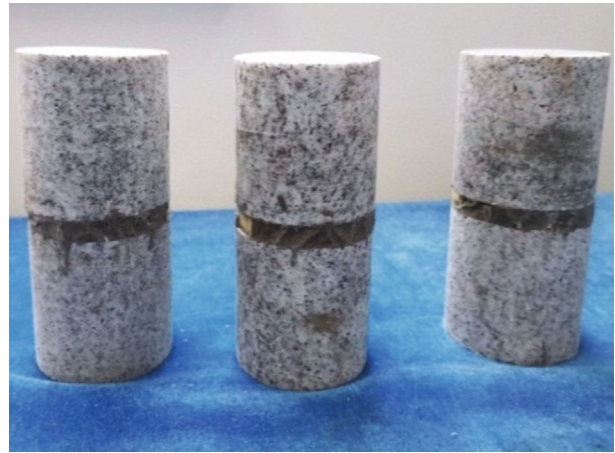
2.2. Capillary Water Absorption Test. Cylindrical specimens with diameters of 150 mm each and heights of 300 mm each were prepared, and the HS admixture was added at proportions of 0% and 3%. After 28 days of maintenance, epoxy resin was applied to the top and sides, and then, the bottom of the specimen was placed in a water absorption device with

TABLE 1: Mix ratios of concrete with different HS admixture dosages.

HS admixture dosage	Quantity of materials used in each cube of concrete (kg/m ³)					
	Water	Cement	Fine aggregate	Coarse aggregate	Water reducer	HS admixture
0%	160	320	747	1169	4.16	0.00
1%	160	320	746	1167	4.16	3.20
3%	160	320	743	1163	4.16	9.60
5%	160	320	741	1159	4.16	16.00



(a) Vertical fissures



(b) Horizontal fissures

FIGURE 2: Specimens with filled fissures.

a water depth of 3-5 mm to measure the water absorption height at different time points. Three tests were conducted for each specimen.

2.3. *Early-Age Anticracking Ability.* Under a temperature of 21° and a relative humidity of 60%, an early-age anticracking test [19] was conducted for concrete mixtures with 0% and 3% HS admixture. The size of the testing device was 800 mm × 600 mm × 100 mm, and the central wind speed was no less than 5 m/s. Two tests were conducted for each specimen.

2.4. *Cube Compressive Strength Test.* Cubic specimens 100 mm × 100 mm × 100 mm in size and containing 0%, 1%, 3%, and 5% of the HS admixture were prepared. After 28 days of maintenance, two cube compressive strength tests [19] were conducted for each specimen.

2.5. *Splitting Tensile Test.* Cubic specimens 100 mm × 100 mm × 100 mm in size and containing 0%, 1%, 3%, and 5% of the HS admixture were prepared. After 28 days of maintenance, two splitting tensile tests [19] were conducted for each specimen.

2.6. *Triaxial Compression Test by Filling Granite Fissures.* The tested granite came from Lanzhou, Gansu, China. Cylindrical granite specimens 50 mm in diameter and 100 mm in height were prepared. To simulate the surrounding rocks, specimens containing vertical and horizontal fissures were prepared by cutting, and then, the fissures were

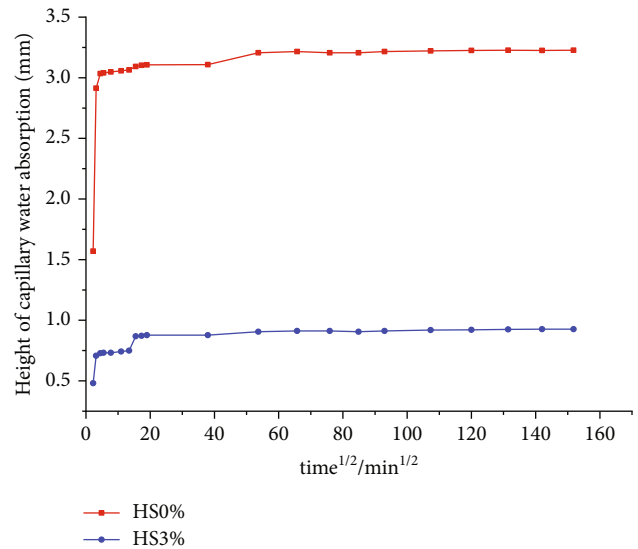


FIGURE 3: Results of the capillary water absorption test.

filled with concrete containing the HS admixture. The specimens are shown in Figure 2.

3. Performance of HS Admixture and Test Results

3.1. *Results of the Capillary Water Absorption Test.* The results of the capillary water absorption test are shown in

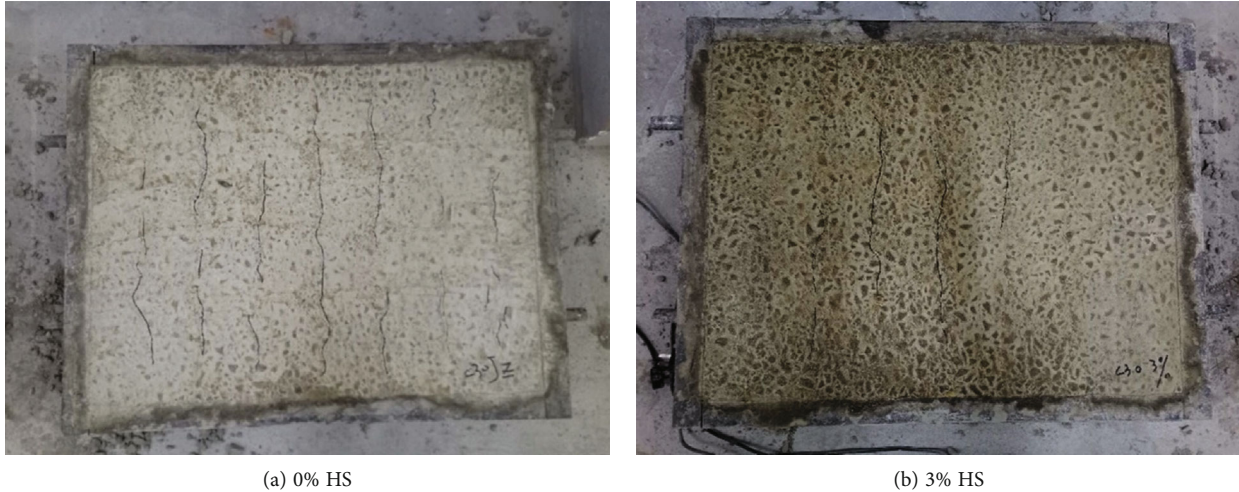


FIGURE 4: Distribution of fissures after 24 h.

TABLE 2: Results of the early-age anticracking test.

HS admixture dosage	Number of fissures per unit area	Cracking area per unit area ($1 \text{ mm}^2/\text{m}^2$)
0%	12.5	1388
3%	8.3	813

Figure 3. The benchmark specimen (0%) had a high capillary water absorption rate, and the capillary water absorption rate of the concrete with a 3% HS admixture was much less than that of the benchmark specimen for the entire process. The benchmark specimen (0%) absorbed water quickly in the first 1,440 min, then the absorption rate slowed, and finally, the water reached a height of approximately 3.21 mm after the adsorption rate stabilized. For the specimen with a 3% HS admixture, the capillary water absorption height was only 0.88 mm at 1,440 min, and it finally stabilized at a height of approximately 0.92 mm. The analysis showed that adding the HS admixture effectively improved the water absorption resistance of the concrete.

3.2. Results of the Early-Age Anticracking Test. The surface conditions of the specimens after the early-age anticracking test are shown in Figure 4. Table 2 shows the number of fissures and the cracking area on the surface of the specimens with the two admixture dosages. As shown in Figure 4, the benchmark specimen (0%) had a much greater number of fissures than the concrete with a 3% HS admixture. Table 2 shows that the concrete with 3% admixture had a significantly lower number of fissures per unit area and a significantly smaller cracking area compared to the benchmark specimen (0%). Therefore, the HS admixture effectively improved the early-age anticracking ability of the concrete. At the same time, the concrete with the 3% HS admixture performed better in terms of the water retention, while that without the HS admixture lost more water.

The HS admixture improved the early-age anticracking ability of the concrete because it contains a substantial

amount of active SiO_2 , Al_2O_3 , and CaO . These components can react with the substances generated by cement hydration and thereby improve the composition of hydrated cement and reduce both the internal and external migrations of water. Hydrated calcium silicate $\text{Ca}_5\text{Si}_6\text{O}_{16}(\text{OH})\cdot 4\text{H}_2\text{O}$ with a low alkalinity, a high strength, and good stability is generated in this process, which improves the composition of hydrated gelatinous substances. In the early stage of concrete molding, adding the HS admixture can restrict contraction and prevent the loss of water from the concrete, which can reduce the amount of desiccation fissures and thereby decrease the cracking area and the number of fissures in the amended concrete.

3.3. Results of the Cube Compressive Strength Test. The results of the cube compressive strength test are shown in Figure 5, which shows that the cube compressive strength of the specimens declined as the HS admixture dosage increased. The benchmark specimen (0%) had a compressive strength of 48.4 MPa. The cube compressive strength values for the specimens with 1% and 3% HS admixture were 48.0 and 43.5 MPa, respectively, which are 0.8% and 10.1% less than the values of the benchmark specimen; for the specimens with 5% HS admixture, the cube compressive strength was 39.5 MPa, which represents a decrease of 18.4% compared to the benchmark specimen.

In this test, the HS admixture lessened the damage to the concrete specimens. The benchmark (0%) specimen showed vertical fissures and a high degree of crushing. The specimen with 1% HS admixture showed a similar failure mode to the benchmark specimen; however, the occlusions between the fragments were more compact, and the degree of crushing was reduced. The specimens with 3% and 5% HS admixture were more intact, with a further decrease in the amount of crushing.

3.4. Results of the Splitting Tensile Test. The results of the splitting tensile test are shown in Figure 6, which shows that the splitting tensile strength first increased and then

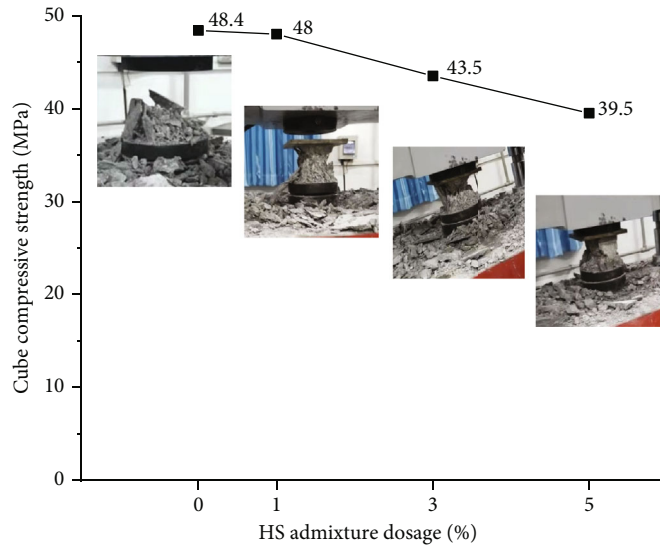


FIGURE 5: Results of the cube compressive strength test.

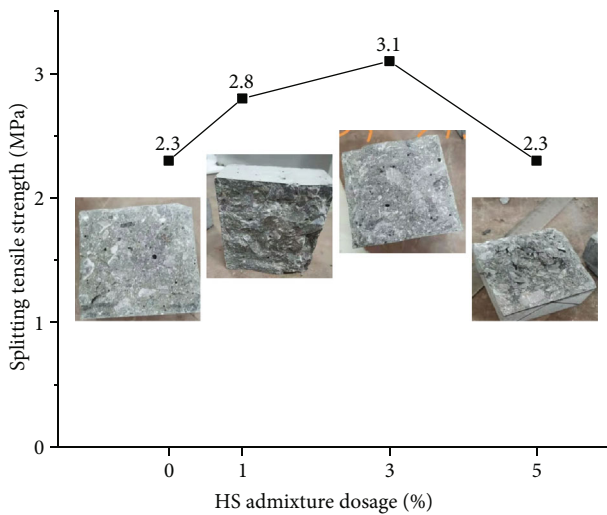


FIGURE 6: Results of the splitting tensile test.

decreased as the HS admixture amount was increased. The splitting tensile strength of the benchmark specimen (0%) was 2.3 MPa; for the specimen with a 1% HS admixture, the splitting tensile strength was 2.8 MPa, which represents an increase of 21.7% compared to the benchmark specimen; for the specimen with 3% HS admixture, the splitting tensile strength reached a peak of 3.1 MPa, which is 34.8% higher than the value for the benchmark specimen; for the specimen with 5% HS admixture, the splitting tensile strength decreased to 2.3 MPa.

The HS admixture dosage also affected the splitting tensile failure mode of the specimens. The fissure surface of the benchmark specimen (0%) was neat, interface fissures were formed, and the specimen had no crush marks. The specimen with 1% admixture cracked locally, and the cracking surface was more rugged than that of the benchmark speci-

men. The specimens with 3% and 5% admixture showed uneven fissures.

4. Triaxial Compression Test of Granite Fissures Filled with Concrete Containing the HS Admixture

4.1. *HS Admixture Dosage.* To study the reinforcement effect of the HS admixture dosage on the rock mass, rock specimens with 4 mm wide vertical fissures were prepared and filled with concrete containing 0%, 1%, 3%, and 5% of the HS admixture. Then, triaxial compression tests were conducted on a TAW-2000 triaxial tester with a confining pressure of 2 MPa. The stress-strain curve and failure mode are shown in Figure 7.

As shown in Figure 7, the damaged benchmark specimen (0%) had one fissure from top to bottom, with a width of 0-2 mm, which was serrated along the depth direction. The entire specimen cracked and peeled off, and the filled layer became fragmented.

The damaged specimen with 1% HS admixture had two fissures from top to bottom on both sides of the filled layer, with depths of 1-2 mm. The specimen cracked and peeled off between the two fissures that were serrated along the depth direction. The surface rock peeled off from the specimen, and the failure surface was characterized by steps.

The specimen with 3% HS admixture had two clear fissures from top to bottom on both sides of the filled layer. The rock and filled layer within these two fissures cracked and peeled off. One serrated fissure was oriented from top to bottom, with a width of 1-1.5 mm, and had pinnate fissures on both sides. The other fissure in the middle was short and oblique, and the entire peeling surface was uneven and had a steep dip angle, with a 2 mm wide crack, which extended upward from the lower part of the specimen through the middle part of the specimen and then gradually

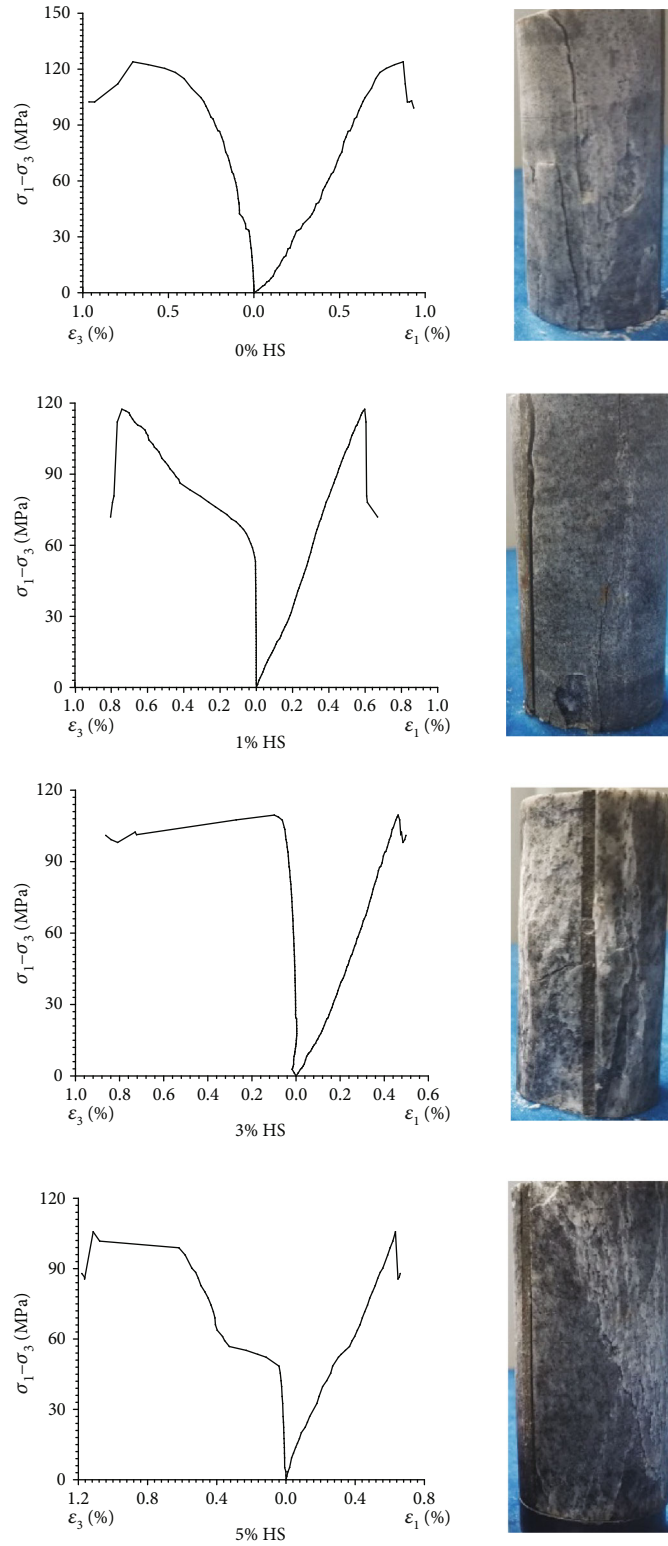


FIGURE 7: Stress-strain curve and typical failure mode of specimens with different HS admixture dosages.

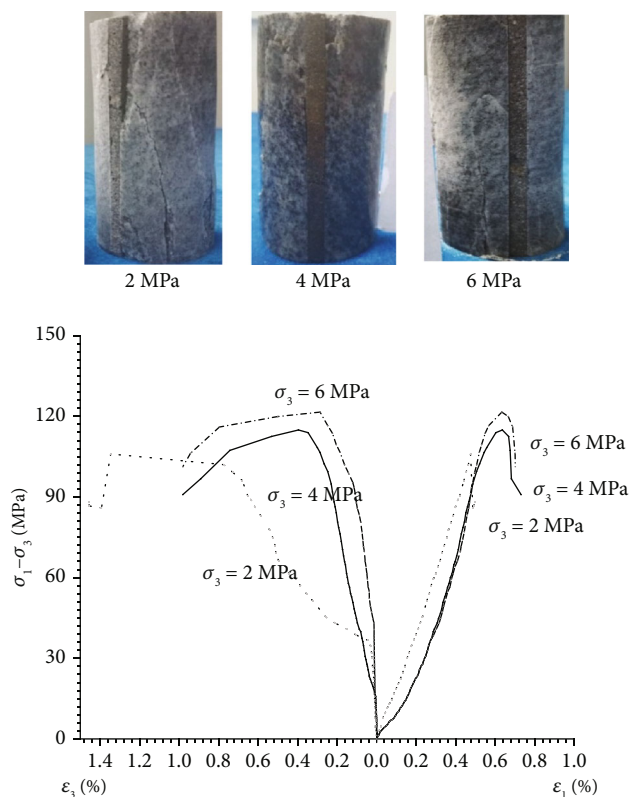


FIGURE 8: Stress-strain curve and typical failure mode under different confining pressures.

ended. In addition, there were longitudinal and transverse cracks and step-like damage in the filled layer.

The damaged specimen with 5% HS admixture had four fissures on the back of the filled layer. In particular, one fissure was a short vertical fissure, two fissures developed obliquely and intersected with the main fissure, and the remaining main fissure was serrated and crescent-shaped on the side face, with a depth of 0.5-2 mm. The rocks between the main fissure and the filled layer cracked and peeled off, and the damaged surface had two steps. The hoop strain at the stress-strain curve was greater than the axial strain.

With the increase in the HS admixture dosage, the overall peak strain decreased, which indicates that adding the HS admixture improved the axial and radial stiffnesses of the specimen with fissures. The specimen with 5% HS admixture showed an evident decrease in the peak strength, while the other specimens had similar peak strength values, which is consistent with the results of the splitting tensile test. Therefore, the concrete containing 3% HS admixture was recommended for filling fissures.

4.2. Confining Pressure. To study how the confining pressure affects the mechanical properties of rocks filled with concrete containing the HS admixture, rock specimens with 6 mm wide vertical fissures were prepared. Samples containing 3% HS admixture were tested under confining pressures of 2, 4, and 6 MPa. The stress-strain curve and failure mode are shown in Figure 8.

Figure 8 shows that under a confining pressure of 2 MPa, the damaged specimen had two inverted Y-shaped fissures and two oblique fissures. One inverted Y-shaped fissure was seriously damaged, and the rocks between this fissure and the filled layer were completely crushed. The rocks between a short oblique fissure in the lower part and the filled layer also peeled off, and the rocks in the upper part of the specimen collapsed. Under a confining pressure of 4 MPa, two small transverse fissures and two small oblique fissures appeared and converged at the filled layer, and the rocks at the upper part were broken. Under a confining pressure of 6 MPa, there was one oblique fissure with a high dip angle on the side of the filled layer, which ran from top to bottom and clearly cracked at the bottom. In addition to the fissure, unclear small closed pinnate fissures appeared.

In conclusion, under different confining pressures, the stress-strain values of the specimens with filled fissures were similar to those of the specimens without fissures. When a specimen was damaged, the filled layer was closely connected to the rock without evident sliding. The broken surface, which ran from top to bottom, appeared on the rock rather than on the filled layer itself, which indicates that concrete containing the HS admixture can effectively fill rock fissures.

4.3. Fissure Width. To study how the concrete containing the HS admixture reinforced rock masses with different fissure widths, rock specimens with vertical fissures of 4 mm and 6 mm were prepared. The HS admixture dosage was 3%, and the confining pressure was 2 MPa. The stress-strain curve and failure mode are shown in Figure 9.

Figure 9 shows that the damaged specimen with a fissure of 4 mm had two fissures that ran from top to bottom on the side of the filled layer, with a depth of approximately 1-1.5 mm. The rocks and filled concrete between the two fissures were broken and peeled off, the fissures showed a zig-zag shape, and there were pinnate cracks on the side. There was a damaged fissure with a width of approximately 2 mm on the peeling surface, which extended upward from the lower part of the specimen through the middle part of the specimen and then gradually ended. There were transverse cracks and step-like damages in the filled layer.

The damaged specimen with a fissure of 6 mm had one inverted Y-shaped fissure on the side of the filled layer that ran from top to bottom. The rocks above the fissure were broken and peeled off, and there were more fissures in the specimen. Two inverted Y-shaped fissures were also formed on the side of the filled layer. For one inverted Y-shaped fissure, the rocks at the fissure bifurcation were broken and fell. The Y-shaped fissure on the side gradually diminished and ended at the convergence of the filled layer. The upper part of the filled layer was broken and peeled off due to the broken and peeled rocks. Although there were many longitudinal fissures in the specimen, the overall skeleton of the specimen was intact.

Overall, the damaged specimen with a fissure width of 4 mm was highly intact, while the specimen with a fissure width of 6 mm had many longitudinal fissures. The peak strengths of the specimens with the two different fissure

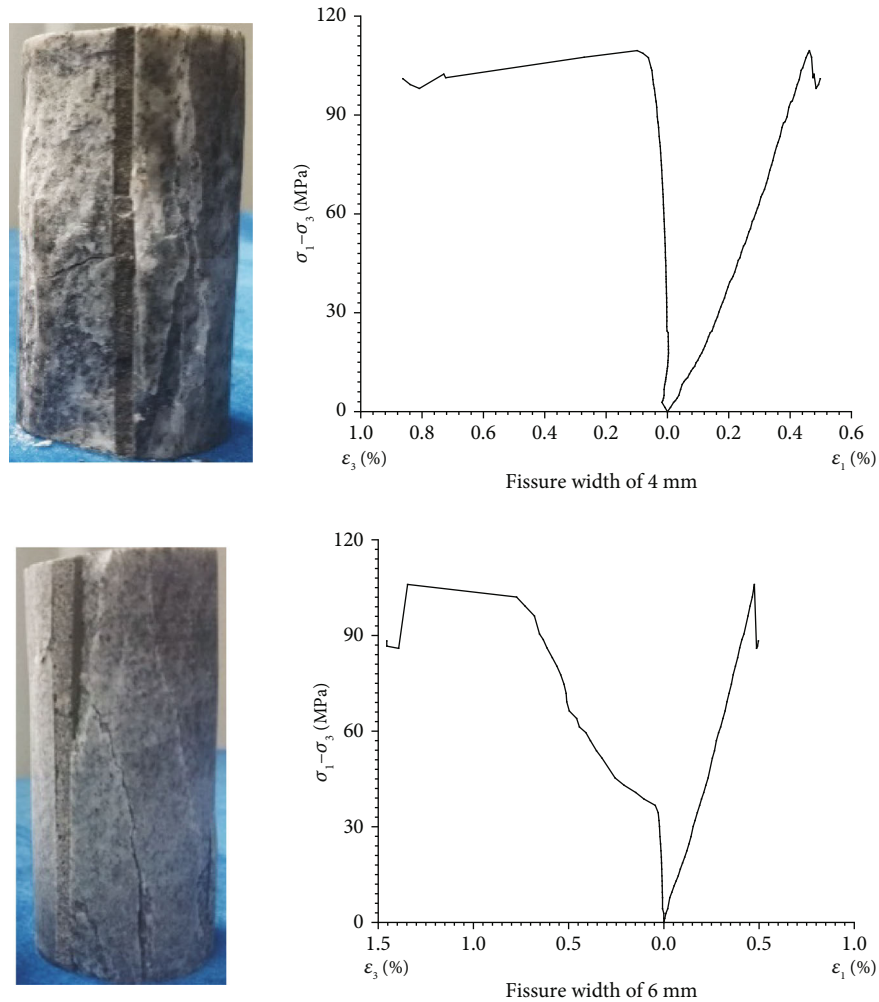


FIGURE 9: Stress-strain curve and typical failure mode of specimens with different fissure widths.

widths did not significantly change, and the axial strains after damage were also almost the same. In addition, both specimens showed high residual strengths after the peaks, which shows that concrete containing the HS admixture can effectively reinforce fissures of different widths.

5. Conclusions

As a new admixture for the concrete linings of surrounding rocks, the HS admixture showed good water retention and superhydrophobic properties, so it is applicable in the harsh working conditions of the linings of surrounding rocks. Through a triaxial compression test, the ability of concrete containing the HS admixture to fill and reinforce rock fissures was evaluated. The conclusions are as follows:

- (1) The HS admixture greatly lowered the water absorption rate of concrete and significantly improved the water resistance
- (2) The HS admixture effectively prevented the concrete from losing water and reduced the number of desiccation cracks in the concrete

- (3) The HS admixture was cemented in the concrete. As the HS admixture dosage increased, the damaged specimen under cube compressive strength was more intact, and the damaged surface of the specimen under the splitting tensile test was coarser
- (4) The concrete containing the HS admixture was applicable to rock specimens with premade fissures because it effectively reinforced the rock fissures

Data Availability

Some or all data, models, or code generated or used during the study are available from the corresponding author by request.

Conflicts of Interest

The authors declare that there are no conflicts of interest regarding the publication of this paper.

References

- [1] J. Sulem, M. Panet, and A. Guenot, "An analytical solution for time-dependent displacements in a circular tunnel," *International Journal of Rock Mechanics & Mining Sciences & Geomechanics Abstracts*, vol. 24, no. 3, pp. 155–164, 1987.
- [2] A. Graziani, D. Boldini, and R. Ribacchi, "Practical estimate of deformations and stress relief factors for deep tunnels supported by shotcrete," *Rock Mechanics and Rock Engineering*, vol. 38, no. 5, pp. 345–372, 2005.
- [3] Z. Ding, H. Zi, X. Ji, C. Shi, and Z. Ren, "Seismic fragility analysis of mountain tunnels considering lining degradation," *Chinese Journal of Rock Mechanics and Engineering*, vol. 39, no. 3, pp. 581–592, 2020.
- [4] Q. Xu, J. Wu, W. Chu, A. Cao, and J. Liu, "Application of temporal and spatial characteristics of shotcrete mechanics in Middle East pumping storage project," *Chinese Journal of Underground Space and Engineering*, vol. 16, no. 3, pp. 852–862, 2020.
- [5] P. P. Oreste, "A procedure for determining the reaction curve of shotcrete lining considering transient conditions," *Rock Mechanics & Rock Engineering*, vol. 36, no. 3, pp. 209–236, 2003.
- [6] G. G. Gschwandtner and R. Galler, "Input to the application of the convergence confinement method with time-dependent material behaviour of the support," *Tunnelling and Underground Space Technology incorporating Trenchless Technology Research*, vol. 27, no. 1, pp. 13–22, 2012.
- [7] Y. Lu, L. Wang, Z. Li, and H. Sun, "Experimental study on the shear behavior of regular sandstone joints filled with cement grout," *Rock Mechanics and Rock Engineering*, vol. 50, no. 5, pp. 1321–1336, 2017.
- [8] G. Xiang, Z. Li, and J. Zhang, "Analysis and treatment for Shi-ziya Tunnel damage," *Soil Engineering and Foundation*, vol. 1, pp. 5–7, 2008.
- [9] Q. Zhang, "Analysis on engineering geological characteristics of Sanchaling Tunnel," *Railway Investigation and Surveying*, vol. 36, no. 3, pp. 50–52, 2010.
- [10] J. Qi, Z. Hou, and S. Jia, "The research on the characteristics of Jinjiguan Tunnel's water penetration and deformation with defects control," *Journal of Disaster Prevention and Mitigation Engineering*, vol. 2, pp. 222–226, 2005.
- [11] J. Zhang and H. Huang, "Analysis and treatment of lining concrete corrosion failure in Liupanshan Tunnel," *Journal of Highway and Transportation Research and Development*, vol. 11, pp. 228–232, 2007.
- [12] S. Ji, Y. TANG, H. U. Degui, J. WANG, and S. TAO, "Analysis of typical seismic damages of highways in Wenchuan earthquake-induced hazard areas in Sichuan Province," *Chinese Journal of Rock Mechanics and Engineering*, vol. 28, no. 6, pp. 1250–1260, 2009.
- [13] G. Cui, D. Y. Wang, S. Z. Ni, and J. X. Yuan, "Model tests on bearing characteristics of steel fiber-reinforced concrete lining of weak surrounding rock tunnel," *Chinese Journal of Geotechnical Engineering*, vol. 39, no. 10, pp. 1807–1813, 2017.
- [14] Y. Guo, *Study of Mechanical Model of Reinforced Soils by Pre-Grouting and Its Application in Tunnelling Practices*, Beijing Jiaotong University, China, 2016.
- [15] W. Li, F. Shaikh, L. Wang et al., "Experimental study on shear property and rheological characteristic of superfine cement grouts with nano-SiO₂ addition," *Construction and Building Materials*, vol. 228, article 117046, 2019.
- [16] D. Cui, *The Research and Performance Test of Type of Tunnel Lining Crack Repairing Material*, Chang'an University, China, 2017.
- [17] T. R. Naik, S. S. Singh, and M. M. Hossain, "Permeability of concrete containing large amounts of fly ash," *Cement & Concrete Research*, vol. 24, no. 5, pp. 913–922, 1994.
- [18] Y. Yu and J. Wang, "The influence of WHDF crack resistance agent on improving crack resistance characteristics of concrete face-slab," *Journal of Hydroelectric Engineering*, vol. 19, no. 3, pp. 112–116, 2006.
- [19] "Test code for hydraulic concrete (China)(DL/T5150-2017)".

Research Article

Stability Analysis and Protection Measures of Large Section Tunnel in Coal Rich Weak Rock Stratum

Guannan Zhou,¹ Zijiang Zhao ,¹ Zhanping Song ,² and Hongjian Wang^{3,4}

¹China Railway Bridge Engineering Bureau Group Co., Ltd., 300300 Tianjin, China

²Xi'an University of Architecture and Technology, Xi'an, 710055 Shanxi, China

³North China University of Water Resources and Electric Power, Zhengzhou, 450045 Henan, China

⁴Zhongyuan Oilfield Branch of Sinopec, Puyang, 457000 Henan, China

Correspondence should be addressed to Zijiang Zhao; hanweige@stdu.edu.cn

Received 8 June 2021; Accepted 17 August 2021; Published 30 August 2021

Academic Editor: Yu Wang

Copyright © 2021 Guannan Zhou et al. This is an open access article distributed under the Creative Commons Attribution License, which permits unrestricted use, distribution, and reproduction in any medium, provided the original work is properly cited.

Due to poor engineering geological conditions of Liujiashuang tunnel on Shanghai-Kunming Passenger Dedicated Line, the large deformation of weak rock occurs repeatedly during tunnel construction. In this paper, the large-scale finite element software ABAQUS is used to simulate the construction process of a large-section tunnel in weak surrounding rock. It is found that when tunnel face passes through the coal seam, the displacement and stress simulated by the bench method increase abruptly. The maximum stress reaches up to 18 MPa, and displacement reaches 45 mm, which is about twice when without crossing coal seam. It is technically feasible to use the bench method for tunnel construction, under the condition when large settlements is allowed; additionally, the bench method has better technical and economic benefits than that of the CD method. Through the comparative analysis of onsite monitoring data and numerical simulation results, it can be seen that the tunnel is in a dangerous state when passing through the coal seam and measures such as strengthening support or auxiliary advance support should be taken immediately to control the surrounding rock and to ensure tunnel construction safety.

1. Introduction

Due to many active faults, wide distribution of weak rock, high ground stress, karst development, and abundant groundwater, the tunnel in weak surrounding rock may produce many disasters such as large deformation, mud outburst and gushing water, collapse and harmful gas [1–3]. By analyzing the characteristics of gas tunnel, the method of multihole cutting directional hydraulic fracturing to prevent gas outburst is proposed [4]. Shucai Li et al. studied the formation mechanism and development trend of karst tunnel water inrush disaster [5]. Zhang et al. conducted a systematic study on the occurrence mechanism and classification method of large deformation of structural weak rock in tunnel surrounding rock [6]. Wang et al. attributed the formation of the soft rock fracture zone of underground caverns to fatigue damage caused by repeated tectonic stress [7,

8]. At present, domestic and foreign methods for tunnel research in weak surrounding rock mainly include numerical simulation analysis, field monitoring measurement, and model test [9].

In weak rock tunnel stability theory analysis, Yang induced the factors affecting the stability of tunnel structure into four indexes, which are overbreak and underbreak volume, tunnel surrounding rock stability coefficient, the seismic intensity, and tunnel ratio. According to these four indices, original data information was collected; then by utilizing the information optimization theory, the relationship between the original data information and the stability of the tunnel structure is established [10]. Liu found that the cause of large deformation of the Muzhailing tunnel was resulting from the comprehensive action of surrounding rock plastic flow and surrounding rock swelling [11]. In recent years, Zuo et al. adopted the instability discriminant

of surrounding rock obtained by the catastrophe theory and achieved satisfying results when analyzing the stability of surrounding rock in the fault section through which the tunnel passes [12]. Yong-Hao et al. obtained the elastoplastic mechanical parameters of rock mass through laboratory tests and Hoek-Brown criterion and obtained the rheological parameters of surrounding rock through finite element inversion analysis. Combined with tunnel deformation monitoring data, numerical simulation of large deformation behavior of tunnel thus was achieved [13]. Peng et al. established the calculation formula of RRC of weak rock roadway related to creep effect [14]. In terms of weak rock tunnel support, Li et al. took into account the rheological properties of surrounding rock and carried out viscoelastic analysis of surrounding rock on the basis of the Poyting-Thomson model. Combined with the monitoring and measurement practice of the Shilong tunnel, the influence of initial support on the stability and displacement of surrounding rock was analyzed [15]. Liu et al. calculated the measured missing displacement according to the measured deformation statistics and the theoretical calculated limit displacement and elastic displacement, obtained the relationship between the measured deformation, the deformation rate before the secondary lining, and the limit displacement [16].

In terms of the physical model analysis of the stability of the weak rock tunnel, Tan et al. studied the displacement pressure of the tunnel with small clear distance in the initial supporting state by using the large-scale physical similarity model test [17]. Wang et al. established a calculation method suitable for prediction of ground subsidence caused by shield construction in weak rock area through indoor model test [18]. In terms of stability numerical calculation and analysis, Dai used numerical simulation to study the stability of shallow tunnel under different retaining schemes [19]. Yang et al. aimed at the influence of construction conditions, shallow burial, and other factors on the left portal of a tunnel, carried out three-dimensional simulation analysis by using numerical simulation, and compared the excavation methods [20]. Based on the numerical model and the improved strength reduction method, Chen et al. studied the influence of short bench, CD, and CRD construction methods on the stability of large section loess tunnel crossing slope [21]. In terms of monitoring means, new methods are emerging continuously. Wu et al. studied the feasibility of the RA/AF ratio in describing the process of rock failure development [22]. Wang et al. studied the characteristics of acoustic emission parameters of layered shale and red sandstone under different fault modes, providing a basis for acoustic monitoring of surrounding rock stability in the field [23, 24]. Hou et al. proposed a tunnel settlement inversion model based on distributed optical fiber strain [25]. Liu et al. applied dynamic parameterized 3D modeling technology into tunnel construction monitoring [26].

When tunnel traverses the soft surrounding rock section and large-section excavation construction technology that were carried out, unlike in the section with good geological conditions, rapid mechanized construction of tunnel lining can be used, and we must analyze the poor geological conditions of the section with weak surrounding rock, through

comparative analysis of multiple construction technical plans, to obtain the optimistic method. If merely in order to speed up the construction progress, blindly choose an inappropriate construction method, it will cause the tunnel excavation instability, on the contrary, delay the construction period and even cause engineering accidents. In this study, the Liujiazhuang tunnel passing through the weak coal seam group was taken as the engineering background, three construction methods were compared by numerical analysis, and the optimized one was obtained. In view of the large deformation problem caused by large section tunnel under such adverse geological conditions, the strengthening support measures are given.

2. Engineering Background

Liujiazhuang tunnel in Guizhou section of Shanghai-Kunming Passenger dedicated railway is located in the middle and low mountainous area of erosion structure in Yungui Plateau. Influenced by the structure, the tunnel body is located in the area with relatively developed folds and faults, with broken rock mass and poor surrounding rock conditions. The 300m section of tunnel D1K923+825 ~ D1K924+125 passes through the weak coal seam with high gas content. The coal bearing stratum at the exit section of the Liujiazhuang tunnel is Longtan Formation of Permian upper series, and the lithology is mainly black mudstone, sandy mudstone, siltstone, fine sandstone, and limestone, with more than 20 layers of coal line, as shown in Figure 1.

According to the *Code for design of railway tunnels in China* (TB10003-2016), based on the basic classification of weak coal tunnel surrounding rock, combined with the groundwater state, initial in situ stress and occurrence of main structural planes in the coal tunnel section, the classification of tunnel surrounding rock in this section is determined as grade IV. The excavation method of class IV surrounding rock of the Liujiazhuang tunnel adopts the bench method and temporary cross bracing.

On March 8, 2012, the primary support arch of the tunnel exit section was seriously deformed, a large number of shotcretes fell off, the primary support shotcrete on site cracked, and the vault sank, as shown in Figure 2. The field monitoring and measurement data show that the maximum vault subsidence is 301 mm, and the clearance convergence is 357 mm. The steel frame was strengthened by adding anchor pipe with locking feet, but the effect was not good, and the initial support continued to deform.

Overall evaluation shows that the engineering geological conditions of tunnel body are poor, and large deformation of weak rock occurs many times during tunnel construction. When the tunnel passes through the weak coal seam, the numerical simulation analysis of the tunnel construction should be carried out and combined with the onsite monitoring measurement, and the monitoring measurement of the tunnel construction deformation and stability should be carried out. And the reasonable reinforcement and prevention measures should be put forward to ensure the safe construction of the tunnel.

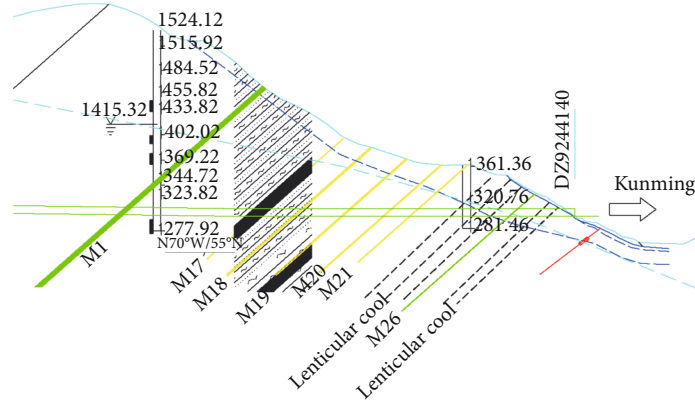


FIGURE 1: Profile of the Liujiazhuang tunnel.



FIGURE 2: Distortion and spalling of shotcrete of steel frame for initial support of arch.

3. Analysis of Mechanical Effect of Tunnel in Weak Surrounding Rock

3.1. Large Deformation of Tunnel in Weak Surrounding Rock. The large deformation of weak surrounding rock is the key problem affecting the stability of surrounding rock. In order to analyze the mechanism of large deformation of tunnel in weak surrounding rock, the rubinite formula is introduced.

$$R_p = R_{p0} + R_{p0}f(\theta)$$

$$= R_0 \left\{ \frac{P_0(1 + \lambda) + 2c \cot \phi(1 - \sin \theta)}{2P + 2c \cot \phi} \right\}^{1 - \sin \phi/2 \sin \phi} \quad (1)$$

$$\times \left\{ 1 + \frac{P_0(1 - \lambda)(1 - \sin \phi) \cos 2\theta}{[P_0(1 - \lambda) + 2c \cot \phi] \sin \phi} \right\},$$

$$R_{p0} = R_0 \left\{ \frac{[P_0(1 + \lambda) + 2c \cot \phi](1 - \sin \phi)}{2P + 2c \cot \phi} \right\}^{1 - \sin \phi/2 \sin \phi}, \quad (2)$$

$$f(\theta) = \frac{P_0(1 - \lambda)(1 - \sin \phi) \cos 2\theta}{[P_0(1 - \lambda) + 2c \cot \phi] \sin \phi}, \quad (3)$$

where R_p and R_0 are plastic zone radius (m) and tunnel radius (m) of surrounding rock of circular tunnel, respec-

tively. R_{p0} is the radius of axisymmetric plastic zone (m). θ is the angle between the polar radius of any point in the surrounding rock and the horizontal axis ($^\circ$); $f(\theta)$ is the relevant radius with θ of the plastic zone (m); P_0 is the vertical initial geostress, which is considered as the self weight stress (kPa); λ is the horizontal initial geostress coefficient; c and ψ are the cohesion (kPa) and internal friction angle of surrounding rock ($^\circ$), respectively; P is the support force (KN). Accordingly, the general elastic-plastic displacement of circular tunnel can be expressed by the formula:

$$U = \frac{1}{4GR_0} [R_{p0}^2 + (1 + \lambda)R_{p0}f(\theta)] \cdot \left\{ \sin \phi[(1 + \lambda)P_0 + 2c \cot \phi] \cdot \left[1 + \frac{(1 - \lambda) \sin \phi}{R_{p0}(1 - \sin \phi)} f(\theta) \right] - P_0(1 - \lambda) \cos 2\theta \right\}, \quad (4)$$

where U is the displacement around the tunnel; G is the shear modulus of surrounding rock. It can be seen from equation (4) that the main factors affecting the tunnel construction deformation include the initial geostress conditions (including the vertical geostress size and horizontal geostress coefficient), the properties of surrounding rock (including deformation parameters and strength index),

and the tunnel size and support resistance. Among them, the horizontal geostress coefficient mainly determines the distribution of the plastic zone (the relative relationship between vertical deformation and horizontal deformation). For the convenience of analysis, assuming that the coefficient of lateral pressure is 1, equations (1) and 4 are transformed into

$$R_p = R_0 \left\{ \frac{[P_0 + c \cot \phi](1 - \sin \phi)}{P + c \cot \phi} \right\}^{1 - \sin \phi / 2 \sin \phi}, \quad (5)$$

$$U = \frac{R_p^2}{2GR_0} (P_0 + c \cot \phi) \sin \phi. \quad (6)$$

It can be seen from equations (5) and (6) that the rock deformation around the tunnel is directly proportional to the square of the radius of the plastic zone. It can be seen that there will be a large range of plastic zone in the process of tunnel construction. The large range of plastic zone mainly depends on the strength index (especially the value) of surrounding rock, the value of in situ stress, and the resistance provided by the supporting structure, as shown in equation (5). The general strength index of weak surrounding rock is relatively low, and it is easy to appear a large range of plastic zone under a certain level of in situ stress. If the support is not timely or the support measures are not appropriate, large deformation is bound to occur. It can be seen from equation (6) that the deformation around the tunnel is inversely proportional to the comprehensive deformation index shear modulus G of surrounding rock. For the weak surrounding rock, its shear modulus is relatively low; so, the probability of large deformation in the corresponding tunnel construction deformation will increase. In addition, the tunnel excavation size is also one of the main factors of construction deformation. The larger the excavation size is, the more significant the construction deformation is.

3.2. Discrimination of Deep and Shallow Buried Tunnel. According to the *Code for design of railway tunnels in China* (TB10003-2016), the judgment standard for deep and shallow buried railway tunnels is $2.5h_q$. The specific discrimination methods are as follows:

when $h \geq 2.5h_q$, the tunnel is deep buried. When $h < 2.5h_q$, the tunnel is shallow, where h is the buried depth of tunnel vault. h_q is the equivalent load height. The calculation method of h_q is as follows:

$$h_q = 0.45 \times 2^{s-1} \times \omega. \quad (7)$$

s is the grade of surrounding rock. ω is the influence coefficient of tunnel width, and its value is

$$\omega = 1 + i(B - 5), \quad (8)$$

where B is the tunnel width (m); when $B > 5$ m, $i = 0.1$; when $B < 5$ m, $i = 0.2$.

In case of the Liujiazhuang tunnel, the Shanghai-Kunming Passenger dedicated railway is a two-way high-

speed line, the design section width of the tunnel is $B = 12$ m, the buried depth of the tunnel vault is $h = 59$ m, and the surrounding rock grade of the Liujiazhuang tunnel passing through the coal seam section is $s = 4$.

According to equations (7) and (8), $\omega = 1.7$ and $h_q = 6.12$ m.

The buried depth of tunnel vault is $h = 59$ m $> 2.5 \times h_q = 2.5 \times 6.12 = 15.3$ m, and the Liujiazhuang tunnel is belonging to deep buried tunnel.

4. Three-Dimensional Numerical Simulation Analysis of Large Cross-Section Tunnel in Weak Surrounding Rock

In this chapter, the ABAQUS numerical software is used to simulate and analyze the construction process of the Liujiazhuang Tunnel in weak surrounding rock. The full-face excavation method, bench cut method, and CD method are used to optimize the tunnel construction scheme. Based on the numerical analysis, the tunnel construction deformation control technology is proposed.

4.1. Finite Element Analysis Software ABAQUS. ABAQUS is one of the most advanced finite element analysis software in the world. Rock, concrete, soil, and other materials are granular friction materials. The compressive yield strength of these materials is much greater than the tensile yield strength, and the particles will expand when the materials are in tension. Therefore, Drucker-Prager yield criterion is often used to simulate these materials. ABAQUS extends the classical Drucker-Prager model. The yield surface of the extended Drucker-Prager model is not circular on the plane, and the yield surface includes linear model, hyperbolic model, and exponential model on the meridian plane.

4.2. Three Dimensional Numerical Simulation of Tunnel Construction Process

4.2.1. Model Parameter. In the calculation model,

- (1) The rock mass and weak coal seam are regarded as continuous, uniform, and isotropic elastic-plastic medium, and the stress-strain relationship of rock mass material is fully elastic-plastic without considering the influence of groundwater, and Drucker-Prager yield criterion is adopted
- (2) Only the stress field of the surrounding rock is considered, and the influence of the tectonic stress is not considered
- (3) In order to simplify the calculation, the coal seam area is analyzed as a whole. In the whole excavation process, considering the role of the first lining, the secondary lining is only designed as a reserved safety reserve

According to the engineering geological data of the Liujiazhuang Tunnel and *Code for design of railway tunnels in China* (TB10003-2016), the material parameters of

TABLE 1: Material parameters of surrounding rock.

Parameters	Bulk density (KN/m ³)	Elastic modulus (GPa)	Poisson's ratio	Cohesion (kPa)	Internal friction angle (°)
Surrounding rock	22	1.295	0.3	280	45

TABLE 2: Rock mass parameters of anchorage zone.

Parameters	Bulk density (KN/m ³)	Elastic modulus (GPa)	Poisson's ratio	Cohesion (kPa)	Internal friction angle (°)
Anchorage zone	22	1.295	0.3	330	45

TABLE 3: Physical and mechanical parameters of surrounding rock layers.

Parameters	Bulk density (KN/m ³)	Elastic modulus (GPa)	Poisson's ratio	Cohesion (kPa)	Internal friction angle (°)
First level	20	5.5	0.31	800	28.8
Second level	22	7.2	0.30	810	26
Third level	23	12.2	0.32	840	30
Fourth level	22	11.2	0.31	740	27
Weak coal seam	15	0.5	0.33	52	25.8
First lining	25	20	0.2	—	—
Grouting reinforcement	22	1.295	0.3	300	45

surrounding rock mass used in numerical simulation are shown in Table 1.

In the calculation, the bolt element is not used, but the method of improving the parameters of bolt and solid surrounding rock is adopted to simulate the role of anchor. According to the literature, the mechanical performance of rock mass reinforced by bolt is improved. The compressive strength and bending strength of surrounding rock are also improved. The anchorage zone parameters used in numerical simulation are shown in Table 2.

To sum up, according to Design drawing of the Liujiashuang Tunnel of Shang-hai-Kunming Passenger Dedicated Line and the current *Code for design of railway tunnels in China* (TB10003-2016), the material parameters of rock and soil mass simulated by the project are shown in Table 3.

4.2.2. Three Dimensional Numerical Model. The calculation range of numerical analysis shows that the transverse length of the whole model is 100 m, the height is 190 m, and the longitudinal length is 210 m (X direction is the vertical to the tunnel centerline, Y direction is the gravity direction, and Z direction is the tunnel centerline direction), which meets the requirements of finite element model calculation and analysis. The tunnel is parallel to the water discharge tunnel. When the tunnel is excavated, half of the excavation has been completed. Therefore, the calculation model of the Liujiashuang Tunnel is shown in Figure 3. The model adopts solid element to simulate coal seam, lining, and rock mass. The hexahedral element mapping is used for the tunnel lining and the lining of the water discharge tunnel. The number of the units is 832 and 904, and the number of nodes is 1650 and 560, respectively. Tetrahedral elements

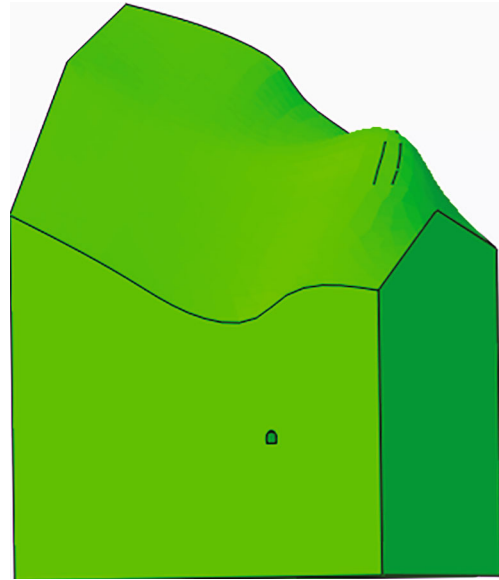


FIGURE 3: Mountain model.

are used to divide the mountain freely. The number of elements and nodes of the whole model is 62686 and 32269, respectively. The mesh is shown in Figure 4.

When meshing at the intersection of tunnel, drainage tunnel, and coal seam, irregular error unit and warning unit often appear. In order to reduce the proportion of wrong elements in meshing, hexahedral elements with neutral axis mapping are used for the excavation of tunnel rock mass and tunnel lining, discharge tunnel rock mass, and discharge tunnel lining. Tetrahedral elements are used for other areas

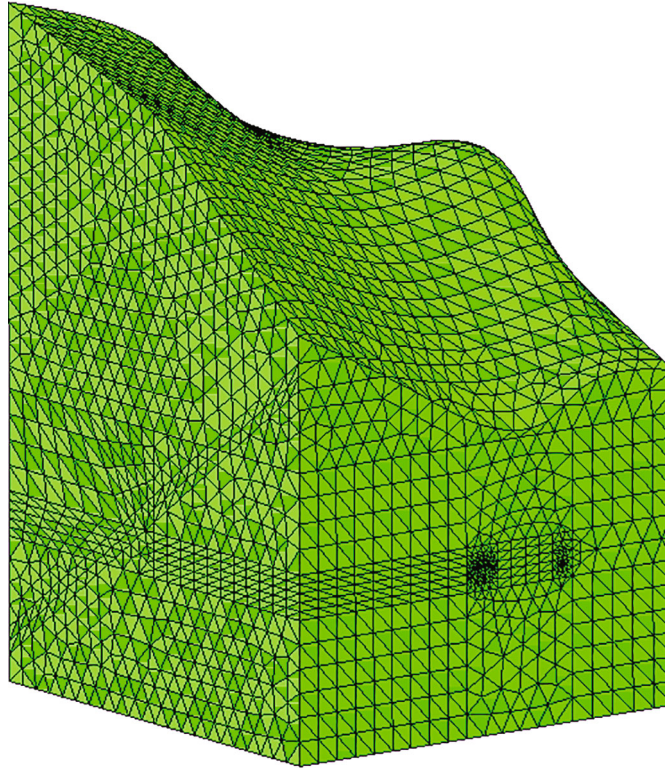


FIGURE 4: Grid graph.

of the mountain. The accuracy of mesh generation is greatly improved by planting seeds locally at intersections and modifying the size of mesh seeds, as shown in Figure 5.

4.2.3. Numerical Calculation and Scheme Optimization of Tunnel Construction through Coal Seam. The simulation steps of the numerical software are as follows: Firstly, set the initial stress of the model to balance the self-weight stress. Secondly, full-face excavation method, bench cut method, and CD method are used to simulate the tunnel excavation and support, respectively, and the stress and displacement of three different excavation methods are analyzed.

(1) Full-Face Excavation Method. The construction process of the tunnel is numerically simulated according to the construction steps of full-face excavation method, and the stress diagram and displacement diagram are shown in Figure 6.

It can be seen from Figures 6(a) and 6(b) that the stress concentration occurs after the excavation of the section. With implementation of the supporting structure, the stress distribution around the tunnel after the excavation is obviously improved, and the maximum stress is gradually transferred from the vault to the arch waist on both sides. After the excavation and support is completed, the maximum stress of the arch waist is 6.35 MPa. In the middle of the tunnel arch and invert, the stress is released more, the minimum principal stress value is 0.316 MPa, and the whole cal-

culational area is in the compression state. It can be seen from Figures 6(c) and 6(d) that the surrounding rock of the tunnel moves towards the excavation chamber after the full-face excavation. The displacement of the horizontal direction of the surrounding rock is the largest at the arch waist, the vertical maximum settlement value of the arch is about 37.58 mm, and the upward displacement of the tunnel bottom is 15.47 mm. The displacement of gravity direction is obvious in the range of 20 m above the vault, which is about 1.6 times of the tunnel diameter. The stress and displacement of the excavated water release tunnel have little influence on the construction of the tunnel during the whole tunnel construction.

(2) Bench Cut Method. The construction process of the tunnel is numerically simulated according to the construction steps of the upper and lower step method, and the stress diagram and displacement diagram are shown in Figure 7.

It can be seen from Figures 7(a) and 7(b) that after the upper bench excavation, the stress concentration appears around the core soil of the upper half section, and the maximum principal stress value can reach 5.35 MPa. After the initial support, the concentrated stress is transferred to the surrounding of the tunnel. After the excavation of the current half section, the rock stress around the tunnel changes greatly. When the inverted arch is completed, the stress distribution around the tunnel is obviously improved after the excavation of the tunnel. The maximum stress is borne by the arch waist on both sides, and the maximum stress of

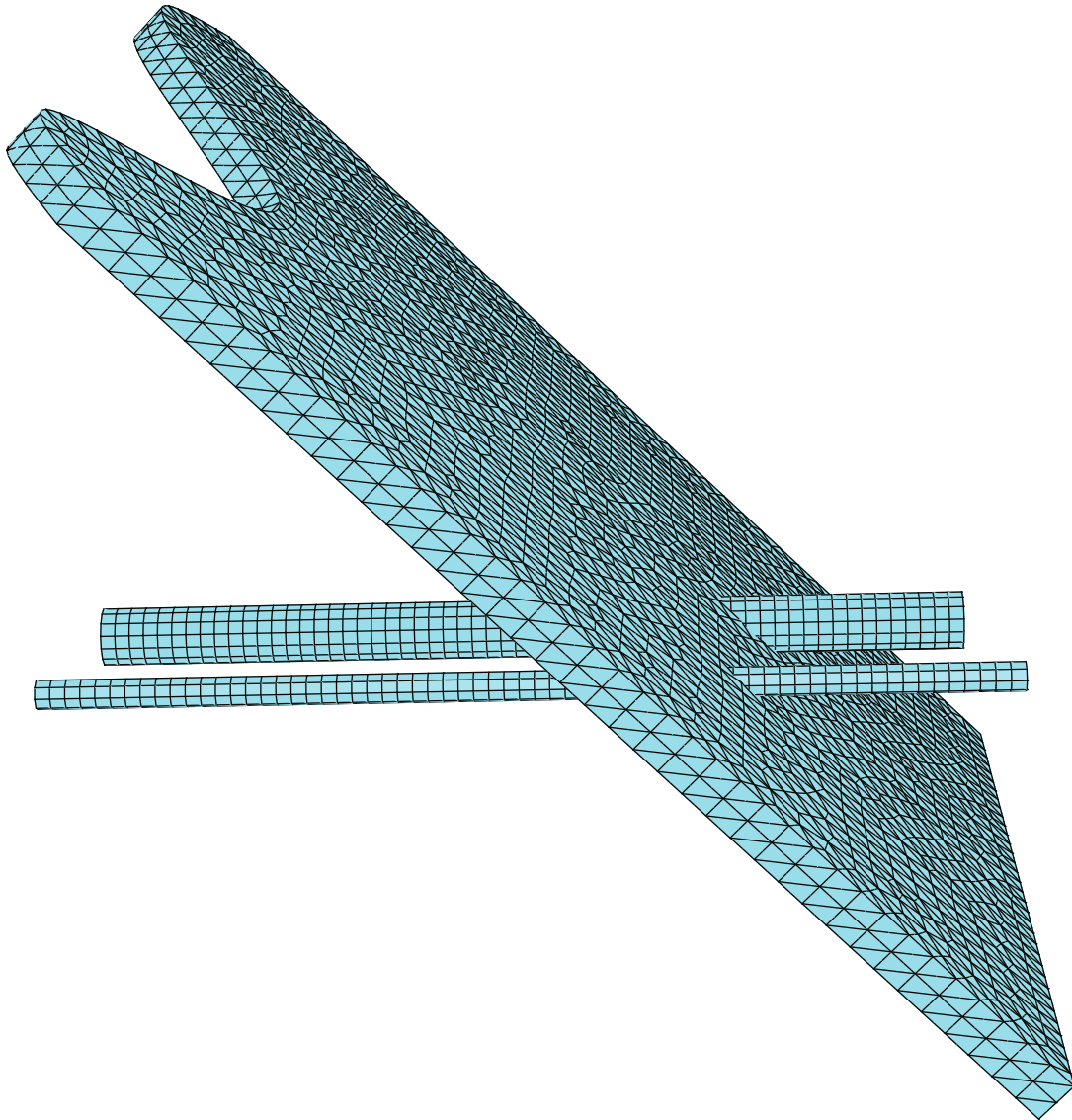


FIGURE 5: Cross diagram of coal seam and lining.

the arch waist is 7.20 MPa. At the top of tunnel and the bottom of invert, the stress is released more, the minimum stress is 0.57 MPa, and the whole calculation area is in the state of pressure.

It can be seen from Figures 7(c) and 7(d): after the excavation and support of the upper half section, the maximum horizontal displacement appears at the arch foot of the upper step, and the maximum displacement in the direction of gravity is at the vault of the tunnel. The maximum settlement of the vault of the tunnel is 17.13 mm, and the upward displacement of the bottom of the tunnel is 5.14 mm. After the excavation and support of the lower half section, the horizontal displacement of the surrounding rock basically does not change, and the vertical displacement changes significantly. The maximum settlement of the vault is about 20.93 mm, and the bottom edge rises 8.03 mm upward. The vertical displacement within 15 m above the vault is obvious, which is about 1.2 times of the tunnel radius.

In the whole process of tunnel construction, the stress and displacement of the excavated tunnel have little influence on the tunnel construction.

(3) *CD Method*. The construction process of the tunnel is numerically simulated according to the construction steps of CD method, and the stress and displacement are shown in Figure 8.

From Figures 8(a)–8(d), it can be seen that (1) since the CD method adopts the excavation of side wall heading by parts, the self-weight stress field formed by this method is asymmetric. When the upper right half of the tunnel is excavated and supported, the stress concentration occurs at the junction of the excavation face, and the maximum value is 3.84 MPa. (2) After the excavation and support of the lower right half section of the tunnel, the stress at the arch waist becomes uniform, and the maximum stress is 5.76 MPa.

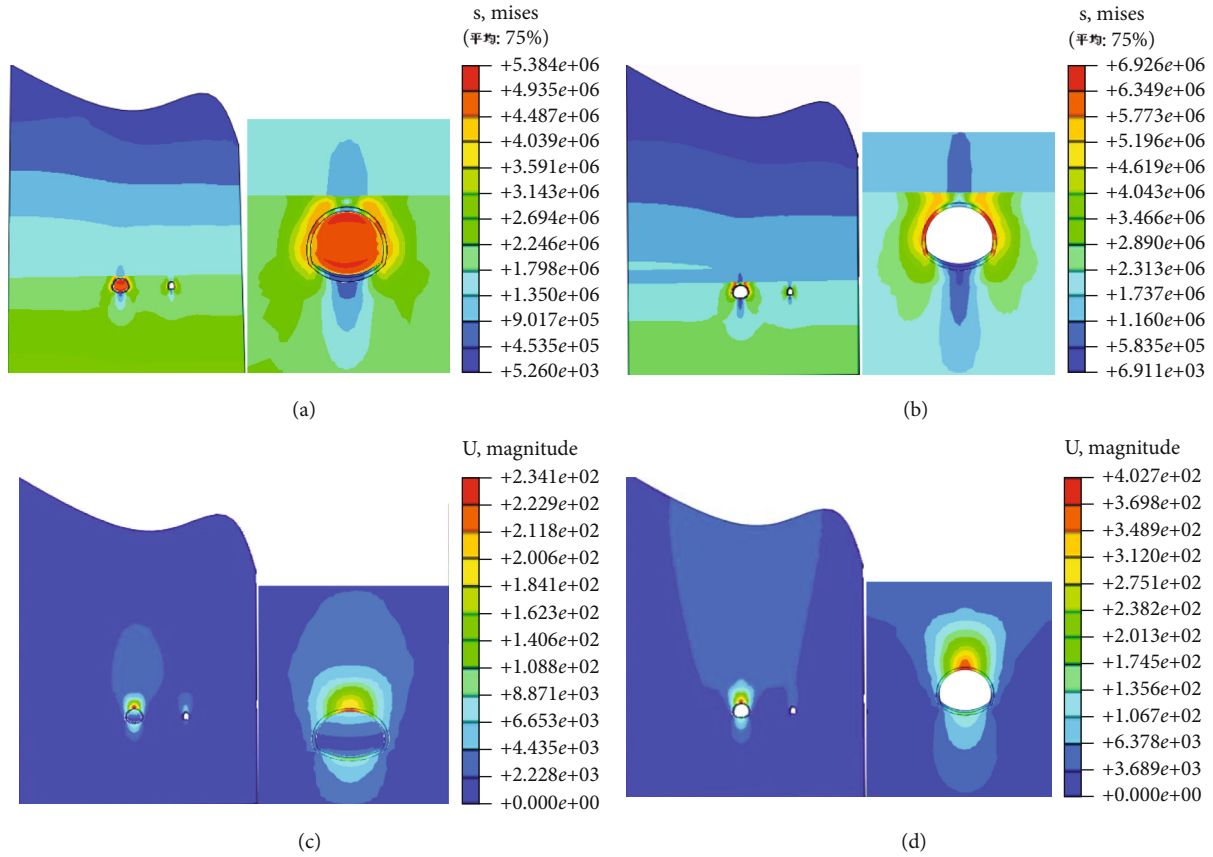


FIGURE 6: Stress diagram and displacement diagram of full section of tunnel crossing coal seam: (a) step 8: excavation stress diagram, (b) step 10: excavation stress diagram, (c) step 8: excavation displacement diagram, and (d) step 10: excavation displacement diagram.

(3) The stress of arch waist is the largest in the excavation of the upper left half section of the tunnel, with the value of 11.61 MPa. After support, only the stress concentration appears on the arch top, and the steel support also bears greater pressure. (4) After the excavation and support of the lower left half section of the tunnel, the stress field of the model is symmetrical, the maximum stress of the surrounding supporting structure is 18.52 MPa, and the surrounding rock and supporting structure of the tunnel are in the state of pressure. (5) The grid steel support can effectively limit the development of horizontal displacement. During the excavation process, the stress of surrounding rock changes significantly in the range of 3~4 m from the tunnel wall. After removing the grid steel support, the change of stress field is small, which indicates that the stress of surrounding rock has been basically released during the partial piloting of the CD method, and the deformation of tunnel is in a stable state.

From Figures 8(e)–8(h), it can be seen that (1) the displacement field is asymmetrically distributed. After the excavation and support of the upper part of the heading, the displacement in the horizontal direction basically does not change, which is because the grid steel frame support plays a role in restraining the deformation. The vertical displacement increases obviously in the upper part of the heading before excavation. Because the vault is greatly constrained, the maximum settlement does not appear in the vault, but

in the right side of the vault, about 4 mm, the bottom rises 4.5 mm. (2) After the excavation of the lower part of the heading, the horizontal displacement of the surrounding rock changes little, and the maximum vertical displacement is 9.7 mm, which occurs in the middle of the excavation tunnel. (3) After the excavation and support of the upper part of the back heading, the displacement of the horizontal side wall is 2.51 mm. The vertical displacement of vault and invert increased by 2.8 mm, and the cumulative displacement reached 12.5 mm, forming a “U” shaped settlement trough above the excavation chamber. (4) After the excavation and support of the lower part of the back heading, the vault settlement displacement is 15.25 mm, the invert displacement is 7.61 mm, and the settlement tends to be stable. (5) After the middle diaphragm is removed, the displacement field is basically unchanged.

(4) *Comparative Analysis of Numerical Simulation Results of Different Construction Methods.* The stress and displacement of surrounding rock disturbed by the above excavation methods are compared and analyzed, as shown in Table 4.

It can be seen from Table 4 that (1) during the construction of full-face excavation method, the displacement around the cavern is the largest, and the stress is the smallest. The maximum stress of full-face excavation method is only 0.37 times of that of the CD excavation method. The

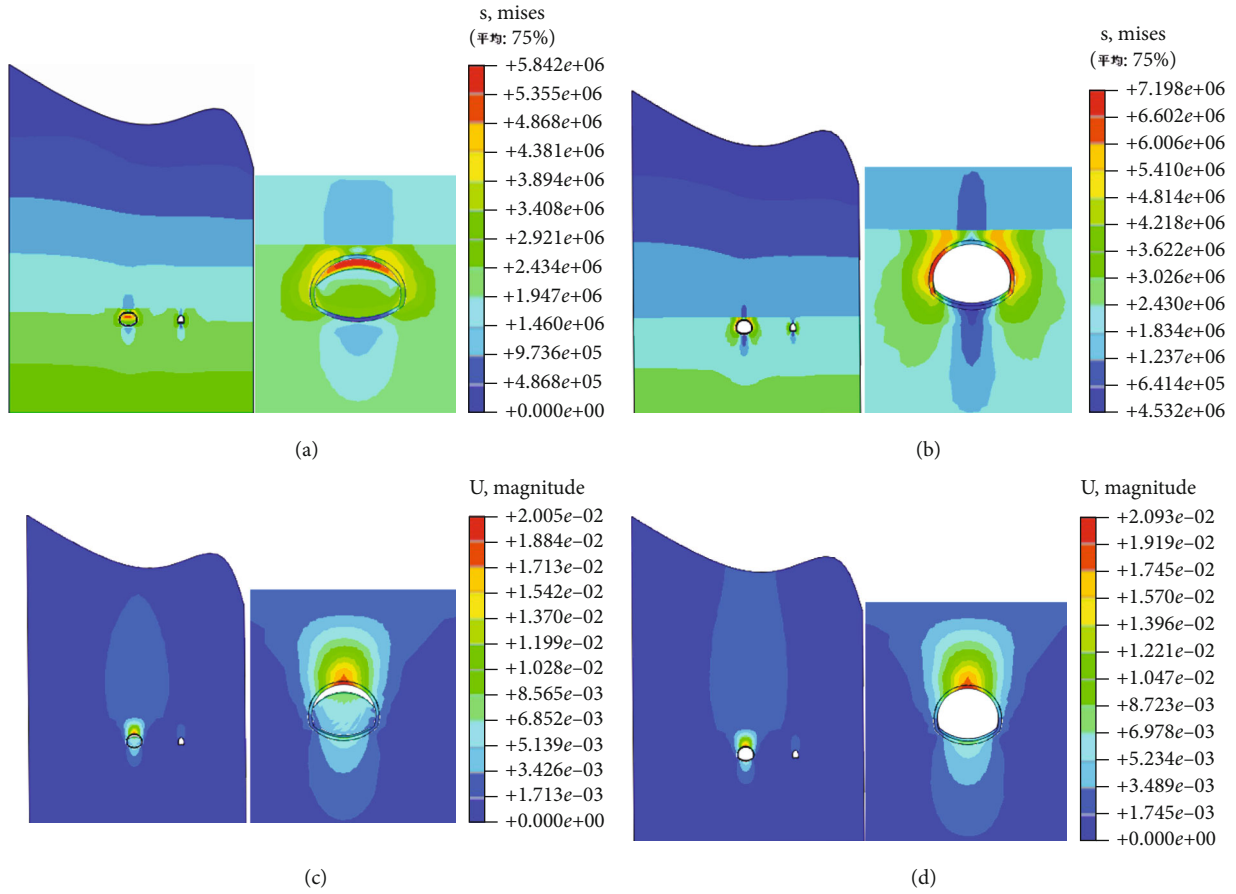


FIGURE 7: Stress diagram and displacement diagram of the upper and lower step method: (a) step 13: excavation stress diagram, (b) step 19: excavation stress diagram, (c) step 13: excavation displacement drawing and local enlarged drawing, and (d) step 19: excavation displacement diagram and partial enlarged drawing.

characteristics of full-face excavation method are small support stiffness, fast construction speed, and simple process; so, this method can be used in tunnel engineering which allowed large deformation. When facing the poor surrounding rock condition, in order to reduce the excavation step, increase the circulating footage, avoid unnecessary temporary support, and simplify the construction sequence, and most of the engineering personnel recommend using “advanced support with full section method” and using large machinery for full section excavation, so as to fully achieve the safe, fast, and efficient construction goal.

During the bench cut method, the displacement and stress around the cavern are between the full-face excavation method and the CD method. The analysis shows that construction process of the bench method is relatively simple compared with the CD method. By reserving the core soil behind the tunnel face, shortening the bench, closing the invert as close as possible to the tunnel face, and strengthening the arch foot support, the overall deformation of the middle arch of shallow buried weak surrounding rock tunnel can be controlled to varying degrees. However, the bench cut method has a greater disturbance to the weak surrounding rock in the excavation stage, and its ability to control the settlement deformation of shallow buried strata is far less than that of the CD method. The technology and

economic benefit of the bench cut method is better than that of the CD method, which is suitable for medium grade surrounding rock. Therefore, for the construction of large section tunnel with weak surrounding rock, the reserved core soil bench cut method can be used when large surface settlement is allowed.

During the construction of the CD method, the displacement around the cavern is the smallest, and the stress is the largest. The maximum displacement of the CD method is only 0.46 times of that of the full-face excavation method and 0.75 times of that of the bench cut method. In the construction of weak surrounding rock, the CD method has no crossbracing, and the inverted arch of heading must be closed in time. Only after the support is closed can a strong overall support stiffness be formed, so as to control the clearance displacement in time for further development. The CD method is safe, but also is a slow and highly cost construction method. The results show that the CD method can be used when the tunnel span is large, the surface settlement is strict, and the surrounding rock condition is very poor and when it is difficult to control the deformation of surrounding rock by bench cut method.

Through the above comparative analysis, in the weak surrounding rock tunnel construction, the bench cut method has the advantages of simple construction technology, large

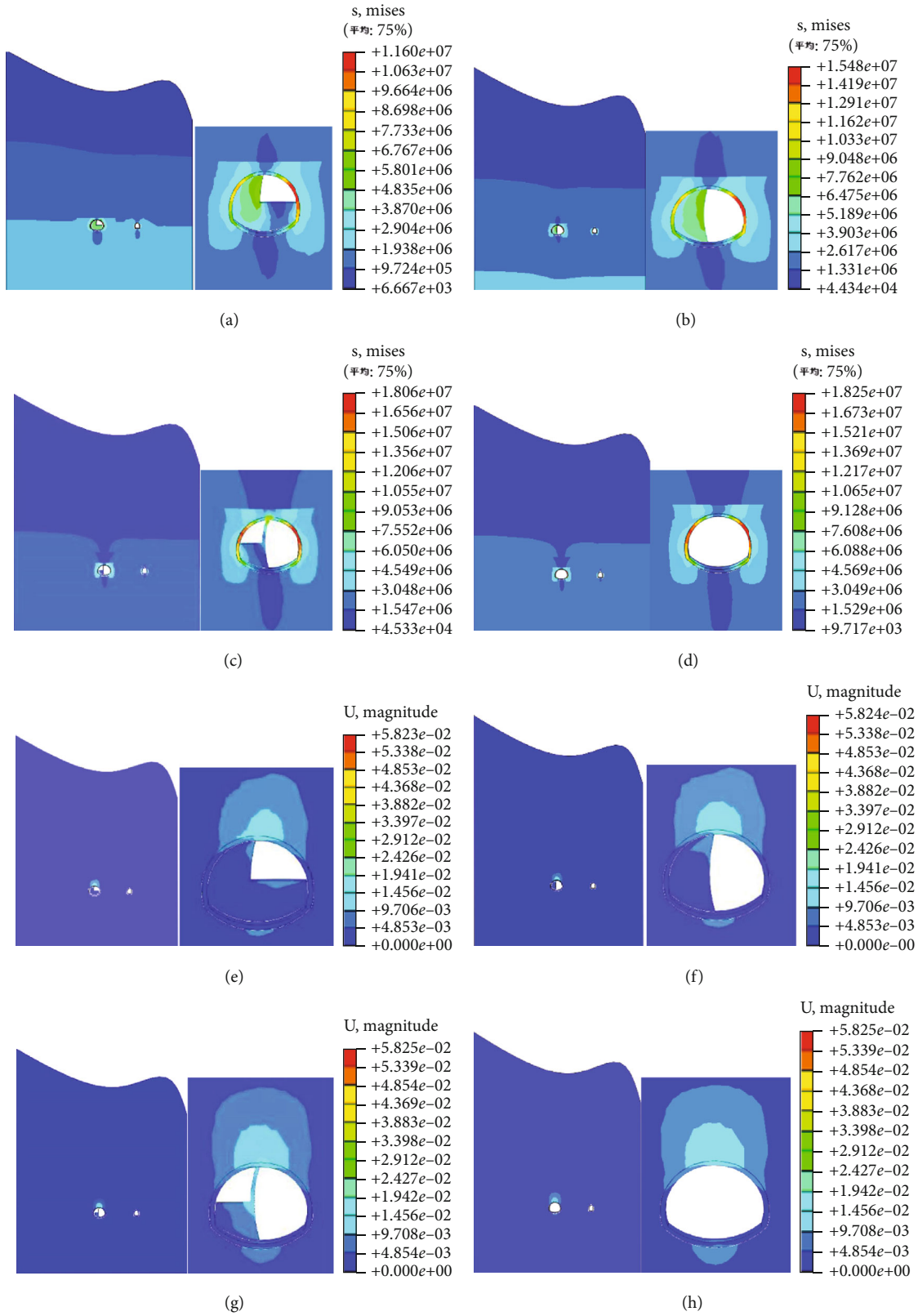


FIGURE 8: Stress diagram and displacement diagram of the CD method: (a) step 19: excavation stress diagram and partial enlarged drawing, (b) step 21: excavation stress diagram and partial enlarged drawing, (c) step 23: excavation stress diagram and local enlarged drawing, (d) step 25: excavation stress diagram and partial enlarged drawing, (e) step 19: excavation displacement diagram and partial enlarged drawing, (f) step 21: excavation displacement diagram and partial enlarged drawing, (g) step 23: excavation displacement diagram and partial enlarged drawing, and (h) step 25: excavation displacement diagram and partial enlarged drawing.

TABLE 4: Stress and displacement of surrounding rock.

Tunnel excavation method	Mises stress (MPa)		Magnitude displacement (mm)	
Full-face excavation method	Maximum	6.35	Vault	-37.58
	Minimum	0.32	Invert bottom	15.47
Bench cut method	Maximum	7.20	Vault	-20.93
	Minimum	0.57	Invert bottom	8.03
CD method	Maximum	18.52	Vault	-15.25
	Minimum	0.37	Invert bottom	7.61

Note: “-” indicates the displacement in the direction of gravity.

operation space, and convenient operation of large mechanical equipment, and its construction speed is obviously better than that of the CD method. Therefore, the bench cut method is widely used in class III and IV surrounding rock with good stability. In the weak surrounding rock of grades IV and V, if the bench cut method is to be used, appropriate advance supporting measures must be selected before excavation to ensure the safety of construction.

5. Onsite Monitoring and Stability Protection Measures

5.1. Monitoring of the Liujiazhuang Tunnel Project. The basis for this project monitoring scheme is *Technical Code for High Speed Railway Engineering Monitoring (DB11/490-2007)*, *Code for Design of High Speed Railway* (trial 2009), *Technical Specification for Monitoring Measurement of Railway Tunnel*. Considering the requirements of Liujiazhuang tunnel monitoring scheme and the actual geological situation of tunnel exit, the layout of vault monitoring points, side wall convergence monitoring points, and inverted arch monitoring points of the Liujiazhuang tunnel is shown in Figure 9.

According to the numerical simulation results of Liujiazhuang tunnel in the previous chapter, D1K923+870~D1K923+660 section is selected for data analysis of monitoring and measurement.

5.1.1. Analysis on Settlement Monitoring Data of Vault of Primary Support. Vault settlement is an important monitoring measurement item in monitoring measurement. The displacement of surrounding rock is related to many factors, and it is a comprehensive index, which can reflect the joint effect of stress, surrounding rock structure, construction method, construction quality, support strength, and other factors. The vault settlement data of the initial supporting of the D1K923+770~D1K923+730 section are analyzed.

According to Figure 10, the monitoring data of five cross-section points show that the stability of surrounding rock takes about 45 days, and the final settlement of each monitoring point is 80.02 mm, 85.62 mm, 83.79 mm, 88.02 mm, and 122.13 mm, respectively. The D1K923+650 section is the fracture surface before crossing the coal seam, and the final settlement of surrounding rock is basically stable at about 85.0 mm. The D1K923+660 section is the fracture surface crossing the coal seam, and the displacement of 122.12 mm occurred in the D1K923+660 section. At this

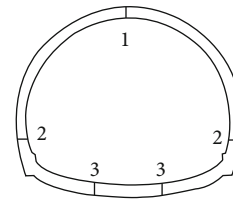


FIGURE 9: Layout of monitoring points for vault, arch waist, and inverted arch: point 1: settlement monitoring point of vault, point 2: convergence monitoring point of side wall, and point 3: settlement monitoring point of inverted arch.

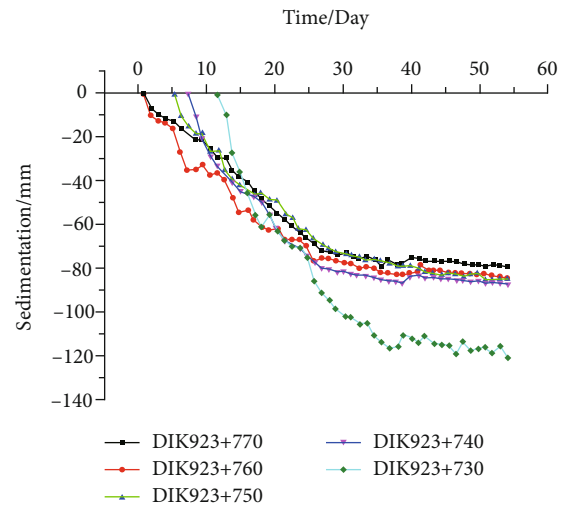


FIGURE 10: Settlement curve of vault.

time, we should increase the monitoring frequency, pay close attention to the development trend of surrounding rock, and ensure the construction safety.

5.1.2. Analysis of Convergence Monitoring Data of Side Wall. The convergence monitoring measurement data of side wall of the D1K923+770~D1K923+730 section are analyzed below.

It can be seen from Figure 11 that the final settlement values of each monitoring point are 12.4 mm, 12.5 mm, 14.7 mm, 16.08 mm, and 16.65 mm, respectively. The final settlement of surrounding rock is basically stable at about 15.0 mm, and the five monitoring sections tend to be stable

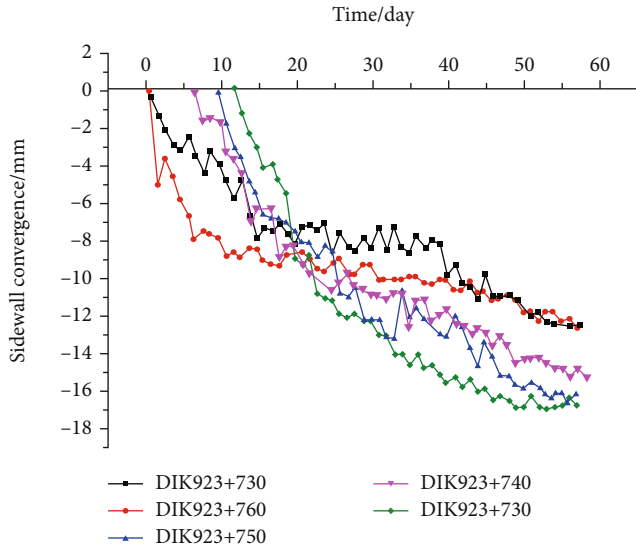


FIGURE 11: Convergence curve of side wall.

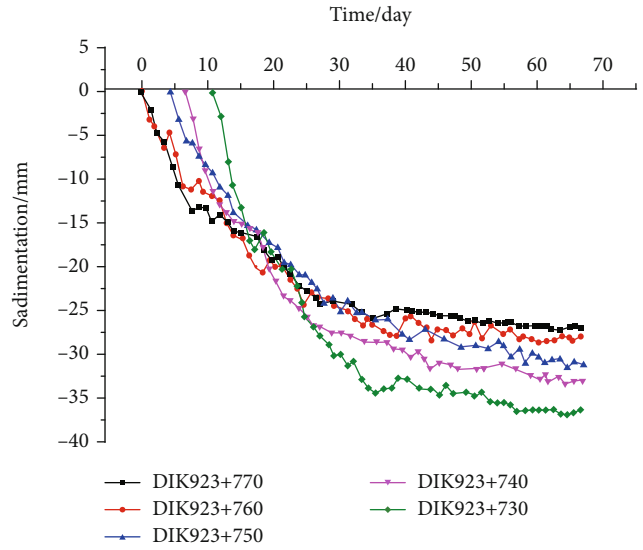


FIGURE 12: Settlement curve of inverted arch.

in about 45 days. Through the comparative analysis of five monitoring sections, it is known that with the excavation of the tunnel, the final convergence value changes about 15 mm. It can be seen that the influence of coal seam excavation on the convergence of side wall is not obvious.

5.1.3. Analysis of Settlement Monitoring Data of Inverted Arch. The settlement monitoring data of inverted arch of DIK923+770 ~ DIK923+730 section are analyzed below.

It can be seen from Figure 12 that the final settlement values of each monitoring point are 26.97 mm, 28.20 mm, 31.00 mm, 33.00 mm, and 36.50 mm, respectively. The final settlement of surrounding rock is basically stable at about 35.0 mm, and the five monitoring sections tend to be stable in about 45 days.

The DIK923+740 section is the fracture surface before crossing the coal seam, and the final settlement of surrounding rock is basically stable at about 33.00 mm. The DIK923+730 section is the fracture surface crossing the coal seam, the inverted arch settlement is 36.50 mm, and the variation is small. This is because at the DIK923+730 section, the coal seam and the tunnel are inclined and intersected, the upper part of the tunnel vault is excavated to the coal seam, and the lower part of the tunnel arch bottom is not excavated to the coal seam; so, the settlement change of the lower part of the tunnel is small.

5.1.4. Monitoring Data Analysis of Pressure Cell and Strain Gauge. From Figures 13 and 14, it can be seen that the internal force of steel arch frame and surrounding rock pressure is basically stable in about 15 days. The DIK923+740 section is the fracture surface before crossing the coal seam, the pressure of surrounding rock is about 0.16MPa, and the internal force of steel arch is 9.8 MPa. The DIK923+730 section is the fracture surface crossing the coal seam, the pressure of surrounding rock is about 0.21Mpa, and the internal force of steel arch is 10.48Mpa. In the section of

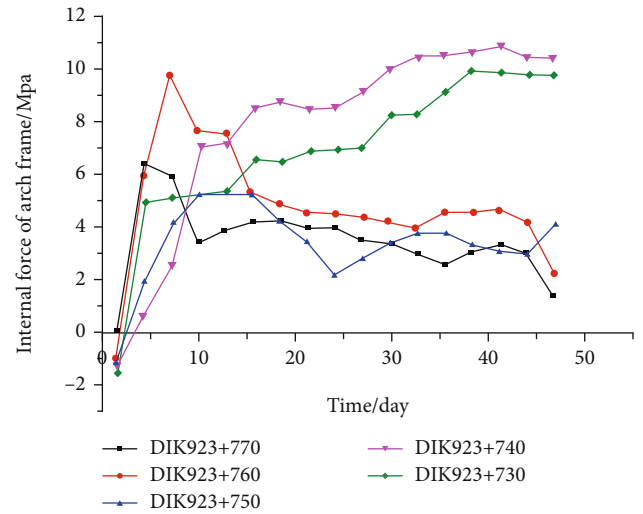


FIGURE 13: Internal force curve of steel arch.

crossing coal seam, the pressure of surrounding rock and the internal force of steel arch frame increases obviously. Therefore, it is necessary to strengthen the monitoring and measurement frequency during the construction to ensure the construction safety.

5.2. Comparative Analysis of Numerical Simulation and Monitoring Results. Through the numerical simulation, we can not only understand the dynamic change law of surrounding rock but also combine the numerical simulation value with the field monitoring data, which can more effectively guide the field construction.

It can be seen from Table 5 that

- (1) The numerical simulation values of vault settlement, horizontal convergence, and inverted arch settlement of the DIK923+730 section are 37.58 mm,

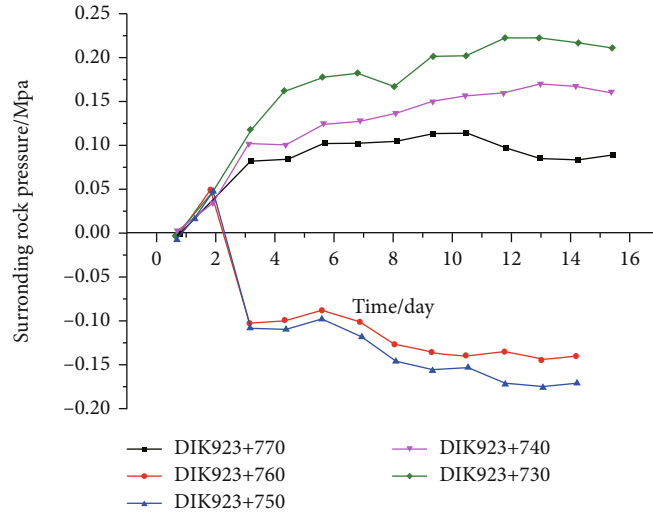


FIGURE 14: Pressure-time curve of surrounding rock.

TABLE 5: Field monitoring value and numerical simulation value.

Measurement items	Field monitoring value (mm)	Numerical simulation value (mm)
Settlement displacement of vault	61.2	37.58
Horizontal convergence displacement	7.5	2.29
Settlement displacement of inverted arch	18.2	15.47

Note: this table shows the measured and simulated values of the DIK923+730 section.

2.29 mm, and 15.47 mm, respectively. The simulation value of ABAQUS software is smaller than the measured value, which is because the mechanical parameters used in the numerical model are from the geological exploration report, which is within a range of statistical result. Compared with the actual mechanical parameters of the surrounding rock, the parameters used in numerical model to a certain extent cannot correctly reflect the stress-strain relationship of the actual surrounding rock in the process of excavation. Therefore, there is a gap between the deformation convergence results of numerical simulation and the convergence values of field monitoring. However, the convergence trend of surrounding rock obtained from numerical simulation and field measurement is consistent; so, the results of numerical simulation can be used to describe the law of tunnel convergence after tunnel excavation

- (2) Onsite monitoring and measurement should be used to design the key parts of tunnel surrounding rock and supporting structure, so as to ensure the economy and safety of engineering construction
- (3) In actual construction, if the measured value is greater than the predicted value, the construction should be slowed down or stopped, and the design parameters of supporting structure should be enhanced. If the

measured value is less than or equal to the predicted value, it shows that the design parameters of the surrounding rock support structure are reasonable, the construction method is feasible, and the normal construction can continue

6. Discussions

For the tunnel with weak surrounding rock, from the perspective of deformation control, the selection of appropriate “support time” and “support stiffness” plays an important role in the stability of the tunnel. Therefore, through the optimization analysis of Liujiazuang tunnel construction process and scheme, the following deformation control measures are proposed.

- (1) Reasonable selection of excavation division and excavation footage can effectively change the stress and deformation of surrounding rock and supporting structure and prevent tunnel instability
- (2) With the excavation of the tunnel, the weak surrounding rock has a large deformation in the face and in front of the face. If not controlled, it will cause partial collapse and large deformation of the vault of the face and then result into the secondary disasters of the surrounding rock. During tunnel construction, the reinforcement measures behind the tunnel face

cannot control the deformation of surrounding rock in front of the tunnel face. Therefore, the advanced support technology with auxiliary measures can effectively control the construction deformation of weak surrounding rock tunnel and ensure the construction safety

7. Conclusions

Based on the project of the Liujiazhuang tunnel exit section of Shanghai-Kunming Passenger Dedicated Line, large-scale finite element software ABAQUS is used to simulate the excavation of large section tunnel in weak surrounding rock and the construction process when crossing coal seam. Through the simulation of the site construction scheme and three different excavation methods, we obtained the variation law of stress and strain of surrounding rock and supporting structure. The field monitoring measurement data and numerical simulation results of tunnel vault settlement, sidewall convergence, inverted arch settlement, surrounding rock pressure, and support internal force are compared and analyzed, and the following conclusions are obtained:

- (1) With the excavation of the tunnel, when palm surface passes through the coal seam, the simulated displacement and stress using bench method increase abruptly. The maximum stress of the supporting structure is 18.13 MPa when crossing the coal seam, and the maximum displacement reaches 45 mm, which is about twice the displacement without crossing the coal seam. Therefore, normally, the tunnel can be constructed according to the bench method without crossing the coal seam, and the design parameters of the supporting structure should be enhanced when crossing the coal seam
- (2) By the comparison of the three construction methods, it can be known that cavern settlement is the largest, and the stress is the smallest under the full-face construction method. The maximum settlement of the step method is 0.57 times of the maximum settlement of the whole section, and the maximum stress of the bench method is 0.39 times of the CD method. Therefore, the bench method can better control the stability of excavation face; furthermore, in the case of allowing large settlement, the technical and economic benefits of the bench method are better than the benefits of the CD method
- (3) Through the comparative analysis of onsite monitoring and numerical calculation of tunnel vault settlement, horizontal convergence of side wall, and tunnel invert settlement data of the Liujiazhuang Tunnel, it can be seen that the tunnel is in a dangerous state when crossing the coal seam section. Engineering measures such as strengthening support or the bench method with auxiliary measures of advanced support should be taken immediately to control the deformation of surrounding rock and ensure the construction safety

Data Availability

The data used to support the findings of this study are included within the article.

Conflicts of Interest

The authors declare that they have no conflicts of interest.

Acknowledgments

This work was financially supported by the National Natural Science Foundation of China (41807254), Key Research & Development and Promotion Projects of Henan Province (212102310374), China Postdoctoral Science Foundation (2020M682372), and Young Talent Support Project of Henan Province (2021HYTP013). We would like to express our sincerest gratitude to the help of Yanzong Cui of North China University of Water Resources and Electric Power for field data collection and analysis.

References

- [1] T. Zhigang, Z. Fei, W. Hongjian, Z. Haijiang, and P. Yanyan, "Innovative constant resistance large deformation bolt for rock support in high stressed rock mass," *Arabian Journal of Geosciences*, vol. 10, no. 15, 2017.
- [2] S. Tian, Y. Zhao, S. Shi, and J. Hu, "The status problems and countermeasures of typical disaster prevention and control methods during the construction period of Chinese railway tunnels," *Hazard Control in Tunnelling and Underground Engineering*, vol. 1, no. 2, pp. 24–48, 2019.
- [3] Z. He, "Analysis of geological problems of railway tunnels: case study of typical tunnels," *Tunnel Construction*, vol. 36, no. 6, pp. 636–665, 2016.
- [4] D. Li, Y. Lu, Y. Rong et al., "Rapid uncovering seam technologies for large cross-section gas tunnel excavated through coal seams using directional hydraulic fracturing," *Rock and Solid Mechanics*, vol. 40, no. 1, pp. 363–369, 2019.
- [5] S. Li, K. Wang, and L. Li, "Mechanical mechanism and development trend of water inrush disasters in karst tunnels," *Chinese Journal of Theoretical and Applied Mechanics*, vol. 49, no. 1, pp. 22–30, 2017.
- [6] G. Zhang, J. Deng, and D. Wang, "Mechanism and classification of tectonic-induced large deformation of soft rock tunnels," *Advanced Engineering Sciences*, vol. 53, no. 1, pp. 1–12, 2021.
- [7] Y. Wang, C. Li, and J. Han, "On the effect of stress amplitude on fracture and energy evolution of pre-flawed granite under uniaxial increasing-amplitude fatigue loads," *Engineering Fracture Mechanics*, vol. 240, article 107366, 2020.
- [8] Y. Wang, Y. Yi, C. Li, and J. Han, "Anisotropic fracture and energy characteristics of a Tibet marble exposed to multi-level constant-amplitude (MLCA) cyclic loads: a lab-scale testing," *Engineering Fracture Mechanics*, vol. 244, article 107550, 2021.
- [9] Z. Tao, C. Zhu, M. He, and M. Karakus, "A physical modeling-based study on the control mechanisms of negative Poisson's ratio anchor cable on the stratified toppling deformation of anti-inclined slopes," *International Journal of Rock Mechanics and Mining Sciences*, vol. 138, article 104632, 2021.

- [10] X. Yang, L. Li, and B. Liu, "Evaluation on structure stability of unsymmetrically tunnels using the theory of information optimization analysis," *Chinese Journal of Rock Mechanics and Engineering*, no. 4, pp. 484–488, 2002.
- [11] G. Liu, F. Zhang, X. Li, and Z. Yang, "Research on large deformation and its mechanism of Muzhailing tunnel," *Chinese Journal of Rock Mechanics and Engineering*, Supplement 2, pp. 5521–5526, 2005.
- [12] Q. Zuo, L. Wu, Z. Lu, Y. Tan, and Q. Yuan, "Instability analysis of soft surrounding rock in shallow tunnel portal under unsymmetrical pressure by catastrophe theory," *Rock and Soil Mechanics*, vol. 36, Supplement 2, pp. 424–430, 2015.
- [13] D. A. Yong-hao, C. H. Wei-Zhong, and T. I. Hong-ming, "Study of large deformation and support measures of daliang tunnel with soft surrounding rock mass," *Chinese Journal of Rock Mechanics and Engineering*, vol. 34, Supplement 2, pp. 4149–4156, 2015.
- [14] Y. Peng, L. Wu, H. Peng, Y. Hao, and Y. An, "Theoretical and experimental study on rock resistance coefficient of soft rock tunnel considering creep effect," *Arabian Journal for Science and Engineering*, vol. 45, no. 5, pp. 4333–4342, 2020.
- [15] X. Li, D. Li, X. Jin, and Y. Gu, "Discussion on influence of initial support to stability and deformation of surrounding rock mass in soft rock tunnel," *Rock and Soil Mechanics-WUHAN*, no. 8, pp. 1207–1210, 2005.
- [16] Z. Liu, W. Li, Y. Zhu, and M. Sun, "Research on construction time of secondary lining in soft rock of large-deformation tunnel," *Chinese Journal of Rock Mechanics and Engineering*, vol. 27, no. 3, pp. 580–588, 2008.
- [17] K. Tan, Q. Yang, and L. Yang, "Effect of uneven pressure and heterogeneous ground on the safety and stability of twin tunnels with small spacing," *Modern Tunnelling Technology*, vol. 47, no. 4, pp. 20–26, 2010.
- [18] H. Wang, P. Su, H. Sun, K. Qi, and J. Shao, "Prediction of ground settlement caused by shield construction in soft rock ground," *Chinese Journal of Rock Mechanics and Engineering*, vol. 39, Supplement 2, pp. 3549–3556, 2020.
- [19] W. Dai, "Numerical analysis on stability of retaining scheme comparison and selection for shallow tunnel under unsymmetrical pressure," *Railway Engineering*, no. 3, pp. 61–65, 2011.
- [20] C. Yang, Y. Zhang, D. Huang, and Y. Lou, "A study of tunnel surrounding rock stability of shallow and unsymmetrical loaded portal section with excavation sequences from inside," *Hydrogeology and Engineering Geology*, vol. 39, no. 4, pp. 49–54, 2012.
- [21] S. Chen, Y. Zhu, Z. Li, L. Huang, and H. Zhang, "Analysis of lateral slope stability during construction of a loess tunnel with a large section," *Modern Tunnelling Technology*, vol. 51, no. 1, pp. 82–89, 2014.
- [22] S. Wu, Y. Gan, Y. Ren, and L. Zheng, "Feasibility research of AE monitoring index in tunnel based on RA and AF," *Chinese Journal of Engineering*, vol. 42, no. 6, 730 pages, 2020.
- [23] H. Wang, F. Zhao, Z. Huang, Y. Yao, and G. Yuan, "Experimental study of mode-I fracture toughness for layered shale based on two ISRM-suggested methods," *Rock Mechanics and Rock Engineering*, vol. 50, no. 7, pp. 1933–1939, 2017.
- [24] H. Wang, D. Liu, Z. Cui, C. Cheng, and Z. Jian, "Investigation of the fracture modes of red sandstone using XFEM and acoustic emissions," *Theoretical and Applied Fracture Mechanics*, vol. 85, pp. 283–293, 2016.
- [25] G. Hou, Z. Li, T. Hu et al., "Study of tunnel settlement monitoring based on distributed optic fiber strain sensing technology," *Rock and Soil Mechanics*, vol. 41, no. 9, pp. 3148–3158, 2020.
- [26] L. Liu, F. Wu, G. Zhang, and Y. Bai, "Research and application of tunnel construction monitoring method based on dynamic 3D parametric modelling technology," *Modern Tunnelling Technology*, vol. 57, Supplement 1, pp. 859–863, 2020.

Research Article

Undrained Cyclic Response and Resistance of Saturated Calcareous Sand considering Initial Static Shear Effect

Baojian Li ¹, Panpan Guo ¹, Gaoyun Zhou,¹ Zhe Wang,² Gang Lei ^{1,3}
and Xiaonan Gong ¹

¹Research Center of Coastal and Urban Geotechnical Engineering, Zhejiang University, Hangzhou 310058, China

²College of Civil Engineering and Architecture, Zhejiang University of Technology, Hangzhou 310023, China

³Beijing Urban Construction Design & Development Group Company Limited, Beijing 100037, China

Correspondence should be addressed to Panpan Guo; pp_guo@zju.edu.cn and Xiaonan Gong; gongxn@zju.edu.cn

Received 5 June 2021; Accepted 1 July 2021; Published 21 August 2021

Academic Editor: Yu Wang

Copyright © 2021 Baojian Li et al. This is an open access article distributed under the Creative Commons Attribution License, which permits unrestricted use, distribution, and reproduction in any medium, provided the original work is properly cited.

Sand elements in the natural or manmade field have often undergone initial static shear stresses before suffering cyclic loading. To explore the effect of static shear stress, a series of undrained cyclic triaxial tests were performed on dense and loose calcareous sand under different initial and cyclic shear stresses. The triaxial test results are used to describe the effect of static shear stress on the cyclic response of the calcareous sand with different relative density. Cyclic mobility, flow deformation, and residual deformation accumulation are the three main failure modes under varying static and cyclic shear stress levels. The cyclic resistance of dense sand is greater than that of loose sand, but the initial static stress has different effects on the cyclic resistance of the two kinds of sand. The dense sand owns a higher cyclic resistance with SSR increasing, while for the loose sand, 0.12 is the critical SSR corresponding to the lowest value of the cyclic resistance. The dense sand has more fast accumulation of dissipated energy, compared with loose sand. Additionally, an exponential relationship is established between static shear stress, relative density, and normalized energy density.

1. Introduction

With the implementation of the Belt and Road Initiative, calcareous sand, biogenic sediment and skeletal remain of marine organism, has been a topic of interest among geotechnical researchers recently [1, 2]. It is widely distributed in the continental shelf and coastline of tropical and subtropical climate between north and south latitude 30 degrees, such as the eastern and western of the Caribbean Sea, the Pacific Islands, the western of the Indian Ocean, and Nansha Islands and Xisha Islands in the South China Sea [3, 4]. Compared to terrigenous sand, the main composition is calcium carbonate [5, 6]. The characteristics of calcareous sand are high crushability, irregular particle shape, complex microstructure, and high intraparticle void [7, 8]. Therefore, the mechanical behaviors are quite different from those of silica sand [9–11]. Over the past few years, calcareous sand has been used

as a kind of filling material in geotechnical engineering, and the engineering challenges (e.g., embankment subsidence, retaining wall stability, and ground improvement) are becoming more and more complex. In order to promote the process of island and reef infrastructure construction, it is necessary to further study calcareous sand.

Many investigations have been carried out to explore the mechanical properties of calcareous sand. Using triaxial tests at high pressure to study uncemented Dog's Bay sand, the results showed that, despite particle breakage, its properties were still similar to those of the common soil observed [12]. And it was consistent with the principle of critical state soil mechanics. However, a series of static and dynamic experimental programs including direct shear tests, compression tests, triaxial tests, and resonant column tests were designed to reveal the difference between silica sand and Cabo Rojo sand with a similar grain size distribution [13, 14]. The

research claimed the latter expressed a more ductile and contractive behavior and had higher peak friction angles which is relative to the shear rate. Besides, liquefaction of calcareous sand has been an interested theme to examine mechanical properties among geotechnical scholars. It is a phenomenon that results from collapse deformation following the unstable behavior of saturated loose or dense sand at the state of low mean effective stress and shear strength [15, 16]. The liquefaction-type behavior, which may produce the most devastating effects of all catastrophic damage (e.g., the spreading of embankments and dams), can be induced under either monotonic or cyclic loading conditions [17, 18].

It is well known that sand elements in the natural or man-made field have often undergone an initial static shear stress prior to suffering from cyclic loading, which is caused by wave, traffic, wind, and earthquakes [19, 20]. Under the combined action of initial static and cyclic stress, the saturated sand foundation is prone to landslide, foundation instability, and subsidence, which is very harmful [21–23]. Therefore, the liquefaction behavior considering initial static shear stress has become one of challenging topics in geotechnical engineering [18, 24]. The results obtained by a lot of triaxial tests, taking into account initial static and cyclic deviatoric stress, proved that different stress conditions resulted in two types of cyclic behavior: CM and RDA [25]. Therefore, how to analyze the liquefaction is becoming more and more important. Since the pioneering work of David and Berrill [26], the dissipated energy concept was a convenient method. It was first introduced following the assumption of Nemat-Nasser and Shokoh [27] that the dissipated energy per unit volume resulting from the breakdown of soil skeleton was directly related to the pore pressure buildup. This could be an efficient way in evaluating the liquefaction potential of sand under both uniform and irregular cyclic stress conditions. In the last few decades, various studies have focused on establishing the relationship between the incremental pore pressure and dissipated energy obtained from stress-strain loops in undrained cyclic tests. As such, Kokusho and Pan and Yang [28, 29] further indicated that the energy dissipation correlated well not only with the generated pore pressure but also with the induced strain. The foregoing studies were mainly concerned with the energy-pore pressure or energy-strain relationship. Apart from these, the experimental work confirmed that the amount of energy dissipation that led to liquefaction failure (full pore pressure buildup or development of a specific strain) increased with soil density, confining pressure, and sustained shear stress level [30–32]. Although these previous studies have afforded valuable data for the energy-based evaluation of liquefaction potential, the validity of this method remains uncertain when it is applied to evaluate the cyclic resistance of calcareous sand under various initial and cyclic stress conditions.

In the present study, undrained cyclic triaxial tests were carried out. The results are composed of two parts: in the first part, through a comparison between loose and dense calcareous sand considering various initial static shear effect, cyclic

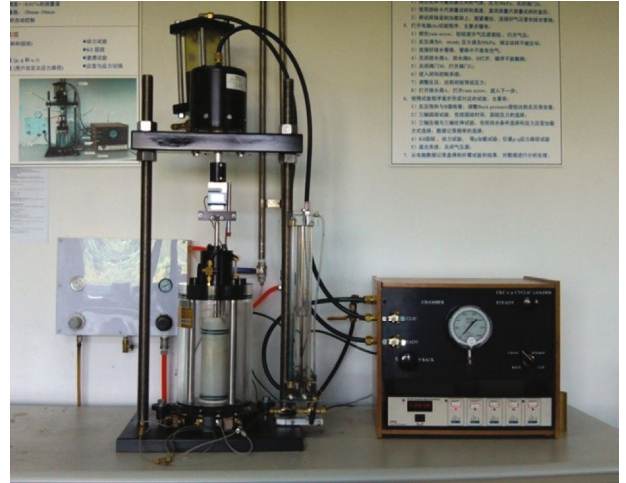


FIGURE 1: CKC automatic triaxial test system.

TABLE 1: Physical properties of calcareous sand.

G_s	d_{60} (mm)	d_{30} (mm)	d_{10} (mm)	C_u	C_c
2.79	2.60	0.88	0.38	6.84	0.78

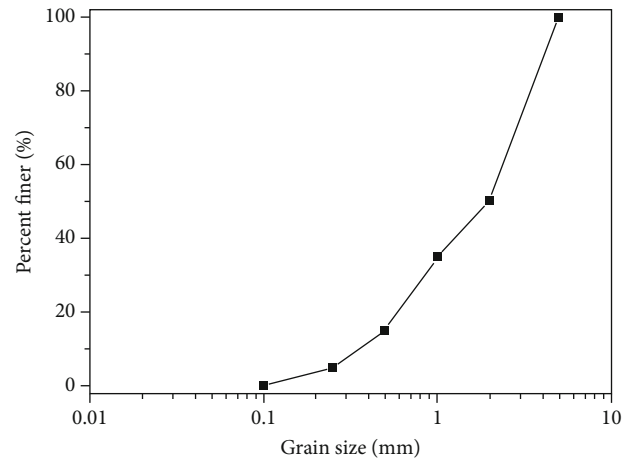


FIGURE 2: Grain size distribution curves of calcareous sand.

shear responses of liquefaction are explored. On the other hand, through the energy-based liquefaction analysis, the dissipated energy could be uniquely correlated with cyclic resistance.

2. Laboratory Test Method

2.1. Apparatus and Material. An advanced system, CKC automatic triaxial test system shown in Figure 1, was used in this study to achieve the undrained circulation triaxial test. The system could convert the computer output digital signal into analog signal and then enter the electric-gas conversion system and control the air pressure amplifier to apply the air pressure. Thus, isotropic and anisotropic

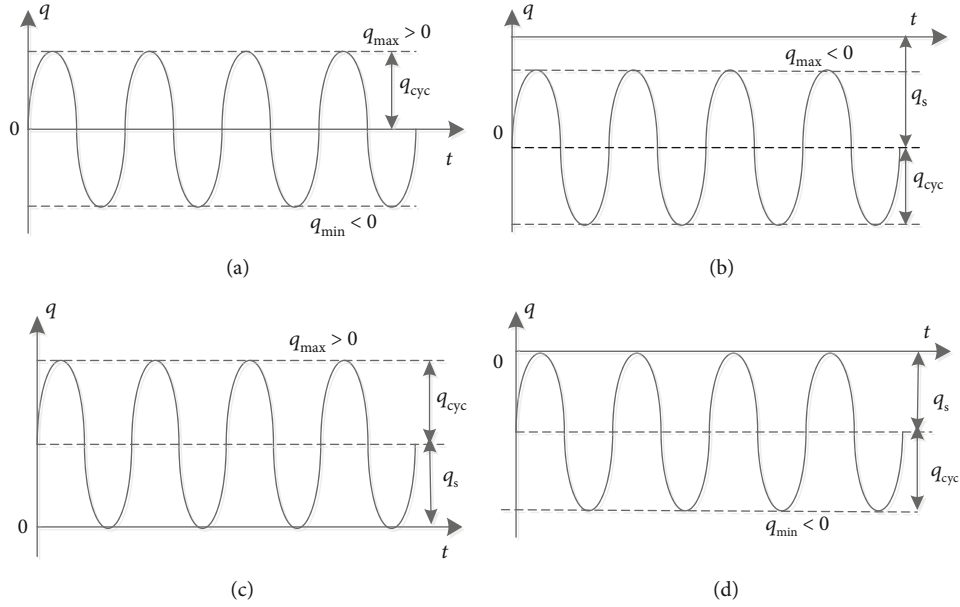


FIGURE 3: Categories of stress conditions considered in this study: (a) stress reversal; (b) no stress reversal; (c, d) intermediate.

consolidation and applying various cyclic loading modes could be realized.

The test material used in this study, calcareous sand, is biogenic sediments and skeletal remains of marine organisms retrieved from the reef reclamation site in Nansha Island, South China Sea. A natural grading with a grain diameter less than 5.0 mm was retained for testing. The physical parameters are shown in Table 1. Figure 2 shows the particle size distribution curve of calcareous sand used in this study. The investigated materials have poor distribution, containing coarse and medium sand without fine particles.

2.2. Test Program. The specimens of 70 mm in diameter and 140 mm in height were used in this triaxial test, which were prepared by using the moist undercompaction method as stated by Kim et al. [33]. Before the triaxial sample was mounted on the loading frame, carbon dioxide and deaired water were circulated through the specimens successively. Subsequently, a backpressure of 300 kPa was applied to obtain a high degree of saturation. And finally, specimens can be considered to reach the saturation state with Skempton's B -values exceeding 0.95 for all of the samples presented in the study.

The saturated specimens were then isotropically consolidated to the mean effective stress $p_0' = 100$ kPa under drainage conditions and subsequently anisotropically consolidated to a desired q_s along a constant $p' = 100$ kPa path under drainage conditions likewise.

The specimens with various q_s were then loaded by the different q_{cyc} as follows:

$$q(t) = q_s + q_{cyc} \sin(2\pi ft), \quad (1)$$

where $f = 1$ Hz and t is the elapsed time. The cyclic stress paths are divided into "shear stress reversal," "no shear stress reversal," and "intermediate" [34], as shown in Figure 3.

As listed in Table 2, undrained cyclic tests were performed with dense calcareous sand samples ($D_r = 70\%$) and loose calcareous sand samples ($D_r = 30\%$) and were designed to consider various combinations of the static stress ratio ($SSR = q_s/2p_0'$) and cyclic stress ratio ($CSR = q_{cyc}/2p_0'$).

3. Cyclic Response and Failure Modes under Initial Shear Stress

Figures 4 and 5 show the typical response of saturated dense sand and loose calcareous sand under cyclic loading. Figures 4(a)–4(c) are the effective stress path (q - p') and stress-strain curve (q - ϵ) relations of dense sand with $D_r = 70\%$ under the condition of isotropic consolidation and initial static deviator-stress of compression and tension, respectively.

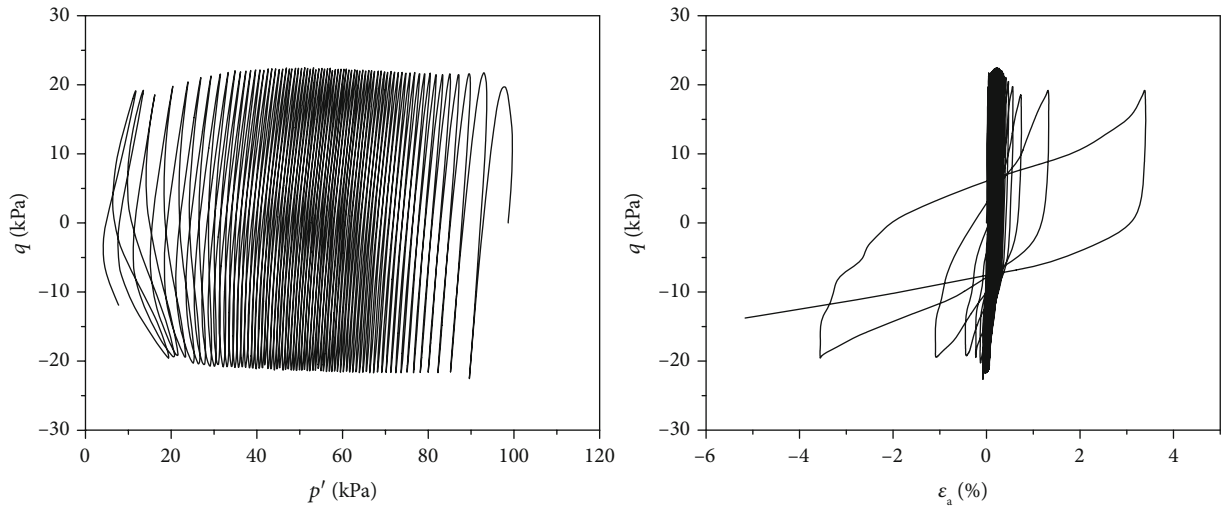
Figure 4(a) shows the typical response of saturated dense sand with isotropic consolidation suffering from symmetric cyclic load ($SSR = 0$, $CSR = 0.125$) under the condition of stress reversal. It can be seen from the effective stress path in the figure that, under the condition of being undrained, the effective stress of the test sample decreases continuously with the cyclic loading. At the end of the cycling stage, cyclic response is characterized by a "butterfly" effective stress path, which can be interpreted as the constant conversion between dilatancy and contraction of the sample throughout loading and unloading; the deviatoric stress approaches zero at an identical time the effective stress of the sample approaches zero. The axial deformation develops slowly in the first 71 cycles and rapidly in the last 3 cycles at both the

TABLE 2: Summary of undrained cyclic triaxial tests.

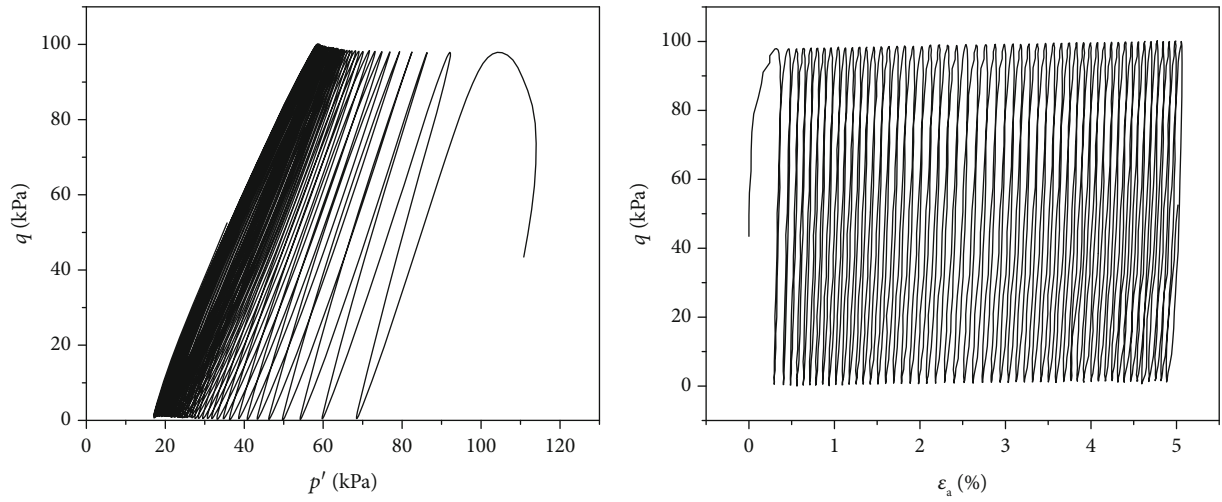
Series	D_r (%)	q_s (kPa)	q_{cyc} (kPa)	SSR	CSR	Stress condition	N_f
I	70	0	20	0	0.1	Reversal	232
		0	25	0	0.125	Reversal	74
		0	30	0	0.15	Reversal	17
		0	40	0	0.2	Reversal	6
		20	30	0.1	0.15	Reversal	168
		20	45	0.1	0.225	Reversal	19
		20	50	0.1	0.25	Reversal	3
		50	50	0.25	0.25	Intermediate	53
		50	60	0.25	0.3	Intermediate	11
		50	70	0.25	0.35	Reversal	6
		80	70	0.4	0.35	Intermediate	14
		80	80	0.4	0.4	Intermediate	7
		-10	25	-0.05	0.125	Reversal	78
		-10	30	-0.05	0.15	Reversal	39
		-10	35	-0.05	0.175	Reversal	8
		-20	20	-0.1	0.1	Intermediate	210
		-20	25	-0.1	0.125	Intermediate	11
		-20	30	-0.1	0.15	Intermediate	8
		-40	20	-0.2	0.1	No reversal	57
		-40	25	-0.2	0.125	No reversal	16
-40	30	-0.2	0.15	No reversal	8		
II	30	0	15	0	0.075	Reversal	943
		0	20	0	0.1	Reversal	120
		0	25	0	0.125	Reversal	37
		0	30	0	0.15	Reversal	18
		24	30	0.12	0.15	Intermediate	61
		24	35	0.12	0.175	Intermediate	16
		24	40	0.12	0.2	Intermediate	5
		40	15	0.2	0.075	No reversal	175
		40	20	0.2	0.1	No reversal	9
		50	12.5	0.25	0.0625	No reversal	17
		50	15	0.25	0.075	No reversal	2
		-10	12.5	-0.05	0.0625	Reversal	382
		-10	15	-0.05	0.075	Reversal	180
		-10	20	-0.05	0.1	Reversal	11
		-20	10	-0.1	0.05	No reversal	246
		-20	12.5	-0.1	0.0625	No reversal	202
		-20	15	-0.1	0.075	No reversal	12
		-40	5	-0.2	0.025	No reversal	104
		-40	7.5	-0.2	0.0375	No reversal	13
		-40	10	-0.2	0.05	No reversal	2

compression and tensile sides, thus forming an “S”-shaped stress-strain curve, and finally failure occurs at the tensile side, until the failure criterion of 5% double-amplitude (DA) axial strain has been satisfied [35]. Both the “butterfly” stress path and the “S”-shaped stress-strain curves were the typical features of the “cyclic mobility” (CM) response [36].

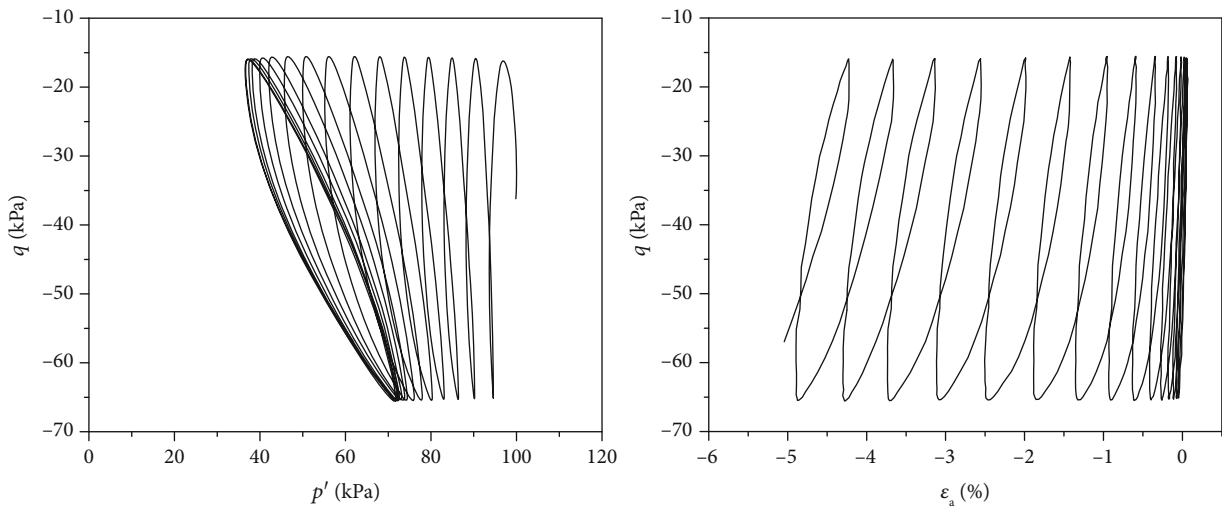
Figure 4(b) shows the typical response of saturated dense sand, which is suffering from positive static deviatoric stress before undergoing undrained cyclic loading (SSR = 0.25, CSR = 0.25), under the condition of the “intermediate” state. It can be seen from the effective stress path in the figure that, in the early stage of cyclic loading, the effective stress decreases with cyclic loading,



(a) $D_r = 70\%$, $SSR = 0$, $CSR = 0.125$, $N_f = 74$, CM (stress reversal)



(b) $D_r = 70\%$, $SSR = 0.25$, $CSR = 0.25$, $N_f = 53$, RAD (intermediate)



(c) $D_r = 70\%$, $SSR = -0.2$, $CSR = 0.125$, $N_f = 16$, RAD (no stress reversal)

FIGURE 4: Cyclic response of dense sand with different initial static deviatoric stresses.

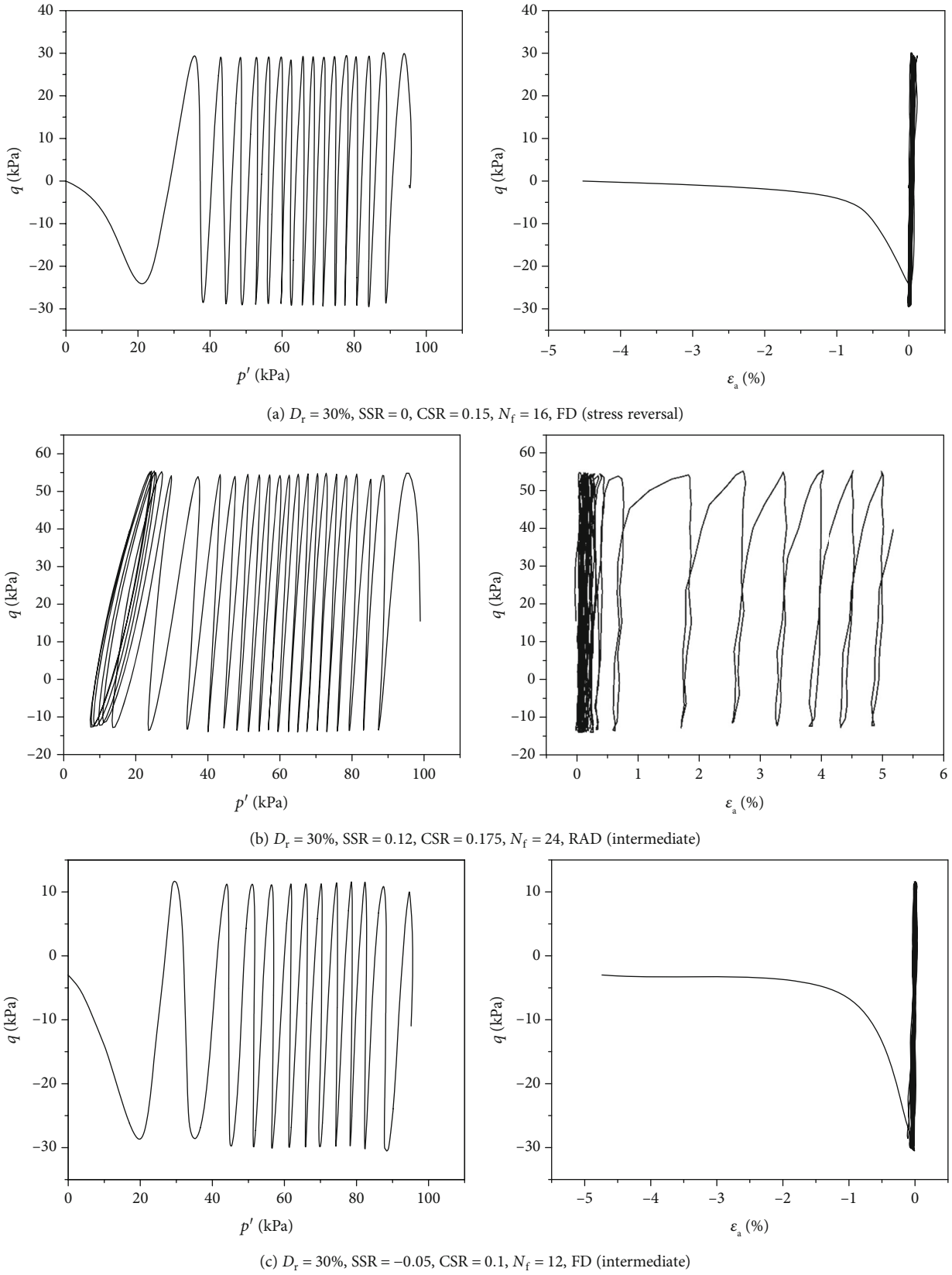


FIGURE 5: Cyclic response of loose sand with different initial static deviatoric stresses.

while in the later stage of cyclic loading, the average effective stress tends to be stable and is always greater than 0. At the same time, due to the existence of static deviatoric stress, the axial strain only accumulates on the compression side, and the rate of strain accumulation is relatively stable until the failure criterion of 5% single-amplitude (SA) axial strain has been satisfied at $N_f = 53$. The above behavior type which is significantly different from the CM behavior type can be named “residual deformation accumulation” (RDA).

Figure 4(c) shows the typical response of saturated dense sand considering static negative deviatoric stress under undrained cyclic loading and no stress reversal conditions ($SSR = -0.2$, $CSR = 0.125$). The same response pattern of “residual deformation accumulation” as shown in Figure 4(b) can also be observed on the tensile side, and the rate of strain accumulation is relatively stable until the failure criterion of 5% single-amplitude (SA) axial strain has been satisfied at $N_f = 16$.

By comparing the effective stress path and stress-strain curve in Figures 4(a)–4(c), it can be seen that under the condition of stress reversal, the undrained cyclic response of saturated dense sand is mainly manifested as CM response. The saturated dense sand under the condition of no stress reversal in Figure 4(c) and the saturated dense sand under the condition of intermediate as shown in Figure 4(b) mainly present the behavior type of RDA. Due to the difference of static deviatoric stress, the effective stress paths of the two show “wing-like” curves with different inclined directions in the later period of cyclic loading.

Figure 5(a) shows the typical response of saturated loose sand with isotropic consolidation suffering from symmetric cyclic load ($SSR = 0$, $CSR = 0.15$). It can be seen from the effective stress path in the figure that, under the condition of being undrained, the effective stress of the test sample decreases continuously with the cyclic loading. Eventually, failure occurs at the extension side, until the failure criterion of 5% double-amplitude (DA) axial strain has been satisfied at a number of cycles $N_f = 16$. This type of cyclic failure is classified as “flow deformation” (FD), manifested by a whole loss of strength and effective stress.

Figure 5(b) shows the typical response of saturated loose sand, which was suffering from positive static deviatoric stress before undergoing undrained cyclic loading ($SSR = 0.25$, $CSR = 0.25$). The same response pattern of “residual deformation accumulation” (RDA) as shown in Figure 3(b) can also be observed on the loose sand. And finally, the failure criterion of 5% axial strain has been satisfied at $N_f = 24$. Figure 5(c) shows the typical response of saturated loose sand considering static negative deviatoric stress under undrained cyclic loading. The same response pattern of “flow deformation” shown in Figure 5(a) can also be observed on the negative side. And the failure criterion of 5% axial strain has been satisfied at $N_f = 16$.

The above experimental results show that the behavior type of saturated sand under undrained cyclic load is not only related to the magnitude and direction of the initial stress state of the sample but also affected by the relative

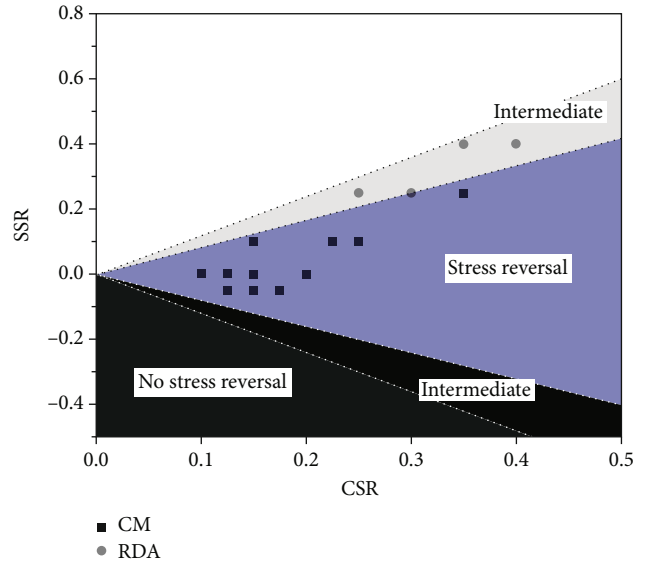


FIGURE 6: Summary of dense sand behavior types under different stress conditions.

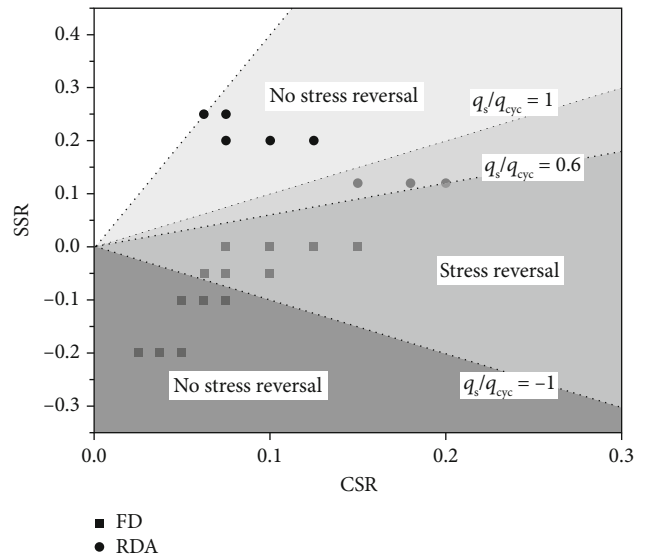


FIGURE 7: Summary of loose sand behavior types under different stress conditions.

density. Figures 6 and 7 show the distribution of dense and loose sand cyclic behavior types under different stress conditions, respectively. For dense sand as shown in Figure 6, the samples under the condition of stress reversal exhibit a “cyclic mobility” characterized by the “butterfly” stress path and the S-shaped stress-strain curves and the samples under the condition of no stress reversal or intermediate exhibit a “residual deformation accumulation” characterized by a stable effective path and axial strain on the initial deviatoric stress side. For loose sand as shown in Figure 7, there are mainly two types: “flow liquefaction” and “residual deformation accumulation.” It is found that the former was presented when $q_s/q_{cyc} < 0.6$,

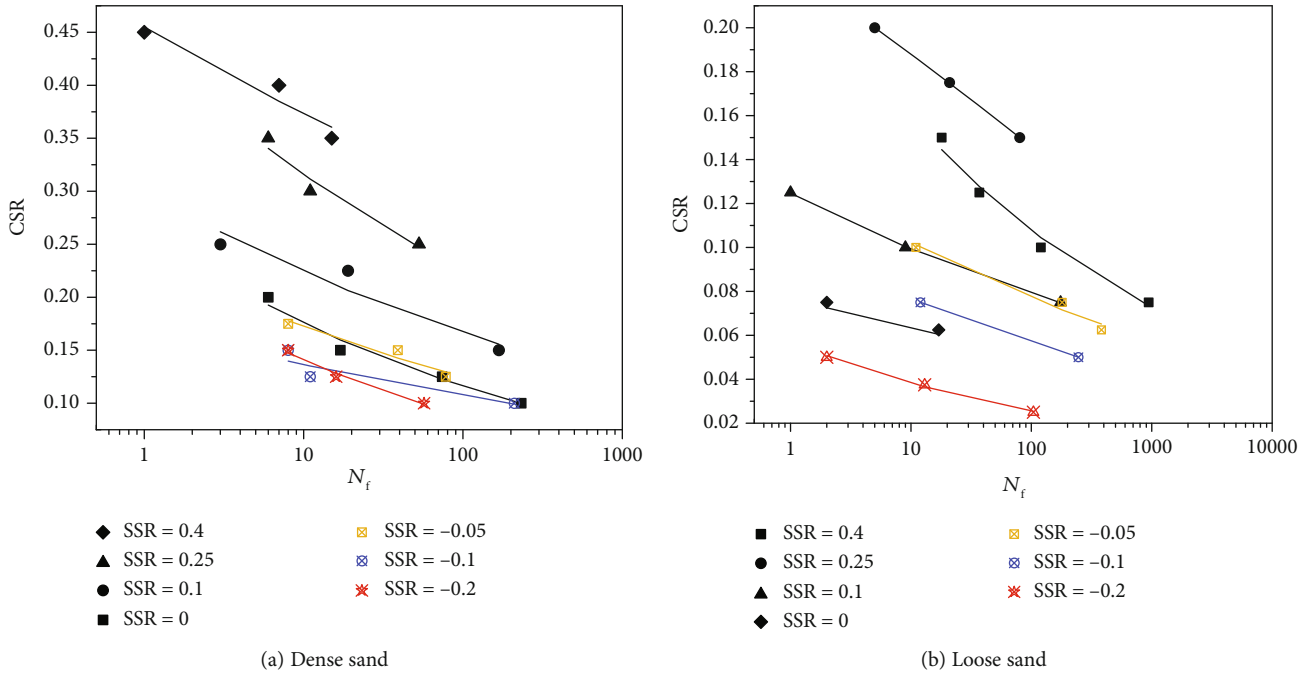


FIGURE 8: Relationship between CSR and N_f with various SSR.

characterized by complete loss of strength and effective stress, and the latter was presented when $q_s/q_{cyc} > 0.6$, indicating that the behavior types of loose sand have no obvious connection with stress reversal.

4. Cyclic Resistance

Figures 8(a) and 8(b), respectively, show the relationship between the number of cycles required to obtain axial strain of 5% N_f (DA or SA) and the cyclic stress ratio CSR required for saturated dense sand and saturated loose sand under different initial static deviatoric stress conditions. It can be seen from the single curve that the saturated dense sand and loose sand under anisotropic consolidation conditions ($SSR \neq 0$) are consistent with those under the condition of isotropic consolidation ($SSR = 0$); that is, for a given initial deviatoric stress, N_f decreases monotonically with the increase in CSR, indicating that the increase in cyclic stress amplitude reduces the cyclic stability of soil. It can be seen from the positions between the curves that the N_f -CSR curves under different initial stress states ($SSR \neq 0$) may appear either above or below the condition of isotropic consolidation ($SSR = 0$), indicating that the existence of initial static shear stress can either promote or inhibit cyclic strength.

To compare the cyclic resistance of various samples effectively, the cyclic resistance ratio $CRR_{N=20}$ is introduced, which is defined as the required CSR to cause failure at $N_f = 20$. It can be seen from Figure 9 that $CRR_{N=20}$ of dense sand increases monotonously with SSR, indicating that the initial deviatoric stress of compression has a promoting effect on the cyclic resistance of calcareous sand, while the initial deviatoric stress of tension has an inhibiting effect on the cyclic resistance of sand. The $CRR_{N=20}$ of

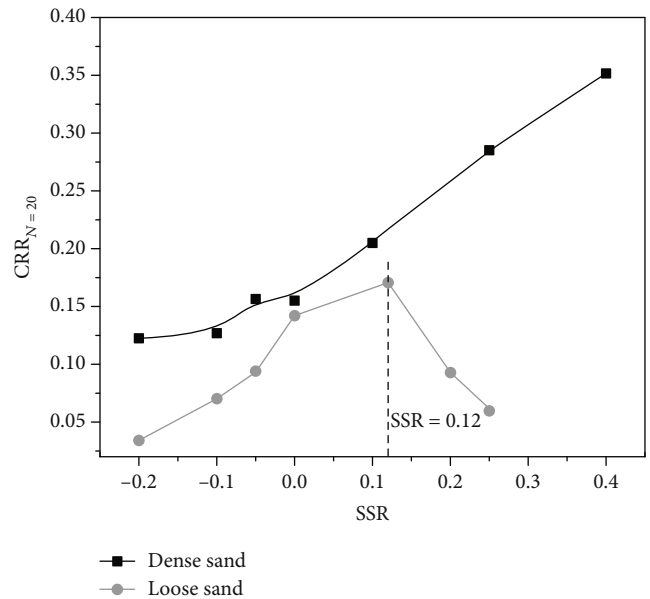


FIGURE 9: Relation curve between CRR for $N_f = 20$ and SSR.

loose sand first increased and then decreased with SSR and reached the peak strength at $SSR = 0.12$. In addition, for a given SSR, the cyclic resistance of dense sand is always above that of loose sand, indicating that the cyclic resistance of saturated sand increases with the increase in relative density D_r .

5. Energy Dissipation

According to formula, the dissipated energy density value W of the sample during cyclic loading can be calculated. The

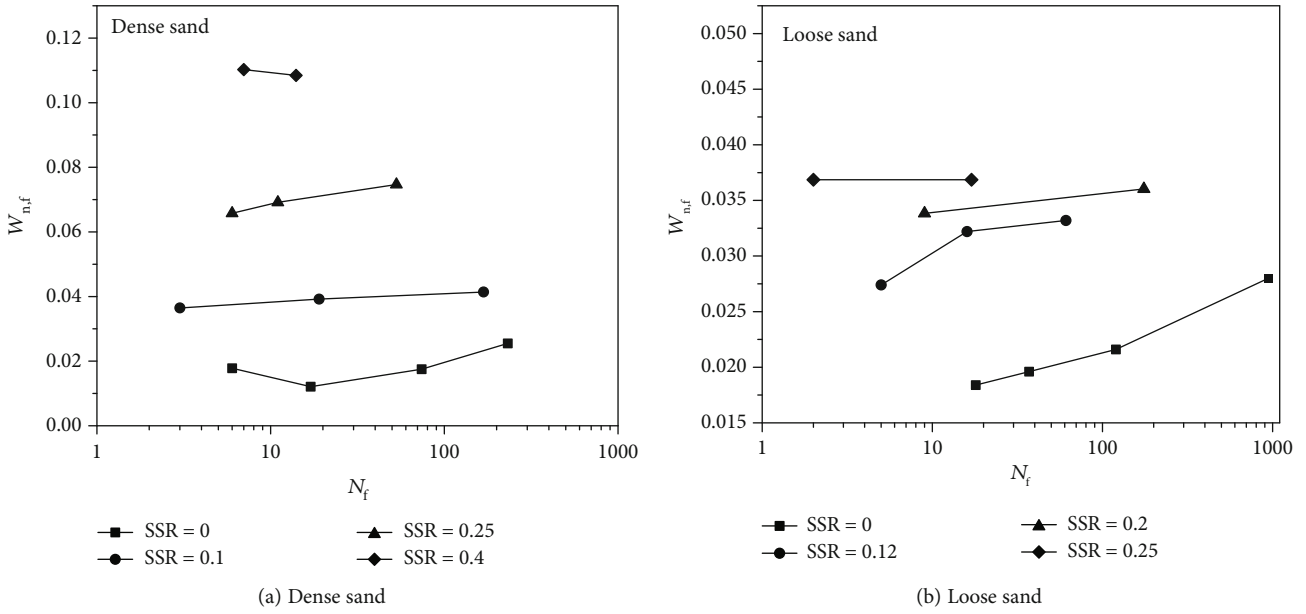


FIGURE 10: Relationship between dissipated energy and number of cycles required to cause liquefaction.

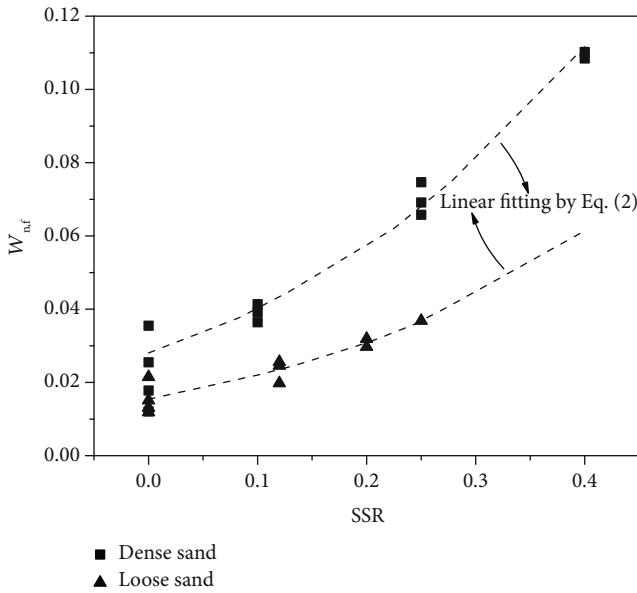


FIGURE 11: Relationship between the dissipated energy and static stress ratio.

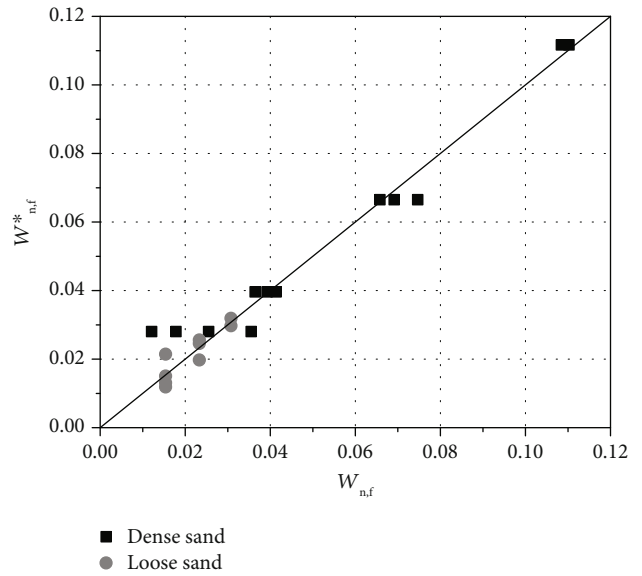


FIGURE 12: Comparison of measured and predicted values of dissipated energy.

normalized energy $W_{n,f}$, that is, the dissipated energy density normalized by the minor principal effective stress σ_3' needed for the failures outlined by 5% strain criteria, is shown in Figures 10(a) and 10(b), versus the specified range of failure cycles N_f for loose and dense sand, severally. As shown in the figure, for a given SSR, the $W_{n,f}$, corresponding to different N_f , fluctuates up and down in a small range without an obvious rule; meanwhile, according to the previous textual intensity law, for a given SSR, the size of N_f is only related to the value of CSR, so the various CSR has a negligible effect on the amount of required energy, which is consistent with the

experimental phenomenon on isotropic consolidated sand; in their opinion, the dissipated energy was virtually unambiguously correlative with elicited strain no matter the cyclic stress ratio (CSR) within the reconstituted sands [37–41].

The required energy dissipation illustrated in Figure 10 can be versus the SSR, as shown in Figure 11. It can be seen from the figure that the dissipated energy required by both loose sand and dense sand reaching the 5% strain standard increases monotonically with the increase in SSR. For a given SSR, the dissipated energy required by dense sand is always greater than that of loose sand.

The above experimental results show that the dissipated energy of saturated calcareous sand under undrained cyclic load is mainly related to the state of SSR and D_r . According to the interpretation conducted by Yang and Pan [36], the relationship between $W_{n,f}$, SSR, and D_r can adopt the following expression:

$$W_{n,f}^* = 10^{a(D_r - 0.78)} \cdot 10^{b(SSR - 1.0)}, \quad (2)$$

where a and b are empirical parameters. $a = 0.65$ and $b = 1.5$ are, respectively, recommended according to the data of this experiment. The dotted line in Figure 8 is the equation curve obtained by Equation (2), which can fit well with the experimental data. In addition, as shown in Figure 12, the measured value ($W_{n,f}$) and the predicted value ($W_{n,f}^*$) of dissipated energy are compared, and it can be found that they basically fall on the diagonal with a slope of 1, indicating that Equation (2) can reasonably predict the dissipated energy.

6. Conclusions

A series of undrained cyclic triaxial tests were conducted on reconstituted samples and principally involved the static shear impact on the cyclic state change behavior of two totally different compactness of saturated calcareous sand below different initial deviatoric stress and cyclic stress. Through the definition of dissipated energy, the energy variation law of loose sand and dense sand under cyclic load is analyzed, and the prediction formula of dissipated energy is given. Here are the main conclusions of this study:

- (1) Calcareous sand exhibits three cyclic response modes under different initial deviatoric stresses and cyclic stress combinations: (a) cyclic mobility, (b) residual accumulated deformation, and (c) flow liquefaction. The “cyclic mobility” response is characterized by the “butterfly” stress path and the “S”-shaped stress-strain curves at the end of cyclic loading. The “residual deformation accumulated” response is characterized by unilateral “wing-like” effective stress path at the end of cyclic loading. The “flow deformation” response is characterized by complete loss of strength, and effective stress occurs at the end of the cycle. The dense sand is mainly manifested as “cyclic mobility” and “residual deformation accumulated.” Loose sand is mainly manifested as “residual deformation accumulated” and “flow deformation.” The cyclic response mode is affected not only by the relative density but also by the initial deviatoric stress and cyclic stress
- (2) The initial deviatoric stress of compression has a promoting effect on the cyclic resistance of dense calcareous sand, while the initial deviatoric stress of tension has an inhibiting effect on the cyclic resistance of dense sand. The cyclic resistance of loose sand first increased and then decreased with SSR and reached the peak strength at SSR = 0.12. For a given SSR,

the cyclic resistance of saturated sand increases with the increase in the density

- (3) The dissipated energy required by saturated calcareous sand reaching the 5% strain standard increases monotonically with the increase in SSR. For a given SSR, the dissipated energy required by dense sand is always greater than that of loose sand. By considering the initial static deviatoric stress ratio and relative compactness, the equation can be obtained to predict the dissipated energy variation law of saturated calcareous sand under undrained cyclic load, and the rationality of the equation is effectively verified
- (4) A systematic experimental study on calcareous sand with fine content concerning the effects of both compressional and extensional static stresses is potential directions for future research on this topic

Nomenclature

a, b :	Fitting parameters for the energy prediction model
C_c :	Coefficient of curvature
C_u :	Coefficient of uniformity
CSR:	Cyclic stress ratio
$CRR_{N=20}$:	Resistance ratio
d_{10}, d_{30}, d_{60} :	Effective, median, and limited particle size, respectively
DA:	Double-amplitude axial strain
D_r :	Relative density of sand
G_s :	Specific gravity of sand
p' :	Mean normal effective stress
q_s, q_{cyc} :	Static and cyclic deviatoric stress, respectively
SA:	Single-amplitude axial strain
SSR:	Static stress ratio cyclic
N_f :	Number of cycles required to obtain axial strain of 5%
W :	Dissipated energy
$W_{n,f}$:	Required energy dissipation for failure (measured value)
$W_{n,f}^*$:	Required energy dissipation for failure (predicted value)
ε_a :	Axial strain.

Data Availability

The data used to support the findings of this study are available from the corresponding author upon request.

Conflicts of Interest

The authors declare that there are no conflicts of interest regarding the publication of this paper.

Acknowledgments

This paper gets its funding from the project (Grant Nos. 51778585 and 5207080379) supported by the National

Natural Science Foundation of China and Joint Fund of Zhejiang Natural Science Foundation Committee Power China Huadong Engineering Corporation (Grant No. LHZ19E090001).


References

- [1] C.-l. Zhu, J.-x. Zhang, N. Zhou, M. Li, and Y.-b. Guo, "Permeability of sand-based cemented backfill under different stress conditions: effects of confining and axial pressures," *Geofluids*, vol. 2021, Article ID 6657662, 13 pages, 2021.
- [2] Z.-h. Yan, C. Cao, M.-y. Xie et al., "Pressure behavior analysis of permeability changes due to sand production in offshore loose sandstone reservoirs using boundary-element method," *Geofluids*, vol. 2021, Article ID 6658875, 10 pages, 2021.
- [3] M. Hyodo, N. Aramaki, M. Itoh, and A. F. L. Hyde, "Cyclic strength and deformation of crushable carbonate sand," *Soil Dynamics and Earthquake Engineering*, vol. 15, no. 5, pp. 331–336, 1996.
- [4] J. Catano and M. A. Pando, "Static and dynamic properties of a calcareous sand from southwest Puerto Rico," *GeoFlorida 2010: Advances in Analysis, Modeling & Design*, pp. 842–851, 2010.
- [5] A. Fourie and G. Papageorgiou, "Defining an appropriate steady state line for Merriespruit gold tailings," *Canadian Geotechnical Journal*, vol. 38, no. 4, pp. 695–706, 2001.
- [6] M. R. Coop, K. K. Sorensen, T. B. Freitas, and G. Georgoutsos, "Particle breakage during shearing of a carbonate sand," *Géotechnique*, vol. 54, no. 3, pp. 157–163, 2004.
- [7] S. Donohue, C. O'Sullivan, and M. Long, "Particle breakage during cyclic triaxial loading of a carbonate sand," *Géotechnique*, vol. 59, no. 5, pp. 477–482, 2009.
- [8] D. Kong and J. Fonseca, "Quantification of the morphology of shelly carbonate sands using 3D images," *Géotechnique*, vol. 68, no. 3, pp. 249–261, 2018.
- [9] Y. Wu, N. Li, X.-z. Wang, and J. Cui, "Experimental investigation on mechanical behavior and particle crushing of calcareous sand retrieved from South China Sea," *Engineering Geology*, vol. 280, p. 105932, 2020.
- [10] S.-j. Rui, Z. Guo, T.-l. Si, and Y.-j. Li, "Effect of particle shape on the liquefaction resistance of calcareous sands," *Soil Dynamics and Earthquake Engineering*, vol. 137, p. 106302, 2020.
- [11] Y. Peng, X.-m. Ding, Y. Zhang, C.-l. Wang, and C.-y. Wang, "Evaluation of the particle breakage of calcareous sand based on the detailed probability of grain survival: an application of repeated low-energy impacts," *Soil Dynamics and Earthquake Engineering*, vol. 141, p. 106497, 2020.
- [12] M. R. Coop, "The mechanics of uncemented carbonate sands," *Géotechnique*, vol. 40, no. 4, pp. 607–626, 1990.
- [13] Y. R. Lv, X. Li, and Y. Wang, "Particle breakage of calcareous sand at high strain rates," *Powder Technology*, vol. 366, pp. 776–787, 2020.
- [14] W. Cai, Z.-l. Long, D.-m. Kuang, J.-m. Chen, and C.-p. Yan, "Effect of shear rate on shear strength and deformation characteristics of calcareous sand in direct shear test," *Rock and Soil Mechanics*, vol. 40, pp. 359–366, 2019.
- [15] T. Kokusho, "Major advances in liquefaction research by laboratory tests compared with in situ behavior," *Soil Dynamics and Earthquake Engineering*, vol. 91, pp. 3–22, 2016.
- [16] J. Yang, "Non-uniqueness of flow liquefaction line for loose sand," *Géotechnique*, vol. 52, no. 10, pp. 757–760, 2002.
- [17] M. Hyodd, A. F. L. Hyde, and N. Aramaki, "Liquefaction of crushable soils," *Géotechnique*, vol. 48, no. 4, pp. 527–543, 1998.
- [18] Z.-x. Yang and K. Pan, "Flow deformation and cyclic resistance of saturated loose sand considering initial static shear effect," *Soil Dynamics and Earthquake Engineering*, vol. 92, pp. 68–78, 2017.
- [19] P. Guo, F. Liu, G. Lei et al., "Predicting response of constructed tunnel to adjacent excavation with dewatering," *Geofluids*, vol. 2021, Article ID 5548817, 17 pages, 2021.
- [20] Y. Wang, C. H. Li, and J. Q. Han, "On the effect of stress amplitude on fracture and energy evolution of pre-flawed granite under uniaxial increasing-amplitude fatigue loads," *Engineering Fracture Mechanics*, vol. 240, p. 107366, 2020.
- [21] P. Guo, X. Gong, and Y. Wang, "Displacement and force analyses of braced structure of deep excavation considering unsymmetrical surcharge effect," *Computers and Geotechnics*, vol. 113, p. 103102, 2019.
- [22] S. S. Sharma and M. Fahey, "Evaluation of cyclic shear strength of two cemented calcareous soils," *Journal of Geotechnical and Geoenvironmental Engineering*, vol. 129, no. 7, pp. 608–618, 2003.
- [23] P. Guo, X. Gong, Y. Wang, H. Lin, and Y. Zhao, "Minimum cover depth estimation for underwater shield tunnels," *Tunnelling and Underground Space Technology*, vol. 115, p. 104027, 2021.
- [24] K. Pan, G.-y. Zhou, Z.-x. Yang, and Y.-q. Cai, "Comparison of cyclic liquefaction behavior of clean and silty sands considering static shear effect," *Soil Dynamics and Earthquake Engineering*, vol. 139, p. 106338, 2020.
- [25] K. Pan and Z.-x. Yang, "Effects of initial static shear on cyclic resistance and pore pressure generation of saturated sand," *Acta Geotechnica*, vol. 13, no. 2, pp. 473–487, 2018.
- [26] R. O. David and J. B. Berrill, "Energy dissipation and seismic liquefaction in sands," *Earthquake Engineering and Structural Dynamics*, vol. 10, no. 1, pp. 59–68, 1982.
- [27] S. Nemat-Nasser and A. A. Shokoh, "A Unified approach to densification and liquefaction of cohesionless sand in cyclic shearing," *Canadian Geotechnical Journal*, vol. 16, no. 4, pp. 659–678, 1979.
- [28] T. Kokusho, "Liquefaction potential evaluations: energy-based method versus stress-based method," *Canadian Geotechnical Journal*, vol. 50, no. 10, pp. 1088–1099, 2013.
- [29] K. Pan and Z.-x. Yang, "Evaluation of liquefaction potential of sand under random loading conditions: equivalent approach versus energy-based method," *Journal of Earthquake Engineering*, vol. 24, no. 1, pp. 59–83, 2017.
- [30] J. L. Figueroa, A. S. Saada, L. Liang, and N. M. Dahisaria, "Evaluation of soil liquefaction by energy principles," *Journal of Geotechnical Engineering*, vol. 120, no. 9, pp. 1554–1569, 1994.
- [31] Y. Jafarian, I. Towhata, M. H. Baziar, A. Noorzad, and A. Bahmanpour, "Strain energy based evaluation of liquefaction and residual pore water pressure in sands using cyclic torsional shear experiments," *Soil Dynamics and Earthquake Engineering*, vol. 35, no. 2, pp. 13–28, 2012.
- [32] Y. Wang, Y. F. Yi, C. H. Li, and J. Q. Han, "Anisotropic fracture and energy characteristics of a Tibet marble exposed to multi-level constant-amplitude (MLCA) cyclic loads: a lab-scale testing," *Engineering Fracture Mechanics*, vol. 244, p. 107550, 2021.

- [33] U. Kim, D. Kim, and L. Zhuang, "Influence of fines content on the undrained cyclic shear strength of sand-clay mixtures," *Soil Dynamics and Earthquake Engineering*, vol. 83, pp. 124–134, 2016.
- [34] R. Mohamad and R. Dobry, "Undrained monotonic and cyclic triaxial strength of sand," *Journal of Geotechnical Engineering*, vol. 112, no. 10, pp. 941–958, 1986.
- [35] S. Tori, F. Tatsuoka, S. Miura, Y. Yoshimi, S. Y. C. Engineer, and Y. M. C. Engineer, "Cyclic undrained triaxial strength of sand by a cooperative test program," *Soils and Foundations*, vol. 26, no. 3, pp. 117–128, 1986.
- [36] Z.-x. Yang and K. Pan, "Energy-based approach to quantify cyclic resistance and pore pressure generation in anisotropically consolidated sand," *Journal of Materials in Civil Engineering*, vol. 30, no. 9, article 04018203, 2018.
- [37] M. Konstadinou and V. N. Georgiannou, "Cyclic behaviour of loose anisotropically consolidated Ottawa sand under undrained torsional loading," *Géotechnique*, vol. 63, no. 13, pp. 1144–1158, 2013.
- [38] T. Kokusho, "Energy-based liquefaction evaluation for induced strain and surface settlement—evaluation steps and case studies," *Soil Dynamics and Earthquake Engineering*, vol. 143, p. 106552, 2021.
- [39] K. T. Law, Y. L. Cao, and G. N. He, "An energy approach for assessing seismic liquefaction potential," *Canadian Geotechnical Journal*, vol. 27, no. 3, pp. 320–329, 1990.
- [40] B. Li, G. Lei, P. Guo, G. Zhou, Z. Wang, and X. Gong, "Experimental investigation into limit void ratio characteristics of calcareous sands considering various factors," *Geofluids*, vol. 2021, Article ID 3686852, 9 pages, 2021.
- [41] S.-H. He, H.-F. Shan, T.-D. Xia, Z.-J. Liu, Z. Ding, and F. Xia, "The effect of temperature on the drained shear behavior of calcareous sand," *Acta Geotechnica*, vol. 16, no. 2, pp. 613–633, 2021.

Research Article

Analysis of Mechanical Properties of Sandstone under Freeze-Thaw Cycles Based on Digital Image Correlation (DIC)

Daguo Quan,^{1,2} Shuailong Lian,^{1,2} Jing Bi ,^{1,2} and Chaolin Wang^{1,2}

¹College of Civil Engineering, Guizhou University, Guiyang 550025, China

²Guizhou Provincial Key Laboratory of Rock and Soil Mechanics and Engineering Safety, Guiyang 550025, China

Correspondence should be addressed to Jing Bi; demonjjun@126.com

Received 23 May 2021; Accepted 5 July 2021; Published 9 August 2021

Academic Editor: Yu Wang

Copyright © 2021 Daguo Quan et al. This is an open access article distributed under the Creative Commons Attribution License, which permits unrestricted use, distribution, and reproduction in any medium, provided the original work is properly cited.

This paper studies the change of physical and mechanical properties of sandstone after freeze-thaw (F-T) cycle treatment. Firstly, the effects of the freeze-thaw treatment on the P-wave velocity of sandstone specimens are analyzed. It is found that the P-wave velocity decreases with the increase of the number of freeze-thaw cycles. Secondly, the effect of freeze-thaw treatment on the mechanical properties of sandstone is analyzed. The results show that the tensile strength and compressive strength of sandstone samples decrease with the increase of the number of freeze-thaw cycles. Finally, the digital image correlation (DIC) technique was used to collect the full-field deformation data of the samples, and the influence of freeze-thaw cycles on the deformation characteristics and fracture process of sandstone was analyzed. Based on the standard deviation of the principal strain in the field deformation data, the damage variables were proposed to characterize the damage process of sandstone samples in the Brazilian splitting test and the uniaxial compression test. The results show that the proposed damage variables can reflect the damage evolution process of the sample effectively. According to the variation of damage variables, the damage evolution process of sandstone specimens during the Brazilian splitting test and the uniaxial compression test can be divided into three stages: slow or negative growth stage, stable growth stage, and rapid growth stage. The research results are of great significance for predicting the failure mode and damage evolution of rock mass engineering by using digital image correlation technology.

1. Introduction

In China, cold regions account for 75.8% of the total land area [1]. In cold areas, ambient temperatures above or below the freezing point can trigger freeze-thaw cycles. The damage and deterioration of rock mass caused by freezing and thawing have caused a series of geological engineering problems, such as frost heave cracking of tunnel linings [2], deformation of high-speed railway subgrades [3], weathering and denudation of rock slope [4], and instability of high and steep dangerous rock mass [5]. Therefore, it is of great significance for engineering construction in cold areas to study the damaged mechanical properties of rock specimens after freeze-thaw treatment under load conditions.

In recent years, the research on freeze-thaw rocks has made rapid progress, and many outstanding achievements have been made [6, 7]. Fukuda et al. [8] studied the effects of temperature, particularly minimum and cooling temperatures, on rocks. Wen et al. [9] analyzed the physical and mechanical properties of rocks at low temperatures (-10°C , -20°C , -30°C , and -40°C), and the results showed that low temperature could greatly affect the frost resistance of rocks. Prick [10] determined the occurrence of freeze-thaw cycle damage based on the saturation threshold. Tan et al. [11] studied the damage mechanism of granite after freeze-thaw treatment and concluded that the mechanical parameters of granite decreased exponentially with the number of freeze-thaw cycles. Khanlari and Abdilor [12] studied the influence

of the pore size on the mechanical properties of sandstone after freeze-thaw treatment and concluded that the particle size and particle contact did not achieve the expected effect on the damage of sandstone samples during the freeze-thaw cycle.

At the same time, with the emergence of some advanced equipment, researchers have applied it in rock mechanics tests and tried to study the damage evolution process of the rock mass from multiscale. The acoustic emission (AE) technique is a common method for the nondestructive testing of rock. The spatiotemporal evolution characteristics of acoustic emission events can be used to reflect the damage state of rock during loading [13, 14]. In order to characterize the failure process of rock more intuitively, some parameters such as acoustic emission energy, event counts, and ringing counts were applied to the damage theory, and a new damage variable was proposed to reflect the evolution of rock damage [15]. The computer tomography (CT) and the scanning electron microscope (SEM) are also extensively used in the study of failure modes and microscopic crack propagation of rock [16, 17].

DIC technology, as a new optical detection method, can be used to study the surface strain field information of materials without out-of-plane motion. It possesses many advantages, such as simple experimental steps, high accuracy, and high computational efficiency [18–22]. At present, many researchers begin to apply DIC in mechanical tests to obtain the full-field strain information on the surface of quasibrittle materials. For example, Leplay et al. [23] analyzed the crack propagation law and failure mode on the surface of ceramic materials by DIC; Zhang et al. [24] studied the fracture mode of sandstone under compression through digital image correlation technology. Ma et al. [25] used DIC to analyze the damage evolution process of granodiorite during the splitting test. Therefore, the DIC technology can be used to effectively characterize the damage evolution process of rock materials.

Compared with CT, SEM, and AE, DIC has many advantages such as full-field observation, high accuracy, low cost, and large test range [26]. Therefore, based on the advantages of the above DIC technology, this paper studies the deformation characteristics and failure process of sandstone after freeze-thaw cycles. The damage evolution process of sandstone under freeze-thaw cycles is quantitatively analyzed using the standard deviation of the principal strain as the damage variable. The research results are of great significance for predicting the failure mode and damage evolution of rock mass engineering by using digital image correlation technology.

2. Experimental Setup and Specimen Preparation

2.1. 2D-DIC Setup. DIC technology has been widely used in recent years because of its unique advantages of noncontact measurement, full-field strain, displacement data extraction, and high precision. This paper adopts the VIC-2D field strain test system. It is mainly composed of an industrial camera, lens, light source, speckle tool, computer, and image analysis software.

2.1.1. Principle of 2D-DIC. As an optical measurement technique, DIC measures the two-dimensional or three-dimensional coordinates of the whole field constantly changing on the sample surface during the entire mechanical test process. The measured coordinate fields can be used to derive further the areas of displacement, strain, strain rate, velocity, and curvature of interest (Quantities-of-Interest, QOI). As shown in Figure 1, the core idea of DIC is to estimate the coordinates and displacements of full-field speckle based on a series of digital speckle images of sample surfaces by solving optimization problems. The basic assumption in DIC is that the speckle pattern on the sample surface should deform along with the sample, whether natural or artificial. Therefore, the speckle image taken on the sample surface can be used for correlation calculation to obtain its full-field coordinates, which can be used to characterize the shape, movement, and deformation of the sample surface. A single-camera system to measure the 2D coordinates of a flat sample surface is called 2D-DIC.

2.1.2. 2D-DIC Image Acquisition Method. As can be seen in Figure 1, the VIC-2D-DIC image acquisition system is mainly composed of a fixed-focus lens with a focal length of 50 mm, a CCD industrial camera, two high-brightness light sources, a computer, and image analysis software. The image size of the CCD industrial camera is 4096×3000 . In the test, the camera should be aligned with the center of the sample, and the image size of the sample should be adjusted to reach the same size as the camera vision. DIC collects images at a rate of 10000 per second during the experiment.

2.2. Sample Preparation and Test Procedure

2.2.1. Sample Preparation. The rock sample used in this paper is fine red sandstone, and the fine red sandstone sample is processed and polished according to the Standard of the International Society for Rock Mechanics (ISRM). According to the requirements of the paper, two sizes of sandstone samples are processed: one is a standard cylinder sample with a height of about 100 mm and a diameter of about 50 mm and the other is a standard disc specimen with a height of about 25 mm and a diameter of about 50 mm. The processed sandstone samples are shown in Figure 2.

2.2.2. Test Procedure. Rock lithology, temperature, water saturation rate, and the number of cycles are the critical influencing factors of the freeze-thaw cycle test. Therefore, according to the requirements, the test plan is as follows:

- (1) To select samples with similar lithology for the test, the wave velocity of the two processed samples was measured, and the sandstone samples with similar wave velocities were selected
- (2) The sample is dried by an electric thermostatic drying oven, making the sample more easily absorb water and saturate. The dried sample is immersed in the vacuum water-filling device for 24 hours to make it fully saturated

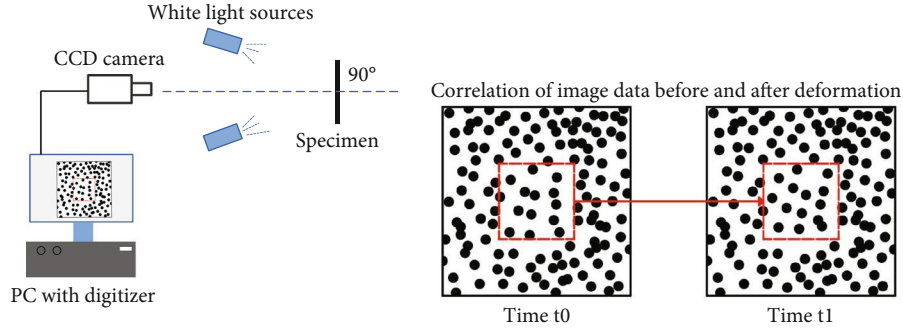


FIGURE 1: 2D-DIC schematic diagram.

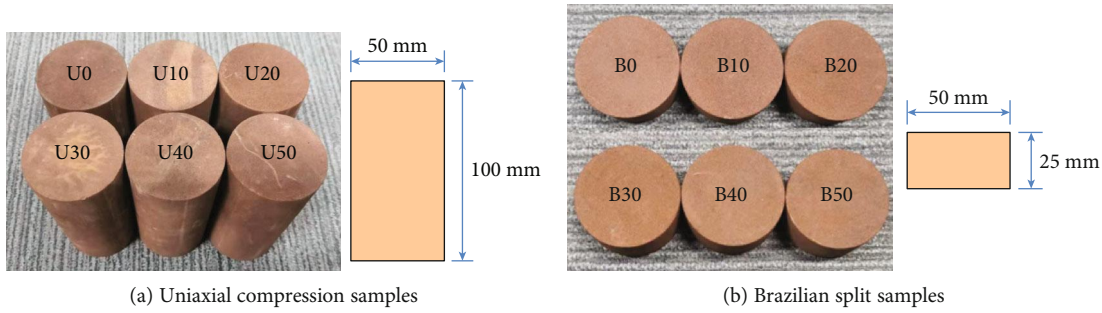


FIGURE 2: The processed sandstone samples.

(3) Then, the samples are placed into the freeze-thaw cycle test equipment for the freeze-thaw cycle treatment. The freezing temperature was set as $-20^{\circ}\text{C} \pm 2^{\circ}\text{C}$, and the freezing time was 3 hours. The thawing temperature was set as $20^{\circ}\text{C} \pm 2^{\circ}\text{C}$, the thawing time was 3 hours, and the one freeze-thaw cycle was 6 hours. The relationship between temperature and time in freeze-thaw cycles can be seen in Figure 3. Then, 0, 10, 20, 30, 40, and 50 freeze-thaw cycle tests were completed. After the freeze-thaw cycle test, the wave velocity of the sample was measured to observe the degree of damage. The grouping of freeze-thaw cycle test samples can be seen in Table 1

(4) The test equipment used in this study is the DSZ-1000 stress-strain controlled rock mechanics testing system, and the maximum axial force that could be applied by the test system was 1000 kN. For the DIC principle, an ideal speckle with a diameter of 0.33 mm should be made on the sample surface by the speckle tool before the start of the mechanical test. After the speckle production, dry the sample surface with the normal temperature air of a hairdryer and put the sample on the DSZ-1000 test machine. Adjust the position of the sample and the angle of the camera lens so that the center of the sample is aligned with the center of the camera field of view. The loading method of this mechanical test is force control; the loading rate was set as 0.05 MPa/s. The primary test devices and their processes are shown in Figure 4

3. Results and Analysis

3.1. Variation of Longitudinal Wave Velocity of Sandstone after Freeze-Thaw Treatment. In this test, ultrasonic equipment was used to test the internal condition of sandstone before and after freeze-thaw treatment. Ultrasonic monitoring is a nondestructive testing method that uses ultrasonic waves to propagate in a certain velocity and direction in the material with internal defects and then obtain the obvious change of its acoustic properties. Because of the fast propagation speed of the P-wave in materials, the P-wave is generally used to detect material properties.

As can be seen in Figure 5, with the increase of the number of freeze-thaw cycles, the wave velocity of saturated rock samples showed a decreasing trend. Quadratic polynomial functions can represent both, and the fitting formula is as follows:

$$\bar{V} = -0.011N^2 - 3.412N + 1728. \quad (1)$$

\bar{V} is the average value of the P-wave velocity, N is the number of cycles, and the relative coefficient between the two is $R^2 = 0.987$. Along with the whole freeze-thaw cycle test, the longitudinal wave velocity of the sandstone sample decreases greatly, with a maximum decrease of 10.84%. The main reason for the decrease of the P-wave velocity is that the water forms change under the action of temperature, which exerts a certain large frost heave force on the interior of the sandstone, resulting in the expansion and increase of microcracks and micropores in the sandstone. At the same time, in the melting process of the ice in the sandstone, the

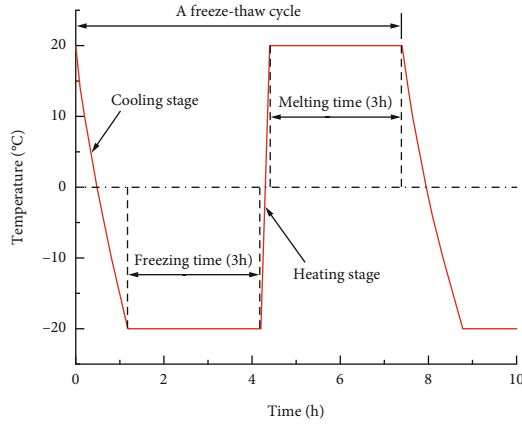


FIGURE 3: The relationship between temperature and time in freeze-thaw cycle test.

external water keeps entering new microcracks and micropores, resulting in the increasing proportion of water in the sandstone. However, the propagation velocity of the P-wave in water is lower than that in rock, so the propagation velocity of the P-wave in the sandstone is significantly reduced after freeze-thaw treatment.

3.2. Study on the Law of Tensile Strength of Sandstone under Freeze-Thaw Cycles

3.2.1. Load-Displacement Curves of Sandstone Samples. The load-displacement curves of B0, B10, B20, B30, B40, and B50 are shown in Figure 6; taking B50 as an example, four key points, O, A, B, and C, were selected from the load-displacement curve of the B50 specimen and analyzed in the following section.

As can be seen in Figure 6, the load-displacement curves of sandstone samples after freeze-thaw treatment were basically the same under the splitting test. By comparing these six groups of load-displacement curves, it is found that when the number of freeze-thaw cycles increases continuously, the tensile strength and displacement of sandstone samples both show a decreasing trend. When the number of freeze-thaw is small, the peak tensile strength and peak displacement decrease slowly, indicating that the effect of freeze-thaw on tensile strength is small in the early stage. With the increase of freeze-thaw times, the internal damage of sandstone accumulates continuously. The peak tensile load and peak displacement decrease rapidly, and the decrease is noticeable compared with that in the early freeze-thaw period. This phenomenon indicates that after multiple freeze-thaw cycles, the sandstone suffered severe damage inside the rock, which led to the more easy failure of the rock under tensile load during the Brazilian splitting test, showing a decreasing trend of both tensile load and displacement.

3.2.2. Failure Characteristics of Sandstone Samples under Different Freeze-Thaw Cycles. In this section, the characteristic X-direction main strain was analyzed by selecting the strain cloud diagram of ROI (region of interest) on the samples B0, B10, B20, B30, B40, and B50. Table 2 shows

the evolution process of the X-direction main strain cloud diagram of the sample before reaching the maximum load in the splitting test.

From the results obtained in Table 2, for the sandstone specimens B0, B10, B20, B30, B40, and B50 under the condition of freeze-thaw cycles, when the load applied reaches $0.2\sigma_c$, the strain field appears in the entire Brazilian disc due to load action. In the Brazilian splitting test, stress concentration was generated at the end of the Brazilian disc due to loading along the diameter. The maximum strain value in the strain field appeared at both ends of the Brazilian disc. When the load reaches $0.9\sigma_c$, a large strain concentration region is formed at the end of the Brazilian disc, and the deformation region of the strain band begins to gather, making the strain band more obvious. With the increase of load, cracks in the Brazilian disc develop rapidly. The strain field is constantly spreading from one end of the sample to the other, which makes the strain concentration area larger. When the load reaches the peak σ_c , microcracks appear on the surface of one end of the disc, indicating that the Brazilian disc starts to crack from one end. Finally, under the continuous action of the load, the microcrack expands rapidly from one end of the disc to the center, resulting in a larger crack.

As mentioned above, during the splitting test of the freeze-thaw-treated sandstone sample, the pores and cracks in the disk will increase, and with the increase of the number of freeze-thaw cycles, the strain difference between the end and the middle of the sandstone gradually decreases. The crack initiation location of the Brazilian disc may change from the end to the middle.

3.3. Study on the Law of Compressive Strength of Sandstone under Freeze-Thaw Cycles

3.3.1. Stress-Strain Curve of Sandstone Samples. The stress-strain curves of U0, U10, U20, U30, U40, and U50 are shown in Figure 7; taking U50 as an example, five key points, O, A, B, C, and D, were selected from the stress-strain curve of the U50 sample and analyzed in the following section.

As can be seen in Figure 7, the stress-strain curves of sandstone samples after freeze-thaw treatment were basically the same under the uniaxial compression test, which all go through the compaction stage, elastic stage, and yield stage, and then, the sample is destroyed abruptly. The failure characteristic is a typical brittle failure. By comparing these six groups of stress-strain curves, it is found that with the increase of the number of freeze-thaw cycles, the peak strength presents a decreasing trend, while the peak strain presents an increasing trend. When the number of freeze-thaw cycles is less than 30 times, the stress-strain curve of sandstone is similar to the stress-strain curve without freeze-thaw, which is relatively smooth, and the peak strain only increases by 6.62%, until the failure occurs suddenly at the ultimate load. When the number of freeze-thaw cycles reaches 50 times, the peak strength decreases, and the peak strain increases significantly. The stress-strain curve is smooth and stable in the compaction zone and the elastic zone. However, after entering the plastic zone, the stress-strain curve fluctuates wildly because the freeze-thaw cycle

TABLE 1: The grouping of freeze-thaw cycle test samples.

Grouping basis and number		U0	U10	U20	U30	U40	U50
Loading method	The uniaxial compression	U0	U10	U20	U30	U40	U50
	The Brazilian splitting	B0	B10	B20	B30	B40	B50

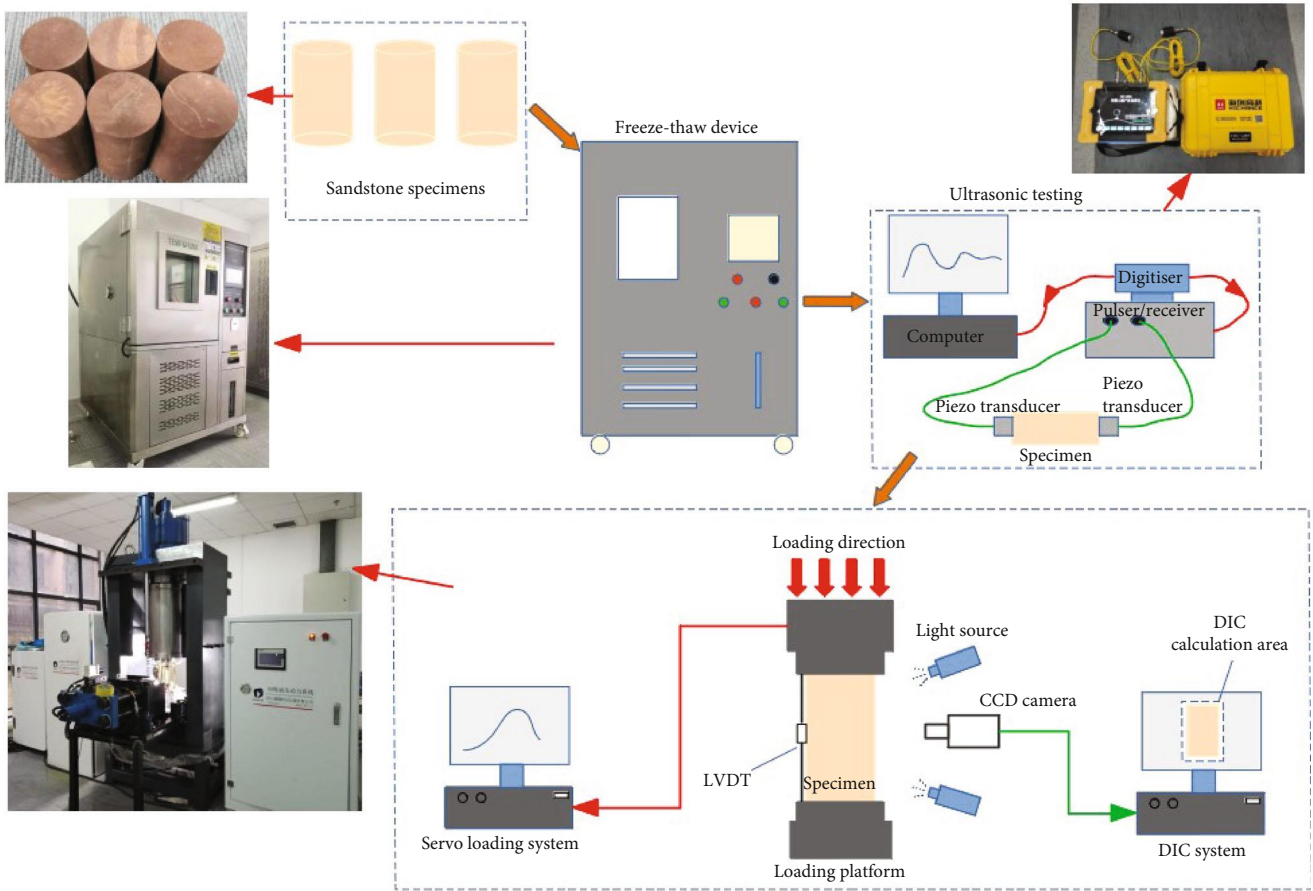


FIGURE 4: The main equipment and test flow chart.

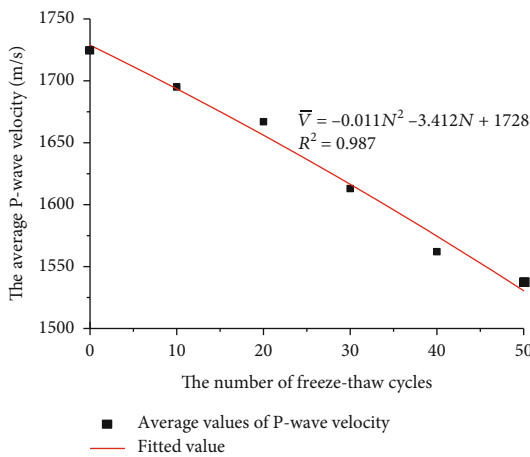


FIGURE 5: Variation of mean P-wave velocity of uniaxial compression samples under different freeze-thaw cycles.

causes irreversible damage to the interior of the sandstone. With the increase of the number of freeze-thaw cycles, the frost heave force caused by water freezing squeezes the micropores inside the sandstone, causing damage to the sample. With the passage of time, the accumulation of damage leads to the continuous expansion of microcracks, which leads to the decrease of peak strength and the increase of peak strain.

3.3.2. *Failure Characteristics of Sandstone Samples under Different Freeze-Thaw Cycles.* In this section, the deformation and failure modes were analyzed by selecting the strain cloud diagram (X-direction) of ROI (region of interest) on the samples U0, U10, U20, U30, U40, and U50. Table 3 shows the evolution process of the X-direction strain cloud diagram of the sample before reaching the maximum load in the uniaxial compression test.

From the results obtained in Table 3, for the sandstone sample U0 without freeze-thaw cycle treatment, before the

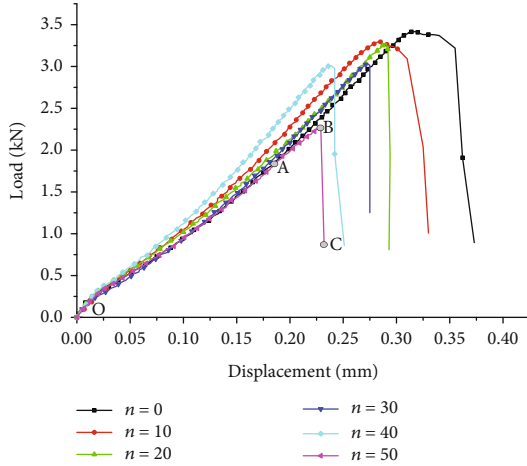


FIGURE 6: Load-displacement curves of Brazilian splitting test.

peak stress reaches $0.4\sigma_c$, some smaller strain concentration regions are distributed in the upper right side of the sample U0. When the peak stress is between $0.5\sigma_c$ and $0.6\sigma_c$, the strain concentration area in the upper right part of the sample begins to diverge to the periphery and gradually develops into a relatively clear strain band. When the peak stress is between $0.7\sigma_c$ and $0.9\sigma_c$, the strain concentration region at both ends of the sample begins to form initially and extends along the vertical direction, slowly connecting with the strain concentration region in the middle of the right side of the sample. When the peak stress σ_c is reached, the strain concentration region at the tip of the specimen develops rapidly, and its propagation path is consistent with the actual failure crack of the specimen.

For the sandstone sample U10 after ten freeze-thaw cycles, before the peak stress up to $0.6\sigma_c$, some small strain concentration areas are scattered at the end of the U10 sample. When the stress increases from $0.7\sigma_c$ to $0.9\sigma_c$, the strain concentration zone develops rapidly at the lower end of the specimen. Unlike the failure process of specimen U0, the width of the strain concentration zone increases gradually. When the peak stress σ_c is reached, a large strain concentration area is formed at the lower end of the sample. For samples U20 and U40, the process from loading to failure is similar to that of U10, and strain concentration areas are formed at the lower end, and when the peak stress σ_c is reached, the lower end of the sample will be damaged first.

For the sandstone sample U30 after 30 freeze-thaw cycles, before the peak stress up to $0.4\sigma_c$, there is a small strain concentration area scattered in the middle of the surface of specimen U30. When the stress reaches $0.5\sigma_c$, the strain concentration area appears at the upper end of the sample. When the stress increases from $0.6\sigma_c$ to $0.9\sigma_c$, the strain concentration area develops rapidly in the middle and the end of the sample. When the peak stress σ_c is reached, an oblique strain concentration area and a strain concentration area parallel to the sample are formed. For the sandstone sample U50, the process from loading to failure is similar to that of U30. A small strain concentration area is formed at one end of the sample of U30 at first. With the increase of stress, the strain

concentration area gradually widens and moves towards the other end of the sample. Finally, an oblique strain concentration area is formed in the sample.

In summary, in the process of uniaxial compression of sandstone samples after freeze-thaw treatment, the more times of freeze-thaw cycles, the greater the strain of sandstone samples will be. The reason is that the freezing and thawing cause irreversible damage in the interior of the sandstone. With the accumulation of freeze-thaw damage, the influence of internal frost heaving force on the microcracks gradually increases, leading to the expansion and connection of microcracks, and the bearing capacity of the specimen decreases, and the number of deformation increases.

4. Damage Assessment of Sandstone Samples under Freeze-Thaw Cycles Based on 2D-DIC

4.1. *Establishment of Damage Variables.* In rock mechanics, the degradation of rock strength is caused by internal damage, and the accumulation of the damage will inevitably lead to the change of the strain field on the surface of the specimen. Therefore, the internal damage of rock can be represented by an index of strain field concentration. Based on the above, damage variables [27] can be expressed by

$$D = \frac{S}{S_{\max}}. \quad (2)$$

In Equation (2), S is the standard deviation of the strain field, as shown in Equation (3). S_{\max} is the maximum value of S (generally at the failure point) during the whole loading process.

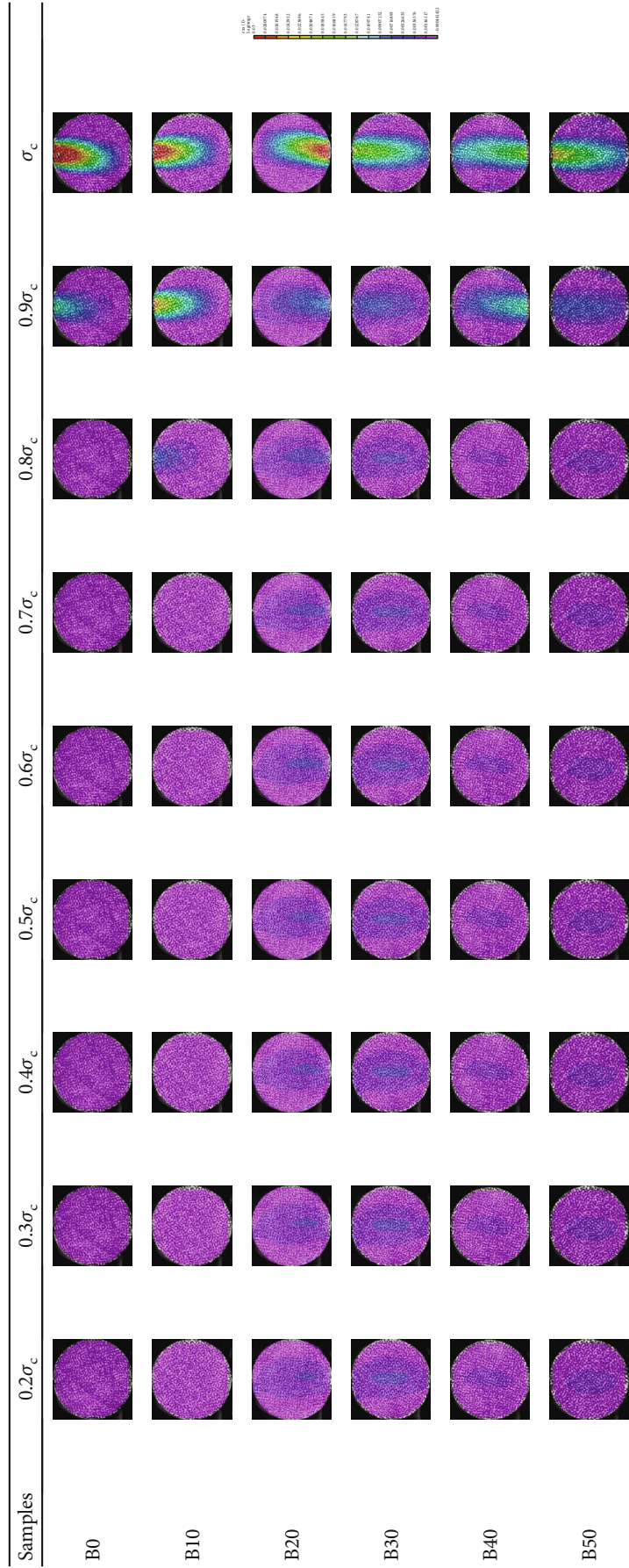
$$S = \sqrt{\frac{1}{n-1} \sum_{k=1}^n (X_k - \bar{X})^2}. \quad (3)$$

In Equation (3), X_k is the strain value at each point within the strain field. \bar{X} is the average of X_k , and n is the total number of data points in the strain field.

4.2. *Damage Analysis of Samples under the Brazilian Splitting Test.* The damage evolution process of B0, B10, B20, B30, B40, and B50 specimens has been analyzed. After the image analysis software was used to obtain the principal strain of the strain field in the X -direction of the sample, and the maximum standard deviation of the principal strain in the X -direction was calculated, the maximum standard deviation was substituted into Equation (2) to calculate the damage variable.

As shown in Figure 8, the damage evolution of sandstone in the splitting process under different freeze-thaw cycles can be divided into three stages: in the first stage (period of slow or negative growth), the damage variable was small. This is because the sample in this stage is subjected to a small load, which is not enough to destroy the cohesion inside the sandstone and is not enough to generate new microcracks and micropores. Even due to the action of the load, the internal microcracks in B0 and B10 are compressed and closed, the

TABLE 2: Evolution process of the X-direction main strain of samples B0, B10, B20, B30, B40, and B50.



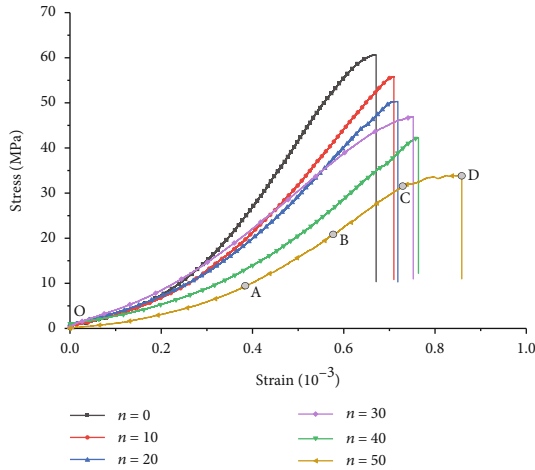


FIGURE 7: Stress-strain curves of uniaxial compression.

elastic modulus increases, and the damage variable decreases, resulting in a negative damage phenomenon. With the loading process, the sample is in the second stage (period of steady growth), the connection between mineral particles is destroyed, primary cracks expand, secondary cracks appear, cracks gradually converge, and the growth rate of the damage variable accelerates. Finally, the damage evolution enters the third stage (period of rapid growth), and a large number of cracks develop rapidly. When the load of the sample reaches the maximum, the main crack expands rapidly until the final barrier is broken through, and the sample is damaged. The damage variable increased sharply.

4.2.1. Damage Evolution Analysis of B50. In this part, the load-displacement curve and the damage-strain curve of sample B50 are compared and analyzed. As can be seen in Figure 9, taking B50 as an example, four key points O, A, B, and C were taken from the load-displacement curve of sample B50 for analysis. The damage-strain curve of sample B50 with 50 cycles of freeze-thaw treatment can be divided into three stages during the splitting test.

In the initial OA stage (linear elastic stage), the sample bears a small load. The damage variable was small, about 0.05. Due to the influence of freeze-thaw cycles, the internal damage of the sample accumulates seriously. Under the action of the load, the damage variable begins to increase. When it reaches the AB stage (elastic-plastic stage), new microcracks and micropores begin to appear inside the sample and continue to develop stably. The growth rate of the damage variable increased significantly and increased to 0.9. When approaching the maximum load, the specimen is in the BC stage (failure stage). The strain develops intensively along the loading diameter, cracks appear on the loading diameter, and transient fracture occurs. The damage variable reached the maximum value [28–35].

4.3. Damage Analysis of Samples under the Uniaxial Compression Test. The damage evolution process of U0, U10, U20, U30, U40, and U50 specimens has been analyzed. After the image analysis software was used to obtain the prin-

cipal strain of the strain field in the X-direction of the sample, and the maximum standard deviation of the principal strain in the X-direction was calculated, the maximum standard deviation was substituted into Equation (2) to calculate the damage variable.

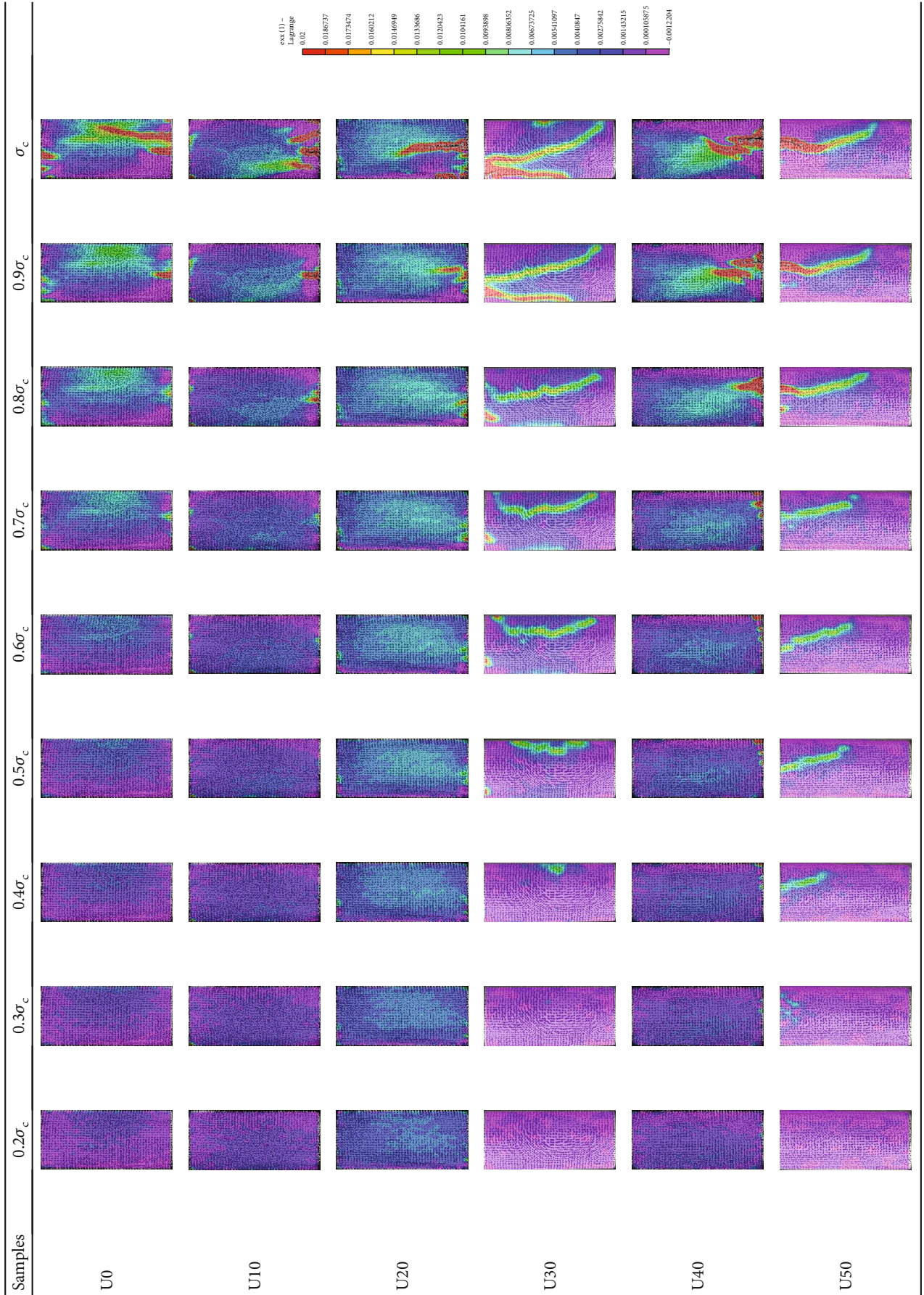
As shown in Figure 10, the damage evolution process of sandstone samples treated by freeze-thaw cycles under uniaxial compression tests can be divided into three stages: in the first stage (period of slow or negative growth), the sandstone will undergo a compaction process at the initial stage of loading, during which the microcracks and micropores in the sandstone will be closed. (Of course, new microcracks and micropores may occur, but the closing trend is greater than the generating trend.) In this way, the rock's elastic modulus will increase, the damage variable of the rock will decrease, and the rock will produce negative damage. This process will approximately continue until the rock enters the linear elastic stage. After that, the damage evolution of rock enters the second stage (period of steady growth), in which the damage variable of rock begins to increase continuously, which means that the generation trend of microcracks and micropores in the rock is greater than the closing trend. This stage occurs until the macroscopic failure of rock. After a macroscopic failure occurs, the damage evolution of rock enters the third stage (period of rapid growth) of accelerated development, in which the damage development of rock is obviously accelerated. Finally, the rock loses its bearing capacity completely, and the damage variable is close to the ultimate damage variable of rock failure [36–46].

When the number of freeze-thaw cycles exceeds 10, the specimen is greatly affected by freeze-thaw cycles. Compared with the Brazilian splitting test, the damage variable of sandstone under uniaxial compression test changes slowly, which is consistent with the actual failure process of the sample and better verifies the feasibility and high precision of DIC used to measure the deformation and failure process of rock.

4.3.1. Damage Evolution Analysis of U50. In this part, the stress-strain curve and damage-strain curve of sample U50 are compared and analyzed. As can be seen in Figure 11, taking U50 as an example, five key points O, A, B, C, and D were taken from the stress-strain curve of sample U50 for analysis. The damage-strain curve of sample U50 with 50 cycles of freeze-thaw treatment during the uniaxial compression test can be roughly divided into four stages.

Due to the accumulation of damage in the sample under freeze-thaw cycles, the damage variable cannot be regarded as 0 before loading. Due to the action of load in the OA stage (crack closure stage), the internal microcracks and micropores of the sample are gradually compacted or even closed, resulting in negative damage to the rock. Then, the entire loading process enters the AB stage (linear elastic stage); that is, the linear elastic stage and the sandstone sample are further compressed. As far as the damage inside the specimen is concerned, it enters the linear elastic damage stage. In this stage, it is found that the apparent damage variable is small, and the damage degree of the specimen is low on the whole. When the loading stress level reaches the stress state of point B, the damage of the sample begins to accumulate, and the

TABLE 3: Evolution process of the X-direction main strain of samples U0, U10, U20, U30, U40, and U50.



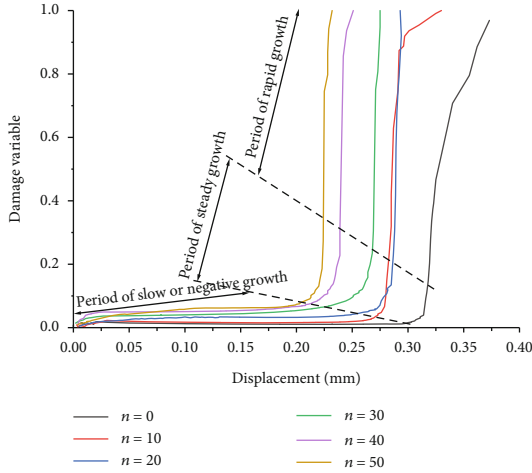


FIGURE 8: The damage variable evolution of B0, B10, B20, B30, B40, and B50 specimens.

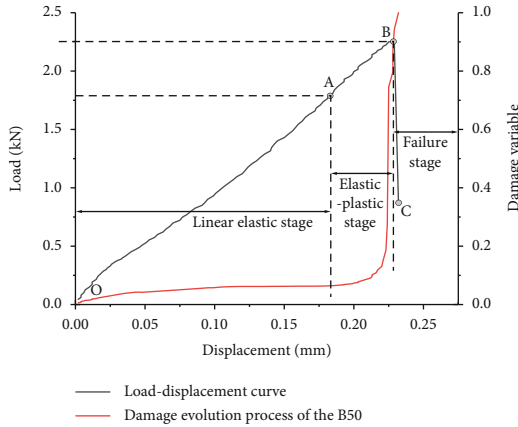


FIGURE 9: The relationship between the damage variable and the loading curve of the B50.

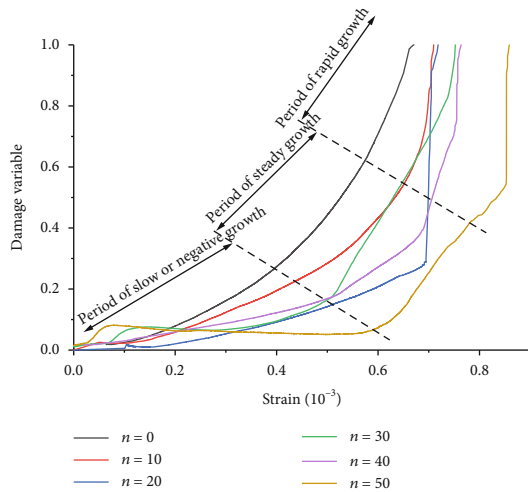


FIGURE 10: The damage variable evolution of U0, U10, U20, U30, U40, and U50 specimens.

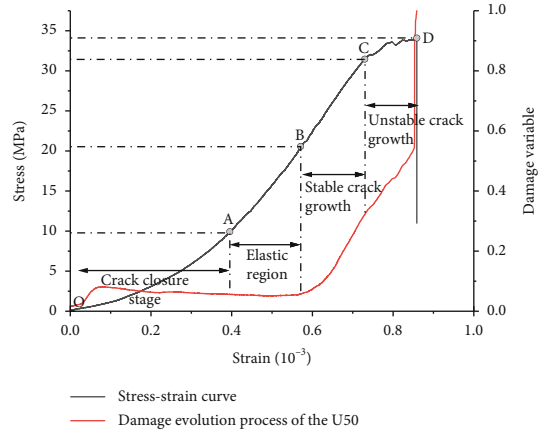


FIGURE 11: The relationship between the damage variable and the loading curve of the U50.

damage variable begins to evolve. The loading BC section (stable crack growth) of the sample is an elastoplastic development stage. Among them, the damage evolution develops from the inside of the specimen to the surface, and the damage variable value steadily increases, namely, the elastoplastic damage. The CD section (unstable crack growth) is the plastic stage, and the failure behavior of the specimen at this stage varies from microscopic failure to macroscopic failure. The damage variable increases sharply and reaches the plastic damage stage. When the whole loading process reached point D, the value of the damage variable changed to 1, and the bearing capacity of the specimen decreased rapidly.

5. Conclusions

The study of mechanical properties and the damage evolution process of rock mass in cold regions is an important issue for practical applications. In this paper, the DIC method is used to study the deformation characteristics and failure process of freeze-thaw-treated sandstone. Taking the standard deviation of principal strain as the damage variable, the damage evolution process of freeze-thaw-treated sandstone was quantitatively analyzed. Based on this study, the following conclusions can be drawn:

- (1) During the whole process of freeze-thaw damage, the frost heave force generated by the constant change of water morphology makes the cracks expand and increase continuously, leading to the emergence of new cracks. The results show that the greater the number of freeze-thaw cycles, the lower the P-wave propagation velocity is
- (2) According to the splitting test and uniaxial compression test of the sandstone samples after freeze-thaw treatment, the tensile strength and compressive strength of the sandstone samples after freeze-thaw treatment show a decreasing trend with the increase of the number of freeze-thaw cycles. Moreover, the more times the freeze-thaw cycles are treated, the faster the tensile strength and compressive strength decrease

- (3) Using DIC technology, it was found that with the increase of the number of freeze-thaw cycles, the internal pores and cracks in the Brazilian splitting disc became more and more intensive during the loading process, and the strain difference between the end and the middle of the sandstone gradually decreased. The crack initiation location of the Brazilian disc may change from the end to the middle. However, for the uniaxial compression test, due to the influence of the end effect, the localization strain band is always generated from one end and gradually widens and moves to the other end of the sample, finally forming an oblique or vertical localization strain band in the middle of the sample
- (4) The full-field strain of the specimen surface was measured by the digital image correlation technique, and the damage variable which could characterize the deformation characteristics of the specimen was proposed based on the standard deviation of the principal strain. The damage evolution process of sandstone specimens after freeze-thaw treatment can be divided into three stages: the period of slow or negative growth stage, the period of steady growth stage, and the rapid growth stage. The results show that the proposed damage variables can better describe the damage evolution process of sandstone specimens after freeze-thaw treatment

Data Availability

Some or all data, models, or code that support the findings of this study are available from the corresponding author (demonjjun@126.com) upon reasonable request.

Conflicts of Interest

The authors declare that they have no conflicts of interest to this work. The authors also declare that they do not have any commercial or associative interest that represents a conflict of interest in connection with the work submitted.

Acknowledgments

This work was supported by the National Natural Science Foundation of China (52064006, 52004072, and 51779021), Science and Technology Support Project of Guizhou ([2020]4Y044, [2021]N404, and [2021]N511), Talents of Guizhou University (Grant No. 201901), and Special Research Funds of Guizhou University (Grant Nos. 201903, 202011, and 202012).

References

- [1] X. Wang, L. Pan, H. C. Lau, M. Zhang, L. Li, and Q. Zhou, "Reservoir volume of gas hydrate stability zones in permafrost regions of China," *Applied Energy*, vol. 225, pp. 486–500, 2018.
- [2] Y. Lai, W. Hui, W. Ziwang, L. Songyu, and D. Xuejun, "Analytical viscoelastic solution for frost force in cold-region tunnels," *Journal of the China Railway Society*, vol. 31, no. 3, pp. 227–234, 2000.
- [3] G. Xu, J. Qi, and H. Jin, "Model test study on influence of freezing and thawing on the crude oil pipeline in cold regions," *Cold Regions Science and Technology*, vol. 64, no. 3, pp. 262–270, 2010.
- [4] M. Krautblatter, D. Funk, and F. K. Günzel, "Why permafrost rocks become unstable: a rock-ice-mechanical model in time and space," *Earth Surface Processes & Landforms*, vol. 38, no. 8, pp. 876–887, 2013.
- [5] S. P. Pudasaini and M. Krautblatter, "A two-phase mechanical model for rock-ice avalanches," *Journal of Geophysical Research Earth Surface*, vol. 119, no. 10, pp. 2272–2290, 2014.
- [6] J. Bi, P. F. Liu, and F. Gan, "Effects of the cooling treatment on the dynamic behavior of ordinary concrete exposed to high temperatures," *Construction and Building Materials*, vol. 248, article 118688, 2020.
- [7] P. C. Li and H. Wang, "A novel strategy for the crossarm length optimization of PSSCs based on multi-dimensional global optimization algorithms," *Engineering Structures*, vol. 238, article 112238, 2021.
- [8] M. Fukuda, T. Harimaya, and K. Harada, "The study on effect of rock weathering by freezing and thawing to rock mass collapse," *Gekkan-Chikyu*, vol. 18, no. 9, pp. 574–578, 1996.
- [9] L. Wen, X. B. Li, H. Y. Tang, and L. Weng, "Study of physico-mechanical characteristics of rock under different frozen-thawed circle temperature range and its engineering application," *Engineering mechanics*, vol. 34, pp. 247–256, 2017.
- [10] A. Prick, "Critical degree of saturation as a threshold moisture level in frost weathering of limestones," *Permafrost and Periglacial Processes*, vol. 8, no. 1, pp. 91–99, 1997.
- [11] X. Tan, W. Chen, J. Yang, and J. Cao, "Laboratory investigations on the mechanical properties degradation of granite under freeze-thaw cycles," *Cold Regions Science & Technology*, vol. 68, no. 3, pp. 130–138, 2011.
- [12] G. Khanlari and Y. Abdilor, "Influence of wet-dry, freeze-thaw, and heat-cool cycles on the physical and mechanical properties of upper red sandstones in Central Iran," *Bulletin of Engineering Geology and the Environment*, vol. 74, no. 4, pp. 1287–1300, 2015.
- [13] L. Dexing, W. Enyuan, K. Xiangguo, J. Haishan, W. Dongming, and A. Muhammad, "Damage precursor of construction rocks under uniaxial cyclic loading tests analyzed by acoustic emission," *Construction and Building Materials*, vol. 206, pp. 169–178, 2019.
- [14] Z. P. Zhang, R. Zhang, H. P. Xie, J. F. Liu, and P. Were, "Differences in the acoustic emission characteristics of rock salt compared with granite and marble during the damage evolution process," *Environmental Earth Sciences*, vol. 73, no. 11, pp. 6987–6999, 2015.
- [15] C. A. Tang and X. H. Xu, "Evolution and propagation of material defects and Kaiser effect function," *Journal of Seismological Research*, vol. 13, no. 2, pp. 203–213, 1990.
- [16] Z. Cui and W. Han, "In situ scanning electron microscope (SEM) observations of damage and crack growth of shale," *Microscopy and Microanalysis*, vol. 24, no. 2, pp. 107–115, 2018.
- [17] X. Y. Wu, P. Baud, and T. F. Wong, "Micromechanics of compressive failure and spatial evolution of anisotropic damage in Darley Dale sandstone," *International Journal of Rock Mechanics and Mining Sciences*, vol. 37, no. 1-2, pp. 143–160, 2000.

- [18] X. Zhang, J. Chen, Z. Wang, N. Zhan, and R. Wang, "Digital image correlation using ring template and quadrilateral element for large rotation measurement," *Optics and Lasers in Engineering*, vol. 50, no. 7, pp. 922–928, 2012.
- [19] B. Pan, K. M. Qian, H. M. Xie, and A. Asundi, "Two-dimensional digital image correlation for in-plane displacement and strain measurement: a review," *Measurement Science & Technology*, vol. 20, no. 6, article 062001, 2009.
- [20] L. B. Jiang, H. M. Xie, and B. Pan, "Speeding up digital image correlation computation using the integral image technique," *Optics and Lasers in Engineering*, vol. 65, pp. 117–122, 2015.
- [21] Z. Y. Jiang, Q. Kemao, H. Miao, J. L. Yang, and L. Q. Tang, "Path-independent digital image correlation with high accuracy, speed and robustness," *Optics and Lasers in Engineering*, vol. 65, pp. 93–102, 2015.
- [22] Y. L. Kang and H. M. Xie, "Micro and nano metrology in experimental mechanics," *Optics and Lasers in Engineering*, vol. 48, no. 11, pp. 1045–1045, 2010.
- [23] P. Leplay, J. Rethore, S. Meille, and M. C. Baietto, "Identification of damage and cracking behaviours based on energy dissipation mode analysis in a quasi-brittle material using digital image correlation," *International Journal of Fracture*, vol. 171, no. 1, article 9624, pp. 35–50, 2011.
- [24] H. Zhang, G. Y. Huang, H. P. Song, and Y. L. Kang, "Experimental investigation of deformation and failure mechanisms in rock under indentation by digital image correlation," *Engineering Fracture Mechanics*, vol. 96, pp. 667–675, 2012.
- [25] S. P. Ma, D. Yan, X. Wang, and Y. Y. Cao, "Damage observation and analysis of a rock Brazilian disc using high-speed DIC method," *Applied Mechanics & Materials*, vol. 70, pp. 87–92, 2011.
- [26] M. M. Kou, X. R. Liu, Z. Q. Wang, and S. D. Tang, "Laboratory investigations on failure, energy and permeability evolution of fissured rock-like materials under seepage pressures," *Engineering Fracture Mechanics*, vol. 247, article 107694, 2021.
- [27] Y. Y. Cao, S. P. Ma, X. Wang, and Z. Y. Hong, "A new definition of damage variable for rock material based on the spatial characteristics of deformation fields," *Advanced Materials Research*, vol. 146–147, pp. 865–868, 2010.
- [28] Y. Zhao, C. L. Wang, and J. Bi, "Analysis of fractured rock permeability evolution under unloading conditions by the model of elastoplastic contact between rough surfaces," *Rock Mechanics and Rock Engineering*, vol. 53, no. 12, article 2224, pp. 5795–5808, 2020.
- [29] Y. Zhao, C. L. Wang, Y. F. Zhang, and Q. Liu, "Experimental study of adsorption effects on shale permeability," *Natural Resources Research*, vol. 28, no. 4, article 9476, pp. 1575–1586, 2019.
- [30] Y. Zhao, P. F. He, Y. F. Zhang, and L. Wang, "A new criterion for a toughness-dominated hydraulic fracture crossing a natural frictional interface," *Rock Mechanics and Rock Engineering*, vol. 52, no. 8, pp. 2617–2629, 2019.
- [31] Z. J. Wu, L. F. Fan, Q. S. Liu, and G. W. Ma, "Micro-mechanical modeling of the macro-mechanical response and fracture behavior of rock using the numerical manifold method," *Engineering Geology*, vol. 225, pp. 49–60, 2017.
- [32] Q. S. Liu, Z. C. Qian, and Z. J. Wu, "Micro/macro physical and mechanical variation of red sandstone subjected to cyclic heating and cooling: an experimental study," *Bulletin of Engineering Geology and the Environment*, vol. 78, no. 3, pp. 1485–1499, 2019.
- [33] Z. J. Wu, X. Y. Xu, Q. S. Liu, and Y. T. Yang, "A zero-thickness cohesive element-based numerical manifold method for rock mechanical behavior with micro-Voronoi grains," *Engineering Analysis with Boundary Elements*, vol. 96, pp. 94–108, 2018.
- [34] L. F. Fan, J. W. Gao, X. du, and Z. J. Wu, "Spatial gradient distributions of thermal shock-induced damage to granite," *Journal of Rock Mechanics and Geotechnical Engineering*, vol. 12, no. 5, pp. 917–926, 2020.
- [35] F. Wu, H. Zhang, Q. L. Zou, C. B. Li, J. Chen, and R. B. Gao, "Viscoelastic-plastic damage creep model for salt rock based on fractional derivative theory," *Mechanics of Materials*, vol. 150, article 103600, 2020.
- [36] W. Fei, L. Jie, Z. Quanle, L. Cunbao, C. Jie, and G. Renbo, "A triaxial creep model for salt rocks based on variable-order fractional derivative," *Mechanics of Time-Dependent Materials*, vol. 25, no. 1, pp. 101–118, 2021.
- [37] X. P. Zhou, J. Bi, and Q. H. Qian, "Numerical simulation of crack growth and coalescence in rock-like materials containing multiple pre-existing flaws," *Rock Mechanics and Rock Engineering*, vol. 48, no. 3, pp. 1097–1114, 2015.
- [38] J. Bi, X. P. Zhou, and Q. H. Qian, "The 3D numerical simulation for the propagation process of multiple pre-existing flaws in rock-like materials subjected to biaxial compressive loads," *Rock Mechanics and Rock Engineering*, vol. 49, no. 5, pp. 1611–1627, 2016.
- [39] J. Z. Zhang and X. P. Zhou, "AE event rate characteristics of flawed granite: from damage stress to ultimate failure," *Geophysical Journal International*, vol. 222, no. 2, pp. 795–814, 2020.
- [40] X. P. Zhou, Y. X. Zhang, Q. L. Ha, and K. S. Zhu, "Micromechanical modelling of the complete stress-strain relationship for crack weakened rock subjected to compressive loading," *Rock Mechanics and Rock Engineering*, vol. 41, no. 5, pp. 747–769, 2008.
- [41] Y. Zhao, J. Bi, C. L. Wang, and P. F. Liu, "Effect of unloading rate on the mechanical behavior and fracture characteristics of sandstones under complex triaxial stress conditions," *Rock Mechanics and Rock Engineering*, no. article 2515, 2021.
- [42] Y. T. Yang, X. H. Tang, H. Zheng, Q. S. Liu, and L. He, "Three-dimensional fracture propagation with numerical manifold method," *Engineering Analysis with Boundary Elements*, vol. 72, pp. 65–77, 2016.
- [43] Y. T. Yang, X. H. Tang, H. Zheng, Q. S. Liu, and Z. J. Liu, "Hydraulic fracturing modeling using the enriched numerical manifold method," *Applied Mathematical Modeling*, vol. 53, pp. 462–486, 2018.
- [44] Y. Zhao, C. L. Wang, M. Y. Teng, and J. Bi, "Observation on microstructure and shear behavior of mortar due to thermal shock," *Cement & Concrete Composites*, vol. 121, article 104106, 2021.
- [45] Y. Zheng, C. X. Chen, T. T. Liu, and Z. H. Ren, "A new method of assessing the stability of anti-dip bedding rock slopes subjected to earthquake," *Bulletin of Engineering Geology and the Environment*, vol. 80, no. 5, article 2188, pp. 3693–3710, 2021.
- [46] S. Q. Yang and H. W. Jing, "Strength failure and crack coalescence behavior of brittle sandstone samples containing a single fissure under uniaxial compression," *International Journal of Fracture*, vol. 168, no. 2, pp. 227–250, 2011.

Research Article

Investigation into Macro- and Microcrack Propagation Mechanism of Red Sandstone under Different Confining Pressures Using 3D Numerical Simulation and CT Verification

Wen Zhang , Yan-yu Chen , Jin-ping Guo , Sai-sai Wu , and Cheng-yuan Yan 

School of Resources Engineering, Xi'an University of Architecture and Technology, Xi'an 710055, China

Correspondence should be addressed to Wen Zhang; zhangwen@xauat.edu.cn and Sai-sai Wu; saisai.wu@xauat.edu.cn

Received 25 May 2021; Accepted 14 July 2021; Published 3 August 2021

Academic Editor: Yu Wang

Copyright © 2021 Wen Zhang et al. This is an open access article distributed under the Creative Commons Attribution License, which permits unrestricted use, distribution, and reproduction in any medium, provided the original work is properly cited.

The growth and evolution features of crack are of great significance to study the failure mechanism of rock mass and evaluate the stability of the cavity. In this study, in order to obtain the mechanics parameters and external macroscopic crack propagation characteristics of red sandstone, triaxial compression tests were carried out. Based on the experimental results, a numerical model was established through the reasonable parameter calibration by the PFC^{3D} software. The internal and external crack propagation processes of red sandstone under triaxial compression were simulated. Moreover, to verify the simulation results, the CT scanning and three-dimensional reconstruction technologies were used to observe the internal crack state of the specimens. The results showed that the internal crack failures occurred first at the end of the rock specimen. Then, the microcracks continued to accumulate and expand under the combined action of axial stress and confining pressure. The accumulated microcracks finally converged to form a macroscopic oblique shear failure. Based on the homogenizing treatment and reasonable parameter calibration, the internal and external crack expansion and evolution processes of the rock were simulated by the PFC^{3D} model and the simulation results are consistent with the results obtained from the triaxial compression test and the CT scanning. The macro- and microfailure mode of crack propagation of the specimen deepens the understanding of rock failure mechanism. The PFC^{3D} homogenization simulation method provides a new feasible method to study the macro- and microfailure mode of internal and external crack propagation of rock under compression.

1. Introduction

The rock mass is an anisotropic heterogeneous body formed by one or more rock-forming minerals in a certain combination that contains structural defects such as cracks and joints. The composition of rock minerals, combination mode, and development degree of cracks and joints determine the physical and mechanical properties of the rock [1–7]. In the ore excavation process, the rock mass is subjected to complex loading and unloading stress processes, which leads to the deformation and destruction of the rock mass. The distribution and expansion of its fissures directly affect mining safety, such as underground water inrush and roof failure which are all developed and evolved from cracks and other weak surfaces [8, 9]. In underground mining, the development of fissures is one of the major causes leading to the destruction

of rock projects [10–12]. Understanding the crack propagation mechanism can provide a feasible basis for engineering safety design. Effective monitoring methods can identify the distribution and expansion of cracks in rock masses for safety early warning, which help achieve safe and efficient mining.

The expansion and evolution of fissures have long been a hot issue of concern to researchers all around the world [13–15]. The laboratorial examination is one of the commonly used methods to study the fissure behavior of rock mass. Mokhtarian et al. used the filling material to simulate the rock and studied its weak plane failure under triaxial compression [16]. Yang et al. studied the strength and failure characteristics of red sandstone by the triaxial compression test [17]. Ma et al. investigated the effects of temperature on granite failure characteristics through high-temperature triaxial tests [18]. Jiang et al. analyzed both the uniaxial

compressive and triaxial compressive strength of sandstone under air-drying, natural, and saturation conditions [19]. Most of the studies above focused on rock mechanical properties and failure characteristics under triaxial action, but only few studies investigated the mechanism of the internal crack prorogation and expansion.

CT scanning technology can accurately characterize the internal fractures of the rock. Kawakata et al. used the X-ray CT scanning system to study the fracture process of granite under different load conditions [20]. Christe et al. evaluated the degree of alteration of highly tectonized carbonate rock specimens based on X-ray computed tomography and led to a diagnosis of alteration which appeared objective, precise, and in agreement with the visual observations [21]. Yang et al. investigated the failure mechanism of transversely isotropic composite rock-like material on the microlevel by CT, and the 3D volume renders were in good agreement with the actual surface crack photographs of specimens [22]. Zhu et al. simulated and predicted the mechanical properties and fracture characteristics of the rock based on the CT three-dimensional numerical simulation [23]. CT scanning technology can respond to changes in the rock specimen's internal fractures in a nondestructive and multi-directional manner, but the expense is high and the current measurement sample size is small, which cannot meet the research of large-size specimens.

Because of its convenience and accuracy, the numerical simulation methods were used by many researchers to study rock behaviors [24–26]. Fan et al. established the bonded particle models containing flaws or/and openings in order to investigate the mechanical properties as well as the crack propagation characteristics of the rock under uniaxial compression [27]. Wu et al. used PFC to simulate rocks with different cavities and fissures and found three rock bridge coalescence modes: tensile, shear, and tensile-shear modes [28]. Zhang et al. studied the cracking process in rock-like material containing a single flaw by PFC^{2D} and found that the numerical simulation could reproduce the indoor test phenomenon [29]. It is worth noting that two-dimensional numerical simulation is a plane stress model, which is easier to limit the boundary conditions and apply the loads, but it is quite different from the actual model. In order to establish a numerical model consisting with the actual simulation, Yang et al. introduced the establishment of a three-dimensional model of agglomerated particles and pores based on CT scanning [30]. Zhao used CT reconstruction technology to compare the PFC^{2D} and PFC^{3D} models and found that the internal structure built in 3D is more complete, which showed more realistic macromechanical behavior and deformation patterns [31]. The consistency between the three-dimensional simulation and the actual model determines that the simulation results are closer to the real macromechanical behavior, which is more conducive to the study of the development of macro- and microfissures inside the specimen.

To reveal the crack evolution process of red sandstone, triaxial compression tests on red sandstone under different confining pressures were carried out to obtain the mechanical parameters and failure characteristics. The typical red

sandstone specimen was scanned by CT experiment after failure to obtain each scan layer CT image, and AVIZO software was used to reconstruct the CT images in three dimensions. Based on homogenization processing, the deformation and failure models of red sandstone were established by PFC^{3D} software. The macro- and microcrack failure characteristics and processes under different confining pressures were simulated. Through the comparison of the results obtained from laboratory tests, CT images, and PFC^{3D} simulations, the feasibility of the PFC^{3D} model to study the crack propagation characteristics of the rock specimen was verified. The proposed methodologies and the obtained results provide a new method for the study of rock mechanical properties and damage mechanisms.

2. Experiment

2.1. Material Preparation. The rock specimens used in the tests are red sandstone, and all the specimens were taken from the same rock. The specimen's homogeneity is good, which reduces the influence of the dispersion of the specimens on the experimental results. The specimens were prepared according to the standards of the "International Society of Rock Mechanics" and cut into standard cylindrical specimens with a diameter of 50 mm and a height of 100 mm.

2.2. Experimental Procedures. The triaxial compression test and CT scan test were carried out on the prepared red sandstone specimens.

2.2.1. Triaxial Compression Test. The SAM-2000 testing machine was used to perform triaxial compression experiments on the specimens (Figure 1). The red sandstone specimens were tested under confining pressures of 5, 10, 15, and 20 MPa. The stress-strain curves and deformation parameters of the rock specimens under different confining pressures were obtained, which provided basic data to study the crack propagation laws and conduct the numerical simulations.

2.2.2. CT Scan Test. The MS-Voxel450 CT scanner (Figure 2(a)) was used to perform CT scanning analysis on the red sandstone specimen to study the inner fracture expansion after the triaxial test.

The CT scanning system principle is based on the different X-ray absorption capabilities of the different materials when X-rays penetrate through the materials (Figure 2(b)). When X-rays pass through an object, part of the X-ray energy is absorbed and the X-rays are attenuated. The unabsorbed X-rays pass through the test material and reach the detector. The detector converts the received X-ray energy into electrical signals, which are digitized by the computer.

3. Triaxial Test Results and Deformation Characteristic Analysis

3.1. Triaxial Test Results and Analysis. In order to reduce the influence of temperature on the test results, the laboratory temperature was strictly controlled at 20(±0.5)°C during the tests. The basic mechanical parameters and the

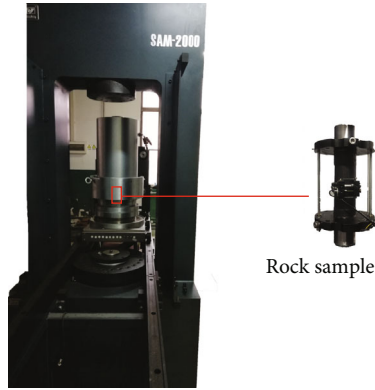


FIGURE 1: SAM-2000 triaxial testing machine.

corresponding stress-strain curves of red sandstone under different confining pressures were obtained, as shown in Table 1 and Figure 3.

From Figure 3(a), it can be seen that the stress-strain curves of red sandstone specimens under different confining pressures can be roughly divided into four stages. The stages are described as the elastic deformation stage, microcrack stable propagation stage, microcrack unstable propagation stage, and the postfailure stage (Figure 3(b)). The characteristics of each stage are described in detail as follows: (1) The elastic deformation stage. The curve is approximately a straight line; the rock undergoes elastic deformation. The strain continues to increase, and no new cracks are generated in this stage. If the load is unloaded at this stage, the strain can be restored. (2) The stage in which microcracks bifurcate and expand stably. The microcracks inside the rock sample begin to branch, expand, or generate new microcracks under the action of axial force. In this stage, the microcracks stop to expand once the load stops increasing. (3) The stage that the microcracks are expanding unstably. The stress at point II is the yield stress. When the stress value exceeds point II, even if the load stops increasing, the microcracks are unceasingly expanding, and this stress-strain curve presents a concave shape. (4) The postfailure stage. The macroscopic failure occurs at point III. As the strain increases, the rock continues to fail, and microcracks continue to penetrate to form a macroscopic fracture plane, and the bearing capacity of the rock decreased, until point IV, the rock broke completely. The stresses σ_I , σ_{II} , σ_{III} , and σ_{IV} correspond to four stages, which are called the elastic limit, yield stress, peak value of strength, and residual strength of rock, respectively.

At the same time, Figure 3(a) can also clearly reflect that the rock specimen's peak strength increases as the confining pressure increases, but the increments are gradually decreasing. At the confining pressures of 5, 10, 15, and 20 MPa, the maximum axial stresses are 59.70, 80.99, 98.21, and 110.12 MPa, respectively. For every additional 5 MPa increasing in confining pressure, the value of maximum axial stress of red sandstone increases by 21.29, 17.22, and 11.91 MPa. The axial strain at the peak increases with the increase of confining pressure. When the confining pressure is 5 MPa, the axial strain at the peak is 0.76×10^{-2} . For each 5 MPa

increase in the confining pressure, the axial strain at the peak increases to 0.92×10^{-2} , 1.27×10^{-2} , and 1.41×10^{-2} . The slope of the elastic phase in the stress-strain curve is the elastic modulus of the rock specimen. It can be seen that the slope of the stress-strain curve increases with the increase of confining pressure, which means that the elastic modulus is also gradually increasing. At the confining pressure of 5, 10, 15, and 20 MPa, the elastic modulus is 8.92, 10.03, 10.05, and 11.17 GPa, respectively.

3.2. Analysis of Deformation and Failure Characteristics. The macroscopic failure modes of red sandstone under different confining pressures are presented in Figure 4. At the confining pressure of 5 MPa, the failure presents shear mode. The failure starts from the upper left side of the rock and ends at the lower right side of the rock's bottom. When the confining pressure is 10 MPa, the main failure surface also shows shear failure. In addition to shear failure, the bottom corners are also damaged. This observation was regarded as one of the typical failure modes of the rock since the rock is a heterogeneous body with joints which will be fractured during the compression process. Due to the internal fissures, local small-scale cracking occurs at the bottom right end of the rock specimen. When the confining pressure is 15 MPa, the failure mode is similar to that of 5 MPa, but the shear inclination angle is reduced. At the confining pressure of 20 MPa, compared with other failure inclination angles, the failure surface inclination angle is the smallest. In summary, the failure mode of red sandstone with different confining pressures is dominated by the shear mode. As the confining pressure increases, the inclination of the failure surface decreases.

4. Numerical Modeling and Simulation Analysis

4.1. Numerical Model and Mesoparameter Calibration. The PFC^{3D} software was used to study the fracture development of red sandstone under different confining pressures, and the numerical models were established to simulate triaxial compression tests.

4.1.1. Numerical Model Construction. The PFC^{3D} simulation first generates a boundary wall according to the size of the rock specimen and then generates compact particles in the wall. By specifying the ratio of the maximum and minimum particle radius, the program can randomly generate a uniformly distributed particle model according to the preset maximum and minimum values. Figure 5 shows the constructed complete PFC^{3D} simulation test piece, which is basically consistent with that of the experimental specimen. The specimen size is 50 mm (diameter) \times 100 mm (height), which consisted of 29,620 particles.

4.1.2. Homogenization Model. In order to make the particle size distribution of the generated model meet the specified requirements, the contact accuracy between particles must be high enough. This requires the overlap between adjacent particles in the particle system generated by the model generation algorithm is small enough. The particles are in close contact with the boundary and completely coupled. Therefore, to meet the above requirements, a self-programming

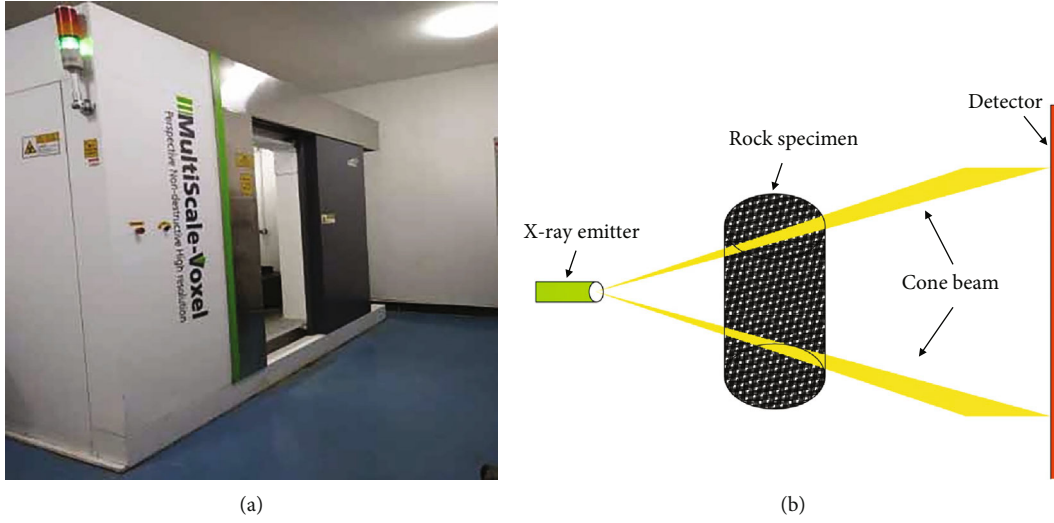


FIGURE 2: Microstructure test equipment: (a) CT scanner; (b) principles of CT scanning.

TABLE 1: Deformation parameters of the specimens under different confining pressures.

Sample number	Average density ($\text{g}\cdot\text{cm}^{-3}$)	Confining pressure (MPa)	Axial stress (MPa)	Elasticity modulus (GPa)	Poisson ratio	Cohesion (MPa)	Internal friction angle ($^{\circ}$)
1	2132	5	59.70	8.92	0.189	12.29	32.84
2		10	80.99	10.03	0.165		
3		15	98.21	10.05	0.188		
4		20	110.12	11.17	0.189		

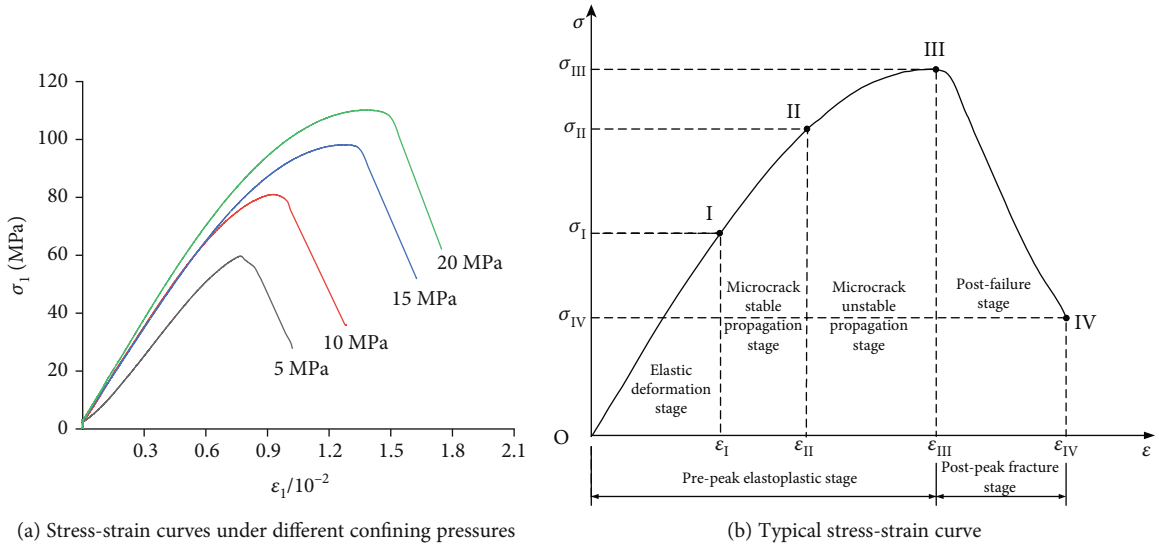


FIGURE 3: Stress-strain curves of red sandstone under different confining pressures.

capable of making the model close to the uniform state is proposed. Figure 6 shows the homogenization process. Through adjusting the model's boundary conditions, the contact between particles can reach the ideal state.

4.1.3. Calibration of Parameters. There are a variety of contact models in PFC^{3D}. Compared with other models,

the parallel bond model can transmit force and moment at the same time. Additionally, the stiffness after the failure of the parallel bond will decrease, which is similar to the plastic characteristics of the rock and better reflect the rock's mechanical characteristics. Therefore, the parallel bond model is chosen to calibrate the mesoparameters of the red sandstone [32–34]. Firstly, a set of mesoparameters are

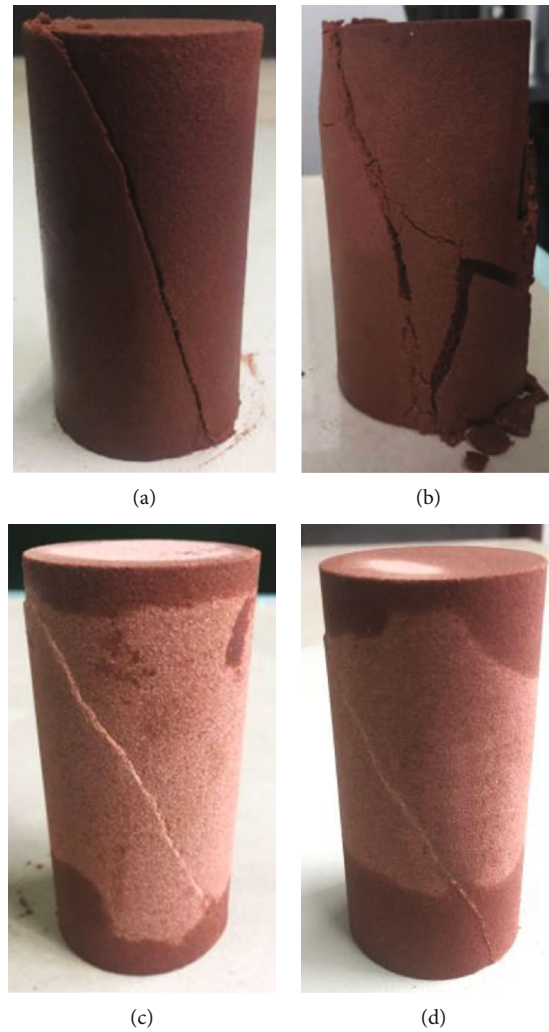


FIGURE 4: Macrofailures of red sandstone under different confining pressures: (a) 5 MPa; (b) 10 MPa; (c) 15 MPa; (d) 20 MPa.

assumed, and the stress-strain curves are obtained through the applying of the axial loads. Then, based on the measured data, the macroscopic compressive strength, the elastic modulus, and other macroscopic parameters are calculated and compared with the laboratory experiment. Finally, through continuously adjusting the mesoparameters, the stress-strain curve obtained by the numerical simulation test is consistent with the curve from the laboratory experiment, and the macroscopic damage is also similar to that observed in the laboratory experiments. A group of mesoparameters that are closest to the laboratory test are identified and applied to the numerical simulation test [35]. The mesoparameters are shown in Table 2.

4.2. Comparison of Test and Simulation. In the simulation test, the upper and lower walls simulate the indoor test loading stress, and the cylindrical wall is used to simulate the loading confining pressure. A self-compiled servo control program is used to control the wall motion. Through constantly updating the wall's speed, the wall contact force reaches the target confining pressure. After getting the target confining pressure, a constant loading rate to the upper and

lower walls is applied. The wall exerts a constant loading rate to compress the model axially. Figure 7 shows the stress-strain curves of the intact red sandstone, and the final failure forms obtained through numerical simulation are shown in Figure 8.

In Figure 7, it was observed that the stress-strain curves under the triaxial compression simulated by PFC^{3D} were in good agreement with the results obtained in the laboratory tests. In the numerical simulation, for each 5 MPa increase in the confining pressure, the maximum axial stress obtained by the triaxial compression simulation is gradually increased, but the increased value of maximum axial stress is gradually reduced. Additionally, the slope of the curve in the elastic stage which is elastic modulus is increasing. When the confining pressure is 5 MPa, the maximum axial stress obtained by simulation is 59.27 MPa, and the elastic modulus is 9.04 GPa. The discrepancies of peak stress and elastic modulus between the simulation and lab test are 0.72% and 1.35%. At the confining pressures of 10, 15, and 20 MPa, the deviations of peak stress between simulations and laboratory experiments are 3.33%, 5.06%, and 1.33%, and the deviations of elastic modulus are 1.99%, 1.59%, and 6.98%. According to

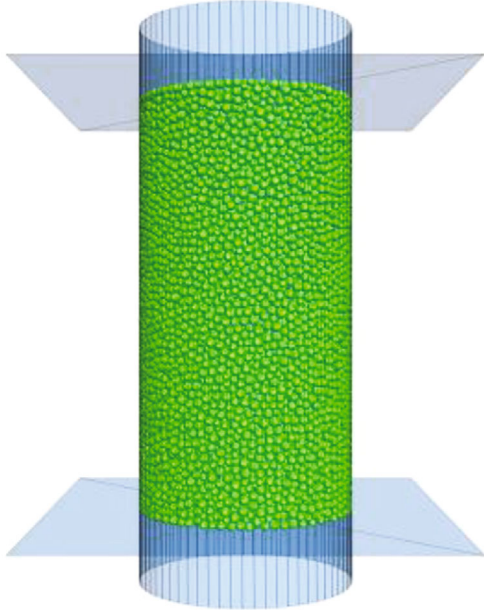


FIGURE 5: The PFC^{3D} model of standard triaxial compression specimen.

the Mohr-Coulomb criterion, the macroscopic mechanical parameters of the simulation experiment can be obtained. The cohesion force is 12.21 MPa, and the internal friction angle is 32.05°. The deviations from the indoor tests are 0.65% and 2.41%, respectively. These deviations are within a reasonable range, indicating that the numerical simulation results are accurate.

Figure 8 shows the fracture characteristics of the specimens under different confining pressures. The green particles represent the areas not broken, and the particles of other colors represent the broken area. The reason for this different color is that different fragments are formed after the fracture of the rock specimen penetrates, and the PFC^{3D} renders in different colors are to make the fracture more intuitive.

The particle failure can clearly show the macroscopic failure of the rock. The failure mainly presents the characteristics of shear failure, and the failure angle obtained by the simulation is basically the same as the real rock failure angle. As the confining pressure increases, the angle between the macroscopic crack of the rock and the horizontal plane is gradually decreasing, and the length of the crack is also decreasing. When the confining pressure is 5 MPa, the particles are affected by the hoop pressure. The damage appears to be shear failure, which is consistent with the failure mode of the test. As the confining pressure increases, the lateral pressure to the particles gradually increases, and the influence of lateral expansion deformation is gradually clear. The rock specimen gradually develops from the failure area of the loading interface to the middle area. The inclination angle of the failure surface also gradually decreases.

4.3. The Propagation Mode of Internal Fissures. The triaxial compression test is a method to study the mechanical behavior and failure mode of rock specimens, but these works have certain limitations. Triaxial tests can only

observe the distribution of cracks on the surface of the rock specimen. The distribution of internal cracks and the path of failure penetration are unclear. The emergence of numerical simulation will solve this problem. The slice function in the numerical simulation can be used to study the distribution of cracks and failure paths in the rock specimen, but there are still doubts about its accuracy. Here, a CT scan is proposed to verify the accuracy of the numerical simulation.

In order to observe the expansion of the internal fractures in the rock more accurately, the reconstructed 3D rock model was sectioned by using the AVIZO software. To observe the internal fracture paths, the failed specimens were cut three times along the axial direction. The location of each cutting is presented in Figure 9.

Figure 10 shows the comparison of the internal fracture mode of red sandstone between the test and simulation under a confining pressure of 15 MPa. In Figure 10, it was observed that the internal fracture behavior of the specimen obtained by numerical simulation is consistent with the CT results. At the slice of Cut 1, there is only one main crack in the numerical simulation. In addition to a main oblique shear crack on the CT image, a small shear crack is observed at the top of the red sandstone. This difference is that the red sandstone in its natural state has microcracks, while the numerical simulation is a homogenization model without microcracks. At the slice of Cut 2, the CT oblique shear main crack moves compared to the main crack observed at Cut 1. The upper rupture line moves up, and the lower rupture line moves down. The rupture angle becomes larger and longer. The numerical simulation appears with the same change, and the position of the main fracture surface also moves upward. At the slice of Cut 3, compared with Cut 2, the rupture line at the lower end of the oblique shear main crack shifts up. The failure angle becomes smaller, and the starting line becomes shorter, which is consistent with the main crack position shown by the numerical simulation. Comparing the CT results with the simulation results, the internal fracture behavior of the red sandstone obtained by the numerical simulation PFC^{3D} is consistent with the experimental results.

4.4. Crack Propagation Process. As shown in the above comparison, the results obtained from the laboratory test and numerical simulation are in good agreement. Numerical simulation can be used to observe the interior of the fracture process of rock specimens as compared to the laboratory test. Therefore, the inside crack evolution process is studied according to the simulation model of red sandstone under different confining pressures. Figure 11 shows the internal crack propagation process and crack changes of red sandstone under different confining pressure conditions, and Figure 12 gives the evolution of the number of microcracks in rocks under different conditions. In Figure 12, the characteristic points are selected to evaluate the crack evolution. Point I is generally selected at 2/5 of the peak stress. Point II is the transition from the elastic stage to the plastic stage, which is generally considered to be about 2/3 of the peak strength [36, 37]. Therefore, the selected characteristic points are 2/5 peak stress, 2/3 peak stress, the peak stress, and failure stress.

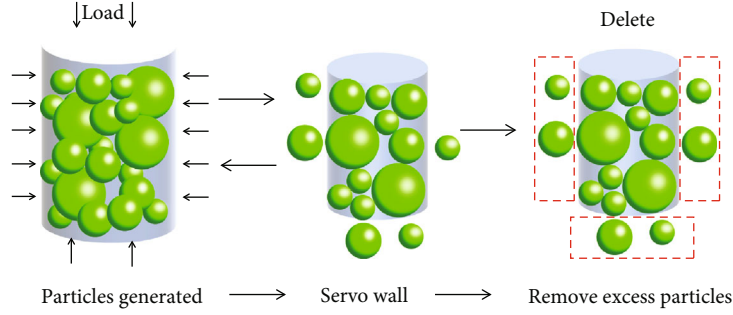


FIGURE 6: Homogenization process of the model.

TABLE 2: Mesoparameter calibration of numerical simulation.

Microparameters	Values
The minimum radius of the ball, R_{\min}/mm	0.85
Ratio of the maximum to the minimum radius of the ball, R_{\max}/R_{\min}	1.5
Density of the ball, $\rho/(\text{kg}/\text{m}^3)$	2132
Ball friction coefficient, μ	0.5
Young's modulus of the ball, E_C/GPa	9.2
Ratio of normal to shear stiffness of the ball, k_n/k_s	2.3
Radius multiplier of the parallel bond, λ	1.0
Young's modulus of the parallel bond, \bar{E}_C/GPa	9.2
Ratio of normal to shear stiffness of the parallel bond, \bar{k}_n/\bar{k}_s	2.3
Normal strength of the parallel bond, σ/MPa	32.5
Shear strength of the parallel bond, c/MPa	32.5
Friction angle of the parallel bond, $\varphi/^\circ$	30

Under the confining pressure of 5 MPa, the simulated crack propagation process of the red sandstone specimen is shown in Figure 11(a), and the corresponding curve of the number of cracks is shown in Figure 12(a). In the process of simulating the fracture of red sandstone, no microcracks were generated at point I ($\sigma_1 = 23.71$ MPa), which is consistent with the theory of microcracks in the experiment. When the axial stress increases to point II ($\sigma_1 = 39.51$ MPa accounts for 2/3 of the peak stress), the microcracks begin to occur at the end of the rock specimen. The number of microcracks is 72, accounting for about 1.22% of the total number of microcracks at peak point III. With the increase of the axial stress, the axial deformation continues to increase. Before the axial stress reaching point III ($\sigma_1 = 59.27$ MPa), the specimen is at the stage of plastic deformation where new microcracks initiate. In this stage, the cracks began to expand; the number of microcracks is up to 5910. Additionally, an oblique shear failure crack was being formed. After reaching the peak stress, the axial stress began to decline, and the specimen was completely destroyed at point IV ($\sigma_1 = 42.10$ MPa). At point IV, a macroscopic oblique

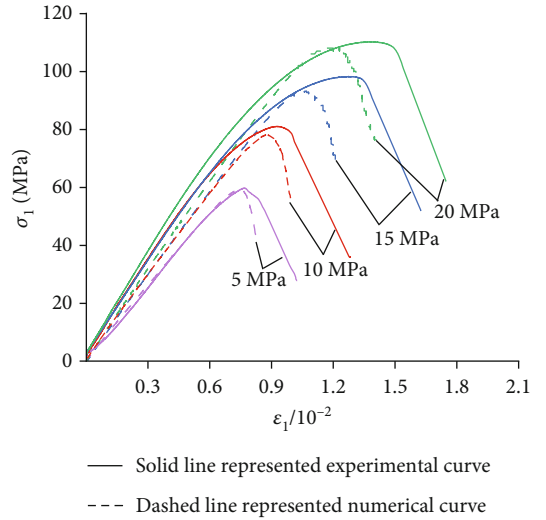


FIGURE 7: Numerical simulation curves of stress-strain.

shear failure formed, with a rapid increase in the number of microcracks. The number of microcracks eventually reached 21700.

Figure 11(b) shows the simulated crack propagation process of the red sandstone specimen at the confining pressure of 10 MPa, and Figure 12(b) shows the corresponding curve of microcrack quantity. The cracking process is consistent with that of 5 MPa. When the axial strain is 0.319×10^{-2} (point I), no cracks occur. As the axial strain increases to 0.537×10^{-2} (point II), 123 microcracks are generated at the end of the rock, accounting for about 2.01% of the total number of microcracks at peak point III. With the continuous increase of strain, the direction of crack propagation is determined in the elastic-plastic region, and it can be clearly observed that the microcracks form an oblique shear crack. At this time, the number of microcracks is 6110. After point III, the specimen steps into the stage of microcrack penetration failure. The number of microcracks continues to increase until the axial strain reaches point IV. At this point, the rock specimen is completely destroyed, and the final number of microcracks reaches 23,100. It is observed that the microcracks interact with each other forming an oblique shear macrocrack. Figures 11(c) and 11(d) are the crack propagation process of red sandstone under confining

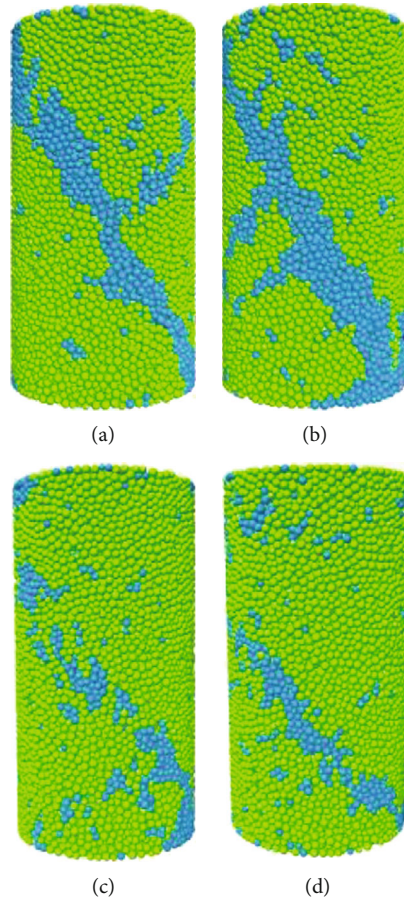


FIGURE 8: Macroscopic failure modes of redstone under different confining pressure by PFC^{3D}: (a) 5 MPa; (b) 10 MPa; (c) 15 MPa; (d) 20 MPa.

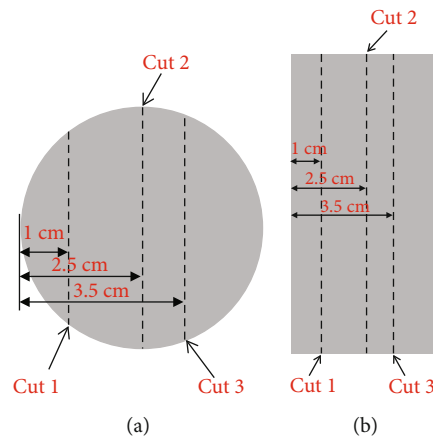


FIGURE 9: Locations of the cuttings: (a) cross-section; (b) longitudinal section.

pressures 15 and 20 MPa, and Figures 12(c) and 12(d) show the corresponding curve of microcrack quantity. The initiation, propagation, and interaction of crack in the specimens are consistent with that of 5 MPa. The cracks also start from the end position of specimen and propagate obliquely under the combined action of axial force and confining pressure. The macroscopic oblique shear failure is eventually formed.

5. Analysis of Experiment and Simulation Results

5.1. Strength Characteristics and Failure Modes. The laboratorial triaxial experiment found that the triaxial compression deformation of red sandstone has elastic deformation stage, microcrack stable propagation stage, microcrack unstable

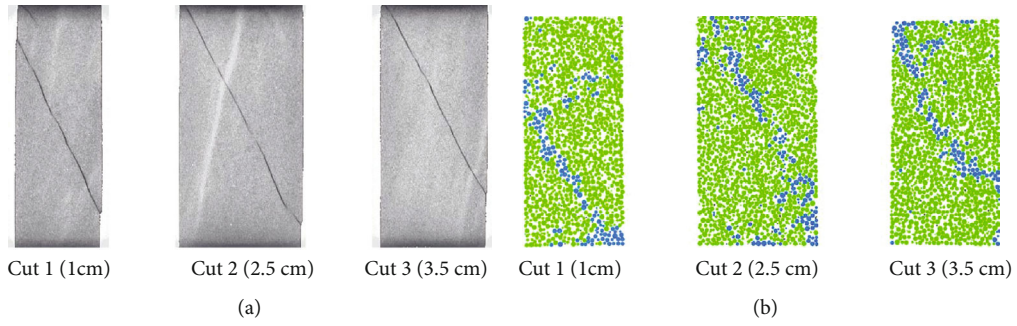


FIGURE 10: Comparison of internal fractures in red sandstone under 15 MPa: (a) CT scan; (b) simulation.

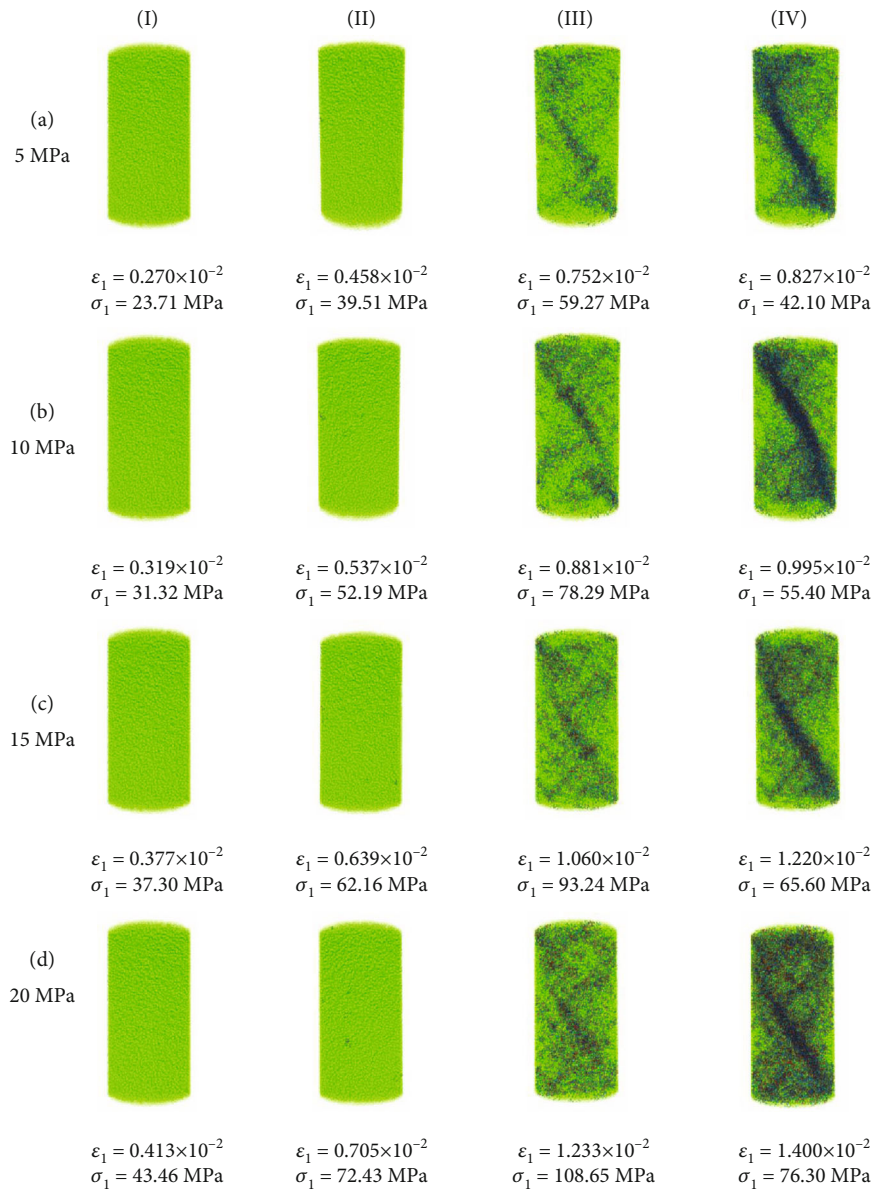


FIGURE 11: Internal crack propagation rules of red sandstone under different confining pressure conditions.

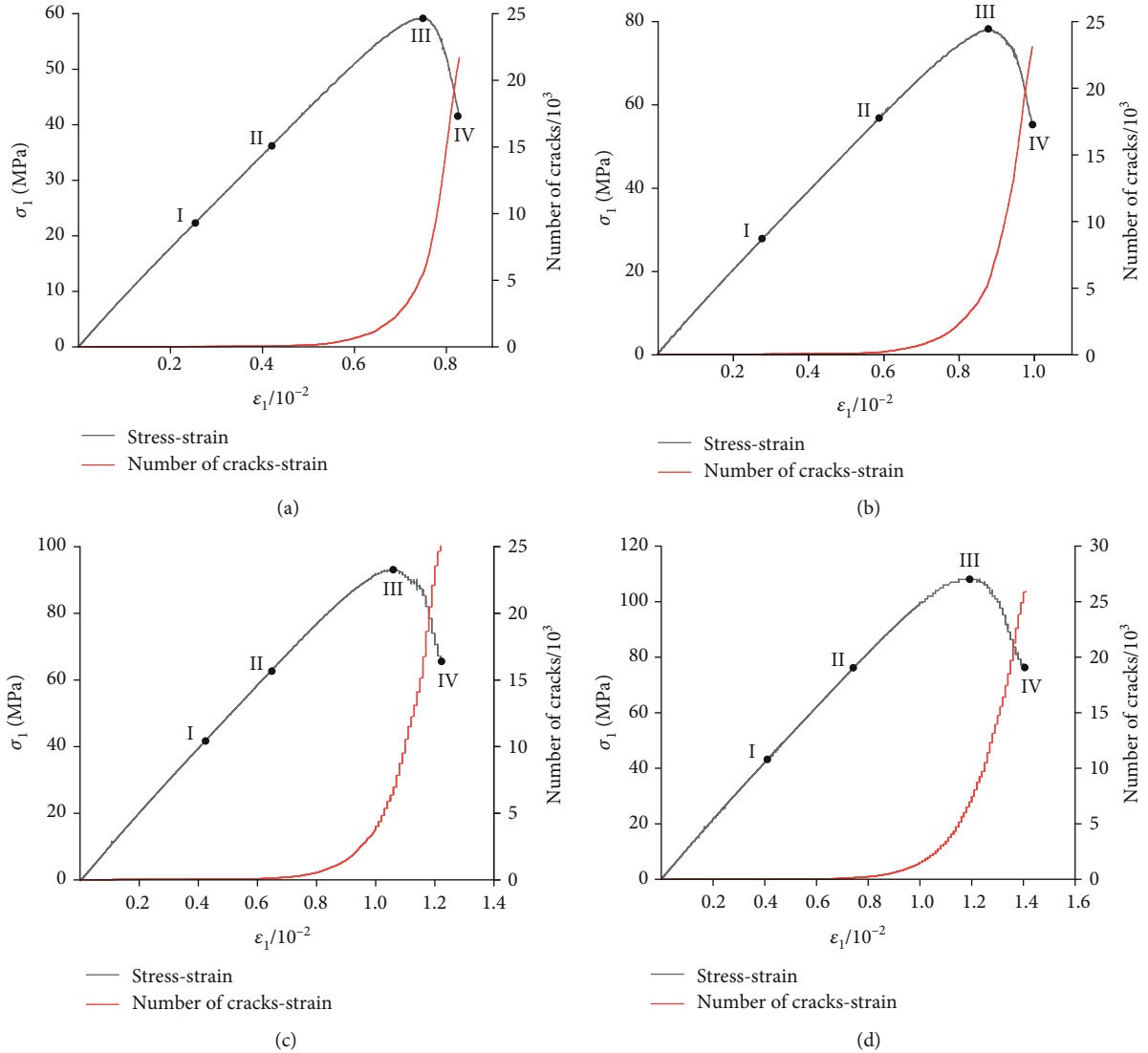


FIGURE 12: The number of microcracks in red sandstone under different confining pressure conditions: (a) 5 MPa; (b) 10 MPa; (c) 15 MPa; (d) 20 MPa.

propagation stage, and postfailure stage. For the model established by the numerical simulation, the deformations and failures are consistent with the laboratorial test. From the triaxial test and PFC^{3D} simulations, it can be seen that the red sandstone failed in the shear mode. The peak strength, elastic modulus, peak strain, and residual stress of red sandstone increase while the inclination of the failure surface decreases as the confining pressure increases. This indicates that the increase of confining pressure can improve the anti-destructive ability of red sandstone to a certain extent, in other words, playing a certain protective effect on the deformation and failure of red sandstone.

5.2. Comparative Analysis of Numerical Simulation. From the rock failure characteristics obtained by the PFC^{3D} simulation, it is observed that the three-dimensional numerical simulation can accurately simulate the macro- and micro-failure mode of the rock under pressure. In laboratory

experiments, the macroscopic failure of red sandstone under different confining pressures all showed oblique shear failure, and the failure angle decreased with the increase of confining pressure. Simulations of red sandstone under different confining pressures are consistent with the laboratorial experiments, with only a few differences on the tiny crack. This is because the rock itself has cracks in nature, which have an influence to rock damage in the laboratorial experiment. The homogeneous model was established by the method of numerical simulation that leads to the slight differences between numerical simulation and experimental results.

The PFC^{3D} homogenization simulation can not only simulate the changes of macroscopic cracks but also analyze the development of its internal cracks. By comparing internal cracks from the CT three-dimensional reconstruction of red sandstone with numerical simulation results under confining pressure of 15 MPa, it is clear that the shape of

the main failure cracks inside the simulated rock specimen is consistent with the internal cracks of the real rock specimen. The good agreement of the results obtained from the numerical simulation and the CT scanning indicates that the numerical simulation is accurate for the distribution of cracks in the red sandstone and the path of penetration failure.

The PFC^{3D} homogenization simulation can obtain the fracture process of the rock specimen under the condition of triaxial compression and reveal the evolution law of microcracks in the rock specimen. In the initial stage, the number of microcracks is very small. In the elastic-plastic deformation stage, the cracks begin to be active and the number of cracks begins to increase. Compared with the first two stages, the number of cracks increases exponentially after the peak stress. It indicates that the microcracks of the rock specimen interact and form the macrocracks at this stage. In addition, it is found that the microcrack propagation mode of red sandstone under different confining pressures is basically the same. The microcracks in red sandstone start from the end of the rock specimen and gradually form oblique shear failure under the action of external force. The consistencies of the mechanical parameters and fracture evolution processes of the red sandstone obtained from numerical simulation and the indoor experiment also confirmed the feasibilities of using the PFC^{3D} numerical simulation to study rock failure.

6. Conclusion

In this study, with the applications of indoor triaxial compression tests, PFC^{3D} numerical simulation, and CT scanning technique, the internal and external deformation and failure characteristics of red sandstone under different confining pressures were analyzed at micro- and macroscales. The following conclusions were obtained:

- (1) The effects of confining pressure on the mechanical properties and failure characteristics of red sandstone are very obvious. The failure surface of the specimens shows shear modes. As the confining pressure increases, the peak stress, elastic modulus, and peak strain of the rock increase, while the inclination angles of the shear surface decrease
- (2) The process of crack initiation and propagation was studied using the PFC^{3D} numerical simulation and CT scanning. The cracks first began to occur at the end, propagated obliquely with the action of axial stress and confining pressure producing a large number of the microcracks, and finally, microcracks interact with each other forming the macrocracks and resulted in oblique shear failure
- (3) The mechanical parameters, fracture evolution processes, and macro/microfracture characteristics of the specimens obtained from PFC^{3D} numerical simulation and the CT three-dimensional reconstruction are consistent. The consistencies confirmed that PFC^{3D} can simulate mechanical properties and the failure characteristics of red sandstone under differ-

ent confining pressures, providing a feasible numerical method for studying the mechanical behavior of rock. In addition, this method can also be used to study the internal micromechanism of the rock failure and provide a theoretical basis for rock strength prediction and safety evaluation under loads

Data Availability

The detailed data used to support the findings of this study are available from the corresponding author upon request.

Conflicts of Interest

The authors declare that they have no conflicts of interest.

Acknowledgments

This work was financially supported by the National Natural Science Foundation of China (Nos. 51904220 and 52004196) and Science and Technology Bureau of the Beilin, Xi'an (GX2016).

References

- [1] Y. Wang, X. Zhou, and Y. Shou, "The modeling of crack propagation and coalescence in rocks under uniaxial compression using the novel conjugated bond-based peridynamics," *International Journal of Mechanical Sciences*, vol. 128, pp. 614–643, 2017.
- [2] V. Sarfarazi and H. Haeri, "A review of experimental and numerical investigations about crack propagation," *Computers and Concrete*, vol. 18, no. 2, pp. 235–266, 2016.
- [3] J. J. Chen, P. Liu, H. B. Zhao, and C. Zhang, "Analytical studying the axial performance of fully encapsulated rock bolts," *Engineering Failure Analysis*, vol. 128, article 105580, 2021.
- [4] S. S. Wu, H. L. Ramandi, H. Chen, A. Crosky, P. Hagan, and S. Saydam, "Mineralogically influenced stress corrosion cracking of rockbolts and cable bolts in underground mines," *International Journal of Rock Mechanics and Mining Sciences*, vol. 119, pp. 109–116, 2019.
- [5] S. S. Wu, X. H. Zhang, J. P. Li, and Z. Wang, "Investigation for influences of seepage on mechanical properties of rocks using acoustic emission technique," *Geofluids*, vol. 1155, 19 pages, 2020.
- [6] S. Xie, H. Lin, Y. Wang et al., "Nonlinear shear constitutive model for peak shear-type joints based on improved Harris damage function," *Archives of Civil and Mechanical Engineering*, vol. 95, 2020.
- [7] H. Lin, X. Zhang, Y. Wang et al., "Improved nonlinear Nishihara shear creep model with variable parameters for rock-like materials," *Advances in Civil Engineering*, vol. 2020, Article ID 7302141, 15 pages, 2020.
- [8] Y. L. Zhao and L. Y. Zhang, "Experimental study on the mud-water inrush characteristics through rock fractures," *Advances in Civil Engineering*, vol. 2018, Article ID 2060974, 7 pages, 2018.
- [9] C. Y. Zhang, C. Z. Pu, R. H. Cao, T. T. Jiang, and G. Huang, "The stability and roof-support optimization of roadways passing through unfavorable geological bodies using advanced detection and monitoring methods, among others, in the

- Sanmenxia Bauxite Mine in China's Henan Province," *Bulletin of Engineering Geology and the Environment*, vol. 78, no. 7, pp. 5087–5099, 2019.
- [10] X. Liu, L. Wu, Y. Zhang, S. Wang, X. Yao, and X. Wu, "The characteristics of crack existence and development during rock shear fracturing evolution," *Bulletin of Engineering Geology and the Environment*, vol. 80, pp. 1671–1682, 2021.
- [11] J. L. Liu, Y. H. Liu, Y. J. Zhu et al., "Study of influences of rock hardness on crack evolution rule under hydraulic fracturing," *IOP Conference Series Earth and Environmental Science*, vol. 558, no. 3, article 032003, 2020.
- [12] Y. Bai, R. L. Shan, Y. Ju et al., "Experimental study on the strength, deformation and crack evolution behaviour of red sandstone samples containing two ice-filled fissures under triaxial compression," *Cold Regions Science and Technology*, vol. 174, article 103061, 2020.
- [13] S. Q. Yang, Y. Z. Jiang, W. Y. Xu, and X. Q. Chen, "Experimental investigation on strength and failure behavior of pre-cracked marble under conventional triaxial compression," *International Journal of Solids and Structures*, vol. 45, no. 17, pp. 4796–4819, 2008.
- [14] C. Y. Zhang, Y. X. Wang, and T. T. Jiang, "The propagation mechanism of an oblique straight crack in a rock sample and the effect of osmotic pressure under in-plane biaxial compression," *Arabian Journal of Geosciences*, vol. 13, no. 15, pp. 736–751, 2020.
- [15] S. Wu, J. Li, J. Guo, G. Shi, Q. Gu, and C. Lu, "Stress corrosion cracking fracture mechanism of cold-drawn high-carbon cable bolts," *Materials Science and Engineering: A*, vol. 769, article 138479, 2020.
- [16] H. Mokhtarian, H. Moomivand, and H. M. Moomivand, "Effect of infill material of discontinuities on the failure criterion of rock under triaxial compressive stresses," *Theoretical and Applied Fracture Mechanics*, vol. 108, article 102652, 2020.
- [17] S. Q. Yang, H. W. Jing, and S. Y. Wang, "Experimental investigation on the strength, deformability, failure behavior and acoustic emission locations of red sandstone under triaxial compression," *Rock Mechanics and Rock Engineering*, vol. 45, no. 4, pp. 583–606, 2012.
- [18] X. Ma, G. L. Wang, D. W. Hu, Y. Liu, H. Zhou, and F. Liu, "Mechanical properties of granite under real-time high temperature and three-dimensional stress," *International Journal of Rock Mechanics and Mining Sciences*, vol. 136, no. 1, article 104521, 2020.
- [19] Y. D. Jiang, X. F. Xian, and J. Xu, "A research on sandstone uniaxial and triaxial compression tests," *China Mining Magazine*, vol. 13, no. 4, pp. 66–69, 2004.
- [20] H. Kawakata, A. Cho, T. Kiyama, T. Yanagidani, K. Kusunose, and M. Shimada, "Three-dimensional observations of faulting process in Westerly granite under uniaxial and triaxial conditions by X-ray CT scan," *Tectonophysics*, vol. 313, no. 3, pp. 293–305, 1999.
- [21] P. Christe, P. Turberg, V. Labiouse, R. Meuli, and A. Parriaux, "An X-ray computed tomography-based index to characterize the quality of cataclastic carbonate rock samples," *Engineering Geology*, vol. 117, no. 3–4, pp. 180–188, 2011.
- [22] S. Q. Yang, P. F. Yin, Y. H. Huang, and J. L. Cheng, "Strength, deformability and X-ray micro-CT observations of transversely isotropic composite rock under different confining pressures," *Engineering Fracture Mechanics*, vol. 214, pp. 1–20, 2019.
- [23] J. B. Zhu, T. Zhou, Z. Y. Liao, L. Sun, X. B. Li, and R. Chen, "Replication of internal defects and investigation of mechanical and fracture behaviour of rock using 3D printing and 3D numerical methods in combination with X-ray computerized tomography," *International Journal of Rock Mechanics and Mining Sciences*, vol. 106, pp. 198–212, 2018.
- [24] X. P. Zhou, Y. X. Zhang, and Q. L. Ha, "Real-time computerized tomography (CT) experiments on limestone damage evolution during unloading," *Theoretical and Applied Fracture Mechanics*, vol. 50, no. 1, pp. 49–56, 2008.
- [25] C. Zhang, H. Lin, C. Qiu, T. Jiang, and J. Zhang, "The effect of cross-section shape on deformation, damage and failure of rock-like materials under uniaxial compression from both a macro and micro viewpoint," *International Journal of Damage Mechanics*, vol. 29, no. 7, pp. 1076–1099, 2020.
- [26] B. Gong, Y. J. Jiang, and L. J. Chen, "Feasibility investigation of the mechanical behavior of methane hydrate-bearing specimens using the multiple failure method," *Journal of Natural Gas Science and Engineering*, vol. 69, article 102915, 2019.
- [27] X. Fan, K. H. Li, H. P. Lai, Y. Xie, R. Cao, and J. Zheng, "Internal stress distribution and cracking around flaws and openings of rock block under uniaxial compression: a particle mechanics approach," *Computers and Geotechnics*, vol. 102, pp. 28–38, 2018.
- [28] T. H. Wu, Y. T. Gao, Y. Zhou, and J. W. Li, "Experimental and numerical study on the interaction between holes and fissures in rock-like materials under uniaxial compression," *Theoretical and Applied Fracture Mechanics*, vol. 106, article 102488, 2020.
- [29] X.-P. Zhang and L. N. Y. Wong, "Cracking processes in rock-like material containing a single flaw under uniaxial compression: a numerical study based on parallel bonded-particle model approach," *Rock Mechanics and Rock Engineering*, vol. 45, no. 5, pp. 711–737, 2011.
- [30] X. Yang, Z. P. You, Z. G. Wang, and Q. L. Dai, "Review on heterogeneous model reconstruction of stone-based composites in numerical simulation," *Construction and Building Materials*, vol. 117, pp. 229–243, 2016.
- [31] Y. F. Zhao, *Stress-induced permeability evolution in coal: laboratory testing and numerical simulations*, [PhD thesis], Technischen Universität Bergakademie Freiberg, Germany, 2020.
- [32] N. Cho, C. D. Martin, and D. C. Segol, "A clumped particle model for rock," *International Journal of Rock Mechanics and Mining Sciences*, vol. 44, no. 7, pp. 997–1010, 2007.
- [33] L. Cheung, C. O'Sullivan, and M. R. Coop, "Discrete element method simulations of analogue reservoir sandstones," *International Journal of Rock Mechanics and Mining Sciences*, vol. 63, pp. 93–103, 2013.
- [34] J. M. Xu, Z. L. Xie, and H. T. Jia, "Simulation of mesomechanical properties of limestone using particle flow code," *Rock and Soil Mechanics*, vol. 31, no. 2, pp. 390–395, 2010.
- [35] B. Gong, Y. J. Jiang, P. Yan, and S. H. Zhang, "Discrete element numerical simulation of mechanical properties of methane hydrate-bearing specimen considering deposit angles," *Journal of Natural Gas Science and Engineering*, vol. 76, article 103182, 2020.
- [36] R. E. Goodman, *Introduction to Rock Mechanics*, Wiley, Canada, 1989.
- [37] M. F. Cai, M. C. He, and D. Y. Liu, *Rock Mechanics and Engineering*, Beijing Publishing House, China, 2013.

Research Article

A Damage Constitutive Model for a Rock under Compression after Freeze-Thaw Cycles Based on the Micromechanics

Hongyan Liu ^{1,2}, Xiaochen Zhang ³, and Xidong Yan ⁴

¹College of Engineering & Technology, China University of Geosciences (Beijing), Beijing 100083, China

²Key Laboratory of Deep Geodrilling Technology of Ministry of Natural Resources, Beijing 100083, China

³School of Safety Engineering, North China Institute of Science and Technology, Beijing 101601, China

⁴RIOH Transport Consultants Ltd, Beijing 100088, China

Correspondence should be addressed to Hongyan Liu; lhyan1204@126.com

Received 12 May 2021; Accepted 8 July 2021; Published 23 July 2021

Academic Editor: Yu Wang

Copyright © 2021 Hongyan Liu et al. This is an open access article distributed under the Creative Commons Attribution License, which permits unrestricted use, distribution, and reproduction in any medium, provided the original work is properly cited.

The freeze-thaw cycles will cause continuous damage to the rock, which is much related to the microcrack length, rock permeability, and frost heaving pressure. However, the failure mechanism of the rock under compression after freeze-thaw cycles is not very clear; therefore, it is studied with the damage theory here. First of all, according to the hydraulic pressure theory, the relationship between the frost heaving pressure and the microcrack propagation length in one single microcrack is established based on the elastoplastic mechanics and fracture theory. Second, by assuming the total strain of the rock under compression is comprised of the initial damage strain, elastic strain, additional damage strain, and plastic damage strain, a constitutive model for a rock based on the deformation and propagation of the microcrack under compression after freeze-thaw cycles is established. Finally, the proposed model is verified with the test result. In all, the proposed model can perfectly reflect the deterioration of the rock mechanical behavior under compression after the freeze-thaw cycles.

1. Introduction

Rock deterioration under freeze-thaw cycles is a hot issue in many engineering projects in cold regions. This deterioration proceeds with the freeze-thaw cycles, and the rock will gradually lose its stiffness and strength.

Water in the microcrack is assumed to be the key factor leading to the rock deterioration under freeze-thaw cycles. The deterioration mechanism of the porous media under freeze-thaw cycles was firstly described by Powers [1]. According to his theory, the frost heaving pressure will be generated by 9% volume expansion when water in the closed microcrack freezes into ice. It will make the microcrack propagate and cause damage to the rock. Thereafter, lots of laboratory tests have been done by many researchers, for instance, Altindag et al. [2], Momeni et al. [3], Nicholson and Nicholson [4], Zhang et al. [5], Wang et al. [6], Tounsi et al. [7], and Tang et al. [8]. All these results indicated that with the increasing number of freeze-thaw cycles, rock will

deteriorate and degrade to some degree in terms of the compressive strength, elastic modulus, mass density, and so on.

No, many research works have been done in this field. Neaupane and Yamabeb [9] proposed a nonlinear elastoplastic constitutive relationship and a two-dimensional (plane stress) numerical modeling on the basis of the finite element method. With the continuum mechanics, Exadaktylos [10] established a coupled model for the saturated porous rocks under freeze-thaw cycles which can be used for analyzing the preliminary thawing experiments on the porous sandstone. According to the freeze-thaw cyclic fatigue tests on sandstone and shale, Tang et al. [8] assumed that the rock damage process included two coupled parts, e.g., the damage induced by the freeze-thaw cycles and the damage evolution caused by stress erosion. And then, a frost damage constitutive model is accordingly established. Based on the mass conservation law, energy conservation law, and the principle of static equilibrium, Kang et al. [11] studied the thermo-hydro-mechanical coupling mechanism and then proposed

a new THM (thermo-hydro-mechanical) coupling model by considering phase change effect, in which the water migration caused by segregation potential and temperature gradient is described. By considering the coupling effects among fluid flow, heat transfer, crystallization, and deformation in porous media, Wu et al. [12] established a thermo-hydro-salt-mechanical coupled model for fully saturated porous media with phase change. From the viewpoint of the energy conservation law, mass conservation law, and the principle of static equilibrium considering water/ice phase change, Huang et al. [13] set up a fully coupled THM model and verified its validity with the laboratory test. Based on a microstructure-based random finite element model for the frozen soil, Dong and Yu [14] established a holistic model to simulate the temperature, stress, and deformation in frozen soil and implement a model to simulate frost heave and stress on water pipelines. In order to consider the migration of unfrozen water during freezing, Wang et al. [15] proposed a general thermo-mechanical-water migration coupled constitutive model to model mechanical degradation of rocks subjected to freeze-thaw cycles. Fan et al. [16] established a universal damage constitutive model under freeze-thaw and loading conditions based on the statistical damage constitutive model. Meanwhile, it can be seen that plasticity theory [17, 18] is often adopted to describe the nonlinear mechanical behavior of rock-like materials under freeze-thaw cycles.

Rock properties including the microcrack size distribution and permeability also have significant influence on rock mass mechanical behavior [19–22]. Hori and Morinoro [23] treated the shape of the microcrack as an ellipse in rock and set up a micromechanical model for the microscopic process. Although they assumed that the rock damage was induced by the microcrack propagation due to the water freezing and movement, they did not discuss the influence of microcrack distribution and permeability on rock deterioration. Therefore, the main objective of this research is to present an elastoplastic damage model for the rock with random distribution of the microcrack and the plastic yield criterion of the homogeneous medium combined with the micromechanical damage model to simulate the rock plastic deformation. The total strain of the rock is assumed to be comprised of initial damage strain, elastic strain, additional damage strain, and plastic damage strain [24], where the initial damage strain caused by the freeze-thaw cycles is calculated by the initial compliance matrix which is the function of freeze-thaw cycles. Meanwhile, the Drucker-Prager criterion is adopted to describe the plastic behavior of rock under compression, in which the microcrack radius is assumed to obey an exponential law [25]. Finally, the validity of the proposed model is verified with the experiment results.

2. Propagation of One Single Microcrack under Frost Heaving Pressure

2.1. The Relationship between the Microcrack Propagation Length and Ice Pressure in One Single Microcrack. Figure 1 illustrates a two-dimensional propagation model for one single microcrack under the frost heaving pressure. The microcrack is an ellipse, and its propagation under the frost

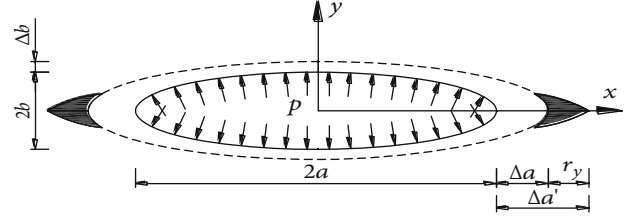


FIGURE 1: The microcrack propagation model under the frost heaving pressure. $2a$ and $2b$ are the length and width of the microcrack, respectively. Δa and Δb are the propagation length of the microcrack along two directions, respectively. r_y is the length of the plastic zone near the microcrack tip. $\Delta a'$ is the equivalent propagation length of the microcrack.

heaving pressure will lead to the rock damage. When freezing, the frost heaving pressure p acts on the inner wall of the microcrack normally and evenly.

The following assumptions are made in this study: (1) the microcrack is always elliptical during the whole freeze-thaw cycles. That is to say, the shape of the microcrack is the same; only its size changes; (2) the rock particle is assumed to be unchanged; (3) the microcrack is always saturated, and the microcrack propagation obeys the linear elastic fracture mechanics; and (4) the propagation process of the microcrack is stable.

Water will change into ice with the volume expansion when temperature decreases to a certain degree. But because of the constraint of the microcrack wall, the stress induced by the ice volume expansion will act on the microcrack inner wall which will produce the elastic strain energy in the rock. When the stress intensity factor K_I is larger than the rock fracture toughness K_{IC} , the microcrack will propagate, which will lead to the release of the elastic strain energy. According to the Griffith energy balance theory, there is

$$W = E - U, \quad (1)$$

where W , E , are U are work done by the frost heaving pressure, elastic strain energy stored in the rock, and the reduced total potential energy of the whole system, respectively.

Assume the elastic strain energy releases completely during the microcrack propagation, Equation (1) can be written into

$$W = -U. \quad (2)$$

The work W done by the frost heaving pressure on the inner wall of the microcrack is expressed as

$$W = 2 \times (p \times 2a \times \Delta b) = 4pa\Delta b, \quad (3)$$

where p is the frost heaving pressure, Δb is the microcrack opening displacement increment, shown in Figure 1.

The reduced total potential energy U of the whole system in Equation (2) can be expressed as

$$U = -2G \times \Delta a, \quad (4)$$

where Δa is the microcrack propagation length and G is the microcrack Griffith energy release rate.

There is a relationship between the volume of water and that of the ice [26]. Without considering the constraint of the microcrack wall, we assume the ice expansion volume is ΔV_i under the free condition. However, in practice, the ice is loaded by the stress p , and accordingly, the corresponding volumetric strain ε_v can be calculated:

$$\varepsilon_v = \frac{3(1 - 2\nu_i)}{E_i} p, \quad (5)$$

where E_i and ν_i are the ice elastic modulus and Poisson's ratio, and here, they are assumed to be 600 MPa and 0.3, respectively.

Then, the actual volume increment $\Delta V_i'$ is

$$\Delta V_i' = \Delta V_i - V_i \varepsilon, \quad (6)$$

where V_i is the volume of water before freezing.

According to the relationship of the water volume before and after the phase change, there is

$$\pi ab + \Delta V_i' = \pi(a + \Delta a)(b + \Delta b). \quad (7)$$

The microcrack propagation length can be obtained by combining Equations(3), (4), (6), and (7)

$$A(\Delta a)^2 + B(\Delta a) + C = 0, \quad (8)$$

where $A = \pi G$, $B = \pi(2pab + aG)$, and $C = -2\Delta V_i' pa$.

Solving Equation (8) yields

$$\Delta a = \frac{-(2abp + aG)\pi + \sqrt{(2abp + aG)^2\pi^2 + 8Gpa \times \Delta V_i'}}{2G\pi}. \quad (9)$$

The microcrack propagation corresponds to the rock damage, and accordingly, the rock elastic modulus and compressive strength will also decrease.

2.2. The Frost Heaving Pressure. According to Walder and Hallet [28], the frost heaving pressure p_i is related to the duration time of the low temperature, the value of temperature, the volume of ice and water, and flow resistance, which can be calculated by

$$p_i(t) = \frac{L(-T_c)}{\nu_s T_a} \left(1 - e^{-(t/\tau)}\right) + p_0 e^{-(t/\tau)}, \quad (14)$$

For the rock especially the soft rock, the plastic zone will be formed near the microcrack tip when the microcrack wall is loaded by the frost heaving pressure. So, in order to satisfy the requirement of the linear elastic fracture mechanics, it is necessary to deal with the plastic zone near the microcrack tip with the equivalent method. The plastic region reduces the stiffness of the rock which is equivalent to a longer microcrack. The equivalent propagation length a' of the microcrack is [27]

$$a' = a + r_y, \quad (10)$$

where a is the original microcrack length and r_y is the length of the plastic zone near the microcrack tip shown in Figure 1, which can be expressed as for a plane stress issue [27].

$$r_y = \frac{1}{2\pi} \left(\frac{K_I}{\sigma_s}\right)^2, \quad (11)$$

where σ_s is the rock yield strength and K_I is the first stress intensity factor at the microcrack tip.

So after amendment, the actual propagation length $\Delta a'$ of the microcrack shown in Figure 1 is

$$\Delta a' = \Delta a + r_y. \quad (12)$$

The shape of the microcrack after propagation is shown as the dotted line in Figure 1.

After m freeze-thaw cycles, the microcrack half-length a_m is

$$a_m = a_{m-1} + \frac{-(2a_{m-1}bp + a_{m-1}G)\pi + \sqrt{(2a_{m-1}bp + a_{m-1}G)^2\pi^2 + 8Gpa_{m-1} \times \Delta V_i'}}{2G\pi}. \quad (13)$$

where the characteristic time τ is [28]

$$\tau = \left(\frac{8}{3\pi}\right) \left(\frac{1 - \nu}{\mu}\right) \left(\frac{g\nu_i}{\nu_s^2}\right) R_f, \quad (15)$$

where $p_i(t)$ is the frost heaving pressure of ice at time t ; $L(-T_c)/\nu_s T_a = 1.1 \text{ MPa}/^\circ\text{C} \times (-T_c)$. $L(-T_c)$ is the fusion heat of ice at $T = T_c$, kJ/mol; ν_s and ν_L are the relative volume of ice and water, respectively; when $T < -1^\circ\text{C}$, $\nu_L = 0.07$ and $\nu_s = 0.93$ [29]; T_a is the absolute temperature, 273.15 K; p_0 is the initial frost heaving pressure, and according to the experiment result, it is 2 MPa; ν is the rock Poisson ratio; μ is the

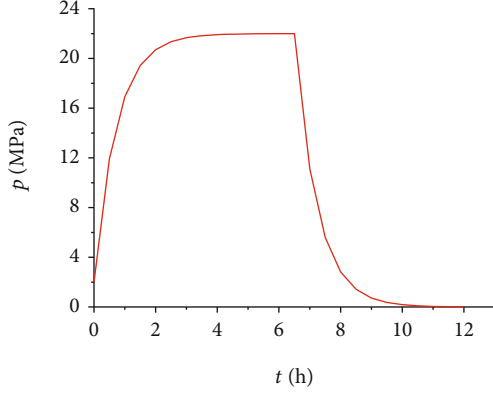


FIGURE 2: Variation of the frost heaving pressure with time during one freeze-thaw cycle.

rock shear modulus, MPa; R_f is the flow resistance, Pa·s/m; g is the gravitational acceleration, m/s²; a is the microcrack half-length. Here, the freezing and thawing temperatures are adopted to be -20°C and 20°C, respectively. The time of one freeze-thaw cycle is 12 h. The detailed calculation method of R_f has been introduced by Walder and Hallet [28].

Therefore, the variation of the frost heaving pressure with time is shown in Figure 2.

The work done by the frost heaving pressure along the microcrack inner wall for one freeze-thaw cycle is

$$W = \int_0^{t_i} 4ap_i(t) \frac{\Delta b}{t_i} dt = 4a \frac{\Delta b}{t_i} \int_0^{t_i} p_i(t) dt, \quad (16)$$

where $t_i = 43200s$ and $p_i(t)$ can be solved with Equation (14).

3. Establishment of the Rock Constitutive Model under Compression after Freeze-Thaw Cycles

3.1. Establishment of the Rock Constitutive Model. It is assumed that the water/ice phase change in freeze-thaw condition is the main reason leading to rock deterioration. The frost heaving pressure is generated by 9% volume expansion of freezing water in closed microcrack. The pressure makes the microcrack propagate and when the temperature rises, the melt water will go into the newly formed microcracks. The repeated freeze-thaw cycles cause continuous damage to the rock. Based on this viewpoint, the propagation of one single microcrack under the frost heaving pressure is studied, and the relationship between the propagation length of the microcrack and the frost heaving pressure is obtained. Because new damage continuously occurs under freeze-thaw cycles, the elastoplastic theory is adopted to study the rock damage mechanical behavior, and finally, a new constitutive model for a rock based on the deformation and propagation of microcracks under compression after freeze-thaw cycles is proposed.

3.2. Strain Decomposition. In this proposed model, the total strain of the rock under compression can be decomposed into the following four components such as the initial dam-

age strain, elastic strain, plastic strain, and additional damage strain induced by the microcrack propagation. It can be expressed as

$$\boldsymbol{\varepsilon} = \boldsymbol{\varepsilon}_d + \boldsymbol{\varepsilon}_e + \boldsymbol{\varepsilon}_{da} + \boldsymbol{\varepsilon}_p, \quad (17)$$

where $\boldsymbol{\varepsilon}$ is the total strain, $\boldsymbol{\varepsilon}_d$ is the initial damage strain, $\boldsymbol{\varepsilon}_e$ is the elastic strain, $\boldsymbol{\varepsilon}_{da}$ is the additional damage strain, and $\boldsymbol{\varepsilon}_p$ is the plastic strain. Their calculation methods are discussed below.

3.2.1. Initial Damage Strain Induced by Freeze-Thaw Cycles. The initial damage strain induced by freeze-thaw cycles is

$$[\boldsymbol{\varepsilon}_d] = [C_d][\boldsymbol{\sigma}], \quad (18)$$

where $[C_d]$ is the initial damage compliance matrix.

Assume the half-length of the i^{th} microcrack becomes a_m^i after m freeze-thaw cycles. α_i is the orientation of the i^{th} microcrack; then, the initial damage compliance matrix due to one single microcrack is given by [25]

$$[C] = [C_0] + ([A_i]^{-1})^T [\Delta C_i] [A_i]^{-1}, \quad (19)$$

where $[C_0]$ is the elastic compliance matrix, $[A_i]$ is the transformation matrix, and $[A_i]^{-1}$ is its inverse matrix.

$$[A_i] = \begin{bmatrix} \cos^2 \alpha_i & \sin^2 \alpha_i & -\sin 2\alpha_i \\ \sin^2 \alpha_i & \cos^2 \alpha_i & \sin 2\alpha_i \\ \frac{1}{2} \sin 2\alpha_i & -\frac{1}{2} \sin 2\alpha_i & \cos 2\alpha_i \end{bmatrix},$$

$$[A_i]^{-1} = \begin{bmatrix} \cos^2 \alpha_i & \sin^2 \alpha_i & \sin 2\alpha_i \\ \sin^2 \alpha_i & \cos^2 \alpha_i & -\sin 2\alpha_i \\ \frac{1}{2} \sin 2\alpha_i & -\frac{1}{2} \sin 2\alpha_i & \cos 2\alpha_i \end{bmatrix}, \quad (20)$$

$$[\Delta C_i] = \begin{bmatrix} 0 & 0 & 0 \\ 0 & \frac{C_n^i a_m^i}{K_n^i 2dh} & 0 \\ 0 & 0 & \frac{C_s^i a_m^i}{K_s^i 2dh} \end{bmatrix}$$

where C_n^i , C_s^i , K_n^i , and K_s^i are the compression transferring coefficient, shear transferring coefficient, normal stiffness, and shear stiffness of the i^{th} crack, respectively. d and h are width and height of the rock sample, respectively.

The total compliance matrix including N microcracks whose half-length a_m is

$$[C] = [C_0] + \sum_{i=1}^N ([A_i]^{-1})^T [\Delta C_i] [A_i]^{-1}. \quad (21)$$

The orientation and size of the microcracks in the rock are assumed to be random, which can be expressed with a

probability density function $\rho(a, \alpha) = \rho(a)\rho(\alpha)$. According to the distribution law of the microcrack, its orientation and size satisfy the following normalization condition [30]:

$$\int_{a_{\min}}^{a_{\max}} \rho(a) da \int_0^{\pi/2} \rho(\alpha) \sin \alpha d\alpha = 1. \quad (22)$$

Assume the total number of the microcracks is N_c , and then, the number N of the microcracks with half-length of a can be expressed as

$$N = N_c \int_{a_{\min}}^a \rho(a) da. \quad (23)$$

Assume the orientation of the microcrack evenly distributes in all directions [31], and according to the definition of the density function, $\rho(\alpha) = 1$ is obtained. Therefore, the total compliance matrix including all microcracks is

$$[C] = [C_0] + N_c \int_{a_{\min}}^{a_{\max}} ([A_i]^{-1})^T [\Delta C_i] [A_i]^{-1} \rho(a) da \int_0^{\pi/2} \sin \alpha d\alpha. \quad (24)$$

With Equation (24), the initial damage compliance matrix for different freeze-thaw cycles can be calculated and then, the initial damage strain can be finally obtained.

3.2.2. Elastic Strain. For a plane stress issue, the elastic constitutive relationship of rock is [32]

$$[\boldsymbol{\varepsilon}_e] = [C_0][\boldsymbol{\sigma}], \quad (25)$$

where $[\boldsymbol{\varepsilon}_e]$ is the elastic strain matrix, $[\boldsymbol{\varepsilon}_e] = [\varepsilon_{11} \ \varepsilon_{33} \ \varepsilon_{13}]^T$, $[\boldsymbol{\sigma}]$ is the stress matrix, $[\boldsymbol{\sigma}] = [\sigma_{11} \ \sigma_{33} \ \sigma_{13}]$, and $[C_0]$ is the elastic compliance matrix,

$$[C_0] = \begin{bmatrix} \frac{1}{E} & -\frac{\nu}{E} & 0 \\ -\frac{\nu}{E} & \frac{1}{E} & 0 \\ 0 & 0 & \frac{1}{\mu} \end{bmatrix}, \quad (26)$$

where E , μ , and ν are the rock elastic modulus, shear modulus, and Poisson ratio, respectively.

3.2.3. Additional Damage Strain due to Compression. Under compression, the microcrack will firstly close, and then, the friction occurs along the microcrack face. When the shear stress along the microcrack face is larger than the friction, the wing crack will initiate and propagate from the microcrack tip. The propagation of the microcrack will lead to the decrease in the rock elastic modulus, strength, and increase in the rock permeability. The sliding microcrack model under compression is shown in Figure 3.

After m freeze-thaw cycles, the microcrack length becomes a_m , and for this moment, the first stress intensity

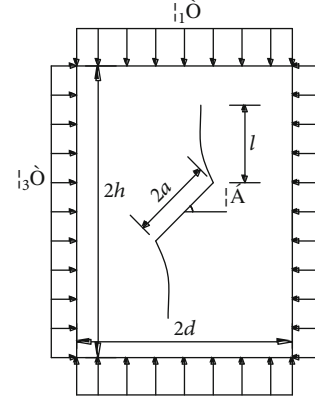


FIGURE 3: The sliding microcrack model under compression. $2a$ and α are the length and dip angle of the microcrack, respectively. l is the wing crack length. $2h$ and $2d$ are the height and width of the model, respectively.

factor K_I at the microcrack tip is [31, 33]

$$K_I = \frac{2}{\sqrt{3}} \tau^* \sqrt{\pi a_m}, \quad (27)$$

where τ^* is the effective shear stress on the microcrack face, $\tau^* = \tau_m - f\sigma_m$, τ_m and σ_m are the shear and normal stresses on the microcrack face, respectively, and f is the friction coefficient of the microcrack face.

$$\begin{aligned} \tau_m &= \frac{\sigma_1 - \sigma_3}{2} \sin 2\alpha, \\ \sigma_m &= \frac{\sigma_1 + \sigma_3}{2} - \frac{\sigma_1 - \sigma_3}{2} \cos 2\alpha. \end{aligned} \quad (28)$$

When $K_I \geq K_{IC}$ (K_{IC} is the rock fracture toughness), the microcrack begins to propagate, and the stress intensity factor K_I^W at the wing crack tip is [31, 33].

$$K_I^W = \frac{2a\tau^* \cos \alpha}{\sqrt{\pi l}} - \sigma_3 \sqrt{\pi l}, \quad (29)$$

where

$$\tau^* = \frac{1}{2} [(\sigma_1 - \sigma_3) \sin 2\alpha - f(\sigma_1 + \sigma_3 + (\sigma_1 - \sigma_3) \cos 2\alpha)]. \quad (30)$$

The wing crack will stop propagating when $K_I^W \leq K_{IC}$, so l can be calculated with Equation (29).

The additional damage of a rock is due to the wing crack propagation. According to Li and Lajtai [34], the

macroscopic strain of a rock can be calculated.

$$\begin{aligned}\varepsilon_1^* &= \frac{8\lambda\chi \cos \alpha}{E} \left[\frac{2\tau^* \cos \alpha}{\pi} \ln \frac{l}{a} - \sigma_3 \left(\frac{l}{a} - 1 \right) \right], \\ \varepsilon_3^* &= \frac{\chi}{E} \left[\frac{16\tau^* \gamma \cos^2 \alpha}{\pi} \ln \frac{l}{a} + \sigma_3 \pi \left(\frac{l^2}{a^2} - 1 \right) \right. \\ &\quad \left. - 8 \cos \alpha \left(\frac{l}{a} - 1 \right) (\sigma_3 \gamma + \tau^*) \right],\end{aligned}\quad (31)$$

where ε_1^* and ε_3^* are the strains along the vertical and horizontal directions, respectively; $\lambda = \sin \alpha \cos \alpha - f \cos^2 \alpha$; $\gamma = -\cos \alpha \sin \alpha - f \sin^2 \alpha$. χ is defined as the initial microcrack density and is expressed as $\chi = Na^2/V$. N is the total number of the microcracks in a two-dimensional body of unit thickness whose volume is $V = 2h \times 2d$.

Finally, the total rock strain due to compression considering the normalization condition is

$$\begin{aligned}\varepsilon_1 &= N_c \int_{a_{\min}}^{a_{\max}} \rho(a) da \int_0^{\pi/2} \rho(\alpha) \sin \alpha d\alpha \cdot \frac{8\lambda\chi \cos \alpha}{E} \\ &\quad \times \left[\frac{2\tau^* \cos \alpha}{\pi} \ln \frac{l}{a} - \sigma_3 \left(\frac{l}{a} - 1 \right) \right], \\ \varepsilon_3 &= N_c \int_{a_{\min}}^{a_{\max}} \rho(a) da \int_0^{\pi/2} \rho(\alpha) \sin \alpha d\alpha \cdot \frac{\chi}{E} \\ &\quad \times \left[\frac{16\tau^* \gamma \cos^2 \alpha}{\pi} \ln \frac{l}{a} + \sigma_3 \pi \left(\frac{l^2}{a^2} - 1 \right) \right. \\ &\quad \left. - 8 \cos \alpha \left(\frac{l}{a} - 1 \right) (\sigma_3 \gamma + \tau^*) \right].\end{aligned}\quad (32)$$

3.2.4. The Plastic Strain due to Compression. The Drucker-Prager model is adopted to describe the rock plastic behavior, whose yield function and plastic potential function are

$$\begin{aligned}F(\sigma, \kappa) &= \beta_1 I_1 + \sqrt{J_2} - \kappa, \\ G(\sigma, \kappa) &= \beta_2 I_1 + \sqrt{J_2} - \kappa,\end{aligned}\quad (33)$$

where $I_1 = \sigma_1 + \sigma_2 + \sigma_3$, $J_2 = (1/6)[(\sigma_1 - \sigma_2)^2 + (\sigma_2 - \sigma_3)^2 + (\sigma_3 - \sigma_1)^2]$, $\beta_1 = 2 \sin \varphi / \sqrt{3}(3 - \sin \varphi)$, $\beta_2 = 2 \sin \psi / \sqrt{3}(3 - \sin \psi)$, and φ and ψ are the friction angle and dilation angle, respectively. κ is the hardening function, which can be expressed as [35]

$$\kappa = \sigma_0 + a_1 \lambda \exp(a_2 I_1 - a_3 \lambda),\quad (34)$$

where a_1 , a_2 , and a_3 are the constants which can be obtained by fitting with the uniaxial compressive stress-strain curve. $\sigma_0 = 6c \cos \varphi / \sqrt{3}(3 - \sin \varphi)$; c is the rock cohesion.

According to Tan et al. [36], the rock internal friction angle is basically the same, but the rock cohesion decreases

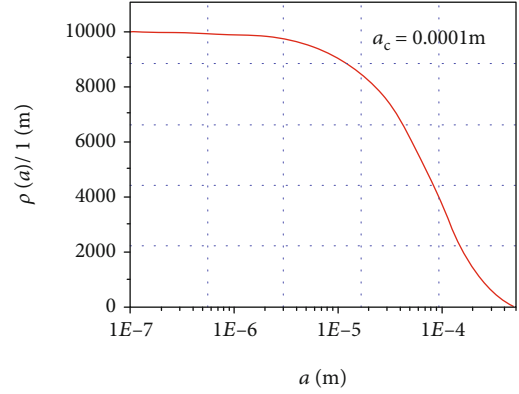


FIGURE 4: Probability density functions of the microcracks.

with the freeze-thaw cycles and obeys the following exponential function:

$$c(m) = c_0 e^{-0.072m},\quad (35)$$

where c_0 is the original cohesion strength (before freeze-thaw cycle) and $c(m)$ is the cohesion after the m^{th} freeze-thaw cycle.

The plastic strain rate is

$$\dot{\varepsilon}_p = \dot{\lambda} \frac{\partial G}{\partial \sigma},\quad (36)$$

where $\dot{\lambda}$ is a proportion coefficient.

3.2.5. The Number of the Microcracks in a Rock. The probability function [37] of the microcrack length can be expressed as

$$\rho(a) = \begin{cases} -\frac{1}{a_c} \exp\left(-\frac{a}{a_c}\right), & a_{\min} \leq a \leq a_{\max}, \\ 0, & \text{otherwise,} \end{cases}\quad (37)$$

where a_c is the characteristic length of the microcrack, $a_c = \int_{a_{\min}}^{a_{\max}} \rho(a) da$. N_c is the total number of the microcracks per unit volume, which is determined by the total volume of the microcrack, $V_c = 2\pi b N_c \int_{a_{\min}}^{a_{\max}} \rho(a) a^2 da$.

Finally, the curve of probability density function of the microcracks is shown in Figure 4.

According to the experiment result of Rostásy et al. [38], the total number of the microcracks basically remains the same after freeze-thaw cycles. The longer microcracks will propagate, while the shorter ones will close under the extrusion of other microcracks. Therefore, it is assumed that the total volume of the microcrack is the same during the freeze-thaw cycles and compression. So the total volume V_c of the microcracks can be expressed with the rock void porosity e and the total volume V of the rock sample, namely, $V_c = eV$.

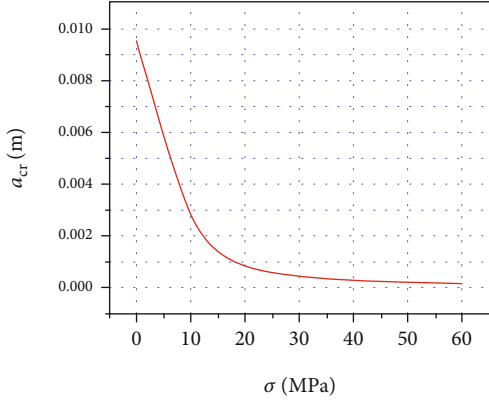


FIGURE 5: Relationship between the microcrack critical length and axial stress.

The first stress intensity factor K_I of the microcrack with different lengths at the same stress condition can be expressed as

$$K_I = \frac{2}{\sqrt{3}} \tau^* \sqrt{\pi a}. \quad (38)$$

Equation (38) can be changed into

$$\left(\frac{\sqrt{3} K_{IC}}{2\tau^*} \right)^2 \frac{1}{\pi} = a_{cr}, \quad (39)$$

where $\tau^* = (1/2)[(\sigma_1 - \sigma_3) \sin 2\varphi - f(\sigma_1 + \sigma_3 + (\sigma_1 - \sigma_3) \cos 2\varphi)]$ where a_{cr} is the critical length of the microcrack which becomes active at the condition of σ_1 and σ_3 when $K_I = K_{IC}$.

As shown in Figure 5, the microcrack whose length is greater than a_{cr} will propagate.

The total number of microcracks that will be actually activated is given by $N = N_c \int_{a_{min}}^{a_{max}} \rho(a) da$, as shown in Figure 6.

3.2.6. The Numerical Algorithm of the Proposed Model. The calculation of the rock plastic strain at different times can be calculated with the semi-implicit return graphical algorithm [17], shown in Figure 7. The plastic variables σ_{n+1} , ϵ_{n+1}^p , κ_{n+1} , r_{n+1} , and h_{n+1} at t_{n+1} are determined by integration flow rule and hardening law and $\Delta\sigma^{tr}$, σ_n , κ_n , $r_n = \partial F / \partial \sigma|_{\sigma=\sigma_n}$, and $h_n = \partial \kappa / \partial \lambda|_{\lambda=\lambda_n}$ at time t_n . The main steps are as follows:

- (1) Update strain tensor, and calculate the elastic strain at time t_{n+1}

$$\begin{aligned} \epsilon_{n+1} &= \epsilon_n + \Delta\epsilon, \\ \Delta\sigma_{n+1}^{tr} &= \mathbf{C}^{-1} : \Delta\epsilon, \end{aligned} \quad (40)$$

where \mathbf{C} is the initial elastic compliance matrix including the initial damage compliance tensor caused by freeze-thaw and elastic compliance tensor.

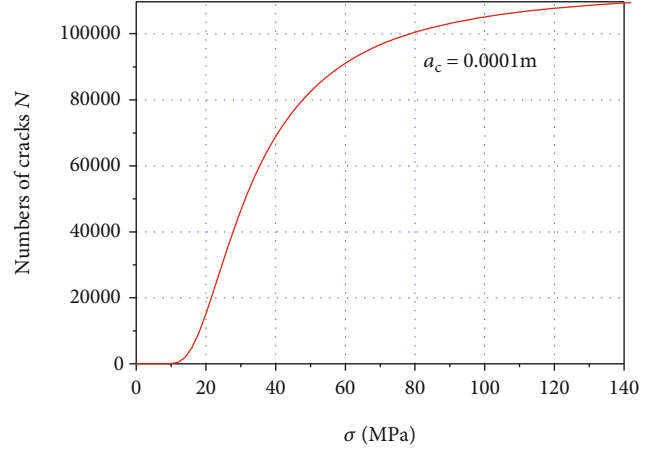


FIGURE 6: Relationship between the microcrack initiation number and axial stress.

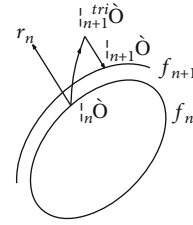


FIGURE 7: Graphic returns method of semi-implicit integration algorithm.

- (2) Update stresses and plastic strain and hardening function κ_{n+1}

$$\begin{aligned} \epsilon_{n+1}^p &= \epsilon_n^p + \Delta\lambda_{n+1} r_n, \\ \kappa_{n+1} &= \kappa_n + \Delta\lambda_{n+1} h_n, \\ \sigma_{n+1} &= \mathbf{C}^{-1} : (\epsilon_{n+1} - \epsilon_{n+1}^p) \\ F_{n+1} &= F(\sigma_{n+1}, \kappa_{n+1}) = 0 \end{aligned} \quad (41)$$

where $r_n = \partial G / \partial \sigma|_{\sigma=\sigma_n}$ and $h_n = \partial \kappa / \partial \lambda|_{\lambda=\lambda_n}$.

Calculate the plastic internal variable $\Delta\lambda_{n+1}$:

$$a_{n+1}^k + \mathbf{C}^{-1} : \Delta\sigma_{n+1}^k + \delta\lambda^k r_n = 0, \quad (42)$$

$$b_{n+1}^k - \Delta\kappa_{n+1}^k + \delta\lambda^k h_n = 0, \quad (43)$$

$$F_{n+1}^k + F_{\sigma}^k : \Delta\sigma_{n+1}^k + F_{\kappa}^k \bullet \Delta\kappa_{n+1}^k = 0, \quad (44)$$

$$\begin{bmatrix} \Delta\sigma \\ \Delta\kappa \end{bmatrix} = - \begin{bmatrix} A^{(k)} \\ \tilde{a}^{(k)} \end{bmatrix} - \delta\lambda^{(k)} \begin{bmatrix} A^{(k)} \\ \tilde{r}_n \end{bmatrix}, \quad (45)$$

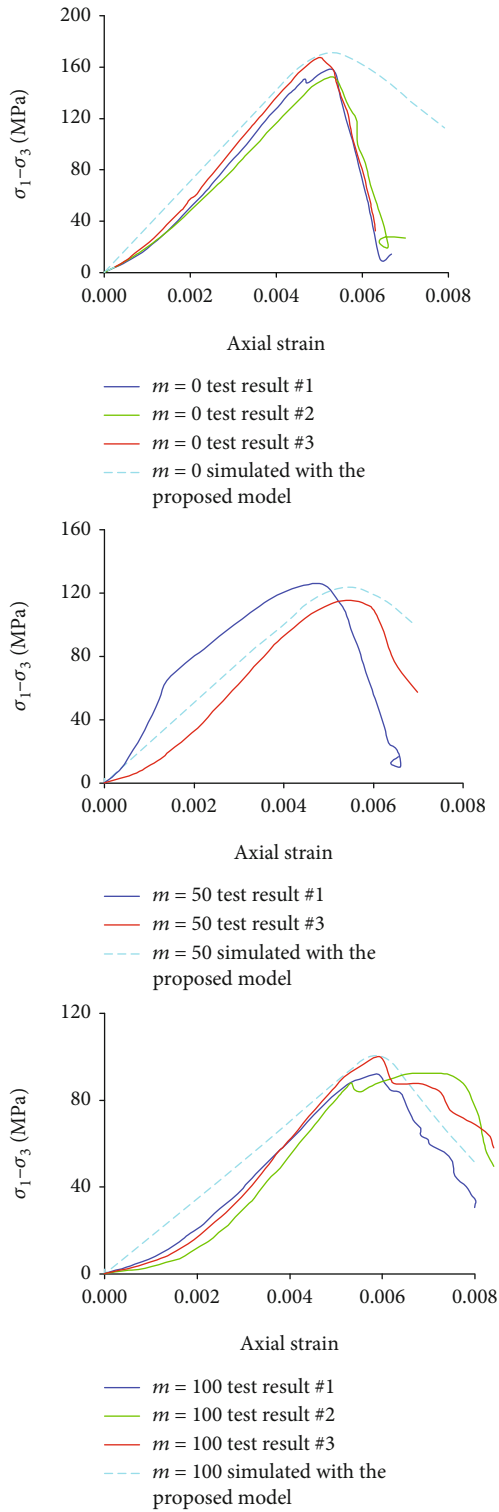


FIGURE 8: Comparison of the stress-strain relationships for triaxial compression tests with confining pressure $\sigma_3 = 5$ MPa by Tan et al. [36] and simulated with the proposed model. The predicted stress-strain relationships agree well with the tested ones.

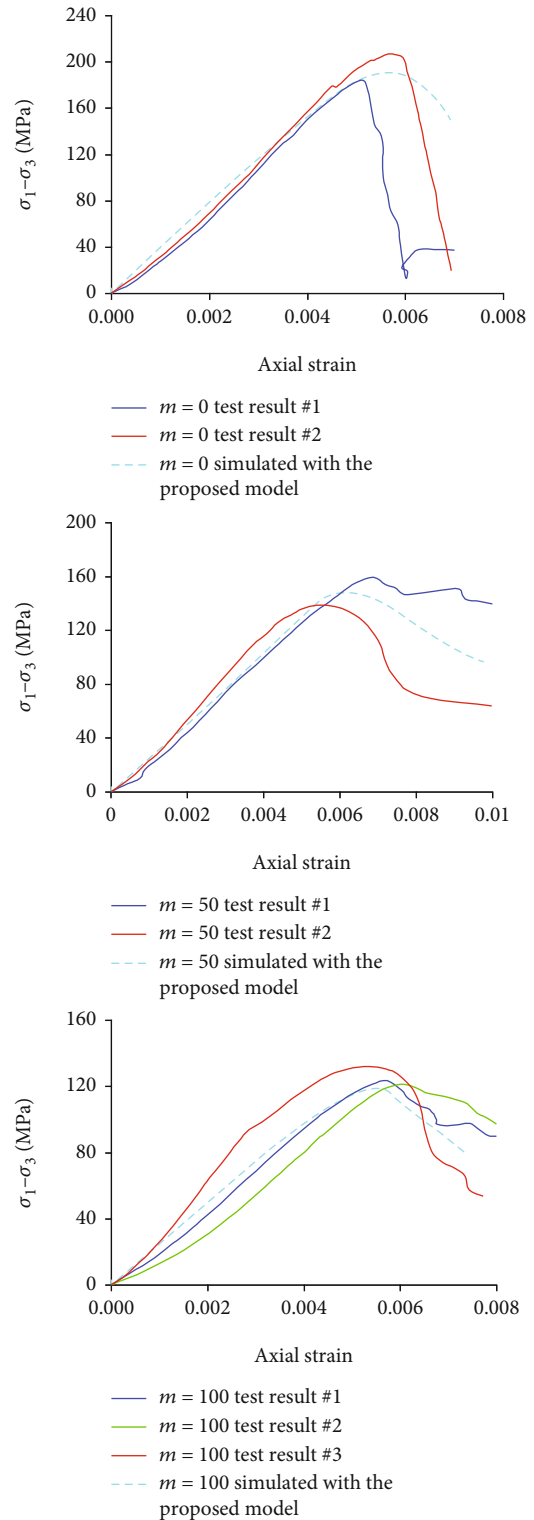


FIGURE 9: Comparison of the stress-strain relationships for triaxial compression tests with confining pressure $\sigma_3 = 10$ MPa by Tan et al. [36] and simulated with the proposed model. The predicted stress-strain relationships agree well with the tested ones.

TABLE 1: The calculation parameters.

E (GPa)	ν	e	c (MPa)	a_1 (MPa)	a_2 (MPa ⁻¹)	a_3	a_c (m)	a_{\min} (m)	a_{\max} (m)
36.71	0.2	0.0067	27.43	5e9	1e-8	100	1e-4	1e-7	0.0012

where

$$\begin{aligned} [A^k] &= \begin{bmatrix} C & 0 \\ 0 & -I \end{bmatrix}, \\ [\tilde{a}^{(k)}] &= \begin{bmatrix} a^k \\ b^k \end{bmatrix} = \begin{bmatrix} 0 \\ 0 \end{bmatrix}, \\ [\tilde{r}_n] &= \begin{bmatrix} r_n \\ h_n \end{bmatrix} \dots \end{aligned} \quad (46)$$

$\delta\lambda^{(k)}$ can be obtained with Equation (45)

$$\delta\lambda = \frac{F^k}{\partial F : A^k : \tilde{r}_n}, \quad (47)$$

where $[\partial F] = [F_\sigma \quad F_\kappa]$.

$$\Delta\lambda_{n+1}^{k+1} = \Delta\lambda_{n+1}^k + \delta\lambda^k. \quad (48)$$

(3) Update N_{n+1} which is the number of microcracks that begin propagating

At time t_{n+1} , the updated normal stress is σ_{n+1} , under which the critical initiation length $(a_{cr})_{n+1}$ of the microcrack is calculated by

$$(a_{cr})_{n+1} = \frac{1}{\pi} \left(\frac{\sqrt{3}K_{IC}}{2(\tau^*)_{n+1}} \right)^2, \quad (49)$$

where

$$\begin{aligned} (\tau^*)_{n+1} &= \frac{1}{2} \left[\begin{array}{c} ((\sigma_1)_{n+1}^{tr} - \sigma_3) \sin 2\varphi \\ -\mu((\sigma_1)_{n+1}^{tr} + \sigma_3 + ((\sigma_1)_{n+1}^{tr} - \sigma_3) \cos 2\varphi) \end{array} \right], \\ N_{n+1} &= N_c \int_{(a_{cr})_{n+1}}^{a_{\max}} \rho(a) da. \end{aligned} \quad (50)$$

(4) Update the additional damage strain $(\boldsymbol{\epsilon}_{ad})_{n+1}$

The additional damage strain matrix of $\boldsymbol{\epsilon}_{ad}$ can be expressed as

$$[\boldsymbol{\epsilon}_{ad}] = [\boldsymbol{\epsilon}_1 \quad \boldsymbol{\epsilon}_3 \quad 0]. \quad (51)$$

Update the length of wing crack l_{n+1}

$$K_I^W = \frac{2a(\tau)_{n+1} \cos \varphi}{\sqrt{\pi l_{n+1}}} - (\sigma_3)_{n+1} \sqrt{\pi l_{n+1}}, \quad (52)$$

where $K_I^W = K_{IC}$.

Update the additional strain

$$\begin{aligned} (\boldsymbol{\epsilon}_1)_{n+1} &= N_{n+1} \int_{(a_{cr})_{n+1}}^{a_{\max}} \rho(a) da \int_0^{\pi/2} \rho(\alpha) \sin \alpha d\alpha \cdot \frac{8\lambda a \cos^2 \alpha}{E} \\ &\quad \times \left[\frac{2(\tau^*)_{n+1} \cos \alpha}{\pi} \ln \frac{l_{n+1}}{a} - \sigma_3 \left(\frac{l_{n+1}}{a} - 1 \right) \right], \\ (\boldsymbol{\epsilon}_3)_{n+1} &= N_{n+1} \int_{(a_{cr})_{n+1}}^{a_{\max}} \rho(a) da \int_0^{\pi/2} \rho(\alpha) \sin \alpha d\alpha \cdot \frac{a^2}{E} \\ &\quad \times \left[\frac{16(\tau^*)_{n+1} \gamma \cos^2 \alpha}{\pi} \ln \frac{l_{n+1}}{a} + \sigma_3 \pi \left(\frac{l_{n+1}^2}{a^2} - 1 \right) \right] \\ &\quad \times \left[-8 \cos \varphi \left(\frac{l_{n+1}}{a} - 1 \right) (\sigma_3 \gamma + (\tau^*)_{n+1}) \right]. \end{aligned} \quad (53)$$

(5) Update the stress

$$\boldsymbol{\sigma}_{n+1}^* = \boldsymbol{\sigma}_{n+1} - \mathbf{C}^{-1} : (\boldsymbol{\epsilon}_{ad})_{n+1} \quad (54)$$

4. Verification of the Proposed Model

In order to verify the proposed model, the experiment by Tan et al. [36] is taken for an example. The rock type is granite, which is obtained from Galongla mountain in Tibet of China, where a highway tunnel passes through the mountain and it is very cold in winter. The tested samples are prepared as cylinders with 50 mm in diameter and 100 mm high. The compression tests with confining pressure 5 MPa and 10 MPa on the rock sample are done with a multifunction rock mechanics test machine, and the corresponding stress-strain curves are shown in Figures 8 and 9. The calculation parameters are shown in Table 1.

The characteristic length a_c of the microcrack under 0, 50, and 100 freeze-thaw cycles is solved to be 0.1 mm, 0.41 mm and 1.64 mm, respectively, with Equation (13). According to the proposed model, the complete stress-strain curve of the rock under compression with confining pressure $\sigma_3 = 5$ MPa/10 MPa is shown in Figures 8 and 9.

It can be seen that the simulated stress-strain curves agree well with the tested ones especially when $\sigma_3 = 10$ MPa. Meanwhile, with the increasing freeze-thaw cycles, both the climax strength and slope of the stress-strain curve decrease; that is to say, the rock compressive strength and elastic modulus both decrease. It indicates that the freeze-thaw cycles have much effect on the rock mechanical behavior.

5. Conclusions

- (1) Based on the fracture mechanics, the calculation method of the microcrack propagation length induced by the freeze-thaw cycles is proposed. Meanwhile, the variation of the frost heaving pressure with time during one freeze-thaw cycle is also calculated
- (2) In the framework of the fracture and damage mechanics, the total strain of the rock under compression after freeze-thaw cycles can be decomposed into the initial damage strain, elastic strain, plastic strain, and additional damage strain. And their calculation methods are discussed in detail. Finally, a constitutive model for a rock based on the deformation and propagation of microcracks under compression after freeze-thaw cycles is established
- (3) By utilizing the semi-implicit algorithm, the stress-strain relationship of the proposed model is calculated. The comparison of the theoretical results of the proposed method and test ones shows that they agree well with each other. Overall, the proposed method provides a new way to simulate the mechanical behavior of a rock under compression after freeze-thaw cycles

Data Availability

All data generated or analyzed during this study are included in this manuscript.

Conflicts of Interest

The authors declare that there are no conflicts of interest regarding the publication of this paper.

Acknowledgments

This study is supported by the National Key Research and Development Plan of China (2019YFC1509701).

References

- [1] T. C. Powers, "Freezing effect in concrete. Durability of concrete," in *ACI SP47*, pp. 1–11, American Concrete Institute, Detroit, Michigan, 1975.
- [2] R. Altindag, I. S. Alyildiz, and T. Onargan, "Mechanical property degradation of ignimbrite subjected to recurrent freeze-thaw cycles," *International Journal of Rock Mechanics and Mining Sciences*, vol. 41, no. 6, pp. 1023–1028, 2004.
- [3] A. Momeni, Y. Abdilor, G. R. Khanlari, M. Heidari, and A. A. Sepahi, "The effect of freeze-thaw cycles on physical and mechanical properties of granitoid hard rocks," *Bulletin of Engineering Geology and the Environment*, vol. 75, pp. 1649–1656, 2016.
- [4] D. T. Nicholson and F. H. Nicholson, "Physical deterioration of sedimentary rocks subjected to experimental freeze-thaw weathering," *Earth Surface Processes and Landforms*, vol. 25, no. 12, pp. 1295–1307, 2000.
- [5] J. Zhang, H. W. Deng, J. R. Deng, and B. Ke, "Development of energy-based brittleness index for sandstone subjected to freeze-thaw cycles and impact loads," *IEEE Access*, vol. 6, pp. 48522–48530, 2018.
- [6] S. R. Wang, Y. L. Chen, J. Ni, M. D. Zhang, and H. Zhang, "Influence of freeze-thaw cycles on engineering properties of tonalite: examples from China," *Advances in Civil Engineering*, vol. 2019, Article ID 3418134, 12 pages, 2019.
- [7] H. Tounsi, A. Rouabhi, E. Jahangir, and F. Guerin, "Mechanical behavior of frozen metapelite: laboratory investigation and constitutive modeling," *Cold Regions Science and Technology*, vol. 175, 2020.
- [8] Z. C. Tang, L. Li, X. C. Wang, and J. P. Zou, "Influence of cyclic freezing-thawing treatment on shear behaviors of granite fracture under dried and saturated conditions," *Cold Regions Science and Technology*, vol. 181, p. 103192, 2021.
- [9] K. M. Neaupane and T. Yamabe, "A fully coupled thermo-hydro-mechanical nonlinear model for a frozen medium," *Computers and Geotechnics*, vol. 28, no. 8, pp. 613–637, 2001.
- [10] G. E. Exadaktylos, "Freezing–thawing model for soils and rocks," *Journal of Materials in Civil Engineering*, vol. 18, no. 2, pp. 241–249, 2006.
- [11] Y. S. Kang, Q. S. Liu, and S. B. Huang, "A fully coupled thermo-hydro-mechanical model for rock mass under freezing/thawing condition," *Cold Regions Science and Technology*, vol. 95, pp. 19–26, 2013.
- [12] D. Y. Wu, Y. M. Lai, and M. Zhang, "Thermo-hydro-salt-mechanical coupled model for saturated porous media based on crystallization kinetics," *Cold Regions Science and Technology*, vol. 133, pp. 94–107, 2017.
- [13] S. B. Huang, Q. S. Liu, A. Cheng, Y. Z. Liu, and G. F. Liu, "A fully coupled thermo-hydro-mechanical model including the determination of coupling parameters for freezing rock," *International Journal of Rock Mechanics and Mining Sciences*, vol. 103, pp. 205–214, 2018.
- [14] S. Y. Dong and X. Yu, "Microstructure-based random finite element method simulation of frost heave: theory and implementation," *Transportation Research Record*, vol. 2672, no. 52, pp. 347–357, 2018.
- [15] Z. Wang, Z. D. Zhu, and S. Zhu, "Thermo-mechanical-water migration coupled plastic constitutive model of rock subjected to freeze-thaw," *Cold Regions Science and Technology*, vol. 161, pp. 71–80, 2019.
- [16] W. Fang, N. Jiang, and X. D. Luo, "Establishment of damage statistical constitutive model of loaded rock and method for determining its parameters under freeze-thaw condition," *Cold Regions Science and Technology*, vol. 160, pp. 31–38, 2019.
- [17] J. C. Simo and R. L. Taylor, "A return mapping algorithm for plane stress elastoplasticity," *International Journal for Numerical Methods in Engineering*, vol. 22, no. 3, pp. 649–670, 1986.

- [18] B. Moran, M. Ortiz, and F. Shih, "Formulation of implicit finite element methods for multiplicative finite deformation plasticity," *International Journal for Numerical Methods in Engineering*, vol. 29, no. 3, pp. 483–514, 1990.
- [19] A. Saad, S. Guédon, and F. Martineau, "Alteration microstructurale de roches sedimentaires par des cycles de gel- degel : etude experimentale de parametres d'etat et de transfert," *Comptes Rendus Geoscience*, vol. 342, no. 3, pp. 197–203, 2010.
- [20] N. Matsuoka, "Mechanisms of rock breakdown by frost action: an experimental approach," *Cold Regions Science and Technology*, vol. 17, no. 3, pp. 253–270, 1990.
- [21] M. Mutluturk, R. Altindag, and G. Turk, "A decay function model for the integrity loss of rock when subjected to recurrent cycles of freezing-thawing and heating-cooling," *International Journal of Rock Mechanics and Mining Sciences*, vol. 41, no. 2, pp. 237–244, 2004.
- [22] H. Yavuz, R. Altindag, S. Sarac, I. Ugur, and N. Sengun, "Estimating the index properties of deteriorated carbonate rocks due to freeze- thaw and thermal shock weathering," *International Journal of Rock Mechanics and Mining Sciences*, vol. 43, no. 5, pp. 767–775, 2006.
- [23] M. Hori and H. Morihoro, "Micromechanical analysis on deterioration due to freezing and thawing in porous brittle materials," *International Journal of Engineering Science*, vol. 36, no. 4, pp. 511–522, 1998.
- [24] R. K. Abu al-Rub and G. Z. Voyiadjis, "On the coupling of anisotropic damage and plasticity models for ductile materials," *International Journal of Solids and Structures*, vol. 40, no. 11, pp. 2611–2643, 2003.
- [25] K. Maleki and A. Pouya, "Numerical simulation of damage-permeability relationship in brittle geomaterials," *Computers and Geotechnics*, vol. 37, no. 5, pp. 619–628, 2010.
- [26] G. P. Davidson and J. F. Nye, "A photoelastic study of ice pressure in rock cracks," *Cold Regions Science and Technology*, vol. 11, no. 2, pp. 141–153, 1985.
- [27] G. R. Irwin, J. A. Kies, and H. L. Smith, "Fracture strengths relative to onset and arrest of crack propagation," *Proceedings-American society for testing and materials*, vol. 58, pp. 640–660, 1958.
- [28] J. Walder and B. Hallet, "A theoretical model of the fracture of rock during freezing," *Geological society of America Bulletin*, vol. 96, no. 3, pp. 336–346, 1985.
- [29] M. Mikkola and J. Hartikainen, "Computational aspects of soil freezing problem," in *In Fifth World Congress on Computational Mechanics*, Vienna, Austria, 2002.
- [30] S. W. Yu and X. Q. Feng, "A micromechanics-based damage model for microcrack-weakened brittle solids," *Mechanics of Materials*, vol. 20, no. 1, pp. 59–76, 1995.
- [31] M. F. Ashby and S. D. Hallam, "The failure of brittle solids containing small cracks under compressive stress states," *Acta Metallurgica*, vol. 34, no. 3, pp. 497–510, 1986.
- [32] H. Martin and Sadd, "Elasticity," in *Theory, Application, and Numerics*, Academic Press, 2005.
- [33] H. Horii and S. Nemat-Nasser, "Compression-induced microcrack growth in brittle solids: axial splitting and shear failure," *Journal of Geophysical Research*, vol. 90, no. B4, pp. 3105–3125, 1985.
- [34] S. Li and E. Z. Lajtai, "Modeling the stress-strain diagram for brittle rock loaded in compression," *Mechanics of Materials*, vol. 30, no. 3, pp. 243–251, 1998.
- [35] R. I. Borja, K. M. Sama, and P. F. Sanz, "On the numerical integration of three-invariant elastoplastic constitutive models," *Computer Methods in Applied Mechanics and Engineering*, vol. 192, no. 9-10, pp. 1227–1258, 2003.
- [36] X. J. Tan, W. Chen, J. Yang, and J. Cao, "Laboratory investigations on the mechanical properties degradation of granite under freeze-thaw cycles," *Cold Regions Science and Technology*, vol. 68, no. 3, pp. 130–138, 2011.
- [37] C. Arson and J. M. Pereira, "Influence of damage on pore size distribution and permeability of rocks," *International Journal for Numerical and Analytical Methods in Geomechanics*, vol. 37, no. 8, pp. 810–831, 2013.
- [38] F. S. Rostásy, R. Weib, and G. Wiedemann, "Changes of pore structure of cement mortars due to temperature," *Cement and Concrete Research*, vol. 10, no. 2, pp. 157–164, 1980.

Research Article

Numerical Simulation of the Effect of Stress on the Seepage of Fractured Rock Mass

Liang Shiwei ^{1,2}, Wang Hongmei,³ Ge Di,² and Zhao Cunqing⁴

¹School of Human Settlements and Civil Engineering, Xi'an Jiaotong University, Xi'an 710049, China

²Xi'an Kedagaoxin University, Xi'an 710109, China

³Xi'an Research Institute of China Coal Technology and Engineering Group Co., Ltd., Xi'an 710054, China

⁴Gansu Lanjin Civil Explosion High-Tech Co., Ltd., Lanzhou 730000, China

Correspondence should be addressed to Liang Shiwei; 176032237@qq.com

Received 9 May 2021; Accepted 16 June 2021; Published 9 July 2021

Academic Editor: Yu Wang

Copyright © 2021 Liang Shiwei et al. This is an open access article distributed under the Creative Commons Attribution License, which permits unrestricted use, distribution, and reproduction in any medium, provided the original work is properly cited.

In our country, the Yellow River Basin ecological protection and development are put forward under the background of high quality. Among the 14 large-scale coal bases in our country, 9 coal bases are located in the Yellow River Basin, and the Shenfu-Dongsheng Coalfield, which is currently the largest under development, is located here. The region is in the process of coal mining, and the movement of overlying strata will cause the stress redistribution and coal seam in overlying aquifers also due to the effect of pore water pressure along the seepage of rock fracture and damage of overlying aquifer, so in the same formation, stress and the coupled action of seepage flow will produce mutual influence. This article through the early stage of the theoretical results discussed the application of numerical simulation method for simulating 2301 face, and the effect of stress on seepage is concluded. It is proved that the numerical simulation analysis has an important reference value for the coupling problem of stress and seepage. At the same time, the protective mining of aquifers is the basic condition for the surface ecological protection of the area, and it also provides a theoretical basis for the restoration of the ecological environment in the coal mining areas of the Yellow River Basin.

1. Introduction

China's Yellow River Basin is rich in coal resources; nine of the 14 large coal bases in our country coal base distribution are in the China Yellow River Basin's many Dongsheng Coalfields which are located in the western Inner Mongolia, and the development of one of the biggest piece of coal is in the northern Shanxi Province, which has simple mining geological conditions; the surface has the salient feature of the fragile ecological environment. In the edge of Maowusu desert and the Loess Plateau, sparse vegetation and wind erosion are serious, and most of the areas covered by thick wind-blown sand; the main aquifer of quaternary system of Sarah WuSu group is an unconformable contact on the Jurassic bedrock; the aquifer is the survival of the whole region water system; water is very precious, mainly by the surface precipitation to supply; we have a clear understanding that the development of coal should not be at the expense of the

destruction of the local ecological environment, especially in the northwest of Yulin and Ordos region; the region is an arid region, there is little rain, wind is big, and the ecological environment is very frail [1–4]. It is well known that the traditional coal mining causes damage of the underground rock mass structure, under the action of mining pressure and the movement of the overburden; the phenomenon such as fracture and overburden belongs to the discontinuous medium rock at the top of the aquifer in discontinuous medium flow, which we referred to as percolation, but due to coal mining, the influence of stress of rock mass will redistribute; it will inevitably affect the formation of the fissure zone of rock mass, which affects fluid seepage in rock mass; in the mining area, ecological restoration, protection, and restoration of aquifer are crucial. At present, scholars at home and abroad have studied more natural rock seepage, but less on the seepage characteristics under the influence of mining. In this paper, combining with the existing theory,

TABLE 1: The face of 2301 of rock physical and mechanical properties.

Serial number	Rock name	Layer thickness (m)	Buried depth (m)	Bulk density (kg/m ³)	Compressive strength (MPa)	Tensile strength (MPa)	Elastic modulus (GPa)
1	Weathered mudstone	43	43	2300	10.6	1.2	1.0
2	Sandstone	104.2	147.2	2550	31.3	1.2	7.6
3	Sand and mudstone	1.7	148.9	2730	66.7	1.8	6.2
4	3 coal seams	3.5	152.4	1420	27		0.4
5	Sandy mudstone	40.2	192.6	2610	35.3	2.8	1.2

the computer numerical simulation method commonly used in the field of geotechnical science is used to analyze this kind of problem, which has very important significance [5–8].

2. Brief Introduction of Previous Research Results

The relation between the permeability coefficient K_h and the stress P obtained by Snow (1966) [9] is

$$K_h = K_0 + A \left[\frac{\rho g b^2}{4\mu_s} \right] \frac{P - P_0}{K_n}, \quad (1)$$

where K_0 is the initial stress; P_0 is the permeability coefficient of action; K_n is the normal stiffness of the crack; and A is the coefficient.

Jones (1975) [9] proposed the empirical equation of permeability coefficient K of rock fractures as follows:

$$K = K_0 \left[\log \frac{P_h}{P} \right]^3, \quad (2)$$

where P_h is the effective stress of healing when $K = 0$.

Louis et al. (1976) [9] obtained the following according to the borehole pumping test:

$$\begin{aligned} K &= K_0 \exp(-\alpha\sigma), \\ \sigma &\approx \lambda H - p, \end{aligned} \quad (3)$$

where K_0 is the surface permeability coefficient; γH is overburden weight; P is water pressure; and α is the coefficient.

Kranz et al. (1979) [9] proposed the following formula to predict the change of permeability coefficient (K):

$$K \propto - \left[\sigma_c - \frac{b}{a} P \right]. \quad (4)$$

In the formula, b and a are constant.

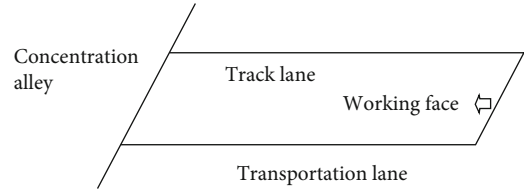


FIGURE 1: Roadway layout of working face.

Walsh (1981) [9] obtained the empirical formula of permeability coefficient and effective stress σ_e as follows:

$$K = K_0 \left\{ 1 - \left(\sqrt{2\xi} \right) \ln \left[\frac{\sigma_e}{\sigma_{e0}} \right] \right\}^3, \quad (5)$$

where K_0 is the initial permeability coefficient; σ_{e0} is the initial effective stress, and ξ is the coefficient related to the crack geometry size.

Kelsall (1984) [9] proposed a method to explain the influence of stress on the permeability coefficient of rock mass:

$$K_e = K_{e0} \frac{[1 + A[\sigma_{e0}/\xi]^t]^3}{[1 + A[\sigma_e/\xi]^t]^3}, \quad (6)$$

where K_e is the permeability coefficient when the effective stress is σ_e and K_{e0} acting on the σ_e main direction; and A , T , and ξ are the material constants of rock mass fractures.

Bai and Elsworth (1989) [9] assumed that cracks were soft, and the following equation was determined:

$$\Delta K = \frac{\rho g}{12s^{\mu}} (b + s\Delta\varepsilon)^3, \quad (7)$$

where $\Delta\varepsilon$ is the strain perpendicular to the fracture group.

Zhang et al. [10] obtained the relationship between pressure, permeability coefficient, and seepage flow as follows:

$$\begin{aligned} K &= K_0 \left[1 + \frac{p - \gamma H (\cos^2\theta + \lambda \sin^2\theta)}{bK_n} \right]^4, \\ Q &= Q_0 \left[1 + \frac{p - \gamma H (\cos^2\theta + \lambda \sin^2\theta)}{bK_n} \right]^4. \end{aligned} \quad (8)$$

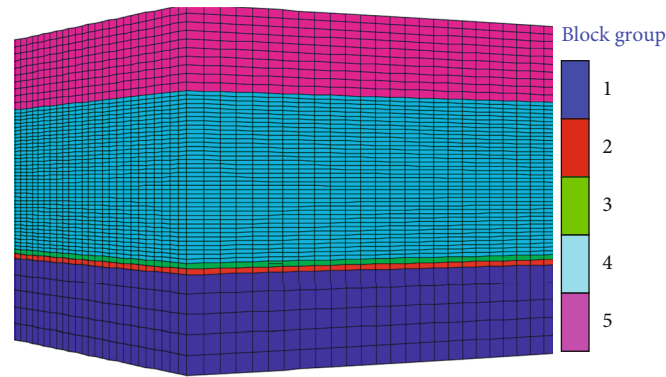


FIGURE 2: The establishment of the mechanical model. 1 sandy mudstone; 2 coal seams; 3 sand and mudstone; 4 sandstone; 5 weathered mudstone.

3. Stress Seepage Coupling Numerical Simulation Analysis of Fractured Rock Mass

3.1. Establishment of Mechanical Model. The 2301 working face of a mine is located in the desert area of Yulin area, the ecological environment is fragile, the working face is located in the 3 coal seam, the average thickness is 3.5 meters, and the overburden contains aquifer, which has an important impact on the mining of coal mine; improper mining will cause the accident of water inrush and sand. According to the rock mechanics experiment, the rock mechanics parameters are obtained (Table 1).

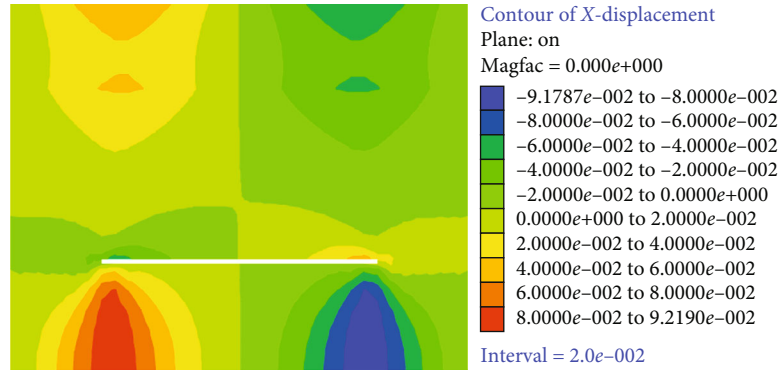
According to the roadway layout characteristics of 2301 working face and the near-horizontal coal seam (as shown in Figure 1), in order to improve the calculation efficiency, the design model is shown in Figure 2. This simulation is mainly to analyze the distribution law and development height of caving zone and fracture zone with overlying aquifers. The entire overlying rock and a small part of the floor should be considered when designing the model, which is to analyze the coordination of coal seam, roof, and floor; this is key to analyze the problem. This thesis has certain pore water pressure of the aquifer as module, located 10 m beneath the floor of the overlying strata in the process of working face advancing; fluid-structure interaction phenomenon has mutual influence, the change of pore water pressure in the rock mass causes stress variation in the mining, and water may exist in the crack, and the crack volume changes; it will have an effect on pore water pressure; this model uses the fluid calculation and mechanical calculation; at the same time, it also is often said that the fluid-structure coupling calculation adopts the model of seepage flow in the calculation and isotropic seepage model, calculating result in order to achieve. In the model, the range of coal seam roof above is until 148.9 m as a model of the upper surface and a layer of rock as a model of the base plate; each side of the model scales out 50 m; boundary treatment is the key problem of the model; the specific process is as follows: on the left and right boundary of the model, take $u = 0$, $v = 0$ (u for the X axis displacement, v for the Y direction

displacement, namely, single constraint boundary). At the bottom boundary of the model, $u = v = 0$ is the fully constrained boundary. The upper boundary of the model is the ground surface [11–15], which is regarded as free boundary without constraint [16–18].

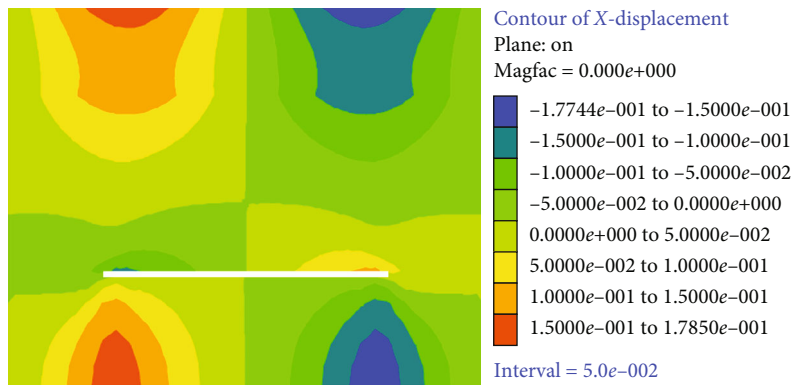
3.2. Coupling Analysis of Stress and Seepage. The movement of the overlying strata in coal mining leads to the redistribution of stress, which is bound to affect the flow of fluid in the fracture, and the key parameter is the permeability coefficient, which reflects the flow law of fluid and also reflects the development law of fracture in the overlying strata.

3.2.1. Horizontal Movement Law of Overburden. Due to the influence of working face mining, each unit of the mathematical model has to undergo continuous deformation. In order to clearly display the horizontal displacement change process of each node unit, the displacement calculation results of each node were output along with the working face advancing, and the displacement cloud maps of 2301 working face with different lengths and different stopping stages were drawn. The horizontal displacement cloud maps of working face advancing with 100 m, 150 m, 200 m, and 250 m are shown in Figures 3–5 respectively.

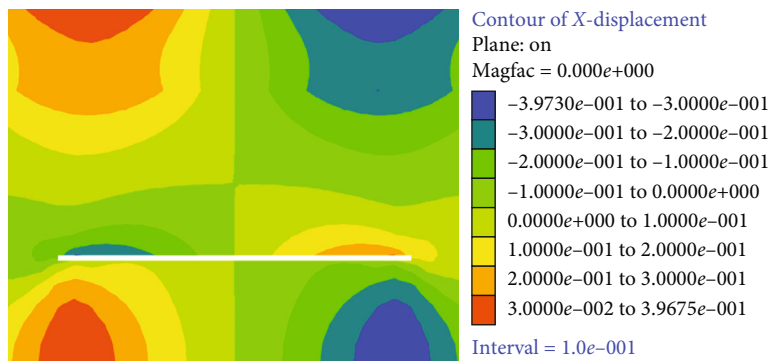
In the working face, the phase of initial overall overburden deformation is not large, including horizontal deformation value; this is due to the fact that the immediate roof is not fully caving; the supporting role, on both sides of the mined-out area, has the opposite change; there is displacement of the change in the opposite direction; its value is nearer the mined-out area; the greater the distance of the far mined-out area, the more and more small, along with the mining, mine pressure release, the overburden, and the horizontal displacement of zero, sometimes at the same time, due to the restriction of the boundary conditions, the model, and the lower part of the border around the border; the strata horizontal displacement value is separated into four areas: there are negative



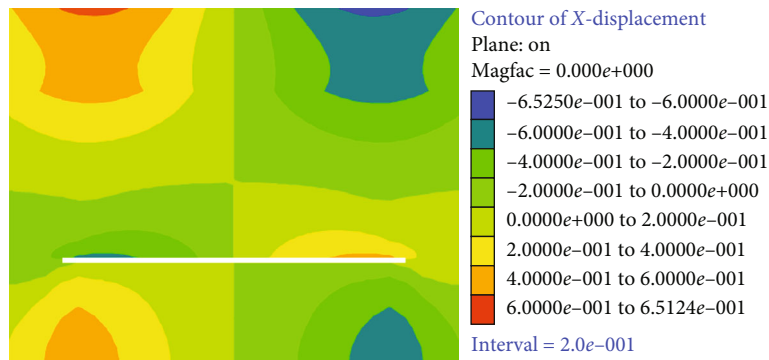
(a) 100 m horizontal displacement cloud map



(b) 150 m horizontal displacement cloud map

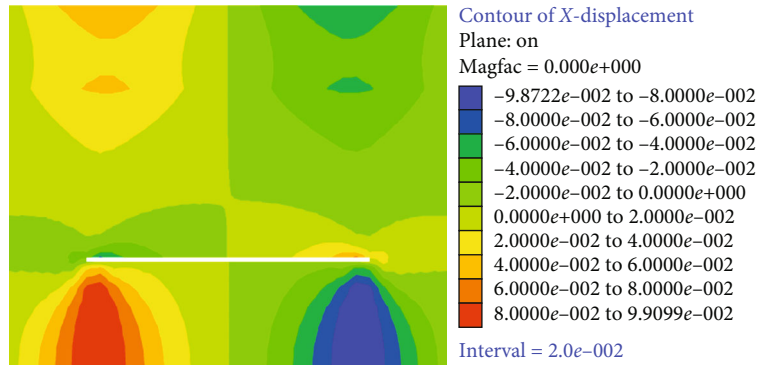


(c) 200 m horizontal displacement cloud map

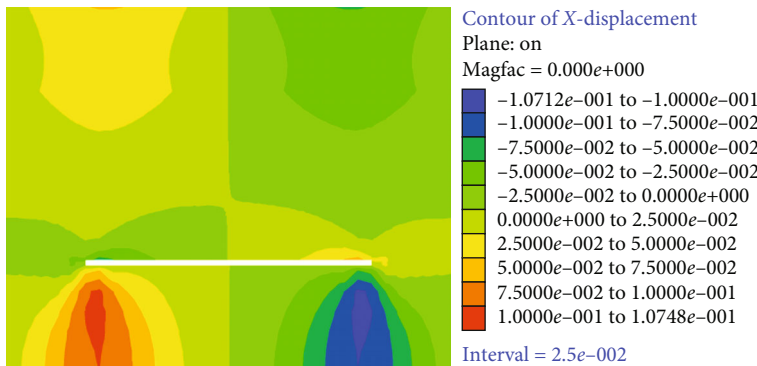


(d) 250 m horizontal displacement cloud map

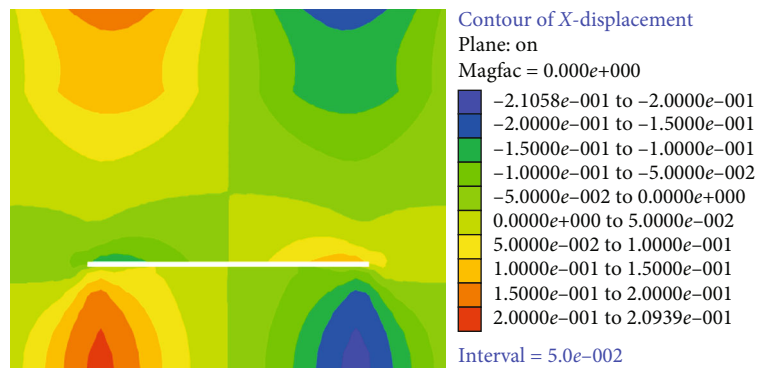
FIGURE 3: Horizontal displacement cloud map of different stopping stages (100 m, 150 m, 200 m, and 250 m) when the length of working face is 200 m.



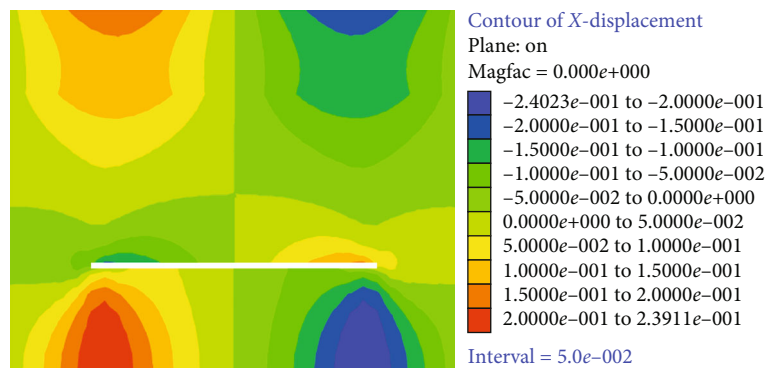
(a) 100 m horizontal displacement cloud map



(b) 150 m horizontal displacement cloud map

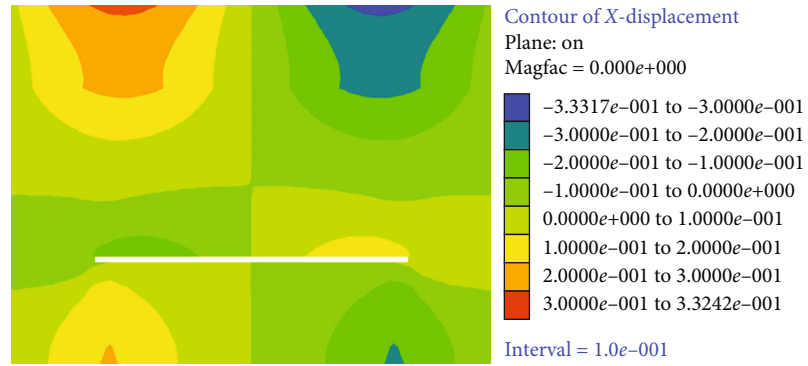


(c) 200 m horizontal displacement cloud map

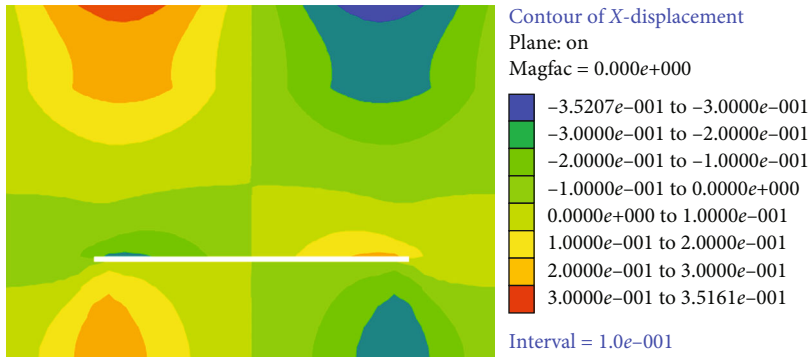


(d) 250 m horizontal displacement cloud map

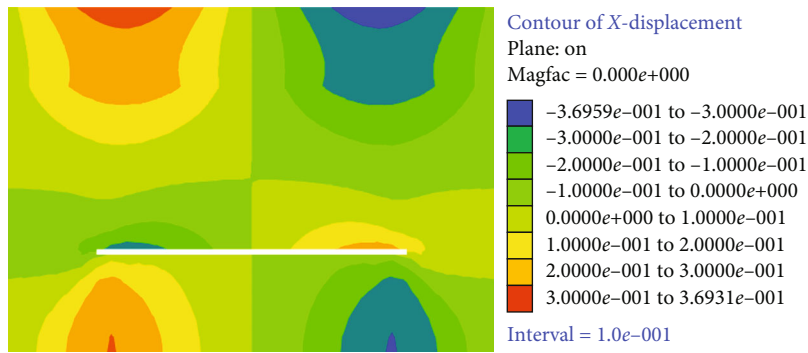
FIGURE 4: Horizontal displacement cloud map of different stopping stages (100 m, 150 m, 200 m, and 250 m) when the working face length is 220 m.



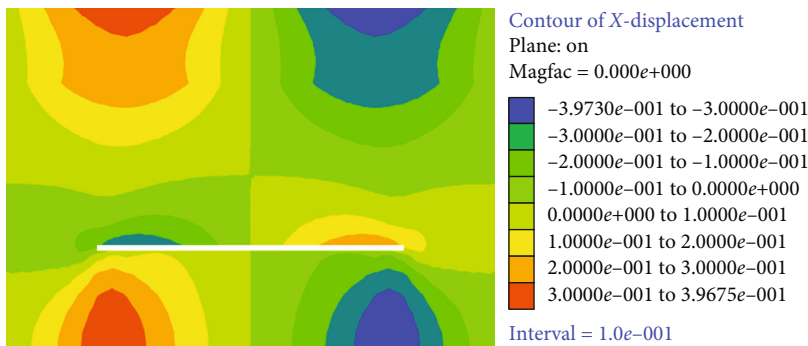
(a) 100 m horizontal displacement cloud map



(b) 150 m horizontal displacement cloud map



(c) 200 m horizontal displacement cloud map

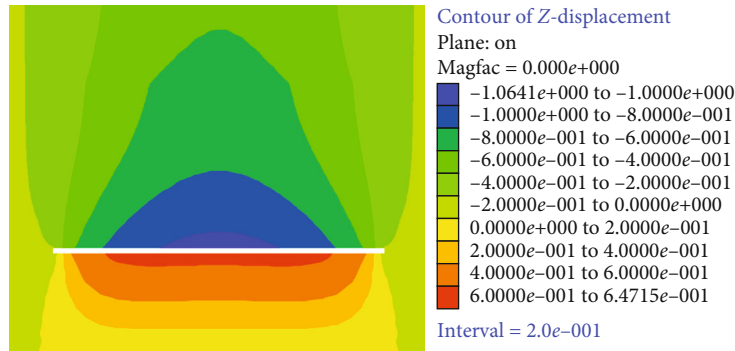


(d) 250 m horizontal displacement cloud map

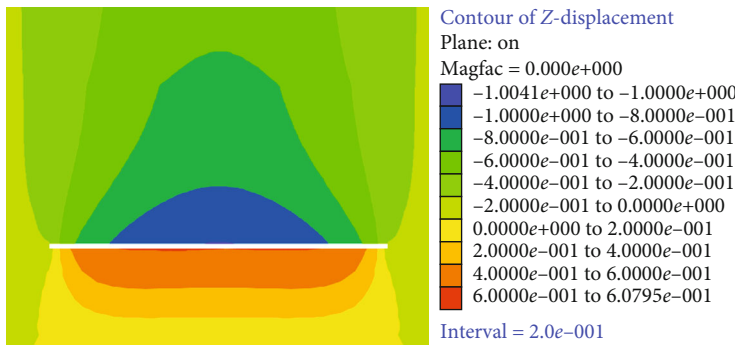
FIGURE 5: Horizontal displacement cloud map of different stopping stages (100 m, 150 m, 200 m, and 250 m) when the working face length is 240 m.

moving area, positive moving area far away from the goaf, and positive moving area and negative moving area near the goaf.

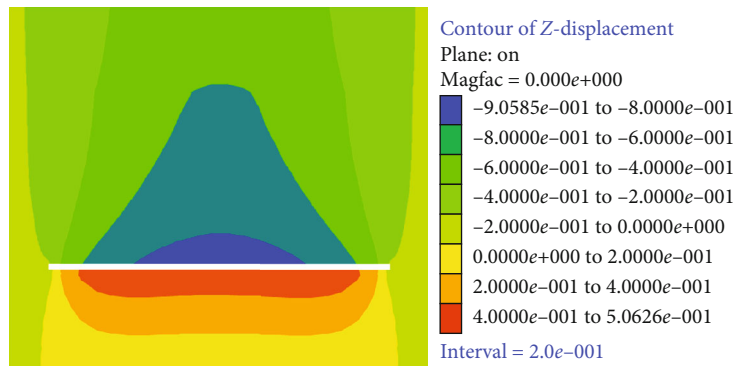
3.2.2. *Vertical Movement Law of Overburden.* In the different stages of 2301 working face, the vertical subsidence curve shape of overlying rocks does not change much in the process



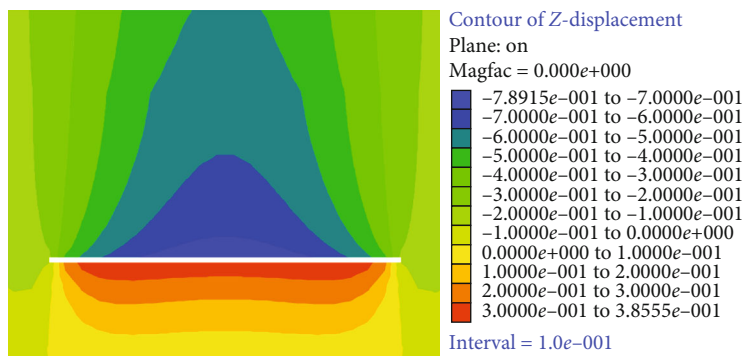
(a) 100 m vertical displacement cloud map



(b) 150 m vertical displacement cloud map



(c) 200 m vertical displacement cloud map

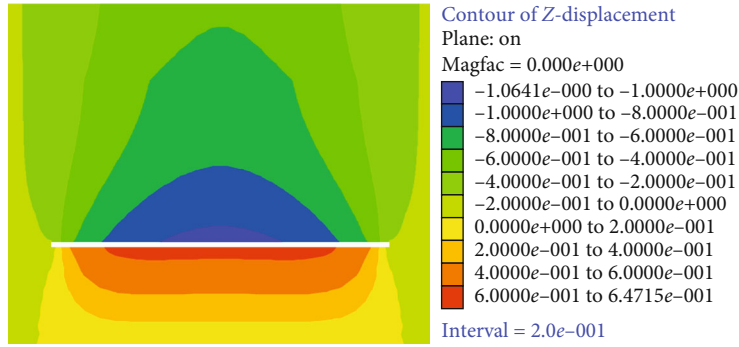


(d) 250 m vertical displacement cloud map

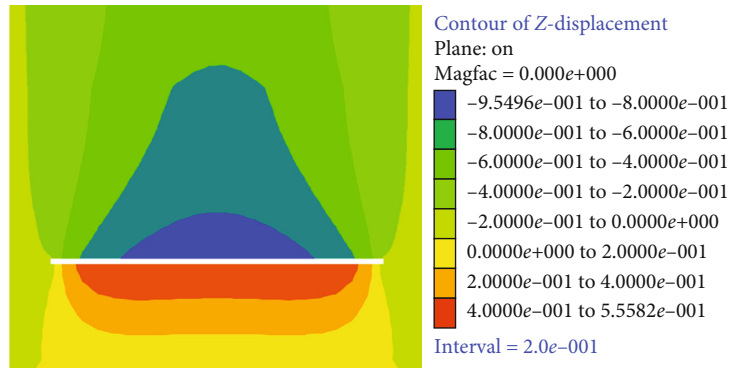
FIGURE 6: Vertical displacement cloud map of different stopping stages (100 m, 150 m, 200 m, and 250 m) when the length of working face is 200 m.

of working face advancement, and the changes of each rock layer are basically the same; whether it is hard rock or soft rock, all are coordinated deformation.

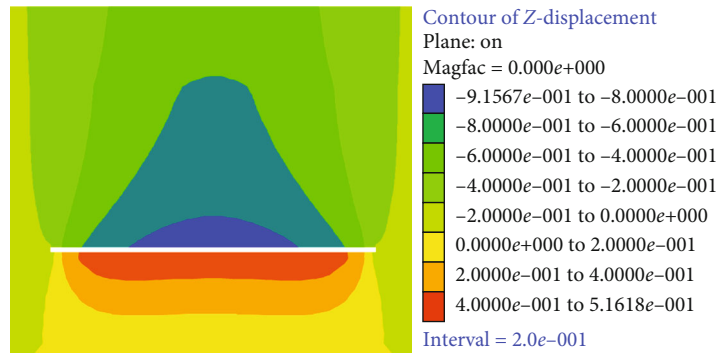
In the overburden on the vertical displacement of the funnel characteristics, in early mining, the vertical displacement is not big, but the amount of propulsion, strata of



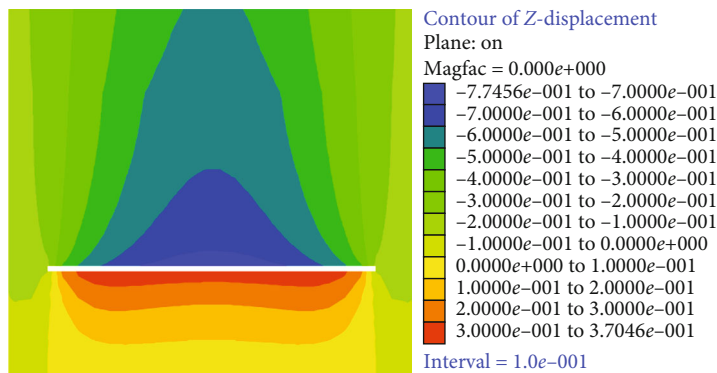
(a) 100 m vertical displacement cloud map



(b) 150 m vertical displacement cloud map



(c) 200 m vertical displacement cloud map

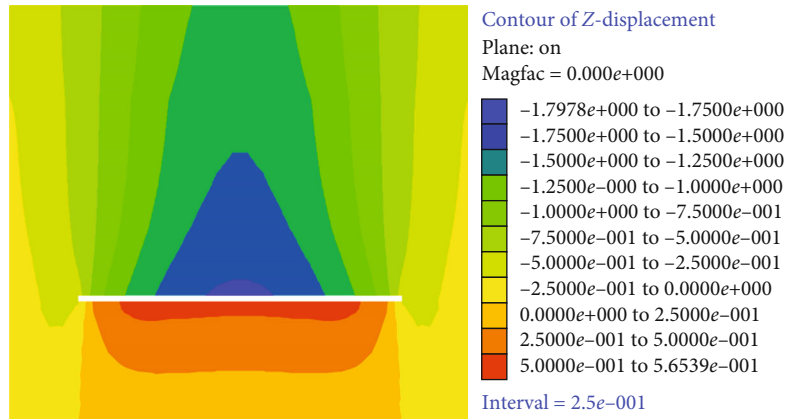


(d) 250 m vertical displacement cloud map

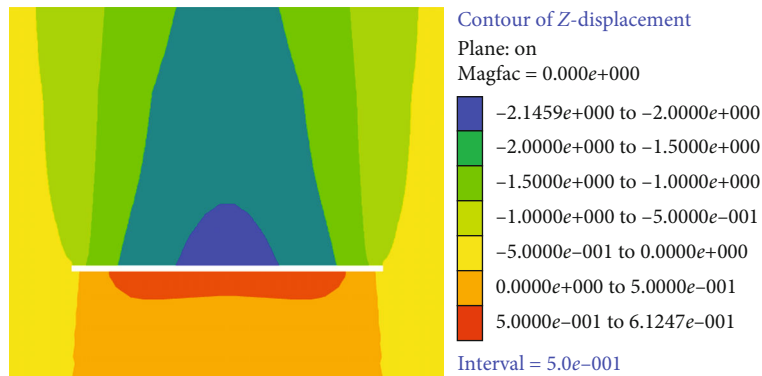
FIGURE 7: Vertical displacement cloud map of different stopping stages (100 m, 150 m, 200 m, and 250 m) when working face length is 220 m.

vertical displacement, and the maximum value appeared in the middle of the mined-out area. This is because in the middle of the mined-out area, without support, the rock strata

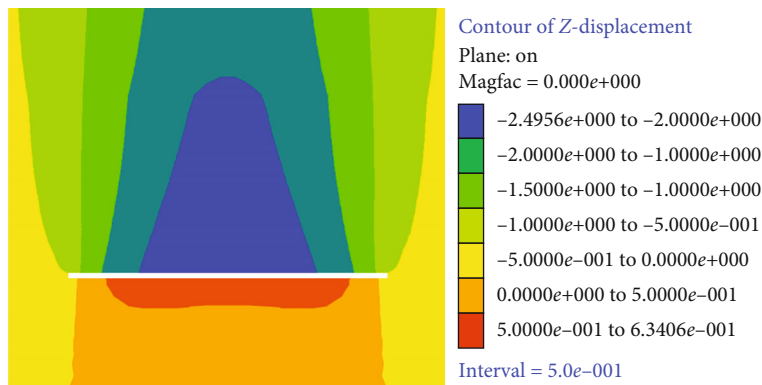
have a greater range of movement, and from the picture that looks like a funnel, when mining fully, strata are not a big change, its change of displacement distribution is



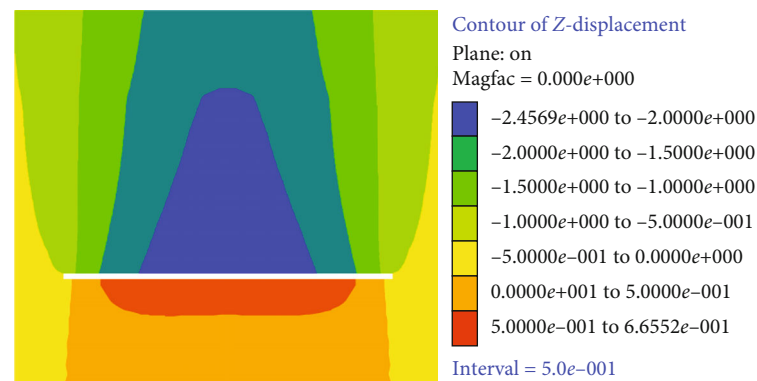
(a) 100 m vertical displacement cloud map



(b) 150 m vertical displacement cloud map

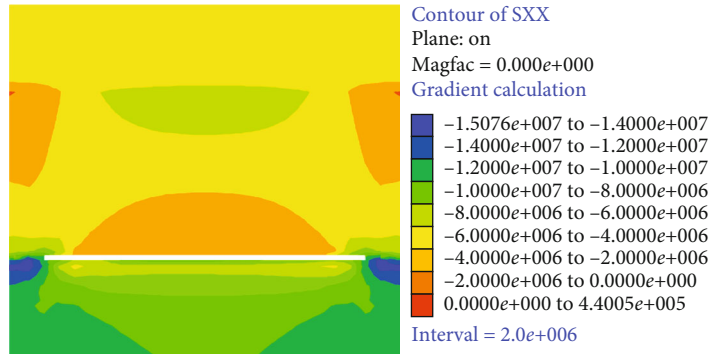


(c) 200 m vertical displacement cloud map

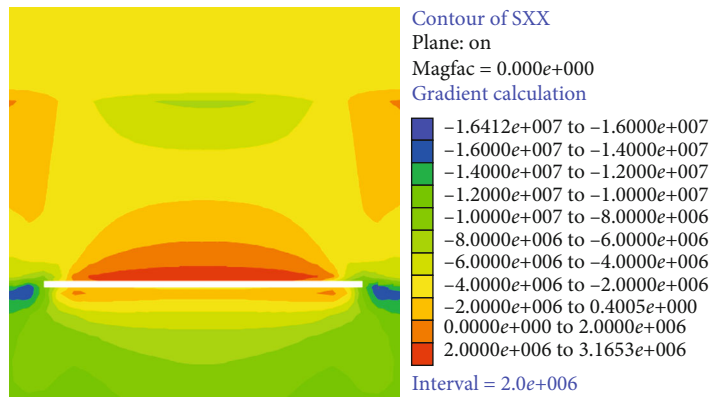


(d) 250 m vertical displacement cloud map

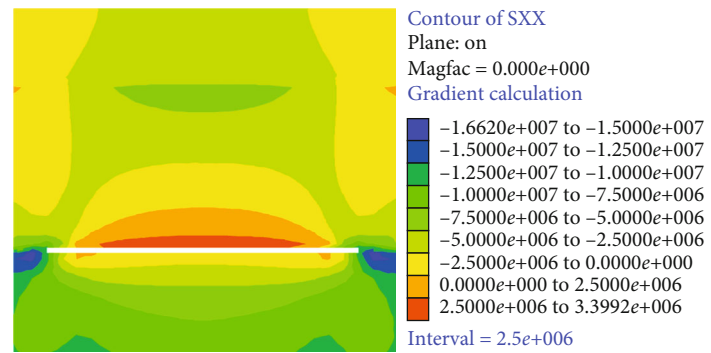
FIGURE 8: Vertical displacement cloud map of different stopping stages (100 m, 150 m, 200 m, and 250 m) when working face length is 240 m.



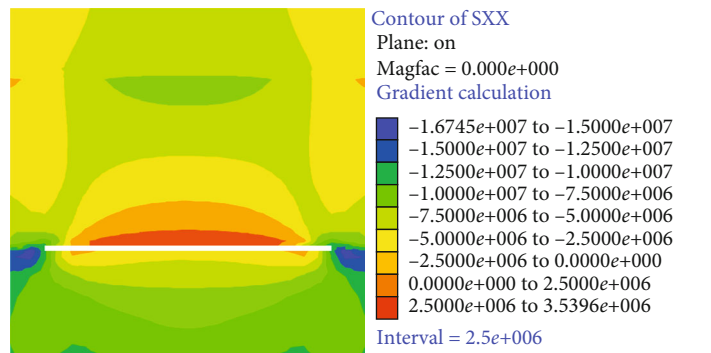
(a) 100 m horizontal stress nephogram



(b) 150 m horizontal stress nephogram

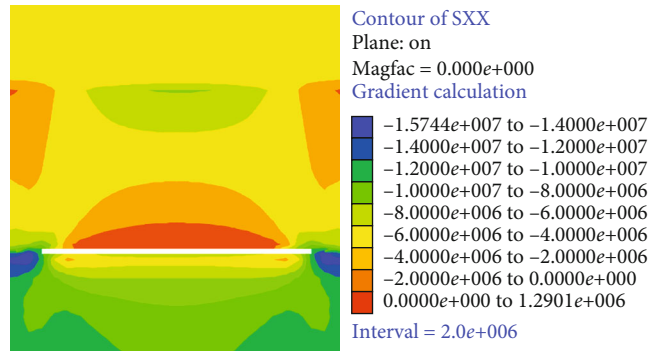


(c) 200 m horizontal stress nephogram

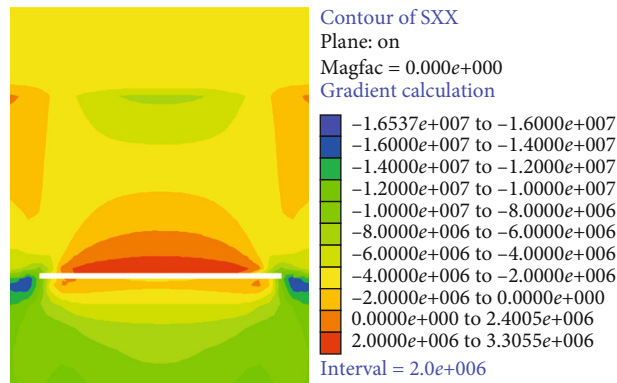


(d) 250 m horizontal stress nephogram

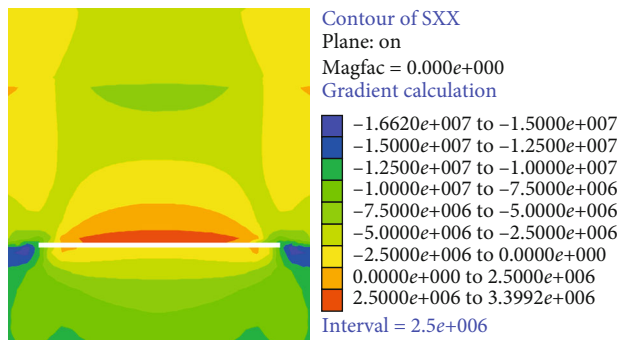
FIGURE 9: Horizontal stress nephogram of different stoping stages (100 m, 150 m, 200 m, and 250 m) when the length of working face is 200 m.



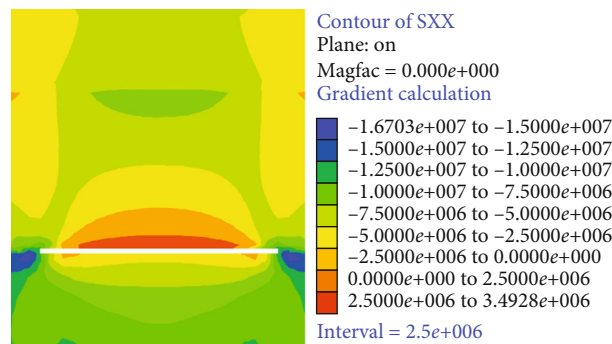
(a) 100 m horizontal stress nephogram



(b) 150 m horizontal stress nephogram



(c) 200 m horizontal stress nephogram

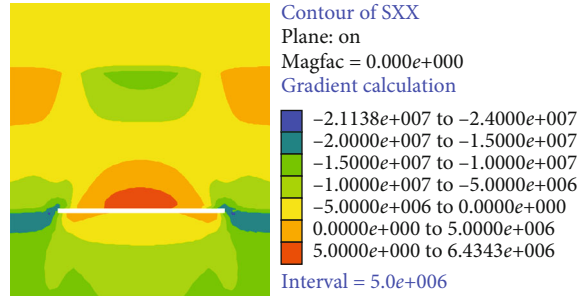


(d) 250 m horizontal stress nephogram

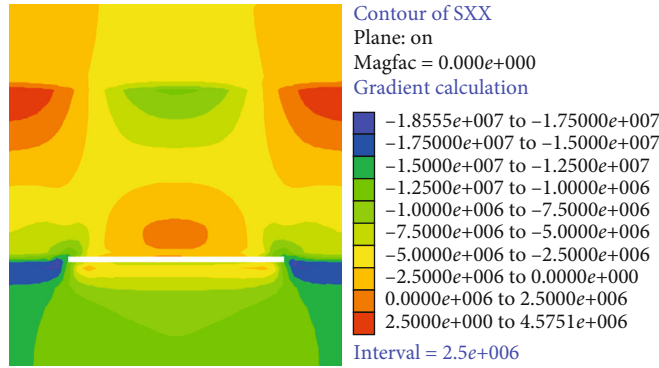
FIGURE 10: Horizontal stress nephogram of different stopping stages (100 m, 150 m, 200 m, and 250 m) when the working face length is 220 m.

symmetrical, goaf in the working face advances continuously in the process of filling, and vertical displacement of overburden rock will then move forward, until it is focused on the coal wall.

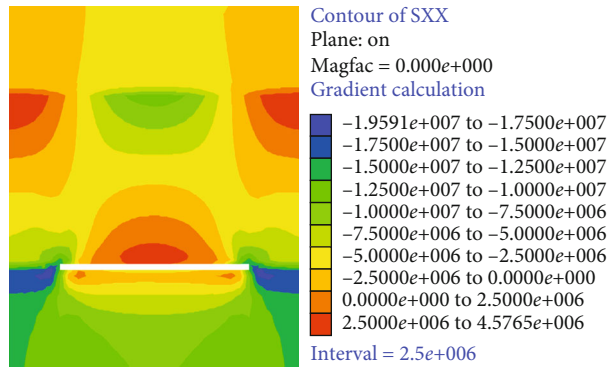
From the vertical displacement cloud maps of different mining stages, in the beginning stage, the displacement cloud maps in the vertical direction are not very large either in size or in advance influence range. With the



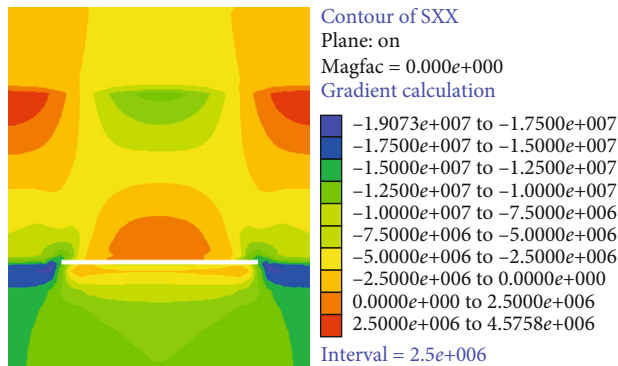
(a) 100 m horizontal stress nephogram



(b) 150 m horizontal stress nephogram



(c) 200 m horizontal stress nephogram

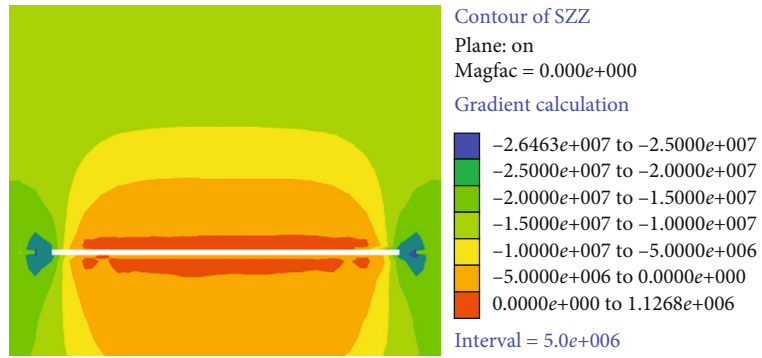


(d) 250 m horizontal stress nephogram

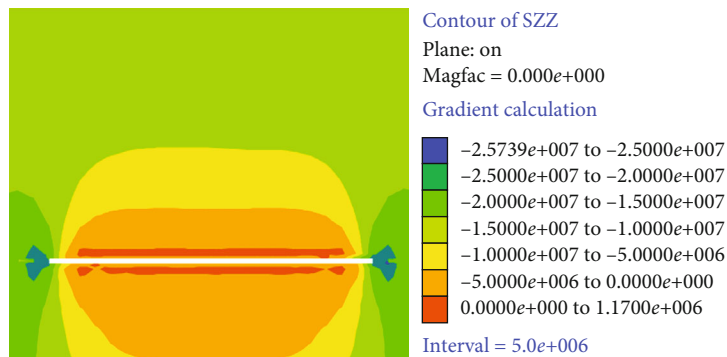
FIGURE 11: Horizontal stress nephogram of different stopping stages (100 m, 150 m, 200 m, and 250 m) when the working face length is 240 m.

increase of distance, these changes also increase, and the vertical displacement cloud map gradually becomes unclosed (Figures 6–8).

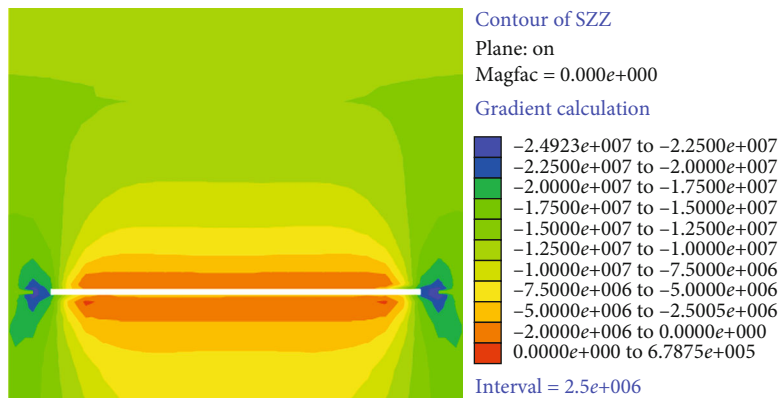
3.2.3. *Horizontal Stress Distribution in Rock Mass.* Numerical simulation results show that the early mining overburden horizontal stress is not big. However, the zoning of the



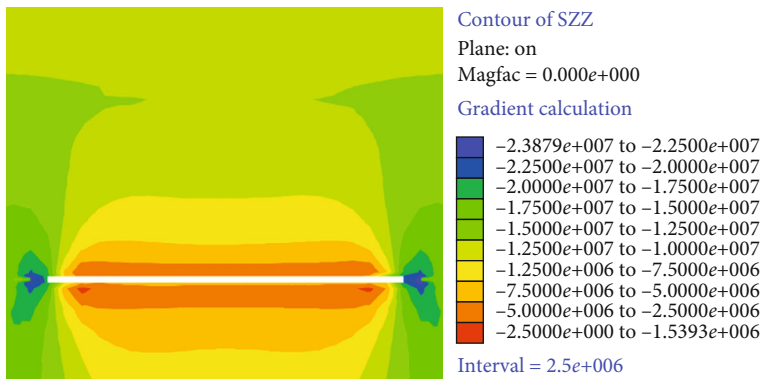
(a) 100 m vertical stress nephogram



(b) 150 m vertical stress nephogram



(c) 200 m vertical stress nephogram



(d) 250 m vertical stress nephogram

FIGURE 12: Vertical stress nephogram of different stopping stages (100 m, 150 m, 200 m, and 250 m) when the length of working face is 200 m.

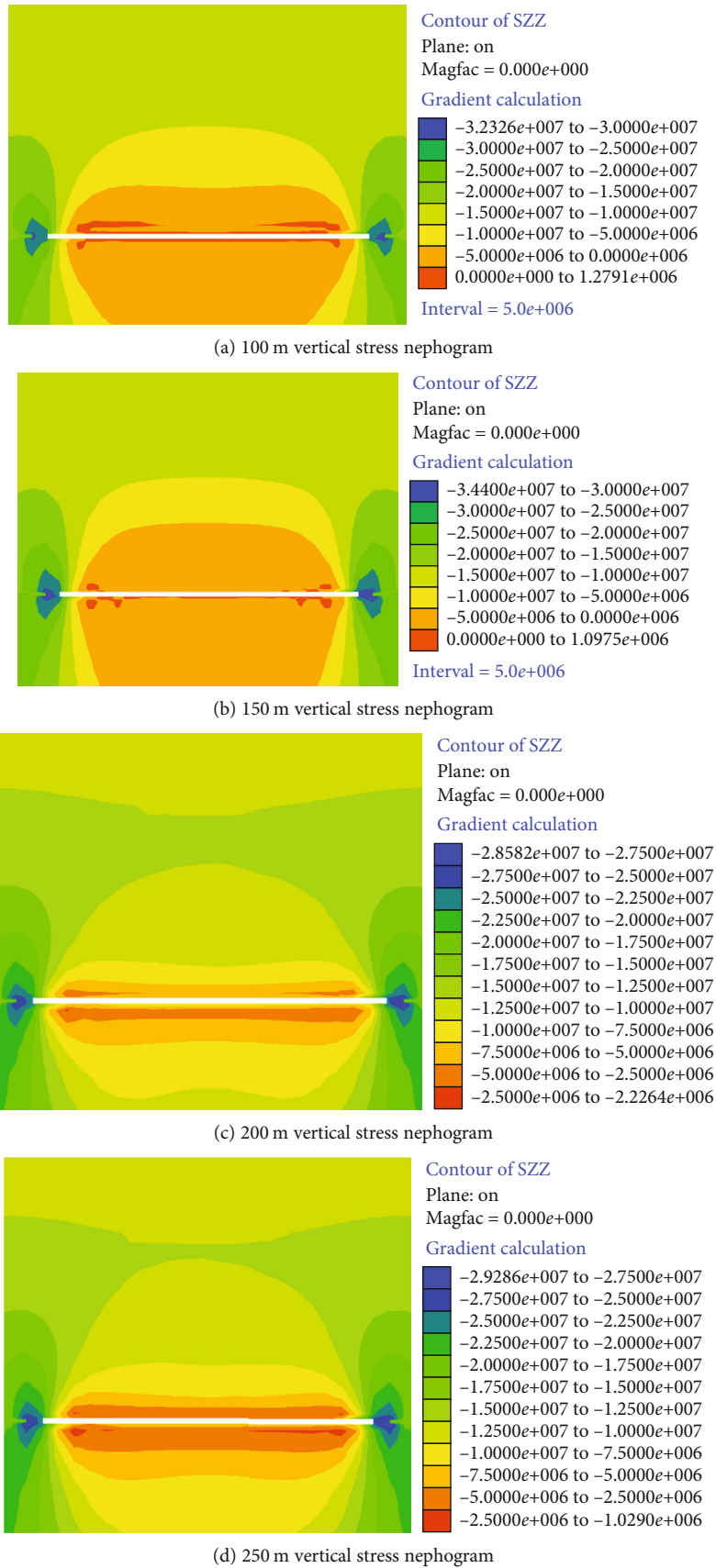
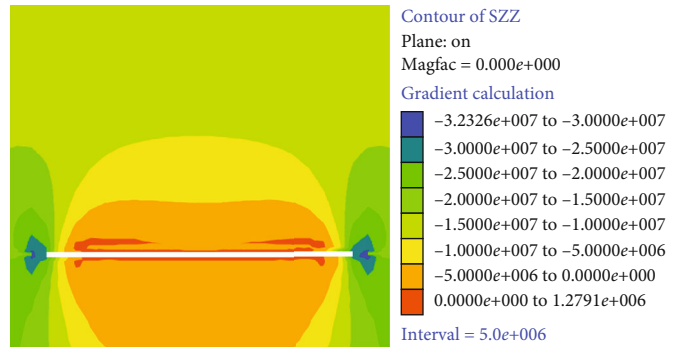
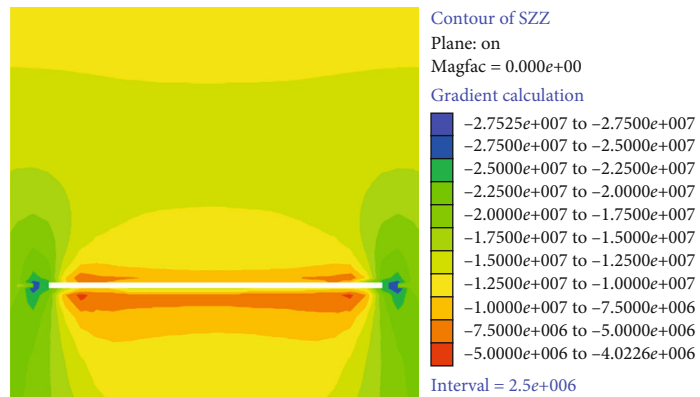


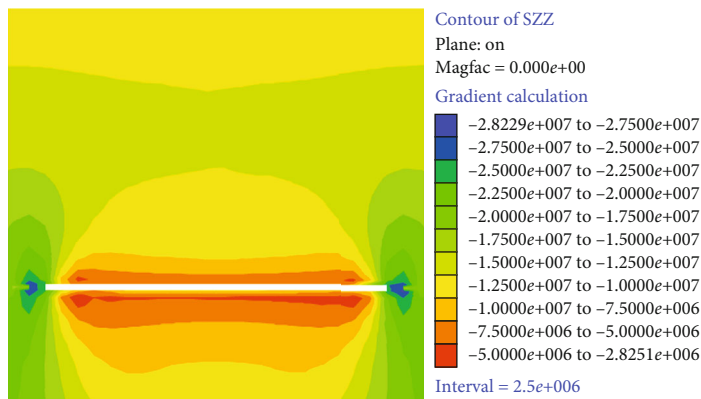
FIGURE 13: Vertical stress nephogram of different stopping stages (100 m, 150 m, 200 m, and 250 m) when working face length is 220 m.



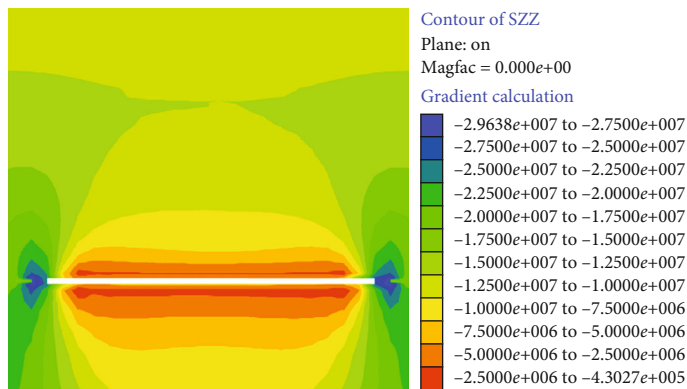
(a) 100 m vertical stress nephogram



(b) 150 m vertical stress nephogram



(c) 200 m vertical stress nephogram



(d) 250 m vertical stress nephogram

FIGURE 14: Vertical stress nephogram of different stopping stages (100 m, 150 m, 200 m, and 250 m) when working face length is 240 m.

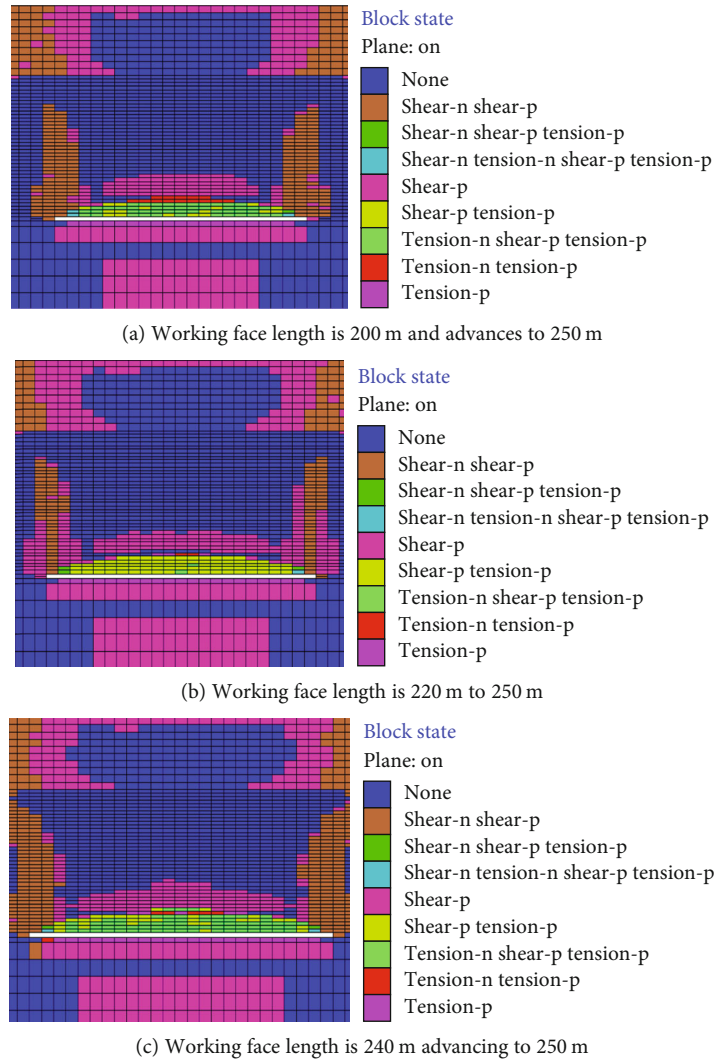


FIGURE 15: The plastic zone distribution when the working face length is 200 m, 220 m, 240 m, and pushed to 250 m.

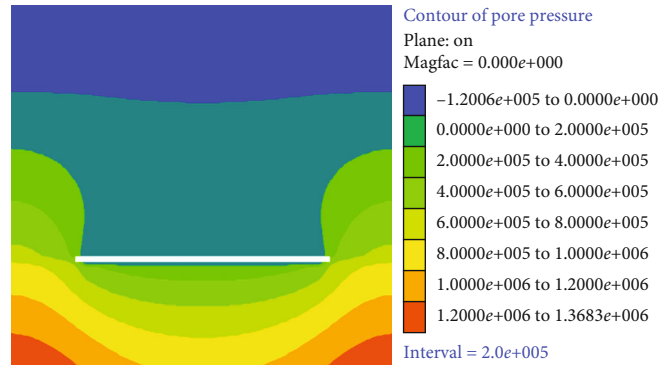
overlying strata in the whole model is obvious. This is because the overlying strata are composed of rock layers of different properties during the deposition process. At the same time, the vertical distance between each layer of rock strata and the working surface is also different, so in the face of the disturbance of underground mining, it will show different characteristics of overlying rock changes. The distribution of strata stress is stress arch, usually in place after the coal for starting cut arch foot, in front of the coal wall stress peak area of stress arch structure of the former arch foot; with the working face advancing, the arch is not fixed but constantly moves forward.

After the end of mining, the horizontal stress distribution in the mined-out area is as follows: the horizontal stress in the mined-out area is larger 20~40 m upward, indicating that the influence of stress mining is greater and strong. The change of horizontal stress in the goaf upward 40-80 m is moderate, and the fluctuation is not large. The horizontal stress from above 80 m to the surface is small. It is due to the mining of the underground working face, which is far

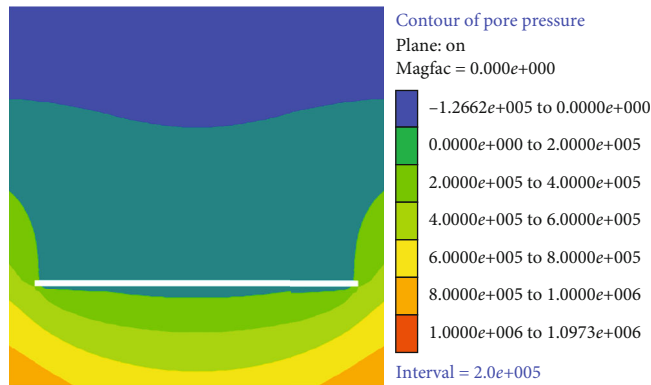
away from the surface of the ground, and the direct roof and basic roof rock layers below have undertaken most of the horizontal deformation. As you can see from the following diagram, there is a significant partitioning phenomenon. It also confirms that the extent of damage to the overlying rock strata caused by mining activities gradually weakens with the increase of distance (Figures 9–11).

3.2.4. Distribution Law of Vertical Stress inside Rock Mass.

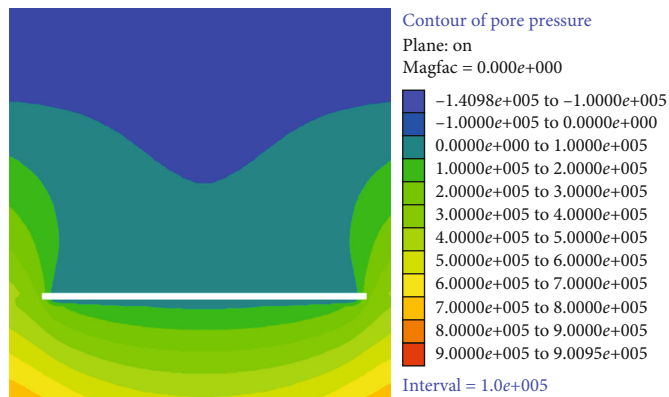
In the process of advancing the working face, the overburden undergoes the process of “deformation-separation-instability.” At the same time, the internal stress of the rock mass also changes accordingly. Because the basic roof is thick and hard and the ability to resist deformation is strong, the duration of each stage is longer. When the working face is advanced to 150 m, the advance influence range of the working face abutment pressure is about 50 m. With the advance of working face, the influence range of leading pressure is also changing, and it has experienced the process of “increase-decrease-increase.” After mining, stress concentration appears



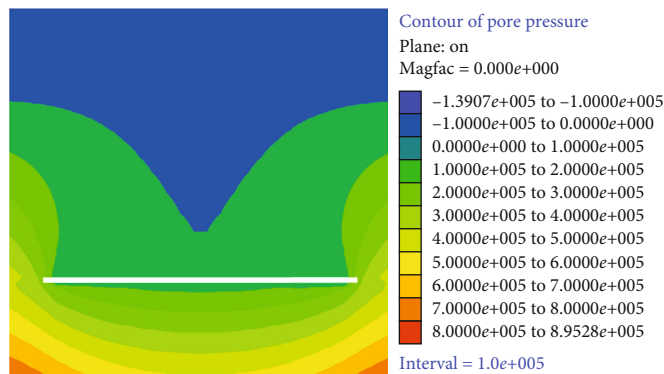
(a) 100 m advance of working face



(b) 150 m advance of working face



(c) 200 m advance of working face



(d) 250 m advance of working face

FIGURE 16: Cloud diagram of overburden pore water pressure at 250 m advance of working face advances to 100 m, 150 m, 200 m, and 250 m.

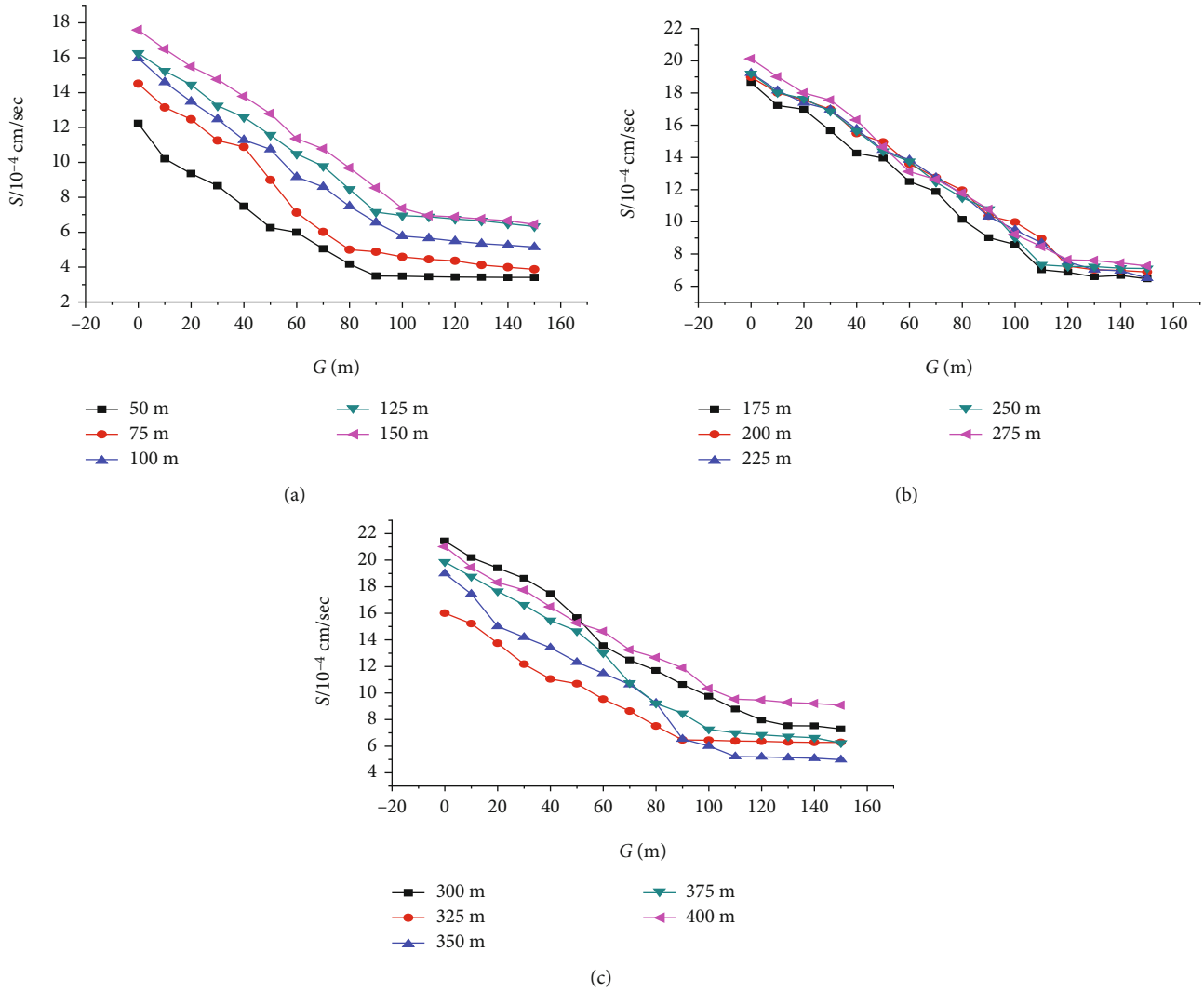


FIGURE 17: Comparison of permeability coefficient variation trend of different advancing distances at different working faces.

especially near the top of the coal pillar. The peak depth of the coal wall is 10 m, and the influence range of abutment pressure is about 60 m in front of the coal wall (Figures 12–14).

3.2.5. Overburden Failure Status and Plastic Zone Distribution. In the elastoplastic analysis, when the FLAC program is dealing with the problem, it will judge the stress state of the point according to the Mohr-Coulomb criterion at the same time when calculating the stress and displacement of each element. In the numerical simulation, the following conventions are made: 0 denoted that the rock mass element is still in elastic state; 1 indicates that the rock mass element is yielding and begins to transition to the plastic state; 2 represents that the rock mass element enters the plastic state; 3 means that the rock mass element has exceeded the uniaxial tensile resistance; 4 represents the yield of rock mass unit and exceeds uniaxial tensile resistance; and 5 indicates that the rock mass element has exceeded the uniaxial tensile resistance. The software uses the existing failure parameters of each unit to integrate, so as to express the failure situation of the whole overburden. The identification of plastic zone is

the main basis of the failure state of overburden, as well as the method to judge the distribution law and development height of the water-conducting fracture zone.

It can be seen from the plastic separation diagram that the main failure places are at the top and left and right sides of the model. Under the influence of mining damage, the overburden failure is symmetrically distributed. By comprehensive comparison of various calculation models, different working face lengths lead to different distribution of plastic zone and development height of the water-conducting fracture zone. According to the analysis in Figure 15, when the working face length is 200 m, the maximum height of plastic zone distribution in overlying rock is 48 m. When the working face length of 220 m strata distribution of plastic zone is in the maximum height of 54 m and when the working face length of 240 m strata distribution of plastic zone in the maximum height has communicated the overlying loose bed, the overlying aquifer water inrush occurs; in production practice, it cannot meet the working face length. Under the action of mining seepage, the length of the working face cannot be expanded indefinitely. Once it exceeds a certain value, the

overburden fissures will communicate with the aquifer and even the surface, causing water inrush accidents. So the working face length of 220 m is the most reasonable [19–22].

3.2.6. Coupling Analysis of Stress and Seepage of Overlying Rock when Working Face Length is 220 m. Under the influence of mining, the stress of the overlying strata changes, which makes the permeability of the overlying strata change. Therefore, the coupling analysis of stress and seepage is particularly important in engineering applications. The seepage problem of overburden rock caused by mining is mainly to study the law of fluid movement in pores and fissures. Among them, the parameter that best reflects the law of change is the permeability coefficient. The change in permeability coefficient reflects the expansion and closure of pores and fissures. This also explains the overburden from the side. In the law of rock movement, we can analyze the law of seepage through the change of stress, that is, the coupling analysis of stress and seepage.

Here, we take the length of the working face 220 m as the basis. In the mining geological conditions, we know that there is an aquifer above the bedrock, which will inevitably generate pore water pressure on the surrounding rock formations. The existence of pore water pressure will affect the surrounding rocks. The nature of the pore water will change, and the change of pore water pressure will affect the stress and strain of the rock formation, which will redistribute the stress of the rock formation. In the mining of the working face, the upper and lower ends of the working face and the cut-off are most affected. At this time, the permeability of the rock formation will increase accordingly. As the work surface advances, the stress of the overlying strata of the stope will be redistributed, and the overlying strata will be closed from the original tensile cracks and the permeability at this time. The rate gradually decreases until the fissure is closed, the pore water pressure is zero, the working face continues to advance, and the pore water pressure may become negative, because the water-conducting fissure zone may spread to the overlying aquifer, affecting the water level of the aquifer.

According to the simulation, the distribution of pore water pressure reflects the movement of the overlying strata in the process of advancing the working face. The figure shows that the stress distribution at both ends of the working face is concentrated, and a falling funnel appears above the goaf (Figure 16).

According to the numerical simulation results, the change rule of overburden stress under the action of overburden pore water pressure can be obtained, which is expressed by the trend in Figure 17.

Through the above analysis, the movement fracture of the overlying strata in coal mining is the result of the joint action of stress and seepage. The change of stress will change the flow law of fluid accordingly.

4. Conclusion

- (1) Summing up the relationship between stress and permeability coefficient in the earlier part, these relations are simple and convenient to apply

- (2) By using computer numerical simulation technology, the influence of stress on the seepage of fractured rock mass is analyzed. The plastic separation diagram shows that the main areas of failure are above and on the left and right sides of the model. Under the influence of mining damage, the overburden failure is symmetrically distributed. By comprehensive comparison of the calculation models, different working face lengths lead to different distributions of plastic zone and development height of water-conducting fracture zone. Through the comparative analysis of cloud image and trend chart, it is found that the pore water pressure acts on the whole overlying strata and affects the development of fractures, and the change of fracture network also affects the subsidence trend of overlying aquifer, both of which influence each other
- (3) The practice shows that the computer numerical simulation analysis of the coupling problem of stress and seepage is intuitive and effective. The application of clear and intuitive diagrams instead of complex theoretical formulas simplifies a lot of work
- (4) The above analysis shows that the mining impact of the coal mining area in the Yellow River Basin has led to the destruction of the overlying rock aquifer and the leakage of surface water, affecting the fragile ecological environment of the surface, leading to lack of water for surface vegetation and soil desertification, so the mining area is underway. In ecological restoration, this method can be used to conduct in-depth research on the protection and restoration of aquifers, so as to provide a theoretical basis for the ecological protection and high-quality development of the Yellow River Basin

Data Availability

The data used to support the findings of this study are available from the corresponding author upon request.

Conflicts of Interest

The authors declare that they have no conflicts of interest to report regarding the present study.

Acknowledgments

The research was funded by special scientific research plan of Education Department of Shaanxi Province (No. 18JK1046).

References

- [1] R. Singh, P. K. Mandal, A. K. Singh, R. Kumar, J. Maiti, and A. K. Ghosh, "Upshot of strata movement during underground mining of a thick coal seam below hilly terrain," *International Journal of Rock Mechanics and Mining Sciences*, vol. 45, no. 1, pp. 29–46, 2008.
- [2] Q. Wang, Z. Jiang, B. Jiang, H. Gao, Y. Huang, and P. Zhang, "Research on an automatic roadway formation method in

- deep mining areas by roof cutting with high-strength bolt-grouting,” *International Journal of Rock Mechanics and Mining Sciences*, vol. 128, 2020.
- [3] Q. Wang, Y. Wang, M. C. He et al., “Experimental research and application of automatically formed roadway without advance tunneling,” *Tunnelling and Underground Space Technology*, vol. 114, no. 3, 2021.
- [4] A. Li, F. Dai, Y. Liu, H. B. Du, and R. C. Jiang, “Dynamic stability evaluation of underground cavern sidewalls against flexural toppling considering excavation-induced damage,” *Tunnelling and Underground Space Technology*, vol. 112, 2021.
- [5] R. D. Miller, D. W. Steeples, and L. Schulte, “Shallow reflection study of salt dissolution well field meal,” *Mining Engineering*, vol. 45, 1993.
- [6] Q. X. Meng, W. Y. Xu, H. L. Wang, X. Y. Zhuang, W. C. Xie, and T. Rabczuk, “DigiSim – an open source software package for heterogeneous material modeling based on digital image processing,” *Advances in Engineering Software*, vol. 148, 2020.
- [7] H. Qingxiang, *Roof Structure and Strata Control of Longwall Mining in Shallow Coal Seam*, China University of Mining and Technology Press, Xuzhou, 2000.
- [8] Q. Mingguo, M. Xiexing, and X. Jialin, *Key Strata Theory of Rock Strata Control*, China University of Mining and Technology Press, Xuzhou, 2000.
- [9] M. Bai and D. Elsworth, “Modeling of subsidence and stress dependent hydraulic conductivity for intact and fractured porous media,” *Rock Mechanics & Rock Engineering*, vol. 27, no. 4, pp. 235–251, 1994.
- [10] Z. Jincai, L. Tianquan, and Z. Yuzhuo, “Research on the permeability characteristics of fractured rock mass,” *Journal of China Coal Society*, vol. 22, no. 5, pp. 481–485, 1997.
- [11] L. Shiwei, “Simulation of water-retaining mining in shallow coal seam with thick soil layer,” *Journal of Liaoning Technical University*, vol. 32, no. 6, pp. 741–744, 2013.
- [12] L. Shiwei, “Numerical simulation of water conducting fracture zone H8 of 2301 working face in Yuyang coal mine,” *Chinese Journal of Production Safety Science and Technology*, vol. 9, no. 3, pp. 46–50, 2013.
- [13] L. Shiwei, “Study on water inrush mechanism of roof in shallow coal seam with thin bedrock,” *Mining Safety and Environmental Protection*, vol. 40, no. 3, pp. 21–24, 2013.
- [14] L. Zhengqiu and B. Shihua, *A Brief Course of Material Mechanics*, Higher Education Press, Beijing, 2000.
- [15] T. Min, “Research on the development height of mining-induced rock mass fracture in Panxie mining area,” *Journal of China Coal Society*, vol. 29, no. 6, pp. 641–645, 2004.
- [16] L. Shiwei, “Study on overburden failure of coal seam mining under coupling of stress and see page,” *Journal of Hulun Buir College*, vol. 25, no. 6, 2017.
- [17] X. Kong, *Advanced Seepage Mechanics*, University of Science and Technology of China Press, Hefei, 1999.
- [18] X. Zhang, Z. Xia, C. Yao, J. Yang, and M. Yang, “Experimental study on seepage properties of postpeak fractured rocks under cyclic loading-unloading confining stress and axial stress,” *Geofluids*, vol. 2021, 12 pages, 2021.
- [19] L. Wen, Y. Li, and J. Chai, “Numerical simulation and performance assessment of seepage control effect on the fractured surrounding rock of the Wunonglong underground powerhouse,” *International Journal of Geomechanics*, vol. 20, no. 12, 2020.
- [20] W. B. Sun, Y. C. Xue, L. M. Yin, and J. Zhang, “Experimental study on seepage characteristics of large size rock specimens under three-dimensional stress,” *Geomechanics and Engineering*, vol. 18, 2019.
- [21] L. Zhou, K. Su, H. Wu, and C. Shi, “Numerical investigation of grouting of rock mass with fracture propagation using cohesive finite elements,” *International Journal of Geomechanics*, vol. 18, no. 7, 2018.
- [22] T. Yang, H. Y. Liu, and C. A. Tang, “Scale effect in macroscopic permeability of jointed rock mass using a coupled stress-damage-flow method,” *Engineering Geology*, vol. 228, pp. 121–136, 2017.

Research Article

Observed Performance and FEM-Based Parametric Analysis of a Top-Down Deep Excavation in Soil-Rock Composite Stratum

Gang Lei ^{1,2}, Panpan Guo ¹, Fucai Hua,² Xiaonan Gong,¹ and Lina Luo³

¹Research Center of Coastal and Urban Geotechnical Engineering, Zhejiang University, Hangzhou 310058, China

²Beijing Urban Construction Design & Development Group Company Limited, Beijing 100037, China

³Guangzhou Railway Polytechnic, Guangzhou 510430, China

Correspondence should be addressed to Gang Lei; 11812105@zju.edu.cn and Panpan Guo; pp_guo@zju.edu.cn

Received 13 May 2021; Accepted 4 June 2021; Published 21 June 2021

Academic Editor: Yu Wang

Copyright © 2021 Gang Lei et al. This is an open access article distributed under the Creative Commons Attribution License, which permits unrestricted use, distribution, and reproduction in any medium, provided the original work is properly cited.

This paper investigates the performance of a top-down deep excavation in soil-rock composite stratum. The behavior of the excavation bracing system, consisting of ground anchors and end-suspended piles, has not been well understood due to the lack of relevant research. Based on the observed data of a typical deep excavation case history for the May Fourth Square Station in Tsingtao, China, the characteristics of the horizontal and vertical pile displacements, ground surface settlements, building settlements, axial forces in ground anchors, earth pressure, and pore water pressure during excavation were analysed. Two-dimensional finite element simulations were carried out to further explore the deformation and internal force responses of end-suspended piles and to capture the effects of pile diameter, embedded depth, and rock-socketed depth on the horizontal displacement and bending moment distributions along the pile shaft. It was found that the pattern of the vertical pile displacements could be categorized into three types: rapid settlement, slow settlement, and rapid heave. The magnitudes of the ground and building responses can be well controlled within allowable limits by combining the top-down method with the adopted bracing system. Among the investigated parameters, pile diameter is dominant in affecting the horizontal pile displacement. The primary influence zone for pile bending moment varies, depending on the parameters. It is recommended that a combination of top-down method, ground anchors, and end-suspended piles be adopted for restraining excavation deformation and lowering construction costs of similar deep excavations in soil-rock composite stratum.

1. Introduction

Excavations are generally made for constructing metros, mass rapid transit systems, high-rise buildings, underground oil tanks, and other facilities. With the rapid development of economy and urbanization, excavations are going deeper and becoming larger in scale. This highlights the significance of investigating the performance of deep excavations, especially for them that are under unsatisfactory geological conditions [1–4] or them that are in close proximity to constructed facilities or infrastructures [5–8].

In the past several decades, extensive studies have been conducted to investigate the performance of deep excavations in terms of excavation-induced deformation and internal force characteristics of retaining walls and bracing

structures [9–11], ground movements [12–14], and response of preexisting structures that are adjacent to the excavations [15–17]. These studies are based mainly on numerical simulations [18, 19], empirical or semiempirical methods [20, 21], analytical solutions [22, 23], in situ monitoring data analysis [24, 25], centrifuge or scaled model testing [26, 27], and machine learning [28, 29]. Among the commonly adopted methods, numerical simulations usually predict better results for excavation-induced wall displacements than for ground movements and can consider the effects of excavation stages and nonlinearity of soil behavior [30, 31]. In addition, as the design of the bracing system for a deep excavation is still heavily dependent on semiempirical and empirical methods [32, 33], an update on the well-documented deep excavation case histories by in situ monitoring data analysis will be

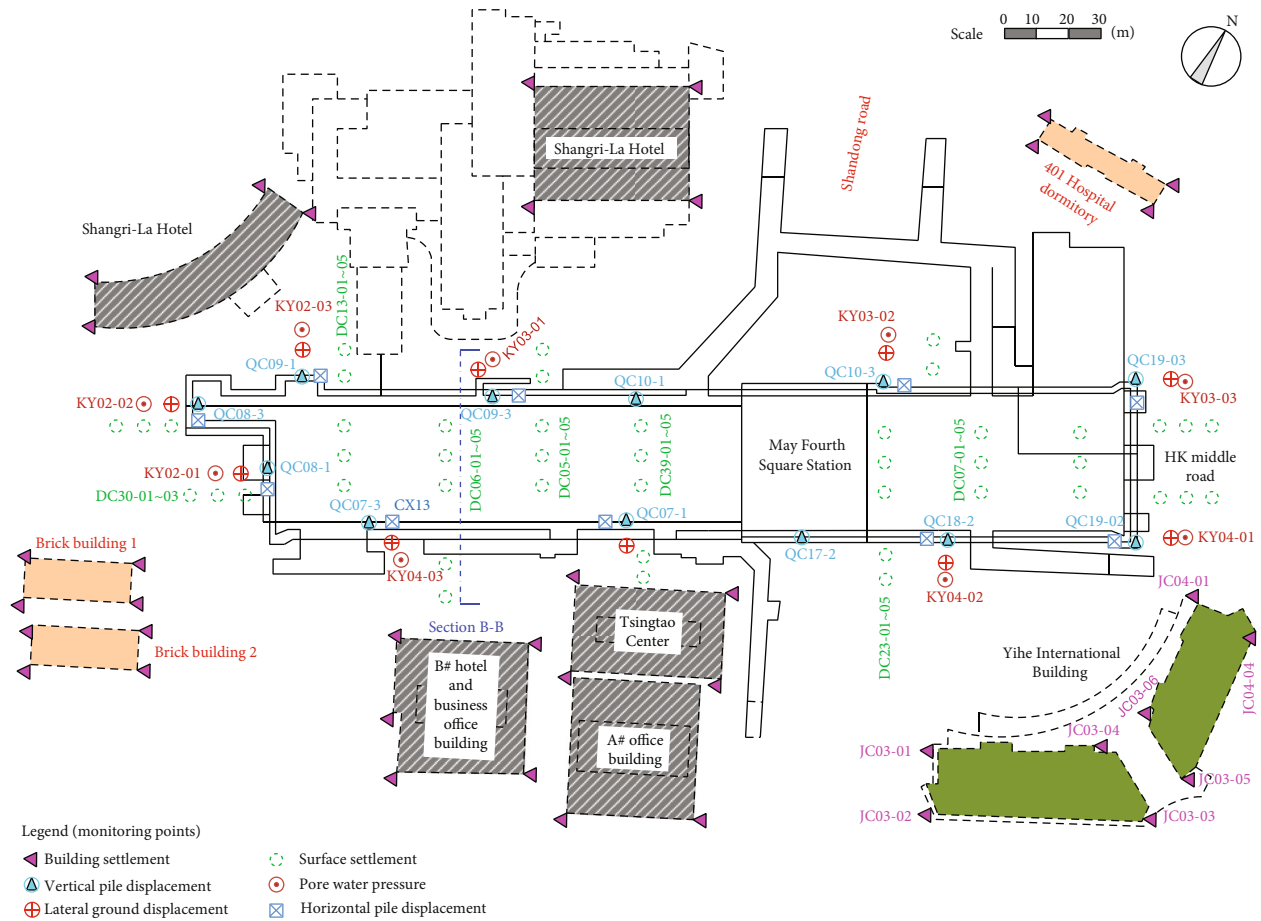


FIGURE 1: Plan view of the May Fourth Square Station excavation case history.

beneficial for relevant researchers, designers, and engineers by providing timely feedback helpful for lowering the risk for construction and design.

The performance of deep excavations varies according to excavation geometry and scale, geological conditions, excavation method, type of retaining structure, and other factors. Tan et al. [34] found that for a long and narrow deep excavation, the minimum wall deflections occurred near the excavation corners while the maximum near the middle span of the excavation. This can be attributed to the corner strengthening effect which has also been investigated by Lee et al. [35] and Ou and Shiau [36]. The geological conditions significantly affect the design of the excavation bracing system and thus the construction duration and cost. A great deal of efforts were made to understand the performance of deep excavations in various types of soils including soft clays [37], sand [38], granite [39], sand covered karst [40], and loess [41].

The commonly adopted excavation methods mainly include the bottom-up method, the top-down method, and the semitop-down method. Due to its advantages of short excavation duration, low construction cost, and easy operation, the bottom-up method was used for constructing many metrostations or basements in soft soils [42, 43]. To avoid the risk of excessive ground movements and tremendous distur-

bance to the existing structures or facilities involved in the bottom-up method, the top-down method is frequently adopted in deep excavations in congested urban environment [44–46]. Recently, an innovative excavation method termed semitop-down method, which is superior to the abovementioned two methods, has been used in several excavations in downtown Shanghai [47]. In addition, as for the type of retaining structure for a deep excavation, flexible retaining systems (e.g., soldier pile walls and sheet pile walls) and stiff diaphragm walls are prevalent and have been extensively investigated. Some observed data has proved that the empirical or semiempirical prediction methods based on flexible retaining systems may overestimate the ground movements and wall deflections corresponding to stiff diaphragm walls [48–51]. Despite the plenty of studies on the performance of deep excavations, the performance of deep excavations braced with ground anchors and end-suspended piles in soil-rock composite stratum has not been well understood.

The end-suspended piles have been successfully applied for supporting deep excavations in the soil-rock composite stratum in many cities in China such as Tsingtao, Guangzhou, Shenzhen, and Wuhan where the bedrock is relatively shallowly buried. Due to the difficulty of constructing cast-in-place pile in hard rock stratum and the limitation of

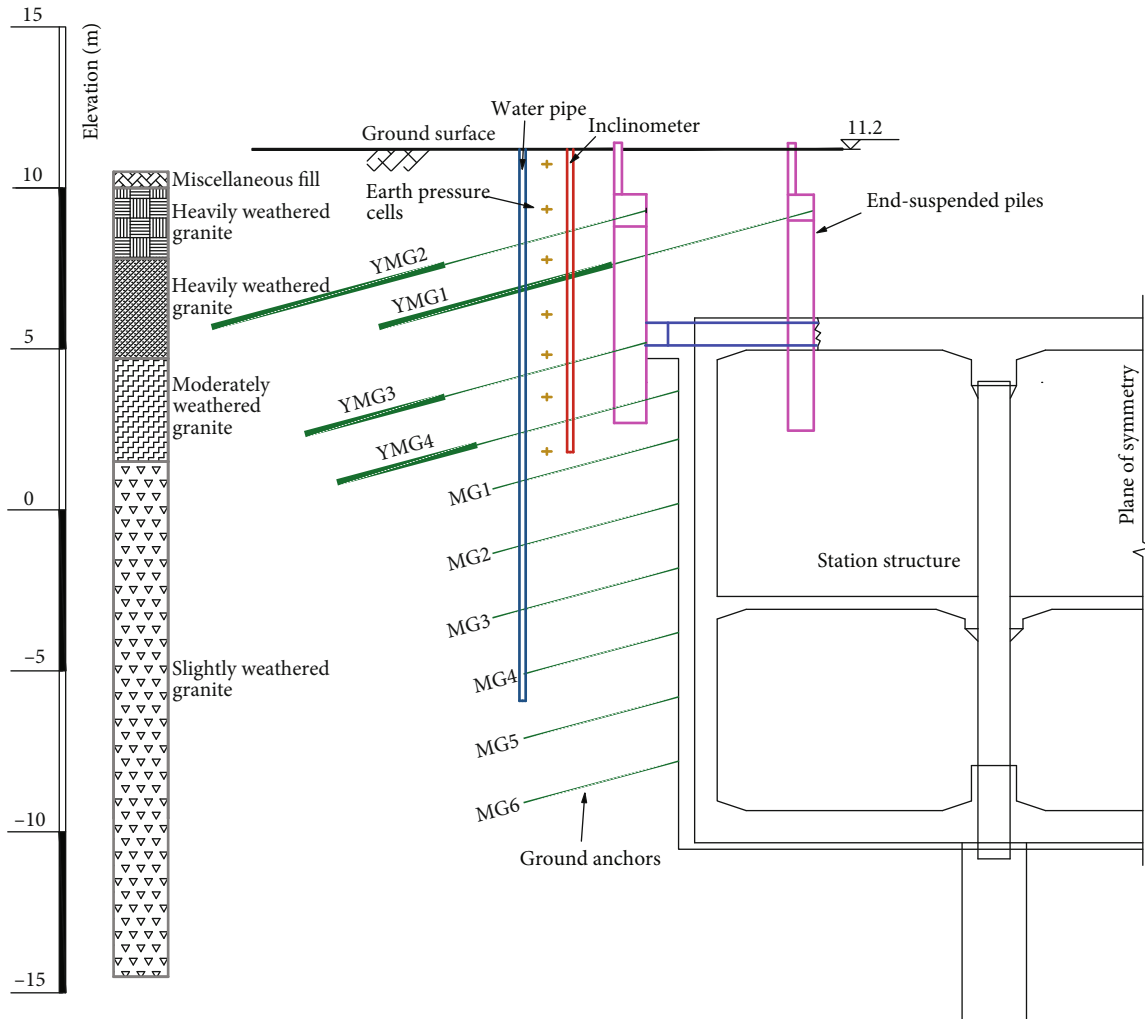


FIGURE 2: Profile of Section B-B.

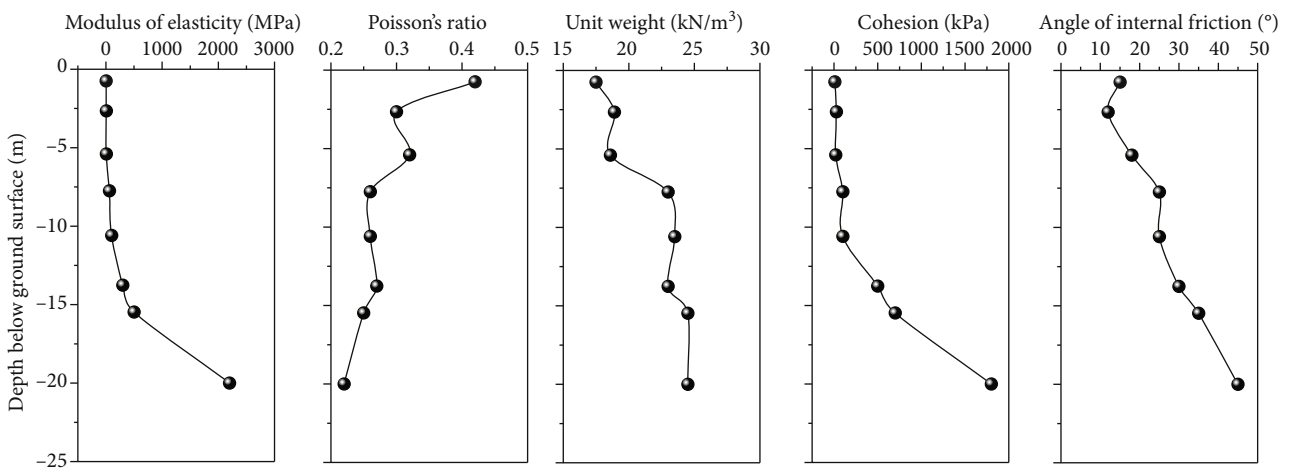


FIGURE 3: Variations of soil parameters with depth below ground surface.

project budget, the bottom of end-suspended pile in this case is above the final excavation bottom. This feature differentiates the deep excavation braced with end-suspended piles

from that braced with conventional piles. In order to further expedite the application of end-suspended piles in deep excavations and optimize their design, a deeper understanding of

TABLE 1: Summary of the main construction activities.

Stage	Construction activities	Duration (days)
1	Excavate to top slab, construct columns and top slab, and backfill and restore traffic	78
2	Construct end-suspended piles, excavate to 2 m BGS	59
3	Install ground anchors YMG1 and YMG2, apply prestress of 200 kN	17
4	Excavate to 5 m BGS	14
5	Construct temporary support	9
6	Excavate to 7 m BGS	12
7	Install ground anchors YMG3, apply prestress of 100 kN	19
8	Excavate to 8 m BGS	22
9	Install ground anchors YMG4, apply prestress of 310 kN	16
10	Excavate to 9.5 m BGS	13
11	Install ground anchors MG1	7
12	Excavate to 12 m BGS	15
13	Install ground anchors MG2	23
14	Excavate to 13.5 m BGS, cast middle slab	17
15	Install ground anchors MG3	26
16	Excavate to 15.5 m BGS	11
17	Install ground anchors MG4	18
18	Excavate to 17.5 m BGS	29
19	Install ground anchors MG5	21
20	Excavate to 20 m BGS	10
21	Cast base slab	19

the performance of deep excavations braced with end-suspended piles and the effects of many important parameters is necessary. In addition, the soil-rock composite stratum is characterized by soft soil in the upper position and hard rock in the lower position. Because of this, blasting excavation may be required and careful design of the excavation bracing system is necessary for reducing the construction cost and ensuring safety and stability.

In this paper, a case history of top-down deep excavation braced with ground anchors and end-suspended piles in the soil-rock composite stratum was reported. The observed performance of the deep excavation in terms of horizontal and vertical pile displacements, ground surface settlements, building settlements, axial forces in ground anchors, earth pressure, and pore water pressure was analysed. Moreover, a parametric study based on two-dimensional (2D) finite element method was conducted to capture the effects of pile diameter, embedded depth, and rock-shoulder width on the deformation and internal force characteristics of end-suspended pile.

2. Case History Description

2.1. Engineering Background. Figure 1 shows a plan view of the considered deep excavation case history. The May Fourth Square (MFS) Station, serving as an interchange station for Lines M2 and M3 of Tsingtao Metro Line 3, is located at the intersection of the HK Road and the Shandong Road. The MFS Station, consisting of 5 passageways and 2 fire-fighting entrances, has a length of 277.8 m and a width of

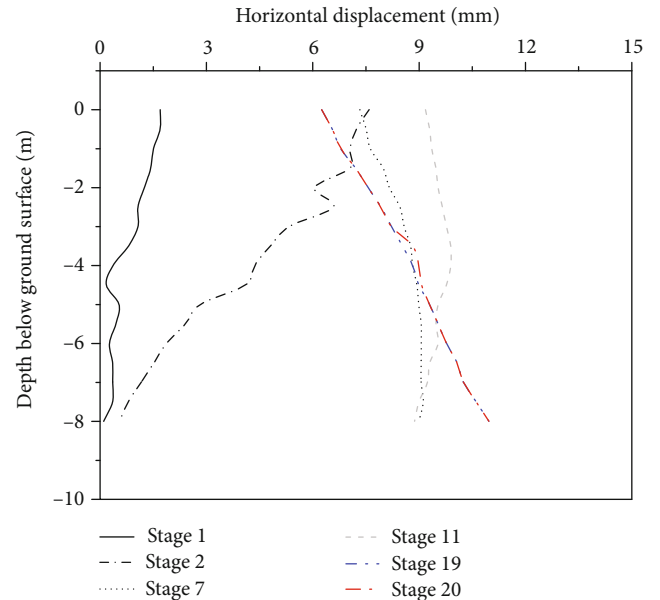


FIGURE 4: Horizontal displacements of end-suspended pile CX13 at various construction stages.

44.8 m. The cover depth of the Station ranges between 3.7 and 6.9 m. The 20 m deep excavation was bounded by the 401 Hospital dormitory to the north, by the Tsingtao Center and its hotel and office buildings to the south, by 2 brick buildings and the Shangri-La Hotel (15–19 stories) to the west, and by the Yihe International Building to the east.

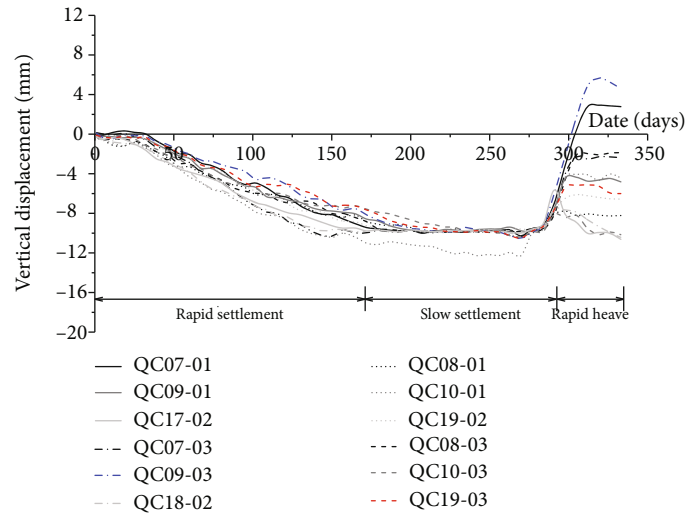


FIGURE 5: Time histories of vertical displacements of the end-suspended piles.

Figure 2 shows a profile of Section B-B as illustrated in Figure 1. The excavation, made using the top-down method, was braced with end-suspended piles and both prestressed ground anchors (i.e., YMG1, YMG2, and YMG3) and general ground anchors (i.e., MG1–MG6). The vertical and horizontal spacings between two ground anchors were, respectively, 1.9 and 1.8 m. The borehole diameter and the inclination angle with respect to the horizontal direction for a ground anchor were, respectively, 0.15 m and 15°. The diameter of the end-suspended piles was 0.8 m on the inner side row and 1.0 m on the outside row. The length of the end-suspended piles ranged between 6.5 and 8.0 m.

The subsurface conditions at the site consist of a miscellaneous fill (MF) layer of 2 m in thickness overlying a sequence of granite layers. The granite layers, in descending order, are heavily weathered granite (HWG) layer, moderately weathered granite (MWG) layer, and slightly weathered granite (SWG) layer. The groundwater mainly consists of pore water and bedrock fissure water which is near to the structural belt. A detailed geotechnical investigation including in situ and laboratory tests was performed to determine the soil parameters for this case history. The variations of several important parameters, which are modulus of elasticity, Poisson's ratio, unit weight, cohesion, and angle of internal friction, with depth below ground surface, are plotted in Figure 3. Evidently, the modulus of elasticity, cohesion, and angle of internal friction for the SWG and MWG layers are significantly greater than that for the HWG and MF layers.

2.2. Field Instrumentation. A plan view of the field instrumentation layout is presented in Figure 1. Figure 2 gives a profile of the instrumentation. The instrumented items included horizontal and vertical pile displacements, ground surface settlements, building settlements, axial forces in ground anchors, earth pressure, and pore water pressure. The horizontal and vertical pile displacements were monitored using inclinometers. Level instruments were used to monitor the ground surface settlements and building settle-

ments with a minimum spacing of 2.0 m. The monitoring points for building settlements were created by drilling on the building corners using percussion drilling and then installing L-shaped iron nails. The axial forces in ground anchors were monitored using steel stress meters welded to the main reinforcement of the ground anchors. The earth pressure was monitored using the earth pressure cells, which were installed on the outside of the end-suspended piles. The elevations of the earth pressure cells corresponded to that of the steel stress meters. Monitoring of pore water pressure was automatically performed throughout the excavation stages using the vibrating-wire piezometer cells located in the water pipe boreholes close to the inclinometers. All instrumentation was installed and calibrated at least two weeks before the beginning of any construction work at the site. Accuracy of the observed data was periodically checked during the excavation.

2.3. Construction Stages. Table 1 summarizes the main construction activities as well as their duration at the site. Work began with the excavation of the soil above the top slab. After this, the columns and the top slab with a thickness of 1 m were constructed. The concrete filled steel tubular columns were of 0.8 m in external diameter, 0.02 m in wall thickness, and 7.8 m in spacing. When the top slab was completed, backfilling of the excavated miscellaneous fill and construction of the pavement were conducted to restore the traffic. Excavation then proceeded as described in Table 1. The inner side row of the end-suspended piles extended to a depth of 8.5 m below ground surface, whereas the outside row penetrated to a depth of 15 m below ground surface. As the construction activities proceeded, 8 levels of ground anchors were installed to brace the end-suspended piles and the excavation. Ground anchors at the first level consisted of YMG1 and YMG2, and they were preloaded with approximately 60% of the design ground anchor load. The second and third levels of ground anchors were preloaded, respectively, with a load of 100 and 310 kN.

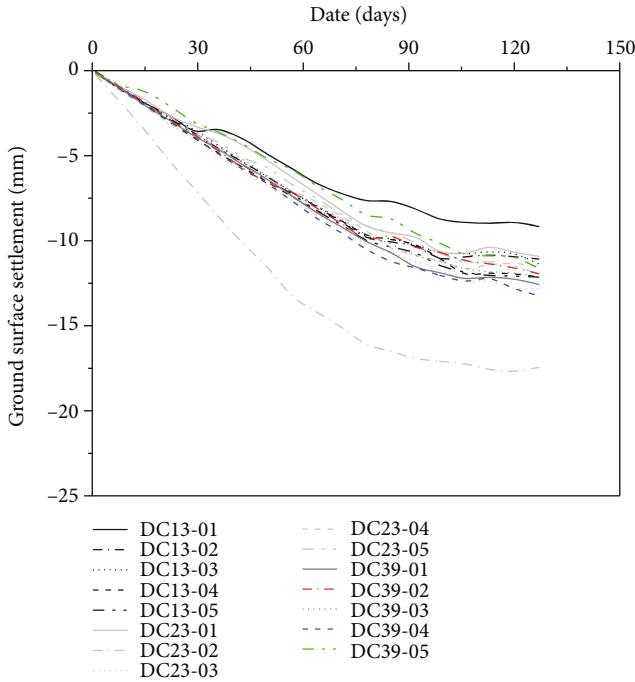


FIGURE 6: Time histories of ground surface settlements along lines of DC13, DC23, and DC39.

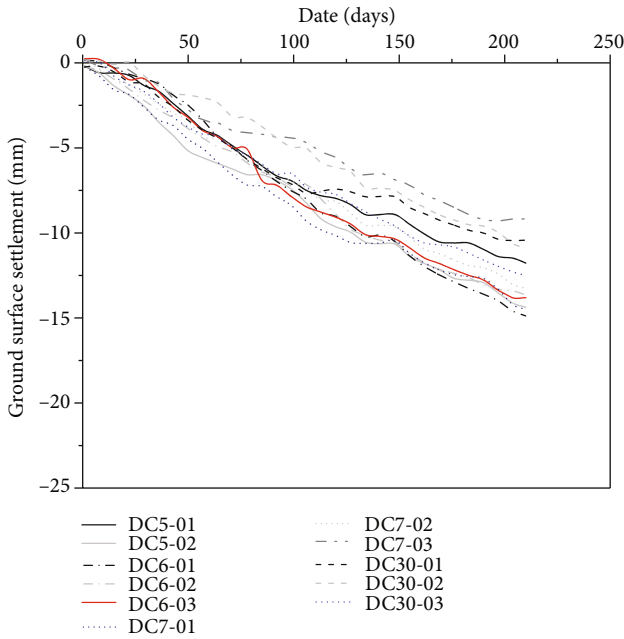


FIGURE 7: Time histories of ground surface settlements along lines of DC05, DC06, DC07, and DC30.

3. Observed Performance during Excavation

3.1. Horizontal and Vertical Pile Displacements. The magnitude of the horizontal displacements of the end-suspended piles affects not only the stability of the pile but also the ground movements surrounding the excavation. Figure 4 presents the subsurface distributions of horizontal pile dis-

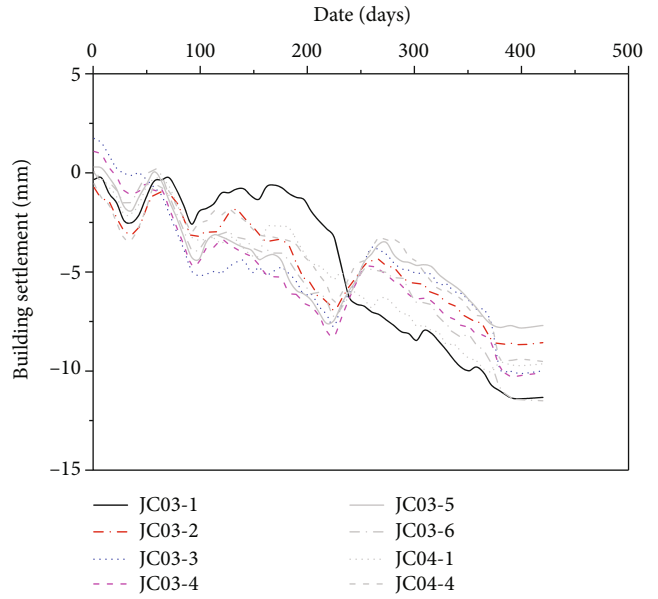


FIGURE 8: Time histories of settlements of the Yihe International Building.

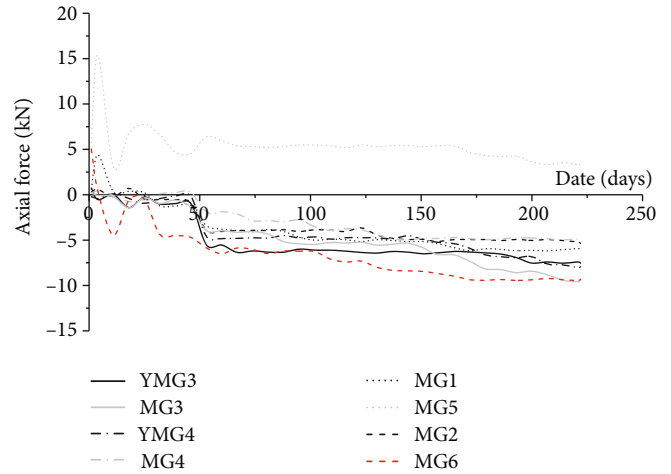


FIGURE 9: Time histories of axial forces in ground anchors.

placements at CX13 for several construction stages as detailed in Table 1. It can be indicated that when the excavation proceeded to 2 m below ground surface, the horizontal pile displacement was trivial with its maximum being less than 3 mm. This could likely be attributed to the fact that the excavation depth was small and the excavation exposure duration was short. As the excavation depth increased, the horizontal pile displacements throughout the entire pile length significantly increased. The maximum horizontal pile displacement occurred initially at the pile top at the first two excavation stages. After the excavation stage proceeding to 7, the maximum horizontal pile displacement occurred at the pile tip. Although the embedded depth of the end-suspended piles into the MWG layer was only 2 m, the restraining effect of the embedded section was sufficient to ensure the stability of the end-suspended pile during excavation.

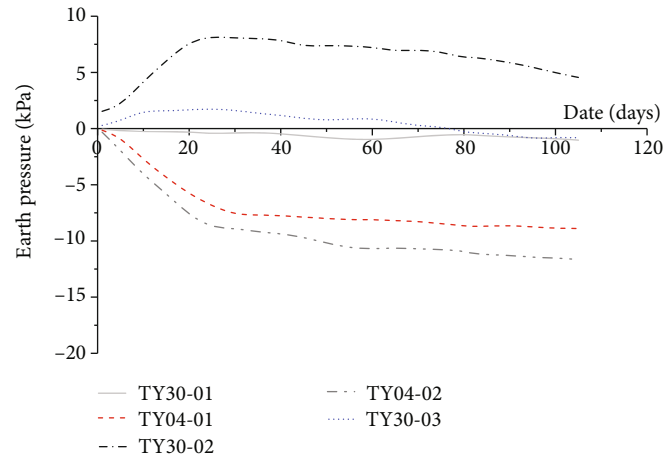


FIGURE 10: Time histories of earth pressure at various monitoring points.

Figure 5 shows the time histories of the vertical displacements atop the end-suspended piles. It can be found that the pattern of the vertical pile displacements could be categorized into three types: rapid settlement, slow settlement, and rapid heave. The rapid settlement pattern occurred before the backfilling of the excavated MF layer above the top slab. Throughout the pattern of slow settlement, the maximum vertical pile displacement of -12.28 m in magnitude was achieved. When the excavation depth proceeded to be greater than 15.5 m, the pattern of rapid heave appeared due to the pronounced stress relaxation effect caused by excavation. The maximum heave of the end-suspended piles was 5.68 mm.

3.2. Ground Surface Settlements. Figure 6 shows the time histories of the ground surface settlements along monitoring lines of DC13, DC23, and DC39. It can be indicated that the rate and the magnitude of the ground surface settlement was much greater at DC23-02 than at other surface settlement monitoring points. Before July 19, 2012, the daily surface settlement was approximately -0.4 mm, and this value decreased to be -0.1 to -0.2 mm as time went on. Up to August 31, 2012, the maximum surface settlement was reached with a magnitude of -17.68 mm. In addition, neither the daily surface settlement nor the accumulated surface settlement exceeded the design value and the alarm value.

Figure 7 shows the time histories of the ground surface settlements along monitoring lines of DC05, DC06, DC07, and DC30. It can be noticed that the ground surface settlements were continuous during the excavation with the daily surface settlement being about -0.2 mm. The rapid settlement phase was replaced by the slow settlement phase after the achievement of the final excavation depth. The maximum surface settlement was -14.88 mm, which was also less than the design and the alarm values. The relatively small ground surface settlement induced by a top-down deep excavation benefited from the bracing effect of the top slab. Therefore, in soil-rock composite stratum, the top-down method is preferable to the bottom-up excavation method.

3.3. Building Settlements. To analyse the excavation induced building settlements, the Yihe International Building, which was, respectively, 24 and 63 m apart from the 4# and the 3# passageways, was selected as the representative. Figure 8 shows the time histories of the Yihe International Building settlements. It is noted that the building settlements occurred at the 8 monitoring points increased in a wave-shaped manner with proceeding the construction date. Several rebounding trends on the time history curves are observable. This phenomenon may be attributed to the preloading of the ground anchors. Among the considered monitoring points, the JC04-1, nearest to the excavation, settled most, with the maximum settlement being -10.71 mm.

3.4. Axial Forces in Ground Anchors. Figure 9 shows the time histories of the axial forces in ground anchors. It can be recognized that the variation of the axial forces in ground anchors was rather complex in the early stage of the excavation. After the backfilling of the soil above the top slab, the axial force in ground anchor MG5 decreased gradually. In the meantime, the axial forces in ground anchors YMG3, MG4, and MG2 remained almost unchanged, while the axial forces in ground anchors YMG4, MG1, MG3, and MG6 increased slightly. For the investigated case history, a combination of ground anchors and end-suspended piles has provided satisfactory bracing effect.

3.5. Earth Pressure. Figure 10 shows the time histories of the earth pressure at monitoring points TY03-01, TY03-02, TY03-03, TY04-01, and TY04-02. It is shown that the earth pressure at TY03-02 and TY03-03 increased before the 25th construction days and then decreased with proceeding the construction days. However, unlike the variational characteristics of earth pressure at TY03-02 and TY03-03, the earth pressure at TY03-01, TY04-01, and TY04-02 consistently decreased with proceeding the construction days. The decreasing trend of the earth pressure could be attributed to the increase in the horizontal displacements of the ground surrounding the excavation.

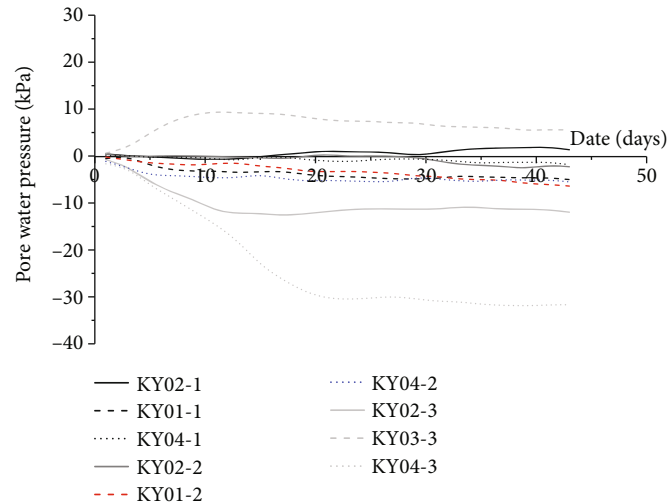


FIGURE 11: Time histories of pore water pressure at various monitoring points.

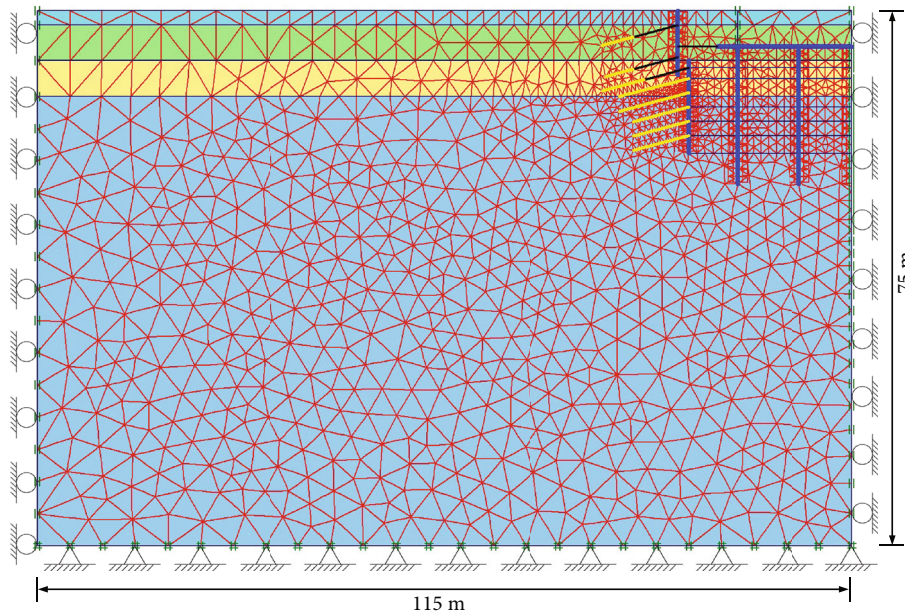


FIGURE 12: Meshing of the finite element analysis model.

3.6. Pore Water Pressure. Figure 11 shows the time histories of pore water pressure at various monitoring points. As is shown, the variational rate of the pore water pressure was slow at the selected monitoring points except the KY04-03. At KY04-03, the pore water pressure initially decreased at a relatively high velocity until the 20th construction day, after which the decreasing velocity was reduced greatly. According to the principle of effective stress, the relationship among total stress σ , effective stress σ' , and pore water pressure μ can be described by $\sigma = \sigma' + \mu$. When the total stress σ is kept constant, a negative correlation exists between effective stress σ' and pore water pressure μ . During the station excavation, the unloading effect will lead to a reduction in the pore water pressure within the ground. Simultaneously, the effective stress increases, which will compress the soil, resulting in a

repeated increase of the pore water pressure at some monitoring points.

4. Finite Element Analysis

4.1. Meshing and Boundary Conditions. The symmetry of the considered deep excavation case history was considered in the finite element analysis. Figure 12 shows the meshing of the finite element analysis model. As the length of the excavation in the longitudinal direction is much larger than that in the transverse direction, a 2D plane strain finite element model was established. According to the previous engineering experience and related numerical analysis results, the primary zone of excavation influence is characterized by a width of 2 to 4 times the final excavation depth and by a depth of 2

TABLE 2: Soil parameters adopted in finite element analysis.

Parameter	Miscellaneous fill	Heavily weathered granite	Moderately weathered granite	Moderately weathered granite
γ_{unsat} (kN/m ³)	17.5	23.5	24.5	25
γ_{sat} (kN/m ³)	20	24.5	25	25.3
E (MPa)	8	45	120	12000
E_{inc} (MPa/m)	0	0	0	500
ν	0.42	0.28	0.25	0.22
c (kPa)	10	40	100	1800
φ (°)	8	25	35	45
ψ (°)	0	0	5	13
R_{int}	0.67	0.8	1	1

Note: γ_{unsat} : natural unit weight; γ_{sat} : saturated unit weight; E : modulus of elasticity; E_{inc} : incremental stiffness; ν : Poisson's ratio; c : cohesion; φ : angle of internal friction; ψ : dilatancy angle; and R_{int} : reduction factor for soil/structure interfacial shear strength.

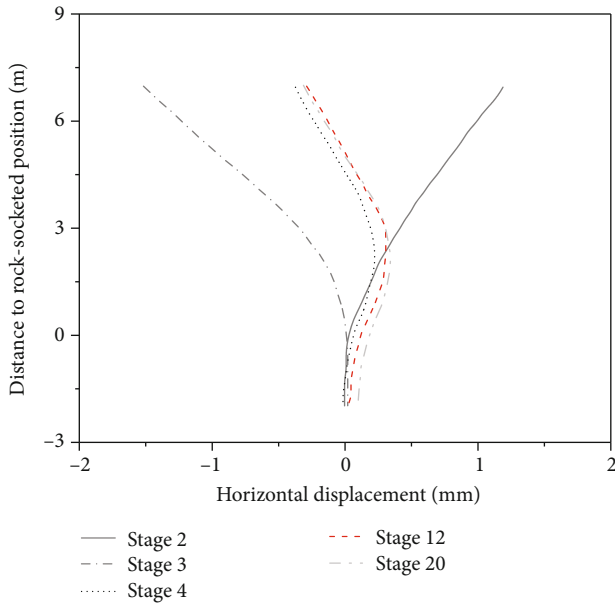


FIGURE 13: Variation of horizontal displacement of end-suspended pile with construction stage.

to 3 times the final excavation depth. Therefore, the dimensions of the established finite element analysis model were of 115 m in horizontal direction and 75 m in vertical direction. Roller supports were applied to the vertical boundaries to restrain the horizontal displacements, while pin supports were applied to the bottom of the mesh to restrict the displacements in all directions.

4.2. Constitutive Models and Parameters. In the numerical analysis, the Mohr-Coulomb model was used to describe the stress-strain behavior of the soils. Table 2 summarizes the soil parameters for the finite element analysis. The parameter, incremental stiffness E_{inc} , is a special option in PLAXIS [52] for the Mohr-Coulomb model. It is activated for inputting the soil stiffness as a function of cover depth, which is beneficial for revising the exaggerated basal heave involved in the application of this soil constitutive model. Considering the fact that the stiffness of the bracing structure

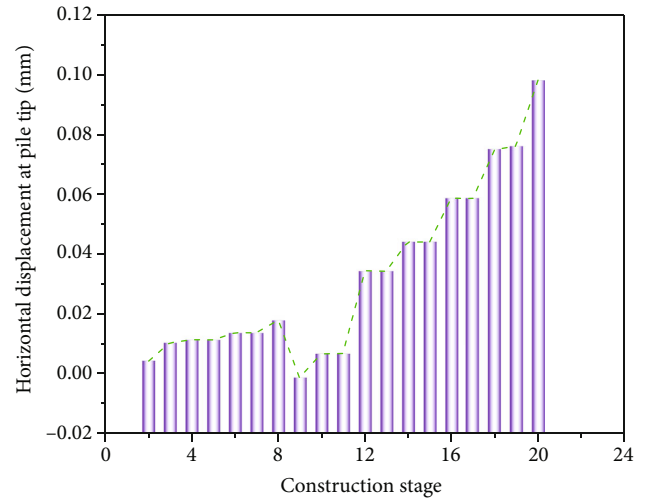


FIGURE 14: Variation of horizontal displacement at the end-suspended pile tip with a construction stage.

and the station structure is much larger than that of the soils, the linear elastic model was adopted to simulate the constitutive behavior of the structures.

The beam element was used to represent the end-suspended piles and steel pipe columns. In the numerical analysis, the real piles and columns of circular cross-section were transformed to beams of a rectangular cross-section. This transformation is based on the principle of equivalent flexural rigidity which has the form of

$$\frac{\pi D^4}{64} = \frac{S d_{\text{eq}}^3}{12}, \quad (1)$$

where D is the diameter of pile or column, S is the spacing between two piles or columns, and d_{eq} is the equivalent thickness of the transformed beams.

A manipulation of Equation (2) yields

$$d_{\text{eq}} = \sqrt[3]{\frac{3\pi D^4}{16S}}. \quad (2)$$

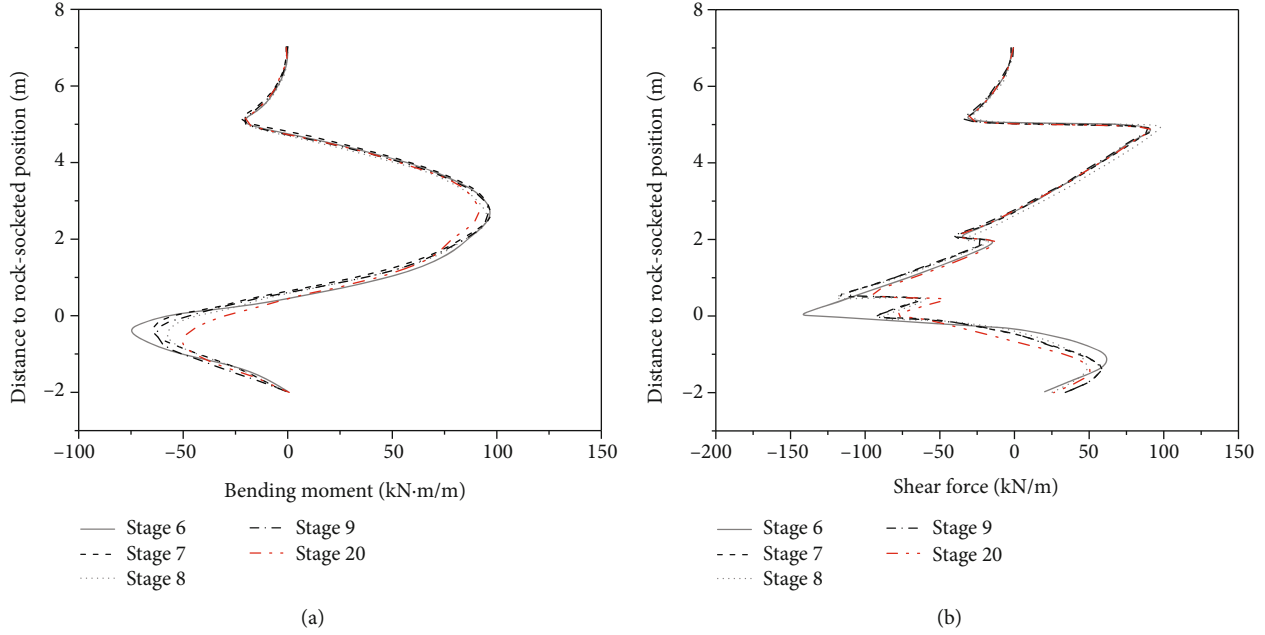


FIGURE 15: Variation of internal forces in the end-suspended pile with the construction stage. (a) Bending moment. (b) Shear force.

By using Equation (2), the equivalent thicknesses for the end-suspended piles, slabs, and steel pipe columns were derived which are, respectively, 0.73, 1, and 0.42 m.

The anchorage sections of the prestressed ground anchors as well as the ground anchors in the granite layers were simulated using the geogrid element. For the geogrid element, the modulus of elasticity E_c was calculated by

$$E_c = \frac{AE_s + A_m E_m}{A + A_m}, \quad (3)$$

where A is the cross-sectional area of the cable or bolt, A_m is the cross-section area of grout, E_s is the modulus of elasticity for the cable or bolt, and E_m is the modulus of elasticity for the grout.

4.3. Deformation and Internal Force Characteristics of End-Suspended Piles. Figure 13 presents the variation of the horizontal displacement of the end-suspended pile with a construction stage. It can be indicated that at the excavation depth of 2 m, the deformation of the pile was characterized by cantilever type. In other words, the horizontal pile displacement peaked at the pile top, while it was almost zero below the rock-socketed position. An observable increase in the horizontal pile displacement below the rock-socketed position occurred when the excavation depth reached 5 m. At the excavation depth of 20 m, the maximum horizontal pile displacement of 0.33 mm appeared at 2.25 m above the rock-socketed position. As a whole, because of the effect of the prestressed ground anchor attached to the pile top, the maximum horizontal displacement of the end-suspended pile, which occurred at the pile top, was achieved at the construction stage 2.

The variation of the horizontal displacement at end-suspended pile tip with construction stage is shown in

Figure 14. It can be noted that the horizontal pile tip displacement increased with an increase in the excavation depth. During the installation of the ground anchor YMG4, a significant change of the horizontal pile tip displacement occurred, indicating that the feet-lock prestressed ground anchor played an important role in controlling the horizontal pile tip displacement. A dramatic increase in the horizontal pile tip displacement was also observed when the rock within the range of pile embedment depth was excavated. This demonstrated that the restraining effect of the rock beneath the pile tip on the pile tip was noteworthy, although the embedment depth of the pile into the MWG layer was only 2 m. Moreover, it can also be indicated from Figure 14 that a significant reduction in the horizontal displacement at the pile tip occurred between construction stages 8 and 12. This may be attributed to the application of a relatively large prestress of 310 kN to the ground anchors of YMG4.

Figure 15 shows the variations of the bending moment and shear force in the end-suspended pile with the construction stage. It is shown that the effect of proceeding the construction stage on the internal forces within the upper 3 m of the pile was negligible. This was because the first level of the ground anchor attached to the pile top had restrained the horizontal pile displacement. As the maximum bending moment in the pile occurred between the first-level ground anchor and the temporary support, the prestress in the lower levels of ground anchors had a negligible effect on the maximum bending moment. Moreover, with a further increase in the excavation depth, the position at which the maximum negative bending moment occurred moved down gradually. When reaching the final excavation depth, the maximum negative bending moment appeared at 0.75 m below the rock-socketed position. Additionally, the shear force in the rock-socketed position decreased with increasing the excavation depth.

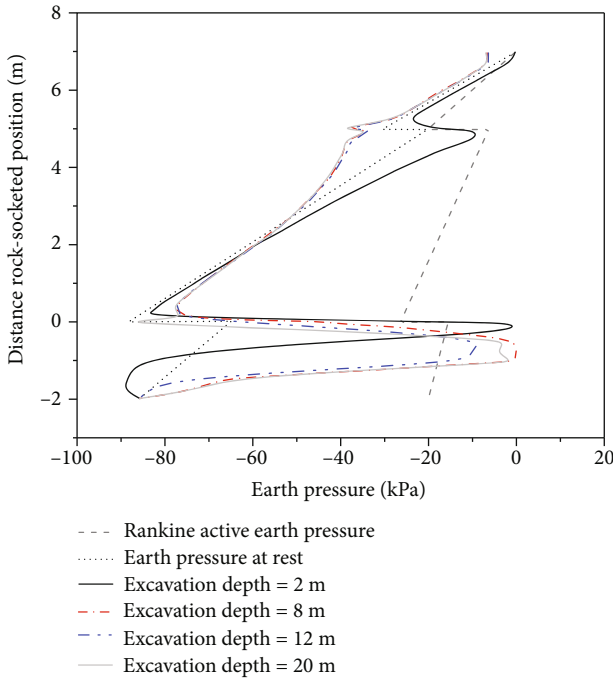


FIGURE 16: Earth pressure applied on the active side of the end-suspended pile at different excavation stages.

Figure 16 shows the variations of the earth pressure applied on the active side of the end-suspended pile with the distance to the rock-socketed position. It can be indicated that at the excavation depth of 2 m, the soil behind the pile above the excavation face did not reach the active limit state due to the small magnitude of the horizontal pile displacement. Below the excavation face, with an increase in the cover depth, the horizontal pile displacement decreased gradually; and therefore, the active earth pressure applied on the pile gradually approached the earth pressure at rest. At the rock-socketed position (i.e., interface between soil and rock), the earth pressure equaled to nearly zero. This could be attributed to the fractures generated in the rock due to the detaching of the pile from the rock. Overall, both the distribution pattern and the magnitude of the earth pressure applied on the pile by the finite element analysis method agreed well with the results of the Rankine earth pressure theory. The discrepancy between them was distinct only at the interface of the soil and rock.

Figure 17 shows the variations of the earth pressure applied on the passive side of the end-suspended pile with the distance to rock-socketed position. The figure indicates that both the distribution pattern and the magnitude of the earth pressure obtained by the finite element method differed greatly from that predicted by the Rankine passive earth pressure theory. Therefore, it can be inferred that the limit equilibrium method may be not applicable for the design of the end-suspended pile. Therefore, it is recommended that the soil springs be adopted to simulate the passive earth pressure applied on the end-suspended pile. Moreover, it can be also indicated that the earth pressure distribution curves were

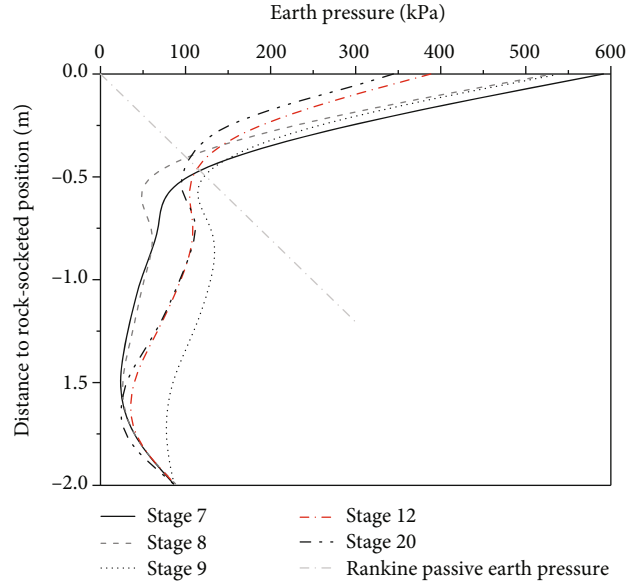


FIGURE 17: Earth pressure applied on the passive side of the end-suspended pile at different excavation stages.

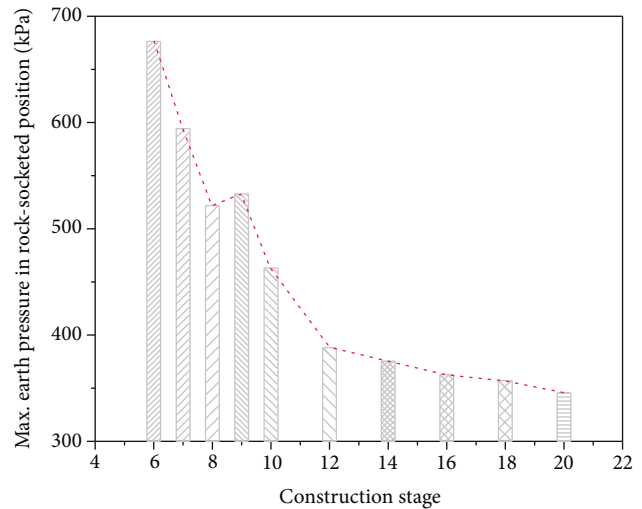


FIGURE 18: Variation of maximum earth pressure in the rock-socketed position with the construction stage.

similar before and after the excavation of the bedrock, and they peaked at the bedrock surface.

The variation of the maximum earth pressure in the rock-socketed position with excavation depth is presented in Figure 18. From the variational curve, it can be indicated that the maximum earth pressure decreased almost linearly with an increase in the excavation depth until reaching construction stage 8. After completing the excavation of the slightly weathered granite, the rate of the decreasing trend for the maximum earth pressure became lower. This was partially attributed to the installation of the ground anchor YMG4. However, the installation of the ground anchor YMG4 did not compensate fully for the loss of the passive earth pressure induced by the excavation of the rock shoulder.

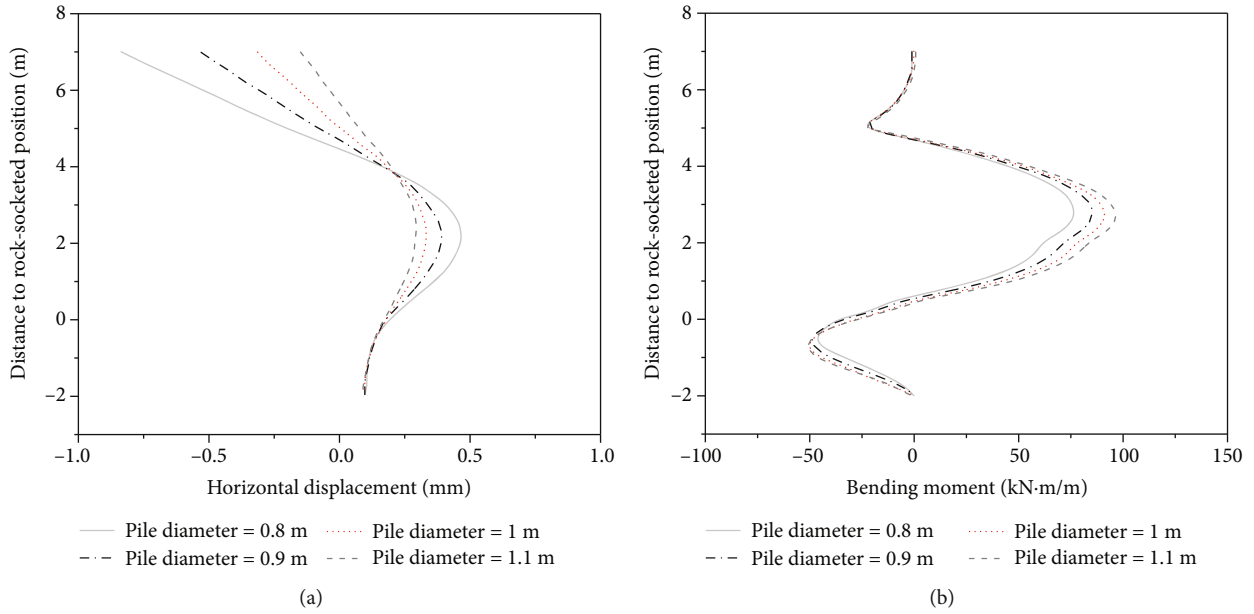


FIGURE 19: Effects of pile diameter on the horizontal displacement and bending moment of end-suspended pile. (a) Horizontal displacement. (b) Bending moment.

5. Discussion

5.1. Effects of Pile Diameter. Figure 19 shows the effects of pile diameter on the horizontal displacement and bending moment of the end-suspended pile. It can be indicated that for most parts of the pile shaft, the horizontal displacements decrease with an increase in pile diameter from 0.8 to 1.1 m. However, the effects of the pile diameter on horizontal displacements are trivial at a distance to rock-socketed position of approximately 4 m or being less than 0 m. From Figure 19(b), it is noted that the primary area of the effects of the pile diameter on the bending moment ranges between 1 and 4 m of the distance to the rock-socketed position. Moreover, within the primary area, the bending moment increases with increasing pile diameter; and the rate of increase in the bending moment decreases with increasing pile diameter.

The variational percentages of the maximum positive horizontal displacement and maximum bending moment of end-suspended pile at the considered magnitudes of pile diameter are presented in Figure 20. Note that the variational percentages are calculated based on the results at the pile diameter of 0.8 m. It is shown that the decreasing trend of the maximum positive horizontal displacement with increasing pile diameter gradually becomes mitigatory. A reduction of approximately 30% in the maximum positive horizontal displacement appears when the pile diameter increases from 0.8 to 1 m. This demonstrates the benefit of controlling excavation deformation by increasing the pile diameter. However, it is inevitable that work amount will be greatly increased with increasing pile diameter. In addition, Figure 20 also shows that with an increase in the pile diameter, the maximum bending moment increases accordingly. An increase of approximately 20% in the maximum bending moment occurs when the pile diameter increases from 0.8 to 1 m.

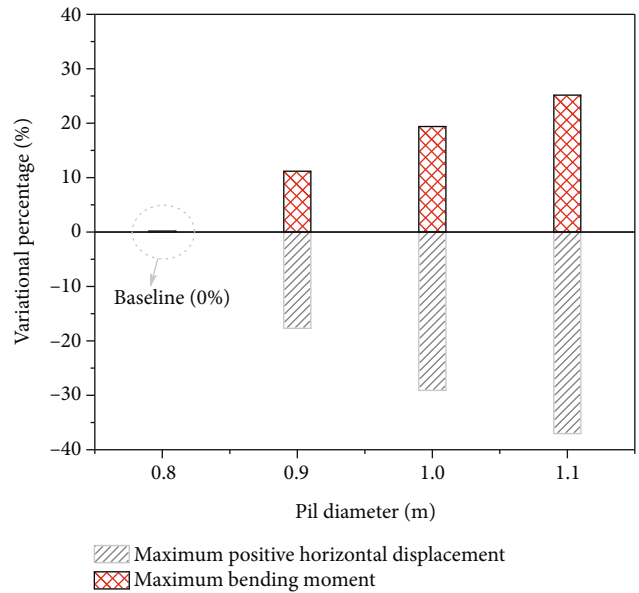


FIGURE 20: Variations of the maximum positive horizontal displacement and maximum bending moment of the end-suspended pile at different pile diameters.

5.2. Effects of Embedded Depth. Figure 21 presents the effects of embedded depth on the horizontal displacement and bending moment of the end-suspended pile. The variational percentages of the maximum positive horizontal displacement and the maximum bending moment at various magnitudes of embedded depth are shown in Figure 22. It is indicated that for the considered magnitudes of embedded depth, all the maximum horizontal displacements uniformly occur at a distance to rock-socketed position of 2.25 m, which is located between the first row of ground anchors and the

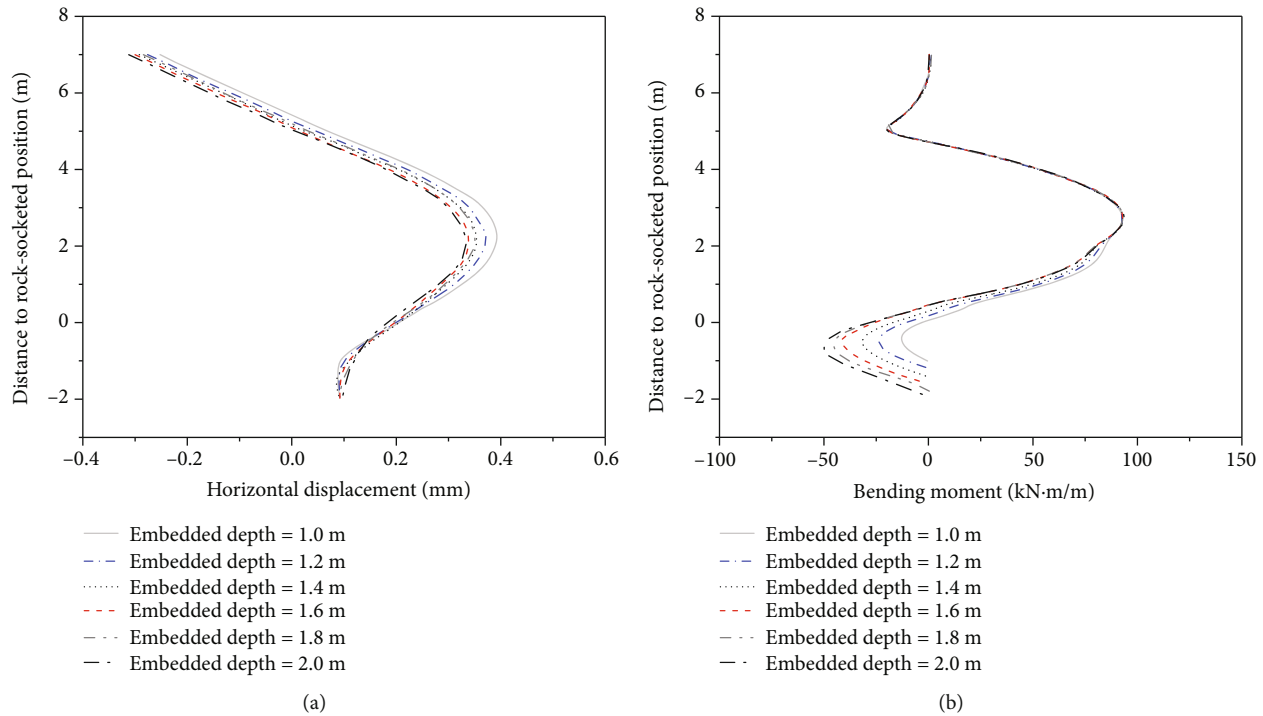


FIGURE 21: Effects of embedded depth on the horizontal displacement and bending moment of the end-suspended pile. (a) Horizontal displacement. (b) Bending moment.

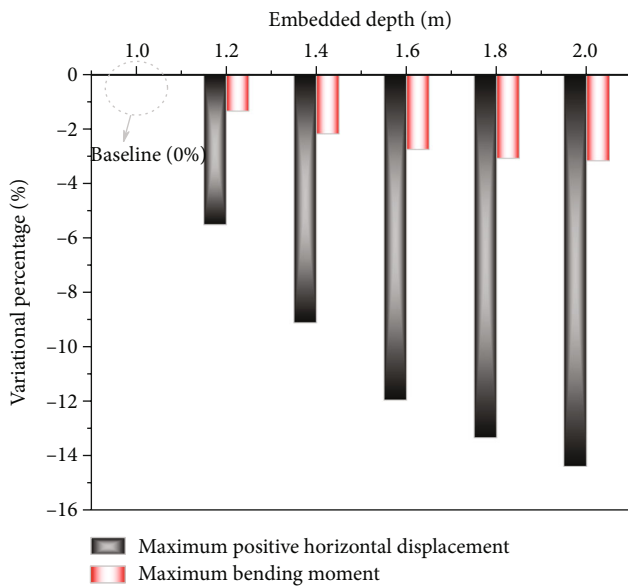


FIGURE 22: Variations of the maximum positive horizontal displacement and maximum bending moment of the end-suspended pile at different embedded depths.

temporary support. With an increase in the embedded depth, the horizontal displacement for the upper part of the end-suspended pile decreases at a relatively low rate. From Figure 22, it can be indicated that when the embedded depth increases from 1 to 2 m, the maximum positive horizontal displacement of the end-suspended pile decreases by 14%.

The position at which the maximum bending moment occurs is also located between the first row of ground anchors and the temporary support. An increase in the embedded depth affects only the bending moment for the part of pile shaft below the temporary support. Therefore, the effects of embedded depth on the maximum bending moment are very inappreciable. This phenomenon can be also observed in Figure 22 which shows a reduction in the maximum bending moment of merely 3.2% when the embedded depth increases from 1 to 2 m.

5.3. Effects of Rock-Shoulder Width. Figure 23 shows the effects of rock-shoulder width on the horizontal displacement and bending moment of the end-suspended pile. It can be indicated that the occurrence position of the maximum horizontal displacement gradually moves upward with an increase in the rock-shoulder width. After reaching the rock-shoulder width of 1.1 m, the occurrence position of the maximum horizontal displacement remains unchanged. This demonstrates that the rock-shoulder with a width of 1.1 m can provide sufficient earth resistance for restraining the tip of the end-suspended pile. An increase in the rock-shoulder width has a relatively big effect on the horizontal displacement of the pile shaft below the temporary support. However, the horizontal displacement of the pile shaft above the temporary support remains nearly unchanged as the rock-shoulder width increases. Figure 24 shows the variational percentages of the maximum positive horizontal displacement and the maximum bending moment of the end-suspended pile at various magnitudes of rock-shoulder

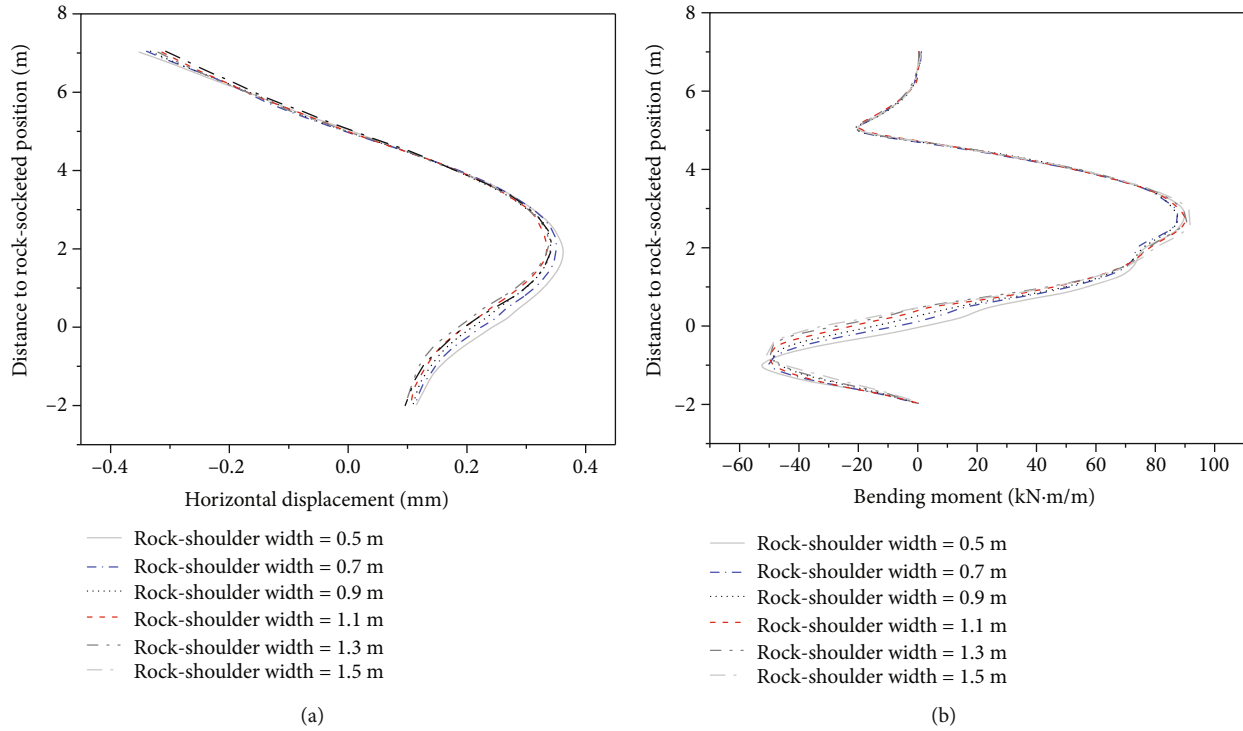


FIGURE 23: Effects of rock-shoulder width on the horizontal displacement and bending moment of the end-suspended pile. (a) Horizontal displacement. (b) Bending moment.

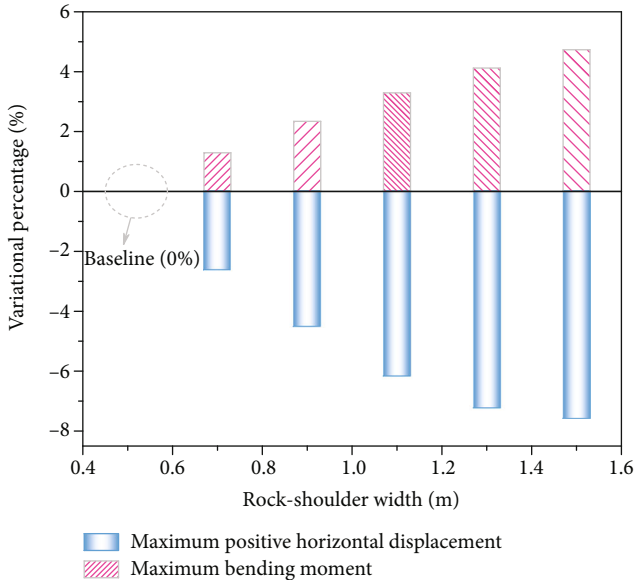


FIGURE 24: Variations of the maximum positive horizontal displacement and maximum bending moment of the end-suspended pile at different rock-shoulder widths.

width. It can be noted that a reduction of merely 6% in the maximum positive horizontal displacement occurs when the rock-shoulder width increases from 0.5 to 1.1 m. Moreover, when the rock-shoulder width increases from 0.5 to 1.5 m, an increase of approximately 4.7% in the maximum bending moment can be achieved.

6. Conclusions

The performance of top-down deep excavation braced with ground anchors and end-suspended piles in a soil-rock composite stratum was investigated by analysing the observed data for a typical case history in Tsingtao, China, and performing a series of finite element simulations. A parametric analysis based on finite element simulations was also made to capture the effects of pile diameter, embedded depth, and rock-shoulder width on the horizontal displacement and bending moment of the end-suspended pile. The conclusions drawn from this study can be summarized as follows.

- (i) The deformation of end-suspended pile during excavation is of cantilever type. Due to the limited socketed force provided by the reserved rock-shoulder with a relatively small width, the horizontal pile displacement is considerable at the rock-socketed position. The position at which the maximum bending moment in pile occurs gradually moves downward as proceeding the construction stages. With an increase in the excavation depth, the horizontal displacements for the socketed section of the end-suspended pile increase accordingly
- (ii) Magnitudes of pile top settlements, ground surface settlements, and building settlements induced by top-down deep excavation braced with ground anchors and end-suspended piles are generally less than 20 mm, indicating that the top-down excavation method has a beneficial effect on restraining

the excavation-induced settlements in a soil-rock composite stratum

- (iii) Within the primary influence zone of pile diameter ranging between 1 and 4 m of the distance to the rock-socketed position, the bending moment increases while the rate of increase in the bending moment decreases with increasing pile diameter. An increase in the embedded depth affects only the bending moment for the part of pile shaft below the temporary support. The horizontal displacement of the pile shaft above the temporary support remains nearly unchanged as the rock-shoulder width increases
- (iv) A combination of the top-down method with a bracing system consisting of ground anchors and end-suspended piles is recommended for deep excavations in a soil-rock composite stratum, as it can effectively restrain the deformation of the excavation. Moreover, by implementing this combination, the construction costs can be significantly lowered due to the reduced rock-socketed depth of the piles as well as to the reduced difficulty of construction, when compared to the conventional excavation bracing system

Data Availability

The data used to support the findings of this study are available from the corresponding author upon request.

Conflicts of Interest

The authors declare that there are no conflicts of interest regarding the publication of this paper.

Acknowledgments

This study was supported by the Fundamental Research Funds for the Central Universities (201962011), the Laboratory for Marine Geology, Qingdao National Laboratory for Marine Science and Technology (MGQNLN-KF201804), and the National Natural Science Foundation of China (no. 41672272).

References

- [1] C. Yuan, Z. Hu, Z. Zhu et al., "Numerical simulation of seepage and deformation in excavation of a deep foundation pit under water-rich fractured intrusive rock," *Geofluids*, vol. 2021, Article ID 6628882, 10 pages, 2021.
- [2] E. Pujades, E. Vázquez-Suñé, J. Carrera, and A. Jurado, "Dewatering of a deep excavation undertaken in a layered soil," *Engineering Geology*, vol. 178, pp. 15–27, 2014.
- [3] Q. Zhang, B. Huang, M. He, and S. Guo, "A numerical investigation on the hydraulic fracturing effect of water inrush during tunnel excavation," *Geofluids*, vol. 2020, Article ID 6196327, 15 pages, 2020.
- [4] P. Guo, F. Liu, G. Lei et al., "Predicting response of constructed tunnel to adjacent excavation with dewatering," *Geofluids*, vol. 2021, Article ID 5548817, 17 pages, 2021.
- [5] R. Zhang, J. Zheng, H. Pu, and L. Zhang, "Analysis of excavation-induced responses of loaded pile foundations considering unloading effect," *Tunnelling and Underground Space Technology*, vol. 26, no. 2, pp. 320–335, 2011.
- [6] C. W. W. Ng, M. Shakeel, J. Wei, and S. Lin, "Performance of existing piled raft and pile group due to adjacent multipropped excavation: 3D centrifuge and numerical modeling," *Journal of Geotechnical and Geoenvironmental Engineering*, vol. 147, no. 4, 2021.
- [7] R.-f. Feng, Q.-q. Zhang, and S.-w. Liu, "Experimental study of the effect of excavation on existing loaded piles," *Journal of Geotechnical and Geoenvironmental Engineering*, vol. 146, no. 9, 2020.
- [8] Y. Tan, R. Huang, Z. Kang, and W. Bin, "Covered semi-top-down excavation of subway station surrounded by closely spaced buildings in downtown Shanghai: building response," *Journal of Performance of Constructed Facilities*, vol. 30, no. 6, 2016.
- [9] P. Guo, X. Gong, and Y. Wang, "Displacement and force analyses of braced structure of deep excavation considering unsymmetrical surcharge effect," *Computers and Geotechnics*, vol. 113, 2019.
- [10] K. Cheng, R. Xu, H. Ying, X. Gan, L. Zhang, and S. Liu, "Observed performance of a 30.2 m deep-large basement excavation in Hangzhou soft clay," *Tunnelling and Underground Space Technology*, vol. 111, 2021.
- [11] Y. M. Hou, J. H. Wang, and L. L. Zhang, "Finite-element modeling of a complex deep excavation in Shanghai," *Acta Geotechnica*, vol. 4, no. 1, pp. 7–16, 2009.
- [12] C. W. W. Ng, Y. Hong, G. B. Liu, and T. Liu, "Ground deformations and soil-structure interaction of a multi-propped excavation in Shanghai soft clays," *Géotechnique*, vol. 62, no. 10, pp. 907–921, 2012.
- [13] Y. M. A. Hashash and A. J. Whittle, "Ground movement prediction for deep excavations in soft clay," *Journal of Geotechnical Engineering*, vol. 122, no. 6, pp. 474–486, 1996.
- [14] D. Wu, K. Xu, P. Guo, G. Lei, K. Cheng, and X. Gong, "Ground deformation characteristics induced by mechanized shield twin tunnelling along curved alignments," *Advances in Civil Engineering*, vol. 2021, Article ID 6640072, 17 pages, 2021.
- [15] M. Son and E. J. Cording, "Numerical model tests of building response to excavation-induced ground movements," *Canadian Geotechnical Journal*, vol. 45, no. 11, pp. 1611–1621, 2008.
- [16] G. B. Liu, P. Huang, J. W. Shi, and C. W. W. Ng, "Performance of a deep excavation and its effect on adjacent tunnels in Shanghai soft clay," *Journal of Performance of Constructed Facilities*, vol. 30, no. 6, 2016.
- [17] M. J. Schuster, C. H. Juang, M. J. S. Roth, and D. V. Rosowsky, "Reliability analysis of building serviceability problems caused by excavation," *Géotechnique*, vol. 58, no. 9, pp. 743–749, 2008.
- [18] S. Burlon, H. Mroueh, and I. Shahrour, "Influence of diaphragm wall installation on the numerical analysis of deep excavation," *International Journal for Numerical and Analytical Methods in Geomechanics*, vol. 37, no. 11, pp. 1670–1684, 2013.
- [19] S. Likitlersuang, C. Surarak, D. Wanatowski, E. Oh, and A. Balasubramaniam, "Finite element analysis of a deep

- excavation: a case study from the Bangkok MRT,” *Soils and Foundations*, vol. 53, no. 5, pp. 756–773, 2013.
- [20] Y. Tang, S. Xiao, and Y. Zhan, “Predicting settlement along railway due to excavation using empirical method and neural networks,” *Soils and Foundations*, vol. 59, no. 4, pp. 1037–1051, 2019.
- [21] W. Zhang, A. T. C. Goh, and F. Xuan, “A simple prediction model for wall deflection caused by braced excavation in clays,” *Computers and Geotechnics*, vol. 63, pp. 67–72, 2015.
- [22] M. Korff, R. J. Mair, and F. A. F. Van Tol, “Pile-soil interaction and settlement effects induced by deep excavations,” *Journal of Geotechnical and Geoenvironmental Engineering*, vol. 142, no. 8, 2016.
- [23] G. T. C. Kung, C. H. Juang, E. C. L. Hsiao, and Y. M. A. Hashash, “Simplified model for wall deflection and ground-surface settlement caused by braced excavation in clays,” *Journal of Geotechnical and Geoenvironmental Engineering*, vol. 133, no. 6, pp. 731–747, 2007.
- [24] L. Masini, D. Gaudio, S. Rampello, and E. Romani, “Observed performance of a deep excavation in the historical center of Rome,” *Journal of Geotechnical and Geoenvironmental Engineering*, vol. 147, no. 2, 2021.
- [25] F.-Y. Zeng, Z.-J. Zhang, J.-H. Wang, and M.-G. Li, “Observed performance of two adjacent and concurrently excavated deep foundation pits in soft clay,” *Journal of Performance of Constructed Facilities*, vol. 32, no. 4, 2018.
- [26] Q. Fu and L. Li, “Vertical load transfer behavior of composite foundation and its responses to adjacent excavation: centrifuge model test,” *Geotechnical Testing Journal*, vol. 44, no. 1, 2021.
- [27] X. S. Cheng, G. Zheng, Y. Diao et al., “Experimental study of the progressive collapse mechanism of excavations retained by cantilever piles,” *Canadian Geotechnical Journal*, vol. 54, no. 4, pp. 574–587, 2017.
- [28] S.-S. Lin, S.-L. Shen, A. Zhou, and Y.-S. Xu, “Risk assessment and management of excavation system based on fuzzy set theory and machine learning methods,” *Automation in Construction*, vol. 122, 2021.
- [29] Y. Pu, D. B. Apel, and R. Hall, “Using machine learning approach for microseismic events recognition in underground excavations: comparison of ten frequently-used models,” *Engineering Geology*, vol. 268, 2020.
- [30] M. N. Houhou, F. Emeriault, and A. Belouнар, “Three-dimensional numerical back-analysis of a monitored deep excavation retained by strutted diaphragm walls,” *Tunnelling and Underground Space Technology*, vol. 83, pp. 153–164, 2019.
- [31] P.-G. Hsieh, C.-Y. Ou, and Y.-L. Lin, “Three-dimensional numerical analysis of deep excavations with cross walls,” *Acta Geotechnica*, vol. 8, no. 1, pp. 33–48, 2013.
- [32] G. Zheng, X. Yang, H. Zhou, Y. Du, J. Sun, and X. Yu, “A simplified prediction method for evaluating tunnel displacement induced by laterally adjacent excavations,” *Computers and Geotechnics*, vol. 95, pp. 119–128, 2018.
- [33] Y. Wang, X. Shang, and K. Peng, “Relocating mining microseismic earthquakes in a 3-D velocity model using a windowed cross-correlation technique,” *IEEE Access*, vol. 8, pp. 37866–37878, 2020.
- [34] Y. Tan, B. Wei, Y. Diao, and X. Zhou, “Spatial corner effects of long and narrow multipropped deep excavations in Shanghai soft clay,” *Journal of Performance of Constructed Facilities*, vol. 28, no. 4, 2014.
- [35] F.-H. Lee, K.-Y. Yong, K. C. N. Quan, and K.-T. Chee, “Effect of corners in strutted excavations: field monitoring and case histories,” *Journal of Geotechnical and Geoenvironmental Engineering*, vol. 124, no. 4, pp. 339–349, 1998.
- [36] C.-Y. Ou and B.-Y. Shiau, “Analysis of the corner effect on excavation behaviors,” *Canadian Geotechnical Journal*, vol. 35, no. 3, pp. 532–540, 1998.
- [37] J. H. Wang, Z. H. Xu, and W. D. Wang, “Wall and ground movements due to deep excavations in Shanghai soft soils,” *Journal of Geotechnical and Geoenvironmental Engineering*, vol. 136, no. 7, pp. 985–994, 2010.
- [38] G. Russo, M. V. Nicotera, and S. Autuori, “Three-dimensional performance of a deep excavation in sand,” *Journal of Geotechnical and Geoenvironmental Engineering*, vol. 145, no. 4, 2019.
- [39] Q.-L. Cui, H.-N. Wu, S.-L. Shen, and Y.-S. Xu, “Geological difficulties and countermeasures for socket diaphragm walls in weathered granite in Shenzhen, China,” *Bulletin of Engineering Geology and the Environment*, vol. 75, no. 1, pp. 263–273, 2016.
- [40] K. Elbaz, S.-L. Shen, Y. Tan, and W.-C. Cheng, “Investigation into performance of deep excavation in sand covered karst: a case report,” *Soils and Foundations*, vol. 58, no. 4, pp. 1042–1058, 2018.
- [41] Y. Mei, Y.-L. Li, X.-Y. Wang, J. Wang, and C.-M. Hu, “Statistical analysis of deformation laws of deep foundation pits in collapsible loess,” *Arabian Journal for Science and Engineering*, vol. 44, no. 10, pp. 8347–8360, 2019.
- [42] H. Chen, J. Li, and L. Li, “Performance of a zoned excavation by bottom-up technique in Shanghai soft soils,” *Journal of Geotechnical and Geoenvironmental Engineering*, vol. 144, no. 11, 2018.
- [43] M. Khoiri and C.-Y. Ou, “Evaluation of deformation parameter for deep excavation in sand through case histories,” *Computers and Geotechnics*, vol. 47, pp. 57–67, 2013.
- [44] M.-G. Li, J.-J. Chen, A.-J. Xu, X.-H. Xia, and J.-H. Wang, “Case study of innovative top-down construction method with channel-type excavation,” *Journal of Construction Engineering and Management*, vol. 140, no. 5, 2014.
- [45] Y. Ikuta, M. Maruoka, M. Aoki, and E. Sato, “Application of the observational method to a deep basement excavated using the top-down method,” *Géotechnique*, vol. 44, no. 4, pp. 655–679, 1994.
- [46] P. Jamsawang, P. Voottipruex, P. Tanseng, P. Jongpradist, and D. T. Bergado, “Effectiveness of deep cement mixing walls with top-down construction for deep excavations in soft clay: case study and 3D simulation,” *Acta Geotechnica*, vol. 14, no. 1, pp. 225–246, 2019.
- [47] Y. Tan, H. Zhu, F. Peng, K. Karlsrud, and B. Wei, “Characterization of semi-top-down excavation for subway station in Shanghai soft ground,” *Tunnelling and Underground Space Technology*, vol. 68, pp. 244–261, 2017.
- [48] M. Long, “Database for retaining wall and ground movements due to deep excavations,” *Journal of Geotechnical and Geoenvironmental Engineering*, vol. 127, no. 3, pp. 203–224, 2001.
- [49] C. Moormann, “Analysis of wall and ground movements due to deep excavations in soft soil based on a new worldwide database,” *Soils and Foundations*, vol. 44, no. 1, pp. 87–98, 2004.
- [50] M. W. Seo, S. M. Olson, K. S. Yang, and M. M. Kim, “Sequential analysis of ground movements at three deep excavation sites with mixed ground profiles,” *Journal of Geotechnical*

and Geoenvironmental Engineering, vol. 136, no. 5, pp. 656–668, 2010.

- [51] G. Lei and X. Gong, “Analysis of lateral displacement law of deep foundation pit support in soft soil based on improved MSD method,” *Advances in Civil Engineering*, vol. 2021, Article ID 5550214, 15 pages, 2021.
- [52] C. Chheng and S. Likitlersuang, “Underground excavation behaviour in Bangkok using three-dimensional finite element method,” *Computers and Geotechnics*, vol. 95, pp. 68–81, 2018.